ESMRMB
European Society for Magnetic Resonance in Medicine and Biology

ESMRMB 2012 Congress

October 4–6, Lisbon/PT

Book of Abstracts

EPOS™ Poster / Paper Poster / Clinical Review Poster / Software Exhibits

DOI: 10.1007/s10334-012-0324-9

EPOS™ Poster

Abdomen

441

WITHDRAWN

442

Estimation of liver function using liver parenchymal enhancement and volume on Gd-EOB-DTPA-enhanced MRI

T. Yoneyama, Y. Fukukura, K. Kamimura, K. Takumi, A. Tateyama, A. Umanodan, M. Nakajo
Radiology, Kagoshima University Graduate School of Medical and Dental Sciences, Kagoshima/JAPAN

Purpose/Introduction: Gadolinium ethoxybenzyl diethylenetriamine-pentaacetic acid (Gd-EOB-DTPA) is widely used to improve the detectability of focal liver lesions and the characterization of liver tumors on MRI. Moreover, the change in the MR signal of the liver parenchyma before and after administration of contrast agent can reflect liver function. However it has been unclear whether liver volumetry improves the precision of liver function estimation by using Gd-EOB-DTPA-enhanced MRI. Therefore, the purpose of this study was to assess the efficacy of liver volumetry for estimation of liver function by contrast enhancement on Gd-EOB-DTPA-enhanced MRI.
Subjects and Methods: A total of 97 patients (mean age, 69 years) with suspected focal hepatic lesions were included in this study. All patients underwent the indocyanine green (ICG) clearance test and Gd-EOB-DTPA-enhanced MRI. 3D T1 weighted images and T1 maps were obtained before and 20 min after Gd-EOB-DTPA injection. The volumes of the liver parenchyma were measured on 20-min-delayed Gd-EOB-DTPA-enhanced MRI. We calculated the following Gd-EOB-DTPA-enhanced MRI based indices with and without liver volume: relative liver-enhancement ratio of T1 relaxation time = (T1pre of the liver − $T1_{20}$ of the liver)/T1pre of the liver; relative liver-enhancement ratio of SI = (SI_{20} of the liver − SIpre of the liver)/SIpre of the liver; liver -spleen contrast ratio of SI = (SI_{20} of the liver − SI_{20} of the spleen)/SI_{20} of the spleen; and corrected liver-enhancement ratio and muscle index of SI = (SI_{20} of the liver/SI_{20} of the muscle − SIpre of the liver/SIpre of the muscle)/(SIpre of the liver/SIpre of the muscle); where SIpre is the signal intensity before Gd-EOB-DTPA administration, SI_{20} is the signal intensity at 20 min after Gd-EOB-DTPA administration, T1pre is the T1 relaxation time before Gd-EOB-DTPA administration and $T1_{20}$ is the T1 relaxation time at 20 min after Gd-EOB-DTPA administration. We also calculated the correlation between Gd-EOB-DTPA-enhanced MRI based indices and ICG-15 by using the Pearson correlation analysis.
Results: Liver volume and all Gd-EOB-DTPA-enhanced MRI based indices were correlated with ICG-15 (Table 1). Each Gd-EOB-DTPA-enhanced MRI based index with liver volume was more correlated with ICG-15 than that without liver volume. Relative liver-enhancement ratio of T1 relaxation time with liver volume had the highest correlation with ICG-15 (Figure 1).

Table 1

Correlation of Gd-EOB-DTPA-enhanced MRI based indices with ICG-15

	r	*P* value
Liver volume	0.315	.002
Index from contrast enhancement alone		
Relative liver-enhancement ratio of T1 relaxation time	0.533	<.001
Relative liver-enhancement ratio of SI	0.488	<.001
Liver-spleen contrast ratio of SI	0.431	<.001
Corrected liver-enhancement ratio and muscle of SI	0.495	<.001
Index from contrast enhancement and liver volume		
Relative liver-enhancement ratio of T1 relaxation time and volume	0.561	<.001
Relative liver-enhancement ratio of SI and volume	0.555	<.001
Liver-spleen contrast ratio of SI and volume	0.492	<.001
Corrected liver-enhancement ratio and muscle of SI and volume	0.509	<.001

Figure 1

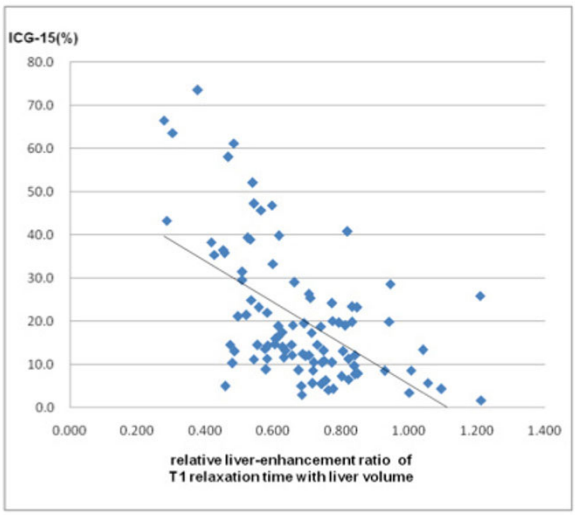

Discussion/Conclusion: The results of our study demonstrated that Gd-EOB-DTPA-enhanced MRI based indices multiplied by liver volume were correlated with ICG-15, and liver volumetry could improve the correlation.

443

WITHDRAWN

444

Quantitative evaluation of liver function with T1 mapping of Gd-EOB-DTPA MRI: comparison with signal intensity-basedmarkers

K. Kamimura[1], Y. Fukukura[1], T. Yoneyama[1], K. Takumi[1], A. Tateyama[1], A. Umanodan[1], T. Shindo[1], Y. Kumagae[1], S. Ueno[2], M. Nakajo[1]
[1]Radiology, Kagoshima University Graduate School of Medical and Dental Sciences, Kagoshima/JAPAN, [2]Department of Surgical Oncology and Digestive Surgery, Kagoshima University Graduate School of Medical and Dental Sciences, Kagoshima/JAPAN

Purpose/Introduction: The aim of this study was to assess the relationship between reduction rate of T1 relaxation time of the liver before and 20 min after gadolinium ethoxybenzyl diethylenetriamine pentaacetic acid (Gd-EOB-DTPA) injection and liver function including Child-Pugh classification and indocyanine green (ICG) clearance in comparison with signal intensity-based liver function indices on Gd-EOB-DTPA MRI.
Subjects and Methods: This prospective study was approved by our institutional review board, and written informed consent was obtained from all patients. A total of 99 patients with suspected liver lesions (mean age, 69.1

years; range, 20-85 years) were selected for evaluation in our study. Twenty-four patients had normal liver function (NLF group). Chronic liver disease was present in 75 patients, and severity of the liver function evaluated according to the Child-Pugh classification showed 64 patients classified as A (LCA group) and 11 as B (LCB group). MRI was performed with a 3-T system. Dynamic images using three-dimensional fat-suppressed T1-weighted gradient-echo volumetric interpolated breath-hold examination axial series were obtained before and after intravenous injection of Gd-EOB-DTPA. In this study, only pre-contrast and 20-min-delayedcontrast enhanced T1-weighted images and T1 maps were evaluated. We compared five Gd-EOB-DTPA MRI-based liver function indices with Child-Pugh classifications and tentative ICG test. From the data acquired, the following contrast enhancement-based liver function indexes were calculated: reduction rate of T1 relaxation time of the liver, relative liver-enhancement ratio of signal intensity (SI), liver-spleen contrast ratio of SI, liver-muscle contrast ratio of SI, and corrected liver-enhancement ratio and muscle index of SI. We evaluated the difference in Child-Pugh classifications by using the Dunnet test. We also calculated the correlation between the imaging-based liver function indices and ICG-15 by using the Pearson correlation analysis.

Results: By using NLF group as a control, Dunnet tests showed reduction rate of T1 relaxation time of the liver was significantly lower for patients with LCA and LCB than for patients with NLF ($P < .001$). The Pearson correlation analysis indicated that reduction rate of T1 relaxation time of the liver had the highest correlation with ICG-15 ($r = -0.605$, $P < .001$), followed by relative liver-enhancement ratio of SI ($r = -0.547$, $P < .001$).

Discussion/Conclusion: We suggest that reduction rate of T1 relaxation time of the liver determined by using Gd-EOB-DTPA-enhanced MRI has the highest correlation with ICG-15 and might be a potential liver function maker.

445

Bismuth classification of hilar cholangiocarcinoma: archaism according recent MRI findings?

O.N. Sergeeva[1], V. Panov[2], B. Dolgushin[2]
[1]Interventional Oncology department, State Institution N.N.Blokhin Cancer Research Center RAMSci, Moscow/RUSSIAN FEDERATION, [2]Radiology, N.N. Blokhin Cancer Research Center, Moscow/RUSSIAN FEDERATION

Purpose/Introduction: Proposed in 1970-th Bismuth classification of hilar cholangiocarcinoma (Klatskin tumor) was based on the cholangiographic proximal bile duct obstruction level. Gd-EOB-DTPA-enhanced MRI demonstration of extramural tumor infiltration changeovers the malignancy margin and spread pattern conception.

Subjects and Methods: Twenty Klatskin tumor (KT) patients have been examined by MRI. 3D/2D MRCP, DWI, Gradient-Echo T1WI and Fast/Turbo Spin-Echo T2WI were obtained on Magnetom Avanto/Espree 1.5T (Siemens). MRCP and DWI had foregone Gd-EOB-DTPA (Primovist, Bayer) enhanced dynamic (4 phases) T1WI's. Respiratory triggered T2WI were made between dynamic and T1WI at hepatocellular/hepatobiliary phase (20-25 min-120 min after Gd-EOB-DTPA 2ml/s i.v. injection (Spectris Solars EP, Medrad)).

Results: The proximal tumor infiltration margin and the conventional cholangiography/MRCP determining bile duct obstruction level were to be significantly distinguished. The proximal tumor spread as the malignancy margin marker was usually underestimated regarding the obstruction level.

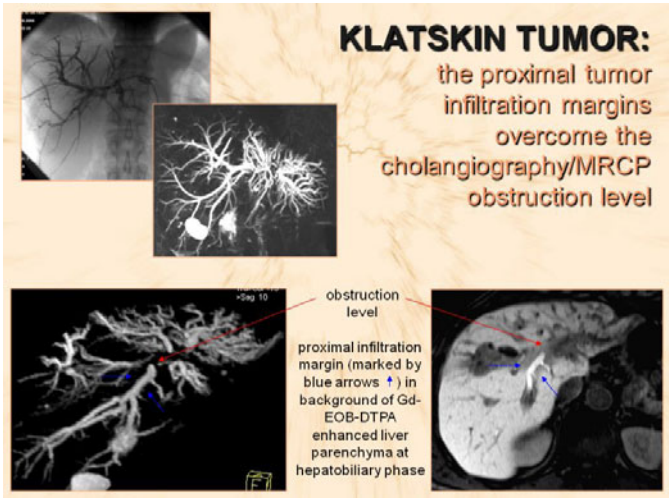

The bile duct diameter didn't reflect the corresponding liver segment/subsegment functioning. Both narrow and dilated bile ducts might be filled up by excreting Gd-EOB-DTPA but the opposite was also true.

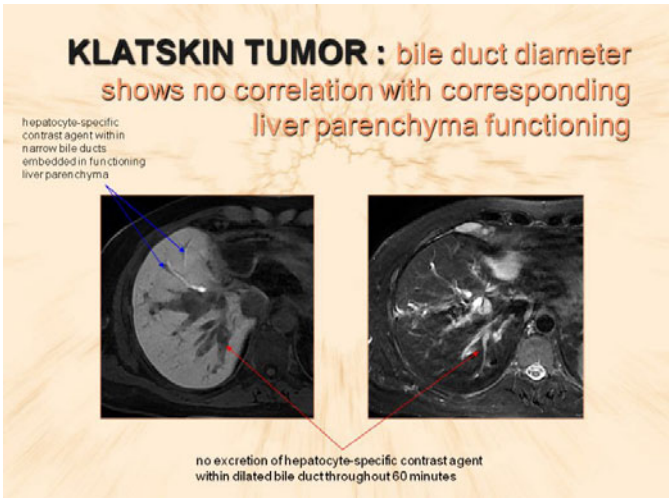

The distribution of Gd-EOB-DTPA within the liver in hepatocellular phase demonstrated periductal fibrotic or desmoplastic liver infiltration as extraluminal tumor spread.

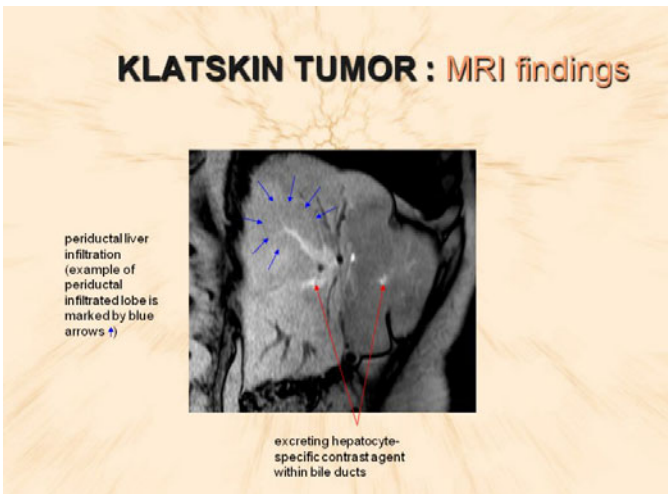

The MIPs accentuated the Gd-EOB-DTPA distribution pattern and set us supposing KT to have a stroma aligned infiltrating growth.

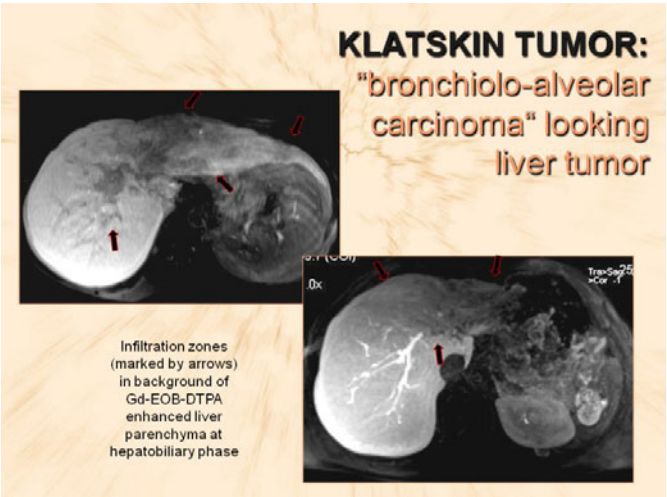

DWI allowed differentiating tumor infiltration from periductal fibrosis.

Discussion/Conclusion: The proximal bile duct obstruction level is the unreliable malignancy margin marker due to the infiltrative periductal tumor spread underestimation. Discussion on Klatskin tumor Bismuth classification revision blows up to the date.

References:

- Klatskin G. Adenocarcinoma of the hepatic duct at its bifurcation within the porta hepatis. An unusual tumor with distinctive clinical and pathologic features. Am J Med. 1965 Feb;38:241-56.
- Bismuth H., Corlett M.B. Intrahepatic cholangioenteric anastomosis in carcinoma of the hilus of the liver. Surg.Gynecol.Obstestet.1975 Feb;140:170-8.
- Shimada H, Niimoto S, Matsuba A, Nakagawara G, Kobayashi M, Tsuchiya S. The infiltration of bile duct carcinoma along the bile duct wall. Int Surg. 1988 Apr-Jun;73(2):87-90.

446

Multifrequency vs monofrequency MR elastography for the characterisation of liver fibrosis and inflammation

P. Garteiser[1], G. D'Assignies[1], **H. Leitao**[2], R. Sahebjavaher[3], S.A. Lambert[1], F. Mouri[1], V. Vilgrain[1], B. Van Beers[1], R. Sinkus[1]

[1]INSERM CRB3-U773, Université Paris Diderot Sorbonne Paris Cité, Clichy/FRANCE, [2]Department of radiology, Hospitais de Universidade de Coimbra, Coimbra/PORTUGAL, [3]Robotic and Control Lab, University of British Columbia, Vancouver/BC/CANADA

Purpose/Introduction: Magnetic Resonance Elastography (MRE) is a non-invasive modality that quantifies the mechanical properties of tissues. Theoretical and physical considerations indicate that the presence of microscopic obstacles may influence not only the absolute value of viscoelastic parameters, but also their relationship with frequency. Yet, most studies use a single excitation frequency thus knowledge about frequency-related mechanical properties is very limited. Our aim is to determine which of multifrequency or monofrequency parameters correlates best with the METAVIR score.

Subjects and Methods: Twenty patients with viral hepatitis B (n=5), C (n=14) and nonalcoholic fatty liver disease (n=1) underwent MRE. Liver inflammation/fibrosis was assessed with METAVIR scoring of percutaneous biopsies. For MRE, a gradient-echo sequence was used (TR/TE=112ms/9.6ms, 4mm resolution). Three-directional motion encoding (eight phase offsets) was performed on simultaneous 28, 56 and 84 Hz mechanical waves transduced by an electromechanical actuator. Complex viscoelastic parameters were calculated by demodulation and local inversion of the linear viscoelastic 3D wave equation. The parameters were: storage modulus, G' (kPa), loss modulus G" (kPa), absolute value of the shear modulus, G_{abs}, β(2π over the wavelength, mm^{-1}) and alpha (the attenuation coefficient, mm^{-1}). The frequency dependence of each parameter (modelled by a power law) was assessed as the exponent parameter, γ. Monofrequency and multifrequency parameters were compared among inflammatory grades and fibrosis stages, using the Kruskal-Wallis test and Dunn's post-test.

Results: At 28Hz G_{abs} and β discriminated between F1vsF3 (P<0.05), but not among the other stages. G', G", and α at 28Hz did not significantly differ between any of the fibrosis stages, and the same was seen with G', G", G_{abs}, α and β at 56Hz and 84Hz. None of the monofrequency parameters was able to discriminate inflammation grades. Using a multifrequency approach, γ_{β} and $\gamma_{G'}$ could discriminate between F0vsF3 and F1vsF3 (P<0.05), and γ_{Gabs} between F0vsF3 (P<0.05). γ_{beta}, γ_{Gabs} and $\gamma_{G"}$ varied significantly between inflammation grades A0vsA1 (P<0.05). A significant correlation was found between inflammation and γ_{β} and γ_{Gabs}.

Discussion/Conclusion: Multifrequency exponent of β and G" provided better discrimination between inflammation grades and fibrosis stages than monofrequency parameters. Moreover, using multifrequency-derived viscoelastic parameters (exponents) will allow standardization among MR elastography research groups.

References:

[1] Holm S. 2010, JASA 127:542-8
[2] Asbach P. 2010, Radiology 257:80-86
[3] Huwart L. 2008, Gastroenterology 135:32-40
[4] Lambert S. 2012, ESGAR procs

447

High diagnostic performance of the quantitative assessment of T2-weighted signal intensity evolution in the tumor for detection of complete response to neoadjuvant chemoradiotherapy in rectal cancer patients

E. Kluza[1], E. Rozeboom[1], M. Maas[1], M. Martens[1], D. Lambregts[1], G. Beets[2], J. Slenter[1], R. Beets-Tan[1]

[1]Department of Radiology, Maastricht University Medical Center, Maastricht/NETHERLANDS, [2]Department of Surgery, Maastricht University Medical Center, Maastricht/NETHERLANDS

Purpose/Introduction: Neoadjuvant chemoradiotherapy (CRT) has become an important component of the treatment for patients with locally advanced rectal cancer. The current CRT schemes result frequently in a significant tumor downsizing, downstaging and even complete remission. For patients with complete response, the omission of surgery in combination with an intensive patient follow-up is considered as a desired clinical pathway. Unfortunately, the selection of complete responders remains a major diagnostic challenge. In the current study, we hypothesized that the quantitative analysis of CRT-induced changes in the T2w signal intensity distribution can improve the accuracy of restaging MRI. Our aim was therefore to determine the diagnostic performance of T2w signal intensity evolution in the tumor for detection of complete response in rectal cancer patients.

Subjects and Methods: 39 patients that were diagnosed with locally advanced adenocarcinoma and treated with CRT, followed by surgery, underwent MRI before and after CRT on a 1.5T scanner using T2-weighted FSE imaging (TE/TR = 150/3427 ms, matrix = 256 × 256, slice thickness = 3 or 5 mm, FOV = 200 × 292 mm^2). The signal intensity in tumor pixels was normalized to the average signal intensity of the obturator internus muscle. The obtained relative T2w signal intensity (rT2wSI) distribution in the tumor and post-CRT residual tissue (**Figure1**) was characterized by means of the descriptive statistical parameters, such as the mean, 95th percentile and SD. Receiver operating characteristic curves were used to determine the diagnostic performance of the CRT-induced alternations in rT2wSI descriptives (Δ). The qualitative image analysis, which served the comparison for the quantitative Δ rT2wSI parameters, was performed by an experienced radiologist. The tumor regression grade (TRG) served as a histopathological reference standard.

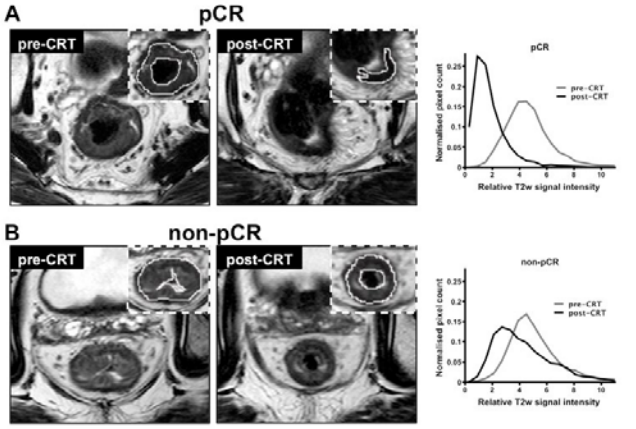

Fig. 1 Relative T2w signal intensity profiles observed for (**A**) a pathological complete responder (pCR) and (**B**) a pathological incomplete responder (non-pCR) before (pre-CRT) and after neoadjuvant chemoradiotherapy (post-CRT). The representative T2w images and corresponding histograms of the T2w signal intensity in the primary tumour and post-CRT residual tissue normalised to the mean T2w signal intensity of the obturator internus muscle. Grey and black lines represent the distribution of relative T2w signal intensity before (pre-CRT) and after the neoadjuvant chemoradiotherapy (post-CRT), respectively

Results: CRT induced a significant decrease of circa 50% in all rT2wSI descriptives in complete responders (TRG1). This drop was significantly larger compared to incomplete response groups (TRG2–TRG4) (**Figure 2**). ΔrT2wSI descriptives produced a high diagnostic performance for identification of complete responders (**Table 1**), e.g., Δ95th percentile, ΔSD and Δmean resulted in the accuracy of 92%, 90% and 82%, respectively. Importantly, the diagnostic performance of Δ95th percentile (AUC = 0.90; 95%CI = 0.75 – 1.00) was significantly higher compared to that achieved by the qualitative image assessment (AUC = 0.65; 95%CI = 0.39 – 0.91) (p = 0.03).

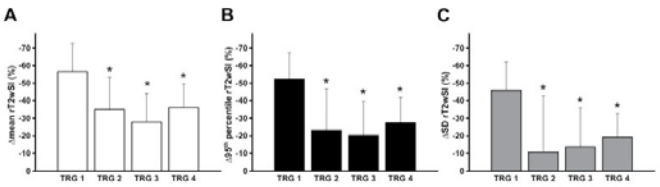

Fig. 2 Comparison between the pathological response groups with respect to the chemoradiotherapy-induced changes in the descriptive parameters of the relative T2w signal intensity (rT2wSI). The graphs display the percentage of change relative to the baseline state for the (**A**) mean (Δmean rT2wSI), (**B**) 95th percentile (Δ95th percentile rT2wSI) and (**C**) standard deviation of the mean (ΔSD rT2wSI). The patients were grouped according to the TRG classification: TRG 1 = the absence of viable tumour cells, exclusively fibrotic tissue (complete response), TRG 2 = rare residual tumour cells scattered throughout the fibrosis, TRG 3 = dominant fibrosis with few tumour cell groups, TRG 4 = residual tumour tissue outgrowing fibrosis. . Bars represent mean ± SD (n = 7, TRG 1; n = 13, TRG 2; n = 13, TRG 3; n = 6, TRG 4). Symbol "*" indicates significant difference compared to the complete response group (TRG 1) at p < 0.05.

Table 1. Diagnostic performance achieved by measuring the percentage of change in rT2wSI descriptive parameters for selection of complete responders to CRT

	AUC 95% CI	Sensitivity 95% CI	Specificity 95% CI	PPV 95% CI	NPV 95% CI	Accuracy 95% CI	Optimal cutoff
Δmean	0.85 0.68–1.00	71 (5/7) 32–94	84 (27/32) 76–89	50 (5/10) 23–66	93 (27/29) 83–98	82 (32/39) 68–90	- 50
Δmedian	0.81 0.61–1.00	71 (5/7) 32–94	72 (23/32) 63–77	36 (5/14) 16–47	92 (23/35) 81–98	72 (28/39) 57–80	- 47
Δ5th percentile	0.74 0.48–1.00	57 (4/7) 24–57	100 (32/32) 92–100	100 (4/4) 43–100	91 (32/35) 85–91	92 (36/39) 80–92	- 78
Δ25th percentile	0.79 0.58–1.00	57 (4/7) 24–57	100 (32/32) 92–100	100 (4/4) 43–100	91 (32/35) 85–91	92 (36/39) 80–92	- 70
Δ75th percentile	0.84 0.66–1.00	71 (5/7) 32–94	84 (27/32) 76–89	50 (5/10) 23–66	93 (27/29) 83–98	82 (32/39) 68–90	- 48
Δ95th percentile	0.90 0.75–1.00	86 (6/7) 47–99	94 (30/32) 85–96	75 (6/8) 42–86	97 (30/31) 88–99	92 (36/39) 78–97	- 46
ΔSD	0.87 0.72–1.00	71 (5/7) 34–92	94 (30/32) 85–98	71 (5/7) 34–92	94 (30/32) 85–98	90 (35/39) 76–97	- 45
ΔIQR	0.85 0.67–1.00	71 (5/7) 34–92	94 (30/32) 85–98	71 (5/7) 34–92	94 (30/32) 85–98	90 (35/39) 76–97	- 43

Note: The optimal cutoff value was determined from the ROC curve as the most distant point with respect to the reference line. All the diagnostic performance parameters are expressed in percentages. Absolute values are shown in parentheses. AUC = area under the ROC curve; PPV = positive predictive value; NPV = negative predictive value.

Discussion/Conclusion: Quantitative assessment of the CRT-induced changes in the tumor T2-weighted signal intensity provides a high diagnostic performance for selection of complete responders.

448

Preliminary experience: a novel DCE-MRI approach based on Functional Volumetric estimation (Standardized Index of Shape, SISV) to differentiate Responder by Not Responder after neo-adjuvant therapy in Locally Advanced Rectal Cancer (LARC).

M. Petrillo[1], R. Fusco[2], V. Granata[2], O. Catalano[2], A. Rotondo[1], A. Petrillo[2]
[1]Section of Radiology, Department "Magrassi-Lanzara,", Second University of Naples, Naples/ITALY, [2]Radiology, INT IRCCS "Foundation G.Pascale", Naples/ITALY

Purpose/Introduction: Our purpose was to evaluate the diagnostic performances of two MRI functional approaches in LARC evaluation after neo-adjuvant therapy (pCRT). A DCE-MRI Time Intensity Curves (TIC) [1,2] evaluation was compared with a novel semi-quantitative dynamic feature, the Standardized index of Shape, calculated on a DCE-MRI Volume (SISV). Respective obtained data were compared with histological Tumor Regression Grade (TRG) to identify responders (R) by not responders (NR) after pCRT.
Subjects and Methods: 14 consecutive LARC affected patients (m.a. 61y) underwent a 1.5 T scanner examination. 11 T1w 3D-FLASH sequences were acquired (one sequence before and ten sequences after Gd-DOTA administration). Region of Interests were drawn inside the tumor and obtained TIC were classified according their shapes: type 1, slow WI, slow WO; type 2, fast WI, slow WO; type 3 fast WI, fas WO. An expert radiologist performed a manual tumor segmentation on a derived series using an open-source software (OsiriX v 4.1) subtracting the 5th post-contrast scan by the 1st non enhanced T1w scan. Drawn tumor volumes were were exported in .XML format and manipulated in MATLAB toolbox. After surgery TRG 1-2 were considered R and TRG 3-5 were considered NR to pCRT. TIC and SISV data from baseline to pre-surgical scans were correlated with TRG. Median times for image segmentation were computed. Sensitivity (SEN), specificity (SPE), receiver operating characteristic (ROC) were computed. Youden Index was used to obtain the optimal ROC analysis cut-off value. Mc Nemar test was performed to underline statistically difference.
Results: Seven patients (50%) were classified R [Fig.1 A-E] and 7 (50%) NR at histology. DCE-MRI TIC and SISV evaluations respectively reached a SEN of 50%, and 90%, an equal SPE of 100%. The best diagnostic performance was reached by SISV that showed an area under ROC of 0,7265 with an optimal cut-off value of 36% (p<0.05). Mean time required for SISV segmentation was 3.2 min, range: 2.1–5.1 min.

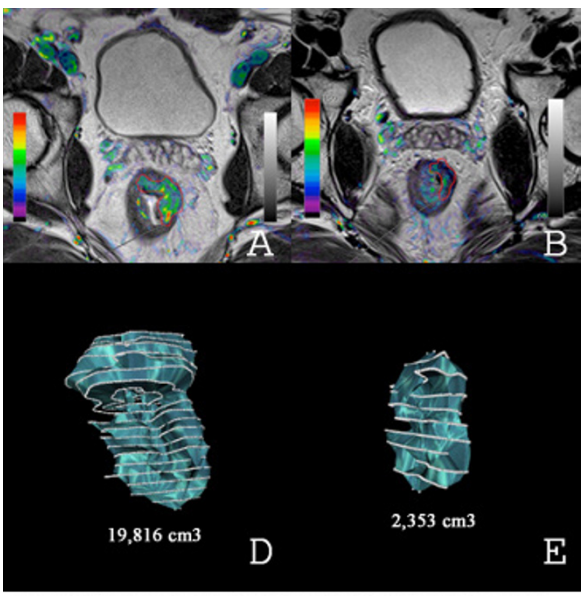

Fig.1 A-E: SIS map combined with a T2w scan (A) before pCRT with corresponding volumetric assessment (SISV, D);
SIS map combined with aT2w scan (A) after pCRT that shows a great decrease in SIS value with a reduction in SISV (E) equal to 60% (Cut-off value=36%) in a Responder patient (TRG=1).

Discussion/Conclusion: SISV could represent a robust semi-quantitative index based on an easy and fast segmentation approach to assess pCRT response to therapy in LARC.

References:

1. Torricelli P, Pecchi A, Luppi G, Romagnoli R. Gadolinium-enhanced MRI with dynamic evaluation in diagnosing the local recurrence of rectal cancer. Abdom Imaging 2003;28(1):19–27

2. Lavini C, de Jonge MC, van de Sande MG, Tak PP, Nederveen AJ, Maas M. Pixel-by-pixel analysis of DCE MRI curve patterns and an illustration of its application to the imaging of the musculoskeletal system. Magn Reson Imaging 2007;25(5):604–612.

EPOS™ Poster

Angiography, blood flow and tissue perfusion

449

Monitoring perfusion during an alcohol infusion using pulsed arterial spin labeling

M. Marxen[1], G. Gan[2], D. Schwarz[1], M. Pilhatsch[1], U.S. Zimmermann[1], M. Guenther[3], M.N. Smolka[1]
[1]Department of Psychiatry und Psychotherapy, Technische Universität Dresden, Dresden/GERMANY, [2]Department of Psychiatry und Psychotherapy, Technische Universitaet Dresden, Dresden/GERMANY, [3]Faculty of Physics and Electrical Engineering, Universität Bremen, Bremen/GERMANY

Purpose/Introduction: A number of studies has investigated the effect of alcohol on brain perfusion [1-3] including three recent arterial spin labeling (ASL) studies [4-6]. One study has reported an increase in perfusion in men but not in women [6]. Reported results are highly variable regarding affected brain regions. The presented study will be the first to monitor perfusion continuously during an alcohol infusion using pulsed ASL.
Subjects and Methods: An ethanol and a placebo infusion were administered to 52 young adults (18-24 years) [7] up to a target blood alcohol concentration (BAC) of 0.6 g/kg 15min. after the start of the infusion. ASL data was acquired before and during the infusions using a pulsed ASL sequence [6]. Eight ASL series with inversion/inflow times TI from 300ms to 2600ms were collected.

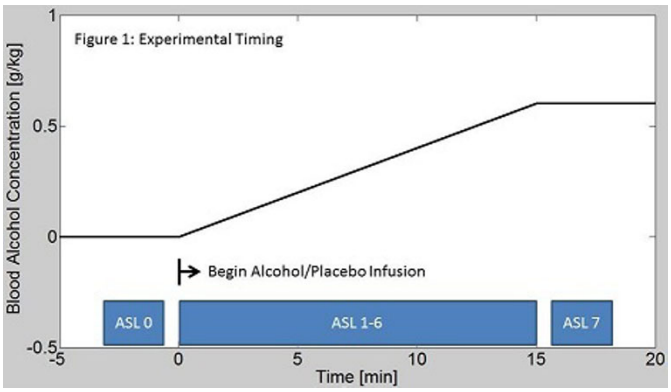

Results: Figure 2: Relative change of global perfusion during the infusion starting at t=0 in 52 subjects. Error bars represent the error of the mean. A highly significant (p<0.0001) alcohol effect is observed. The effect was present in both man (N=35) and women (N=17) with no significant gender effect.

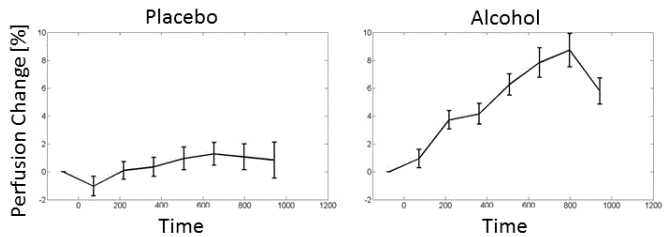

Figure 3: Group activation map (N=30) for the contrast alcohol vs. placebo ramp at P<0.05 (FWE).

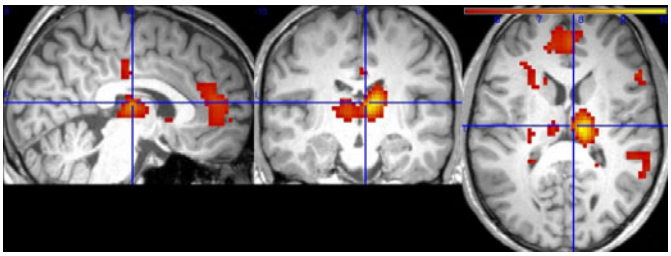

Table 1: Clusters k > 25 voxels (3x3x3mm), maxT - t-value maximum.

MNI x	MNI y	MNI z	k	maxT	Name
12	-19	10	512	10.06	Thalamus
0	47	1	498	6.89	Cingulum Ant
-15	14	19	183	6.58	Caudate L
54	11	28	46	6.53	Frontal Inf Oper R
21	20	7	89	6.36	Caudate R
51	-37	19	187	6.26	Temporal Sup R
57	23	10	30	6.2	Frontal Inf Tri R

Discussion/Conclusion: 1) A steady increase of BAC to 0.6 g/kg lead in average to an increase in global perfusion of ~8%.
2) Gender differences [6] could not be reproduced.
3) Regional effects were identified with high power and differ partially from previous studies potentially due to measurement timing. Particularly, the strong thalamic effect has not been reported.

References:

References: [1] Schwartz, J.A. et al. (1993), Alcohol Clin Exp Res 17(6); [2] Sano M. et al. (1993),J Stud Alcohol 54(3); [3] Volkow, N.D. et al. (1988), Psychiatry Res 24; [4] Khalili-Mahani N. et al. (2011), J Cereb Blood Flow Met; [5] Tolentino, N.J. et al. (2011), Alcohol Clin Exp Res 35(6); [6] Rickenbacher, E. et al. (2011), Alcohol 45(8); [7] O'Connor S. et al. (1998), Alcohol Clin Exp Res 22(1); [8] Guenther, M. et al. (2005), MRM 54.

EPOS™ Poster

Animal models - brain pathologies

450

fMRI study of malnourished brain in rats

R. Martin, R. Godinez, A.O. Rodriguez
Dep. Ingenieria Electrica, UAM Iztapalapa, Mexico DF/MEXICO

Purpose/Introduction: Malnutrition is a worldwide health problem, especially in infants. Animal models have been widely used to study this problem. The cerebellum is one of the structures importantly affected by malnutrition: a decrease in the volume of granular cells [1], abnormalities in the electrophysiological activity of the Purkinje cells, and low neuronal synapses can be observed [2]. There is also a neural cell decrease in the hippocampus [3]. We used BOLD fMRI to investigate regions of brain activity in malnourished rats resulting by stimulating the trigeminal nerve.
Subjects and Methods: To provoke malnutrition, food competition method was applied [4]. Twelve male Wistar rats aged 18 to 21 days, equally divided into control (41.9±4.9g) and experimental (29.1±3.3g) groups, were induced with isoflurane in O2. Rat's head and ears were fixed with a stereotactic frame to minimize motion artifacts and to supply anesthetic during experiments. ECG, breathing monitoring, and rat's temperature control were done with a small animal monitoring and gating system (Model 1025, SA Instruments, NY, USA). Right trigeminal nerve was stimulated using percutaneous electrodes, in the whiskers and in the masticatory muscles. For stimulation an electric stimulator (Grass S-48 Stimulator, Grass Technologies, RI, USA) with constant current pulses (500 mV and 2 mA) at 1Hz was used. 60s OFF was alternated with 60s ON periods. All experiments were performed on a 7T/21cm imager and a transceiver 16-rung birdcage. Brain images were acquired using a standard gradient echo sequence: TR/TE=107.82/3.8 ms, Flip_angle=20°, FOV=30x30mm, matrix size=128x128, thickness=0.3mm, NEX=1.
Results: All brain images were digitally processed using the toolbox SPMMouse [5]. We acquired BOLD signals of the regions: cerebellum, hippocampus, hypothalamus and somatosensory cortex. Fig. 1 shows an example of the signals obtained at the cerebellum and the somatosensory cortex in the experimental group. In Fig. 2, it is shown the mean responses in the four regions of the experimental group.

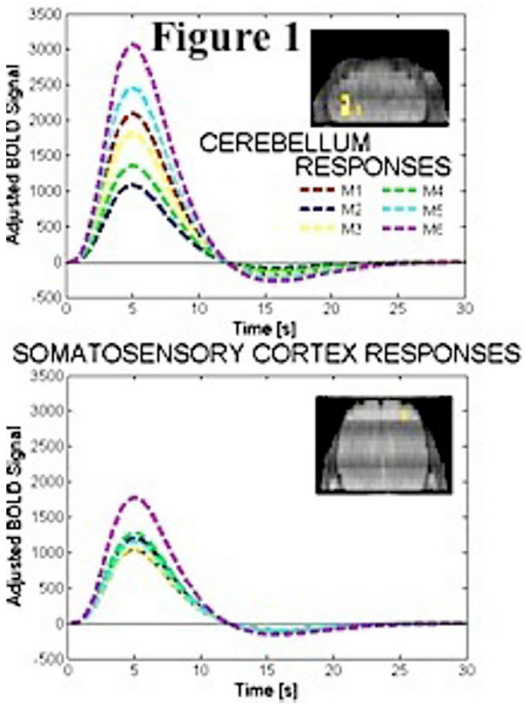

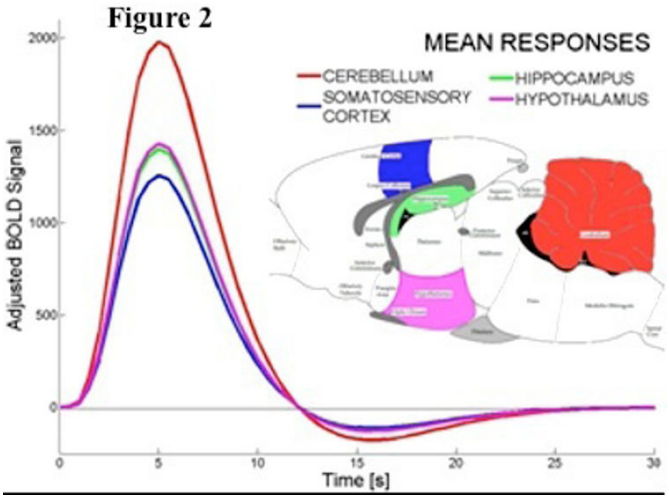

Discussion/Conclusion: These results may pave the way into the treatment of this health problem and other possible rehabilitation procedures.
References:
1. Hillman, D.E. et al. Neurosc.1981; 6:1263-1275. 2. Neurologic Consequences of Malnutrition. World Federation of Neurology; 2008. 3. Lister, J.P. et. al. Hippocampus 2005; 15:393-403. 4. Ortiz R. et al. Med. Sci. Res. 1996;24:843. 5. Sawiak SJ. et. al. Proc. Intl. Soc. Mag. Reson. Med. 2009:1086.
Acknowledgement. R. M. thanks the CONACyT Mexico for Ph. D. scholarship, email: arog@xanum.uam.mx.

451

Effect of Simvastatin on brain creatine kinase reaction in animal model of vascular dementia. The magnetization transfer ^{31}P MRS study

R. Tusková[1], A. Gálisová[1], M. Jozefovicová[1], A. Kebis[2], K. Ambrušová[2], I. Just Kukurová[3], L. Bačiak[1], S. Kasparova[1]
[1]Faculty of Food & Chemical Technology, Slovak University of Technology, Bratislava/SLOVAK REPUBLIC, [2]Faculty of Public Health, Slovak Medical University, Bratislava/SLOVAK REPUBLIC, [3]MR Centre of Excellence, Department of Radiology, Medical University of Vienna, Vienna/AUSTRIA

Purpose/Introduction: Potentially beneficial effects of statins on Alzheimer disease or vascular dementia (VD) have been demonstrated by a number of investigators in human and animal models [1]. In our studies we showed that creatine kinase (CK) plays a central role in energy transfer in brain, it is very susceptible to oxidative stress and the rate constants of CK reaction can be investigated by magnetization transfer *in vivo* ^{31}P MRS in rat brains during modeled VD [2].
The aim of these experiments was to demonstrate that the pseudo first-order rate constant k_{for} of the CK forward reaction could not only be a more suitable indicator of changes in the brain energy metabolism compared to the conventional MRI during chronic pathological states but can also reflect the therapy
Subjects and Methods: Aged (15 month-old) Wistar rats divided into 3 groups (control, VD and VD+Simvastatin treated) were used. VD model was induced by four-vascular occlusion of internal carotides [3]. Simvastatin (20 mg/kg) was administered during 4 weeks after the last occlusion. ^{31}P MRS saturation transfer measurements were performed on a 4.7 T system with a surface HP coil. We used the time dependent saturation transfer method that allows one to measure simultaneously two parameters, k_{for} and T_1. The k_{for} was obtained via nonlinear regression analysis according to McConnel's equation for a two-state exchange under condition of g-ATP resonance saturation. The time of irradiation of the g-ATP resonance varied from 0.3 to 10s.
Results: We found highly significant decrease in k_{for} in all rat brains during chronic hypoperfusion 4 weeks after the occlusion compared to control rats. However, CK rate constant increased to almost control levels in simvastatin-treated rats.

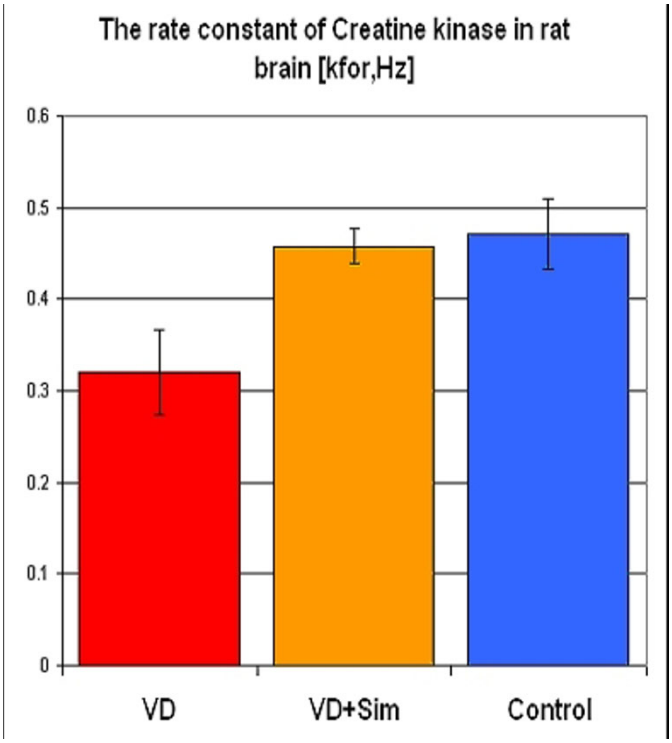

Discussion/Conclusion: Bioenergetic dysfunction, of CK in particular, plays a key role in the pathophysiology of cell death in vascular dementia [2]. Changes in cerebral CK kinetics may result in cognitive impairment. Our results show that simvastatin can improve energetic status of cells in VD, providing temporary protection.
The investigation of the kinetic parameters using magnetization transfer methods can be used as a relatively noninvasive *in vivo* biomarker for neurodegenerative diseases and can possibly predict energy metabolism damage in brain and reflect the effect of therapy not detectable by conventional MRI methods.
References:
[1] Shepardson NE et al. Arch. Neurol 68 (11):1385-92 (2011)
[2] Kasparova S. et al. Nerochem Inter. 46:601-611 (2005)
[3] Ferreira E.D.F. et al., EJN 1, 10 (2011)
Supported by grant VEGA 2/0084/11.

452

Effects of fructose diet on brain: anatomical MRI and DTI study in the rat.

M. Beauvieux[1], G. Raffard[1], A. Bouzier-Sore[2], B. Hiba[1], P. Machet-Maquat[1], M. Urdaci[3], E. Richard[4], J. Gallis[1]
[1]UMR5536 RMSB, CNRS Université Victor Segalen, Bordeaux/FRANCE, [2]CNRS/University, RMSB Center, Bordeaux/FRANCE, [3]Laboratoire Microbiologie, Bordeaux Sup Agro, Gradignan/FRANCE, [4]Laboratoire Biochimie, Hôpital Pellegrin, Bordeaux/FRANCE

Purpose/Introduction: An early diagnostic remains the best hope to prevent and/or to diminish the progression of neurodegenerative diseases (ND). Insulin resistance (IR), frequent consequence of nutritional life-style in industrialized countries is suspected to be implicated in the onset of ND. The Alzheimer disease (AD) brain is associated with reductions in insulin, insulin receptors and insulin signaling (Steen2005). There is probable association between refined sugar intake, particularly high-fructose corn syrup, and the possible promotion of the development of dementia (Stephan2010). In the rats, chronically high fructose (HF) diet leads to hepatic and extrahepatic IR (Tappy2010). Our aim was to explore anatomical MRI and diffusion tensor imaging changes in rat submitted to fructose diet.
Subjects and Methods: 7wks-old male Wistar rats were pair-fed during 10wks with 2 diets (10g/d.100g body weight): Control group: standard chow; HF group: 60% fructose (instead of starch) (n=8 each). At the 3rd, 6th and 10th wks, blood was collected for plasma parameters. Anatomical images (20 axial 1mm-slices; TurboRARE acquisition; TE/TR: 70/3700 ms) and diffusion tensor images (B-value 1000; 30 diffusion directions; resolution) were acquired, using a Bruker biospin 4.7T scanner, after 10wks diet. Fraction Anisotropy (FA) and apparent diffusion coefficient were computed for hippocampus and using region of interests manually defined on diffusion maps. The volumes of total brain, brain ventricular and hippocampus were assessed after a semi-automatic segmentation of anatomical images. Post-hoc statistical tests were used.
Results: HF induced a systemic IR (normoglycaemia+hyperinsulinemia) from 3wks. At 10wks, HF induced oxidative stress (plasmatic a-tocopherol, 2-fold higher than control) and inflammation (plasmatic IL6, 2-4-fold higher than controls). HF changed volumes of brain structures: increase of ventricules (35.2±4.2 mm^3 *vs* control =31.4±5 mm^3) and decrease of hippocampus (123±4mm^3 *vs* control =140±2 mm^3; p=0.015). HF decreased FA (0.32±0.02 *vs* control =0.41±0.03; p=0.01).
Discussion/Conclusion: Fructose consumption seemed to induce very early impairments which can be linked to neurodegenerative process. Hippocampal volume is proposed to predict memory decline and progression to AD (Mielke2012). Ventricular enlargement is also associated with mild-cognitive impairment (Apstolova2012). Moreover, DTI can be used to estimate the white matter impairment in dementia patients with significant regional reductions of FA values (Fu2012). Luo (2011) has found that 10%-fructose during 16wks induced Aβ overproduction; it could be supposed that daily consumption of fructose induces early brain impairments.
References:
ApostolovaLG, AlzheimerDisAssocDisord. 2012;26:17; FuJL, ActaRadiol.2012;53:312-7 ; LuoD, EurJPharmacol.2011;664:14-9; MielkeMM, Alzheimers Dement.2012;8:105-13; Steen E,JAlzheimerDis.2005;7:63;StephanBCM ,JGerontol2010;65:809;TappyL, MetabolicPhysiolRev.2010;90,:23

453

Longitudinal multi-parametric MRI of cerebral amyloidosis in transgenic arcAbeta mice

J. Klohs[1], I. Wojtyna Politano[1], A. Deistung[2], J. Grandjean[1], A. Drewek[3], M. Dominietto[1], R. Keist[4], F. Schweser[2], J.R. Reichenbach[2], I. Knuesel[4], M. Rudin[1]
[1]Institute for Biomedical Engineering, University of Zurich and ETHZ, Zurich/SWITZERLAND, [2]Medical Physics Group, Institute of Diagnostic and Interventional Radiology I, Jena University Hospital – Friedrich Schiller University Jena, Jena/GERMANY, [3]Seminar für Statistik, ETH Zurich, Zurich/SWITZERLAND, [4]Institute of Pharmacology and Toxicology, University of Zurich, Zurich/SWITZERLAND

Purpose/Introduction: Biomarker of Alzheimer`s disease (AD) are critical for providing an early clinical diagnosis during early stages of the disease and for staging the disease progression. The main goals of this animal study were to characterize the effects of progressive amyloid-β (Aβ) accumulation on tissue water content, magnetic susceptibility, on blood-brain barrier integrity and occurrence of cerebral microbleeds (CMBs) as well as to investigate if these measures may serve as biomarkers of AD pathology. For this purpose, T1-mapping, diffusion-weighted imaging (DWI), quantitative susceptibility mapping (QSM) and dynamic contrast-enhanced MRI (DCE-MRI) were applied in a longitudinal study in the arcAβ mouse, modeling aspects of AD.
Subjects and Methods: ArcAβ and wild type mice were serially assessed over an age range of 7 to 22 months. DWI, T1-mapping and DCE-MRI experiments were performed on a Bruker 200MHz MR system. Apparent diffusion coefficient (ADC) maps were computed from DWI data [1,2]. T1 maps were computed by pixel-wise non-linear least-squares fitting of 6 inversion recovery spin echo data sets acquired with TE=8.2 ms and inversion times of 90.3/150/500/1000/3000/5500ms. The vascular transfer constant (K^{trans}) and the contrast agent volume of the extracellular compartment (v_e) were computed from DCE-MRI data [3]. 3D velocity compensated gradient-echo data were acquired on a Bruker 400MHz MR system with TE/TR/FA=12/250/15° and converted into quantitative susceptibility maps [4]. For analysis, regions-of-

interest were identified separately on each parameter map. To assess whether age or genotype was a determinant of an MRI parameter a linear mixed model was built [5].
Results: ADC values were significantly associated with age and genotype (p= 0.01and p=0.006 respectively). T1 showed a statistical association with age, but not with genotype p=0.001 and p=0.38 respectively). v_e was significantly associated with age, but not genotype, while K^{trans} were neither associated (p=0.008, p=0.73, p=0.02 and p=0.34 respectively). Magnetic susceptibility was found to be associated with age and genotype (p=0.0001 and 0.0002). Focal areas of increased magnetic susceptibility, i.e. presumably CMBs became apparent with 13 month of age and increased in number with increasing age.
Discussion/Conclusion: Most MRI parameters were associated with age. T1 mapping and DCE-MRI do not seem suitable for detecting Aβ pathology in the arcAβ mouse whereas DWI and QSM appear promising as biomarkers of AD.
References:
[1] Mueggler Eur. J. Neurosci 2004
[2] Brunberg AJNR Am J Neuroradiol 1995
[3] Rudin NMR Biomed 2005
[4] Schweser Proc Intl Soc Mag Reson Med 2012
[5] R Development Core Team, 2012

454

Correlations between MRI biomarkers and gene expression in a mouse model of high grade glioma

A.R. Borges[1], J.M. Bravo Marques[2], G. Rodriguez-Tarduchy[3], L. Barrios[4], P. Lopez-Larrubia[3], S.G. Cerdan[5]
[1]Radiology, Instituto Português de Oncologia Centro de Lisboa, Lisbon/ PORTUGAL, [2]Neurology, Instituto Português de Oncologia Centro de Lisboa, Lisboa/PORTUGAL, [3]Instituto Investigaciones Biomedicas "Alberto Sols" CSIC-UAM, Madrid/SPAIN, [4]Informática, Consejo Superior de Investigaciones Científicas, Madrid/SPAIN, [5]Modelos Experimentales de Enfermedades Humanas, Instituto de Investigaciones Biomédicas Alberto Sols, Madrid/SPAIN

Purpose/Introduction: High grade glioma (HGG) is a heterogeneous neoplasm. Its genetic profile varies over time and drifts after different treatments. Clinical management of these tumors is increasingly based on pharmacogenomics but, in clinical practice, the serial assessment of gene expression is invasive and unpractical. On these grounds we explore the correlations between MRI biomarkers and the *in vivo* expression of crucial tumor genes, to assess the potential inference of gene expression profiles from MRI scans. More specifically we aim;

- To provide multiparametric MRI and genetic characterization of the Gl261 mouse model of HGG.
- To evaluate and validate MR imaging methods
- as non-invasive biomarkers of gene expression in an animal model of HGG.

Subjects and Methods: 10^6 Gl261 cells were orthotopically implanted in the putamen of adult CD1 mice. Serial MR studies (T2*, DWI and PWI maps) were performed at 4 day intervals after implantation. Upon development of morbid, neurologic signs or weight loss over 15%, mice were sacrificed (high power microwaves 5KW) and tumors excised for RNA extraction and RT-qPCR. The MR data set collected on the last study before sacrifice was correlated with gene expression modules of proliferation, angiogenesis, hypoxia, invasion and migration, using Pearson's and Spearman's correlations (SPSS http://ibm-spss statistics.softronic.com/).
Results: MR imaging characterization of this model over time showed a progressive decrease in ADC values until week 3 after which they started to increase due to tumor necrosis; T2* values decreased also until week 3, increasing afterwards coinciding with the angiogenic shift; perfusion values included an increase in CBV after the 2nd week and a steady increase of MTT over time. Statistically significant correlations (Pearson and Spearmann correlations) were found between mADC and EGF, IDH_1 and IGFBP genes; between mT2* and GLUT3 gene, between mCBF and mCBV with VEGF-A, VEGFR2, HIF1α, GLUT3, EGF, EGFR, CDH_5 (VE-chaderin), $IDH1_1$, IGFBP2, CD71 (TfR1) genes and between MTT and VEGF-A, VEGFR2, EGF, CD51 (integrin), BIRC5 (AIP14), CDH5 and CA9 genes. Similarly, important correlations were also found in the expression of some of the genes investigated (Fig. 1).

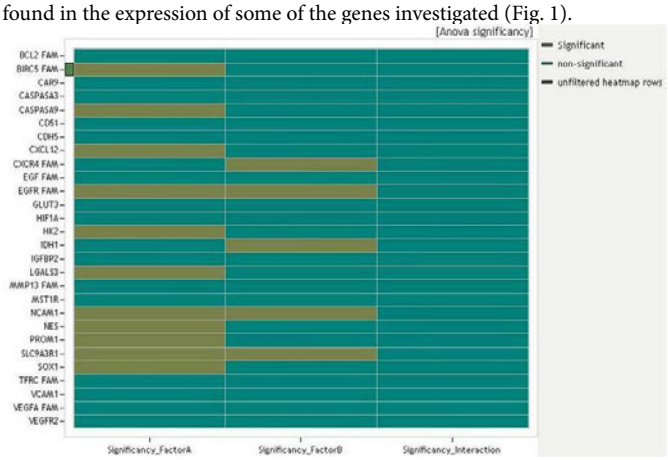

Discussion/Conclusion: We provide an extensive MRI and genetic characterization of the Gl261 mouse model and correlations thereof. Significant correlations were found between MR parameters (mADC, mT2*, mCBF, mCBV and mMTT) and different modules of gene expression, making it possible to infer the genetic alterations from a single non-invasive, phenotypic, MRI measurement.

455

MRI tracking of human mesenchymal stem cells distribution and migration in rats with focal brain ischemia

L. Gubskiy[1], **D. Namestnikova**[2], R. Tairova[1], K.N. Yarygin[3]
[1]Fundamental and Clinical Neurology, The Russian National Research Medical University named after N.I.Pirogov, Moscow/RUSSIAN FEDERATION, [2]Center of Magnetic Tomography and Spectroscopy of Faculty of Basic Medicine, M.V.Lomonosov Moscow State University, Moscow/RUSSIAN FEDERATION, [3]Cell biology, The Russian National Research Medical University named after N.I.Pirogov, Moscow/RUSSIAN FEDERATION

Purpose/Introduction: Transplantation of human mesenchymal stem cells (hMSCs) has been shown to improve functional outcome and decrease infarct size in rodent models of stroke and in humans during first clinical trials[1]. However, the mechanism of therapeutic effects, optimal route of administration, migration and fate of transplanted hMSCs has not been fully understood yet. In our study we evaluate distribution and migration of magnetically labeled hMSCs stem cells in rats with focal brain ischemia using MRI.
Subjects and Methods: Male Wistar rats (n=75) were subjected to 60-minutes MCAO by an intraluminal monofilament[2]. Two days after MCAO hMSCs derived from placenta and labeled with superparamagnetic iron oxide nanoparticles (SPIO) and fluorescence mark (ME02F-Bangs Laboratories) were transplanted intravenous (n=20) and intraparenchymal into contralateral to ischemic lesion hemisphere (n=15). Before and after MCAO and hMSCs transplantation rats were examined at 7T Bruker BioSpec MR tomograph: DWI, T2-WI and T2*-WI were obtained. Tracking of hMSCs were detected as a strong hypointense areas on T2*-WI. Other cause of signal decrease on T2*-WI were excluded by comparing with group of control (rats just with MCAO, n=30). For conformation of hMSCs migration immunohistochemistry was performed.
Results: In rats with intravenously injected hMSC we found tracking after 1 day post-transplantation in superficial cortex; after 7 days around major blood vessels, in subventricular zone (SVZ), corpus callosum (CC) and also few in ischemic lesion; after 14 and 21 days there was significant migration of hMSC into the infarct area and SVZ. In rats with intraparenchymal injection after 1 day hMSC were detected at the site of transplantation; after 7 days along the injection canal and near semilateral to it SVZ; only after 14 days migration to CC, SVZ of the other site and ischemic lesion were detected.

Discussion/Conclusion: We evaluate the ability of hMSC to migrate into the brain after transplantation, reach and accumulate in the ischemic area and SVZ. Intravenous injected hMSC have shown more rapid spread in the ischemic rat brain.

References:

[1]Koizumi J., 1986, Jpn J Stroke 1-8; [2]Honmou O., 2011, Brain 1790-1807.

456

fDWI predicts obesity development in rats

B. Lizarbe[1], P. Lopez-Larrubia[1], S. Cerdan[1], V. Caz[2], M. Tabernero[2], E. De Miguel[2], C. Largo[2]

[1]Instituto Investigaciones Biomedicas "Alberto Sols" CSIC-UAM, Madrid/ SPAIN, [2]Cirugía Experimental, [2]Instituto de Investigación Sanitaria La Paz IdIPaz, Madrid/SPAIN

Purpose/Introduction: Obesity is a pandemic syndrome underlying the most morbid and prevalent diseases in developed countries. It results from an imbalance in the appetite regulation, affecting global energy turnover. Our group has shown that appetite can be detected by MEMRI[1] and Diffusion Weighted Imaging (DWI) through changes in the hypothalamus of mice and humans[2, 3]. Here we show that changes observed by DWI are different in the hypothalamus of rats gaining weight or not under high fat diets, and that they affect differently the Dorsomedial (DM), Ventromedial (VM) and Arcuate (ARC) nuclei. Results suggest that global energy balance and response to diet can be monitored by DWI of the hypothalamus

Subjects and Methods: *Animal model*: Wistar rats (8 weeks, n=6) were fed *ad libitum* during 6 months with high-fat diet (17.4% Protein, 35.8%Lipids, 35% Carbohidrates, purified diet 230 HF, SAFE). Three rats developed obesity, weighting 638±11g ("Obese" group), and the remaining three showed a normal weigh 438±15g ("Non Obese" group).

DWI: Rats were imaged in a 7T magnet (90mm gradient coil-36G/cm,^{1}H surface coil, TR/TE=3000/51ms, in-plane resolution=0.296mm/pixel, axial slices 1.5mm, δ=4ms, Δ=20ms, eight b-values 300<b<1800s/mm^2, L-R/A-P/H-F directions) in a fed state and after an overnight fasting .

Data analysis: Data was analyzed in the DM, VM and ARC hypothalamic nuclei and fitted (MATLABv7a) to a biexponential model $S(b)/S(0)=SDP\cdot\exp(-b\cdot D_{slow})+FDP\cdot\exp(-b\cdot D_{fast})$, with the slow (SDP) and fast (FDP) diffusion phases characterized by slow (D_{slow}) and fast (D_{fast}) diffusion coefficients

Results: Biexponential fittings presented significant differences between the mean values of SDP and D_{slow} in the different regions investigated. Fed Non Obese rats have significantly higher SDP in DM than Obese rats. The Obese group showed upon fasting a significant increment of SDP and D_{slow} in the ARC and in the VM, respectively. The Non Obese rats, showed decreased SDP in the DM upon fasting.

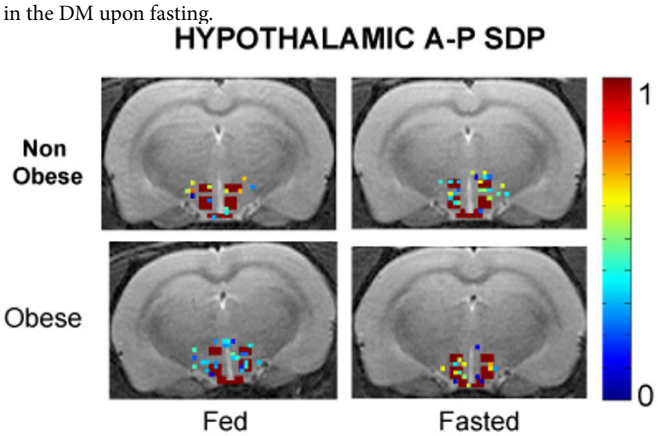

Figure 1. A-P SDP parameter maps (blue-red color code) in the hypothalamus of representative Non Obese Fed (upper left), Non Obese Fasted (upper right), Obese Fed (lower left) and Obese Fasted (lower right) rats. Parameter maps are shown superimposed to the localisation of hypothalamic nuclei ARC (most anterior), VM (middle) and DM (most posterior) shown by the brown pixels.

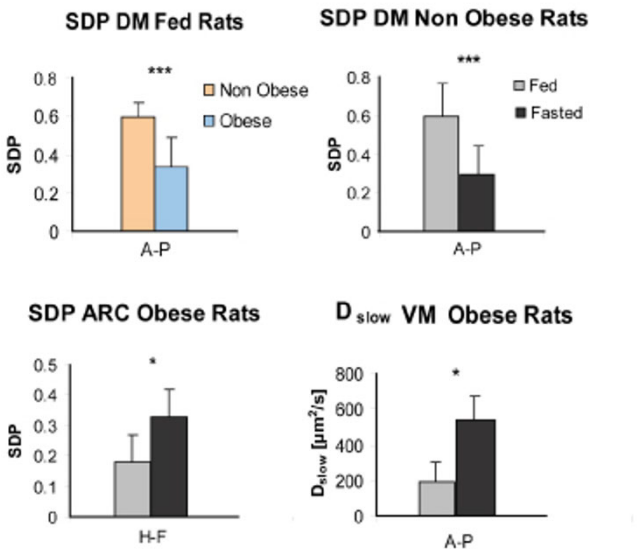

Figure2. Bar graphs of SDP and D_{slow} (mean ±SD) from all animals investigated, showing the main differences between fed and fasted states of Obese and Non Obese rats in the DM, VM and ARC. (* $p<0.05$), (*** $p<0.001$)

Discussion/Conclusion: Increments of SDP and D_{slow} are associated to activation-induced astrocytic swelling[2-4]. Here, we report significant increments of SDP and D_{slow} with fasting in the orexigenic ARC and VM hypothalamic nuclei in Obese rats, and decreases with fasting in the anorexigenic DM nuclei of the Non Obese rats. Our results suggest that obesity development may be identified through quantification of DWI parameters of hypothalamic nuclei.

References:

[1]Delgado et al.JCBFM(2011), [2]ESMRMB 2011(#103), [3]ISMRM 2012(#3909), [4]Le Bihan D et al. PNAS(2006)

457

Effect of manganese chloride on rat hippocampus metabolism studied by proton HRMAS NMR

A. Daoust[1], E. Barbier[2], S. Bohic[3], S. Maunoir-Regimbal[4], **F. Fauvelle**[4]

[1]NeuroImagerie Fonctionnelle et Perfusion Cérébrale, Inserm U 836, Institut des neurosciences de Grenoble, La Tronche/FRANCE, [2]NeuroImagerie Fonctionnelle et perfusion cérébrale, INSERM U836, Institut des neurosciences de Grenoble, La Tronche/FRANCE, [3]Rayonnement sychrotron et recherche médicale, European Synchrotron Radiation Facility (ESRF), Grenoble/ FRANCE, [4]NMR laboratory, IRBA-CRSSA, La Tronche/FRANCE

Purpose/Introduction: Manganese (Mn) Enhanced Magnetic Resonance Imaging (MEMRI) can be used for different applications such as tract tracing neuronal connection.[1-2]However, Mn cellular distribution and toxicity in brain tissue are still unclear. The aim of this study was to measure metabolic perturbations in rat hippocampus due to Mn by High Resolution Magic Angle Spinning (HRMAS) NMR, in order to get better insights in MEMRI mechanisms.

Subjects and Methods:

***Mn injections*:** An intracerebral (IC) injection of $MnCl_2$ (10μL, 50mM) was performed in the right hippocampus dentate gyrus of 8 Sprague-Dawley rats, while 8 other received vehicle (Fig. 1A).

***In vivo MRI*:** 24h post-injection, T1-weighted images (Spin-echo, TR/TE=300/12ms) were acquired on a 7T MRI system (Bruker) using a surface/volume cross coil configuration.

***Sample preparation*:** After MRI, animals were quickly killed by decapitation and left and right hippocampus removed on ice. They were divided in 3 equal parts (anterior, middle and posterior) and rapidly frozen in liquid nitrogen.

HRMAS: ^{1}H HRMAS NMR spectra were acquired at 400MHz using a CPMG pulse sequence (30ms echo time) and 4Kz spinning rate. NMR data were quantified using jMRUI software (www.mrui.uab.es/mrui/).
Results: Animals that received Mn exhibited an hyper MR signal in both sides of the hippocampus (Fig. 1C). In HRMAS NMR spectra, only lactate, NAA, glutamate and aspartate resonances were broadened due to the Mn paramagnetic effect (Fig. 2A). At the injection site, an important impact on cerebral metabolism was observed (Fig 2B). Moreover, these effects were not identical in each of the three parts of the hippocampus, and in right and left hippocampus (data not shown).

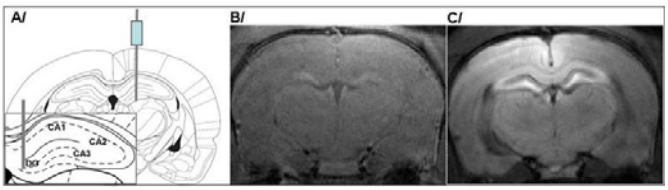

Fig 1: MEMRI images 24h after intra-cerebral Mn injection in the right hippocampus.

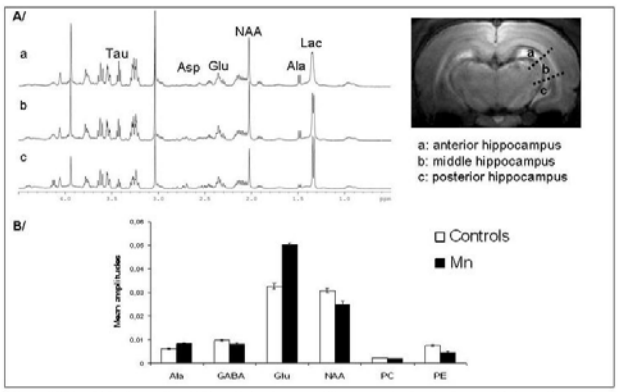

Fig 2: ^{1}H HRMAS NMR study at 9.4 T of the impact of Manganese 24 h after injection in the right anterior hippocampus A/ spectra obtained in the three right hippocamus sub-regions, showing the differential broadening of lactate B/ Mean amplitudes ±SEM of metabolites that vary significatively (student-test, $p<0.05$) in right anterior hippocampus

Discussion/Conclusion: It is known that organic acids chelate Mn. This could explain the specific broadening of some resonances in HRMAS NMR spectra.[3] Moreover, both metabolism and broadening variations seem to follow a Mn concentration gradient along hippocampus. The disturbance of glutamine-glutamate-GABA cycle observed is consistent with literature.[4] To conclude, these preliminary data are encouraging and could shed some light on how Mn interacts with brain cells.
References:
[1] I. Aoki et al., Neuroimage, 22:1046-1059, 2004.
[2] R.G. Pautler, NMR Biomed, 17: 595-601, 2004.
[3] K. Kishi et al., Biochemistry, 33:8694-701, 1994.
[4] C. Zwingmann et al., Neurotoxicol, 25: 573-587, 2004.

458

Comparison of different contrast agents in cerebral perfusion assessment by MRI studies at 7 T: Follow-up of a high-grade glioma rat model

E. Cañadillas-Cárdenas[1], R. Pérez-Carro[1], **P. Lopez-Larrubia**[2]
[1]Departamento de Modelos experimentales de enfermedades humanas, Instituto de Investigaciones Biomédicas "Alberto Sols", Madrid/SPAIN, [2]Modelos experimentales de enfermedades humanas, Instituto Investigaciones Biomedicas "Alberto Sols" CSIC-UAM, Madrid/SPAIN

Purpose/Introduction: Cerebral perfusion assessment by Dynamic Susceptibility Contrast MRI involve the intravenous administration of a contrast agent (CA) followed by the rapid, time-resolved, MR signal of its first pass through the microvasculature of the imaged slice[1,2]. In brain, analysis of the kinetic curves allows for the determination of the blood volume, blood flow, mean transit time[3]. In this study we compared the results obtained from bolus tracking measurements performed in a high-grade glioma rat model by using contrast media with different relaxation and plasma half-life properties. We used Endorem®, an iron oxide nanoparticle with high relaxivity values and two Gd-based chelates: Magnevist®, that shows rapid vascular clearance to the extracellular fluid and Multihance®, a blood pool agent that strongly and reversibly binds to plasma proteins increasing its relaxivity and retention time in the vascular system.
Subjects and Methods: High grade gliomas were induced in Wistar rats (200-220g) by stereotaxic injection of C6 cells in the right caudate nucleus. MRI evaluations were carried out in a horizontal 7T system at several time points of the cancer development. Acquisitions were performed using single-shot EPI and 0.2M contrast agent solutions rapidly injected in the tail vein as a bolus (1mL/kgBW), wiht parameters: TR/TE=250/7ms, Av=1, angle=30º, in-plane resolution of 594x475µm^2 and 150 repetitions. Parametric maps (CBF, CBV and MTT) were generated on a pixel-by-pixel basis with a home-made software application. Pixel time-evolution signals were fitted to the following expression: $\Delta R2^*(t)=-k.\ln(S(t)/S0(t))$. Haemodynamic parameters were analysed in four ROI's (cortex, white matter, peripheral-tumor and core-tumor).
Results: Parameters measured showed no significant differences with the three contrast agents (figure 1). By comparing the data from early-stage tumors (<20 mm^3) with those in more advanced stages (>100 mm^3) Magnevist was the unique agent that provided significant differences in the measurements (figure 2). Results clearly evidenced that this medium detected the malignant progression of the tumor by an increasing in CBV whereas the other CA's did not.

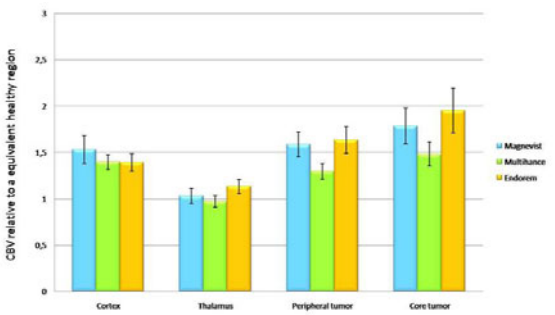

Fig. 1. Relative CBV mean values and SD in four brain regions of interest for measurements performed with Magnevist, Multihance and Endorem in rats with a glioma induced by stereotaxic injection of C6 cells

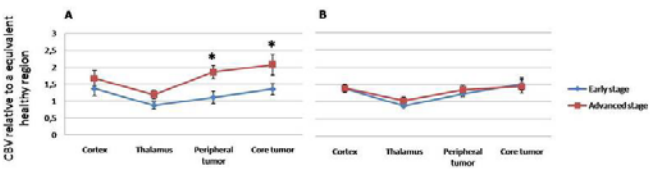

Fig. 2. Relative CBV mean values and SD in four brain regions of interest for measurements performed with Magnevist (A) and Multihance (B) by comparing early stage (tumor volume lower than 20 mm^3) and advanced stage (tumor volume bigger than 100 mm^3) * p<0-05

Discussion/Conclusion: Although different efforts have been made to solve the problems associated to the contrast media in the measurements of haemodynamic parameters by DSC-MRI, in this work we show that Magnevist, the most extended CA in clinical routine, is good enough to quantify microvasculature alterations associated to the development of an intracranial neoplasm in a rat model.
References:
1. L. Ostergaard. Top.Mag.Res.Imag. 2004,15:3-9; 2 F. Calamante et al. Stroke 2002, 33:1146-52, 3 L. Ostergaard, J.Mag.Res. 2005, 22:710-717.

EPOS™ Poster

Animal models - normal brain function

459

Functional proton MR spectroscopy of the rat barrel cortex

N. Just[1], L. Xin[1], R. Gruetter[2]
[1]LIFMET, CIBM-EPFL, Lausanne/SWITZERLAND, [2]LIFMET, CIBM-EPFL-LIFMET-SB, Lausanne/SWITZERLAND

Purpose/Introduction: For a better understanding of the processes underlying brain activity, we propose to investigate the neurochemical consequences of brain activation using functional MR Spectroscopy (fMRS) at high field. Lactate, Glutamate, Aspartate and Glucose concentration changes were evaluated in the barrel cortex of the rat during prolonged barrel cortex activation.
Subjects and Methods: The barrel cortex of Sprague-Dawley rats was activated with prolonged trigeminal nerve electrical stimulation [1] (10 minutes, 1Hz, 2mA, 0.5ms) under α-chloralose anesthesia. All the experiments were performed on an actively shielded 9.4T/31cm bore magnet (Magnex, Varian) with a surface coil. Shims were adjusted using FASTMAP resulting in water linewidths of 12-15Hz in a 216µl volume. The BOLD response was assessed using single shot gradient echo EPI. Each rat was exposed to alternate periods of 10 minutes of rest and 10 minutes of TGN stimulation. Localized Proton spectroscopy was performed using SPECIAL [2] in a VOI (2x2x4mm^3) localized on the motion-corrected T-value BOLD maps ((GLM model) with t>3) obtained after a 10-minute TGN stimulation (fig.1) in the activated barrel cortex and after adjusting once more the shims using FASTMAP (12-15Hz). The raw 1HMRS spectra corrected for frequency drift and summed were used for LCmodel analysis with a basis set of 21 simulated metabolites. For metabolite concentration time courses, blocks of 16 fids were summed using a moving average (3 x 16 fids ~ 1 minute, $SNR_{LCmodel}$> 8; Full width at half maximum<0.040ppm) over each 10-minute period per rat and then further summed over all the animals. Statistics were performed using a paired t-test. A pvalue <0.05 was considered significant.
Results: An average increase of 1.7% of the peak height due to the BOLD effect was observed in the activated barrel cortex. The time courses for 11 rats of Lac , Glu, Glc and Asp (CRLB <40%) were plotted (fig.2) for 10 minute TGN stimulation and rest periods. The average metabolite concentrations during TGN stimulation and rest for Lac, Glu, Glc and Asp were compared. [Lac] (p=0.001) and [Glu] (p<0.005) increased significantly during sustained TGN stimulation relative to the rest period while [Glc] (p<0.02) showed a significant decrease. Aspartate also demonstrated a tendency to decrease during TGN stimulation.

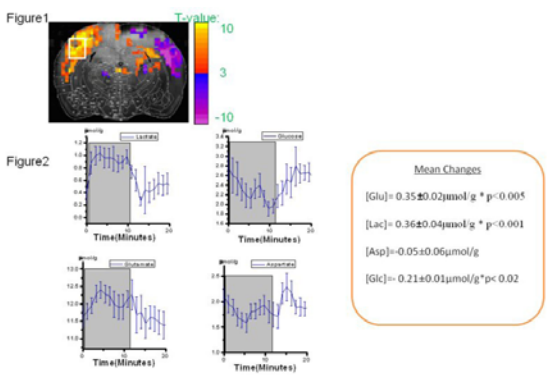

Discussion/Conclusion: The present study reports for the first time the dynamics of [Lac], [Glu], [Glc] and [Asp] and demonstrates the feasibility of fMRS during sustained TGN stimulation in rodents.
References:
1. Just N . 2010. MRI. 1143-51
2. Mlynarik V. 2006. MRM. 965-70

460

fDWI reveals reduced feeding impulse in NPY knockout mice

B. Lizarbe, P. Sánchez, P. Lopez-Larrubia, S. Cerdan
Instituto Investigaciones Biomedicas "Alberto Sols" CSIC-UAM, Madrid/SPAIN

Purpose/Introduction: Cerebral activation is associated to intracellular, extracellular and transcellular ion fluxes between neural cells, accompanied by water movements and cellular swelling. Diffusion Weighted Imaging (DWI) is excellently endowed to detect these changes in a fully non invasive manner. Recently, our group has shown that appetite can be detected by DWI through changes in the diffusion behaviour of water in the hypothalamus of mice and humans[1, 2]. Here we investigate the effects of orexigenic activation by fasting in the hypothalamus of neuropeptide Y knockout mice (NPY)[3], as detected through DWI methods. Hypothalamic NPY neurons are thought to provide a relevant contribution to the orexigenic response. Our results reveal that orexigenic activation in NPY knockout mice is reduced in comparison to normal mice and that this effect can be conveniently detected by fDWI.
Subjects and Methods: *Animal model:* Adult C57BL/6 mice (n=6), and 129S-*Npy*^{tm1Rpa}/J (n=10) were imaged in two experimental conditions, fed *ad libitum* and fasted (48 h). Food intake was measured in metabolic cages, in normal conditions and after the fasting period.
DWI: Mice were imaged in a 7T Magnet (90mm gradient coil-36 G/cm, 23mm mouse head resonator, δ=4ms, Δ=20ms, TR/TE=3000/51ms, in-plane resolution=0,296mm/pixel, axial slices 1.5mm, eight b-values 300<b<1800 s/mm^2, L-R/A-P/H-F directions).
Data analysis: Data was fitted (MATLABv7a) to a biexponential model $S(b)/S(0)=SDP\cdot\exp(-b\cdot D_{slow})+FDP\cdot\exp(-b\cdot D_{fast})$, with slow (SDP) and fast (FDP) diffusion phases characterized by slow (D_{slow}) and fast (D_{fast}) diffusion coefficients.
Results: Measurements in metabolic cages indicate that food consumption is similar in both mouse strains under normal conditions (Figure 1). However, NPY knockout mice show reduced food intake in response to fasting. Concomitantly, DWI shows significant differences between the mean values of SDP, D_{slow} and D_{fast}, in the hypothalamus of fed and fasted mice (Figures 2,3), and these changes are more pronounced –and more significant- in wild type than in knockout mice.

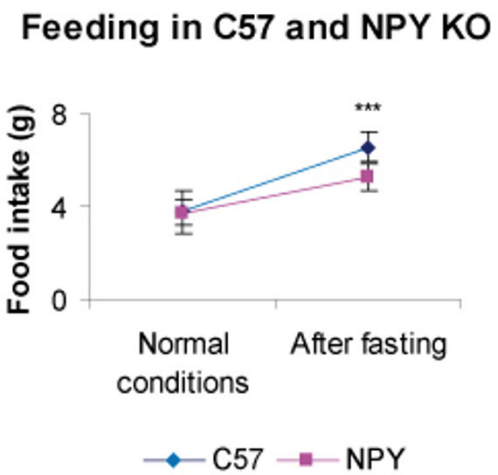

Figure 1. Amount of food consumed (mean±SD) by C57 BL/6 and NPY knockout mice, measured during 24h in normal conditions and during 24h after 48h of fasting. (***p<0.001).

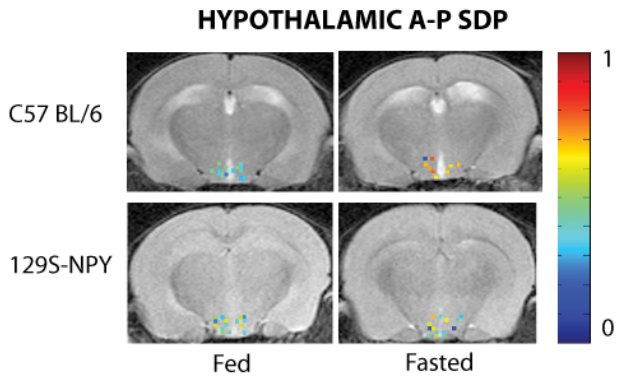

Figure 2. A-P SDP Parameter maps in the hypothalamus of representative C57 BL/6 mice (upper pannels) and 129S-NPY knockout mice (lower pannels), in the fed and the fasted states

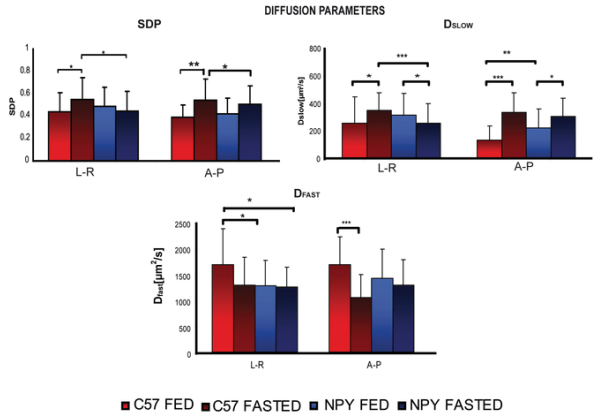

Figure 3. SDP, D_{slow} and D_{fast} values (mean±SD) in the hypothalamus of C57 BL/6 mice (red) and 129S-NPY (blue) mice, in the fed and fasted states. (*p<0.05,**p<0.005,***p<0.001)

Discussion/Conclusion: We report that hypothalamic activation by fasting, detected by DWI as a significant increase in the SDP, D_{slow} and decrease in D_{fast}, is significantly reduced in NPY knockout mice, demonstrating a smaller orexigenic activation, in agreement with the metabolic measurements detecting a reduction in food intake as a response to fasting. Together our results show that the food intake desire may be measured by DWI of the hypothalamus.

References:

[1]ESMRMB2011(#103)[2], ISMRM2012(#3909), [3]Bannon A.W et al. Brain Research(2000)

461

The control of strong emotional reactions in response to affective pictures by high harm avoidand females during an fMRI experiment.

P. Van Schuerbeek[1], C. Baeken[2], R. Luypaert[1], J. De Mey[1]
[1]Radiology, UZ Brussel (VUB), Brussels/BELGIUM, [2]Psychatry and medical Psychology, UGent, Gent/BELGIUM

Purpose/Introduction: In our previous study [1], in response to aversive stimuli less amygdala activity was found in correlation to the personality trait 'Harm Avoidance' (HA) in females while watching passively to blocks with positive or negative affective pictures. However, high HA means stronger negative reactions and paying more attention towards aversive stimuli, resulting in more amygdala activity [2]. To explain this discrepancy, we hypothesized that our volunteers anticipated to the negative stimuli either by shifting their attention away from the pictures or by suppressing their emotional reaction. In an attempt to test this hypothesis, we repeated the fMRI experiment but now we restricted the possibility to anticipate by presenting the pictures in random order and asking to evaluate the valence of the shown pictures.

Subjects and Methods: We included 33 non-depressed female volunteers (22±3 years) and quantified their personality with the temperament and character inventory (TCI). During the MRI, they had to evaluate pictures of happy smiling baby faces as positive and unhappy crying baby faces with a severe dermatological condition as negative affective pictures. The associated brain activity was measured with a standard EPI sequence (dynamic resolution: 3s) at a 1.5T MRI scanner. Based on the individual response maps and for each affective condition, we performed a multiple regression analysis with all personality traits and age as regressors on circular ROI's (radius: 5mm) defined on the maximum response in the amygdalae, subregions of the PFC known to regulate the amygdalae response and the visual cortex.

Results: Using a significance threshold of p<0.05, the response to the negative pictures correlated with HA in the right amygdala, the left ACC, the left MOFC and the left DLPFC (figure 1). The response to the positive pictures correlated with HA in the ACC bilateral, the left OFC, the left MOFC, the left DLPFC and the VLPFC bilateral (figure 2). None of our results survived multiple comparison correction.

Response to the negative pictures							
		Response			Regression with HA		
Region	Position	T	p(uncorrected)	p(corrected)	T	p(uncorrected)	p(corrected)
Amygdala L	{-20;-4;-16}	3.10	0.002	0.032	1.33	0.098	0.809
Amygdala R	{20;-4;-16}	3.61	0.001	0.008	**2.50**	**0.010**	**0.147**
ACC L	{-8;38;-2;}	-4.47	<0.001	<0.001	**2.12**	**0.022**	**0.302**
ACC R	{10;36;-8}	-5.47	<0.001	<0.001	1.26	0.109	0.843
OFC L	{-20;32;-16}	-2.80	0.004	0.066	0.93	0.182	0.959
OFC R	{34;28;-6}	5.11	<0.001	<0.001	0.82	0.209	0.976
MOFC L	{-6;54;-6}	-4.95	<0.001	<0.001	**1.88**	**0.036**	**0.447**
MOFC R	{10;36;-10}	-5.46	<0.001	<0.001	1.12	0.138	0.906
DLPFC L	{-22;34;38}	-8.54	<0.001	<0.001	**1.82**	**0.041**	**0.485**
DLPFC R	{24;34;40}	-6.49	<0.001	<0.001	0.69	0.247	0.989
VLPFC L	{-58,14;30}	5.31	<0.001	<0.001	0.45	0.329	0.998
VLPFC R	{54;14;30}	8.67	<0.001	<0.001	0.95	0.177	0.956
MDPFC L	{-4;58;22}	-1.24	0.112	0.851	1.28	0.107	0.837
MDPFC R	{2;56;2}	-3.60	0.001	0.008	0.97	0.172	0.951
VC L	{-36;-84;2}	16.79	<0.001	<0.001	0.96	0.174	0.953
VC R	{32;-90;6}	19.27	<0.001	<0.001	0.71	0.243	0.988

Figure 1: The brain response to the negative pictures and its regression to the personality trait 'Harm Avoidance' (HA) in the left (L) and right (R) amygdala, anterior cingulate cortex (ACC), orbitofrontal cortex (OFC), medio-orbitofrontal cortex (MOFC), dorsolateral prefrontal cortex (DLPFC), ventrolateral prefrontal cortex (VLPFC), medio-dorsal prefrontal cortex (MDPFC) and the visual cortex (VC).

Response to the positive pictures							
		Response			Regression with HA		
Region	Position	T	p(uncorrected)	p(corrected)	T	p(uncorrected)	p(corrected)
Amygdala L	---	---	---	---	---	---	---
Amygdala R	---	---	---	---	---	---	---
ACC L	{-6;52;0}	-5.66	<0.001	<0.001	**2.46**	**0.011**	0.142
ACC R	{10;38;-2}	-5.45	<0.001	<0.001	**2.64**	**0.007**	0.096
OFC L	{-50;28;-4}	-3.16	0.002	0.024	**2.48**	**0.010**	0.135
OFC R	{44;28;-6}	3.50	0.001	0.010	1.46	0.079	0.684
MOFC L	{-4;54;-4}	-5.41	<0.001	<0.001	**2.31**	**0.015**	0.188
MOFC R	{8;44;-10}	-4.92	<0.001	<0.001	1.20	0.122	0.837
DLPFC L	{-24;32;48}	-7.68	<0.001	<0.001	**1.71**	**0.050**	0.512
DLPFC R	{52;44;18}	4.04	<0.001	0.002	0.84	0.205	0.960
VLPFC L	{-46;38;8}	-3.40	0.001	0.013	**1.75**	**0.046**	0.483
VLPFC R	{44;12;24}	6.14	<0.001	<0.001	**1.89**	**0.035**	0.395
MDPFC L	{0;56;10}	-6.08	<0.001	<0.001	1.43	0.082	0.699
MDPFC R	{2;56;10}	-5.92	<0.001	<0.001	1.23	0.116	0.822
VC L	{-30;-90;2}	14.29	<0.001	<0.001	0.64	0.263	0.986
VC R	{34;-94;10}	15.06	<0.001	<0.001	0.84	0.205	0.960

Figure 2: The brain response to the positive pictures and its regression to the personality trait 'Harm Avoidance' (HA) in the left (L) and right (R) amygdala, anterior cingulate cortex (ACC), orbitofrontal cortex (OFC), medio-orbitofrontal cortex (MOFC), dorsolateral prefrontal cortex (DLPFC), ventrolateral prefrontal cortex (VLPFC), medio-dorsal prefrontal cortex (MDPFC) and the visual cortex (VC).

Discussion/Conclusion: Although statistically weak, restricting the posibility to anticipate to the presented stimuli seems to result in the expected behavior for the amygdala activity in relation to HA (figure 3). In an attempt to control the emotional reaction, more PFC activity was seen. In conclusion, the high harm avoidand females in our experiments tried to avoid or suppress strong emotional reactions to negative stimuli.

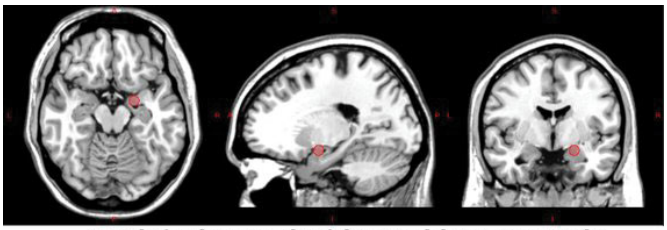

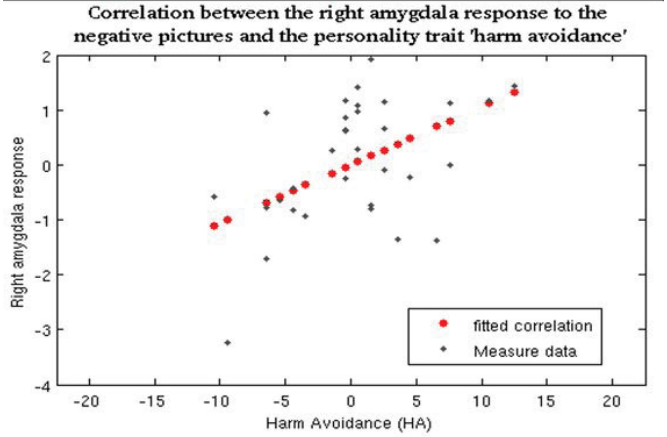

Figure 3: The location of the right amygdala ROI on an axial, sagital and coronal plane (top) and the correlation plot between the response to the negative pictures in the right amygdala and the personality trait 'Harm Avoidance' (bottom).

References:
[1] Baeken C. et al. (2009): Brain Research; 1296:94-103
[2] Most S. et al. (2006): NeuroImage; 31:1016-1027

462

Brain CSF distribution of gadolinium contrast agent with using simultaneous microdialysis & MRI methods

F. Noury[1], N. Brandhonneur[2], P. Eliat[3], F. Chevanne[2], P. Le Corre[2], H. Saint-Jalmes[1]
[1]Université de Rennes 1, LTSI, Rennes/FRANCE, [2]IRSET, TEAM 9, Rennes/FRANCE, [3]PRISM, Biosit, CNRS UMS 3480, INSERM UMS 018 - Biogenouest, Rennes/FRANCE

Purpose/Introduction: The objective was to evaluate the biodistribution of methotrexate in the brain cerebrospinal fluid (CSF) after intraventricular administration. Previously, we have conducted a microdialysis study to compare CSF kinetics of methotrexate and gadolinium, and obtained similar CSF biodistributions.
Microdialysis gives measurements of absolute drug concentrations versus time only in the specific area where the probe is positioned. Magnetic resonance imaging (MRI) on the other hand gives a relative 3-dimensional distribution as a function of time of a contrast agent of the entire tissue or organ.
The idea was to combine MRI and microdialysis after intrathecal administration of gadolinium to study its biodistribution in all brain CSF, in order to obtain information of methotrexate brain CSF biodistribution.
Subjects and Methods: Microdialysis
Microdialysis probe was inserted into the intrathecal 3rd ventricular space after skull trepanation in New Zealand White rabbits under general anesthesia. 3rd ventricle administration of 100 µg of gadolinium was performed. Intrathecal dialysate concentrations of gadolinium were analyzed by inductively coupled plasma mass spectroscopy.
MRI
Acquisitions were performed at 4.7 T (47/40 Bruker Biospec), using a linear birdcage coil (emission) and a custom surface coil (reception). T1-weighted images were acquired using a 3D gradient echo sequence: TR/TE=15/6.6 ms, θ=30°, voxel dimensions 176*176*625 µm³, T_{acq}=5 min. A reference image was obtained before the intrathecal administration of gadolinium. Acquisition was then repeated during and over 180 min after gadolinium administration, in synchronization with the microdialysis protocol.

Calculation of gadolinium concentrations
Signal intensities were measured from each image in 4 regions of interest (ROI) in the brain: 3rd ventricle, right and left lateral ventricles and magna cisterna (fig. 1).
Gadolinium concentrations (mmol.ml-1) were calculated. The kinetics of gadolinium concentrations decay versus time, for each ROI and each animal were determined. These kinetics were compared to kinetics obtained from microdialysis data.
Results: The kinetics of gadolinium concentrations calculated by MRI in the 3rd ventricle and the lateral ventricles paralleled the elimination of gadolinium in the 3rd ventricle obtained by microdialysis (fig. 2). In the magna cisterna, we obtained delayed kitenics compared to 3rd ventricle. A robust mathematical correlation was observed between MRI and microdialysis CSF gadolinium concentrations.

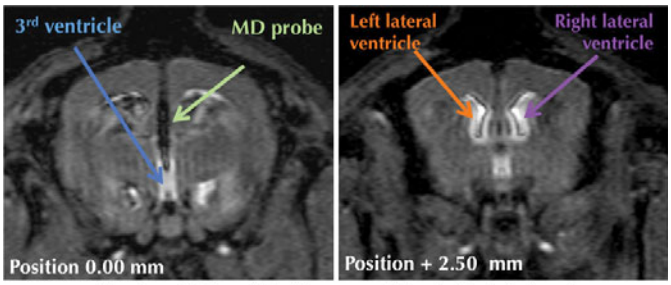

Fig. 1: axial T_1-weighted images obtained after intrathecal administration of gadolinium. See position of MD probe, 3rd ventricle and right and left lateral ventricles.

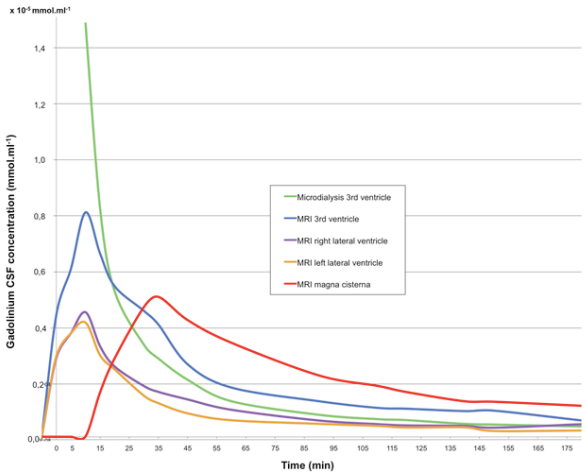

Fig. 2: kinetics of gadolinium concentrations obtained by MRI in the 3rd ventricle, lateral ventricles and magna cisterna and by microdialysis in the 3rd ventricle.

Discussion/Conclusion: Combination of microdialysis and MRI allows the determination of the 3D distribution of contrast agents in the brain CSF and will be important to better understand the biodistribution of drugs injected in the CSF, as methotrexate.

463

MRI investigation of brain aging in rats

S. Tambalo[1], E. Mosconi[2], A. Daducci[1], S. Fiorini[1], **P. Marzola**[1]
[1]Dept. Computer Science, University of Verona, Verona/ITALY, [2]Dept. of Clinical Physiopathology, University of Florence, Florence/ITALY

Purpose/Introduction: Studies on healthy aging are fundamental to seek factors related to mental and physical wellbeing. MRI findings in normal brain aging in humans have been reported (1). Aim of this work was to investigate

normal brain aging in rats in order to assess which MRI findings are common with healthy brain aging in humans.

Subjects and Methods: T2w and DTI images were obtained for old (n= 13, age=26 months) and young (n=7, age=3-4 months) rats by using a Bruker Biospec scanner operating at 4.7 T and a cross coil configuration. T2w images were analysed using the FSL software (FMRIB Software Library, http://www.fmrib.ox.ac.uk/), adapted here for rat brain analysis. To compute GM, WM and CSF volumes, T2w brain images were first processed using the FAST segmentation procedure and volumes were quantified for each tissue-type. Statistical significance for volumes of brain structures volumes was evaluated using the Mann Whitney U-test.

Results: Figure 1 shows WM, GM and CSF volumes expressed as mean±standard deviation. CSF volume in old rats is statistically higher than young ($p<0.001$) rats, while no significant difference was detected in WM and GM. Figure 2 shows FA and ADC values measured over the whole brain. A decrease in FA and an increase in ADC are evident ($p<0.05$) in elder rats when compared to young subjects.

Fig.1

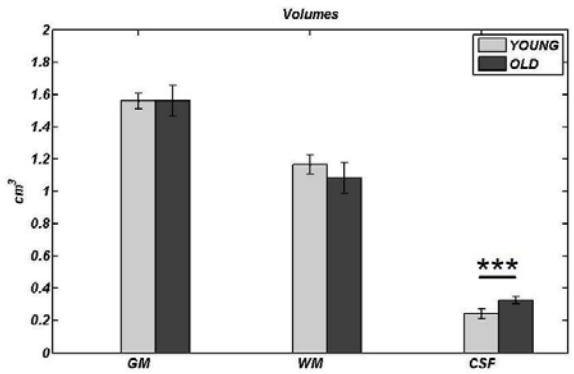

Fig.2

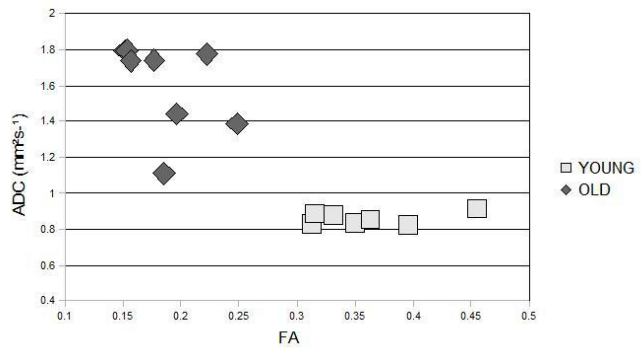

Discussion/Conclusion: Brain aging was investigated by MRI in rats. Morphologically, a statistically significant increase in CSF volume in aged rats was observed. In addition, DTI images revealed an increase in ADC, paralleled by a decrease in FA, in aged animals. These findings are in agreement with previously reported results obtained in humans (1-4). The present study shows that some relevant features of brain aging as detected by MRI in humans are also detectable in rats therefore validating the experimental model.

References:

(1) Minati et al, J Geriatr Psychiatry Neurol 2007; 20:3-21
(2) Wozniak et al., Neurosci Biobehav Rev 2006; 30:762-74.
(3) Bennett et al. Hum Brain Mapp 2010; 31:378-90
(4) Takao et al. Magnetic resonance imaging 2010; 28:65-9.

464

functional MRI with specific frequency stimulations in mice

Y. Komaki[1], K. Hikishima[2], T. Konomi[3], S. Shibata[1], M. Yamada[4], N. Miyasaka[5], K. Fujiyoshi[3], K. Yagi[6], N. Tamaoki[2], M. Nakamura[3], H.J. Okano[7], H. Okano[1]

[1]Department of Physiology, Keio University, Tokyo/JAPAN, [2]Pathology Research Department, Central Institute for Experimental Animals, Kanagawa/JAPAN, [3]Department of Orthopaedics, Keio University, Tokyo/JAPAN, [4]Faculty of Radiological Technology, Fujita Health University, Aichi/JAPAN, [5]Department of Comprehensive Reproductive Medicine, Tokyo Medical and Dental University, Tokyo/JAPAN, [6]Department of Radiological Sciences, Tokyo Metropolitan University, Tokyo/JAPAN, [7]Institute of DNA Medicine, Jikei University School of Medicine, Tokyo/JAPAN

Purpose/Introduction: We are committed to translational researches for the treatment of spinal cord injury by using methods of behavior, histology and MRI. Although previous study succeeded in recovering motor function, a study about allodynia (experiencing pain by non-painful stimulation) caused by spinal cord injury do not reveal successful result yet. The purpose of this study is creating the path to develop the treatment for allodynia by revealing the mechanism of brain with fMRI technology for mice.

Subjects and Methods: This study was approved by the local Animal Experiment Committee and was conducted in accordance with the Guidelines for Conducting Animal Experiments of the Japanese Central Institute for Experimental Animals.

Animal preparation: For 5 male mice(26.6±3.6 g / ave. ±SD), we made modified Chung model which was a neuropathic pain model of L5 denervation under isoflurane anesthesia.

Behavior Analysis: We temporally performed behavior analysis to evaluate allodynia.

functional MRI: On the basis of results of Neurometer, first, we performed electric stimulation of specific frequency (5Hz, 250Hz, 2,000Hz: 250uA) to left forepaw and measured functional MRI in healthy mice.Secondly, using the electric stimulation which selectively depolarized Aβ fiber , we measured functional MRI on preoperation and POD7 in modified chung model mice.

MRI equipment: 7.0T Biospec 70/16 MRI, CryoProbe (Bruker BioSpin: Ettlingen,Germany)

Data analysis: Using SPM8 (Wellcome Trust Centre for Neuroimaging, UCL Institute of Neurology, London, UK), we standardized anatomical images of C57Bl/6 mice brain and achieved group analysis.

Results:

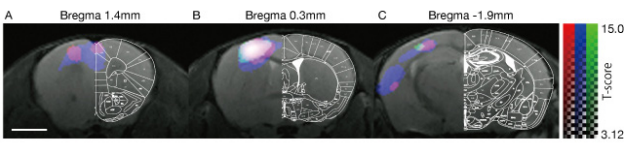

Red:5Hz, Blue:250Hz, Green:2000Hz (500μA, forepaw, $P<0.001$). A scale bar is 2mm. Stimulation of 2,000Hz (A β fiber, sense of touch) showed activation only in contralateral S1(section B). Stimulation of 250Hz (Aδ fiber, Primary pain) showed activation in contralateral S1, secondary somatosensory cortex (S2, section C), anterior cingulate cortex (ACC, section A). Furthermore, stimulation of 5Hz (C fiber, Second pain and sense of warmth) showed activation in S1, ACC.

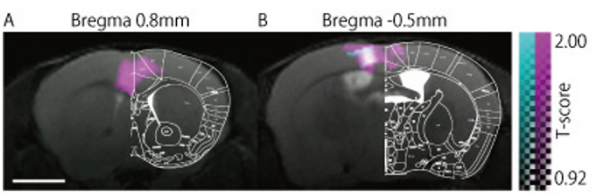

BOLD activations with left hindpaw stimulation(2000Hz) of neuropathic pain model. Cyan:preoperative, Magenta:POD 7($P<0.05$, n=5).The stimulation of

2,000Hz for healthy mice observed activation only in contralateral S1. On the other hand, the stimulation for neuropathic pain model mice observed activation in S1 and ACC.

Discussion/Conclusion: We established functinal MRI for mice and succeeded in clarifying brain function localization. Examining fMRI when each peripheral nerve fibers received specific frequency stimulations showed the relation with allodynia and brain.

References:

Adamczak, et al. Neuroimage 2010
Baltes C., et al. NMR Biomed 2010
Bosshard S.C., et al. Pain 2010
Takemura Y., et al. Synapse 2011

EPOS™ Poster

Animal models - other

465

Myostatin deficiency impairs both mechanical performance and metabolic efficiency of contracting mouse gastrocnemius muscle in vivo

B. Giannesini[1], E. Mousiel[2], C. Vilmen[1], C. Dalmasso[1], Y. Lefur[1], P.J. Cozzone[1], H. Amthor[2], D. Bendahan[1]
[1]CNRS - Aix-Marseille Université UMR 6612 CNRS Université de la Méditerranée, CRMBM UMR 7339, Marseille/FRANCE, [2]UMR S974 UMR S 787, Institut de Myologie, Paris/FRANCE

Purpose/Introduction: While it has been well established that the lack of myostatin (Mstn) expression promotes skeletal muscle hypertrophy [1], the corresponding changes regarding both muscle function and energetics have been poorly documented and remains conflicting. Here, we have tested in situ whether Mstn depletion affects energetic efficiency in contracting muscle.
Subjects and Methods: Gastrocnemius muscle function and energetics were investigated strictly noninvasively in 4-month old Mstn-targeted knockout (*Mstn*$^{-/-}$) and wild-type (WT) mice during a fatiguing protocol (6 min of repeated isometric contractions electrically induced by transcutaneous stimulation at a frequency of 1.7 Hz). For this purpose, we used an innovative experimental device allowing mechanical performance, energy metabolism, anatomy and physiology to be accessed in situ in contracting gastrocnemius muscle using ^{1}H-magnetic resonance (MR) imaging and ^{31}P-MR spectroscopy [2]. Experiments were performed in the 4.7 T horizontal magnet of a 47/30 Biospec Avance MR system (Bruker, Karlsruhe, Germany) equipped with a Bruker 120-mm BGA12SL (200 mT/m) gradient insert. ATP production from creatine kinase reaction, mitochondrial oxidative phosphorylation and glycolysis during the stimulation period were calculated using the method initially described by Kemp at al. [3].
Results: In *Mstn*$^{-/-}$ group, although body weight and gastrocnemius muscle volume were both larger (+ 38 % and + 118 %, respectively) when compared to WT mice, specific force (i.e., force normalized to gastrocnemius volume calculated by MR imaging) was significantly lower (- 36 %) and fatigue development was more important. Besides, Mstn deficiency did not affect basal energy metabolism but caused a strong increase (up to + 206 %) of ATP cost of contraction during the stimulation period. Further, Mstn deficiency limits the shift toward oxidative metabolism throughout muscle activity despite oxidative ATP synthesis capacity was not impaired.
Discussion/Conclusion: Our data demonstrate that the absence of Mstn impairs both mechanical performance and energy metabolism efficiency during muscular activity in situ, and therefore does not confer any functional advantage over wild-type animals. These findings must be kept in mind when considering postnatal blockade of Mstn as a potential strategy for treating patients with muscle-wasting disorders.
References:
[1] Lee, SJ, 2001, Proc Natl Acad Sci USA, 98, 9306-9311
[2] Giannesini, B, 2010, Magn Res Med, 64, 262-270.
[3]. Kemp, GJ, 1994, Magn Reson Q, 10, 43-63.

466

In-vivo pHe measurment by 1H MRS in HT-29 mice model

P. Eliat[1], F. Noury[2], S. Jouan-Lanhouet[3], G. Gambarota[1], M. Dimanche-Boitrel[3], H. Saint-Jalmes[2]
[1]PRISM, Biosit, CNRS UMS 3480, INSERM UMS 018 - Biogenouest, Rennes/FRANCE, [2]Université de Rennes 1, LTSI, Rennes/FRANCE, [3]UMR 1085, INSERM, Rennes/FRANCE

Purpose/Introduction: Tumor microenvironment, characterized by hypoxia, high lactate concentration and acidic extracellular pH (pHe) due to high glycolytic metabolism, could modify cancer cell sensitivity to treatments. Several approaches had been proposed to measure pHe *in vivo*, using ^{31}P-MRS, ^{19}F-MRS and ^{1}H-MRS combined with the administration of a specific compound. Here we propose to measure pHe in HT-29 tumor model in mice with ISCUA([(+/-)2-(imidazol-1-yl)succinic acid]) administration combined with ^{1}H-MRS acquisition.
Subjects and Methods: HT-29 colon carcinoma cells (2.5 10^{6}) were injected subcutaneously in the right flank of 9 MF1 nude mice (Harlan). MRS was performed two weeks after cells inoculation on a 4.7 T MR system (BIOSPEC 47/40, Bruker). Before acquisitions, a catheter was placed in the tail vain for continuous infusion of ISUCA (1 ml.h^{-1} during 20 min and 0.5 ml.h^{-1} during 40 min). Spectra were acquired in a voxel (3mm)^{3} using a PRESS sequence (TR/TE = 1700/11ms, 4 dummy scans, 256 scans). Chemical shift of the pH-sensitive peak of ISUCA was measured and converted to pHe according to the the Henderson-Hasselbalch equation: pH = pKa + log{(δ1- δ) / (δ-δ2)}, where δ is the chemical shift and δ1 > δ2 are the asymptotic values.
Results: Spectra of tumours showed several peaks : total choline (tCho, δ=3.22 ppm), creatine-containing compounds (tCr, δ=3.01 ppm) and "lactate + lipids" peak (lac + lip, δ=1.33 ppm). pH-sensitive resonance of ISUCA was detected near 8.3 ppm allowing pHe measurement. An acidification was observed with a mean pHe of 6.73±0.45.

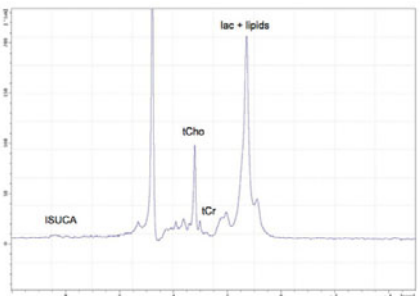

Figure 1 : Typical *in-vivo* 1H single-voxel spectrum obtained in HT-29 xenografts showing total choline (tCho, δ=3.22 ppm), creatine-containing compounds (tCr, δ=3.01 ppm) and "lactate + lipids" peak (lac + lip, δ=1.33 ppm)

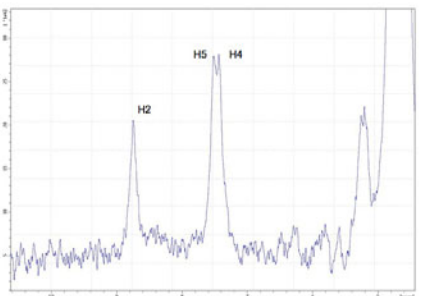

Figure 2 : Zoom in the ISUCA region showing peak corresponding to the pH-sensitive H2 resonance at 8.75ppm and H4-H5 peaks at 7.35 and 7.55 ppm

Discussion/Conclusion: These preleminary results reports the use of ISUCA for pHe measurement by 1H-MRS on HT-29 subcutaneous xenografts. We observed an acidification of pHe two weeks only after cells injection wihich is in agreement with previous studies on several cell-lines using other techniques
References:
Ojugo et al. (1999). *NMR in biomedicine*, *12*(8), 495–504.
van Sluis et al. (1999). Magnetic resonance in medicine, 41(4), 743–750.
García-Martín et al. (2001). Cancer research, 61(17), 6524–6531. Jordan et al. (2005). NMR in biomedicine, 18(7), 430–439.
Provent et al. (2007). Cancer research, 67(16), 7638–7645.

467

Improving the evaluation of cardiac function in rats at 7T by using non-local means filtering

B. Tricot[1], M. Descoteaux[2], M. Lepage[1], O. Lesur[3], L. Tremblay[1], F. Chagnon[3], **A. Lalande**[4]
[1]Centre d'Imagerie Moléculaire de Sherbrooke, Université de Sherbrooke, Sherbrooke/QC/CANADA, [2]Sherbrooke Connectivity Imaging Lab, Université de Sherbrooke, Sherbrooke/QC/CANADA, [3]Centre de Recherche Clinique Etienne-LeBel, Université de Sherbrooke, Sherbrooke/QC/CANADA, 4LE2I (UMR CNRS 6306), University of Burgundy, Dijon/FRANCE

Purpose/Introduction: Multi-element cardiac coil arrays are often required for signal reception to attain high-quality images of the rat heart [1]. These coils are not yet widely available. We investigated the effect of the non-local means filter [2] on lower quality cardiac cine-MR images, particularly on the accuracy and the variability of cardiac function parameters.
Subjects and Methods: Nine rats (n=9) were scanned using a 7T Varian scanner, with a 63mm-diameter volume coil. Series of short-axis cine images covering the left ventricle were obtained with an ECG and respiratory-gated cine-FLASH sequence (in plane resolution: 195x195µm² ; slice thickness : 1mm ; 16 frames).
Hearts were excised after image acquisition, and the left ventricle mass (LVM) was determined by ex vivo measurement of the weight of the heart.
Each 3D image of the cardiac cycle was denoised using non-local means filtering with automatic noise standard deviation estimation of the background, search volume of 1331 neighbors and neighboring size of 26 neighbors [2] (Figure 1).
Cine images were manually segmented using Segment , twice by the same observer, and by two different observers. The end-diastolic and end-systolic volumes (EDV, ESV), the ejection fraction (EF) and the LVM were calculated. A two-tailed paired Student's t-test was used to determine any significant differences between measurements from different segmentations ($p<0.05$).

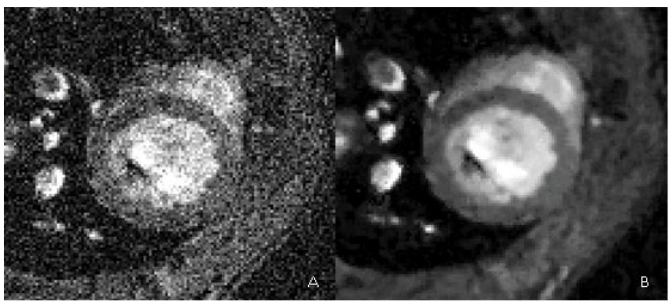

Figure 1 – Short-axis image of the rat heart A) acquired from the MR scanner (non-denoised) B) after non-local means filtering (denoised). Contrast-to-noise ratio (CNR) was 7±2 for non-denoised images and 23±8 for denoised images.

Results: There was a good agreement between values of the LVM from ex vivo measurements and from manual segmentation of both sets of images (Table 1). Significant differences were found for observer B with the non-denoised images whereas there were no significant differences with the denoised images. Intra-observer variability (Table 2) was small in general with both datasets with the exception of ESV and no significant differences were found. The variability decreased for every parameter with the denoised images.
The inter-observer variability decreased for all the parameters with the denoised images except for the EDV.

	Non-denoised images			Denoised images		
	Mean difference (mg)	Relative difference (%)	r	Mean difference (mg)	Relative difference (%)	r
Observer A	-1.8 ± 22.4	-0.6 ± 4.5	0.99	1.8 ± 21.3	0.6 ± 3.6	0.99
Observer B	28.6 ± 32.8*	4.5 ± 5.7	0.98	22.9 ± 34.0	3.3 ± 5.5	0.99

Table 1 – Mean values ± standard deviation (SD) and correlation coefficient *r* for the comparison of LVM obtained from ex-vivo measurement and from the segmentation of cine images. *$p<0.05$

	Non-denoised images		Denoised images	
	Mean difference	Relative difference (%)	Mean difference	Relative difference (%)
Intra-observer				
EDV (µL)	-2.1 ± 15.0	-0.4 ± 3.7	4.7 ± 14.9	1.1 ± 3.1
ESV (µL)	-5.3 ± 15.4	-5.2 ± 12.8	-2.8 ± 11.6	-1.4 ± 7.7
EF (%)	1.2 ± 2.8	1.7 ± 3.9	0.5 ± 2.0	0.6 ± 2.7
LVM (mg)	13.9 ± 30.3	1.6 ± 4.2	-4.4 ± 27.7	-0.3 ± 4.6
Inter-observer				
EDV (µL)	28.8 ± 9.7*	5.5 ± 2.1	27.11 ± 25.72*	5.4 ± 5.0
ESV (µL)	21.4 ± 21.9*	12.4 ± 13.1	14.2 ± 18.0*	8.2 ± 11.1
EF (%)	-1.9 ± 4.0	-2.7 ± 5.7	-0.7 ± 2.7	-1.0 ± 3.7
LVM (mg)	1.0 ± 39.9	0.6 ± 6.6	27.3 ± 40.2	3.2 ± 5.6

Table 2 – Intra and inter-observer variability for manual segmentation of non denoised images and denoised images. *$p<0.05$

Discussion/Conclusion: Each observer had to determine the most basal slice to include in the analysis, resulting in significant differences for EDV and ESV. Overall, intra and inter-variability of cardiac function parameters were reduced with the denoised images, comparing well with results from previous reports [1,3]. Denoising could be an interesting alternative to the need of better contrast between myocardium and surrounding tissues. The influence of denoising on semi-automatic segmentation will be the object of future work.
References:
[1] Riegler, J., JMRI, 2010, 869-877
[2] Coupé P., IEEE Trans. Med. Imag., 2008, 425-441
[3] Heijman E., JMRI, 2008, 86-93

468

Optimisation of Diffusion Weighted MRI in mouse liver in vivo at 9.4T

W.P. Węglarz, K. Jasinski, T. Skorka
Department of Magnetic Resonance Imaging, Institute of Nuclear Physics PAN, Kraków/POLAND

Purpose/Introduction: Due to presence of abundant blood carrying capillaries dependence of the diffusion weighted signal on applied *b*-values in the liver shows presence of two components: the fast decaying due to perfusion (pseudodiffusion) and the slow decaying related to true diffusion [1]. So far most of the reported MRI work on characterization of diffusion in liver was done on human subjects in clinical environment. Mice models of liver pathologies bring opportunities for studying conditions for development of pathologies and searching for efficient therapies. The aim of this work is characterization of the diffusion in liver of the laboratory mice and optimization of the measurement protocols in order to minimize experimental time necessary to collect quantitative data at 9.4 T preclinical MRI scanner.
Subjects and Methods: BALB/c mice were anesthetized with 2% isoflurane and placed in the prone position. Respiratory trigger was supplied using pneumatic pillow sensor (SA Instruments Inc., Stony Brook, NY, USA). Single Shot Diffusion Weighted EPI (TE=17ms, TR=3000ms, D=10.3ms, NA=18) was accomplished using 9.4T/21cm horizontal bore Bruker Biospec MRI scanner, equipped with 30 mm birdcage quadrature rf coil. Matrix size was 96x64, FOV 30x23mm and slice thickness 1mm. Sixteen MR images for different b-values ranging from 60 to 2300 s/mm², covering fast and slow diffusing parts of the signal decay were collected. For analysis, the DW images obtained for three orthogonal diffusion gradients were averaged to improve SNR. Biexponential, pixel-by-pixel analysis based on IVIM model [1] was applied using custom written Matlab (MathWorks, Natick, MA, U.S.A.) script.
Results: Reasonably artifact free DWI images (see Fig. 1) were obtained. Maps of the true diffusion (D_{true}), pseudodiffusion (D_p) and perfusion fraction (f) resulting from biexponential analysis of the full data set are shown in Figs. 2-4 respectively. The regions of major arteries were excluded from analysis. Example of the two different dependence of the signal decay on b-values from two chosen regions is shown in Fig. 4. In general, for b-values smaller than 300 s/mm2 significant fraction of pseudodiffusion is observed albeit it depends on the region of the liver.

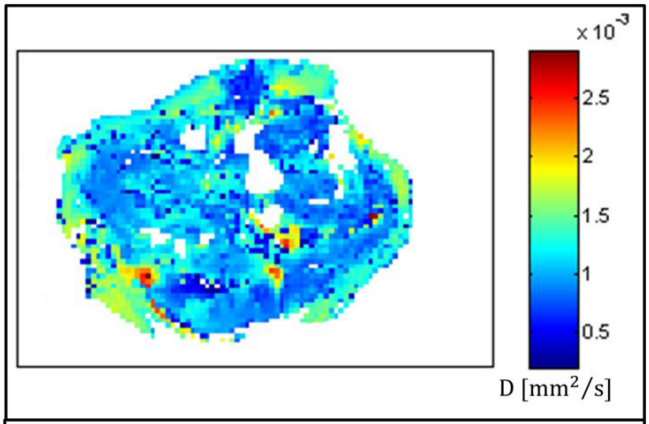

Fig.2. Calculated map of the true diffusion in mouse liver.

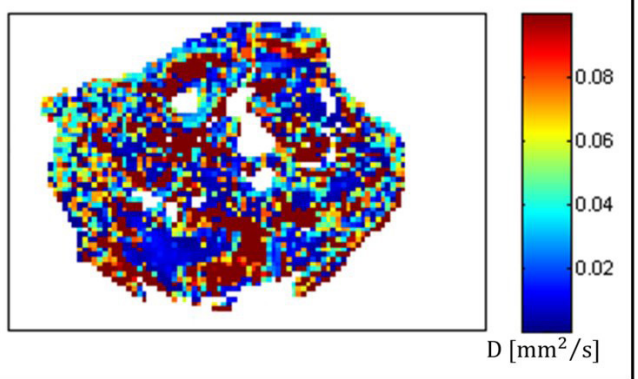

Fig.3. Calculated map of the psudodiffusion in mouse liver.

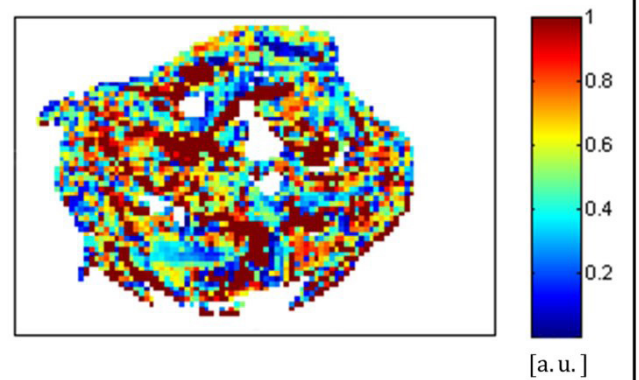

Fig.4. Calculated map of the perfusion fraction in mouse liver.

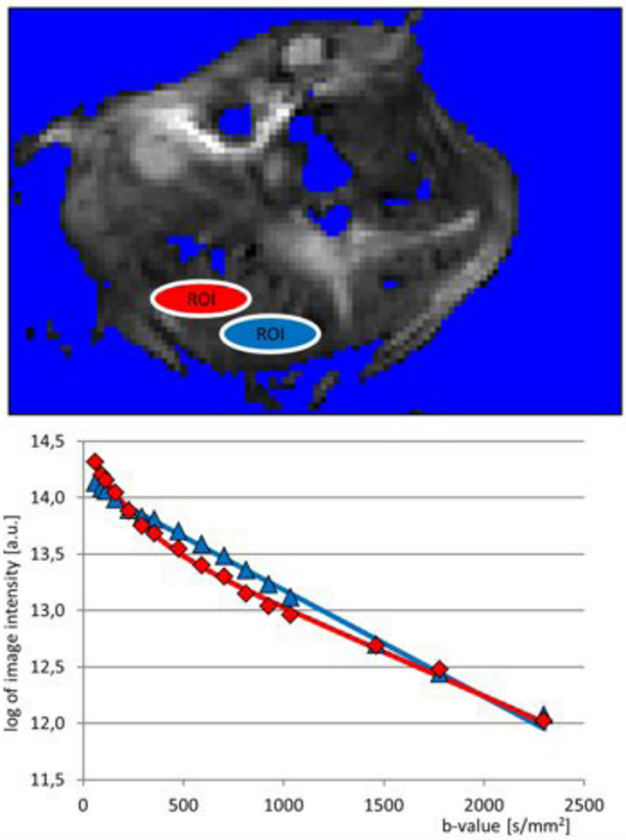

Fig.1. Anatomical single shot EPI image of mouse liver *in vivo* with two examples of the diffusion weighted signal dependence on b-factor for two chosen ROIs. Areas of large arteries are excluded from the imge.

Discussion/Conclusion: Characterization of the diffusion/pseudodiffusion relations for different regions of liver allows for optimization of the measurements protocols in order to save experimental time and still get quantitative results.
This research was supported through grant coordinated by JCET-UJ, NoWND-POIG.01.01.02-00-069/09-00.

References:

1. Le Bihan D (2008) Radiology; 249:748–52

EPOS™ Poster

Animal models - pathologies

469

MRI characterization of a novel mouse model of Staphylococcus aureus chronic osteomyelitis

V. Hoerr[1], S. Horst[2], C. Kreis[3], L. Tuchscherr[4], J. Kalinka[4], B. Löffler[4], E. Medina[2], **C. Faber**[1]
[1]Department of Clinical Radiology, University Hospital Muenster, Muenster/GERMANY, [2]Infection Immunology Research Group, Helmholtz Centre for Infection Research, Braunschweig/GERMANY, [3]Clinic of Trauma-, Hand-, and Reconstructive Surgery, University Hospital Muenster, Muenster/GERMANY, [4]Institute of Medical Microbiology, University Hospital Muenster, Muenster/GERMANY

Purpose/Introduction: *Staphylococcus aureus* is the major cause of severe bone infection known as osteomyelitis [1], but its pathogenesis remains poorly understood and treatment options are unsatisfactory [2,3]. Therefore, a major need exists for development of novel diagnostic and therapeutic tools. Here, we have characterized and validated a novel mouse model of staphylococcal osteomyelitis using MRI and radiography.
Subjects and Methods: Mouse-model: 10-weeks-old female C57BL/6 mice were inoculated with 10^6 CFU of *S. aureus* (strain 6850) in 150 µl PBS via a lateral tail vein and developed metastatic chronic osteomyelitis.
Imaging: 3D gradient echo images (TE/TR=3.1/20.0 ms, resolution: 88x98x196 µm) were acquired on a Bruker BioSpec94/20. X-ray radiography was performed on a Kodak imaging system using an exposure time of 40 seconds.
Analysis: Volume of tibiae and lesions was segmented and quantified using Amira. Biomechanical stability of the tibiae was assessed with a torsion angle test (Llyod-Instruments "LE5K-plus", UK). Animal data were compared to X-ray, MRI and histology of two human osteomyelitis patients.
Results: Sequential MR and X-ray imaging was performed to investigate the progression of osteomyelitis in *S. aureus*-infected mice during the acute and chronic phase. Inflammatory lesions in the tibia became apparent by MRI but not by X-ray already 3 days after bacterial inoculation and expanded continuously over time. During the chronic phase both MR and X-ray images revealed progressive bone deformation which resulted in increased bone volume up to a factor of five. Inflammatory lesions and bone deformation in the murine model varied between animals, but perfectly reproduced observations in human osteomyelitis patients.
Biomechanical measurements showed that flexibility of deformed tibiae decreased, resulting in increased risk for fractures. Histology of infected bones during both early and chronic phase of infection revealed intense bacterial multiplication, massive neutrophil infiltration, and bone remodeling by osteoclast activity and formation of woven bone structures. All these observations were in full concordance with findings in tissue samples from osteomyelitis patients.

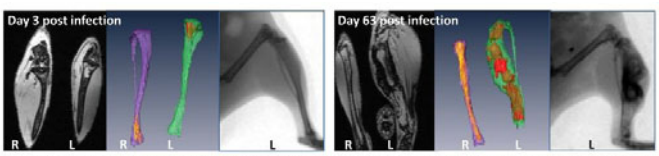

MR characterization and quantification of *S. aureus* induced osteomyelitis. Inflammation and bone deformation was investigated in the tibia of mice in vivo on day 3 through day 63 post infection. Tibiae and inflammatory lesions (bright areas in the bone) were segmented in the MR images and were reconstructed three dimensionally: non-inflamed area of the right leg shown in magenta, non-inflamed area of the left leg shown in green. Red and orange color represents inflammatory lesions.

Discussion/Conclusion: The animal model of staphylococcal haematogenous osteomyelitis precisely mimics the pathophysiological features of the human disease. Compared to radiography, MRI proved to be more sensitive for charcterization of osteomyelitis. Due to the inter-animal variations, non-invasive imaging is required to use this model for the assessment of novel treatment modalities.

References:
[1] Wright JA et al (2010) Int J Med Microbiol 300:193-204. [2] Foster TJ et al (2005) Nat Rev Microbiol 3:948-958. [3] Lowy FD et al (1998) N England J Med 339:520-532.

470

Preclinical evaluation of diffuse changes in operated liver with a cold plasma hemostasis, in rat: morphofunctional study, MRI with Gd-EOB-DTPA

O.Y. Borodin[1], E. Semichev[2], M. Belyanin[3], V. Ussov[1], V. Filimonov[3], M. Sannikov[4], P. Bushlanov[2], A. Baikov[2], G. Dambaev[5]
[1]Tomography Research Lab, Institute of Cardiology of the Siberian Branch of the Russian Academy of Medical Sciences, Tomsk/RUSSIAN FEDERATION, [2]Central research laboratory, Siberian State Medical University, Tomsk/RUSSIAN FEDERATION, [3]Biotechnology and organic chemistry, Tomsk Polytechnic University, Tomsk/RUSSIAN FEDERATION, [4]MRI facility, Siberian State Medical University, Tomsk/RUSSIAN FEDERATION, [5]Department of Hospital Surgery, Siberian State Medical University, Tomsk/RUSSIAN FEDERATION

Purpose/Introduction: Magnetic resonance imaging (MRI) is the most promising method for noninvasive diagnosis of morphological and functional changes in the hepatobiliary system. The purpose of this study was to examine various parameters reflecting the severity of liver damage in a cold plasma hemostasis using the MRI contrast in dynamics.
Subjects and Methods: The study was performed on a commercial MRI magnetic field strength 1.5 Tesla. In in vivo experiments involved rats of Wistar breed n = 15. The study design consisted of the 1st control group (n = 5) - intact animals without surgical intervention; group 2 - after removal of the left lobe of the liver in 90 days (n = 5) and the third - after the surgery through 180-th day (n = 5). Hemostasis site removal of the left lobe of the liver produced using non-equilibrium plasma. Sterile solutions were injected bolus Gd-EOB-DTPA against a dynamic scanning protocol 3D FFE for 45 minutes. And the average rate of contrast-noise ratio (CNR) and standard deviation (SD) for the liver. Statistic analysis was performed with Kruskal-Wallis test and Mann — Whitney U-test.
Results: In the morphological study of postoperative 90th day of the observed vascular disorders that are manifested edema, thrombosis and in the expansion of the central and interlobular veins (Fig.1 and 2).

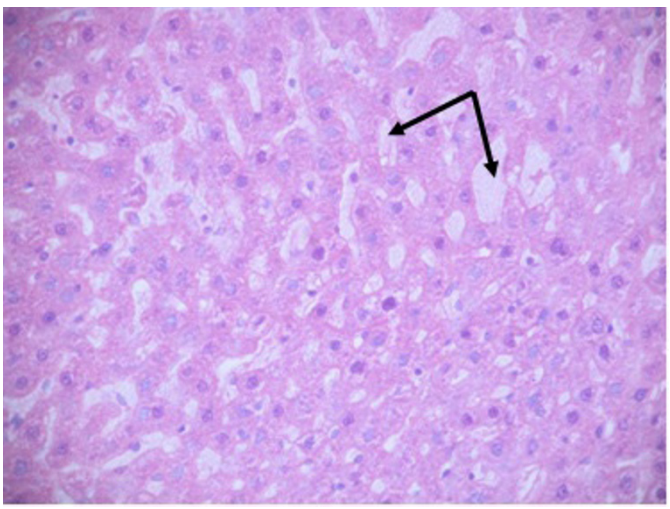

Fig.1. Histological preparation of the liver parenchyma on the 90th day after hemostasis with a cold plasma. Stained with hematoxylin and eosin. The arrows indicate the enlarged sinusoids.

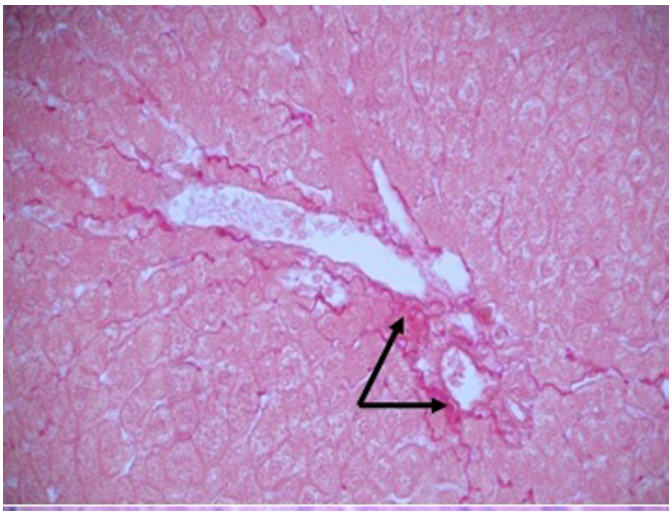

Fig.2.Also, Van Gieson stain. The arrows indicate fibrosis.

In the study with Gd-EOB-DTPA on 90-th day there was a significant (p<0,05) reduction in the contrast effect (Fig.3).

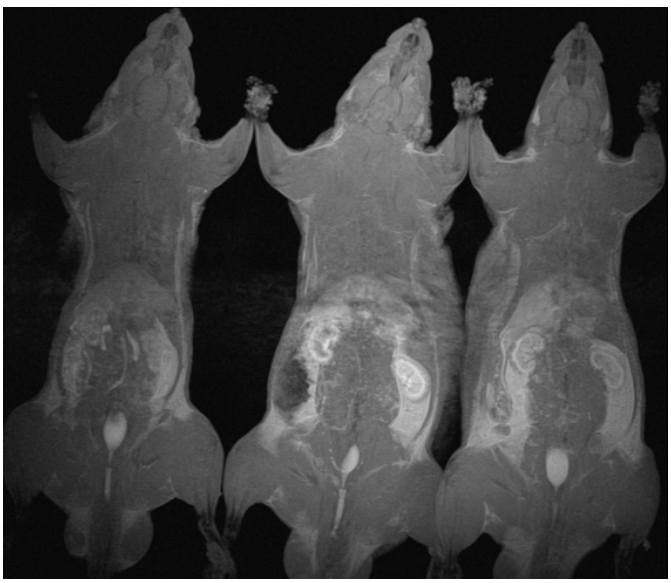

Fig.3. 3D FFE on the 90-th day after syrgery on 12 minute contrast enchance with Gd-EOB-DTPA.

By the 180th days significantly increased contrast effect of the liver, compared with 90-days, but no significant differences (p>0,05) with respect to the control were detected (Fig.4).

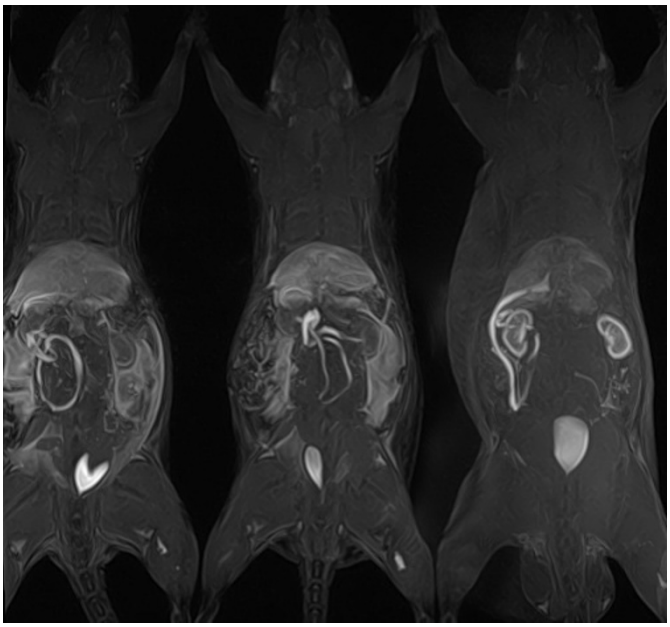

Fig.4. Also, on 180-th day.

Biochemical blood parameters revealed significant differences in the groups studied only in terms of glucose.
Discussion/Conclusion: Liver specific contrast media Gd-EOB-DTPA can detect diffuse changes in liver tissue and to assess their dynamics in time for the expression of contrasting nature of the effect. Using a non-equilibrium plasma hemostatis operated rats on the liver to the 180th days was accompanied by restoration of the morphology of the liver parenchyma.

471

Visualizing lung infection with retrospectively gated MRI in a mouse model for cryptococcosis

G. Vande Velde[1], T. Dresselaers[1], E. Verbeken[2], K. Lagrou[3], **U. Himmelreich**[1]
[1]Biomedical MRI unit, KU leuven, Leuven/BELGIUM, [2]Imaging & Pathology, KU Leuven, Leuven/BELGIUM, [3]Laboratory of Clinical Bacteriology and Mycology, KU Leuven, Leuven/BELGIUM

Purpose/Introduction: *Cryptococcus neoformans* and *C.gattii* are pathogenic yeasts causing life-threatening disease in both immuno-competent and immuno-suppressed individuals. Cryptococcosis mostly affects the lung and may spread to the brain, causing meningitis and/or pseudocystic lesions in the brain. It remains unknown why, how and when the cryptococci are able to cross an apparently intact blood-brain-barrier. Histology remains essential to unravel cellular and molecular interactions, but imaging techniques are indispensible to define the relevant time frames for each animal individually to investigate crucial events in pathogenesis. As current imaging tools cannot evaluate cryptococcal pneumonia with good temporal and spatial resolution *in vivo* (for example, µCT is limited because of radiotoxicity concerns), advances in lung MRI techniques to follow-up disease progression non-invasively will greatly enhance this research. We aimed at dynamically monitoring cryptococcosis non-invasively in individual animals in a mouse model for cryptococcal pneumonia and meningo-encephalitis, establishing the kinetics of cryptococcal lung infection and spreading to the brain, thereby defining the critical time points for histological and immunological analysis of key events in the pathogenesis of cryptococcosis.
Subjects and Methods: Immunocompetent mice (Balb/C) were infected by inhalation of a *C. gattii* R265 cell suspension, scanned at baseline and weekly up to 5 weeks post infection with retrospectively gated MRI (9.4T, Bruker, Paravision 5.1, IntraGate) and CT (SkyScan 1076) and lung parameters quantified. Lungs and brains were isolated for histology and quantification of fungal load.

Results:

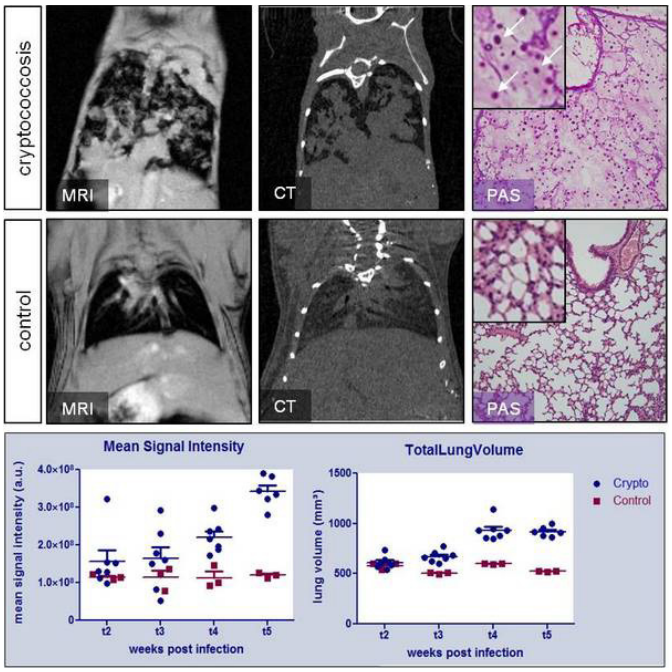

Pneumonial cryptococcosis was successfully and reproducibly induced in immunocompetent mice. While the mice showed no clinical signs of cryptococcosis, progression of the lung pathology and compensatory mechanisms could be non-invasively visualized and quantified using the here evaluated protocol for IntraGate MRI and validated by CT, histochemistry and fungal load quantification at all time points post infection (Figure).

Discussion/Conclusion: This is the first study showing that non-invasive monitoring of pneumonial cryptococcosis is feasible with retrospectively gated MRI (Intragate, Bruker) and CT resulting in high resolution and contrast images. This imaging approach will allow longitudinal screening of animals, without radiotoxicity concerns when using MRI, thereby visualizing infection onset and progression on an individual basis and far before the appearance of any phenotypical signs of disease. We will further fine-tune the timing of disease onset and correlate this with the time of traversal of *C. neoformans* and *C.gattii* cells to the CNS. MR imaging of cryptococcosis will greatly help unraveling the still enigmatic pathogenesis of this life-threatening disease.

472

Correlation of late gadolinium enhancement in cardiac Magnetic Resonance Imaging with wall thickness, heart mass and histopathological examinations in a rat model of autoimmune myocarditis

W. Kromen[1], H.K. Korkusuz[2], S. Lindemayr[1], R.W. Bauer[1], T.J. Vogl[1]
[1]Dept. of Diagnostic and Interventional Radiology, J.W. Goethe University Hsopital Frankfurt am Main, Frankfurt am Main/GERMANY, [2]Clinic of Nuclear Medicine, J.W. Goethe University Hospital Frankfurt am Main, Frankfurt am Main/GERMANY

Purpose/Introduction: Myocarditis is a possibly life-threatening disease which clinically presents with a large spectrum of symptoms and which is still not fully understood in all details. The objective of the current study was to examine localisation and extent of late gadolinium enhancement in cardiac MRI and to correlate these findings to inflammatory reactions like mycardial wall thickening and increase of heart mass and to underlying histopathological changes in an experimental animal model of autoimmune myocarditis.

Subjects and Methods: Twenty male Lewis rats were randomly allocated to an experimental and a control group of ten animals each. Experimental autoimmune myocarditis (EAM) was induced by application of porcine Cardiac Myosin (pCM) and Complete Freud's Adjuvance (CFA). On day 21, all the animals were examined with Turbo Flash and Turbo Spin Echo sequences in cardiac MRI. Serological levels of Haptoglobin and Troponin T were determined and histopathologically identified grade and localisation of myocardial inflammation as well as inflammatory changes like increase in heart mass and thickening of the myocardial wall were correlated to extent and distibution of late gadolinium enhancement (LGE) in cardiac MRI.

Results: Histopathological signs of myocardial inflammation and LGE were mainly found in the left lateral and in the left anterior sections of the rat heart. Localisation of the LGE in cardiac MRI and the histopathological loci of inflammation showed high correlatinon. Myocardial mass and left ventricular wall thickness were significantly elevated in the experimental animal group. Myocyardial wall thickness and heart mass were well correlated to the amount of LGE in cardiac in the left lateral wall section of the myocardium and myocardial wall thickness showed good correlation to the histopathological severity of inflammation. Troponin T and haptoglobin levels were not correlated to myocardial mass and wall thickness.

Discussion/Conclusion: We were able to show a typical distribution pattern of LGE in a rat animal model of experimental autoimmune myocarditis (EAM). The pattern of LGE showed a good correspondence to the histopathologically determined distribution of myocardial lesions. Myocardial wall thickness and heart mass indicate the extent of LGE and the myocardial damage and are thus good markers for the severity of myocardial inflammation. Despite of the tininess of the rat heart the used experimental setup is a well working model for human myocarditis.

References:

Cooper LT Jr (2009) Myocarditis. N Engl J Med 360(15):1526–1538
Izumi T, Takehana H, Matsuda C, Yokoyama H, Kohno K,Suzuki K, Inomata T (2000) Experimental autoimmune myocarditis and its pathomechanism. Herz 25(3):274–278

473

Functional MRI for Assessment of Novel Chemokine-Directed Therapy of Renal Allograft Rejection in a Murine Animal Model

M. Notohamiprodjo[1], A. Kalnins[2], M. Kolb[1], A. Tischer[2], M. Reiser[1], K. Nikolaou[1], J. Andrassy[2]
[1]Department of Radiology, University Hospitals Munich, Munich/GERMANY, [2]Surgery, University Hospitals Munich, Munich/GERMANY

Purpose/Introduction: Renal allograft rejection is associated with monocyte chemoattractant CC chemokine ligand 2(CCL2) - dependent glomerular and interstitial macrophage recruitment. CCL2 blockade with the Oligonucleotide/Spiegelmer mNOX-E36-3'PEG inhibits leukocyte recruitment in inflammatory kidney disease. The purpose of this study was to evaluate functional MRI, e.g. MR-Renography and Diffusion Weighted Imaging (DWI) for assessment of this novel chemokine-directed therapy in an experimental murine animal model.

Subjects and Methods: An orthotopic renal transplant mouse-model with acute allograft rejection (balb/c into C57/BL6) was used. 5 animals were treated with low-dose Cyclosporin A in combination with mNOX. 7 animals did not receive treatment. 3 syngenic controls (C57/BL6 into C57/BL6) were performed.

Functional MRI was conducted at 3T (Magnetom VERIO, Siemens Healthcare Sector) with a dedicated mouse coil (Rapid Biomedical). Diffusion weighted imaging was performed with b-values ranging 0 to 800 s/mm² (0.8x0.8x3mm). MR-Renography with deconvolution analysis was performed with a TWIST-sequence with a temporal resolution of 1.5 seconds. (0.6 x 0.6 x 3mm) following a bolus of 10µl Gadobutrol (Bayer Schering Pharma) in 100µl NaCl. Significance between subgroups was assessed with Wilcoxon´s rank-sum test.

Results: Syngenic allograft showed substantially higher plasma flow (53.2 ± 17.2 ml/100ml/min) and significantly lower ($p<0.05$) ADC (1.20 ± 0.02mm²/s) than native kidneys (44.1±7.1 ml/100ml/min and 1.29±0.09 mm²/s). Allograft-ADC of treated animals (0.98±0.14mm²/s) was substantially higher than of untreated animals (0.76±0.17mm²/s). Cortical plasma flow (24.5±5.5ml/100ml/min) was significantly lower ($p<0.05$) for untreated animals compared to treated animals (37.4±7.6ml/100ml/min). Volume of distribution and mean transit time did not show significant differences between the subgroups.

Discussion/Conclusion: Chemokine-directed treatment ameliorates acute renal allograft rejection. Functional MRI is able to non-invasively assess these

therapy effects in this experimental model and holds high potential to become an alternative to invasive organ biopsy.

474

A non-invasive ^{23}Na MRI study revealing that Nitroglycerin may be a synergistic factor for apoptotic propagation in tumors after photodynamic therapy.

C.D. Thomas[1], **F. Poyer**[1], M. Lupu[1], P. Maillard[2], J. Mispelter[1]
[1]Imagerie Intégrative, Inserm U759/ Institut Curie/Université Paris XI, Orsay/ FRANCE, [2]UMR 176, Institut Curie/ UMR176 CNRS/ Université Paris XI, Orsay/FRANCE

Purpose/Introduction: The aim of the study was to assess by sodium magnetic resonance imaging (^{23}Na MRI) the efficacy of a treatment protocol that combines photodynamic therapy (PDT) and nitroglycerin (NG) on human retinoblastoma tumors xenografted on nude mice. PDT implies the use of a non-mutagen photosensitizing agent (PS : glycoconjugated-meso-substituted-porphyrin derivative) activated by visible light. Absorption of light initiates the photochemical reactions leading to the generation of cytotoxic products responsible for the therapeutic effects. Vasculature damage and necrosis or apoptosis decrease cell density and increase the local sodium concentration [1]. 23Na MRI directly monitors variations of sodium concentrations in a non-invasive way, it can be used to follow-up the tumor response to therapy [2]. NG is known to dilate vessels and enhance the permeability and retention of macromolecules in solid tumors [3].
Subjects and Methods: PDT (650nm), targeting both blood vessels and cancer cells, was followed by ^{23}Na/^{1}H MRI. NG ointment (0.2mg) was applied 1h before the first PS i.v. injection. The first dose of PS was followed by a second dose, separated by a 3h interval. This time lapse allowed the first dose of PS to penetrate into tumor cells. Ten minutes after the second dose, tumors were exposed to red light. Two PDT treatments were performed at 4 days interval.
Results: PDT treatments hindered the tumoral progression, stopped it and increase the % of necrosis (Fig.1-2). The NG acted as a synergistic factor in decreasing the tumor by increasing the PS concentration at the tumor level. On the other hand the increased quantity of cellular debris generated by PDT may initiate a bystander effect (Fig. 3).

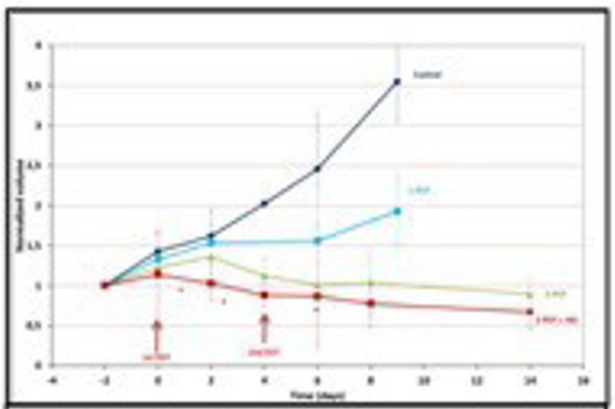

Fig.1 : Normalized tumor volume evolution of Retinoblastoma

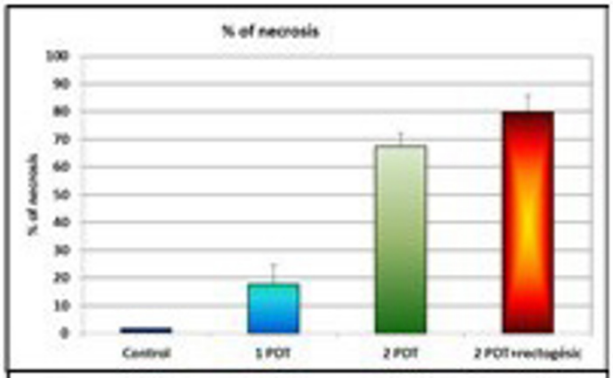

Fig.2 : Percentage of necrosis at the end of the follow-uo

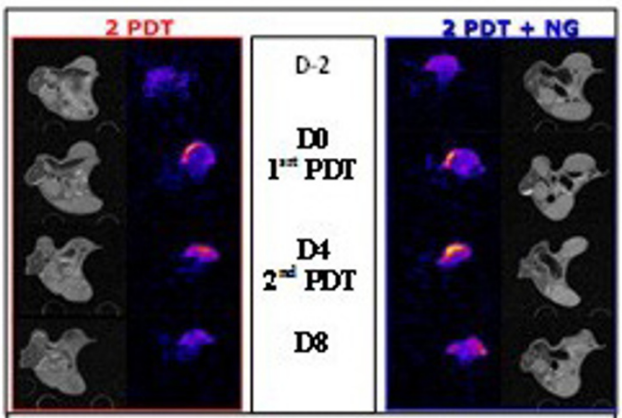

Fig.3 : Longitudinal follow-up of Retinoblastoma xenografted tumors imaged by ^{23}Na/^{1}H MRI.

Discussion/Conclusion: In this study we reported that the PDT effect was enhanced by applying nitroglycerin ointment on the tumor-bearing animal's skin. PDT initiates the bystander effect on retinoblastomas, NG increases this effect. Our work indicates that in vivo dual ^{1}H and ^{23}Na MRI is a non-invasive technique well suited for both longitudinal follow-up and early treatment assessment. The transition from low sodium signal before treatment to high sodium signal characteristic of damaged areas is very rapid, sometime over a couple of hours. The sodium imaging is well suited for longitudinal studies and for assessing treatment protocols especially anti-tumoral ones.
References:
[1] Thomas CD et al., Proc.Intl.Soc.Mag.Reson.Med., 2008, 16: 2795.
[2] Lupu M et al., PDPDT, 2009, 6: 214.
[3] Matsumura Y., Cancer Res, 1986, 46: 6387-92.

475

VO(dmpp)$_2$ reverts pre-diabetic features in fatty Zucker rats: MRI/MRS techniques as non-invasive powerful tools in drug development

A.M. Martins Metelo[1], R. Pérez-Carro[2], M. Castro[3], P. Lopez-Larrubia[1]
[1]Experimental models of human disease, Instituto de Investigaciones Biomédicas, CSIC/UAM, Madrid/SPAIN, [2]Departamento de Modelos experimentales de enfermedades humanas, Instituto de Investigaciones Biomédicas "Alberto Sols", Madrid/SPAIN, [3]Life Sciences, University of Coimbra, Coimbra/PORTUGAL

Purpose/Introduction: Type 2 Diabetes *mellitus* is characterized by a deregulation of the glucose metabolism, which contributes to the development of other pathologies such as obesity, cardiovascular diseases and cancer[1]. Different studies have showed the anti-diabetic properties of vanadium compounds (as BMOV) and their efficacy encouraged their use in human clinical trials[2]. Recently, bis-[3-hydroxy-1,2-dimethyl-4-pyridinonato]oxovanadium(IV), also called VO(dmpp)$_2$, was shown to be more efficient than BMOV *in vitro* without showing any toxicity signs[3]. In this study, the therapeutic effect of VO(dmpp)$_2$ was evaluated *in vivo* using obese Zucker rat as an animal model of pre-diabetes. Moreover, here we show the ability of MRI/MRS to be used as a non-invasive tool in drug development and early diagnosis of diabetes.
Subjects and Methods: Lean Zucker (fa/+) and obese Zucker (fa/fa) rats (7 weeks-old) were used to test the insulin-mimetic properties of VO(dmpp)$_2$. During four weeks, animals were daily weighted and intraperitoneally injected with VO(dmpp)$_2$ (15mg/Kg body weight) or serum (n=8 per group). Once a week, the hepatic triglyceride (HTG) content and subcutaneous fat width was analysed using ^{1}H MRS and T1W MR images, respectively. On the last day of the experiment, a glucose tolerance test was performed to confirm the glycaemic profile of the animals.
Results: After VO(dmpp)$_2$ treatment, different parameters indicative of obesity, insulin resistance and pre-diabetes were completely reverted in obese Zucker rats, such as gain of body weight, subcutaneous fat width and glucose intolerant profile. The high HTG content of obese Zucker rats was also significantly and continuously decreased (P<0.0005) during VO(dmpp)$_2$ treatment.

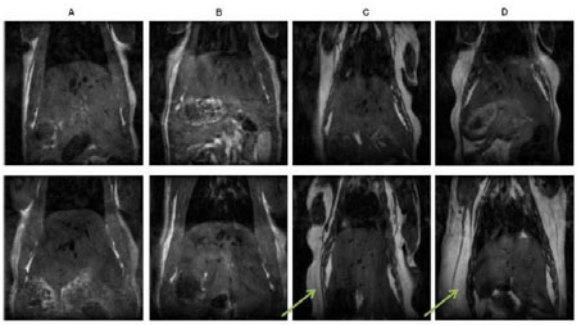

Figure 1 – Coronal T1W images of the liver of four different rats acquired with MSME sequence: non-treated lean Zucker rat (A), $V^{IV}O(dmpp)_2$-treated lean Zucker rat (B), $V^{IV}O(dmpp)_2$-treated obese Zucker (C) non-treated obese Zucker rat (D), in the 1st (top) and in the 30th day of the study (bottom). The difference between the subcutaneous fat width of obese-treated and obese non-treated rat is shown by the arrows.

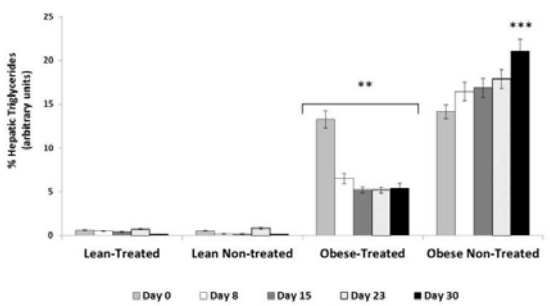

Figure 2 – Graphical representation of HTG content (%) in the four groups of rats during the study. HTG content was quantified by ^{1}H MRS. ^{1}H MR spectra were acquired from four different ROIs (Region Of Interest) in the liver of each animal. The intensity of the water and fat signals was used to calculate the HTG percentage in arbitrary units. Data are shown as mean values ± SEM. Paired bilateral *t* test and one-way ANOVA were used in statistical analysis to compare two or more groups respectively, where P < 0.05 was considered to be significant. ** P < 0.005; Obese-treated rats at Day 0 *vs.* Day 8 *vs.* Day 15 *vs.* Day 23 *vs.* Day 30. *** P < 0.0005; Obese-treated *vs.* Obese non-treated at Day 30.

Discussion/Conclusion: Here we show that VO(dmpp)$_2$ treatment reverts different physiologic parameters of obese Zucker rats which are usually associated with pre-diabetes. Since VO(dmpp)$_2$ is more efficient than BMOV *in vitro* and it is therapeutically active *in vivo*, it becomes a strong candidate to enter in future steatosis, obesity or Type 2 diabetes clinical trials. Moreover, by using MRI techniques we were able to follow the activity of this compound *in vivo*. Consequently, MRI/MRS showed to be *in vivo* accurate and non-invasive tools to be used for an early diagnosis of diabetes and other metabolic disorders in humans.
References:
[1]Hsueh W *et al.*(2010) *Postgrad Med.* 122(4):129-43. [2]Sakurai H *et al.* (2008) *Chemical Society Reviews*. 37(11):2383-2392. [3]Passadouro M *et al.* (2010) *Journal of Inorganic Biochemistry*. 104(9):987-992.

476

Lipomatous Metaplasia in Rabbits with Chronic Myocardial Infarction: 3.0T MRI and Histopathological Findings

Y. Feng[1], F. Chen[2], Y. Xie[3], M. Miranda Cona[1], Y. Ni[1]
[1]Radiology, UZLeuven, Leuven/BELGIUM, [2]Radiology, KULeuven, Leuven/BELGIUM, [3]ELIS, Gent Univercity, Gent/BELGIUM

Purpose/Introduction: Cardiac lipomatous metaplasia (LM) occurs in patients with chronic ischemic heart disease and heart failure with undetermined mechanisms. We report an animal of LM in rabbits with healed myocardial infarction (MI).
Subjects and Methods: This study was approved by the institutional ethical committee for animal care and use. Under anesthesia and ventilation, MI was surgically induced in dozens of rabbits by open-chest occlusion and close-chest reperfusion of a coronary artery. During follow-up in three cases of them for nine months, multiparametric cardiac magnetic resonance imaging (cMRI) was performed to monitor the evolution of the MI. After animal euthanization, histochemical stainings with triphenyltetrazolium chloride, Masson's trichrome, and hematoxylin-eosin were used for determination of diagnosis.
Results: Morphological and functional changes of the MI from ischemic infarction in acute phase to scar tissues in chronic phase were documented using cMRI. In all three rabbits, scar transformation and fat deposition at infarct sites were suggested by *in vivo* cMRI and the diagnosis of varying degrees of LM was finally established by postmortem techniques.

Table 1 Comparing the global MI size in MRI, SPECT and TTC

The global MI size (%LV)	MRI	123I-MIH SPECT	^{99m}Tc-MIBI SPECT	TTC
No.1	24,23%	27,96%	30,37%	25,30%
No.2	47,12%	51,96%	49,89%	41,68%
No.3	28,32%	37,44%	34,38%	30,35%
No.4	40,89%	44,86%	48,32%	37,40%
No.5	12,24%	16,80%	19,70%	8,84%
No.6	6,45%	8,23%	7,56%	5,32%
No.7	38,05%	47,27%	51,23%	34,93%
No.8	28,19%	35,53%	38,06%	24,13%
Mean±SD	28,19±13,94%	33,76±15,24%	34,94±15,50%	25,99±13,10%

MRI vs MIH p=0.5; MRI vs MIBI p=0.4; MRI vs TTC p=0.8; MIH vs MIBI p=0.8; MIH vs TTC p=0.3; MIBI vs TTC p=0.2.
Obtained from unpaired t-tests, p < 0.05 indicates a significant difference

Table 2 Comparing the MI size slice by slice on autoradiography to MRI, HE and TTC

MI size (n=24)	MRI (% LV)	HE (% LV)	TTC (% LV)	Rx (% LV)
Mean	38,23%	29,03%	31,66%	33, 41%
SD	16,51%	14,44%	15,82%	16,36%

Rx-MRI p=0.3; Rx-TTC p=0.7; Rx-HE p=0.4
Obtained from unpaired t-tests, p <0.05 indicates a significant difference

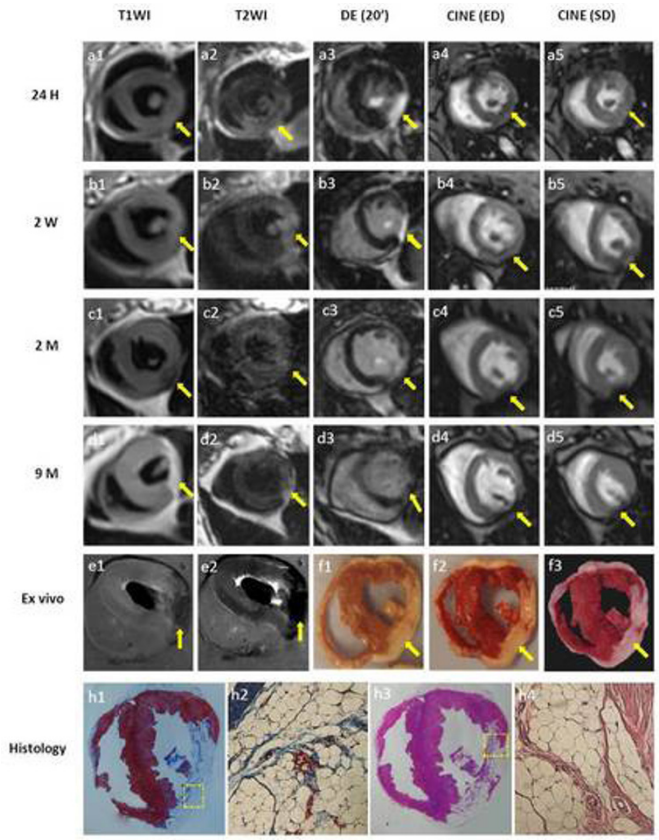

Figure 1 Longitudinal evaluation of progressive changes from infarcted myocardium to large LM (yellow arrow) by in vivo, ex vivo cMRI and histological study.

Discussion/Conclusion: LM can be induced in rabbits with healed MI and visualized by cMRI. Further study using this animal model may provide insights into the mechanisms of LM and contribute to translational research in cardiology.

References:

Kimura F et al. *RadioGraphics*, 2010. 30(1): p. 1587–1602.
Lucke C et al. *Eur Radiol*. 20(9): p. 2074-83.
Feng Y et al. *J Cardiovasc Imaging*, 2009. 25(3): p. 289-98.
van der Laarse A et al. *Int J Cardiovasc Imaging*, 2009. 25(3): p. 299-301.
Feng Y et al. *Journal International Journal of Modelling, Identification and Control* 2010 9 P. 288-310.

477

MRI Monitored Myocardial Therapy: High Dose of Mononuclear Cells in Myocardium after Injection Predicts Improved Recovery after Acute Myocardial Infarction

K. Alestalo[1], R. Korpi[2], S. Lehtonen[1], J. Mäkelä[3], T. Mäkelä[3], F. Yannopoulos[3], E. Rimpiläinen[3], H. A.Jensen[3], K. Ylitalo[4], V. Anttila[3], T. Juvonen[3], E. Lappi-Blanco[5], R. Blanco Sequeiros[2], P. Lehenkari[1]
[1]Department of Biomedicine, Division of Anatomy and Cell Biology, University of Oulu,, Oulu/FINLAND, [2]Department of Radiology, University of Oulu, Institute of Diagnostics, Oulu/FINLAND, [3]Department of Surgery, Clinical Research Center,, University of Oulu and Oulu University Hospital, Oulu/FINLAND, [4]Department of Internal Medicine, Centre of Excellence in Research, University of Oulu, Clinical Medicine, Oulu/FINLAND, [5]Department of Pathology,, Oulu University Hospital, Oulu/FINLAND

Purpose/Introduction: Stem cell therapy has potential in restoring cardiac function after acute myocardial infarction(AMI)(1,2). The mechanisms behind beneficial effects of cell transplantation for myocardial repair remain largely unknown. Superparamagnetic iron oxide (SPIO) and other nanoparticles are used to label cells for direct visualization (3). Our object was to investigate the key mechanisms leading to the myocardial recovery and to study visualization and localization of the transplanted SPIO labeled bone marrow mononuclear cells (BMMC) by using MRI and histology.

Subjects and Methods: 18 pigs were randomized to SPIO labeled BMMC (108 cells/ 2 ml) or saline group. Therapy was administered with direct injection to myocardium after 90 minute occlusion of the circumflex artery. MRI was performed postoperatively and after 3 weeks to evaluate cardiac function and BMMC localization. The heart was divided to 16 segments to compare the localization and amount of the BMMCs between the histology and MRI.

Results: Both MRI and histological evaluation showed that cells were localized in the infarction area. There was a higher increase in EF in BMMC group after 3 weeks of AMI (11% vs. 0.8%) (Fig.1B). The animals with higher EF increase (>11%) during the follow-up, had also more detectable BMMCs by using histology and MRI.

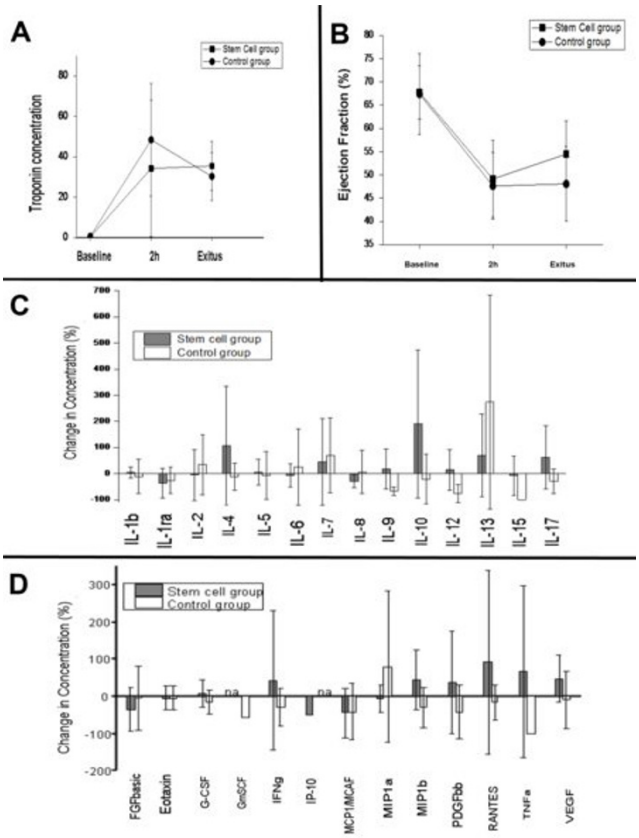

Discussion/Conclusion: MRI is a useful method to evaluate the localization of the transplanted cells. The high dose of BMMCs in myocardium after transplantation predicts improved cardiac function after AMI.

References:

(1) Gyöngyösi M. Lang I. Dettke M. Beran G. Graf S. Sochor H. et al. Combined delivery approach of bone marrow mononuclear stem cells early and late after myocardial infarction: the MYSTAR prospective, randomized study. Nat Clin Pract Cardiovasc Med 2009 Jan;6(1):70-81.

(2) Makela J, Ylitalo K, Lehtonen S, Dahlbacka S, Niemela E, Kiviluoma K, et al. Bone marrow-derived mononuclear cell transplantation improves myocardial recovery by enhancing cellular recruitment and differentiation at the infarction site. J Thorac Cardiovasc Surg 2007 Sep;134(3):565-573.

(3) Addicott B, Willman M, Rodriguez J, Padgett K, Han D, Berman D, et al. Mesenchymal stem cell labeling and in vitro MR characterization at 1.5 T of new SPIO contrast agent: Molday ION Rhodamine-BTM. Contrast Media Mol Imaging 2011 Jan-Feb;6(1):7-18.

478

Lung sodium-23 MRI using ultra-short echo time sequence at 9.4 Tesla

R. Kalayciyan[1], F. Wetterling[2], B. Jung[3], D. Stiller[3], L.R. Schad[1]

[1]Computer Assisted Clinical Medicine, Heidelberg University, Mannheim/ GERMANY, [2]Faculty for Engineering, Mathematics and Science, Trinity College, Dublin University, Dublin/IRELAND, [3]x, Boehringer Ingelheim Pharma GmbH & CO. KG, biberach/GERMANY

Purpose/Introduction: Sodium MRI (^{23}Na-MRI) is a non-invasive technique which already enabled to measure extravascular lung water in rats [1]. The aim of this study was to develop a ^{23}Na-MRI technique for lung tissue imaging in a rodent model of cigarette smoke-induced bronchitis (1 healthy and 3 diseased). In order to maximize the ^{23}Na-signal sensitivity at 9.4T a 3D-Ultrashort Echo Time (3D-UTE) sequence was adapted and a planar transceiver surface resonator was developed.

Subjects and Methods: Five days prior to the imaging experiments the bronchitis-exposed rats (Wistar,male, 305±20g) were exposed to smoke (equivalent 20 cigarettes per day) for four days. All experiments were carried on a Bruker BioSpec 94/20 MRI system (Bruker BioSpin,Germany) under consideration of an appropriate animal license and with institutional ethics approval. For ^{23}Na-scanning a 3D-Ultrashort Echo Time (3D-UTE) pulse sequence [2] was adapted to achieve as short echo time as 135µs with TR/TA=80ms/15min, and nominal voxel size = (1x1x4)mm^3. The double-tuned ^{1}H/^{23}Na resonator system used in this study was composed of a single-tuned ^{1}H birdcage resonator and a home-built single-tuned ^{23}Na surface coil (5x6cm^2 side length, 1.2mm thick silver wire), both being geometrically-decoupled Qloaded/unloaded=140/100). A 3D-FLASH sequence was used for ^{1}H scanning with TE/TR = 3ms/22ms, and a nominal resolution of (1x1x2)mm^3.

Results: The mean and standard deviation of the SNR averaged across all lungs was measured to be 7.5±0.8, which was three times less than the mean ^{23}Na-signal measured in ventricular blood. The ^{1}H and ^{23}Na-MR images for one representative bronchitis rat are presented in Fig. 1 and 2, respectively. The quantitative results for all rats are listed in Table 1. The ^{23}Na-signal was reduced in all three bronchitis rats (37.1± 3.6%) compared to the healthy lung tissue (42.5± 3.5%).

Discussion/Conclusion: The ^{23}Na-signal in lung tissue was reduced by 5-10 % in smoke exposed rats. Considering that smoke induces vascular constriction it was expected that intravascular mean sodium signal can decrease in the used smoke model. In conclusion, ^{23}Na-MRI can be used to measure intravascular ^{23}Na signal in rats. More experiments and higher significance are required to confirm the ^{23}Na-signal reduction in bronchitis rats and to monitor drug efficiency with ^{23}Na-MRI in this model.

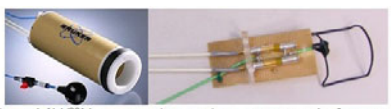

Fig. 1: Double-tuned ^{1}H/^{23}Na resonator system composed of a commercial single-tuned ^{1}H birdcage resonator (left) and a home-built single-tuned ^{23}Na transceiver surface coil.

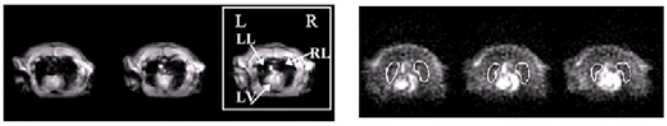

Fig. 2: (left) ^{1}H 3D-FLASH images of rat lung in three axial slices. Left ventricle, left lung, and right lung are labeled as LV, LL, and RL, respectively. (right) ^{23}Na 3D-UTE images of the smoke-treated lung with appropriate ROIs used for the right and left lobe of the lung.

	left lung	right lung	heart
1- **CONTROL**	38.9±10 %	46±10 %	100±11.1 %
2- **COPD**	35.6±12 %	38.3± 10 %	100±14.2 %
3- **COPD**	36.6± 7.4 %	41±8.3 %	100±19.3 %
4- **COPD**	35.6±9.5 %	35.5±7.8 %	100±9.5 %

Tab. 1: Lung sodium intensity values normalized on blood signal of heart in five experiments.

References:

1- L. Lancaster et al., MRM,19: 96–104(1991); **2**- J. Rahmer et al., MRM,55:1075-1082(2006)

EPOS™ Poster

Brain - functional

479

Neuroanatomy associated with emotional distractor during working memory task in patients with generalized anxiety disorder

G. Kim[1], M. Lee[2], **G. Jeong**[3]
[1]Radiology, Chonnam National University Hospital, Gwang-ju/KOREA, [2]Psychology, Chonnam National University Hospital, Gwang-ju/KOREA, [3]Radiology, Chonnam National University Hospital, Chonnam National University Medical School, Gwang-ju/KOREA

Purpose/Introduction: Patient with generalized anxiety disorder (GAD) is associated with abnormalities in the processing and regulation of emotion, and neuropsychological impairment as well. Despite recent studies for identifying the neural circuitry contributing to emotional control, the neural mechanisms for emotional inhibition components of cognitive control during a delayed-response working memory (WM) in patient with GAD have not yet been completely specified. The purpose of this study was to assess the differential brain activation patterns associated with the effects of emotional and non-emotional distractors during the WM maintenance for the human faces between the healthy controls and patients with GAD by using an fMRI.
Subjects and Methods: A total of 14 patients (mean age = 36.5±7.8 years) with GAD and 16 healthy controls (mean age = 36.1±7.8 years) with no history of neurological or psychiatric illness were participated in this study.The paradigm consisted of a string of "encoding - WM maintenance - retrieval - fixation baseline". In the encoding task, three different human faces sequentially appear onec. The subjects performed a WM maintenance for faces with either non-emotional distractors (faces or scrambled faces) or emotional distractors (unpleasant or neutral scenes). In retrieval task, either of the previously used human face or a new human face appears. The brain activation maps and their resulting qualification were analyzed by SPM8.
Results: The scores for the face recognition task of the face and unpleasant scene distractors in healthy controls were 64.7% and 64.7%, respectively, while the scores in patients with GAD were 63.5% and 61.1%, respectively. Non-emotional (face) distractor influenced the same brain areas during the delay interval of a WM task between patients with GAD and healthy controls. In both groups with GAD and healthy controls, non-emotion distracters showed increase of signal intensities in the superior frontal gyrus, dorsolateral prefrontal cortex, ventrolateral prefrontal cortex, superior/inferior parietal gyri, anterior cingulate gyrus, and fusiform gyrus ($p<0.005$). In emotional (unpleasant) distractor, patients with GAD showed significantly increased activation in the ventromedial and dorsolateral prefrontal cortices (VMPFC/DLPFC), hippocampus, parahippocampal gyrus, amygdala, and caudate nucleus during a delayed-response WM ($p<0.005$).
Discussion/Conclusion: These results demonstrate the differential functional neuroanatomy between patients with GAD and healthy controls during a delayed-response working memory with emotional distractor. This finding will be helpful to assess the neural mechanisms related to general impairment of emotional function observed in patient with GAD.
References:
1. Dolcos et al, Brain Research 2007;1152:171-181
2. Etkin et al, Am. J. Psychiatry 2011;168:968-978

480

Patterns of cortical activations during visual tasks of emotional faces in subjects with depression: a coordinate-based meta-analysis

C. Lai
Department of Psychiatry, Buddhist Tzu-Chi General Hospital, Taipei Branch, Xindian/TAIWAN

Purpose/Introduction: Visual processing of emotional faces is an important function in depression, which constitutes a possible theory to explain the pathogenesis of depression. We designed this study to integrate current studies of functional magnetic resonance imaging (fMRI) associated with visual tasks of emotional faces to perform a robust quantitative review and elucidate consistent patterns while visual emotional processing in depression.
Subjects and Methods: We retrieved 10 fMRI studies about visual task for emotional faces in subjects with depression from the database of BrainMap. Among these 10 articles, 8 were chosen for the systematic meta-analysis of activated pattern for "depression vs. control". The "depression vs. control" group of meta-analysis included 238 subjects and 140 foci of activations, which were extracted and computed to estimate the brain locations. Eight studies were enrolled for the meta-analysis of activations for "control vs. depression" and this group included 253 subjects and 68 foci of activations, which was also analyzed with similar procedure.
Results: "depression vs. control" group showed significantly increased activations of likelihood in left striatum (activation likelihood estimation: 2.54x10-3) and left parahippocampal gyrus (3.02x10-3). "control vs. depression" group showed left medial frontal gyrus (1.89x10-3), left middle frontal gyrus (1.88x10-3), right thalamus (1.71x10-3), left anterior cingulate (1.56x10-3) and superior frontal gyrus (1.34x10-3). All the significant clusters and statistical significance reached false discovery rate < 0.05 and cluster-extent threshold > 200 mm3.
Discussion/Conclusion: Our study suggested that depressive patients had limbic activations and controls had fronto-thalamic activations while visual processing of emotional faces.
References:
Buchsbaum, M. S., Wu, J., Siegel, B. V., Hackett, E., Trenary, M., Abel, L., & Reynolds, C. Effect of sertraline on regional metabolic rate in patients with affective disorder. Biol Psychiatry 1997; 41: 15-22.
Calder, A. J., Keane, J., Lawrence, A. D., & Manes, F. Impaired recognition of anger following damage to the ventral striatum. Brain 2004; 127: 1958-1969.
Cardinal, R. N., Parkinson, J. A., Hall, J., & Everitt, B. J. Emotion and motivation: the role of the amygdala, ventral striatum, and prefrontal cortex. Neurosci

481

Glutamatergic metabolism in the pre-genual cortex and cognitive performance – a pilot study in multiple sclerosis patients and healthy volunteers

R.A. Dineen[1], A. French[1], C. Constantinescu[2], D. Auer[1]
[1]Radiological and Imaging Sciences, University of Nottingham, Nottingham/UNITED KINGDOM, [2]Neurology, Division of clinical Neurology, Nottingham/UNITED KINGDOM

Purpose/Introduction: A recent study in healthy adults has shown that individuals with lower glutamate levels in the dorsal anterior cingulate cortex (dACC) have increased blood oxygen level dependent response during a task requiring cognitive control than those with high dACC glutamate [1]. We examine whether glutamate concentration in the pre-genual anterior cingulate cortex (pgACC), an area more commonly associated with emotional processing, has any relationship to cognitive performance in patients with multiple sclerosis (MS).
Subjects and Methods: The study was approved by the local Research Ethics Committee. Eleven MS patients without overt cognitive dysfunction (median age 45 years, range 25 to 62 years) and 7 age-matched healthy volunteers underwent 3T MRI (Philips Achieva) with single-voxel proton Magnetic Resonance Spectroscopy (point resolved spectroscopy sequence, TE=80 ms and TR=2000ms, 128 averages, voxel size35x15x15mm^3) of the pgACC. Glutamate (Glu), N-acetyl aspartate and total creatine (tCr) concentrations were estimated

using linear combination model (LCModel) [2]. Glu and NAA concentrations were expressed relative to tCr (Glu/tCr). All participants underwent cognitive testing with the paced auditory serial addition test (PASAT) which tests sustained attention, working memory and processing speed [3].

Results: PASAT scores from MS patients and controls did not differ (mean 44.6 v 44.7, p=.989). Glu/tCr did not differ between groups (mean 0.81 v 0.92, p=.315). An inverse correlation was found between pgACC Glu/tCr levels and PASAT performance (figure) for all subjects (-0.57, p=.017), and for the patient and control groups separately.

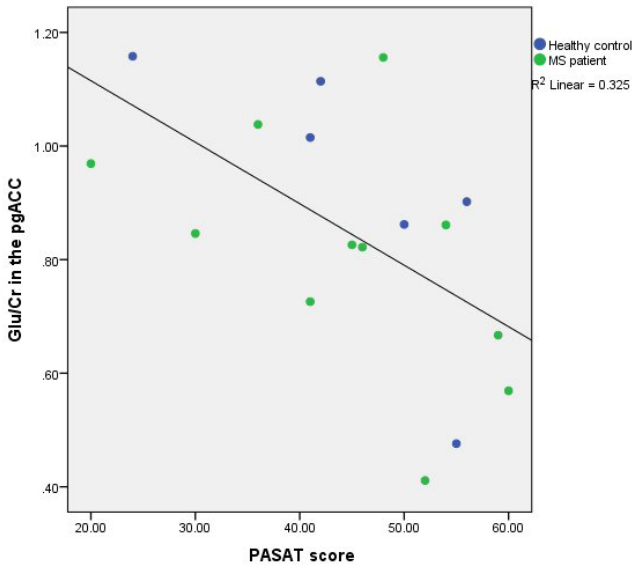

Discussion/Conclusion: In this pilot study we identify a relationship between pgACC glutamatergic metabolism and cognitive performance, and this does not appear to be an MS-specific effect. Speculatively, the inverse relationship between pgACC glutamate concentration and cognitive performance may indicate that high glutamate in the pgACC reduces cognitive control by the dACC.

References:

1. Falkenberg, L.E., et al., *Resting-state glutamate level in the anterior cingulate predicts blood-oxygen level-dependent response to cognitive control.* Proceedings of the National Academy of Sciences, 2012. **109**(13): p. 5069-5073.

2. Provencher, S.W., *Automatic quantitation of localized in vivo ^{1}H spectra with LCModel.* NMR in Biomedicine, 2001. **14**(4): p. 260-264.

3. Gronwall, D.M.A., *Paced auditory serial-addition task: A measure of recovery from concussion.* Perceptual and motor skills, 1977. **44**: p. 367-373.

EPOS™ Poster

Brain - ischemia and angiography

482

Ultra-High-Field MRI of stroke at 7T: first experiences

F.C. Von Samson-Himmelstjerna[1], V.I. Madai[2], E. Tovar-Martinez[1], K. Stengl[2], M. Bauer[2], J. Wuerfel[3], J. Sobesky[2], T. Niendorf[1]
[1]Berlin Ultrahigh Field Facility (BUFF), Max Delbrueck Centre for Molecular Medicine (MDC), Berlin/GERMANY, [2]Centre for Stroke Research (CSB), Charite Universitätsmedizin Berlin, Berlin/GERMANY, [3]Institute of Neurology, University Medicine Göttingen, Göttingen/GERMANY

Purpose/Introduction: Magnetic resonance imaging (MRI) up to field strengths of 3 Tesla (T) has emerged as the most favorable modality for the imaging of stroke [1]. Recently, ultrahigh-field (UHF) MRI at 7T has shown encouraging results for the depiction of brain pathology and chronic inflammatory diseases [2–5]. This potential diagnostic improvement has not yet been applied to stroke imaging.
We present the first evaluation of a stroke imaging protocol at 7T in comparison to 3T MRI. The development of this 7T protocol focused on equivalent diagnostic information, similar acquisition time and choosing existing clinical 3T-sequences as a starting point. The challenges here inherent to 7T imaging like B0- and B1-inhomogeneities, increased T_1-relaxation, decreased T_2-relaxation and increased RF power-deposition.
Subjects and Methods:

7T	sequence	TR	TE	accelera-tion	BW	Voxel size	Matrix size	FA	No. of	t
	type	ms	ms	factor (R)	Hz/Px	mm³		°	slices	min
MPRAGE	3D	2750	1.81	3	350	0.7x0.7x0.7	384x384	10	17 cm coverage	05:40
FLAIR	2D	9000	89	1	283	1.2x0.9x3.0	256x192	130	11	03:56
T_2	2D	14300	73	2	260	0.6x0.6x3.5	384x384	144	20	03:36
T_2^*	2D	600	15	3	260	0.7x0.7x3.0	320x320	25	45	02:38
TOF	3D	32	3.53	1	305	0.4x0.4x0.4	512x512	25	5.1 cm coverage	08:16
										Σ 24:06

3T	sequence	TR	TE	accelera-tion	BW	Voxel size	Matrix size	FA	No. of	t
	type	ms	ms	factor (R)	Hz/Px	mm³		°	slices	min
MPRAGE	3D	1900	2.93	1	170	1.0x1.0x1.0	256x256	9	16 cm coverage	04:35
FLAIR	2D	9010	136	2	252	0.6x0.6x4.0	320x320	140	20	03:02
T_2	2D	6000	96	2	220	0.7x0.7x4.0	320x320	150	25	01:20
T_2^*	2D	800	20	1	260	1.1x0.7x4.0	256x230	25	25	02:35
TOF	3D	24	3.60	2	186	0.6x0.6x0.6	384x364	18	8.2 cm coverage	05:54
										Σ 17:26

Table 1: Parameters of the 3T and 7T sequences. The development of the 7T sequences was based on generally available, clinical 3T sequences. Several UHF intrinsic aspects like B0- and B1-inhomogeneities, increased T1-relaxation, decreased T2-relaxation and increased RF power-deposition had to be taken into account for the development of the protocol. Increased T1 relaxation time and/or RF-power-deposition led to increased acquisition time and/or reduced brain coverage in the B0 direction in most sequences. Only the T2*-weighted-HemoFLASH sequence at 7T had a comparable acquisition time and even better brain coverage, while offering superior spatial resolution, anatomical detail and depiction of presumable perilesional hemosiderin deposits. All in all the acqisition time remains longer at 7T compared with 3T (24 min vs. 18 min).

As part of an ongoing prospective observational imaging study [6] 12 patients with subacute and chronic stroke were imaged. 3T imaging (Magnetom Verio, Siemens Healthcare, Germany) was followed immediately by 7T imaging (Magnetom 7T, Siemens Healthcare, Germany). Both protocols included T_1-weighted 3D-MPRAGE, 2D-T_2-weighted FLAIR, T_2^*-weighted 2D-TSE, 2D-FLASH (HemoFLASH) and 3D-TOF-angiography (table 1).
Results: In FLAIR-imaging, all lesions were readily visible at both field strengths. In all other sequences a higher spatial resolution was achieved showing more anatomical details at 7T with respect to vessel structure, per-infarct alterations and infarct microstructure (figures 1-3).
Increased relaxation times and/or higher RF-power-deposition resulted in acquisition time prolongation and/or reduced brain coverage for 2D-FLAIR, 2D-T_2-TSE, 3D-TOF and 3D-MPRAGE sequences. This was not an issue in the 2D-HemoFLASH sequence.
Discussion/Conclusion: In our sample of stroke patients, 7T MRI yielded all relevant diagnostic information currently acquired at 3T MRI. Additionally, 7T MRI provided higher spatial resolution and a relevant improvement in the visualization of infarct related alterations in stroke. These findings substantiate a preliminary report on diagnostic advantages of stroke imaging at 8T over 3T [7]. Its benefit in terms of clinical stroke imaging, as well as the solution of remaining technical issues related to 7T-MRI have to be evaluated in the future.
References:

[1]Merino J.G., Warach S.,2010, *Nat Rev Neurol,* 560-71
[2]Lupo J.M. et al.,2011, *Curr Opin Neurol*, 605-15
[3]Dammann P. et al.,2010, *Neurosurg FOCUS* , E5
[4]Kwon D.-H. et al.,2012, *Ann Neurol* , 267-77
[5]Tallantyre E.C. et al.,2011, *Neurology* , 534-9
[6]Madai, V.I., von Samson-Himmelstjerna, F.C. et al.,2012, *PLoSONE*, e37631
[7]Novak V. et al.,2005, *Magn Reson Imaging*, 539-48

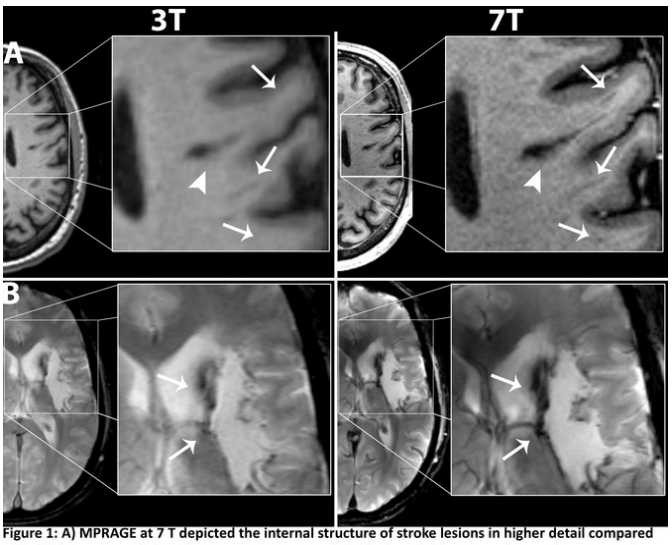

Figure 1: A) MPRAGE at 7 T depicted the internal structure of stroke lesions in higher detail compared with 3 T (arrowheads). Small anatomical structures like Virchow-Robin-spaces (arrows) were seen in more detail and more often than at 3 T. B) HemoFlash at 7 T provided higher spatial resolution and enhanced sensitivity for the depiction of presumed perilesional hemosiderin deposits (arrows).

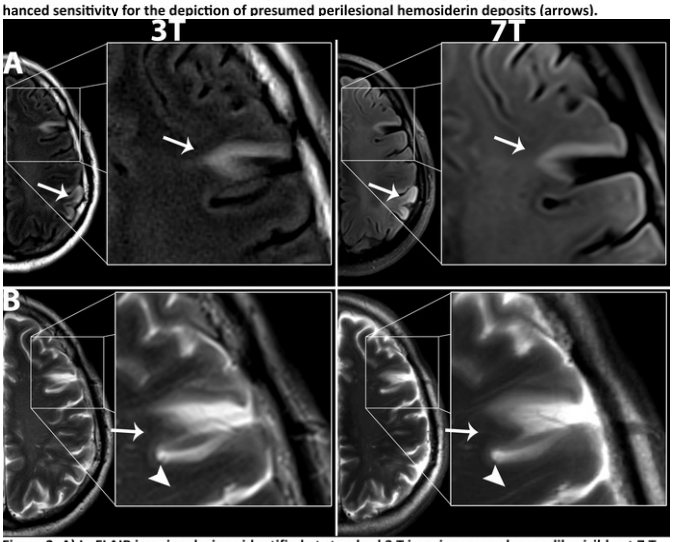

Figure 2: A) In FLAIR imaging, lesions identified at standard 3 T imaging were also readily visible at 7 T imaging (arrows).B) T2 imaging at 7 T allowed for the identification of lesions seen at 3 T (arrows) and provided higher spatial resolution, e.g. for the depiction of Virchow-Robin-spaces (arrowheads).

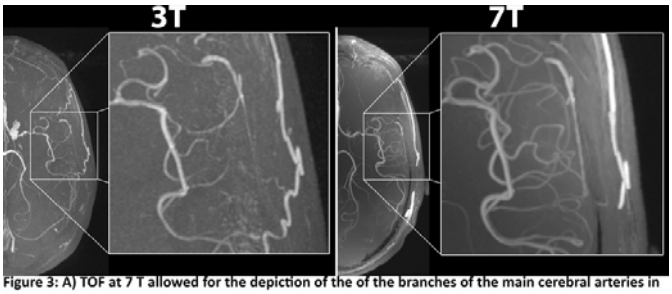

Figure 3: A) TOF at 7 T allowed for the depiction of the of the branches of the main cerebral arteries in higher anatomical detail. In this exemplary patient, more second and third order branches are seen in the left MCA territory compared with 3 T.

483

Effect of echo time and spatial resolution on delineation of aneurysm remnant with 3D time-of-flight magnetic resonance angiography

L. Cerwén[1], L. Borota[1], E. Ronne-Engström[2], E. Larsson[1], J. Wikström[1]
[1]Department of Radiology, Uppsala University, Uppsala/SWEDEN,
[2]Department of Neuroscience, Uppsala University, Uppsala/SWEDEN

Purpose/Introduction: Three-dimensional time-of-flight magnetic resonance angiography (3D TOF MRA) is increasingly used instead of x-ray angiography (DSA) to examine patients with coiled intracranial aneurysms. One limitation of MRA is the occurence of artefactual signal loss in the vicinity of the coil mesh, which would be expected to decrease with shorter echo time and smaller voxel size. Phantom and animal studies (1,2) and limited clinical data (3) support this but larger clinical studies are lacking.
The purpose of this study was therefore to assess the effect of echo time and slice thickness on delineation of aneurysm remnants.
Subjects and Methods: Twenty-eight patients with coiled intracranial aneurysms underwent 3D TOF MRA at 3 Tesla with three different echo times and two different slice thicknesses, totalling six sequences (Table).
The diameters of the circulating remnant and of the coil mesh in the three main directions were measured. Non-parametric tests were used to assess the significance of differences in diameter products between the sequences, with a p-value of 0.05 as threshold.
Results:

Table

Slice thickness (mm)	Echo time (ms)	Mean diameter product of aneurysm remnant (mm^3)	Mean diameter product of coil mesh (mm^3)
1	3.45	45.2	472
1	2.7	45.7	414
1	1.85	52.6	304
0.5	3.45	53.9	504
0.5	2.7	57.8	420
0.5	2.0	60.6	413

With decreasing echo time there was a statistically significant increase in size (P=0.030) of the circulating remnant at a slice thickness of 1.0 mm and a trend for increase in size (P=0.131) at a slice thickness of 0.5 mm.
A numerical increase in mean size of circulating remnant with decreasing slice thickness was observed at all echo times. The size difference was statistically significant at echo time 3.45 ms (P=0.031) and close to significant at echo time 2.7 ms (P=0.085).
The mean size of the coil mesh decreased with shorter echo time. The size difference was statistically significant at a slice thickness of 1.0 mm (P= 0.012).

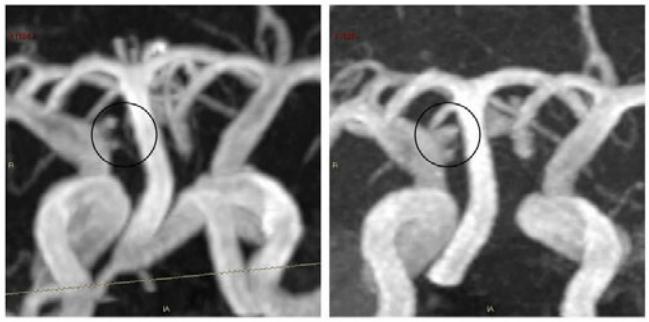

Figure. Larger aneurysm remnant is seen at echo time 2.0 ms and slice thickness 0.5 mm (right) than at echo time 3.45 ms and slice thickness 1 mm (left).
Discussion/Conclusion: An increase in size of the aneurysm remnant with decreasing echo time and slice thickness was observed, suggesting reduced susceptibility related but maybe also turbulence related intravoxel dephasing.
References:
•1. Kakeda et al. JMRI 2008
•2. Spilberg et al. AJNR 2012
•3. Gönner et al. AJNR 1998

484

Cardiovascular risk factors associated with recognized and silent brain infarcts on magnetic resonance imaging in an elderly population

R. Nylander[1], J. Wikström[1], H. Ahlström[2], L. Johansson[2], L. Lind[3], **E. Larsson**[2]
[1]Department of Radiology, Uppsala University Hospital, Uppsala/SWEDEN,
[2]Department of Radiology, Uppsala University, Uppsala/SWEDEN,
[3]Department of Medicine, Uppsala University, Uppsala/SWEDEN

Purpose/Introduction: The purpose of this study was to assess the association of established and new cardiovascular disease risk factors with recognized and silent brain infarcts in a 75-year-old population
Subjects and Methods: Cerebral magnetic resonance imaging (MRI) was performed on 407 randomly selected 75-year old subjects in a prospective population based study. Imaging was performed using a 1.5 Tesla MRI scanner. The protocol included sagittal 3D T1-weighted gradient echo images, transverse proton density-weighted and transverse T2-weighted turbo spin echo images. Images were assessed for lacunar and cortical infarcts. Infarcts were further categorised as clinically recognized (symptomatic) or silent, based on review of clinical records. Cardiovascular risk factor data was obtained from clinical records and from dedicated questionnaires. Odds ratios for the different infarct types were calculated for the cardiovascular risk factors.
Results: One or more infarcts were seen in 102 (25%) of the subjects. Recognised brain infarcts were found in 5% and silent brain infarcts in 20%. Out of all subjects with infarcts, 76% had only lacunar infarcts, 11% had only cortical infarcts and 13% had both.
Several established cardiovascular risk factors were associated with increased risk for all types of brain infarcts. Lacunar infarcts were associated with hypertension and diabetes, while cortical infarcts were associated with hypertension and smoking. Recognized brain infarcts were related to hypertension, abdominal obesity, diabetes and low HDL-cholesterol, while silent brain infarcts were related to hypertension only. New cardiovascular risk factors had only slight impact. N-terminal pro-brain natriuretic peptide and cystatine C were associated with slightly increased odds-ratios for recognized infarcts but not for silent brain infarcts. The odds ratios of different risk factors are shown in Fig 1 A-D.
Fig 1 Standardized odds ratios of different risk factors adjusted for gender

A. Odds ratios for lacunar infarcts

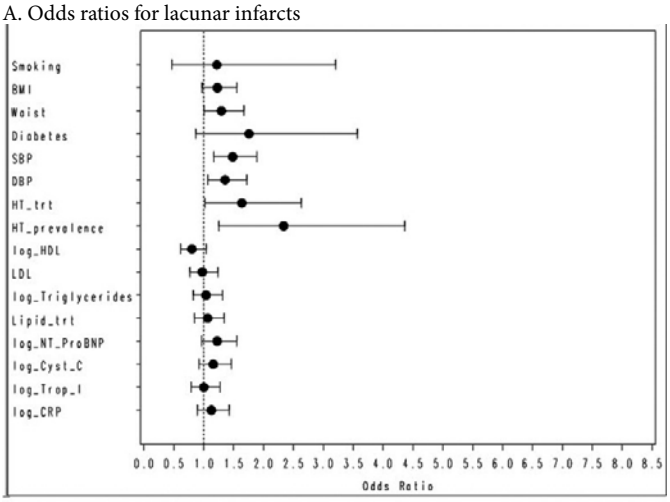

B. Odds ratios for cortical infarcts

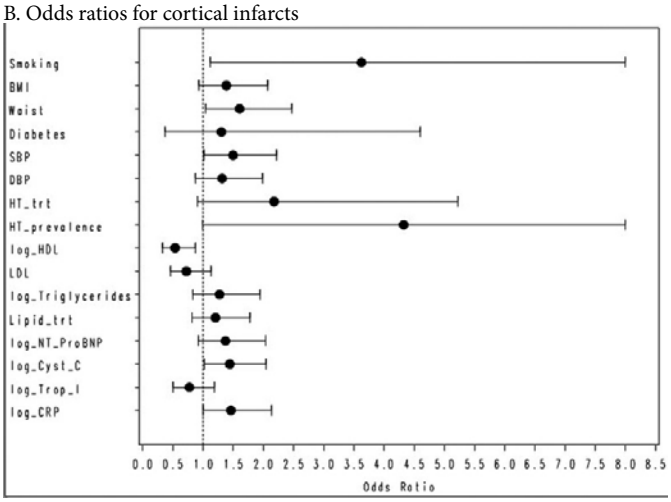

C. Odds ratios for recognized brain infarcts

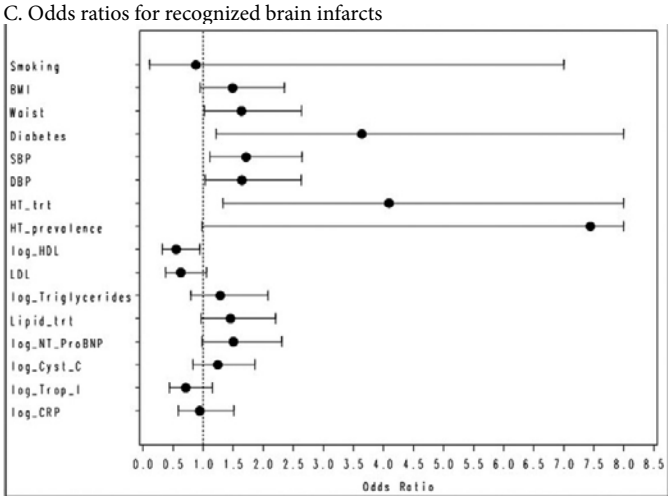

D. Odds ratios for silent brain infarcts

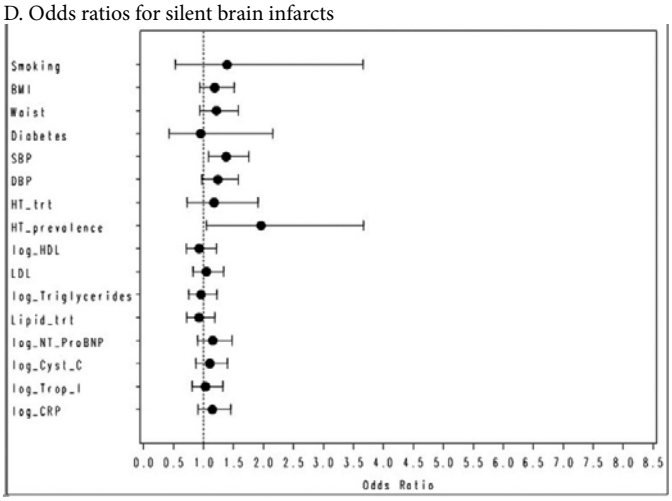

Abbreviations in figures: BMI- body mass index, waist - waist circumference, SBP - systolic blood pressure, DBP - diastolic blood pressure, HT - trt - hypertension treatment, HT - prevalence - hypertension prevalence, HDL and LDL - high and low density lipids, Lipid trt - lipid lowering treatment.
Discussion/Conclusion: Established cardiovascular risk factors are associated with increased odds ratios for all types of brain infarcts, but the different infarct types have slightly different risk factor profiles. New cardiovascular risk factors showed only slight impact on the risk for brain infarcts.

485

Visualization of the lenticulostriate arteries at 3T: optimization of TOF-MRA with SORS-MTC and comparison with FSBB-MRA

T. Okada[1], M. Miyazaki[2], A. Kido[3], K. Fujimoto[3], A. Yamamoto[3], M. Kanagaki[3], S. Okuchi[3], X. Zhou[2], K. Togashi[3]
[1]Diagnositc Imaging and Nuclear Medicine, Kyoto Uniservisty Graduate School of Medicine, Kyoto/JAPAN, [2]MRI, Toshiba Medical Research Institute USA, Inc., Vernon Hills/IL/UNITED STATES OF AMERICA, [3]Diagnostic Imaging and Nuclear Medicine, Kyoto University Graduate School of Medicine, Kyoto/JAPAN

Purpose/Introduction: The lenticulostriate arteries (LSAs) give blood supply to the basal ganglia and the internal capsule, and its occlusion results in infarct at its territories. The LSAs have been well visualized by Time-Of-Flight (TOF)-MRA at 7T (1). At 1.5T, flow-sensitive black blood (FSBB) angiography successful visualized LSAs (2). Most recently, however, TOF-MRA has successfully visualized LSAs at 3T (3) and 1.5T (4). In the latter study at 1.5T, Slice-Selective Off-Resonance Sinc Pulse Saturation Transfer Contrast (SORS-STC) was used. Therefore, we investigated visualization of LSAs at 3T by comparing 3D TOF-MRA with SORS-STC with FSBB-MRA.
Subjects and Methods: Firstly, 20 volunteers (mean age 52 y.o.) were scanned using a 3T-MR system (Vantage, Toshiba medical systems, Ohtawara, Japan) for axial TOF-MRAs (TR/TE 35/6.8ms, FA 20) with SORS-STC pulses of 3 different flip angles (FAs: 0, 400 and 750 degrees), which were reconstructed coronal with 2mm-thick MIP. Numbers of LSA branches were counted and compared to investigate the optimal FA. Thereafter, coronal FSBB-MRA (TR/TE 35/13ms, FA 15 and b-value 0.3s/mm^2) with the same spatial resolution was acquired and compared with TOF-MRA with the optimal FA in 21 volunteers (mean age 55 y.o.). Numbers and length of LSA branches were measured. Statistical analysis was conducted with paired *t*-tests.
Results: The average numbers and 95% confidence intervals of visualized LSAs by TOF-MRA were 3.7 [2.9-4.5], 5.8 [4.9-6.6] and 4.2 [3.2-5.1] for FAs of 0, 400 and 750 degrees, respectively. The FA 400 degree visualized significantly more LSA branches. In the following study, visualized LSA branches / their total length were 5.3 [4.6-6.0] / 81.4 [70.0-92.9] mm and 10.6 [9.5-11.6] / 209.0 [183.7-234.4] mm, respectively for TOF-MRA with FA of 400 degree and FSBB-MRA. Both were significantly higher in FSBB-MRA.

Discussion/Conclusion: TOF-MRA with SORS-STC visualized LSA branches most, when FA of 400 degree was adopted. However, FSBB-MRA could visualize them significantly more and longer. FSBB-MRA is considered a choice at 3T.

References:

(1) Cho ZH, et al. Stroke, 2008. (2) Gotoh K, et al. JMRI 2009. (3) Chen YC, et al. AJNR 2011. (4) Admiraal-Behloul F, et al. ISMRM abstract p363, 2011.

EPOS™ Poster

Brain - neurodegenerative diseases and epilepsy

486

A Magnetic Resonance Signal-Based Approach to deal with Partial Volume Effects

Q. Duché[1], H. Saint-Jalmes[2], O. Acosta[2], G. Gambarota[3], I. Merlet[2], O. Salvado[4]
[1]INSERM, UMR 1099, RENNES/FRANCE, [2]LTSI - UMR INSERM 1099, Université de Rennes 1, Rennes/FRANCE, [3]PRISM, Biosit, CNRS UMS 3480, INSERM UMS 018 - Biogenouest, Rennes/FRANCE, [4]CSIRO, AEHRC, BRISBANE/QLD/AUSTRALIA

Purpose/Introduction: Accurate quantification of small structures in magnetic resonance (MR) images is often limited by partial volume (PV) effects which arise when more than one tissue type is present in a voxel. Different image processing methods have been proposed. Here, we describe a signal-based method to estimate PV by modeling the MR signal per voxel with at most two magnetic contributions representing two tissues in each voxel. It is based on sound physical grounds and tackles a well-known problem from the acquisition point of view.
Subjects and Methods: Based on the bi-exponential formulation, fractional contents can be retrieved by solving a linear system of two equations with two unknowns, namely tissue magnetizations. The mixing of tissues is explicit at each voxel in the bi-exponential model. Then, it becomes implicit, when reduced to a linear system solved per voxel, thereby leading to a strong robustness to high RF inhomogeneities. The idea strongly relies on the novel-of-the-art acquisition methods such as MP2RAGE and its derivatives (FLAWS) which are becoming product sequences on clinical scanners. This method requires two co-registered images acquired with different parameters.
The first tests were conducted on images acquired on a physical phantom composed of two gel-layers simulating respectively GM and white matter (WM) tissue relaxation properties. We varied the partial volumed zone (PVZ) by gradually rotating the acquisition plane by 5° from the middle of the GM/WM interface. Each position was acquired twice with a Spin Echo sequence of parameters TR1=800ms and TR2=3600ms on a Bruker Biospec 4.7T scanner. Those parameters have been optimized for this purpose by running Monte Carlo simulations minimizing the error on fractional contents for two tissues. The PVZ were measured on the fractional contents maps and were confronted to the theoretical size given by the conditions of acquisition (slice thickness and orientation). Preliminary in vivo tests were also conducted on a FLAWS sequence.

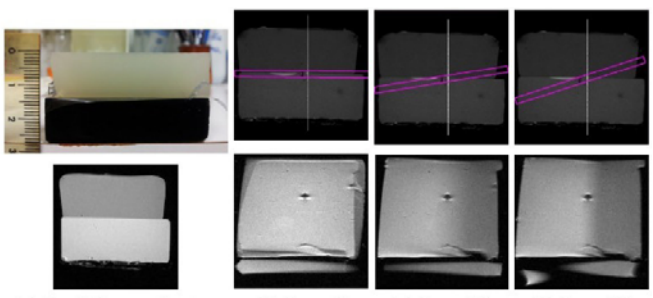

(a) DoubleLayer phantom (b) $\theta_0 = 0°$ (c) $\theta_2 = 10°$ (d) $\theta_4 = 20°$

Results: The PV protocol used on the physical phantom gave errors inferior to the voxel resolution, showing good agreement with the theoretical measurements of the PVZ.

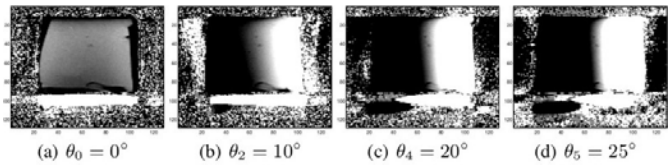

(a) $\theta_0 = 0°$ (b) $\theta_2 = 10°$ (c) $\theta_4 = 20°$ (d) $\theta_5 = 25°$

θ	$\theta_1 = 5°$	$\theta_2 = 10°$	$\theta_3 = 15°$	$\theta_4 = 20°$	$\theta_5 = 25°$
s (mm)	45.72	22.69	14.92	10.99	8.58
s_{exp} (mm)	44.38	23.75	15.00	11.25	8.13
$s - s_{exp}$ (mm)	1.35	1.06	0.07	0.26	0.45
$s - s_{exp}$ (px)	>2	>1	<1	<1	<1

Table 1. Theoretically and experimentally computed sizes (in mm) of the partial volume zones for five angles on the DoubleLayer phantom. In this experiment, $r_x = 0.625mm$. Errors are shown in the last two rows (in mm and pixels).

Discussion/Conclusion: We proposed a simple and fast method to accurately estimate fractional content of tissues using a bi-exponential model. It is intrinsically robust to RF inhomogeneities as the signal is identically biased in the two images. It gives a numerical estimation of the fractional contents most of the common use heavy computationally models. It may be easily implemented.
References:
M. Tanner et al. J Magn Reson Imaging. (2011) *doi: 10.1002/jmri.23532*

487

Correlating motor and cognitive function to voxelwise myelin water measurements across whole multiple sclerosis brain

S. Kolind[1], A. Seddigh[2], N. Sibtain[2], S. Deoni[3], G.J. Barker[4], A. Traboulsee[1], S.C.R. Williams[4], P.A. Brex[2]
[1]Medicine, University of British Columbia, Vancouver/BC/CANADA, [2]Neurology, King's College Hospital, London/UNITED KINGDOM, [3]Engineering, Brown University, Providence/RI/UNITED STATES OF AMERICA, [4]Neuroimaging, King's College London, London/UNITED KINGDOM

Purpose/Introduction: Myelin water fraction[1] (MWF), a measure related to myelin content[2], can be assessed using multi-component relaxation imaging. mcDESPOT[3] permits high-resolution whole-brain multi-component relaxation imaging in less than 12 minutes. Previously[4], we demonstrated significant correlations (R=-0.58) between decreased MWF and greater disability (as measured by the Expanded Disability Status Scale[5] (EDSS)) diffusely throughout the white matter in primary progressive multiple sclerosis (PPMS). Two of the functional system scores that make up the EDSS showed more regionally focused correlations with MWF decreases: the mental score was correlated in frontal brain and corpus callosum while the sensory score was correlated near the sensory cortex, suggesting that MWF reflects changes in pathology that are relevant to disease expression.
In this study, we assessed the relationship between MWF and the Multiple Sclerosis Functional Composite[6] (MSFC) score and its component measures of motor function (nine-hole peg test (9HPT) and timed walk) and cognitive function (paced auditory serial addition test (PASAT)).
Subjects and Methods: mcDESPOT imaging and MSFC assessments were performed for 15 PPMS patients. Voxelwise MWF maps were derived, and a white matter tract skeleton was created from the MWF maps using tract-based spatial statistics[4,7]. Voxelwise non-parametric testing was performed on the skeletonised MWF data across the brain to assess correlations with mean time for the 9HPT and timed walk, PASAT score, and MSFC.
Results: Reduced MWF correlated significantly with longer 9HPT times in the corpus callosum and minor forceps (R = 0.67 in significant regions). No significant correlations were found between MWF and timed walk or PASAT scores. Significant correlations (R = 0.55) between the MSFC score and MWF were observed in very similar regions to the 9HPT.

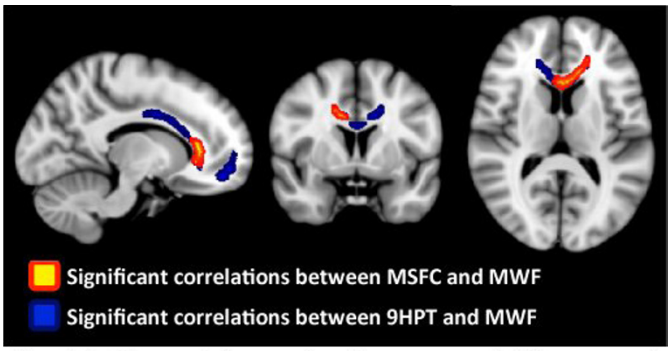

Figure 1: Significant correlations were found between greater disability as measured by the MSFC and reduced MWF values, which overlap largely with areas of significant correlation between longer times to complete a 9HPT and reduced MWF.

Discussion/Conclusion: In this small PPMS cohort, the modest correlations found between MWF and the MSFC score appear to have been driven by the results of the 9HPT. Future work will involve serial studies and include spinal cord imaging; changes in these scores over time may correlate more strongly with MWF, and motor-related scores may correlate more strongly with spinal cord MWF.

References:

1 MacKay A. 1994. Magn Reson Med; 673-677.
2 Laule C. 2008. Neuroimage; 1575-1580.
3 Deoni SC. 2008. Magn Reson Med; 1372-1387.
4 Kolind S. 2012. Neuroimage; 263-270.
5 Kurtzke JF. 1983. Neurology; 1444-1452.
6 Fischer JS. 1999. Mult Scler; 244-250.
7 Smith SM. 2006. Neuroimage; 1487-1505.

488

Cortical atrophy in advanced stage of parkinson disease

D. Khaimov[1], A. Trufanov[2], L. Voronkov[1], A.Y. Efimtcev[1], V. Fokin[1], I. Litvinenko[2], A.A. Yurin[2]
[1]Radiology, Military Medical Academy, Saint Petersburg/RUSSIAN FEDERATION, [2]Neurology, Military Medical Academy, Saint Petersburg/RUSSIAN FEDERATION

Purpose/Introduction: The Parkinson disease (PD) pathology is not only nigrostriate dophaminergic system degeneration, but also includes wide-spread lesion of brain cortex. This is the reason not only motor function impairment in classic PD pattern, but also cognitive and spatio-visuale deficit. The main goal of our study was to determine differences of brain thickness in patients with 2nd and 3rd stage of Parkinson disease.

Subjects and Methods: 67 patients with idiopathic Parkinson disease were examined. Diagnosis was made using criteria of British Brain bank. 28 patients were with Hoehn-Yahr stage 2, 39-with stage 3. In all patients T_1 gradient-echo protocol with recounting on PC with FreeSurfer software was performed. 240 right and left hemisphere structures were statistically manipulated using Statistica 8.0 software using Mann-Whitney.

Results: Significant differences of brain cortex thickness in left and right hemispheres were determined (Table 1 and 2)

Table 1
Differences of cortical thickness (mm) in left hemisphere in patients with Hoehn-Yahr stage 2 and 3 of Parkinson disease.

Localization	stage 2 M [LQ;UQ]	stage 3 M [LQ;UQ]	p
Lingual area	1,864 [1,786;1,917]	1,729 [1,635;1,883]	0,046
Pericalcarine area	1,556 [1,453;1,599]	1,443 [1,387;1,522]	0,048
Frontopolar area	2,586 [2,529;2,844]	2,446 [2,366;2.598]	0,030
Girus cingulum posterior dorsalis	2,759 [2,681;2,871]	2,623 [2,401;2,795]	0,017
Girus occipitalis middle	2,576 [2,447;2,740]	2,385 [2,198;2,576]	0,013
Fusiform girus	1,831 [1,797;1,940]	1,758 [1,630;1,855]	0,042
Girus precuneus	2,392 [2,335;2,703]	2,265 [2,084;2,474]	0,039
Broadman area 3a	1,601 [1,578;1,720]	1,532 [1,438;1,604]	0,046
Broadman area MT	2,319 [2,279;2,548]	2,236 [2,140;2,366]	0,023

Table 2
Differences of cortical thickness (mm) in right hemisphere in patients with Hoehn-Yahr stage 2 and 3 of Parkinson disease.

Localization	stage 2 M [LQ;UQ]	stage 3 M [LQ;UQ]	p
Paracentral area	2,219 [2,083;2,404]	2,102 [1,956;2,288]	0,044
Postcentral area	2,008 [1,912;2,088]	1,849 [1,726;2,062]	0,015
Precentral area	2,351 [2,248;2,447]	2,173 [1,974;2,341]	0,027
Girus postcentralis	2,128 [2,001;2,244]	1,883 [1,729;2,194]	0,017
Girus precentralis	2,539 [2,470;2.753]	2,401 [2,145;2,541]	0,015
Sulcus centralis	1,731 [1,656;1,879]	1,555 [1,429;1,779]	0,015
Sulcus postcentralis	1,996 [1,833;2,071]	1,787 [1,717;1,974]	0,025
Sulcus suborbitalis	2,642 [2,529;2,928]	2,389 [2,153;2,557]	0,015
Broadman area 1	2,313 [2,177;2,704]	2,101 [1,892;2,412]	0,030
Broadman area 2	2,017 [1,945;2,140]	1,899 [1,758;2,051]	0,025
Broadman area 3a	1,580 [1,548;1,677]	1,535 [1,446;1,596]	0,014
Broadman area 4a	2,239 [2,106;2,469]	2,003 [1,687;2,371]	0,013
Broadman area 4p	2,109 [1,931;2,268]	1,809 [1,494;2,172]	0,010

Discussion/Conclusion: Our study allows better understanding a lot of pathogenetic mechanisms of Parkinson disease. It was found that most structures responsible for cognitive, motoric and psychic functions primarily suffer in dominant hemisphere.

489

Cortical And Whole Brain Volume Assesment And Diffusion Tensor Imaging Findings In Alzheimer's Disease And Mild Cognitive Impairment

G. Aktas[1], B. Cavusoglu[2], **E. Ada**[1], P. Kurt[2], F. Tetik[1], G. Yener[3]
[1]Radiology, Dokuz Eylul University Faculty of Medicine, Izmir/TURKEY, [2]Neuroscience, Dokuz Eylul University Institute of Health Sciences, Izmir/TURKEY, [3]Neurology, Dokuz Eylul University Faculty of Medicine, Izmir/TURKEY

Purpose/Introduction: To compare the whole brain and cortical gray matter volume, fractional anisotropy (FA) and mean diffusivity (MD) of white matter in patients who were clinically diagnosed as Alzheimer's disease (AD) and mild cognitive impairment (MCI) patients with a healthy control group.

Subjects and Methods: Alzheimer's disease (26), mild cognitive impairment (18) and healthy control (16) subjects were assessed. Gray matter and whole brain were annotated and volume calculated with a lesion annotation and volume assessment tool (LAVA, Mimlabs) from 3D T1A coronal images. DTI measurements were made by determining the ROI values in the splenium, anterior and posterior pericallosal and parietal white matter, cingulate gyrus, and hippocampus from MD and FA maps. Results were compared statistically.

Results: Total brain volumes of AD and MCI were found to be decreased compared to the healthy control (HC) group, but the difference between AD and MCI was not significant. Gray matter volumes of Alzheimer patients were significantly decreased but this is not significant in MCI according to the HC. MD was found to be significantly different in all ROIs but not in splenium between AD and HC. In bilateral hippocampus, anterior and posterior pericallosal and right parietal white matter ROIs, MD values were significantly different between AD and MCI. MD was found to be significantly higher in all points except splenium and bilateral posterior cingulate gyrus in MCI than HC. Bilateral anterior pericallosal and left posterior pericallosal white matter

FA values were significantly different in AD and MCI. FA values were found to be significantly lower in all points in MCI than HC and in AD than HC except splenium and right anterior cingulate gyrus.
Discussion/Conclusion: Whole brain and/or gray matter volumes and DTI can contribute to differentiate AD and MCI, MCI and HC. But this is not sufficient to differentiate exactly, it needs more refined researches help to do early diagnosis and better management of the patients.

490

^{1}H-magnetic resonance spectroscopy reveals increased Glutamate levels in the nucleus accumbens after acute detoxification in alcohol dependent patients

J. Bauer[1], H. Kugel[2], N. Scherbaum[3], J. Bening[1], J. Patschke[1], A. Pedersen[1], P. Ohrmann[1]
[1]University of Muenster, Department of Psychiatry, Muenster/GERMANY, [2]Institut for Clincal Radiology, University of Muenster, Muenster/GERMANY, [3]Klinik für abhängiges Verhalten und Suchtmedizin, Kliniken der Universität Duisburg-Essen, Essen/GERMANY

Purpose/Introduction: Excessive glutamatergic neurotransmission has been held responsible for acute withdrawal symptoms and craving in patients with alcoholism. Most physiological evidence for this hypothesis has been retrieved from animal, mostly rat studies. In humans, gabaergic and glutamatergic medications have given indirect evidence for glutamatergic dysfunction in alcohol withdrawal, whereas in-vivo data of the glutamatergic metabolism in alcoholism are still rare.
Subjects and Methods: We used ^{1}H magnetic resonance spectroscopy to measure glutamate levels within 10 days after detoxification in alcohol-dependent male patients (n = 29) and healthy control subjects (n = 31). A Point Resolved Spectroscopy Sequence (PRESS) was applied on a 3T scanner (Philips Gyroscan Intera 3T) with the following parameters: TE 32 ms, TR 2000 ms, 2048 datapoints, bandwidth 2000 Hz, an iterative shim procedure and water suppression. The two 3.375 ml sized regions of interest were the nucleus accumbens, one of the most important brain structures in the reward system, and the anterior cingulate cortex, a interconnected region that has been related to willed action and cognitive and emotional decision making. Spectroscopic data were analyzed with LCModel [1] and corrected for cerebrospinal fluid.
Results: Glutamate levels in the nucleus accumbens were significantly increased after acute detoxification in patients compared to controls. Craving as measured with the obsessive-compulsive drinking scale was positively correlated with levels of glutamate and glutamine in the nucleus accumbens and the anterior cingulate cortex. There were no other significant differences in metabolites between patients and controls.
Discussion/Conclusion: Our data are the first to demonstrate increased glutamate levels in the nucleus accumbens after detoxification in patients with alcohol dependence in- vivo and thus support animal data on ethanol withdrawal. They also support the relevance of the glutamatergic system in craving. Longitudinal studies might be able to further elucidate the relationship between glutamatergic neurotransmission and relapses in order to develop successful pharmacological interventions in chronic alcoholism.
References:
[1] Provencher, S.W. (1993):
Estimation of metabolite concentrations from localized in vivo proton NMR spectra. Magn Reson Med 30, 672-679.

491

Pharmacog: Multi-site MRI calibration to study the progression of Alzheimer's disease using brain morphometry

J. Jovicich[1], M. Marizzoni[2], R. Sala-Llonch[3], D. Bartrés-Faz[4], L. Roccatagliata[5], F. Nobili[5], C. Zeeh[6], P. Schonknecht[6], A. Monnet[7], R. Bordet[7], G. Zoccatelli[8], A. Beltramello[8], S. Meyer[9], J. Wiltfang[9], V. Chanoine[10], O. Blin[10], H. Gros-Dagnac[11], P. Payoux[12], H. Hardemark[13], G.B. Frisoni[14]
[1]Center for Mind/Brain Sciences, University of Trento, Mattarello/ITALY, [2]LENITEM Laboratory of Epidemiology, Neuroimaging, & Telemedicine, IRCCS San Giovanni di Dio Fatebenefratelli, Brescia/ITALY, [3]Dept de Psiquiatria i Psicobiologia Clinica, Universitat de Barcelona and IDIBAPS, Barcelona/SPAIN, [4]Dept. de Psiquiatria i Psicobiologia Clinica, Facultat de Medicina, Universitat de Barcelona and IDIBAPS, Barcelona/SPAIN, [5]Dept of Neuroscience, Ophthalmology and Genetics, University of Genoa, Genoa/ITALY, [6]Dept of Psychiatry and Dept of Neuroradiology, University of Leipzig, Leipzig/GERMANY, [7]UL2, Universitè Lille, LILLE/FRANCE, [8]Dept of Neuroradiology, General Hospital, Verona/ITALY, [9]Department of Psychiatry and nuclear medicine, Universitaet Duisburg-Essen, Essen/GERMANY, [10]Bât F – 1er étage, Hôpital La Timone CIC – UPCET, Marseille/FRANCE, [11]U825, Inserm, TOULOUSE/FRANCE, [12]Institut National de la Sant et de la Recherche Medicale, Institut National de la Sant et de la Recherche Medicale, Toulouse/FRANCE, [13]Clinical Neuroscience Therapy Area, AstraZeneca R&D, Sodertalje/SWEDEN, [14]LENITEM, IRCCS Fatebefratelli, Brescia/ITALY

Purpose/Introduction: Pharmacog is an industry-academic European project aimed at identifying reliable biomarkers that are sensitive to disease progression in patients with Mild Cognitive Impairment (MCI) [1]. The ultimate goal is to validate biomarkers that can predict conversion from MCI to Alzheimer's disease (AD) using longitudinal biochemical, neuroimaging, neuropsychological and neurophysiological data. Here we present preliminary work aimed at implementing standardized procedures to acquire multi-site structural MRI data for automated brain morphometry using clinical 3T scanners from different vendors and models.
Subjects and Methods: Eight 3T MRI sites participate across Italy, Spain, France and Germany. MRI systems consist of one GE HDxt, two Philips Achieva and five Siemens (two TrioTim, one Verio, one Allegra, and one Skyra) scanners. The acquisition protocol (35 min) includes two structural T1 volumes for brain morphometry: 3D MPRAGE, acceleration factor 2 where possible, 1x1x1mm^3 following recommendations from the ADNI project [2]. After local ethics approval each site is recruiting 5 local healthy volunteers in the age range of the clinical population (55-90 years) for two acquisitions a week apart of the full protocol. Data analysis of each MPRAGE includes a visual quality assurance to control for various artifacts followed by full brain automated segmentation with Freesurfer [3]. A Bland-Altman analysis is used to examine the test-retest reliability of volume and cortical thickness estimates from each site. Spatial reproducibility of the segmented volumes across sessions is examined using the Dice coefficients computed for the volume overlap.
Results: Preliminary morpohometry analysis was done for two sites (Siemens TrioTim and Allegra) with their completed test-retest acquisitions of 5 different volunteers each (Allegra: 68±10 years; Trio Tim: 75±3 years). Segmented voumes, cortical thickness, and their across session reproducibility are comparable across sites (see Figures 1 - 4) and with the literature [4-5].

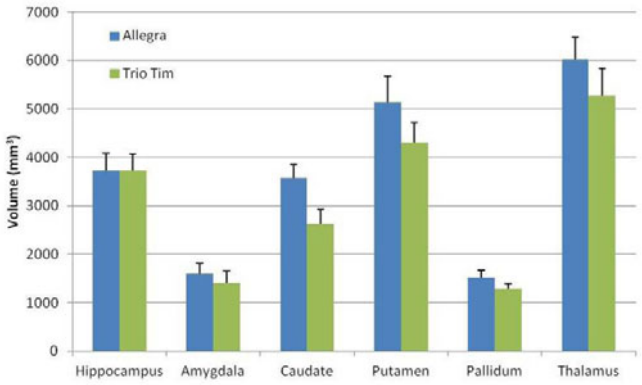

Figure 1: Subcortical volume estimates

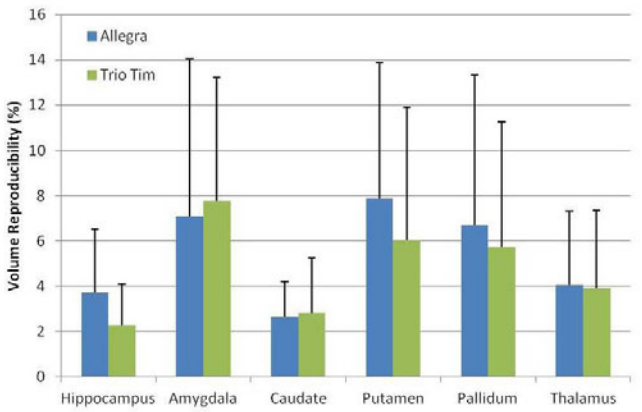

Figure 2: Subcortical volume reproducibility

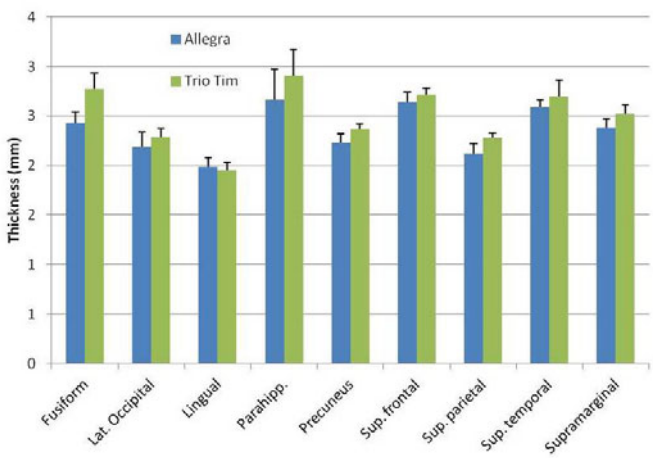

Figure 3: Cortical thickness estimates

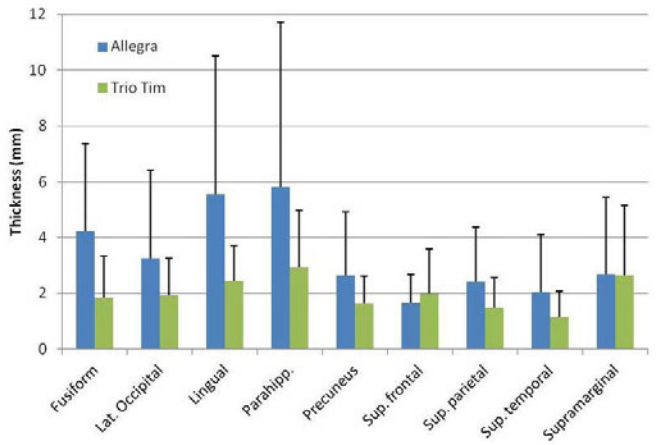

Figure 4: Cortical thickness reproducibility

Discussion/Conclusion: A European multi-site 3T MRI protocol for brain morpohometry analysis was implemented in eight sites covering four countries. Data acquisition is ongoing, preliminary test-retest reproducibility results show good consistency with the literature. These results extend previous test-retest reproducibility studies of Freesurfer-derived metrics [4-5] by considering eight 3T systems.

Pharmacog is funded by the EU-FP7 for the Innovative Medicine Initiative (grant n°115009).

References:

[1] http://www.alzheimer-europe.org/FR/Research/PharmaCog.
[2] Jack et al., J Magn Reson Imaging. 2008; 27(4):685-91.
[3] http://surfer.nmr.mgh.harvard.edu/fswiki
[4] Jovicich et al., Neuroimage 2009; 46(1):177-92.
[5] Han et al., Neuroimage 2006; 32(1):180-95.

492

Differentiation between idiopathic Parkinson's disease, atypical Parkinsonian syndromes and other neurodegenerative diseases with similar symptoms using 3D-MRSI

A. Gröger[1], B. Bender[2], I. Wurster[1], G.L. Chadzynski[2], D. Berg[1], **U. Klose**[2]
[1]Department of Neurodegeneration, Hertie Institute for Clinical Brain Research and German Center for Neurodegenerative Diseases (DZNE), University of Tübingen, Tübingen/GERMANY, [2]Department of Diagnostic and Interventional Neuroradiology, Magnetic Resonance Research Group, University Hospital Tübingen, Tübingen/GERMANY

Purpose/Introduction: Idiopathic Parkinson's disease (iPD) and atypical Parkinsonian syndromes (aPS) are frequent neurodegenerative disorders which are difficult to differentiate among each other. Especially in early stages of diseases the clinical symptoms are non-specific. Additionally, morphological neuroimaging techniques can only be used to rule out some forms of secondary PS (sPS) and other neurological/degenerative diseases with similar symptoms. The pathophysiological difference between iPD and other forms of PS is the primary affection of dopaminergic neurons in the substantia nigra (SN) pars compacta. Therefore, the aim was to estimate the diagnostic value of 3D-MRSI in the SN region for differentiation between iPD, aPS, and sPS.

Subjects and Methods: So far, 20 patients with iPD, 11 with aPS (MSA, PSP, CBD), 7 with sPS or other neurological/degenerative diseases (NPH, tumor, PKAN), and 26 age-equivalent healthy controls were included. All subjects were examined on a 3T whole-body MR scanner (TimTrio, Siemens) using 3D-MRSI as described recently (1). The excitation volume for MRSI was exactly localized in the same position in all 4 groups according to anatomical structures. It was positioned in a way that in each hemisphere one voxel defines the rostral and one the caudal region of the SN. Using a fully automatic evaluation of spectra without any manual changes the metabolite ratios of NAA/Cr were calculated in the four relevant voxels after curve fitting und peak integrating.

Results: In all relevant voxels spectra with good quality could be obtained. For all 4 groups the spectra quality was comparable and enabled evaluation of the rostral-to-caudal ratios of NAA/Cr ratios (Fig. 1). The differences in these rostral-to-caudal NAA/Cr ratios were significant between patients with iPD and all other 3 groups (p<0.001 for all). For healthy controls, NAA/Cr in rostral voxels was greater than in caudal, whereas in iPD patients, this ratio was reversed. Patients with aPS and sPS or other neurological/degenerative diseases showed similar ratios as the control group.

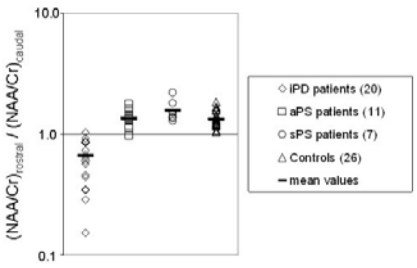

Fig. 1: Logarithmic plot of the rostral-to-caudal ratios of the NAA/Cr ratios with mean values in patients with iPD, patients with aPS, patients with sPS, and healthy controls

Discussion/Conclusion: The typical reversed rostral-to-caudal NAA/Cr ratios in iPD patients compared to healthy controls (1) could be confirmed in larger cohorts. Additionally, aPS and sPS patients showed similar ratios as controls. These results suggest that the ratio is linked to the specific pathology of neuronal loss in the SN pars compacta in iPD. Therefore, 3D-MRSI may aid in the differential diagnosis of patients with clinically unclassifiable PS which do not fulfill the established diagnostic criteria yet.

References:

1 Gröger et al., Eur Radiol 2011; 21(9):1962-9.

493

Comparison of visual assessment of medial temporal lobe atrophy (MTA) on MRI, automatic hippocampal volume measurement and cognitive performance in a 75-year-old population

V. Velickaite[1], L. Cavallin[2], J. Kullberg[3], R. Nordenskjöld[3], A. Simmons[4], L. Lind[5], H. Ahlström[6], L. Wahlund[7], E. Larsson[3]

[1]Department of Radiology, Uppsala University Hospital, Uppsala/SWEDEN, [2]Department of Radiology, Karolinska University Hospital Huddinge, Stockholm/SWEDEN, [3]Department of Radiology, Uppsala University, Uppsala/SWEDEN, [4]Institute of Psychiatry, King's College, London/UNITED KINGDOM, [5]Department of Medicine, Uppsala University, Uppsala/SWEDEN, [6]Radiology, Oncology and Radiation sciences, Uppsala University Hospital, Uppsala/SWEDEN, [7]Department of Geriatrics, Karolinska University Hospital Huddinge, Stockholm/SWEDEN

Purpose/Introduction: Medial temporal lobe atrophy (MTA) is a useful imaging biomarker in early Alzheimer's disease and is less common in normal ageing. Visual scoring of MTA on magnetic resonance imaging (MRI) using the Scheltens scale from 0-4 is a useful, fast and simple technique in a clinical radiological setting [1]. Automatic hippocampal volumetric methods are emerging but are not widely used clinically. An MTA-score of 2 or more is usually considered abnormal below the age of 75 years, and MTA-scores 3 and 4 are considered abnormal above 75 years, although there is no distinct cut-off value. No large study of the MTA-score has been performed in a population of normal 75 year olds.

The purpose of this study was to compare visual scoring of MTA and automatic hippocampal volumetry with cognitive performance in 75-year-old subjects.

Subjects and Methods: In a prospective population based study, 407 subjects (211 men, 196 women), all aged 75 years, underwent MRI of the brain at 1.5T. Visual MTA assessment using the Scheltens scale was performed on coronal T1-weighted 3D gradient echo images. Automatic hippocampal volumetry and measurement of total intracranial volume (ICV) were performed with Freesurfer, version 5.1.0. The results were compared with cognitive tests.

Results: (1) Most subjects had an MTA score of 1-2 (grade 0- 7 subjects, grade 1- 261, grade 2- 96). Only a few had grade 3 (37 subjects) and grade 4 (6 subjects) scores. MTA score is compared with automatic hippocampal volumetry in Figs 1 and 2.

(2) MTA score was significantly higher (p=0.002 and 0.021) and hippocampal volume (HV) significantly larger (p=0.004 and 0.009) in men than in women. The ratio HV/intracranial volume (ICV) was significantly larger in women (p=0.000).

(3) MTA scores as well as hippocampal volumetry showed significant correlation with cognitive tests (Table 1).

Fig 1 and 2. Comparison of right-and left-sided MTA scores and HV (ml) in 407 subjects

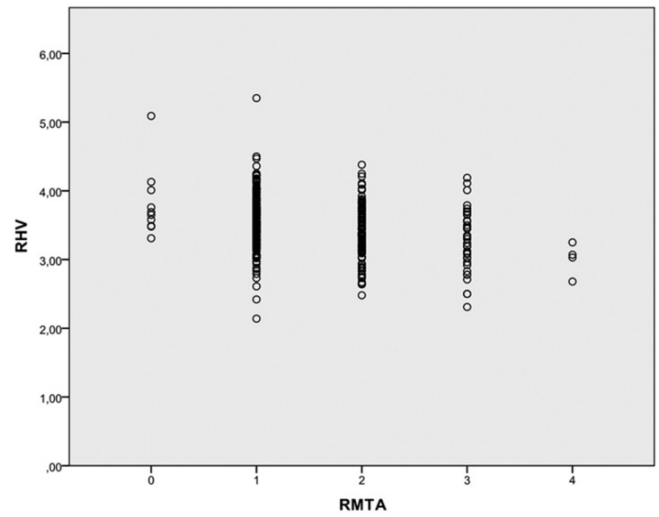

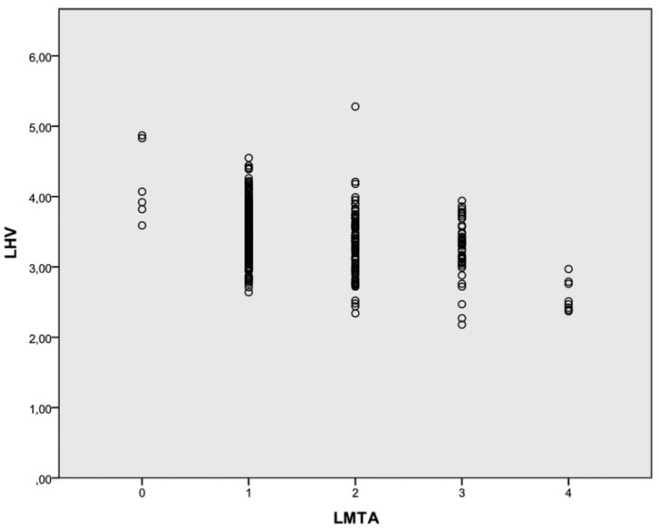

Table 1

	Males (n=211)		Females (n=196)		Cognition-Correlation	
	Left	Right	Left	Right	MMSE	7MS
MTA (mean score +/- SD)	1.57+/- 0.86	1.55+/- 0.75	1.33+/-0.66	1.38+/-0.71	-0.161, p=0.001	0.192, p=0.000
Mean HV (ml,+/- SD)	3.50+/-0.41	3.53+/-0.41	3.38+/-0.42	3.43+/-0.39	+0.146, p=0.003	-0.120, p=0.020
HV/ICV (ratio+/- SD)	0.21+/-0.025	0.22+/-0.026	0.24+/-0.029	0.24+/-0.027	+0.156, p=0.001	-0.104, p=0.042

Abbreviations:
MTA- medial temporal lobe atrophy.
HV- hippocampal volume.
ICV- intracranial volume.
MMSE - mini mental state examination
7MS - 7 minutes screen

Discussion/Conclusion: (1) In a 75 year-old population, most subjects had MTA score 1-2, but 11% had score 3-4.
(2) There is a difference in HV between men and women in agreement with earlier studies [2].
(3) MTA visual scoring and hippocampal volumetry significantly correlated with cognitive tests.
References:
1. Scheltens et al. Journal of Neurology 1995;242:557-60
2. Pruessner, et al. Journal of Neuroscience 2001;21194–200

494

The Substantia Nigra and the Subthalamic Nucleus in Parkinsonian Disorders: a Multimodal MRI Assessment at 3T

O. Al Helli, L. Massey, E. De Vita, J. Thornton, T. Yousry
Neuroimaging Analysis Centre, University College London Institute of Neurology, London/UNITED KINGDOM

Purpose/Introduction: The substantia nigra (SN) and the subthalamic nucleus (STN) are key nuclei in the pathogenesis, pathology, and even treatment of Parkinsonian disorders. Differentiation among them is important for therapeutic and prognostic reasons. The increasing availability of clinical 3T MRI scanners, with their advantages of higher spatial resolution, increased susceptibility effect of iron, and the application of rather sophisticated sequences might help in providing more accurate diagnostic approach and providing a potential surrogate biomarkers for disease progression and effect of novel treatments.
We performed a clinico-radiological, case-control multimodal MRI study including measurement of multi-echo T2 relaxometry, T2* relaxometry, fractional anisotropy (FA) and mean diffusivity (MD) at 3T in a cohort of patients with PD, PSP and MSA with neurological controls.
Subjects and Methods: 59 subjects were recruited from movement disorder clinics and informed consent obtained.
20 patients with PD, 20 with PSP and 19 with MSA in addition to 20 age- and gender- matched control subjects were scanned using multi-sequence MRI protocol that included: multi-echo (3 and 31 echo times) T2 relaxometry, T2* relaxometry and MTR sequences, as well as 3D T1-weighted structural sequence.
ROIs were defined in the SN and the STN by two neuroradiologists, as per anatomical landmarks of the nuclei. ROIs were defined on T2-weighted images and transferred to the co-registered T2, T2*, FA and MD maps.
Results: Our T2, T2*, MD and FA values of the STN are comparable to those in the published literature. Those values were overlapping between the four subject groups. They were not correlated with age, disease duration or clinimetric scores.
T2 measurements, using 31-TE sequence, of the posterior part of the SN in the PD patients is significantly lower than in PSP, MSA and controls. Whereas T2 obtained from 3-TE sequence showed only a trend for lower values.
T2* values were lower in the posterior part of the SN in the PD group in comparison to the other groups. However, such difference was not statistically significant. FA and MD values between disease groups did not show significant differences.
Discussion/Conclusion: Using 31-TE T2 sequence, we found significant differences in T2 relaxation times in the posterior part of the SN in PD in comparison to control and PSP groups.
References:
BARSOTTINI, et al 2007. Differentiation of Parkinson's disease and progressive supranuclear palsy with magnetic resonance imaging: the first Brazilian experience. *Parkinsonism &disorders,* 13**,** 389.
BROOKS, D. 2002. Diagnosis and management of atypical parkinsonian syndromes. *Journal of Neurology*.

495

Reduced functional connectivity of the executive network and cognitive impairment in Parkinson's disease

M. Abaei[1], S.T. Schawrz[1], N. Dashdorj[1], N. Bajaj[2], D.P. Auer[1]
[1]Radiological and Imaging Sciences, University of Nottingham, Nottingham/ UNITED KINGDOM, [2]Neurology, Queens Medical Centre, Nottingham/ UNITED KINGDOM

Purpose/Introduction: Resting state fMRI(RsfMRI) is an established method to assess functional connectivity(FC) of spontaneous brain activity based on temporo-spatial coherence in the low-frequency(<0.1Hz)[1,2]. Previous RsfMRI studies in Parkinson's disease(PD) confirm abnormal connectivity in motor and non motor networks. This study aimed to explore the most prominent features of abnormal brain oscillatory function in ealry PD, and to relate findings with clinical/cognitive assessments.
Subjects and Methods: All participants gave written informed consent, and the relevant governance bodies approved the study. 11 patients (65.7±4.6years,5 male) and 9 controls (63.2±4.7years,5 male) underwent multimodal MRI scans at 3T including RsfMRI (TR/TE=2200/35msec,flip angle 90°,matrix size=64x64x35,slice thickness=3mm). A total of 145 volumes were acquired. Data were pre-processed and analysed using FSL(www.fmrib.ox.ac.uk), including motion correction and removal of non-brain structures with BET. Gaussian spatial smoothing was applied with a FWHM of 5mm, and high pass temporal filtering was used; independent component analysis (ICA) was performed after temporal concatenation to generate group components .ICA maps were subjected to dual-regression analysis, and difference between controls and patients were tested by permutation (5000) tests. Significant activations were identified using threshold free cluster enhancement with corrected P≤ 0.05.
Results: ICA identified 36 components with all main resting state networks. Dual regression analysis identified a disease effect only in executive or so called dorsal attention network (DAN): patients with PD showed reduced connectivity in the left inferior parietal cortex and precuneus compared to controls[Fig1]. In PD,we found significant correlations between the connectivity of the precuneus and DAN (expressed as mean Z scores) and cognitive performance (total and memory subscores of the Addenbrook's cognitive examination,r^2=0.48 and r^2=0.43 respectively).

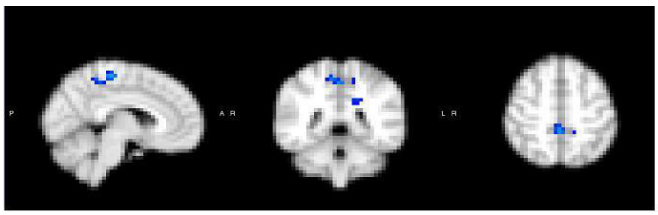

Fig 1: Reduced connectivity in the area of *precuneus resulting from dual-regression analysis with corrected p<0.05(blue)overlaid on template.*

Discussion/Conclusion: Using dual regression ICA anlaysis in non-demented patients with PD, we found most prominent network abnormality in the executive-attention network. Reduced connectivity with the precuneus was furthermore related to cognitive impairment.Our findings in line with [3,4] suggest that fronto-parietal disconnection underlies executive dysfunction in PD.Our findings are well in line with previous PET study [5]positing that the precuneus and inferior parietal lobule form part of dysfunctional cognitive network in PD.
This preliminary study suggests that reduced functional connectivity in the dorsal attention network may explain cognitive impairment in early PD patients. The findings further add to the evidence that RsfMRI is a particular powerful tool to characterise neurodegenerative diseases.
References:
1. Auer,D.P,MagnResonImaging,2008.26(7):p.1055-64.
2. Zuo,X.N,et al.,Neuroimage,2010.49(3):p.2163-77.
3. Tessitore, A,et al.,Parkinsonism Relat Disord,2012.
4. Seeley,W.W,et al.,J Neurosci,2007.27(9):p.2349-56.
5. Dusek,P,et al.,PLoS One,2012.7(1):p.e29635.

496

Pharmacog: Multi-site MRI calibration to study the progression of Alzheimer's disease using brain diffusion data

J. Jovicich[1], M. Marizzoni[2], R. Sala-Llonch[3], N. Bargalló[4], J. Wiltfang[5], L. Roccatagliata[6], F. Nobili[6], P. Schonknecht[7], A. Monnet[8], R. Bordet[8], V. Chanoine[9], A. Auffret[10], J. Ranjeva[9], O. Blin[10], H. Gros-Dagnac[11], G. Zoccatelli[12], P. Payoux[11], D. Bartrés-Faz[4], H. Hardemark[13], G.B. Frisoni[2]
[1]Center for Mind/Brain Sciences, University of Trento, Mattarello/ITALY, [2]LENITEM, IRCCS Fatebefratelli, Brescia/ITALY, [3]Dept de Psiquiatria i Psicobiologia Clinica, Universitat de Barcelona and IDIBAPS, Barcelona/SPAIN, [4]Dept. de Psiquiatria i Psicobiologia Clinica, Facultat de Medicina, Universitat de Barcelona and IDIBAPS, Barcelona/SPAIN, [5]Department of Psychiatry and nuclear medicine, Universitaet Duisburg-Essen, Essen/GERMANY, [6]Dept of Neuroscience, Ophthalmology and Genetics, University of Genoa, Genoa/ITALY, [7]Dept of Psychiatry and Dept of Neuroradiology, University of Leipzig, Leipzig/GERMANY, [8]UL2, Universitè Lille, LILLE/FRANCE, [9]Centre de Resonance Magnetique Biologique et Medicale, Aix Marseille Université, Marseille/FRANCE, [10]Bât F – 1er étage, Hôpital La Timone CIC – UPCET, Marseille/FRANCE, [11]Institut National de la Sant et de la Recherche Medicale, Institut National de la Sant et de la Recherche Medicale, Toulouse/FRANCE, [12]Dept of Neuroradiology, General Hospital, Verona/ITALY, [13]Clinical Neuroscience Therapy Area, AstraZeneca R&D, Sodertalje/SWEDEN

Purpose/Introduction: Pharmacog is an industry-academic European project aimed at identifying reliable biomarkers that are sensitive to disease progression in patients with Mild Cognitive Impairment (MCI) [1]. The ultimate goal is to validate biomarkers that can predict conversion from MCI to Alzheimer's disease (AD) using longitudinal biochemical, neuroimaging, neuropsychological and neurophysiological data. Here we present preliminary work aimed at implementing standardized procedures to acquire and analyze multi-site diffusion tensor imaging (DTI) data for the characterization of white matter (WM) changes using clinical 3T scanners from different vendors and models.
Subjects and Methods: Eight 3T MRI sites participate across Italy, Spain, France and Germany. MRI systems consist of one GE HDxt, two Philips Achieva and five Siemens scanners (two TrioTim, one Verio, one Allegra, and one Skyra) . The acquisition protocol (35 min) includes a single DTI acquisition: b-value= 700 s/mm^2, 5 b0 volumes, 30 gradient directions, 2x2x2mm^3, acceleration factor 2, axial slice acquisition. After local ethics approval each site is recruiting 5 local healthy volunteers in the age range of the clinical population (55-90 years) for two acquisitions a week apart. Data analysis of each DTI volume included eddy current and motion correction followed by the estimation of fractional anisotropy (FA) and mean diffusivity (MD) [2]. Group across-session reproducibility of FA and MD at each site was assessed using an ROI-based analysis from a WM atlas (JHU-ICBM-DTI-81), imported to FSL, non-linear registration to each session FA, mean FA and MD values estimated within each transformed atlas label.
Results: The DTI analysis was done for two sites (Siemens TrioTim and Allegra). The ROI analysis was initially focused on the hippocampus, corpus callosum (CC, genu, body, splenium) and the fornix [3-4], giving consistent results across sites (Figs. 1-2).

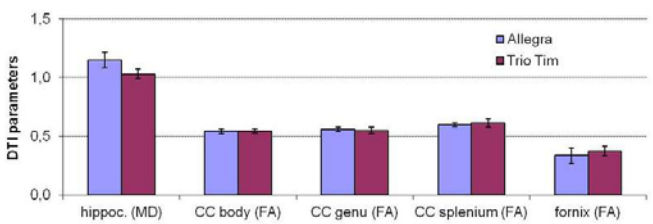

Fig. 1: Mean MD and FA results

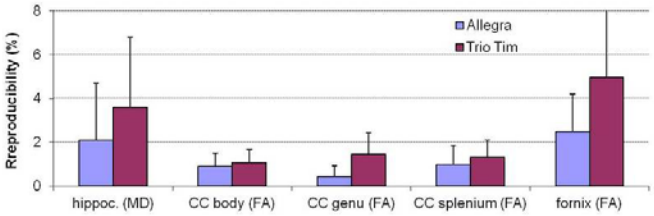

Fig. 2: Mean MD and FA reproducibility

Discussion/Conclusion: A multi-site 3T MRI protocol for brain DTI analysis was implemented in eight sites covering four countries. Data acquisition is ongoing, as well as tuning of the analysis workflow. Preliminary test-retest reproducibility results show good consistency with the literature [5].
Pharmacog is funded by the EU-FP7 for the Innovative Medicine Initiative (grant n°115009).
References:
[1] http://www.alzheimer-europe.org/FR/Research/PharmaCog.
[2] Smith S.M. et al., NeuroImage 23: S208-S219 (2004).
[3] Liu Y. et al., Neurobiol Aging 32, 1558-71 (2011).
[4] Di Paola M. et al., Neurology 74, 1136-42 (2010).
[5] Vollmar et al., Neuroimage 51, 1384-94 (2010).

497

Diffusion tensor tractography of the posterior cingulate gyrus and corpus callosum does not identify MCI-patients at high risk for conversion to Alzheimer's disease in a heterogeneous MCI cohort

D. Svärd[1], F. Szczepankiewicz[2], J. Lätt[1], M. Nilsson[2], K. Nägga[3], S. Palmqvist[3], O. Hansson[3], D. Van Westen[1]
[1]Center for Medical Imaging and Physiology, Lund University Hospital, Lund/SWEDEN, [2]Medical Radiation Physics, Lund University, Lund/SWEDEN, [3]Neuropsychiatric clinic, Skane University Hospital Malmö, Malmö/SWEDEN

Purpose/Introduction: In mild cognitive impairment (MCI) conversion to Alzheimer's disease (AD) is predicted by CSF-biomarkers [1]. Diffusion tensor imaging (DTI) is sensitive to neurodegeneration with diffusivity changes in MCI and AD in the posterior cingulate gyrus (PCG) and corpus callosum (CC) [2]; thus DTI is a potential non-invasive tool for identifying incipient AD. Our aim was to investigate if DTI-parameters mean diffusivity (MD) and fractional anisotropy (FA) can differentiate MCI-patients with pathological CSF (MCIp-CSF) from MCI-patients without pathological CSF (MCInp-CSF) as well as from controls using tractography-based analysis of the PCG and CC.
Subjects and Methods: DTI was performed in sixty-two MCI-patients and thirty-one healthy controls (mean age 70.3±4.0; 51.6% females). MCI-patients were defined as MCIp-CSF (n = 32; mean age 71.6±5.1; 53.1% females) if Aβ42:P-tau ratio < 6,5, T-tau > 350 ng/L and Aβ42 < 530 ng/l in CSF, and as MCInp-CSF (n = 30; mean age 69.1±6.2; 60.0% females) if Aβ42:P-tau ratio > 6,5, T-tau < 400 ng/L and Aβ42 > 530 [1]. DTI data were acquired on a Siemens Trio 3T MRI using a PGSE pulse sequence (TE/TR = 86 ms/8200 ms). Two *b* values were used (0 and 1000 s/mm2) along 64 diffusion encoding directions. Sixty contiguous axial slices with thickness 2 mm and pixel size 2x2 mm were acquired. Whole-brain tractography was generated with FA threshold of 0.20 using TrackVis [3]. Tracts of the PCG and CC were generated and divided into four and three segments, respectively. Global values for each segment were extracted and compared between groups (see Figure 1 and 2).

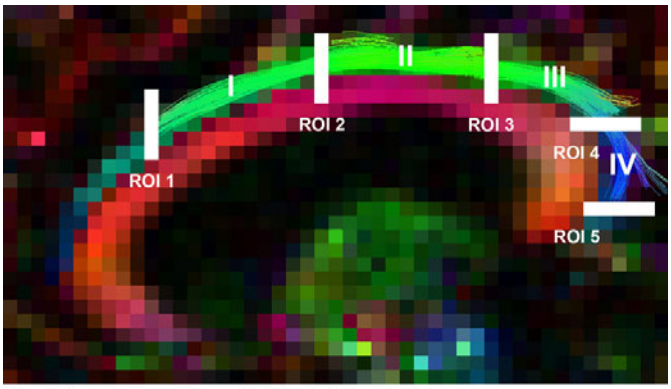

Figure 1. Illustrating generated segment I, II, III and IV of the right PCG tract and positions of ROI 1, 2, 3, 4 and 5 used in the process.

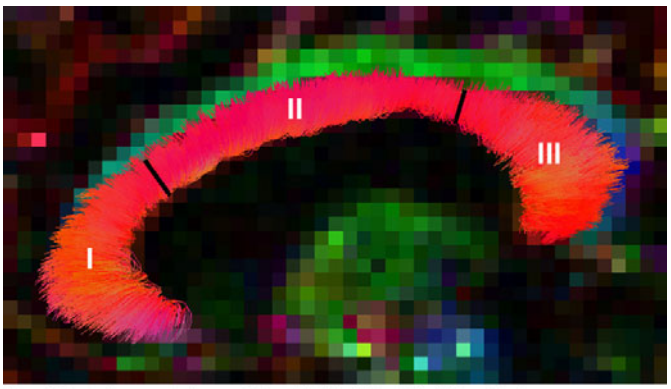

Figure 2. Illustrating generated segment I, II and III of the CC tract. The ROIs used in the process are not shown.

Results: Results are shown in Table 1. DTI-metrics did not differ between MCIp-CSF and MCInp-CSF. In the MCIp-CSF and MCInp-CSF groups together, FA was reduced in segment I and III of the right PCG and MD and FA was increased and reduced, respectively, in segment IV of the left PCG compared to controls.

Table 1. Global diffusion parameters from tractography-based analysis for patients with $MCI_{p\text{-}CSF}$, $MCI_{np\text{-}CSF}$, MCI and controls. Independent-samples t-tests were used to compare differences between groups.

	$MCI_{p\text{-}CSF}$ (n = 32)	$MCI_{np\text{-}CSF}$ (n = 30)	MCI (n = 62)	Controls (n = 31)
Cingulum right MD	0.74 (0.04)	0.74 (0.05)	0.74 (0.04)	0.73 (0.04)
Cingulum right FA	0.52 (0.04)	0.53 (0.04)	0.53 (0.04)	0.54 (0.04)
Cingulum right I MD	0.74 (0.06)	0.75 (0.05)	0.75 (0.05)	0.74 (0.05)
Cingulum right I FA	**0.51 (0.06)** [1]	0.53 (0.05)	**0.52 (0.06)** [3]	0.54 (0.05)
Cingulum right II MD	0.74 (0.05)	0.74 (0.05)	0.74 (0.05)	0.73 (0.04)
Cingulum right II FA	0.55 (0.05)	0.56 (0.04)	0.55 (0.05)	0.56 (0.04)
Cingulum right III MD	0.73 (0.04)	0.74 (0.06)	0.74 (0.05)	0.72 (0.06)
Cingulum right III FA	0.50 (0.05)	**0.49 (0.04)** [2]	**0.50 (0.05)** [3]	0.52 (0.04)
Cingulum right IV MD	0.74 (0.05)	0.73 (0.06)	0.73 (0.05)	0.72 (0.05)
Cingulum right IV FA	0.45 (0.04)	0.45 (0.04)	0.45 (0.04)	0.46 (0.05)
Cingulum left MD	0.74 (0.05)	0.74 (0.03)	0.74 (0.04)	0.72 (0.04)
Cingulum left FA	0.56 (0.04)	0.56 (0.05)	0.56 (0.04)	0.57 (0.04)
Cingulum left I MD	0.76 (0.07)	0.74 (0.04)	0.75 (0.05)	0.73 (0.05)
Cingulum left I FA	0.58 (0.06)	0.58 (0.06)	0.58 (0.06)	0.60 (0.05)
Cingulum left II MD	0.73 (0.06)	0.73 (0.04)	0.73 (0.05)	0.72 (0.04)
Cingulum left II FA	0.58 (0.04)	0.58 (0.05)	0.58 (0.04)	0.60 (0.04)
Cingulum left III MD	0.73 (0.05)	0.74 (0.04)	0.73 (0.04)	0.72 (0.05)
Cingulum left III FA	0.49 (0.04)	0.48 (0.05)	0.49 (0.05)	0.50 (0.04)
Cingulum left IV MD	0.74 (0.06)	**0.75 (0.05)** [2]	**0.74 (0.06)** [3]	0.71 (0.05)
Cingulum left IV FA	**0.44 (0.04)** [1]	**0.44 (0.04)** [2]	**0.44 (0.04)** [3]	0.47 (0.04)
CC MD	0.83 (0.08)	0.83 (0.06)	0.83 (0.07)	0.81 (0.05)
CC FA	0.72 (0.03)	0.71 (0.04)	0.72 (0.04)	0.73 (0.02)
CC I MD	0.88 (0.09)	0.88 (0.10)	0.88 (0.09)	0.84 (0.09)
CC I FA	0.68 (0.05)	0.67 (0.05)	0.68 (0.05)	0.69 (0.04)
CC II MD	0.88 (0.09)	0.90 (0.08)	0.89 (0.08)	0.87 (0.06)
CC II FA	0.71 (0.04)	0.69 (0.05)	0.70 (0.05)	0.71 (0.03)
CC III MD	0.77 (0.08)	0.78 (0.06)	0.77 (0.07)	0.75 (0.05)
CC III FA	0.75 (0.04)	0.75 (0.04)	0.75 (0.04)	0.75 (0.03)

Numbers denote mean (standard deviation). MD = mean diffusivity (mm^2/s), FA = fractional anisotropy, A = anterior segment, CC = corpus callosum and I, II, III and IV = segment I, II, III and IV in an anteroposterior direction.
[1]Statistically significant vs. controls ($p < 0.05$).
[2]Statistically significant vs. controls ($p < 0.05$).
[3]Statistically significant vs. controls ($p < 0.05$).

Discussion/Conclusion: In the present study, MD and FA from tractography-based analysis of DTI-data in the PCG and CC did not differentiate the MCIp-CSF group from the MCInp-CSF group or from controls, suggesting that this technique might not be sensitive enough to identify incipient AD in MCI-patients. However, the differences in diffusivity between MCI-patients and controls indicate that DTI is sensitive to microstructural changes due to neurodegeneration, supporting previous findings [2].

References:

[1] Hansson et al. Lancet Neurol 2006;5:228-34.
[2] Sexton et al. Neurobiol Aging 2011;32:2322.e5-2322.e18.
[3] Wang and Wedeen. Proc Intl Soc Mag Reson Med 2007;15:3720.

498

White and Gray Matter Microstructural Alternations Revealed by Diffusional Kurtosis Imaging Correlated with Cognitive Decline in Alzheimer's Disease and Mild Cognitive Impairment

N. Gong[1], C. Wong[1], C. Chan[2], L. Leung[2], Y. Chu[3]
[1]Diagnostic Radiology, The University of Hong Kong Li Ka Shing Faculty of Medicine, Hong Kong/CHINA, [2]Radiology, United Christian Hospital, Hong Kong/CHINA, [3]Radiology, Kwong Wah Hospital, Hong Kong/CHINA

Purpose/Introduction: The newly introduced Diffusional Kurtosis Imaging (DKI), which is a natural extension of Diffusion Tensor Imaging (DTI), can characterize non-Gaussian diffusion. We tried to investigate the capability of DKI parameters for detecting microstructural alternations of both white and gray matters between patients with mild cognitive impairment (MCI) and Alzheimer's disease (AD), and to investigate if the parameters can serve as biomarkers to indicate cognitive decline.

Subjects and Methods: Diffusion-weighted imaging was performed on 18 ADs and 12 MCIs. Fractional anisotropy, kurtosis parameters, and diffusivity parameters in temporal, parietal, frontal, and occipital lobes were compared between 2 groups using Mann–Whitney U test. Receiver operating characteristic analysis was used to assess regional parameters in differentiating AD from MCI. The correlations between regional parameters and Mini-Mental State Examination (MMSE) scores were investigated using Pearson's correlation.
Fig. 1 MPRAGE (A), segmented white matter (B), gray matter (C), and corresponding parameter maps of FA (D), MD (E), and MK (F) from a typical patient

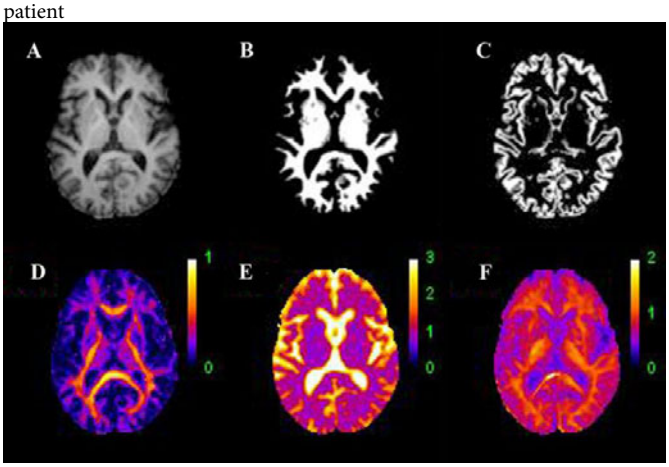

Results: Significant differences of diffusivity and kurtosis parameters were found in both white and gray matters of parietal and occipital lobes. In ROC analysis mean kurtosis in parietal white matter showed the highest area under curve (AUC) of 0.782. Except radial kurtosis and fractional anisotropy, significant correlations with MMSE score were found for all other 5 DKI parameters in several cerebral lobes' white and gray matter.
Fig. 2 ROC curves of MK (AUC = 0.782) and FA (AUC = 0.769) in parietal white matter for differentiating between MCI and AD
PL = parietal lobe, WM = white matter

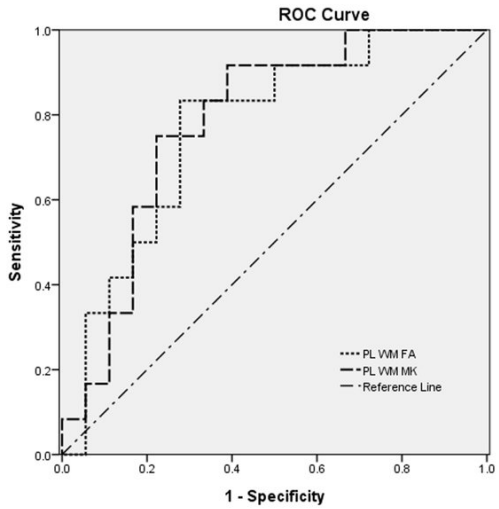

Fig.3 Sample correlations between regional parameters and MMSE scores. MD in temporal white matter (A, r = -0.435, P = 0.016), MK in occipital white matter (B, r = 0.361, P = 0.050), FA in parietal white matter (C, r = 0.323, P = 0.081)

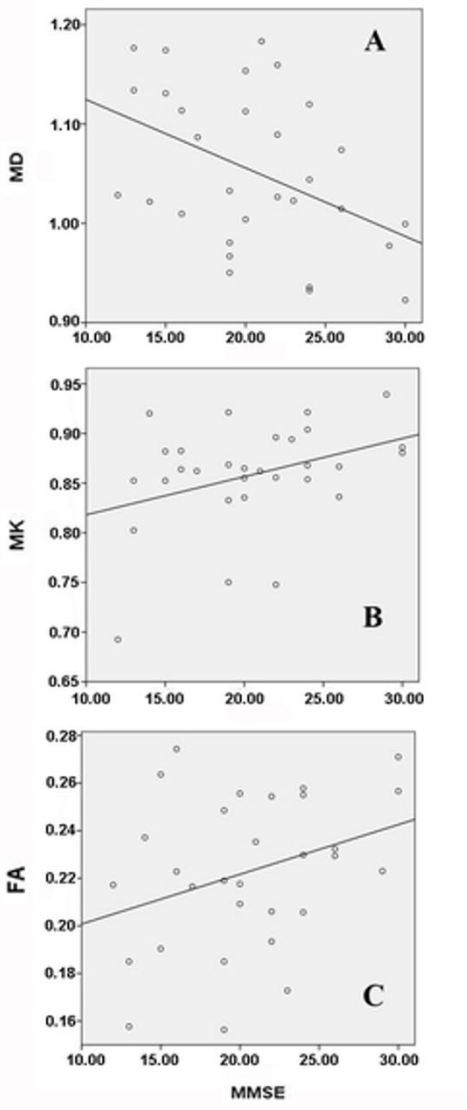

Discussion/Conclusion: Bearing additional information, DKI may provide sensitive biomarkers for disease's early detection and monitoring based on characterizing microstructure in both white and gray matters, and for indicating cognitive decline with reference to the MMSE score.

References:

1. Stahl R (2007) Radiology 243 (2):483-492 2. Huang J (2007) Ann N Y Acad Sci 1097:259-264 3. Liao J (2010) Alzheimer Dis Assoc Disord. 4. Fellgiebel A (2004) Dement Geriatr Cogn Disord 18 (1):101-108 5. Jensen JH (2005) Magn Reson Med 53 (6):1432-1440 6. Lu HZ (2006) NMR Biomed 19 (2):236-247 7. Helpern JA (2011) J Magn Reson Imaging 33 (1):17-23

499

Longitudinal test-retest reproducibility of cortical thickness measurements

F. Ruiz De Arcaute[1], L. Emsell[2], C. Mcdonald[3], S. Sunaert[4], W. Van Hecke[5], D. Loeckx[1]

[1]icoMetrix, icoMetrix, Leuven/BELGIUM, [2]Translational MRI, University of Leuven, Leuven/BELGIUM, [3]Department of Psychiatry, National University of Ireland, Galway/IRELAND, [4]Radiology, University Hospitals Leuven, Leuven/BELGIUM, [5]Dept. of Radiology, Antwerp University Hospital, Antwerp/BELGIUM

Purpose/Introduction: Cortical thickness is a promising biomarker that can provide valuable information about normal and abnormal neuroanatomy [1]. It could be highly relevant in research, clinical trial and clinical settings. Starting from high-resolution MRI, multiple image processing methods exist to measure the thickness automatically. However, to gain widespread acceptance, the biomarker should be highly reproducible in all settings, fast and easy to use. Within this abstract, we perform a test-retest evaluation of voxel-based cortical thickness quantification over 10 acquisitions of the same 27 year-old healthy subject acquired over 17 months.

Subjects and Methods: Images were acquired on a 1.5T Siemens system using an MPRAGE sequence and reconstructed with 0.9 mm isotropic resolution. Cotical thickness was estimated using an in-house developed pipeline, similar to [2]. First, the baseline image (first timepoint) is registered to an atlas. Next, each follow-up image is registered to the registered baseline image. Then, the brain is extracted and segmented using a maximum likelihood expectation maximisation method. Subsequently, the cortical thickness is calculated using a Lagrangian initialisation and Eulerian solution. Finally, the cortex is subdivided in multiple regions by an atlas to evaluate the regional thickness.

Results: All scans were processed without manual intervention. An overview of the images before and after co-registration is provided in respectively Figure 1 and Figure 2. Figure 3 represents the variability of each region over time. Quantitative results of the reproducibility are provided in Table 1.

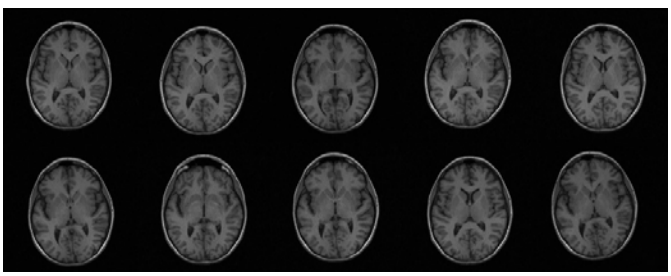

Figure 1: Images prior to registration

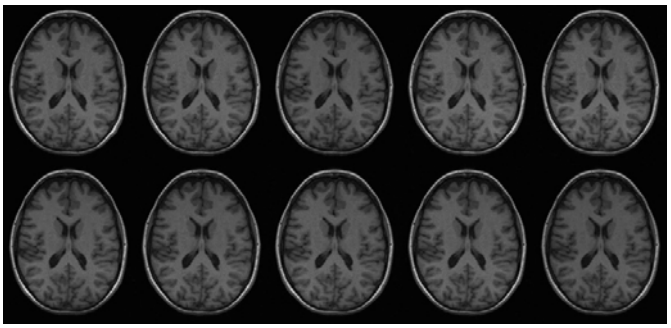

Figure 2: Images after registration to atlas

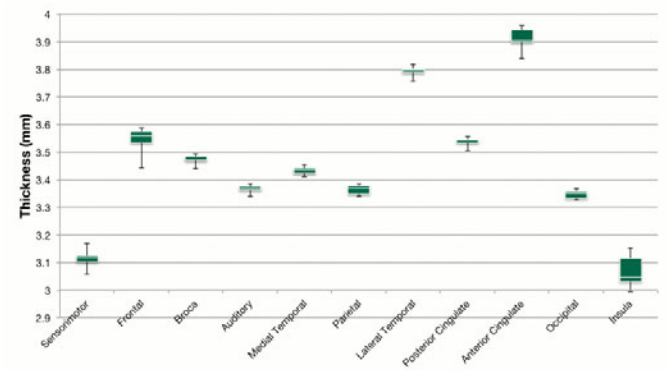

Figure 3: Thickness variability in each region.

Table 1: Quantitative reproducibility results

	Sens	Frontal	Broca	Audi-tory	Med Temp	Parie-tal	Lat Temp	Post Cing	Ant Cing	Occipital	Insula	All
Mean (mm)	3.12	3.55	3.47	3.37	3.43	3.37	3.80	3.54	3.92	3.35	3.07	3.45
Std-dev (mm)	0.03	0.04	0.02	0.01	0.01	0.02	0.02	0.02	0.04	0.02	0.06	0.03
% diff.	3.53%	4.07%	1.54%	1.36%	1.30%	1.40%	1.64%	1.43%	3.05%	1.23%	5.20%	2.34%

Discussion/Conclusion: The standard deviation ranges from 0.01mm to 0.06mm; the relative difference ((max-min)/mean) ranges from 1.23% to 5.20%. This is relatively small compared to the variability over the different regions, with a standard deviation of 0.25mm and a relative difference of 24.52%. Cortical thickness measurement using our technique demonstrates high reproducibility when applied to single-centre longitudinal data.

References:

[1] Voxel-based cortical thickness measurements in MRI, Hutton C et al, Neuroimage. 2008 May 1;40(4):1701-10.

[2] LoAd: a locally adaptive cortical segmentation algorithm, Cardoso MJ et al, Neuroimage. 2011 Jun 1;56(3):1386-97.

500

Identification of the ventrointermediate thalamic nucleus using Q-ball calculation

C. Kiefer[1], T. Lönnfors-Weitzel[2], L.S. Stieglitz[1], M. Oertel[3], M. Schüpbach[4], A. Kaelin-Lang[4], A. Pica[5], N. Meier[4], C. Pollo[3]

[1]Institute of Diagnostic and Interventional Neuroradiology, University Hospital of Bern, Bern/SWITZERLAND, [2]DRNN, Institute of Diagnostic and Interventional Neuroradiology, Inselspital, University of Bern2, Bern/SWITZERLAND, [3]Department of Neurosurgery, Universityhospital Bern, Inselspital, Bern/SWITZERLAND, [4]Department of Neurology, Universityhospital Bern, Inselspital, Bern/SWITZERLAND, [5]Department of Radiooncology, Universityhospital Bern, Inselspital, Bern/SWITZERLAND

Purpose/Introduction: Introduction:
Localization of thalamic nuclei for targeting in deep brain stimulation (DBS) is challenging. They are not clearly identifiable on standard MRI. The dentato-rubro-thalamic tract connects thalamic ventrointermediate nucleus (Vim) with cerebellum. We evaluated the reliability of Q-ball calculation (QBC) in predicting position of the functional target compared to coordinate based localization of Vim in patients who underwent DBS for essential tremor (ET)

Subjects and Methods: Methods:
5 patients received bilateral DBS in Vim for treatment of ET 2011/2012. Conventional targeting was based on atlas coordinates and high resolution MRI (0.57 isotropic 3D TR 3000, TE 241). MRI was performed at 3 Tesla (Trio or Verio, 32 channel head coil, Siemens Medical Solutions, Erlangen, Germany). QBC is based on a 42 directional diffusion-sequence and performed with a house intern developed software. We analyzed connectivity by QBC of dentate nucleus with thalamus and thereby retrospectively identified Vim. Co- registration of the connective-imaging target compared to atlas-based pre-op targeting and with postoperative CT coordinate of the active contact of the implanted lead, which was correlated with the best clinical effect on tremor, was performed. Euclidian distances were measured between the coordinate of the active contact of the implanted lead, the seed voxel for QBC , preoperative target and the connective imaging target..

Results: We were able to localize Vim according to connectivity via the dentato-rubro-thalamic tract in all patients on both sides. Average localization of active contacts was 14.6mm lateral (SD 1.24), 5.37mm (SD 0.94) posterior and 2.21mm cranial of MC (SD 0.69). The lead contacts were found medial to the connectivity target in 7/10 of the implanted electrodes and inside the connectivity target in 3/10 cases, reflecting the tract starting at the boarder of VIM. The average distance between the active contact and the connectivity target was 3.38 mm (SD 1.57). The active contact was found at an average of 1.5 mm (SD 1.22) anterior of the connectivity target. The antero-posterior as well as the vertical position showed good correlation with sites of effective DBS.

Discussion/Conclusion: Conclusions:
Connectivity analysis of Vim position by QBC provided direct visualization in all cases. Our preliminary results suggest that the reliability of QBC in determining pre-op targeting of the Vim is comparable to atlas-based targeting. Larger prospective calculations are needed to determine the robustness of QBC in providing refined information useful for neurosurgical and radiosurgical treatment of tremor.

References:

Reference: DS Tuch. Q-Ball imaging. Magnetic Resonance in Medicine 52,1358-72 (2004).

EPOS™ Poster

Brain - other

501

Cerebral perfusion changes in preterm infants during early brain development

R. O'Gorman[1], H. Bucher[2], B. Koller[2], H. Speckbacher[3], D. Alsop[4], A. Shankaranarayanan[5], J. Fauchere[2], C. Hagmann[2]
[1]Center for MR Research, University Children's Hospital, Zurich/SWITZERLAND, [2]Neonatology, University Hospital, Zurich/SWITZERLAND, [3]Diagnostic Imaging, University Children's Hospital, Zurich/SWITZERLAND, [4]Radiology, Beth Israel Deaconess Medical Center and Harvard Medical School, Boston/MA/UNITED STATES OF AMERICA, [5]Global Applied Science Laboratory, GE Healthcare, Menlo Park/CA/UNITED STATES OF AMERICA

Purpose/Introduction: Diffuse white matter injury is the most prominent brain injury reported in preterm infants and is associated with neurodevelopmental impairment. [1] Since cerebral ischemia represents a major risk factor for white matter injury, [2] perfusion abnormalities in preterm infants may reflect a selective vulnerability to brain injury. The purpose of this study was to investigate the development of cerebral perfusion during the neonatal period.
Subjects and Methods: The patient group consisted of 8 unsedated preterm infants (4 male) born between 26 and 31 weeks gestation. Cerebral perfusion images were acquired at term equivalent age (37-43 weeks) using a pulsed continuous arterial spin labelling (pCASL) sequence. Perfusion images were normalised to a neonatal template and correlations between perfusion, gestational age at birth (GA), corrected gestational age at scan (CGA), and postnatal age were assessed by permutation testing. [3]
Results: Perfusion was increased in the basal ganglia, brainstem, and sensorimotor areas relative to other cortical and subcortical regions. Postnatal age correlated positively with global perfusion ($p<0.05$, corrected), and CGA correlated positively with perfusion in the occipital lobe and sensorimotor regions (figure 1). No significant correlations between perfusion and GA were observed. Haemoglobin (Hb) levels were not significantly associated with age or CGA ($p>0.4$).

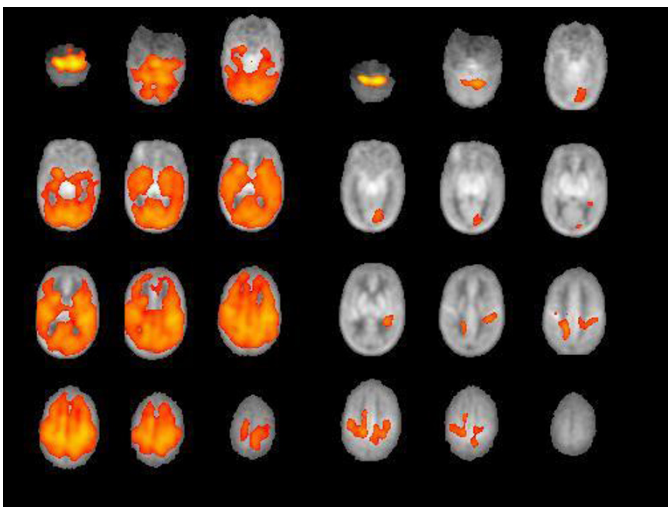

Figure 1. Perfusion vs. postnatal (left) and corrected gestational age (right).

Discussion/Conclusion: Although the perfusion values could be confounded by hematocrit-related blood T1 differences [4], the lack of a significant correlation between age and Hb suggests that the observed age-related perfusion changes are unlikely to be driven by T1 effects. While both the postnatal age and CGA influence the development of perfusion, postnatal age appears have a larger effect on the global perfusion while CGA affects local perfusion in regions of high metabolism and myelination. The rapid increase in perfusion with postnatal age is consistent with the known increase in vascular flow during the neonatal period, [5] and may account for the increased cortical perfusion seen in preterms at term-equivalent age relative to term infants. [6] These results underscore the importance of taking developmental effects into account when interpreting perfusion or fmri studies in neonates.

References:
1. Volpe JJ. (2003) Pediatrics 112;176
2. Hagberg H., et al.(2002) Ment Retard Dev DR 8: 30–38
3. Bullmore, E. et al. (1999) IEEE Trans Med Imag. 18(1):32
4. Lu H., et al. (2004) Magn Reson Med 52:679–682
5. Kehrer M., Schöning M. (2009) Ped Research 66(5):560-564
6. Miranda M., et al. (2006) Ped Research 60(3):359-363

502

Fractional cerebral blood volume quantification with the Rapid Steady State T1 MRI technique in humans

T. Perles-Barbacaru[1], I. Tropres[2], D. Chechin[3], S. Grand[4], J. Le Bas[5], F. Berger[1], H. Lahrech[1]
[1]Grenoble Institute of Neurosciences, INSERM U836, La Tronche/FRANCE, [2]SFR Biomedical NMR and Neurosciences, [3]T Facility, La Tronche/FRANCE, 3/, Philips Healthcare, Suresnes/FRANCE, [4]CHU Grenoble,, INSERM U836, La Tronche/FRANCE, [5]3T Facility, SFR Biomedical NMR and Neurosciences, CHU Grenoble,, La Tronche/FRANCE

Purpose/Introduction: Accurate arterial input function (AIF) determination for blood volume fraction (BVf) quantification by MRI, is not straightforward in the clinical setting. RSST1-MRI yields quantitative cerebral BVf measures without requiring the AIF, and has been validated in rodents at high magnetic field(1,2). In this work, the RSST1-technique is transferred to clinics and the Dotarem® (Guerbet) dose is established at 1.5T.
Subjects and Methods: With approval by the Research Ethics Committee, RSST1-MRI was included in the neuroimaging examination on a Philips Achieva scanner of neurooncological patients (n=9) requiring Dotarem® administration for routine follow up. RSST1-MRI consists of a dynamic (NR=120, duration 90s) single-shot 2D turbo-field-echo acquisition (non-selective inversion pulse, Tinv/TR/TRecho/TE/α = 325ms/750ms/4ms/1.27ms/10deg, 64x37 matrix), during which Dotarem® was administered at a dose of 0.1 - 0.2mmol/kg using an automatic injector (3mmol/s).
The signal was normalized according to Snorm(t)=(Spost(t)-<Spre>)/S0, where Spost(t) is the post-contrast signal, <Spre> is the average pre-contrast signal, and S0 is the equilibrium signal from the vascular and extravascular compartment(1) acquired in 30s with TR/NR =10s/3 using the same sequence without inversion pulse.
Results: At 1.5T, Spre is ≈0 for tissues with T1≥900ms such as blood (T1=1250ms(3)) and cortical gray matter. For a dose ≥0.13mmol/kg (n=7), Snorm(t) in blood and brain tissue with Dotarem® confined to the vascular space reaches a steady state at maximum amplitude lasting ≈8s during which BVf=Snorm(1,2) (Figure1). We found BVf≈1 in large vessels with little partial volume effect and BVf=0.04±0.1 in healthy appearing gray matter.

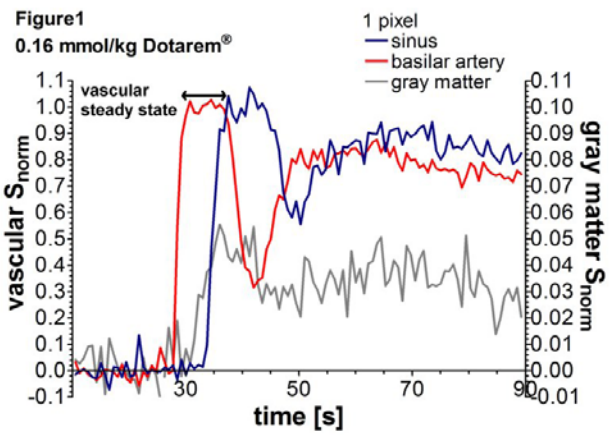

Figure2: BVf map
spatial resolution 3.4mm × 3.4mm × 6mm

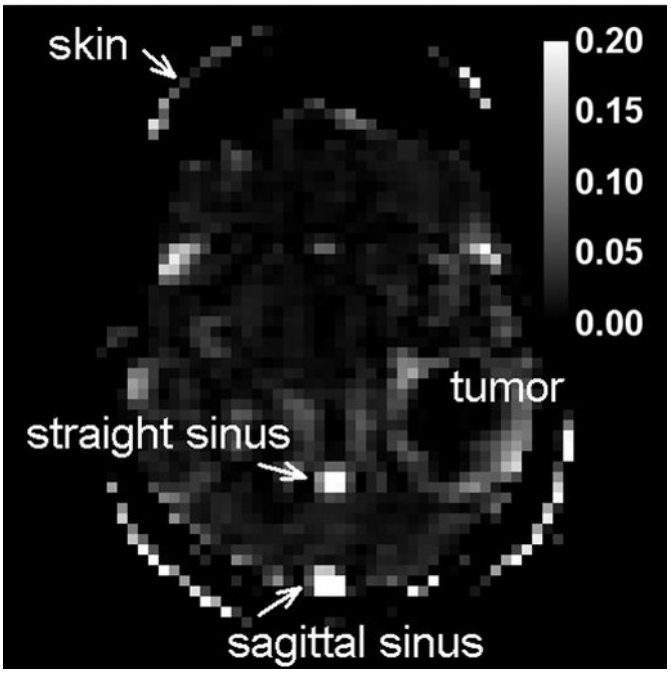

Discussion/Conclusion: RSST1-MRI yields quantitative cerebral BVf maps (Figure2) with clinically approved Dotarem® doses. This study shows the clinical feasibility of RSST1-MRI for direct BVf quantification without AIF measurement. In case of permeable vasculature in brain lesions, a pharmacokinetic model can be applied(4).

References:

(1)…Perles-Barbacaru and Lahrech, JCBFM 2007;
(2)…Perles-Barbacaru et al, MRM accepted;
(3)…Rohrer et al, Invest Radiol 2005;
(4)…Perles-Barbacaru et al, ESMRMB 2008;

503

Impact of Diffusion Tensor Imaging in surgical planning of patients with intra-axial eloquent region brain lesions

S.S. Gupta[1], Z.M. Patel[2], A. Bagadia[3], B.K. Misra[3], H. Purandare[3]
[1]MRI, P.D. Hinduja Hospital, Mumbai/INDIA, [2]Radiology, Hinduja Hospital, mumbai/INDIA, [3]Neurosurgery, Hinduja Hospital, Mumbai/INDIA

Purpose/Introduction: To assess the role of diffusion tensor imaging (DTI) to strategise surgical planning in patients with intra-axial lesions in the eloquent areas.

Subjects and Methods:

60 patients (M:F =41:19) were preoperatively evaluated with DTI (25 directions) and image guidance on 1.5 T MRI. These patients had intra-axial lesions near or involving the eloquent cortex and tracts (mainly peri-rolandic/ corticospinal tracts: n = 45, perisylvian/ arcuate fasciculus; n = 7 and parieto-occipital / optic radiation: n=5; thalamic deep insular / internal capsule n=3).

Images were post-processed to obtain fractional anisotropy (FA) maps, directionally-encoded color FA maps; and 3D fiber tractography maps. The surgeon reviewed the routine MRI images to determine a pre-operative approach, followed by evaluation of DTI data to reassess surgical planning. The frequency of change of strategy of the surgical approach was graded in the form of a scale (table below), to quantify the usefulness of the DTI data in pre-operative decision making and helping a more radical yet safe excision.

DTI score	Description	Surgical re-evaluation
1	Tracts not in close proximity	No benefit
2	Tracts in close proximity but with intervening normal tissue	Gives overall orientation between tumor and fiber tracts
3	Tracts in close proximity to tumor	Demarcates / restricts direction of resection or retraction
4	Tracts in very close proximity/ abnormally displaced	Change in surgical approach

Results: The impact of DTI on pre-operative planning, intra-operative technique & approach was graded by the above mentioned score. Significant alteration in surgical planning (DTI score=4) was seen in 21 patients (35%); definite impact on the surgical procedure by limiting retraction & resection margins (DTI score=3) in 15 cases (25%); DTI score =2 in 12 patients (20%) and no benefit (DTI score =1) in 12 cases (20%).

Discussion/Conclusion:

- Intraoperative cortical & subcortical electrical stimulation, which remains the gold standard of functional mapping in neurosurgery, is invasive with risks and may at times fail due to cortical dysfunction[1]. DTI provides a non-invasive technique, which when integrated with intra-operative motor evoked potential, positively impacts operative planning, confidence and surgical outcome.

In our study, pre-operative DTI showed a significant impact (DTI score >/= 3) in 60% of patients. The surgical approach was changed based on the predicted location of the fibers allowing for aggressive and safe resection of the lesion.

References:

1) Kamada K, Sawamura Y, Takeuchi F, et al. Functional identification of the primary motor area by corticospinal tractography. Neurosurgery 2007; 61 (Suppl. 1): 166–76.

504

Does skull thickening have any effect on the association between cognition and brain in older adults?

B.S. Aribisala[1], N.A. Royle[1], M.C. Valdes Hernandez[1], C. Murray[2], L. Penke[2], A. Gow[2], S. Maniega[1], J.M. Starr[3], M.E. Bastin[1], I.J. Deary[4], J.M. Wardlaw[1]
[1]Brain Research Imaging Centre, Division of Clinical Neurosciences, University of Edinburgh, 2XU/UNITED KINGDOM, [2]Department of Psychology, University of Edinburgh, 9JZ/UNITED KINGDOM, [3]Geriatric Medicine Unit, Uiversity of Edinburgh, 2DN/UNITED KINGDOM, [4]Psychology, University of Edinburgh, Edinburgh/UNITED KINGDOM

Purpose/Introduction: Intracranial volume (ICV) is commonly used as a marker of premorbid brain size in neuroimaging studies because it is thought to remain fixed throughout adulthood and not be affected by disease or age-related changes [1]. However, thickening of the inner skull table would encroach on ICV and could mask true brain atrophy [2]. We investigated the effect that skull thickening might have on the associations between brain atrophy and cognition in a group of community dwelling older adults in their seventies.

Subjects and Methods: The sample comprised 60 non-demented older adults who underwent MRI at mean age 73 years and assessed on cognitive ability at mean age 11 and 73 years. PCA was used to derive factors of general cognitive ability (g), information processing speed and memory from the recorded cognitive ability data. Imaging was performed using a GE Signa Horizon HDxt 1.5T clinical scanner. Scan data [3] included: T_2W, T_2*W, and FLAIR sequences. The total brain tissue volume (TBV) and ICV with (estimated original ICV) and without (current ICV) adjusting for the effects of inner table skull thickening were measured. Image segmentation used, MCMxxxVI [4] and inner table skull thickening was identified as described elsewhere [2]. General linear modelling was used to test for associations.

Results: All cognitive ability variables measured in old age were significantly ($P<0.01$) associated with percentage TBV in current ICV (Table, g: $\eta^2=0.177$, speed: $\eta^2=0.264$ and memory: $\eta^2=0.132$). However, only speed was significantly associated with percentage TBV in estimated original ICV ($\eta^2=0.085$,$P=0.034$), not g ($\eta^2=0.048$,$P=0.11$) or memory ($\eta^2=0.044$,$P=0.127$). The association

between cognitive ability measures and the percentage of TBV in current ICV was significantly larger than with percentage of TBV in estimated original ICV (Figure, g: t= 2.67,P=0.01; speed: t=3.16,P=0.003).

Table: Association between brain atrophy measures and cognitive ability (g, speed, memory) using general linear modelling with and without accounting for skull thickening in the computation of ICV.

	g			Speed			Memory		
	F	p	η^2	F	p	η^2	F	p	η^2
Percentage of TBV in current ICV	**11.2**	**0.002**	**0.177**	**18.3**	**<0.001**	**0.264**	**7.88**	**0.007**	**0.132**
Percentage of TBV in Estimated original ICV	2.6	0.11	0.048	**4.7**	**0.034**	0.085	2.4	0.127	0.044

Model controlled for age in days, age 11-IQ and gender. Dependent variables were g, speed and memory. Gender was used as fixed factor while percentage of TBV in current ICV, percentage of TBV in estimated original ICV, age in days and age-11 IQ were used as covariates. n= 60, the degree of freedom for each of the covariates and the fixed factor was 1. η^2 = partial Eta Squared.

Discussion/Conclusion: Not accounting for skull thickening when computing ICV could distort the association between brain atrophy and cognitive ability, though further investigations in larger samples are required to determine the true effect of skull thickening on the association between brain atrophy and cognitive ability. Future studies of cognitive ageing using structural imaging should consider accounting for inner table skull thickening when measuring ICV.

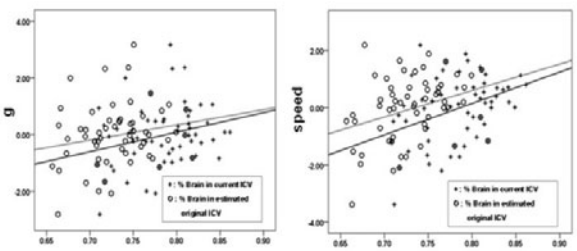

Figure : Scatter plots with regression lines of (left) g against percentage of TBV in current ICV (bold line), and in estimated original ICV (dotted line). (right) speed against percentage of TBV in current ICV (bold line), and in estimated original ICV (dotted line). The association between *g* and the percentage of TBV in current ICV was significantly larger than with percentage of TBV in estimated original ICV (Steiger's paired t= 2.67, n=60, P=0.01). The association between speed and the percentage of TBV in current ICV was also significantly larger than with the percentage of TBV in estimated original ICV(Steiger's paired t= 3.16, n=60, P=0.003).

References:
[1] Skoog I et al.,2011, NBA.
[2] Royle NA et al., Under Review,Neuroradiology.
[3] Wardlaw, J.M et al., 2011, International-Journal-of-Stroke.
[4] Hernández, M.C., et al., 2012, Open-Journal-of-Radiology.

505

Towards the differentiation between calcified regions and iron deposits in ageing brains on conventional structural MRI

M.C. Valdes Hernandez[1], A.J. Kiker[2], D.A. Dickie[1], A. Glatz[1], N.A. Royle[1], B.S. Aribisala[1], S. Munoz Maniega[1], M.E. Bastin[3], I.J. Deary[4], J.M. Wardlaw[1]
[1]Clinical Neurosciences, University of Edinburgh, Edinburgh/UNITED KINGDOM, [2]Medicine and Veterinary Medicine, University of Edinburgh, Edinburgh/UNITED KINGDOM, [3]Medical and Radiological Sciences, University of Edinburgh, Edinburgh/UNITED KINGDOM, [4]Psychology, University of Edinburgh, Edinburgh/UNITED KINGDOM

Purpose/Introduction: Minerals such as iron and calcium accumulate in ageing brains mainly in basal ganglia structures. Their presence has been linked with adverse effects from specific diseases to cognitive decline[1]. Here we explore the differentiation between calcified regions and non-calcified iron deposits on conventional structural MRI sequences.
Subjects and Methods: We used co-registered T1- and T2*-weighted(W) sequences from 100 MRI datasets of community-dwelling individuals aged 72-73 years old. Potential deposits of both minerals were identified as areas of hypointensity on T2*W images. "Mainly iron" areas showed no signal change on T1W, and "calcified areas" showed a significant signal change on this sequence [1,2]. Despite being mutually exclusive according to the criterion followed for their identification, in some cases, the size of these accumulations and the intensity inhomogeneities in the region, made it impossible to separate one from the other. When this was the case, the region was double-labelled. We developed a statistical framework for characterising the differentiation between both types of regions after been segmented, based on Euclidean distance analyses, of joint T1W_T2*W intensity histograms (Figure 1).
Figure 1
Results: Iron deposits were identified in 82/100 subjects, calcified regions in 91/100 and both types in 77/100. We found two statistically significant distinct distributions for calcified regions and non-calcified iron deposits in the cumulative joint T1W_T2*W intensity histograms from all subjects (t=16.934, p<0.001) (Figure 2).
Figure 2
The mean volume of affected tissue per subject for calcified and non-calcified deposits were 236.74±309.70mm^3 and 283.76±581.51mm^3; respectively. Further, location-based analysis showed that iron deposits were mainly found in the basal ganglia, while calcified regions were mainly identified in the choroid plexus. We also found a positive association between both types of regions (ß=0.32, p<0.005), consistent with existent literature reports[1].
Discussion/Conclusion: The method described here offers high reliability in the differentiation of both minerals from conventional structural MRI. Higher cross-correlation in the joint T1W_T2*W histograms of the iron deposits with respect to calcified regions suggests that, although there is an unavoidable overlap between both, depositions of iron macromolecules alone cause a more definable signal change in these sequences than when there are other mineral aggregates sharing the same physical region, and therefore, the automatic segmentation of iron deposits can be more plausible than that of calcified regions.
References:
[1] Valdes Hernandez MC, Maconick LC, Tan EMJ and Wardlaw JM (2012) Eur Radiol (in press)
[2] Curtis AR, Fey C, Morris CM, et al. (2001) Nature Genetics 28, 350-354

506

Post Partum Convulsions a Mystery to Solve: Value of Brain MRI Study

N.F. El Ameen[1], H.S. Abdel Ghany[2], A.K. Kotib[3]
[1]Radiology, El Minia univeristy hospital, El Minia/EGYPT, [2]Radiology, El Minia university, El Minia/EGYPT, [3]Obstetric and gynecology, El Minia univeristy, El Minia/EGYPT

Purpose/Introduction: The aim of this study was to evaluate the role of MRI of the brain in women with post partum convulsion and correlate them with clinical data.
Subjects and Methods: In a prospective study, a total of 48 patients (age range from 25 – 37ys; mean 31years) with post partum convulsions and suspected to have CNS complications were collected. The patients were referred from Obstetric and Gynecology Department from a time interval between January 2010 and October 2011. MRI was performed for all patients using a 1-T scanner. All patients were included after meting the inclusion criteria which depends on the clinical history and examination. MRI findings were collected and classified according to final diagnosis.
Results: MRI examination of the brain was positive in 27 (56.3%) out of 48 patients who presented with post partum convulsions. Dural sinus thrombosis was the most frequently encountered finding representing 12/27 (44.4%). Intra cerebral hemorrhage was encountered in 6/27 (22.2%). Posterior reversible encephalopathy and subarachnoid hemorrhage were encountered in 5/ 27 (18.5%) and 3/27 (11.1%) patients respectively. Only one patient had pituitary apoplexy 1/27 (3.7%). The remaining 21 (43.7%) patients had negative MRI.

Discussion/Conclusion: Post partum convulsion is a serious condition and may be caused by delayed eclampsia or other neurological condition. MRI can solve this mystery and differentiate between variable causes. So MRI of the brain must be routinely done for these patients without delay to ensure correct diagnosis and appropriate treatment.

References:

Ginzburg VE and Wolff. Headache and seizure on postpartum day 5: late postpartum eclampsia. Canadian Medical Association 2009; 17, 180(4): 425–428.

507

Measuring brain stiffness using MRE: Are we there yet?

C.H. Rua, T.A. Carpenter, M.O. Mada
Wolfson Brain Imaging Centre, Wolfson Brain Imaging Centre, Cambridge/ UNITED KINGDOM

Purpose/Introduction: Brain MR Elastography has been developed as a non-invasive imaging biomarker to measure brain stiffness. Using a phase contrast MRI technique together with an external mechanical actuation device, it is possible to detect propagating shear waves inside the brain. Stiffness can then be estimated by applying inversion methods to the phase data. The most simple and commonly used methods, the Algebraic Helmholtz Inversion (AHI) and Local Frequency Estimation (LFE), have been widely applied for brain stiffness studies[1] or to detect changes in brain elasticity in pathologies such as multiple sclerosis[2] and normal pressure hydrocephalus[3]. However, the cost of the model's oversimplification and a wrong processing scheme may lead to incorrect elasticity quantification. Here both methods were studied on healthy brain data in order to compare and test their performance.

Subjects and Methods: Five healthy volunteers were scanned on a 3T scanner using a modified SS-EPI sequence with incorporated sinusoidal motion-encoding gradient (MEG) (1-3 cycles; 40mT/m). 32 phase offsets were acquired with 5 slices positioned above the third ventricle. A piezoelectric system coupled to a head cradle via a transmission rod, produced oscillations at low frequencies (25.0, 37.5, 50.0, 62.5, 75.0Hz) synchronized with the MEG.

A MATLAB script was built for AHI processing according to [4]. The real part of the complex wave maps were taken as the elasticity measures, G', at each spatial position. Stiffness maps applying the LFE algorithm were obtained using MRE/Wave software (http://mayoresearch.mayo.edu/mayo/research/ehman_lab/mrw-wave.cfm). In order to evaluate WM/GM stiffness, T2-weighted amplitude images from the MRE dataset were used to build tissue-type ROIs with FSL software.

Results: An example of the inversion methods' outcome at 50Hz and 75Hz is shown in figure 1. Averaged G' results were obtained over the five healthy volunteers and slices for each excitation frequency (figure 2). Figure 3 shows G' variations at 75Hz with the slice number.

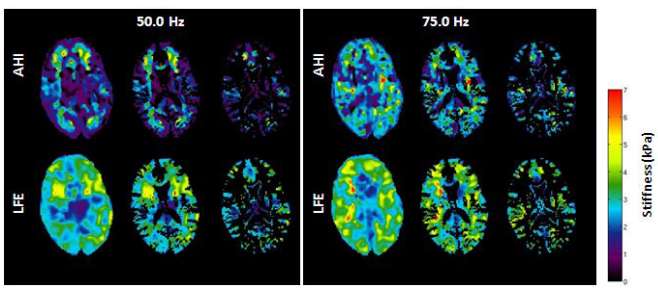

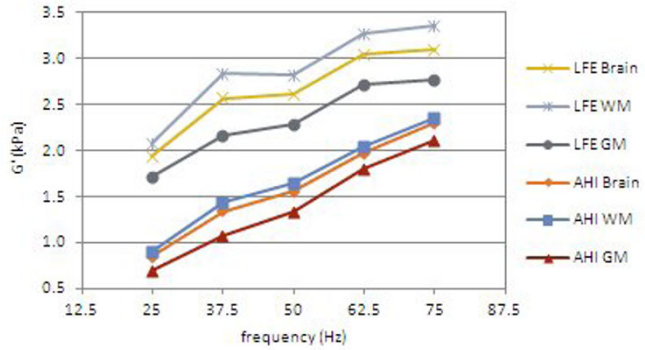

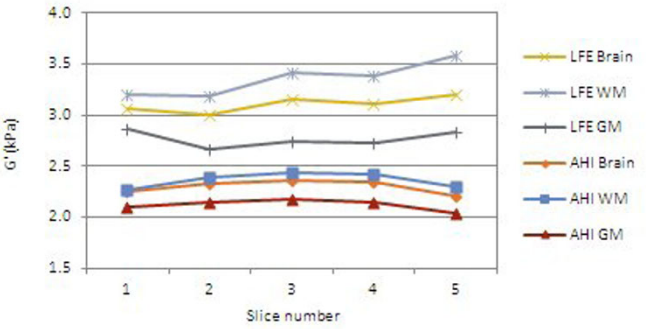

Discussion/Conclusion: This study showed that both methods followed the same trend when estimating brain stiffness and no significant influence with slice position was detected, but a systematic difference thought to be caused by overfiltering in LFE and noise induced by Laplacian estimation in AHI is observed between algorithms. WM was shown stiffer than GM; however the simplicity of the models will bias the results, which may underestimate WM/GM elasticity.

References:

[1] Kruse, S A, et al.(2008) NeuroImage, 231-7.
[2] Streitberger, K-J, et al.(2012) PLoSone.
[3] Freimann, F B, et al.(2010) Diagnostic Neuroradiology, 189-96.
[4] Papazoglou, S, et al.(2008) Phys Med Biol., 3147-58.

508

The callosal angle measured on MRI of the brain as a prognostic imaging biomarker in iNPH

E. Larsson[1], J. Virhammar[2], K. Cesarini[3], K. Laurell[2]
[1]Department of Radiology, Uppsala University, Uppsala/SWEDEN, [2]Department of Neurology, Uppsala University Hospital, Uppsala/SWEDEN, [3]Department of Neurosurgery, Uppsala University Hospital, Uppsala/ SWEDEN

Purpose/Introduction: Many radiological imaging biomarkers have been studied to find one that could predict response to CSF shunting in idiopathic normal pressure hydrocephalus (iNPH). The callosal angle has been described as useful in discriminating iNPH from ventricular dilation secondary to atrophy in patients with Alzheimer's disease [1]. The aim of this study was to evaluate whether measurement of the callosal angle is a useful supplement in the selection of shunt candidates in iNPH

Subjects and Methods: The pre-operative MRI scans of the brain in 137 patients who had undergone shunt surgery for iNPH during 2006-2010 were evaluated retrospectively. The study was approved by the local ethical committee. Multiplanar reconstruction (MPR) was performed interactively to obtain a coronal image through the posterior commissure, perpendicular to the anterior-posterior commissure (AC-PC) plane (Fig 1). The callosal angle was measured as the angle between the lateral ventricles on the coronal image (Fig. 2). The patients were evaluated thoroughly clinically before surgery and at three and twelve months post operatively.

Fig. 1. Sagittal T1-weighted image with AC-PC plane and position of coronal slice
Fig. 2. Coronal T1-weighted MPR image with callosal angle measurement

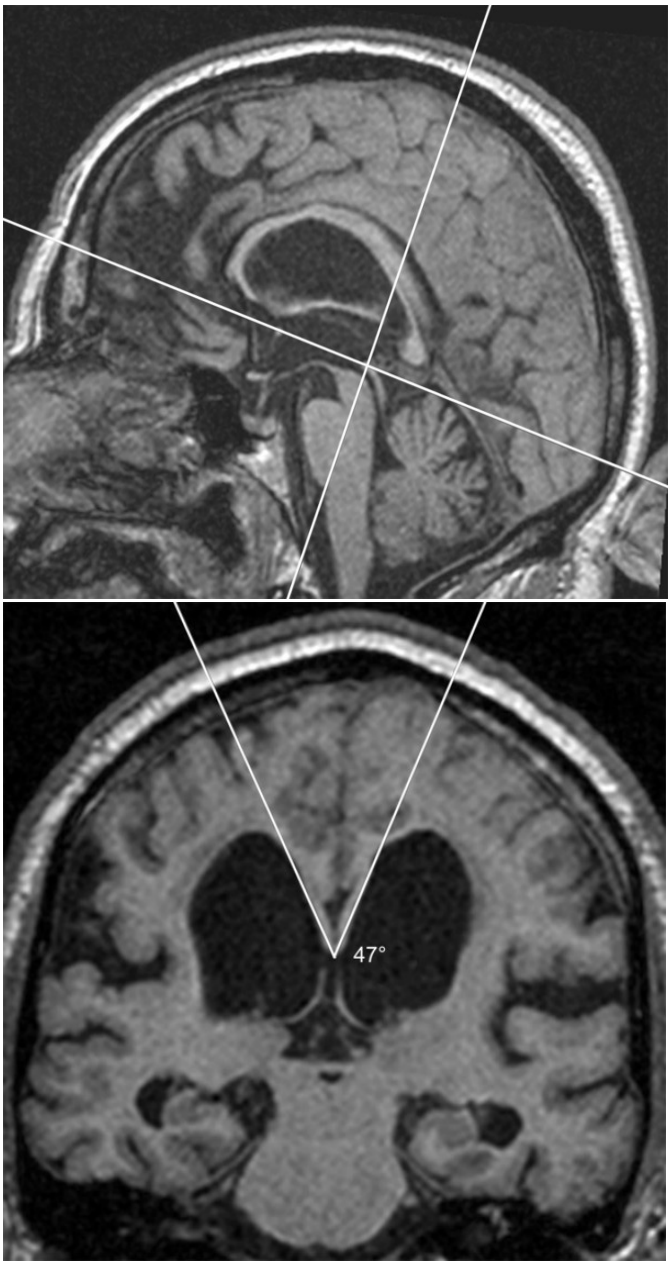

Results: Patients who were shunt-responders had a significantly smaller pre-operative callosal angle compared with non-responders (58.8° ± 16 vs 68.9° ± 17.9, p<0.01). The sensitivity was 55% and specificity 79% to predict a shunt-responder with cut off for a callosal angle of 58°. The cut off 90° gave a sensitivity of 95% and specificity 12.5%.
Discussion/Conclusion: The preoperative callosal angle is smaller in patients who improve after shunt surgery and could be a useful supplement in the selection of shunt candidates.
References:
1. Ishii, K., et al., *Clinical impact of the callosal angle in the diagnosis of idiopathic normal pressure hydrocephalus.* Eur Radiol, 2008;18(11):2678-83.

509

PET/MR quantification of cerebral metabolic rate with an image derived input function

N.A. Da Silva[1], H. Herzog[2], C. Weirich[2], L. Tellmann[2], E. Rota Kops[2], H. Hautzel[3], P. Almeida[1]
[1]Faculty of Sciences of the University of Lisbon, Institute of Biophysics and Biomedical Engineering, Lisboa/PORTUGAL, [2]Institute of Neuroscience and Medicine, Forschungszentrum Jülich, Jülich/GERMANY, [3]Department of Nuclear Medicine, University of Düsseldorf, Jülich/GERMANY

Purpose/Introduction: The combination of a high-resolution MR-compatible BrainPET scanner operated within a 3T-MRI is an excellent prerequisite for obtaining an image derived input function (IDIF), due the perfect image co-registration (figure1). The good soft tissue contrast from MR offers a more precise VOI definition compared to PET images. In this study we quantified cerebral metabolic rate for glucose (CMRglu) with an IDIF measured in a 3TMR-BrainPET scanner.

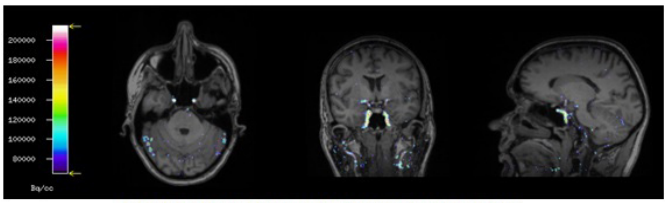

Figure 1. PET MR carotid co-registration in the different anatomical planes.

Subjects and Methods: Three patients without brain disease were investigated in listmode for 1 h after injection (p.i.) of 370MBq FDG. There were 23 frames reconstructed with AW-Poisson-OSEM including all corrections. There were 8 frames per 5sec at the beginning and 3 frames per 10min at the end. Six venous blood samples (VB) were drawn from 5 to 55min p.i.. MPRAGE-MRI was recorded during the early part of the PET scan for 6min.VOIs at 50%-isocontour were defined bilaterally over the carotid arteries (CAs) in the MPRAGE image and transferred to the dynamic PET images to obtain IDIF-A, from the VOI average. BrainPET offers a central resolution of 3mm [1] and consequently the IDIF-A is influenced by partial volume effect (PVE), since the diameter of the CAs measured from the MR images was 5,56+/-0,20mm. Furthermore, spillover (SP) from cerebral radiotracer uptake onto the arteries has to be considered. To correct for both effects a the measured signal (Cmea) is considered as a linear combination of the "true" activity (Ctrue) and the neighboring tissue signal (Csurround) [2]:
Cmea=PV*Ctrue+SP*Csurround.
To estimates the PV and SP coefficients, based on the VB a non-linear least squared fit method were applied (figure2). The corrected curve is IDIF-AC. Moreover, a theoretical PV coefficient (PVt) was calculated. PATLAK plot was used to calculate the CMRglu[3].

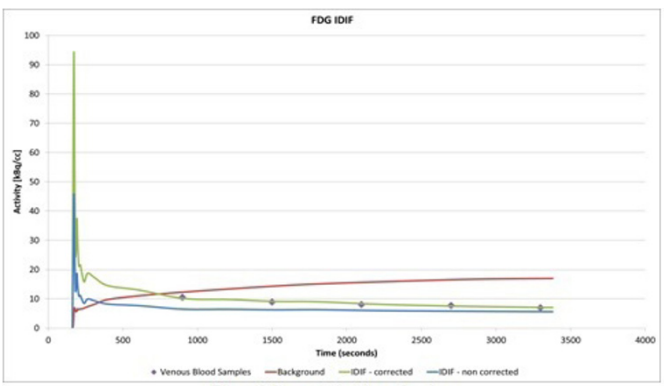

Figure 2. Image derived input function

Results: The fitting procedure delivered a PVE of 0.39+/-0.06 and an SP of 0.2+/-0.04 for data based on VOI average. The PVt was 0.40+/-0.03. The whole brain CMRglu for IDIF-A was 25.7+/-2.1 µmol/min/100g and for IDIF-AC 21.4+/-0.3 µmol/min/100g (figure3).

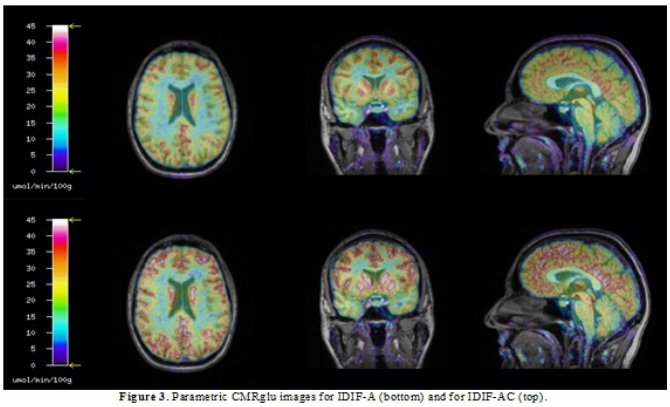

Figure 3. Parametric CMRglu images for IDIF-A (bottom) and for IDIF-AC (top).

Discussion/Conclusion: The integration of a high resolution BrainPET in an MR scanner allows obtaining an IDIF from VOI drawn on the MR, overcoming the reported co-registration errors [4,5]. Nevertheless, IDIF must be corrected for partial volume effect and spillover in order to obtain an accurate CMRglu estimation.

References:

[1]Herzog,H., et.al. (Nuklearmedizin.) 50,n.º2(2011):74-82.
[2]Chen,Kewei, et.al. (Journal of Cerebral Blood Flow and Metabolism) 18(1998):716-723.
[3]Patlak,CS, et.al(J Cereb Blood Flow Metab) 3,n.º1(1983):1-7
[4]Litton,Jan Eric.(J Comput Assist Tomogr)21(1997):907-909.
[5]Mourik,Jurgen,et. al. (NeuroImage)39(2008):1041-50.

510

Synthetic MRI compared with conventional MRI of the brain in a clinical setting

I. Blystad[1], M. Warntjes[2], Ö. Smedby[2], A. Landtblom[2], P. Lundberg[3], **E. Larsson**[4]
[1]Centre for Medical Image Science and Visualization, CMIV, Linköping/SWEDEN, [2]CMIV, Centre for Medical Image Science and Visualization, Linköping/SWEDEN, [3]Department of Medical and health sciences, Radiation Physics, Linköping/SWEDEN, [4]Radiology, Uppsala University, Uppsala/SWEDEN

Purpose/Introduction: Conventional MRI has relatively long scan times for routine examinations. The signal intensity of the images is related to the specific MR scanner settings and it is impossible to compare images in terms of absolute image intensity. Synthetic MRI [1], a method to generate conventional images based on MR quantification, potentially both decreases examination time and enables quantitative measurements [2] in a clinically applicable time.
Purpose: To evaluate synthetic MRI of the brain in a clinical setting by assessment of the contrast, the contrast-to-noise ratio (CNR), and the diagnostic quality compared with conventional MR images.
Subjects and Methods: 22 patients from the neurology department had synthetic imaging added to their clinical MR examination. Patients either had MS, ischemia or unclear diagnosis. In each patient, 12 regions of interest were placed in the brain images to measure contrast and CNR. Furthermore, general image quality, probable diagnosis, and lesion conspicuity were investigated. Synthetic images were compared with conventional images.
Conventional images.

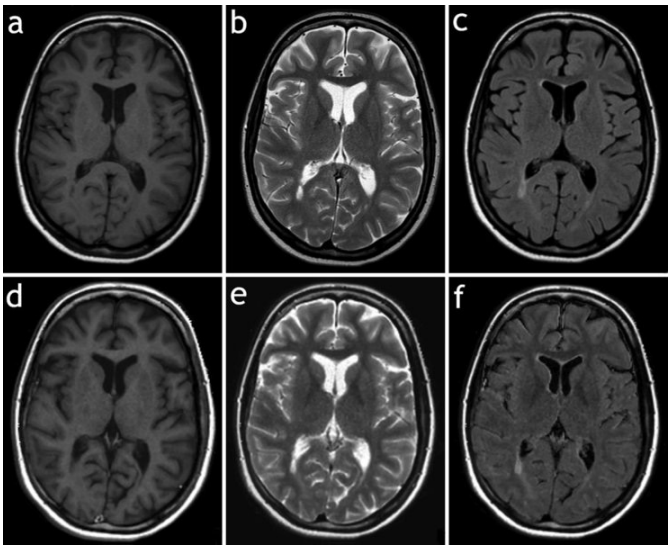

Synthetic images.

Results:

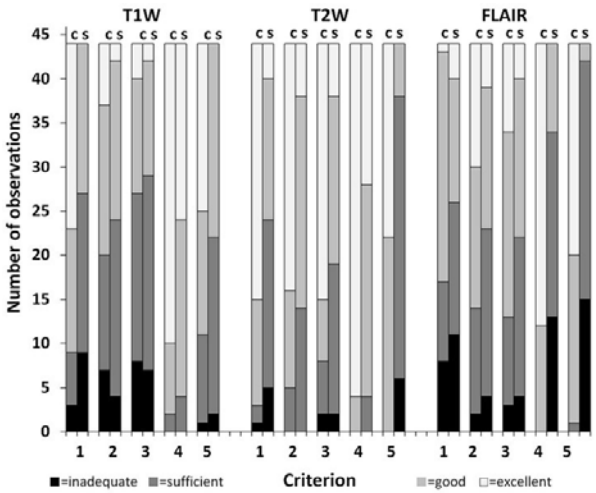

Synthetic T1-weighted and T2-weighted images had higher contrast but also a higher level of noise, resulting in a similar CNR compared with conventional images. Synthetic T2-weighted FLAIR images had lower contrast and a higher level of noise, which led to a lower CNR. Synthetic images were generally assessed to be of inferior image quality, but agreed with the clinical diagnosis to the same extent as the conventional images. Lesion conspicuity was higher in the synthetic T1w images, which also had a better agreement with the clinical diagnoses than the conventional T1w images.
Discussion/Conclusion: Synthetic MRI can potentially shorten the MR examination time and in addition it has a great potential for tissue characterization and volume estimation since it is a quantitative technique. Even though the image quality is perceived to be inferior, synthetic images agreed with the clinical diagnosis to the same extent as the conventional images in this study. The application of synthetic MRI in the clinical setting would be facilitated by further improvements of the quantitative MRI sequence, especially with respect to reducing the current noise level. A potential may be to apply the method at 3T, with its inherent improved noise characteristics.

References:

1. Warntjes JB, Leinhard OD, West J, Lundberg P. Rapid magnetic resonance quantification on the brain: Optimization for clinical usage. Magn Reson Med 2008 Aug;60(2):320-329.
2. West J, Warntjes JB, Lundberg P. Novel whole brain segmentation and volume estimation using quantitative MRI. Eur Radiol 2011 Nov 24.

511

High-energy metabolism in the human brain: Initial results of a 31P magnetic resonance spectroscopy study with LCModel quantitation

X. Wang[1], H. Lanfermann[2], P.B. Barker[1], **X. Ding**[2]
[1]Department of Radiology and Radiological Science, Johns Hopkins University School of Medicine, Baltimore/UNITED STATES OF AMERICA, [2]Institute of Diagnostic and Interventional Neuroradiology, Hannover Medical School, Hannover/GERMANY

Purpose/Introduction: The aim of this study was to investigate the feasibility of rapid, whole-brain ^{31}P MRS in normal volunteers with automated LCModel analysis, and to investigate dependence of metabolite levels on gender and body mass index (BMI).
Subjects and Methods: Twenty-three healthy volunteers (12 females and 11 males, 31–65 years old, mean age 53± 4 years for female, and 54 ± 7 for male) were examined with non-localized whole brain ^{31}P-MRS on a 3T scanner (Siemens, Erlangen, Germany). A double-tuned ^{1}H/^{31}P volume head coil (Rapid Biomedical, Würzburg, Germany), and FID sequence with TR/TE=1700/0.23 ms, 64 acquisitions, and a flip angle of 50° were used, with a scan time of about 2 min. In a separate acquisition (TR 9s), 50mM potassium phosphate monobasic (KH2PO4) was used as calibration standard. Spectra were processed with the 'LCModel' (Provencher 1993) to estimate the content of phosphorylethanolamine (PE), phosphocholine (PC), glycerophosphoethanolamine (GPE), glycerophosphocholine (GPC), nicotinamide adenine dinucleoide (NAD), inorganic phosphate (Pi), phosphocreatine (PCr) and Adenosine-5'-triphosphate (ATP). Spectral basis sets were calculated using the VeSPA program. After a coil loading correction based on the transmitter amplitude required for a 50° pulse in each spectrum, whole brain metabolite content was estimated by referencing to the phantom (arbitrary units (a.u.)). The relative (%) concentration of each metabolite was also calculated as ratio to the sum of all ^{31}P components (TP).
Results: Whole brain metabolite content (a.u., n = 23, mean ± standard deviations) was as follows: ATP 2.0±0.3, PCr 2.3±0.4, PC 0.43±0.06, NAD 0.28±0.05, GPC 0.3±0.10, GPE 0.6±0.2, PE 0.8±0.2, Pi 0.6±0.2. Relative concentrations of all metabolites were follows: ATP/TP 28%, PCr/TP 31%, PC/TP 6%, NAD/TP 4%, GPC/TP 4% , GPE/TP 8%, PE/TP 10%; Pi/TP 8%. No differences between males and females, and no correlation of any metabolite with BMI were found ($p > 0.05$).
Discussion/Conclusion: The relative concentrations reported here are comparable to those previously reported for localized brain structures (Miller et al. 2009). A rapid 2 min data acquisition coupled with automated LCModel analysis can provide reliable whole-brain ^{31}P MRS measures of phosphorus containing metabolites, particularly for the high-energy metabolites ATP and Cr. Clinical applications of these measurements remain to be determined.
Acknowledgement We thank Dr. Provencher for the valuable discussions concerning adaption of the LCModel. The work was partly founded by Deutsche Forschungsgemeinschaft.
References:
Miller J, et al. (2009) Psychiatry Res 173 (2):155-157
Provencher SW (1993) Magn Reson Med 30 (6):672-679.

512

Comparison of shim quality in spectroscopy acquired in patients with intraaxial metastatic process examined with and without stereotactic frame. Technical note.

M. Horak[1], J. Vymazal[1], R. Zacek[1], P. Kozubikova[2], A. Rulseh[1], R. Liscak[3]
[1]Radiology, Homolka hospital, Prague/CZECH REPUBLIC, [2]Clinical Physics, Homolka hospital, Prague/CZECH REPUBLIC, [3]stereotactic neurosurgery, Homolka hospital, Prague/CZECH REPUBLIC

Purpose/Introduction: The effect of treatment with Leksell Gamma Knife (LGK) in patients with intraaxial tumors can be evaluated in time by MR spectroscopy (MRS). In classical workout each patient undergoes one MRS evaluation before start of LGK-treatment without stereotactic frame. And same day or next day undergoes planning MR with stereotactic frame. Thus each patient must be scanned twice in short time. The goal was to evaluate the real difference between MRS with and without frame in short period of time. Data were compared with quality of signal/noise ratio and peak integral.
Subjects and Methods: Ten patients with intraaxial tumor without any prior treatment were taken into this study. Planned treatment was Leksell Gamma Knife. 1.5T MR-system was used (Avanto, Siemens). Standard protocol for imaging brain (T1se, T2tse, Flair, DWI) and MRS 2Dcsi (automatic shim) positioned at plane of corpus callosum at proper position for lesion.
Each patient was examined one day without stereotactic frame. And next day the same patient was examined with stereotactic frame with same scanning protocol. MRS will be used also later for follow up evaluation of effect of LGK. Same contrast agent was administered before MRS for tumor imaging, the same amount was used on each patient.
Results: MRS had proper shim and low noise in 9 out of 10 patients. Results was only with minimal change in peak integral of observed molecules (N-AcetylAspartate, cholin, creatin).
In one case both MRS (with and without stereotactic frame) were with high noise and the evaluation was not valid. Stereotactic frame played no role in this case. High noise was probably due close bonny structure and MR system was unable to make proper shim.
Discussion/Conclusion: Observations could lead to the result, that it is possible to examine patients for MRS follow up before LGK treatment with stereotactic frame only.
In one case both MRS were with high noise and the evaluation was not valid. Stereotactic frame played no role in this case. High noise was probably due close bonny structure and MR system was unable to make proper shim.
MRS (2Dcsi) is one of methods to evaluate the effect of LGK in intraaxial tumors. In ten cases MR-spectroscopic evaluation showed no real difference if examined with or without stereotactic frame. In the future, it can save time if doing just one examination.
References:
1. Patrick Weybright et al. Differentiation Between Brain Tumor Recurrence and Radiation Injury Using MR Spectroscopy. *AJR* 2005; 185: 1471-1476

513

Characteristic appearance of basal ganglia iron deposits of healthy, elderly subjects on clinical MRI volumes

A. Glatz[1], M.C. Valdes Hernandez[1], A.J. Kiker[2], M.E. Bastin[1], S. Munoz Maniega[1], I.J. Deary[3], J.M. Wardlaw[1]
[1]BRIC, Division of Clinical Neurosciences, University of Edinburgh, Edinburgh/UNITED KINGDOM, [2]College of Medicine and Veterinary Medicine, University of Edinburgh, Edinburgh/UNITED KINGDOM, [3]School of Philosophy, Psychology and Language Sciences, University of Edinburgh, Edinburgh/UNITED KINGDOM

Purpose/Introduction: Basal ganglia iron deposits (BGIDs) have been proposed as a biomarker for small vessel disease[1] and cognitive ageing[2]. They appear hypointense on T2*-weighted volumes and, depending on their degree of calcification, hypo- or isointense on T1-weighted volumes[3]. However, little is known about their spatial distribution and connected components.
Here we analyzed BGIDs on clinical MRI volumes of healthy, community-dwelling, elderly subjects and present their characteristic intensity and spatial distributions, and connected component statistics.

Subjects and Methods: We randomly selected 50 subjects with BGIDs (25 female, 70 to 71years) from the Lothian Birth Cohort 1936 Study[4]. A trained analyst manually segmented BGIDs on affine registered T1- and T2*-weighted volumes.
We calculated the joined BGID intensity distribution by combining the linearly normalized T1- and T2*-weighted BGID intensities of all subjects (Figure 1). We calculated the spatial distribution by joining the BGID masks of each subject in the MNI152 space after nonlinear transformation from T2* space. Finally, we subsampled the BGID masks to obtain isotropic voxels with (1x1x1) mm^3 and calculated distributions of the BGID connected component count, volume and area.

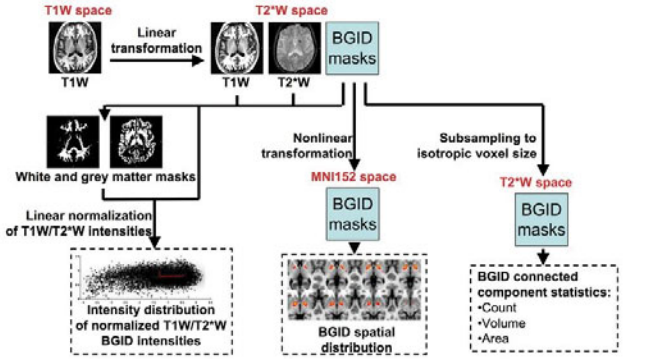

Figure 1: Flow diagram of our method for calculating the basal ganglia iron deposit (BGID) intensity and spatial distributions, and BGID connected component statistics. We used FSL tools (www.fmrib.ox.ac.uk/fsl/) for brain extraction, registration and segmentation, N4 (Slicer3, www.slicer.org) for bias field correction and implemented the remaining processing steps in MATLAB (www.mathworks.com). We linearly normalized the T1- and T2*-weighted intensities (T1W, T2*W) of all subjects so that the normalized, mean T1W and T2*W white and grey matter intensities were 1 and 0.5, and 0.5 and 1, respectively. The connected component area is the largest extent of a connected component on axial T2*W scans.

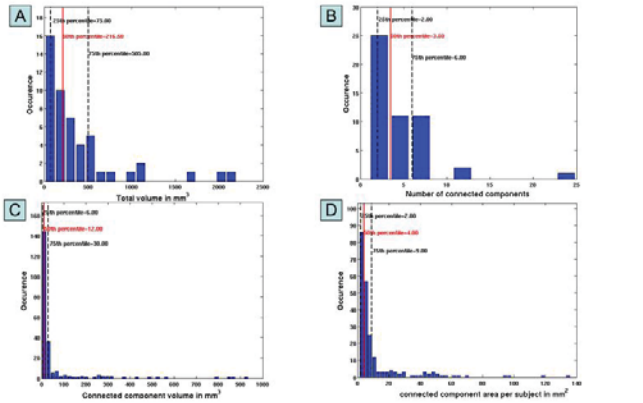

Figure 4: Connected component statistics of basal ganglia iron deposits (BGIDs) masks. (A) shows the distribution of the total BGID mask volumes from all subjects. (B) shows the distribution of the BGID connected component counts from all subjects. (C) shows the distribution of the volumes from all connected components. (D) shows the distribution of the connected component areas from all subjects.

Results: Figure 2A shows the joined BGID intensity distribution and its principal components. The distribution of the first principal component orientations from all subjects has three modes (Figure 2B). Figure 2C and 2D show the projections of the joint distribution on its first and second principal components, which resemble triangular and Gaussian distributions, respectively. The spatial BGID distribution (Figure 3B) indicates a high occurrence of BGIDs in the medial globus pallidus. Figure 4 shows the distributions of the total BGID mask volumes, connected component counts, connected component volumes and connected component areas.

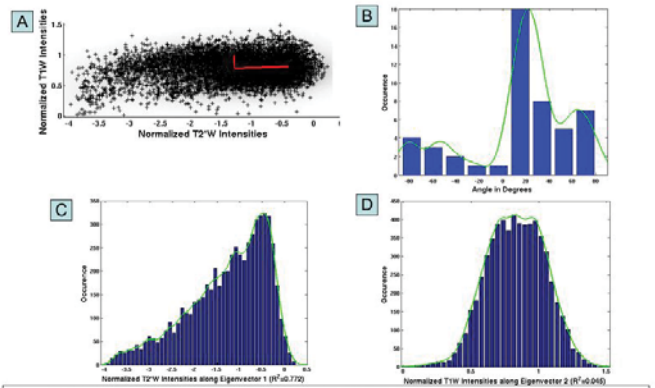

Figure 2: BGID intensity distribution. (A) shows the joint BGID intensity distribution of normalized T1- and T2*-weighted intensities. The red lines indicate the principal components (Eigenvectors of the covariance matrix) of the distribution. The angle between the first principal component and the x-axis is the first principal component orientation. (B) shows the distribution of the first principal component orientations from all subjects, which has three modes. (C) and (D) show projections of the joint BGID intensity distribution on its principal components, which resemble triangular and Gaussian distributions, respectively.

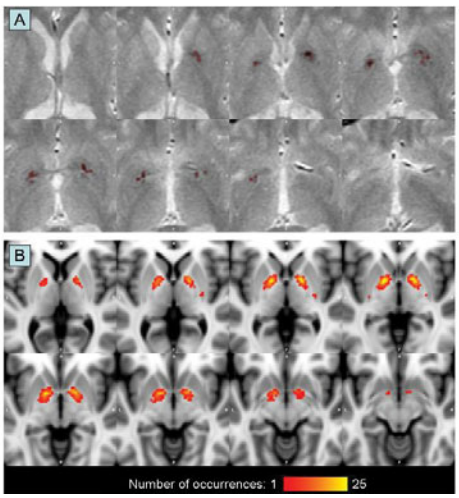

Figure 3: Spatial distribution of basal ganglia iron deposits (BGIDs). (A) shows the T2*-weighted volume of a representative subject with BGIDs (hypointensities) and the perimeters of the masks from our trained analyst (red). (B) shows the spatial distribution of BGIDs over the MNI 152 T1-weighted template volume, which indicates a high occurrence of BGIDs in the medial globus pallidus.

Discussion/Conclusion: We showed that the joined BGID intensity distribution does not resemble a Gaussian distribution, as its projection on the first principal component is not a Gaussian distribution. The principal component orientation distribution suggests that BGIDs have three characteristic appearances on T1-weighted volumes, as the orientations correlate with the appearances of the BGIDs on T1-weighted volumes. The spatial distribution and the connected component statistics of the BGIDs show that the connected components are very small (median volume of 12mm3, median area of 4mm2), have a scattered appearance and occur symmetrically in the left and right medial globus pallidus[5].

References:

[1]Pantoni L.,2010,Lancet Neurol.,9(7):689-01
[2]Penke L. et al.,2010,Neurobiol. Aging,in press
[3]Valdés Hernández M.C. et al.,2012,Eur. Radiol.,in press
[4]Wardlaw J.M. et al.,2011,Int. J. Stroke,6(6):547-59
[5]Harder S.L. et al.,2008,AJNR Am. J. Neuroradiol.,29(1):176-83

EPOS™ Poster

Brain tumours

514

Inter-observer and Intra-observer Agreement of rCBV Measurements in Glial Tumour Using Different Proprietary Software Analysis Tool

S.M. Fallatah[1], A. Krishnan[1], M. Brisson[1], M. Adams[1], X. Golay[2], R. Jager[1]
[1]Radiology, UCL Institute of Neurology, London/UNITED KINGDOM, [2]Institute of Neurology, University College London, London/UNITED KINGDOM

Purpose/Introduction: To assess interobserver and intraobserver agreement of relative cerebral blood volume (rCBV) measurements in glioma using different software-packages.
Regional CBV measurements derived from magnetic resonance perfusion imaging have become important for the differential diagnosis, follow-up and outcome prediction in glial brain tumours (1-3).
For proper implementation of rCBV measurements in clinical practise the technique should fulfil the following criteria: It should be reliably identifying areas of high rCBV values; it should be reproducible, independent of the manufacturer; the degree of inter/intraobserver variability should be known to enable critical interpretation; it should be time efficient (4).
Subjects and Methods: Dynamic susceptibility contrast MRI of 17 histologically confirmed glioma (7 glioblastoma, 4 low-grade astrocytoma, 2 anaplastic astrocytoma, 2 low-grade oligodendroglioma, 1 high-grade oligodendroglioma,1 low-grade oligoastrocytoma) were analysed by two independent operators blinded to the histopathology. A previously described validated method (4) used to choose the means of the higher rCBV value of several intratumoral ROIs and ROIs in the contralateral white matter for normalisation. Three proprietary software-packages are used from three different MRI manufacturers (A, B and C). For software A three methods were used: A1, rCBV maps obtained without contrast leakage correction; A2, with automatic leakage correction; A3, with manual leakage correction. For software B two methods were used: B1, where baseline of the time-intensity curve is constant and B2 where an interpolated baseline is used.
Lesions were classified into two groups: low-grade, rCBV<1.7 and high-grade, rCBV≥1.7 according to (5).
Calculations of intraclass correlation coefficient, Kappa test and Bland Altman plots were used to determine the levels of agreement. Paired T-test is also used.
Results: The intraobserver agreement varied from good to excellent, average ICC: 0.74 (observer 1), 0.66 (observer 2). Method A3 showed the best interobsarver agreement, ICC: 0.87. Method A2 demonstrated kappa value of 1 in grouping lesions into low and high grade, respectively. The variations between observers are correlated with increasing rCBV values.
Discussion/Conclusion: Perfusion imaging in glioma has important clinical and diagnostic implications. Our study assessed the degree of agreement depending on the type of analysis software used.
All three perfusion analysis software-packages showed quite variable however acceptable intra/ interobserver reproducibility of rCBV measurements and were deemed suitable for clinical use. However software A showed the best agreement in our study.
References:
(1)-Danchaivijitr etal. 2008 Radiology ;247(1):170-178.
(2)-Haris M etal. 2008. Neuroradiology;50(6):531-540.
(3)-Di Costanzo etal. 2008. Radiol Med;113(1):134-14.3
(4)-Wetzel SG, etal. 2002. Radiology; 224(3):797-803.
(5)-Law M, etal. 2008. Radiology;247(2):490-498.

515

Monitoring of Glioblastoma response with resting-state Functional and Structural Magnetic Resonance Imaging

H. Wang[1], E.R. Gerstner[2], S. Stufflebeam[1], D. Jennings[1], B.R. Rosen[1]
[1]Department of Radiology, Massachusetts General Hospital, Athinoula A. Martinos Center for Biomedical Imaging, Charlestown/MA/UNITED STATES OF AMERICA, [2]Department of Neurology, Massachusetts General Hospital, Boston/MA/UNITED STATES OF AMERICA

Purpose/Introduction: Early and accurate assessment of anti-angiogenic therapies for glioblastoma (GBM) is extremely important for clinical decision-making. Although conventional magnetic resonance imaging (MRI) can reveal a great deal of information about the structure and physiology of the tumor, a better understanding of the functional disruption of brain regions is greatly needed in order to predict the impact of treatment. We sought to monitor patient treatment response with functional and structural connectivity of brain regions using resting-state functional magnetic resonance imaging (rs-fMRI) and diffusion tensor imaging (DTI).
Subjects and Methods: Three newly diagnosed GBM patients treated with a VEGF-signaling inhibitor, cediranib, and standard chemoradiation, were monitored with longitudinal MRI studies including resting-state fMRI and DTI image acquisition. Post-gadolinium T1-weighted and FLAIR images were collected after tumor resection.
Results: An example of one patient with a right parietal GBM is shown in Fig.1 for three selected visits (Day +14, +121, +237). The tumor shrank at the second visit and progressed at the third visit. The functional connectivity was analyzed with seed region mapping. The tumor region, located in the right parietal cortex, was closely related with the default mode network that involves the vACC (ventral anterior cingulate cortex) and PCC (posterior cingulate cortex) regions. The functional connectivity maps for the seed regions vACC and PCC were reconstructed and the mean connectivity z-scores for the corresponding network regions were used to quantify the related functional network connectivity (Fig.2-3).[1] When the tumor size shrank, the connectivity of the default network involving vACC and PCC increased. On the other hand, when the tumor progressed, the connectivity for the default network involving vACC and PCC decreased.
DTI images were analyzed and the white matter fiber tracks for the whole brain were reconstructed with TrackVis.[2] The seed regions vACC and PCC were applied to view the inter-connected tracks. The number of tracks and the FA (fractional anisotropy) values were evaluated. The number of fiber track connections between the two seed regions changed along with the tumor size (Fig.4) whereas the FA values for all of the three visits were similar. This is because the FA values were calculated mean values for the fiber track volume.

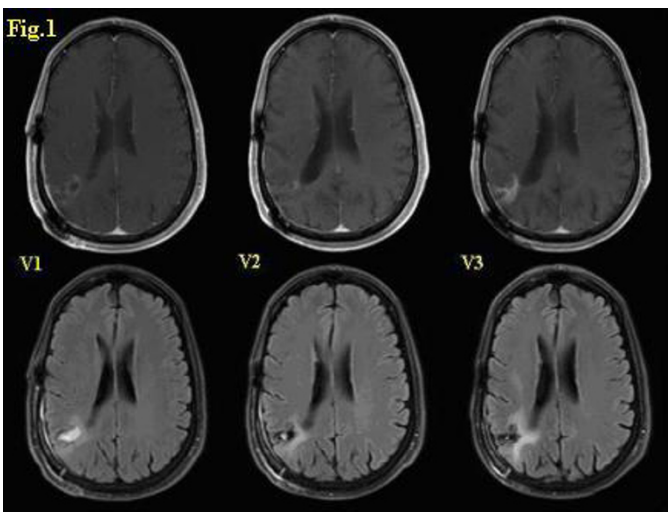

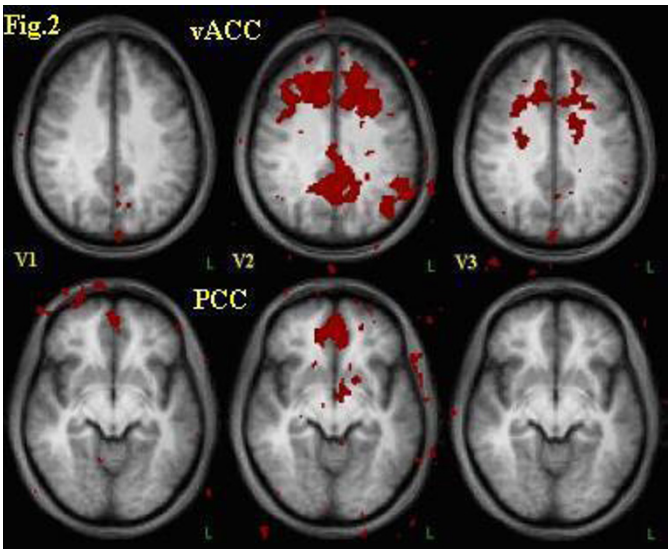

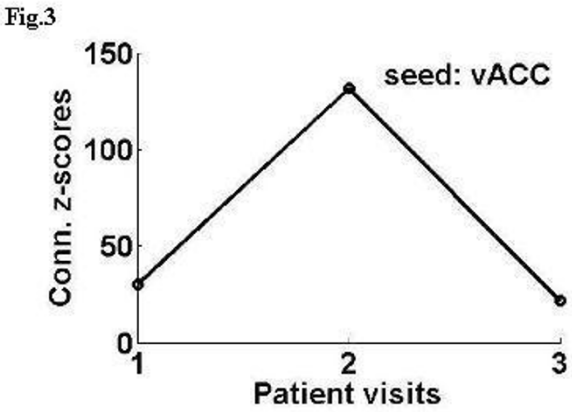

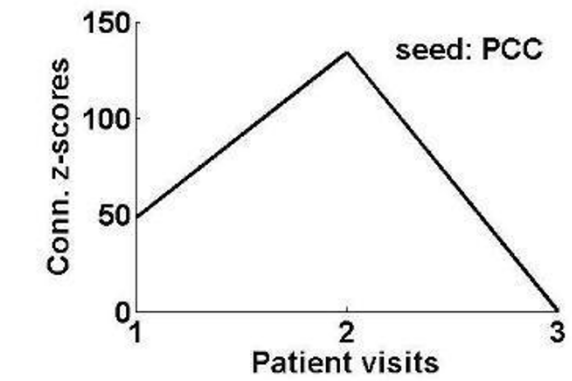

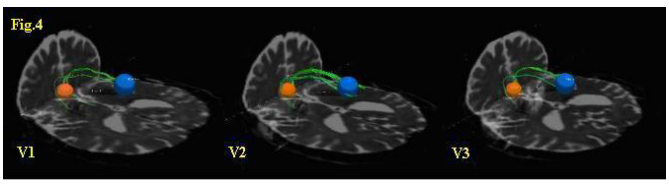

Discussion/Conclusion: Compared to the functional connectivity map, the number of fiber tracks decreased as the functional connectivity decreased. These results suggest that functional and structural connectivity were closely related to tumor volume.

References:
[1] Vincent, JL et al, 2006, J Neurophysiol, 3517-31.
[2] Wang, RP and Wedeen, VJ, http://trackvis.org/

516

Segmentation-based estimation of relative Cerebral Blood Volume in Dynamic Susceptibility Contrast (DSC) enhanced MR images of brain tumors

A. Fathi Kazerooni[1], M. Mohseni[2], M. Miri[2], K. Firouznia[3], **H. Saligheh Rad[4]**
[1]Medical Physics and Biomedical Engineering Department, Tehran University of Medical Sciences, Medical School, Tehran/IRAN, [2]Neurosurgery Department, Tehran University of Medical Sciences, Tehran/IRAN, [3]Department of Radiology, Tehran University of Medical Sciences, School of Medicine, Tehran/IRAN, [4]Laboratory for Advanced MR Imaging and Spectroscopy (LAMIS), Research Center for Science and Technology (RCSTIM), Tehran/IRAN

Purpose/Introduction: Diagnosing tumor grade non-invasively is clinically important. Previous works suggest assessing relative Cerebral Blood Volume (rCBV), which positively correlates with tumor grade and increased vascularity, for predicting tumor grade [1]. Reliable calculation of rCBV requires accurate determination of the region of interest in the reference white matter (WM) tissue, which is difficult to discriminate visually from gray matter (GM) in Dynamic Susceptibility Contrast Enhanced (DSC) MR images. In this work, an automatic segmentation-based approach for calculating rCBV in patients with brain tumors is proposed.

Subjects and Methods: DSC-MR images of eight patients (with non-enhancing gliomas) were acquired on a 3-*T*scanner (gradient echo planar imaging with *TE*/*TR*=45/2340 *ms*, Flip Angle=60, Image Matrix=128x128, FOV=23x23 *cm*, Slice Thickness=5 *mm*, No gap, Measurement Number=50, Slice Numbers=21). GM and WM were segmented from the first scan of the images using an automatic parametric mapping segmentation method by SPM software [2] and automatically registered to the sequence of images. Regional CBVs were computed in tumor and contra-lateral (normal) WM. rCBV was obtained by normalizing regional CBV value in tumor to that of WM.

Results: Figures 1(b) and 1(c) illustrate the segmented GM and WM from the first scan of the image sequence (Figure 1(a)). Table 1 lists the calculated rCBV values for each patient with and without applying automatic segmentation. Figures 2(a) and (b) display correlation between the tumor grade and the calculated rCBV values with and without segmentation, respectively.

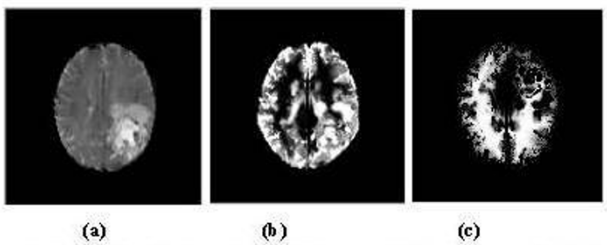

Figure 1: (a) DSC-MR first scan image; (b) Segmented GM; (c) Segmented WM.

Table 1:The rCBV calculated in each patient

Patient No./ Age/Sex	Tumor/Grade	rCBV (with segmentation)	rCBV (without segmentation)
1/58/M	GBM/IV	6.9	3.69
2/33/M	Oligodendrocytoma/III	4.3	4.8
3/50/M	Anaplastic Astrocytoma/III	2.28	2.62
4/30/M	Fibrillary/II	1.08	1.08
5/32/F	Fibrillary/II	2.22	1.1
6/15/M	Astrocytoma/II	1.21	1.33
7/38/M	Oligodendroglioma/II	2.74	2.75

Table 1:The rCBV calculated in each patient

Patient No./ Age/Sex	Tumor/Grade	rCBV (with segmentation)	rCBV (without segmentation)
8/45/M	Oligodendroglioma/II	2.29	3.15

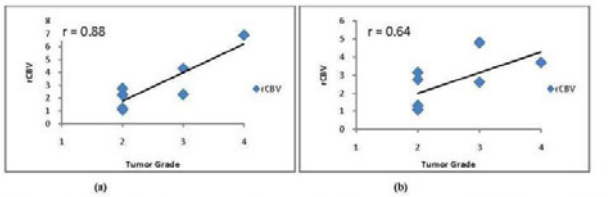

Figure 2: Correlation between rCBV and tumor grades calculated (a) with segmentation; and (b) without segmentation

Discussion/Conclusion: In this work, it was shown that employing automatic segmentation significantly increases the correlation between calculated rCBV values and tumor grades (r=0.88 with segmentation vs. r=0.64 without segmentation). As visual discrimination of the WM from the GM in DSC-MR brain images is a difficult and operator-dependent task, automatic segmentation of GM and WM is advantageous for reliable rCBV estimation for tumor grading.

References:

[1]Kennan,R.P. and Jäger,H.R.(2004)T_2- and T_2^*-W DCE-MRI:Blood Perfusion and Volume Estimation using Bolus Tracking,in Quantitative MRI of the Brain:Measuring Changes Caused by Disease(ed P.Tofts),John Wiley&Sons,Ltd,Chichester,UK. doi:10.1002/0470869526.ch11.

[2]Friston K, Ashburner J, Frith C, Poline J-B, Hether J,Frackowiak R (1996) Spatial registration and normalization of images.Human Brain Mapping 2,165–189.

517

Imaging of recurrent medulloblastomas and mimickers

S. Vinhais[1], S. Nunes[2], I. Costa[3], D. Salgado[3]
[1]Radiology, Portuguese Institute of Oncology, Lisbon/PORTUGAL, [2]Department of Child and Adolescent Oncology, Portuguese Institute of Oncology, Lisbon/PORTUGAL, [3]Neurology, Portuguese Institute of Oncology, Lisbon/PORTUGAL

Purpose/Introduction: Recurrence of medulloblastomas predicts a bad outcome. A precocious diagnosis could help dealing with the disease, and the MR techniques are recruited as fundamental tools for the task.
Our aim was to evaluate this pathological condition, with focus on the MR role.
Subjects and Methods: Two series of medulloblastomas cases followed in our institution, 89 children/adolescents and 45 adults. All 134 patients were further stratified into categories of standard (SR) and high-risk (HR), following criteria of age (<3 years or older), total resection *versus* residual disease, and absence or disseminated disease at presentation. A total of 32 recurrent medulloblastomas was identified by follow-up MRI studies, CSF analysis or even biopsy (9 with multiple relapses). Other cases representative of differential diagnostic lesions were also reviewed.
Results: Medulloblastomas recurred similarly in children/adolescents (24,7%) and adults (22,2%), these two series with a HR/SR proportion of 50:39 and 18:27. Overall mean follow-up was 7,8 years; 12 patients lost to follow-up. Mean time of first recurrence was 1,9 years. Although most patients had clinical complaints (53,1%), asymptomatic disease was largely observed. All had positive MRI findings, yielding the diagnosis: local relapse 21,9%, combined with leptomeningeal spreading to the brain/neuroaxis 21,9%, isolated brain metastasis 21,9%, or pure leptomeningeal disease 34,3%. Classic medulloblastomas predominated, the remainders being of the desmoplastic/nodular variant (15,6%). Overall mortality rate was 29,1%, and from recurrent disease 84,3%; the specific survival rates at 3 and 5-years of 31,5% and 9,4% respectively.
MRI was false positive in 2 patients with radionecrosis, false negative in 4, and gave doubtful results in other 3 cases of favorable evolution, these corresponding to post-operative complications/squealer lesions.
The use of proton MR spectroscopy, recently available in our hospital, was very limited. Applied to differentiate recurrent tumor from radiation necrosis in few cases, it provided satisfactory discriminative results, offering a complementary analysis in the imaging monitoring process.
Discussion/Conclusion: Results are in consonance with other studies.
MR diagnosed the recurrences, but gave some equivocal and false results, the main problem being the differentiation of radionecrosis. Thus, some limitations render a place for advanced MR techniques, namely spectroscopy.
We expect that the use of tailored MR protocols, with a judicious employment of the newest MR techniques help to fulfill this gap, to better treat these patients.

References:

[1]. Rollins *AJR Am J Roentgenol.* 1990;155:153-157.
[2]. Loree *J Neurosurg Pediatr.* 2010;6:87-91.
[3]. Warren *J Clin Oncol.* 2000;18:1020-1026.
[4]. Schubert *Acta Radiol.* 2006;47:1100-1104.

518

Feasibility and reproducibility of resting state fMRI in the presurgical patient with a primary brain malignancy.

T. De Beule[1], **S. Van Cauter**[1], F. D'Arco[1], R.R. Peeters[2], S. Sunaert[1]
[1]Radiology, UZLeuven, Leuven/BELGIUM, [2]Radiology, University Hospitals of Leuven, Leuven/BELGIUM

Purpose/Introduction: To determine the feasibility of resting state functional MRI (rfMRI) in patients with brain tumors in the presurgical workup in order to map eloquent functional areas.
Subjects and Methods: Resting state fMRI was performed in 13 patients, (two third male with a mean age of 42) with known brain tumors. This sequence as added to the routine presurgical workup, consisting of task-based fMRI (language and motor), diffusion tensor imaging and anatomical imaging.
Analysis of rfMRI data was done in FSL with an independent component analysis. The results were visually scored for the following resting state networks: default mode network, dorsal attention network, ventral attention network, extrastriate visual network, right and left parietofrontal network (1-2). We furthermore scored the classical primary motor network, primary visual network, auditory and the language areas.
Results: The rfMRI sequence showed data of good quality and a full analysis could be achieved in all scanned patients. The default mode network and the primary visual cortex were demonstrated in all patients, dorsal attention and ventral attention networks in 8 patients, motor functions in 10, language and auditory function in 7 patients. In almost all patients the supplementary motor area (SMA) was visible. We did a visual correlation with the standard task based fMRI. The full language network correlated visually in 8 out of 13 patients. The SMA had a positive correlation in 10 patients. The motor areas looked similar for the rfMRI and the fMRI in about 5 patients.
Discussion/Conclusion: Resting state fMRI is feasible to perform in the presurgical workup of patients with brain tumors. We could demonstrate the typical resting state networks, the motor and language network with rfMRI in a fairly high percentage of the patients in our study group.

References:

1. Martijn P. van den Heuvel , Hilleke E. Hulshoff Pol Exploring the brain network: A review on resting-state fMRI functional connectivity. European Neuropsychopharmacology (2010) 20, 519–534
2. J. S. Damoiseaux, S. A. R. B. Rombouts, F. Barkhof, P. Scheltens, C. J. Stam, S. M. Smith, and C. F. Beckmann Consistent resting-state networks across healthy subjects PNAS (2006) www.pnas.org_cgi_doi_10.1073_pnas.0601417103

519

Investigation of the necessity of pre-contrast T1-determination in DCE-MRI; simulations and clinical data

C. Larsson[1], M.M. Kleppestø[2], A. Bjørnerud[1]
[1]*Intervention centre, Rikshospitalet, Oslo University Hospital, Oslo/NORWAY,*
[2]*The Intervention Centre, Oslo University Hospital, Oslo/NORWAY*

Purpose/Introduction: Quantification of DCE-derived kinetic parameters requires accurate estimation of the CA induced change in T_1 relaxation rates in tissue and blood which in turn requires knowledge of pre-contrast T_1 values ($T_{1,0}$) . The need for $T_{1,0}$-data results in additional scan-time, and raises challenges related to inaccuracies in $T_{1,0}$ estimates. The necessity of using $T_{1,0}$ maps in DCE analysis has thus been questioned [1].
We compared kinetic parameters obtained using fixed $T_{1,0}$ values to calculated pixel-wise values through simulations and clinical data.
Subjects and Methods: A total of 45 examinations in 6 patients with glioblastoma were included in the study. The protocol included a 3D Look-Locker (LL) based inversion recovery sequence for T_1-measurements [2] and a DCE 3D saturation recovery sequence. All images were acquired on a 3 Tesla Philips Achieva scanner.
The transfer constant, K^{trans} was estimated either using $T_{1,0}$-maps estimated at each exam (Method 1) or by assigning the median $T_{1,0}$ of the tumor from the patient's first exam (baseline) to all pixels in all exams (Method 2). The effect of varying $T_{1,0}$-values on K^{trans} estimates was simulated by estimating the variation in K^{trans} due to deviations in $T_{1,0}$ from the nominal value.

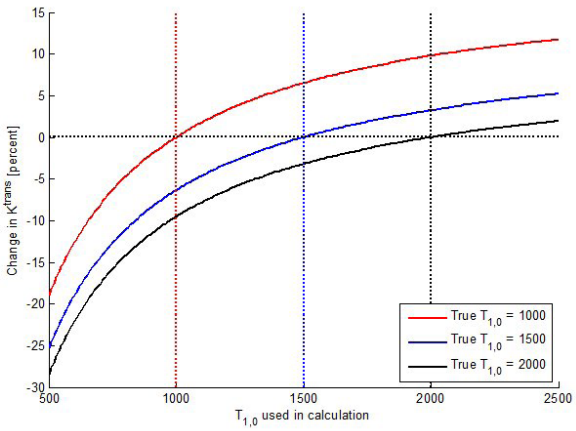

Results: Figure 1 shows the simulated error in K^{trans}-estimates when using $T_{1,0}$-values different from the true $T_{1,0}$. Figure 2 shows the median change in tumor $T_{1,0}$ for all patientsduring a one-year follow-up. Figure3 shows similar $T_{1,0}$ data from a single patient and the corresponding tumor K^{trans} values obtained using method 1 and 2. The K^{trans}-values are seen to be almost identical despite the increase in $T_{1,0}$. The difference in median tumor K^{trans} calculated with method 1 versus method 2 in figure 4 did not correlate with the measured variation in $T_{1,0}$ relative to the baseline scan.

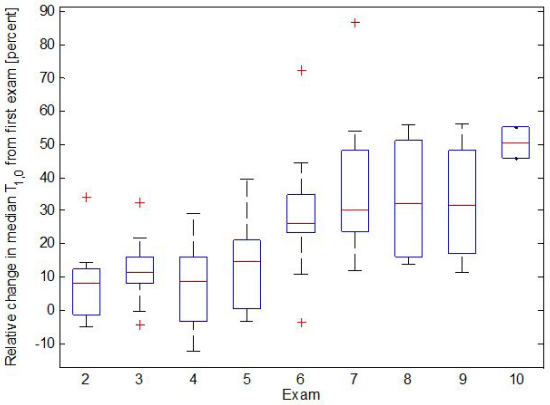

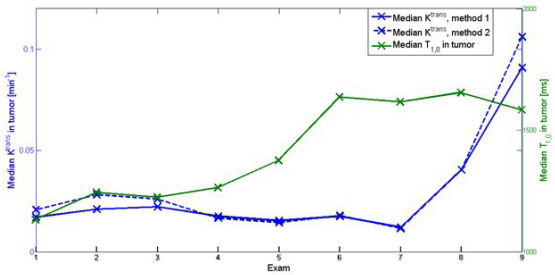

Discussion/Conclusion: In spite of a marked increase in $T_{1,0}$ observed in glioblastoma patients one-year after treatment, the use of exam specific $T_{1,0}$ maps did not result in significant differences in tumor K^{trans} values; suggesting that the use of fixed $T_{1,0}$ values may be adequate; reducing analysis complexity and total scan-time.

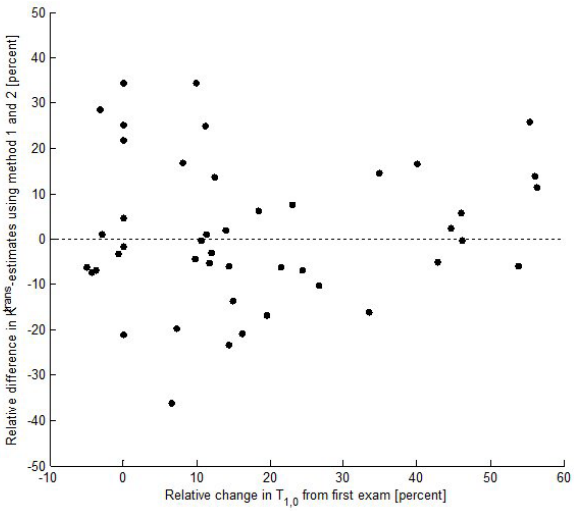

References:
1. E. M. Haacke et al., Magn Reson. Med. 58, 463 (2007).
2. D. C. Look and D. R. Locker, Rev. Sci. Instrum. 41, 250 (1970).

520

Surgical proven location of the Facial Nerve in the vicinity of Cerebellopontine Angle Tumours depicted pre-operatively by Tractography

P.M. Gonçalves-Pereira[1], G. Neto D´almeida[2], R. Manaças[3], P. Escada[4], T. Taoka[5]
[1]Serviço de Radiologia, Hospital dos Lusíadas, Lisboa/PORTUGAL, [2]Neurosurgy dept, Hospital Egas Moniz, Lisboa/PORTUGAL, [3]Neuroradiology dept, Hospital dos Capuchos, Lisboa/PORTUGAL, [4]ENT dept, Hospital Egas Moniz, Lisboa/PORTUGAL, [5]Radiology dept, Nara University Hospital, Nara/JAPAN

Purpose/Introduction: To determine the clinical utility of pre-operative diffusion tensor (DT) tractography of the facial nerve in the vicinity of cerebellopontine angle (CPA) tumours. The location of the facial nerve was established pre-operatively by tractography and compared with in-vivo electrode stimulation during microsurgery of vestibular schwannomas and rare CPA masses (meningiomas and arachnoid cysts).
Subjects and Methods: We have evaluated 19 patients with histologically proven CPA vestibular schwannomas (n=15), meningiomas (n=2) and arachnoid cysts (n=2). The location of the facial nerve on the cerebellopontine angle was assessed intra-operatively by visual inspection and mapping (using a monitoring electrical equipment) and compared with pre-operative DT tractography. DT images were obtained at 1,5T using a single-shot, high-resolution echo-planar sequence with six-axis encoding. Tractography of the facial nerve was performed accordingly to the method of Taoka T. et al[1,2].
Results: The facial nerve position was depicted intra-operatively in all the patients and illustrated by DT tractography in 18 patients (Figures 1 and 2). In 17 patients (>90%) there was a precise correspondence between the CPA course of the facial nerve found at surgery and DT tractography. In one patient the facial nerve was found anterior/cranial to the tumor while tractography seemed to depict an anterior/caudal course.

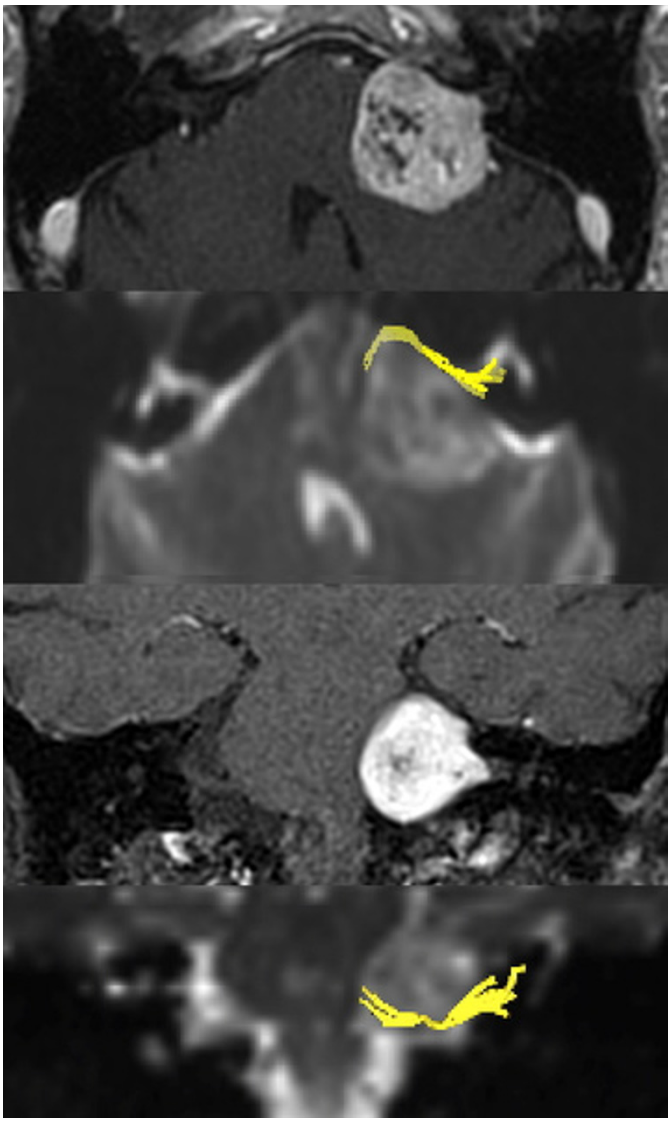

Figure 1: *Vestibular Schwannoma* on the left CPA. Axial and coronal T1 pós-Gad and equivalent tractography images. The facial nerve was identified during surgery with a similar antero-inferior location as predicted by tractography.

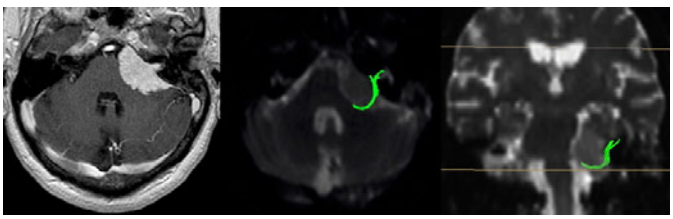

Figure 2: Left CPA *Meningioma* extending through the *porus accusticus*. Axial T1 pós-Gad. Axial and coronal tractography images predicted a postero-inferior displacement of the facial nerve, which was confirmed during surgery.
Discussion/Conclusion: DT tractography of the facial nerves is feasible and has a consistent correspondence with the surgical findings. This technique may deliver useful pre-operative information and contribute to lower the risk of facial nerve injury during CPA surgeries.
References:
1 - Taoka T, Hirabayashi H, et al. Displacement of the facial nerve course by vestibular schwannoma: preoperative visualization using diffusion tensor tractography. J Magn Reson Imaging. 2006 Nov;24(5):1005-1010.

2 - Gonçalves Pereira PM, Neto d´Almeida, et al. Tractography of the Facial Nerve in Tumors of the Cerebellopontine Angle. Proceedings of the ASNR 50th Annual Meeting. 2012:405-406.

521

Application of clusterization techniques to dynamic susceptibility-weighted MR quantitative parameters: relationship with survival time in high grade gliomas

R. Sanz-Requena[1], A. Revert-Ventura[2], L. Marti-Bonmati[3], A. Alberich-Bayarri[1], G. Garcia-Marti[1]
[1]Radiology, Hospital Quiron Valencia, Valencia/SPAIN, [2]Radiology, Hospital de Manises, Manises/SPAIN, [3]Radiology, Universitat de Valencia, Valencia/SPAIN

Purpose/Introduction: Survival time in high-grade gliomas is influenced by a number of factors, including clinical factors, histological grade and therapeutic strategy. In this context, the quantitative assessment of the tumor microvascular environment is important to establish the lesion aggressiveness [1]. Our aim is to group similar vascular behaviors in high-grade gliomas and relate them to survival time.
Subjects and Methods: 39 patients with high-grade gliomas were included in the study (8 grade-III, 31 grade-IV, 60±10 y.o.). They underwent a T2*-weighted MR perfusion study (1.5T, TR/TE/FA=836ms/30ms/40º, 1.8x1.8x7mm, 40 dynamics, 2.4 s/dynamic, 0.2mmol/kg @5 ml/s) before biopsy or therapeutic procedure. At the time of the study all patients had died (survival 267±191 days).
Tumor regions were manually selected in all the slices where the lesion was visible, according to the enhanced region in the late-enhancement T1-weighted sequence.

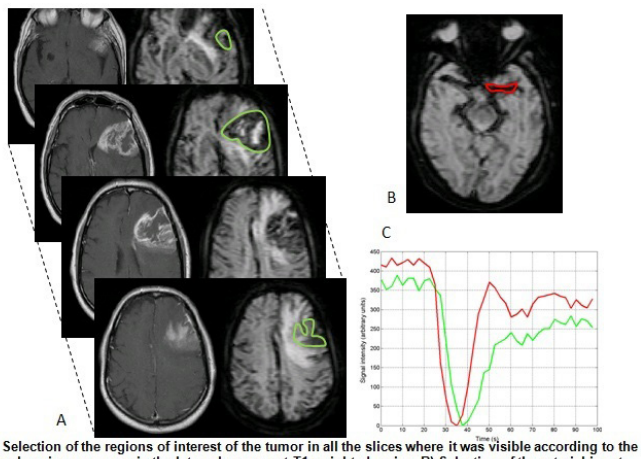

A) Selection of the regions of interest of the tumor in all the slices where it was visible according to the enhancing area seen in the late-enhancement T1-weighted series. B) Selection of the arterial input function (AIF) at the mean cerebral artery. C) Examples of uptake curves for the AIF (red) and the lesion (green).

These regions were merged into a volume and a voxel-based analysis was performed to obtain several quantitative parameters from the uptake curves [2,3]:

- Single-compartment model: cerebral blood volume (CBV), cerebral blood flow (CBF) and mean transit time (MTT).
- Pharmacokinetic model: transfer constant (K^{trans}), interstitial space fraction (v_e) and vascular space fraction (v_p), using the mean cerebral artery as arterial input function.

The volumetric data of each lesion was summarized as the mean for each parameter. The mean of the 10% maximum values was also obtained to consider the most aggressive parts of the tumor. A two-step cluster analysis was applied to obtain natural groupings both for each individual parameter and for their combination (SPSS, IBM). Finally, ANOVA tests were applied to search statistical differences in survival time among the groupings.
Results: The analysis of CBV, CBF, K^{trans} and v_p released two groups, both individually and combining them, and both using the whole volumetric mean and the mean of the 10% maximum. However, depending on the parameter and the combination, these groups comprised different cases. When comparing the survival time of the clusters, only the groups associated to the mean of the 10% maximum K^{trans} showed statistical differences (p=0.04). There were no statistical correlations between the clustered groups and the patients' age or the lesion size.

	Parameters	Groups	Survival time	p
Whole tumor volume	CBV	1 (31)	278 ± 185	0.455
		2 (8)	221 ± 222	
	CBF	1 (7)	189 ± 218	0.239
		2 (32)	284 ± 184	
	K^{trans}	1 (24)	281 ± 193	0.570
		2 (15)	244 ± 192	
	v_p	1 (34)	277 ± 194	0.360
		2 (5)	192 ± 172	
	{CBV,CBF,K^{trans},v_p}	1 (8)	221 ± 222	0.455
		2 (31)	278 ± 185	
10% maximum values	CBV	1 (25)	268 ± 176	0.945
		2 (14)	264 ± 223	
	CBF	1 (34)	272 ± 185	0.673
		2 (5)	232 ± 248	
	K^{trans}	1 (31)	298 ± 192	0.040
		2 (8)	144 ± 135	
	v_p	1 (34)	277 ± 194	0.360
		2 (5)	192 ± 172	
	{CBV,CBF,K^{trans},v_p}	1 (31)	282 ± 181	0.338
		2 (8)	208 ± 231	

Results of the clusterization showing the groups and number of cases per group for each individual parameter or combination (in brackets), both for the whole tumor and the 10% maximum means; the mean and standard deviation of the survival time and the statistical significance between the clusterized groupings. CBV: cerebral blood volume, CBF: cerebral blood flow, K^{trans}: transfer constant, v_p: vascular space fraction. Survival time is shown in days.

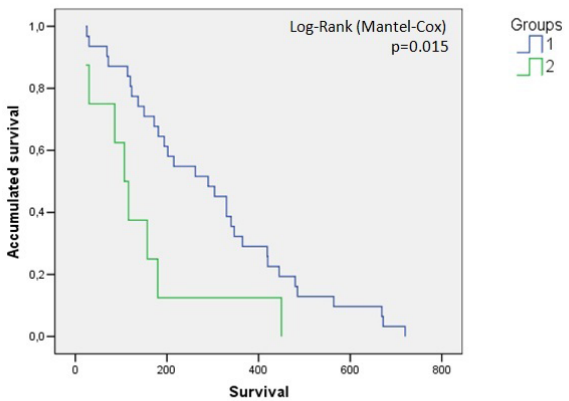

Kaplan-Meier curve showing the survival of each group, obtained from the clusterization of the 10% maximum K^{trans} values. The log-rank test shows a p-value=0.015.

Discussion/Conclusion: Quantitative MR perfusion parameters, specifically the highest values of K^{trans}, can be potentially used as independent predictors of survival time in high-grade gliomas.
References:

1. Mills SJ et al. AJNR 2006;27:853-58.
2. Law M et al. AJNR 2006;27:1975-82.
3. Revert-Ventura AJ et al. Radiologia 2010;52:432-41.

522

Conribution of Diffusion MRI for Glioblastoma Radioherapy

R. Turcat[1], L. Simon[2], **A. Deviers**[3], S. Ken[4], J. Lotterie[4], E. Moyal Cohen-Jonathan[5], R. Ferrand[2], A. Laprie[4]
[1]EEA - Physique Médicale, Université Paul Sabatier, Toulouse/FRANCE, [2]Département d'Ingénierie et de Physique Médicale, Institut Claudius Regaud, Toulouse/FRANCE, [3]Anatomie-Imagerie médicale, Ecole Nationale Vétérinaire de Toulouse, Toulouse/FRANCE, [4]UMRS 825, INSERM, Toulouse/FRANCE, [5]Department of Radiotherapy, Institut Claudius Regaud, Toulouse/FRANCE

Purpose/Introduction: Glioblastoma (GBM) is the most frequent and aggressive primary brain tumour in adults. Despite the standard treatment (surgery/biopsy and chemotherapy concomitant with radiotherapy (RT)) relapse is

local and occurred in 95% within the irradiated fields. To consider a RT dose escalation on new target volumes, we proposed in this study to assess MR diffusion parameters for the optimisation of target delineation.
The ability of MR diffusion to predict areas of relapse is assessed and the integration feasibility of these MR diffusion parameters in the Treatment Planning System (TPS) is presented.
Subjects and Methods: Thirty-six patients with GBM included in previous clinical trials were followed before RT (M0), after RT and until relapse. In total, MRI acquisitions at 1.5T consisted of: 3D-axial-T1 images before injection, 3D-axial-T1 after injection (T1-Gd), T2, FLAIR, perfusion, spectroscopy, diffusion-weighted imaging (DWI) and diffusion tensor imaging (DTI).
Morphological abnormalities were defined by contrast-enhancing areas on T1-Gd images (at M0 and at relapse) and co-registered on Apparent Diffusion Coefficient (ADC) maps at M0: the differences between ADC at M0 and contrast-enhancing areas are evaluated. Abnormal ADC threshold at M0 was assessed as predictive indicator.
Brain areas infiltrated by tumor can be highlighted by diffusion parameters such as the isotropic component (p) and the fractional anisotropy (FA) [1]. These parameters are different from morphological abnormalities; they give additional information on tumor infiltration and could then characterize an "optimal" tumor delineation.
Results: ADC maps acquired at M0 spatially matched with areas of relapse (contrast-enhancing areas on T1-Gd) (Figure 1a). Characterization of an ADC threshold could not have been found to overlap perfectly with areas of relapse (Figure 1b).
Tumor infiltration defined by area of p>10% from controlateral [1] gave regions of interest different from contrast-enhancing areas on T1-Gd at M0. These areas defined according to p presented a better overlap with contrast-enhancing areas on T1-Gd at relapse (Figures 2 and 3). These new regions of interest and also fiber tracts from FA maps have been successfully integrated in TPS (Eclipse, v8.9) (Figure 4).

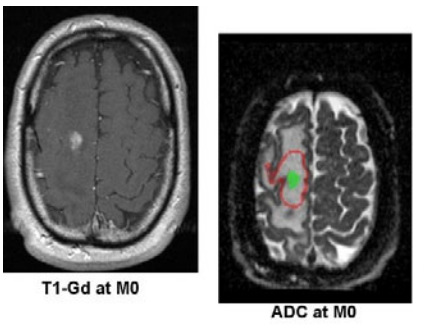

Figure 1a : Predictive information from ADC maps before treatment
The filled green area corresponds to *PRIMARY TUMOR*
The red outline corresponds to *RECURRENCE*

Figure 2 : T1-Gd images at M0 and after RT with « *p* » *threshold overlaid*
(blue area = *p* > of 10% from contralateral)
« areas of *p*+10% » measured at M0 spacially match with tumor progression at 3 months follow-up

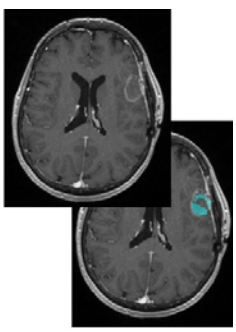

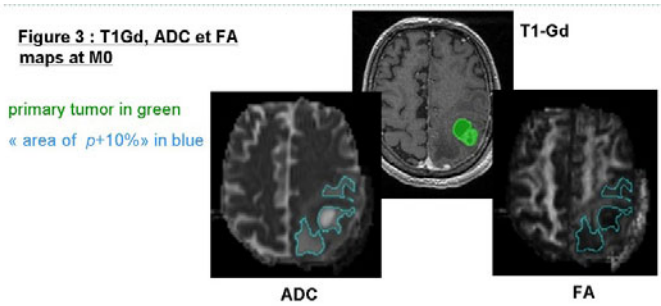

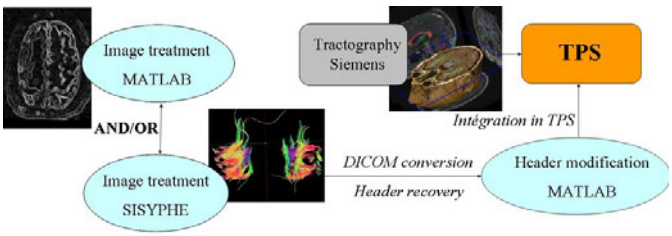

Figure 4 : integration of calculated images in the TPS

Discussion/Conclusion: Consideration of MR diffusion parameters (ADC maps, isotropic component p and fiber tracts) from DWI and DTI modalities could bring new information for RT target delineation compared to other MR modalities (T1-Gd, Spectroscopy, etc...) Technical feasibility of integration of these MR diffusion parameters into TPS is established.
References:
[1] Price AJNR 2006
[2] Tensouati&Lotterie ESMRMB 2008

523

Spatial Relationship Between Subventricular zone, Cortex Proximity and Progression Free Survival Time

F. Tensaouti[1], V. Lubrano[2], J. Lotterie[2], I. Berry[3], P. Celsis[2], E. Moyal Cohen-Jonathan[4]
[1]Université Paul Sabatier Toulouse III, INSERM UMR 825, TOULOUSE/FRANCE, [2]UMRS 825, INSERM, Toulouse/FRANCE, [3]Rangueil, Centre Hospitalier Universitaire, Toulouse/FRANCE, [4]Department of Radiation Oncology, Institut Claudius Regaud, Toulouse/FRANCE

Purpose/Introduction: Glioblastoma multiforme (GBM) are very aggressive and radioresistant tumors whose standard treatments associate surgery followed by radio-chemotherapy. GBM are most often characterized by recurrence within the original tumor site, but distant recurrence and dissemination also exists.The objective of this study is to use volumetric analysis and morphometrics to measure the spatial relationship between subventricular zone (SVZ), cortex proximity and progression free survival time in a cohort of 48 diagnosed GBM patients.
Subjects and Methods: The study cohort included 35 male and 13 female patients. All patients had undergone resection of glioblastoma at our academic institution from 2006-2010. Flair and gadolinium-enhanced T1-weighted magnetic resonance images (MRI) at pre-operative, post-operative, pre-radiation therapy, and post-radiation therapy time points were collected. RANO criteria [1] are used for the assesement of progression. Tumor volumes and distances from the edge and center of the abnormality to the ventricles (EDV, CDV) and cortex (EDC, CDC) were measured on pre-operative GdT1WI. Progression-free survival (PFS) time was calculated in months from the post-operative MRI. All post-processing and measurements were done by using Sisyphe Software [2].
Results: Mean post operative PFS was 8,31 months, mean age 61 years, mean follow up time 12 months, mean EDV 6,46 mm, mean CDV 33,8mm, mean EDC 0.16 mm and mean CDC 18,07 mm and the mean pre-operative volume was 44789mm^3.

In the univariate and multivariate analysis. The age, CDV, EDC, CDC, and Tumor pre-operative volume were not a significant predictors of PFS. However, EDV was a significant predictor of PFS in the univariate and multivariate analysis (p=0.038, p=0,05).
Discussion/Conclusion: Our retrospective analysis showed that patients with GBM abutting the ventricles to have outcomes inferior to those whose tumors are some distance from the SVZ. This result should be taken with care because other factors (clinical data) were not considered, they will be introduced to complete the study.
References:
[**1**] Patrick Y. Wen et al. 2010 J Clin Oncol. April 10
[**2**] Tensaouti, F. et al. (2008). Proc ESMRMB. 991

524

Assessment of Progression In Glioblastoma Using Multimodality Imaging and the Response Assessment in Neurology Oncology Criteria

F. Tensaouti[1], V. Lubrano[2], J. Lotterie[2], I. Berry[3], P. Celsis[2], E. Moyal Cohen-Jonathan[4]
[1]Université Paul Sabatier Toulouse III, INSERM UMR 825, TOULOUSE/FRANCE, [2]UMRS 825, INSERM, Toulouse/FRANCE, [3]Rangueil, Centre Hospitalier Universitaire, Toulouse/FRANCE, [4]Department of Radiation Oncology, Institut Claudius Regaud, Toulouse/FRANCE

Purpose/Introduction: Glioblastoma multiforme (GBM) are very aggressive and radioresistant tumors whose standard treatments associate surgery followed by radio-chemotherapy. GBM are most often characterized by recurrence within the original tumor site, but distant recurrence and dissemination also exists.The objective of this study is to investigate the added value of volume on post-contrast (3D) T1WI and volume on 2D Flair over classical cross-sectional area in evaluating tumor progression in GBM.
Subjects and Methods: The study cohort included 35 male and 16 female patients. All patients had undergone resection of glioblastoma.The area and volume measurements were performed on 262 MRI studies on post-contrast 3D T1WI and on 2D Flair imaging. Measurements were performed using Sisyphe Software [1]. The area was calculated as the product of the largest diameter and its maximum perpendicular diameter in the largest cross-sectional area of tumor [2]. The tumor size measurement included all regions of tumor enhancement [2]. Radiographic progression was determined based on change in either area, volume on 3D T1WI, Volume on Flair or new lesion. Progressive disease (PD): ≥25% increase in tumor area [2] relative to baseline. For volumetric measurements, we used a volume increase greater than 40% for PD [3]. The comparison of measurement methods was performed and the correlation was analyzed.
Results: A high correlation was revealed between the area and volume on 3D T1 ($r = 0.84$, 95% $p < 0.05$, Fig 1) and between the percentage increase of area or volume ($r = 0.75$, $p < 0.05$). When evaluating progression, the correlation between the area and volume on 3D T1 was 0.84 ($p < 0.05$). A good correlation between Volume on flair and volume on 3DT1 ($r = 0.66$, $p < 0.05$) and between the area on 3D T1 and volume on flair ($r = 0.65$, $p < 0.05$). When evaluating progression, the correlation between the area measurement method and volume on 2D Flair measurement method was 0.56 ($p < 0.05$) and the correlation between the measurement methods : volume on 3D T1 and volume on 2D Flair was 0.86 ($p < 0.05$).

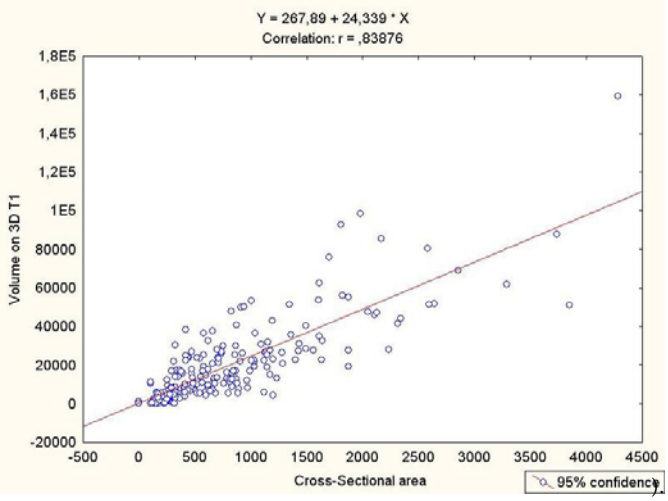

Discussion/Conclusion: Tumor cross-sectional area appears comparable to volume on 3D T1WI and volume on 2D Flair and should still be a practical alternate of volume on 3D for evaluating tumor progression.
References:
[**1**] Tensaouti, F. et al. Proc ESMRMB. 2008
[**2**] Wen, P Y. et al. J Clin Oncol. 2010 April 10
[**3**] Wanga, M-Y et al. Eur J Rad. 2011 Jun 6

525

Diffusion-weighted MR imaging findings of the intracerebral metastasis of breast cancer

S. Kavak, **N. Ciledag**, K. Arda, B. Savran, E. Aktas, B. Gulpinar, H. Kaygusuz
Radiology, Ankara Oncology Research and Education Hospital, Ankara/TURKEY

Purpose/Introduction: We aimed to show the diffusion-weighted imaging(DWI) findings of the intracerebral metastasis of the breast cancer cases and to detect whether there is a correlation between the histopathologic type of the primary tumor and the adherent diffusion coefficient (ADC) values.
Subjects and Methods: Between May 2008 and April 2011, 57 female patients with breast cancer (46 with invasive ductal carcinoma, 7 with invasive lobular carcinoma, 2 with comedocarcinoma and 2 with papillary cribriform carcinoma) were included in the study. The cases were divided into two main groups according to the histopathologic type. The patients were examined with routine MR imaging and DWI. Then the diffusion coefficient was measured from the solid components of the lesions in all patients and from the cystic components if present. The comparison was made between the two main histopathologic type of the breast cancer.
Results: In the first group, the mean ADC value was $1{,}105 \times 10^{-3}$ mm²/sn for the solid components of the lesions, $2{,}012 \times 10^{-3}$mm²/sn for the cystic components and $0{,}780 \times 10^{-3}$mm²/sn for the normal brain parenchyma. In the second group, the mean ADC value was $1{,}099 \times 10^{-3}$mm²/sn for the solid components of the lesions, $2{,}542 \times 10^{-3}$mm²/sn for the cystic components and $0{,}801 \times 10^{-3}$mm²/sn for the normal brain parenchyma. The results of the statistical analysis showed that for the both groups, the ADC values of the solid and the cystic components of the lesions were higher than the ADC values of the normal brain parenchyma. Among each group, the ADC values of the solid components were lower than that of the cystic components. There was no statistical difference of the ADC values of the solid, cystic components and the normal brain parenchyma between the two breast cancer groups.
Discussion/Conclusion: On DWI, metastatic tumors of the brain may exhibit different signal intensities depending on their histology and cellularity(1). Detection of restricted diffusion on DWI in cerebral metastases of the primary lung or breast cancer, is not rare(1).In our study, there was no statistical difference of the ADC values of the metastasis according to the histopathologic

type of the breast cancer. Prospective studies with larger series are necessary regarding the correlation between the primary tumor histopathology and the ADC values of the metastasis.

References:

1. Y.Hayashida,T.Hira,S.Morishita,M.Kitajima,R.Murakami,Y.Korogi,K. Makino, H.Nakamura, I.Ikushima, M.Yamura, M.Kochi, JI.Kuratsu, Y. Yamashita. DWI of metastatic brain tumors:comparison with histologic type and tumor cellularity.AJNR.2006;27(7):1419-25.

526

Combining Diffusion Kurtosis Imaging, Dynamic Susceptibility Contrast-Enhanced Perfusion MR and Short Echo time Chemical Shift Imaging in the grading of gliomas.

S. Van Cauter[1], F. De Keyzer[1], D.M. Sima[2], J. Veraart[3], F. D'Arco[1], A. Leemans[4], R.R. Peeters[1], S. Van Gool[1], S. Sunaert[1], U. Himmelreich[5]
[1]Radiology, University Hospitals Leuven, Leuven/BELGIUM, [2]Electrical Engineering - ESAT, Katholieke Universiteit Leuven, Leuven/BELGIUM, [3]Vision Lab, University of Antwerp, Antwerp/BELGIUM, [4]Radiology, Images science institute, Utrecht/NETHERLANDS, [5]Biomedical MRI unit, KU leuven, Leuven/BELGIUM

Purpose/Introduction: To assess the diagnostic accuracy of diffusion kurtosis imaging (DKI), dynamic susceptibility-weighted imaging (DSC) and short echo time chemical shift imaging (CSI) in the grading of gliomas, as separate techniques and in a multimodal approach in order to determine the best discriminative parameter(s).

Subjects and Methods: 35 patients with cerebral gliomas prior to any treatment (12F/23M; age range: 22-78, median age: 55) underwent DKI, DSC and CSI imaging at a 3T MR scanner. Scanning and data analysis was done according to previously described protocols (1-4). Diffusion parameters - mean diffusivity (MD), fractional anisotropy (FA), mean kurtosis (MK) -, perfusion parameters – mean relative regional cerebral blood volume (mean rrCBV) – and CSI ratio markers as defined in (5)- were compared in the solid part of 22 high grade gliomas (HGG) and 14 low grade gliomas (LGG) (Mann-Whitey-U, $p<0.05$ significance, Bonferroni corrected). Sensitivity, specificity, diagnostic accuracy and optimal thresholds were determined from a receiver operating curve analysis.

Results: MK, meanrrCBV, Lips/Cho and Lips/Cre were significantly higher in HGG compared to LGG. FA, MD and normalizedCho/NAA and normalizedCho/Cre did not significantly differ between glioma grades. Highest sensitivity, specificity and diagnostic accuracy to discriminate between HGG and LGG was found for meanrrCBV and MK (79%, 92%, 84% and 80%, 92%, 85% respectively). Optimal thresholds for MK and meanrrCBV to differentiate HGG from LGG were 0.50 and 1.78 respectively. Combining MK, meanrrCBV and Lips/Cho ratio to determine tumor grade demonstrated a sensitivity of 85%, a specificity of 93% and diagnostic accuracy of 88%.

Discussion/Conclusion: Combining the parameters mean kurtosis, meanrrCBV and Lips/Cho to determine the grade of gliomas, yields a diagnostic accuracy up to almost 90%. The best performing parameters in single use were found to be mean kurtosis and meanrrCBV.

References:

(1) Poot D et al. IEEE Trans Med Imaging: 1504-1505 (2) Van Cauter S et al. (2012) Radiology: 492-501 (3) Van Cauter S et al. (2011) Neurolradiology: 721-31 (4) Van Cauter S et al. Submitted, (5) Kounelakis MG et al. Meas Sci. Technol. (2011)

527

Artificial neural networks and ^{1}H in vivo MRS in classification of posterior fossa tumors progression or recurrence

Ł. Boguszewicz[1], M. Sokół[1], S. Blamek[2], **M. Kijonka**[1]
[1]Department of Medical Physics, Maria Sklodowska-Curie Memorial Cancer Center and Institute of Oncology, Gliwice/POLAND, [2]Department of Radiotherapy, Maria Sklodowska-Curie Memorial Cancer Center and Institute of Oncology, Gliwice/POLAND

Purpose/Introduction: This work assesses the ability of artificial neural networks to classify ^{1}H in vivo MRS spectra and to predict tumor recurrence/progression. The benefits of application of such a decision support system before pathological changes are manifested in MRI are invaluable.

Subjects and Methods: The 166 short TE spectra were acquired from 31 patients using the whole-body 2T MRI/MRS scanner. VOIs were located at the border between the tumor (or tumor bed) and the healthy tissue, and in the normal appearing tissue at the opposite cerebellar hemisphere. Multilayer perceptron (MLP) was chosen as a simple and reliable classifier. Number of variables was reduced by PCA and backward feature selection algorithm. The network structure and learning parameters were chosen by trial and error procedure. The classification accuracy was assessed with an independent test set.

Results: Network trained with principal components correctly classified 87.5% of tumor free, 100% of stable tumor and 80% of tumor progression/recurrence cases. Network trained with reduced number of original variables correctly classified 75% of tumor free, 75% of stable tumor and 60% of tumor progression/recurrence cases.

Discussion/Conclusion: As compared to the following studies [1,2,3,4] the accuracy of our PCA based MLP is high. On the other hand, the BFS algorithm was found to lead to poor classification, which is probably due to removal of too many of important variables. The main drawback of our study is a rather small number of cases, especially in the TPR group. Thus making far-reaching conclusions is risky at the moment. Nevertheless, it may be expected that such adaptive systems - like ANN - should be precise enough in learning of features of samples that are unique in a population. We strongly believe that, when trained with a large number of samples, ANN can constitute the core of fast working and reliable DSS.

References:

1.Lisboa PJG et al (2008) Classification, Dimensionality Reduction, and Maximally Discriminatory Visualization of a Multicentre 1H-MRS Database of Brain Tumors. ICMLA '08 613-618

2.Poptani H et al (1999) Diagnostic assessment of brain tumours and non-neoplastic brain disorders in vivo using proton nuclear magnetic resonance spectroscopy and artificial neural networks. J Cancer Res Clin Oncol 125(6):343-349

3.García-Gómez JM et al (2009) Multiproject-multicenter evaluation of automatic brain tumor classification by magnetic resonance spectroscopy. MAGMA. 22(1):5-18 (2009).

4.Menze BH et al (2006) Optimal classification of long echo time in vivo magnetic resonance spectra in the detection of recurrent brain tumors. NMR Biomed 19(5):599-609

528

Usefulness of MR spectroscopy in differentiation between recurrent/residual brain glioma and post-therapeutic changes

A. Bieza, G. Krumina
Department of Radiology, Riga Stradins University, Riga/LATVIA

Purpose/Introduction: Differentiation between glial tumor recurrence and radiation and/or chemotherapy induced effects is a serious clinical as well as radiological problem, because structural magnetic resonance imaging (MRI) is not specific enough, and tends to have similar visual appearance.

Magnetic resonance spectroscopy (MRS) is widely used for metabolic characterization of the brain parenchyma. Our purpose was to determine the efficiency of standard brain metabolites measurements: choline (Cho), creatine (Cr), lipid and lactate (LL), myo-inositol (MI), N-acetylaspartate (NAA) in

distinguishing between recurrent/residual brain glioma zones and radiation/chemotherapy induced changes in the brain parenchyma.
Subjects and Methods: 73 patients with visually typical and subsequently morphologically proved glial brain tumors on structural MRI before surgical intervention and 77 patients in clinical remission after combined surgical and radiation and/or chemotherapy with visually recognized pathological changes around the removed tumor bed underwent MRS of the brain with a 1.5 tesla MRI system. Metabolites ratios (Cho/Cr, NAA/Cr, MI/Cr and LL/Cr) were computed for manually selected areas: the solid tumor part (in the first group) and the abnormal signal intensity area around the removed tumor bed (in the second group). Differences in metabolites ratios among two groups were tested using the Wilcoxon signed rank test.
Results: Following mean metabolite ratios (± standard deviation) were observed in the solid tumor part: Cho/Cr 2.305 (± 1.543), NAA/Cr 1.031 (± 0.517), MI/Cr 0.814 (± 0.509), LL/Cr 3.933 (± 1.547). Patients in remission after combined therapy had following measurements results: Cho/Cr 1.355 (± 0.606), NAA/Cr 1.153 (± 0.507), MI/Cr 0.607 (± 0.362), LL/Cr 2.304 (± 1.213). The difference between true tumor tissues and post-therapeutic changes in the Cho/Cr and LL/Cr ratios was statistically more significant ($p < 0.001$) than in MI/Cr ratio ($p = 0.010$). We found no statistically significant difference in NAA/Cr ratios.
Discussion/Conclusion: Cho/Cr, MI/Cr, LL/Cr ratios in the solid, vital parts of glial tumors are statistically significantly higher compared to post-treatment injury areas. MRS is an adequate and sufficiently accurate MRI method for differentiation between vital glial tumor parts and post-therapeutic changes. We recommend including MRS in the standard follow-up MRI protocol for glioma patients, who underwent combined surgical and radiation and/or chemotherapy.
References:
1. Nelson SJ (2011) Assessment of therapeutic response and treatment planning for brain tumors using metabolic and physiological MRI. NMR Biomed 24(6):734-749
2. Sundgren PC (2009) MR spectroscopy in radiation injury. Am J Neuroradiol 30:1469 –1476

529

Differentiating diffuse WHO grade II and IV Astrocytomas using ex vivo MR Spectroscopy

R. Vettukattil[1], M. Gulati[1], T.E. Sjøbakk[1], A.S. Jakola[2], S.H. Torp[3], N.A.M. Kvernmo[2], T.F. Bathen[1], S. Gulati[4], I.S. Gribbestad[1]
[1]Department of Circulation and Medical Imaging, Norwegian University of Science and Technology, Trondheim/NORWAY, [2]Department of Neurosurgery, St. Olavs University Hospital, Trondheim/NORWAY, [3]Department of Pathology and Medical Genetics, St. Olavs University Hospital, Trondheim/NORWAY, [4]Department of Neuroscience, St. Olavs University Hospital, Trondheim/NORWAY

Purpose/Introduction: Astrocytomas are among the most common primary brain tumors in humans and are subdivided into histological grade II - IV according to the WHO classification [1]. Management of diffuse astrocytomas differs considerably depending on their grade, and identification of factors that may stratify these patients with regards to optimal prognosis and treatment is essential. Magnetic resonance spectroscopy (MRS) is an emerging noninvasive tool to improve diagnostic accuracy and has the potential to detect 2-hydroxyglutarate (2HG), associated with isocitrate dehydrogenase (IDH) gene mutations and better survival in gliomas [2]. The aim of this study was to investigate whether ex vivo MRS could differentiate diffuse astrocytomas WHO grade II (A-II) and IV (glioblastomas; GBM) and to correlate metabolic profiles with histopathology.
Subjects and Methods: Patients with A-II and GBM (n=58) scheduled for surgical resection were enrolled. Tumor specimens were collected during surgery and stored in liquid nitrogen before analysis with high resolution magic angle spinning (HR-MAS) MRS as previously described [3]. The tumors were histopathologically classified according to WHO criteria as A-II (n=10) and GBM (n=48). After HR-MAS analysis immunohistochemical analyses with respect to IDH1 expression and histological estimation of necrosis were done. The spectra were analyzed by multivariate analysis.
Results: The spectra showed differences in the metabolic profiles of different grades of astrocytomas (fig.1). A-II had higher levels of glycerophosphocholine (GPC) and myo-inositol than GBM. The latter had more phosphocholine (PCho), glycine and lipids. Phosphorous spectroscopy improved the delineation between PCho and GPC. A significant metabolic difference between recurrent GBM versus non recurrent ($P<0.001$) was observed. Primary GBM had more PCho than recurrent GBM. In GBM, there was a significant correlation ($P<0.001$) between lipid, lactate and necrosis. 2HG was detected in the HR-MAS spectra of five patients. IDH1 mutation analysis and its concordance with 2HG detection is summarized in Table 1.
Discussion/Conclusion: This study demonstrates that ex vivo MRS can differentiate various types of diffuse astrocytomas based on their metabolic profiles. A comprehensive approach using 31P MRS, 1H MRS and markers for IDH1 mutation may offer additional clinical benefits in the classification, treatment, and management of astrocytomas.
References:
1 Louis, DN, 2007, Acta Neuropathol, 114(2):97-109.
2 Elkahled, A., 2012, Sci Transl Med, 4(116):116ra115.
3 Sitter, B., 2002, NMR Biomed, 15(5): p. 327-337.

Table1: IDH1 mutation and 2HG detection among astrocytomas (n=58)

Parameter	Total	IDH1+	2HG detected	2HG+/IDH1+
Primary GBM	44	2	0	0
Secondary GBM	4	3	2	1
A-II	10	3	3	3

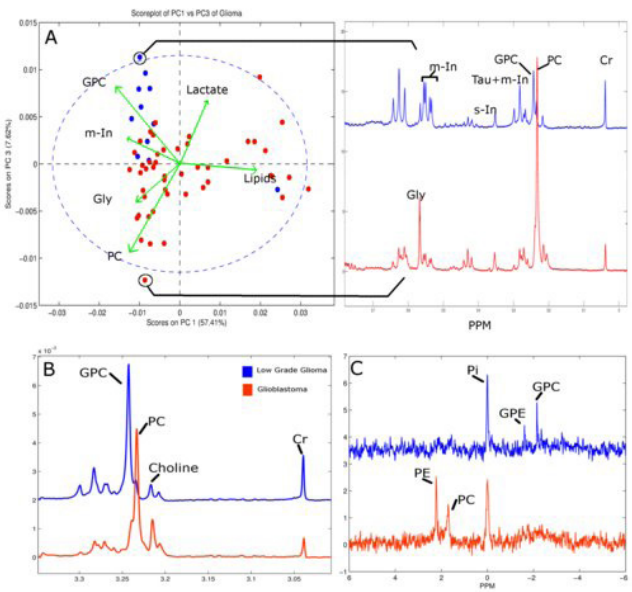

Figure1: A) PCA of Glioma 1H MR Spectra: GBM and A-II patients are shown in red and blue respectively. Green arrows are drawn on the basis of loadings plot to show the important metabolites. Corresponding normalized spectra from individual patients pointed by arrows are shown in the right side. A-IIs have more GPC and m-In than GBM. The later has more PCho, Gly and Lipids. B) Representative 1H and C) 31P HR-MAS of astrocytomas showing the differences in choline signals

530

Brain tumour classification using quantitative MR imaging and spectroscopy

D. Wagnerova[1], V. Herynek[1], A. Malucelli[2], M. Dezortova[1], J. Vymazal[3], D. Urgosik[4], M. Syrucek[5], F. Jiru[1], A. Skoch[1], R. Bartos[2], M. Sames[2], M. Hajek[1]
[1]MR-Unit, Department of Diagnostic and Interventional Radiology, Institute for Clinical and Experimental Medicine, Prague 4/CZECH REPUBLIC, [2]Department of Neurosurgery, JE Purkyne University and Masaryk Hospital, Usti nad Labem/CZECH REPUBLIC, [3]Department of Radiology, Na Homolce Hospital, Prague 5/CZECH REPUBLIC, [4]Stereotactic and radiation neurosurgery, Na Homolce Hospital, Prague 5/CZECH REPUBLIC, [5]Department of Pathology, Na Homolce Hospital, Prague 5/CZECH REPUBLIC

Purpose/Introduction: Coregistration of MR spectroscopic (SI), diffusion (DTI), relaxation images and their subsequent correlations based on pixel-by-pixel quantitative analysis have a potential to distinguish pathological states (a tumour, oedema, tumour infiltrated oedema, necrosis) and a healthy tissue and therefore help assess the brain tumour extent1. Patients with low and high grade gliomas (LGG, HGG resp.), lymphomas (LYM), recurrent tumours or radiation necrosis were involved in the study to validate the use of this method in clinical practice.

Subjects and Methods: Two groups of patients with a suspected intracranial tumour and 55 healthy subjects were examined on a 3T system. Group 1 consists of 24 patients with untreated brain lesions, group 2 of 17 patients with a tumour recurrence or radiation necrosis after resection of a primary brain tumour and consequent chemo/radiotherapy.

The measurement protocol consisted of anatomical T2-weighted MR images, SI, DTI and T2 relaxometry. SI data were analyzed by a program SIPRO2 and correlations by a program CORIMA1 with automatic identification of pixels in the normal tissue according to control data.

All the subjects provided an informed consent according to the ISO 9001:2008 norm.

Results: Specific correlation patterns between metabolic concentrations and mean diffusivity (MD) or T2 relaxation times (T2) were found for given lesion localization and for given tumour type (HGG-Fig.1, LYM-Fig.2). These patterns are based on different tissue states involved in the examined area, i.e. healthy tissue (Fig.1 and 2, region 1), tissue infiltrated by tumourous cells (region 2), active tumour (region 3), tumour infiltrated oedema (reg.4), oedema (reg.5), etc. Recurrent tumours exhibited the same correlation patterns as untreated ones, but different parameter values were found in the surrounding irradiated tissue. Metabolic values did not correlate with MD and T2 in the case of radiation necrosis. Correlations of the following MR parameters are suitable for tumour and tissue differentiation: MD, T2, choline, N-acetylaspartate, creatine, inositol, lactate, macromolecules, lipids and metabolite ratios.

Discussion/Conclusion: A quantitative analysis of different MR methods is able to describe the complexity of a highly heterogeneous tissue in the tumour and its vicinity and determine crucial parameters for tumour and tissue differentiation and for assessment of the tumour extension. However this method can be used only in semiautomatic mode due to an unavoidable chemical shift artifact in SI and image distortions in DTI.

References:

[1]Wagnerova D et al. Magn Reson Mater Phy 2009;22(1):19-31,
[2]http://www.sites.google.com/site/jsiprotool/

Acknowledgements
Supported by MZCR projects IGA NS/9654-4 and Institutional grant 00023001IKEM.

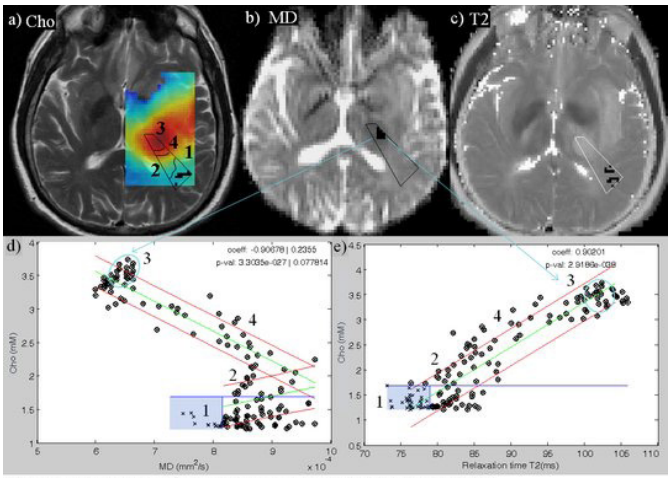

Figure 1: An example of correlation patterns in the high grade glioma.
a) A T2 weighted image merged with a choline map. b) Mean diffusivity map. c) T2 relaxation map. d) Cho-MD correlation. e) Cho-T2 correlation. Black pixels inside the selected area on images a,c correspond to the healthy tissue according to control data. Black pixels on MD map correspond to localisation of biopsy specimen. Data points indicated by a cross in the correlation plots represent an ordered pair of parameter values corresponding to one pixel in the analysed area. Values corresponding to control values (determined by blue lines) are visible as crosses inside the blue area, all values above the blue lines visible as crosses in circles correspond to tissue abnormalities. Region 1 - healthy tissue, 2 - infiltrative tumour to the healthy tissue, 3 - active tumour, 4 - oedema infiltrated by tumour. The green lines represent the best linear fit of the data. The red lines indicate the 95% confidence interval for the linear regression fit. Cho - choline containing compounds; NAA - total N-acetyl aspartate; T2 - T2 relaxation time; MD - mean diffusivity.

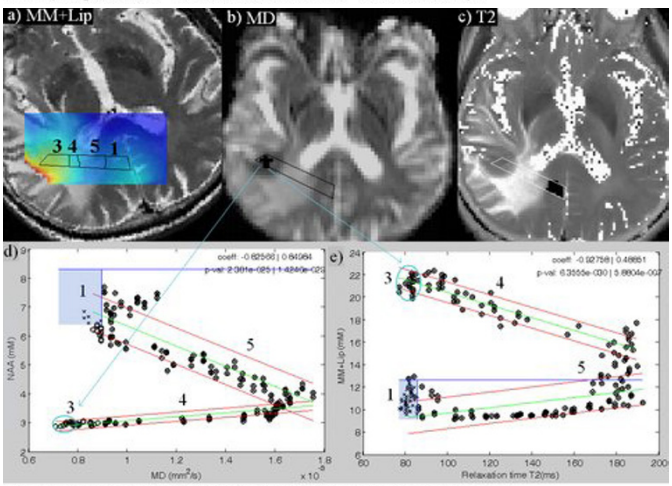

Figure 2: An example of correlation patterns in the lymphoma.
a) A T2 weighted image merged with a metabolite map. b) Mean diffusivity map. c) T2 relaxation map. d) NAA-MD correlation. e) MM+Lip-T2 correlation. Black pixels inside the selected area on images a,c correspond to the healthy tissue according to control data. Black pixels on MD map correspond to localisation of biopsy specimen. Data points indicated by a cross in the correlation plots represent an ordered pair of parameter values corresponding to one pixel in the analysed area. Values corresponding to control values (determined by blue lines) are visible as crosses inside the blue area, all values above the blue lines visible as crosses in circles correspond to tissue abnormalities. Region 1 - healthy tissue, 3 - active tumour, 4 - oedema infiltrated by tumour, 5 - oedema. The green lines represent the best linear fit of the data. The red lines indicate the 95% confidence interval for the linear regression fit. NAA - total N-acetylaspartate; MM+Lip - macromolecules and lipids; T2 - T2 relaxation time; MD - mean diffusivity.

531

Diffusion weighted imaging and magnetic resonance spectroscopy in assessment of methylation status of glioblastoma multiforme

M. Daković[1], T. Petrović[1], J. Mihailović[2], T. Stošić-Opinćal[3], G.G. Bačić[4], D. Grujičić[5]
[1]Department of Biophysical Chemistry, Faculty of Physical Chemistry, Belgrade/SERBIA, [2]Department of biophysical chemistry, Faculty of Physical Chemistry, Belgrade/SERBIA, [3]Magnetic resonance department, National Cancer Research Center, Belgrade/SERBIA, [4]Center for Radiology and Magnetic Resonance, Clinical Center of Serbia, Belgrade/SERBIA, [5]Department of Radiochemistry, Faculty of Physical Chemistry, Belgrade/SERBIA, [6]Neurosurgery Clinic, Clinical Center of Serbia, Belgrade/SERBIA

Purpose/Introduction: Efficiency of glioblastoma (GBM) treatment with methylating agents largely depends on expression of enzyme O6-alkylguanine–DNA alkyltransferase (MGMT) which removes methyl group from methylated guanine and diminishes efficiency of therapeutic agents. It has been proven that methylation status correlates with outcome of GBM patients treated with concomitant radiation and methylation agent therapy [1]. Standard procedure determines methylation status using by methylation-specific polymerase chain reaction (MPCR) and requires specimen obtained by biopsy or surgery.
The aim of this retrospective study is to test ability of DWI and proton magnetic resonance spectroscopy to discriminate between methylated and non-methylated GBM.
Subjects and Methods: Twelve patients were subjected to MRI examination before surgery and chemotherapy. Diagnosis of GBM was confirmed by histopathological analysis and methylation status was determined using MPCR. MRI protocol at 1.5 T SIEMENS AVANTO imager included use of 8-channeled phased array head coil and T1W, T2W, T2*, FLAIR and postcontrast T1W sequences. In addition DWI using three b-values (0, 500, 1000 smm^{-2}) and chemical shift imaging (CSI) with echo time of 30 ms were performed; for 4 subjects CSI at 135 ms was added as well.
Histogram analysis of ADC maps in regions that correspond to postcontrast enhancement in T1W images was performed using MIPAV software. Components in histograms were deconvoluted and ratio of areas beneath the curves was calculated. This parameter should represent relative contributions of microvascularity and cellularity [2]. CSI was performed in area which coincided to area of hyperintensity in T2 images. Ratios choline to creatine (Cho/Cr) and myoinositol to creatine (mIno/Cr) were determined for voxel placed in the same region as for ADC histogram calculation.
Results: No significant differences were found for average ADC values and relative contributions of microvascularity and cellularity between methylated and non-methylated GBMs. This could be attributed to similar microstructure in analyzed region in both types. Methylated GBMs had significantly higher values of mIno/Cr ratios (0.65 vs 0.26, $p<0.05$), while no differences were found between Cho/Cr ratios. The observed difference could be explained by contribution of glycine which has resonance at same position as mIno (3.53 ppm). This is supported by observed resonance of inhibitory neurotransmitter glycine in 135 ms spectra of methylated tumors.

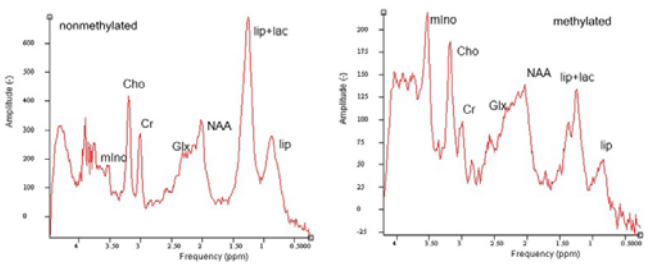

Discussion/Conclusion: MRS can help in assessment of methylation status of GBM and hence in prediction of outcome of therapy with methylation agents.
References:
[1] M. E. Hegi et al, Clin Canc Res, 2004; 10:1871-1874.
[2] W.B. Pope et al, AJNR, 2011; 32:882– 889.

EPOS™ Poster

Brain - white matter

532

Voxel-based morphometry and MR-spectroscopy in complex MR diagnostics of multiple sclerosis.

A. Sokolov, V. Fokin, A. Efimtcev, G. Trufanov
Radiology, Medical Military Academy, Saint-Petersburg/RUSSIAN FEDERATION

Purpose/Introduction: MRI is the best test to visualize the changes caused by multiple sclerosis. The precise image produced by MRI gives the neurologist clear evidence of lesions in white matter of the brain or spinal cord that is characteristic of MS. But it does not give quantitative data about pathological changes of the brain, such as the level of brain atrophy and metabolic changes in MS lesions or abnormal areas on the brain. Therefore, voxel-based morphometry (VBM) and MR-spectroscopy make MR diagnostics of multiple sclerosis more complex.
Subjects and Methods: 32 patients with relapsing-remittng multiple sclerosis (age from 18 to 38) and 20 healthy volunteers underwent complex MR investigation, which included conventional MRI, MR-spectroscopy and MR morphometry. Investigation was repeated after 2 years of treatment. SPM8 software package was used for voxel-based morphometry.
Results: The investigation showed reduction of N-acetylaspartate (NAA) and creatine (Cr) concentrations, NAA/Cho and NAA/Cr ratios and increase of choline (Cho) and lactate (Lac) concentrations, Cho/Cr ratio in brain lesions of patients with relapsing-remittng multiple sclerosis. VBM measures differences in local concentrations of brain tissue through a voxel-wise comparison of multiple brain images. VBM showed atrophy of gray matter of both hemispheres in particular in cingulated gyrus, hippocampus, uncus, basal ganglia and increase of crerbrospinal fluid volume between baseline and 2 year point.
Discussion/Conclusion: Voxel-based morthometry and MR-spectroscopy give additional quantitative information of brain lesions in patients with multiple sclerosis, which takes effects on future prognosis of such patients.

EPOS™ Poster

Breast

533

Effects of motion correction on pharmacokinetic parameters of dynamic contrast-enhanced magnetic resonance imaging (DCE MRI) of breast cancer

L.B. Nilsen[1], T. Seierstad[2], A. Fangberget[2], D.R. Olsen[3], O. Engebråten[1], O.M. Geier[4]
[1]Institute for Cancer Research, Oslo University Hospital, Oslo/NORWAY, [2]Department of Radiology and Nuclear Medicine, Oslo University Hospital, Oslo/NORWAY, [3]Faculty of Mathematics and Natural Sciences, University of Bergen, Bergen/NORWAY, [4]The Intervention Centre, Oslo University Hospital, Oslo/NORWAY

Purpose/Introduction: Quantitative parameters obtained from pharmacokinetic modelling of the contrast enhancement curve (CTC) from DCE MRI reflecting tumour vascularisation are increasingly being evaluated as potential biomarkers that may improve radiological diagnosis, characterization and monitoring of breast cancer patients [1]. A prerequisite for reliable determination of these pharmacokinetic parameters is a CTC that reflects the contrast dynamics of the tumour tissue precisely. Displacements during acquisition alter the CTC and reduce the validity of the obtained parameters. The purpose of this study was to quantify the effect of breast movement during the scan on the vascular rate constant K^{trans}.
Subjects and Methods: Ten women with confirmed invasive breast cancer were included. Pre-treatment T1-weighted DCE MRI (K-space-weighted imaging contrast; temporal resolution=13.8s; TR/TE=5.46ms/2.59ms; spatial resolution=1x1x1mm^3) was performed on a 1.5T scanner (ESPREE, Siemens) using Gadovist (0.08mmol/kg body weight; 3ml/s+20ml saline flush). The degree of tumour displacement was categorized as no/little (group0) or high (group1). Motion correction was performed by a non-rigid 3D co-registration based on mutual information and B-spline transformation using the elastix software package [2]. K^{trans} was calculated using nICE (Nordic NeuroLab) with the Tofts model including individual AIFs. Median K^{trans} was obtained from a single ROI and from the whole tumour volume (VOI). The ROI was placed in the slice with the greatest tumour extent of the image volume being the baseline for motion correction. The VOI was found by semi-automatic segmentation of the uncorrected and co-registered images, respectively. Comparisons between median K^{trans} for uncorrected and co-registered images were performed with Wilcoxon signed ranks test.
Results: Fig.1A shows the effect of motion correction on DCE MR images with significant displacements. After co-registration the shape of the mean CTC was altered (Fig.1B). Resulting K^{trans} maps from uncorrected and co-registered images are shown in Fig.1C. Table 1 shows the result from comparing differences in uncorrected and motion-corrected median K^{trans} between group0-1.

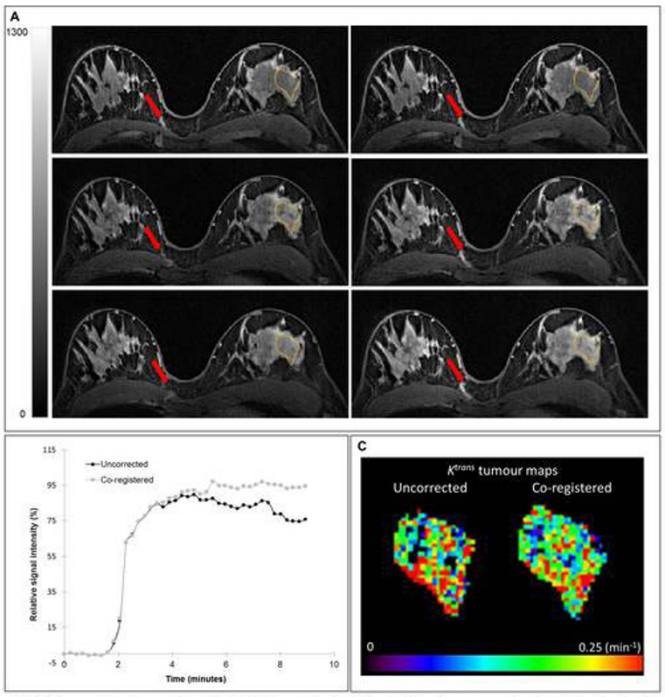

Fig.1. Uncorrected and co-registered DCE MR images in the left and right columns, respectively, prior to (top) and 2 (middle) and 6 (bottom) minutes after contrast agent injection (A). The yellow ROI placed within the enhancing breast tumour of the left breast was drawn in the 2 minutes post-contrast image (middle). After motion correction the tumour was no longer spatially displaced and also small vessels did not appear blurred (red arrow). Difference in mean relative single intensity-time curves from the ROI of the uncorrected (black) and corrected (grey) is shown in B. The uncorrected and co-registered K^{trans} tumour maps are shown to the left and right (median K^{trans}=0.18 and 0.16 min^{-1}), respectively in C.

Table 1. Comparison of median K^{trans} obtained from pharmacokinetic modelling of corrected and uncorrected DCE MR images

	Difference in median K^{trans} (%)				Wilcoxon signed ranks test
	Group0		Group1		
	Median	Range	Median	Range	p-value
Single ROI	0.7	0.1-5.4	8.5	2.7-9.8	0.04
VOI	1.8	0.1-3.35	8.6	4.6-12.2	0.04

Discussion/Conclusion: Only small differences in uncorrected and motion-corrected median K^{trans} values were found in group0, where there had been little displacement of the tumour during the scan. In contrast there were significantly larger differences in K^{trans} in group1. The results of this preliminary study thus indicates that motion correction should be performed on DCE MR images prior to pharmacokinetic modelling in order to obtain more accurate parameters.
References:
[1] Padhani AR, Khan AA, 2010, Target Oncol, 39-52
[2] Klein S *et al.*, 2010, IEEE Trans Med Imag, 196-205

534

DCE-MRI transfer coefficient Ktrans as a surrogate marker for neoadjuvant treatement in breast cancer patients: Comparison of manual versus automatic segmentation of region of interest

S. Drisis, K. Stathopoulos, S. Chao, M.R. Capelan, M. Lemort
Radiology, Institut Jules Bordet, Bruxelles/BELGIUM

Purpose/Introduction: To compare the predictive value of DCE-MRI transfer coefficient Ktrans for distinguishing responders from non responders breast cancer patients receiving neoadjuvant chemotherapy (NAC) when manual versus automatic segmentation of region of interest (ROI) was applied.
Subjects and Methods: A retrospective study including 50 patients was performed where all patients underwent two DCE MRI examinations, one before and one during NAC. DCE-MRI transfer coefficient Ktrans was calculated by

manual segmentation (KtransManual) and compared with automatic region growing segmentation algorithms with the following different configurations: i) a threshold value of Ktrans more than two standard deviations than the Ktrans value of the normal mammary gland (Ktrans2sd) ii) more than three standard deviations (Ktrans3sd) and iii) more than three standard deviations with a 3D propagation of the seed (3DKtrans3sd). Post-operative pathological examination was used as the golden standard with a binary response: responders, patients showing complete remission or "in situ" residual disease and non-responders for the rest of the patients. ROC curves and comparison of ROC with the method of Delong were employed for the statistical analysis.
Results: The Ktrans3sd showed the highest area under the curve (AUC) followed by 3DKtrans3sd, Ktrans2sd and KtransManual with the values of 0.694, 0.639, 0,596 and 0,533 respectively. However, the comparison of Ktrans3sd and KtransManual showed a non significant value of p = 0.368. In addition, no significant difference was found for the comparison between the different segmentation methods.
Discussion/Conclusion: Automatic region growing segmentation of ROI showed non significant difference of AUC in comparison with manual segmentation. However, Ktrans3sd automatic algorithm showed better predictive value of Ktrans than manual segmentation for distinguishing responders from non responders.
References:
[1] Pickles MD, Lowry M, Manton DJ, Gibbs P, Turnbull LW. Role of dynamic contrast enhanced MRI in monitoring early response of locally advanced breast cancer to neoadjuvant chemotherapy. Breast Cancer Res Treat. 2005 May;91(1):1-10.
[2] Padhani AR, Hayes C, Assersohn L, Powles T, Makris A, Suckling J, Leach MO, Husband JE. Prediction of clinicopathologic response of breast cancer to primary chemotherapy at contrast-enhanced MR imaging: initial clinical results. Radiology. 2006 May;239(2):361-74. Epub 2006 Mar 16.
[3] Fisher B, Bryant J, Wolmark N, Mamounas E, Brown A, Fisher ER, et al. Effect of preoperative chemotherapy on the outcome of women with operable breast cancer. J Clin Oncol. 1998 Aug;16(8):2672-85.

535

Value of MR-spectroscopy in differential diagnosis of breast lesions

S. Ternovoy, **N. Meladze**, A. Solopova, A. Abduraimov
Tomography, I. M. Sechenov State Medical University, Moscow/RUSSIAN FEDERATION

Purpose/Introduction: To evaluate the value of single proton MR-spectroscopy and dynamic contrast MR-mammography in differential diagnosis of breast lesions.
Subjects and Methods: The study involved 87 women with breast lesions at the age from 32 to 69 years.
The diagnostic algorithm consisted of clinical examination, ultrasound, Roentgen mammography, MR-mammography with dynamic contrast enhancement (DCE) and MR-spectroscopy. MR-mammography was performed at Philips Achieva 3.0 T TX using seven-channel coil MammoTrack. Dynamic of contrast accumulation was assessed by constructing "signal intensity-time" curves. Signal voxel proton MR-spectroscopy was performed using PRESS sequence with voxel size 1-3cm, before and after contrast agent administration.
Results: Breast cancer was diagnosed in 62 cases (71,3%), fibroadenoma in 21 (24,1%), cysts 9 (10,3%), lipoma 2 (2,3%). Lesion size ranged from 4 to 38 мм. MR-mammography with DCE of 52 (83,9%) patients with breast cancer was characterized by a rapid washout curve, when the peak intensity of accumulation observed in first two minutes. In 10 (16%) patients with cancer and in 7 patients with fibroadenoma (33,3%) "signal intensity-time" curve was characterized by a linear increase within 2-3 minutes after contrast injection, followed by a plateau phase. In 14 (66,6%) cases of fibroadenoma there was gradual ramp signal intensity over a long time period. In 9 cases (100%) of cysts and 2 (100%) cases of lipoma increased contrast accumulation was not determined. Increasing concentration of choline in malignant lesions were obtained only in 11 cases (17,7%). Lesion size in all these cases exceeded 2 cm. In all other cases we failed to identify the peak of choline. Choline positive signal was also given in 3 (14,2%) cases of fibroadenoma. MR-spectroscopy comparative analysis performed before and after contrast enchainment showed better results of MR-spectroscopy performed after contrast agent administration as the tumor size could be easily evaluated.
Discussion/Conclusion: The main diagnostic limitations of MR-spectroscopy were observed if the voxel size exceeded the lesion. MR-spectroscopy could not be used as an accurate method in primary evaluation and differential diagnosis of breast lesions. MR-spectroscopy showed better results while performed after contrast agent administration as it helped in voxel positioning. MR-mammography with DCE is an accurate method for infiltrating breast cancer evaluation, and should be used at the final stage of diagnosis.

536

Improving MRI Sensitivity, Specificity and Accuracy in Breast Cancer Diagnosis by ^{1}H-MRS

G. Russo[1], **S. Nicolosi[2]**, I. D'Angelo[3], G. Vicari[3], M.C. Gilardi[4], G. Borasi[2]
[1]Fisica Sanitaria, CNR-IBFM, UOS Cefalù, Cefalù/ITALY, [2]Radiologia, CNR - LATO, Cefalù/ITALY, [3]Radiologia, San Raffaele G. Giglio, Cefalù/ITALY, [4]Medicina Nucleare, CNR - IBFM, Segrate (MILANO)/ITALY

Purpose/Introduction: Purpose
Magnetic Resonance Imaging has gained popularity in breast cancer diagnosis with the introduction of contrast media. Recent development in MRI demonstrated new potential use in diagnosis. In particular, application of in vivo spectroscopy (MRS) to mammary tissue shows that spectral appearance of choline could be a marker of malignancy [1]. For early diagnosis and unambiguous breast cancer characterization it would be desirable a standardized protocol which provides for the simultaneous use of more than one techniques. It is in fact intuitive to think that the sensitivity, specificity and accuracy associated with different diagnostic tests is always less than that associated to their combination.
Subjects and Methods: Subjects and Methods
In this retrospective study, a total number of 29 female patients were included. Patients were consecutively referred for MR imaging at 1.5 T from Division of Senology (Operative Unit of Radiology) at our institution if there were clinically suspicious finding and/or abnormalities detected with mammography and/or ultrasonography. The MRI/MRS protocol have been performed on a General Electric Signa HDtx 1.5 Tesla clinical magnetic resonance. Data analysis of DCE has been performed throw the evaluation of ROI signal intensity over time. Data analysis of MRS has been performed throw the evaluation of absolute choline concentration and signal to noise ratio of choline peak. Sensitivity, specificity and accuracy of the two markers and their best linear combination have been assessed by Receiver Operating Characteristic (ROC) methodology.
Results: In this paper we have developed an empirical methods to obtain a high level diagnostic index combining Dynamic Contrast Enhancement MRI and in vivo Magnetic Resonance Spectroscopy (MRS). Individually, choline and DCE show specificity of 85,7% and 90,9%, sensitivity of 68,2% and 42,8%, and accuracy of 81,2% and 84,0%, respectively. Their best linear combination shows a specificity of 100%, a sensitivity of 86.4% and an accuracy of 96%. ROC curves of the three indexes are displayed in Figure.

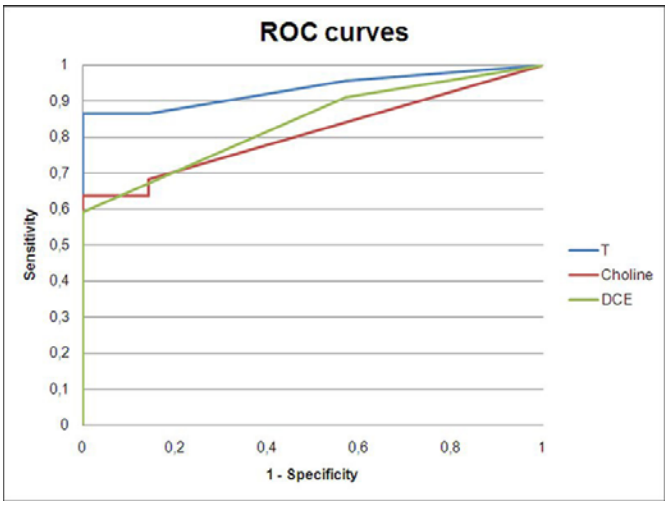

Fig. Comparison of Receiver operating characteristic curves among the linear combination T of the two tests and the individual ones (Choline and DCE)

Discussion/Conclusion: The joint use of the two diagnostic test results in a new, high level, diagnostic index T able to discriminate among disease and non-disease patient in an excellent way.

References:

[1] Begley JKP, Redpath TW, Bolan PJ et al (2012) In Vivo proton magnetic resonance spectroscopy of breast cancer: a review of the literature. Breast Cancer Research 14:207(10 pp)

EPOS™ Poster

Cardiac and coronaries

537

Comparison of Models for the Quantification of Myocardial Perfusion using MRI

F. Schwab[1], R. Marcus[1], K. Hildebrand[1], D. Theisen[1], F. Bamberg[1], M. Reiser[1], M. Ingrisch[2]
[1]Department of Clinical Radiology, University Hospital Grosshadern, Munich/GERMANY, [2]Institute for Clinical Radiology, Ludwig-Maximilians-University Hospital Munich, Munich/GERMANY

Purpose/Introduction: The analysis of myocardial perfusion is of fundamental importance in clinical routine for the detection of ischemic heart regions. However, analysis generally proceeds either only qualitatively or semiquantitatively, using descriptive curve parameters such as the upslope [1, 2]. It was the purpose of this work to compare several established models for perfusion quantification in the context of cardiac perfusion.
Subjects and Methods: 5 patients underwent rest and stress perfusion measurements on a clinical 3 Tesla scanner (Magnetom Verio, Siemens) using an ECG-triggered SR-FLASH sequence (TR=160.5ms, TE=0.86ms, Matrix=128×96, FoV=360×270 mm²). 3 slices were acquired for each patient, which were divided into 6 (basal, midventricular) or 4 (apikal) sectors using commercially available software (ARGUS, Siemens). Data curves were analyzed on software written in house for the following models: A one-compartment model, a Fermi model, a two-compartment exchange model, an uptake model as well as a Tikhonov-regularized deconvolution using an optimized L-curve criterion [3]. Analysis was limited to the first pass.
Results: Median values for the plasma flow and plasma volume over all patients and sectors are given in Table 1 and all data are presented as box plots in the figure.

Table 1 Median values for perfusion quantities determined using various models.

Quantity \ Model	Deconvolution	One Compartment	Fermi Model	2 compartment Exchange	Uptake Model
Plasma Flow (Rest) (ml/100ml/min)	59.0	60.3	57.2	88.1	77.6
Plasma Flow (Stress) (ml/100ml/min)	111.5	128.2	129.8	554.7	205.5
Plasma Volume (Rest) (ml/100ml)	11.7	14.2	13.2	1.8	10.2
Plasma Volume (Stress) (ml/100ml)	14.5	14.2	14.0	4.7	10.0

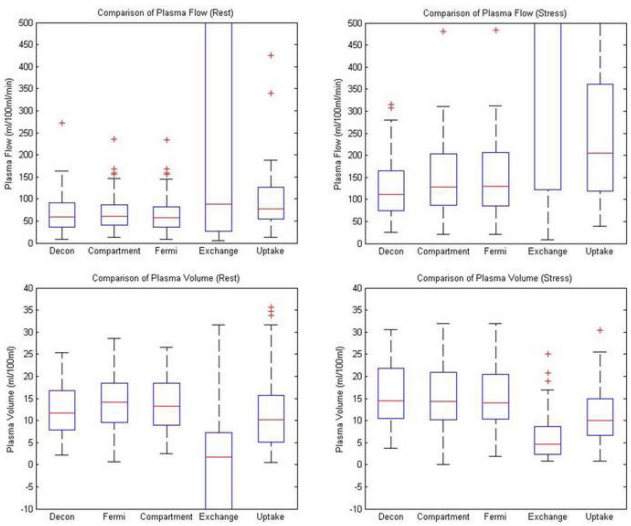

We find good agreement between the deconvolution, the one compartment and Fermi model, while the uptake model does not agree as well and the exchange model differs rather strongly. Correlation analysis using a Wilcoxon rank sum test shows a significant difference for the exchange and uptake models, but mostly good individual agreement between the other three methods (Table 2 and 3).

Table 2 *P*- values denoting statistical correlation between results for plasma flow at rest (above diagonal line) and stress (below diagonal line).

Plasma Flow	Decon (Rest)	Fermi (Rest)	Comp (Rest)	Exchange (Rest)	Uptake (Rest)
Decon (Stress)		0.8	0.7	0.03	0
Fermi (Stress)	0.1		0.5	0.02	0
Comp (Stress)	0.2	0.8		0.05	0.002
Exchange (Stress)	0	0	0		0.9
Uptake (Stress)	0	0	0	0.003	
	Decon (Stress)	Fermi (Stress)	Comp (Stress)	Exchange (Stress)	Uptake (Stress)

Table 3 *P*- values denoting statistical correlation between results for plasma volume at rest (above diagonal line) and stress (below diagonal line).

Plasma Volume	Decon (Rest)	Fermi (Rest)	Comp (Rest)	Exchange (Rest)	Uptake (Rest)
Decon (Stress)		0.2	0.06	0	0.2
Fermi (Stress)	0.5		0.6	0	0.02
Comp (Stress)	0.5	0.96		0	0.01
Exchange (Stress)	0	0	0		0
Uptake (Stress)	0	0	0	0	
	Decon (Stress)	Fermi (Stress)	Comp (Stress)	Exchange (Stress)	Uptake (Stress)

Discussion/Conclusion: This work compares several models used for perfusion quantification in the context of myocardial perfusion. The one-compartment model, the Fermi model and the model independent deconvolution all agree with each other while the two-compartment exchange and uptake models are underdetermined and hence yield parameter estimates with large deviations. This is most likely due to the fact that the analysis was limited to the first pass only, while the time scale of the extravasation is longer, so that extravascular parameters cannot be reliably determined [4]. Many of these results are in accordance with a previous study [5], which, however, used a different deconvolution method as well as a different two-compartment model.
References:
[1] Jerosh-Herold, M.; J Cardiovasc Magn Reson. 2010;12:57.
[2] Sourbron, S et al; Phys. Med. Biol. 2007:52(2):425-47.
[3] Ingrisch, M, et al; World Congress 2009 IFMBE Proceedings 25I: 356-358
[4] Pack, N.; DiBella, E.; Magn Reson Med. 2010;64(1):125-37.

538

Influence of the Spatial Resolution in Functional Cardiac Cine Imaging

F. Schwab[1], D. Theisen[1], F. Schwarz[1], M. Reiser[2], O. Dietrich[2]
[1]Department of Clinical Radiology, University Hospital Grosshadern, Munich/GERMANY, [2]Institute for Clinical Radiology, Ludwig-Maximilians-University Hospital Munich, Munich/GERMANY

Purpose/Introduction: Functional cardiac MRI is the current gold standard for the evaluation of parameters describing left ventricular function, such as the end-diastolic volume (EDV), the end-systolic volume (ESV) and the ejection fraction (EF). It has been found [1], that the temporal resolution for these analyses must be lower than T_{res}=50 ms, while for the spatial resolution only a limited influence was found in the analyzed range from 1-3mm². In this work, the analysis of [1] with respect to the spatial resolution is extended and the methodology is different.
Subjects and Methods: 6 healthy volunteers underwent cardiac imaging on a clinical 3 Tesla Scanner (Magnetom Verio, Siemens Healthcare) using a segmented k-space read-out cine protocol (matrix=224×168, FoV=360×270 mm², in plane res=1.6×1.6 mm², T_{res}=30.4 ms). These reference data sets are scaled down using linear interpolation to the following lower resolutions: pixel lengths ds=2, 2.5, 3, 3.5, 4, 4.5, 5, 5.5, and 6 mm, corresponding to base

matrix sizes of 180, 144, 120, 103, 90, 80, 72, 65, and 60. EDV, ESV and EF were evaluated off-line in all images using Segment [2].
Results: Quantitative results for EDV, ESV as well as EF (each normalized to the reference value obtained at the best spatial resolution) are shown in Fig. 1 as a function of the spatial resolution.

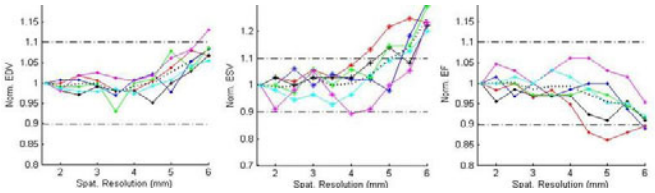

Results become unstable above 4 mm, leading to a slightly decreasing EF. At worse resolutions than 5 mm, both volumes are systematically found too high and also a smaller EF is obtained. In particular, the mean ESV is found to differ from the reference value by more than 10 % for a pixel size of 5 mm and for some volunteers at pixel sizes between 4 and 5 mm and the EF differs by 10 % for one volunteer. Table 1 demonstrates the impact of the spatial resolution on the temporal resolution obtained in clinical single-shot real-time protocol[3] (FoV=360×247 mm², GRAPPA with separate ref scan and *R*=5, TE optimized automatically).

ds(mm)	1.9	2.5	2.8	3.8	4.5
T_{res}(ms)	48.8	34.2	30.6	21.3	18.2
Matrix	192	144	128	96	80
T_E(ms)	1.37	1.28	1.24	1.19	1.17

Discussion/Conclusion: The determination of the functional parameters EDV, ESV, and EF is surprisingly robust over a large range of spatial resolutions. A spatial resolution of 4×4 mm² appears to be sufficient for an acceptable quantification; to be on the safe side, however, a spatial resolution of 3×3 mm² should be used.
References:
[1] Miller, S et al, Radiology. 2002;223(1):263-9.
[2] Heiberg, E et al, BMC Medical Imaging, 10:1.
[3] Wintersperger, B et al, Eur. Radiol. 2003;13(8):1931-6.

539

Left ventricular diastolic dysfunction in patients with the metabolic syndrome

K. Nyman[1], M. Granér[2], M.O. Pentikäinen[2], R. Sirén[3], M.S. Nieminen[2], M. Taskinen[2], N. Lundbom[1], K. Lauerma[1]
[1]Department of Radiology, HUS Radiology, HUS, Helsinki/FINLAND, [2]Department of Medicine, University of Helsinki, University of Helsinki/FINLAND, [3]Department of General Practice, University of Helsinki, University of Helsinki/FINLAND

Purpose/Introduction: Left ventricular (LV) diastolic dysfunction refers to abnormal diastolic filling of LV due to abnormal ventricular relaxation and/or increased ventricular stiffness (1). Diastolic dysfunction is encountered concomitant with preserved systolic function and ejection fraction in heart failure (2). In the early course of disease, a majority of these patients may be asymptomatic thus making this entity both a diagnostic and therapeutic challenge. Metabolic syndrome (MetS) has been shown to contribute to diastolic dysfunction in echocardiographic studies measuring trans-mitral in-flow velocities (3) or by speckle tracking (4). Cardiac magnetic resonance (CMR) studies of this subject are rather limited. Owing to its 3D nature, CMR has become the golden standard for the quantification of dynamic LV volume physiology allowing accurate analysis of the LV filling pattern. The aim of our study was to investigate the presumed association of the LV diastolic dysfunction and the MetS using CMR.
Subjects and Methods: The study subjects included 32 non-diabetic (aged 35-51 years, BMI 31.8 ± 4.5 kg/m²) males who met the IDF criteria of the MetS and 32 age-matched controls (BMI 24.0 ± 2.3 kg/m²). Patients with coronary artery disease or any known heart disease were excluded. CMR data was acquired with a 1.5T MR imager (Avanto, Siemens) followed by analysis of the LV short-axis cine series with dedicated software. LV diastolic peak filling rates (PFR) and times to PFR were obtained from the LV volume versus time curves. Student's t-test was performed to compare the mean values of the groups. P-values ≤0.05 were considered statistically significant.
Results: Subjects with the MetS had lower mean LV early diastolic PFRs (502.8 ml/s; 95% confidence interval (CI): 443.3, 562,2 ; SD ±164.9) than controls (647.8 ml/s; 95% CI: 584.6, 711.0; SD ±175.3) (p=0.001) by CMR. They also had longer time to PFR from end-systole (176.6 ms; 95% CI: 161.5, 191.2; SD ±41.2) than controls (158.2 ms; 95% CI: 147.0, 169.4; SD ±31.2) (p=0.05). LV ejection fractions did not differ between the study groups.
Discussion/Conclusion: Low LV PFR and elevated time to PFR are signs of diastolic dysfunction. Our data indicates that subjects with the MetS are at risk of developing LV diastolic dysfunction while systolic function and normal ejection fraction are still preserved. CMR analysis of the LV filling pattern may be useful to detect subclinical diastolic dysfunction in patients with the MetS.
References:
(1)Zile MR et al.:2002;Circulation:105:1387-1393.
(2)Maeder MT, Kaye DM:2009;JAmCollCardiol:53:905-918.
(3)Masugata H et al.:2006;HypertensRes:29:897-903.
(4)Orhan et al.:2010;Echocardiography:27:236-243.

540

Prognostic role of contrast-enhanced MRI of the heart in patients after transmural myocardial infarction

A.A. Bogunetsky[1], T.A. Shelkovnikova[1], V.E. Babokin[1], R.V. Aimanov[2], **W.Y. Ussov**[1]
[1]Lab. of Tomography, Institute of Cardiology, Tomsk/RUSSIAN FEDERATION, [2]Cardiac Surgery, Institute of Cardiology, Tomsk/RUSSIAN FEDERATION

Purpose/Introduction: Preoperation diagnosis of myocardial viability and of extent of postinfarction aneurismatic changes has been carried out with contrast-enhanced MRI of the heart as "gold standard". Nevertheless the vital prognosis in patients with extensive post-infarctional aneurisms usually not quantified in routine patients. Thus we tested the quantitative indexes of the contrast-enhanced MRI of the heart as possible predictors of survival in patients with severe post-infarctional left ventricular disfunction.
Subjects and Methods: Patients. 48 patients were included to the study, everybody after the extensive transmural infaction. In everybody the coronary artery bypass surgery (CABS) with LV aneurismectomy (by Dor or Menicanty) was carried out. Six persons of them died during first year after the surgery. Contrast-enhanced MRI was carried out in everybody as ECG-synchronized T1-w, T2-w , ssfp perfusion protocols and delayed enhancement scanning both in T1-w. spin-echo modes, and also as inversion recovery protocols.
In everybody the semiautimated quantitative analysis has been carried out with calculation of ventricular volumes, of extent of aneurism, thicknesses of viable and scarred myocardium and of indexes of contractility.
Discriminant inter-group analysis was applied in order to obtain a predictive function of patient's survival.
Results: The most prominent highly significant difference between survivors and non-survivors groups of patients was observed in EDVLV, in maximal thickness of viable myocardium of LV, and in extent of aneurism (Table 1).

	Survivors	Non-survivors
$EDV_{LV,}$ cm^3	165,3 s.d. 79	215,5 s.d. 49,7 p<0,05
Maximal thickness of viable myocardium, mm	14,2 ± 3,1	7 ± 1,8 p<0,05
Maximal extent of aneurism, mm	29 s.d.12	78 s.d. 23 p<0,02

Co-existance of maximal thickness of viable myocardium below 10 mm with EDV_{LV} over 165 predicted the mortality during the first year after surgical treatment (i.e. aneurismectomy with coronary bypass surgery). Also discriminant prognostic function was carried out as DF = 2,57*(Extent of aneurism, in mm) +0,78 * (EDV, in cm3). Patients with negative prognosis of post-operation survival demonstrated DF values over 310. All persons with pre-operation DF value below 310 remained alive for one year and also improved the functional class of heart insufficiency.

Discussion/Conclusion: Hencefore we conclude the quantitative analysis of contrast-enhanced MRI data in patients with previous transmural myocardial infarction and extensive LV aneurism provides quantitative prognosis of life after aneurismectomy using discriminant prognostic function. Further and more numerous analysis is in progress in order to apply probabylistic Bayesian analysis as well.

References:

Slavin M.B. Computer multiparametric analysis of medical data. Moscow. 1989

EPOS™ Poster

Contrast agents (excluding molecular and cellular imaging)

541

A study of acute brain penetration of Omniscan after blood-brain barrier disruption by ultrasound in mice

N.G. Spencer[1], B. Austen[1], E. Stride[2], F.A. Howe[3]
[1]Basic Medical Sciences, St. George's University, London/UNITED KINGDOM, [2]Institute of Biomedical Engineering, University of Oxford, Oxford/UNITED KINGDOM, [3]Clinical Sciences, St. George's University, London/UNITED KINGDOM

Purpose/Introduction: The brain penetration of magnetic resonance imaging (MRI) contrast agents in mice with an intact blood-brain barrier (BBB) can be achieved by applying ultrasound with concomitant injection of microbubbles. Global BBB disruption can be achieved using unfocused ultrasound when there is need to treat the whole brain such as in Alzheimer's disease.
Aims: To assess the early time course of delivery of an MR contrast agent to whole mouse brain.
Subjects and Methods: Two 8 month old 5xFAD Alzheimer's disease transgenic mice (Jackson Laboratories) and three, aged matched, wild-type controls were used. BBB disruption was achieved using an ultrasound transducer (Imasonic) to apply four sets of eight 10 ms 1 MHz ultrasound pulses at a nominal intensity of 4.8 W/cm^2 at the centre of the mouse brain following intravenous injections of 50 µl Optison, 20 µl Omniscan and 130 µl phosphate buffered saline. T_1-weighted gradient echo images with 20 and 45 degree flip angles were acquired 10 min post injection of Omniscan and every ten minutes up to 2 hours. Imaging parameters were 60/6.51 ms TR/TE, 4 averages, 256 x 256 matrix, 30 x 30 FOV and a 1 mm slice.
Results: BBB extravasations of Omniscan after ultrasound exposure were evident on the T_1-w images (Figure). ROIs placed in the thalamus on the T_1 maps at each time point show reduced T_1 up to 60 min post injection with an average T_1 of 746 ms (Chart). An average pre-contrast T_1 in this region of 1138 ms has been measured using the same imaging parameters. At 60 minutes post contrast, image enhancement in the brain had greatest homogeneity. There were few differences seen between transgenic and control mice in terms of the time profile of T_1 changes.

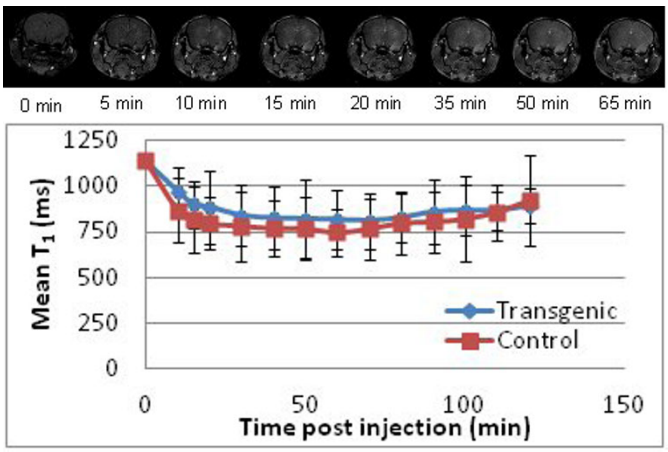

Discussion/Conclusion: Greatest BBB disruption is expected to occur immediately after the US pulses and this was represented by spots of focal contrast enhancement (CE) in the thalamus. Visually the subsequent CE was then suggestive of diffusion of Omniscan within the extracellular/extravascular space from these focal regions to the outer regions of the brain. Although global brain CE was achieved, the time course of CE was anatomical region dependent. Future experiments will evaluate these effects to enable selection of optimum parameters for global and uniform delivery of contrast agents or drugs for studies in non-focal brain disease.
We gratefully acknowledge the support of the Alzheimer's Association

542

MRI monitored USPIO-labelled intracardial cell therapy in acute myocardial infarct, imaging features with pathologic correlation in porcine model

R.M. Korpi[1], K. Alestalo[2], R. Borra[3], F. Yannopoulos[2], S. Lehtonen[4], E. Lappi-Blanco[5], V. Anttila[2], P. Lehenkari[4], T. Juvonen[2], R. Blanco Sequeiros[6]
[1]University of Oulu, Department of radiology, 90029 Oulu/FINLAND, [2]Department of Surgery, Clinical Research Center,, University of Oulu and Oulu University Hospital, Oulu/FINLAND, [3]General Hospital, A.A.. Martinos Center for Biomedical Imaging, MA/MA/UNITED STATES OF AMERICA, [4]Department of Biomedicine, Division of Anatomy and Cell Biology, University of Oulu,, Oulu/FINLAND, [5]Institute of Diagnostics, Department of Pathology, University of Oulu, Oulu/FINLAND, [6]Department of Radiology, University of Oulu, Institute of Diagnostics, Oulu/FINLAND

Purpose/Introduction: Acute myocardial infarction is the most common cause of death in western populations and has a high mortality rate.[1] In clinical and experimental settings the stem cell therapy has shown potential to improve myocardial function after infarction.[2,3] Accurate monitoring of cell homing and events related cell therapy *in vivo* is vital, and with MRI using iron nanoparticles as means to increase cellular contrast in images achievable.[4] The objective of this study was to investigate radiological-pathological correlation of cell therapy in acute myocardial infarction with MRI and super paramagnetic iron oxide (SPIO) labelled bone marrow derived mononuclear cells (BMMCs). A large animal model was used as means to stimulate the clinical situation.
Subjects and Methods: An acute myocardial infarction was induced to a swine by ligating the circumflex artery. BMMCs were labelled with SPIO and transplanted. Labelled cells were visualized *in vivo* MRI one hour after cell delivery and *ex vivo* MRI one day upon sacrificing the animal. The hearts were prepared. Cardiac tissue was stained with Prussian blue.
Results: A high spatial correlation was observed between labelled cells on MRI and histology. Corresponding to the macrosopic observation and histology, altered kinesia and abnormalities were detected in MRI at the region perfused by the circumflex artery. (Fig. 1)
Fig. 1 Localisation of labeled stem cells in infracted myocardium. (**A**) SPIO labeled MSCs in infracted myocardium in a short axis view (arrows). (**B**) SPIO labeled MSCs in infracted myocardium in a DE image. SPIO label induced area of hypointensity (arrows). (**C**) SPIO labeled MSCs in infarced myocardium in an *ex vivo* MRI image. Intramyocardial hemorrhage in the infracted area is shown hyperintence in the picture. SPIO label induced area of hypointensity (arrows). (**D**) Intramyocardial hemorrhage in macroscopic slice of pig cardiac.
Discussion/Conclusion: Cell homing can be satisfactorily monitored with a clinical MRI scanner, with clinical parameters. Imaging findings and tissue pathology show a high correlation. However, SPIO labelling potentially complicates the diagnostic evaluation of contrast enhanced MRI sequences when measuring the myocardial vitality.
[1]Yusuf S, Hawken S, Ounpuu S, *et al.* 2004 Lancet 364:937– 952. [2]Wollert KC, Meyer GP, Ltz J, *et al.* 2004 Lancet 364:141 – 148. [3]Lee RH, Pulin AA, Seo MJ, Kota DJ, *et al.* 2009 Cell Stem Cell 5:54 – 63. [4]Tallheden T, Nannmark U, Lorentzon M, *et al.* 2006 Life Sci 79:999 – 1006

543

Physiological Effect of Caffeine on Susceptibility Weighted Imaging (SWI)

A.R. Caseiro[1], P. Sousa[1], R. Manaças[2], **P.M. Gonçalves-Pereira**[2]
[1]Radiology, Higher School of Health Technology of Lisbon - ESTeSL, Lisboa/PORTUGAL, [2]Radiology dept, Hospital dos Lusíadas, Lisboa/PORTUGAL

Purpose/Introduction: Susceptibility-weighted imaging (SWI) is a relatively new contrast in MR. Previous studies have found an effect of caffeine in the contrast generated by SWI images[1]. The present study investigates the effect of caffeine on contrast-to-noise ratio (CNR) in SWI images[2]
Subjects and Methods: Twenty-four healthy volunteers (12 females, 26,54 ±3,12 years) were enrolled in the study. SWI images were acquired before and post-ingestion of 100ml of coffee (≈200mg of caffeine). All the volunteers were caffeine-free for 24h prior to the test. The volunteers were divided into groups of six and evaluated 15, 25, 30, 45 min after caffeine. High-resolution T2* 3D gradient-echo (SWI) was acquired with the following parameters: TR=49; TE=40; flip-angle=15; FOV=187x230; matrix=221x320. The caffeine effect was quantified by calculating the Contrast-to-Noise Ratio[3] [CNR=(*Sa*–*Sb*)/*Sref*], in magnitude and MIP images, whereas *Sa* corresponds to signal intensity measured by a ROI placed at the internal cerebral vein, *Sb* at the white mater of the corona radiata and *Sref* at the lateral ventricle (CSF). Image processing was performed using OsiriX[4]. Statistics were performed with GraphPad Prism.
Results: The SWI images post-caffeine showed an enhanced contrast in brain venous vasculature in all participants. Pre-caffeine CNR differed significantly from CNR measured post-caffeine in images of magnitude and MIP ($p < 0.0001$). There was no difference between groups evaluated at different times post-caffeine.

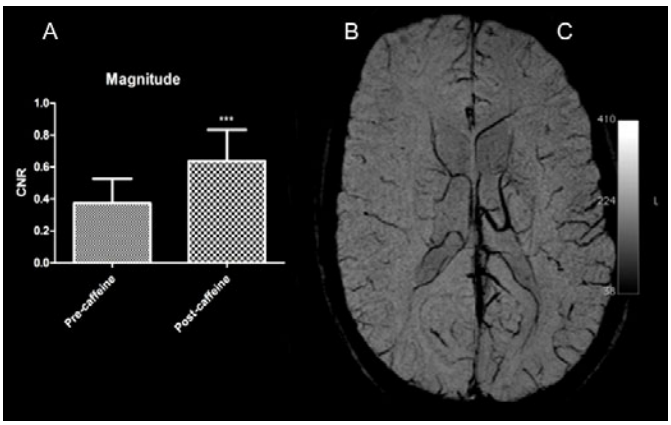

Figure: *A* – Mean and standard deviation of CNR pre and post ingestion of ≈100ml of coffee, (***,0,0001), obtained in internal cerebral vein for the entire sample (n=24) in magnitude images. *B* – Right hemisphere pre-caffeine (MIP image). *C* – Left hemisphere 15min post-caffeine (MIP) with the same window settings.

Discussion/Conclusion: There was a significant reduction of signal within the veins solely due to the effect of caffeine intake. Contrast differences pre and post-caffeine were not significant in white matter and in CSF. We speculate that caffeine can be used as a cost-effective, safe and easy to administrate contrast agent on SWI images.
Ana Rita Caseiro is a Master student at the Higher School of Health Technology of Lisbon - ESTeSL

References:

1- Chen Y and Parrish TB, *Neuroimage* 2009: 44: 647-652.
2- Gonçalves Pereira PM, Caseiro A, et al. Proceedings of the ASNR 50th Annual Meeting 2012: 484-485
3- Edelstein WA, Bottomley PA, et al. *Journal of Computer Assisted Tomography* 1983: 3: 391–401.
4- Rosset A, Spadola L et al. J Digit Imaging. 2004: 3: 205-216.

544

T_1 and T_2^* Mapping of Magnetic Nanoparticles for the Detection of Breast and Pancreatic Cancer Cells

D. Krueger[1], G. Salas[2], M. Calero[2], S. Lorrio Gonzalez[3], M.D.P. Morales[4], R. Botnar[3]
[1]Division of Imaging Sciences & Biomedical Engineering, King's College London, London/UNITED KINGDOM, [2]Facultad de Ciencias Módulo C-IX, 3ª planta, Instituto IMDEA Nanociencia, Madrid/SPAIN, [3]Division of Imaging Sciences and Biomedical Engineering, King's College London, London/UNITED KINGDOM, [4]Biomaterials and Bioinspired Materials, Instituto de Ciencia de Materiales de Madrid, Madrid/SPAIN

Purpose/Introduction: The aim of this project is to develop and validate multifunctionalised magnetic nanoparticles (MF-MNP) to selectively target and monitor delivery and treatment response of MNPs by MRI. MNPs can be used as contrast agents and magnetic heating inductors (fig 1) and can be functionalised with targeting ligands to increase their affinity towards cancer[1]. Here we sought to investigate imaging properties of MNPs and validate these in breast and pancreatic cancer cell lines.

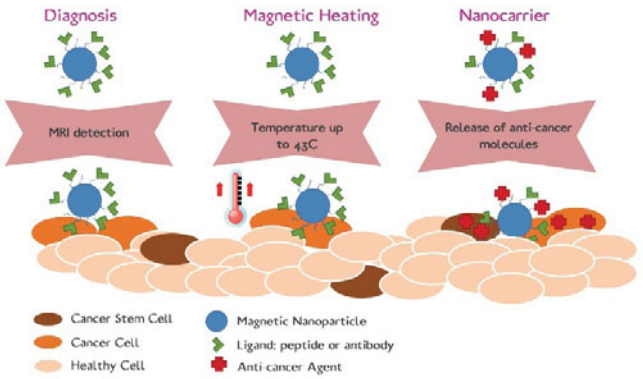

Figure 1: MNPs for theragnosis: MRI detection + multimodal therapeutic approach.

Subjects and Methods: We used a water phantom to investigate the longitudinal and transversal relaxation rates of various MNP alone and 24 hours post incubation with human pancreatic carcinoma cells (i.e. PANC-1). We used a 2D multi-gradient-echo sequence (echoes = 5, slice thickness = 3 mm, TE = 1.7 ms, TR = 11 ms, FA = 25°) to measure T_2^* and a 2D multi spin-echo sequence to measure T_2. T_1 was determined by using a sequence that employs two non-selective inversion pulses with inversion times ranging from 20 ms to 2000 ms, followed by eight segmented readouts for eight individual images.
Results: Three MNPs (ADNH, ASi and OD15) that have been synthesized in the Multifun consortium (fig 2) show excellent r_1 and r_2^* values making them promising contrast agent prototypes for both T_1 and T_2^* imaging (tab 1). We also showed that MRI can be used to monitor the dose dependent uptake of those nanoparticles (e.g. F1563) by PANC-1 cancer cells as demonstrated by T_2^* mapping (fig 3).

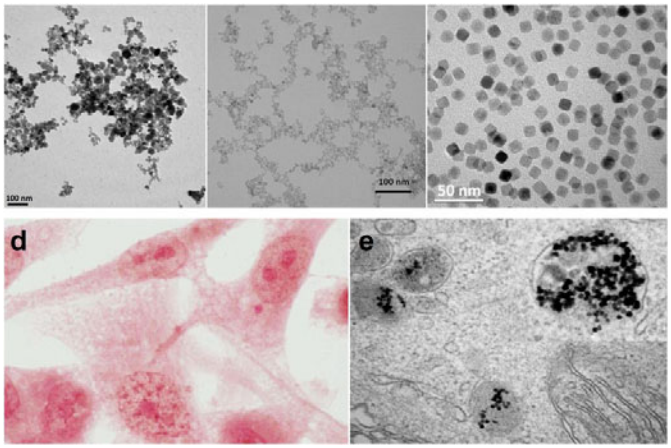

Figure 2: Transmission electron microscopy (TEM) images of a) ADNH, b) ASi and c) OD15. d) Light microscopy image of MDA-MB-231 carcinoma cells without any nanoparticles and e) TEM image after incubation with 15 nm particles (OD15).

Table 1: Promising SPIO nanoparticles

Name	Particle size TEM [nm]	Hydrodynamic size [nm]	Nature of coating	r_1 $[mM^{-1} * s^{-1}]$	r_2^* $[mM^{-1} * s^{-1}]$
ADNH	6	150	Aminodextran	10.5	743.81
ASi	8.5	60	Aminosilane	10.1	359.07
OD15	15	45	DMSA	10.1	292.74
F1563	10	1235	PEI	3.3	174.27

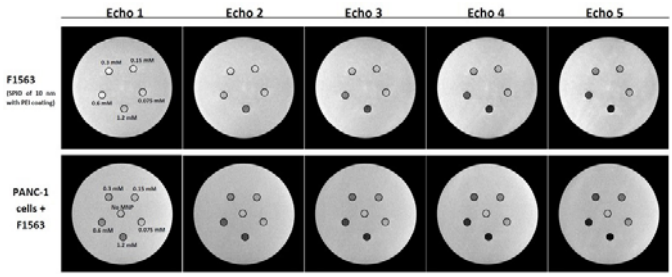

Figure 3: T_2^* weighted images acquired at 3T of five different MNP (F1563) concentrations and of pancreatic carcinoma cells after incubation with different concentrations of F1563.

Discussion/Conclusion: We demonstrate that the investigated nanoparticles have good MR imaging properties and can be used to label carcinoma cell lines. The investigated MNPs show promising imaging and labelling properties and will now be investigated in nude tumour bearing mice (BT474, MDA-MB-231, BxPc-3, PANC-1) to evaluate biodistribution, specificity and suitability for in vivo imaging and therapy.

References:

[1] Peng, X.-H., et al., 2008. *Int J of Nanomed*, 3,pp.311-21.

545

In vivo imaging of mouse pancreatic volume using manganese-enhanced MRI (MEMRI)

J. Jung[1], S. Lamprianou[2], L. Vinet[2], P. Meda[2], R. Gruetter[3], H. Lei[4]
[1]Physics, Imperial College London, London/UNITED KINGDOM, [2]PHYME, Medical School Geneva, Geneva/SWITZERLAND, [3]Department of Radiology, University of Geneva and Lausanne, Geneva Lausanne/SWITZERLAND, [4]CIBM - Centre d'Imagerie Biomédicale, EPFL - École Polytechinque Fédérale de Lausanne, Lausanne/SWITZERLAND

Purpose/Introduction: Aims of this study were to evaluate the pancreatic volume and to visualize pancreatic substructures which could lead to the development of improved, non-invasive monitoring methods for pancreatic disease models.

Subjects and Methods: All experiments were performed using a 26cm horizontal bore scanner Varian 14.1T with a quadrature surface coil (18mm inner-diameter). Male C57BL/6J mice (~30g) were anesthetized with 1.5-2% isoflurane during scanning and positioned sideways with the left side of abdomen facing upwards towards the coil. For MEMRI, animals were injected i.p. with 150µL 20% glucose, followed after 5 min by the injection of 23.5, 47, 70.5 or 94 mg/kg $MnCl_2$ (a 15 mmol/L solution in 0.9% NaCl), and continuously monitored till they featured regular breathing. To sustain a high surviving rate for this protocol, all animals were scanned 5, 7, 22 and 24h after the latter injection. T1-weighted images (TE=6ms, flip=95°, 40×0.3mm coronal slices, 78x90µm² in-plane-resolution) were acquired using a respiratory-gated multi-slice GRE sequence and the resulting TR was ~700ms. The volumes were calculated by multiplying the slice thickness by the surface area of pancreas in individual slices.

Results: Motion-free, coronal images were obtained (Fig.1), which allowed for the identification of the pancreas (red bound area in Fig2) and the surrounding spleen, kidney, liver and intestines.

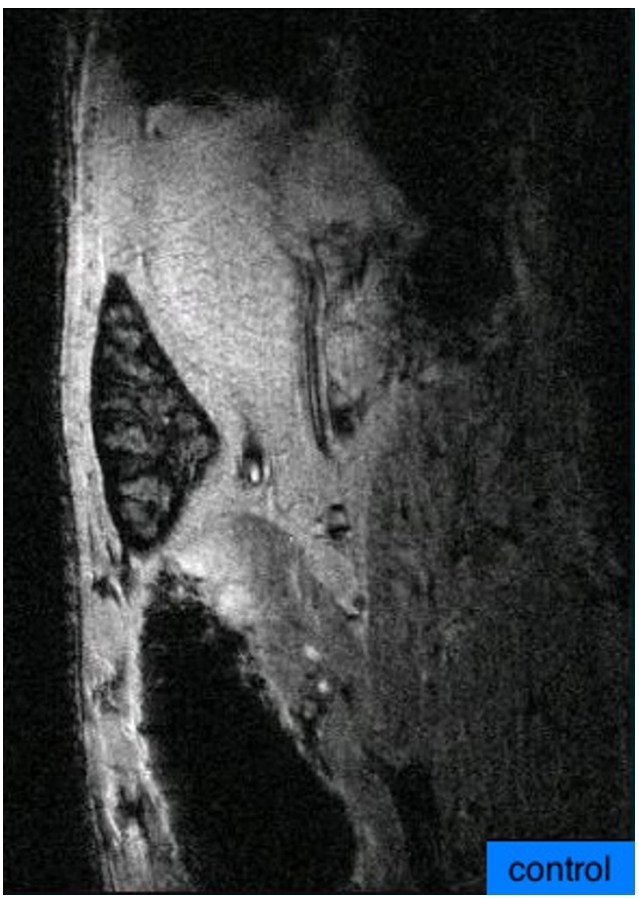

Fig.1 control without manganese.

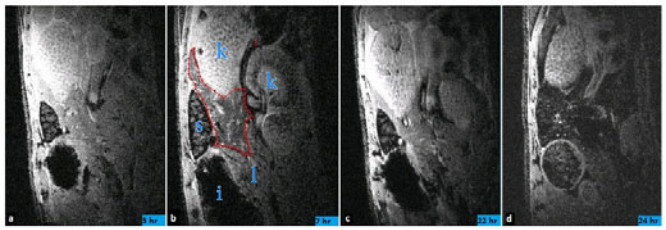

Fig.2 MEMRI at different time points after injection of various amounts of MnCl2 (a)5h, 23.5mg/kg. (b)7h, 47mg/kg. (c)22h, 70.5mg/kg (d) 24h, 94mg/kg. Pancreas = red bound area; s = spleen; k = kidney; l = liver; i = intestine.

Animal	Identified pancreas volume (mm³)		% Difference of pancreas volume after manganese injection
	Without MnCl2	With MnCl2	
1	157.8	210.4	33.3
2	91.1	151.9	66.7
3	75.7	113.4	49.7
4	81.4	133.6	64.1
Mean	101.5	152.3	53.5
STD	38.1	41.8	15.4

Fig.3 7h after manganese injection, the enhancement of MEMR images allowed us to visualize increased volumes of pancreas.

Motion-free images allowed us to visualize increased pancreas tissue volumes after MnCl2 injection (average increase 53.5±15.4%, n = 4, Fig 2b), due to the enhancement of the gland contrast which facilitated the pancreas detection as well as highlighting its substructures (Fig. 2d).

Discussion/Conclusion: MEMRI allows for longitudinal monitoring of pancreatic volume and the visualization of pancreatic substructures, in a fully non-invasive way and with minimal side effects.

References:

Lamprianou S, Immonen R, High-resolution magnetic resonance imaging quantitatively detects individual pancreatic islets. Diabetes. 2011 Nov;60(11):2853-60

Alan P. Koretsky and Afonso C. Silva, Manganese-enhanced magnetic resonance imaging (MEMRI), NMR Biomed. 2004;17:527–531

Patrick F. Antkowiak, Sarah A. Tersey, Noninvasive assessment of pancreatic b-cell function in vivo with manganese-enhanced magnetic resonance, Am J Physiol Endocrinol Metab 296:E573-E578, 2009.

546

Imaging of intracranial extra- and intraaxial tumors using non-gadolinium paramagnetic contrast agent Mn-DCTA pre-clinical and clinical study

W.Y. Ussov[1], A.I. Bezlepkin[1], M. Belyanin[2], A.A. Churin[2], V. Filimonov[2]
[1]Lab. of Tomography, Institute of Cardiology, Tomsk/RUSSIAN FEDERATION, [2]Biotechnology and organic chemistry, Tomsk Polytechnic University, Tomsk/RUSSIAN FEDERATION

Purpose/Introduction: In order to avoid risks of Gd release from paramagnetic complexes and of it's toxicity we have developed the synthesis, obtained the injection form and tested in-vivo the Manganese complex Mn-trans-1,2-Diaminocyclohexane N,N,N',N'-Tetraacetate (Mn-DCTA, Cyclomang) as possible paramagnetic agent for the contrast-enhanced MRI diagnosis of cerebral tumors. Previous toxicologic studies have shown the Mn-DCTA is an entirely non-toxic agent, with LD50 over 21 ml/KgBW (when tested as 0,5M solution), and with R1 relaxivity in saline as high as 3,68 1/(mM*s) [1].

Subjects and Methods: The in-vivo imaging has been carried out in dogs and in human subjects. In dogs: twelve animals with meningeal (ten) and glial (two) tumors were referred from a local veterinary clinics.

In twenty patients with suggested relapses of low-grade gliomas and glioblastomas and nine with newly revealed meningeal tumors were included. In patients with suggested relapses of glial tumors in eleven the relapses were verified, whereas nine remained recidive-free.

In everybody the dose of injection was kept as 2 ml of 0,5M solution per 10 Kg of BW.

T1-weighted GRE and SE protocols with TR i400 ms - 2000 ms were carried out using 1,5 T MRI scanner. To quantify the Mn-DCTA uptake the index of enhancement (IE) was calculated, as ratio of post- and precontrast intensities of T1-w SE images. In humans the blood clearance was measured also.

Results: In humans the Mn-DCTA demonstrated biexponential blood clearance with $t_{1/2}$ = 8,3 min and $t_{1/2}$ = 54 min, respectively.

The Mn-DCTA enhanced MRI of the brain in dogs with cerebral meningeomas , with IE = 1,94 s.d. 0.21 (see a typical case of enhancement of T1-w SE images of fossa olfactoria meningeoma in a shepherd's dog brain with Mn-DCTAfigure 1).

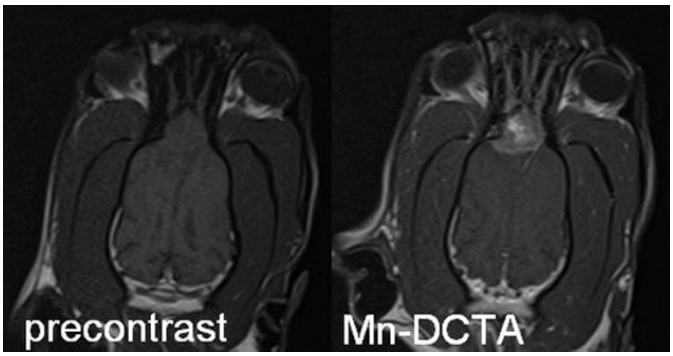

In humans the Mn-DCTA provided enhancement of both extraaxial (IE = 1,86 s.d. 0.24)and glial tumors (IE = 1,43 s.d. 0.16)(see in figure 2 a typical case of enhancement of T1-w with Mn-DCTA in relapse of low-grade glioma).

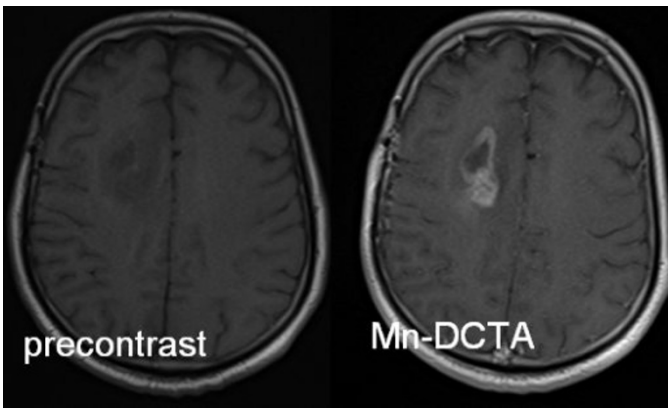

Mn-DCTA demonstrated 100% sensitivity in meningeomas both in animals and in humans. Also ten of eleven patients with relapses of gliomas were revealed, with 90% sensitivity.

Discussion/Conclusion: Hencefore Mn-DCTA can be suggested as possible paramagnetic agent for enhancement of tumors in patients with high risk of Gadolinium toxicity

References:

V.Yu. Ussov, M.L. Beljanin, A.A. Churin et al. Synthesis and Preclinical Evaluation of Mn-trans-1,2-Diaminocyclohexane N,N,N',N'-Tetraacetate (Cyclomang) as Paramagnetic Contrast Agent for Magnetic Resonance Imaging. Medical Visualization (Moscow). 2009(5). p.121-133.

547

Preclinical evaluation of GDOF-Mn-DTPA as liver specific contrast media, in rat

O.Y. Borodin[1], M. Belyanin[2], V. Ussov[1], V. Filimonov[2], E. Semichev[3], P. Bushlanov[3], M. Sannikov[4]
[1]Tomography Research Lab, Institute of Cardiology of the Siberian Branch of the Russian Academy of Medical Sciences, Tomsk/RUSSIAN FEDERATION, [2]Biotechnology and organic chemistry, Tomsk Polytechnic University, Tomsk/RUSSIAN FEDERATION, [3]Central research laboratory, Siberian State Medical University, Tomsk/RUSSIAN FEDERATION, [4]MRI facility, Siberian State Medical University, Tomsk/RUSSIAN FEDERATION

Purpose/Introduction: Liver specific contrast agents significantly increase the sensitivity and specificity of magnetic resonance imaging (MRI) in detecting hepatocellular carcinoma (HCC), improve the differential diagnosis of HCC with benign focal changes in the type of arterio-venous shunts in cirrhosis. The aims is to pre-clinical evaluation of contrasting effects of the potential liver specific contrast media GDOF-Mn-DTPA.

Subjects and Methods: The study was performed on a commercial MRI with magnetic field strength 1.5 Tesla. Technique Fast-Spin-Echo (FSE) with an inversion-recovery used to measure R1 of phantoms with known concentration of Gd-EOB-DTPA and GDOF-Mn-DTPA (2-(2-carboxymethyl-(4-hexadecyloxyphenyl-carbamoilmethyl)-aminoethyl)-aminoethyl-(4-hexadecyloxyphenyl-carbamoilmethyl)-aminoacetat acid complexonat manganese(II)) (Fig.1).

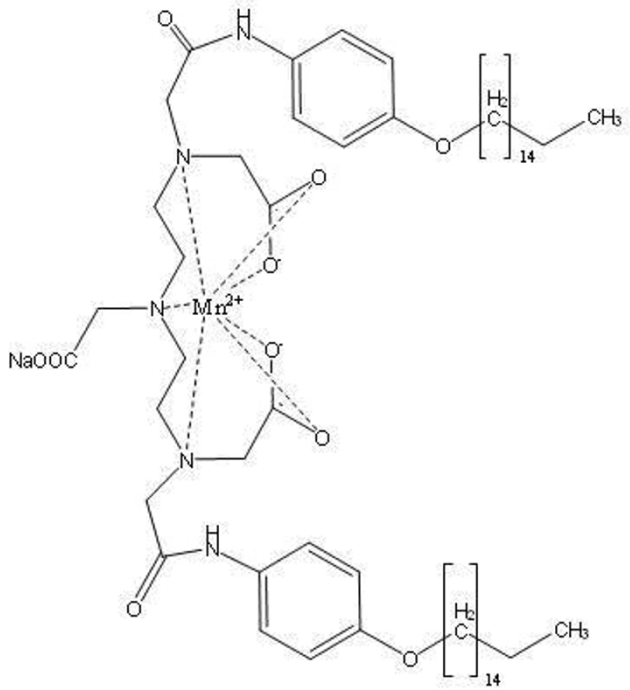

Fig.1. Chemical structure of GDOF-Mn-DTPA.

In vivo experiments involved female rats of Wistar breed. Sterile solutions GDOF-Mn-DTPA (n = 5, dose 0,025 mM/kg) and Gd-EOB-DTPA (n = 5, dose 0,025 mM/kg) were bolus injected over 2-3 seconds, at the same time performs a dynamic scanning protocol 3D FFE due to 45 minutes. The mean contrast-to-noise ratio (CNR) and standard deviation (SD) was measured every 3 minute due to 45 minutes for the liver, kidneys and heart relative to muscle tissue.

Results: According to phantom studies, the values of R1(Gd-EOB-DTPA) = 12,7 $mmol^{-1}$ s^{-1} *, R1(GDOF-Mn-DTPA) = 8,25 $mmol^{-1}$ s^{-1}. For GDOF-Mn-DTPA determined rapid increasing contrast enhancement of liver tissue to a plateau from early 5-6 minutes iv injection (Fig.2, tabl.1). All animals were living in the remote period after the study.

Table 1. Ratio contrast-to-noise due to 30 minutes for liver with Gd-EOB-DTPA and GDOF-Mn-DTPA

	Gd-EOB-DTPA		GDOF-MN-DTPA	
	M	SD	M	SD
0	6,6	6,4	18,0	3,8
3	26,2	13,1	24,5	5,1
6	33,6	12,8	24,6	4,8
9	47,9	25,3	26,9	4,9
12	47,8	25,3	25,3	5,9
15	44,1	24,3	26,2	5,3
18	31,1	16,5	27,1	5,5
21	26,7	10,6	27,5	6,4
24	25,3	13,7	25,5	5,4
27	20,8	12,7	26,8	6,4
30	20,4	12,2	27,8	5,2

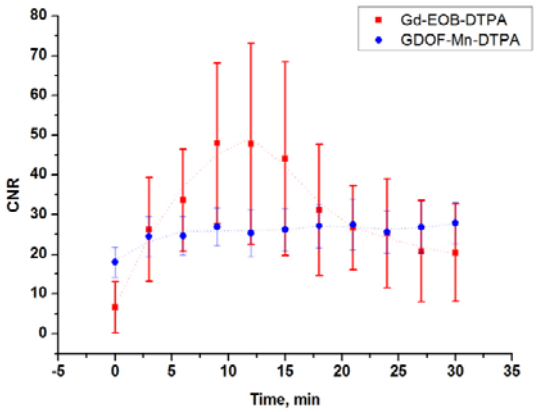

Fig.2. Contrast-to-noise ratio for liver MRI with Gd-EOB-DTPA and GDOF-Mn-DTPA. After 20 minutes output on the plateau for Gd-EOB-DTPA, in contrast to GDOF-Mn-DTPA from early 3-5 minutes.

There is no accumulation or excretion GDOF-Mn-DTPA by the kidneys (Fig.3).

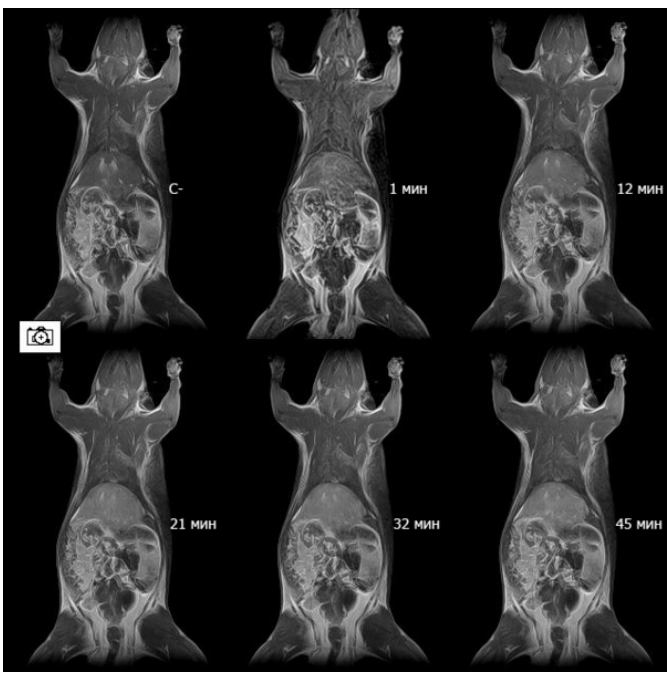

Fig.3. 3D FFE weighted images with GDOF-Mn-DTPA.

There are no contrast enhancements of the liver as compared with baseline at the next day.
Discussion/Conclusion: Macromolecular nanocolloidal compound of GDOF-Mn-DTPA is a potentional liver specific contrast media with a 100% accumulation in liver and removed from the body through the liver by metabolism. Pharmacokinetics GDOF-Mn-DTPA differs from that for Gd-EOB-DTPA .

548

In-vitro study of Gadoxetate uptake and inhibition in rat hepatocytes

L. Georgiou[1], J. Naish[1], P. Hubbard[1], J. Penny[2], N. Woodhouse[3], G. Nicholls[4]
[1]School of Cancer and Enabling Sciences, University of Manchester, Manchester/UNITED KINGDOM, [2]School of Pharmacy and Pharmaceutical Sciences, University of Manchester, Manchester/UNITED KINGDOM, [3]Biomarker Imaging Group, AstraZeneca, Macclesfield/UNITED KINGDOM, [4]DMPK, AstraZeneca, Macclesfield/UNITED KINGDOM

Purpose/Introduction:
Gadoxetate is a hepatobiliary MRI contrast agent whose uptake into hepatocytes is mediated by members of the organic anion transporter polypeptide family. There are several methods available to measure cellular uptake of compounds, which generally involve the use of radiolabelled compounds (which may not be readily available) or the use of HPLC and LC/MS (which require more extensive sample preparation). This study introduces preliminary results investigating the potential to use MRI to detect the active uptake of Gadoxetate into isolated hepatocytes in the absence and presence of a known OATP inhibitor [1,2].
Subjects and Methods: Fresh rat hepatocytes, diluted (final volume 5ml (9x106cells)) in a fresh suspension medium prepared with KH buffer, were pre-incubated at 37°C. Following pre-incubation, either Gadoxetate and Rifampicin (OATP inhibitor) or Gadoxetate alone were added to the respective suspension, incubated at 37°C for 5 minutes and centrifuged in microtubes. Six microtubes were scanned (Table1) using a RARE-T_1 sequence (TE=13.63ms, variable TR=633-6000ms, 256x128 matrix). T1 maps were generated (Figure1a) and ROIs were drawn in the top layer (incubation medium) and bottom layer (KOH, cell debris and compound taken up) of all tubes.

Table 1. Description of the samples scanned.

Tube	Incubation Compounds		Description of study
	Gadoxetate (100µM final concentration)	Rifampicin (100µM final concentration)	
A	✗	✗	Control Tube 1
B	✗	✔	Control Tube 2
C	✔	✗	Uptake study 1
D	✔	✔	Inhibition study 1
E	✔	✗	Uptake study 2
F	✔	✔	Inhibition study 2

Results: T_1 values of the bottom layer were not normally distributed due to inhomogeneities (mixture of two Gaussians) in the volume (Figure1d) and were not quantitatively analyzed. Two-sampled t-test of the top layers (Figure1c) showed statistically different mean T_1 values between inhibition and uptake studies but no difference for the control tubes (Table2).

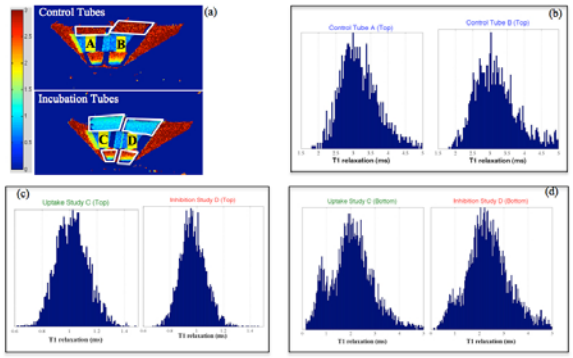

Figure 1. (a) T_1 map of sample tubes A, B, C, D (Table1). (b) Histogram of T_1 values from the top layer of control tubes. (c) Histogram of T_1 values from the top layer of incubation tubes. (d) Histogram of T_1 values from bottom layer of incubation tubes.

Table 2. Two sampled t-test on the top layer of the sample tubes.

Tube (Top Layer)	Mean	Standard Deviation	p value
A	3.1805	0.5484	0.8240
B	3.1853	0.6215	
C	1.0027	0.0879	p < 0.001
D	0.9565	0.0969	
E	1.018	0.1169	p < 0.001
F	0.9740	0.0948	

Discussion/Conclusion: Qualitative analysis of the bottom layers shows that both peaks were shifted towards lower T_1 compared to inhibition tubes, indicating an increased amount of Gadoxetate taken up by hepatocytes. The homogeneous top layer and lower mean T_1 value obtained in inhibition studies (Table2), is interpreted as more Gadoxetate remaining in the incubation medium, reflecting uptake inhibition due to Rifampicin. Two-sampled t-test demonstrates that the means of uptake and inhibition studies are significantly different, whereas the control tubes show no statistical difference.
We report a method to determine the uptake of Gadoxetate into hepatocytes, as well as inhibition of the uptake process by co-administration of Rifampicin. Future experiments aim to test variability and reproducibility between tubes, in order to quantify Gadoxetate uptake and determine the translatability of this *in-vitro* method in predicting the outcome of planned *in-vivo* and clinical studies.
References:
[1] Jessica E. van Montfoort et al. 1999. [2] Leonhardt et al. 2010.

549

Highly Fluorescent and Paramagnetic Silica Nanoparticles as Multimodal Contrast Agent: Synthesis and Characterization

E. Lipani, L. Vander Elst, R. Muller, **S. Laurent**
NMR and Molecular Imaging Laboratory, UMONS, Mons/BELGIUM

Purpose/Introduction: Silica nanoparticles are popular thanks to their interesting physico-chemical properties and because they are known to be biocompatible and not subjected to microbial attacks. They seem to be a good candidate for biomedical purposes and more precisely as contrast agents for medical imaging.
Magnetic Resonance Imaging (MRI) has become the most powerful tool and displays high spatial resolution, unlimited tissue penetration, non-ionizing and non-invasive nature. Nevertheless its sensitivity located limits certain examinations, that's why researchers are interested in combining imaging tools to overcome their limitations.
The combination of MRI with optical imaging (OI) would lead to high spatial resolution and high sensitivity analysis.
The goal of the project is to develop silica nanoparticles with a highly fluorescent core and a paramagnetic coating as a new promising multimodal contrast agent for the combination between MRI and OI.

Subjects and Methods: Silica nanoparticles were synthesized by the well-known microemulsion pathway which gives the advantage to produce uniform tunable-size nanoparticles[1]. The fluorescent core is composed of a ruthenium complex that is directly entrapped into silica shell during the nanoparticle synthesis.
Silica nanoparticles were then coated with polyethylene glycol and with a paramagnetic Gd-DTPA complex.
This new promising multimodal contrast agent was comprehensively characterize in terms of morphology, photophysical and relaxometric properties.
Results: Paramagnetic and fluorescent silica nanoparticles were successfully synthesized. TEM and DLS results are well correlated and estimate the average diameter around 23 nm.
When excited at 455 nm, the sample strongly emits in the near infrared region (around 590 nm). That makes him a good candidate for optical imaging as it avoids the autofluorescence of tissues.
NMRD profiles of paramagnetic silica nanoparticles and of the free paramagnetic complex were recorded (figure 1, table 1). The shape of NMRD profile of paramagnetic silica nanoparticles is characteristic of high molecular weight paramagnetic species and proves that the paramagnetic complex is well grafted. The relaxivity of paramagnetic silica nanoparticles is higher than the one of the small complex alone.

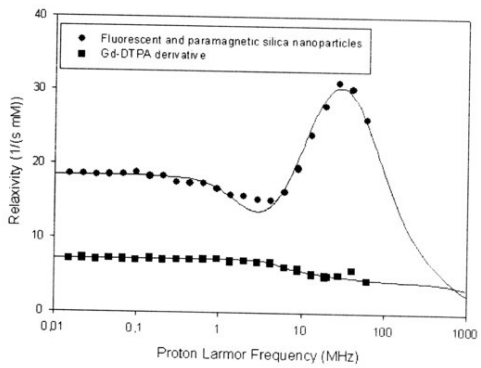

Figure 1 NMRD profiles of paramagnetic entities

Table 1 Parameters exctracted from the NMRD curves

	Free Gd-DTPA derivative	Fluorescent Paramagnetic silica nanoparticles
τ_r (ns)	0,09	$\tau_r g = 2,04$ $\tau_r l = 0,35$ $S^2 = 0,455$
τ_M (µs)	0,1	0,1
τ_{sc} (ps)	73,6	163
τ_v (ps)	31,8	44

Discussion/Conclusion: Paramagnetic fluorescent silica nanoparticles have been successfully synthesized and are a promising candidate for combined MRI/OI studies, moreover it could also find applications in computed tomography as an opaque contrast agent thanks to the ruthenium core and Gd could also be used as a radiosensitizer in neutron capture therapy. Further manipulations will consist in grafting a specific peptide for molecular imaging.
References:
[1] Y. Jin, et al. Chem. Mater., 2008, 20 (13), 4411-4419

550

MRI Characterization of Mastocytoma Rejection in Mice: a Semi-Quantitative DCE Approach

S. Boutry[1], M. Bali[2], J. Vanderlinden[3], M. Roch[1], N. Wathelet[4], G. Rahir[4], A. Hanoteau[4], Q. Zhou[3], S. Laurent[3], L. Vander Elst[3], M. Moser[4], R.N. Muller[1]
[1]University of Mons, Center for Microscopy and Molecular Imaging, Gosselies/BELGIUM, [2]Erasme Hospital-Radiology, Université Libre de Bruxelles, Brussels/BELGIUM, [3]NMR and Molecular Imaging Laboratory, University of Mons, Mons/BELGIUM, [4]Laboratory of Immunobiology, Université Libre de Bruxelles, Gosselies/BELGIUM

Purpose/Introduction: Murine mastocytoma (P815) undergoes spontaneous (immune reaction-based) rejection when subcutaneously implanted for the second time in DBA/2 mice, after cyclophosphamide treatment of the primary tumor. This rejection can be prevented by anti-CD4 antibody administration (1). A semi-quantitative approach of dynamic contrast-enhanced (DCE) MRI was set up, using a "fast diffusion" (low molecular weight) contrast agent and a "slow diffusion" (intermediate molecular weight) contrast agent, for attempting to characterize tumor vascularization in conditions of rejection and non-rejection of the tumor (2).
Subjects and Methods: MR imaging was performed on a 9.4T Biospec (94/20, Bruker, Ettlingen, Germany). Anatomic T_2-weighted RARE sequence was used to evaluate tumor volume changes. A FLASH sequence (time resolution: 2.391 s) was used for dynamic assessment of tumor enhancement in a 1-mm axial slice, after i.v. administration of Gd-based contrast agents (Dotarem (560 Da) or P846 (3.5 kDa), both from Guerbet, Aulnay-sous-Bois, France). Signal enhancement curves and semi-quantitative parameters (maximum signal (peak), time-to-peak, AUC) were obtained by ROI drawing on the tumor using PMI software 0.4 (3). Preliminary data were collected on 4 mice tumors (2 rejecting and 2 non-rejecting).
Results: Dotarem and P846 showed different enhancement features related to their trans-endothelium diffusion properties only in non-rejection conditions. The time-to-peak values were 318 s (Dotarem) vs 373 s (p846) for rejecting, and 100 s (Dotarem) vs 476 s (P846) for non-rejecting, with the latter case indicating an easier distribution for Dotarem as compared to P846. Comparing rejecting-tumor and non-rejecting-tumor with comparable peak values and volumes, a higher time-to-peak value for Dotarem was observed for the rejected-tumor (~600s vs 100s), also suggesting a more difficult distribution of the contrast agent in tumor tissue under rejection conditions.
Discussion/Conclusion: In mastocytoma spontaneous tumor rejection model, preliminary data obtained with semi-quantitative DCE-MRI suggested that decrease ("normalization") of vessel permeability might occur in tumors undergoing rejection. These findings will be further investigated.
References:
1. V. Flamand et al., Immune surveillance: both CD3+ CD4+ and CD3+ CD8+ T cells control in vivo growth of P815 mastocytoma, Int J Cancer. 45(4):757-762, 1990
2. B. Lemasson et al., Monitoring blood-brain barrier status in a rat model of glioma receiving therapy: dual injection of low-molecular-weight and macromolecular MR contrast media, Radiology. 257(2):342-352, 2010
3. S.P. Sourbron et al., MRI-measurement of perfusion and glomerular filtration in the human kidney with a separable compartment model, Invest Radiol. 43(1):40-48, 2008

551

MRI contrast agent for CD34+ stem cell isolation and post-transplantation monitoring

H.M. Huang[1], **H.W. Tseng**, Y.S. Lin[1], W.Y. Hsieh[1], S.J. Wang[2], W.C. Shyu[3], C.H. Lin[3], H. Shen[1]
[1]Biomedical Technology and Device Research Laboratories, Industrial technology research institute, Chutung, Hsinchu/TAIWAN, [2]Material and Chemical Research Laboratories, Industrial technology research institute, Chutung, Hsinchu/TAIWAN, [3]China Medical University, Graduate Institute of Immunology, Taichung/TAIWAN

Purpose/Introduction: Cell based therapeutics face an important issue in monitoring cell localization to ensure cell homing at the desired region in vivo. This is important because the distribution of transplanted cells strongly correlates with the effectiveness and safety [1-2]. Due to this reason, we developed a contrast agent "iron oxide material" with high relaxivity. The ion oxide contrast agent was also conjugated with antibodies to have specific CD34+ cell binding ability. The ion oxide-antibody complexes are used to isolate CD34+ cells in vitro from either cell solutions or cord blood by elutined from a sorting device. In the animal model, the purified cells were transplant into rat brains. The MRI and histochemistry analysis indicated the nanoparticles bond to selected cells and can be traced in living organisms.
Subjects and Methods: New MRI contrast agent was made in four steps: (1) Coprecipitation of iron oxide and dispersed nanoparticles in oleic acid; (2) carboxylated functional PEG-silane (simple type and mixed type PEG) were prepared; (3) the PEG-silane were made to react with the IO respectively; and then (4) the material was activated by EDC/NHS and conjugated with anti-CD34 antibody to obtain the final product.
Results: In this investigation, we conjugated either secondary antibody (Alexa594 IgG) or primary antibody (CD34+ antibody) onto the IOP individually. The photos of fluorescence electrophoresis of the contrast agent revealed the conjugation process was accomplished. The physical properties of the contrast agent were also measured: the core size is between 8~15nm and the hydrodynamic diameter is in the order of 50~150nm depending on the coating polymer types. Preliminary study show that over 95% KG1a CD34+ cell can bind to optimal IOP-antibody batch. Further cell isolation experiment indicated IOP-My10 can effectively bind to KG1a CD34+ cell in mixed PBMC cell solution, and more than $3*10^6$ of CD34+ cells can be purified by sorting tube with strong magnetic field. Moreover, MRI in animal model indicated that the nanoparticles remain in living organisms for at least 4 weeks after cell transplantation. The results indicate that the IOP-antibody still bind to the target cell tightly and remain in the injection location.
Discussion/Conclusion: The contrast agent has the ability for CD34+ cell isolation, enrichment and cell tracing in patients. The study reveals the potential of the contrast agent for further cell therapy application.
References:
1. Philippe et al. , *Investigative Radiology* (2006) 41, No.3, March
2. Peter Reimer, Thomas Balzer, *Eur Radiol* (2003) 13:1266–1276

552

In vivo relaxivities for gadodiamide in blood and cerebral tissue in pig

A. Morell[1], F. Lennmyr[2], O. Jonsson[2], T. Tovedal[2], J. Pettersson[3], J. Bergquist[3], V. Zemgulis[2], G. Myrdal[2], S. Thelin[2], H. Ahlström[1], A. Bjornerud[4]
[1]Radiology, Uppsala University, Uppsala/SWEDEN, [2]Surgical sciences, Uppsala University, Uppsala/SWEDEN, [3]Analytical chemistry, Uppsala university, Uppsala/SWEDEN, [4]Physics, Oslo University, Oslo/NORWAY

Purpose/Introduction: Perfusion assessment by monitoring the transport of a tracer bolus depends on correct conversion of signal intensity variation into corresponding tracer concentration [1]. One of the main assumptions in MRI applications of the first pass method is that the contrast agent relaxivity is identical in blood and tissue [2, 3]. The purpose of this study was to investigate the validity of this assumption.
Subjects and Methods: Blood and cerebral tissue relaxivities r1, r2 and r2* for gadodiamide were measured at steady state blood concentration levels up to 20-30 mM in four pigs at cardio pulmonary bypass at 1.5T. Regions of gray- and white matter (GM, WM) were defined by thresholding in baseline T1 maps and the sagittal sinus was used for the blood measurements. The gadolinium concentration levels in blood were determined by inductively coupled plasma atomic emission spectroscopy. Tissue relaxivities with respect to tissue concentration was estimated by assuming tissue blood volume fractions of 4% and 2% for GM and WM respectively.
Results: In vivo relaxivities ($s^{-1}mM^{-1}$) for GM, WM and blood are presented in Fig 1. Tissue relaxivities differed significantly from blood relaxivity for all three relaxivity parameters.

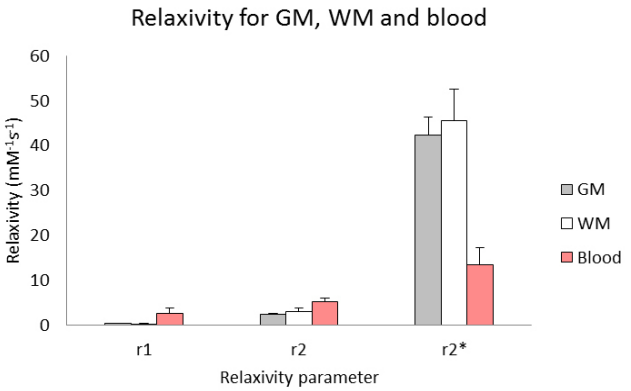

Discussion/Conclusion: The observed r1 response seem low but the r2* measurements are in good agreement with previously published values by van Osch [4] and Kjølby [5], see Fig 2. The ratio between blood and tissue relaxivity is not unity and not independent of relaxation mechanism. There is in particular a very substantial difference in the blood to tissue relaxivity relation in T1-based versus T2*-based analysis. When striving for truly quantitative perfusion measurements using tracer based MRI techniques, these differences must be taken into consideration.

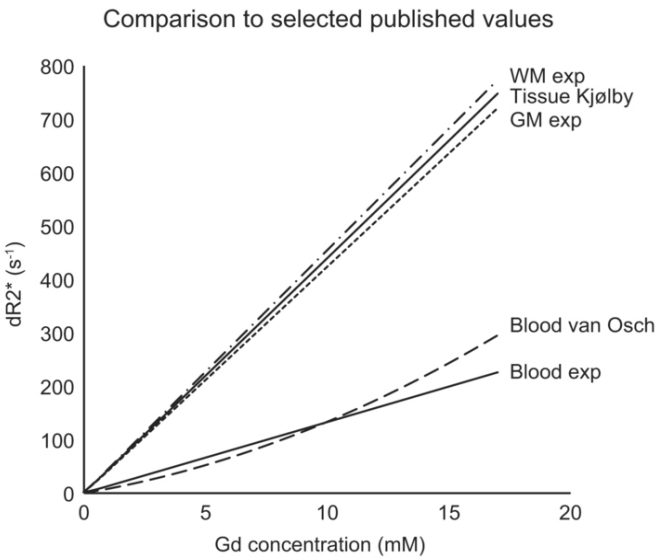

References:
1. Kiselev, V., 2005, J Magn Reson Imaging, 22:693-696
2. Gückel, F., 1994, J Comput Assist Tomogr, 18:344-351
3. Rempp, K., 1994, Radiology, 193:637-641
4. van Osch, M., 2003, Magn Reson Med, 49:1067-1076
5. Kjølby, B., 2006, Magn Reson Med, 56:187-197

EPOS™ Poster

Diffusion

553

Towards optimization of diffusion kurtosis imaging to study brain changes with age

R. Neto Henriques[1], M. Morgado Correia[2], C.A. Cam-Can[3]
[1]Faculty of Sciences of the University of Lisbon, Institute of Biophysics and Biomedical Engineering, Lisboa/PORTUGAL, [2]Medical Research Council, Cognition and Brain Sciences Unit, Cambridge/UNITED KINGDOM, [3]Biotechnology and Biological Sciences Research Council, Cambridge Centre for Ageing and Neuroscience, Cambridge/UNITED KINGDOM

Purpose/Introduction: Diffusion kurtosis imaging (DKI) is an extension of diffusion tensor imaging (DTI), which provides an estimate of microstructural barrier complexity in addition to the diffusion tensor[1]. However, DKI is more sensitive to noise, motion and image artefacts than DTI. Our main goal is to optimize the DKI pipeline to provide reliable measures for the large collaborative aging project, the CamCAN (Cambridge Centre for Ageing and Neuroscience). In this study, we will compare different fitting methods to extract the quantitative parameters for DKI. Secondly, the optimal value of FWHM of the Gaussian kernel used to reduce the impact of noise and image artefacts[2] on the diffusion weighted (DW) images is investigated.
Subjects and Methods: Ordinary linear squares (OLS), weighted linear squares (WLS), non-linear squares (NLS), constrained linear squares[3] (CLS) and a newly proposed method, direct linear squares (DLS), for directly fitting the values of mean kurtosis (MK) and mean diffusivity (MD), are tested on simulated data corrupted with different levels of Rician noise. In addition, the methods are tested on real data for two groups of subjects: 14 young adults (mean 26.2, sd 3.9) and 14 middle aged adults (mean 53.4, sd 2.0). DW-images were acquired on a 3T Siemens Trio and filtered with different Gaussian kernel sizes to access the optimal value of FWHM, defined as the one which is more sensitive to the age changes between the two age groups. Both synthetic and real data were based on 63 DW-images (3 for b-value 0, and 30 direction for b-values 1000 and 2000s/mm²).
Results: OLS, WLS and NLS fits underestimate the values of kurtosis, while CLS overestimates them (Figure 1).

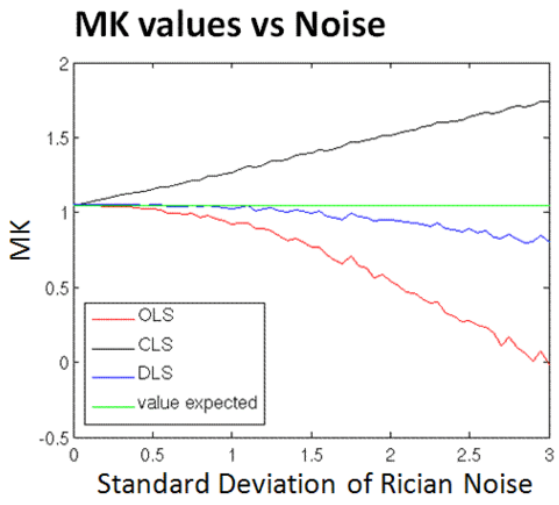

Fig.1 Mean MK values extracted from simulated data using OLS, DLS and CLS. The WLS and NLS method (not shown in figure) had the same behaviour as OLS.

By smoothing the DW-images, the Gaussian kernel seems to reduce noise effects and consequently the artefacts of underestimation or overestimation of MK are reduced for all different fitting methods (Figure 2).

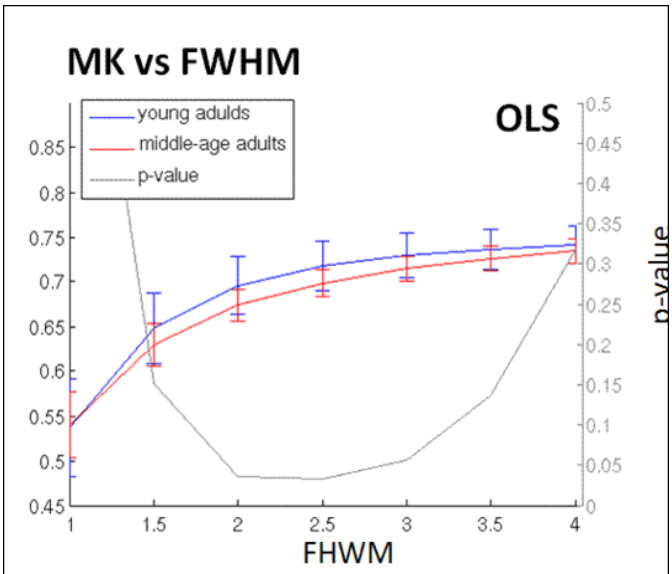

Fig.2 Performance of the Gaussian filter on real data. This example corresponds to gray matter values of the prefrontal brain. MK values in this figure were extracted using the OLS method.

Discussion/Conclusion: Our results using simulated data suggest that DLS is the most robust fitting method since it provides MK values that are less sensitive to increasing noise levels. For our data, we found that a kernel with FWHM of 2.5 mm provides a good compromise between accuracy of measures and resolution. Consequently, data filtered with this kernel is more sensitive to differences between the two age groups.
References:
1. Lu H et al., 2006, NMR Biomed, 19(2): 236-247 **2.** Jones DK & Cercignami M, 2010, NMR Biomed, 23(7): 803-820 **3.** Tabesh A et al., 2011, Magn Reson Med, 65(3):823-836

554

The influence of frontal glutathione levels on white matter connectivity in healthy and early psychosis subjects: a preliminary study

A. Griffa[1], P. Baumann[2], L. Xin[3], S. Crespi[2], C. Ferrari[4], R. Mekle[5], R. Gruetter[6], J. Thiran[1], K.Q. Do[4], P. Conus[2], **P. Hagmann**[7]
[1]Signal Processing Laboratory (LTS5), Ecole Polytechnique Fédérale de Lausanne (EPFL), Lausanne/SWITZERLAND, [2]Department of Psychiatry, Lausanne University Hospital (CHUV), Prilly - Lausanne/SWITZERLAND, [3]Laboratory for Functional and Metabolic Imaging, Ecole Polytechnique Fédérale de Lausanne, Lausanne/SWITZERLAND, [4]Center for Psychiatric Neuroscience, Lausanne University Hospital (CHUV) and University of Lausanne, Prilly - Lausanne/SWITZERLAND, [5]Medical Physics, Physikalisch-Technische Bundesanstalt, Berlin/GERMANY, [6]EPFL-SB-IPSB-LIFMET, Functional and Metabolic Imaging Laboratory, Lausanne/SWITZERLAND, [7]Department of Radiology, Lausanne University Hospital (CHUV) and University of Lausanne, Lausanne/SWITZERLAND

Purpose/Introduction: Schizophrenia is a brain disorder involving faulty connectivity, and developmental redox-dysregulation leading to oxidative stress and myelination impairment [1]. A decrease in prefrontal glutathione levels ([GSH]), a major antioxidant, has been observed in patients with schizophrenia [2].

The combination of diffusion imaging, tractography and graph analysis is emerging as powerful instrument for the characterization of the human connectome, in health and disease. These methods allow the investigation of white matter connectivity through tract-based analysis, and global network measures able to quantify the whole brain efficiency of information transfer [3].
Here we investigate the relationship between prefrontal [GSH] measured with magnetic resonance spectroscopy (MRS), and white matter connectivity measures, in healthy and early psychosis (EP) subjects.
Subjects and Methods: 18 EP subjects (13M/5F) (25.4 yo+/-5.6) and 19 age and gender matched healthy controls (14M/5F) (23.9+/-3.7) underwent an MR session composed by MRS, high-resolution T1w imaging, and diffusion spectrum imaging (DSIq4, b8000 s/mm^2).
An anatomical connectivity matrix was generated for each subject, combining segmentation of brain tissues, subdivision of cortical and subcortical volumes into 83 anatomical regions, and streamline tractography on DSIq4 data [4]. Each connection was weighted by the mean generalized fractional anisotropy (gFA) value along the tract. The gFA is an indicator of anisotropy of the local diffusion profile, and is therefore linked to fibers myelination status and efficiency of information transfer. A graph was derived from each connectivity matrix, and global network measures were computed.
The frontal GSH levels were correlated with the average gFA values along the cingulate tract (given the anatomical proximity of this tract with the MRS measurement) and with global network metrics.
Results: We found in healthy subjects positive correlation of [GSH] with gFA values along the cingular tract (right r=0.59,p=0.008; left r=0.74,p=0.0003); with network efficiency (r=0.50,p=0.03), global strength (r=0.49,p=0.03), clustering coefficient (r=0.52,p=0.02); negative correlation with network characteristic path length (r=-0.50,p=0.02). No correlation was found in patients.
Discussion/Conclusion: Frontal [GSH] is positively associated with gFA, and with higher global efficiency of the connectome, as indicated by measures of both integration and segregation. These results suggest that GSH is involved in the normal development of white matter tracts and highlight the role of cingular region in schizophrenia physiopathology. The absence of this correlation in EP subjects deserves further investigations.
References:
[1] Do, K.Q. et al., 2009, CurrOpinNeurobiol, 220-230
[2] Do, K.Q. et al., 2000, EurJNeurosci., 3721-3728
[3] Bullmore, E.T. et al., 2011, AnnuRevClinPsycho, 113-140
[4] Hagmann, P. et al., 2010, JNeurosciMeth, 34-45

555

Investigation of phase and diffusion tensor imaging correlations at ultra-high magnetic field

Y. Van De Looij[1], N. Kunz[2], R. Maddage[2], P. Hüppi[1], R. Gruetter[3], S. Sizonenko[1]
[1]Division of Child Growth & Development, University of Geneva, Geneva/SWITZERLAND, [2]EPFL-SB-IPSB-LIFMET, Functional and Metabolic Imaging Laboratory, Lausanne/SWITZERLAND, [3]Department of Radiology, University of Geneva and Lausanne, Geneva Lausanne/SWITZERLAND

Purpose/Introduction: Diffusion Tensor Imaging (DTI) and Phase Imaging (PI) are two MR techniques used to probe brain microstructure. DTI gives useful white matter information such as fiber direction and integrity. The phase of gradient echo images has been used to create anatomical images with excellent grey/white matter contrast [1]. Even if the contrast mechanisms of these two techniques are different (i.e. spin mobility for DTI *vs.* signal phase variation for PI), several similarities such as an influence of myelin and fiber orientation have been shown [1,2]. The aim of this work was to investigate the potential correlations between DTI and PI in the rat brain at 9.4T.
Subjects and Methods: MR experiments were performed on an actively-shielded 9.4T/31cm magnet (Varian/Magnex) with a quadrature transceive 20-mm surface RF coil. For each rat (n=6), DTI acquisitions were performed using a semi-adiabatic double spin-echo sequence [3] (FOV=23×15mm^2, matrix size=128×64, 9 axial slices 0.8mm thick, 8 averages, TE/TR=42/2000 ms, 21 directions and b=1000s.mm^{-2}). Gradient-echo images were acquired (TE/TR=18/900ms; SW=30KHz, FOV=23×15mm^2, Matrix size=512×340, 18 slices 0.4 mm thick and 8 averages). To remove the effect of large-scale phase shifts across the phase images, a 2D Gaussian high-pass filter was applied (kernel size: 121voxels, width: 10 voxels) [1].
Results:

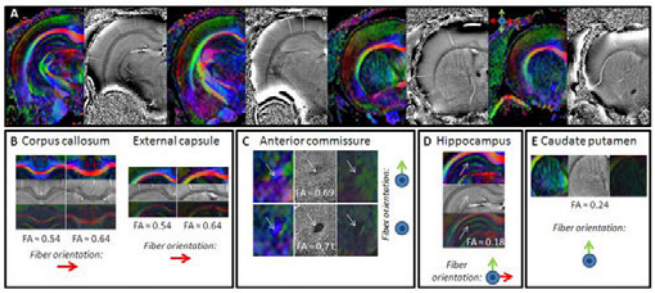

Figure 1: A: Typical DT color maps and phase images at four different image-planes. B-E: color maps, phase images and eigenvectors zoomed on different regions of interest: corpus callosum and external capsule (B), anterior commissure (C), hippocampus (D) and caudate putamen (E). Below each zoom is displayed the FA and the direction of the fibers in the corresponding region. In highly anisotropic regions such as corpus callosum (B), the phase contrast is different as a function of the anisotropy degree whereas in anterior commissure the contrast changes with the fiber orientation (higher contrast in the anterior part corresponding to marked anteroposterior fiber orientation). In myelinated regions with very low FA such as hippocampal layers (D, arrows) the contrast is very low on phase images whereas in caudate-putamen (E) with a mix of fiber directions (up-down and antero-posterior) the contrast seems predominantly related to the up-down fibers.

In the corpus callosum, the phase contrast changes as a function of the FA (Fig.1B). The frequency shift between white and grey matter in this region was inversely correlated ($p<0.05$) with the FA (r=-0.32) and the axial diffusivity (r=-0.54). This suggests a possible effect of the axonal compaction in white matter on the phase contrast. In the anterior commissure (Fig.1C), the highest contrast was observed at the anterior part corresponding to an area with a marked anteroposterior fiber orientation (dark blue on color maps), confirming the known effect of the fiber orientation. In myelinated regions with low FA such as the hippocampal layers (Fig.1D, arrows), contrast between white and grey matter on phase images was extremely low whereas the different layers were visible on color maps.
Discussion/Conclusion: To conclude we show for the first time a correlation between DTI derived parameters and frequency shift of phase images. Further experiments are in progress to quantify more accurately these results by an assessment of the correlations between DTI and susceptibility maps.
References:
[1]Marques JP. Neuroimage2009; [2]Lodygensky G. Neuroimage2011 [3]van de Looij Y. MRM2011;
Supported by the SNF-N°31003A-135581, the CIBM of UNIL, UNIGE, HUG, CHUV, EPFL, Leenards-Jeantet foundation.

556

Extensive follow-up of biexponential diffusion coefficients in ischemic rat brain

M. Pitkonen[1], U. Abo-Ramadan[2], I. Marinkovic[2], D. Strbian[2], A. Durukan[1], T. Tatlisumak[1]
[1]Experimental MRI Laboratory, Biomedicum Helsinki, Helsinki/FINLAND, [2]Dept of Neurology, Helsinki University Central Hospital, Helsinki/FINLAND

Purpose/Introduction: In clinical practice, two to three measurements of signal intensity with different b-values are collected for apparent diffusion coefficient (ADC) calculation. ADC result is further founded on the hypothesis of monoexponential signal intensity decay. It has been reported that the signal intensity of brain water shows non-monoexponential decay when measured over an extended b-value range (1-3). Further, two separate diffusion coefficients and the volume fractions of those pools may be detected (4-5). (6). Herein, we investigated the long-term evolution of the biexponential brain diffusion signal decay parameters (fast and slow apparent diffusion coefficient ADC_f and ADC_s and fast and slow fraction f_{fast} and f_{slow}) post permanent middle cerebral artery occlusion (pMCAO) in rats over the period from hyperacute to chronic phase of ischemia.
Subjects and Methods: Wistar rats (n = 9) were subjected to focal cerebral ischemia by permanent suture MCAO (7). They were imaged at 2 and 3.5 hours, 1, 2, 3, and 4 days, 1, 2, 4, 6, and 8 weeks. Sham-operated rats were

used as healthy controls (n = 8). The MRI measurements were performed with a 4.7 T MR Scanner (PharmaScan, Bruker BioSpin, Germany). Diffusion measurements were acquired from multi-shot spin-echo echo-planar image (EPI) with 3 directions (x, y, z) and 31 b values from 0 to 6000 s/mm². Data were analyzed with two-compartment (biexponential) model that accounted for exchange between two diffusion compartments. For comparison we calculated monoexponential ADC curves.

Results: The plots in Figure 1 depict characteristic diffusion attenuation curves post pMCAO. ADC_f is more sensitivity compared to ADC_s in characterizing ischemic tissue phases. ADC originates mainly from ADC_f. In the hyperacute phase, there is massive increase in the slow fraction of diffusion, which reduces over the 8 weeks period, whereas f_{fast} has an opposite trend (Table 1.)

Table 1. Evolution of slow (f_{slow}) and fast (f_{fast}) fractions post permanent MCAO in cortex, subcortex, and corpus callosus. Normal is enhanced with blue.

f_{slow}	normal	2h	3.5h	1d	2d	3d	4d	1w	2w	4w	6w	8w
cortex	7,1	43,8	46,5	38,8	31,6	28,8	31,7	34,4	38,1	23,2	22,3	25,7
subcortex	8,9	45,0	54,7	43,7	39,1	40,4	50,1	52,8	42,3	33,3	31,5	25,4
corpus callosum	14,0	42,8	53,3	46,3	40,9	37,3	45,0	47,8	36,6	30,0	32,3	28,0

f_{fast}	normal	2h	3.5h	1d	2d	3d	4d	1w	2w	4w	6w	8w
cortex	77,3	56,2	53,5	61,2	68,4	71,2	68,3	65,6	61,9	76,8	77,7	74,3
subcortex	69,7	55,0	45,3	56,3	60,9	59,6	49,9	47,2	57,7	66,7	68,5	74,6
corpus callosum	72,3	57,2	46,7	53,7	59,1	62,7	55,0	52,2	63,4	70,0	67,7	72,0

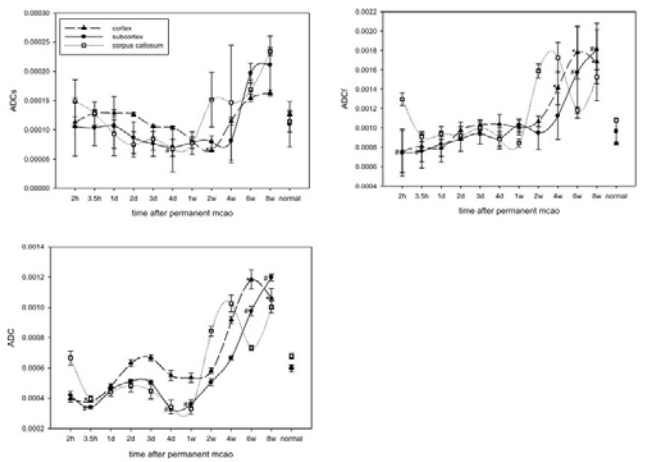

Figure 1. Temporal evolution of diffusion multicomponent parameters; up: ADC$_s$ (x10 mm²/s) (left), ADC$_f$ (x10 mm²/s) (right), and down: ADC (x10 mm²/s), within the cortex, subcortex, and corpus callosum, following permanent MCAO. Each point represents the mean in the region of interests (n = 9). Time points with values that differ significantly from that of the normal are marked in the cortex (*), subcortex (#), and corpus callosum (**) (p < 0.05).

Discussion/Conclusion: Our work showed that biexponential analysis give information about water compartments post ischemia but the link to cellular damage should be further discussed.

References:

(1) Niendorf et al, 1996, MRM 36:847-857
(2) Brugieres et al, 2004, AJNR Am J Neuroradiol 25:692–698
(3) Assaf & Cohen, 1998, J. Magn. Reson. 131, 69–85
(4) Clark & Le Bihan, 2000, Magn. Reson. Med. 44, 852–859
(5) Le Bihan, 2006, Proc.Nat. Acad. Sci. 103, 8263–8268
(6) Baird & Warach, 2000, J. Cereb. Blood Flow Metab. 18, 583–609
(7) Koizumi et al., 1986, Jpn J Stroke. 8:1-8

557

Tract-Based Spatial Statistical analysis of diffusion tensor imaging in patients with relapsing-remitting multiple sclerosis

I. Ibrahim[1], A. Skoch[2], J. Tintera[1], K. Rasova[3]
[1]MR Unit, Department of Diagnostic and Interventional Radiology, Institute for Clinical and, IKEM, Prague/CZECH REPUBLIC, [2]MR-Unit, Department of Diagnostic and Interventional Radiology, Institute for Clinical and Experimental Medicine, Prague/CZECH REPUBLIC, [3]Department of Rehabilitation, 3rd Faculty of Medicine, Charles University in Prague and Faculty Hospital Královské Vinohrady, Prague 10/CZECH REPUBLIC

Purpose/Introduction: Multiple sclerosis (MS)-related pathological changes can modify the integrity of white matter (WM) bundles, leading to diffusion tensor imaging (DTI)-detectable changes. The aim of the study was to assess microstructural changes in white matter using Tract-Based Spatial Statistical (TBSS) analysis of DTI in patients with relapsing-remitting multiple sclerosis (RRMS) (1-2).

Subjects and Methods: Eleven patients (43.27 ± 9.28) with RRMS and 11 age-matched healthy controls (39.45 ± 12.2) underwent MRI examination on a 3T Siemens Trio scanner using diffusion spin-echo echo-planar imaging in 20 directions. Data was analyzed using TBSS tool of FSL for voxelwise analysis of multi-subject diffusion data (http://www.fmrib.ox.ac.uk/fsl/fsl/whatsnew.html). JHU DTI-based white matter atlas was used to parcelate voxels with significantly reduced FA into specific antomic white matter to regions (3). Together with DTI examination, Paced Auditory Serial Addition Test (PASAT) and Expanded Disability Status Scale (EDSS) were also measured to assess cognitive functions and impairment in patients (4-5).

Results: TBSS analysis of patients with MS showed reduction of anisotropy (FA) compared to controls in a number of brain regions, including the corpus callosum, optic radiations, fornix, cingulum, the superior longitudinal fasciculus and internal capsule in both hemispheres. *p* values <0.05 were considered statistically significant. The PASAT mean score was lower in MS (43.0 ± 13.66) compared to controls (51.40 ± 9.22), however, the differences were not statistically significant (p = 0.23). The EDSS mean score in patients was 3.50 ± 0.80. In patients, no correlation was observed between reduction of the FA values and EDSS or PASAT scores. **Figure 1** shows clusters in regions with reduced FA in patients compared to controls (TBSS findings).

Fig. 1. TBSS findings

Locations	Cluster size (voxels)	Patients with MS (FA)	Controls (FA)
Optic radiation - L	11605	0.48	0.59
Optic radiation - R	11792	0.49	0.60
Genu of CC	12045	0.64	0.71
Body of CC	23408	0.62	0.69
Splenium	16027	0.68	0.75
Anterior limb of internal capsule - L	3784	0.54	0.60
Anterior limb of internal capsule - R	4224	0.56	0.61
Posterior limb of internal capsule - R	440	0.66	0.69
Posterior limb of internal capsule - L	198	0.47	0.52
Cingulum - L	1155	0.47	0.56
Cingulum R	1199	0.46	0.52
Fornix	1375	0.31	0.45
Superior longitudinal fasciculus - L	3529	0.45	0.52
Superior longitudinal fasciculus - R	3773	0.48	0.54

Fig. 1. Regions of significantly reduced FA values in patients with MS compared to control subjects (p < 0.05). FA: fractional anisotropy. L: left. R: right. CC: corpus callosum

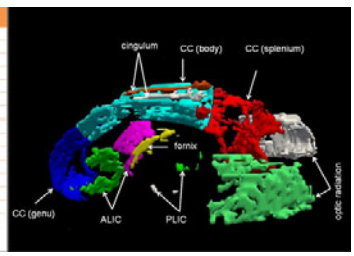

Discussion/Conclusion: The results of the study show that the integrity of white matter in patients is broken in a number of brain regions. Reduced FA in patients did not correlate with PASAT or EDSS in any of the mentioned-above areas.

References:

- Smith SM. et. Neuroimage 2006 Jul 15;31(4):1487-505.
- Ibrahim I. et al. Neuroradiology 2011 Nov;53(11):917-26.
- Morris LC. Demos, New York 2000, pp 236–290.
- Kurtzke JF. Neurology 1983, 33:1444–1452.
- Mori S et al. Neuroimage. 2008 Apr 1;40(2):570-82.

This study was supported by Institutional grant **00023001 IKEM,** and IGA **1A/8628-5**, Ministry of Health**, Czech Republic.**

558

FREBAS Transform for q-Space Compressed Sensing in Accelerated Diffusion Spectrum Imaging

J.I. Sperl[1], E.T. Tan[2], M.I. Menzel[1], K.F. King[3], C.J. Hardy[2], L. Marinelli[2]
[1]Diagnostics & Biomedical Technologies Europe, GE Global Reseach, Garching n. Munich/GERMANY, [2]MRI Laboratory, GE Global Reseach, Niskayuna/NY/UNITED STATES OF AMERICA, [3]MR Physics, GE Healthcare, Waukesha/WI/UNITED STATES OF AMERICA

Purpose/Introduction: Diffusion spectrum imaging (DSI)[1], in which the diffusion encoding space (*q-space*) is Nyquist sampled, allows for resolving crossing fiber tracts in the brain or characterizing diffusional kurtosis[2]. To overcome its long acquisition times, q-space can be randomly undersampled and reconstructed using compressed sensing (CS)[3]. Various denoising methods based on total variation (TV) and randomly translated wavelet transform (rWT) have been successfully applied in CS-DSI[4]. This work transfers the Fresnel band-split (FREBAS) transform, which has been used in CS methods for conventional MR imaging[5], to CS-DSI yielding superior convergence rates.

Subjects and Methods: In CS-DSI, the undersampled q-space signal y is used to reconstruct the r-space data x by solving $\min_x ||Ax-y||_2+l||\Psi x||_1$ with A=MF (undersampling operator and Fourier transform) and Ψ a sparsifying transform. The minimization is addressed by an iterative shrinkage algorithm with Nesterov update (ISA+NU)[6] (Tab 1.).

ISA+NU[6]	denoising functions	
$u^t = a_t x^t + b_t x^{t-1}$ $z^t = y - Au^t$ $w^t = A^H z^t + u^t$ $x^{t+1} = \eta_t(w^t)$	**TV**[7] $(\Psi w = \nabla w)$	**soft thresholding**[8] (Ψ: rWT or FREBAS)
	$\eta_t(w) = w - \sigma_t \nabla \mathrm{TV}(w)$ $\nabla \mathrm{TV}(w) = -\mathrm{div}\left(\frac{\nabla w}{\|\nabla w\|}\right)$	$\eta_t(w) = \Psi^{-1} T_{\sigma_t}(\Psi w)$ $T_\sigma(s) = \begin{cases} s - \mathrm{sgn}(s)\sigma & \text{if } \|s\| \geq \sigma \\ 0 & \text{else.} \end{cases}$

Tab. 1: Iterative shrinkage algorithm (iteration t) with Nesterov update and denoising functions h_t.

For TV, the denoising function η_t incorporated the gradient of the TV operator; for other transforms like rWT and FREBAS, η_t employs soft thresholding. Furthermore, the methods can be combined either by subsequently applying different denoising methods or by changing η_t over the iterations t.
Fiber simulations were performed using a Gaussian Mixture Model (2 fibers, fractional anisotropy FA=0.85, 70° crossing angle) on a 17^3 cube. Complex Gaussian noise was added (level 5%). The q-space data was randomly undersampled with acceleration factor R=4. CS reconstruction was performed using ISA+NU and various denoising techniques (Tab 2.). Root mean square error (RMSE) between reconstruction and noiseless ground truth was analyzed. Averages were taken over 1000 sampling/noise patterns.

name	denoising function η_t at iteration t	
	$t \leq 5$	$t > 5$
TV	TV	TV
rWT	rWT	rWT
FREBAS	FREBAS	FREBAS
TV+rWT	TV+rWT	TV+rWT
TV+FREBAS	FREBAS	TV
rWT+FREBAS	FREBAS	rWT
TV+rWT+FREBAS	FREBAS	TV+rWT

Tab. 2: Denoising strategies.

Results:

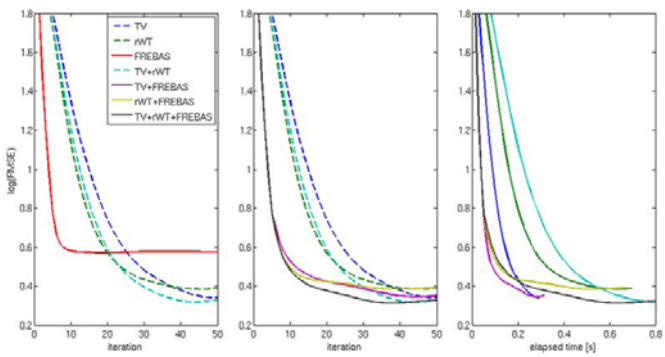

Fig. 1: Fiber simulation results.

The simulation results in Fig.1 show that FREBAS yields fastest error reduction during the first iterations but relatively high residual error. Combining FREBAS with some of the other methods exploits this property yielding superior convergence rates (in particular when taking the reconstruction time into account) and comparable error reduction.

Discussion/Conclusion: If combined with other sparsifying transforms, FREBAS transform has been shown to improve convergence rates in CS-DSI. Further work should focus on finding optimal combinations of various denoising methods to achieve maximal acceleration of DSI.

References:

[1]Wedeen, MRM, 2005
[2]Jensen., NMR Biomed, 2010
[3]Menzel, MRM, 2011
[4]Sperl, ISMRM, 2012
[5]Ito, ISMRM, 2011
[6]Khare, MRM, 2012
[7]Sidky, Phys. Med. Biol., 2008
[8]Daubechies, Commun. Pure Appl. Math. 2004

559

Influence of intravoxel incoherent motion (IVIM) effects on diffusional kurtosis measurements

O. Dietrich[1], A. Graser[2], M. Karpitschka[2], M. D'Anastasi[2], M. Reiser[2]
[1]Josef Lissner Laboratory for Biomedical Imaging, Institute for Clinical Radiology, Ludwig-Maximilians-University Hospital Munich, Munich/GERMANY, [2]Institute for Clinical Radiology, Ludwig-Maximilians-University Hospital Munich, Munich/GERMANY

Purpose/Introduction: Diffusional kurtosis imaging (DKI) can be used to assess the extent of non-Gaussian diffusion, which reflects properties of tissue microstructure[1]. DKI is based on the non-monoexponential signal attenuation at high b-values (b_{max}≈2000s/mm²). Microcapillary tissue perfusion is an additional cause of non-monoexponential signal attenuation present at very low b-values (0<b<200s/mm²), described by intravoxel-incoherent-motion (IVIM) MRI[2,3]. In DKI of the brain, the IVIM influence is generally neglected because of the low cerebral blood volume[1]. However, the influence of IVIM effects on DKI measurements can be relevant e.g. in abdominal or pelvic applications. The purpose of the present study was to analyze the potential influence of IVIM effects on DKI measurements.
Subjects and Methods: The diffusional kurtosis, K, of prostate tissue was obtained by a DKI measurement with b=0/150,500,1000,1500,2000s/mm². The IVIM influence on DKI was simulated for fixed D (diffusivity) and a broad range of IVIM parameters f (perfusion fraction) and D^* (pseudo-diffusion) based on published reference values[4,5]: D=1.3×10⁻³mm²/s, 0<f<0.25, 2×10⁻³mm²/s<D^*<14×10⁻³mm²/s. The simulated signal attenuation including IVIM and kurtosis contributions is:
$S(b)/S_0=(1-f)\cdot\exp(-bD+(bD)^2\cdot K/6) + f\cdot\exp(-b\cdot(D+D^*))$.
We determined D and K from simulated values $S(b)$ using a non-linear least-squares fit to a DKI model without IVIM contribution: $S(b;S_0,D,K)=S_0\exp(-bD+(bD)^2\cdot K/6)$. Two sets of b-values 0,500,1000,1500,2000s/mm² and 150,500,1000,1500,2000s/mm² were used. The relative deviation of the determined values D and K from the original values was calculated.
Results: Measured prostate kurtosis was K=0.59 based on the standard approach (b_{min}=0) and K=0.56 based on the IVIM-suppressed approach (b_{min}=150s/mm²) (Fig.1). The simulated relative deviation of D and K due to the IVIM influence is shown in Fig.2. For b_{min}=0, a substantial increase of K and D was observed. An improved estimation of K and D was obtained for b_{min}=150s/mm².

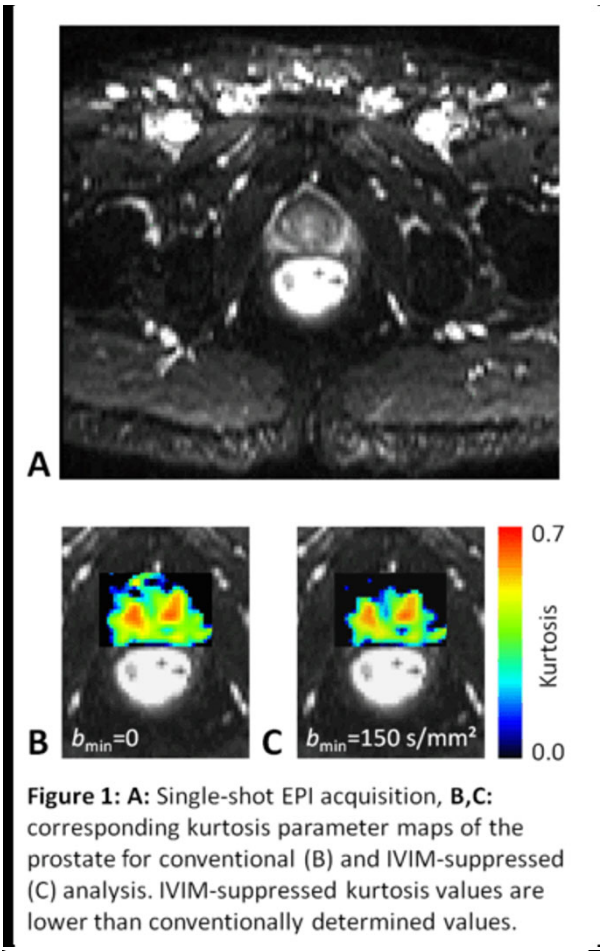

Figure 1: A: Single-shot EPI acquisition, **B,C:** corresponding kurtosis parameter maps of the prostate for conventional (B) and IVIM-suppressed (C) analysis. IVIM-suppressed kurtosis values are lower than conventionally determined values.

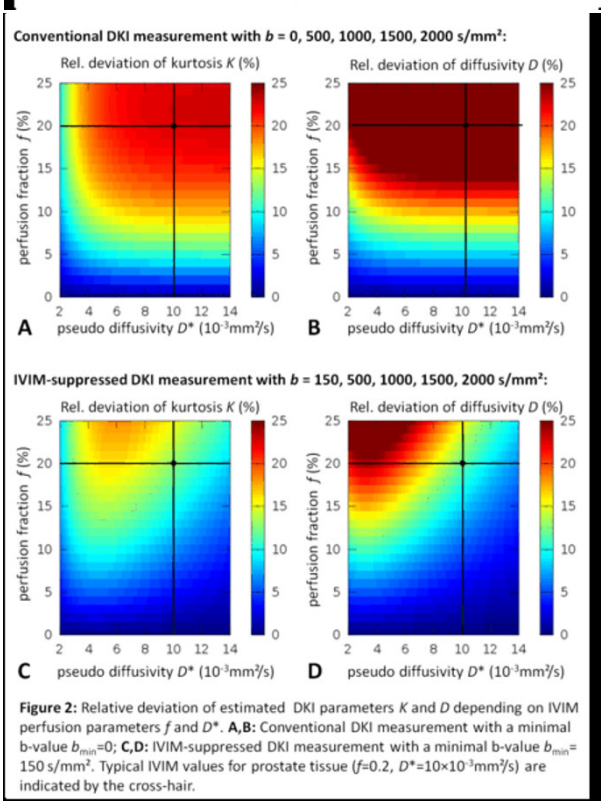

Figure 2: Relative deviation of estimated DKI parameters *K* and *D* depending on IVIM perfusion parameters *f* and *D**. **A,B:** Conventional DKI measurement with a minimal b-value b_{min}=0; **C,D:** IVIM-suppressed DKI measurement with a minimal b-value b_{min}= 150 s/mm². Typical IVIM values for prostate tissue (*f*=0.2, *D**=10×10⁻³mm²/s) are indicated by the cross-hair.

Discussion/Conclusion: IVIM effects can considerably influence the diffusivity and kurtosis determined in DKI leading to a parameter bias of about +20%. Using a minimum b-value of 150s/mm² reduces this bias substantially.

References:

[1]Jensen-JH et al. NMRBiomed. 2011;24:452. [2]Le Bihan-D et al. Radiology 1988;168:497 [3]Koh-D et al. AJR 2011;196: 1351 [4]Döpfert-J et al. MagnResonImaging 2011;29:1053 [5]Riches-SF et al. NMRBiomed 2009;22:318

560

Comparison of Diffusion Kurtosis Tensor Estimation Methods in an Advanced Quality Assessment Framework

V. Golkov[1], J.I. Sperl[2], T. Sprenger[1], H. Bungartz[3], M. Sedlacek[3], E.T. Tan[4], L. Marinelli[4], C.J. Hardy[4], K.F. King[5], M.I. Menzel[2]

[1]Diagnostics & Biomedical Technologies Europe, GE Global Research, Garching N. Munich/GERMANY, [2]Diagnostics & Biomedical Technologies Europe, GE Global Reseach, Garching N. Munich/GERMANY, [3]Department of Informatics, Technische Universität München, Garching N. Munich/GERMANY, [4]MRI Laboratory, GE Global Reseach, Niskayuna/NY/UNITED STATES OF AMERICA, [5]MR Physics, GE Healthcare, Waukesha/WI/UNITED STATES OF AMERICA

Purpose/Introduction: Diffusion (D) and kurtosis (K) tensor estimation [1] suffers in the presence of low-SNR data, as noise introduces bias and uncertainty. In contrast to common linear least-squares methods (ordinary/weighted (OLS/WLLS)), maximum likelihood estimation (MLE) takes Rician signal distribution into account [2]. This work compares three tensor estimation methods (OLS, WLLS and MLE) using diagnostically relevant quality criteria. Estimates of tensor-derived scalar measures (FA, maximal/radial/mean diffusivity/kurtosis) were evaluated with respect to healthy/diseased tissue discriminability, stability (precision after n repetitions), SNR-independence and accuracy (proximity to result of noiseless fit).

Subjects and Methods: Diffusion and kurtosis tensors were estimated using OLS/WLLS/MLE, with and without three constraints (#1:diffusivity>0, #2:kurtosis≥0, #3:monotonic signal decay with b-value) [2,3] using both simulated (Fig.1) and experimental diffusion spectrum imaging (DSI, [4,5]) data for different noise levels in 100 simulations each (Fig.1).

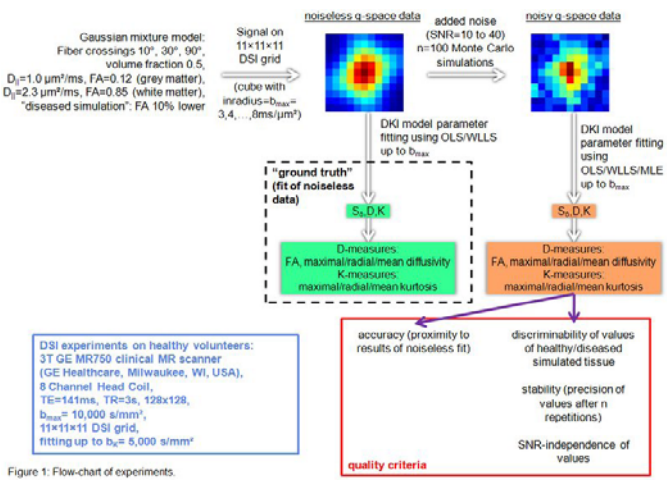

Figure 1: Flow-chart of experiments.

WLLS weighting was $1/(1+b/(ms/\mu m^2))^2$. OLS was employed in two-step (first D, then K) and one-step variants [3].

A novel DKI-visualization (Fig.3) illustrates OLS/WLLS-fitting bias, unconstrained/constrained modelled signal, and OLS-neglecting of the few low-b DSI-points.

Results: Most methods yielded similar results, with the following particularities:

Fitting Option/Method	Observation
unconstrained fitting	inferior stability (K-measures)
two-step fitting (i.e.fewer data points for estimation of D)	inferior stability (all measures); superior SNR-independence and accuracy (for D-measures only)
OLS	inferior stability, SNR-independence and accuracy (most measures)
b_{max}=6000, 7000, 8000s/mm² with constraint#3	failed for up to 20% of simulations
b_{max}=3000 and 4000s/mm²	inferior stability (especially all K-measures)
MLE	in many cases (examples in Fig.2a-b): superior in all four quality criteria; sometimes inferior stability; results less affected by constraints
SQP algorithm for MLE	convergence superior to originally proposed Nelder-Mead algorithm [2]

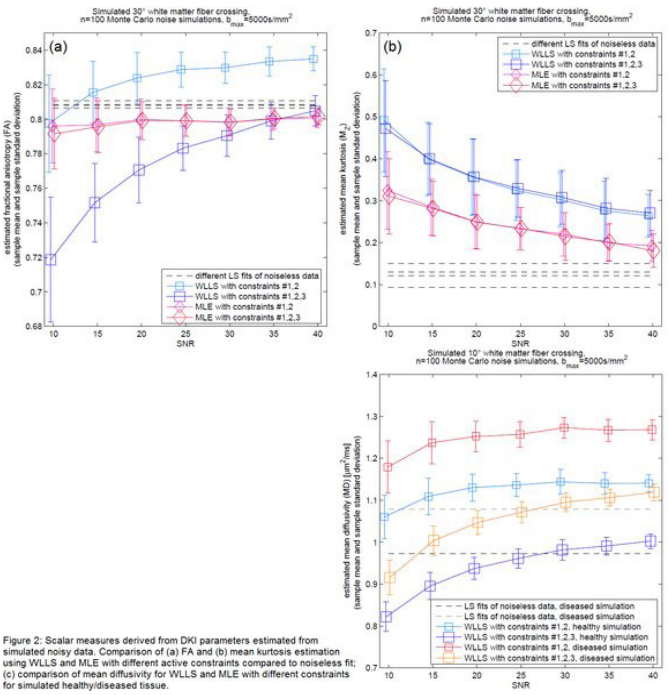

Figure 2: Scalar measures derived from DKI parameters estimated from simulated noisy data. Comparison of (a) FA and (b) mean kurtosis estimation using WLLS and MLE with different active constraints compared to noiseless fit; (c) comparison of mean diffusivity for WLLS and MLE with different constraints for simulated healthy/diseased tissue.

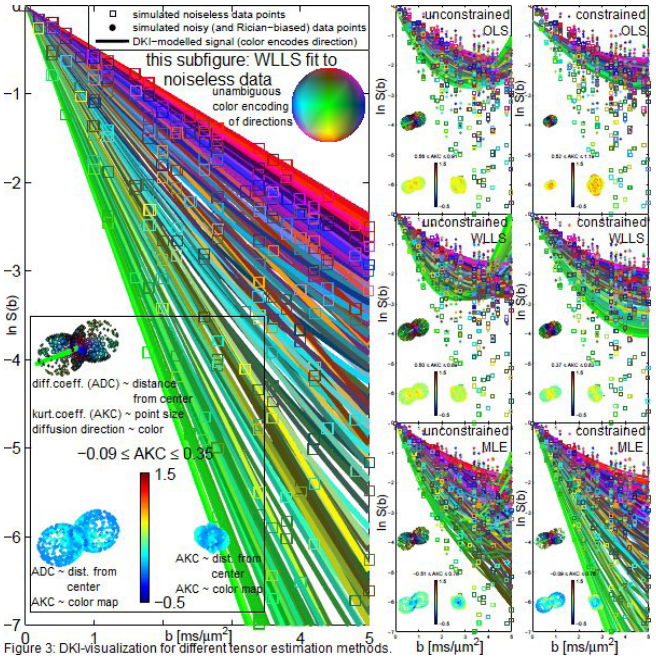

Figure 3: DKI-visualization for different tensor estimation methods.

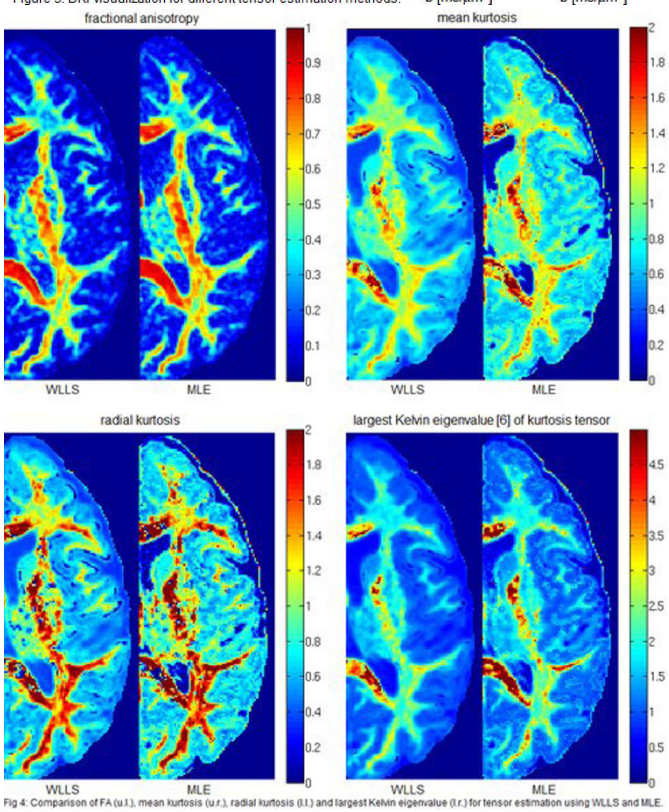

Fig 4: Comparison of FA (u.l.), mean kurtosis (u.r.), radial kurtosis (l.l.) and largest Kelvin eigenvalue (l.r.) for tensor estimation using WLLS and MLE.

Discussion/Conclusion: Unconstrained fitting, OLS, fitting with b_{max} considerably different from 5000s/mm² (validity range of DKI model), and the original MLE algorithm could all be rejected for their evident disadvantages. A final choice of one of the remaining methods requires more knowledge of details of diagnostic procedure and expected differences for healthy/diseased tissue. Values of measures obtained with different methods and/or SNRs should not be confounded (different ranges, Fig.2c). For brain data, MLE reveals more contrast details but also slightly higher noise (Fig.4).

References:

1. Jensen JH *et al.*, 2005, Magn.Reson.Med., 53(6):1432-1440.
2. Veraart J *et al.*, 2011, Magn.Reson.Med., 66:678-686.

3. Sperl JI *et al.*, 2011, Proc.Intl.Soc.Mag.Reson.Med., 19:4011.
4. Wedeen VJ *et al.*, 2005, Magn.Reson.Med., 54:1377-1386.
5. Menzel MI *et al.*, 2011, Magn.Reson.Med., 66:1226-1233.
6. Qi *et al.*, 2009, J.Math.Anal.Appl., 349:165-180.

561

Flow dependency of diffusion coefficients of the human brain measured by ECG gated diffusion weighted imaging

A. Müller-Lutz[1], J. Gross[2], G. Pentang[2], R.S. Lanzman[2], H.J. Wittsack[2], G. Antoch[2]
[1]Institute of Diagnostic and Interventional Radiology, University Duesseldorf, Medical Faculty, Dusseldorf/GERMANY, [2]Institute of Diagnostic and Interventional Radiology, University Dusseldorf, Medical Faculty, Dusseldorf/GERMANY

Purpose/Introduction: Usually the determination of apparent diffusion coefficients (ADC) in the brain is performed at arbitrary time points with respect to the blood flow in the carotid artery [1-3]. Nevertheless, the pulsatile cerebral blood flow might affect the diffusion of water molecules according to the time point within the heart cycle. The aim is to investigate the influence of pulsatile blood flow on ADC values obtained at well-defined time points within the heart cycle from ECG-gated diffusion weighted imaging of the human brain.
Subjects and Methods: 10 volunteers (7 males, 3 females, 23±2 years) were investigated at a 3T MRI scanner (Siemens Magnetom TIM Trio). Blood flow within the carotid arteries was measured by ECG gated phase contrast (PC) flow measurements with the following acquisition parameters: FOV=240x165mm², slice thickness 6mm, MxP=256x154, T_R/T_E=54.4ms/3.75ms, VENC=80cm/s and 20 acquired phases. Thereafter, ECG-gated DWI data acquisition was performed in one transversal slice at low (LF) (22.9±5.3cm/s) and at high (HF) (48.8±10.6cm/s) carotid blood flow. The acquisition parameters were: FOV=240mm², slice thickness 6mm, MxP=128x128, TR/TE=1700ms/92ms, 3 orthogonal diffusion directions using 16 different b-values from 0 to 2500s/mm². ADC was determined by regional analysis in white matter (WM), cortex (C), insular tissue (I) and cerebrospinal fluid (CSF) from DWI acquired at LF and HF.
Results: No differences of ADC for HF and LF were obtained in C (HF:ADC=0.69±0.02 μm²/ms; LF:ADC=0.69±0.03 μm²/ms; p-value:0.74) and I (HF and LF:ADC=0.75±0.05 μm²/ms; p-value:0.86). A small, but significant difference was obtained in WM (HF:ADC=0.65±0.02 μm²/ms; LF:ADC =0.64±0.02 μm²/ms; p-value:0.02). The CSF shows the highest flow-dependency (HF:ADC=2.25±0.55 μm²/ms; LF:ADC=1.91±1.03 μm²/ms; p-value <0.01). Figure 1 shows ADC maps obtained at time points of HF and LF in the carotid artery.

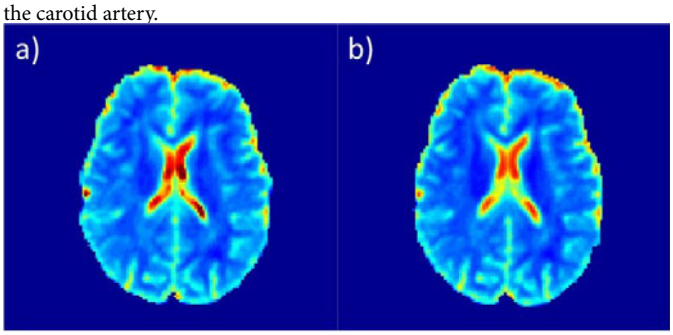

Figure 1: ADC maps at high (a) and low (b) carotid flow. Visually, differences of ADC can only be observed in the CSF.

Discussion/Conclusion: No differences in ADC values obtained at HF and LF were observed in C and I, whereas a small but significant difference was found for WM. The highly significant differences in ADC values of the CSF may be caused by the liquor pulsation with the heart cycle. In conclusion, measurements of mono-exponential ADC seem not to be influenced by the pulsation of cerebral blood flow. These findings are probably related to autoregulatory effects in the brain.

References:
[1] Turner et al. Radiology 1990;177:407-414
[2] De Lano et al. AJNR Am J Neuroradiol 2000;21:1830-1836
[3] Rizzo et al. Brain 2008;I31:2690-2700

562

Relaxation time corrected diffusion weighted imaging

D.G. Chong[1], L.J. Bains[1], D. Nanz[2], M. Ith[3]
[1]Dept. of Diagnostic, Interventional and Pediatric Radiology (DIPR), University & Inselspital Bern, Bern/SWITZERLAND, [2]Institute für Diagnostische und Interventionelle Radiologie, Universitätsspital Zürich, Zürich/SWITZERLAND, [3]Institute of Diagnostic Interventional and Pediatric Radiology, University Bern, Bern/SWITZERLAND

Purpose/Introduction: The signal intensity in DWI is affected by TE (1,2), which is largely dictated by b-values. If miniumum TE for each b value is used, then the maximum signal intensity can be achieved. The purpose of this abstract is to determined if same ADC values can be obtained by accounting for T_2 relaxation.
Subjects and Methods: Model
We propose that T_2 relaxation effects in DWI can be accounted for by modifying the classic ADC signal model:

$$S(TE,b) = S_0 \cdot \exp\left(-\frac{TE}{T_2}\right) \cdot \exp\left(-b \cdot ADC\right)$$

Phantom
Sucrose solutions at various concentrations (1) and cream (3) were investigated.
MR Imaging
Imaging was performed on Siemens Verio 3T with the following sequences

- DWI EPI with TE/b= 50/0, 50/50, 50/100, 55/300, 60/500, 66/1000, 66/0 (in ms and s/mm², respectively).
- Standard DWI EPI with TE = 66ms and the same b values.
- Fast spin echo with different TE

Results: Figure 1 shows the signal intensities of data acquired at constant TE and minimum TE at each b value. Figure 2 shows ADC maps generated by classic ADC model and Relax-DWI. In addition, T_2-maps obtained with Relax-DWI and fast spin-echo based mapping are shown. Table 1 summarizes the ADC and T_2 values observed with both models. The SNRs observed with RELAX-DWI were up to 50% higher than with standard DWI. ANOVA shows that ADC values obtained with both methods did not differ ($p > 0.4$). However, T_2 values estimated were shorter.

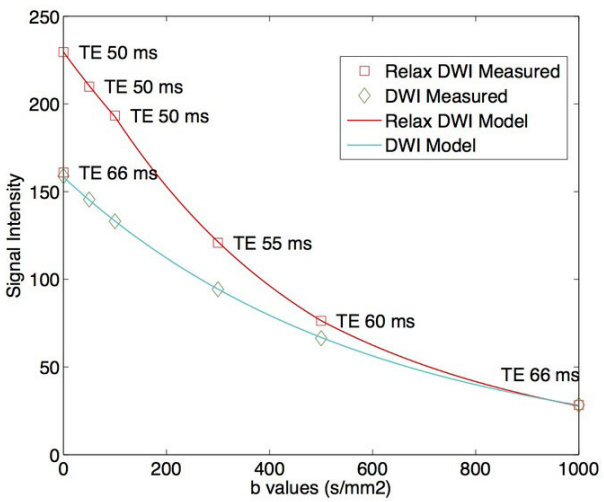

Figure 1 Signal intensities observed for classic DWI and Relax-DWI.

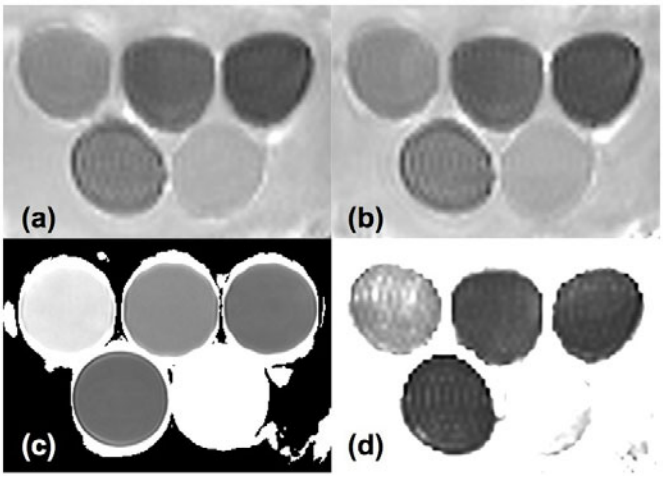

Figure 2 ADC (a,b) and T_2 (c,d) parametric maps from standard DWI (a) and T_2 measurements (c) and from Relax-DWI (ADC (b) and T_2 (d), respectively).

Table 1 Apparent diffusion (ADC, x10^{-5} mm²/s) and T_2 relaxation constants (T2, ms) from standard experiments and from Relax-DWI (mean ± std dev).

Phantoms	ADC	ADC (Relax-DWI)	T2	T2 (Relax-DWI)
Cream	125.7 ± 0.6	126.6 ± 1.3	83 ± 1	56 ± 1
Sucrose 05%	173.0 ± 0.6	169.9 ± 0.3	577 ± 26	294 ± 48
Sucrose 15%	136.2 ± 1.0	138.4 ± 1.1	188 ± 5	139 ± 7
Sucrose 25%	96.5 ± 0.7	95.0 ± 1.7	113 ± 3	61 ± 3
Sucrose 35%	79.1 ± 1.7	81.7 ± 1.7	91 ± 2	58 ± 3

Discussion/Conclusion: The strength of Relax-DWI is to maximize signal intensity for DWI. Figure 1 demonstrates and visualizes this effect nicely. Our experiments imply that the ADC values may be correctly estimated with RELAX-DWI.

Outlook

Further investigations are necessary to understand the true nature of the T_2 determined using this model. T_1 effects may also need to be accounted for. This model may be of clinical importance if it could be used to reduce T2 shine through effects in high b value images.

References:

1. Laubach JMRI 1998 8(6):1349–54
2. Ogura Eur J Radiol 2011 77(1):185–8
3. Ababneh Magma 2004 17(2):95–100

563

Revised mono-exponential model for intra-voxel incoherent motion

D.G. Chong, L.J. Bains
Dept. of Diagnostic, Interventional and Pediatric Radiology (DIPR), University & Inselspital Bern, Bern/SWITZERLAND

Purpose/Introduction: Mazaheri (1) introduced a model to calculate IVIM parameters with only three b values. However, the second approximation as published is not valid for all possible perfusion fractions (*f*). This paper introduces improved revised mono-exponential model (Rev-mono).

Subjects and Methods: Model

Mazaheri (1) showed that the bi-exponential IVIM model (Bi-exp) can be reduced to [1] by approximation. Instead of using a second approximation, we propose to substitute the log function temporary variable, κ in [2]. Equation [3] can be derived via rearrangement. Solving equation [3] gives a valid κ value which allows the IVIM parameters D and *f* to be determined using equation [4] and [5].

$$ADC_b = D + log\left(\frac{1}{1-f}\right)/b \quad [1]$$

$$ADC_b = D + \frac{\kappa}{b}. \quad [2]$$

$$\kappa = \left(\frac{b_1 \cdot b_2}{b_2 - b_1}\right) \cdot \left(ADC_{b_1} - ADC_{b_2}\right) \quad [3]$$

$$D = ADC_{b_1} - \frac{\kappa}{b_1} \quad [4]$$

$$f = \frac{1}{1-\exp(\kappa)} \quad [5]$$

Simulation

Simulation calculations were performed to understand the difference between Rev-mono and Bi-exp. Signal intensity was calculated for a selection of b values with IVIM parameter combinations lying within a wide physiological range. Signal intensities were then fitted using the Rev-mono. Differences between the two models were then calculated for *f* and D and visualized using a 3D parameter space map.

MRI Measurement

Five healthy subjects were each measured five times in Siemens Verio 3T. DWI measurement with b=0, 10, 20, 40, 60, 150, 300, 500, 750, 1000 s/mm². For Rev-mono fitting, only b=0, 60, 300, 750 s/mm² data were used. The additional 60 s/mm² data allows for calculation of D*.

Results: The green area in Figure 1 shows that both models agree with each other within a large segment of the parameter space. Figure 2 shows the spread of parameter estimates for kidney cortex and medulla using Rev-mono is significantly lower than Bi-exp. Smoother parameter maps are also generated using Rev-mono as shown in Figure 3.

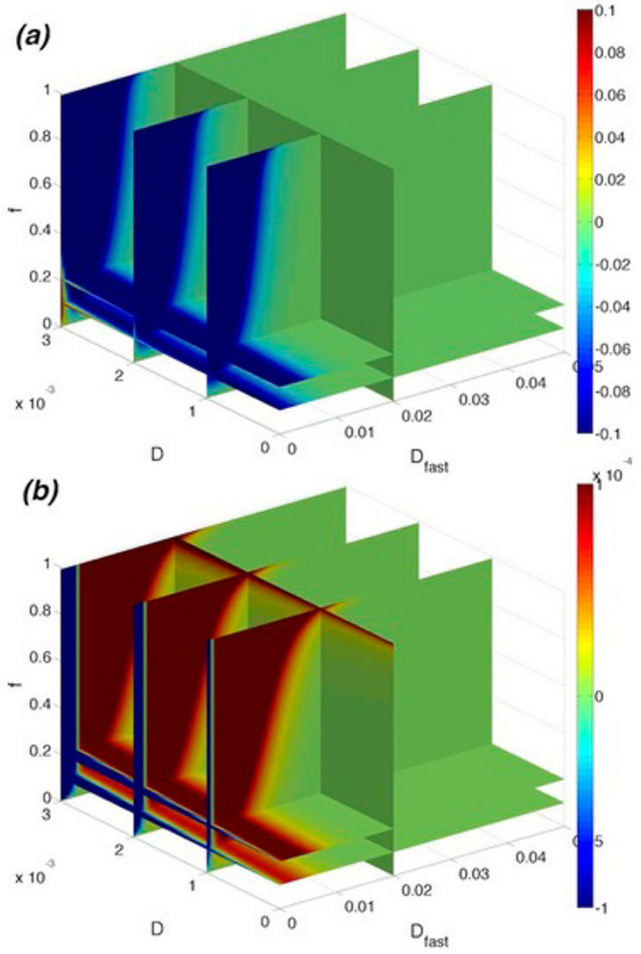

Figure 1 (a) Perfusion fraction (b) and D difference between Rev-mono and Bi-exp using b=0,400 and 700 s/mm². The green color area indicates zero difference between the models.

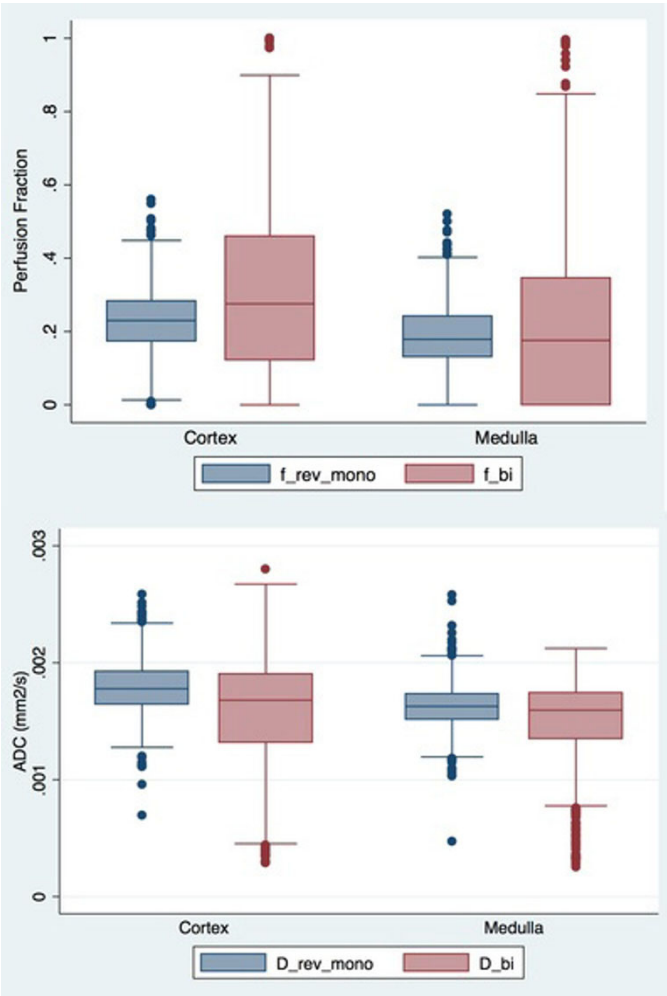

Figure 2 (a) Perfusion fraction and (b) D values for kidney cortex and medulla. Rev-mono gives a lower interquartile range than Bi-exp.

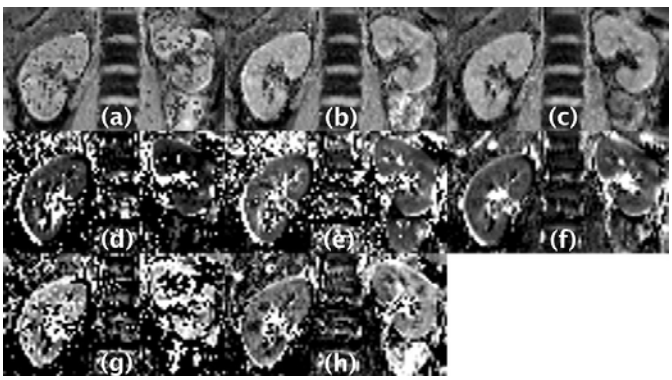

Figure 3 Parameter maps fitted using Bi-exp (a,d,g), Rev-mono (b,e,h) , ADC_{High} (c) and ADC_{Low} (f). The maps include D (a-c), D* (d-f) and perfusion fraction (g,h) parameters.

Discussion/Conclusion: The improved Rev-mono can produce comparable parameter values with lower spread and smoother parameter maps as compared to the classic Bi-exp.

References:

1.Mazaheri JMRI 2012 35(3):660–8

564

Optimal ROI Size for IVIM Imaging parameter determination

M. Montelius[1], M. Ljungberg[2], E. Forssell-Aronsson[3]
[1]*Department of Radiation Physics, Institution of Clinical Sciences, Gothenburg/SWEDEN,* [2]*Sahlgrenska University Hospital, Department of Medical physics and Biomedical Engeneering, Gothenburg/SWEDEN,* [3]*Radiation Physics, Clinical sciences, Gothenburg/SWEDEN*

Purpose/Introduction: The use of multiple b-values in diffusion weighted (DW) imaging allows quantification of the tissue molecular diffusion parameter D, the perfusion-related diffusion parameter D* and the perfusion fraction f, by applying the intravoxel incoherent motion (IVIM) model [1]. Tumor tissue can thus be characterized non-invasively, and since perfusion and diffusion strongly influence the delivery of therapy agents to tumor cells, careful monitoring of these parameters prior to and during the course of treatment would facilitate e.g. decision-making regarding treatment strategy. However, the quantification is highly affected by the size of the analyzed region of interest (ROI). Our aim was to investigate the optimal ROI size for quantification of D, D* and f.
Subjects and Methods: Liver IVIM MRI was performed on healthy volunteers using a 3T Philips Achieva and a phased array surface coil. DW SE-EPI with respiratory navigator; b-values:0-800; fat suppression=SPIR; TR/TE/NSA=2000/53/2; pixel size:1.46*1.46mm²; slice thickness:5mm; SENSE factor=2; scan time~12 min. ROI averaged signal-intensity decay curves were acquired from four positions in the liver parenchyma (Fig.1a). Eight ROI sizes, each with a one pixel increase in radius compared to the preceding ROI, were analyzed for each position [ROI 1-8: 2,19,53,104,173,258,360 and 480mm²]. Each resulting signal decay curve was fitted to the bi-exponential model [1] using Matlab (The Mathworks, USA), and D, D* and f were extracted together with the sum of squares due to error (SSE). The variation of the parameters with increasing ROI radius was analyzed by calculating the derivative of D, D* and f with regard to ROI radius, thus producing dD/dr, dD*/dr and df/dr for each liver position. The magnitudes of the derivatives were averaged for each size increment and their standard deviations were calculated. This was plotted vs. ROI radius.
Results: The variation of D, D* and f with increasing ROI size approaches zero at ~5-6 pixels ROI radius (Fig.1b-d), corresponding to 170-260mm² using the above described parameters. The model fit (SSE) (Fig.1e) is strongly improved with increasing ROI size (from 0.02 for the smallest ROI to approximately 0.005 using 5-6 pixels ROI radius).

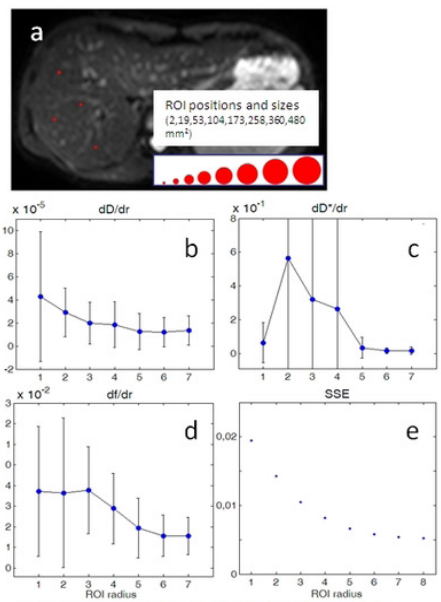

Figure 1a) IVIM (b=0) image of liver with ROI positions and sizes. Parameter variation with ROI radius vs. ROI radius in b), c) and d) for diffusion (D), perfusion-related diffusion (D*) and perfusion fraction (f), respectively (bar = std). 1e) shows average SSE. Note the scales of the y-axes in b), c) and d).

Discussion/Conclusion: The parameter variation does not reach zero. This is probably due to the heterogeneity of the tissue. Nevertheless, the initial higher variation decrease and we suggest using a ROI area close to the stabilization, i.e. a 5-6 pixels ROI radius or approximately 170-260 mm², where the parameters are least affected by ROI size.
References:
D. Le Bihan, *Radiology* 1988

565

WITHDRAWN

566

Quantitative analysis of the limits of the mono-exponential tensor model in DTI.

L. Squarcina[1], D. Peruzzo[1], F. Arrigoni[2], F.M. Triulzi[3], A. Bertoldo[1]
[1]*Department of Information Engineering, University of Padova, Padova/ITALY,* [2]*Neuroimaging Unit, Scientific Institute IRCCS Eugenio Medea, Bosisio Parini (LC)/ITALY,* [3]*Neuroimaging Unit, Fondazione IRCCS Ca' Granda, Ospedale Maggiore Policlinico, Milano/ITALY*

Purpose/Introduction: DTI data analysis in a clinical context is usually performed assuming the mono-exponential tensor model. Moreover, fiber direction is assumed to be parallel to the main eigenvector when deterministic tractography is performed [1], e.g. in connectome studies. The aim of this study is to evaluate the impact of these assumptions on the results.
Subjects and Methods: Data set: 6 healthy subjects (M/F=3/3, mean age±SD=28.8±1.7 years) were acquired on a 3T 32 channels Philips-Achieva. DTI data include 32 non-collinear directions acquired at different b-values (500, 1000, 1500, 2000, 2500 s/mm²).
Analysis: the mono-exponential model was identified using the b=1000s/mm² data with the weighted linear least squares estimator, whereas the bi-exponential one was identified using the weighted nonlinear least squares estimator on the whole data set [2]. Comparison was performed in terms of differences in FA values and direction of the main eigenvectors. In the bi-exponential model the FA and the main eigenvector have been computed on the most relevant compartment.
Results: The mono-exponential tensor model significantly underestimates the FA compared to the bi-exponential one (Figure 1), both in the white (-32%±5%) and in the gray matter (-27%±2%) (Figure 2, p<0.05 in both cases).

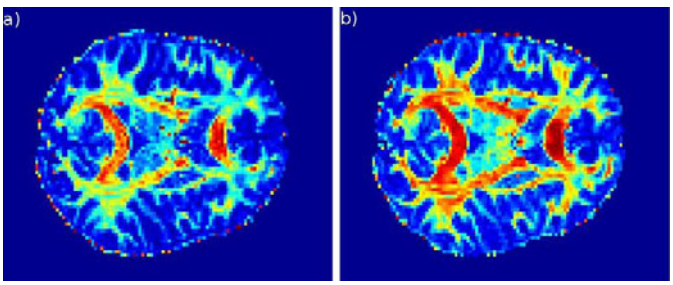

Figure 1: FA maps obtained using the mono-exponential (a) and the bi-exponential (b) models.

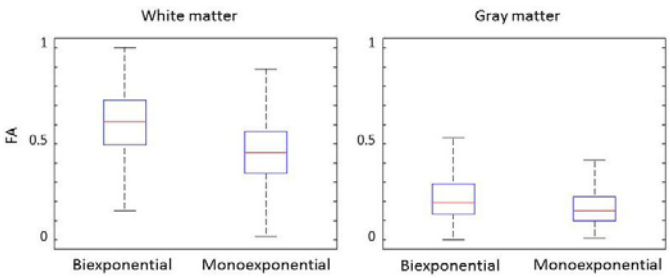

Figure 2: impact of the model on the FA.

Differences have been highlighted also in the direction of the main eigenvectors. In particular, clusters with FA>0.2, a volume larger than 120 mm³ and direction differences larger than 30° have been detected in the putamen, in the thalamus, in the cortico-spinal tract (Figure 3a), in the corona radiata and in the superior longitudinal fasciculus (Figure 3b). FA>0.2 has been considered to avoid areas where the tensor model yields particularly uncertain results.

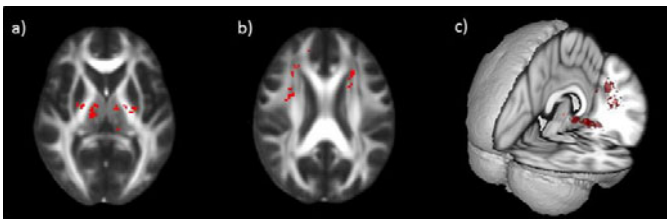

Figure 3: clusters with a direction difference between the main eigenvectors obtained with the mono- and the bi-exponential models greater than 30°. Axial views (a and b) and 3D rendering (c).

Discussion/Conclusion: Assuming a mono-exponential tensor model corresponds to assume that only one fiber compartment is present in each voxel. This has a significant impact on the analysis results, not only when FA is evaluated but also when deterministic tractography is performed, since the direction of the main eigenvector in the mono-exponential model is modified by the presence of multiple fiber bundles.

References:

[1] Mori, S. et al., (1999), *Ann. Neurol.*, 45:265-9.
[2] Maier, S.E. et al., (2008), *Magn Reson Med*, 51:321-30.

567

Improved Signal-to-Noise Ratio in High-Resolution Diffusion-Weighted Imaging Offered by Center-out EPI

M. Shrestha, T. Mildner, T. Schlumm, H.E. Möller
Nuclear Magnetic Resonance (R&D Unit), Max Planck Institute for Human Cognitive and Brain Sciences, Leipzig/GERMANY

Purpose/Introduction: Diffusion-weighted imaging (DWI) has become an important biomedical tool. Recent efforts have been spent to increase the spatial resolution by parallel acquisition techniques or by reduced field-of-view imaging. This study investigates the feasibility of DWI at minimum TE by high-resolution center-out EPI. It is shown that substantial signal-to-noise ratio (SNR) improvements may be achieved.

Subjects and Methods: The pulse sequence (Fig. 1) was adapted from the DEPICTING approach [1]. It consists of two consecutive slice loops with diffusion preparation. The upper tile of k-space is acquired in the first loop whereas the lower tile is obtained with inverted blips in the second loop. The central k-space line is acquired twice for inter-segment phase correction [1]. Nyquist-ghost correction is based on a template scan acquired with minimum b-value. Twelve axial slices were recorded at 3 T (Siemens TIM Trio) in a healthy volunteer with b=1000s/mm² (G_{max}=26 mT/m) with nominal voxel size 1×1×1.5mm³ (acq. matrix 192×192) and TE=72ms. Standard twice-refocused DWI images [2] were recorded for comparison (6/8 partial Fourier imaging, GRAPPA acceleration factor 3 to achieve TE=102 ms). The same total scan time was employed for both methods (i.e. 4 vs. 8 averages).

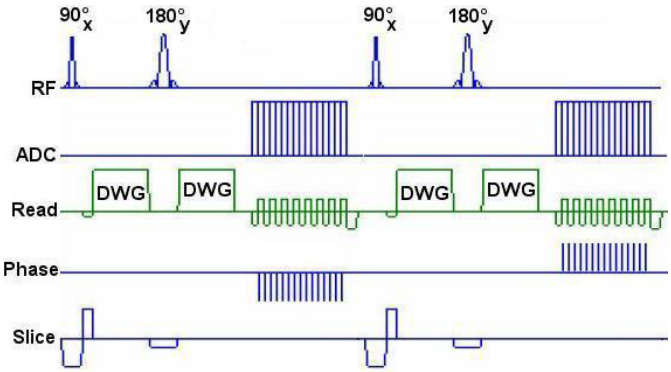

Figure 1: *Sequence diagram of diffusion-weighted two-shot center-out EPI.*

Results: Visual inspection demonstrated the expected diffusion contrast (Fig. 2). A gain in SNR by 3-11% was obtained in the corpus callosum for the center-out technique. This is consistent with estimates of the signal decay due to transverse relaxation at the different echo times based on published white-matter T_2 values with additional consideration of SNR loss resulting from parallel imaging and partial Fourier acquisition.

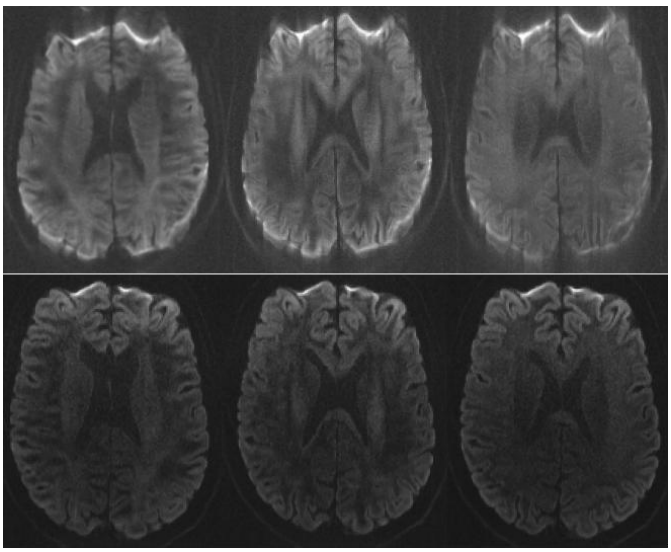

Figure 2: *DWI along x/y/z directions; Upper: center-out EPI; Lower: standard partial-Fourier EPI.*

Discussion/Conclusion: The center-out acquisition achieves DWI with an optimized TE that is independent of the acquisition matrix, whereas standard EPI suffers from prolonged TE, and hence an additional SNR penalty, with increasing resolution. A drawback is an increased susceptibility to image artifacts related to involuntary head motion and/or vibrations of the patient table resulting from rapid gradient switching. Occurrence of residual vibration artifacts strongly depends on the direction of the diffusion-weighting gradients leading to signal loss and blurring. This behavior is common to all segmented DWI approaches and would strongly benefit from mechanical stabilization of the patient table [3].

References:

[1] Hetzer S 2011, MRM 65:165-175. [2] Reese TG 2003, MRM 49:177-182. [3] Gallichan D 2010, HBM 31:193-202.

568

A new anisotropic multiple-fibre phantom for diffusion MRI

E. Farrher, A. Celik, F. Grinberg, N.J. Shah
Institute of Neuroscience and Medicine - 4, Forschungszentrum Juelich GmbH, Juelich/GERMANY

Purpose/Introduction: Anisotropic fibre phantoms have become a useful tool for diffusion MRI, particularly in the validation of tractography algorithms, theoretical models and simulations [1,2]. In this work a new anisotropic fibre phantom made of polyethylene fibres [1,2] is presented. The valuable feature of the new design is the integration of several geometrical configurations in a single phantom.

Subjects and Methods: The phantom was built using hydrophobic polyethylene fibres (Dyneema®DTX70) of 8 μm radius, wound around a Plexiglas® support (Fig.1a) [1]. It includes four regions with different interwoven fibre configurations: one region contains a single fibre orientation with uniform fibre density (blue ROI in Fig.1a); two regions contain interwoven fibres with different orientations at a distribution of angles in the range $50°<\varphi<90°$ and with variable fibre density (FD) (black ROIs in Fig.1a); a fourth region with triple-crossing fibres (red ROI in Fig.1a). Dashed arrows in Fig.1a) denote the fibre direction in each ROI. The whole setup was immersed in a cylindrical container filled with distilled water. Measurements were performed with a 3T Siemens Magnetom Trio scanner (Siemens, Erlangen). A spin-echo multi-contrast sequence was used to estimate FD and T_2 relaxation time [1]. A twice-refocused spin-echo diffusion-weighted EPI sequence was performed for 64 gradient directions and *b*-values 0-1000 s/mm². Diffusion metrics such as mean diffusivity (MD) and fractional anisotropy (FA) were calculated with the help of the ExploreDTI toolkit [3].

Results: Figure 1b) shows a map of FD of a selected slice. One can see that while the single- and triple-fibre regions have approximately uniform FD, the double-fibre has a gradient of FD.

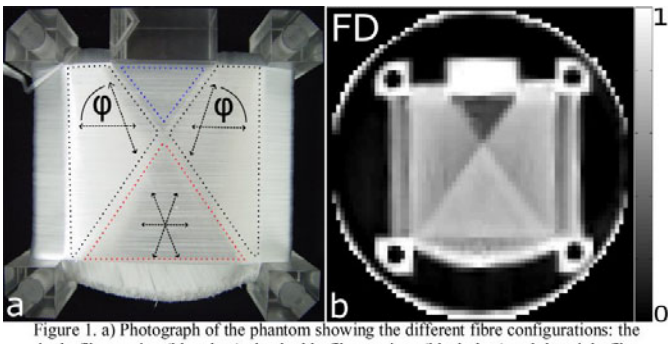

Figure 1. a) Photograph of the phantom showing the different fibre configurations: the single-fibre region (blue dots), the double-fibre regions (black dots) and the triple-fibre region (red dots). Arrows in each area denote the fibre directions. b) The fibre density map [1].

Figure 2 shows the map of T_2 (a) and its correlation with FD for each of the ROIs (b).

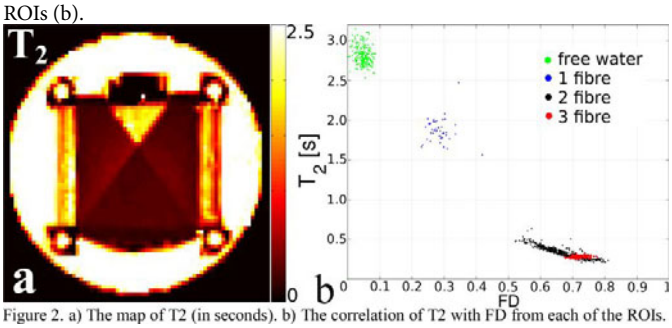

Figure 2. a) The map of T2 (in seconds). b) The correlation of T2 with FD from each of the ROIs.

Figure 3 is a map of MD (a) and its correlation with FD for each of the ROIs (b).

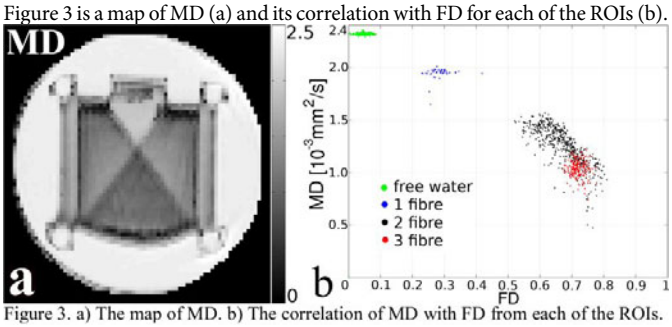

Figure 3. a) The map of MD. b) The correlation of MD with FD from each of the ROIs.

Figure 4 shows a map of FA (a) and its correlation with FD for each of the ROIs (b).

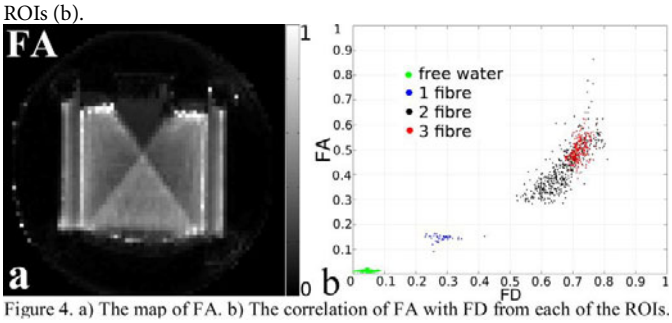

Figure 4. a) The map of FA. b) The correlation of FA with FD from each of the ROIs.

Discussion/Conclusion: The new design combines several useful features in a single phantom; a single-fibre region with constant FD, two double-fibre areas with a distribution of crossing angle and variable FD and a triple-fibre region with uniform FD. Relaxation and diffusion properties have been assessed. Further investigation of the diffusion properties using high angular resolution diffusion imaging methods [4] are currently being carried out in our laboratory.

References:

[1]Farrher,E.,Kaffanke,J.,Celik,A.A.,Stöcker,T.,Grinberg,F.,Shah,N.J.,2012. *Magn.Reson.Imaging***30**,518-526;[2]Fieremans,E.,DeDeene,Y.,Delputte,S.,Özdemir,M.S.,D'Asseler,Y.,Vlassenbroeck,J.,Deblaere,K.,Achten,E.,Lemahieu, I.,2008.*J.Magn.Reson.***90**,189-199;[3]Leemans,A.,Jeurissen,B.,Sijbers,J.,Jones ,D.K.,2009.*Proc.Intl.Soc.Magn.Reson.Med.***17**,3537.[4]Anderson,A.W.,2005. *Magn.Reson.Med.***54**,1194-1206.

569

Probing micro-structural information using the CHARMED model in the non-myelinated human newborn brain at 3T

N. Kunz[1], H. Zhang[2], K. O'Brien[3], Y. Assaf[4], D. Alexander[2], F. Lazeyras[5], P. Hüppi[6]
[1]Division of Child Growth & Development, University of Geneva, Genève/SWITZERLAND, [2]Computer Science, University College London, London/UNITED KINGDOM, [3]Advanced Clinical Imaging Technology, CIBM-Siemens Development group, University of Lausanne, Geneva and EPFL, Lausanne/SWITZERLAND, [4]Neurobiology, Tel Aviv University, Tel Aviv/ISRAEL, [5]Radiology - CIBM, Geneva University Hospital, Genève/SWITZERLAND, [6]Division of Child Growth & Development, University of Geneva, Geneva/SWITZERLAND

Purpose/Introduction: Many neurobiological disorders and disabilities originate from disruptions in structural and functional development, which motivates the need for a better understanding of brain development. Diffusion tensor imaging (DTI) provides a unique insight into the brain microstructure and development. New modelling approaches such as CHARMED[1], can potentially provide more specific information than DTI such as axonal volume fraction. The aim of this study was to investigate the application of the CHARMED model on newborns.

Subjects and Methods: 3 human preterm newborns were scanned during the first week of life (BIRTH) and 9 were scanned at term (40 weeks gestational age, GA40).

At BIRTH, experiments were performed on a 1.5T Avanto system and at GA40 on a 3T Trio Tim system (Siemens-Medical-Solutions, Erlangen-Germany) The data were acquired using a DSE-EPI sequence[2] (resolution=2×2×2mm³; matrix=80×80). CHARMED protocols consisted of 5 b-value shells with a total of 66 directions (bmax=2000s/mm² at BIRTH and 2500s/mm² at GA40)[1]. 5 ROIs were drawn manually on FA maps (splenium,body,genu corpus callosum, s-b-g-CC, posterior,frontal cortico-spinal tract, p-f-Cst).
The CHARMED model composes of 3 compartments: Intra-axonal (cylinder); Extra-axonal (ellipsoid); CSF (isotropic). Axonal parallel diffusivities=2·10⁻³mm²/s, and CSF diffusivity=3·10⁻³mm²/s. Extra-axonal compartment was modelled using a tortuosity approach ($D_{rad}=(1-VF_{ia})D_{long}$). The intra-axonal and CSF volume fraction (VF_{ia},VF_{CSF}) and S_0 were fitted using a maximum-likelihood gradient-descent algorithm.
Results:

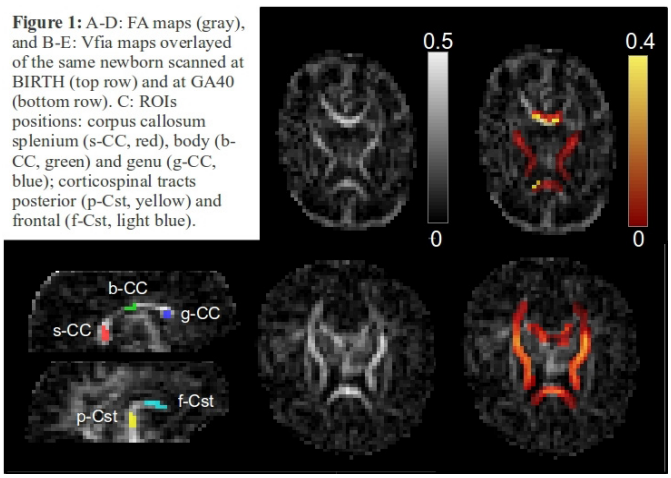

Figure 1: A-D: FA maps (gray), and B-E: Vfia maps overlayed of the same newborn scanned at BIRTH (top row) and at GA40 (bottom row). C: ROIs positions: corpus callosum splenium (s-CC, red), body (b-CC, green) and genu (g-CC, blue); corticospinal tracts posterior (p-Cst, yellow) and frontal (f-Cst, light blue).

Overall data quality was good (Fig-1), except for 3 subjects at GA40, which were rejected due to large motion artifacts. Regular DTI analysis shows FA values significantly higher at GA40 compared to BIRTH in the s-CC, f-Cst and p-Cst mainly due to a reduction of the radial diffusivity. With the CHARMED analysis, only VF_{ia} in the p-Cst was significantly higher at GA40, but the same trend for FA was visible in the other regions (Table-1).

Table 1: Mean Fractional anisotropy (FA) and intra-axonal volume fraction (Vfia), in five white-matter regions: splenium (s-CC), body (b-CC) and genu (g-CC) of the coprus callosum, posterior (p-Cst) and frontal (f-Cst) cortical spinal chords in pretrem newborns during first week (BIRTH, n=3) and at term (GA40, n=6). Error are standard deviation over the group. *: t-test p<0.05

	FA		VFia	
	BIRTH	GA40	BIRTH	GA40
s-CC	0.41 ± 0.02	0.55 ± 0.08 *	0.28 ± 0.04	0.31 ± 0.05
b-CC	0.33 ± 0.01	0.38 ± 0.06	0.21 ± 0.00	0.26 ± 0.08
g-CC	0.36 ± 0.03	0.43 ± 0.08	0.20 ± 0.03	0.27 ± 0.05
p-Cst	0.34 ± 0.03	0.48 ± 0.04 *	0.18 ± 0.01	0.26 ± 0.03 *
f-Cst	0.26 ± 0.03	0.31 ± 0.03 *	0.13 ± 0.00	0.16 ± 0.03

Discussion/Conclusion: VFia and FA seems to correlate with WM maturation, with values increase with development and lower values were observed in f-Cst than the p-Cst, which is known to myelinate later. Limited statistical significance may be explained by the low number of subjects and also the large range of GA of the subject at birth (26 to 31weeks).
In conclusion, these preliminary results demonstrate the feasibility to acquire CHARMED data for studying brain development in human newborns.
References:
[1]Assaf,MRM-2005,[2]Clayeden,IPMI-2009
Suppored by: FP7-CONNECT, SNF-SPUM-124101, the CIBM of UNIL-UNIGE-HUG-CHUV-EPFL, Leenards-Jeantet foundations.

570

WITHDRAWN

571

WITHDRAWN

572

Tumor cell migration as detected by microscopic 3D-DTI and two-photon microscopy in a novel mouse model of glioma.

U.P.Y. Gimenez, T. Perles-Barbacaru, B. Van Der Sanden, D. Wion, M.F. Nissou, F. Appaix, F. Berger, H. Lahrech
Grenoble Institute of Neurosciences, INSERM U836, La Tronche/FRANCE

Purpose/Introduction: Glio6 is an orthotopic tumor model (1) derived from human glioma stem cells with similar growth pattern and invasiveness to clinically encountered glioma. Glio6 cells are likely to migrate along fibers of the corpus-callosum. The sensitivity of microscopic 3D-Diffusion Tensor Imaging (3D-DTI) to detect this migration was assessed and validated using two-photon microscopy ex-vivo.
Subjects and Methods: Nude mice were injected with 500000 Green Fluorescent Protein (GFP) labeled Glio6 cells (n=11) or with physiological liquid (n=5) in the caudate-nucleus. The tumor development was monitored in vivo every 15 days with T2-weighted imaging. At 60 days after tumor implantation, the mice were fixed by transcardiac perfusion with 4% paraformaldehyde in phosphate buffered saline containing 6.25mmol/L Gd-DOTA (Guerbet, France). Brains were preserved in Flomblin-oil (Solvay-Solexis, Italy).
3D-DTI was performed at 7T (Bruker, 600mT) using a spin-echo sequence (TE/TR= 16/90ms, NA=34). Diffusion gradients (d=3.5ms D=8ms) were applied in six different gradient diffusion directions ([1 1 0],[1 -1 0],[0 1 1],[0 1 -1],[1 0 1],[-1 0 1]) with a b-value 1500s/mm². The FOV and the spatial resolution were set to 20x8.5x11.5mm³ and 100x100x100mm³ respectively. Total time was 59 hours. The diffusion data was analyzed with MedINRIA software (https://gforge.inria.fr/frs/?group_id=727&release_id=4541, INRIA, France). Fractional anisotropy (FA), parallel (Dpara) and perpendicular (Dperp) diffusivities were computed (2) for symmetrical ROIs in the corpus-callosum.
300µm thick coronal brain slices were observed with a two-photon microscope consisting of a Biorad (MRC 1024) scanhead and an Olympus BX50WI microscope using a 20x water immersion objective and an 800nm excitation beam.
Results: In tumor bearing mice, thickening of the corpus-callosum (Figure 1) and changes in DTI parameters were observed (Figure 2) Elongated tumor cells (green in Figure 3) distinctly migrate along fibers of the corpus-callosum, invading the cortex, but not the hippocampal formation.

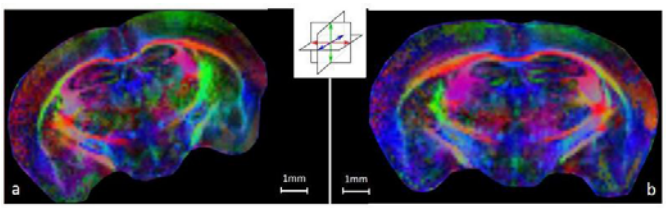

Figure 1: Color maps of axial fiber directions: sham mouse (a), glioma bearing mouse (b)

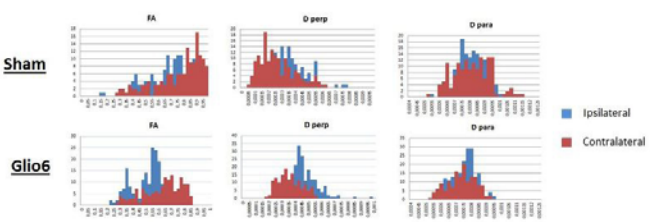

Figure 2 : Fractional anisotropy (FA), parallel and perpendicular diffusivity (Dpara, Dperp) in corpus-callosum of both mice.

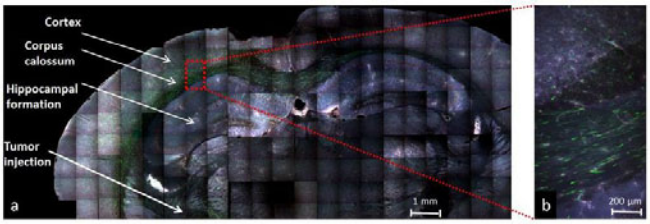

Figure 3: Two-photon microscopy of GFP marked glioma cells. (A) composite image with tumor site (red arrow) and invaded corpus-callosum. (B) Enlargement of a ROI in the ipsilateral corpus-callosum.

Discussion/Conclusion: The 3D-DTI data conveys a decrease of geometric organization in the tumor area and in the corpus-callosum. The FA and Dpara are lower (-24%,-12%), and Dperp is higher (+27%) due to the presence of tumor cells between fibers.
The Glio6 tumor model and 3D-DTI are appropriate to study tumor cell migration and asses new treatments. This study demonstrates that FA, Dpara and Dperp parameters are biomarkers of tumor cell migration using microscopic 3D-DTI and validating with two-photon microscopy. However, they are also exptected to be useful biomarkers in clinical applications with shorter acquisition times.

References:

1……Platet, 2007
2……Pierpaoli, 1996

573

White Matter Grid Tracking in Living Humans

C.M. Santos, R. Lavrador, N.F. Lori
IBILI, Faculty of Medicine – University of Coimbra, Coimbra/PORTUGAL

Purpose/Introduction: White Matter (WM) Fiber Tracking [1,2] can be done using Low Angular Resolution Diffusion Imaging (LARDI), High Angular Resolution Diffusion Imaging (HARDI) or High Grid Resolution Diffusion Imaging (HGRDI). In HARDI, the data is often converted into an orientation distribution function (ODF) using, for example, the FMRIB Software Library (FSL) [3]. The work of Wedeen et al. [4], obtained using Diffusion Spectrum Imaging (DSI) says that there are only 3 almost orthogonal WM fiber orientations at each WM point. The purpose of this work is to develop WM grid tracking, with the grid defined by having 3 orientations for each brain voxel. For each voxel, the orthogonality condition is tested.
Subjects and Methods: We used FSL in brain anatomical MRI data to segment air or background, Cerebrospinal Fluid (CSF), Gray Matter (GM) and White Mater(WM).
Orthogonality Within Voxels (OWV): The OWV is defined using eq. 1 and eq. 2 in Figure 1; where u, v, and w are the 3 orientations obtained for each voxel by FSL. This parameter is computed in WM and GM regions. If the voxels are not in WM and GM or if there are two or more null vectors, the OWV will be set to a negative value to differentiate between valid values and non-defined or out-of-interest values. Finally, a set of color maps for each slice about the OWV is obtained.
Grid Tracking: WM Grid tracking is done for every point of WM, the grid is defined by starting in a point at the center of the voxel and going in the 6 directions defined by the 3 vector orientations at each voxel, and then propagating line points using the discretized Frenet equation, eq. 3, Figure 1.

$$OWV(\vec{u},\vec{v},\vec{w}) = \frac{1}{\sqrt{3}}\sqrt{\frac{|\vec{u}\times\vec{v}|^2}{|\vec{u}|^2|\vec{v}|^2}+\frac{|\vec{u}\times\vec{w}|^2}{|\vec{u}|^2|\vec{w}|^2}+\frac{|\vec{v}\times\vec{w}|^2}{|\vec{v}|^2|\vec{w}|^2}}\;;\text{for } |\vec{u}|,|\vec{v}|,|\vec{w}| \neq 0 \quad (1)$$

$$OWV(\vec{u},\vec{v},\vec{0}) = \frac{|\vec{u}\times\vec{v}|}{|\vec{u}||\vec{v}|} \qquad ;\text{for } |\vec{u}|,|\vec{v}| \neq 0 \quad (2)$$

$$\vec{r}_{k+1} = \vec{r}_k + h\,\frac{\vec{u}(\vec{r}_k)}{|\vec{u}(\vec{r}_k)|} \qquad ;\text{for } |\vec{u}(\vec{r}_k)| \neq 0\;;k = 0,1,2,\ldots \quad (3)$$

Figure 1: Orthogonality within voxels equations.

Results: The Figure 2 shows the color maps of OWV in six slices. We also did statistical analysis about OWV, using a T-test, obtaining the results of Figure 3. For the WM Grid Tracking, the results are showed in Figure 4.

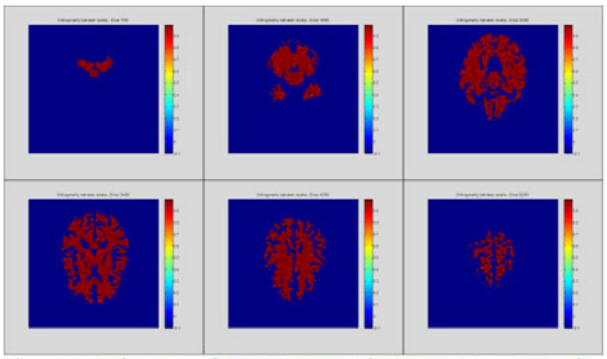

Figure 2: Color map of OWV in WM and GM using as a JET color map. Localization of cut brains: slice 7 (line 1, column 1), slice 17 (line 1, column 2), slice 25 (line 1, column 3), slice 34 (line 2, column 1), slice 43 (line 2, column 2) and slice 52 (line 2, column 3).

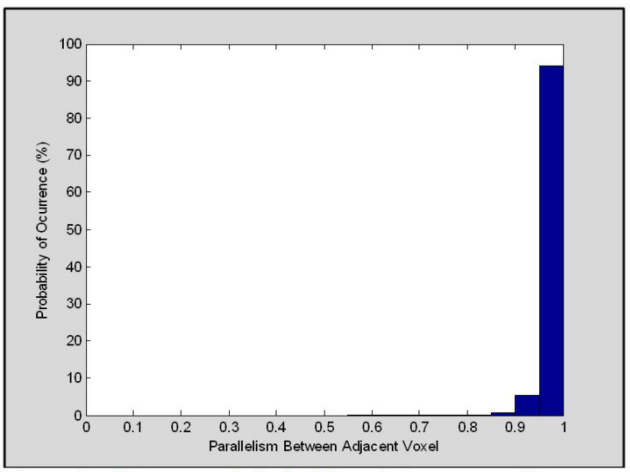

Figure 3: Histogram of Probability of Occurrence (%) versus discretized OWV com T=0.05.

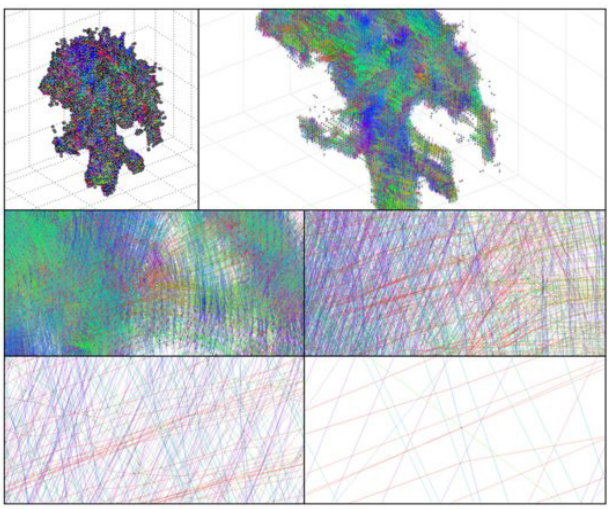

Figure 4: 3D-Plot of Fiber Tracking of brain in original and enlarged sizes of region of Callosum Corpus in remaining images. The gray points are seeded points. Sizes: original size (line 1, column 1), 2x zoom (line 1, column 2), 4x zoom (line 2, column 1), 6x zoom (line 2, column 2), 8x zoom (line 3, column 1) and 12x zoom (line 3, column 2). Coloration of lines: red: x-axis, green: y-axis, blue: z-

Discussion/Conclusion: In OWV analysis, from Figure 3, we can conclude that the three orientations are considered almost orthogonal in 99.2482% of WM or GM regions with OWV ≥ 0.90. The WM Grid tracking obtained is completely new as this approach has not been done before.

References:

1.Basser P.J., et al.,Magn. Reson.Med. (2000); 44: 625-632.
2.Mori S., Zijl P.C.M., NMR Biomed (2002); 15: 468-480.
3.Smith S.M., et al., NeuroImage (2004); 23: S208-S219.
4.Weeden V.J., Science (2012); 335: 1628-1634.

574

Detection of white matter fibers 2D planes in living humans using q-ball imaging

C.M. Santos, R. Lavrador, **N.F. Lori**
IBILI, Faculty of Medicine – University of Coimbra, Coimbra/PORTUGAL

Purpose/Introduction: The work of Wedeen et al. [1] using Diffusion Spectrum Imaging (DSI) obtained that the cerebral fiber pathways are formed by a rectilinear three-dimensional grid, and that the cerebral path crossings formed well-defined 2D sheets with 2 almost orthogonal orientations inside this sheet. But in 3D structure, there are exceptions in the cubic grid configuration, specifically in white matter (WM) regions. For example, the grid orientations in central sulcus of some species as rhesus can be an oblique twisted 2D sheet. Thus, the orthogonality between 3 WM fiber orientations is not guaranteed in every region of the brain. The purpose of this work is to test the orthogonality between 2 of the 3 WM orientations, and the parallelism of 2D-plane obtained from these 2 orientations with the 2D-plane formed by other 2 orientations, in WM regions only.

Subjects and Methods: We used FSL [2] in brain anatomical MRI data to segment Air, Cerebrospinal Fluid (CSF), Gray Matter (GM) and WM.

Parallelism Between Adjacent Voxels (PBAV): The PBAV is computed in WM, using eq. 5, Figure 1; where v_1, v_2, and v_3 are the 3 WM orientations obtained for each voxel by FSL, PBAV is based on the Orthogonality Within Voxels (OWV) defined by eq. 1, Figure 1; x^+ is the pseudo inverse of x and sign(x) = $|x|\,x^+ = x\,|x^+|$ is the signal of x. If the voxels are not in WM region or if denominator of eq. 5 is null, the PBAV will be set to a negative value to differentiate between valid values and non-defined or out-of-interest values. Finally, a set of color maps for each slice about the PBAV is obtained.

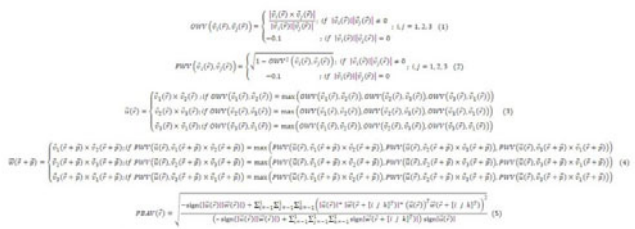

Figure 1: Parallelism between adjacent voxels equations.

Results: The Figure 2 shows the color maps of PBAV in six slices. We also did a PBAV histogram, Figure 3. In Figure 4 are the experimental 2D-plane results in a living human brain.

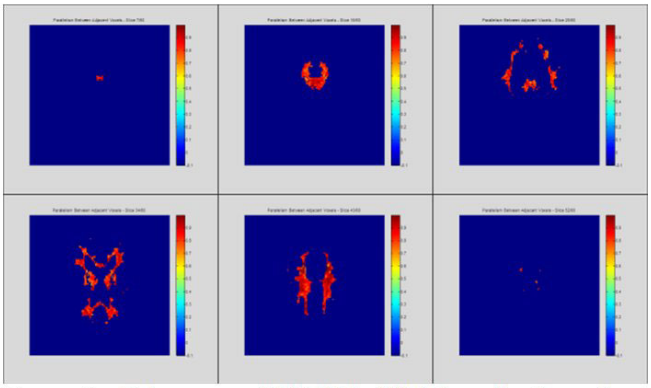

Figure 2: Color map of PBAV in WM. Localization of cut brains: slice 7 (line 1, column 1), slice 16 (line 1, column 2), slice 25 (line 1, column 3), slice 34 (line 2, column 1), slice 43 (line 2, column 2) and slice 52 (line 2, column 3).

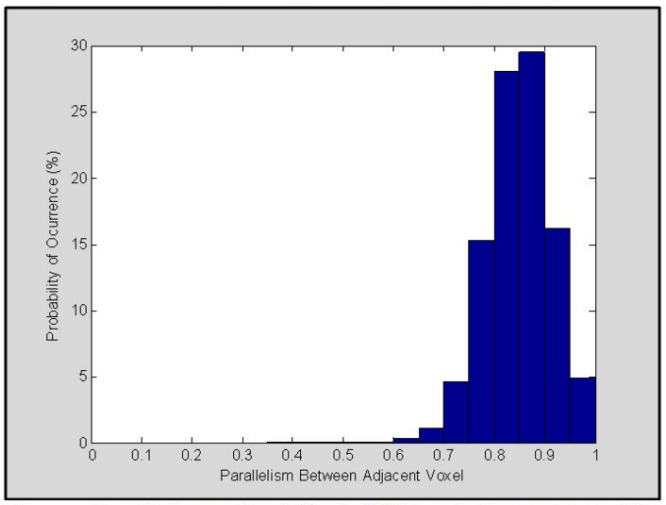

Figure 3: Histogram of Probability of Occurrence (%) versus discretized PBAV.

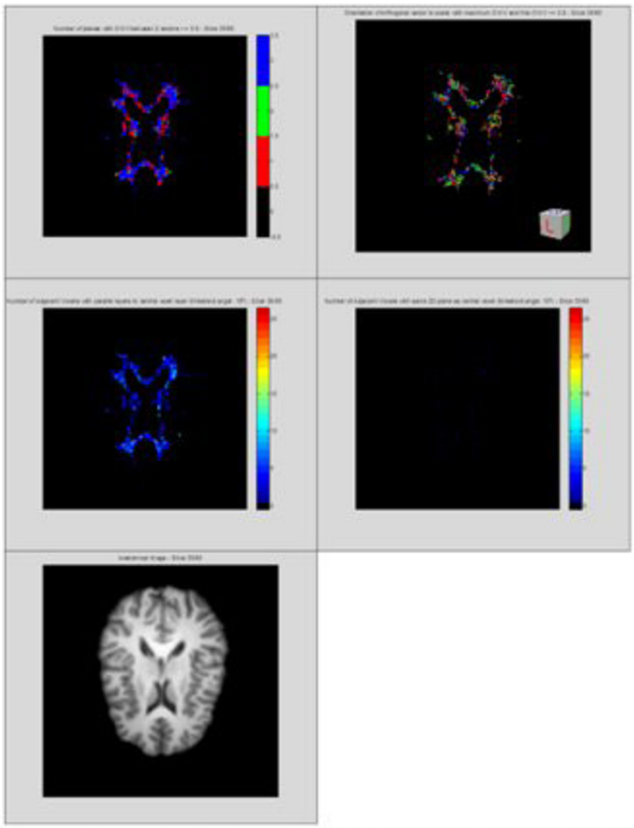

Figure 4: *Color maps in slice 35 about information of 2D-plane disposition in WM regions: Number of planes with OWV between 2 vectors >= 0.9 (94.87% of WM voxels): red: 1, green: 2, blue: 3 (line 1, column 1), Orientation of orthogonal vector to plane with maximum OWV and this OWV >= 0.9: red: x-axes, green: y-axes, blue: z-axes (line 1, column 2), Number of Adjacent Voxels with parallel layers to central voxel layer (threshold angle: 10°), (line 2, column 1), Number of Adjacent Voxels with same plane as central voxel (threshold angle: 10°), (line 2, column 2), anatomical MRI image of the same slice(line 1, column 3).*

Discussion/Conclusion: The 2D plane results put agree with the results in [1] that the 2D surfaces have orthogonal orientations. We were not able to obtain 2D planes going for more than 1 voxel except for a few voxels, but we were able to obtain that layers of parallel 2D surfaces go for several voxels in agreement with [1]. More MRI data is being acquired in order to further validate the results.

References:

1.Weeden V.J., Science (2012); 335:1628-1634.
2.Smith S.M., et al., NeuroImage (2004); 23:S208-S219.

EPOS™ Poster

Functional imaging (acquisition methods)

575

Turbulent Shear Stress Quantification using Phase Contrast MRI

C. Binter[1], V. Knobloch[1], A. Sigfridsson[1], S. Kozerke[2]
[1]Institute for Biomedical Engineering, University and ETH Zürich, Zürich/SWITZERLAND, [2]Division of Imaging Sciences and Biomedical Engineering, King's College London, London/UNITED KINGDOM

Purpose/Introduction: Excessive shear stresses in the cardiovascular system can lead to platelet activation and damage of red blood cells [1]. While Phase-Contrast (PC) MRI velocity measurements are routinely used for quantification of coherent blood flows, the encoding principle may also be modified to enable the assessment of velocity fluctuations[2]. In this work, a robust method to determine turbulent shear stresses using generalized PC-MRI is presented. Accuracy and noise sensitivity are analyzed using computer simulations and the feasibility of the method is shown on in-vivo data acquired in healthy volunteers.

Subjects and Methods: In PC-MRI, velocity fluctuations lead to a signal attenuation depending on the first gradient moment k_v[2], allowing to quantify the variance of the fluctuating velocities σ^2(**eq. 1**). Assuming a Gaussian distribution of velocities in a voxel, the full Reynolds stress tensor R can be acquired by measurements in the 3 principal and the 3 bisecting directions and solving **eq. 2**. Principal stress analysis yields the maximum shear stress as well as the turbulent kinetic energy[3]. 3D PC flow measurements were combined with a Bayesian analysis method modified from [4]. For the simulations, Particle Tracking Velocimetry data of a home-built flow phantom was used. In-vivo data were acquired in 5 healthy volunteers. All data were acquired on a 3T Philips system. With 8-fold undersampling and k-t PCA reconstruction, the nominal scan time was 15 min.

$$S(k_v) = S_0 e^{-\frac{\sigma^2 k_v^2}{2}} e^{i(v_m k_v + \varphi)} \qquad \text{eq. 1}$$

$$|\mathbf{S}| = |S_0| e^{-\frac{1}{2\rho}\begin{bmatrix} k_{v,x} & k_{v,y} & k_{v,z} \end{bmatrix} \cdot \mathbf{R} \cdot \begin{bmatrix} k_{v,x} \\ k_{v,y} \\ k_{v,z} \end{bmatrix}} \qquad \text{eq. 2}$$

Results: The results of the simulations are shown in Fig. 1. It is seen that a minimum SNR of 15 is required to keep errors of turbulent shear stress below 20% when using 43 k_v encoding points. Peak turbulent shear stress and kinetic energy are 113±23 Pa and 153±42 J/m³, respectively. Mean values are 19.6±3.4 Pa and 26±5 J/m3, respectively. Exemplary results of one volunteer are shown in Fig. 2.

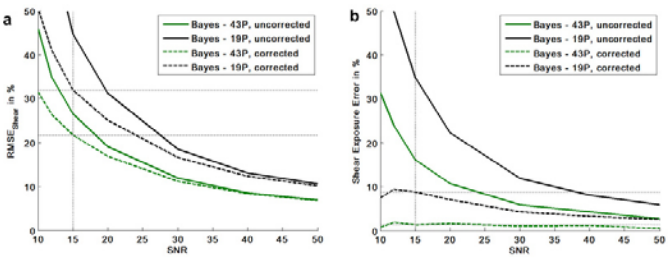

Fig. 1: Computer simulations. a) Root Mean Square Error of measured turbulent shear stress with 19 and 43 acquired k_v points (3 and 7 k_v points per direction). b) Estimated error of shear exposure obtained by averaging shear stresses along calculated pathlines. The exponential decay of the signal leads to an overestimation of measured shear stress, which is corrected in post-processing (dashed lines).

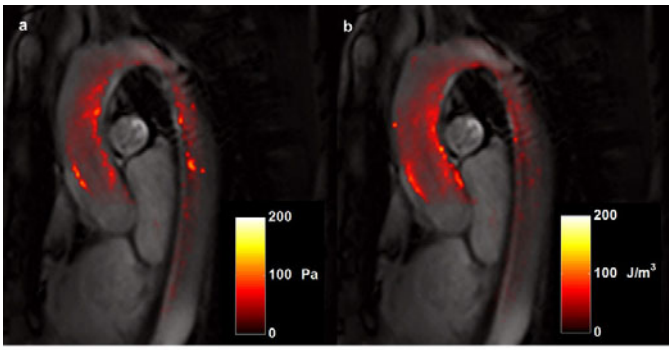

Fig. 2: Maps of Turbulent Shear Stresses (a) and Turbulent Kinetic Energy (b) in a healthy volunteer.

Discussion/Conclusion: In this work an approach for a detailed assessment of the turbulent flow field has been presented. It has been demonstrated that in vivo measurements of turbulent shear stresses are feasible, and the SNR requirements for reasonable error levels have been shown. By obtaining time-resolved shear stress and velocity maps it is possible to quantify the exposure time of red blood cells and platelets to damaging shear stress levels, leading to a more comprehensive picture about the load conditions.

References:

[1]Lu et al.,J Biomech 2001,34(10):1361-1364.
[2]Dyverfeldt et al.,MRM 2006,56(4):850-8.
[3]Malvern et al.,Prentice-Hall 1969.
[4]Xing et al.,J Magn Reson B 1995,106(1):1-9.

576

Brain activity during bladder filling – synchronic study using fMRI and urodynamics

J. Tintera[1], J. Krhut[2], P. Holy[3], P. Zvara[4], R. Zachoval[3]
[1]ZRIR MR, IKEM, Prague/CZECH REPUBLIC, [2]Department of Urology, University Hospital Ostrava, Ostrava/CZECH REPUBLIC, [3]Department of Urology, Thomayer's Hospital, Prague/CZECH REPUBLIC, [4]Division of Urology, University of Vermont, Burlington/VT/UNITED STATES OF AMERICA

Purpose/Introduction: The research of neural control of the lower urinary tract (LUT) function has been paid much attention in the recent years. We used fMRI to map brain activations during urinary bladder filling with a synchronous performance of a standard urodynamic examination.

Subjects and Methods: A total of ten voluntary female patients (age 20-68 years) were enrolled into the study with repeated cycles of filling and emptying of the bladder in order to strengthen the sensory input.

All measurements were performed on Siemens Trio 3T scanner using GRE-EPI sequence (FOV=192x192mm, voxel 3x3x3mm, TR/TE=2000/30ms, 35 slices). During the first fMRI measurement, the urinary bladder was filled until 100 ml and then two cycles of filling and emptying of only 15 ml (F/E15ml) was performed. Following, the bladder was filled until maximal capacity and strong urgency to void reported by the subject. During the next fMRI measurement, 4 cycles of F/E15ml were performed. Each cycle lasted over 28 scans, 56s (7pause-7filling-7pause-7emptying). Total of 168 dynamical scans was analyzed after data concatenation.

Statistical analysis was done in SPM8 using GLM. We defined two models describing the situation simultaneously: A- step function (empty versus full bladder), B-periodic cycling with F/E15ml. Final group statistics using t-test was calculated (p=0.001 uncorrected).

Results: Group analysis of the brain activity contrasting empty and full bladder (model A) detected activations in the area of the orbital surface of the inferior frontal lobe (olfactory cortex, bordering with frontal cingulum) [-5,20,-10], in the left gyrus parietalis superior [-25,-60,52] and theleft central area (gyrus postcentralis) [-5,-35,60] – fig.1.

Analyzing activations in reaction to rapid filling/emptying cycles of the urinary bladder (model B), two regions of activity were found: area of the brainstem [7,-10,-10] and thalamus with subcortical gray matter nuclei [10,-15,0] – fig.2.

In the subject level, we also frequently identified activation in the area of right cingulate gyrus [5,-47,22], left thalamus [-9,-10,11], left middle frontal gyrus [-36,33,45], inferior frontal gyrus in left orbital part [-46,20,-6] and in right orbital part [47,30,-14].

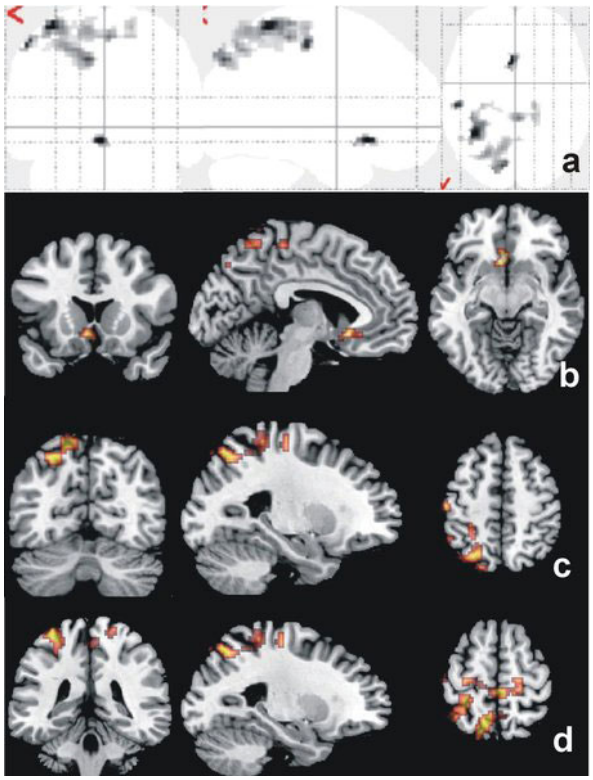

Fig.1 activations with model A: a) MIP, b) [-5,20,-10], c) [-25,-60,52], d) [-5,-35,60]

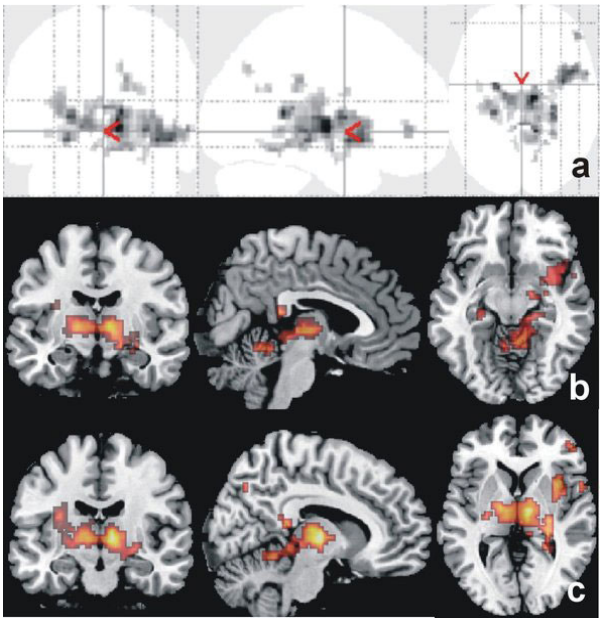

Fig.2 activations with model B: a) MIP, b) [7,-10,-10], c) [10,-15,0]

Discussion/Conclusion: Our work further broadened the protocol suitable for research of neural control of LUT with the use of fMRI. Our results correspond with available literary data and are coherent with the present hypothetical functional model of LUT neural control.

References:

Supported by MZCR Institutional grant 00023001IKEM

EPOS™ Poster

Functional imaging (data analysis)

577

ASL perfusion and structural MRI for computer aided diagnosis in dementia

M. Sousa[1], M. Silveira[1], P. Vilela[2], S. Nunes De Oliveira[2], P. Figueiredo[1]
[1]Department of Bioengineering, Institute for Systems and Robotics / Instituto Superior Tecnico, Technical University of Lisbon, Lisbon/PORTUGAL,
[2]Imaging Department, Hospital da Luz, Lisboa/PORTUGAL

Purpose/Introduction: Computer aided diagnostic techniques have shown promising results in the early diagnosis of dementia. Diagnostic criteria include neuroimaging biomarkers, based on structural MRI and functional radiotracer techniques [1]. Arterial Spin Labelling (ASL) is currently being evaluated as an alternative, non-invasive and cost-effective MRI technique to obtain functional information from brain perfusion measurements [2]. Here, we aim to investigate the value of using ASL perfusion as well as structural MRI, for automatic diagnosis of Alzheimer's disease (AD) and Mild Cognitive Impairment (MCI).
Subjects and Methods: MRI data from 10 AD, 15 MCI and 13 cognitively normal (CN) subjects, matched for age and gender, were used for development and validation of the classification method. For each subject, both high-resolution T1-weighted images (MPRAGE, 1x1x1mm^3) and ASL perfusion images (Pulsed ASL PICORE-Q2TIPS, 4x4x10mm^3) were collected on a 3T Siemens system. Images were preprocessed using FSL (www.fmrib.ox.ac.uk/fsl) to obtain two types of features: 1) structural: grey matter density (GMD) images; and 2) functional: perfusion or cerebral blood flow (CBF) images. Both images were registered to a common template (MNI152, Montreal Neurological Institute) using non-linear registration (www.fmrib.ox.ac.uk/fsl/fnirt). Two methods were used for feature extraction: 1) voxel-by-voxel values selected using Mutual Information criteria; and 2) ROI-averaged using the Harvard-Oxford ROIs. Based on these features, a Support Vector Machine classifier was applied using the LibSVM toolbox (www.csie.ntu.edu.tw/~cjlin/libsvm/) on the following experiments: AD vs. CN, MCI vs. CN, and AD vs. MCI. The fusion of output labels from structural and perfusion classifiers was then performed for each experiment using Weighted Majority Vote (Wmaj) or Naive Bayes (NB).
Results: The accuracies obtained by voxel-by-voxel and ROI-based analyses of GMD, CBF and their fusion, in each experiment, are presented in Table 1. Maps of the voxels with the most relevant GMD and CBF features are shown in Figure 1. These include voxels bordering gray matter for GMD and exhibit an asymmetrical pattern for CBF, as expected.

Table 1. Accuracy (%) obtained for each experiment and for each type of features.

	GMD	CBF	Fusion	Fusion (NB)
Voxe-by-voxel				
AD vs. CN	91.3	65.2	91.3	82.6
MCI vs. CN	57.1	82.1	82.1	82.1
AD vs. MCI	96.0	64.0	84.0	76.0
ROI-based				
NC vs AD	73.9	52.2	73.9	73.9
NC vs MCI	64.3	57.1	57.1	53.6
AD vs MCI	64.0	52.0	56.0	56.0

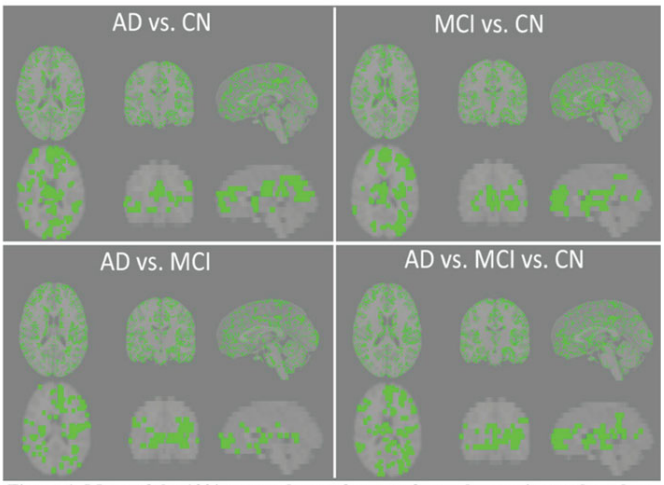

Figure 1. Maps of the 10% most relevant features for each experiment, based on GMD (top) and CBF (bottom).

Discussion/Conclusion: The results obtained show that good classification performances based on structural and perfusion features can be achieved; however, the multimodal fusion of the individual classifiers requires further investigation. The size of the samples must be extended in order to allow final conclusions about the utility of the proposed methodology. Nevertheless, our results indicate that ASL perfusion images may be useful in computer aided diagnosis methods in dementia.
References:
[1] Perrin RJ et al. (2009), Nature, 461(7266):916-922.
[2] Golay X, Guenther M. (2012) MAGMA, 25(2):79-82.

578

Correlation of SPECT and DCE-MRI in a neuroendocrine tumour model

K. Bol[1], J.C. Haeck[2], H.C. Groen[3], W. Niessen[1], M.R. Bernsen[4], M. De Jong[5], J.F. Veenland[1]
[1]Biomedical Imaging Group Rotterdam, Erasmus MC, Rotterdam/NETHERLANDS, [2]Radiology, Erasmus MC, Rotterdam/NETHERLANDS, [3]Nuclear Medicine, Erasmus MC, Rotterdam/NETHERLANDS, [4]Radiology & Nuclear Medicine, Erasmus MC, Rotterdam/NETHERLANDS, [5]Nuclear Medicine & Radiology, Erasmus MC, Rotterdam/NETHERLANDS

Purpose/Introduction: Neuroendocrine tumours overexpress somatostatin receptors on the cell membrane. Using radiolabeled somatostatin-peptide-analogues that bind to these receptors, tumours can be imaged with SPECT or PET, and treated (Peptide Receptor Radionuclide Therapy - PRRT). High resolution SPECT imaging with ^{111}In -DTPA-Octreotide (Octreoscan) often reveals a heterogeneous peptide uptake in preclinical tumour models[1]. Tumour vascular characteristics that may influence the peptide distribution and uptake can be studied non-invasively using DCE-MRI. In this study we investigate the relation between radiolabeled peptide uptake imaged with SPECT, and Dynamic Contrast-Enhanced (DCE) MRI derived perfusion parameters, in a neuroendocrine pancreatic rat tumour.
Subjects and Methods: Lewis rats (n=2) were inoculated subcutaneously with receptor-positive pancreatic tumour cells (CA20948). When the tumour reached a diameter of 1.5 cm, the animals were injected with 50 MBq ^{111}In-DTPA-Octreotide and imaged with SPECT-CT and MRI (SWI, T1-weighted and DCE). MRI was registered to SPECT-CT and the SWI sequence was used to outline the tumours. For voxel-based quantification of DCE-MRI data three different analysis methods were used: semi-quantitative (area-under-the-curve (AUC), AUC first 60 seconds (AUC60), maximum enhancement (Smax), washin, washout), quantitative analysis using the standard Tofts equation (K^{trans}, k_{ep}), and principal component analysis (pc-score)[2]. Spearman's rank correlation coefficients between SPECT and DCE parameters were computed

over all voxels in the tumour. In addition SPECT tumour uptake values were grouped into quintiles, and median DCE parameter values for the first, third and fifth quintile were compared using the t-test.

Results: Clear trends can be seen in SPECT versus DCE parameters: all parameter values increased at increasing peptide uptake (figure 1). Spearman's rank correlation coefficient (ρ) between SPECT and DCE parameters was significant for all DCE-parameters for both tumours ($p<0.001$). For the semi-quantitative and quantitative parameters ρ was between 0.34 and 0.65 (table 1). Although ρ was low for the first pc-score, for the second pc-score ρ was comparable to semi- and quantitative parameters. Median DCE parameter values were all significantly different ($p<0.05$) between first and third and between third and fifth quintile of SPECT uptake.

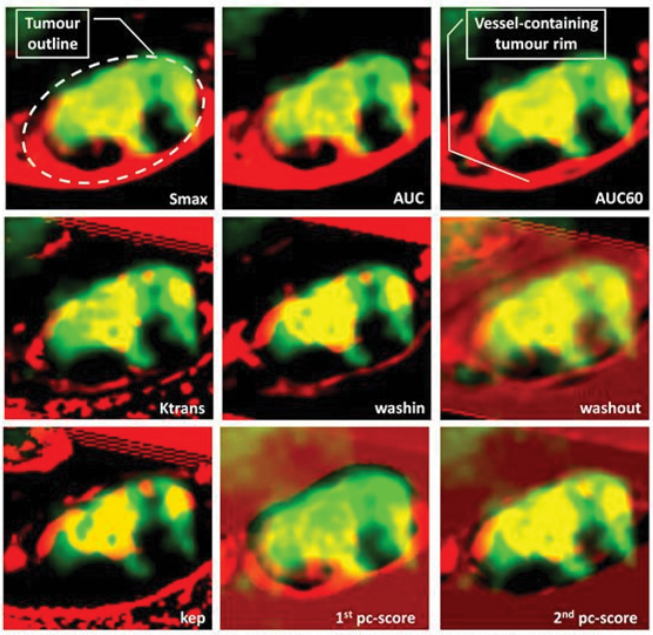

Figure 1: Example of overlap (yellow) between DCE-parameter maps (red) and SPECT peptide uptake (green); AUC = area under the curve, AUC60 = area under the curve fist 60 seconds, Smax = maximum enhancement, pc-score = principal component score

Table 1: Spearman's correlation coefficient between SPECT uptake and different DCE parameters (p<0.005)

DCE parameter	Tumour 1	Tumour 2
Smax	0.52	0.48
AUC	0.43	0.34
AUC60	0.62	0.57
washin rate	0.65	0.60
washout rate	0.62	0.62
K^{trans}	0.59	0.46
k_{ep}	0.58	0.55
1st pc-score	0.19	0.25
2nd pc-score	0.54	0.59

Discussion/Conclusion: In our pancreatic tumour model, tumour perfusion measured with DCE-MRI shows a substantial correlation with radiolabeled peptide uptake in SPECT. With DCE-MRI influences of vascular characteristics on uptake and distribution of radiolabeled peptides in the tumour can be quantified, opening opportunities for treatment response prediction.

References:

[1] Müller, C., 2007, Cancer Biotherapy & Radiopharmaceuticals, 151-159
[2] Bruwer, M.-J., 2008, J. Chemometrics, 708–716

579

Comparing MELODIC and the conn toolbox and the impact of physiological artifact correction in resting state fMRI using DRIFTER

S. Bollmann[1], K. Payette[1], C. Ghisleni[1], S.S. Poil[1], R. O'Gorman[1], D. Brandeis[2], P. Klaver[3], E. Martin[1], L. Michels[1]
[1]Zentrum fuer MR Forschung, Kinderspital Zuerich, Zürich/SWITZERLAND, [2]Department of Child and Adolescent Psychiatry, University of Zürich, Zürich/SWITZERLAND, [3]nstitute of Psychology, Division of Abnormal Psychology and Clinical Intervention, University of Zurich, Zürich/SWITZERLAND

Purpose/Introduction: Spontaneous fluctuations of the blood oxygenation level dependent signal at rest have contributed significantly to an improved understanding of brain networks in health and disease. Currently two different methods are widely used to analyze resting state fMRI data: seed-based correlation analysis (SCA), and independent component analysis (ICA) (Cole et al. 2010). However, the relative merits of each method are not well understood as few studies have directly compared these approaches.

Two state of the art software packages were compared: MELODIC (Beckmann et al. 2005) as an example of ICA and the conn toolbox (http://web.mit.edu/swg/software.htm) for SCA. The effects of physiological artifact correction on each method were investigated using DRIFTER (Särkkä et al. 2012), a recently published method for removing physiological noise from fMRI data.

Subjects and Methods: We studied 15 adult subjects (mean age 34.63±10.8 years, 7 females). MRI data was acquired on a 3.0 T (GE Healthcare, Milwaukee, WI, USA) whole-body scanner. For fMRI, 35 axial slices covering the whole brain were acquired with a T2*-sensitive multi-slice echo planar imaging sequence (repetition time =1.925 s; echo time=32 ms; voxel size = 3x3x3 mm; flip angle =75°).

Physiological data was recorded with the standard GE respiratory belt and heart rate photo plethysmogram.

The resting state session consisted of alternating eyes-open (EO) and eyes-closed (EC) blocks of 2.5 min duration (in total 10 minutes: EC-EO-EC-EO).

Results: Both MELODIC and the conn toolbox deliver similar results, demonstrating typical resting state networks described in the literature (Cole et al. 2010) and are altered after removing physiological confounds using DRIFTER. MELODIC rearranges the importance of some components drastically post-DRIFTER, however the two main components remain unchanged. The SCA approach shows a difference in resting state patterns after removing physiological artefacts in both ROI-ROI and seed-voxel correlations.

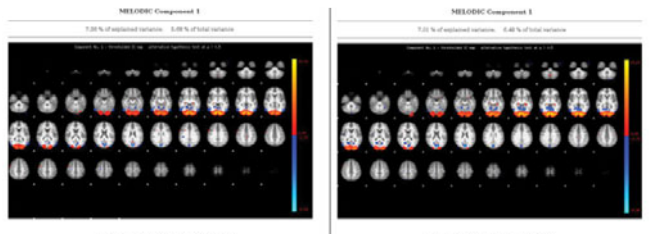

Figure 1 - In the above two images we see that the component with the highest explained variance (a resting state network component titled "extrastriate visual cortex") did not change drastically. This shows that MELODIC is able so separate resting state patterns from physiological noise in case the network is very prominent.

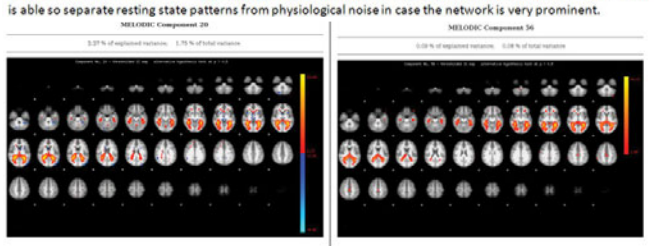

Figure 2 – Here we see a component which lost a lot of explained variance after DRIFTER ran – we think that this is a component with lots of physiological noise (since it is close to the brainstem and it is not a typical pattern found in the resting state literature). This shows that even the ICA approach cannot fully distinguish between physiological noise and real components. In this case DRIFTER simplified the interpretation of the results drastically.

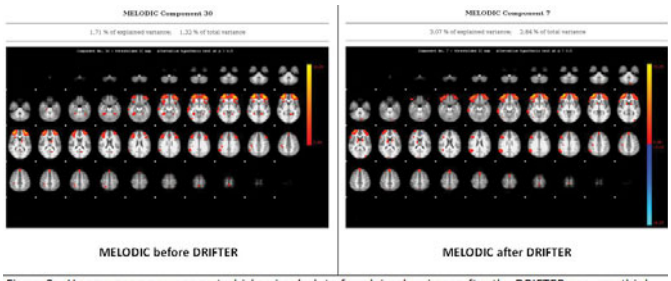

MELODIC before DRIFTER | MELODIC after DRIFTER

Figure 3 – Here we see a component which gained a lot of explained variance after the DRIFTER ran – we think that this is a component that got more important after removing physiological noise.

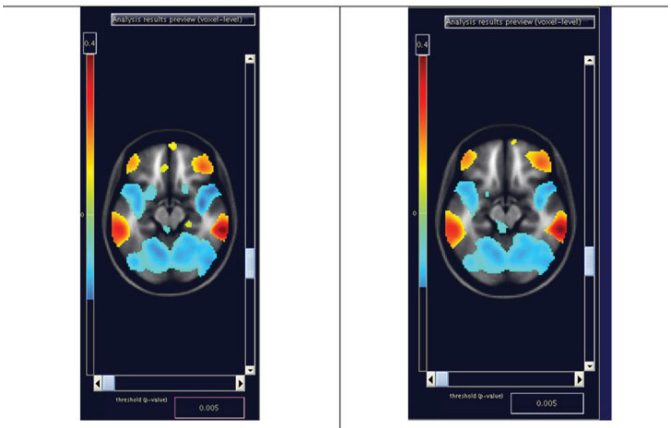

CONN toolbox before DRIFTER | CONN toolbox after DRIFTER

Figure 4 – In the above two images we see the correlation pattern of the Seed Region "RLP". DRIFTER removes some spots close to the brainstem and the midline making the interpretation of the pattern easier and more similar to the patterns described in the literature.

Discussion/Conclusion: Both the conn toolbox and MELODIC improve after the removal of physiological noise components. The MELODIC method appears to be more robust against the presence of physiological noise as the two main components remain the same after DRIFTER. However, ICA is not able to completely separate the physiological data into components separate from those of brain activation. Also with the SCA method, after DRIFTER had been run on the data the interpretation of the resting state networks was easier.

References:

Beckmann, C.F. et al., 2005, Philos Trans R Soc Lond B Biol Sci, pp. 1001-1013.
Cole, D.M., et al., 2010, Front Syst Neurosci, pp. 1-15.
Särkkä, S. et al., 2012, NeuroImage, pp. 1517-1527.

580

FMRI oddball paradigm in the first-episode patients with schizophrenia

M. Ublinskiy[1], N. Semenova[1], I. Lebedeva[2], V. Kaleda[2], S. Sidorin[3], A. Petryaykin[1], T. Akhadov[3], A. Tyurneva[1]
[1]Radiology, Children's Clinical and Research Institute Emergency Surgery and Trauma, Moscow/RUSSIAN FEDERATION, [2]Laboratory of neurophysiology, National Mental Health Research Center, Moscow/RUSSIAN FEDERATION, [3]Radiology Department, Children's Clinical and Research Institute of Emergency Surgery and Trauma, Moscow/RUSSIAN FEDERATION

Purpose/Introduction: The study was aimed to the research of the first episode of schizophrenia. fMRI variant of the auditory oddball paradigm was used to estimate localization of areas of hemodynamic response (HR) and to identify the cerebral structures which are involved in the processes of selective attention.
Subjects and Methods: Nine male right-handed patients (17-28 years) with the first episode of schizophrenia were examined. Nine healthy right-handed subjects comprised the control group. fMRI was conducted on 3T Philips Achieva scanner EPI BOLD (T2 EPI, TR 2000 ms, TE 30 ms, EPI Factor 69, FOV 240, Thk 4 mm, NSA 1, 150 dynamics, 30 slice in one dynamic). The standard two-tones auditory oddball paradigm (non-target (1000 Hz), target (2000 Hz), tones) was applied. The subjects were instructed to press button by the right thumb in response to targets. FMRI data were processed using a workstation Philips EBWS. Intergroup analysis and voxel-based morphometry (VBM) were done by SPM8. In both groups the HR time dependency analysis was done for the motor cortex subarea associated with the right thumb.
Results: No differences in the speed and accuracy of executing the task between two groups were detected. In both groups HR (target vs non-target) was mostly pronounced in the voxels attributed to parietal and frontal cortex. The intergroup analysis didn't show statistically significant ($p<0.001$) differences. The most expressed HR was revealed in the motor and auditory cortexes.
No statistically significant differences were identified between groups according to VBM. The analysis of the raw fMRI data has revealed that the time corresponding to the maximum value of the HRF for two groups is equal to 6 sec. The curves of the relative increase of HR in both groups reduced to the level of the initial value since 10 seconds. A significantly higher increase of HR in control group than in patients has been found.
Discussion/Conclusion: In patients with the first episode schizophrenia there was found the decreased amplitude of the HRF in area involved in the support of task required motor response. Considering the absence of statistically significant intergroup differences in the behavioral measures, the mechanisms should involved the differences in hemodynamic and consequently metabolic brain functioning support. As the intensity of HR is proportional to the level of the glucose consumption [1], a hypothesis on the lower demands of glucose in patients brain cells metabolism was suggested.

References:

1. Sokoloff L. 1977. J. Neurochem. 29:13–26.

581

Comparing PCA with model-free and compartment-model-based methods in DCE-MRI

K. Bol[1], L. Alic[2], J.C. Haeck[3], M.R. Bernsen[4], W. Niessen[2], J.F. Veenland[2]
[1]Biomedical Imaging Group Rotterdam, ErasmusMC, Rotterdam/NETHERLANDS, [2]Biomedical Imaging Group Rotterdam, Erasmus MC, Rotterdam/NETHERLANDS, [3]Radiology, Erasmus MC, Rotterdam/NETHERLANDS, [4]Radiology & Nuclear Medicine, Erasmus MC, Rotterdam/NETHERLANDS

Purpose/Introduction: Although Dynamic Contrast-Enhanced Magnetic Resonance Imaging (DCE-MRI) is increasingly used in oncology to quantify vascular tumour characteristics, a standard analysis method has not yet been adopted. Principal component analysis (PCA) was recently proposed as an alternative to the more conventional model-free and compartment-model-based analysis methods[1]. The advantage of PCA over the other two methods is that no additional data is required, no model assumptions are made, and the whole time trajectory of contrast-enhancement is included. To identify the significance of PCA in DCE-MRI, we used both simulated data and a tumour model to compare PCA-derived parameters, the so-called pc-scores, with the two conventional models.
Subjects and Methods: In this two-part study we first simulated contrast-concentration-over-time curves with the compartment-model-based standard Tofts equation, using a range of K^{trans} values (0-0.5 min^{-1}), arterial input function from literature[2], a temporal resolution of 5 seconds, and various scanning times (3.5 - 10 - 30 minutes). These simulated curves were then used to perform model-free analysis and PCA. The second part of the study included two preclinical datasets (scan times 10 and 30 minutes) from a pancreatic tumour model (CA20948). From these datasets we derived model-free parameters (area under the curve (AUC), maximum enhancement (Smax), washin and washout rate), compartment-model-based parameters (K^{trans}, k_{ep}), and pc-scores. Spearman's rank correlation coefficients between all DCE-parameters were computed.
Results: Spearman's correlation coefficient in the simulated data was high (>0.9) between the first pc-score, K^{trans} and washout. The correlation between the second pc-score and K^{trans} was 0.6, between the second pc-score and washout 0.75. The preclinical datasets showed two distinct groups with strong correlations (0.7-0.9): group1 consisted of the first pc-score, Smax and AUC, group 2 of the second pc-score, k_{ep}, washin and washout (figure 1). Only in the 30-minute preclinical dataset K^{trans} correlated strongly with the second

pc-score (0.8), for the 10-minute dataset the correlation between K^{trans} and the second pc-score was 0.6.

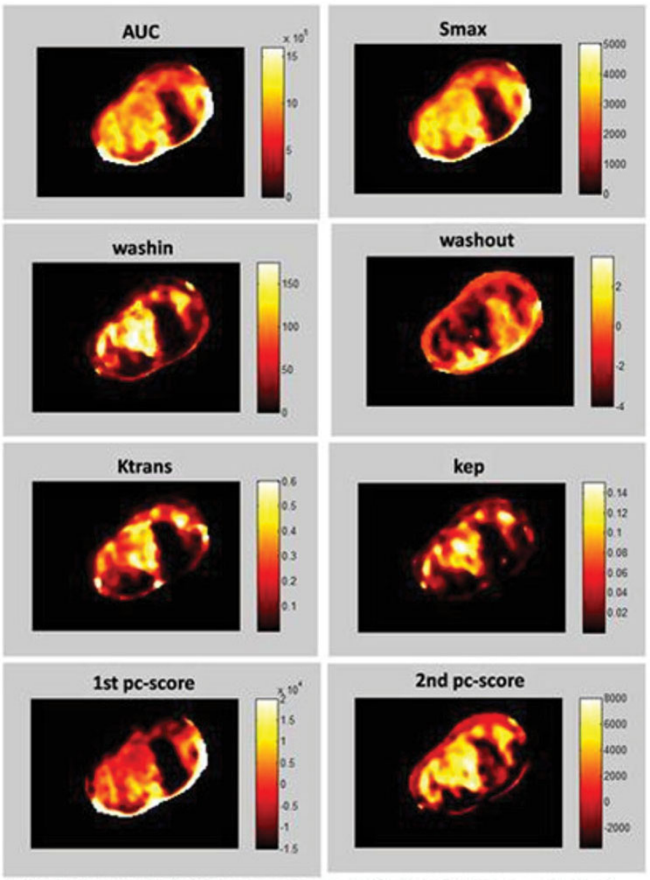

Figure 1: Example of DCE-parameter maps for the 10-minute preclinical dataset; AUC = area underthe curve, Smax = maximum enhancement

Discussion/Conclusion: While our results indicate that the amount of contrast entering the tumour is correlated with the first pc-score, the second pc-score appears to be more related to pharmacokinetic dynamics inside the tumour. Thus while PCA appears to be a promising tool for quantifying DCE-MRI in oncology, the correlation between the pc-scores, K^{trans} and model-free parameters should be investigated further.

References:

[1] Bruwer, M.J., 2008, J. Chemometrics, 708–716
[2] McIntyre, D.J.O, 2004, NMR Biomed.132–143

582

Volume definition in pancreatic cancer using Diffusion Weighted MRI and FDG PET

R. Haase[1], G. Wolf[2], T. Paulus[3], C. Zimmermann[4], R. Grützmann[4], K. Zöphel[5], N. Abolmaali[3]
[1]Biological and Molecular Imaging Group, OncoRay, TU Dresden, Dresden/GERMANY, [2]Institut für Klinische Chemie und Labormedizin, University Hospital Carl Gustav Carus, TU Dresden, Dresden/GERMANY, [3]Institue and Policlinic for Radiology, University Hospital Carl Gustav Carus, TU Dresden, Dresden/GERMANY, [4]Klinik und Poliklinie für Viszeral-, Thorax- und Gefäßchirurgie, University Hospital Carl Gustav Carus, TU Dresden, Dresden/GERMANY, [5]Clinic and Policlinic for Nuclear Medicine, University Hospital Carl Gustav Carus, TU Dresden, Dresden/GERMANY

Purpose/Introduction: For inoperable pancreatic cancer patients, neoadjuvant radiochemotherapy may be an option to reach operability. In morphologic imaging, tumour volume definition is often difficult. Alternatively, functional imaging such as [18F]fluorodeoxyglucose positron emission tomography (FDG-PET) or diffusion weighted magnetic resonance imaging (DWI) can be used for volume definition. DWI may further aid to detect early response after initiation of therapy. Aim of the study was to compare DWI derived volumes with those from FDG-PET.

Subjects and Methods: Between January 2011 and February 2012 15 patients were examined for an ongoing mono-institutional prospective study on neo-adjuvant therapy of pancreatic cancer. As part of the imaging protocol, 13 of these patients initially retrieved a whole body FDG-PET/CT scan and an abdominal DWI (six b-values from 50 to 800 s/mm in 11 cases, four b-values from 50 to 800 s/mm² in two cases) scan before therapy start. An experienced radiologist (NA) drew a spherical region of interest (ROI) around the tumour using in house developed software on FDG-PET and b=800 DWI images. The procedure is shown in figure 1. The software allowed delineation of the object in the ROI that shows signal intensity above the average. For both modalities the volume V was measured. Bland-Altman analysis was performed for corresponding VPET and VDWI values. Standard uptake values SUVmax and SUVmean of the target volume in the FDG-PET data set were determined. Additionally, the apparent diffusion coefficient ADCmean in the DWI data set was calculated by mono-exponential fitting based on all available b-values.

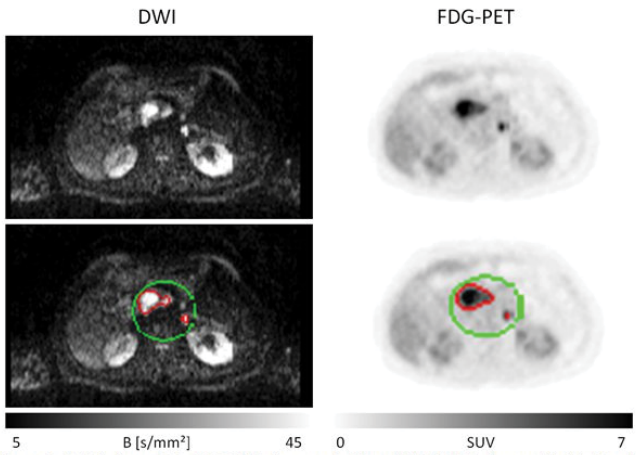

Figure 1: Axial slices of b=800 DWI data set (left) and FDG-PET data set (right) showing contours (bottom row) which were analysed. The three dimensional spherical ROI which was placed by the observer is shown in green, the afterwards automatically generated target volume definition is shown in red.

Results: Target volume delineation in FDG-PET resulted in V_{PET}=46.2±13.8 ml, SUV_{max}=7.4±2.8 and SUV_{mean}=3.5±1.0 respectively. DWI segmentation resulted in V_{DWI}=39.2±18.7 ml and ADC_{mean}=1768±326 µm²/s. Bland-Altman analysis, shown in figure 2, showed that FDG PET based volume definitions are slightly higher than DWI based volumes (bias is about 7ml or 24%). A detailed view on the determined V, SUV and ADC measures is given in table 1.

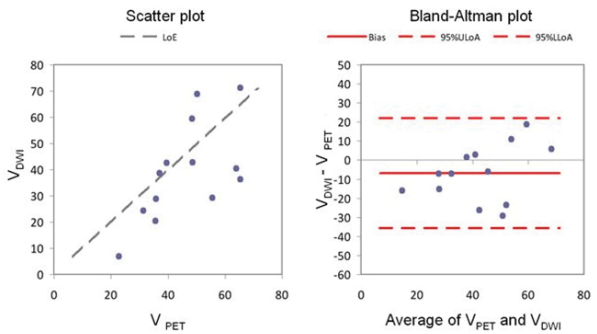

Figure 2: Scatter plot and Bland-Altman plot of V_{PET} versus V_{DWI} show that FDG PET based volumes are slightly overestimated in comparison to DWI.

Table 1: Detailed view on measured Volume, SUV and ADC values.

Patient	V_{PET} [ml]	SUV_{max}	SUV_{mean}	+/-	V_{DWI} [ml]	ADC_{mean} [µm²/s]	+/-
1	31,4	7,1	3,0	0,8	24,3	1650	162,3
2	35,9	3,4	2,3	0,3	28,8	1605	59,3
3	64,0	6,4	3,2	0,7	40,4	1686	55,6
4	48,6	7,2	3,7	0,8	42,7	1639	53,7
5	50,2	7,3	3,5	0,8	68,8	1477	76,6
6	22,8	2,6	1,6	0,2	6,8	2459	152,6
7	48,4	7,5	3,7	1,1	59,4	1674	49,3
8	65,4	13,0	5,6	1,7	71,2	1757	101,4
9	65,4	4,7	2,9	0,4	36,3	2506	175,3
10	35,7	9,9	4,0	1,4	20,3	1596	87,0
11	39,6	8,9	4,3	1,3	42,5	1744	48,3
12	37,1	8,3	3,5	1,1	38,7	1650	162,3
13	55,6	10,1	4,0	1,1	29,3	1540	76,6
Average	46,2	7,4	3,5		39,2	1768	
StdDev	13,8	2,8	1,0		18,7	326	

Discussion/Conclusion: FDG-PET based tumour volumes are slightly higher than DWI based volume definitions. DWI data sets acquired two days after therapy start are currently analysed to determine benefits for early response monitoring.

583

EPI versus real-time fMRI autoregressive modeling

R. Mutihac[1], A. Braun[2], T. Balkin[3]
[1]Department of Physics, University of Bucharest, Bucharest/ROMANIA, [2]Department of Intramural Research, NIH / NIDCD, Bethesda/MD/UNITED STATES OF AMERICA, [3]Psychiatry and Neuroscience, WRAIR, Silver Spring/MD/UNITED STATES OF AMERICA

Purpose/Introduction: Analysis of real-time fMRI signals is subject to temporal dispersion of the hemodynamic response and aliasing of physiological noise. Yet echo-volumar imaging [1], inverse imaging [2], and highly undersampled projection imaging [3] enable temporal resolution down to 100 ms. Short acquisition poses the problem of serial correlations among voxels studied here in the context of univariate autoregressive (AR) models.
Subjects and Methods: No direct means exist to determine the model order p of a model AR(p). As p increases the estimates are more accurate. Yet the plot of the root mean square between the series estimated by the AR(p) coefficients and the actual series typically decreases rapidly up to a certain order and much slowly thereon (Fig.1). Both the time series of residuals and the significance level were computed by a modified Li-McLeod portmanteau test.

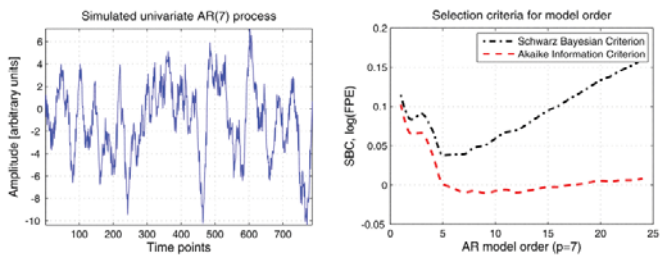

Fig. 1 - Simulated univariate autoregressive time series (left) and selection citeria for model rank (right).

Results: Full brain fMRI data were analyzed in terms of BOLD contrast in a finger-tapping multi-subject multi-session task. Both fast spin echo EPI and multi-slab EVI [4] data acquisitions were carried out at 3 T. ARfit algorithm [5] provided approximations to Schwarz's Bayesian Criterion [6] leading to the smallest mean-squared prediction error, and to the logarithm of Akaike's final prediction error [7] as model order selection means (Fig.2 & Fig.3). Parameters not statistically significant were discarded and the adequacy of representation was evaluated by the uncorrelatedness of residuals (Fig.4).

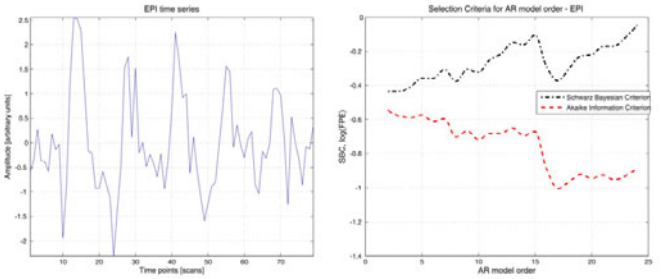

Fig. 2 - EPI time series (left) and model order selection (right).

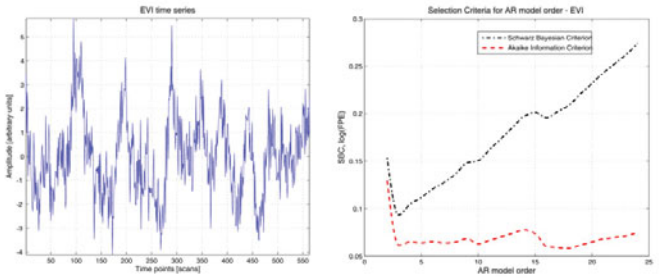

Fig. 3 - EVI time series (left) and model order selection (right).

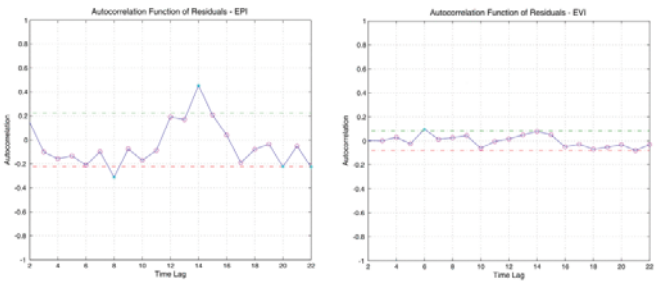

Fig. 4 - Uncorrelatedness of residuals: EPI (left) and EVI (right).

Discussion/Conclusion: Dynamics of complex systems can be inferred from analyses of stochastic time series models fitted to experimental data. The high order of fMRI data AR models entails that correction of serial correlations is crucial in statistical analysis.
Since each voxel is represented as a time series of neurophysiological activity summing up the cognitive and sensorimotor conditioning that underlies the BOLD response, a multivariate autoregressive model (MAR) would be more realistic. MAR models are fully connected and fitting them to data generates sub-networks that may explain the observed brain dynamics.

References:

- Rabrait C. et al. (2008) *J Magn Reson Imaging* **27**(4):744-53.
- Lin F.H. et al. (2010) *Neuroimage* **49**(4):3086-98.
- Grotz T. et al. (2009) *Magn Reson Med* **62**(2):394-405.
- Posse S. *et al.* (2010) ISMRM *Abstracts*, 3590.
- Neumaier A. et al. (2001) *ACM Trans Math Software* **27**(1):27-57.
- Schwarz G (1978) *Ann Statist* **6**:461-64.
- Akaike H. (1974) *IEEE Transactions on Automatic Control* **19**(6):716-23.
- Akaike H (1971) *Ann Inst Statist Math* **23**:163–180.

Aknowledgements: Mutihac gratefully acknowledges the support from NAS/NRC Award #W81XWH-07-2-0001-0114.

584

Functional MR to monitoring cystic fibrosis (CF) lung disease

F. De Leo[1], S. Bertolo[1], P. Ciet[2], M. Ros[3], G. Morana[1]
[1]Radiology, Ca' Foncello Hospital, Treviso/ITALY, [2]of Radiology and Pediatrics Pulmonology, Erasmus-MC Rotterdam, Rotterdam/ NETHERLANDS, [3]Pediatrics, Ca' Foncello, Treviso/ITALY

Purpose/Introduction: CF is the most common lethal hereditary disease in the caucasian population. Currently, no sensitive, radiation-free methods are available to localize lung inflammation. Developments in MR imaging technique have made possible its larger use in thoracic imaging to obtain morphological and also functional information. The aim of our study is assess the sensitivity of chest-MRI to monitor inflammation and disease in CF lung.
Subjects and Methods: In this study will be enrolled, during 10 months, 20 patients (age>8), 10 cases e 10 controls. Each patients will perform 2 RM examinations: pre and post antibiotic treatment for the case group, after and before 2 weeks for the control group.
The MR examinations were performed on a 1.5-T MRI (Siemens Avanto): Propeller BLADE PD (TR/TE/α: 1030/26 ms/150°) with navigator, TRUFI (TR/TE/α: 3/0.99 ms/66°), DWI_EPI with 11 b-value (TR/TE: 4100/52 ms). In post processing can be calculate the diffusion and perfusion maps with ICE-program_Siemens and ventilation/perfusion maps with lung_fmri software_Siemens. Moreover we can be calculate the IVIM (Intravoxel Incoherent Motions) features with the software that we have implementated with Matlab2010: D and D*(diffusion and pseudodiffusion coefficient), ADC (apparent diffusion coefficient) and pf (perfusion fraction). Statistics Analysis: Pearson test; Kruskal-Wallis and Wilcoxon test, ROC analysis (Spss and Matlab).
Results: The study is a working in progress, but preliminary results seem to be really interesting. IVIM features in inflammation area are: ADC 1.16 x 10 $^{-3}$ mm^2/sec ± 0.29, D 0.76 x 10 $^{-3}$ mm^2/sec ± 0.34, D* 0.94 x 10 $^{-3}$ mm^2/sec ± 0.23, pf 23%+ 6.1 in case group (pre-antibiotic); ADC 1.24 x 10 $^{-3}$ mm^2/sec ± 0.31, D 0.98 x 10 $^{-3}$ mm^2/sec ± 0.23, D* 1.03 x 10 $^{-3}$ mm^2/sec ± 0.35 , pf 38%+ 5.2 in case group (post-antibiotic); 1.19 x 10 $^{-3}$ mm^2/sec ± 0.42 , D 1.01 x 10 $^{-3}$ mm^2/sec ± 0.37 , D* 1.1 x 10 $^{-3}$ mm^2/sec ± 0,45, pf 34%+ 3.9 in control group. D increases after antibiotic and is not far from the coefficient found in the control group.

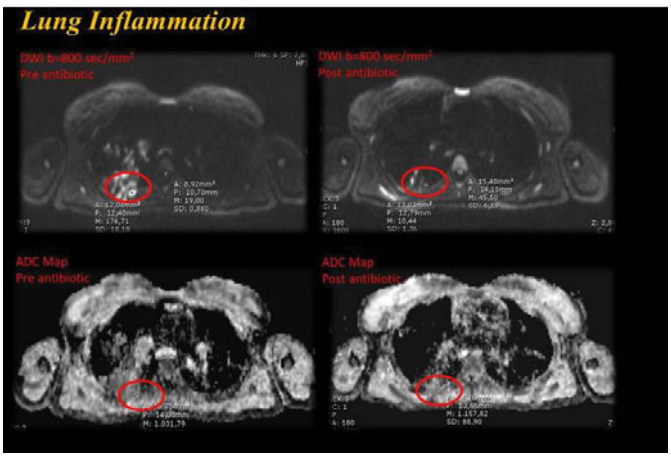

Discussion/Conclusion: The DWI seems to be sensitive to lung inflammation in CF population. The promising preliminary results obtained so far open new therapeutic scenario in CF and in other chronic lung diseases.
References:
Le Bihan; Effects of intravoxel incoherent motions (IVIM) in SSPF imaging: application to molecular diffusion imaging; Magn Reson Med

EPOS™ Poster

Head and Neck

585

Porous polyethylene reconstruction of orbital floor and roof defects-clinical and radiological evaluation

N.F. El Ameen[1], A.M. Mahrous[2], E.Z. Zahran[3]
[1]Radiology, El Minia univeristy hospital, El Minia/EGYPT, [2]Plastic surgery unit, El Minia university, El Minia/EGYPT, [3]Neurosurgery, El Minia university, El Minia/EGYPT

Purpose/Introduction: Clinical and radiological evaluation of the use of high porous polyethylene (Medpor) for reconstruction of post-traumatic orbital roof and floor defects.
Subjects and Methods: A prospective study included 37 patients had traumatic orbital wall defects. They classified into three groups. Group (A) 22 patients had orbital floor defects. Group (B) 10 patients had orbital roof defects. Group (C) 5 patients had combined orbital roof and floor defects. All defects were reconstructed by medpor. All of them were underwent MRI to evaluate vascular in growth.
Results: All patients showed vascular ingrowth denoted by enhancement in the implants in post Gad evaluation as early as one month post operative in 23 patients and 2 months postoperative in the remaining 14 patients. All patients showed improvement in immediate postoperative period and maintained in the postoperative follow up period clinically. Neither extrusion nor infection was recorded in any case.
Discussion/Conclusion: Porous polyethylene was found to be flexible, strong, porous and is highly biocompatible in orbital wall reconstruction. Its porosity enables vascular and bony ingrowth leading to tissue adhesion and a reduced risk of infection. Gadolinium enhanced MRI can detect vascular ingrowth into medpor orbital sheets as early as one month post operative.
References:
Farwell DG, Strong EB. Endoscopic repair of orbital floor fractures. Otolaryngol Clin North Am 40:319–28, 2007.
Ducic Y, Verret D. Endoscopic transantral repair of orbital floor fractures. Otolaryngol Head Neck Surg 140:149–54, 2009.
Lin C, Liao SH, Luke LK , Lin J . Porous Polyethylene Implants in Orbital Floor Reconstruction .Formos Med Assoc Vol 106 No 1. 2007.
Sarvananthan N, Liddicoat AJ, Fahy GT. Synthetic hydroxyapatite orbital implants: a clinical and MRI evaluation. Eye 13:205-208, 1999.

586

WITHDRAWN

EPOS™ Poster

Interventional - Safety, bioeffects

587

Spin-echo phase imaging allows differentiation between wattless and active currents in metallic needles surrounded by media with variable conductivity

F. Eibofner, H. Graf, F. Schick
Diagnostic and Interventional Radiology, University Hospital Tuebingen, Tübingen/GERMANY

Purpose/Introduction: Elongated metallic structures in a magnetic resonance (MR) environment can cause serious heating due to electric currents in the surrounding medium. Especially, when the length of the structure matches the in water wavelength of the applied radiofrequency (RF), efficient RF-coupling between the transmit coil and the structure results. However, medium heating in addition will depend on its conductivity (maximum power transfer theorem) [1,2]. Assessing this point as worst case for medium heating by MR imaging might be preferable [3].

Subjects and Methods: The electromagnetic RF-field applied during MR imaging couples to a highly conductive metallic structure and a secondary RF-field B1' is produced. If the structure is placed in an isolating medium like distilled water, a wattless current on the metal (low ohmic resistance, high frequency) results. An increase of medium conductivity is connected to an active current through the medium, which will be related to potential heat production. The transition from wattless to active current in the structure comes along with a difference in RF-phase between the applied and the B1'-field near the metallic structure. RF-phase difference can be measured with spin-echo phase imaging. A biopsy needle was placed off-center in a container which was filled with gadolinium doped, distilled water (Fig.1). Conductivity was increased in 10 steps to 0.39 S/m by adding NaCl. Phase images were acquired with a spin-echo sequence. The phase values were evaluated along a column from an unaffected area toward the edge of the needle. The phase changes near the needle as a function of conductivity were determined.

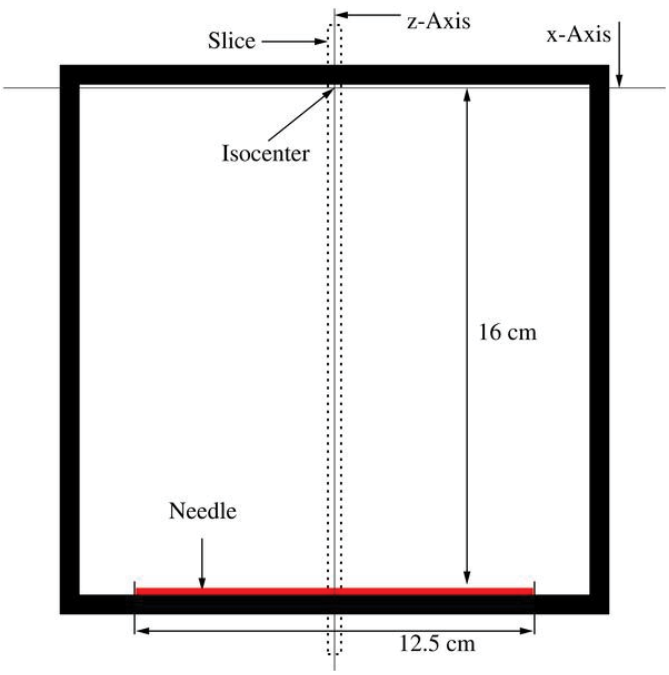

Results: Whereas the phase is relatively stable for all conductivities in the unaffected area, a phase offset is observable near the needle, depending on the conductivity of the medium (Fig.2). Here, RF-excitation near the needle is dominated by the induced secondary B1'-field. In the isolating medium, no phase offset is visible, because B1' is in phase with the RF-field.

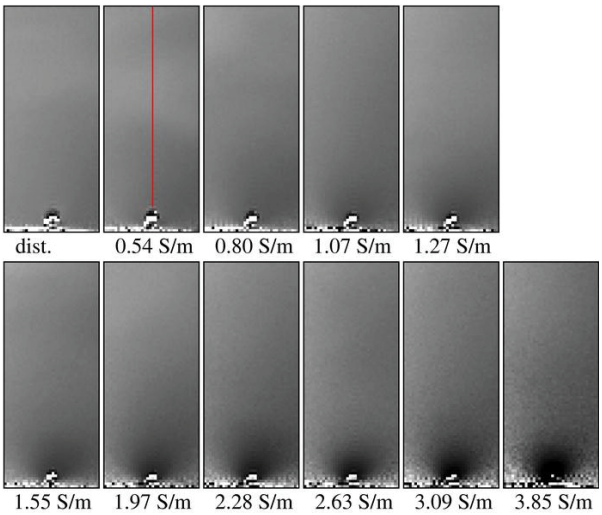

Phase progressions for the different conductivities from a column of the images are shown in Fig.3.

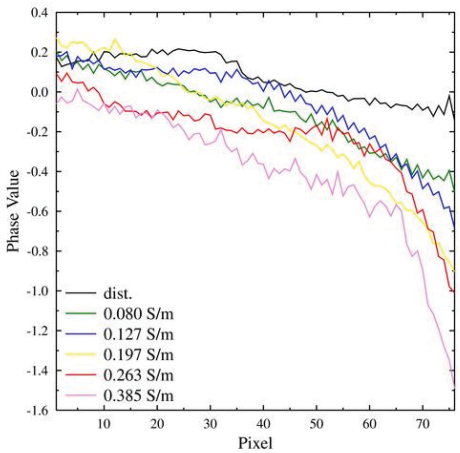

The differences between the unaffected phases and the phases near the needle are shown in Fig.4.

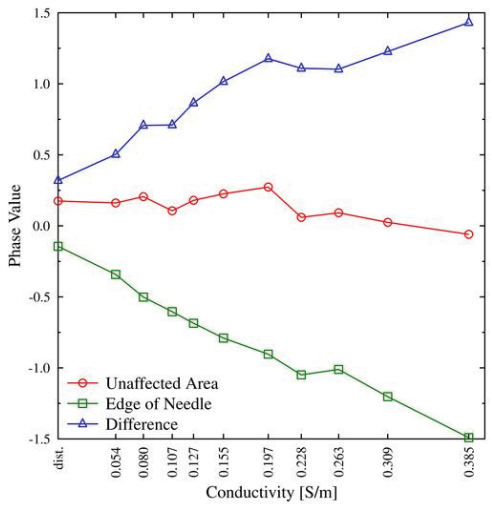

Discussion/Conclusion: RF-phase determination could be a helpful tool for the assessment of potentially heat producing active currents near metallic structures. Further investigations have to be performed in order to elucidate the relation between shifted phase values and possible heating in surrounding media.

References:

[1] Ballweg V, MedPhys, 2011:5522-5529.
[2] Langman D, MagResonMed, 2012:DOI:10.1002/mrm.23235.
[3] Van den Bosch MR, MedPhys, 2010:814-821.

588

Acoustic noise levels in an MR-conditional neonatal incubator during 3T MRI

D.L. Price[1], T. Burrows[2], G. Kendall[3], E. Cady[1], N. Robertson[3]
[1]Medical Physics & Bioengineering, UCLH NHS Foundation Trust, London/UNITED KINGDOM, [2]Dept Medical Physics & Bioengineering, UCLH NHS Foundation Trust, London/UNITED KINGDOM, [3]Academic Neonatology, University College London, London/UNITED KINGDOM

Purpose/Introduction: The aim of this study was to measure acoustic noise levels in an MR-conditional neonatal incubator during 3T MRI and determine whether ear protection is adequate to safeguard the neonatal ear.

Subjects and Methods: At our centre newborn infants are scanned at 3T (Achieva, Philips Medical Systems, Best, The Netherlands) whilst in an MR-conditional neonatal incubator (LMT, Luebeck, Germany).

Hearing protection comprises both ear plugs (Earo, Indianapolis, USA) and neonatal ear muffs, (Natus, San Carlos, USA). The neonate is also immobilised within the neonatal head RF coil using foam pads covering the sides of the head. Phantoms were used to simulate the neonate. Acoustic noise was measured using an integrating sound level meter (Brüel and Kjaer, Denmark) with a microphone at a position representative of the neonatal ear. The continuous equivalent acoustic noise level on the A-weighted scale (LAeq) and peak acoustic noise on the linear scale (L_{peak}) were recorded for each neonatal MRI pulse sequence.

Octave band acoustic noise levels were collected so that the effective noise at the ear could be calculated using the earplug manufacturer's assumed protection values (APVs).

Results:

Table: Acoustic noise levels for 3T neonatal MRI

Scan	TR(ms)/TE(ms)/ pixel(mm)/ scantime(mins:secs)	LA_{eq} (dB)	L_{peak} (dB)
Survey	11.1/4.6/0.97/0:32	98.8	114.4
SENSE reference	4/0.75/5.5/0:44	114.7	123.8
2D T2 TSE	10042/130/0.49/7:28	103.0	118.5
3D T1 MPRAGE	17/4.6/0.82/7:42	104.4	122.0
DTI	7857/46/1.75/5:41	103.3	119.0

The highest effective noise level at the ear was 79dB(A) for the SENSE reference scan.

Discussion/Conclusion: 3T MRI involves high acoustic noise levels exceeding 100 dB(A) for several different pulse sequences. The Health Protection Agency UK recommends that noise levels are reduced to below 85dB(A) at the ear in all patients. Our measurements indicate that earplugs would reduce the noise at the neonatal ear to below 80dB(A) when the LMT neonatal incubator is used. This may be an overestimate of the real situation since APVs are based on adult exposures.

However, combined earplugs and earmuffs typically provide 5-10dB more noise reduction than that of the most effective protection used alone [1]. The foam head-imobilising pads provide further protection [2]. Therefore we are confident that noise levels at the neonatal ear are reduced to well below 80dB(A). Such combined protection measures effectively protect the neonatal ear and allow MRI of both sedated and unsedated naturally sleeping infants.

References:

[1] Berger, 1983, Am. Ind. Hyg. Assoc. J.,44(5):321-329.
[2] Wagner, W,et al, 2003, Laryngoscope, 113:1216-1223.

589

13C spectroscopy in the human head at 7T: a feasibility study

A.W. Magill[1], E. Serés Roig[1], L. Xin[1], M. Meyerspeer[2], R. Gruetter[1]
[1]Laboratory for Functional and Metabolic Imaging, Ecole Polytechnique Fédérale de Lausanne, Lausanne/SWITZERLAND, [2]Center for Biomedical Engineering and Physics, MR Centre of Excellence, Vienna/AUSTRIA

Purpose/Introduction: Carbon-13 spectroscopy in humans at ultra-high field is challenging in terms of SAR management. Main sources of energy deposition are J-decoupling and NOE, both of which excite at the proton frequency for ^{13}C-direct detection. This study uses RF coil simulation to estimate the power deposition in a typical NOE enhanced, WALTZ-16 decoupled pulse-acquire sequence in the human head at 7T.

Subjects and Methods: An RF coil, consisting of the linear ^{13}C loop (7cm diameter) and a ^{1}H quadrature pair (12cm diameter) [1], was simulated using Microwave Studio (CST) while loaded with a human head model [2] (fig.1a). Loops were matched to better than -30dB; B_1^+ (75MHz) and B_2^+ (300MHz) fields, and global and 10g local SAR, were then calculated.

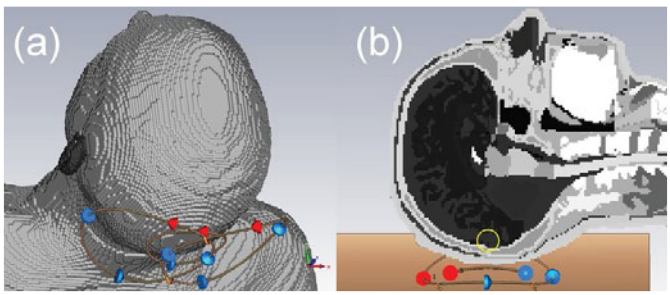

Figure 1: (a) simulation coil model and (b) calibration target location (yellow circle).

The modelled pulse sequence (fig.2) consists of a series of 90° NOE pulses (40×1ms, 99ms gaps), a 90° carbon excite pulse (1ms), followed by simultaneous acquisition and WALTZ-16 decoupling (80ms). Transmit voltages for the NOE and excite pulses were calculated using simulated B_1^+ and B_2^+ fields at a point 20mm inside the head (fig.1b). The decoupling voltage was set to twice that used for NOE, based on calibration measurements using a glucose phantom. Specific absorption due to each pulse was calculated, and hence the minimum repetition time that stays within IEC-guidelines [3].

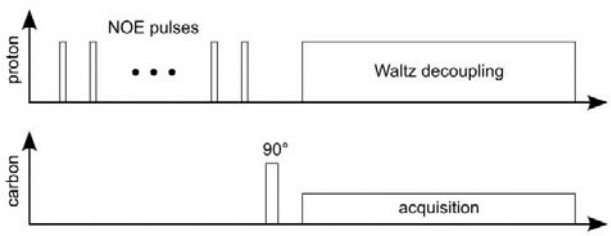

Figure 2: The pulse sequence.

Results: B_1^+ and B_2^+ field strengths at the target location were 1.22μT/V and 0.118μT/V respectively. Table 1 shows the SAR budget calculation. The maximum 10g energy deposition for the complete pulse sequence is 31.6J/kg and the sequence duration is 4.1s. The minimum permitted T_R is 3.16s (i.e. shorter than the sequence duration), or 2.81s if the NOE block is excluded.

	NOE	^{13}C excite	WALTZ-16
Duration /ms	4000	1	80
Duty cycle	1%	100%	100%
Transmit voltage /V	49.5	19.1	99.0
Transmit power /W	49.0	7.29	196
SAR, 10g max /Wkg^{-1}W^{-1}	1.79	2.42	1.79
SA, 10g max /Jkg^{-1}	3.51	0.0176	28.1
Proportion of total SA	11.1%	<0.1%	88.8%

Table 1: SAR budget calculation.

Discussion/Conclusion: This simulation study suggests that it is realistic to run NOE enhanced, WALTZ-16 decoupled ^{13}C acquisitions in the human head in reasonable time without exceeding SAR guidelines. Assuming 256 averages with T_R=4.1s, the total acquisition time is 18 minutes. Calculated values for ^{13}C and ^{1}H transmit voltages are comparable to those calibrated in a phantom using the same coil design. Further work is now required to calibrate these values in vivo.

References:

[1] Adriany & Gruetter, JMR 125, 1997;
[2] Christ et al, PMB 55(2), 2010;
[3] IEC 60601-2-33, 2002.

EPOS™ Poster

Interventional (including invasive MRA)

590

On exploiting the connectomics for thalamic nuclei localization: application of pattern recognition techniques

D. Bolis[1], **A. Jakab**[2], O. Goksel[1], G. Szekely[1]
[1]*Computer Vision Laboratory, ETH Zürich, Zürich/SWITZERLAND,* [2]*Department of Biomedical Laboratory and Imaging Sciences, University of Debrecen, Debrecen/HUNGARY*

Purpose/Introduction: During deep brain stimulation and ablative therapies, sub-cortical structures are targeted by transferring a stereotactical atlas onto the patient's anatomical images. We hypothesize that mapping of thalamocortical connections could serve as surrogate markers of individual anatomy and could be used for localizing specific targets in the thalamus. Here we demonstrate the application of a supervised machine learning tool that is optimized to predict the locations of various thalamic nuclei which are commonly used as targets in image guided therapies (e.g. Vim, central median nucleus).
Subjects and Methods: Previously, a 3D atlas of the human thalamus was non-rigidly matched with an MR template. Anatomical, diffusion tensor MR imaging and probabilistic tractography to 52 cortical and subcortical areas were performed for 40 subjects. After comparing a variety of different learning schemes, a support vector machine (SVM) and random forests based approach followed by morphological post-processing is proposed for the thalamic nuclei localization, employing the connectivity values to cortical areas as features.
Results: We demonstrate our method for 10 different nuclei. Successfully classified voxel percentages ranged from 55-90%, the Dice's coefficient was 0.35-0.65. The random forest classifier was more effective than the SVM approach. To demonstrate the feasibility, we visualized of nuclei probability maps after registering back to the subject's anatomical MRI space.
Discussion/Conclusion: Our results indicate that thalamocortical connectivity data do contain discriminant internucleus information. This kind of information could be potentially exploited for individual thalamic nuclei localization. Misregistration in calculating the ground truth was considered as a potential source of limitation during the learning procedure.

591

Quantification of the targeting error in MRI-guided biopsy using Monte Carlo simulations

F. Galassi[1], D. Brujic[1], M. Rea[2], P. Ferreira[1], M. Ristic[1]
[1]*Mechanical Engineering, Imperial College, London/UNITED KINGDOM,* [2]*Radiological Sciences Unit, NHS Trust, Imperial College London, London/UNITED KINGDOM*

Purpose/Introduction: MRI-guided interventional procedures require accurate tracking of devices. Recently, we proposed the projection pairing algorithm to localise N RF markers from 1D projections [1]. Here we analyse how the errors in localising the markers translate into erroneous targeting. We implemented Monte Carlo simulations of MRI-guided biopsy for analysis of targeting accuracy in relation to markers configuration and needle length.
Subjects and Methods: *Experimental analysis.* Wireless micro-circuits, filled with 27mm^3 water-gel, were constructed (123.5MHz). Sets of 13 1D-projections were acquired with a modified FLASH sequence(TR=4.57ms, TE=2.13ms, BW=390 Hz/pixel, FE=320, FOV=300mm, flip angle=0.3).
The peak's location is detected with sub-pixel accuracy using Gaussian-approximation. A Chi-square test over 500 acquired 1D-projections showed a Gaussian distribution of the error in peak's location with standard deviation $\sigma_{projection}\approx 0.05$ mm. If two peaks are close they can merge into one. We have found this happens when they are closer than d=2.5 mm. $\sigma_{projection}$ and d are input to Monte Carlo simulations.
Monte Carlo Simulations. We analysed 4 configurations of 3 markers and 4 needle lengths relevant to MRI-guided transrectal biopsy systems (Fig.1). For random rotations of the probe, 13 1D-projections of the markers are computed. Gaussian noise is added to the projections and the effect of peak merging is introduced. From these projections the positions of markers and needle tip are computed using our algorithm [1]. The targeting error $|tip_{computed} - tip_{correct}|$ was statistically analyzed.

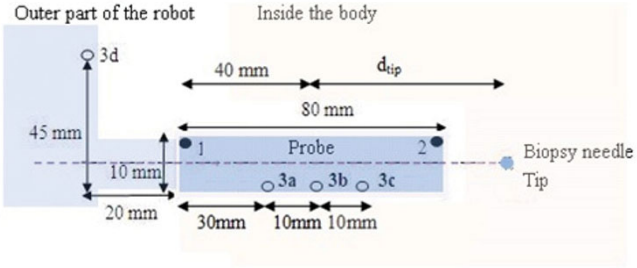

Fig.1.Configurations: (1,2,3a); (1,2,3b); (1,2,3c)); (1,2,3d).

Results: Each configuration was simulated 10^6 times and for $\sigma_{projection}$=0.05, 0.1, 0.15 and 0.2 mm. The lowest and highest maximum errors in targeting are 2.7mm and 4.1mm, for configuration (1,2,3d) and (1,2,3a) respectively. Among configurations within the probe, (1,2,3b) has the highest accuracy. Targeting accuracy improves for shorter length of the needle (Fig.2).

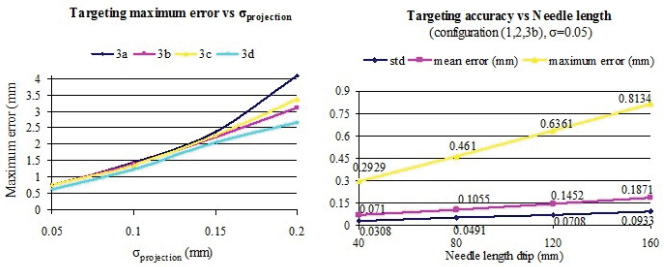

Fig.2. Simulations results.

Discussion/Conclusion: Optimal targeting requires optimal placement of the markers within the geometry of the system. Monte Carlo simulations enabled quantification of the dependence of the targeting accuracy on the markers configurations and needle length using experimentally obtained characteristics of the MRI data. Our analysis introduces guidelines in targeting error minimisation, as crucial as the ones defined in target registration error [2].
References:
1)Brujic D, Galassi F, Rea M, Ristic M 'A novel algorithm for fast 3D localisation of N fiducial markers from 1D projections', ISMRM 2012, Melbourne.
2)Labadie RF, Davis BM, Fitzpatrick JM. 'Image-guided surgery: what is the accuracy?', Otolaryngology Head Neck Surgery. 2005 Feb;13(1):27-31.

592

On Percutaneous Ablation of Liver Metastases: a Method for MRI-Guided and monitored Laser Ablation of Challenging Lesions

S.G. Nour[1], D.A. Kooby[2], C.A. Staley 3Rd[2], H.D. Kitajima[3], T.E. Powell[3], M.A. Bowen[3], A. Gowda[4], B. Burrow[3], W.C. Small[3], W.E. Torres[3]
[1]*Interventional MRI Program, Emory University Hospital, Atlanta/GA/UNITED STATES OF AMERICA,* [2]*Surgical Oncology, Emory University Hospital, Atlanta/GA/UNITED STATES OF AMERICA,* [3]*Rdiology and Imaging Sciences, Emory University Hospital, Atlanta/UNITED STATES OF AMERICA,* [4]*Visualase Laser, Inc, Visualase Laser, Inc, Houston/TX/UNITED STATES OF AMERICA*

Purpose/Introduction: To develop and evaluate an alternative technique to standard CT/US guided thermal ablations of liver metastases, aiming at avoiding hepatic resections in the subset of patients with CT/US invisible lesions, subcentimeter lesions, and/or lesions at challenging locations.
Subjects and Methods: MRI-guided laser ablations were performed in 14 patients (9M, 5F, age=45-84y) with 21 liver metastases (10 colon, 2 gastric,

3 melanoma, 5 pancreatic neuroendocrine, 1 pancreatic adenocarcinoma). Procedures were performed within an interventional MRI suite equipped with 1.5T wide bore scanner. Interventions were performed within the scanner bore while viewing real-time image updates on an in-room monitor. A laser fiber with 15mm diffusing tip encased in 5.5 F cooling catheter (Visualase, TX) was inserted in the target lesion under interactive visualization on a tri-orthogonal plane FLASH sequence (TE/TE=1220/1.92). A test dose of diode laser energy (980nm,30sec,4.5W) was applied to verify the location of ablation nidus on real-time temperature and cumulative damage estimate mapping(TE/TE=24/10). Subsequently, ablative energy dose was delivered with treatment endpoint based on on-line thermal monitoring of growing ablation. Fiber repositioning for additional ablation was conducted as needed. Final ablation was evaluated on TSE T2 (TE/TE=3000/84) and enhanced TSE T1(TE/TE=436/4.4) in 3 planes.

Results: Accurate targeting was achieved in all tumors regardless of size and location. Target tumor sizes were 0.9-2.9 cm (median=1.5cm). Locations were segment 2 (n=2), segment 4 (n=5), segment 5 (n=3), segment 6 (n=2), segment 7 (n=4), and segment 8 (n=5). Complete ablation was achieved in 1 session for each lesion. Applied laser energy was 1080-26975J per lesion (median=5340). Post procedure pain ratings were 0-7. No complications were encountered on follow-up durations of up to 31 weeks. Laser ablation zones demonstrated central iso-to-hypointense signal surrounded by hyperintense/enhancing rim on T2&T1, respectively. Follow-up scans showed involution of ablation zones. One patient with 2 ablated gastric sarcoma metastases underwent subsequent resection of ablated zones during partial hepatectomy performed for additional lesions. Pathology demonstrated complete necrosis of resected ablations.

Discussion/Conclusion: Percutaneous focal laser ablation of subtle liver metastases under real-time MR-guided fiber placement and temperature mapping is feasible, well tolerated, and effective on short and intermediate term follow-up. The technique maintains a minimally invasive option for treating liver metastases that cannot otherwise be approached under CT or ultrasound guidance.

593

Morphologic and metabolic changes in uterine fibroids after FUS treatment

Z. Ryznarova[1], M. Dezortova[2], D. Wagnerova[2], A. Skoch[2], Z. Fucikova[3], M. Hajek[2]

[1]MR Unit, Dept. Diagnostic and Interventional Radiologz, Institute for Clinical and Experimantal Medicine, Prague 4/CZECH REPUBLIC, [2]MR-Unit, Dept. Diagnostic and Interventional Radiology, Institute for Clinical and Experimental Medicine, Prague 4/CZECH REPUBLIC, [3]Dept. Gynecology, Thomayer Hospital, Prague 4/CZECH REPUBLIC

Purpose/Introduction: The study presents morphologic and metabolic changes observed by MR imaging and 1H MR spectroscopy in uterine fibroids after MR-guided focused ultrasound (MRgFUS) ablation. The method uses high-energy ultrasound waves that cause irreversible thermal tissue damage of fibroid tissue. MRI ensures correct wave focusing and temperature monitoring of treated tissues during the whole intervention (approx. 2-4 hours).

Subjects and Methods: Seven symptomatic female patients (age from 44 to 51 years) underwent MRgFUS ablation of eight uterine fibroids using the MRgFUS system (ExAblate 2000, InSightec).

MR examination prior to treatment was performed at Signa 1.5 MRI scanner (GE Medical Systems) using T2 TSE TR/TE=6000/108 ms, T1 TSE fat saturation TR/TE=708/11 ms with an intravenous injection of contrast agent (10 ml Multihance) sequences. 1H MR spectroscopy at 3T Siemens Trio system was performed (PRESS: TR/TE=2000/30 and 135 ms) using body matrix coil one week before and 4, 12 and 24 weeks after the MRgFUS treatment. Evaluation of spectra was done by LCModel software.

Results: Mean diameter of eight fibroids was 61 mm (range, 50–90 mm), hypoperfusion seen immediatelly after the treatment was in the range of 50-91% of the starting fibroid size.

There were no clinical complications. In one case the treatment was unsuccessful due to the depth of the fibroid. Clinical symptoms were significantly improved in all treated women. The tumor was reduced by the mean size of 39% (range, 20–70%) in the following six months, (see Figure).

Metabolic profile of the fibroid before ablation is characterized by the strong signal of cholines which disappeared six months after the treatment and was replaced by strong lipid signals, (see Figure). Surrounding tissue to the tumor was not influenced by thermal ablation.

Figure

MR image (T2TSE sequence) and spectra (PRESS TE=30ms) of fibroid a,b) before MRgFUS ablation; c,d) six months after the treatment.

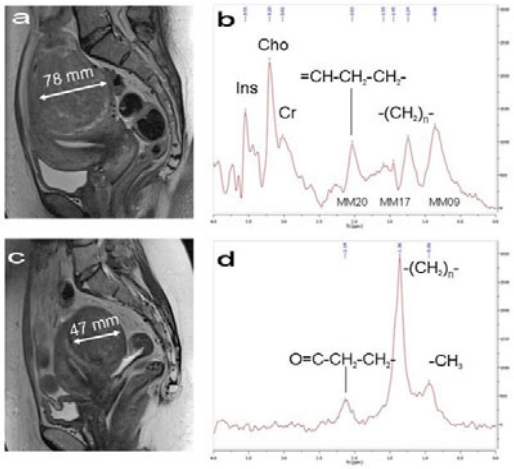

Discussion/Conclusion: The MRgFUS targeted heat-ablation is well tolerated minimally invasive treatment of symptomatic uterine fibroids and is a beneficial alternative to generally used hysterectomy. Due to thermal ablation, the shrinkage of fibroid volume in six months following the treatment was observed and significant metabolic changes characterized by increased lipid signals were visible in 1H MR spectra in all treated fibroids. MR is thus a useful tool to check the treatment process itself as well as the subsequent morphologic and biochemical changes.

References:

The study was supported by the MZCR institutional project 00023001IKEM.

EPOS™ Poster

Magnets and gradients

594

Characterization of Concomitant fields of a PatLoc gradient coil

A.M. Welz[1], H. Weber[1], A. Dewdney[2], F. Testud[1], J. Korvink[3], J. Hennig[1], M. Zaitsev[1]

[1]Department of Radiology, Medical Physics, University Medical Center Freiburg, Freiburg i. Brsg./GERMANY, [2]Healthcare, Siemens, Erlangen/GERMANY, [3]Freiburg Institute of Advanced Studies (FRIAS), University Freiburg, Freiburg/GERMANY

Purpose/Introduction: For spatial encoding in magnetic resonance imaging only the Bz component of the magnetic vector is of interest. In conventional imaging Bz is varied linearly along the three directions x, y and z to allow for imaging with orthogonal and rectangular voxels. One source of voxel distortion or signal dephasing are the concomitant fields [1]. With the introduction of non-linear magnetic fields for imaging [2], concomitant fields of higher-order harmonics become less trivial. This work studies the calculated and measured concomitant fields of a PatLoc-gradient-coil [3].

Subjects and Methods: A model of the PatLoc-gradient-coil was set up in Cobham_OPERA_14_3D and the full magnetic field B_x, B_y and B_z was calculated. This data was used to calculate the concomitant field component $B_c=\mathrm{sqrt}(B_x^2+B_y^2)$. This PatLoc-gradient-coil has been integrated in a 3T_Siemens_Trio_Tim modified to control up to 6 gradients simultaneously. The linear gradients were used for slice selection and acquisition of fieldmaps with a GRE sequence. This sequence was modified to induce a phase accumulation due to concomitant fields of the two PatLoc-gradients, Figure 1.

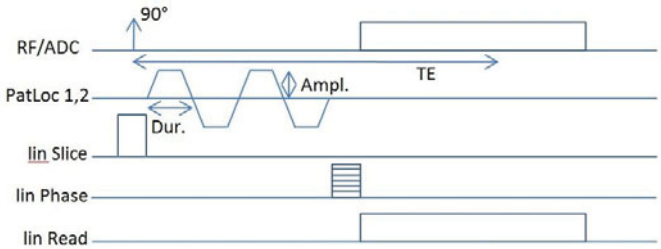

Results: The simulated concomitant fields of the PatLoc-coil were found to be approximately rotation-symmetric. From the data a 1D-representation along the y-axis is chosen at different positions along the z-axis to demonstrate the spatial variation of the concomitant fields, Figure 2. In positive z-direction the concomitant fields are stronger due to the asymmetric coil design with all return paths placed at the service end of the coil. In negative z-direction the concomitant fields are weaker, Figure 3. In Figure 4 the comparison of the simulated and measured field profiles is presented and showing good agreement in amplitude and shape. The difference may be related to the effect that the physical PatLoc-coil was rotated relative to the simulation. Additionally the concomitant fields show strong dependency in z-direction and a precise positioning of the PatLoc-coil is difficult in the current setup.

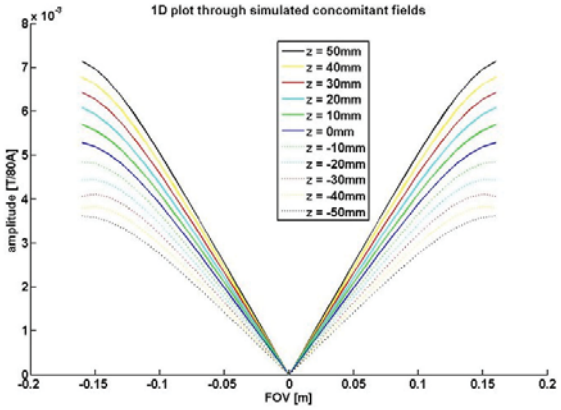

Figure 3: simulated concomitant field along z

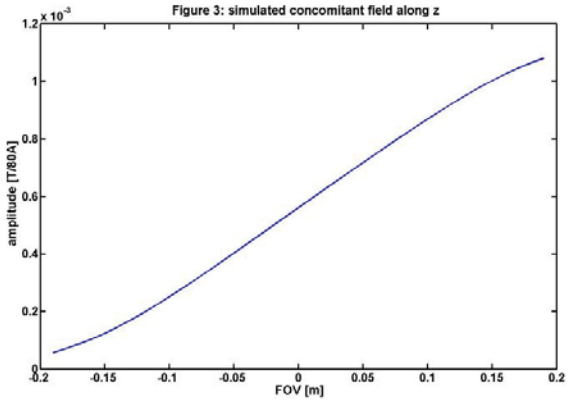

Figure 4: simulated and measured concomitant fields @isocentre

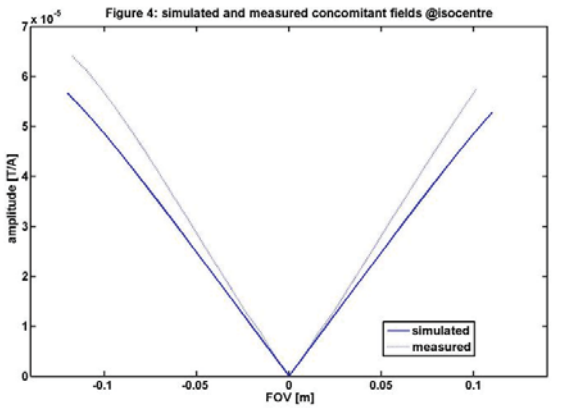

Discussion/Conclusion: It is important to know the concomitant fields in order to evaluate their effect on imaging and for the prediction of PNS which is induced by the total vector B and not only by B_z.

For realistic gradient coils the positioning of the return paths has to be considered for their significance.

References:

[1] Bernstein et al, MRM 39(2):300-308 (1998); [2] Hennig et al, MAGMA 21(1-2):5-14 (2008); [3] Welz et al, ISMRM 2009, p.3073;

EPOS™ Poster

Microscopy

595

Toward in vivo functional neuroimaging of Aplysia using manganese enhanced MRI

G. Radecki[1], I.O. Jelescu[1], R. Nargeot[2], D. Le Bihan[3], L. Ciobanu[1]
[1]I2BM NeuroSpin, CEA, Gif-sur-Yvette/FRANCE, [2]CNRS, Université Bordeaux 1, Bordeaux/FRANCE, [3]DSV/I2BM/NeuroSpin, CEA, Gif-sur-Yvette/FRANCE

Purpose/Introduction: Manganese Enhanced MRI (MEMRI) has become an established technique in neuroimaging with numerous applications including the detection of neuronal activity and neuronal tract tracing [1]. Recently, we used MEMRI in excised ganglia of *Aplysia californica* to highlight networks of identified neurons [2]. In the present work we demonstrate that the MEMRI technique can underline neuro-physiological processes as they take place in the living Aplysia. Specifically, we show that an injection of $MnCl_2$ solution leads to Mn^{2+} accumulation into the neurons in less than two hours. Preliminary results indicate that the Mn^{2+} distribution varies among different neuronal networks.
Subjects and Methods: Adult *Aplysia* (140g) were injected with 0.750ml MnCl2 solution (100mM). After 1½ hours the buccal and abdominal ganglia were resected, inserted into a 2mm diameter capillary filled with artificial sea water (ASW) and imaged. MRI was performed in a 17.2T magnet using a home-built solenoid. 3D FLASH images and T_1 maps were acquired. The ganglia from two animals (without $MnCl_2$ injection) were used as control. Mn^{2+} relaxivity at 17.2T was estimated from T_1 measurements in ASW solutions of known Mn^{2+} concentrations and was found to be $5.1(mM.s)^{-1}$.
Results: The uptake of the Mn^{2+} into the cells is visible on FLASH images acquired on both ganglia (Fig. 1). In the control experiments (data not shown) the contrast does not allow cell identification. Signal intensity differences in the FLASH images reveal a stronger manganese accumulation in the abdominal ganglion which is probably related to its persistent electrical activity underlying respiratory and circulatory functions.

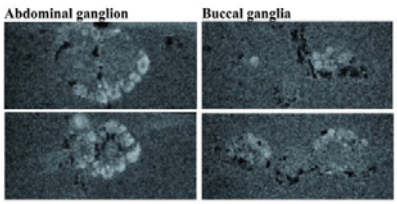

Fig. 1. Slices extracted from FLASH acquisitions of abdominal and buccal ganglia. The hyperintense regions are neurons which accumulated manganese. Acquisition parameters: TR = 150ms, TE = 2ms, 25 µm isotropic resolution.

Relaxometry reveals a shortening of T_1 in the cells from injected animals compared to controls (Table 1). Given the measured T_1s, we estimate an intracellular manganese concentration ranging from 0.078 to 0.135mM, which, according to previous electrophysiological measurements, does not impair the functionality of the ganglia [2].

Table 1: T1 relaxation times measured in the cells labeled in **Fig. 2**. For the control experiment the measurement was performed on one cell.

Cell	B9L	B5L	B5R	B8R	control
T1(ms)	713 ± 70	651 ± 39	897 ± 84	828 ± 116	1436 ± 167

Fig. 2. T2w image of the buccal ganglia showing the cells for which T1 values are reported in **Table 1**. The T1 maps were computed from variable TR RARE acquisitions (8 TR values ranging from 50 to 6000ms, 25µm isotropic resolution).

Discussion/Conclusion: This study demonstrates the feasibility of performing functional MEMRI studies in the *Aplysia*. Given the high scientific significance of the *Aplysia* as a model system in neuroscience, this approach promises to provide insight into crucial neurological processes and into how specific molecular alterations (i.e. dopamine excess) give rise to modifications of neuronal circuitry. We are currently investigating how the stimulation (controlled feeding) of the buccal neuronal network alters the Mn^{2+} distribution.
References:
[1] Pautler R.G.,1998, MRM, 740 [2] Jelescu I.O, 2011, ICMRM, Jelescu I.O, 2012, ENC.

596

Parameter selective MR-microimaging for non-invasive characterization of archaeological wet wood: A novel methodology for dendrochronology and a new approach in conservation science to assess wood species and condition?

A. Berg[1], R. Fürhacker[2], A. Klatz[2], M. Grabner[3]
[1]Center for Medical Physics and Biomedical Engineering, MR Center of Excellence - Medical University Vienna, Vienna/AUSTRIA, [2]n/a, Fürhacker & Klatz GesbR, Gutenberg an der Raabklamm/AUSTRIA, [3]Institute of Wood Science and Technology, University of Natural Resources and Life Sciences, Vienna, Tulln/AUSTRIA

Purpose/Introduction: Non-invasive high-resolution 3D-imaging based on X-ray-CT has been proven recently to be useful for the characterization of archaeological finds with regard to the annual ring (AR)-structure in ancient wood[1,2,3]. The sequence of varying AR-distance is dependent on local climate like precipitation and temperature and such specific for the individual time-period (dendro-chronology[2]). Moreover the visualization of the microstructure of archaeological wet wood is interesting for conservatory purposes with regard to degradation-status and wood-species. However CT-imaging has shown to fail for archaeological wet wood due to missing X-ray absorption contrast [3,5,6].
We, therefore, propose here to use parameter-selective MR-micro-imaging for the non-invasive characterization of archaeological wet wood. We present, to our knowledge for the first time, high-resolution MR-image data, relevant for dendro-chronological dating and micro-characterization as proof of principle.
Subjects and Methods: Specimen of different size (~1-100cm) are originating from a middle bronze-age (~1500 b.C.) well (Obj.764) recently discovered in Wohlsdorf /Steiermark/Austria [5,6].
Different MR-methodologies ranging from Ultra-High-Field (UHF) large scale imaging (cp-head-coil, i.d.28 cm), down to microscopic spatial resolution, from T2-mapping at standard echo-times (ms) down to Ultra-short-Encoding-Time (UTE) imaging (TE=70µs) have to be applied specific to the size and characteristics of the archaeological wet wood sample. For MR-microscopy we use a customer designed strong micro-gradient-insert (G=750mT/m) and a sensitive cp-birdcage resonator (i.d.19mm) on the same UHF-7T human scanner [4]. The software is based on clinically available Syngo pulse sequences and WIP-packages for UTE from the manufacturer with microimaging adapted protocols.
Results: Micro- and microscopic MR-images relevant for dendrochronological dating and microstructural characterization are shown in fig.1-3.

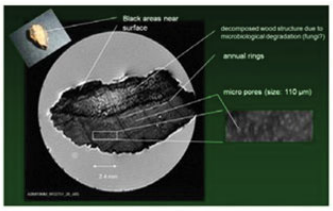

Fig. 1 MR-microscopy (VS:56x56x200µm³, Mtx:320x320x128) of small-sized (≥ 2cm³) archaeological wet wood (sample_2751). The bright micro-pores (d.≥110 µm) belong to small vessels for water transport in the xylem. Their spatial distribution is indicative of the type of wood. T2w-MR-microimaging is capable of distinguishing between degraded (presumably fungi) wood as bright region on top separated by a hypointense demarkation line in the middle from normal wood in the inner part (bottom). Annual rings appear dark, indicative of higher cell density.

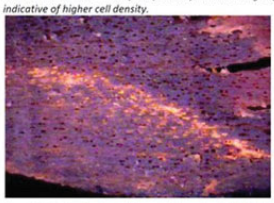

Fig. 2b Optical microscopic image of sample_2751. The bright yellow line in the centre delineates the demarcation between the degraded and normal wood. The histological images confirm the degradation in the upper part and allow for the interpretation of the hypointense MR-signal at low water concentration in the demarcation line as region of tylosis, the occlusion of xylem vessels for protection from fungi. The dark spots represent the vessels for water supply.

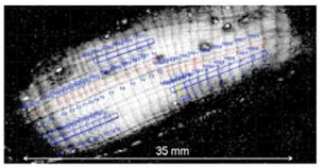

Fig. 3a T2-weighted high-resolution MR-image (VS:203x203x200µm³) of the ancient sample 2526. Bright areas correspond to a higher concentration of larger sized vessels, intersected by regions of none growth in winter. These intersections indicate the frontier of the annual rings (top-down). Horizontal lines (left-right) are indicative of the radial running wood rays. Note the varying distance between the annual rings due to different growth conditions in the corresponding year. Profile pathways (cf. Fig.3b) for the evaluation of the spatial distance between the annual rings are indicated.

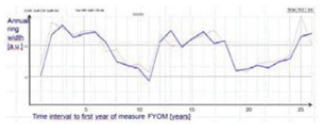

Fig. 3b: Annual ring analysis for dendrochronology: the distance between the annual rings is plotted vs. the time interval to the first year of measurement. The intra wood variance is estimated by the second (red) profile along the pathway indicated in fig. 3a. The sequence of varying distances (profile) between the annual rings is indicative of climate conditions and specific for the climate region and time period. The MR-data may thus allow for the cross dating of the sample if sufficient dendrochronological reference data from other wood specimen for this climate zone is available.

Discussion/Conclusion: The MR-appearance of archaeological wet wood is varying strongly, dependent on wood-species, sample-size and extraction point and thus demands for an extensive variety of hardware, pulse-sequences and MR-protocols. MR-microimaging (ps~200x200µm²) allows in principle for the evaluation of annual rings (AR). However an even higher spatial resolution would be preferable for more accurate determination of the AR-width (~1mm, dependent on sample). Using MR-microscopy (ps<100µm) on small samples, the AR-width can be determined at a sufficient spatial resolution. However, due to the small FOV, the number of detected ARs is limited in this case. MR-microimaging and microscopy is capable of detecting regions of degradation and wood-microstructure allowing in many cases the identification of wood-species, which is important within the conservation process of archaeological wet wood. It may thus be in future a valuable tool for the non-destructive characterization of unique wood-samples and in principle even for dendrochronological dating.

References:

[1] Grabner M, Salaberger D, Okochi T. *The Need of High Resolution µ-X-ray CT in Dendrochronology and Wood Identification.* (2009) in: Zinterhof P. et al. (Eds.), ISPA, Salzburg/Austria.

[2] Haneca K, Cufar K, Beeckman H. *Oaks, tree-rings and wooden cultural heritage: a review of the main characteristics and applications of oak dendrochronology in Europe.* (2009) J ARCHAEOL SCI **36**(1) 1-11.

[3] Bill J, Daly A, Johnsen O, Dalen K. *DendroCT– Dendrochronology without damage.* (2012) Dendrochronologia in press

[4] Berg A, Potthast A, Starewicz P. *MR-Microscopy on a human 7T-Scanner (2010).* Proc. ISMRM/ESMRMB 2010,1048, Stockholm, Sweden.

[5] Grabner M *Untersuchungen des Brunnenkastenholzes aus Wohlsdorf (2010)* in *Fundberichte aus Österreich*, Hrsg. Bundesdenkmalamt, **49**, S: 196 ff

[6] Fürhacker R, Klatz A K *Der mittelbronzezeitliche Brunnen aus Wohlsdorf. Fundbergung und bisher erfolgte Maßnahmen der Konservierung und Restaurierung* (2010) in *Fundberichte aus Österreich*, Hrsg. Bundesdenkmalamt, **49**, S: 194

597

Ex vivo Assessment of Skin Hydration by High Resolution 2.35 T MRI

A. Galante[1], A. Rosa[2], M. Alecci[2]
[1]*Laboratori Nazionale Gran Sasso, INFN-LNGS, L'Aquila/ITALY,*
[2]*Dipartimento di scienze della salute, Universita' dell'Aquila, L'Aquila/ITALY*

Purpose/Introduction: Human skin hydration of individuals depends on several factors: normal or pathological physiology, food consumption, physical activity, stress and climate. Moisturizing agents are widely used to regulate skin water content, and over the past decade a number of in vivo and ex vivo methods were proposed to assess moisturizing effects. Skin water content can be measured with attenuated total reflectance–Fourier transform infrared (ATR-FTIR), near infrared spectroscopy (NIR), nuclear magnetic resonance imaging (MRI) and spectroscopy, electrical and thermal conductivity, and biomechanical properties (1-3). This study describes an ex vivo porcine model for the quantitative assessment of skin hydration by means of 2.35 T high resolution MRI.
Subjects and Methods: Ex vivo porcine model studies were conducted using a 2.35 T MRI Biospec equipped with a TX-only volume coil and a RX-only surface coil of 2.5 cm in diameter, see Fig.1. GEFI images of the whole sample, composed by fresh abdominal porcine skin/fat/muscle layers (10-12g, about 3cm each side), were acquired with: TR=3000ms; FOV=3cm2; 1024*64 (470µm*30µm); thickness=2.6mm; NEX=4; TAQ=13min. Data processing was done with Paravision and ImageJ software.
First, the fresh sample was positioned at about 10 mm from the RF surface coil by using a Pedri dish and plastic spacers (Fig. 3d) and preliminary GEFI images were acquired with TE=2.9, 4.5, 6.0, 10.0ms (Fig. 2 a-d). The best SNR in the skin layers was observed with the shortest TE available (2.9ms).
Second, contact for 2 hours with a solution of 5% glycerol in water induced skin hydration (Fig. 3e). MRI images were acquired before (Fig.3a, T=0hour) and following treatment with 5% glycerol at T=3hours (Fig.3b) and T=16hours (Fig.3c).
Results: The normalized MRI signal profiles along the A/P direction (Fig. 4) showed a clear hydration effect (+30%) of the external layers due to the moisturizing agent and also an increase (10%) of the skin thickness (T=3hours) and a subsequent in air dehydration phase (T=16hours). Following the literature (3), we found (data not shown) that skin treatment with 20% glycerol in water for a few hours produces a significant de-hydration of the external skin layers and a reduction of the skin thickness.
Discussion/Conclusion: In summary, the combination of high resolution (30µm) MRI and ultra short TE (2.9ms) is capable to show with excellent detail the skin anatomy of an ex vivo porcine model and to follow the time course of hydration due to moisturizing agents.

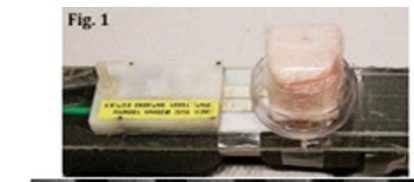

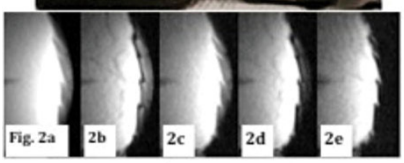

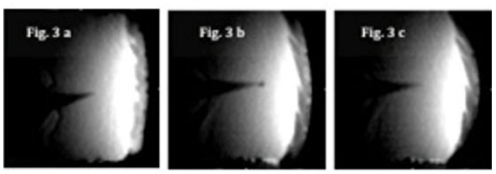

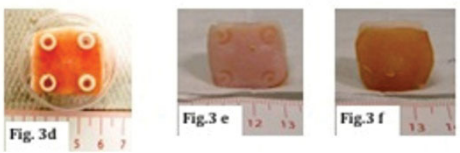

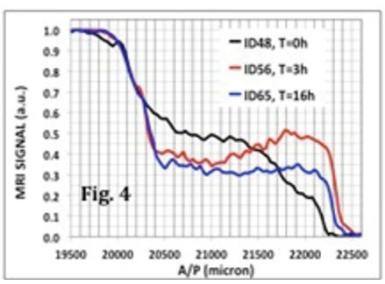

References:
[1] Girard P, et al. Skin Res Technol (2000) 6:205-213.
[2] Stefanowska J, et al. JEADV (2010) 24:875–880.
[3] Barrel JK, et al. MRM (2010) 63:790-796.

598

High-field high-resolution and microscopic T2-maps of a cartilage repair sheep model on a 7T human scanner: first results

J. Friske[1], A. Berg[2], G.H. Welsch[3], M. Pachowsky[3], K. Gelse[3], S. Trattnig[4]
[1]Department of Radiology, MR Center of Excellence - Medical Universtity of Vienna, Vienna/AUSTRIA, [2]Center for Medical Physics and Biomedical Engineering, MR Center of Excellence - Medical University Vienna, Vienna/AUSTRIA, [3]Department of Traumatic Surgery, Friedrich-Alexander Universität Erlangen-Nuremberg, Erlangen/GERMANY, [4]MR Centre of Excellence, Department of Radiology, Medical University of Vienna, Vienna/AUSTRIA

Purpose/Introduction: Surgical treatments of cartilage defects like microfracture technique (MFX) and cell based techniques such as autologous cartilage transplantation (ACT) require a high quality MRI follow up procedure. For improvement an adequate animal model reflecting closely the morphological/biochemical status of the human joint is needed. Therefore Merino sheep were used in our study.
T2-mapping based on a multi-slice-multi-echo sequence has shown to be sensitive to changes in collagen network/water content of the knee cartilage in humans.It can also be used for the biochemical assessment in our model. Moreover the zonal T2 variation of the cartilage reflects the grade of tissue repair after surgery (Welsch et al. 2011). Results on high resolution parameter mapping are presented using two scanner setups, a clinical and a microimaging-system (Berg et al. 2011) for improved spatial resolution.
Subjects and Methods: Two types of surgical procedures (MFX/ACT) (Welsch et al. 2008) were applied to a living Merino sheep. After 20 weeks the treated animal was sacrificed.Samples of the whole knee were taken and imaged ex vivo on a clinical scanner using a 28-channel knee coil (Res:0,37x0,37x1mm³).

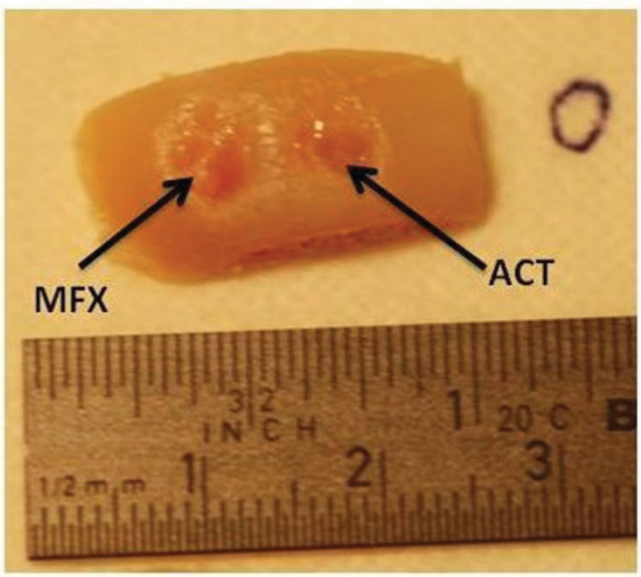

Fig 1. Sheep knee cartilage sample harvested 20 weeks after MFX/ACT surgery.

Subsequently samples of the cartilage were removed and examined using a microimaging-system on the same scanner equipped with a resonator coil (d=19mm) (Berg et al. 2011) for T2-mapping (Res:78x78x250 µm³). In both cases we used a multislice-multiecho-sequence with 10-20 echo times. T2-maps were calculated using a pixel-by-pixel based monoexponantial fit procedure.

Results: Both lesions can be distinguished in T2 maps of the whole cadaver knee joint (Fig2).

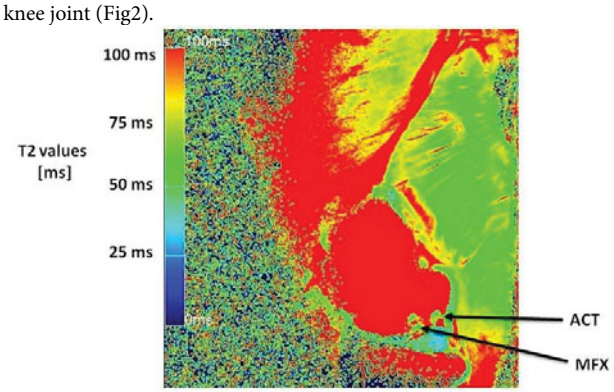

Fig 2. T2 map of a surgical treated knee where both lesions can be clearly distinguished however the resolution is too low to identify a zonal variation of the T2 values inside the cartilage. (Seq: spinecho-multiecho 28 channel knee coil GRAPPA PAT=2 TR 4960ms 10 Echos 11,7 -117 [ms] 0,37x0,37x1mm³ Mono-exponential Map-It (Siemens-Syngo))

As sheep cartilage is rather thin (0.7-1.2 mm) a clear zonal structure of the cartilage cannot be evaluated by standard T2-mapping (Fig2).

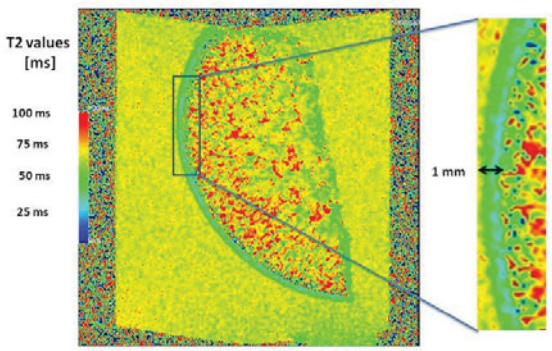

Fig 3. Micro-image of a healthy sheep cartilage showing the rather small thickness of the cartilage (approx. 1 mm) with two distinct zones of T2 values (green, blue) . (Seq: spinecho-multiecho TR 2000 ms 78*78*250 µm³ 20 Echos TE : 9,6-186 [ms])

For the quantitative characterization of the cartilage ultrastructure microscopic spatial resolution,significantly improves the visibility of micro-morphological changes in repair tissue after cartilage surgeries (Fig4).

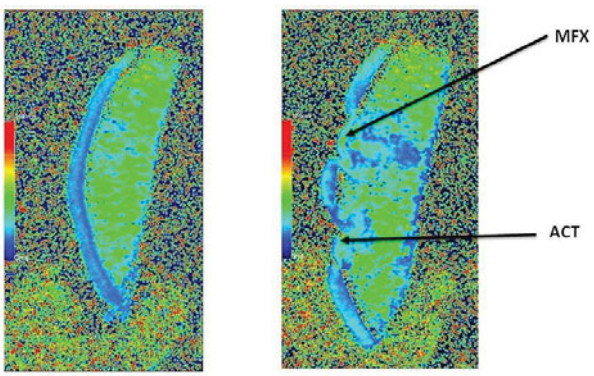

Fig 4. Micro-image of a sheep cartilage showing a healthy region of the cartilage (left) and a region showing irregular variations of the T2 due to MFX/ACT surgery (right). (Seq: spinecho-multiecho TR 3000 ms 78*78*250 µm³ 15 Echos TE : 7,2 - 108 [ms])

Discussion/Conclusion: We show that an improved spatial resolution (78x78x250 μm^3) using a microimaging-system is needed to analyze zonal variation of the cartilage in sheep. A clear zonal T2-difference in the healthy regions of the cartilage can be observed however in both surgery procedures no reorganization took place. We assume that the time period after surgery is too short for the repair tissue to migrate into the cartilage. We will analyze samples at different times after surgery.

References:

Berg, A. et al. (2011): http://dx.doi.org/10.1594/ecr2011/C-2029, **Welsch, G. et al. (2011)**: *Eur Radiol* 21(6),S.1136–1143., **Welsch, G. et al. (2008)**: *J. Magn. Reson. Imaging* 28 (4),S.979–986.

EPOS™ Poster

Molecular and cellular imaging

599

Non-invasive iron quantification of magnetically labeled cells using Electron Paramagnetic Resonance

A. Ketkar- Atre[1], P. Vaes[2], J. Trekker[1], S. Sharma[1], S. Teughels[2], U. Himmelreich[1]
[1]Department of Diagnostic and Pathology, KU Leuven, Leuven/BELGIUM, [2]Pepric NV, Pepric NV, Leuven/BELGIUM

Purpose/Introduction: Labeling of cells with SPIOs has become a routine to follow their location in vivo using high resolution MRI (1). But quantification of MR signal has been hindered, giving limited insight on the fate of transplanted cells (2). Methods like ICP- OES or ICP-MS require lysed cells or digested tissue where samples cannot be used for further experiments. Here, we report on the performance of several commercial and in-house SPIOs investigated by highly sensitive, direct, quantitative and non invasive iron detection technique based on electron paramagnetic resonance (EPR).
Subjects and Methods: SPIO characterization: Endorem and Resovist were used as described previously (1). Small core SPIOs (7nm – mPEGSi-7) and large core SPIOs (13nm – mPEGSi-13) were synthesized by thermal decomposition and were functionalized with a PEGylated silane. Magnetoliposomes (MLs) were prepared by co-precipitation and enwrapped by liposomes. Measurements were done with a PEPRIC particle spectrometer (PPS) (Pepric NV, Leuven BE) and the signal was measured at ~100 Gauss. The excitation frequency was set to ~300 MHz.
Cell labeling: MSCs and adult progenitor cells (Cl2slow) were labeled with different concentrations of SPIOs. Cells were suspended in 150 µl of PBS. These measurements were compared with ICP-OES values.
Results: The sensitivity of five SPIOs was tested. Endorem and Resovist had a sensitivity of 1.43 mV/µmol Fe. Different concentrations of Endorem were tested and a linear behavior of concentration versus EPR signal was found. A higher sensitivity was detected for ML (2.5 mV/µmol Fe). The effect of core size was studied by measuring PEGlayted particles . The mPEGSi-7 had a sensitivity of 0.85 mV/µmol of Fe. A ten-fold increase in sensitivity was measured for the mPEGSi-13 SPIO to ~9 mV/µmol Fe, indicating that a larger core produces higher EPR signals. Signals measured for labeled cells were lower than for suspended SPIOs, but we were still able to detect less than 50000 cells labeled with mPEGSi-13 SPIOs.

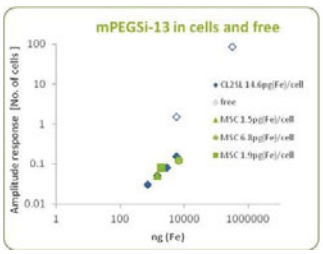

Sample	mV/µmol Fe
Resovist	1.43
Endorem	1.43
ML	2.50
mPEGSi-7	0.85
mPEGSi-13	8.93

Discussion/Conclusion: The EPR approach is an easy to use, completely non-invasive method to determine the iron concentrations in magnetically labeled samples. In addition, it is non destructive; thus samples can be used post measurements. Further investigations with the PPS will focus on mechanisms involved in the signal change after internalization of SPIOs and the characterization in tissue samples.
References:
1. A. Crabbe, et al. Cell Transpl. 19: 919 2010
2. U. Himmelreich et.al. Methods, 48:112 2009
3. S. Soenen, et al. WIREs Nanomed. Nanobiotech. 3: 197 2011

600

New gadolinium particles for high efficiency in MR-cell detection

P. Mowat[1], A. Mignot[1], W. Rima[2], R. Di Corato[3], C. Wilhelm[4], S. Laurent[5], L. Vander Elst[5], R.N. Muller[5], C. Louis[6], P. Perriat[2], L. Sancey[1], F. Lux[1], O. Tillement[1]
[1]LPCML, LPCML CNRS UMR 5620 - University Lyon 1, VILLEURBANNE/ FRANCE, [2]MATEIS CNRS UMR 5510, INSA-Lyon, VILLEURBANNE/ FRANCE, [3]CNRS UMR 7057, University Paris Diderot, PARIS/FRANCE, [4]CNRS UMR 7057, University Paris Diderot, Paris/FRANCE, [5]NMR and Molecular Imaging Laboratory, University of Mons, Mons/BELGIUM, [6]Nano-H SAS, Nano-H SAS, SAINT-QUENTIN FALLAVIER/FRANCE

Purpose/Introduction: Challenges in imaging for diagnosis have lead to an explosion of interest in designing original tracers that can permit a high efficiency of detection. It is the case of gadolinium-based particles, a new kind of contrast agents, made of a polysiloxane matrix with covalently grafted gadolinium complexes (Gd-DTPA).
Subjects and Methods: **Gadolinium particles :**
Different contents of APTES and TEOS, silane precursors, can be added during the synthesis to reach a Si/Gd ratio between 1 and 4 (particles called 1Si, 2Si or 4Si DTPA).
Cell labelling and characterization :
Cells were incubated in presence of particles at a concentration till 10mM of Gd in the appropriate medium (RPMI or DMEM) during a few hours. Toxicity was measured by classical viability tests as Trypan-blue or MTT-assay and MR-efficiency was evaluated by calculating the r_1 in cells at 1.4T (Minispec mq60 NMR analyser, Bruker).
Results: These 5-nm particles are very interesting for MR-detection of cells because their longitudinal relaxivity (r_1) is more important than this of usual molecular gadolinium complexes (i.e Magnevist®) and does not drop when the magnetic field increases, as shown in NMRD profiles.
Before *in vivo* studies, particles were selected by evaluating the toxicity and the MR-efficiency in cells like lymphocytes or mesenchymal stem cells. Toxicity was measured by classical viability tests as Trypan-blue or MTT-assay and MR-efficiency was evaluated by calculating the r_1 in cells at 1.4T (Minispec mq60 NMR analyser, Bruker). The 2Si DTPA-particles were found as the best particles allowing both good cell viability (superior to 90% on lymphocytes till 5mM Gd in the incubation medium, with no impact on stem cells differenciation) and sufficient r_1 in cells to obtain a significant contrast (2.7 $mM^{-1}.s^{-1}$ for a Gd concentration of 0.1mM in cells). These particles permit also a stable labelling for a long time of MR- detection (till 3 weeks).

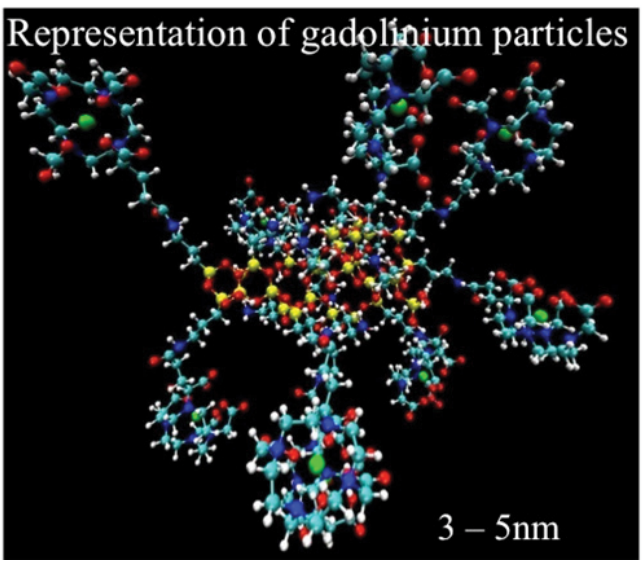

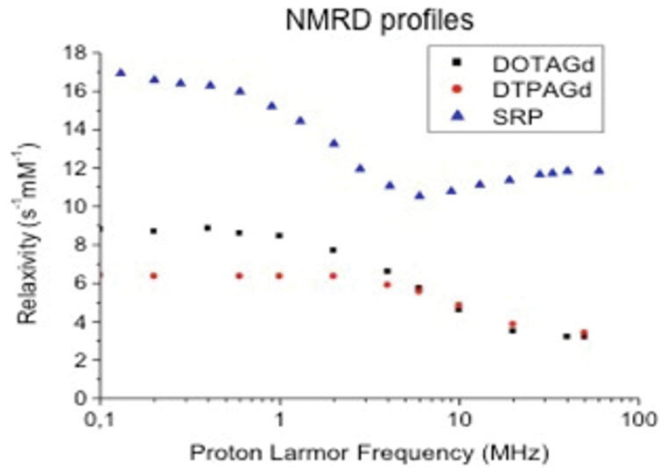

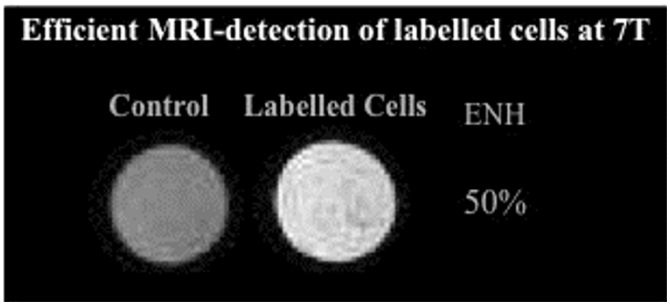

Discussion/Conclusion: To conclude, these new gadolinium particles are efficient to obtain a high MR-effect in cells what should be hopeful to track them *in vivo*. Nuclear and optical imaging can also be performed with these same particles to improve diagnosis and ripen therapeutic strategies.

References:

- F. Lux et al., Nanoparticules ultrafines à matrice polyorganosiloxane fonctionnalisée..., Brevet n° FR 2 959 502 – A1 (avril 2010).
- F. Lux, A. Mignot, P. Mowat, et al., Ultrasmall rigid particles as multimodal probes for medical applications, *Angewandte Chemie*. 2011 ; 50 : 12299-12303.

601

Two Approaches to Stem Cell Magnetic Resonance Imaging: Advantages and Limitations

L. Ostrovska
The Russell H. Morgan Department of Radiology and Radiological Science, The Johns Hopkins University School of Medicine, Baltimore/MD/UNITED STATES OF AMERICA

Purpose/Introduction: We develop strategies for noninvasive monitoring of mesenchymal stem cell (MSC) incorporation into the tumor neovasculature. For stem cell magnetic resonance imaging (MRI), we used two approaches: a) stem cell loading with magnetic nanoparticles and b) utilizing engineered MSC expressing a unique cell surface CD4-receptor (truncated human CD4) with the specific vascular contrast agent targeted to this receptor.

Subjects and Methods: In our experiments, we utilized murine bone marrow derived mesenchymal stem cell line. For MR imaging, we loaded MSC with iron oxide particles: 0.9 μk Bangs particles or 100 nm bionized nanoferrite (BNF) particles. Overnight labeling procedure was performed in the presence of Poly-L-Lysine.

For the second approach, we constructed a recombinant plasmid pEF1α-GFP-IRES-CD4 and determined its expression in transfected recipient MSC. The EGFP coding sequence was cloned into the pEF-1α Myc/His vector along with an internal ribosome entry site (IRES) sequence coupled to the coding sequence of a truncated human CD4 (ΔCD4) receptor giving: pEF-1α-GFP-IRES- ΔCD4. Transfected cells were labeled with superparamagnetic MACS CD4-MicroBeads and isolated on MACSelect magnetic column. Stable pEF-1α-GFP-IRES-ΔCD4 expressing MSCs clones were prepared in selection media with G418. ΔCD4 receptor expression was evaluated immunocytochemically and by FACS using ΔCD4-PE antibodies.

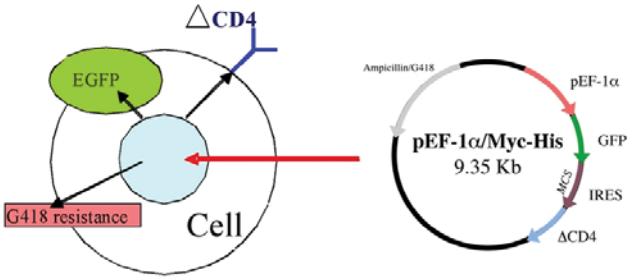

Transfection strategy to generate MSC with double GFP/ΔCD4 expression

Results: Both types of iron oxide particles provided excellent MR contrast for effective MSC imaging. BNF particles had enhanced imaging characteristics and hyperthermic qualities. They did not change stem cell proliferation and differentiation and allowed for therapeutic stem cell applications.

Plasmid transfection resulted in stable and efficient GFP fluorescence; however, expression levels of CD4 were neither efficient nor stable possibly due to limited functionality of the IRES construct. We also noticed that transfected MSC in long-term culture spontaneously formed foci of transformation (comprising cells that lost contact inhibition) with higher frequency. Subpopulations of genetically modified stem cells (transfected with the reporter gene) also changed their differentiation ability.

Discussion/Conclusion: Although the *in vitro* iron oxide labeling protocol resulted in efficient cell labeling for MRI, such labeling might be transient *in vivo* due to the label dilution during subsequent cell divisions. Iron oxide loading/imaging of MSC also does not provide information about survival and function of the loaded cells.

Genetically engineered stem cells in long-term culture are unstable; they may change their behavior, and transform at higher frequency.

In conclusion, we demonstrated that both approaches have advantages and limitations. Our findings indicate importance of bio-safety studies for long-term imaging and efficient clinical applications of stem cells.

602

Ferromagnetic nanoparticles for MR imaging and hyperthermic ablation

V. Herynek[1], P. Jendelová[2], E. Pollert[3], K. Turnovcová[2], P. Veverka[3], D. Jirak[1], M. Burian[1], M. Hajek[1], E. Syková[2]
[1]MR-Unit, Department of Diagnostic and Interventional Radiology, Institute for Clinical and Experimental Medicine, Prague 4/CZECH REPUBLIC, [2]Department of Neuroscience, Institute of Experimental Medicine ASCR, Prague_4/CZECH REPUBLIC, [3]Department of Magnetics and Superconductors, Institute of Physics ASCR, Prague 6/CZECH REPUBLIC

Purpose/Introduction: Ferromagnetic nanoparticles may serve for both diagnostic and therapeutic purposes. The aim of our study was to test encapsulated perovskite ferromagnetic particles as a contrast agent for MRI, a cellular label, and an agent for guided temperature-controlled thermoablation.

Subjects and Methods: Perovskite nanoparticles ($La_{1-x}Sr_xMnO_3$), varying in size over a range of 18-21 nm (Curie temperature 55-65°C) and with different La/Sr ratios, were synthesized and subsequently coated by $Si0_2$ to minimize their toxicity; the coating thickness was 20 nm.

Toxicity was tested after 48-hour incubation of rat mesenchymal stem cells with the nanoparticles in the medium. Cell viability was evaluated using trypan blue. Cell proliferation was evaluated using the Xcellingence System. For in vivo MRI, the nanoparticles (2.5ug in 5ul susp.) were injected into the brain of a rat and scanned with a Bruker Biospec imager 4.7 T using a T2-weighted image sequence, 1 and 7 days post-injection.

In vivo thermal ablation was performed by exposition of the rat to a high frequency magnetic field (480 kHz, 12 mT) for 60 minutes 1 day after injection of the nanoparticles. The lesion was assessed by histology (NeuN + DAPI, cresyl violet and Hematoxylin-Eozin staining).
Results: Viability of cells incubated with the nanoparticles was in the range of 72 – 85%, whereas a control sample reached 92%. Although the coating substantially improved cell viability, the nanoparticles were still slightly toxic. This also resulted in the lower adhesion of a small part of the labeled cells after 48 hours of incubation. Proliferation was slowed down at the time the nanoparticles were added to the media; however, overall proliferation was not changed. The injection of the nanoparticles into the cortex of a rat provided superior MR contrast. Histology staining confirmed damage to the tissue around the injection site after exposition to the high frequency magnetic field (see Figure).

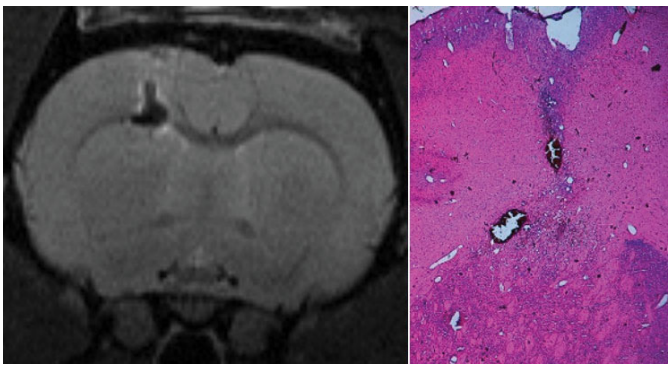

Figure: MR image (left) of a rat brain with applied nanoparticles. Histology (right, Hematoxylin-Eozin) confirmed black particle deposits and tissue destruction after ablation.

Discussion/Conclusion: The nanoparticles can be easily tracked by MRI in vivo. Due to their ferromagnetic properties, they can be locally heated by an external high frequency magnetic field which leads to tissue ablation in their vicinity. Coating of perovskite nanoparticles is crucial for toxicity reduction. It can be also improved by surface functionalization.
Grant support: Grant project MPO CR No. FR-TI3/521, Institutional grant 00023001IKEM MZ CR.

603

MRI artifacts in the ferric chloride thrombus animal model: an alternative solution

M. Wolters[1], R.H.M. Hoof[1], K. Douma[2], M.A.M.J. Van Zandvoort[3], T.M. Hackeng[4], M.J. Post[3], W.H. Backes[1], M.E. Kooi[1]
[1]Department of Radiology, Maastricht University Medical Center (MUMC+), Maastricht/NETHERLANDS, [2]Department of Biomedical Engineering, Maastricht University Medical Centre (MUMC+), Maastricht/NETHERLANDS, [3]Cardiovascular Research Institute Maastricht (CARIM), Maastricht University Medical Center (MUMC+), Maastricht/NETHERLANDS, [4]Department of Biochemistry, Maastricht University Medical Centre (MUMC+), Maastricht/NETHERLANDS

Purpose/Introduction: Visualization of thrombi with molecular Magnetic Resonance Imaging (MRI) may improve the diagnosis and affect therapeutic decisions of thrombotic complications. In pre-clinical molecular MRI studies (1-5) animal models were used in which thrombus induction was achieved with ferric-chloride ($FeCl_3$). However, residual $FeCl_3$ can cause magnetic susceptibility artifacts at MRI and should therefore be used with care. The objective of this study is to investigate $AlCl_3$, as an alternative to $FeCl_3$, in phantom and in vivo animal experiments.
Subjects and Methods: Phantom. Four tubes were filled with 0.05%-$FeCl_3$, 10%-$FeCl_3$, 0.05%-$AlCl_3$ and 10%-$AlCl_3$ and embedded in water. T1-weighted and T2-weighted gradient echo images were acquired on a 7Tesla Bruker Biospec MRI system.
In-vivo. Thrombi were induced in mice. A strip of filter paper soaked in 10%-$FeCl_3$ or 20%-$AlCl_3$ was applied to the right carotid artery (RCA). When the flow dropped to 10% of the original flow in the RCA, the filter paper was removed and and the artery was rinsed. Coronal gradient-echo images were acquired covering both carotid arteries. Afterwards, the RCA was excised and examined with two-photon-laser-scanning-microscopy (TPLSM). Thrombi were stained with anti-fibrin Oregon-Green to visualize fibrin networks (2).
Results:

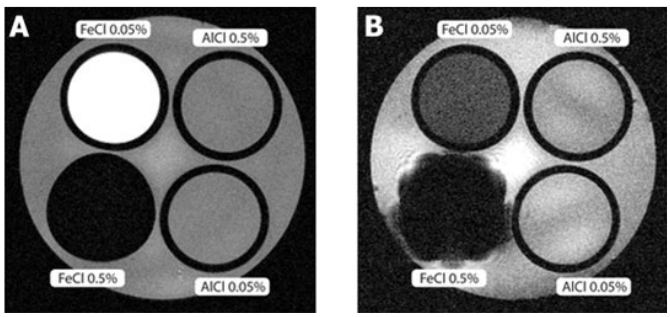

Figure-1A, T1-weighted image (TE 3.3ms/TR 100ms), **Figure-1B**, T2-weighted image (TE 20ms/TR 1000ms). The 0.05%-$FeCl_3$ solution appears hyperintense on the T1-weighted and hypo-intense on the T2-weighted images. 0.5%-$FeCl_3$ is hypo-intense on both images, with susceptibility artifacts. $AlCl_3$ shows similar signal intensity as the surrounding water and no artifacts.

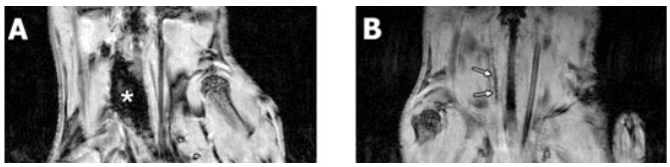

Figure-2A, In-vivo MRI with a large artifact (asterisk) at the RCA originating from $FeCl_3$. **Figure-2B**, In-vivo MRI of an RCA with an $AlCl_3$-induced thrombus. At the site of the thrombus in the artery (arrows) no susceptibility artifacts are observed.

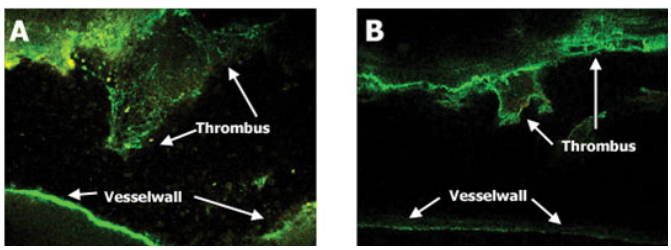

Figure-3A and **Figure-3B**,Two-photon images of thrombi induced with $FeCl_3$ and $AlCl_3$, respectively.

Discussion/Conclusion: This study shows that severe artifacts can occur in MRI when using $FeCl_3$ for inducing thrombi. $FeCl_3$ can cause hypo- or hyper-intensities in the vicinity of a thrombus at MRI. This artifact can seriously complicate the interpretation of potential contrast effects of a thrombus targeting contrast agent. We advise to use $AlCl_3$ to induce (arterial) thrombosis in MRI experiments.
References:
1. D.Duerschmied et al.InvestRadiol.2011
2. RJ.Miserus et al.JACC.2009
3. C.von zur Muhlen et al.Circulation.2008
4. HT.Ta et al.CirculationResearch.2011
5. JR.McCarthy et al.BioconjugateChemistry.2009

604

Evaluating the effect of ultra small superparamagnetic iron oxide nanoparticles for long-term magnetic cell labeling

S. Shanehsazzadeh[1], M.A. Oghabian[1], B.J. Allen[2], M. Amanlou[3], A. Masoudi[4], F. Johari Daha[5]
[1]Emam Hospital, Research Center for Sciences and Technology in Medicine,, 14197/IRAN, [2]St George Hospital, Centre for Experimental Radiation Oncology,, NSW Sydney/AUSTRALIA, [3]Faculty of Pharmacy and Drug Design and Development Research Center, Tehran University of Medical Sciences, Department of Medicinal Chemistry, 14197/IRAN, [4]Sharif University of Technology, Department of Materials Science and Engineering,, Tehran/IRAN, [5]Nuclear Research Center, Radioisotope Division, Tehran/IRAN

Purpose/Introduction: To evaluate the long-term viability, iron content stability and labeling efficiency of mammalian cells when using the ultra small, superparamagnetic, iron oxide nanoparticles with plain surfaces (USPIO) for magnetic cell labeling.
Subjects and Methods: Iron oxide magnetic nanoparticles (MNP) were manufactured locally and by Micromod GmBH, Rostock, Germany. Tests were carried out in four groups of 5 flasks of $5.5*10^6$ AD-293 embryonic kidney cells. The cell lines were incubated with both products for 24 hours with 4 different iron concentrations (0, 0.25, 0.5 and 0.7 mg/mL) with and without protamine sulfate (USPIO-Pro or MNP-Pro), washed with PBS and centrifuged at 900 rpm for cleaning the unbounded MNPs three times. Iron uptake using MNP-Pro was evaluated with Prussian blue test, MRI imaging, ICP test and cell viability. The iron concentrations in the media were also assessed at different time points. Statistical tests for significant differences between original and labeled cells were performed.
Results:

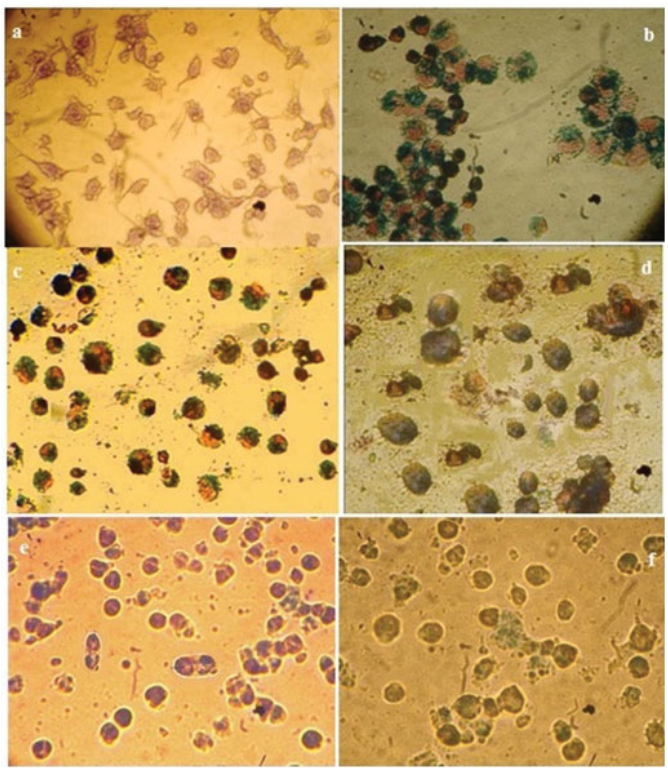

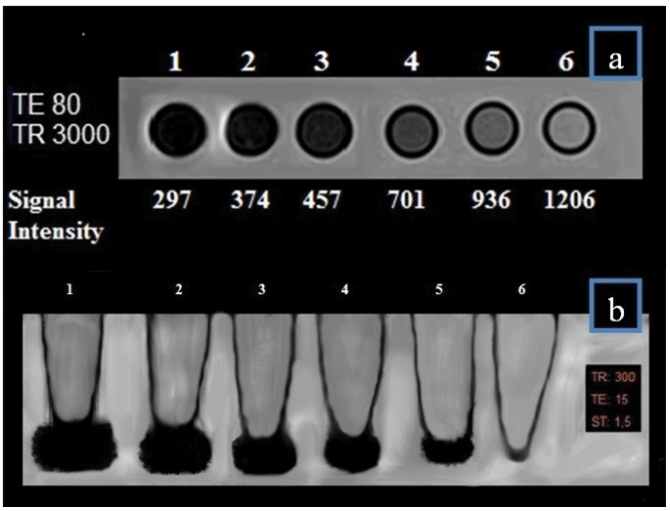

Table 1: Showing viability, Iron concentration (ICP results), % of Iron labeled by Prussian Blue staining and signal changes. Sample properties are defined in figure 1.

% Signal Loss in T2 weighted	No of particles per Cell	Iron Content per cell pictogram/ cell	Prussian Blue (%)	Iron Content ppm or µg/mL	Post labeling day	viability	Sample No. Sample No.
-10±3	53	0.67	25±3	3.7±0.3	1*	>90%	0
-75±4	909	11,36	98±2	62.5±1.1	1	>90%	1
-69±4	789	9,87	89±5	54.3±0.9	3	>90%	2
-62±4	720	9,00	50±7	49.5±0.8	7	>90%	3
-42±3	368	4,60	31±5	25.3±0.5	14	>87%	4
-22±5	157	1,26	25±4	10.8±0.4	21	>85%	5
0	NA	0,1	0	0.6±0.2	Control	>90%	6

There were no significant differences in cell viability between the control group of cells and those groups with iron uptake at the specified iron concentrations. The average iron uptakes ratio compared to the control group was (114±1). The MRI images at post-labeling days 1 and 21 showed (75±4)% and (22±5)% signal decrements compared to the control, respectively. The Prussian blue test showed that 98% of the cells were labeled and the media iron concentration did not affect the cell iron-uptake.
Discussion/Conclusion: Magnetic cellular labeling with the MNP-Pro complex had no short or medium term (3 weeks) toxic effects on embryonic kidney cells. These results hold promise for MRI monitoring of the temporal migration of cells into tissues and the development of cell tracking strategies for the repair or replacement of tissues and other novel cell therapies.

605

The use of Apoferritin for the MRI guided delivery of curcumin for the treatment of acute hepatitis.

S. Geninatti Crich[1], J.C. Cutrin[2], D. Burghelea[1], S. Aime[1]
[1]Dipartimento di Chimica & Centro di Imaging Molecolare, Univ. Torino, Torino/ITALY, [2]Clinical and Biological Sciences, ININCA-CONICET, Torino/ITALY

Purpose/Introduction: Much attention is currently devoted to the development of agents for procedures in which disease diagnosis and therapy are combined. These "theranostics" contain both drugs and imaging reporters within a single formulation. Usually, theranostics are made up by synthetic nanoparticles that, as a consequence of their size, can deliver a high number of diagnostic and therapeutic molecules. Drawbacks associated to their nano-size

are the long extravasation time and low diffusion at the pathological target site. For these reasons, the use of nanosized carriers may reduce the omogeneous distribution of the drug and the imaging agent in the tumor region. In this work, to overcome these problems the use of a natural protein such us apoferritin as theranostic carrier with a smaller size and higher biocompatibility is proposed. Apoferritin is an interesting carrier for molecular imaging agents since its internal cavity can be loaded with Mn^{2+} ions or Gd-complexes to yield a system endowed with high T_1 relaxation enhancement capability. Furthermore, ferritin is taken up by specific receptors (SCARA 5) that are expressed in liver and developing kidneys. Thus for the treatment of these organs ferritin can be used without further modifications. Recently, there is an increasing interest in the use of curcumin in different therapeutic applications as a consequence of its anti-oxidant, anticarcinogenic, anti-infiammatory activities. In this work we propose the use of apoferritin as a simultaneous carrier of curcumin and GdHPDO3A for the attenuation of thioacetamide-induced hepatitis together with the evaluation by MRI of drug delivery efficiency.

Subjects and Methods: Gd-HPDO3A and curcumin have been included in the apoferritin cavity by exploiting the protein dissociation at pH=2 followed by its re-association in the presence of the two compounds at pH=7. Mice were treated intraperitoneally with a curcumin dose of 20 mg/kg 24h before the thioacetamide treatment (60mg/kg).

Results: Biodistribution of apoferritin loaded with curcumin and Gd-HPDO3A was followed by MRI measuring liver signal intensity enhancement of T_1-weighted images. The high relaxation enhancement efficiency of Gd complexes inside the cavity permits the detection of low concentrations of the imaging probe. The efficacy of the prevention treatment in the attenuation of hepatitis has been evaluated by measuring alanine aminotransferase (ALT) activity in serum and by histology.

Discussion/Conclusion: Curcumin-loaded-Apoferritin has shown beneficial properties in thioacetamide-induced liver damage. Drug concentration at the pathological site was measured by MRI in order to plan optimal treatment timing.

References:

S. Geninatti-Crich, et al CMMI 2012, 7.

606

Imaging pathogens by MR: Distribution of SPIO-labeled parasitic protozoan Entamoeba histolytica in the liver of a mouse model at 7T

T.M. Ernst[1], H. Bernin[2], E. Helk[2], M. Zaruba[2], M.G. Kaul[3], G. Adam[1], H. Lotter[2], H. Ittrich[1]

[1]Department for Diagnostic and Interventional Radiology, University Medical Center Hamburg-Eppendorf, Hamburg/GERMANY, [2]Molecular Parasitology Department, Bernhard Nocht Institute for Tropical Medicine, Hamburg/GERMANY, [3]Department of Diagnostic and Interventional Radiology, University Medical Center Hamburg-Eppendorf, Hamburg/GERMANY

Purpose/Introduction: To evaluate the labeling efficacy, migration behavior and *in vivo* distribution of the enteric parasite protozoan *Entamoeba histolytica* (*E.h.*) within the liver in MRI after injection in a mouse model.

Subjects and Methods: In vitro magnetic labeling of *E.h.* was performed with commercially available superparamagnetic iron oxide nanoparticles (SPIO) with polyethylene glycol (PEG) coating (nano-screenMAG-PEG/P, Chemicell, Germany, hydrodynamic diameter 200 nm) by incubation for 48h in culture medium. Labeling efficiency and migration behavior of SPIO-*E.h.* was proven in MRI in vitro in culture medium in the static magnetic field of a preclinical 7T MRI system (ClinScan, Bruker) using T2w and T2*w dynamic susceptibility contrast MR sequences (DSC-MRI) for 88 hours (temporal resolution 4 min./image, effective voxel size 80x80x600(μm)^3). Movement patterns were analyzed using ImageJ (NIH, USA).

For *in vivo* experiments 10^5 SPIO-*E.h.* were injected in the left liver lobe of mice followed by serial respiration triggered T2*w and T2w MRI up to 3 days after injection. Furthermore *ex vivo* high resolution MRI was performed on removed liver specimens for *in/ex-vivo* comparison.

MR images were matched with histology (PAS and Prussian Blue stains) as well as immunohistochemistry.

Results: Efficient magnetic labeling of *E.h.* could be performed by incubation with PEG-coated SPIO keeping the pathogenity and viability of *E.h.*. *In vitro* dynamic MRI showed an undirected migration of single SPIO-*E.h.* in culture medium with pathogen movement in macroscopic dimensions with typical speeds of up to 4 mm/h.

In vivo and ex-vivo MRI of SPIO-*E.h.* showed strong *E.h.* presence at the site of amebic liver abscess formation and broad distribution within the left liver lobe, whereas no SPIO-*E.h.* could be detected in liver lobes different from lobe of injection. All MR findings were confirmed by histology.

Discussion/Conclusion: Efficient magnetic labeling and non-invasive *in-vivo* migration monitoring of pathogenic E.h. within the murine liver tissue is feasible in MRI.

607

Amphiphilic Mn(II) complexes for incorporation into nanosized lipidic systems for MRI applications

G.A. Rolla[1], L. Tei[1], M. Botta[1], L.W..E. Starmans[2], G.B. Giovenzana[3], V. De Biasio[3], G. Mulas[4], E. Terreno[5]

[1]DiSIT, Università del Piemonte Orientale "Amedeo Avogadro", Alessandria/ITALY, [2]Department of Biomedical Engineering, Eindhoven University of Technology, Eindhoven/NETHERLANDS, [3]Dipartimento di Scienze del Farmaco, Università del Piemonte Orientale "Amedeo Avogadro", Novara/ITALY, [4]-, Porto Conte Ricerche Srl, alghero/ITALY, [5]Chemistry-University of Turin, Molecular Imaging Center, Torino/ITALY

Purpose/Introduction: To achieve both human-safe and highly contrast-efficient Mn(II)-based Magnetic Resonance Imaging contrast agents, ligands forming stable complexes associated with first sphere hydration are required.[1] In this work, EDTA and 1,4-DO2A (1,4,7,10-tetraazacyclododecane-1,4-diacetic acid) were chosen as platform to develop amphiphilic Mn(II) complexes bearing aliphatic chains of different length (C_{12} or C_{16}) suitable for liposome formation. The two independent hydrophobic chains (Scheme) improve the motional coupling between the paramagnetic unit and the nanoparticle.[2] Liposomes are clinically established nanosized systems which pharmacodynamic properties can be fine tuned. Therefore they are an ideal platform do deliver MRI contrast.

Subjects and Methods: Mn(II) complexes of the ligands reported in the figure were studied by ^{1}H NMR relaxometry. In water, all complexes formed aggregated structures of variable shape even at very low concentration (< 0.2 mM). Liposomes were also prepared by hydration of a thin lipidic film consisting of DPPC, DSPE-PEG2000 and the amphiphilic Mn(II) complex (or the corresponding diamagnetic Zn(II) complex) in molar ratio 85:5:10 or 75:5:20. Both aggregates and vesicles were characterized by dynamic light scattering in order to assess the mean hydrodynamic diameter and the polydispersity of the system. Cryo-transmission electron microscopy allowed to characterize size and shape of the aggregated structures.

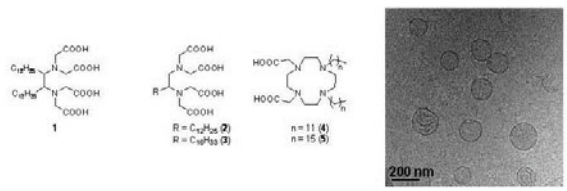

Ligands structures. Cryo-TEM image of Mn(**4**)-based liposomes

Results: Small unilamellar vesicles (~30 nm) were formed by incorporation of 10% Mn(**1**), while incorporating more chelate (20%), smaller micellar aggregates were obtained (~15 nm). The relaxivity (r_1) of both particles were determined as 9.2 and 11.0 $mM^{-1}s^{-1}$ (20 MHz, 310 K), respectively.

Discussion/Conclusion: The two adjacent C_{12} chains seems to force the vesicle to assume this curvature as, using Mn(**2**), the corresponding liposomes have size of about 110 nm. In case of Mn(**4**) and Mn(**5**), liposomes of 109 and 124 nm and with r_1 of 12.3 and 13.0 $mM^{-1}s^{-1}$ (20 MHZ, 310 K) were obtained, respectively. Analogous vesicles were formed by incorporating the corresponding Zn(II) chelates in the membrane and ProHance® in the aqueous compartment to estimate the rate of water diffusion through the membrane which resulted to be faster for liposomes containing chelates with shorter chains. These system seem promising for application.

References:
1) Toth E. *et al.* **2012**, *Eur. J. Inorg. Chem.* 1975–1986
2) Botta M. *et al.* **2010**, *J. Am. Chem. Soc.* 7836–7837

EPOS™ Poster

Motion, artefacts, quality control

608

The study of stimulus correlated motion fMRI artifacts using the computer controlled motion inducing device.

L. Budinsky[1], L.C. Konerth[2], A. Hess[2]
[1]*MRI lab., Institute of Pharmacology FAU, Erlangen/GERMANY,*
[2]*Experimental and Clinical Pharmacology and Toxicology, University of Erlangen Nuremberg, Erlangen/GERMANY*

Purpose/Introduction: The stimulus correlated motion of head is very well known source of artifacts in BOLD fMRI [1]. Such motion can leads to measured signal intensity changes that can mimic the BOLD signal. Very specific situation is in animal pain research. Animals are measured under influence of anesthetics, but still can response to painful stimulus by series of short body and head movements. Such motion is generally correlated with used stimulus, but has random nature. To study such influence we used home build computer controlled device which is capable of simulate this problem.
Subjects and Methods: fMRI experiments were performed on a 4.7 T BRUKER *Biospec* scanner using dead Wistar male rats. A functional series of 500 sets of eleven axial GE EPI images (slice thickness 1 mm, field of view 25 x25 mm, matrix 64x64, TR = 1000 ms, TE_{ef} = 23.4 ms) was acquired. The measurement was repeated with SE EPI, with the same parameters but TE_{ef} = 64ms. During EPI experiments motion was induced by an air driven device integrated into the cradle which secures the animals in the scanner. Two inverted combs located at 2 cm of both sides of the snout allowed stimulations at frequencies between 0-15 Hz. For this study the head of the rat was connected with a rubber string to the combs. Different softness of the rubber string was used for the different degree of the coupling between the moving combs and the rat head, or the phantom, respectively. For minimal coupling no rubber string was used and the motion was induced just by vibration in the cradle. Combs were driven from an external console running a custom stimulation software. Functional analysis was performed using BrainVoyager and custom made IDL programs [2].
Results: We performed a series of experiments with dead rats to show the character of false BOLD activation. All experiments were performed with both spin and gradient echo EPI. Typical result is on Fig. 1a for GE EPI and Fig. 1b for SE EPI. In all our experiments we saw systematically lower number of false area of activation for SE EPI compare to GE EPI.

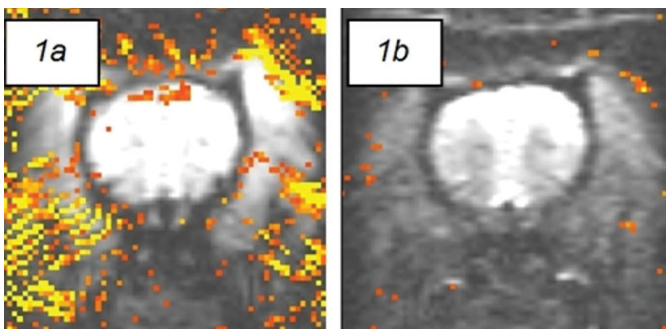

Discussion/Conclusion: The computer controlled motion inducing device is powerful tool for study of stimulus correlated motion artifacts in BOLD fMRI. We present series of experimental results showing different aspects of this problem.
References:
1. Birn et al (1999) Human Brain Mapping 7;106-114 2. Knabl et al (2008) Nature 451: 330-335,

609

The need for quality testing of multi-channel phased array coils

W. Nordhøy, T.E.D. Orheim
The Intervention Centre, Oslo University Hospital, Oslo/NORWAY

Purpose/Introduction: Since the introduction of multi-channel phased array coils, the number of channels and coil elements has increased. This has improved SNR and enabled faster imaging by parallel imaging techniques. At our hospital we have developed a quality assurance (QA) program to identify and monitor the stability of the image quality of our MRI images.
The vendors' QA programs are extensive and include dedicated phantoms, phantom holders for the different coils and analysis software. They offer quarterly or semi-annual testing of scanner performance, but it's very variable how often, and which, coils they test. Some vendors only test the coils upon installation, while others include coil testing in their periodic maintenance (PM).
Subjects and Methods: Recently, we have revealed many failures on our system after the PM, and most often on coils. Phased array coils produce one image per channel, which are combined to make the final or composite image. The most common failure is that one of the coil elements in a phased array coil has very reduced SNR or no signal at all. This usually happens without warning from the MRI system and is very often difficult to reveal in the clinical images. Since there often is significant overlap between channels, problems with single channels can be masked, especially using parallel imaging.
Therefore, we have started to check the coils on our MRI scanners, where two interesting cases are presented here.
Results: When we started testing the coils on one of our MRI scanners, we discovered that the knee coil did not pass the vendors coil test even though there had been no complaints about the image quality in the knee images. When we notified our vendor about the problem, they replaced the coil. Figure 1 shows the scaled SNR and noise in the images from the coil elements, where element number six failed the test.
On another MRI scanner the technicians discovered an artefact that appeared as a wide horizontal stripe in a patient's thigh. A coronal image of a phantom showed a large and defined area of reduced signal intensity, indicating coil failure (figure 2). When we did a quality check of the coil, two elements failed the test.

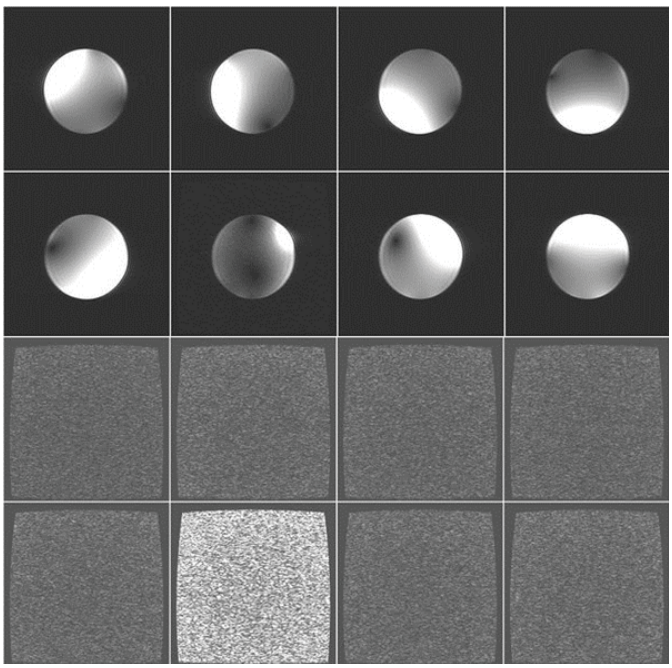

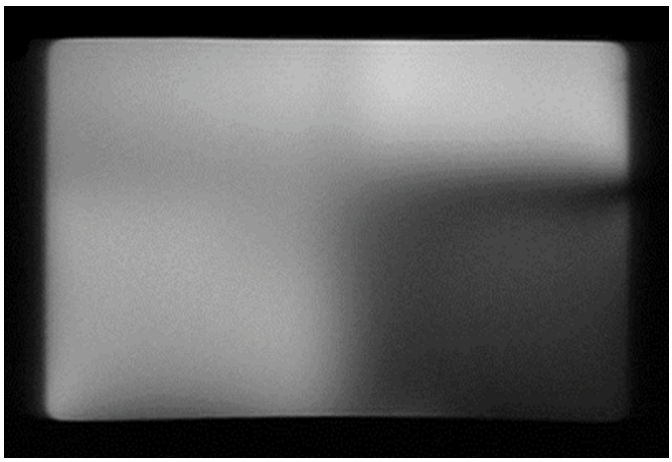

Discussion/Conclusion: Based on our experience we strongly recommend that the technicians check the quality of their coils on a regular basis, and not only the final composite image, but also the individual coil elements.

References:

RSNA 2011 ACR Performance Evaluations by Moriel NessAiver: http://www.simplyphysics.com/MRI%20QA%20RSNA%202011.pdf

EPOS™ Poster

Musculoskeletal

610

Comparison of spinal cord markers on Magnetic Resonance Imaging (MRI) with surgical findings for accurate detection of intracanalicular space occupying lesions

M. Goldust
Student research committee, Tabriz university of medical sciences, Tabriz/IRAN

Purpose/Introduction: Spinal canal space occupying lesions (SOL) fall into a distinct category because their timely diagnosis. Precise localization of these lesions is very important in cases undergoing surgery. This study aims at evaluating preoperative skin marking by using magnetic resonance imaging in locating these lesions in candidates of surgery due to spinal canal SOLs.
Subjects and Methods: In a cross-sectional analytic-descriptive study, 20 patients with spinal canal SOLs who were candidates of operation were studied. Adhesive radio-opaque markers were placed on the skin over predicated location of lesion. Magnetic resonance imaging without contrast was performed in all patients and accordingly, upper and lower limits of the lesion were marked on the skin. Operation was performed through these markers and the consequences were reported by the surgeons.
Results: Twenty patients, 14 males and 6 females with a mean age of 45.0±16.2 (20-72) years were enrolled on the study. There were 12 extradural and 8 intradural lesions; 3, 9 and 8 cases in cervical, thoracic and lumbar/coccygeal regions, respectively. The skin markers exactly represented the location of spinal canal SOLs determined during operation in 18 (90%) cases. In two (10%) cases, there was a little difference between the two locations.
Discussion/Conclusion: Preoperative imaging with adhesive skin markers facilitates positioning for surgery for spinal canal SOLs. The localization error is minor and negligible.
References:
1. Filippi M, Rocca MA, Calabrese M et al. Intracortical lesions: relevance for new MRI diagnostic criteria for multiple sclerosis. Neurology. 2010;75:1988-1994.
2. Hoch B, Hermann G. Migrated herniated disc mimicking a neoplasm. Skeletal Radiol. 2010;39:1245-1249.
3. Meurin A, Cernicanu A, Molinier S et al. [Diffusion-weighted MR imaging of the spine and cord]. J Radiol. 2010;91:352-366.
4. Peruzzotti-Jametti L, Ferrari S, Politi LS et al. Giant anterior arachnoid cyst associated with syringomyelia: implications for treatment and follow-up. Spine (Phila Pa 1976). 2010;35:E322-E324.
5. Hazzard MA, Patel NB, Hattab EM et al. Spinal accessory nerve cavernous malformation. J Clin Neurosci. 2010;17:248-250.
6. Mignarri A, Dotti MT, Battisti C et al. Occurrence of ankylosing spondylitis and multiple sclerosis-like syndrome in a HLA-B27 positive patient. Neurol Sci. 2009.

611

Optimizing the lesion-to-bone-marrow contrast of diffusion-weighted steady-state free-precession (DW-SSFP) acquisitions of the spine

O. Dietrich[1], A. Biffar[1], A. Baur-Melnyk[2], G. Schmidt[2], M. Reiser[2]
[1]Josef Lissner Laboratory for Biomedical Imaging, Institute for Clinical Radiology, Ludwig-Maximilians-University Hospital Munich, Munich/GERMANY, [2]Institute for Clinical Radiology, Ludwig-Maximilians-University Hospital Munich, Munich/GERMANY

Purpose/Introduction: Diffusion-weighted steady-state-free-precession (DW-SSFP) sequences are extremely valuable for the differential diagnosis of benign osteoporotic and malignant neoplastic vertebral compression fractures, which appear hypo- to isointense (benign lesions) or hyperintense (malignant lesions)[1,2]. However, the DW-SSFP signal depends not only on the apparent diffusion coefficient (ADC), but also in a complex way on the tissue relaxation times and pulse-sequence parameters. A recently published analysis of the DW-SSFP signal in vertebral bone marrow (VBM) indicated that the observed image contrast is rather fat- and T_2*-weighted than diffusion-weighted[3]. The purpose of the present study was to extend these results by analyzing if an optimal choice of acquisitions parameters can provide even better lesion contrast than currently used protocols.
Subjects and Methods: The DW-SSFP signal in VBM and vertebral lesions was analyzed as described by Biffar et al.[3] This signal model is an extension of the theory by Wu&Buxton[4,5] with additional terms describing T_2*-relaxation and effects of the combined fat and water signal in VBM. The signal depends on T_1, T_2, T_2*, and ADC of both signal components (fat and water), on the fat fraction and the sequence parameters TR,TE, flip angle α, and diffusion-gradient moment $M_D = G \cdot \tau$ (gradient-amplitude-duration product).
Tissue parameters for normal-appearing VBM, osteoporotic, and neoplastic lesions were obtained from 1.5-Tesla measurements in 40 patients. Initial (non-optimized) sequence parameters were taken from[3].
Lesion contrast was defined as contrast-to-noise ratio (CNR) of the lesion and (neighboring) normal-appearing VBM. To optimize acquisition parameters for both types of lesions at once, the product P_{CNR}=−CNR(malignant)·CNR(osteoporotic) of the CNRs of both lesion types was chosen as target quantity. (Hypointense-vs.-hyperintense lesion contrast is reflected by the positive sign of P_{CNR}.) P_{CNR} was evaluated for a broad range of acquisition parameters (1) by varying only one or two parameters and (2)by finding the global optimum when all parameters were varied.
Results: The simulated contrasts(Fig.1,2) indicate that the initial sequence parameters(P_{CNR}=24.2) are already relatively close to the optimum if only 1 parameter is varied. The global optimum was P_{CNR}=36.1 for TR=17.0ms(min. possible TR), α=52.6°,M_D=0,TE=7.3ms.

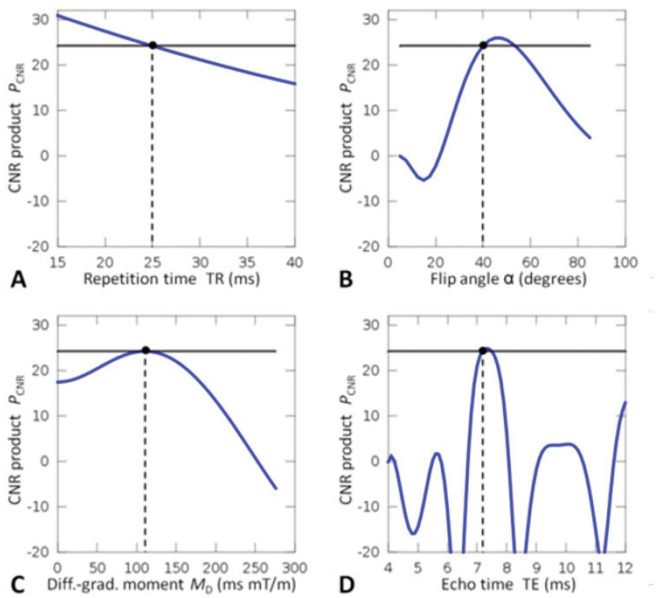

Fig. 1: Obtainable CNR products between lesion and normal-appearing bone marrow (product of CNRs of benign and malignant lesions) for varying acquisition parameters: **A:** TR, **B:** flip angle, **C:** diffusion-gradient moment, **D:** TE. The solid black line indicates the CNR product of the initial (non-optimized) protocol; the initial parameter value is indicated by the dashed line and black circle. The parameters were chosen already close to their optimal values in the initial protocol.

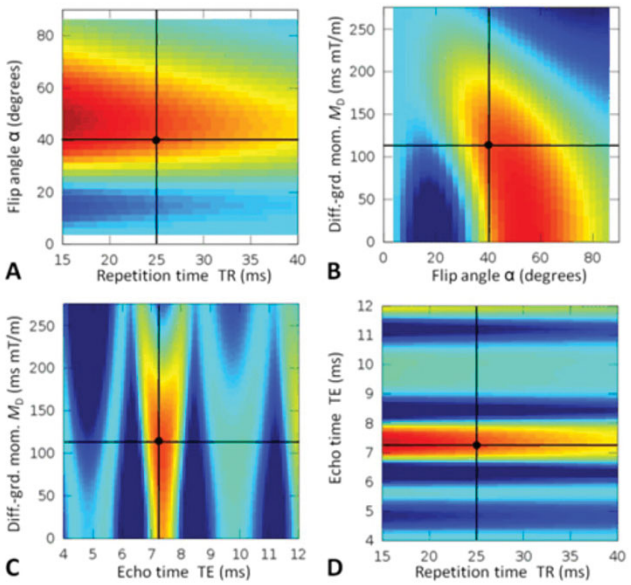

Fig. 2: Obtainable CNR products between lesion and normal-appearing vertebal bone marrow (product of CNRs of benign and malignant lesions) for varying acquisition parameters: **A:** TR & flip angle, **B:** flip angle & diffusion-gradient moment, **C:** diffusion-gradient moment & TE, **D:** TE & TR. High CNR products are shown in red, low values in blue. The initial parameters are indicated by the black circle. Most interesting is the relationship between diffusion weighting and flip angle (B) indicating that lower diffusion weightings are preferred at slightly higher flip angles.

Discussion/Conclusion: The established DW-SSFP protocol[3] provides a very good lesion differentiation due to opposed-phase effects that can be further optimized by decreasing TR, slightly increasing α, and reducing the diffusion-weighting.

References:

[1]Baur-A,… Radiology 1998;207:349. [2]Karchevsky-M,… SkeletalRadiol 2008;37:791. [3]Biffar-A,… InvestRadiol 2011;46:601. [4]Wu-EX… JMagnReson 1990;90:243. [5]Buxton-RB. MRM 1993;29:235.

612

When compared to pre-contrast MR images assessing tumors following neoadjuvant therapy, does gadolinium-enhanced MR change diagnosis or reader confidence?

P.D. Afonso[1], C. Spritzer[2]
[1]Radiology, Hospital Beatriz Angelo, Loures/PORTUGAL, [2]Radiology, Duke University Medical Center, NC/NC/UNITED STATES OF AMERICA

Purpose/Introduction: 1.Evaluate if gadolinium enhanced MR(GeMR) changes the final diagnosis in the assessment of musculoskeletal(MSK) tumor following neoadjuvant therapy (radiotherapy, chemotherapy or radiochemotherapy) before surgical resection.
2.Determine if GeMR improves the confidence of the interpreting radiologist
3.Assess if different experience levels change the above results

Subjects and Methods: This is an IRB approved retrospective review of 49 studies (26men,23women; mean age 51years [18-91]) with clinical indication of ongoing or completed neoadjuvant therapy (radiotherapy, chemotherapy or radiochemotherapy) of aggressive or malignant soft tissue (n=41) or bone (n=7) tumors, all prior to definitive surgical resection. All were imaged with T1WSE, T2WFSE or STIR and post contrast non-fat sat T1wSE.
Initially, the precontrast images were reviewed by 2 radiologists, one with 25 years of experience(reader1) and one undergoing MSK specialty training(reader2). Three questions were answered: 1.Mass or scar present? 2.Cystic or solid? 3.Likelihood of malignancy? Subsequently, both contrast and postcontrast images were reviewed. The same questions were answered again and 6 other questions were answered including if: GeMR defined cystic vs solid mass better,better defined extent,improved conspicuity,improved confidence, and changed the final diagnosis. All reads were independent.
Histologic diagnosis was available in 48 cases.

Results: GeMR defined cystic versus solid better for reader1 (reader2) in 28 (41) cases, increased conspicuity in 13(24), defined extent better in 5(5) for reader1 (reader2). GeMR significantly improved confidence in 3(10) and slightly improved confidence in 6(27) cases. The final diagnosis was changed in 4(4) cases for reader1 (reader2). Experience did change GeMR utility. There was no significant correlation between the readers(k=0.09)

Discussion/Conclusion: Compared to nonenhanced images, GeMR helped to define cystic/necrotic areas better in 57,1% (83,6%) for the more and less experienced readers; it changed the diagnosis in 8% for both readers. Reader confidence was improved either significantly in 6.1%(20%) or slightly in 12.2% (55,1%) for reader1 (reader 2). Experience did lessen GeMR utility; the lesser degree of expertise, the higher the utility of contrast.
Where possible, GeMR should be used in the MR assessment of patients with ongoing or completed neoadjuvant therapy prior to resection.

References:

Fletcher M., Unni K, Mertens F. (Eds.): WHO Classification of Tumours. Pathology and Genetics of Tumours of Soft Tissue and Bone. IARC Press: Lyon 2002
Vanel D et al, MRi in the Follow-up of Malignant Soft-Tissue Tumors: Results of 511 Examinations; Radiology 1994; 190: 263-268
D.Vanel *et al*; Musculoskeletal tumors: Follow up with with MRI after treatment with Surgery and Radiation Therapy; Radiology 1987; 164: 243-245

613

Bilateral Magnetic Resonance Imaging of the Hand and Wrist in Early and Very Early Inflammatory Arthritis: Tenosynovitis is Associated with Progression to Rheumatoid Arthritis

M. Navalho[1], A.M. Rodrigues[2], J.E. Fonseca[2], H. Canhao[2]
[1]Radiology, Hospital dos Lusíadas, Lisboa/PORTUGAL, [2]Rheumatology Research Unit, Instituto de Medicina Molecular, Lisboa/PORTUGAL

Purpose/Introduction: To identify bilateral hand and wrist findings of synovial inflammation that are associated with progression to Rheumatoid Arthritis (RA) in a very early arthritis cohort (VERA, disease duration < three months) and in an early arthritis cohort (ERA, disease duration < 12 months). Also to test tenosynovitis as an MRI additional parameter for improving the diagnostic accuracy of the 2010 American College of Rheumatology/European League against Rheumatism (ACR/EULAR) RA classification criteria. Lastly, to evaluate the symmetry of joint and tendon involvement.

Subjects and Methods: Institutional review board approval and informed patient consent were obtained. Thirty-five patients (32 women, 3 men; mean age 45 years) with untreated recent-onset inflammatory arthritis participated in this prospective study and were examined using an MRI approach including both wrists and hands. After a follow-up of 12 months, 25 patients fulfilled the criteria for RA (10 VERA patients and 15 ERA patients). Ten patients did not fulfil the criteria for RA (Non-RA) and had other diagnosis. Possible associations between synovitis for each joint and tendon and RA diagnosis at 12 months were tested by univariate logistic regression analysis. The diagnostic performance of the ACR/EULAR RA classification criteria was evaluated using receiver operating curve (ROC) analysis. Asymmetry prevalence was also calculated considering all the joints and tendons in the analysis.

Results: Tenosynovitis of the extensor carpi ulnaris (odds ratio [OR], 3.21) and of the flexor tendons of the second finger (OR, 14.61) in the VERA group and synovitis of the radioulnar joint (OR, 8.79) and tenosynovitis of the flexor tendons of the second finger (OR, 9.60) in the ERA group were the most significantly associated with progression to RA ($p < 0.05$). Consideration of tenosynovitis improved area under the curve values of the ACR/EULAR criteria performance for the diagnosis of RA from 0.942, $p < 0.0001$ (sensitivity, 52%; specificity, 100% for the cutoff score ≥ 6) to 0.972, $p < 0.0001$ (sensitivity, 76%; specificity, 100% for the cutoff score ≥ 6). Asymmetry was found in 80.0% and 69.3% of joint or tendon pairs of VERA and ERA patients, respectively ($p < 0.05$).

Discussion/Conclusion: Tenosynovitis is an imaging finding in early RA, and its inclusion as a scoring criterion might contribute for a better diagnostic

performance of the 2010 ACR/EULAR classification. Furthermore our study showed that early RA is an asymmetrical disease.

614

Quantitative Assessment of Fat Infiltration using MRI and correlation with clinical symptoms in the Rotator Cuff Muscles of the shoulder.

L. Nardo[1], D. Karampinos[1], J. Carballido-Gamio[1], D. Lansdown[2], H. Misung[3], B. Ma[2], R. Maroldi[4], T.M. Link[1], R. Krug[3], A. Lai[3]
[1]Radiology, University of California San Francisco, San Francisco/CA/UNITED STATES OF AMERICA, [2]Orthopedic Surgery, UCSF, San Francisco/UNITED STATES OF AMERICA, [3]Radiology, UCSF, San Francisco/UNITED STATES OF AMERICA, [4]Radiology, University Of Brixia, Brescia/ITALY

Purpose/Introduction: The goals of our study were (i) to validate the semi-quantitative Goutallier's classification (GC) using objective MR based IDEAL fat quantification[1] and (ii) to assess whether GC and IDEAL fat quantification predict clinical parameters (range of motion and pain).
Subjects and Methods: A cohort of 56 patients with rotator cuff tear symptoms (30 males, 26 females, aged 22-69) were scanned using 3T MRI with a 4 channel shoulder coil. MRI sequences included sagittal T1-w and PD-w FSE and a six-echo spoiled gradient echo pulse sequence. Fat fraction maps were reconstructed online from the gradient echo images using the IDEAL algorithm with T2* correction and a multi-peak model for the fat spectrum

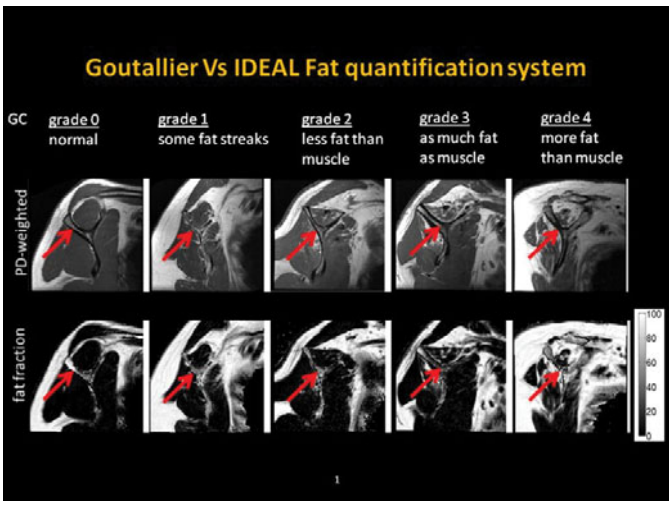

. Clinical parameters concerning pain (using Visual Analog Scale), strengt range of motion (intra/extrarotation, abduction, flexion and extension) of the shoulder were recorded. Fisher's exact test was used to compare GC grades and IDEAL fat fraction values; Spearman rank correlation (SRC) test compared GC grades and IDEAL fat fraction values to clinical variables.

Results: Based on Fisher's exact test result, GC grade correlated with the quantitative IDEAL fat fraction values ($p < 0.0001$ with an associated kappa estimate > 0.9). Mean fat fraction values consistently increased with Goutallier grade: grade 0 ranged from 0% to 5.59%, grade 1 from 1.1% to 9.70%, grade 2 from 6.44% to 14.86%, grade 3 from 15.25% to 17.77%, grade 4 from 19.85% to 24.61%. A significant correlation between fat infiltration of the subscapularis muscle quantified with IDEAL versus a) deficit in internal rotation (SRC= 0.39, 95% CI 0.13-0.60, $p < 0.01$) and b) pain (SRC= 0.313, 95% CI 0.049-0.536, $p = 0.02$) was found. Also high degrees of fat infiltration in the infraspinatus muscle were correlated to deficit in external rotation (SR: 0.37; $p < 0.01$). Additionally, fat infiltration of the supraspinatus muscle was significantly correlated with deficit in abduction of the shoulder (SRC= 0.45, 95% CI 0.19-0.65, $p < 0.01$). GC grade did demonstrate only a borderline correlation with deficit in internal rotation of the subscapularis muscle (SRC= 0.30, 95% CI 0.00-0.53, $p = 0.04$); no other correlations were demonstrated between GC grade and other variables (Spearman p-values >0.05).
Discussion/Conclusion: Semi-quantitative grading of fat infiltration using GC and quantitative fat fraction values derived using quantitative IDEAL were strongly correlated. However, only quantitative measures from IDEAL significantly correlated with pain and range of motion of the rotator cuff muscles.
References:
1. Karampinos DC et al., J Magn Reson Imaging.

615

DTI of the lumbar multifidus in subjects with and without symptoms of low back pain at 3T

G.E. Jones[1], D.A. Kumbhare[2], **M.D. Noseworthy**[3]
[1]School of Biomedical Engineering, McMaster University, Hamilton/ON/CANADA, [2]Physical Rehabilitation, McMaster University, Hamilton/ON/CANADA, [3]Electrical and Computer Engineering, McMaster University, Hamilton/ON/CANADA

Purpose/Introduction: Currently, there is no objective clinical method to evaluate the muscular impairment associated with low back pain (LBP) symptoms. Diffusion tensor imaging (DTI), a rotationally invariant method to measure water diffusivity has been shown useful in assessing muscle damage **[1]**. We hypothesized that increased diffusion is associated with inflamed or injured muscle and can be used to quantify impairments of the lumbar multifidus.
Subjects and Methods: In a study approved by our local ethics committee, 28 patients with lower back pain, and 26 healthy controls, were scanned using a GE Signa HD 3T MRI (GE Healthcare, Milwaukee WI). Axial DTI scans covered L3-L5 (TR/TE=10000/67ms, 15 directions, b=400s/mm^2, 5mm thick, NEX=4, matrix=64X64, FOV=40cm). Regions of interest (ROIs) were traced on 3D-fSPGR images of right and left multifidii from level T2-T5 (**Fig.1**). Also, an asymmetry index (AI) was calculated:

$$AI = \frac{\eta_{left} - \eta_{right}}{\eta_{left} + \eta_{right}}$$

Where η is the calculated DTI parameter of interest (eigenvalues, fractional anisotropy (FA), mean and radial diffusivity (MD, RD)). In addition questionnaires for LPB were administered (Oswestry, Godin Activity, and Visual Analog scale for pain). Statistical analysis was done using repeated measures ANOVA.

Results:

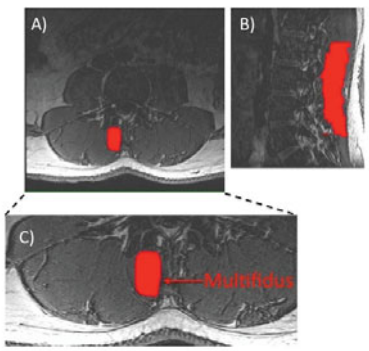

Figure 1 – Sample (a) axial, (b) sagittal, and (c) expaned T2W image of a 32 year old asymptomatic male, with the multifidus in red.

None of the DTI absolute measures were significantly different from healthy controls (**Table1**). However, the asymmetry index (AI) was significantly greater in LBP, relative to healthy controls, for FA and λ_1, (**Fig.2**). Furthermore, within-ROI standard deviation of these metrics was significantly greater in LBP, compared to healthy controls ($P<0.05$).

	Controls	LBP
FA	0.21±0.03	0.22±0.04
MD	1.67±0.15	1.65±0.17
λ_1	2.07±0.18	2.05±0.25
λ_2	1.56±0.15	1.55±0.18
λ_3	1.38±0.10	1.35±0.15
RD	1.46±0.14	1.45±0.16

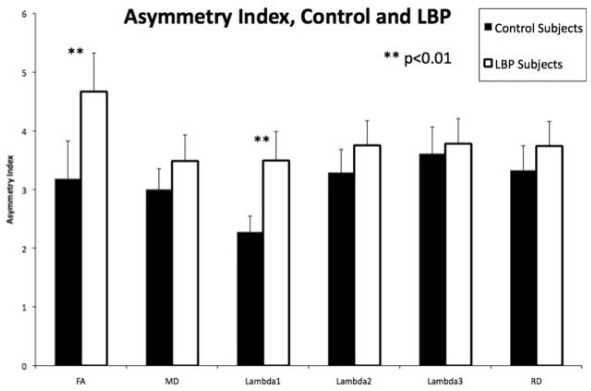

Figure 2 Asymmetry Index in controls and LBP.

Asymmetry index is related to both VAS (**Fig.3A**) and ODI (**Fig.3B**), as expected, but also subject weight (**Fig.3C**).

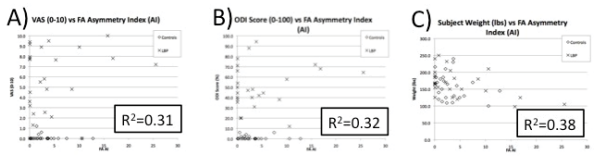

Figure3 – correlation between FA AI and A) VAS, B) ODI, C) subject weight, and BMI Pearson's R^2 is also shown.

Discussion/Conclusion: Neither DTI measures of λ_1, λ_2, λ_3, MD, RD or FA resolve the symptoms of LBP. However, bilateral asymmetry and intra-multifidus variability were both greater in the LBP compared to controls. FA asymmetry scales with both the symptoms of LBP and also subject's weight/BMI. Increased asymmetry in DTI metrics such is consistent with asymmetric damage to the multifidus based on previous work on tonic muscle activity [**2**] and cross sectional area [**3,4**].

References:

[**1**] Zaraiskaya, et al. (2006) JMRI 24:402-408.
[**2**] Hanada, et al. (2011) PMR 3:920-928.
[**3**] Hides, et al. (2010) Br J Sports Med 44:563-567.
[**4**] Hides, et al. (2008) J Orthop Sports Phys Ther. 38:101-108.

616

Magnetic resonance imaging in acute ankle inversion injures

I.S. Pashnikova, I.G. Pchelin, G.E. Trufanov
The Roentgenology and Radiology, The Kirov Military Medical Academy, St. Petersburg/RUSSIAN FEDERATION

Purpose/Introduction: Due to a numerous combinations of movements in a moment of ankle inversion trauma, different types of injures can develop. We present the pattern of injuries in acute ankle inversion trauma and show relations between these injured structures.

Subjects and Methods: 89 patients (male – 49, female – 40, average age – 31,3 years) with acute inversion ankle injury without fractures seen on radiographs were clinically assessed and performed magnetic resonance (MRI) examination.

Results: The pathologic findings seen on MRI were: anterior tibiotalar ligament (ATFL) tear (partial - n=56; 62,9%; complete - n=24; 26,9%), calcaneofibular ligament (CFL) tear (partial n=34, 38,2%; complete – n=16, 17,9%), peroneus brevis tendon partial tear (n=47, 52,8%); peroneus longus partial tear (n=41, 46,0%), peroneus longus complete tear (n=1, 1,1%), superior peroneal retinaculum tear with peroneal tendons dislocation (n=8, 8,9%); partial tear of sinus tarsi ligament complex and sinus tarsi fat inflammation (n=32, 35,9%), synovitis (n=87; 97,7%), talar dome osteochondral lesion (n=9; 10,1%); anterior process calcaneus fracture (n=4; 4,5%), fifth metatarsal tuberosity avulsion fracture (n=3, 3,3%). There were associated tears of ATFL and CFL in 21 cases; CFL tears were associated with the injury of sinus tarsi structures in 32 cases; with the peroneal tendon tears in 36 cases. All cases of osteochondral lesions and fractures of the anterior process calcaneus were associated with the ATFL tear.

Discussion/Conclusion: Different types of injures can occur in acute ankle inversion trauma. The most often pathologic changes to be revealed were anterior talofibular, calcaneofibular ligaments tears, peroneus longus and brevis tears and injury of sinus tarsi structures in different combinations. MRI can assess both soft tissue and osseous pathologic changes in acute ankle inversion injury.

References:

1. Bahel, A. Lateral plantar pain: diagnostic considerations / A. Bahel, J. S. Yu // Am. soc. emergency radiol. – 2010. – Vol. 10 – P. 1–8.
2. Bare, A. Peroneal tendon tears: associated arthroscopic findings and results after repair / A. Bare, R. D. Ferkel // Arthroscopy: j. arthr. rel. surgery. – 2009. – Vol. 25 (11). – P. 1288–1297.
3. Chan, K. W. Acute and chronic lateral ankle instability in the athlete / K. W. Chan, B. C. Ding, K. J. Mroczek // Bull. NYU hosp. joint dis. – 2011. – Vol. 69 (1). – P. 17–26.

617

Muscle 'mitochondrial capacity' inferred from ^{31}P MRS recovery kinetics compared with published invasive maximal-exercise measurements: implications for systems physiology

E.A. Ahmad[1], **G.J. Kemp**[2]
[1]MARIARC, University of Liverpool, Liverpool/UNITED KINGDOM, [2]Department of Musculoskeletal Biology, University of Liverpool, Liverpool/UNITED KINGDOM

Purpose/Introduction: A popular approach to assessing muscle mitochondrial function *in vivo* from ^{31}P MRS measurements of post-exercise phosphocreatine (PCr) recovery is based on the roughly hyperbolic relationship of oxidative ATP synthesis rate (Q, ≈ PCr resynthesis rate, V) to cytosolic [ADP]; this relationship resembles that obtainable with mitochondria *in vitro*, and is consistent with [ADP] as a feedback signal matching ATP supply to demand. Inference of 'mitochondrial capacity' (Q_{MAX}), as V extrapolated to 'infinite' [ADP], depends on the shape of Q *vs* [ADP], which appears to be sigmoid (Hill coefficient $n_H \approx 2$) [1], consistent with results of detailed computational simulation (2). We compared this apparent Q_{MAX} with representative published measurements by various methods.

Subjects and Methods: 11 healthy participants performed isometric 0.25 Hz knee-extension in a 3T Siemens Trio. ^{31}P spectra (3200 Hz bandwidth; 2s TR)

were collected from quadriceps using a dual-tuned (^{1}H/^{31}P) surface coil during 2-3 min exercise at 60% and 90% maximal voluntary contraction (MVC) followed by 5 min recovery. Data were analysed by monoexponential PCr recovery fit [1]. Extensive comparative data came from published O_2 consumption studies using arteriovenous difference (AVD) in maximal quadriceps exercise.
Results: Fig A shows Q vs [ADP] throughout recovery (mean±SEM), showing little difference between apparent Q_{MAX} for 60% and 90% MVC (26±2 vs 34±2 mM min^{-1}; P<0.005). Fig B shows that the common fit is consistent with some published ^{31}P MRS studies [3,4], including one used to test a computational model [2]. Fig C shows that Q_{MAX} implied by ^{31}P MRS is lower than multiple published AVD estimates using maximal knee extension, although similar to those using bicycle exercise (space precludes citing references).

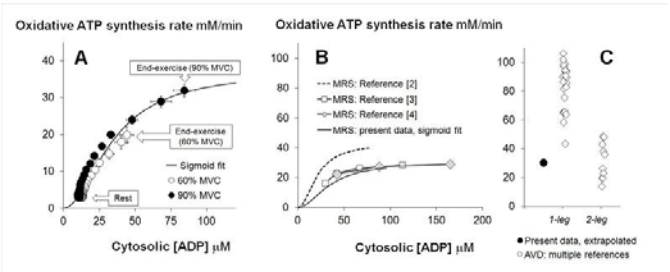

Discussion/Conclusion: The discrepancy between maximal O_2 consumption in 1-leg knee extension and 2-leg cycle ergometry evident in Fig C is attributed to cardiovascular limitations in the latter. Note the equally striking discrepancy between 1-leg knee extension AVD and 1-leg ^{31}P MRS, for which a 'system' explanation might perhaps involve 'parallel activation', or complex interactions between O_2 supply/demand and cellular PO_2.
Supported by the Government of Malaysia
References:
[1] Jeneson JAL et al. J Biol Chem 271:27995-27998,1996; [2] Jeneson JAL et al. Am J Physiol 297: E774-E784, 2009; [3] Takahashi H et al. Eur J Appl Physiol 71: 396-404, 1995; [4] Vanderthommen M et al. Int J Sports Med 20: 279-283, 1999.

618

ATP turnover and the coupling of mitochondrial oxidative phosphorylation during dynamic exercise in humans: a study combining skeletal muscle ^{31}P MRS and breath-by-breath gas exchange measurements

D.T. Cannon[1], T.S. Bowen[1], S.R. Murgatroyd[1], W.E. Bimson[2], H.B. Rossiter[3], **G.J. Kemp**[4]
[1]Institute of Membrane and Systems Biology, University of Leeds, Leeds/UNITED KINGDOM, [2]MARIARC, University of Liverpool, Liverpool/UNITED KINGDOM, [3]Division of Respiratory & Critical Care Physiology & Medicine, Los Angeles Biomedical Research Institute at Harbor-UCLA Medical Center, Torrance/CA/UNITED STATES OF AMERICA, [4]Department of Musculoskeletal Biology, University of Liverpool, Liverpool/UNITED KINGDOM

Purpose/Introduction: During constant work rate exercise (CWRE) above the lactate threshold (LT), the kinetics of oxygen uptake (VO_2) are supplemented by a slow component (VO_{2sc}), reflecting reduced work efficiency. Most of VO_{2sc} originates from active locomotor muscles, but intracellular contributions might include increased ATP cost of power production (P:W) or increased O2 cost of ATP synthesis (P:O) [1]. To distinguish these we used ^{31}P MRS to quantify ATP turnover in relation to VO_2 during sub- and supra-LT CWRE.
Subjects and Methods: Seven healthy participants performed prone bilateral knee-extension CWRE using a computer-controlled ergometer in a 3T Siemens Trio. ^{31}P spectra (3200 Hz bandwidth; 2s TR) were collected from quadriceps using a dual-tuned (^{1}H/^{31}P) surface coil. Moderate (MOD; sub-LT) and heavy (HVY; supra-LT) CWRE was completed for 3 and 8 min allowing total ATP turnover (ATP_{tot}) to be estimated at cessation from the early post-exercise dynamics of phosphocreatine (PCr) and proton handling [2-4]. In parallel experiments VO_2 was measured breath-by-breath using a mass spectrometer and turbine.
Results: VO_{2sc} was insignificant during MOD (0.07±0.15 L.min^{-1}) but larger (p<0.05) at 0.32±0.11 L.min^{-1} (20±6% fundamental VO_2 amplitude) during HVY (Fig A). The difference in [PCr] between 3 and 8 min was not significant (-2.8±4.0 mM) in MOD, but larger (p<0.05) at 2.1±1.5 mM (17±13% fundamental amplitude) during HVY (Fig B). ATP_{tot} was constant during MOD (19±12 vs 15±8 mM.min^{-1}; p>0.2) but increased 17±22% between 3 and 8 min HVY (24±13 vs 28±10 mM.min^{-1}; p<0.098). Despite similar mean relative magnitudes, ΔATP_{tot} was not correlated with VO_{2sc} during HVY (r=0.2; p>0.6).

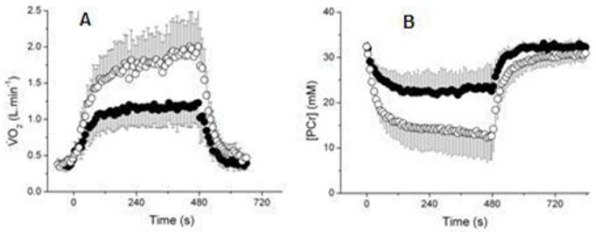

Figure shows (A) VO_2 and (B) [PCr] timecourse for moderate (●) and heavy (○) exercise and recovery (points = means; bars = SD).

Discussion/Conclusion: ATP turnover increased between 3 and 8 min of supra-LT but not sub-LT exercise. However, poor correlation between ΔATP_{tot} and VO_{2sc} suggests that reduced work efficiency in HVY exercise is not wholly explained by high P:W, but that reduced P:O may also contribute [1].
Supported by BBSRC UK BB/I001174/1 & BB/I00162X/1
References:
1] Rossiter et al. J Physiol 541:991-1002, 2002; [2] Layec et al. Exp Physiol 94:704-719, 2009; [3] Kemp et al. Magn Reson Med 33:601-609, 1995; [4] Lanza et al. J Appl Physiol 99:1736-1744, 2005.

619

An alkaline Pi pool and other possible markers of Duchenne Muscle Dystrophy by ^{31}P NMR spectroscopy of forearm at rest.

C. Wary[1], N. Azzabou[2], B. Matot[2], J. Hogrel[3], L. Servais[3], T. Voit[4], P.G. Carlier[2]
[1]IdM NMR Laboratory, CEA, I^{2}BM, MIRCen,, Paris/FRANCE, [2]NMR Laboratory, Institute of Myology AIM CEA, Paris/FRANCE, [3]Institute of Myology, AIM, Paris/FRANCE, [4]Institute of Myology, UM76-UPMC/U974-Inserm/UMR7215-CNRS, Paris/FRANCE

Purpose/Introduction: Duchenne muscular dystrophy (DMD) is the most common of the muscle wasting disorders, (~1:3500 male births). Replacement therapy has begun in the GRMD canine model and in human patients, and non-invasive, quantitative tools are required to evaluate its effects.
Known anomalies of resting muscle 31P spectra of DMD patients (low phosphocreatine, high phospho-monoesters and -diesters and increased pH) are non-specific but grade with disease severity when comparing DMD, to the milder Becker dystrophy and to disease carriers(1,2). More recently, we observed an additional alkaline component (Pib) at 0.3ppm from cytosolic Pi (Pia) in GRMD dog muscle(3). These 31P NMRS indices were measured in DMD patients as part of an observational evaluation protocol.
Subjects and Methods: Seven Duchenne boys, aged 8 to 14, successively underwent 31P spectroscopy of both forearms. Patients lay supine in a 3T-60cm bore magnet (Magnetom TRIO, Siemens, Germany), with a flex 1H-31P surface coil (RAPID Biomedical, Germany) facing the inside of the arm (11cm-diameter 31P loop). The arm rested either flat along the body, or on a slope when patients had retractions, Axial T1w images were acquired, and shims were optimized before 31P acquisition (TR=4s, NA=64, BW=3000Hz, 2048 points, hard pulse 500us). Spectra were processed combining time domain fittting (AMARES, jMRUIv4.0), and integration (TOPSPINv.1.5, Bruker, Germany).
Results: Signal-to-noise decreased strongly with fatty infiltration, but all resonances could be quantified in all 14 measurements, except for Pia which

was not detectable in one arm of one patient. Notably, Pib was observed even in the least affected subject (AH, Fig.1).

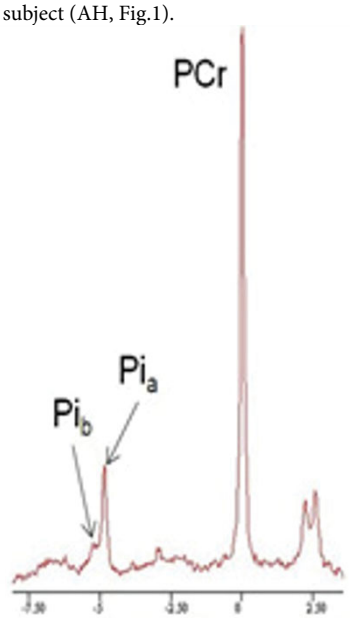

Fig. 1. Spectrum of right forearm of least affected patient **AH** showing Pi_b

Spectra ranged from almost normal appearance, to totally abnormal, extremes are tabulated below.

	Pi tot /PCr	Pib /PCr	Pia /PCr	Pi tot /ATP	Pib /ATP	Pia /ATP	PCr /ATP	PDE /ATP	PDE /PCr	PME /ATP	PME /PCr	pH_b	pH_a	mean pH
min	0.21	0.03	0.17	0.68	0.13	0.30	0.54	0.23	0.08	0.30	0.10	7.37	7.02	7.10
max	1.57	0.99	0.61	1.72	1.20	0.90	3.94	1.35	1.22	2.53	1.37	7.65	7.21	7.48

When patients were sorted according to degree of fat infiltration, several metabolic ratios followed the same ordering. In particular, Pib/PCr and PDE/PCr varied well over 10 fold across patients (Fig.2).

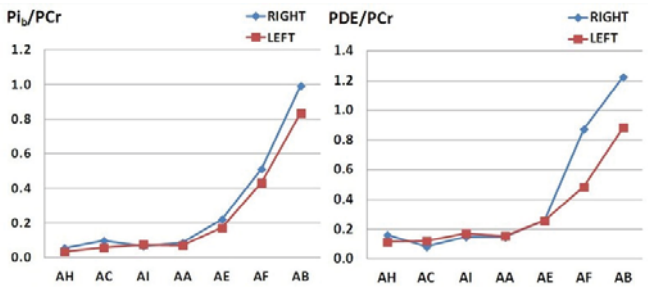

Fig. 2. Values for Pi_b/PCr and PDE/PCr. Individual patients are presented in order of increasing fat infiltration on T1w images

As in GRMD(3), Pib/Pitot correlated inversely with PCr/ATP (Fig.3).

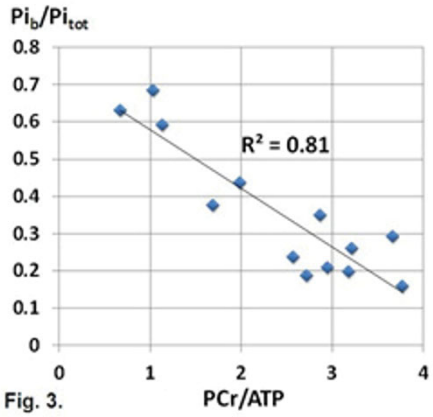

Fig. 3.

Discussion/Conclusion: Phosphorus spectroscopy at rest demonstrated a broad range of metabolic abnormalities in upper limbs of DMD patients. Among these, the Pib component suspected to originate from degenerating muscle cells(3) was systematically observed, and the increasing proportion of Pib with decreasing PCr/ATP confirms a relation to inadequate cell homeostasis. Several indices, as Pib/PCr and PDE/PCr, also related to membrane disruption, graded with disease progression, and may provide biomarkers of therapeutic efficacy, including in non ambulant patients.

References:

1. B. Barbiroli, et al., J Neurol Sci, 1992
2. G.J. Kemp, et al., J Neurol Sci, 1993
3. C. Wary, et al., NMR Biomed, 2012

EPOS™ Poster

Clinical Applications - Other

620

Advanced imaging processing supporting clinical practice: a description of an experience

A. Moscato[1], M. Minella[1], N. Colombo[2], F. Cardinale[3], **A. Torresin**[1]
[1]Medical Physics, Niguarda Ca' Granda Hospital, Milano/ITALY, [2]Neuroradiology, Niguarda Ca' Granda Hospital, Milano/ITALY, [3]Epilepsy Surgery, Niguarda Ca' Granda Hospital, Milano/ITALY

Purpose/Introduction: The purpose of this paper is to describe how in our hospital the Medical Physics Department is able to support clinical demand in the field of multimodal (but mainly MR-based) advanced imaging through the institution of an Imaging Laboratory.
The aim of this Laboratory is to develop solutions in order to allow the physicians to exploit some of the most recent imaging techniques, with the active contribution of physics support concerning methodologies, technical support and training
Subjects and Methods: The main activities of the laboratory could be summed up as follows: quality controls on scanners, service on demand about acquisition and processing of fMRI, DTI and Fiber Tracking, Spectroscopy, multimodality image fusion (PET-MR) and creation of advanced image series for radiotherapy treatment planning or neuronavigation in neurosurgery.
Results: The final result of every image processing is converted in DICOM format and stored in PACS with a technical report, which describes the performed image processing.
Finally, the collaboration with the physicians extends to radiological report drawing up and case discussion with surgeons.
Discussion/Conclusion: At this moment the activity of the Imaging Lab is mostly linked with Neuroscience Department. In fact multimodal neuroimaging offers a wide range of clinical applications (e.g. diagnosis, functional imaging, high resolution imaging for neuronavigation, 3D modeling for neurosurgery planning) that often need to be integrated.
However, some of the techniques and activities could be shared between neuro and body departments in a relatively simple way: for example magnetic proton spectroscopy, 3D modeling with scene creation for surgical planning. Multimodal imaging fusion are similarly applicable to neuro and body fields from a technical point of view.
A strong collaboration between Physicists and Physicians can enhance the quality of imaging laboratory skills and the ability to communicate reciprocally. In addition, some instruments or frameworks (e.g. customized softwares), once developed, could be directly available from the physicians without the need of a constant support.
Image analysis and manipulation often requires high computational performances. This is referable not only to single task computational speed, but also to the capability to perform multiple processing tasks at the same time.
To explore this feature we set up a cluster composed by our hardware managed with a grid-engine (SGE - Sun Grid Engine), which has the possibility to extend itself adding new machines with a relatively simple procedure. The cluster could be accessed directly from end users (e.g. physicians) for a wide range of imaging processing.

EPOS™ Poster

Preclinical Studies & Basic Science - Other

621

NMR-analysis of different galactocerebrosides in pig brain

S. Acikgöz, D. Leibfritz
Institute for Organic Chemistry, AK Leibfritz, University of Bremen, Bremen/GERMANY

Purpose/Introduction: Cerebrosides, a family of glycosphingolipis, are components of cellular membranes in eukaryotic cells. They mediate biological processes, such as intracellular communication and cell development.[1] In mammals, galactose and glucose are the main sugars in cerebrosides. Galactocerebrosides (GalCer) are enriched in neuronal tissue while glucocerebrosides are more abundant in non-neuronal tissue.
Analysis of lipids using NMR-spectroscopy enables lipid profiling in order to identify biomarkers for an early detection of diseases. Cancer and Alzheimer´s disease show disorders in ceramide metabolism. Therefore, it is essential to analyse the involved metabolites. In this study lipophilic extracts of pig brain were examined with NMR-spectroscopy after separation with solid phase extraction (SPE) in different lipid fractions.
Subjects and Methods: Frozen brain tissue from swine was extracted with chloroform/methanol/water (1:1:1). Afterwards, the organic phase was separated into five fractions using SPE following a modified method after Schweisguth et al. 1989[2]. The fractions were analysed in 600µL deuterated chloroform-methanol (2:1) with a Bruker Avance DRX-600 at 300K.
Results: The first fraction mainly included cholesterol, but also GalCer. This exists in two types. Type I comprises α-hydroxylated and type II non-hydroxylated fatty acids (Fig.1). Both species could be identified due to the different chemical shift of the α-CH_2-group next to the galactosyl linkage, which is 3,72+4,07/68,65ppm for type I and 3,59+4,16/68,96ppm for type II (Fig.2).

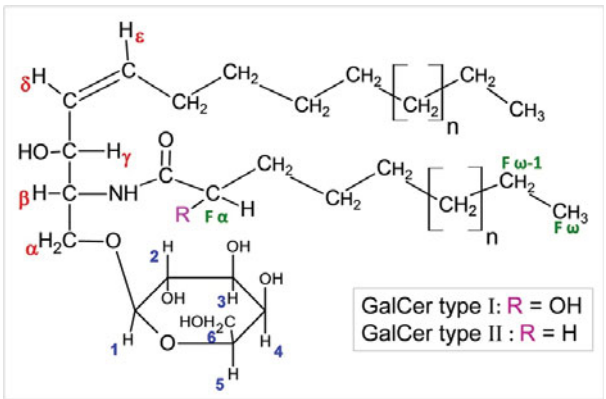

Figure 1: Structure of GalCer

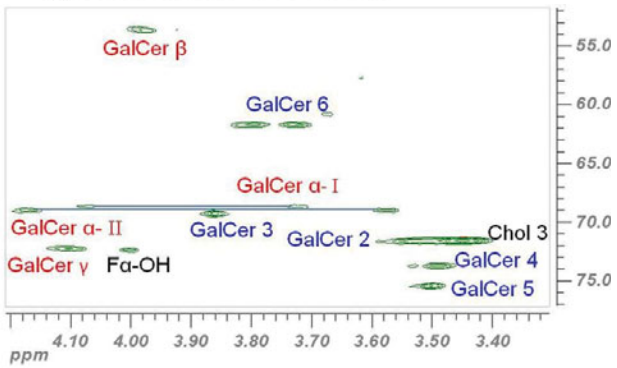

Figure 2: $^1H,^{13}C$-HSQC-Spectrum, Fraction 1

In the next fraction GalCer type I was identified. Comparison of ^1H-NMR-spectra of the first and second fraction showed that also the coupling pattern of the olefinic protons ε and δ for the two species were different.
The third fraction contained phosphatidylethanolamine (PE) and its plasmalogen derivatives. Another ceramide species was identified, which showed different chemical shifts for its headgroup in the HSQC-spectrum (Fig.3, encircled signals). Although various homo- and heteronuclear 2D-spectra were recorded, the proper structure is not clear yet.

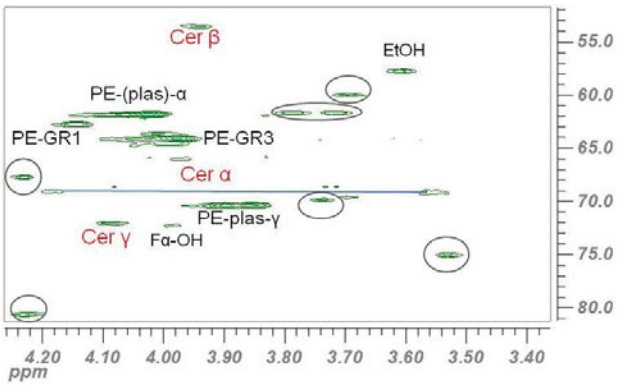

Figure 3: $^1H,^{13}C$-HSQC-Spectrum, Fraction 3

Phosphatidylcholines (PC) were separated from other lipids in the fourth fraction.
The last fraction, which is the expanding modification, was eluted with methanol. PC and sphingomyelin were detected.
Discussion/Conclusion: Three ceramide species in pig brain could be identified. α-hydroxy-GalCer is more polar than the non-hydroxylated type, therefore it eluted later. Accordingly, the unknown species must be the most polar of the ceramides. Furthermore, it is worth mentioning that it was possible to approximately separate such similar molecules with SPE.
References:
[1] R. X. Tan et al., Natural Product Reports; 2003; 20, 509-534
[2] D. C. Schweisguth et al., Biochemichal Education; 1989; 17; 211-213

622

Blood serum demonstrates antyoxidative mechanism: a Magnetic Resonance Relaxation Study

L.W. Skorski[1], B. Blicharska[2]
[1]Radiospectroscopy Department, Jagiellonian University, Krakow/POLAND, [2]Department of the Radiospectroscopy, Jagiellonian University, Krakow/POLAND

Purpose/Introduction: Reactive oxygen species (ROS) were indicated as a factor accelerating ageing process. There are produce in a number of biological processes. Cytotoxic action of ROS includes protein, lipid and DNA structure damage and can be primer to many human diseases, such as cancer, Parkinson's, Alzheimer's, multiple sclerosis, Huntington's and many others. ROS have paramagnetic properties and they significantly shorten relaxation times. Hydroxyl free radicals can be produced from hydrogen peroxide in a Fenton type reaction, classically written as such:
$Fe^{2+} + H_2O_2 \text{ ----> } Fe^{3+} + .OH + OH^-$
$Fe^{3+} + H_2O_2 \text{ ----> } Fe^{2+} + .OOH + H^+$
Here, we compared the effects of adding hydrogen peroxide to human blood serum and selected protein solutions on relaxation times to evaluate their antioxidative effects.
Subjects and Methods: Hydrogen peroxide was added to blood serum in-vitro, lyophilized bovine hemoglobin, bovine serum albumin and Fe2+ solution in relation 1:10. Fe and Cu concentrations in blood serum were estimated using spectrophotometry methods.
Proton NMR measurements of relaxation times were performed using a 60 MHz Minispec Bruker spectrometer Relaxation time T1 was measured by

the Inversion Recovery (IR) sequence, relaxation time T2 by CPMG method. Finally, experiments were repeated with various concentrations of vitamin-C or glutathione added to blood serum.
Results: Fig.1 illustrates the change in relaxation times as a function of time in blood serum contatining Fe an Cu, after addition of hydrogen peroxide. Please note increase in T_1 of blood serum after initial drop due to addition of hydrogen peroxide. This process was not observed in some ingredients of blood (hemoglobin, albumin and iron salt) which were separately performed. Interestingly, after addition of vitamin C and/or glutathione, the initial drop in T_1 is smaller than in blood serum, suggesting that these substances enhance the antioxidative properties of blood serum.

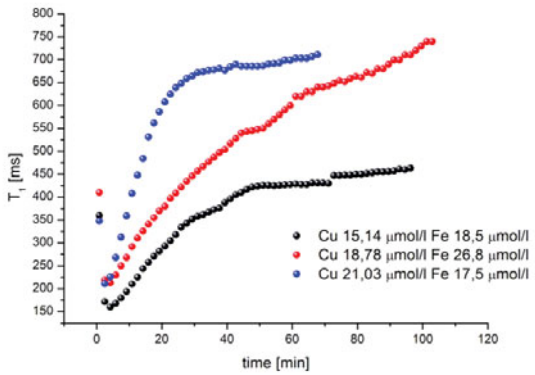

Fig.1

Discussion/Conclusion: ROS created from hydrogen peroxide in Fenton reaction significantly shorten the relaxation times. The mechanism likely reflects removal/deactivation of ROS by some components of blood serum. More importantly, this antioxidative mechanism is enhanced by addition of known antioxidants: vitamin C and glutathione. Antioxidants concentration dependence of relaxation behaviour show that presence of these media in solution restrain progress of oxidation. Our results indicate that measurements of relaxation times may be used for the studies of oxidative processes in biological liquids, and in the future, be helpful in investigation of some human diseases background.

623

WITHDRAWN

624

Imaging cold activated brown adipose tissue using functional MRI and ^{18}F-FDG PET

B.D. Van Rooijen[1], A.A.J.J. Van Der Lans[2], B. Brans[3], J.E. Wildberger[4], F.M. Motthagy[3], P. Schrauwen[2], W.H. Backes[1], W.D. Van Marken Lichtenbelt[2]
[1]Radiology, Maastricht University Medical Center, Maastricht/NETHERLANDS, [2]Human Biology, Maastricht University, Maastricht/NETHERLANDS, [3]Nuclear Medicine, Maastricht University Medical Center, Maastricht/NETHERLANDS, [4]Department of Radiology, Maastricht University Medical Center (MUMC+), Maastricht/NETHERLANDS

Purpose/Introduction: Brown adipose tissue (BAT) represents a major thermogenic system for newborn humans. Recently it was discovered, that adult humans still posses active BAT. As the activation of BAT increases the metabolic rate, pharmaceutical targeting of BAT is a potential strategy in the treatment of obesity. The current methodology to characterize BAT is the use of positron emission tomography (PET). However, the radiation burden limits the application of this method in research. The study presented reports the use of magnetic resonance imaging (MRI) to characterize BAT in adult humans using 2-deoxy-2-[^{18}F]fluoro-D-glucose (FDG) PET as validation.
Subjects and Methods: FDG-PET and MRI of BAT was performed on 11 healthy volunteers. Water-fat images were derived from a multi-echo Dixon technique. For fMRI of BAT activation, dynamic T2* imaging was used. Activation was performed by cold stimulation using a water perfused suit inside the scanner. To identify responses, the time-series were analyzed using independent component analysis (ICA). The response in the BAT depot was quantified by regression with a model based on the cooling paradigm.
Results: The MRI derived fat fraction of the BAT depots was 66.0 ± 9.3 % and 81.5 ± 5.4 % for subcutaneous white adipose tissue. The BAT fat fraction did not correlate significantly with the presence of active BAT on PET/CT. ICA identified signal fluctuations in the T2* weighted time-series with a similar temporal signature as the cooling paradigm. Subsequently, activation was quantified by regression with a model based on the paradigm. The fraction of activating voxels in the BAT depot correlated significantly with BAT FDG uptake on PET/CT (r=0.626, p<0.05).

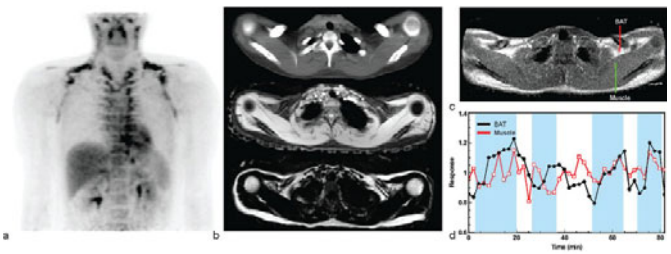

Figure 1. (a) FDG uptake in BAT depots on PET/CT.**(b)** Corresponding axial slices on CT (top) and the MRI water- (middle) and fat- (bottom) images. **(c)** T1-weighted axial MRI slice of BAT. The high fat content of BAT identifies the depot. **(d)** Fluctuations of the T2* weighted fMRI signal from muscle and BAT. The signal fluctuations in BAT correlated with the cooling paradigm (labelled blue).

Discussion/Conclusion: The presence of active BAT cannot be predicted based on MRI water-fat imaging. Active BAT can be detected by fMRI since the T2* weighted signal from BAT contains temporal components that were sensitive to BAT activation. The results indicate that MRI is a promising addition to PET for the characterization of BAT and its responses to stimulation.

625

B1 improvement for travelling MRI using a parallel-plate waveguide at 3T

F. Vazquez[1], A.O. Rodriguez[2]
[1]Dep Fisica, FC UNAM, Mexico DF/MEXICO, [2]Dep. Ingenieria Electrica, UAM Iztapalapa, Mexico DF/MEXICO

Purpose/Introduction: The travelling wave approach has been proved successful at 7T [1] and 3T [2-3] for larger magnet bores. The parallel-plate waveguide can propagate any frequency for the principal mode (TM_{00}), because its cut-off frequency is zero. B1 numerical simulations for the TM_{00} of a parallel-plate waveguide were computed at 3T varying the plate separation using two different types of RF coils.
Subjects and Methods: The parallel plate waveguide is the simplest structure and allows us to easily compute the transverse electromagnetic (TEM) mode. The finite element method was used to numerically compute the principal mode, TM_{00} with propagation along the z-direction as in [3]. Simulations were computed using COMSOL MULTIPHYSICS (Comsol, Burlington, MA, USA) at 128 MHz. The simulation arrangement is shown in Fig. 1: the waveguide was 100cmx50cm with g, varying from 35cm to 65cm with a 5 cm step and assuming, $\mu=4\pi \times 10^{-7}$ H/m, $\varepsilon_0 = 1\times10^{-9}/36\pi$ F/m . The cylindrical phantom was 30 cm in diameter and 40 cm long with σ =73.16. Magnetic field simulations were performed for a pair of circular coils and patch antennae for the different values of g. One coil was used for transmission and the other one for reception and positioned as shown in Fig. 1.

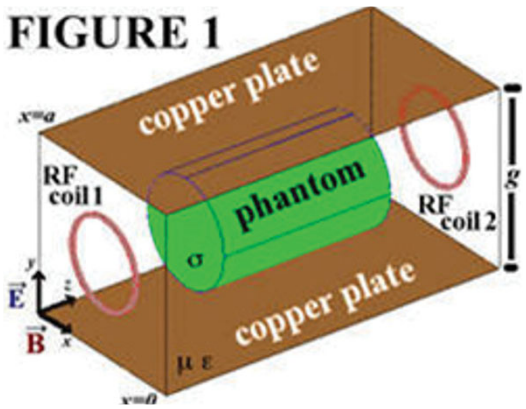

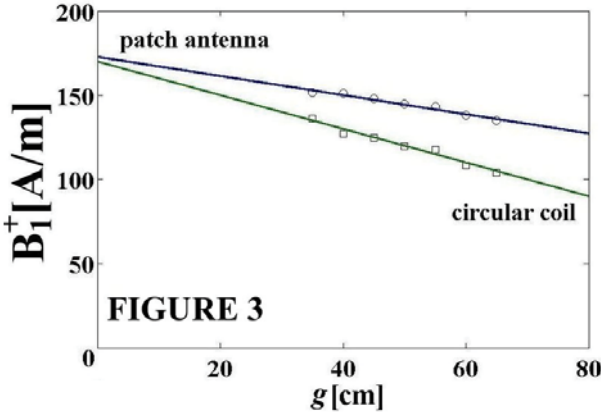

Results: The magnetic field simulations of the parallel plate waveguide are shown in Fig. 2. A region of interest at the centre of the phantom was taken to compute the magnetic field. Linear fittings of gap versus magnetic field for both coil types were computed: B_1(cir)=-0.36g+60 and B_1(patch)=-0.27g+81 and plotted in Fig. 3.

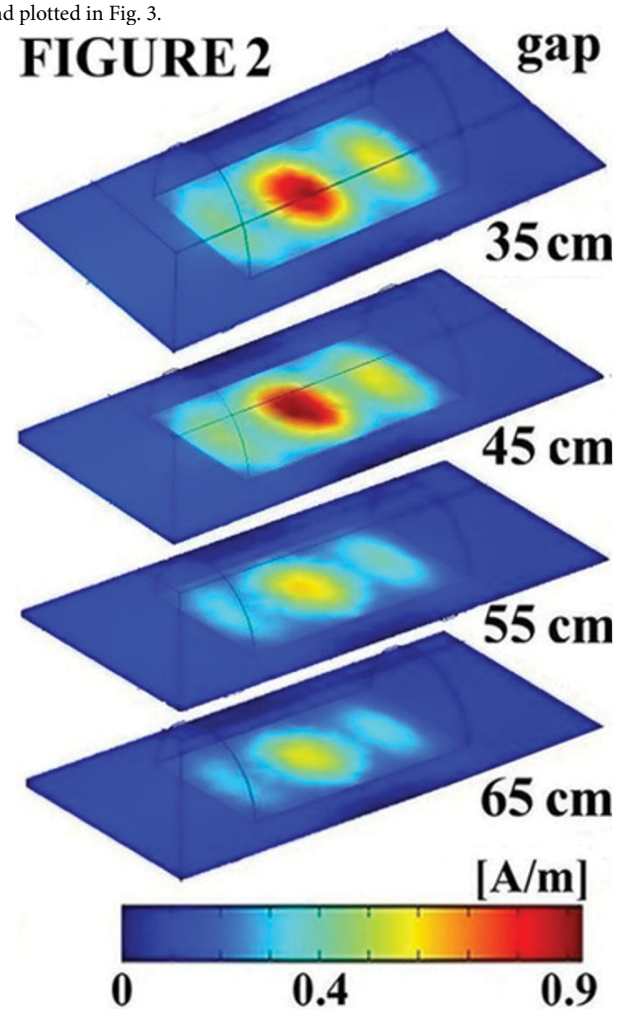

Discussion/Conclusion: Both coil types showed a similar magnetic field intensity for different gaps. A clear increment in the magnetic field magnitude can be appreciated as the plate separation is reduced for both coil types. A parallel-waveguide with a adequate low g can be fitted into small magnet bores regardless the coil type. Waveguides with smaller dimensions are able to increase the magnitude of the magnetic field. These results may be useful to develop waveguides for applications with imagers having smaller bores.

References:

1. Brunner DO, et.al. Nature 457, 994, 2009. 2. Vazquez F, et.al. ISMRM-ESMRMB, 3792, 2010. 3. Vazquez F, et.al. ISMRM, 3792, 2011.

Acknowledgments. F. V. thanks CONACYT Mexico for a Ph. D. scholarship and grant no. 166404. Email: arog@xanum.uam.mx.

626

A phantom based validation framework for EEG-fMRI acquisition methods

M. Andersen, L.G. Hanson
Danish Research Center for MR, Copenhagen University Hospital Hvidovre, Hvidovre/DENMARK

Purpose/Introduction: Scanner generated artefacts on EEG in combined EEG-fMRI recordings is a major problem. Different acquisition methods and filtering algorithms for reducing artefacts have been developed, but most validations lack the knowledge of the true signal, or are based on simulations with assumptions. To our knowledge, Negishi et al performed the most realistic phantom-based validation described in literature [1]. We present an enhanced electronic phantom-based set-up that includes motion sensitivity and avoids perfectly periodic generated signals. Two methods providing EEG free of gradient artefacts in combined EEG-fMRI recordings are compared for demonstration.

Subjects and Methods: The methods chosen for demonstration were 1) the fMRI gradient artefact slice template removal (FASTR) algorithm [2] and 2) artefact avoidance using the Magstripe MRI technique (Magstripe system) [3]. The validation set-up is schematized in figure 1. An artificial EEG voltage signal was generated from a PC with an IO card (Polabs, PoKeys55) outside the scanner room, dampened to μV-range and lead into the scanner room and split. One output was connected to a channel on a conventional EEG-system (Brainproducts GmbH, BrainAmp MR plus). This was considered the true signal used as a reference. The other output was mixed with the signal from electrodes on an EEG-cap, which where short-circuited to form a high-impedance loop. The mixed signal was recorded with the Magstripe system, and with a second channel on the Brainproducts system. The latter was subsequently filtered by the FASTR algorithm. The signals were recorded during MR imaging with an EPI sequence (20 slices, matrix 64x64, TE/TR=41ms/1220ms) and temporally aligned using scanner-generated trigger signals. During the scanning, a test subject was wearing the EEG-cap and made small movements such as deep breaths, coughing and swallowing.

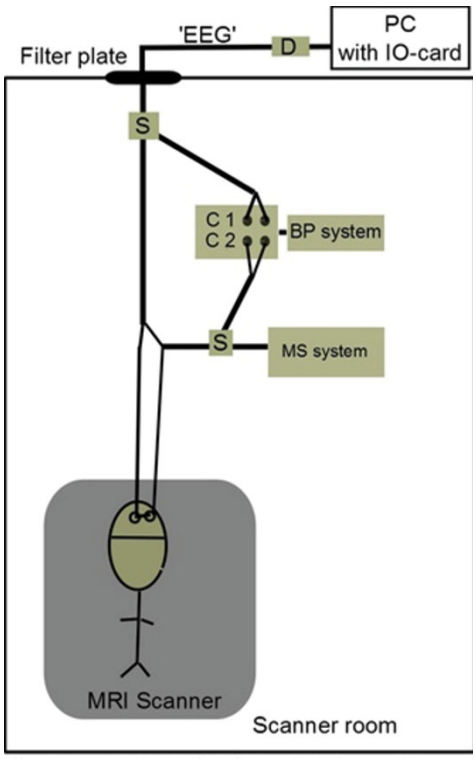

Figure 1: Schematic drawing of the validation set-up. D: Damping circuit; S: Splitter; BP-system: Brainproducts GmbH, BrainAmp MR plus EEG-system; C1: channel 1; C2: channel 2; MS system: Magstripe EEG system.

Results: Figure 2 shows a segment of the resulting signals. High resemblance is seen between the signals exposed to scanner noise and the true signal.

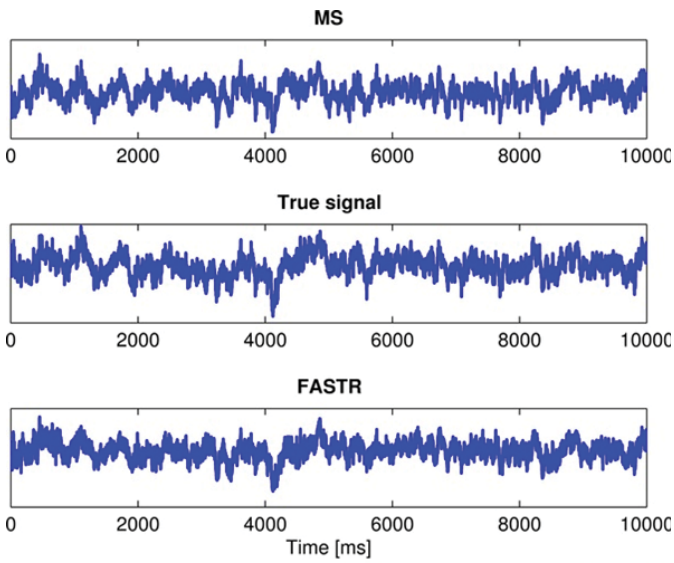

Figure 2: Time series of the recorded and filtered signals. MS: Signal recorded and filtered with the Magstripe system; True signal: EEG signal not exposed to scanner noise; FASTR: The signal exposed to scanner noise after subsequent filtration with the FASTR algorithm.

Discussion/Conclusion: Knowledge of the true signal is the great benefit of electronic phantom-based evaluation methods. Lack of realism can be the drawback. Motion of a subject during scanning is one of the challenges for reducing the scanner induced artefact on the EEG, as motion makes the artefact non-stationary. With the demonstrated set-up, motion aspects can be included in comparisons of methods.

References:
[1] Negishi, M. et al, 2004, Clin Neurophysiol, 2181-92
[2] Niazy, R. K. et al, 2005, NeuroImage, 720-37
[3] Hanson, L. G. et al, 2007, J Magn Reson Med, 1059-66

627

The effects of a finite RF transmit bandwidth on low-flip pTx pulse design

R. Gumbrecht, H. Fautz
Healthcare MR, Siemens AG, Erlangen/GERMANY

Purpose/Introduction: Parallel RF transmission (pTx) offers flexible control of magnetization generation and has been successfully applied for spatially tailored excitations [1,2]. Some of these methods rely on a linear approximation of the Bloch equation [3,4]. There, the RF is sampled at discrete intervals in time where the RF is instantaneous. This implies an infinite bandwidth of the RF within one time-step which causes inaccuracies in the pulse design process if the RF sampling time is not properly adjusted to the applied peak gradient field. In this work, we demonstrate the artifacts created by this effect and how they can be avoided.
Subjects and Methods: The linear approximation of the Bloch equation used here is based on the first-order Taylor series expansion. Therefore, the Bloch equation is discretized in time according to the sampling scheme used on the scanner. Within one time-step, the RF phase and amplitude is constant. The corresponding linear system of equations can be stated as,

$$\vec{m} = J\vec{b}$$

with the resulting transverse magnetization (m), the Jacobi matrix (J) and the RF pulse (b). The Jacobi matrix is calculated analytically from the Bloch equations, with one equation for each voxel. The resulting matrix elements are:

$$a_{ij} = C_{ij} i\gamma\Delta t e^{i\gamma\Delta B_0(\vec{x}_i)(t_j - T)} e^{i\vec{x}_i\vec{k}_j}$$

$$C_{ij} = \frac{2\sin\left[(\vec{x}_i\vec{g}_j + \Delta B_0(\vec{x}_i))\gamma\Delta t/2\right]}{(\vec{x}_i\vec{g}_j + \Delta B_0(\vec{x}_i))\gamma\Delta t}$$

The difference to the known linear approximation is the factor C. It's value is shown in figure 1.It models the transmit bandwidth of the RF within one time-step.

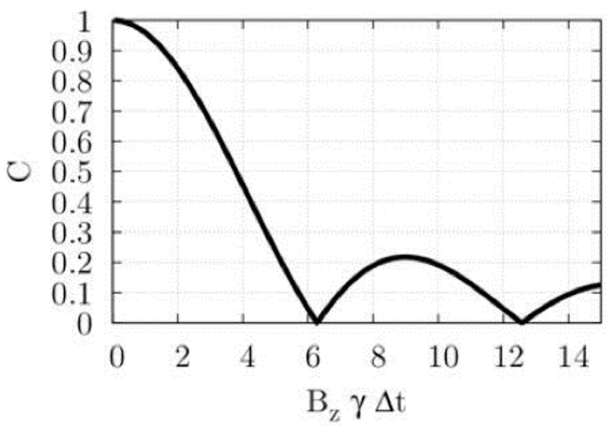

Results: In figure 2, transmit sense pulses were designed using the well known linear approximation without (fig.2a,b) and with (fig.2c,d) the transmit bandwidth correction factor C. In both cases, strong gradients (10mT/m) and a long sampling time (20us) was used. The Bloch simulation of both pulses shows that inaccuracies in the pulse design are restore by adding the factor C to the pulse design problem. However, the pulse energy is higher for the corrected pulse.

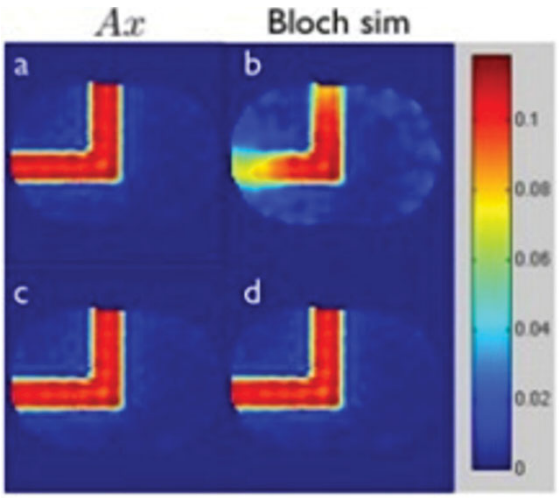

Discussion/Conclusion: We presented a correction factor for currently usedpTx pulse design methods based on the linear approximation shown in [4] whichs explains artifacts in designed pulses when high gradient amplitudes and long RF pulse sampling times are used. Including the finite transmit bandwidth of each RF sample in the design removes the artifacts, but causes a higher pulse energy. This leads to a hard limit for the maximum sampling time for a given peak gradient which should be a design criteria for energy-efficient RF pulses.

References:

[1]Setsompop et al, MRM 59:908-915(2008), [2]Katscher et al, Transmit SENSE, MRM 49:144-150(2003), [3]Yip et al, MRM 54:908-917(2005), [4] Grissom et al, MRM 56:620-629(2006)

628

Validation of temperature monitoring for MRI-guided HIFU therapy on ex-vivo model

T. Saliev[1], I. Karakitsios[1], H. Mcleod[1], R. Eisma[2], A. Melzer[1]
[1]Institute for Medical Science and Technology, University of Dundee, Dundee/UNITED KINGDOM, [2]College of Life Sciences, University of Dundee, Dundee/UNITED KINGDOM

Purpose/Introduction: MRI-guided ultrasound therapy is a promising method for non-invasive cancer treatment, where MRI provides a real-time temperature feedback based on Proton Resonance Frequency (PRF) shift of water protons [1-3]. The aim of this study was to validate the precision of PRF thermometry on *ex-vivo* organ model (explanted Thiel embalmed liver). The Thiel embalming is a well-established technique for post-mortem preservation of body's life-like properties [4]. The second goal of the study was to investigate the effect of Thiel embalming on PRF measurement.

Subjects and Methods: The temperature measurements were conducted concurrently by using the MRI-based PRF-temperature mapping (MRI Signa HDx 1.5 Tesla, GE Healthcare, USA) and fibre optic thermometers (FOTEMP-4, Optocon AG, Germany) during sonication procedures. The MR-safe fibre optic GaAs (gallium arsenide) temperature sensors were placed into the liver within the treatment focal area. The applied acoustic energy was 554 J (with an ultrasound frequency 1.14 MHz). The sonication chamber was covered by special acoustic absorber (Precision Acoustics, UK) to prevent reflection of ultrasound beam and formation of standing waves.

Results: After pre-planning MR imaging and localizing position of thermocouples, the liver was sonicated by HIFU machine (Exablate 2000 UF System, Insightec, Israel). The application of focused ultrasound resulted in a heating effect, which was independently recorded by MRI-based temperature measurement and fibre optic monitoring system (FOTEMP-4). For PRF-thermometry the residual from basal and maximal temperature was detected as 27 C (SD ± 1.73), whilst for fibre optic system it was 28.7 C (SD ± 1.35). The difference between two data was calculated as 1.73 (SD ± 2.19).

Discussion/Conclusion: The results of experiments on an *ex-vivo* model demonstrate that a MRI-based method of temperature measurement provides precise and adequate thermal feedback, which is highly important for effective ablation of organ tissue by MR-guided focused ultrasound. The data indicate that Thiel embalming does not affect significantly on PRF temperature mapping, but this aspect of the study requires further investigation.

References:

[1] Hazle, J. D., C. J. Diederich, et al. (2002). J Magn Reson Imaging 15(4): 409-417.
[2] McDannold, N. (2005). Int J Hyperthermia 21(6): 533-546.
[3] Rieke, V. and K. Butts Pauly (2008). J Magn Reson Imaging 27(2): 376-390.
[4] Thiel, W. (1992). Ann Anat 174(3): 185-195.

629

Does the amygdala responds stronger to snakes appearing in the periphery? A fMRI study on visual detection systems.

I. Almeida[1], S. Soares[2], M. Castelo-Branco[1]
[1]Visual Neuroscience Laboratory, IBILI - FMUC, Coimbra/PORTUGAL, [2]Education Department, University of Aveiro, Aveiro/PORTUGAL

Purpose/Introduction: Previous research in animals and humans has suggested the amygdala responds preferentially to peripheral menacing stimuli, in particular animals [1][2]. However, in humans, relevant stimuli such as faces are processed in central vision [3]. In a previous work, we showed the amygdala responds stronger for central presented faces. However, this might arise from a bias to process detailed stimuli in central vision [4]. Other objects that do not require detailed processing, such as animal shapes (e.g. snakes), may benefit from primitive detection systems related with peripheral visual systems [2]. Amygdala activity is also affected by the type of task performed, although conflicting results have shown that it can be either inhibited [5] or increased [6] while performing explicit emotion recognition tasks.

Subjects and Methods: An fMRI slow event-related design was carried-out with participants being request to perform 2 different tasks while fixating a central cross: snake identification (either face or body; implicit task) and recognition of threat signals (explicit task). Picture duration was kept short (150 ms) and eye movements were recorded to ensure central fixation. Preliminary results are shown for a group of 8 healthy participants (age range 18-37, 5 males).

Results: Whole brain analysis were done separately for each *Task* (implicit, explicit) taking *Spatial Location* (central, right, left) and *Stimulus Type* (snake faces, snake shapes, snake-alike shapes) as measures. For the Animal (snake) identification, a ANOVA RFX 3 x 3 revealed no main nor interaction effect in any of the amygdalas. However, for the Threat recognition, a main effect of Spatial Location arose in the right amygdala. Planned contrasts for central > right presentations elicited bilateral amygdala activation while central > left locations showed increased activity only in the left amygdala.

Discussion/Conclusion: The present findings show that amygdala responds stronger for stimuli presented centrally, as shown before. This effect depended on task type, with stronger (right) amygdala responses only when the participants were asked to explicitly recognize threat. No effect for stimulus type was found, suggesting that shapes of ecologically relevant stimuli benefit as much of central vision as faces.

References:

[1] Bayle, DJ, 2009, *PLoS ONE*, 4, e8207.
[2] Isbell, L, 2006, *J Hum Evol.*, 51, 1-35.
[3] Kanwisher, N, 2001, *Nat Neurosci.*, 4, 533-9.
[4] Vuilleumier, P, 2004, *Nat Neurosci.*, 7, 1271-78.
[5] Hariri, A., 2000, *NeuroReport*, 11, 43-48.
[6] Habel, U, 2007, *Neuropsychologia*, 45, 2369-77.

EPOS™ Poster

Paediatric

630

Central nervous system of children exposed to alcohol during the prenatal life.

A. Urbanik, M. Nardzewska-Szczepanik, P. Karcz, J. Kozub, T. Jadczak-Szumiło
Radiology, Jagiellonian University Collegium Medicum, Kraków/POLAND

Purpose/Introduction: The aim of the study was to define influence of alcohol to central nervous system (CNS) children exposed to alcohol whose mothers were affirmed to drinking alcohol during their pregnancy.
Subjects and Methods: This presentation shows results of the research concerning CNS of 200 children (group A) exposed to alcohol while in a foetus period of life and group of 30 children (group B), whose mothers did not drink alcohol while being pregnant and during lactation. The Project has obtained the consent of bioethical committee. Each child was examined using following imagining techniques :
• MRI– size of the sagittal corpus callosum section was analised as well as its shape
• DWI – the diffusion of CNS in six chosen localizations was examined
• HMRS– performed in SVS technique – in six chosen localizations voxels were localized.
Results: Statistically significant decrease of the section area as well as change of a shape (thinning) of the corpus callosum in the group A has been affirmed in relation to the group B.
The research also confirmed statistically significant increase of diffusion in group A in relation to group B. In case of HMRS significant changes mostly in concentration NAA/Cr (decrease in subcortical nuclei), Cho (decrease in hippocampi and right hemisphere), mI (increase in frontal lobes) were revealed in group A.
Discussion/Conclusion: The result of examining the CNS in children exposed to alcohol during their fetal life using MR techniques indicate that alcohol causes some alteration in brain structure on both macroscopic and microscopic level as in its metabolism.

631

Pixel-by-pixel analysis of DCE-MRI curve shapes in knees of juvenile idiopathic arthritis patients

R. Hemke[1], **C. Lavini**[1], M. Van Rossum[2], C. Nusman[1], M. Van Den Berg[3], D. Schonenberg[2], K. Dolman[4], T. Kuijpers[2], M. Maas[1]
[1]Department of Radiology, Academic Medical Center, Amsterdam/NETHERLANDS, [2]Department of Pediatric Rheumatology, Emma Children's Hospital AMC, Amsterdam/NETHERLANDS, [3]Department of Pediatric Rheumatology, Reade, Amsterdam/NETHERLANDS, [4]Department of Pediatric Rheumatology, St. Lucas Andreas Hospital, Amsterdam/NETHERLANDS

Purpose/Introduction: Juvenile idiopathic arthritis (JIA) is characterized by prolonged synovial inflammation that can lead to destruction of joints, pain and loss of function (1). It is the most common rheumatic disease in childhood. Despite MRIs superiority in assessing disease activity and structural damage in JIA, it lacks objectivity, and quantitative analysis methods for the assessment of disease activity and monitoring response to therapy are desired. Therefore, we applied a Dynamic-Contrast-Enhanced–MRI (DCE-MRI) analysis method based on a 3D pixel-by-pixel classification, which helps to visualize differently shaped time-intensity curves (TIC) within a volume of interest as well as a semi-quantitative analysis (2). The objective of our study was, therefore, to compare the results of these methods between clinically active and clinically inactive JIA patients.
Subjects and Methods: DCE-MRI datasets of knees of JIA patients were prospectively obtained using an open-bore magnet (1.0T). Patients were classified into two clinical subgroups: active arthritis (n=39) and inactive disease (n=21, median inactive disease duration 11 months (IQR 9-16 months)). Parametric maps, showing the 7 different TIC shape types (non-enhancing (1), slow enhancing (2), fast enhancing followed by either a plateau phase (3), washout phase (4) or gradual increase (5), artery (6) and undefined (7)), were created per slice. Spatial information on the synovial TIC shape distribution pattern, relative number of TIC-shapes, ME, IAUC, and slope were calculated in a three-dimensional volume of interest of the synovial membrane. DCE-MRI parameters were compared using the Mann-Whitney U test.
Results: No differences between active and inactive JIA patients were found regarding the relative number of type 2 TIC-shapes and type 3 TIC shapes (P=0.792, P=0.834 respectively). However a significant higher relative number of type 4 TIC shapes was seen in clinical active patients compared with the inactive group (7.6% vs. 5.2%, P=0.016). In contrast a significant higher relative number of type 5 TIC shapes was observed in clinical inactive patients compared with active JIA patients (16.3% vs. 14.2%, P=0.039). Also a trend towards higher ME, IAUC and slope was observed in the active arthritis group compared with the clinically inactive group (P=0.076, P=0.024, P=0.052, respectively).

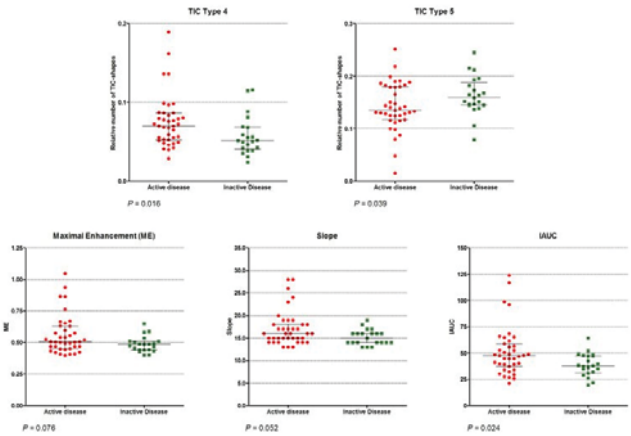

Discussion/Conclusion: Both TIC-shape analysis and the semi-quantitative analysis alone are able to differentiate between clinically active and inactive JIA disease.
References:
1. Ravelli A, Martini A. Juvenile idiopathic arthritis. Lancet 2007;369:767-778.
2. Lavini C, de Jonge MC, van de Sande MG et al. Magn Reson Imaging 2007;25:604-612.

632

Magnetic Resonance Imaging in Pediatric Acute Hip Pain

M.R. Matos[1], J. Raposo[2], P. Alves[2], R. Carneiro[1], R.M. Marques[2]
[1]Radiology, Hospital Dona Estefânia - Centro Hospitalar Lisboa Central, Lisboa/PORTUGAL, [2]Radiology, Hospital São José - Centro Hospitalar Lisboa Central, Lisboa/PORTUGAL

Purpose/Introduction: Magnetic resonance imaging is excellent in the evaluation of the form, position and size of the femoral head and also in the investigation of the acetabulum, bone marrow and surrounding soft tissues.
The aim of this study is to present MRI features concerning the pediatric hip in the sudden onset and persistence of pain.
Subjects and Methods: The authors conducted a retrospective study focusing on pediatric examinations aimed at the hip joint in children complaining about pain/ limping child performed in the institution (Hospital de São José - Centro Hospitalar de Lisboa Central) between 2009 and 2011.
Results: 25 exams were performed, of which seven were normal, 12 cases were confirmed of septic arthritis, four of those associated with osteomyelitis, a situation of osteomyelitis alone, 1 case of transient synovitis, 2 of avascular necrosis and two of pyomyositis.

Discussion/Conclusion: Magnetic resonance imaging may confirm the diagnosis and evaluates the extent of changes in acute pediatric hip pain, and also is important in guiding therapy in certain situations. Often it conducts to the diagnosis when radiographic findings are negative or equivocal.

References:

Wan Jik Yang, et al. MR imaging of transient synovitis: differentiation from septic arthritis. Pediatric Radiology, 2006 (36) 11, 1154-58

G. Ranner, et al. Magnetic resonance imaging in children with acute hip pain. Pediatric Radiology, 1989, (20), 67-71

Swischuk LE. Pediatric hip pain. Emerg Radiol. 2002 (4) 219-24

Jaramillo D et al. Legg-Calvé-Perthes disease: MR imaging evaluation during manual positioning of the hip--comparison with conventional arthrography. Radiology 1999 (2):519-25

EPOS™ Poster

Pelvis, GU

633

Pelvic floor atrophy assessment using a 2-point Dixon technique to measure muscle fat fraction

D.L. Price[1], D. Patel[2], S.A. Taylor[3], S. Halligan[3], P. Lally[1], A. Bainbridge[1], E.B. Cady[1], A. Emmanuel[2]
[1]Medical Physics & Bioengineering, UCLH NHS Foundation Trust, London/UNITED KINGDOM, [2]Department of Gastrointestinal Physiology, UCLH NHS Foundation Trust, London/UNITED KINGDOM, [3]Department of Radiology, UCLH NHS Foundation Trust, London/UNITED KINGDOM

Purpose/Introduction: Fat fraction (FF) measurement by fat/water decomposition may provide a useful measure of atrophy in pelvic-floor muscles including the external anal sphincter (EAS). Our aims were to compare:
1) a 2-point Dixon MRI technique with proton MRS, using the adjacent gluteus maximus (GM) as a larger skeletal muscle surrogate for the EAS as the EAS is unsuitably small for MRS.
2) EAS Dixon FF measurements in asymptomatic controls and incontinent subjects, with both subjective atrophy grades from T2-weighted images and incontinence scores.
Subjects and Methods: Thirteen controls (mean(SD) age 29.9(5.2) y) and 19 patients (age 51.7 (19.3) y) were scanned at 1.5T. Transverse and coronal T2-weighted images were acquired. Identically positioned fat and water images were obtained using a 3D VIBE gradient echo sequence (TR 11.1ms; TE 4.76/7.14ms; FOV 280mmx238mm, matrix 320x258) incorporating a 2-point Dixon technique. FF maps were then processed using MATLAB.
PRESS MRS was performed only on the controls with a 1cm^3 cubic voxel positioned in the GM on the T2-weighted images. Fat and water peaks were determined using jMRUI (AMARES) [1]. The voxel was then localised on the GM FF maps and a mean MRI FF calculated over the slices of interest.
ROIs were outlined on the thickest EAS portion in the T2-weighted images and transferred onto the corresponding FF maps.
EAS atrophy was graded from the T2-weighted images as 1(0% thinning or 0% replacement of muscle by fat), 2(<50%) or 3(>50%) and symptoms were rated according to the St Mark's Incontinence Score (SMIS) [2].
Results: There was good agreement between MRS and Dixon control GM FF (mean (sd) 15.0(8.4) % vs 16.1(7.7) % respectively) with 95% limits of agreement of -6.0% to 3.9%.
A significant correlation was found between subject age and FF% (p=0.001). There was also a significant FF difference between grade 1 and grade 3 EAS atrophy (p=0.027) and between the mild and severe symptom subgroups (p=0.024).

EAS atrophy grade(no. of subjects)	1(13)	2(14)	3(5)
Mean(sd) EAS FF%	19.8(14.2)	26.4(8.6)	36.0(8.4)

SMIS(no. of subjects)	Mild(17)	Moderate(2)	Severe(13)
Mean(sd) EAS FF%	20.1(8.6)	28.0(10.6)	31.6(13.9)

Discussion/Conclusion: To our knowledge this is the first pelvic-floor use of the Dixon technique. 2-point Dixon FF compares well with MRS FF. EAS FF is significantly lower in subjects qualitatively graded with good sphincter quality. FF was higher with worse symptom load.
References:
[1] Stefan, D, et al. 2009, Meas Sci Technol, 20:104035
[2] Maeda, Y, et al. 2007, Dis Colon Rectum, 50(12):2252

EPOS™ Poster

Perfused organs, biopsies, cells, fluids and extracts

634

Assessment of cell growth in biomaterial scaffolds designed for tissue engineering by means of magnetic resonance microscopy

J.M. Morales[1], D. Monleón[2], M. Salmerón-Sánchez[3], D. Moratal[3]
[1]Laboratorio Imagen Molecular y Metabolomica, Universitat de València UCIM, Valencia/SPAIN, [2]Laboratorio Imagen Molecular y Metabolomica, Fundación para la Investigación del Hospital Clínico Universitario de Valencia, Valencia/SPAIN, [3]Center for Biomaterials and Tissue Engineering, Universitat Politècnica de València, Valencia/SPAIN

Purpose/Introduction: One of the main purposes of tissue engineering is to regenerate biological tissues to repair or replace injured or damaged tissues. There is therefore a need to study non-invasively and quantitatively tissue-engineered constructs before implantation to assess the appropriateness of these structures. This work investigates the use of magnetic resonance microscopy to evaluate the presence of cells inside the biomaterial scaffold permitting a non-invasive assessment of cell growth inside the structure.

Subjects and Methods: Scaffolds synthesis.

Poly(methyl methacrylate) porogen spheres of known size 90 µm were employed. MC3T3-E1 osteoblast-like cells were injected into the scaffolds and these were incubated at 37 ºC under 5% of CO_2 conditions for 7 days with media consisting of DMEM+ 10% FBS + 1% P/S. Scaffolds were washed in a Phosphate-Buffered Saline (PBS) solution and fixed with formalin solution for 1h at 4 ºC and washed trice in PBS.

Magnetic Resonance Microscopy (MRM). Samples were embedded in a gel matrix and placed inside the imaging tube of 1 cm diameter. Magnetic resonance images were acquired at 298 K in a 14 Teslas vertical axis scanner Bruker-AVANCE 600 equipped with a 10 mm microimaging ^{1}H coil. Maximal gradient strength was 210 gauss/cm (80% of maximum nominal strength). Our protocol included T1- and T2-weighted images and Diffusion weighted images (16 B values).

Data analysis

Images were converted to DICOM format for further analysis.T2 and Diffusion coefficients were calculated using MATLAB in-house scripts. Relative intensity values of a sample were expressed as the mean intensity in the selected region of interest (ROI).

Results: We have obtained high resolution MRM images on scaffolds embedded in a gel matrix (Figure 1). T2 values calculated on samples MRM images showed statistically relevant differences between scaffolds full of cells and the equivalent ones empty of cells. In addition, we observed two statistically different regions of the scaffold (inner and outer area) based on T2 values (Figure 2 and 3).

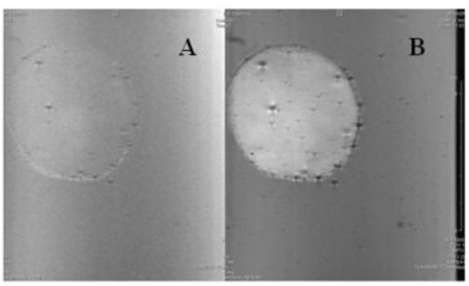

Figure 1. T1-(A) and T2-weighted (B) images from some representatives samples measured at 14.1 Tesla scanner.

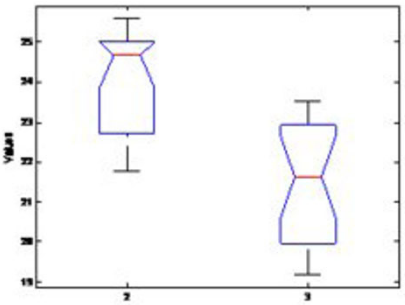

Figure 2. T2 mean values calculated from the inner region of the scaffold for three samples full of cells (full) and for three empty of cells (empty). *** $p < 0.005$.

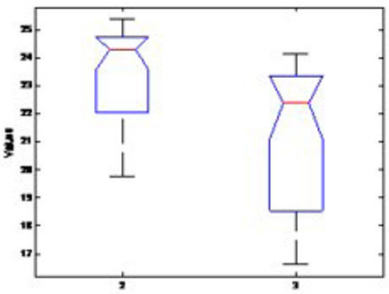

Figure 3. T2 mean values calculated from the outer region of the scaffold for three samples full of cells (full) and for three empty of cells (empty). *** $p < 0.005$.

Discussion/Conclusion: MRM is a useful tool for detecting presence of cells inside of scaffolds. We have developed an alternative method for biomaterials compatibility characterization. Our preliminary results show the cell penetration inside the biomaterial can be monitored by T2 measurements.

References:

Cruz DM, Gomes M, Reis RL, Moratal D, Salmerón-Sánchez M, Ribelles JL, Mano JF. *J Biomed Mater Res A*. 2010; 95(4) : 1182-93

Gonzalez-Segura A, Morales JM, Gonzalez-Darder JM, Cardona-Marsal R, Lopez-Gines C, Cerda-Nicolas M, Monleon D. *PLoS One*. 2011;6(11): e27442

635

Long life NMR metabolomics study of aging in mice

D. Monleón[1], J.M. Morales[2], C. Borras[3], K. Mohamed[3], J. Viña[3]
[1]Laboratorio Imagen Molecular y Metabolomica, Fundación para la Investigación del Hospital Clínico Universitario de Valencia, Valencia/SPAIN, [2]Unidad Central de Investigacion en Medicina, Universidad de Valencia, Valencia/SPAIN, [3]Departamento de Fisiología, Universidad de Valencia, Valencia/SPAIN

Purpose/Introduction: Ageing is a universal, intrinsic, progressive and deleterious process. Understanding it is of major interest to scientist, physicians as well as to the general population. There is a metabolic component in the aging process clearly suggested by the effects of calorie restriction or intervention over the insulin/IGF1 pathways. Our aim was to obtain further insights into

metabolic changes through the aging process by using metabolomic characterization of mice in a long life study.
Subjects and Methods: Blood serum from OF1 male micewas taken at the age of 4, 6, 10, 11, 12, 14, 15, 16, 17, 18, 19 and 20 months. We studied the metabolic profiles of these blood sera by NMR spectroscopy. The whole study was performed at 37C. The spectra were recorded in a Bruker-AVANCE600 spectrometer. All spectra (presaturation and single-pulse) were preprocessed with 0.3Hz line broadening. Alanine doublet was used for spectral referencing. Statistical multivariate analysis was performed using the PLS Toolbox library and in-house script for the MATLAB sofwtare.
Results: Metabolomic analysis of samples collected at different ages reveals metabolic differences between young and old mice. Principal Component Analysis reveals that the plasma metabolome of mice follows a curved trajectory but that young and old mice are easily distinguisable (see Figure 1). Most of changes are related to fatty acid metabolism (changes in glycerol, fatty acids and unsatared fatty acids signals), glucose metabolism (changes in lactate, glucose and acetate signals), protein synthesis (branched chain aminoacids signals) and redox equilibrium (total glutathione and taurine signal). Most of these changes have been previously reported. Interestingly, these changes are not linear with age. Metabolic alterations in different pathways seem to occur at different points of life.

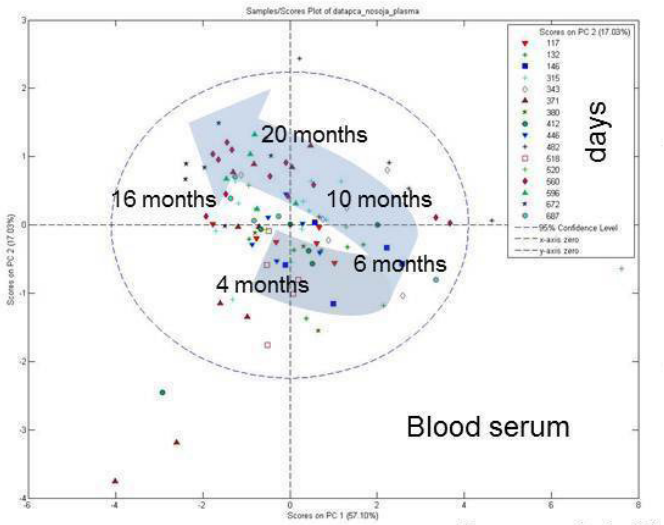

Figure 1. Principal Component Analysis of blood sera from mice at different ages showing a curve age trajectory of the global metabolome.
Discussion/Conclusion: NMR metabolics is a useful tool for the study of metabolism along the aging process. Most previous metabolic studies on aging compared young and old individuals. Our results suggest that metabolic pathways are affected by aging in a non-linear manner. This conclusion may change our way to interpret aging biomarkers and biological age.
References:
Houtkooper RH, Argmann C, Houten SM, Cantó C, Jeninga EH, Andreux PA, Thomas C, Doenlen R, Schoonjans K, Auwerx J. The metabolic footprint of aging in mice. Sci Rep. 2011;1:134.

636

NMR Metabolic Profiling In Blood from Umbilical Cords of Low Birth Weight Newborns

D. Monleón[1], J.M. Morales[2], V. Gonzalez-Marracchelli[1], C. Ivorra[3], E. Lurbe[3]
[1]Laboratorio Imagen Molecular y Metabolomica, Fundación para la Investigación del Hospital Clínico Universitario de Valencia, Valencia/SPAIN, [2]Unidad Central de Investigacion en Medicina, Universidad de Valencia, Valencia/SPAIN, [3]Servicio de Pediatria, Hospital General Universitario de Valencia, Valencia/SPAIN

Purpose/Introduction: Low birth weight has been linked with an increased risk to develop obesity, type 2 diabetes, and hypertension in adult life although the mechanisms underlying the association are not well understood. The objective was to determine the metabolomics profile of plasma from umbilical cord of low birth and normal birth weight newborns and explore the potential differences found.
Subjects and Methods: Fifty healthy pregnant women and their infants were selected. The eligibility criteria were born at term after normal pregnancy and the pairs were grouped according the birth weight, small gestational age (SGA, birth weight<10th percentile, n=20) and appropriate gestational age (AGA, birth weight between the 75th-95th percentiles, n=30). NMR was used to generate metabolic fingerprints of umbilical cord plasma samples. Simultaneously metabolomics profile in their mothers was analysed. The resulting data were subjected to chemometric analysis, principal component analysis and partial least squares discriminant analysis.
Results: Umbilical cord plasma from SGA and control newborns displays a clearly differentiated metabolic profile in the PLS-DA discriminating model (see Figure 1). Seven metabolites were identified that discriminate the SGA from the AGA. SGA newborns had lower levels of choline, proline, glutamine, alanine and glucose than the AGA newborns, while plasma levels of phenylalanine and citrulline were higher in SGA newborns ($p<0.05$). No significant differences between two groups of the mothers were found (Figure 2).

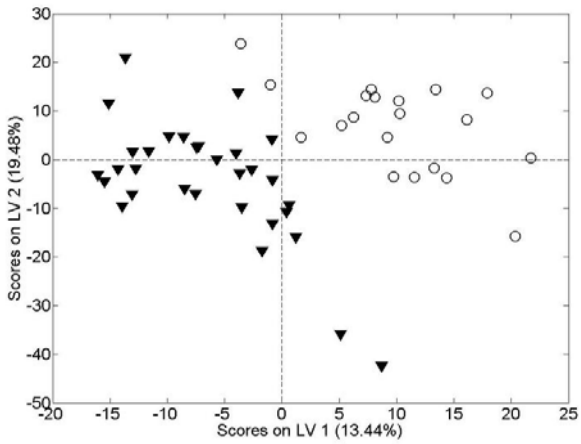

Figure 1. PLS-DA scores plot for discriminating plasma from low (white circles) and normal (black triangles) weight at birth babies.

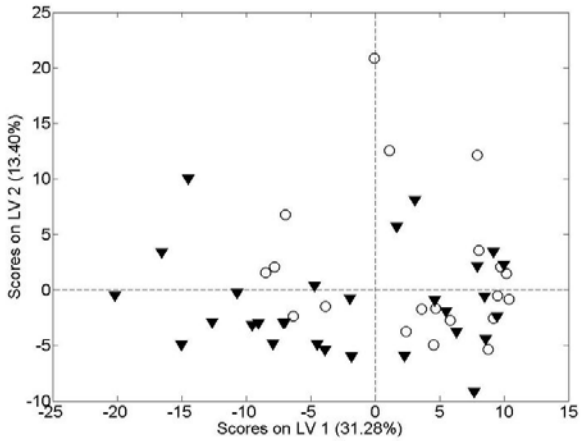

Figure 2. PLS-DA scores plot for discriminating plasma of mathers of low (white circles) and normal (black triangles) weight at birth babies.

Discussion/Conclusion: Our findings suggest that a substantial component of metabolic disease risk has a prenatal developmental basis. The finding of discriminatory metabolites in umbilical cord blood plasma from SGA newborns with a higher risk to develop cardio-metabolic diseases can offer potential biomarkers for early prediction of risk. Further studies should be performed in order to assess if some of these metabolites assessed at birth can become useful biomarkers of cardiometabolic risk later in life.

References:

Cetin I, Ronzoni S, Marconi AM, Perugino G, Corbetta C, Battaglia FC, Pardi G. Maternal concentrations and fetal-maternal concentration differences of plasma amino acids in normal and intrauterine growth-restricted pregnancies. Am J Obstet Gynecol. 1996 May;174(5):1575-1583.

29. Sabatine MS, Liu E, Morrow DA, Heller E, McCarroll R, Wiegand R, Berriz GF, Roth FP, Gerszten RE. Metabolomic identification of novel biomarkers of myocardial ischemia.Circulation. 2005 Dec;112(25):3868-3875.

EPOS™ Poster

Processing and quantification: imaging

637

Demyelination in epilepsy: MR tractography

A.Y. Efimtcev[1], V. Fokin[1], A. Sokolov[1], S. Bazilevich[2], A. Trufanov[3]
[1]Radiology, Military Medical Academy, Saint Petersburg/RUSSIAN FEDERATION, [2]Neulological Diseases, Military Medical Academy, St. Petersburg/RUSSIAN FEDERATION, [3]Neurology, Military Medical Academy, Saint Petersburg/RUSSIAN FEDERATION

Purpose/Introduction: Damage to the brain pathways are not visible on conventional MRI but can be found at the microstructural level using diffusion tensor imaging (DTI). In order to detect abnormalities in the white matter of the brain, DTI has been used in the study of patients with temporal lobe epilepsy. We retrospectively analyzed data to assess the quantitative indicator of the DTI - fractional anisotropy.
The aim of the study was to identify areas of fractional anisotropy changes in patients with TLE.
Subjects and Methods: DTI was performed on the MRI (1.5 T). We've examined 18 patients with TLE, aged 11 to 47, 8 female, 10 male. Control group were 23 persons, healthy, aged 7 to 59. All patients underwent MRI to obtain T1-and T2-WI, DT images. Statistical analysis was performed on the basis of FSL (Functional MRI Software Library).
Results: We found decrease in FA (p <0,04; picture): temporal lobes WM (a, b), frontal lobes WM (c), inferior longitudinal fascicle (ILF) (d), superior longitudinal fascicle (SLF).

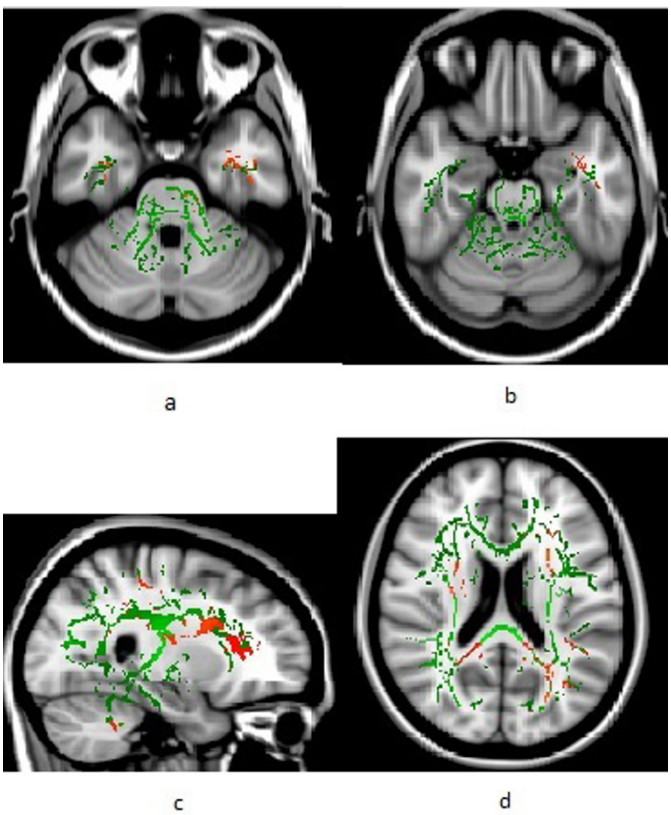

Picture shows the decrease of FA in TLWM, in projection of lower hook and LongitFasc in patients with left-TLE. In patients with right-TLE FA was reduced in WM of left and right TL, as well as in projection of SLF, left and right (p <0,04).

The results of FA coefficient measurements in areas of decline (by FSL) are presented in Table.

FA meanings in patients with TLE

	Controls	Epilepsy (total)	Left-sided TLE	Right-sided TLE
Right TL	0,312±0,021	0,293±0,031	0,296±0,043	0,266±0,037
Left TL	0,307±0,034	0,284±0,032	0,269±0,044	0,301±0,041
Right SLF	0,456±0,052	0,401±0,047	0,429±0,047	0,352±0,040
Left SLF	0,476±0,050	0,387±0,070	0,360±0,066	0,428±0,061
ILF (both sides)	0,684±0,025	0,649±0,053	0,628±0,067	0,675±0,057

Reduce of FA on affected side was observed in patients with left-TLE in left TL, SLF and the hook on the left (p <0,003).
Differences between FA in patients with left-TLE and controls were present in projection of optic radiation, SLF and anterior thalamic radiance. (P <0,05).
In patients with right-TLE FA was lower in right temporal lobe, ILF, but the percentage ratio, compared to rates in patients with left-TLE, was less.

Discussion/Conclusion: Using DTI technique, we found changes in the white matter of the temporal lobes. According to some studies, patients with epilepsy, especially in its long course, a process of demyelination takes place in brain WM. Taking into account these results, we can talk about the confirmation of data on demyelination and its prospects for early detection and quantification of its severity using DTI.

638

Differentiation of superficial (SSCAT) and deep subcutaneous adipose tissue (DSCAT) in a cohort at increased risk for type 2 diabetes – a retrospective cross-sectional analysis

J. Machann[1], J. Lang[2], N. Stefan[3], H. Häring[4], C. Claussen[5], A. Fritsche[4], F. Schick[6]
[1]Section on Experimental Radiology, Institute for Diabetes Research and Metabolic Diseases (IDM) - Metabolic Imaging - of the Helmholtz Center Munich at the University of Tübingen, Tübingen/GERMANY, [2]Section on Experimental Radiology, University Hospital Tübingen, Tübingen/GERMANY, [3]Department of Internal Medicine, Division of Endocrinology, Diabetology, Angiology, Nephrology and Clinical Chemistry, University Hospital Tübingen, Tübingen/GERMANY, [4]Department of Endocrinology and Diabetology, Angiology, Nephrology and Clinical Chemistry, University Hospital Tübingen, Tübingen/GERMANY, [5]Department of Diagnostic and Interventional Radiology, University Hospital Tübingen, Tübingen/GERMANY, [6]Section on Experimental Radiology, Department of Diagnostic and Interventional Radiology, University Hospital Tübingen, Tübingen/GERMANY

Purpose/Introduction: Quantification of different adipose tissue compartments in human body is of increasing interest due to the increasing prevalence of obesity and its concomitant diseases. Mainly visceral adipose tissue (VAT) seems to play an important role in the pathogenesis of insulin resistance, whereas subcutaneous adipose tissue (SCAT) is just thought to be the protective mantle. However, there are two compartments of SCAT which can be differentiated due to an intermediate septa: superficial (SSCAT) and deep subcutaneous adipose tissue (DSCAT). Aim of this retrospective analysis was the quantification of SSCAT and DSCAT in subjects at increased risk for type 2 diabetes.
Subjects and Methods: Retrospective analysis was performed in 240 subjects (106 males, 134 females) in different age- and BMI-groups and separated for gender. MR images were recorded by axial T1-weighted MRI and the slice at the umbilical level was manually segmented to calculate total SCAT, SSCAT and DSCAT. Figure 1 shows an example for a male volunteer. For analysis of age-effect, males and females were separated in 3 subgroups being AG1: younger than 30, AG2: between 30 and 50 and AG3: older than 50. BMI was between 25 and 30kg/m². Additionally, three BMI-groups were set with BMI_G1: <25kg/m², i.e. normal weight, BMI_G2: between 25 and 30kg/m², i.e. overweight, and

BMI_G3: >30kg/m², i.e. obese. Ratios of SSCAT and DSCAT were calculated to the total SCAT in this cross-section.
Results: Males have a significantly higher share of DSCAT compared to females (58% for males, 42% for females). In males there is a significant shift in SCAT distribution with age with DSCAT increasing from 53% in AG1 to 59% in AG3, but not for females (42% to 44%). Obese females (BMI_G3) have a significantly lower amount of DSCAT compared to normal weight females in BMI_G1 (38% vs. 45%, p<0.01). This is just the other way round for males without reaching statistical significance (55% vs. 57%, n.s.).
Discussion/Conclusion: Differences in adipose tissue distribution between males and females are well known. The significantly higher amount of DSCAT reflects the well known fat distribution with VAT being about twice as high for males compared to females with comparable BMI. However, according to these results, a special role of the two SCAT compartments cannot be claimed. Further analyses including metabolic parameters (insulin sensitivity) and probable redistribution after lifestyle intervention are advised to go into more detail.

639

A Multiple Classification System for classification of breast lesions using dynamic and morphological features in DCE-MRI

R. Fusco[1], M. Sansone[2], S. Filice[1], A. Petrillo[1]
[1]Radiology, INT IRCCS "Foundation G.Pascale", Naples/ITALY, [2]Biomedical, Electronic and Telecommunication Engineering, University of Naples 'Federico II', Naples/ITALY

Purpose/Introduction: To evaluate the performance of a Multiple Classification System (MCS) using dynamic and morphological features [1] of breast lesions in Dynamic Contrast Enhanced-Magnetic Resonance Imaging (DCE-MRI). Four classifiers were examined: multilayer perceptron, support vector machine, Bayes classifier and decision tree classifier. The proposed MCS combines the results of two classifiers trained with dynamic and morphological features respectively.
Subjects and Methods: 38 women (average age 46 years) with benign or malignant lesions histopathological proven were enrolled. 22 lesions were malignant and 17 were benign. The lesions were subdivided in two groups: training-test (12 benign and 16 malignant) and test-set (5 benign and 5 malignant).Volumes of Interest (VOIs) have been both manually extracted by an expert radiologists and automatically extracted via a segmentation procedure assessed in a previous study. Both dynamic and morphological features were extracted. The performance of the MCS have been compared with histological classification.
Results: Results showed that with manually segmented VOIs the best combination included two Bayes classifiers (75% of training-set and 70% of test-set correctly classified); when using automatic segmented VOIs the best combination included a decision tree and Bayes classifiers (68% of training-set and 70% of test-set correctly classified).
Discussion/Conclusion: The main difference between our approach and previous studies lies in the combination scheme that allows to take advantage of both dynamic and morphological features of DCE-MRI examinations. In the future, our preliminary study will be extended on a larger number of patients, manual segmentation will be done by multiple readers and morphological, dynamic and texture feature combination will be done.
References:
1. Wedegrtner U, Bick U, Wrtler K, Rummeny E, Bongartz G. Differentiation between benign and malignant findings on MR mammography: usefulness of morphological criteria. Eur Radiol. 2001;11(9):1645-50.

640

Discrete algebraic reconstruction in MRI: a simulation study

Q. Collier, H. Segers, J. Sijbers
Physics: IBBT-Vision Lab, University of Antwerp, Antwerp/BELGIUM

Purpose/Introduction: Compressed sensing (CS) techniques allow an image to be reconstructed from far fewer measurements than needed by traditional methods [1-2]. In magnetic resonance imaging (MRI), as well in other domains, CS exploits prior knowledge about the sparseness of the signal in some transform domain [3]. In this work, we propose the use of prior knowledge about the discreteness in grey level of homogeneous regions in the object in order to achieve compressed sampling. For reconstruction, the `discrete algebraic reconstruction technique' (DART) is employed, which has already proven to be successful in computed tomography and electron microscopy [4]. In this abstract, we introduce the concept of discrete tomography to magnetic resonance imaging and compare its effectiveness to standard iterative reconstruction schemes.
Subjects and Methods: MRI k-space data was generated from a brain phantom that was composed of a small number of gray levels. These phantoms were sampled using a radial k-space trajectory. Undersampled data was generated by (a) introducing a missing wedge in de radial acquisition pattern, (b) reducing the number of equidistant radial spokes and (c) selectively removing radial spokes which resulted in undersampled data combined with a missing wedge. Subsequently, data sets with increasing amounts of noise were generated. These data sets were then reconstructed using DART and compared, in terms of the reconstruction error, to conventional algebraic techniques such as ART and SART.
Results: Our results show that for the limited data problems described above, DART outperforms ART and SART. This is illustrated in figures 1 to 4. Since ART consistently produced better results compared to SART , the SART reconstruction results were left out in the figures for clarity. DART with ART as a subalgorithm (DART-ART) yields the best results for both undersampled k-space sampling and noisy data sets.
Discussion/Conclusion: This work showed that DART allows us to use data that has been severely undersampled by limiting the number of k-space lines or reducing the k-space coverage. DART will still produce good reconstructions by exploiting prior knowledge about the discreteness of the object.
References:
[1] Donoho D (2006) IEEE trans. inform. theory 52(4): 1289-1306. [2] Candès E (2008) IEEE sign. proc. magazine 25(2): 21-30. [3] Lustig M et al. (2008) IEEE sign. Proc. Magazine 25(2): 72-82. [4] Batenburg K et al. (2011) IEEE trans. image proc. 20(9): 2542-53

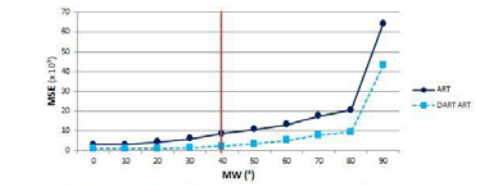

(a) Mean squared error (MSE) as a function of the missing wedge (MW)

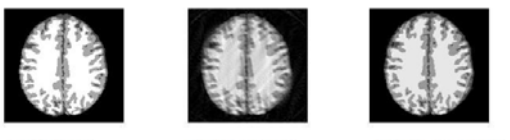
(b) Original image
(c) ART reconstruction MW = 40° MSE = 8,6 x 10³
(d) DART-ART: reconstruction MW = 40° MSE = 2,0 x 10³

Fig. 1. Impact of increasing the angle of the missing wedge (MW) on the image reconstruction

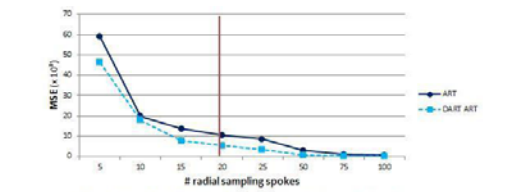

(a) Mean squared error (MSE) as a function of the number of radial spokes

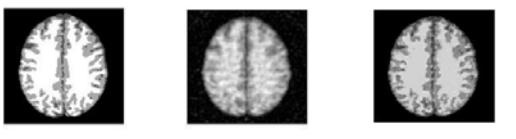
(b) Original image
(c) ART reconstruction # spokes: 20 MSE = 10,4 x 10³
(d) DART-ART reconstruction # spokes: 20 MSE = 5,4 x 10³

Fig. 2. Impact of reducing the number of equidistant radial spokes on the image reconstruction

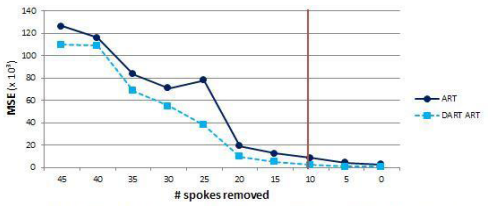

(a) Mean squared error (MSE) as a function of the number of radial spokes removed

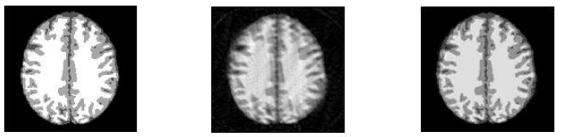

(b) Original image

(c) ART reconstruction
# spokes removed : 10
MSE = 8,9 x 10³

(d) DART-ART reconstruction
# spokes removed : 10
MSE = 2,4 x 10³

Fig. 3. Impact of removing radial spokes on the image reconstruction

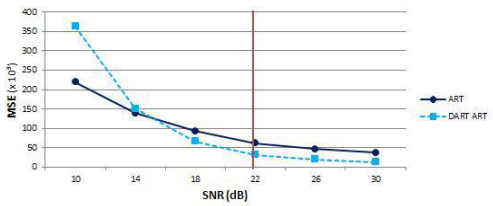

(a) Mean squared error (MSE) as a function of noise in the k-space data

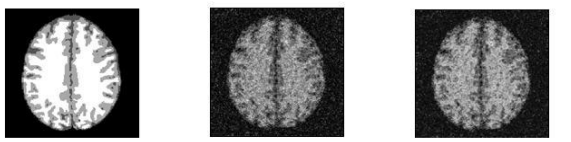

(b) Original image

(c) ART reconstruction
SNR = 22dB
MSE = 61,3 x 10³

(d) DART-ART reconstruction
SNR= 22dB
MSE = 32,1 x 10³

Fig. 4. Impact of SNR in the k-space data on the image reconstruction

641

A New Compressed Sensing Technique by Iterative Truncation of Small Transformed Coefficients

C.B. Ahn
Electrical Engineering, Kwangwoon University, Seoul/KOREA

Purpose/Introduction: A sparsity-enforced compressed sensing technique is proposed for cardiac MRI to achieve high spatial and temporal resolutions without excessive hardware requirements. The performance of the technique appears superior to that of existing technique such as k-t FOCUSS.
Subjects and Methods: Random sampling and nonlinear reconstruction are essential to the compressed sensing. The probability density function of the k-space lines along the phase encoding direction has a Gaussian distribution centered at dc. A given band of low frequency is obtained in every other frame. Stationary and moving regions are classified, and small transformed coefficients below thresholds are set zero to enforce sparsity in the moving region, yet data consistency is maintained with a regularization. A triangular window is used as the thresholds with the highest value at the dc. The process is applied in the spatial-temporal (r-t), spatial frequency-temporal (k-t), and spatial-temporal frequency (r-f) domains back and forth iteratively.
Results: The proposed algorithm is applied to 2D cardiac CINE images obtained at 1.5 Tesla whole body MRI. Balanced SSFP technique is used with TR and TE of 4.7ms and 2.35ms. Image matrix is 256x256, and total 27 frames are acquired with the number of views per segment of 8 within a breath-hold. Reconstructed images with an acceleration factor of 8 for several acquisition and reconstruction methods are shown in Fig.1. As shown in Fig.1, reconstructed image by the proposed technique shows sharper edges with least aliasing error. Average mean square error (MSE) in total 27 frames of images is summarized in Table1 for various acceleration factors. As shown in Table 1 the proposed ITSC method has the lowest MSE among other techniques.

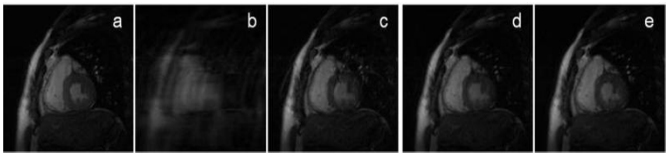

Fig.1 Reconstructed images with an acceleration factor of 8: image by full scan (a), zero filling (b), sliding window (c), k-t FOCUSS (d), and the proposed ITSC technique (e).

Table 1 Average mean square error (MSE) of the reconstructed images by various imaging methods with acceleration factors of 2, 4, and 8.

Acceleration fator	Zero-filling	Sliding window	k-t FO-CUSS	ITSC
2	24.37	3.24	2.81	2.77
4	70.65	7.54	5.31	5.02
8	119.28	14.39	7.80	7.01

Discussion/Conclusion: A new sparsity-enforced compressed sensing technique is successfully applied to a breath-hold cardiac CINE imaging. Although some loss of resolution is found for large acceleration factors, the technique is useful when measurement time is strictly restricted. A wide use of data compression techniques such as JPEG and MPEG suggests an optimistic future of the compressed sensing.

642

Variable Flip Angle T1 Mapping with Dixon Fat Suppression: Preliminary Study

Y. Le[1], F. Akisik[1], **C. Lin**[2]
[1]Radiology and Imaging Science, Indiana University, Indianapolis/IN/UNITED STATES OF AMERICA, [2]Department of Radiology and Imaging Science, Indiana University School of Medicine, Indianapolis/IN/UNITED STATES OF AMERICA

Purpose/Introduction: Spoiled gradient echo sequence with variable flip angle (VFA) is commonly used for fast T1 mapping in contrast enhanced MRI (1). In many applications fat signal needs to be removed (2-3). Interleaved fat suppression (FS) RFs disrupt steady state and may cause T1 measurement error (4). This work shows that Dixon technique allows accurate T1 measurement of water signal and can be used in liver T1 mapping.
Subjects and Methods: A phantom with solutions of various T1s was scanned on a 3T scanner (Tim Trio, Siemens, Germany) using 1)VIBE (no FS) (5), 2) VIBE with interleaved FS (VIBE- QFS); 3) VIBE-QFS with zero FS RF and 4) TWIST-Dixon (6), with flip angles of 5°, 10°, 15° and 25°. Results were compared with IR-TSE (TI/TR=50-4000 ms/10s) measured T1s. For all VIBE sequences, TE/TR=2.42 /6ms. For TWIST-Dixon, TE1/TE2/TR=2.45/3.68/6 ms. With the approval from institutional review board and written informed consent from patients, pre-contrast liver T1 maps were acquired in 15 patients using TWIST-Dixon on a 3T scanner (TIM Verio, Siemens, Germany) with flip angles=5°, 10°, 20° and TE1/TE2/TR=2.45/3.68/5.6 ms.
Results: T1s measured with VIBE and TWIST-Dixon were consistent with IR-TSE even without B1 correction (1); while T1s from VIBE-QFS (fat-suppression RF on/off) shows a systematic difference (Figure 1, Table 1) due to the inconsistent TR, not the RFs.
T1 maps from TWIST Dixon in-phase images (without FS) and water-only images were similar in patients with little liver fat(Figure 2a, c, and e); while obviously different in patient with more liver fat (2b, d, and f).

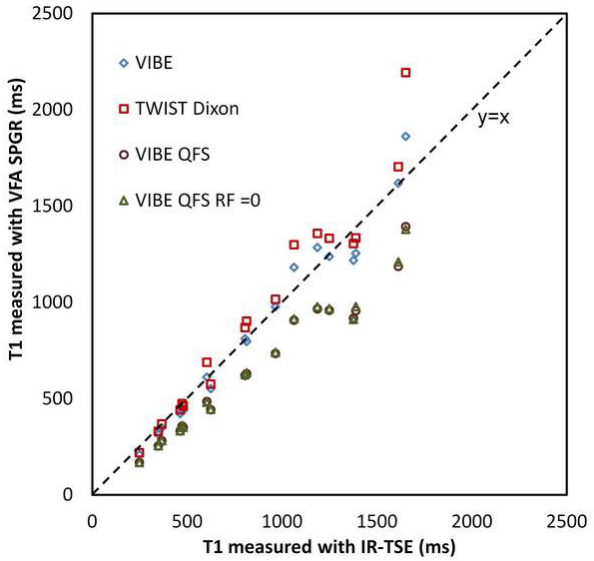

Figure 1. VFA measured T1 vs. IR-TSE measured T1.

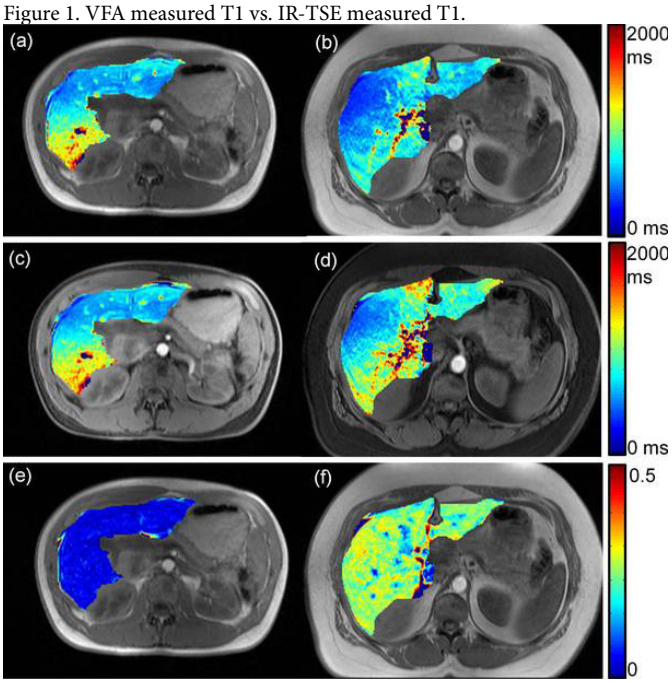

Figure 2. Liver T1 maps from in-phase (a,b) and water-only images (c,d), and fat/in-phase signal ratio maps (e,f).

Table 1. Slopes and R^2s of VFA measured T1s vs. IR-TSE measured T1s.

	Slope	R^2
VIBE without FS	1.01	0.97
TWIST-Dixon	1.09	0.94
VIBE-QFS	0.77	0.97
VIBE QFS FS RF=0	0.76	0.97

Discussion/Conclusion: Dixon technique allows accurate T1 measurement with fat suppression. Preliminary clinical study results show the difference in liver T1 maps with and without fat suppression depends on the fat signal level.

References:

1. Treier R *et al.*, MRM 2007;57(3):568-576. 2. Biffar A *et al.* MRM 2010;64(1):115-124. 3. Rakow-Penner R, *et al.*, JMRI 2006; 23(1):87-91. 4. Desmond KL *et al.* JMRI 2007;25(6):1293-1298. 5. Rofsky NM *et al.* Radiology 1999;212(3):876-884. 6. Le Y *et al.* JMRI 2012.

643

Modelling of Contrast Changes in Soft Tissue Hematomas

B. Neumayer[1], E.M. Hassler[2], T. Widek[1], A. Petrovic[3], E. Scheurer[1]
[1]Clinical Forensic Imaging, Ludwig Boltzmann Institute, Graz/AUSTRIA, [2]-Ludwig Boltzmann Institute for Clinical Forensic Imaging, Graz/AUSTRIA, [3]Institute of Medical Engineering, Graz University of Technology, Graz/AUSTRIA

Purpose/Introduction: Dating hematomas in soft tissue is an important task in forensic investigations in living victims. It is essential for the reconstruction of events, and often implicates legal consequences. Recently, it has been shown that evaluating the colour of bruises is unreliable [1]. While MRI is a standard for the assessment of intracranial bleedings it has not been applied to soft tissue, yet. The aim of this study was the modelling of contrast behaviour in soft tissue hematomas and the validation of the model.

Subjects and Methods: In 20 volunteers own blood (4ml) was injected into the subcutaneous tissue of the thigh. The hematomas were examined with MRI (0, 3, 24, 72, 168, and 336h after injection) on a clinical 3T scanner using PDw FatSat TSE SPAIR (TR/TE=3400/11ms), IR (TR/TE/TI=7000/11/200ms), and MSE (TR/τ=5000/12ms, 16 echoes) of which echo 9 was used. Data of 12 persons (6f&6m, age 26.9±3.98y) was analyzed for model creation. Signal intensities were determined in 3 ROIs, one each in the hematoma, muscle and subcutaneous fat, respectively, and the Michelson Contrast C_M=(I1-I2)/(I1+I2) [2] was calculated. After analysis of the contrast of all sequences the model found for the PD-weighted sequence was cross validated (leave-one-out method) using a 3-parameter LMS fit as a lookup table and by calculating the inverse solution of the model function.

Results: Fig.1 shows the time courses (±SD) of the contrast between hematoma and muscle tissue in the different sequences. For PDw data a mono-exponential decrease was found with the inverse function t=-ln((C_M+0.56)/0.86))*275.45. The cross validation resulted in a good agreement between estimated and real hematoma age (linear regression R^2=0.89/0.87 for lookup table/inverse solution; Fig.2). The Bland-Altman plot showed some outliers, however, no systematic deviations (μ=-0.52).

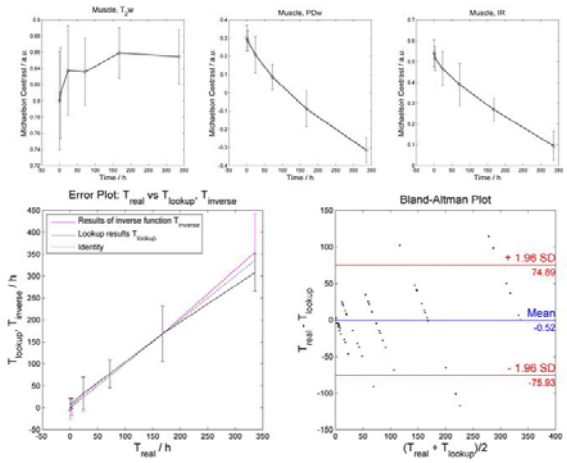

Discussion/Conclusion: The Michelson Contrast is a relatively reliable measure for assessment of contrast between tissues. The inverse of the mono-exponential function of the time course of the contrast between blood and muscle tissue in PDw data can be used to calculate the time since the origin of a hematoma in soft tissues based on a single MRI measurement. However, in contrast to the lookup table this calculation can produce negative values and times above 336h. Additionally, associated variations leading to relatively large age ranges have to be considered. Future work will focus on combining contrast of different measurements to improve accuracy.

References:

[1] Pilling ML et al., 2010, JForensicLegMed 17:143–149
[2] Michelson A, 1927, Studies in Optics

644

Geometric and Intensity EPI Distortion Correction for 7T fMRI Using Simultaneous Classification and Registration

H. Lu[1], W. Van Der Zwaag[2], L. Nolte[1], M. Reyes[1]
[1]Institute for surgical technology and biomechanics, University of Bern, Bern/SWITZERLAND, [2]CIBM-LIFMET, École Polytechnique Fédérale de Lausanne, Lausanne/SWITZERLAND

Purpose/Introduction: Echo planar imaging (EPI) is a rapid imaging sequence widely used for fMRI acquisitions. However, it is prone to geometrical distortions, especially at ultra high-field. Deformable image registration is used to correct the distortions by registering EPI image to an undistorted structural image. However, within the field of view of the object, any change in geometry can redistribute the acquired signal over the reconstructed voxels (Fig. 1). Such intensity changes often cause matching ambiguity during the registration process. To address this limitation and to tackle both geometric and intensity distortion at the same time, we propose to correct these distortions using simultaneous tissue classification and image registration.

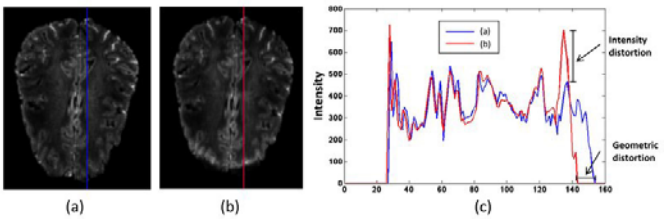

Fig. 1. (a) Distorted 7T EPI image, (b) Corrected EPI image of (a), (c) Intensity profile along the line from top to bottom in (a) and (b). Geometric distortion more than a centimeter occurs in the frontal lobe, causing signal intensity attenuation.

Subjects and Methods: The geometrical distortion is corrected using the multimodal diffeomorphic demons algorithm [1], which co-registers the distorted EPI image to a T1 image; the intensity distortion is separately estimated via tissue classification. Since the geometric and intensity distortions are correlated by the Jacobian of the deformation field, the estimated intensity distortion can provide a new Jacobian factor to refine the deformation field obtained from the non-rigid registration step.
Five volunteers were scanned on a 7T MR scanner (Siemens, Germany). A structural T1 image was acquired using the MP2RAGE [2] sequence and a resting-state fMRI run (matrixsize=160x160x64, TE=29ms, TR=5000ms) was acquired using a standard EPI sequence. The proposed simultaneous classification and registration (SCR) is compared with the multimodal diffeomorphic demons (MDD).
Results: From visual assessment, the SCR registration results show clear advantages over the MDD method for all five cases (Fig. 2). The registration accuracy was also improved quantitatively, as validated by measuring the brain shape recovery ratio (DICE) (Fig. 3(a)), and the geometric distance error computed from 10 manually-defined landmarks located in regions with large distortions (Fig. 3(b), p=0.01).

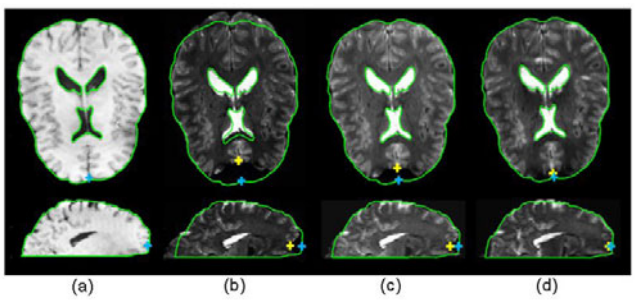

Fig. 2. Correction results from different methods on case 2, (a) T1 image, (b) distorted EPI image, recovered images by (c) MDD, (d) Proposed SCR method. Green line is the contour of reference brain overlaid on each result. Blue cross represents one manually-defined landmark in the T1 reference and yellow cross is the corresponding landmark in the EPI images.

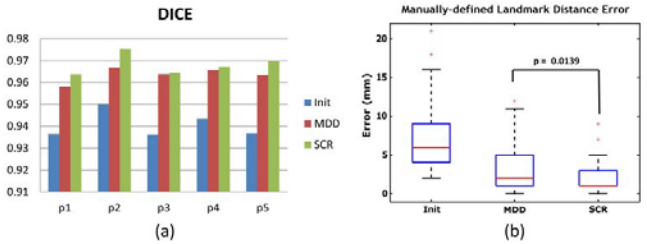

Fig. 3. (a) DICE coefficient between the T1 structural images and the recovered images using the initial EPI, MDD and proposed SCR. (b) Manually-defined mean geometrical distance errors of registration results from MDD and SCR.

Discussion/Conclusion: The results demonstrate that the proposed method achieves better distortion correction compared to a standard registration algorithm. Due to the high signal sensitivity of 7T scanner, the classification of EPI image on which the proposed method highly depends is generally better than that of a comparable 3T image. Moreover, the bias field, although stronger than at 3T, is also easier to correct. Future work will be addressed to validations in a realistic task-fMRI study.
References:
[1] Lu et al., ISBI 2010. [2] Marques et al., Neuroimage. 2010
Acknowledgements: Funded by SNF-205321_135361/1. Data provided by Centre d'Imagerie BioMédicale (CIBM) of the UNIL, UNIGE, HUG, CHUV, EPFL and the Leenaards and Jeantet Foundations.

645

Ex vivo measurements of sodium T1 and T2* relaxation times in human lumbar spine discs at 7 Tesla using vTE-GRE sequence

S. Zbyn[1], S. Apprich[1], V. Juras[1], S. Walzer[2], X. Deligianni[3], O. Bieri[3], S. Trattnig[1]
[1]MR Centre-Highfield MR, Department of Radiology, Medical University of Vienna/Vienna General Hospital, Vienna/AUSTRIA, [2]Department of Orthopedic Surgery, Medical University of Vienna/Vienna General Hospital, Vienna/AUSTRIA, [3]Division of Radiological Physics - Department of Radiology and Nuclear Medicine, University of Basel Hospital, Basel/SWITZERLAND

Purpose/Introduction: Degeneration of intervertebral discs (IVD) is associated with loss of glycosaminoglycans (GAG). Sodium concentration has been shown to correlate well with GAG concentration in IVDs[1]. Decrease of GAG content in bovine cartilage resulted in change of sodium relaxation times[2]. The aim of this study was to measure sodium relaxation times in lumbar IVDs with different grades of degeneration.
Subjects and Methods: Proton and sodium MRI of five IVDs (L1-L5) from human spine specimen were performed at 3T and 7T Siemens whole body systems respectively. Degree of IVD degeneration was evaluated on T2-weighted 2D-TSE images (TR/TE=3790/104ms; resolution=0.6×0.6×3.0mm^3, BW=150Hz/pix, TA=4:18min) using Pfirrmann grading[3]. Progressive saturation using spoiled 3D-GRE sequence with variable echo time scheme (vTE-GRE)[4] was employed for sodium T1 measurements (seven repetition times=10, 18, 28, 40, 75, 120, 250ms, TE=1.82ms, resolution=1.6×3.2×6.0mm^3, BW=320Hz/pix, TA=3:03hours) Sodium T2* measurements were acquired with multi-echo vTE-GRE (eighteen echo times=0.95, 2.33, 3.57,…, 54.47ms, TR=60ms, resolution=1.6×3.2×6.0mm^3, BW=300Hz/pix, TA=1:24hours). T1 and T2* relaxation maps were calculated from intensities of noninterpolated pictures on pixel-by-pixel basis using three parameter nonlinear least squares fitting routine written in IDL (Fig.1,2). Similarly, maps of fast (T2*f) and slow (T2*s) components of sodium biexponential transverse relaxation were created in IDL routine. Fitting precision was evaluated using goodness-of-fit maps. Five regions of interest were defined for each IVD on proton image, and subsequently transferred to relaxation times maps.

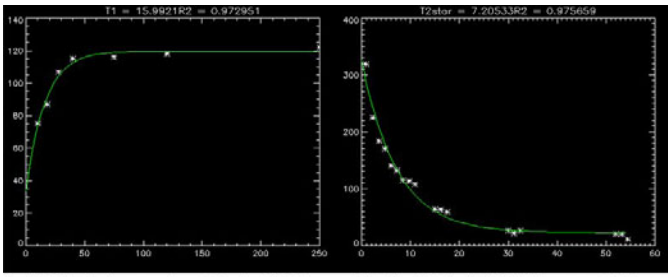

Fig.1 The T1 fit of data from progressive saturation using vTE-GRE sequence (left) and the T2* fit of multiecho vTE-GRE measurement (right). Fitted T1 and T2* values together with goodnes-of-fit are noted on the top of each graph.

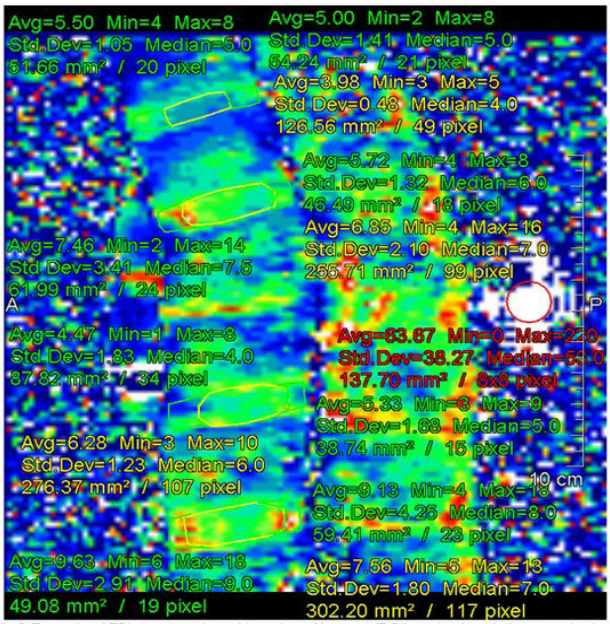

Fig.2 Example of T2* map together with region of interest (ROI) evaluations in intervertebral discs. From top of the image, ROIs in L1, L2, L4 and L5. Yellow ROIs mark nucleus pulposus and green annulus fibrosus.

Results: IVDs were divided into more degenerated (L1, L2; Pfirrmann: L1=4, L2=4) and less degenerated group (L4, L5; Pfirrmann: L4=2, L5=3). L3 was excluded due to severe degeneration. Mean T1 of IVDs from more degenerated (T1=18.4ms) and less degenerated (T1=19.7ms) group were comparable with previously published T1=22ms[1]. However, mean T2* of more degenerated (T2*=5.8ms) and less degenerated (T2*=7.3ms) group corresponded better to T2*=9.7ms reported by Moon[5], than to T2*=16ms published by Wang[1]. Our mean T2*f=1.9ms and T2*s=7.8ms of degenerated annulus are very similar to T2*f=1.7ms and T2*s=7.3ms of degenerated annulus measured by double-quantum-filter MRS[6]. Significantly lower T2*s values were found in more degenerated (T2*s=7.5ms) compared to less degenerated group (T2*s=11.3ms) (Table 1).

Grade of Degeneration	Compartment	T1			T2*			T2*fast			T2*slow			
		Mean (ms)	S.D. (ms)	R2 (a.u.)	Mean (ms)	S.D. (ms)	R2 (a.u.)	Mean (ms)	S.D. (ms)	Part (%)	Mean (ms)	S.D. (ms)	Part (%)	R2 (a.u.)
More Degen.	Annulus	20.7	6.9	0.909	6.3	1.3	0.976	1.9	1.6	42	7.8	1.4	58	0.979
	Nucleus	16.8	3.9	0.864	5.5	0.7	0.984	1.0	1.1	61	7.4	2.0	39	0.984
Less Degen.	Annulus	20.4	6.1	0.893	8.1	1.7	0.983	1.7	1.3	51	12.5	3.8	49	0.981
	Nucleus	19.3	4.7	0.963	6.8	1.0	0.970	1.3	0.9	56	10.7	3.0	44	0.968
More Degen.	Ann. + Nuc.	18.4	5.1	0.936	5.8	0.9	0.982	1.2	1.2	56	7.5	1.9	44	0.983
Less Degen.	Ann. + Nuc.	19.7	5.2	0.935	7.3	1.3	0.967	1.5	1.0	55	11.3	3.2	45	0.966

Table 1. Means, standard deviations and measure of goodnes-of-fit of T1, T2*, T2*fast and T2*slow values in groups of less and more degenerated annulus fibrosus and nucleus pulposus. The two bottom lines represent average T1, T2*, T2*fast and T2*slow values from the whole intervertebral disc. Part is the average percentage of signal from T2*fast or T2*slow component.

Discussion/Conclusion: Sodium relaxation times seem to differ between healthy and degenerated IVDs. This knowledge is essential for correct absolute quantification of sodium concentration in IVDs.

References:

[1] Wang Ch., *Spine*, 2010;35(5):p.505–510.
[2] Borthakur A., *JMRI*, 2002;15:p.315–323
[3] Pfirrmann CW., *Spine*, 2001;26:p.1873–1878.
[4] Deligianni X., *ESMRMB*, 2011
[5] Moon C., *ISMRM*, 2011
[6] Ooms KJ., *MRM*, 2008;60:p.246–252

646

A comparison of cortical thickness determination at 3T and 7T of the human brain using high resolution data

F. Lüsebrink, A. Wollrab, O. Speck
Biomedical Magnetic Resonance, Otto-von-Guericke University Magdeburg, Germany, Magdeburg/GERMANY

Purpose/Introduction: The analysis of the human cerebral cortex and the measurement of its thickness based on MRI data can provide insight into normal brain development and neurodegenerative disorders. Accurate and reproducible results of the cortical thickness measurement are desired for sensitive detection. This study compares ultra-high resolution data acquired at 7T with 3T data for determination of the cortical thickness of the human brain. The impact of field strength, resolution, and processing method is evaluated systematically.

Subjects and Methods: Five subjects were scanned at 3T (1mm isotropic resolution) and 7T (1mm and 0.5mm isotropic resolution) with 3D MP-RAGE and 3D gradient echo methods (Figure 1). The inhomogeneous B_1 field was corrected by the division of the MP-RAGE with the GE [1] (Figure 2). For further investigation the isotropic 0.5mm 7T data was down-sampled to an isotropic resolution of 1mm and zero-mean Gaussian noise was added to the isotropic 1mm 7T data. Three software toolkits (FSL [2], SPM8 [3] and ARCTIC [4]) were used to generate segmentations (Figure 3). ARCTIC was used to compute the cortical thickness of the 3T and 7T data of all resolutions including the different segmentation methods. To compare the results FreeSurfer [5] was used to process the 3T and 7T data with an isotropic resolution of 1mm.

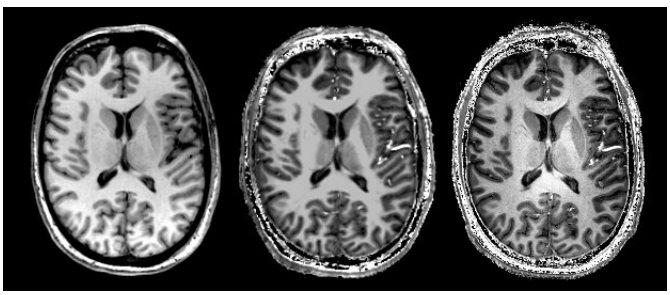

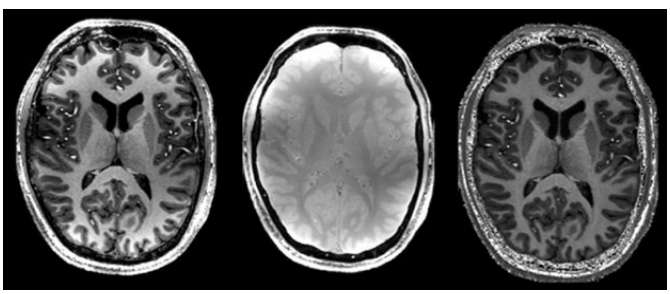

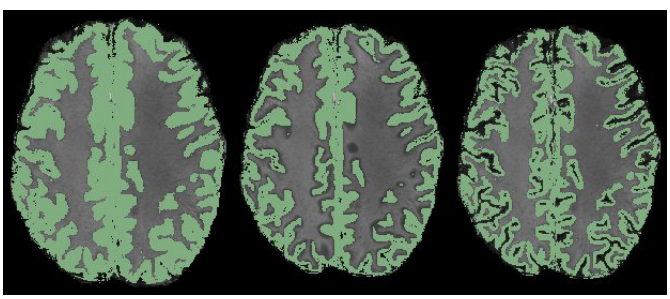

Results: At identical resolution, the cortical thickness determination yielded consistent results between 3T and 7T confirming the robustness of the acquisition and processing against potential field strength related effects. However, the ultra-high resolution 7T data resulted in significantly reduced values for

the cortical thickness estimation compared to the lower resolution data. The down-sampled data and the data with artificially added noise yield similar cortical thickness estimations compared with the 1mm isotropic data acquired at 7T (Figure 4).

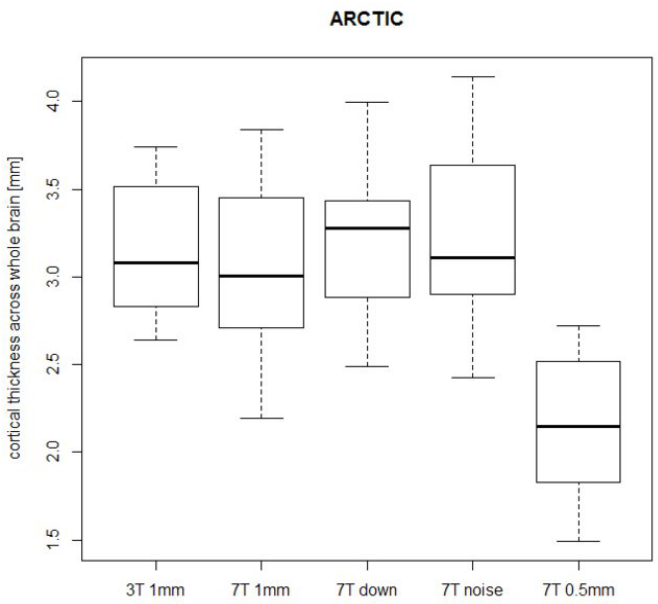

Discussion/Conclusion: The reduction in thickness of the ultra-high resolution data suggests a bias in the gray matter segmentation due to partial volume effects and indicates that true cortical thickness is overestimated by most current MR studies using voxel-based methods and can be more accurately determined with high resolution imaging at 7T.

References:

[1] van de Moortele et al., 2009, T1 weighted brain images at 7 Tesla unbiased for Proton Density, T2 contrast and RF coil receive B1 sensitivity with simultaneous vessel visualization, NeuroImage 46 (2009) 432-446
[2] http://www.fmrib.ox.ac.uk/fsl/
[3] http://www.fil.ion.ucl.ac.uk/spm/
[4] http://www.na-mic.org/Wiki/index.php/DBP2:UNC:Regional_Cortical_Thickness_Pipeline
[5] http://surfer.nmr.mgh.harvard.edu/

647

Principle component analysis of textural features based oncontrast-enhanced MR images of liver with acute hepatitis in murine model.

K. Byk[1], K. Jablonski[2], W. Szczepanski[3], B. Tomanek[4], T. Skorka[1]
[1]Department of Magnetic Resonance Imaging, Institute of Nuclear Physics PAN, Krakow/POLAND, [2]Chair of Gastroenterology, Hepatology and Infectious Diseases, Jagiellonian University Medical College, Krakow/POLAND, [3]Chair of Pathomorphology, Jagiellonian University Medical College, Krakow/POLAND, [4]Institute for Biodiagnostics, National Research Council, Calgary/CANADA

Purpose/Introduction: Chronic liver diseases are very frequent worldwide and are becoming a serious health problem. The standard approach of liver disease diagnosis is a biopsy. For additional, noninvasive data one can use MRI techniques and quantitative image analysis [1].
The purpose of this study was to apply a texture analysis (TA) – an image processing technique, and a principal component analysis (PCA) – statistical approach of reducing issue dimensionality, to distinguish between disease stages in murine model of acute hepatitis.

Subjects and Methods: Dynamic series of the contrast-enhanced (Gd-EOB-DTPA, Primovist, Bayer-Shering) images of the mice liver (10 weeks BALB/c) at different stages of the concanavaline induced hepatitis (Fig. 1) were collected. I–control, II–ConA, 10 mg/kg, III–ConA, 20 mg/kg, and IV–2×10 mg/kg ConA. Time gap between subsequent images was 30 s during uptake and 10 min during rinsing.

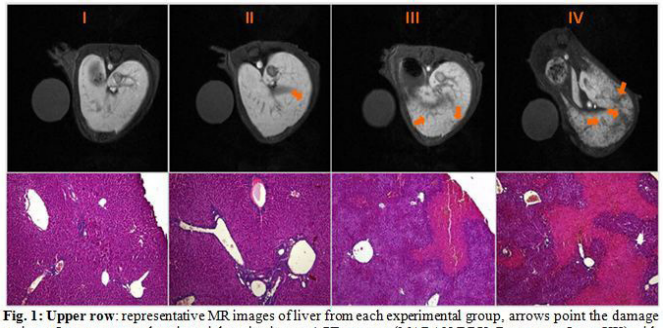

Fig. 1: Upper row: representative MR images of liver from each experimental group, arrows point the damage regions. Images were taken in axial projection at 4.7T magnet (MARAN DRX, Resonance Instr, UK) with GRE_MSMF T_1-weighted sequence with parameters: TE: 3ms, TR: 40ms, FOV: 30×30 mm², slice thickness: 1,2 mm, and matrix size: 256×128. **Lower row**: images of histology samples stained with hematoxylin-eosin, the necrosis areas have a light pink color. Hepatitis starts form central veins in hepatic lobules (second image).

Textural features were computed from histograms, co-occurrence matrixes (GLCM) and run length vectors matrixes (RLVM) [2] using ImageJ (NIH, USA) software. The time course for each texture parameter was approximated in the rinsing phase using linear regression. The slope of the regression line, the intercept, and the value at the time=2000s were taken into account for PCA [3] (Statistica, StatSoft, Inc, USA). Histological samples were studied under light microscope.

Results: Contrast agent was metabolized faster in groups with none or slight injury (I, II) than in those with severe tissue injury (III, IV) (Fig. 2).

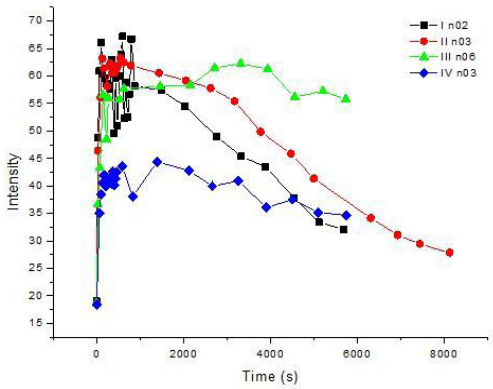

Fig. 2: Representative time courses of pixel intensities for each group. One can see that contrast agent metabolism in group I and II is faster than in group III or IV. This is caused due to fact that livers in groups III and IV are heavily damaged. Intensity-time plots for those groups are almost vertical, what means that contrast agent stays longer inside hepatic lobules without being rinse out.

Four significant factors were determined using eigenvalues, percent of explained variance (Tab. 1), and the scree-plot (Fig. 3).

Tab. 1: Eigenvalues of correlation matrix, and related statistics. Four significant eigenvalues were taken into account in following analysis. They explain more than 83% of original data variation.

Value number	Eigenvalue	% Total variance	Cumulative eigenvalue	Cumulative %
1	60,61912	41,23750	60,6191	41,2375
2	38,21273	25,99506	98,8319	67,2326
3	16,73979	11,38761	115,5716	78,6202
4	7,46594	5,08091	123,0406	83,7011
5	5,82366	3,96167	128,8642	87,6628
6	3,41958	2,32624	132,2838	89,9890
7	2,81395	1,91425	135,0978	91,9032
8	2,24407	1,52658	137,3418	93,4298
9	2,19040	1,49007	139,5322	94,9199
10	1,87270	1,27394	141,4049	96,1938
11	1,53995	1,04759	142,9449	97,2414
12	1,33640	0,90912	144,2813	98,1505
13	0,99807	0,67896	145,2794	98,8295
14	0,76366	0,51949	146,0430	99,3490
15	0,61826	0,42058	146,6613	99,7696
16	0,33873	0,23043	147,0000	100,0000

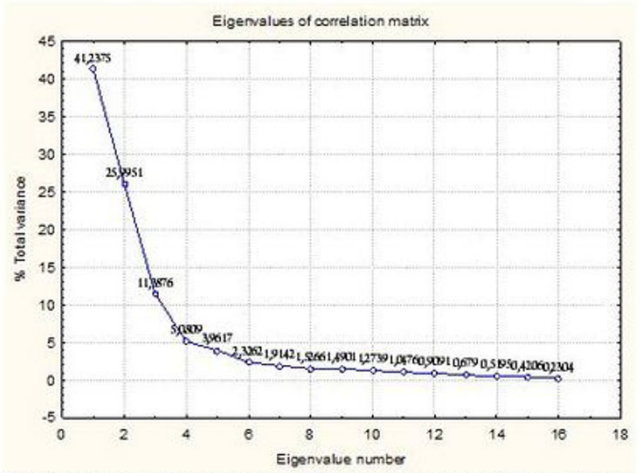

Fig. 3: Scree-plot of eigenvalues of correlation matrix based on texture parameters. Four meaningful factors, explicating more than 80% of total variance, were chosen for further analysis, and rest of component was ruled out. Starting from 6th eigenvalues points are arranging into a straight line and can be excluded from analysis based on Cattell's scree test. The 5th component was expelled because its eigenvalues was notably lower than average of eigenvalues.

The first factor consisted mostly of GLCM parameters the second of parameters based on RLVM whereas the third included remained features. Analysis permitted well-defined discern between groups I or II and groups III or IV (Fig. 4).

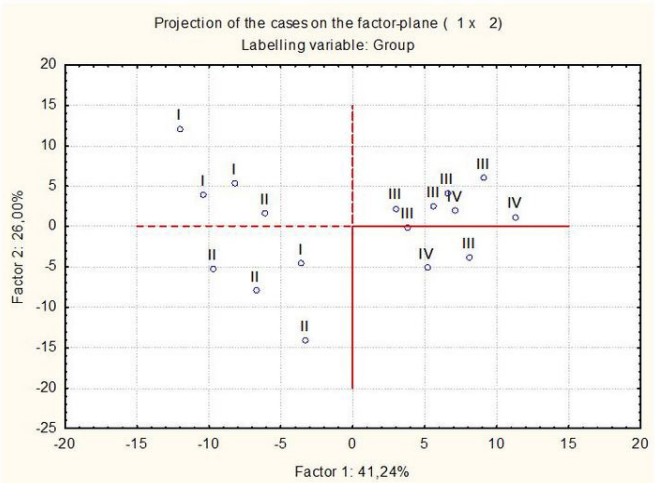

Fig. 4: PCA graph shows separations between groups (I, II) and (III, IV). Moreover distinction among I and II group is also possible because cases from control group are placed rather in 2nd quarter of plot, while mice from group II take negative values in Factor 2 and are in 3rd quarter. Heavily injured groups cannot be so easily divided into two groups on this plot.

Histology showed percentage of hepatocytes necrosis among groups: <5%, 10-25%, >50% (II, III and IV, respectively).

Discussion/Conclusion: Principal component analysis of the textural parameters deriving from the time series of dynamic contrast enhanced images may be useful method for the assessment of the liver injury severities. It gains the possibility of the case classification and is a step towards the classification method that is not biased.

This work was supported by the European Regional Development Fund from European Union (grant coordinated by JCET-UJ, No WND-POIG.01.01.02-00-069/09-00).

References:

[1] Faria, S, 2009, RadioGraphics 29: 1615-1635.
[2] Tuceryan, M, 1998, World Scientific Publishing Co., 207-248.
[3] Larose, DT, 2008, John Wiley $ Sins, Inc., 1-35.

648

A New Method for Receiver Profile Correction for Quantitative Proton Density Mapping

S. Volz[1], U. Noeth[1], A. Jurcoane[2], U. Ziemann[3], E. Hattingen[2], R. Deichmann[1]
[1]Brain Imaging Center (BIC), University of Frankfurt, Frankfurt/Main/GERMANY, [2]Department of Neuroradiology, University Frankfurt, Frankfurt/Main/GERMANY, [3]Department of Neurology, University Frankfurt, Frankfurt/Main/GERMANY

Purpose/Introduction: Techniques for proton density (PD) mapping usually correct image signals for any T1-, T2*- and B1-bias, yielding M0 maps, M0 being the product of PD and the receiver profile (RP). Thus, the knowledge of RP is crucial for correct PD mapping. The method presented here applies the following concept: (1) PD values are calculated from T1-maps for sparse sample points in normal grey and white matter, assuming a linear relationship between 1/PD and 1/T1. (2) RP_sparse is calculated at these points from M0/PD_sparse. (3) Since RP is a smooth spatial function, full RP maps can be obtained from RP_sparse by interpolation. (4) Final PD maps are obtained from M0/RP_interpol. The method is compared to a previously published method based on bias field correction [1].

Subjects and Methods: Measurements were performed at 3T on six healthy subjects and two patients (multiple sclerosis (MS), glioblastoma). Methods for mapping T1, T2* and B1 were based on the techniques described in [1,2,3] (total scan time 15:40min). M0 maps (whole brain, 1mm isotropic resolution), were calculated and converted into PD maps using the two methods described above.

Results: Fig.1 shows PD maps for two healthy subjects, based on bias field correction (top) and the new method (bottom).

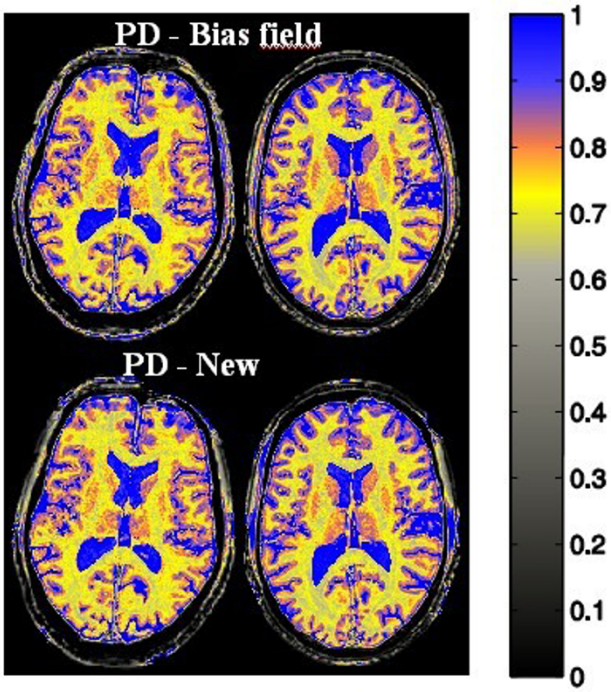

Fig.2 shows for both methods histograms of PD values in healthy brain tissue, pooled across all subjects. There is no significant difference between results.

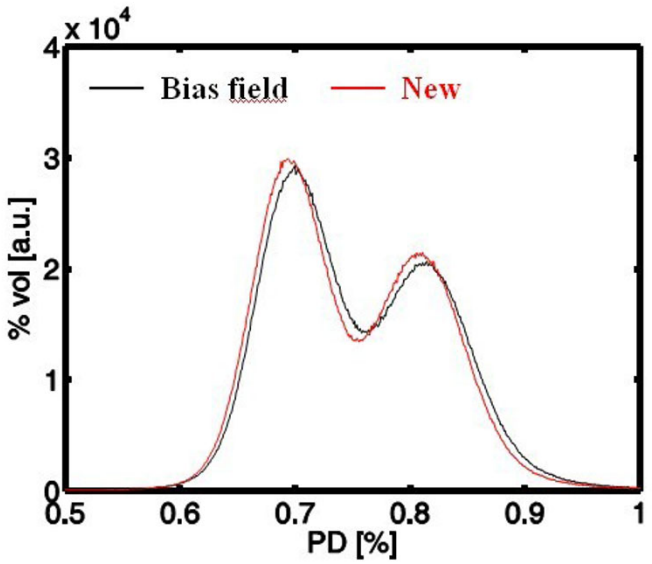

Fig.3 shows PD maps for the MS patient (top) and the tumor patient (bottom), based on the new method (left) and on bias field correction (right). For the MS patient, similar results are obtained with both methods in lesions and normal tissue. In the glioblastoma, the new method yields high PD values (similar to gray matter and edema), whereas the bias field correction yields relatively low PD values (similar to white matter).

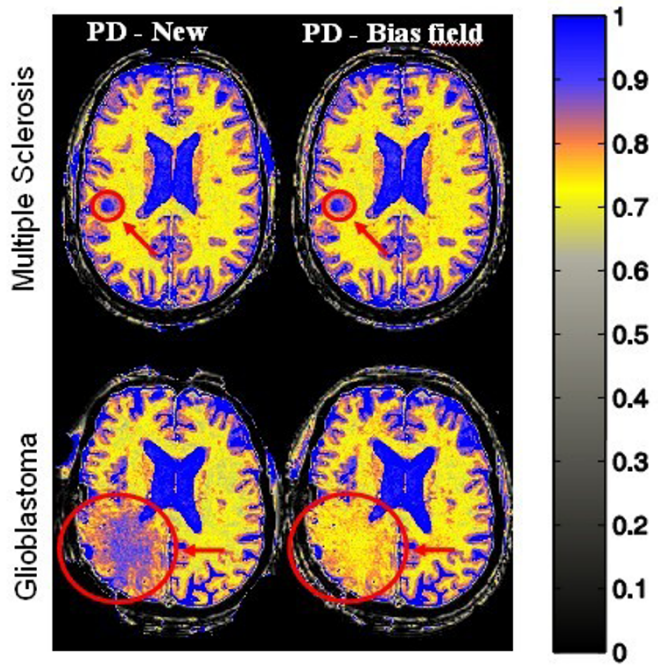

Discussion/Conclusion: The results suggest that both methods yield similar PD values for healthy brain tissue. However, the advantage of the new method is the fact that pathological tissue can be excluded from the sample points, avoiding erroneous PD values in these areas. For the MS patient, results obtained with both methods were still identical. In contrast, there were large PD differences in the glioblastoma, the results obtained with the new method being closer to gray matter and edema values. This result corresponds to literature [4], in contrast to the low PD values obtained with the bias field method.

References:
[1] Volz;DOI: 10.1002/mrm.23206.
[2] Venkatesan;1998;MRM;40:592-602.
[3] Volz;2010;NeuroImage;49:3015-3026.
[4] Neeb;2006;NeuroImage;31:1156-1168.

649

A quantitative analysis of glioma response to antiangiogenic therapy using intelligent image processing

A. Benítez[1], **A.R. Borges**[1], P. Lopez-Larrubia[2], L. Lago-Fernández[3], M. Sánchez-Montañés[3], S. Cerdán[1]
[1]Modelos Experimentales de Enfermedades Humanas, Instituto de Investigaciones Biomédicas "Alberto Sols", Madrid/SPAIN, [2]Instituto Investigaciones Biomedicas "Alberto Sols" CSIC-UAM, Madrid/SPAIN, [3]Escuela Politécnica Superior, Departamento de Ingeniería Informática, Universidad Autónoma de Madrid, Madrid/SPAIN

Purpose/Introduction: Clinical management of high grade gliomas (HGG) often involves antiangiogenic therapies using monoclonal antibodies, mainly against VGEF. Responses to this treatment are highly heterogenous, with similar cohorts of patients behaving as "responders" or "non-responders". It would be then very useful to discriminate by non invasive criteria the two populations as early as possible, to tailor treatment accordingly. Here we report on a multivariate analysis approach on the discriminant power of T2w and DWI, or their combination to predict the treatment outcome of mice bearing implanted Gl621 tumors to anti-VGEF therapy.
Subjects and Methods: We evaluated treatment response in 13 mice bearing implanted Gl261 tumors on a 7T MR scanner (RECIST criteria, mAb against VEGF B20-4.1, 5mg/Kg twice weekly for 8 weeks). MRI studies included T2w and DWI performed sequentially at 3/4 day intervals until completion of treatment or obvious, treatment independent, tumor growth. Fisher's discriminant analysis was then applied to the complete data set in order to find the linear projection that best discriminates the pixels as belonging to "responder" or "non-responder" animals to anti-VGEF treatment. We compared the discriminant power of T2w alone, DWI alone or the combination of both.
Results: Among a total of 13 treated mice, 8 responded to treatment and 5 did not respond. Figure 1 shows the histograms of average pixel intensities in T2w (A) and DWI (B) in responder (red) and non-responder (blue) groups.

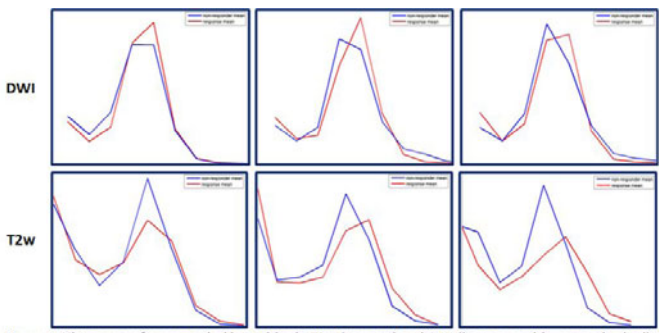

Figure 1. Histograms of average pixel intensities in T2w (top row) and DWI (bottom row) in responder (red) and non responder (blue) groups. Left column: *Day -1* of treatment, Middle column: *Day-2* of treatment and Right column: *Day-finish* of treatment. There are differences that can be used for a classification method to predict the course of treatment.

We used the Fisher´s discriminant analysis to find out the optimal separation between these groups using the T2w, DWI, or the combination of both imaging data sets. Using a leave one out strategy, we obtained the following percentages of accurate predictions of a given mouse between the "responder" and "non-responder" groups: (i) smaller than 50% using DWI only (A), (ii) 61% using T2w images only (B) and (iii) 92% when using the combination of T2w and DWI data sets (C). Figure 2 illustrates the classification between responders (red) and "non-responders" under the three cases.

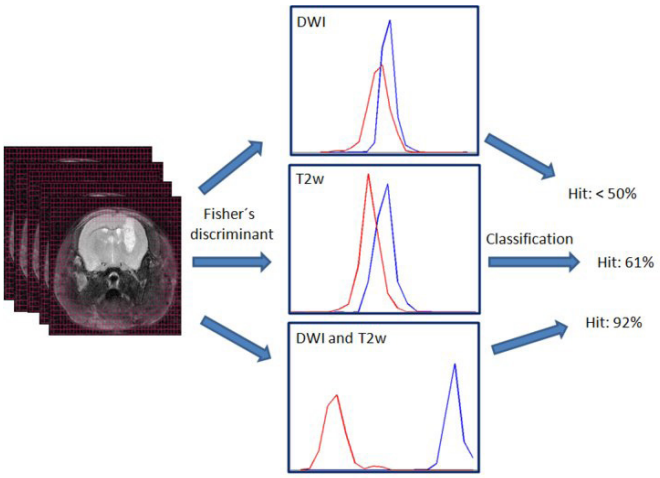

Figure 2. Result of the Fisher´s discriminant analysis and the classification of data set into "responders" (red) and "non-responders" (blue) using DWI (top), T2w (middle) and combination of both (bottom).

Discussion/Conclusion: We provide a protocol for the prediction of therapy response to antiangiogenic therapy in mouse glioma models, based on non invasive parameters as T2w and DWI. Present results provide 92% successful predictions when using combinations of T2w and DWI data sets. Prediction accuracy may be improved by increasing the number of mice investigated or including in the discriminant function additional perfusion parameters as CBF, CBV and MTT. The method is easily extendable for human use.

650

Volumetric Reconstruction of Post Mortem Human Brain Histological Sections using 7T MRI Volume as Guidance

S. Yang[1], Z. Yang[2], D. Reutens[2], O. Speck[1], M. Walter[3]
[1]Biomedical Magnetic Resonance, Otto-von-Guericke-University, Magdeburg/GERMANY, [2]the University of Queensland, Centre for Advanced Imaging, Brisbane/QLD/AUSTRALIA, [3]Clinical Affective Neuroimaging Laboratory, University of Magdeburg, Magdeburg/GERMANY

Purpose/Introduction: It is difficult to analyze 3D structural characteristics on 2D histological sections. Volumetric reconstruction by stacking the 2D sections after alignment between adjacent sections would fail due to registration error accumulation and a reference volume is preferred [1]. High-field MRI resolution (150 µm isotropic) is approaching to histological section thickness [2] and we reconstructed a post mortem human brain using its 7T MRI volume as guidance.
Subjects and Methods: One block of human post-mortem brain (the middle 1/3) was scanned using 7T whole body MRI scanner (Siemens, Erlangen) with FLASH and 200 micron isotropic voxel size. Nissl stained sections with 230 micron thickness were digitized using a flat-bed scanner. Inter-section intensity inhomogeneity was corrected using histogram matching. The affine transformation between any two adjacent histological sections was obtained using ANTS toolbox. By composing these transformations, the series of 2D sections were stacked into a 3D volume, to which the MRI volume was affine registered and resliced. The corresponding MR slice for each histological section was found. The histological sections were registered to their corresponding MRI slices and then stacked to form a volume, to which the MR volume was aligned again. These steps were repeated until there was no significant improvement in the volume similarity. Finally, histology sections were warped to corresponding MR slices.
Results: The tri-planar view of the reconstructed histology is shown in Figure 1. The intensity inhomogeneity correction was satisfactorily performed to yield visually plausible intensity smoothness across sections. A side-by-side view of corresponding histology-MRI image pairs before the final deformable registration step is shown in Figure 2. The histology warped to MRI volume is illustrated in Figure 3 and misalignment can be observed.

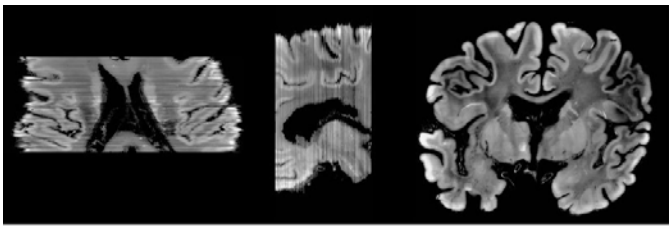

Figure 1: The tri-planar view of the reconstructed histology after the affine transformation between two adjacent histological sections

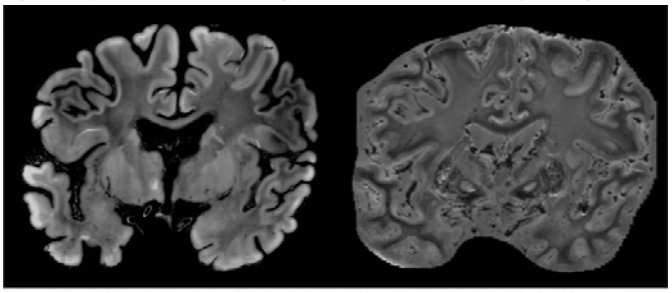

Figure 2: histological 2D section (left) and the corresponding MR 2D slice (right) after the affine transformation from MR to histological volume.

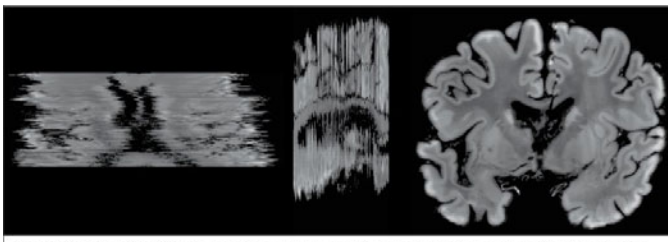

Figure 3: histological 3D-volume after cross correlation-based deformable registration to MR

Discussion/Conclusion: We successfully reconstructed the histological volume and the corresponding MR slice for each histological section was found, although many sections were severely corrupted by poor stain and overexposure. A nonlinear registration of histology to MR should improve the alignment [1, 3], but it was not effective in this study because of the background signal from formalin. In the future, this background issue will be resolved by acquiring images with two different sequences, based on which the signal from formalin can be removed. This pioneer study demonstrated that a 7T MRI guided histology reconstruction is promising.
References:
[1] Yushkevich PA et al. 2006.
[2] Yang, S. et al, ESMRMB 2011.
[3] Yang, Z. et al, ISMRM 2011.

651

Correction of geometrical distortion in EPI sequences through a radial basis function expansion

R. Sghedoni[1], M. Foracchia[2], A. Nitrosi[1], M. Iori[1]
[1]Medical Physics Department, Arcispedale Santa Maria Nuova, Istituto di Ricovero e Cura a Carattere Scientifico, Reggio Emilia/ITALY, [2]Information Technology Department, Arcispedale Santa Maria Nuova, Istituto di Ricovero e Cura a Carattere Scientifico, Reggio Emilia/ITALY

Purpose/Introduction: As it is well known Magnetic Resonance Imaging (MRI) is affected by geometrical distortion both system and patient related. Modern MR scanners largely overcome these issue in almost all sequences but echo planar imaging (EPI). EPI are the basis for the most advanced MR techniques, which are now starting to be used in clinical applications where geometrical accuracy is important (neurosurgery, radiotherapy). In this study a method for correcting distortion in EPI acquisition is described.
Subjects and Methods: A T1-weighted and an EPI sequence of a grid-phantom were acquired in identical geometry in the head coil. Then the phantom was

moved and the acquisitions repeated in 5 different positions. A Matlab script was built to
a) automatically identify corresponding points of the grids in the 2 acquisitions of the phantom
b) transform point positions from EPI to T1.
The transformation binding EPI images to T1 (reference) images has been modeled as (x',y',z')=f(x,y,z;b) where b is the set of parameters identifying the model and f is a radial basis function (RBF) expansion, defined as a mixture of gaussians. To achieve a continuous interpolation in z, different models are identified at different slices, and a simple linear interpolation on final projected coordinates was used.
Results: A set of 5 calibration image pairs (EPI,T1) at different z levels spaced 80mm apart was used. The RBF model has been identified for every image pair. Then, the model has been tested by projecting EPI points on T1 space for a set of 3 validation image pairs, acquired in different positions. The distances between corresponding points in EPI and T1 space after application of the model decreased respectively from 8.2mm (simple traslation correction) to 2.9mm (RBF model), from 9.7mm to 5.3mm, from 9.7mm to 1.3mm. Standard deviation of the distances decreased too.

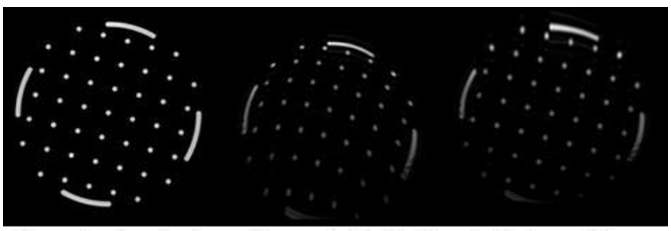

Example of application of the model. Left: T1-weighted acquisition of the grid phantom. Middle: EPI acquisition Right: EPI acquisition corrected by the model

Discussion/Conclusion: Distortion in EPI sequences is still an open issue in MRI. In this study a method for correcting system related distortion through phantom calibration and a transformation based on a radial basis function expansion is proposed. Preliminary results on phantom show a significant reduction in image distortion and a correct positioning of points compared to a non distorted T1 sequence. Further analyses are required to transfer the method to clinical settings.
References:
Yang J., The thin plate spline robust point matching (TPS-RPM) algorithm……..., Pattern Recognition Letters, 32(7),2011
Taso J., Ultrafast imaging: principles,……, JMagnResonImaging, 32(2),2010
Jezzard P., Correction of geometric distortion in fMRI data,Neuroimage,2011

652

The comparison of mono- and bi-exponential fitting for T2* calculation of Achilles tendon using variable-echo-time sequence

V. Juras[1], X. Deligianni[2], S. Apprich[3], O. Bieri[4], S. Zbyn[3], I. Frollo[5], S. Trattnig[6]
[1]MR Centre-Highfield MR, Department of Radiology, Medical University of Vienna/Vienna General Hospital, Vienna/AUSTRIA, [2]Division of Radiological Physics - Department of Radiology and Nuclear Medicine, University of Basel Hospital, Basel/SWITZERLAND, [3]MR Centre of Excellence, Medical University of Vienna, Vienna/AUSTRIA, [4]Department of Radiology and Nuclear Medicine, Division of Radiological Physics, University of Basel Hospital, Basel/SWITZERLAND, [5]Department of Imaging Methods, Institute of Measurement Science, Bratislava/SLOVAK REPUBLIC, [6]Department of Radiology, MR Center of Excellence, Medical University of Vienna, Vienna/AUSTRIA

Purpose/Introduction: A novel multi-echo, variable echo time (VTE) with sequentially shifted echo times [1] sequence enables quantitative MR imaging of certain tissues with very low echo times such as the Achilles tendon (AT). The purpose of this study was to compare the mono- and bi-exponential curve fitting performance for T2*-relaxation times calculation in comparison with clinical scoring in patients with AT injury and healthy volunteers at 3T [2,3].
Subjects and Methods: Institutional Review Board approval and written, informed consent were obtained. Ten patients (mean age 43.9 ± 13.4 years) with a painful AT and 10 age-matched, healthy volunteers (mean age 43.7 ± 11.2 years) were examined with a 3T whole-body system, using an 8-channel knee coil. Morphological imaging included a sagittal T2-w fast spin echo sequence. T2* maps were calculated from an isotropic 3D-multi-echo-VTE-sequence (TE =0.8,2.2,3.1,4.1,5.1,6.1,7.1,8.1,9.1,10.1,11.1,12.1,13.1,14.1,15.1,16.1,17.1, 18.1,19.1,20.1 ms) using a mono- and bi-exponential fit least square analysis (performed in IDL). T2* values were calculated using a manually drawn ROI analysis for the most severe pathology within patients and for the distal two-thirds of the AT in volunteers. All subjects completed the Achilles tendon Total Rupture Score (ATRS; 0-100 points). Statistical measures included an analysis of variance and Pearson-Correlation Coefficient(r).
Results: In volunteers, the mean T2*mono was 2.61±0.63 ms, T2*short was 1.53±0.43 and T2*long was 27.03±5.37. In patients, the mean T2*mono was 7.25±2.37 ms, T2*short was 8.09±7.26 and T2*long was 21.49±10.12. Respective T2* values of patients and volunteers were significantly different. Mean ATRS for patients was 56.30±24.94. Strong correlation was found between the ATRS and mean T2*mono (r=-0.793,R2=0.629,P<0.001), as well as for T2*short (r=-0.676, R2=0.45, P<0.001). No correlation was found for T2*long (r=0.084,R2=0.007,P<0.001).

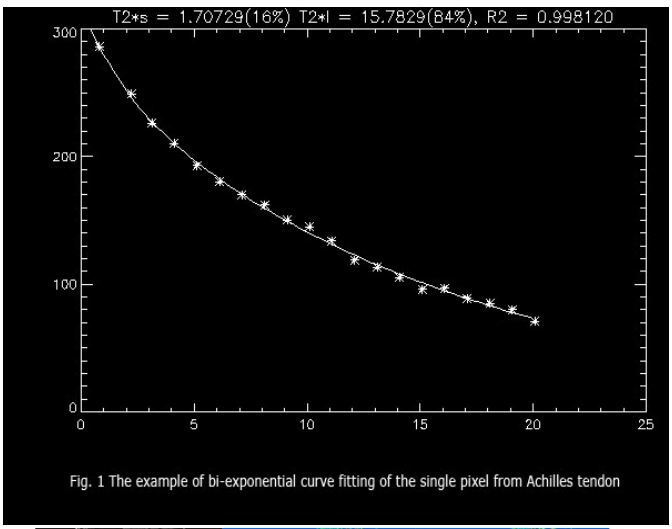

Fig. 1 The example of bi-exponential curve fitting of the single pixel from Achilles tendon

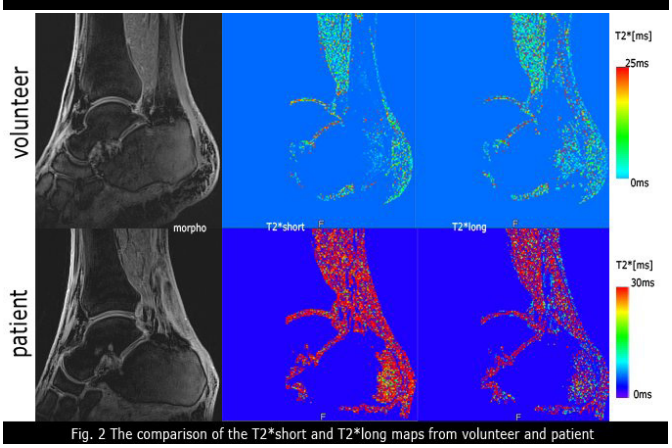

Fig. 2 The comparison of the T2*short and T2*long maps from volunteer and patient

Discussion/Conclusion: Mono-exponential curve fitting for T2* calculation in AT is satisfactory for using T2* as a predictive marker for the probability of an AT rupture as well as for a re-rupture after surgery. Bi-exponential fitting, which is computationally more demanding but more precise due to distinguishing between different types of water molecule binding, did not provide better results.

References:
[1] Song, H.K et al., MRM 1998;39:pp251-258
[2] Filho GH et al, Am J Roentgenol 2009;192:pp117-124
[3] Peto S et al Magn Reson Imaging 1990;8:pp705–712

653

Comparison of quantitative and semi-quantitative cerebral distribution volume values from DCE- and DSC-based perfusion in glioblastoma multiforme.

M.I. Dujardin[1], M. Lowry[2], S. Sourbron[3], Y. Fierens[4], B. Neyns[5], L. Turnbull[1]
[1]Center for Magnetic Resonance Investigations, University of Hull in association with Hull York Medical School, Hull/UNITED KINGDOM, [2]Centre for Magnetic Resonance Investigations, University of Hull in association with HYMS, Hull/UNITED KINGDOM, [3]Division of Medical Physics, University of Leeds, Leeds/UNITED KINGDOM, [4]Radiologie/Befy, UZBrussel, Brussels/BELGIUM, [5]Medical Oncology, UZBrussel, Brussel/BELGIUM

Purpose/Introduction: To compare the cerebral distribution volume (CDV) values of Gd-DTPA estimated from T1-DCE-based and T2*-DSC-based perfusion sequences in both glioblastoma multiforme (GBM) and contralateral white matter (CWM) using a semi-quantitative and quantitative approach.
Subjects and Methods: 12 proven recurrent GBM were measured at 1.5T before and after anti-angiogenesis therapy. IR-prepared-FLASH(TR=2.4ms/TE=2ms/TI=190ms/FA=50°/matrix=146*256, FOV=219-270mm/phases=250/0.3s/slice/slice thickness=5mm/slices=3) was performed during a 15 ml Gd-DTPA injection(2ml/s). Ten minutes later, T2*-weighted GE-EPI-perfusion(TR=1590ms/TE=52ms/FA=90, matrix=128*128/FOV=230mm/phases=50/1.4s/11 slices/slice thickness=5mm/slices=11) was performed during a 20 ml Gd-DTPA injection(4ml/s). Data were processed using PMI0.4[1]. DCE-datasets were truncated to match the acquisition time of the DSC-data(71s). Signal intensity was converted to tracer concentration and deconvolved pixel-by-pixel with an AIF from an artery close to the tumour. The same AIF-region was chosen for DSC and DCE. Comparable ROIs were manually drawn on CBF maps for whole tumour and CWM, avoiding necrosis and large vessels. Semi-quantitative measures for tumour and CWM were calculated as the area under the concentration-time curve for DCE[AUC_{T1}] and DSC[AUC_{T2*}]. Quantitative CDV for both DCE[CDV_{T1}] and DSC[CDV_{T2*}] was calculated by deconvolving tracer concentrations on ROI-basis, and integrating the impulse response.
Results: In 7/24 datasets DSC-based analysis in tumour was impossible due to susceptibility artifacts from surgical clips. Figures 1 and 2 show scatter plots of CDV_{T1} versus CDV_{T2*} and AUC_{T1} versus AUC_{T2*}. No significant correlation was found between CDV_{T1} and CDV_{T2*} in tumour(R=-0.1, p=0.6) or CWM(R=0.03, p=0.9). However AUC_{T1} and AUC_{T2*} showed a significant correlation in both tumour(R=0.5, p=0.03) and CWM(R=0.5, p=0.02).

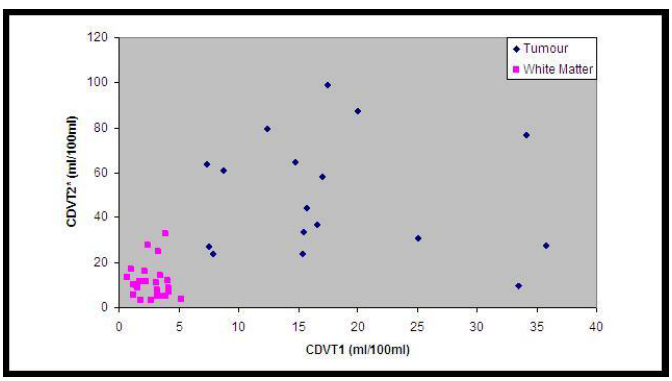

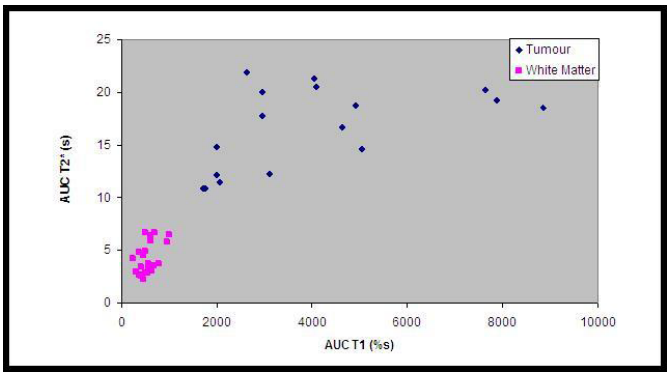

Discussion/Conclusion: CDV_{T2*} were systematically higher than CDV_{T1}, an observation consistent with the overestimation expected by the difference in relaxivity between artery and tissue[2]. Semi-quantitative CDV from both sequences were significantly correlated in both whole tumour and CWM. This agrees with Haroon *et al*[3], who found a correlation using a semi-quantitative approach and with Ludemann *et al*[4], who reported a correlation between perfusion values using various methods not involving an AIF. However, after deconvolution the correlation was destroyed, likely caused by the introduction of significant errors through inflow(DCE) and partial volume errors(DCE and DSC) in the AIF. The results suggest that a quantitative analysis of DSC or DCE should only be considered if the AIF can be measured accurately. If this cannot be guaranteed, semi-quantitative parameters may have a higher diagnostic value.

References:
[1]Sourbron et al;PMB(2007);52:429-447
[2]Kiselev et al;MRM(2001);46:1113-1122
[3]Haroon et al;BJR:(2007);80:161-168
[4]Ludemann et al;EJR:(2009)70:465-474

654

Combining fiber-tracking parameters with functional information into effective connectivity models

G. Garcia Marti[1], J. Sanjuan[2], **L. Marti-Bonmati[3]**
[1]Neuroimaging, CIBERSAM, Valencia/SPAIN, [2]Psychiatry, CIBERSAM, Valencia/SPAIN, [3]Radiology, Universitat de Valencia, Valencia/SPAIN

Purpose/Introduction: Brain functional integration should be considered in relationship to both anatomical and functional connectivity. Diffusion tensor imaging (DTI) allows studying the basis of anatomical connections, estimating the main diffusion of the principal interstitial water component [1]. Functional connectivity can be used to assess the influence that a neuronal system exerts over another [2], providing an interesting tool to evaluate the cause and effect consequences of the functional brain activation. In this work we will propose a quantitative approach to study regional brain connectivity integrating both anatomical and functional information into models of effective connectivity.
Subjects and Methods: The DTI images with 16 directions and the B_0 image were used to calculate parametric maps of Fractional Anisotropy (FA) as the primary indicator of white matter tracts. This process (done by FSL software) included a quality-check procedure, a head motion correction and a normalization step. The normalization parameters were determined by the T1W image relative to the MNI template.
The tracking procedure was performed by positioning the seeds in several different areas, according to the different connectivity models to evaluate. Tracks were generated from every voxel including only those paths with a p>0.10. Then, a "connectivity weighted" variable was created for the connectivity model, indicating the likelihood of a connection between two regions.
MRI scans were obtained on a 3T magnet (Philips Achieva, Best, Netherlands) with the following parameters:
- T1W: 3D, GRE, TE/TR:3.9/8.3, FA:8º, matrix:256x256, slices:160, voxel size: 0.94x0.94x1, gap:0.

- T2*: EPI, TE/TR:19/2275, FA:90°, matrix:80x80, slices:48, voxel size: 2.88x2.88x2.60, gap:0, dynamics:80.
- DTI: SE, TE/TR:55/10237, FA:90°, matrix:144x144, slices:80, voxel size:1.59x1.59x1.76, gap:0, number of directions:16.

Results: The computation of the two different connectivity models (functional and functional+DTI) showed that the connection strengths were higher with the inclusion of the anatomical information. The Bayesian model selection procedure also showed a better posterior probability values for the model with DTI values included as a previous knowledge (0.7 vs 0.3).

Discussion/Conclusion: The inclusion of *a priori* anatomical tensor information in functional connectivity models improve the connection strengths and may be useful to increase the identification of patterns and interactions between different brain regions in terms of neuronal responses.

References:

1.Le Bihan D. et al. MR imaging of intravoxel incoherent motions: application to diffusion and perfusion in neurologic disorders. Radiology.(1986)161:401–7.
2.Friston, KJ. Functional and effective connectivity in neuroimaging: a synthesis. Human BrainMapping.(1994)2:56–78.

655

A Novel Image Processing Pipeline for Quantitative Magnetic Resonance Elastography (MRE): Application in Dynamic Studies of Human Thigh Muscles

E. Barnhill[1], P. Kennedy[1], C. Brown[2], N. Roberts[1]
[1]Clinical Research Imaging Centre, The University of Edinburgh, Edinburgh/UNITED KINGDOM, [2]Research and Development, The Mentholatum Company, Glasgow/UNITED KINGDOM

Purpose/Introduction: Introduction Patterns of muscular activation in a limb provide keys to diagnosis, recovery, and rehabilitation in scenarios of neuromuscular damage or disease[1]. Magnetic Resonance Elastography (MRE) allows for measurement of shear modulus throughout a volume of tissue imaged in vivo, and skeletal muscle stiffness is an indication of the level of muscle activation[2].

A new image processing pipeline was created, using algorithms from other domains of physics and image processing to enhance spatial resolution and robustness of quantification. The pipeline was applied to quantify individual neuromuscular activation patterns within the human thigh.

Subjects and Methods: Subjects and Methods The MRE data were obtained for 11 subjects using a Siemens Verio 3T MRI system (Siemens Medical Systems, Erlangen, Germany) using an EPI sequence with the tissue subjected to forced vibration at 50 Hz. Images were obtained in the transverse plane of the thigh during different states of contraction as well as after application of a topical treatment. The contraction conditions were a rest condition, a straight leg raise which activated quadriceps, and a straight leg press which activated hamstrings.

The new image processing pipeline was created as an ImageJ plugin[3] with libraries from Apache commons-math[4], offering choice among unwrapping, decomposition, and inversion methods.

Results: The pipeline yielded high anatomical specificity without null filling, interpolation, or other manipulations, and without leaving the pixel resolution of the original image. When the elastogram is overlain on the corresponding anatomical image, intensity of individual muscular contraction as well as varied neuromotor strategies to lift and press the leg can be identified.

Average stiffness for each condition was 1.90 Kpa for rest, 2.15 KPa for lift and 2.02 KPa for press. Flexor and extensor muscle group averages during each of the three tasks are in Table 1.

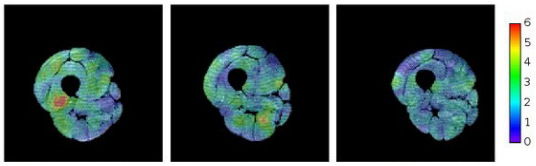

Fig. 1 Sample Subject in Lift, Press, and Rest Conditions.Stiffness in KPa.

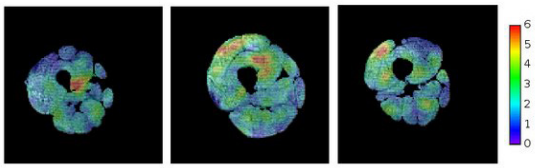

Fig. 2 Examples of individual variety in lift condition.Stiffness in KPa.

Muscle	Rest	Lift	Press
Vastus Medialis	2.081	2.448	1.967
Vastus Intermedius	2.269	2.823	2.144
Vastus Lateralis	1.886	2.432	1.982
Rectus Femoris	1.570	2.064	2.138
EXTENSOR AVERAGE	1.479	2.429	2.066
Biceps Femoris	2.029	2.127	1.956
Semitendinosus	1.861	1.548	1.888
Semimembranosus	1.795	1.803	2.416
Sartorius	2.074	1.783	2.153
Gracilis	1.504	1.260	1.789
FLEXOR AVERAGE	1.457	1.829	2.058

Discussion/Conclusion: The elastograms from the new pipeline allow for the direct measurement and quanitification of an individual's unique functional neuromuscular strategies through a transverse slice of a limb. This information may allow for a more targeted approach to movement rehabilitation and rehabilitation research. It may also yield novel ways to quantify and classify dimensions of athletic or other specialized performance.

References:

[1] Cheng et al. 2004 *Am J Phys Med Rehabil* 83:10-16
[2] Klatt et al. 2010 *Phys Med Biol* 55:21 6445-6559
[3] ImageJ, US National Institutes of Health, Bethesda, Maryland, USA
[4] Apache commons-math release 3.0, 2010 Apache Commons Foundation

656

Model-based Magnetization Transfer Imaging Parameters and their impact on the differentiation of age matched MCI, Alzheimer and healthy patients

C. Kiefer, Y. Burren, M. Hauf, G. Schroth, J. Pruessner, M. Zbinden, K. Cattapan-Ludewig, R. Wiest
Institute of Diagnostic and Interventional Neuroradiology, Support Center for Advanced Neuroimaging (SCAN), University Hospital Bern, Bern/SWITZERLAND

Purpose/Introduction: Alzheimer disease (AD) is one of most dominant challenges in our health system. In this work it was investigated to which degree the magnetic resonance technique of model-based magnetization transfer (mMT) (1,2) contributes to a differentiation of patients with AD, Mild Cognitive Impairment (MCI) and healthy persons of equal age.

Subjects and Methods: Model-based quantification in general is an approach in order to become independent of hardware technology. Compared to the MT ratio (MTR) the mMT technique enables a more precise description of MT phenomena. The sequences and post-processing steps are described in Kiefer et al. (2). We investigated de-novo AD (n = 18), MCI (n = 18) patients and CTRLs (n = 18). A region-of-interest analysis of the entorhinal cortex (EC), hippocampal head and body, insula, and temporal neocortex was performed. The classification of the regional mean mMT parameter values was performed using Fuzzy clustering.

Results: Cluster analysis achieved a concordance of 0.92 (50 of 54 subjects) between a combination of the calculated mMT parameters in the EC and the neuropsychological diagnosis. The sensitivity and specificity for the discrimination of AD from MCI reached 1 and 0.94, with a PPV of 0.95 and a NPV of 1.

Compared to mMT, the concordance for MTR was 0.83 (45 of 54 subjects) with a lower specificity of 0.5 and PPV of 0.67 to discriminate AD and MCI patients.
Discussion/Conclusion: MMT imaging allows an improved patient classification of early AD and MCI patients compared to MTR.
References:
1) Sled, J.G., Pike, G.B., 2001. Quantitative imaging of magnetization transfer exchange and relaxation properties in vivo using MRI. Magn. Reson. Med. 46 (5), 923–931.
2) Kiefer C, Brockhaus L, Cattapan-Ludewig K, Ballinari P, Burren Y, Schroth G, Wiest R: Multi parametric classification of Alzheimer's disease and mild cognitive impairment: The impact of quantitative magnetization transfer MR imaging NeuroImage 2009; 48: 657–667

657

A TGV-Rician based denoising model for DTI

A. Martin[1], J.A. Hernández-Tamames[1], E. Schiavi[2]
[1]*Electronical Technology, Universidad Rey Juan Carlos, Móstoles/SPAIN,*
[2]*Applied Mathematics, Universidad Rey Juan Carlos, Móstoles/SPAIN*

Purpose/Introduction: Tensorial diffusion imaging (DTI) is an emergent MR-technique which allows the analysis of white matter structures of the brain so providing early diagnostic of some degenerative diseases as Alzheimer or Parkinson. To reconstruct the DTI a set of Diffusion-Weighted-MR-Images (DWI) is obtained from the scanner. The obtained DWI data are magnitude low Signal-to-Noise-Ratio (SNR) MR Images severely affected by Rician noise. Our proposal is the numerical resolution and application of a new variational denosing model which takes into account the Rician distribution of the data (as in [1]) together with a regularizing Total-Generalized-Variation (TGV) operator originally proposed for MRI TGV-Gaussian denoising in [2]
This TGV-Rician denoising model leads to the following energy minimization problem: given a noisy MR-image $f \in L^\infty(\Omega)$, $\Omega \subset R^d$ and fixed parameters $\alpha 0$,$\alpha 1$ and σ the noise standard-deviation, recover the denoised image u solving:

$$\min_{u \in BGV^2_\alpha(\Omega), v \in BD(\Omega)} \alpha_1 \int_\Omega |\nabla u - v| + \alpha_0 \int_\Omega |\mathcal{E}(v)| + \int_\Omega \left[\frac{u^2}{2\sigma^2} - \log I_0\left(\frac{uf}{\sigma^2}\right) \right]$$

For the numerical resolution a first-order primal-dual method is applied following [3].

Subjects and Methods: A 15 directions DWI phantom described in [4] was used for model validation. The proposed algorithm was implemented in Matlab and for the DTI reconstruction and visualization the 3d Slicer tools were used (www.slicer.org).
Results: A DWI-phantom is perturbed with Rician noise and a parametric study of σ, α0 and α1 is performed to compare TGV-Rician and TGV-Gaussian in terms of the PSNR between phantom and denoised images. In Table-1 the best PSNR values obtained with both algorithms are shown:

Algorithm	σ=0.0025	σ=0.005	σ=0.0075	σ=0.01	σ=0.025
TGV - Rician	55.24dB	53.72dB	52.26dB	50.78dB	45.55dB
TGV - Gaussian	55.12dB	53.30dB	52.51dB	49.67dB	42.35dB

DWI-denoising also improves the quality of DTI reconstruction. In Table-2 the Fractional Anisotropy calculated from the noisy (FA_n) and the denoised DTI (FA_d) are compaired with the original DTI phantom (FA_p).

Noise	$\|\|FA\_n-FA\_p\|\|_2$	$\|\|FA\_d-FA\_p\|\|_2$
σ=0.005	51.9171	37.0675
σ=0.01	126.0061	48.9898

The denoising effect can be observed in figures 1-2 where the main eigenvector of the tensor is represented for the noisy-free-DTI, the noisy-DTI and the denoised-DTI over the FA images.

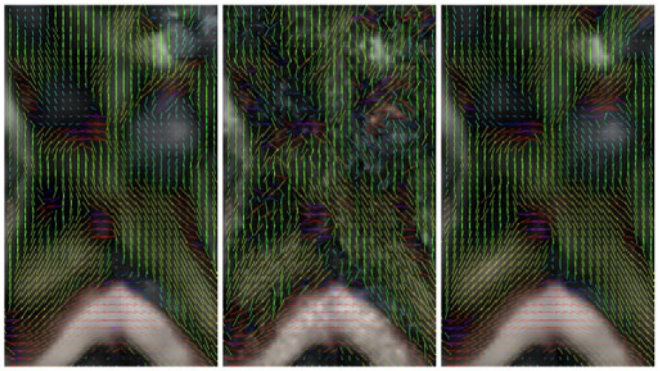

(a) DTI reconstructed from original phantom DWI (b) DTI reconstructed from noisy phantom DWI ($\sigma = 0.005$) (c) DTI reconstructed from TGV-Rician denoised DWI

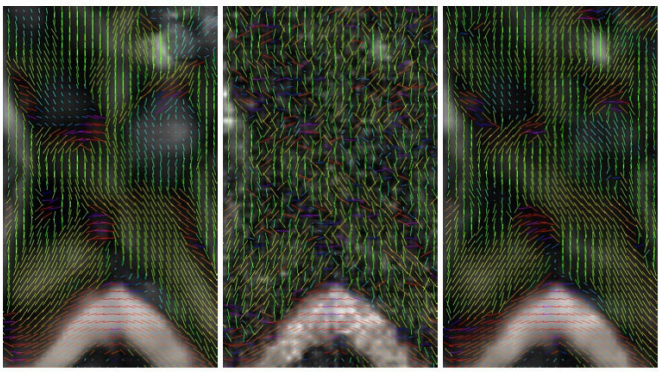

(a) DTI reconstructed from original phantom DWI (b) DTI reconstructed from noisy phantom DWI ($\sigma = 0.01$) (c) DTI reconstructed from TGV-Rician denoised DWI

Discussion/Conclusion: We showed a new model for DTI-denoising validated with phantom images. The next step is validation with real DTI where noise estimation will be crucial (see [5]). Preliminary results will be shown in the presentation.
References:
[1] Martín, A. 2011 IPCV'11 Proc. 959–963
[2] Knoll, F. 2011 Magn. Reson. Med. 65(2):480–491
[3] Chambolle, A. 2011 J. Math. Imaging Vision 40(1):20–145
[4] Tristán-Vega, A. 2009 LNCS 5761:951–958
[5] Coupe,P 2010 Med. Image Anal 14(4):483-93

658

A reference free approach for the comparative evaluation of eight segmentation methods for the estimation of the left ventricular ejection fraction in cardiac MRI.

A. Lalande[1], J. Lebenberg[2], I. Buvat[3], P. Clarysse[4], C. Casta[4], A. Cochet[1], C. Constantinidès[2], J. Cousty[5], A. De Cesare[2], S. Jehan-Besson[6], M. Lefort[2], L. Najman[5], E. Roullot[7], L. Sarry[8], C. Tilmant[9], M. Garreau[10], F. Frouin[2]
[1]*LE2I (UMR CNRS 6306), University of Burgundy, Dijon/FRANCE,*
[2]*Laboratoire d'Imagerie Fonctionnelle, Inserm/UPMC, Paris/FRANCE,*
[3]*IMNC (CNRS UMR 8165), Université de Paris Sud, Orsay/FRANCE,*
[4]*CREATIS (CNRS UMR 5220), Université de Lyon, Lyon/FRANCE,* [5]*LIGM-A3SI (UMR 8049), Université de Paris Est, Marne la Vallée/FRANCE,*
[6]*LIMOS (CNRS UMR 6158), LIMOS, Aubière/FRANCE,* [7]*PRIAM, ESME-Sudria, Ivry sur Seine/FRANCE,* [8]*ISIT (CNRS UMR 6284), Université d'Auvergne, Clermont-Ferrand/FRANCE,* [9]*Institut Pasteur (CNRS UMR 6602), Université Blaise Pascal, Clermont-Ferrand/FRANCE,* [10]*LTSI (INSERM UMR 1099), Université Rennes 1, Rennes/FRANCE*

Purpose/Introduction: Objective evaluation and comparison of segmentation algorithms for medical imaging is still a challenging issue. The most frequently used evaluation method consists in comparing the segmentation with a manual delineation. Since obtaining such manual segmentation can be tedious, we proposed a method based on the "extended Regression Without Truth" ap-

proach (eRWT)(1). This approach is applied to the comparative evaluation of 8 segmentation algorithms with different degrees of automation from the estimated left ventricular ejection fraction (LVEF).

Subjects and Methods: Series of short-axis cine MR images covering the left ventricle were obtained in 36 patients and 9 healthy volunteers (20 frames per cycle). For each series, five automated segmentation methods(2-6) with different degrees of automation were used, and manual contouring was also performed by three operators, providing 8 independent estimates of the LVEF (eLVEF). The principle of our non-supervised method consists in estimating the parameters of a linear model linking the measurements (eLVEF) and the true value (tLVEF). The distribution of the tLVEF is assumed to follow a Beta distribution (mu=4 and nu=5) :

$$\Pr(tLVEF) = \frac{tLVEF^{\mu-1} \times (1 - tLVEF)^{\upsilon-1}}{B(\mu,\upsilon)} \text{ with } B(\mu,\upsilon) = \int_0^1 x^{\mu-1}(1-x)^{\upsilon-1}dx$$

The relationship between the tLVEF and the eLVEF is given by :

$$eLVEF = a \times tLVEF + b + error$$

The determination of a, b and the standard deviation of the error makes it possible to compare the accuracy of the methods. Methods are ranked as a function of their accuracy, based on a figure of merit (Fm) :

$$Fm = (a-1)^2 \times \frac{\mu(\mu+1)}{(\mu+\upsilon)(\mu+\upsilon+1)} + 2(a-1) \times b\frac{\mu}{\mu+\upsilon} + b^2 + {\sigma_{error}}^2$$

Results: The obtained ranking suggests that the LVEF estimations provided by manual methods were the most accurate and the least variable.

Methods	Fm
Manual	0.002
Manual	0.004
Manual	0.004
Semi-automatic(2)	0.006
Semi-automatic(3)	0.009
Automatic(4)	0.010
Semi-automatic(5)	0.011
Semi-automatic(6)	0.012

Discussion/Conclusion: All automated methods considered in our study were less accurate than manual delineations. The main limitations are due to segmentation failures in some particular slices. Their combination to provide one optimized mutual contour is currently under study.

The eRWT approach proved to be relevant to compare different segmentation methods without the use of gold standard and without any prior concerning the automation degree of the method. Moreover, it can be used to evaluate the improvement of a method in progress.

References:

(1) Lebenberg J. et al, 2012, IEEE Trans Med Imaging, in press
(2) Constantinides C. et al, 2009, The Midas Journal
(3) Lalande A. et al, 2004, JCMR, 817-827
(4) Constantinides C. et al, 2012, IEEE EMBC, in press
(5) Schaerer J. et al, 2010, Med Image Anal, 738-749
(6) Cousty J. et al, 2010, Image Vision Comput, 1229-1243

EPOS™ Poster

Processing and quantification: spectroscopy

659

Intra-CardiomyoCellular Lipid (ICCL) Levels Change in Healthy Lean Subjects During the Day and Between Days as Observed by In-Vivo ^{1}H-MR Spectroscopy

R. Kreis[1], C. Stettler[2], J. Xu[3], C. Boesch[1], M. Ith[4]
[1]Depts of Clinical Research & Radiology, University Bern, Bern/SWITZERLAND, [2]Division of Endocrinology, Diabetes &, University Bern, Bern/SWITZERLAND, [3]-, Siemens Medical Solutions USA, New York/NY/UNITED STATES OF AMERICA, [4]Institute of Diagnostic Interventional and Pediatric Radiology, University Bern, Bern/SWITZERLAND

Purpose/Introduction: Myocardial steatosis has been hypothesized to represent an early manifestation of type-2 diabetes[1]. ^{1}H-MRS with double triggering offers an in-vivo assessment of cardiac lipids (Intra-CardiomyoCellular Lipids, ICCL), but its reproducibility is not well established. Our goal was to determine methodological and physiological reproducibility of ICCL levels as determined by navigator-based cardiac MRS and their potential diurnal variations[2].
Subjects and Methods: Five independent single-voxel MRS measurements were distributed over two days (n=9). Both days included morning (fasted) and afternoon (after breakfast and lunch) measurements. The afternoon measurement was repeated to define measurement reproducibility. Volunteer preparation included restricted physical activity for two days. A diary enabled repetition of diet and exercise. MRS conditions: 3T MR system (Siemens), PRESS-sequence, TE=35ms; TR≈5s depending on respiration, ROI in cardiac septum, respiratory (navigator on diaphragm) and cardiac double-triggering (end-systole in end-expiration), 64 scans with and 16 scans without water suppression, triggered shimming in breathhold. Spectra were evaluated with jMRUI (AMARES). Ratios of ICCL and trimethyl-ammonium compounds (TMA) vs. the CH_3-signal of creatine are given.
Results: The median CV of water was 4.7%. Four of 45 measurements were excluded, with the criterion of CV_{water}>20%. This yielded complete datasets from 8 subjects for methodological reproducibility and six datasets for day-to-day physiological reproducibility (morning and afternoon) and for morning-evening diurnal changes. Fig.1 shows a complete set of cardiac spectra for one volunteer. Average CVs from immediate repetition were 8.7±3.9% (ICCL/Cr) and 7.7±7.8% (TMA/Cr). Analysis of intra-individual "long term" reproducibility showed much larger variation for ICCL/Cr (34±19%/30±26% for morning/evening), but similar values for TMA/Cr (4.1±3.3%/8.2±4.8%). Comparison of morning vs. evening revealed a strongly significant diurnal variation with a decrease of 37±19% for ICCL/Cr (p<<0.001), but no change for TMA/Cr (p=0.95). This is illustrated in Fig.2 with individual data for ICCL/Cr.

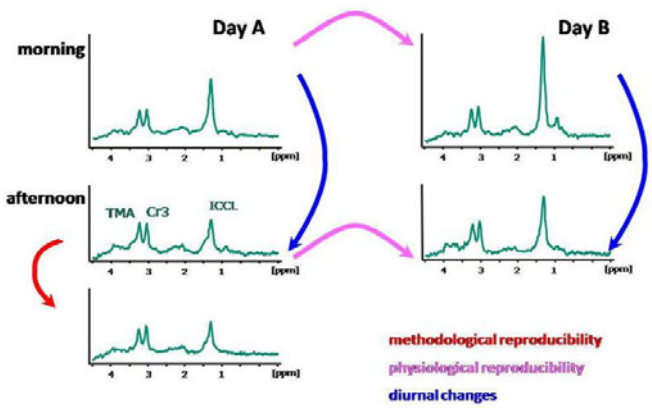

Fig. 1 Complete set of spectra from a single volunteer illustrating methodological reproducibility (2 sessions in afternoon A with immediate repetition), "long-term" reproducibility (morning A vs. morning B; afternoon A vs. afternoon B), and diurnal changes (morning A vs. afternoon A; morning B vs. afternoon B)

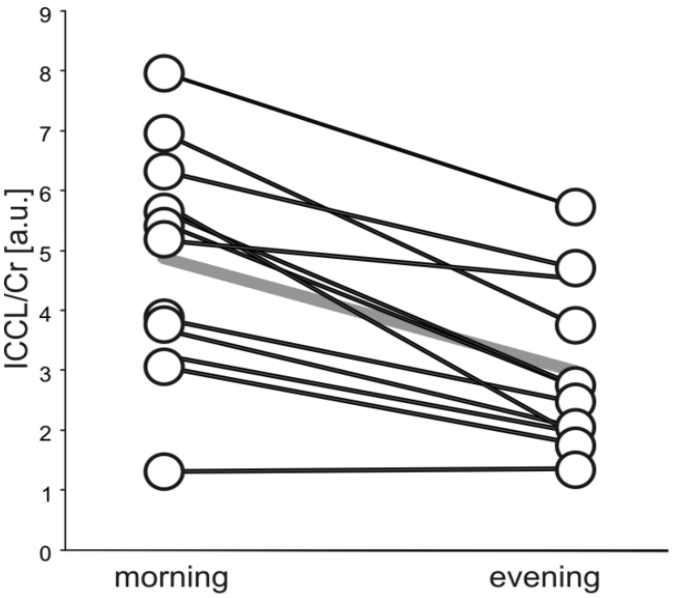

Fig. 2. Individual diurnal changes in ICCL/Cr levels

Discussion/Conclusion: An excellent methodological reproducibility for spectra obtained upon immediate repetition was found for the present implementation of cardiac MRS. In contrast, ICCL/Cr showed a higher variation for repetitions after one to two weeks in spite of identical two day preparation periods. Furthermore, this study revealed a significant diurnal difference in ICCL levels between morning (fasted) and afternoon (fed), indicating that the cardiac fuel depot does not remain constant over the day. These findings place severe limits on the study designs when investigating cardiac lipid metabolism.
References:
1. van de Weijer T et al. Cardiovasc Res. 92:10.
2. Tsai JY et al. J Biol Chem 285:2918.

660

Production of acetylcarnitine and utilization of IMCL at different exercise intensities - A pilot-study applying SVS and MRSI

A. Boss[1], R. Kreis[1], T. Züger[2], J. Bucher[2], C. Stettler[3], C. Boesch[1], P. Vermathen[1]
[1]Depts of Clinical Research & Radiology, University of Bern, Bern/SWITZERLAND, [2]Division of Endocrinology, Diabetes and Clinical Nutrition, University Hospital and University of Bern, Bern/SWITZERLAND, [3]Division of Endocrinology, Diabetes &, University Bern, Bern/SWITZERLAND

Purpose/Introduction: Exercise-induced utilization of intramyocellular lipids (IMCL) and the buildup of acetylcarnitine (AcCar), a buffer for acetyl-CoA, can be monitored using (1)H-MR Spectroscopy (MRS)[1]. With short exercise, AcCar production is increased with higher exercise intensity[2]. It is however not known if this also applies for prolonged exercise.
To our knowledge, the effect of exercise intensity on muscle-specific IMCL-depletion using MR spectroscopic imaging (MRSI)[3] has not been performed before.
Purpose: to assess the effect of low vs. moderate intensity exercise of prolonged duration on the production and recovery of AcCar using single voxel spectroscopy (SVS), and to study regional differences in AcCar-production and utilization of IMCL by MRSI.
Subjects and Methods: Subjects: 3 young, physically active males
Design:
• VO2max test: ramp protocol, determination of power/VO2
• MR/exercise: subjects were tested after an overnight fast. Exercise: 80min ergometer cycling, 30 or 50%VO2max. MRS: Before and after exercise, clinical 3T-system (Siemens), extremity coil.

SVS: PRESS (TR=3000ms, TE=110ms), 32 averages, VOI: 11x16x22mm³, vastus intermedius.
MRSI: PRESS volume pre-selection (TR=1230ms, TE=200ms), matrix: 32x32, FOV: 140x160x15mm³ (regional saturation bands for suppression of subcutaneous fat).
Post-processing: Details were described previously[3]. IMCL and AcCar (acetyl-group at 2.13ppm) peak areas were scaled by creatine as internal reference.
Results: VO2max was 61 in subjects 1 and 2, and 60ml/kg/min in subject 3.
Figure1 displays AcCar-areas from the SVS-experiment. AcCar was observable in each test 25min after exercise. Comparing intensities, AcCar-production varied between subjects. At 60min, AcCar returned to zero in 2 subjects at 30%, and in 1 at 50%VO2max.
Table1 displays differences in AcCar-production between muscles.
IMCL utilization was similar for both intensities. ΔIMCL at 30%VO_2max was significantly correlated with ΔIMCL at 50%VO_2max for the individual muscles (R^2=0.70, p<0.001, **Figure2**). Pre-exercise IMCL correlated significantly with ΔIMCL in all subjects.

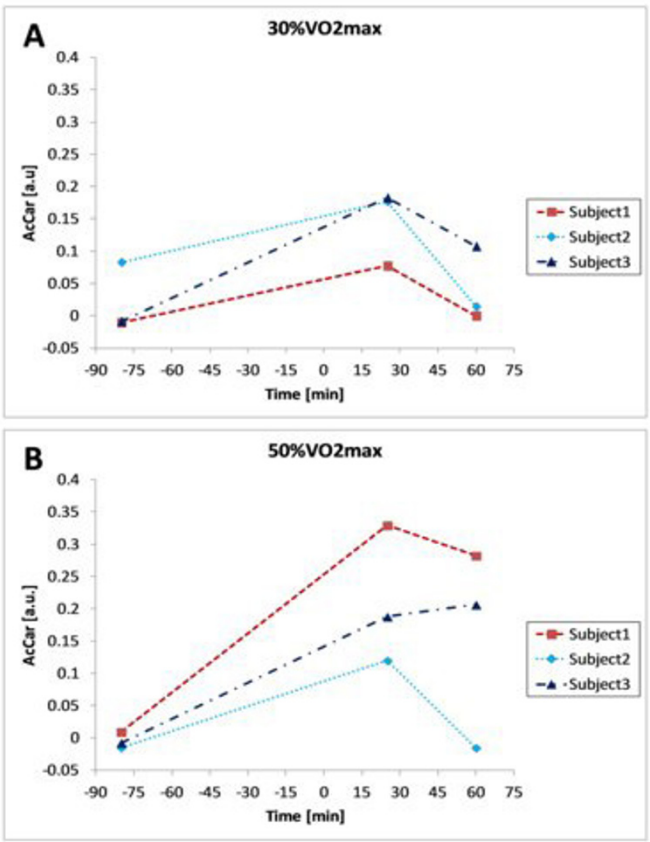

Figure1: AcCar from SVS-experiment in vastus intermedius. Spectra were obtained before, ~25, and ~60 min after exercise; the 80-min exercise ends at time 0. **A)** 30%VO_2max, corresponding to an average power output of 95W; **B)** 50%VO_2max, corresponding to an average power output of 170W.

ΔAcCar

Muscle	Position	Median
Adductor magnus	p	0.50
Caput breve	p	0.52
Caput longum	p	0.96
Semidentinosus	p	0.91
Semimembranosus	p	0.47
Vastus intermedius 1	a	1.07
Vastus intermedius 2	a	1.12
Vastus lateralis 1	a	0.92
Vastus lateralis 2	a	1.06
Vastus medialis 1	a	1.04
Vastus medialis 2	a	1.08

Table1: Difference between muscles in AcCar-production. For the muscle-wise analysis, the MRSI-data of both intensities were pooled, thereby obtaining up to 6 measurements for each muscle. To account for inter-individual differences in AcCar production, normalization was performed by dividing each muscle's increase by the median increase within this subject. p: posterior; a: anterior

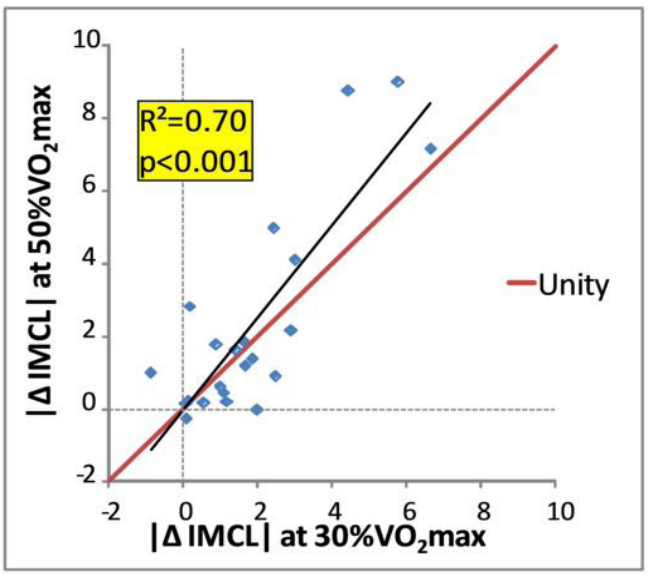

Figure2: IMCL from the MRSI-experiment. Spectra were obtained before and ~45min after exercise. The utilization of IMCL (=|Δ IMCL|) is shown. |Δ IMCL| at 30% is significantly correlated with |Δ IMCL| at 50% VO2max over all muscles and subjects.

Discussion/Conclusion: Despite the small number of subjects it can be concluded: **1)** Contrary to a 4min-exercise[2], prolonged exercise of low intensity is sufficient to increase AcCar. **2)** More AcCar is produced in anterior than in posterior muscles, possibly due to increased activation of anterior muscles during cycling. The remarkable variation between subjects in production and rate of decline of AcCar cannot be explained by differences in fitness. **3)** Muscle specific IMCL utilization was not affected by exercise intensity in the low to moderate regime.

References:

1. Boesch, JMRI;25:321.
2. Stephens, JPhysiol;581:431.
3. Vermathen, MRM;2012.doi:10.1002/mrm.24168.

661

Post-exercise intramyocellular acetylcarnitine levels in endurance trained and sedentary subjects measured with ^{1}H-MRS

L. Lindeboom[1], B.M.W. Brouwers[1], T. Van De Weijer[1], C.I.H.C. Nabuurs[2], M.E. Kooi[3], M.K.C. Hesselink[2], P. Schrauwen[1], J. Wildberger[3], V.B. Schrauwen-Hinderling[3]

[1]Department of Human Biology, Maastricht University Medical Center (MUMC+), Maastricht/NETHERLANDS, [2]Department of Human Movement Sciences, Maastricht University Medical Center (MUMC+), Maastricht/NETHERLANDS, [3]Department of Radiology, Maastricht University Medical Center (MUMC+), Maastricht/NETHERLANDS

Purpose/Introduction: When the rate of acetyl-CoA formation exceeds utilization by the tricarboxyclic acid cycle, carnitine can function as an acetyl group acceptor, to form acetylcarnitine[1]. We have previously shown that using long TE enhances visibility of the acetylcarnitine peak in ^{1}H-MRS in the vastus lateralis muscle, which allows to dynamically study this metabolite *in vivo*[2]. Rapid normalization of acetylcarnitine after exercise may be indicative of good tuning of substrate supply and use, as we expect to find in endurance trained subjects.

Subjects and Methods: Four endurance trained and four sedentary subjects (subject characteristics in table 1) cycled for 30 minutes on 50% of their predetermined W_{max} and acetylcarnitine concentrations were determined before and after exercise. The left leg of the subjects was positioned parallel to the main field in a whole body MRI-scanner (Achieva, 3T, Philips Healtcare). A two-element flexible surface coil was placed over the vastus lateralis. PRESS was used to acquire spectra from a voxel (40x20x60 mm) in the vastus lateralis (TR 6000 ms, bandwidth 2 kHz and 2048 points). The total creatine (t-Cr) peak was used as internal reference. To correct for T_2 relaxation of both the t-Cr and acetylcarnitine peaks in each subject individually, a series of 6 spectra with different TE (300,325,350,400,450 and 500 ms) were acquired. Spectra with a fixed TE of 350 ms were measured before and after each spectrum of the series to determine changes in concentration and to use these to correct T_2 of acetylcarnitine. Duration of the protocol was 35 minutes and post-exercise acquistion of spectra started approximately 15 minutes after cycling.

Results: Exercise-induced elevations of acetylcarnitine levels were similar in both groups ($\Delta_{pre\text{-}post}$ 3.1±1.9 mmol/kg wet weight(ww)). However, post-exercise *kinetics* were significantly different (group, time and group*time effect, P<0.05). In sedentary subjects the concentration continued to increase during recovery towards a plateau at 40 minutes (8.5±0.3 mmol/kgww). In contrast, the acetylcarnitine concentration started to decrease from 20 minutes after exercise in the endurance trained subjects (towards 4.4±1.0 mmol.kgww at 40 minutes).Pre- and post-exercise acetylcarnitne kinetics are shown in figure 1.

Discussion/Conclusion: These results indicate that determination of post-exercise acetylcarnitine kinetics can reveal differences in mitochondrial imbalance, as seen in endurance trained versus sedentary subjects. This opens a window towards investigation of acetylcarnitine in relation to metabolic flexibility and insulin resistance.

Table 1. Subject characteristics

Group	Age [years]	BMI [kg/m^2]	50 % W_{max} [W]	$VO_{2\text{-}max}$ [ml/min/kg]
Endurance trained (2f, 2m)	29±4	21±1	155±12*	56±2*
Sedentary (3f, 1m)	30±4	20±0	90±7	39±1

Data presented as mean ± SEM. *P<0.05 versus sedentary

Figure 1. Dynamic pre- and post-exercise acetylcarnitine concentrations

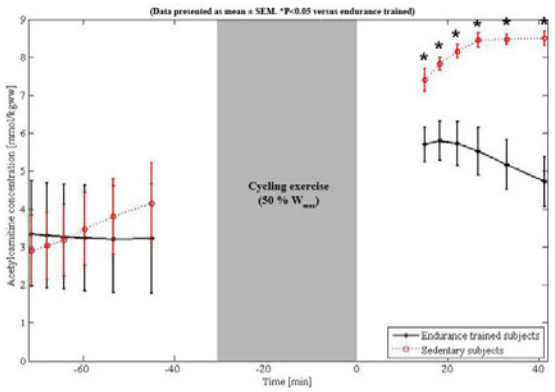

References:

1.Stephens et al. 2007.J Physiol 581.2:431-444
2.Lindeboom et al. 2011.Proceedings annual meeting ISMRM (Montreal), abstract 1161

662

Fraction of unsaturated fatty acids in visceral adipose tissue (VAT) shows strong negative correlation to total VAT volume - a ^{1}H spectroscopic study in male subjects

J. Machann[1], E. Schleicher[2], H. Häring[2], C. Claussen[3], A. Fritsche[2], F. Schick[4]

[1]Section on Experimental Radiology, Institute for Diabetes Research and Metabolic Diseases (IDM) - Metabolic Imaging - of the Helmholtz Center Munich at the University of Tübingen, Tübingen/GERMANY, [2]Department of Endocrinology and Diabetology, Angiology, Nephrology and Clinical Chemistry, University Hospital Tübingen, Tübingen/GERMANY, [3]Department of Diagnostic and Interventional Radiology, University Hospital Tübingen, Tübingen/GERMANY, [4]Section on Experimental Radiology, University Hospital Tübingen, Tübingen/GERMANY

Purpose/Introduction: Visceral adipose tissue (VAT) is thought to play an important role in the pathogenesis of obesity and insulin resistance [1]. However – little is known about the composition of VAT regarding amount of monounsaturated (MUFA) and polyunsaturated fatty acids (PUFA). Volume selective MRS was performed in addition to MRI for quantification of VAT. Main interest was set on methyl (CH_3) signal at 0.9ppm being the only peak with a defined number of protons/triglyceride (n=9), vinyl group (H-C=C-H) at 5.3ppm including protons from MUFA+PUFA, and PUFA at 2.75ppm.

Subjects and Methods: Fourteen overweight/obese male subjects (mean age 46 years, BMI between 28 and 39 kg/m^2) participated in this prospective study and underwent MRS of VAT on a 3 T whole-body unit (Magnetom Trio, Siemens Healthcare). Spectra were recorded by a single-voxel STEAM technique with following measurement parameters: TE/TM/TR 20/10/4000ms, VOI between 20x25x20 and 30x30x20 mm^3 depending on the extension of VAT, 48-80 Acq. depending on size of VOI, BW 1200 Hz. Post processing was performed by jMRUI (AMARES). Volume of VAT was quantified in a separate session on a 1.5 T imager (Magnetom Sonata, Siemens Healthcare) a few days

prior to the MRS-session by T1-weighted fast spin-echo imaging [2]. Relative amount of VAT was calculated as percentage of body weight (%VAT). Ratios of MUFA+PUFA to CH_3 and PUFA to CH_3 were calculated.
Results: All spectra recorded from VAT were of high quality, enabling reliable quantification of the mentioned resonances (see Fig. 1 c and d). There was no significant detectable contamination by water. %VAT and (MUFA+PUFA)/CH_3 were in a broad range (4.4-8.6% and 0.45-0.64). Interestingly, there is a strong negative correlation between these two parameters (r=-0.86). PUFA/CH_3 is clearly less correlated to %VAT (r=-0.39). Figure 1 shows axial T1-weighted images of two volunteers with different %VAT (a,b) and the corresponding spectra (c,d) indicating strong differences in the MUFA+PUFA-signal at 5.3 ppm. There is only a relatively weak negative correlation to BMI (r=-0.38).

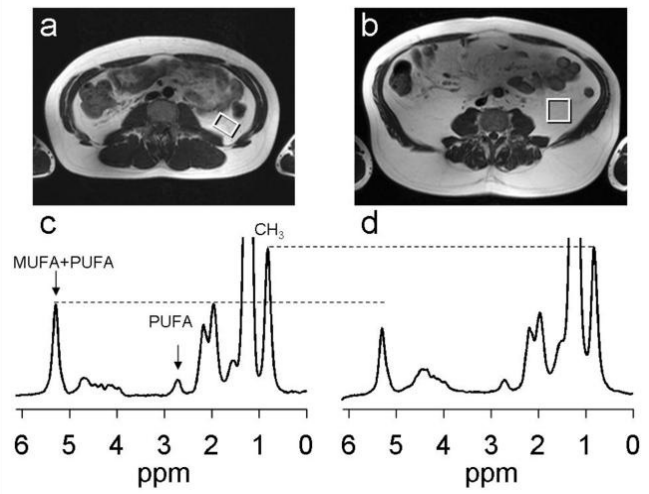

Figure 1: Axial slices indicating the position of VOI for spectroscopic examination of VAT in a subject with low amount of VAT (a) and a subject with high amount of VAT (b). Corresponding spectra indicate higher unsaturation of lipids in subject with low VAT (c compared to d)

Discussion/Conclusion: The composition of VAT shows strong interindividual variations. The higher the total amount of VAT, the less unsaturated lipids are present. This is a preliminary result in mainly obese male subjects and it remains to be determined whether this correlation holds for lean subjects or if there are changes in composition during weight loss or different forms of diet.
References:
[1] Machann J et al. Radiology 2010;257:353-363
[2] Machann J et al. JMRI 2005;21:455-462

663

Variations in lipid composition at different locations of the body – regional and interindividual variabilities assessed by ^{1}H-MRS

J. Machann[1], A. Fritsche[2], C. Schabel[3], H. Häring[2], C. Claussen[4], E. Schleicher[2], F. Schick[3]
[1]Section on Experimental Radiology, Institute for Diabetes Research and Metabolic Diseases (IDM) - Metabolic Imaging - of the Helmholtz Center Munich at the University of Tübingen, Tübingen/GERMANY, [2]Department of Endocrinology and Diabetology, Angiology, Nephrology and Clinical Chemistry, University Hospital Tübingen, Tübingen/GERMANY, [3]Section on Experimental Radiology, Department of Diagnostic and Interventional Radiology, University Hospital Tübingen, Tübingen/GERMANY, [4]Department of Diagnostic and Interventional Radiology, University Hospital Tübingen, Tübingen/GERMANY

Purpose/Introduction: There is an increasing interest not only in quantification of different adipose tissue compartments but also in the analysis of its composition. Mainly the amount of mono-(MUFA) and poly-unsaturated fatty acids (PUFA) promises new non-invasive insight in the fat metabolism of humans. This study was performed to detect probable inter- and intraindividual differences in fatty acid composition in various adipose tissue compartments.

Subjects and Methods: Fourteen healthy male volunteers participated in this prospective study and underwent ^{1}H-MRS on a 3 T whole-body imager (Magnetom Trio, Siemens Healthcare). Following locations were chosen: subcutaneous adipose tissue (SCAT) in the neck ($SCAT_{neck}$) and in the calf ($SCAT_{calf}$), superficial (SSCAT) and deep (DSCAT) in the abdomen, bone marrow in the tibia (BM) and visceral adipose tissue (VAT). Spectra were recorded applying a STEAM technique with following parameters: TE/TM/TR 20/10/4000ms, VOI between 10x12x20 and 30x30x20 mm³ depending on the location, 32-80 Acq. depending on size of VOI, BW 1200 Hz. Post processing was performed by jMRUI (AMARES) and ratios of MUFA+PUFA (vinyl group at 5.3ppm) to CH_3 and PUFA (at 2.75ppm) to MUFA+PUFA were calculated.
Results: Fatty acids showed significantly different mean ratios of MUFA+PUFA/CH_3 with the lowest for VAT (0.517) and the highest for $SCAT_{calf}$ (0.670), which is furthermore characterized by the highest coefficient of variance (CV=0.121). Figure 1 exemplarily shows two extreme spectra from BM (Fig.1c, ratio 0.45) and $SCAT_{calf}$ (Fig.1d, ratio 0.84) with VOI indicated in the T1-weighted images. PUFA/MUFA+PUFA is highest in VAT (0.203) and lowest in $SCAT_{calf}$ (0.157). This indicates a higher amount of poly-unsaturated fatty acids in VAT which is also significantly lower in DSCAT but not in SSCAT.

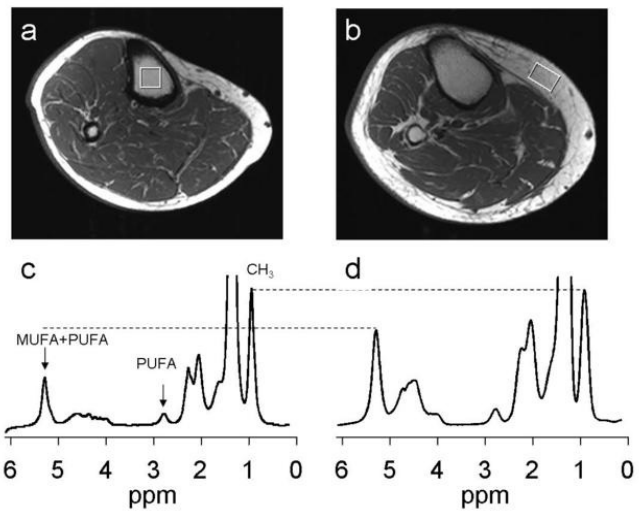

Figure 1: T1-weighted images of the calf with indicated VOI for MRS in bone marrow (a) and subcutaneous adipose tissue (b). Corresponding spectra in (c) and (d) indicate clear differences in the composition of fatty acids.

Discussion/Conclusion: Determination of composition of fatty acids in different adipose tissue compartments of the body reveals significant intra- and interindividual differences regarding the amount of mono- and polyunsaturated fatty acids. There is even a large variability in different locations of subcutaneous adipose tissue. Interestingly, yellow bone marrow has the highest variation. VAT seems to be of special interest due to the highest amount of PUFA. There are only week correlations to BMI and age. The study was limited to males in order to rule out gender related differences – further studies are needed to assess differences for different anthropometric and metabolic status.

664

Non-linear age-related metabolite changes obsereved with ^{1}H MRS

G. Ende[1], N. Tunc-Skarka[1], M. Sack[1], A. Reitz[2], E. Aufhaus[1], C. Schmahl[2], C. Diener[1], T. Schulze[1], W. Weber-Fahr[1]
[1]Neuroimaging, Central Institute of Mental Health, Mannheim/GERMANY, [2]Psychosomatic Medicine, Central Institute of Mental Health, Mannheim/GERMANY

Purpose/Introduction: We aimed to investigate the metabolite changes associated with aging in a large group of healthy subjects detected with single voxel 1H MRS in two brain regions: the anterior cingulate cortex (ACC) and a frontal white matter location (fWM).

Subjects and Methods: In vivo single voxel 1H MR spectra were acquired at a 3.0 T MR scanner (Siemens Magnetom TIM Trio). All MRS voxel placement was planned on a high resolution anatomical data and spectra were brain-matter-corrected. The relatively large ACC voxel (40x30x20mm^3) was chosen for GABA editing (results not shown, TE = 68 ms, TR = 3000 ms) and was acquired with a thirty-two channel head coil from75 (51 female) healthy controls aged 33 ± 10ys (20-52 ys).
The fWM location (1x1x4 cm3, Point-Resolved Spectroscopy (PRESS) sequence with TE = 30 ms, TR = 3000 ms) was investigated in 80 (46 female, 34 male) subjects, aged 48 ± 17 years (21- 82 ys).

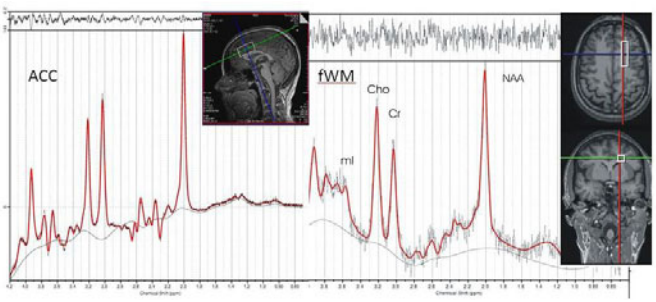

Results: In both locations some of the previously reported age-related metabolite changes (1,2) could be observed.
In the ACC voxel we found a positive correlation for total choline (tCh) and tNAA and age. Whereas for the fWM location we observed positive linear correlations of total Creatine (tCr) and myo-inositol (mI) and a negative correlation was observed for total N-acetylaspartate (tNAA).
Furthermore, for some metabolites non-linear age-dependencies were observed: in fWM tCh increased up to the age of about 51 (maximum in a quadratic fit to the data) whereafter it seems to decrease with increasing age. This observation in fWM fits well with the observation that tCh is on a linear rise up to the age of 52 in the ACC voxel (no older subjects included). In contrast to the fWM we observe a U-shaped age-dependency for tCr and mI in the ACC with turning points at around 30ys of age.

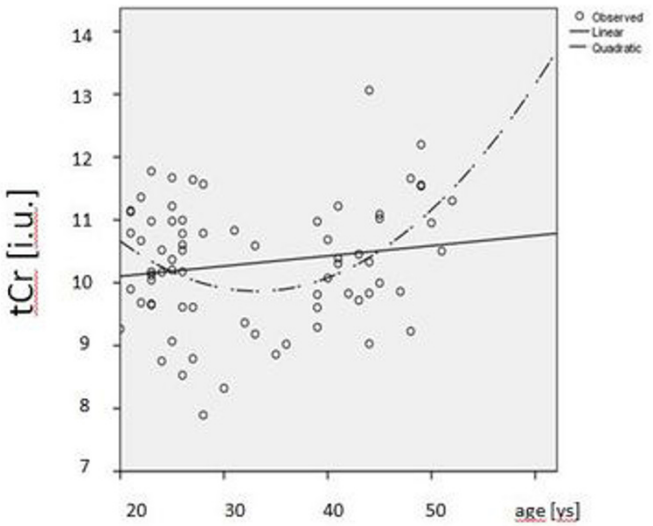

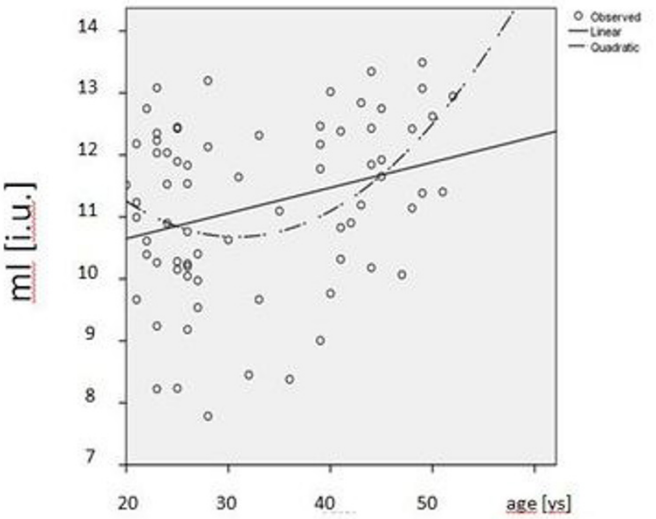

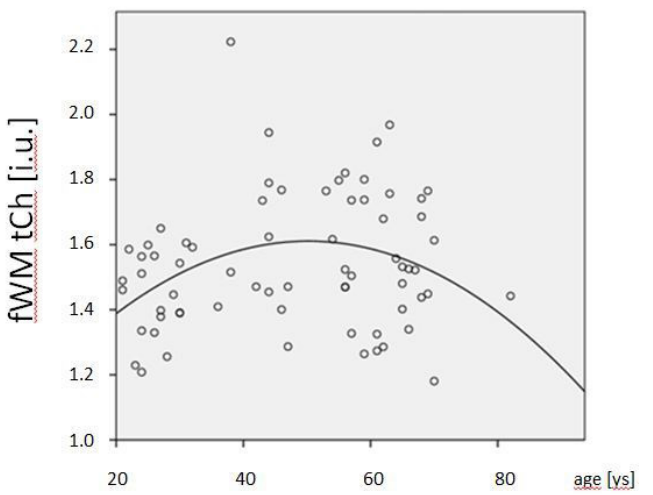

Discussion/Conclusion: We conclude that there are non-linear metabolite developments in healthy subjects younger than 30 and older subjects beyond 50 years. These observations might be region specific. Our data hint that the

declining tCr and mI signals within the third life decade are specific for the ACC since we did not observe a similar trend in the fWM. The decline of tCh observed in fWM beyond the age of 50 could not be investigated in the ACC since we did not include sibjects older than 52.

References:

Maudsley et al. MRM 2009 61:548-59.
Gruber et al. Eur J Radiol. 2008 68:320-7.

665

Quantitative identification of prostate cancer metabolomic markers using High Resolution Magic Angle Spinning 1H Magnetic Resonance Spectroscopy and Immunohistochemistry

F. Loebel, L.L. Cheng, C. Wu, G. Mutter
Radiopathology, Massachusetts General Hospital, Harvard Medical School, Charlestown/UNITED STATES OF AMERICA

Purpose/Introduction: Since the implementation of prostate specific antigen (PSA) screening, Prostate cancer (PCa) has become the most frequently diagnosed malignant disease in adult males in the USA and the second leading cause of cancer deaths in men. [1] Radical treatment procedures, such as prostatectomies, often result in impotence and/or incontinence of urine. Due to the lack of diagnostic tools that are able to differentiate highly malignant and aggressive from indolent PCas, overtreatment has become very common. [2] New diagnostical methods to determine biological status, malignant potential and aggressiveness of PCa are urgently needed.
High Resolution Magic Angle Spinning ^{1}H Magnetic Resonance Spectroscopy (HRMAS-^{1}HMRS) [3] is a novel method providing PCa metabolomic profiles while preserving tissue architecture for subsequent histopathological analysis. [4] In contrast to conventional histopathology, immunohistochemistry has the potential to provide objective, more accurate and quantitative knowledge of tissue pathology. This study is the first to use immunohistochemistry methods to identify and quantify PCa metabolomic markers quantified by HRMAS-^{1}HMRS. The aim of our work was to quantitatively identify PCa metabolomic markers with the assistance of immunohistochemistry.
Subjects and Methods: Prostate tissue samples of 50 patients with biopsy-proven PCa were subjected to HRMAS-^{1}HMRS on a 14.1 T spectrometer (Bruker Biospin). Subsequent immunohistochemistry was carried out using immunomarkers to identify cancerous (alpha-methylacyl.CoA-racemase P504S) and benign glands (high molecular weight cytokeratin CK903 and p63). Spectroscopy results and immunohistochemistry were correlated to identify cancer metabolomics markers using the commercial software JMP. Patient outcomes four years after prostatectomy were collected and included in the correlation.
Results: We identified statistically significant correlations of quantitative immunohistochemistry results with HRMAS ^{1}HMRS outcomes for several metabolic regions such as phosphocholine (3.22 ppm, p=0.017), glutamate (2.34ppm, p=0.0351) and lipids (0.9ppm, p=0.0469).
Discussion/Conclusion: PCa metabolomic markers established with the assistance of immunohistochemistry have the potential to sensitively, objectively and quantitatively determine malignancy, aggressiveness and biological status of cancer. The in-vivo application of these markers could serve as highly sensitive, non-invasive, observer-independant diagnostical tool, avoiding overtreatment and reducing complication rates in PCa patients.

References:

[1] Siegel, R., Naishadham, D., Jemal, A., 2012, CA Cancer J Clin 62(1):10-29.
[2] Ransohoff, DF., McNaughton Collins, M., Fowler, FJ., 2002, Am J Med., 113(8):663-7.
[3] Cheng, LL., Lean, CL, Bogdanova, A., Wright, SC Jr., Ackerman, JL, Brady, TJ., Garrido, L., 1996, Magn Reson Med., 36(5):653-8.
[4] Cheng, LL., Anthony, DC., Comite, AR., Black, PM., Tzika, AA., Gonzalez, RG., 2000, Neuro Oncol., 2(2):87-95.

666

Quantification of Phoshorus MR Spectroscopic Imaging of Human Brain Using Time Domain Fitting versus Frequency Domain Analysis at 3T

B. Bulut[1], N.C. Askin[1], J.C. Crane[2], **E. Ozturk-Isik**[1]
[1]Biomedical Engineering, Yeditepe University, Istanbul/TURKEY, [2]Department of Radiology and Biomedical Imaging, University of California at San Francisco, San Francisco/CA/UNITED STATES OF AMERICA

Purpose/Introduction: Phosphorus magnetic resonance spectroscopic imaging (31P MRSI) provides information regarding the energetic status, pH, magnesium concentration, and membrane synthesis and degradation of brain tissue in vivo. However, phosphorus is 15 times less MR sensitive than proton, and low signal to noise ratio (SNR) makes 31P MRSI quantification quite challenging. In this study, time domain fitting and frequency domain analysis were compared for accurate quantification of 31P MRSI data of human brain at 3T.
Subjects and Methods: Eight healthy volunteers (mean age=34.7±11.4) were scanned on a 3T MR scanner (Philips Medical Systems) using a surface 31P coil. 31P spectra were acquired with image selected in vivo spectroscopy (ISIS) [1] (TR=4500ms, 256 averages, 3000Hz, 1024 points, 27-36cc voxel size). The spectra were first processed in jMRUI with phase correction, apodization with a 10 Hz Lorentzian filter and baseline removal. AMARES [2] within jMRUI was used for time domain fitting. The amplitude, damping, and frequency factors were calculated for each peak with AMARES. SIVIC program [3] was used for frequency domain analysis. The spectra were converted into a SIVIC readable format in MATLAB. After Fourier transform, the area under each peak were estimated in frequency domain in SIVIC. The area under each peak for SIVIC or amplitude for AMARES was normalized with that of PCr. A Bland Altman statistical test, which plots the difference against the mean of two observations, was used to test the agreement of SIVIC and AMARES methods.
Results: Figure 1 shows an example 31P spectrum quantification of a volunteer with AMARES. Table 1 shows mean peak amplitudes and areas relative to PCr of all volunteers estimated by AMARES and SIVIC, respectively, and the results of Bland Altman statistical test. There were no outliers below or above two standard deviations of the mean difference for all peak ratios except GPE/PCr and PE/PCr for two different volunteers. Figure 2 shows the Bland Altman test results for α-ATP/PCr and GPE/PCr.

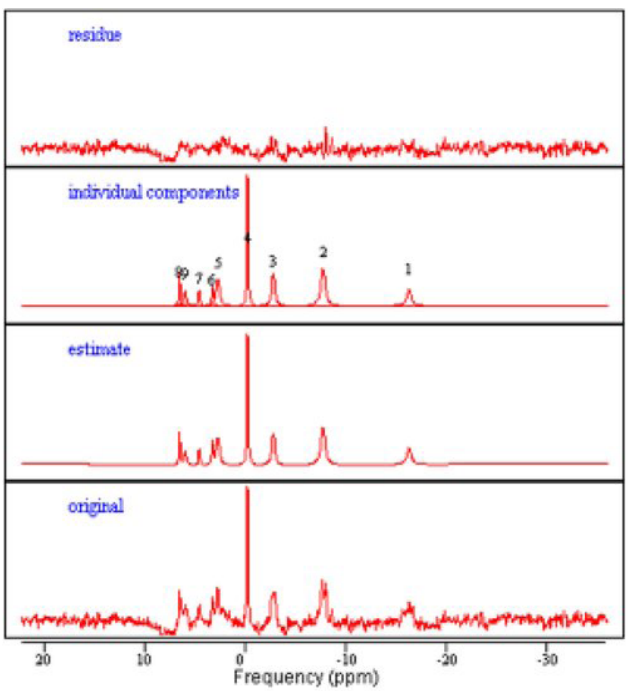

Figure 1. The original, estimated and residual signals and the individual peak estimates of a 31P MR spectrum of a volunteer using AMARES.

Table 1. Mean peak amplitudes and areas of phosphorus containing metabolites in human brain relative to PCr estimated by AMARES and SIVIC, the number of volunteers contributing to each estimate, and the results of the Bland Altman statistical test.

/PCr	# volunteers	mean(amplitude) (AMARES)	mean(area) (SIVIC)	Bland Altman statistic	# outliers	mean(diff)	std(diff)
PCr	8	1.0	1.0	1	0	0	0
γ-ATP	8	0.401	0.465	1	0	0.131	0.112
α-ATP	8	0.782	0.644	1	0	0.169	0.140
β-ATP	4	0.543	0.348	1	0	0.285	0.233
GPC	6	0.280	0.212	1	0	0.108	0.081
GPE	7	0.424	0.376	0	1	0.231	0.270
Pi	4	0.360	0.213	1	0	0.262	0.376
PC	5	0.204	0.260	1	0	0.068	0.065
PE	7	0.597	0.621	0	1	0.127	0.099

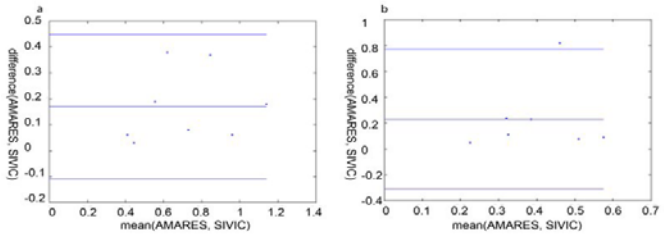

Figure 2. The Bland Altman test results for □-ATP/PCr (a) and GPE/PCr (b). The lines correspond to mean and (+/-) two standard deviations of the difference between AMARES and SIVIC results.

Discussion/Conclusion: Both SIVIC and AMARES provided an accurate quantification of phosphorus metabolites in human brain at 3T. The peak ratio estimates of AMARES and SIVIC were very similar according to the Bland Altman test results. AMARES was observed to provide better peak estimates for more noisy spectra.

References:

This study was supported by Marie Curie IRG grant FP7-PEOPLE-RG-2009 256528. [1]Ordidge, P et al. J. Magn. Reson.1986,66:283-4. [2] Vanhamme, L et al. J. Magn. Reson.1997, 129:35-4. [3] Crane, JC et al. Proc. Intl. Soc. Mag. Reson. Med. 18(2010), 3354.

667

Optimisation of the CMRS quantitation model

M.C. Sohlin[1], S. Holmquist[2], Å. Carlsson[1], E. Forssell-Aronsson[1], M. Ljungberg[1]

[1]Sahlgrenska University Hospital, Department of Medical physics and Biomedical Engeneering, Göteborg/SWEDEN, [2]Department of Radiation Physics, University of Gothenburg, Göteborg/SWEDEN

Purpose/Introduction: Localized cardiac MR-spectroscopy (CMRS) is the only method that facilitates non-invasive localization and quantification of triglycerides within cardiomyocytes (1) and could therefore be an important tool in the search for the unfamiliar link between obesity, cardiovascular disease and diabetic cardiovascular disease. To be able to quantify MRS signals in an efficient and user-independent way, a prior knowledge model is required, but little work have been done to optimise this model. In this work, various prior-knowledge models are evaluated in order to enhance the quantitation process of cardiac ^{1}H-MRS signals.

Subjects and Methods: ^{1}H-MRS of human myocardium was performed in one healthy volunteer on two occasions using a 1.5T whole body MRI-system equipped with an MRS research package (Philips Medical Systems, The Netherlands), and Philips 5-channel cardiac coil for signal reception. On the first occasion the MRS acquisition was repeated six times within one examination. On the second occasion, the examination was again repeated six times, now as separate examinations. PRESS (TE/TR=35/3000ms) and CHESS was used for volume selection and water suppression respectively. 128 water suppressed dynamics and eight non-water suppressed dynamics (TR=6000ms) were acquired. The spectroscopy scans were cardiac triggered to end systole and respiratory triggered at end expiration using a pencil-beam navigator (3). The VOI (4.5cm^3) was planned within the ventricular septum. The spectra (Fig. 1) were fitted with the AMARES algorithm of the jMRUI-package (4) using four prior knowledge models with different choices of lineshapes (Table 1), and subsequently evaluated by comparison of their residual sum of squares (RSS).

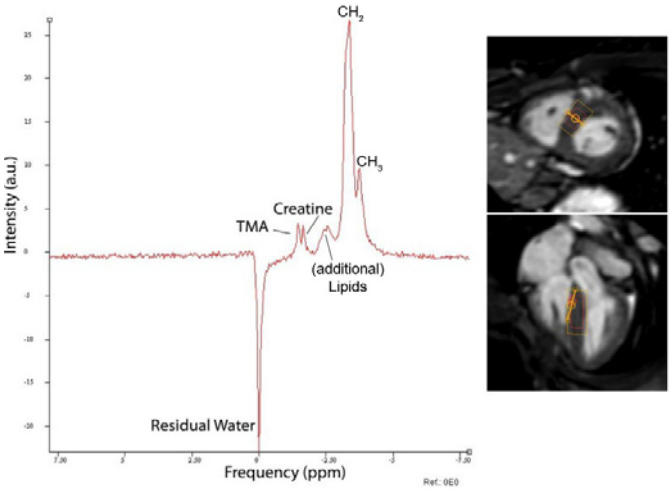

Figure 1 ^{1}H-MR spectrum of the septum myocardium in a healthy volunteer.

Table 1 Lineshapes used in the different models. Lorentzian lineshapes are denoted with L, and Gaussian lineshapes are denoted with G.

Model	TMA	Cr	Lipids	CH_2	CH_3
A	L	L	G	G	G
B	L	L	G	L	G
C	L	L	G	L	L
D	L	L	2 L*	L	L

* In model D, the additional lipid peak at 2.1 ppm was fitted with two components.

Results: For a majority of the signals, model C was found to have the smallest RSS (Table 2).

Table 2 RSSs for signals quantified using different prior knowledge models. For the major part of the signals, the RSS was smallest for model C. The smallest RSS for each spectrum is indicated in bold.

	Intra-examination reproducibility measurements					
Model	1	2	3	4	5	6
A	0.0997	0.0991	0.0927	0.0988	0.1096	0.1028
B	0.0761	0.0797	0.0725	0.0778	0.0841	0.0805
C	**0.0756**	**0.0786**	**0.0718**	**0.0771**	**0.0834**	0.0805
D	0.0757	0.0790	0.0719	0.0779	0.0841	**0.0803**

	Inter-examination reproducibility measurements					
Model	7	8	9	10	11	12
A	0.0824	0.0883	0.0919	0.0745	0.0867	0.0996
B	0.0657	0.0606	0.0653	**0.0570**	0.0611	0.0650
C	**0.0648**	**0.0599**	**0.0651**	0.0573	**0.0610**	0.0645
D	0.0654	0.0607	0.0655	0.0576	0.0620	**0.0644**

Discussion/Conclusion: A large improvement of the quantitation process of CMRS can be achieved when using a Lorentzian lineshape instead of the commonly found Gaussian lineshape to fit the methyl and methylene peak.

References:

1. Singhal A. et al. (2009) Prog Nucl Magn Reson Spectrosc 54(3-4):255-77.

668

T2 relaxation measurements of brain tissue metabolites: effect of age, hearing state and processing methodology

A. Skoch[1], J. Nahodilova[2], F. Jiru[1], D. Wagnerova[1], M. Dezortova[1], J. Syka[3], M. Hajek[1]
[1]MR-Unit, Department of Diagnostic and Interventional Radiology, Institute for Clinical and Experimental Medicine, Prague/CZECH REPUBLIC, [2]St. Anne's University Hospital, International Clinical Research Center, Brno/CZECH REPUBLIC, [3]Department of Auditory Neuroscience, Institute of Experimental Medicine, Academy of Sciences of the Czech Republic, Prague/CZECH REPUBLIC

Purpose/Introduction: The aim of the study was a) comparison of different LCModel basis-set types to T2 relaxation times (T2r) determination; b) to test relation of T2r on age and hearing state.
Subjects and Methods: Group of young controls with physiologic hearing (YC) (25±2 y), elderly controls with normal presbyacusis (EC) (68±1 y) and elderly patients with expressed presbyacusis (EP) (75±6 y) were measured on 3T MR scanner (Trio, Siemens) by SVS PRESS sequence (TR=5000ms). The VOI was centered around the Heschl gyrus of temporal lobe (Fig.1).

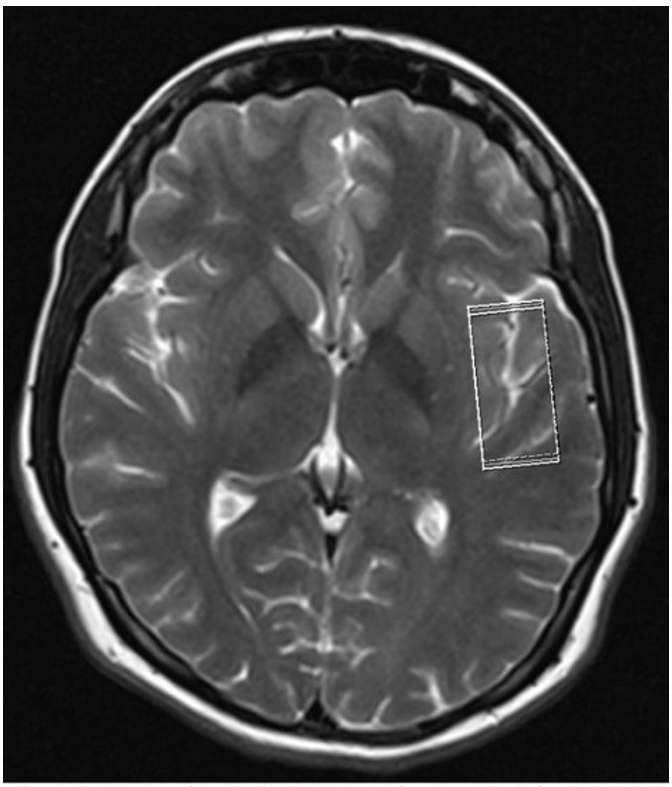

Fig. 1. Positioning of the SVS VOI (volume of approx. 18 ml) for SVS PRESS experiment.

Sets of MR spectra with different TE (30-135 ms) were processed by LCModel [1] with TE-specific basis-sets simulated by SIMPSON [2]. To test the influence of different T2r of coupled and uncoupled parts of metabolite signal, two basis-set types were constructed: Split_basis with coupled and uncoupled signals of glycerophosphocholine (GPC), phosphocholine (PCh), N-acetylaspartate (NAA), N-acetylaspartylglutamate (NAAG) as separate basis components, NoSplit_basis with the coupled and uncoupled parts in one component. The T2r estimations were performed by: a) individual fitting for each subject using the model C=Am*exp(-TE/T2r) and averaging the T2r value within the group; b) "multi-branch" fitting by fixed group T2r (but individual Am) for all subjects in one group. To test the deviation from the expected exponential shape, the concentrations of all subjects in the group were normalized to their Am factor determined in b) fitting approach and plotted with their confidence intervals along the formula exp(-TE/T2r_group).
Results: NAA+NAAG T2r's were significantly higher in group YC with respect to the group EC and EP as well as for Split_basis with respect to NoSplit_basis in group YC (Fig.2).

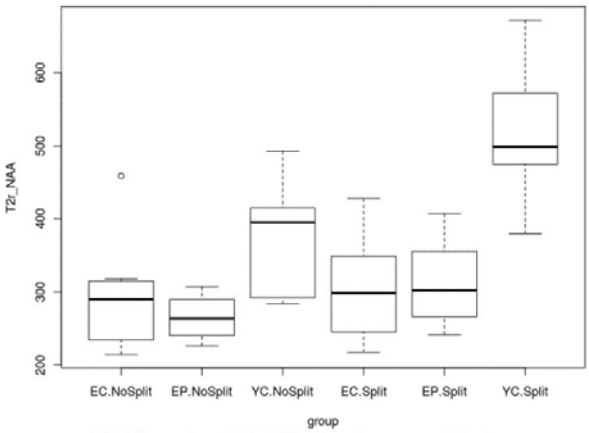

Fig. 2: Comparison of T2r of NAA for subject groups and basis-set types.

The lower T2r of NoSplit_basis is probably due to lower T2r of the coupled part in comparison to the uncoupled part. T2r's of other metabolites were not significantly different. In contrast to GPC+PCh, Cr+PCr (Fig.3), relaxation curves of NAA show systematic deviation from exponential shape (Fig.4): decline in TE=50-60 ms and ascent in TE=70-80 ms.

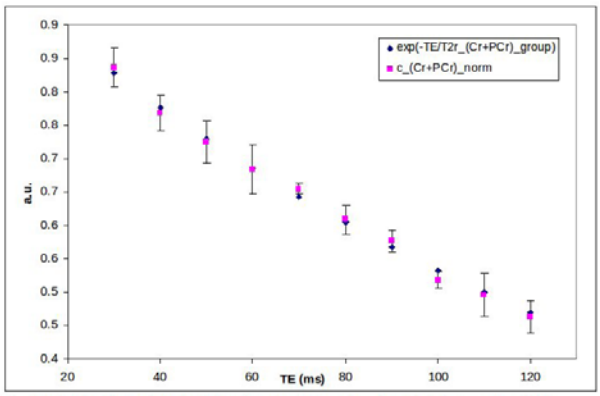

Fig. 3: The plot illustrating deviation from the expected exponential shape: normalized average concentrations of (Cr+PCr) processed by LCModel with NoSplit_basis in the group of young controls (YC) with their confidence intervals along with the group T2 relaxation curve.

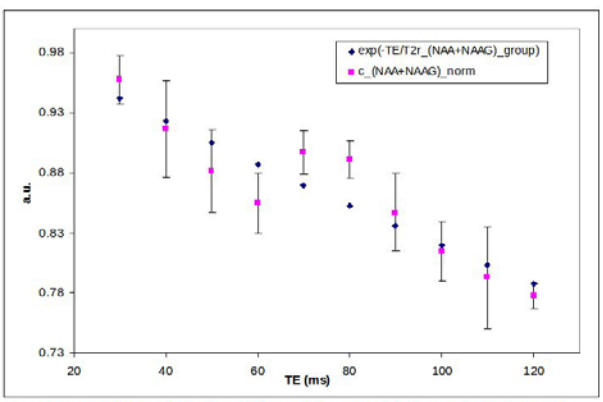

Fig. 4: The plot illustrating deviation from the expected exponential shape: normalized average concentrations of (NAA+NAAG) processed by LCModel with NoSplit_basis in the group of young controls (YC) with their confidence intervals along with the group T2 relaxation curve.

Discussion/Conclusion: The results show that aging decreases T2r of NAA+NAAG in auditory area. No significant influence of hearing loss to T2r of the other metabolites has been observed. Systematic fluctuations of NAA+NAAG relaxation curve shape were found which can significantly influence its T2r estimation. The fluctuations are most likely due to the J-coupling effects studied in [3].

Supported by grants GACR P304/10/1872, P208/11/P059, and European Regional Development Fund-Project FNUSA-ICRC(No.CZ.1.05/1.1.00/02.0123).

References:

[1] Magn. Reson. Med. 1993 Dec;30(6):672-9.
[2] J Magn. Reson. 2000 Dec;147(2):296-330.
[3] Magn. Reson. Med. 1998 Feb;39(2):169-78.

669

Comparison of spectra analysis methods for the quantification of mice liver fatty acid composition by MR spectroscopy

A. Coum[1], **F. Noury**[2], G. Gambarota[3], K. Begriche[4], B. Fromenty[4], H. Saint-Jalmes[3]
[1]INSERM, UMR 1099, Rennes/FRANCE, [2]Université de Rennes 1, LTSI, Rennes/FRANCE, [3]PRISM, Biosit, CNRS UMS 3480, INSERM UMS 018 - Biogenouest, Rennes/FRANCE, [4]INSERM, U991, Rennes/FRANCE

Purpose/Introduction: The objective was to quantify the fatty acids (FA) composition in obese mice liver by magnetic resonance spectroscopy (MRS). In the literature, there are different methods to analyze *in vivo* spectra in order to quantify FA composition of a tissue.

The idea of this study was to compare these various analysis methods in the context of our experimental conditions to determine the optimal method for assessment of FA composition in mice liver.

Subjects and Methods: Phantoms and animals

We used 4 tubes containing pure oil chosen for their various composition in FA, and 10 tubes of water/rapeseed oil emulsions (fat fraction 5% to 50%). *In vivo* experiments were performed using 4 female obese C57BL/6J Rj-ob (ob/ob) mice (8 weeks old).

MRS

Experiments were performed at 4.7 T (47/40 Bruker Biospec). Localized spectra were acquired with PRESS (TR/TE=2500/11ms, VAPOR, 64 averages) (Fig. 1-A and 1-B). For *in vivo* acquisitions on liver, we used respiratory gating, a voxel of 3*3*3mm^3 and 256 averages (Fig. 1-C). T_1 and T_2 relaxation times of each FA component were also measured by MRS using pure oil phantoms.

Spectra analysis

We used jMRUI to integrate the resonance of each FA component. These data were used to calculated FA composition of pure oil and emulsion phantoms using 5 analysis methods, with or without T_1 and/or T_2 correction.

Results: Best performances were obtained with Ren *et al.*, Young *et al.* and Strobel *et al.* methods. Results obtained with the two others analysis methods (Zancaro *et al.* and Corbin *et al.*) gave incoherent results and are not shown. Ren *et al.* analysis method gave the results closest to theoretical composition in FA with, for pure oil data, an error about 3% for saturated an unsaturated FA, 4% for mono-unsaturated FA and 7% for poly-unsaturated FA (Table 1).

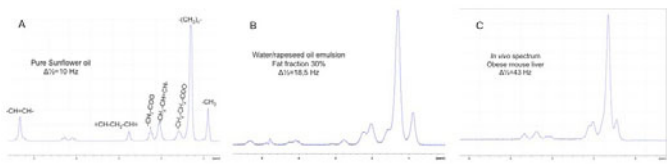

Fig. 1: examples of spectra acquired for a pure oil phantom (A), a water/oil emulsion phantom (B) and ob/ob obese mouse liver (C).

Olive oil	Theoritical composition (%)	REN (%)	YEUNG (%)	STROBEL (%)
SFA	15	14	14	14
UFA:	86	86	86	86
MUFA (*ω9*)	77	77	83	
PUFA:	9	10	3	
MUFA (*ω6*)	7	10	-3	
PUFA (*ω3*)	2		6	

Sunflower oil	Theoritical composition (%)	REN (%)	YEUNG (%)	STROBEL (%)
SFA	12	12	12	12
UFA:	89	88	88	88
MUFA (*ω9*)	23	27	34	
PUFA:	66	61	54	
MUFA (*ω6*)	65	61	48	
PUFA (*ω3*)	1		7	

Table 1: examples of results for olive and sunflower oils obtained for 3 analysis methods. Composition in satured FA (SFA), unsatured FA (UFA), mono-unsatured FA (MUFA) and poly-unsatured FA (PUFA).

ob/ob mice liver FA composition (%)	Mouse 1	Mouse 2	Mouse 3	Mouse 4
SFA	6,0	27,1	18,6	20,4
UFA:	94,0	72,9	81,4	79,6
MUFA (*ω9*)	93,9	72,7	81,4	79,6
PUFA:	0,1	0,2	0,0	0,0
(*ω6*)	0,1	0,2	0,0	0,0

Table 2: *in vivo* results of FA composition of obese mice liver obtain with Ren *et al.* analysis method. Composition in satured FA (SFA), unsatured FA (UFA), mono-unsatured FA (MUFA) and poly-unsatured FA (PUFA).

Discussion/Conclusion: We used Ren *et al.* method to analysis our *in vivo* spectra and determinate FA composition of obese mice liver (Table 2).

References:

- Ren J. *et al.* (2008). *J lipids research.* **49**: 2055-2062.
- Yeung D.K. *et al.* (2008). *Chem phys lipids.* **151**: 103-109.
- Strobel K. *et al.* (2008). *J lipids research.* **49**: 473-480.
- Zancaro C. *et al.* (1994). *J lipids research.* **35**: 2191-2199.
- Corbin I.R. *et al.* (2009). *Biochim Biophys Acta.* **1791**: 757-763.
- Naressi A. *et al.* (2001). *MAGMA.* **12**: 141–52.

670

Fat unsaturation in bone marrow, leg and deep abdominal subcutaneous adipose depots with long echo time ^{1}H MRS at 3 Tesla.

A. Hakkarainen[1], H. Viljakainen[2], T. Saukkonen[2], M. Lipsanen-Nyman[2], O. Mäkitie[2], N. Lundbom[1], J. Lundbom[3]
[1]Medical Imaging Centre, Helsinki University Central Hospital, Helsinki/FINLAND, [2]Children's Hospital, Helsinki University Central Hospital and University of Helsinki, Helsinki/FINLAND, [3]Medical Imaging Center, Helsinki University Central Hospital, Helsinki/FINLAND

Purpose/Introduction: Proton MRS can be used to study bone marrow fat unsaturation noninvasively *in vivo*. The combination of traditionally used short TE and relatively low clinical field strengths (1.5T), however, lead to overlap between the resonances from olefinic fat protons (-CH=CH-, 5.35 ppm) and water protons (H_2O, 4.8 ppm) (1). We have previously shown that long TE ^{1}H-MRS can be used to resolve the olefinic and water resonances in fatty liver (2). Recently, we also showed that the superficial and deep subcutaneous adipose depots differ in fat unsaturation (3).

The aim of this study was to provide an improved method for determining bone marrow unsaturation by using long TE ^{1}H-MRS at 3T. Furthermore, we aimed to determine bone marrow (BM) fat unsaturation in relation to the unsaturation of deep (DSAT) and leg subcutaneous adipose (LSAT) depots.

Subjects and Methods: Fifteen subjects (13F) were measured on a clinical 3 Tesla MR Imager (Verio, Siemens). PRESS localization was used to collect long TE spectra (TE/TR = 200/4000 ms) from three fat depots; DSAT, LSAT and

BM (right tibia). A flex coil was used to obtain spectra from DSAT and a knee coil for LSAT and BM. All spectra were analyzed by AMARES (jMRUI) using prior knowledge. Intensities of olefinic , methylene (-CH2)n-) at 1.3 ppm and methyl (-CH3) at 0.9 ppm were determined. The unsaturation index (UI) was calculated as 100 x $I_{olefinic}/(I_{olefinic}+I_{methylene}+I_{methyl})$.

Results: Bone marrow spectra had no discernible water resonance. The measured unsaturation indices are shown in Table 1. The mean BM unsaturation was similar to the unsaturation in DSAT but significantly less unsaturated than LSAT ($P < 0.001$). Bone marrow unsaturation did not, however, correlate with DSAT or LSAT unsaturation ($R < 0.14$), whereas DSAT and LSAT unsaturation correlated ($R = 0.57$, $P < 0.05$).

Table 1.

UI	DSAT	LSAT	BM
Mean	10.1	12.8*	10.1
SD	1.2	1.3	0.6

*) $P < 0.001$ paired t-test.

Discussion/Conclusion: Using long TE 1H-MRS at 3 Tesla can be used to measure bone marrow unsaturation *in vivo*. Bone marrow fat unsaturation appears comparable to deep subcutaneous adipose tissue unsaturation but is significantly more saturated than lower body subcutaneous adipose tissue.

References:

(1) J Magn Reson Imaging. 2005 Aug;22(2):279-85.
(2) NMR Biomed. 2011 Apr;24(3):238-45.
(3) Int J Obes (Lond). 2012 May 29. doi:10.1038/ijo.2012.72

EPOS™ Poster

RF Systems

671

A multichannel $^{1}H/^{31}P$ transmit-receive coil for spectroscopy in the human calf at 7T

S. Goluch[1], R. Kriegl[2], E. Moser[1], T. Herrmann[3], J. Mallow[3], J. Bernarding[3], K. Kim[4], S. Hong[4], H. Jeong[4], Z. Cho[4], E. Laistler[5]
[1]MR Center of Excellence, Medical University of Vienna, Vienna/AUSTRIA, [2]IR4M (Imagerie par Resonance Magnetique Medicale et Multi-Modalites), UMR8081 CNRS, Université Paris Sud 11, Orsay/FRANCE, [3]Department of Biometry and Medical Informatics, OvG University Magdeburg, Magdeburg/GERMANY, [4]Neuroscience Research Institute, Gachon University of Medicine and Science, Incheon/KOREA, [5]CMPBMT, MR Center of Excellence, Medical University of Vienna, Vienna/AUSTRIA

Purpose/Introduction: Phosphorus-31 spectroscopy is employed for studying energy metabolism in the muscle. At 7T, it benefits from higher sensitivity, increased spectral resolution and shorter relaxation times[1]. The purpose of this work is to design a sensitivity-optimized double-tuned $^{1}H/^{31}P$ transmit-receive surface coil fitting the human calf for muscle metabolism studies at 7T.
Subjects and Methods: The coil (Fig.1) consists of two proton channels ($12.5x12.5cm^2$) with shared conductor and a three channel overlapped phosphorus array (element size $10x7cm^2$). The structure was bent into cylindrical shape (Ø=16.9cm(^{1}H) and Ø=14.9cm(^{31}P)). Segmenting capacitors were evenly distributed over the wire length at distances<λ/20. Proton channels were decoupled with a capacitor on the shared conductor, adjacent phosphorus channels were overlapped. The coil was loaded with a cylindrical phantom (Ø=13.3cm) filled with a gel consisting of 30mmol/l phosphorus in K_2HPO_4, 1ml/l Magnevist, 1.25g/l NaCl, and 10g/l polyacrylic acid. With a conductivity of 0.77 S/m and a physiological phosphorous concentration[2] it should act as a realistic model of the calf muscle. To achieve best B1+ efficiency and homogeneity, 3D EM simulation using XFdtd 7.2.2 (Remcom,State College,PA,USA) and Matlab (MathWorks,Natick,MA,USA) was used to determine the optimal phase relation between channels. Due to homogeneity of the phantom, spatial distribution of the ^{31}P signal amplitude can serve as a measure for relative B1+ distribution. Therefore, a metabolic map (fitted area under peak) was acquired with a 2D CSI sequence on a Siemens 7T whole-body system.

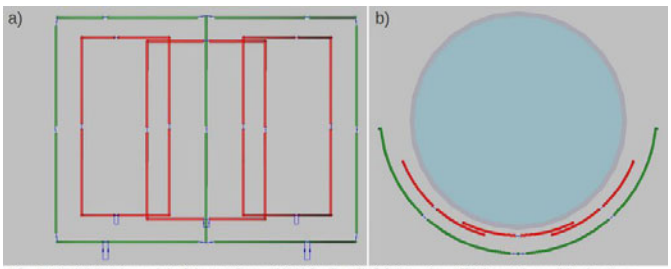

***Fig. 1** XFdtd 7.2.2 model of the ^{1}H (green)/^{31}P (red) coil. **(a)** Top view, **(b)** front view with phantom.*

Results: Decoupling of -27dB was achieved for the proton coils, decoupling between phosphorus channels was <-12dB. Cross-coupling between ^{1}H and ^{31}P channels was <-14dB@120.3MHz and <-21dB@297MHz. Simulation showed optimal B1+ distribution for the proton coil in CP mode and phase shifts of 0°/60°/120° for the phosphorus array. The metabolic map is overlaid on a GRE proton image of the phantom in Fig.2a. Comparison with the simulation result (Fig.2b) for the combined phosphorus B1+ field shows good agreement.

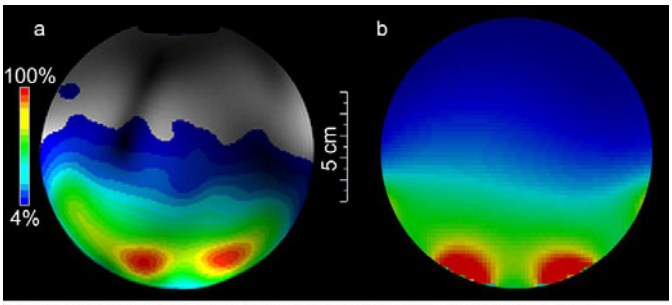

***Fig. 2 (a)** Metabolic map from 2D CSI (TR=400ms, TE=1ms, FOV=14x14x4cm³, MA=14x14, reconstructed to 32x32), post-processing was performed unsing the manufacturer's spectroscopy software. **(b)** Combined simulated B_1^+ field.
The pictures are scaled from the maximum ^{31}P signal (100%) to a threshold of 4%, where the signal could still be accurately fitted. Note that the lower signal intensity at the border area of the CSI measurement data is due to partial volume effects.*

Discussion/Conclusion: We constructed a highly sensitive ^{31}P array coil with optimized phase combination for 7T. First results are in good agreement with 3D EM simulation. The obtained phosphorus sensitivity pattern is well-suited for studies examining the gastrocnemius[3]. In a next step, second-order traps will be inserted to minimize cross-coupling between proton and phosphorus coils. Further improvement should be achieved by phase-corrected combination of the individual ^{31}P-signals.
References:
[1] Bogner et al, MRM(2009), 62(3):574-82
[2] Kemp et al, NMR Biomed(2007), 20:555-65
[3] Meyerspeer et al, MRM(2012), doi:10.1002/mrm.24205

672

A short transmit array optimized for spectroscopy at high field

A.W. Magill[1], R. Gruetter[2]
[1]Laboratory for Functional and Metabolic Imaging, Ecole Polytechnique Fédérale de Lausanne, Lausanne/SWITZERLAND, [2]Department of Radiology, University of Geneva and Lausanne, Geneva Lausanne/SWITZERLAND

Purpose/Introduction: Transmit arrays for the human head are usually designed for whole-brain coverage. Smaller loops offer higher B_1-per-transmit-power close to the loop, but the generated field penetrates less far into the load. This study investigates the design of an eight-loop transmit array for use at 7T, optimized for high B_1 efficiency over a small volume, rather than whole-brain coverage. Such a probe would be suited to spectroscopy, where large coverage is usually unnecessary but SAR is often a limiting factor.
Subjects and Methods: An array of eight rectangular loops was designed to fit onto a 258mm diameter cylinder, leaving a 10mm gap between adjacent loops. A series of arrays of different lengths along the z-axis (30-240mm) were simulated (Microwave Studio, CST) while loaded with a human head model (Duke, Virtual Family [2]) (fig.1a,b). Loops were capacitively divided to maintain conductor lengths <50mm (λ/20 at 300MHz). Ideal decoupling was modelled by exciting each loop in turn, while inactive elements were damped by adding a 1kΩ resistor in series with tuning capacitor. Sum-of-magnitude (SoM) transmit B_1 fields [2] and worst-case 10g SAR maps (assuming the electric field is in phase at all locations) [3] were then calculated.
Results: Figure 1c-f shows a typical example of the SoM B_1 field and worst-case SAR, here for the 60mm array. Figure 2a shows the SoM B_1 field strength at the centre of the array (the weakest point) versus array length, for fixed transmit power. Figure 2b shows the same result scaled for constant worst-case 10g SAR.

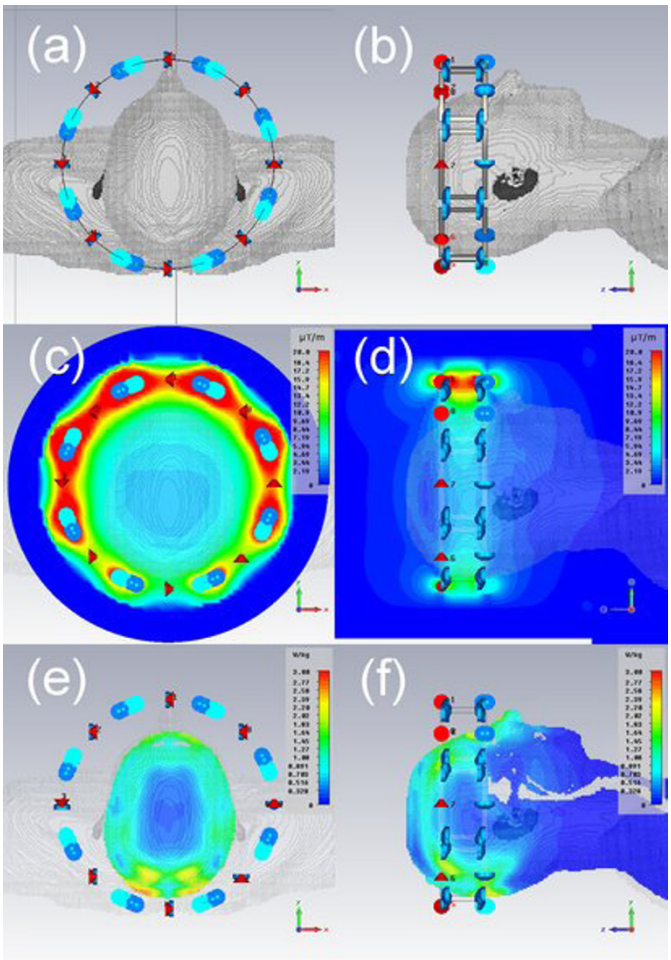

Figure 1: The (a,b) simulation mode, (c,d) SoM B_1 fields and (e,f) worst-case SAR for the 60mm array.

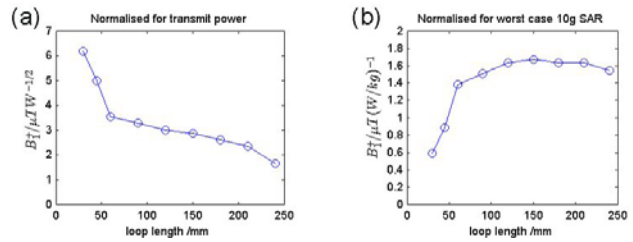

Figure 2: B_1 field strength vs. array length normalised for (a) transmit power and (b) worst-case 10g SAR.

Discussion/Conclusion: SoM B_1 field intensity at the array centre increases as the array length is reduced, even for extremely short loops, due to reduced probe loading. However, shortening the array also increases worst-case 10g SAR, as loop capacitors come into close proximity to the head. Highest B_1/SAR is given by the 120-210mm arrays; within this range the 120mm array generates highest $B_1/\sqrt{(power)}$. A 120mm array will now be built, using transformers to decouple neighbouring loops [4].

References:

[1] Christ et al, PMB 55(2), 2010;
[2] Van de Moortele et al, MRM 54(6), 2005;
[3] Collins et al, ISMRM 2007;
[4] Avdievich et al, MRM 62(1), 2009.

673

A quantitative comparison of electromagnetic computational methods for RF coil design

R. Stara[1], N. Fontana[2], G. Tiberi[3], M. Tosetti[4], G. Manara[2], A. Monorchio[2], M. Alfonsetti[5], A. Vitacolonna[6], A. Galante[6], M. Alecci[5], A. Retico[1]
[1]INFN, Istituto Nazionale Fisica Nucleare, Pisa/ITALY, [2]Dipartimento di scienze dell'informazione, Universita' di Pisa, Pisa/ITALY, [3]University of Pisa, Imago7, Pisa/ITALY, [4]MR laboratory, IRCCS Stella Maris Scientific Institute, Pisa/ITALY, [5]Dip. SDS, Università dell'Aquila, L'Aquila/ITALY, [6]Dipartimento di scienze della salute, Universita' dell'Aquila, L'Aquila/ITALY

Purpose/Introduction: Several clinical MRI/MRS applications require an appropriate design of the RF coil, in order to optimize the RF spatial distribution and sensitivity. As frequency increases, RF fields interact more strongly with the sample, rendering quasi-static approaches [1] less reliable for electromagnetic (EM) characterization. On the other hand, many different numerical methods can be employed, including the Finite-Difference Time-Domain (FDTD) [2,3], the Finite Element Methods (FEM) [4,5] and the Method of Moments (MoM) [6,7]. Those techniques allow EM characterization of low and UHF MR coil, each one having its own advantages and drawbacks. To the best of ourknowledge, a quantitative comparison of the computationperformances of the EM simulation methods is not available in a widefrequency range, making the methods selection difficult and,sometimes, not optimal.

Subjects and Methods: The software CST MW uses the Finite Integration Technique (FIT) inthe time domain, this methodology being similar to the traditionalFinite Difference but the integral form of Maxwell's equations is solved, instead of the differential form. Frequency-domain numerical simulations were used with the Method of Moment (MoM), implemented in the FEKO software and a Finite Element Method (FEM) developed by CST MW Studio. The quantitative comparison was made using two prototypes of surface coils, a Figure of Eight (Fo8) at 1.5 T [8] and a Dual Tuned 1H/31P coil, made with two concentric loops of radius 5 cm (1H) and 3.5 cm (31P), operating at 7T. The comparison comprised workbench measurements (S11/S12 parameters), electromagnetic fields, simulation time and allocated memory.

Results:

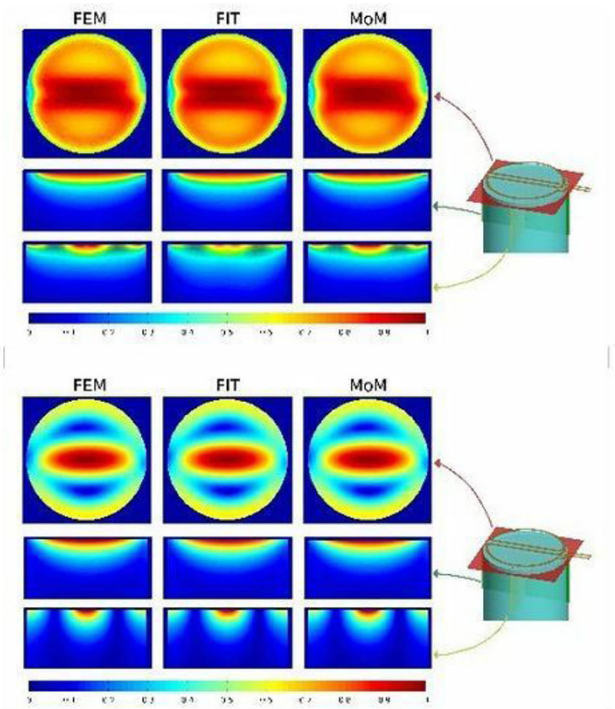

Fig. 1. Effective magnetic field and electric field in three different planes with the three different simulation methods.

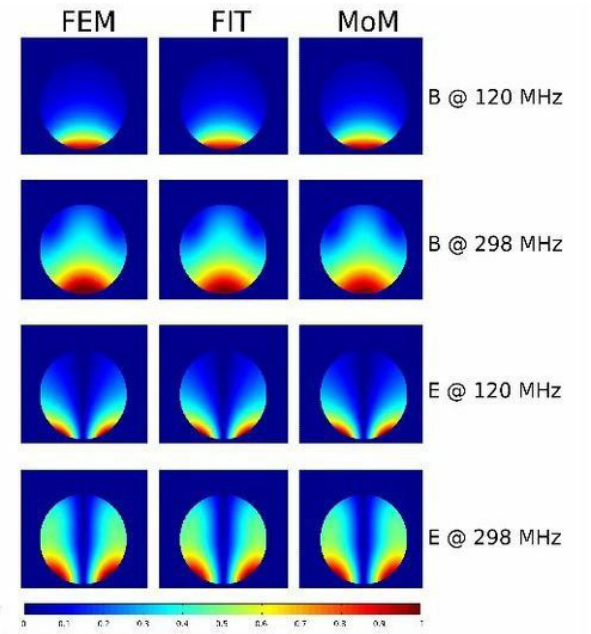

Fig. 2. Effective magnetic field and electric field simulated at 298 MHz (^{1}H) and 120.6 MHz (^{31}P) in the transverse plane of the phantom.

TABLE I
1.5T FIGURE OF EIGHT COIL: S PARAMETER SIMULATIONS

Quantity	Measure	MoM	FEM	FIT
Frequency	63.94	0.3 %	2 %	2%
Matching	-24 dB	0.2%	0.4%	0.4%
Simulation time	/	25 min	2 h 15 min	36 h 25 min
Physical memory	/	40 MB	2.92 GB	423 MB

TABLE II
7T DUAL TUNED 31P/1H COIL: S PARAMETER SIMULATIONS

Quantity	Measure	MoM	FEM	FIT
Frequency, 1H	298.6 MHz	6%	4%	2%
Matching, 1H	-47 dB	0.4%	1 %	10 %
Frequency, 31P	120.5	5 %	5 %	4 %
Matching, 31P	-24 dB	0.1 %	1 %	2 %
S12 at H freq.	-65 dB	0.01 %	0.01 %	0.01 %
S12 at P freq.	-13 dB	0.2 %	1%	0.6 %
Simulation time	/	15 min	2 h 57 min	17 h 6 min
Physical memory	/	50 MB	16 GB	1 GB

Table 1 and 2 show the difference between the results obtained with the three methods and the experimental result for the Fo8 and DT coils, respectively. Figure 1 and 2 show the electromagnetic fields simulations for the Fo8 and the DT coils, respectively.

Discussion/Conclusion: The three methods showed to be all suitable for this kind of simulation, since the parameters accuracy is very similar. The main differences is observed in the simulation time and in the physical memory allocated during the simulation.
We can therefore say that frequency domain methods, especially MoM, due to the very short computation time, are suitable for simulations performed in the prototype stage. The FIT method is more suitable for simulations of complex dielectric model (human body), at the expense of increased computation time, due to the different meshing rules and algorithm.

References:

- Giovannetti, 2002.
- Collins,1998.
- Ibrahim, 1999.
- Simunic, 1996.
- Singerman, 1997.
- Chen, 1998.
- Fuijita 1999.
- Alfonsetti, 2005.

674

A comparison of high-pass birdcage coils for small animal imaging at 9.4 and 14T

T. Cheng[1], J. Jung[2], A. Comment[1], R. Gruetter[3], H. Lei[2], A.W. Magill[4]
[1]SB IPSB GR-CO, Ecole Polytechnique Fédérale de Lausanne Lausanne, Lausanne/SWITZERLAND, [2]Laboratory of Biomedical Imaging, École Polytechnique Fédérale de Lausanne, Lausanne/SWITZERLAND, [3]Department of Radiology, University of Geneva and Lausanne, Geneva Lausanne/SWITZERLAND, [4]Department of Radiology, University of Lausanne, Lausanne/SWITZERLAND

Purpose/Introduction: The birdcage coil was developed to acquire homogenous whole-body human images at relatively low magnetic field (1.5T) several decades ago [1]. In this study two high-pass birdcage coils with same dimensions, aimed for small animal MRI, were simulated, built and tested in both in vitro and in vivo experiments at 9.4T and 14.1T.
Subjects and Methods: High-pass 16-rungs resonators (OD=51mm, L=30mm) with an RF shield (OD=94mm), operating at 400MHz and 600MHz, were simulated using Microwave Studio (CST) to find suitable capacitor values. A prototype of each coil was then built, designed to operate in quadrature transceive mode, with a tunable balancing capacitor inserted between the two ports for decoupling. Unloaded and loaded Q-factors were measured using a network analyzer (E5071C, Agilent) and a cylindrical saline-solution phantom (OD=27mm, L=100mm).MR data were then acquired using 9.4T and 14.1T scanners (Agilent), both with a bore diameter of 26cm. The region of interest (ROI) was shimmed using fastmap [2]. B_1^+ maps were generated using the double angle method (60°/120° FA) (Table 1) [3]. Axial and coronal gradient echo images of the phantom and mice were then acquired.

Parameters used for both coil performance tests and results.

	phantom					*in vivo*		
B_0 (T)	Q_U/ Q_L	TR/TE [ms/ms]	FOV [mm^2]	FA	$SNR_{Phantom}$	TR/TE [ms/ms]	FOV [mm^2]	$SNR_{in\ vivo}$
9.4	1.4	20,000/2.83	40*40	60°±1°	1305±39	20,000/3.31	20*20	196±38
14.1	1.1	20,000/2.83	40*40	51°±6°	2207±252	20,000/3.31	20*20	224±39

Results: Simulated field maps, and phantom and in vivo FA maps at both field strengths are shown in Fig 1. The signal-to-noise ratios of phantom and mouse brains are shown in Table 1.

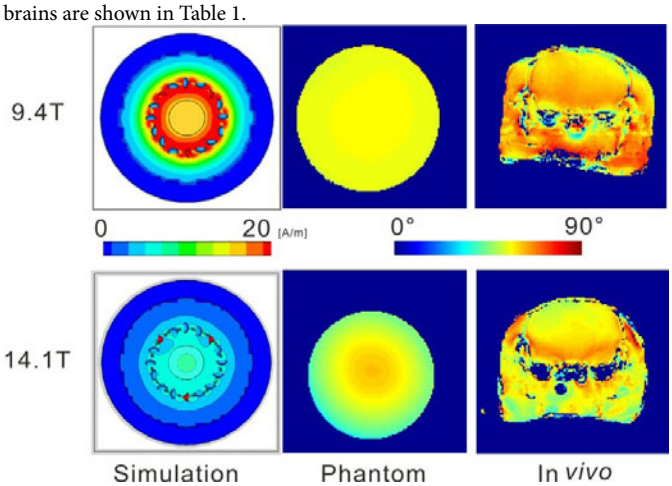

Discussion/Conclusion: In this study we demonstrated that at 9.4T with the high-pass birdcage coil a homogenous B_1^+ field can be generated. At 14T the homogenous B_1^+ region is slightly smaller, due to the standing wave effect, but most of the animal brain can be covered by the reasonably homogenous region in the center of the coil. The SNR values at 14.1T was 1.7 times higher than that at 9.4T since SNR is dependent on the B_0 field strength and B_1 field homogeneity. For the 14T coil, the maximum free conductor length is slightly longer than λ/20, which may produce significant radiation losses.

References:
[1] Hayes, JMR 63, 622 (1985); [2] Gruetter, MRM 29, 804 (1993); [3] Insko et al, JMR A 103: 82–85 (1993).

675

Double crossing volume coil for MRI of rodents at 7 Tesla

O. Marrufo[1], F. Vazquez[2], R. Martin[3], A.O. Rodriguez[3]
[1]Dep Neuroimagen, Instituto Nacional de Neurologia y Neurocirugia MVS, Mexico DF/MEXICO, [2]Dep Fisica, FC UNAM, Mexico DF/MEXICO, [3]Dep. Ingenieria Electrica, UAM Iztapalapa, Mexico DF/MEXICO

Purpose/Introduction: Transceiver volume coils for high field MRI of rats is still a very dynamic field of investigation and development [1]. A transceiver volume coil for rodents was developed inspired on Temnikov's coil [2] for rodents at 7T. It was named double crossing (DCROS) coil. Phantom images were acquired to test its viability.

Subjects and Methods: The finite element method was used to numerically compute the B_1 field of the coil in Fig. 1 and a birdcage coil, using COMSOL MULTIPHYSICS (COMSOL, Burlington, MA, USA) at 300 MHz. A transceiver DCROS coil (length=11.3cm and diameter=6.6cm) was built using copper strips and mounted on an acrylic cylinder. 8 fixed-value capacitors and 4 trimmers were used for tuning at 299.47 MHz and 50Ω matching. A 4-leg birdcage coil was built with similar dimensions for comparison purposes. Both prototypes were linear driven. One 50Ω-coax cable was attached to each coil to transmit/receive the MR signal. Quality factors were computed using a saline solution phantom (4cm diameter). To test the validity of the coils, T1-weighted phantom images were acquired on a 7T/21cm imager and using gradient echo sequences with TE/TR=4.11/530.70ms, FOV=80mmx80mm, matrix size=256x256, slice thickness=2mm, NEX=3.

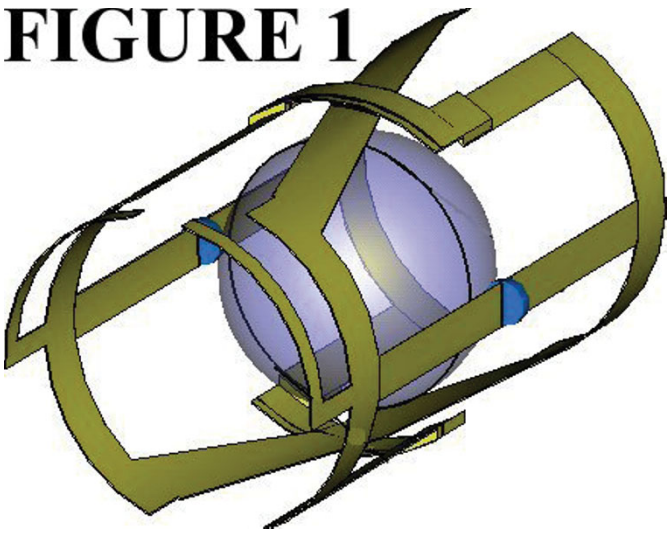

Results: B1 numerical calculations of the two coils are shown in Fig. 2. The coil quality factors were $Q_{unloaded}/Q_{loaded}$(DCROS)=105/93 and $Q_{unloaded}/Q_{loaded}$(birdcage)=97/53. Phantom images were acquired and shown in Figure 3. The signal-to-noise ratios (SNR) and uniformity profiles were calculated and shown in Fig. 4. The $SNR_{double\ crossing}/SNR_{birdcage}$=85.26/76.54.

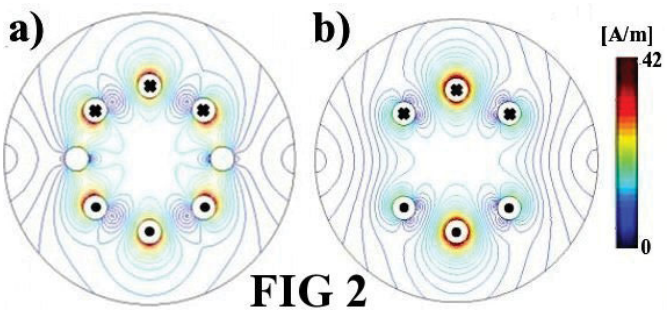

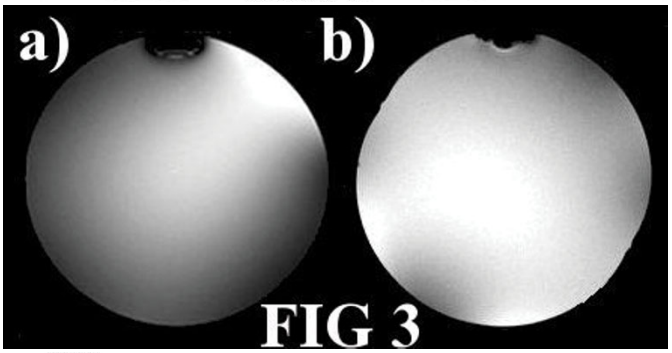

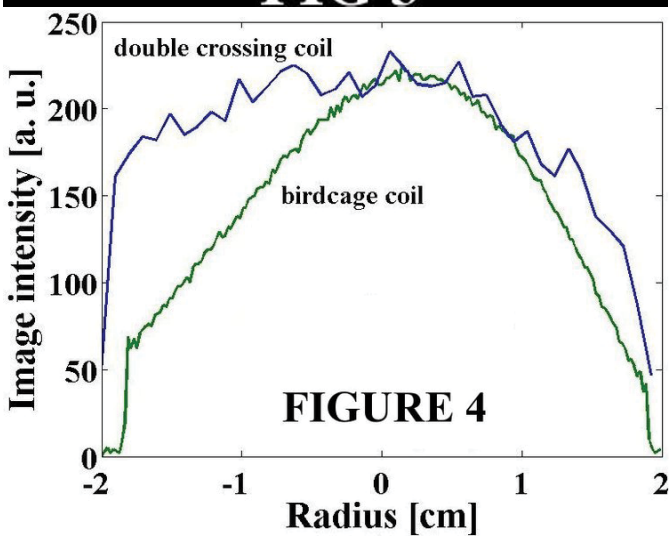

Discussion/Conclusion: The DCROS coil uniformity profile in Fig. 4 shows a smoother behaviour and corroborates very well with results in the literature. Therefore, the double crossing coil outperformed the birdcage coil. This is an important result because our coil is comparatively easier to build. Phantom images confirmed the viability of our coil and its compatibility with high field imagers and pulse sequences. The double crossing coil offers an alternative coil design to the traditional birdcage coil for MRI applications of animal models at high fields. It still remains to investigate the coil SAR and the suitability of this coil to be driven in quadrature mode.

References:
References. 1. Doty FD, et.al. NMR Biomed. 2007;20:304. 2. Temnikov A. Inst Exp Tech. 48:2005:636.
Acknowledgments. O. M., F. V. and R. M. thank CONACyT for Ph. D. scholarships and grant no. 166404. S. S. acknowledges DGAPA-UNAM for postdoc stipend. email: arog@xanum.uam.mx.

EPOS™ Poster

Sequences and techniques

676

MRI of fibrous tissue with short T2 based on a modified Double Echo Steady State (DESS) sequence with adapted post-processing

P. Martirosian[1], C. Schraml[2], N.F. Schwenzer[2], F. Springer[2], C. Würslin[1], F. Schick[1], M. Deimling[3]
[1]Section on Experimental Radiology, University Hospital of Tübingen, Tübingen/GERMANY, [2]Diagnostic and Interventional Radiology, University Hospital of Tübingen, Tübingen/GERMANY, [3]Magnetic Resonance, Siemens Healthcare, Erlangen/GERMANY

Purpose/Introduction: Fibrous tissues as tendons, ligaments, and fibrocartilage structures as menisci show short T_2 values and therefore nearly lacking signal intensity in images recorded by conventional MRI sequences. This work aims at improving the visualization of these tissues with positive contrast by utilizing a modified *Double-Echo-Steady-State* (DESS) sequence. In contrast to the conventional DESS sequences working with an addition of both echo signals [1-2], in the presented sub-DESS sequence the final image is derived by subtraction of the signals of both echoes acquired.
Subjects and Methods: Fibrous structures in the knees of four healthy volunteers were examined on a 3T MR-scanner using an eight-channel-transmit-receive knee coil. The 3D modified DESS-sequence was implemented in a manner that two echoes (S^+,S^-) are acquired separately within two "rephased" readout gradients [3] and reconstructed separately. To keep echo time TE_1 as short as possible S^+-echo is acquired with a strong asymmetry factor of 0.2, and rf excitation is done by non-selective RF-pulses with duration of 100µs. Subtraction images (S^+-S^-) and also relative-subtraction images corresponding to (S^+-S^-)/(S^++S^-) were computed. Contrast in subtraction images was assessed for different sets of TR,TE_1,TE_2,BW (Tab.1). Other imaging parameters were: flip angle (FA)=7°, in-plane-resolution=0.75×0.75mm², slice-thickness=3mm, matrix=256×256, FoV=192×192mm², number-of-slices=40. For each parameter set, CNRs between posterior-cruciate (pc) ligament and menisci and muscle tissue were determined in subtraction images. With an optimal parameter set (maximizing CNR) established, measurements with FA ranging from 1-45° were performed. For improved depiction of tendon-like structures, water-selective excitation pulses were applied.

Tab. 1: Parameter sets in sub-DESS sequence used for the variation of the contrast in S^+ and S^- images.

Meas. #	TR (ms)	TE_1 (ms)	TE_2 (ms)	BW (Hz/Pixel)
1	6.14	1.2	11.08	575
2	6.86	1.3	12.48	444
3	7.50	1.4	13.60	369
4	8.22	1.5	14.94	310
5	8.94	1.6	16.28	268
6	9.60	1.7	17.50	238
7	10.32	1.8	18.84	212
8	10.96	1.9	20.02	193
9	11.68	2.0	21.36	176

Results: Contrast behavior of the tissue pairs (pc-ligament vs. muscle) and (meniscus vs. muscle) for measurements with different parameter sets are depicted in Fig.1. The time-normalized-CNR tend to decline with increasing TE_1 (Fig.1a) and the maximum contrast is obtained at approximately 8° (Fig.1b). The parameter set of FA=8°,TR=6.14ms,TE_1=1.2ms,TE_2=11.08ms, BW=575Hz/pixel was selected as an appropriate choice providing high signal intensity of fibrous tissue and high contrast to other tissues. Fig.2 presents images recorded with the optimized sub-DESS sequence. Images acquired using water-selective pulses are shown in Fig.3.

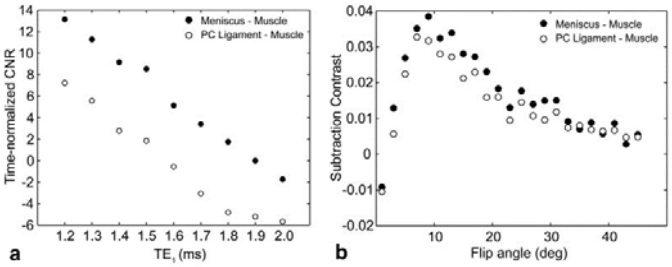

Fig. 1: Time-normalized CNR values **(a)** and subtracrion contrast **(b)** for posterior cruciate ligament (pc) vs. muscle and meniscus vs. muscle in a healthy volunteer obtained using a sub-DESS sequence. Maximum CNR can be achieved with the parameter set: TR = 6.14 ms, TE_1 = 1.2 ms, TE_2 = 11.08 ms, and BW = 575 Hz/pixel. The contrast in the subtraction image is maximal at approximately of 8°.

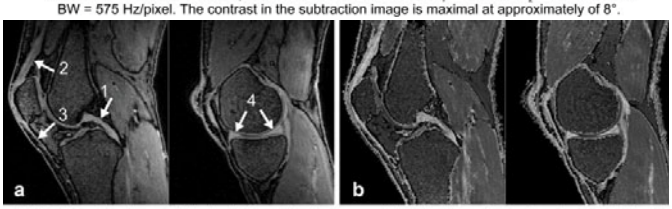

Fig. 2: Subtraction images (a) and relative subtraction images (b) of the knee of a healthy volunteer obtained with a sub-DESS sequence using optimal parameter set. Posterior cruciate ligament (1), quadriceps (2), patellar tendon (3), posterior and anterior horn of the medial meniscus (4) are visualized as areas with "positive" signal intensity in the both types of subtraction images.

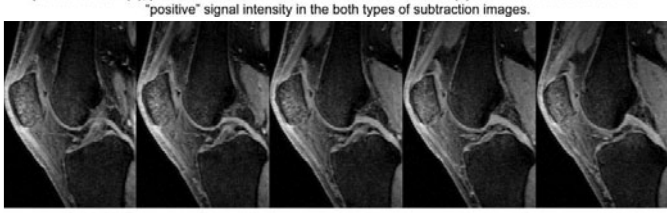

Fig. 3: Sub-DESS subtraction images of a healthy volunteer acquired with WE pulses. Posterior and anterior cruciate ligament, quadriceps and patellar tendon could be clearly delineated in consecutive slices of the knee.

Discussion/Conclusion: The presented sub-DESS approach is based on a common Cartesian data sampling and was adapted in order to achieve high signal-to-noise-ratio per measuring time from fibrous tissue and good contrast to adjacent tissues (fat, musculature) at the same time.
References:
[1]H.Bruder,MRM,1988;7:35-42.
[2]P.A.Hardy,JMRI,1996;6:329-35.
[3]O.Bieri,MRM,2012;doi:10.1002/mrm.24154

677

Variable Flip Angle Schedules in bSSFP Imaging for Fourier Decomposition MRI

D.M.R. Corteville[1], Å. Kjørstad[1], F.G. Zöllner[1], C. Fink[2], L.R. Schad[1]
[1]Computer Assisted Clinical Medicine, Heidelberg University, Mannheim/GERMANY, [2]Institut für Klinische Radiologie und Nuklearmedizin, Heidelberg University, Mannheim/GERMANY

Purpose/Introduction: Proton pulmonary imaging using the recently proposed fourier decomposition (FD) technique [1,2] requires an imaging sequence with a rapid acquisition rate. Best suited for these cases are balanced steady-state free precession (bSSFP) sequences. However due to the high flip angle required to obtain signal from the lung parenchyma [3] the specific absorption rate (SAR) limits the signal to noise ratio (SNR) and the usability of the technique at higher field strengths. One possible approach to address this problem is the variation of flip angles in the pulse sequence, which was successfully used for other modalities already [4]. The purpose of this study was to evaluate the capabilities of variable flip angle bSSFP sequences for proton FD pulmonary imaging.
Subjects and Methods: Measurements were performed on two healthy male volunteers using a 1.5T MR scanner (Magnetom Avanto, Siemens Healthcare, Germany).
An untriggered time resolved 2D-bSSFP sequence was used. The difference in the pulse patterns between the standard and the modified sequence are outlined in Figure 1.

Figure 1. RF excitation schemes.
Section 1 marks the 10 step Kaiser Bessel preparation ramp.
Section 2 and 3 sketch the position of the k-space center and periphery.

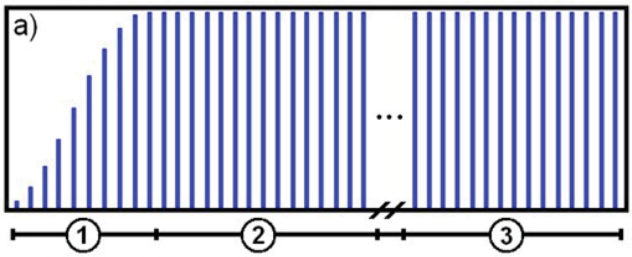

a) Standard bSSFP sequence.

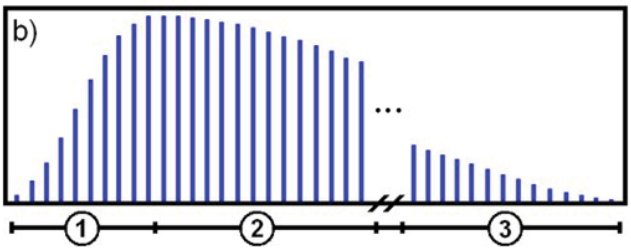

b) Modified bSSFP sequence.
The amplitude of the excitation pulses is reduced from 90° to 0° over the course of the acquisition of an image. To maintain the steady state the ramp down follows the Kaiser Bessel Scheme as well.

The imaging parameters of the utilized sequence were as follows: TR/TE/TA = 1.90/0.95/260ms, acquisition mode = centric, ST = 15mm, FOV = 400mm², matrix = 128x128, bandwidth = 1302Hz/px, total acquisition time = 1minute.

Results: The standard sequence used a flip angle of 75° and was limited by SAR restrictions requiring an additional wait time of 351ms between measurements. The modified sequence was able to achieve flip angles of 90° and reduce the additional wait time to 246ms. Figure 2 shows example images acquired with the standard and the modified sequence.

Figure 2. Example images acquired with the bSSFP sequences.

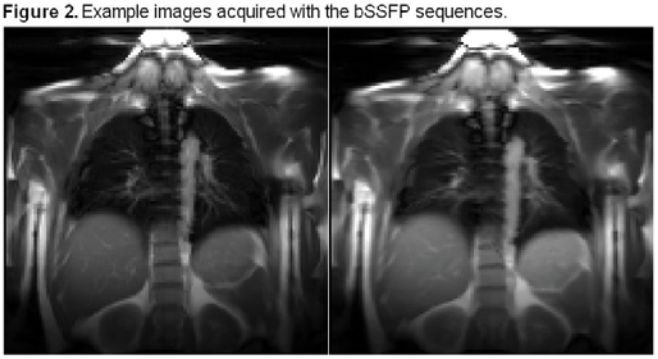

Standard bSSFP Modified bSSFP

Increasing the flip angle from 75° to 90° in the center of k-space resulted in an increase of the signal to noise ratio (SNR) by 21% in the lung parenchyma, while additionally it was possibly to increase the acquisition speed by 16%. The ventilation maps acquired with the FD method are shown in Figure 3.

Figure 3. Ventilition maps of the manually segmented lung.

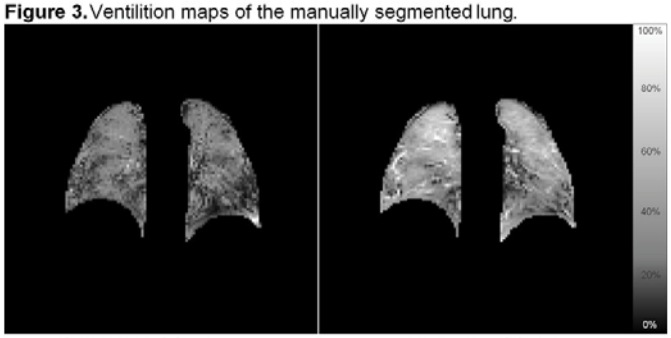

Standard bSSFP Modified bSSFP

Discussion/Conclusion: The modified sequence was able to both improve the SNR and the sampling speed compared to the standard sequence. The expected drawback of signal loss in small structures is barely observable in the source images and not visible in the ventilation maps acquired with the FD method.

References:

[1]Deimling M. et al. Proc. of ISMRM 2008, p.2202.
[2]Bauman G. et al. Magn. Reson. Med. 2009,62(3):656-664.
[3]Zapke M. et al. Resp. Research 2006,7:106.
[4]Paul D. et al. Magn. Reson. Imaging 2009,27:933–941.

Acknowledgments This work was supported by EU FP7 Pi-net.

678

Active Feedback MR Imaging for Early Tumor Detection

Z. Li[1], C. Hsu[2], N. Dimitrov[1], L. Hwang[2], Y. Lin[1]
[1]Department of Chemistry and Biochemistry, University of California, Los Angeles, Los Angeles/CA/UNITED STATES OF AMERICA, [2]Department of Chemistry, National Taiwan University, Taipei/TAIWAN

Purpose/Introduction: Early detection of high-grade malignancy, such as pancreatic cancers (PC) and glioblastoma multiforme (GBM), using enhanced MRI techniques significantly increases not only the treatment options available, but also the patients' survival rate. For this purpose, a conceptually new approach, termed "Active-Feedback MR", was developed. An active feedback electronic device was homebuilt to implement active-feedback pulse sequences to generate avalanching spin amplification (Fig. 1), which enhances the weak magnetic-field perturbations from magnetic nanoparticles in targeted PC (Fig. 2) or malignant physiological conditions in GBM (Fig. 3).

Subjects and Methods: The general principles of the "Active-Feedback MR" can be found in our publications [1-4]. Here, its specific applications to early tumor detection were developed and demonstrated [5,6]. First, an active-feedback electronic device was home-built to generate feedback fields from the received FID current (Fig. 1). The device is to filter, phase shift, and amplify the signal from the receiver coils and then retransmit the modified signal into the RF transmission coil, with adjustable and programmable feedback phases and gains controlld by the console. Next, an active-feedback pulse sequence was developed for early tumor detection (Fig. 3A) and was statistically tested on *in vivo* mice tumor models (Figs. 2 and 3). In essence, the enhanced tumor contrast arises from "selective self-excitation" and "fixed-point dynamics" generated by the bulk water 1H under active feedback fields.

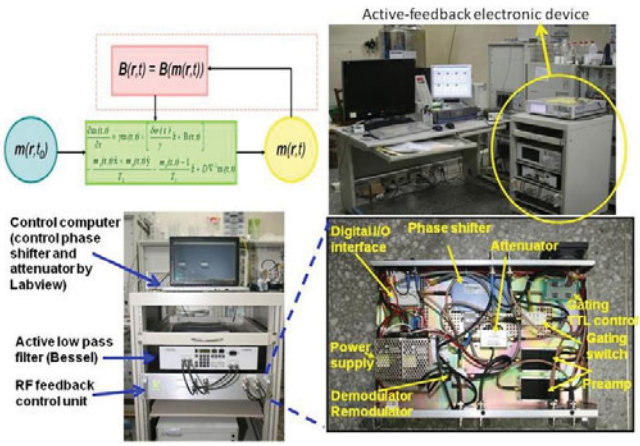

Results: Early PC Detection: Anti-CA 19-9 antibodies were conjugated to NH2-PEG-coated magnetic nanoparticles. *In vivo* images of human PC from nude mouse xenografts (Fig. 2A) show that, while T2-weighted image cannot clearly locate the magnetic nanoparticles (Fig. 2B), the active-feedback images (Fig. 2C) successfully highlight the magnetic nanoparticles with a close correlation with iron-stained histopathology (Fig. 2D).

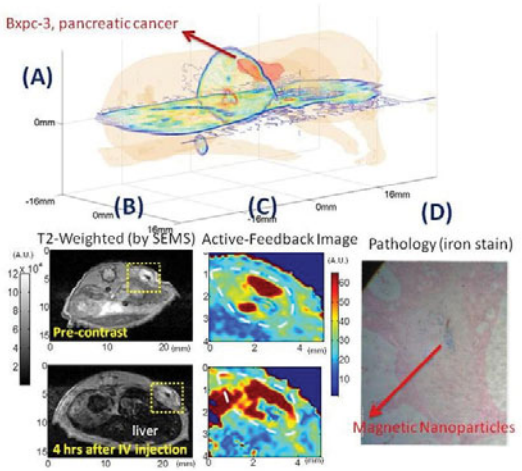

Early GBM Detection: Stage-1 orthotopic GBM mouse models infected with human U87 cell-line were imaged. Our active-feedback images (Fig. 3C) and decay constant mapping (Fig. 3B) provide 4-5 times of improvements in GBM contrast than conventional spin echo or CPMG methods through sensitively imaging the susceptibility variations due to irregular water and deoxyhemoglobin contents.

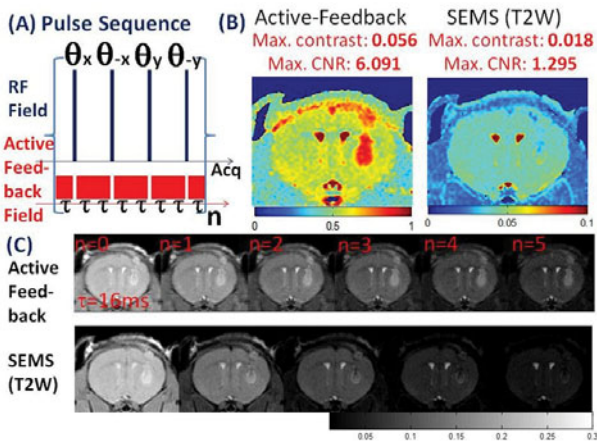

Discussion/Conclusion: *In vivo* PC and GBM mouse models validated the superior contrast/sensitivity and robustness of the "Active-Feedback MR" for early tumor detection. Statistical results at various cancer stages and alternative active-feedback pulse sequences with improved performance will also be presented.

References:

[1] Science 290, 118 (2000) [2] Magn. Reson. Med. 56, 776 (2006) [3] Magn. Reson. Med. 61, 925 (2009) [4] J. Phys. Chem. B 110, 22071 (2006) [5] MAGMA submitted [6] Manuscript submitted

679

Globally optimal design of spatial selectivity for accelerated parallel transmit excitation

K. Vahedipour[1], N.J. Shah[2]
[1]*INM-4 Medical Imaging Physics, Forschungszentrum Juelich, Juelich/GERMANY,* [2]*Department of Neurology, RWTH Aachen University, JARA, Aachen/GERMANY*

Purpose/Introduction:

$$\mathbf{m}_T = R_n \cdot R_{n+1} \cdot \cdots \cdot R_2 \cdot R_1 \mathbf{m}_0$$

The design of pulses for spatially selective excitations beyond 90 degrees has been a hot topic for ultra-high-field MRI. The difficulties arise from the fact that unlike in the small tip angle domain (STA)[1], the non-linear behaviour of the spins cannot be estimated in a general case. Optimisation algorithms have been proposed which are generally seeded with the STA solution; a solution, which is produced with the most opposed assumptions one could imagine. We propose here the use of a modern method of theoretical informatics for best describing the non-linear dynamics plugged into a global search algorithm. We present results from parallel transmit excitation of 150 degrees which display 80% less global energy deposition than the optimal control solution.

Subjects and Methods: The large-tip angle (LTA), selective excitation is analogously to the STA regime performed by the simultaneous action of gradient and arbitrary number of transmitters.
Generally, an STA solution is used for initialising, search algorithm such as NLCG or Optimal control to achieve LTA excitations while some control was used to minimise global or local SAR [2,3].
In order to be able to engage in a global and self-organised optimisation search, one needs a paradigmatic change in computing the derivatives of the 3D SLR[4] spin evolution function [Fig 1], while not neglecting Mz.
We propose the use of automatic derivatives (AD)[5], not to be mistaken with analytic or numeric derivatives together with SOMA[6], an evolutionary optimisation algorithm.
AD is able to compute Hessian matrices of functions of many thousand unknowns to desired precision.
dcc [7] was used to derive the C-code representing [Fig 2] to obtain the Hessian of a 8-channel 3-fold accelerated LTA excitation with 382 time samples (i.e. 6112 unknowns) to reduce the global energy deposition in a water phantom by 83% without prolonging the pulses' durations. Pulse calculation took for 256 search seeds 30s.
Results: The flip angle map (b, 8% NRMSE) of the 150 degree excitation intended along with the pattern (a) are depicted in Fig 2.
Discussion/Conclusion: A method is proposed for LTA pulse design. The code and its Hessian are provided for the conference.
References:

[1] Pauly et al, JMR 1988, 81(1), 43-56
[2] Xu et al, MRM 2008, 59(3), 547–560
[3] Grissom et al, MRM 2008, 59(4), 779–787
[4] Naumann, Math Program 2008, 112(2), 427-441
[5] Zelinka et al, 13th Int Conf Proc Control, High Tatras, Slovakia, 2001
[6] Naumann, The Art of Differentiating computer programs, ISBN 9781611972061

680

Combining ZOOPPA and blipped CAIPIRINHA for Diffusion Weighted Imaging at 7T

C. Eichner[1], K. Setsompop[2], A. Anwander[1], T. Feiweier[3], S. Cauley[2], H. Bhat[4], R. Turner[1], L.L. Wald[2], R.M. Heidemann[5]
[1]Neurophysics, Max Planck Institute for Human Cognitive and Brain Sciences, Leipzig/GERMANY, [2]A. Martinos Center for Biomedical Imaging, Massachusetts General Hospital, Charlestown/UNITED STATES OF AMERICA, [3]Healthcare Sector, Siemens, Erlangen/GERMANY, [4]Healthcare Sector, Siemens, Malvern/PA/UNITED STATES OF AMERICA, [5]Max Planck Institute for Human Cognitive and Brain Sciences, Leipzig/GERMANY

Purpose/Introduction: Sub-millimetre isotropic-resolution diffusion MRI (dMRI) of in-vivo human brain is feasible at 7T [1]. Combining zoomed and parallel imaging (ZOOPPA) enables high acceleration factors (AF) with low g-factor penalty, but the long acquisition time (TA) of about an hour (4 averages) limits this technique. TA can be shortened by recording multiple slices at the same time, unfolding them using parallel imaging [2]. The CAIPIRINHA approach reduces the g-factor noise penalty [3], and was recently applied to EPI acquisitions [4]. This study combines ZOOPPA [1] and blipped CAIPIRINHA [4] to obtain high-spatial and high-angular resolution dMRI.
Subjects and Methods: Experiments were performed on a 7T whole-body MR scanner (MAGNETOM 7T, Siemens AG, Healthcare Sector, Erlangen, Germany) with gradients up to 70mT/m. A 24-element phased-array RF head coil (Nova Medical, USA) was used. A Stejskal-Tanner diffusion-weighted EPI sequence [5] was modified to employ ZOOPPA and blipped CAIPIRINHA. RF-pulses were calculated using a Shinnar-Le Roux algorithm and VERSE to reduce energy deposition. In ZOOPPA, the overall AF is the product of the zoomed AF_{ZOOM} and the parallel imaging AF_{PPA}. Different in-plane AFs were tested using a spherical oil phantom (Fig 1). In-vivo diffusion-weighted images with isotropic resolution of 1mm were acquired using 4 averages of 60 diffusion directions with a b-value of 1000s/mm², 7 interspersed b0 images, a Simultaneous Multi-Slice (SMS) factor 3 and AF=AFppa*AFzoom=2*1.4. Multiple fibre orientations were modelled with constrained spherical deconvolution [6] for each voxel, followed by streamline-tracking using MRtrix.

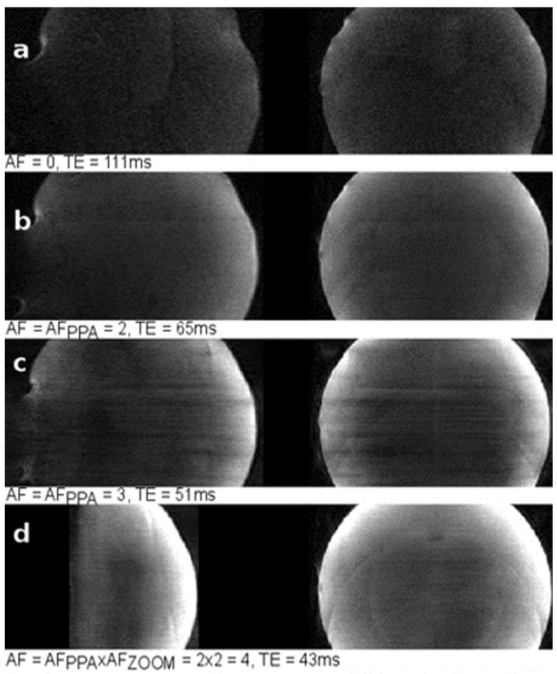

Figure 1: Saggital (left) and axial (right) view of threefold simultaneous multislice acquisition of an oil-filled spherical phantom with different AFs. Imaging parameters: b0 image, 1mm isotropic resolution, SMS=3, FoV=180x180 (180x90 for AF_{ZOOM}=2), TR=11400, BW=1190 Hz/Px. 75% Partial Fourier

Results: With no in-plane acceleration, TE=111ms (Fig.1a). Accelerating the acquisition (Fig.1b-1d) shortens TE. However, a high AF_{PPA}=3 in combination with blipped CAIPIRINHA gives imperfect slice separation (Fig.1c). Use of ZOOPPA with AF_{PPA}=2 and AF_{ZOOM}=2 addresses this problem, with a lower g-factor than GRAPPA alone. ZOOPPA therefore gives better slice separation, even with AF=4 (Fig.1d). However, the multislice pulses increase in amplitude with the number of simultaneously excited slices. The resultant significantly higher power deposition limits the minimal TR.

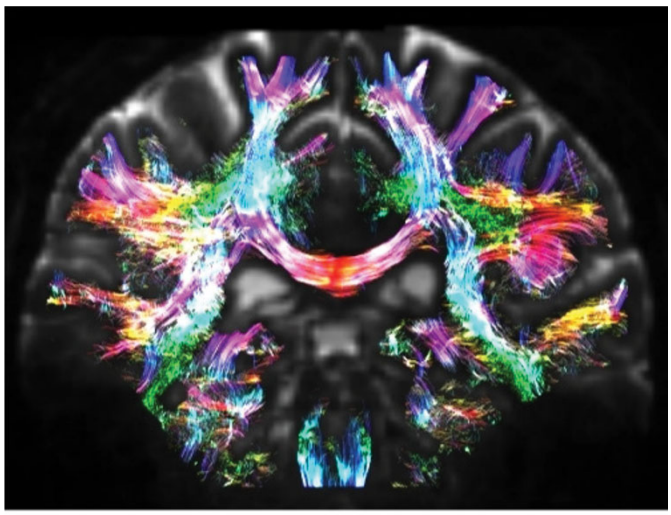

Figure 2: Diffusion-weighted data with the following imaging parameters SMS=3, 99 axial slices, TR=11400ms, TE=66ms, PAT=2, AF_{ZOOM}=1.4, BW=1112Hz/Px, FoV=180x130mm². Whole-brain tracking of $5x10^5$ streamlines in white matter, displayed in 1mm coronal slap.

Discussion/Conclusion: For high-resolution dMRI at 7T, high in-plane AFs are essential for short TE. TA can be shortened for high-resolution dMRI at 7T with ZOOPPA using blipped CAIPIRINHA. Optimized sequence code will reduce TA for this ZOOPPA protocol to approx. 11 minutes per average. Since SAR is the limiting factor, the use of multislice pulses with a lower energy deposition as introduced by Norris and colleagues [8] will be highly beneficial.
References:
[1]HeidemannRM.NeuroImage2012;60:967-78.[2]LarkmanD.JMRI2001;13:313-7.[3]BreuerF.etAl.MRM2005;53:684-91.[4]SetsompopK.MRM2011;67:1210–1224.[5]StejskalE.andTannerJ.J.Chem.Phys.1965;42:288.[6]TournierJ.D.NeuroImage2007;35:1459-72.[7]CalamanteF.NeuroImage2011;56:1259-1266.[8]NorrisD.MRM2011;66:1234-40.

681

Density weighted echo planar imaging for optimized SNR and shortened effective echo time

M. Zeller[1], A. Müller[1], M. Gutberlet[2], D. Stäb[1], D. Hahn[1], H. Köstler[1]
[1]Institute of Radiology, University of Würzburg, Würzburg/GERMANY, [2]Radiology, Hannover Medical School, Hannover/GERMANY

Purpose/Introduction: Echo planar imaging (EPI) intrinsically provides T_2^* weighting and is therefore the first choice for functional MRI. However, the short acquisition time limits the achievable signal to noise-ratio (SNR). Retrospectively filtering the k-space proportional to the signal decay improves the SNR, yet amplifies sidelobes of the point spread function (PSF) leading to Gibbs ringing artifacts. On the other hand, filtering with smoothing functions (e.g. a Kaiser window) reduces the side lobes, but does not provide optimal SNR. Density weighting (DW, [1-4]) is able to combine the advantages of both filters: The Kaiser window for artifact suppression is achieved by acquiring the k-space in phase encoding direction with a non-Cartesian trajectory, while filtering proportional to the T_2^* decay allows for optimal SNR.
Subjects and Methods: Cartesian and DW phantom and in-vivo images were acquired on a 3 T scanner (Siemens Magnetom Trio, 12-channel head

coil) with a single-shot EPI sequence (TR: 2 s, slices: 16, TA: 125 ms, matrix: 128x128, resolution: 1.7x1.7x2.5 mm^3). DW was incorporated using a k-space trajectory that results in a Kaiser window function after retrospective filtering proportional to a signal decay with T_2^*=50 ms. The minimum k-space density was limited to a factor of 0.5. DW yielded an effective echo time $TE_{eff,DW}$=32 ms compared to $TE_{eff,Cart}$=54 ms for Cartesian acquisition (see Figure 1). Image reconstruction was performed using a non-Cartesian GRAPPA/PARS algorithm [2]. Off-resonance effects were corrected utilizing a multifrequency reconstruction method [5]. For SNR assessment, a pseudo multiple replica technique was employed [6].

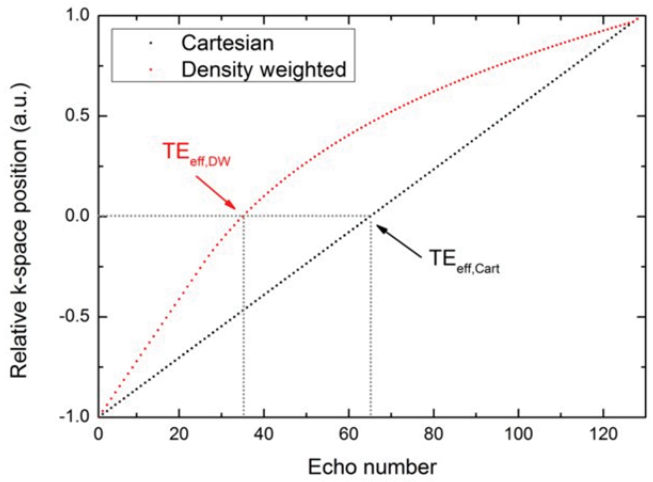

Figure 1 k-space position as a function of the echo number for Cartesian acquisition (black) and density weighting (red). Because of the reduced sampling density at the beginning of the echo train, the k-space center is reached at earlier echoes with density weighting, resulting in a shorter effective echo time $TE_{eff,DW}$.

Results: With respect to Cartesian acquisitions with identical spatial resolution and measurement time, DW resulted in an average SNR increase of (30±3) % for phantom and (30±8) % for in-vivo images (Figure 2). In addition, the application of DW shortened TE_{eff} and reduced the PSF side lobes (Figure 3).

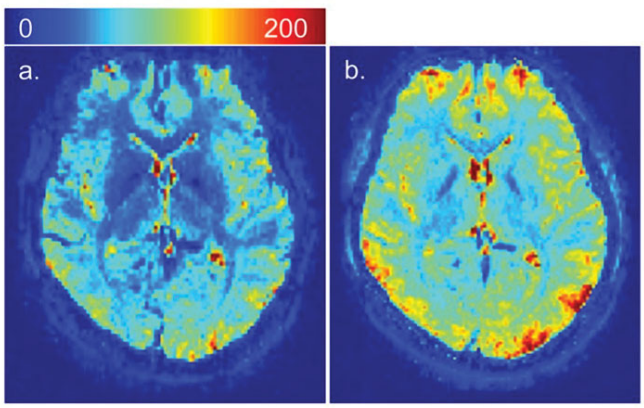

Figure 2 SNR maps of one selected slice for Cartesian (a.) and density weighted acquisition (b.) illustrating the SNR advantage of density weighting throughout the whole brain.

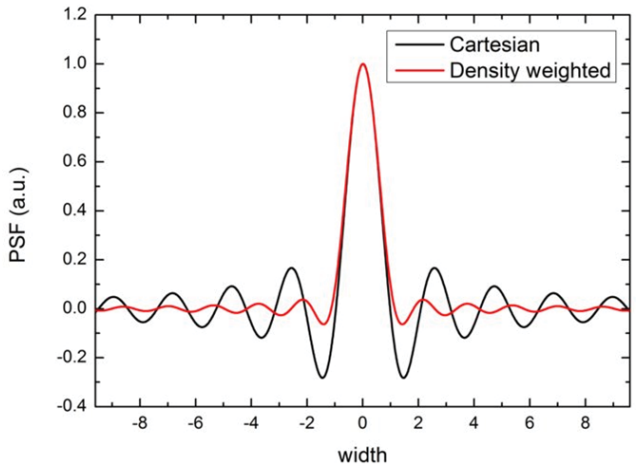

Figure 3 Comparison of the PSFs achieved with standard Cartesian acquisition (black) and density weighting (red). The side lobes of the density weighted PSF are significantly reduced.

Discussion/Conclusion: Employing DW in EPI allows imaging with optimal SNR, reduced PSF side lobes and shorter echo time compared to Cartesian acquisition. Thus fMRI BOLD sensitivity in regions with short T_2^*, especially at high field strength, is expected to profit from DW.

References:

[1] Greiser et al., 2003, MRM, *50*(6)
[2] Geier et al., 2007, MAGMA, *20*(1)
[3] Gutberlet et al., 2010, JMRI, *28*(3)
[4] Zeller et al., Proceedings ESMRMB 2011, 608
[5] Man et al., 1997, MRM, *37*(5)
[6] Robson et al., 2008, MRM, *60*(4)

682

K-Space Weighted Acquisition for High-Resolution Imaging

R. Pohmann[1], K. Scheffler[2]
[1]*Magnetic Resonance Center, Max-Planck-Institute for Biological Cybernetics, Tübingen/GERMANY,* [2]*Biomedical Magnetic Resonance, University Tübingen, Tübingen/GERMANY*

Purpose/Introduction: K-space weighting by acquiring different numbers of averages depending on position in k-space [1,2] is a well-known and often-used technique to avoid signal contamination due to the the unfavorable shape of the point-spread function (PSF) in chemical shift imaging. In addition, it is well-known that this technique can improve the apparent SNR by avoiding negative signal contributions from other regions of the sample [3]. This advantage, however, has so far barely been used in imaging, mainly because it requires averaging [4]. For high-resolution images, where averaging is anyway necessary for SNR reasons, k-space weighted acquisition can help to improve resolution and SNR without sacrificing scan time.

Subjects and Methods: To demonstrate the SNR gain that is possible by k-space weighted acquisition, a 3D-FLASH sequence with weighting in both phase encode directions was implemented. The scheme of the radial weighting function was adjusted to yield equal resolution in the same scan time as a standard FLASH sequence with otherwise identical parameters.

Results: Figure 1 shows a comparison of PSFs of the weighted and unweighted sequences. While the width of the PSF is equal in both cases, implying equal spatial resolution, signal contributions from outside the voxel are strongly suppressed by weighted acquisition, resulting in reduced Gibbs-ringing and improved apparent SNR.

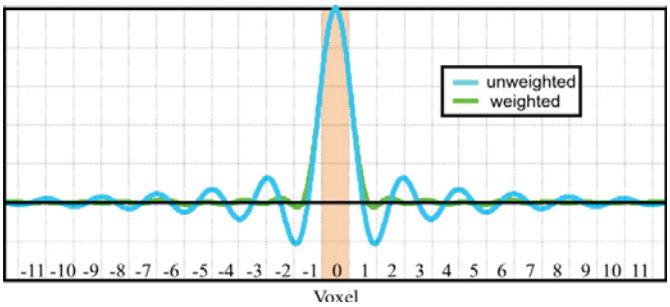

Fig. 1: PSF of the central 24 voxels of the unweighted and weighted sequences. The identical width of the central peak indicates equal spatial resolution.

Images from a phantom (Figs. 2,3) illustrate the reduced Gibbs-ringing in phase direction, while yielding a 30% increased SNR within the same scan time.

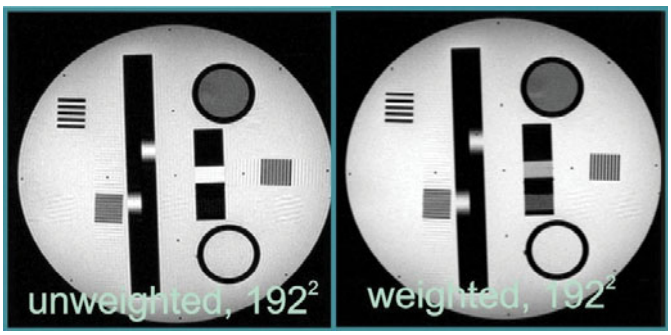

Fig. 2: FLASH images with a standard unweighted sequence (192×192×32, 3 averages), and a weighted sequence with equal nominal resolution, number of phase encoding steps, and imaging parameters.

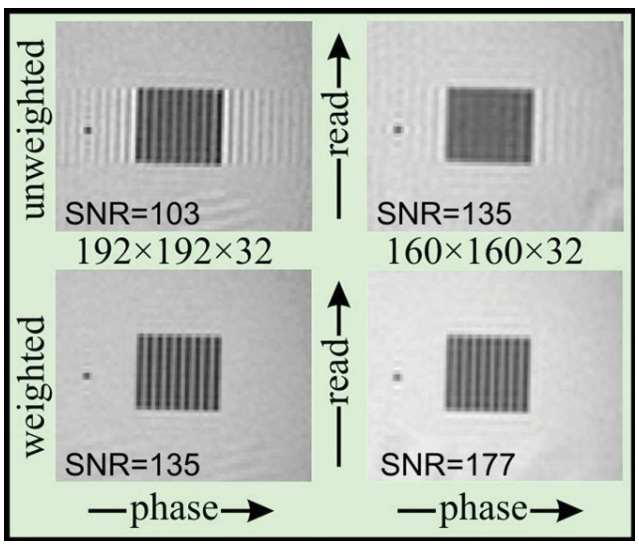

Fig. 3: Zoomed images with two resolutions and equal total duration for weighted and unweighted sequences. The visibility of the grid is at least as good in weighted as in unweighted sequences, demonstrating the unchanged resolution. The SNR is significantly improved in the weighted images. Since weighting is only applied in the phase direction, the vertical ringing is not changed.

Discussion/Conclusion: For high-resolution imaging, where averaging is required for SNR-reasons, k-space weighted acquisition can help to significantly improve SNR and image quality with no extra cost in scan time.

References:

[1] Mareci, Brooker, JMR **57** (1984)
[2] Garwood et al: JMR **65** (1985)
[3] Pohmann, von Kienlin, MRM **45** (2001)
[4] Geier, Hahn, Köstler, MAGMA **20** (2007)

683

Optimization of Compressed Sensing/RARE Combining Acquisition Schemes

M. Naeyaert[1], J. Aelterman[2], J. Van Audekerke[1], K. Claes[1], A. Van Der Linden[1], J. Sijbers[3], M. Verhoye[1]
[1]Biomedical sciences, Bio-Imaging Lab, University of Antwerp, Wilrijk/BELGIUM, [2]TELIN-IPI, Ghent University, Ghent/BELGIUM, [3]IBBT - Vision Lab, University of Antwerp, Antwerp/BELGIUM

Purpose/Introduction: While numerous Compressed Sensing (CS) reconstruction algorithms have been developed, little regard has been given to optimized sampling sequences for these methods. We investigated possible sequences for combining the Rapid Acquisition with Repeated Echoes (RARE) sequence with CS, leading to faster acquisition schemes. The properties of CS could allow for a mitigation of RARE specific artifacts.

Subjects and Methods: A Cartesian, 50% undersampled CS acquisition was made by undersampling the phase lines. 25%, 32% or 40% of the central phase lines were sampled, while the remaining percentage was randomly sampled at the periphery, according to a quadratically weighted chance (1). For RARE acquisition, the lines were ordered into blocks which should be recorded at the same echo time (fig. 1a). A variation of this scheme with the blocks in the centre ordered symmetrically around the centre was also considered . This prevents intensity variations too close near the centre of k-space (fig. 1b).

K-space data was recorded on a 7T Pharmascan (Bruker, Ettlingen) using an MSME and a RARE acquisition with a fruit as a phantom. TE=46.06 ms, TE_min=11.51ms, TR=4s, ETL=8, FOV=(6cm)^2, 256x256 image size. The MSME k-space data was used for simulating the RARE+CS acquisition by taking the appropriate k-space lines from k-spaces recorded at the appropriate echo times. For reconstruction of the RARE+CS data, the COMPASS algorithm was used (2).

Images were compared against the MSME image using peak signal-to-noise ratio (PSNR), Structural SIMilarity (SSIM) (3) and visual inspection.

Results: Figure 2 shows PSNR and SSIM values for the two types of sampling scheme and different central sampling percentages. It is clear that the symmetrical variation gives better results, while the central sampling percentage has a further effect on the image quality, as is confirmed by visual inspection (fig. 3).

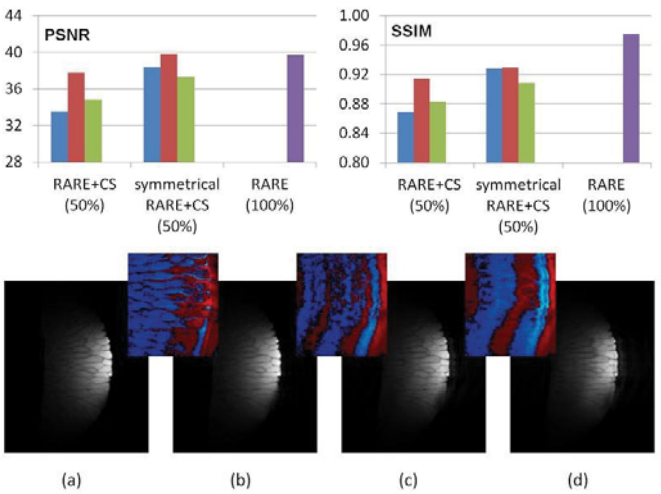

Discussion/Conclusion: The central sampling percentage is an important parameter when deciding on a CS sampling scheme, and should be easy to calculate beforehand from a few simple parameters such as dimensions of the object, FOV and in-plane resolution. Moreover, the scheme should be adjusted so that ET-block boundaries are symmetrical with respect to the centre of k-space. Further refinement of the method will be done, where the effect of mixing lines at different echo times will be investigated, as well as real acquisitions using these schemes.

References:
(1) Lustig, M., 2007, MRM: 1182–1195
(2) Aelterman, J., 2010 IEEE ICIP: 1653 – 1656
(3) Wang, Z., 2004 IEEE Trans.Image.Process, 600-612

684

Matched Filter Anatomical Brain Imaging

L. Kasper[1], M. Haeberlin[1], B.J. Wilm[1], K.E. Stephan[1], K.P. Pruessmann[2]
[1]University and ETH Zurich, Institute for Biomedical Engineering, Zurich/SWITZERLAND, [2]Institute for Biomedical Engineering, University and ETH Zurich, Zurich/SWITZERLAND

Purpose/Introduction: •Ringing filters are commonly used in post-processing of anatomical MR images to suppress Gibb's artifact.
•This smoothing operation translates into a re-weighting of measured samples in Fourier k-space, usually over-emphasizing central and disregarding peripheral samples, though both initially exhibit identical noise content.
•According to the matched filter theorem, this leads to suboptimal SNR, because signal is optimally sampled, if the acquisition density in k-space is equal to the effective filter[1]. •We propose a 2D-matched filter gradient echo acquisition scheme to match a Gaussian filter for ringing suppression.

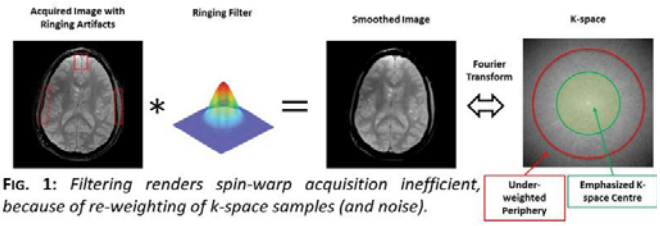

FIG. 1: *Filtering renders spin-warp acquisition inefficient, because of re-weighting of k-space samples (and noise).*

Subjects and Methods: •2D matched filter trajectories augment previous approaches which use 1D-density weighting in phase encoding direction: There, weighting was achieved by variable spacing of k-space lines.[2]
•We additionally introduce a gradient velocity modulation in measurement direction to mimic a Gaussian density: $G(t)=C\cdot\exp(\mathrm{erf}^{-1}(A\cdot t+B))$ (A,B,C=const.)
•As this is demanding for the gradient system, we concurrently monitor the gradients and encoding higher order magnetic fields using a 11-channel T/R 19F NMR field probe-setup.[3],[4] •Data of a healthy volunteer (10 dynamics) was acquired on a Philips Achieva 3 T system using an 8-channel SENSE head coil.

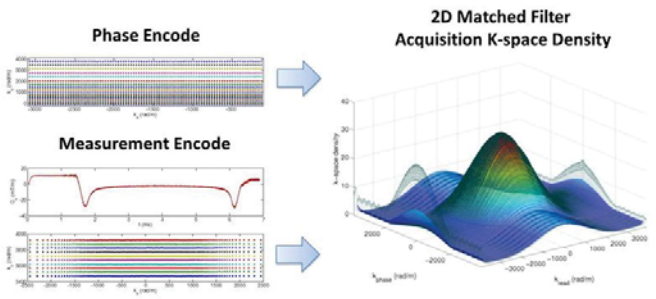

FIG. 2: *A combined modulation of spacing between and gradient velocity within phase encoding lines enables 2D matched filter weighting in k-space.*

Results: •Starting from a uniform acquisition with 0.8 mm resolution and a Gaussian smoothing of 2 mm FWHM, we evaluated different degrees of matched filter weighting (green curve, SNR maps):
•Both, the 1D-matched filter weighting in readout- and phase-encoding direction increased the SNR in the smoothed images by about 30 %. •A combined 2D-matched filter weighting as described above yields an overall SNR increase of 50 %, which can be slightly improved by different density approximations respecting the gradient limitations (combined plateau). •The matching of acquisition weighting and ringing filter is essential, for SNR gain is greatly reduced, if a non-matching (or no) filter is used (cyan, red and black curve). Thus, sampling the k-space center more densely only increases SNR, if it matches the desired post-processing step.

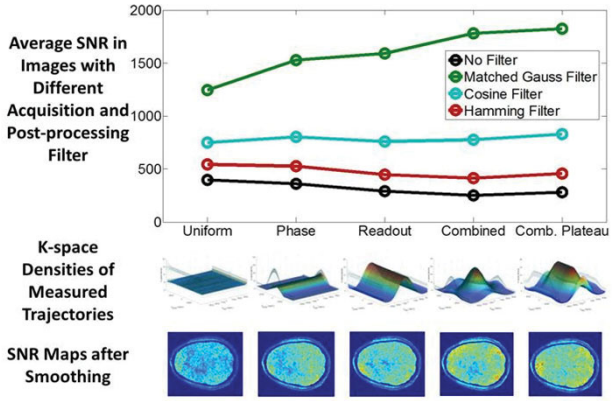

FIG. 3: *SNR in brain images increases with different degrees of matched-filter acquisition weighting, but only if the applied post-processing ringing filter is indeed matched to that acquisition density.*

Discussion/Conclusion: •2D-matched filter spin-warp acquisition improves SNR in-vivo by up to 50 %, if the applied post-processing filter matches the k-space weighting of the trajectory.
•This method is easily adaptable towards other ringing filters (e.g. Hamming) and may become a versatile tool in high-resolution imaging due to its SNR-optimality.

References:
[1] Kasper, L et al, 2011, *Proc. Proc. ISMRM. 11*, p. 1634
[2] Greiser, A & von Kienlin, M, 2003, *MRM 50*
[3] Barmet, C et al, 2010, *Proc. ISMRM. 10*, p. 216
[4] Barmet, C et al, 2008, *MRM 60*

685

Comparison of multi echo approaches in ASL T2 imaging

J. Kramme, J. Gregori, M. Günther
MEVIS, Fraunhofer MEVIS, Bremen/GERMANY

Purpose/Introduction: T2 measurements of the difference signal in Arterial Spin Labeling (ASL) experiments can be improved with a multi-TE 3D-GRASE readout, regarding stability as well as signal-to-noise-ratio (SNR) [1]. However, due to time constraints in in-vivo experiments, a tradeoff between the number of acquired echoes and SNR is necessary. In this work, T2 fits with different numbers of echoes obtained with different turbo factors (TF) at constant time are evaluated to find the optimal imaging scheme with regard to stability and measurement time.
Subjects and Methods: T2 experiments were performed on a 3T Siemens scanner with a 20 channel head coil, at two healthy volunteers (male 40 and female 28 years). A 3D-GRASE ASL sequence [2] (figure 1) with a spatial resolution of 5.2x5.0x6.0mm was used.

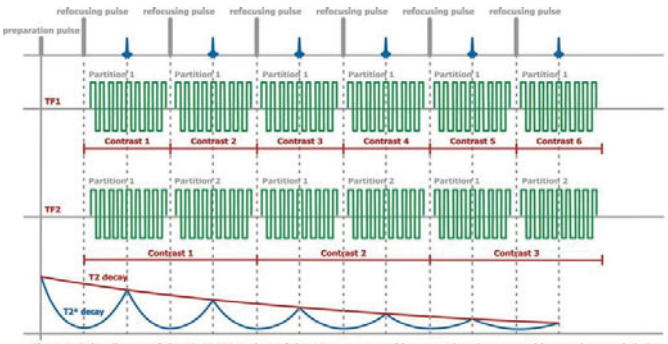

Figure 1: Pulse diagram of the 3D-GRASE readout of the ASL sequence. With every spin echo one partition can be encoded. For example with TF1 (upper row) partition 1 is encoded at six different contrasts. For TF2 (lower row) only three contrasts are encoded since every second refocusing pulse is used to encode partition 2. To encode partition 2 with TF1 the whole experiment needs to be repeated and therefore the measurement time is doubled compared to TF2. On the other hand the echo time with TF1 is half as long as with TF2.

Measurements were performed at a inflow time TI of 1800ms, using refocusing flip angles of 180°. TE was 29ms, the measurement time was kept constant at 2 minutes while varying TF and averages. The different combinations can be found in table1.

	number of echoes	number of averaged images
TF1	12	1
TF2	6	2
TF3	4	3
TF4	3	4
TF6	2	6

Table 1: Number of echoes and averages at different TFs. For TF1, 12 echoes were obtained, whereas in the same echo train length for TF2 half as much echoes are possible, since two refocusing pulses are used for the readout. On the other hand, scan time is halved and a second average becomes possible.

A voxel-wise exponential fit was done in MeVisLab [3] to calculate T2 maps. SNR was calculated by the two region approach [4].

Results: *SNR* increases with higher TFs due to multiple averaging. Its deviation in the difference images is strongest in the first half of the echo train. *Blurring* is significantly increased with higher TF, compare figure 2.

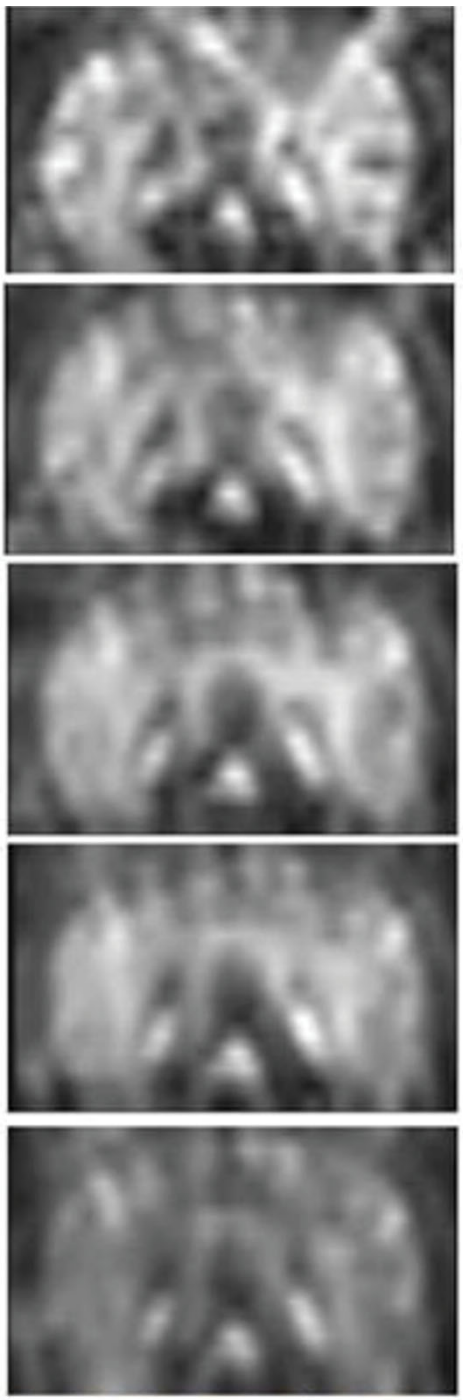

Figure 2: Blurring in z direction. Label image. From top to bottom TF1, TF2, TF3, TF4, TF6

T2 fitting at different TFs: With increasing TF the fluctuations in the T2 values become less. Especially white matter regions with smaller T2 values and therefore faster signal decay profit from multiple averaging, resulting in a more stable T2 fit. For a single average only the first six to eight echoes have intensities clearly distinguishable from noise.

Discussion/Conclusion: Fitting four to six echoes is sufficient for T2 calculation. The longest TE shouldn't exceed 200ms otherwise many averages are

needed for sufficient SNR. In this study the best tradeoff was obtained with TF3, the T2 map is shown in figure3.

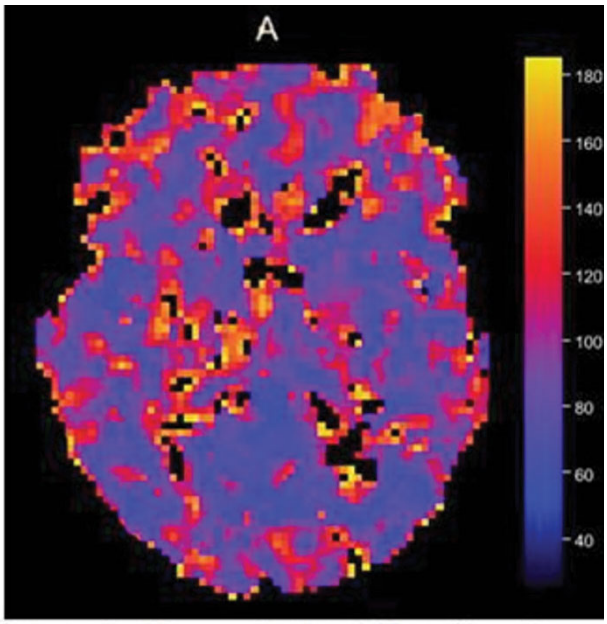

Figure 3: T2 map, TF3 and four fitted echoes

Blurring is stronger with higher TFs. Smaller flip angles for the refocusing pulses can reduce blurring, but T2 values should then be corrected [5]. Choosing an optimal combination of TF, number of echoes and averages makes stable in-vivo T2 measurements possible in a reasonable scan time.

References:
[1]Kramme et al., Proceedings:ISMRM,Stockholm2010,page.1772
[2]Günther et al., Magn Reson Med,2005,54(2):p.491-498.
[3]Ritter et al., Medical image analysis. IEEE pulse,2011,2(6):60–70.
[4]Dietrich et al. Magn Reson Med,2007,26:p.375-385
[5]Kramme et al., Proceedings:ESMRMB CONGRESS 2011,LEIPZIG, Program number:20

686

T_1-corrected Rapid T_2 Estimation Using Double Echo Steady State (DESS)

R. Heule, O. Bieri
Division of Radiological Physics - Department of Radiology and Nuclear Medicine, University of Basel Hospital, Basel/SWITZERLAND

Purpose/Introduction: Double echo steady state (DESS) offers high contrast between cartilage and synovial fluid and thus provides high specificity for the detection of chondral abnormalities (1,2). Recently, rapid T_2 estimation of cartilage was shown to be feasible based on a single morphological DESS scan (3), but becomes independent of T_1 only for flip angles ~ 90°. As a result, DESS-based T_2 quantification is generally biased by T_1 (3). We show that based on a simple rough global T_1 estimator, a considerable reduction in the systematic error of DESS-based T_2 estimation can be achieved. Thus, the proposed method is of high interest for combined morphological and accurate quantitative T_2 imaging of the musculoskeletal system.

Subjects and Methods: Generally, the ratio of the two echo paths (FID and Echo), as acquired with DESS, depends on T_1 and T_2, but becomes independent of T_1 for flip angles ~ 90°, as presented in (3):

$$s(\alpha,T_1,T_2,\ldots) := \frac{S_{Echo}(\alpha,T_1,T_2,\ldots)}{S_{FID}(\alpha,T_1,T_2,\ldots)} \xrightarrow{\alpha\to 90^\circ} \exp\left(\frac{-2\cdot(TR-TE)}{T_2}\right) \qquad Eq.\,[1]$$

Using a simple global estimator for tissues (T_1 ~ 1200 ms), Eq. [1] can be solved for T_2 based on a golden section search.

Results: Simulations reveal that the T_1-related bias for DESS-based T_2 calculation of cartilage can be considerably reduced over a large range of T_1-values (0.5s<T_1<2s) using a global estimator for T_1, as compared to the T_2 estimate derived in the α= 90° limit (Fig. 1). The improvement is particularly evident in the range of low flip angles (15° < α < 30°) as commonly used for morphological DESS imaging, while the two approaches converge in the limit of α = 90°, as expected (see Eq. [1]). The same behavior is observed for in vivo T_2 estimation of cartilage (Fig. 2). Besides the expected T_1-bias reduction in T_2 of about 25% at 15° and 10% at 30°, increased zonal variation between deep and superficial cartilage layers are observed.

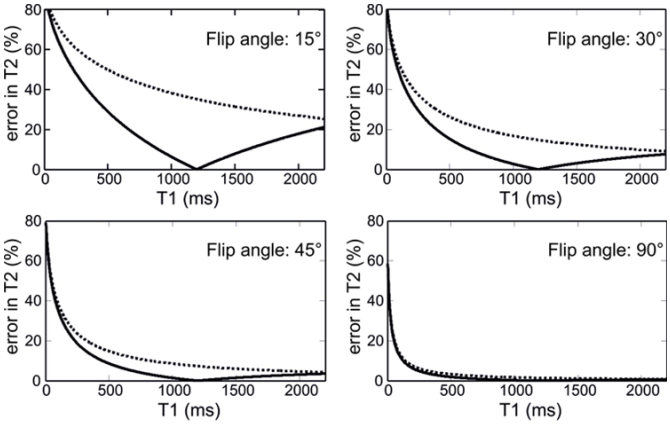

Fig. 1: Plots of the error in the T_2 calculation as a function of T_1 for four different flip angles (15°, 30°, 45°, 90°). Simulation parameters are: TR = 10 ms, true T_2 = 70 ms, global T_1 estimate = 1200 ms. Dotted line: T_2 estimate using Eq. [1] in the limit of α = 90°, see ref. (3). Solid line: T_1-corrected approach.

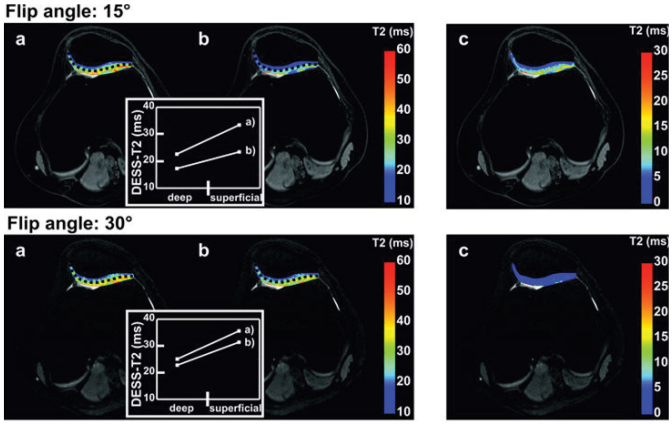

Fig. 2: DESS images of a healthy volunteer with coloured T_2 maps of patellar cartilage in the knee for 15° and 30°. Our T_1-corrected method (**a**) is compared to the T_2 estimate used in ref. (3) (**b**). The dotted black curve divides the patellar cartilage in deep (above) and superficial (below) layers. The zonal gradient in T_2 between these two regions is plotted in the insets. The map in (**c**) shows the absolute difference between (a) and (b).

Discussion/Conclusion: A considerable reduction in the T_1-related bias for DESS-based T_2 estimation can be achieved using a simple global T_1 estimate. Our results emphasize the potential of DESS imaging to combine accurate quantitative T_2 and morphological image analysis of the musculoskeletal system with high resolution.

References:
[1] Eckstein F et al., 2006, Ann Rheum Dis 65:433–441.
[2] Eckstein F et al., 2007, Osteoarthritis Cartilage 15:1326–1332.
[3] Welsch GH et al., 2009, Magn Reson Med 62:544–549.

687

High temporal resolution DCE-MRI with T_2^* compensation for evaluation of the effects of HIFU treatment

I. Jacobs, S.J.C.G. Hectors, G.J. Strijkers, K. Nicolay
Biomedical NMR, Department of Biomedical Engineering, Eindhoven University of Technology, Eindhoven/NETHERLANDS

Purpose/Introduction: DCE-MRI is a valuable tool to evaluate tumor ablation with High Intensity Focused Ultrasound (HIFU), a promising non-invasive treatment. Accuracy of derived pharmacokinetic parameters may be poor if contrast agent induced T2* changes are neglected [1][2]. The aim of this study was to perform high temporal resolution DCE-MRI with T2* compensation. To this aim a dual-gradient echo planar imaging (GE-EPI) based dynamic T1 and T2* mapping protocol was developed. The effect of T2* compensation on dynamic T1 values was investigated and the protocol was used to evaluate HIFU treatment in a murine tumor model.

Subjects and Methods: *In vitro validation*

A DCE-MRI measurement was mimicked by a series of Endorem filled phantoms (30-800 uM) at 6.3T. T1 mapping was performed using a Look-Locker-based EPI (LL-EPI) sequence and dynamic T1 and T2* mapping was performed using a multi-slice dual gradient-echo EPI sequence (TR=1250ms, TE1/TE2=7.5/26.1ms, NA=2, segments=2, flip angle=80°, temporal resolution=5sec.

In vivo application

Tumor-bearing (CT26 colon carcinoma, hind limb) Balb/c mice were subjected to MRI before (n=14), directly after (n=14) and 3 days after (n=7) HIFU ablation (TIPS, Philips). A non-treated control group of 4 animals was included. Two minutes after start of the dynamic acquisition, a Dotarem bolus (0.3 mmol Gd/kg) was injected. Total acquisition time was 30min. A post-contrast single-slice LL-EPI T1 map was made for validation of the dynamic T1 values at t=30min.

Results: *In vitro*

A strongly improved agreement between the dual-gradient echo EPI R1 values and LL-EPI R1 values of the Endorem filled phantoms was observed after T2* compensation (Fig 1).

In vivo

Compensation for T2* resulted in a large increase in peak R1 values compared to without compensation (Fig 2A,B). The linear fit in figure 3B demonstrates a good agreement between the dynamic T1 values at t=30min and the post-contrast LL-EPI T1 values after T2* compensation. After HIFU ablation, lack of contrast enhancement was observed in the treated region (Fig 4).

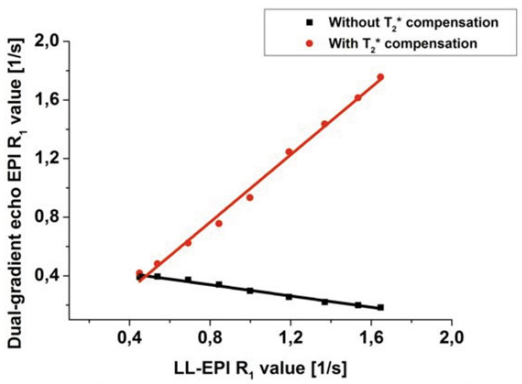

Fig. 1 Scatter plot of the dual-gradient echo EPI R1 values and the LL-EPI R1 values of the Endorem filled phantoms. Linear fit without T2* compensation (black): y= -0.19x + 0.49 and with T2* compensation (red): y=1.15x – 0.15. With T2* compensation the agreement between the dynamic R_1 values and the LL-EPI R_1 values has strongly improved.

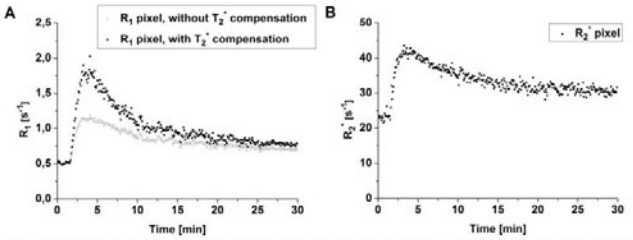

Fig. 2 (A) Representative dynamic R1 curves with (black) and without (gray) T2* compensation of a single tumor pixel. A large increase in peak R1 values is observed after T2* compensation. **(B)** The corresponding dynamic R2* curve. A strong increase in dynamic R2* values can be observed upon contrast agent administration.

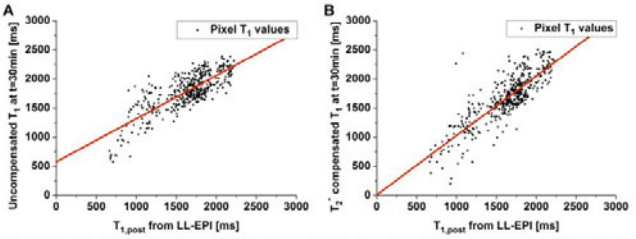

Fig. 3 Scatter plot of the dynamic T1 values at t=30min without T2* compensation **(A)** and with T2* compensation **(B)** and the post-contrast LL-EPI T1 values of all tumor pixels in a representative slice (before HIFU treatment). Linear fit (red line) without T2* compensation: y=0.74x+576.5 and with T2* compensation: y=1.02x+7.7. Without T2* compensation, especially the lower dynamic T1 values deviated from the post-contrast LL-EPI values. With T2* compensation there is a good agreement between the dynamic T1 values at t=30min and the post-contrast LL-EPI T1 values, as demonstrated by the linear fit in fig 3B.

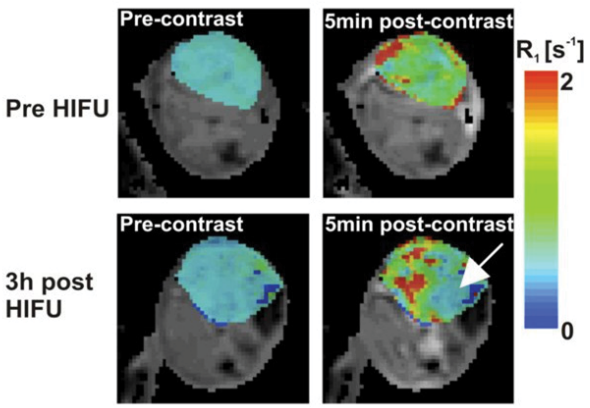

Fig. 4 Representative dynamic R1 maps (with T2* compensation) of the tumor pre- and 5min post Dotarem injection, before and after ablation. The HIFU-treated region is indicated with the white arrow. After HIFU treatment, a region with a lack of contrast enhancement can be clearly observed.

Discussion/Conclusion: High temporal resolution DCE-MRI with T2* compensation can be performed using the dual-gradient echo EPI approach. T2* compensation had major effects on the dynamic R1. Tumor regions with a lack of contrast enhancement were observed after HIFU treatment. In a next step, pharmacokinetic modeling will be applied to investigate the effect of T2* compensation on pharmacokinetic parameters and changes in these parameters after HIFU treatment.

References:

[1] Quarles, C.C., 2009, Phys. Med. Biol. 54, 5749–5766.
[2] Yu, Y., 2011, Proc. Intl. Soc. Mag. Reson. Med. 19, 2060.

688

Motion-corrected Single-sequence Single-quantum and Triple-quantum Filtered Imaging of ^{23}Na at 9.4T in vivo

D.P. Fiege[1], S. Romanzetti[1], F.E. Boada[2], S.R. Yutzy[2], Y. Qian[2], J. Felder[1], N.J. Shah[1]
[1]INM-4, Medical Imaging Physics, Forschungszentrum Jülich GmbH, Juelich/GERMANY, [2]Radiology and Bioengineering, University of Pittsburgh, Pittsburgh/UNITED STATES OF AMERICA

Purpose/Introduction: Monitoring sodium levels is a good indicator of cell viability [1]. Triple-quantum filtering has been suggested as a means to observe primarily the intracellular sodium [2]. Single sequence acquisition of triple-quantum filtered (TQF) and single quantum (SQ) sodium has recently been demonstrated [3]. In this work we present a modified imaging approach using two signal-to-noise efficient Twisted Projection Imaging (TPI) readouts at 9.4T. We show how the motion information of one of the readouts can be used to correct the other.

Subjects and Methods: All experiments were performed on a Siemens (Erlangen, Germany) 9.4T whole-body scanner. A home-built birdcage coil (Affinity Imaging, Jülich, Germany) was used for imaging. The sequence diagram is shown in Figure 1. Two TPI waveforms (204 and 1224 projections) were used to collect data. An extended phase cycling was used to correct for B0 inhomogeneities [5]. Data from a healthy volunteer was acquired after informed consent was obtained according to the local IRB.

Figure 2 shows the motion correction for the SQ readout. The motion estimation is obtained from co-registration (SPM 8) of the six TQF images. This is then applied to the SQ image reconstructed to six intermediate steps of identical duration. The re-combination of these yields a fully sampled motion-corrected SQ image. The TQF image is motion corrected by summation of the co-registered images.

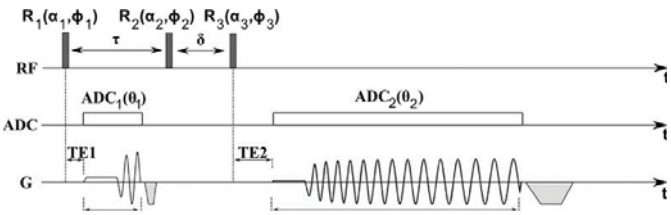

Figure 1: SISTINA sequence diagram. Readout 1 fits between the first two RF pulses and is rewound (light grey gradient). The second readout is considerably longer, rewound (light grey) and spoiled (dark grey).

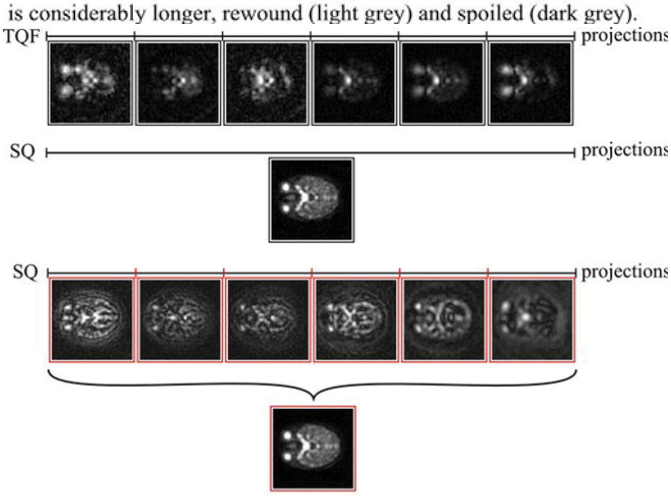

Figure 2: The standard reconstruction yields 6 TQF and 1 SQ fully sampled images (black frame). The TQF images can be co-registered to each other. The motion information is applied to SQ images reconstructed from a reduced number of projections (indicated by the red bars). The undersampling artefacts disappear upon complex summation.

Results: *In vivo* results are shown in Figure 3. SQ images (a) show very good CSF delineation and brain structures. The TQF image (b) is necessarily lower in SNR and resolution. Compared to a T2* weighted image (c) of the same slice, the signal dropouts, attributable to the cerebrospinal fluid, are visible. They are marked by red arrows in the TQF image (b).

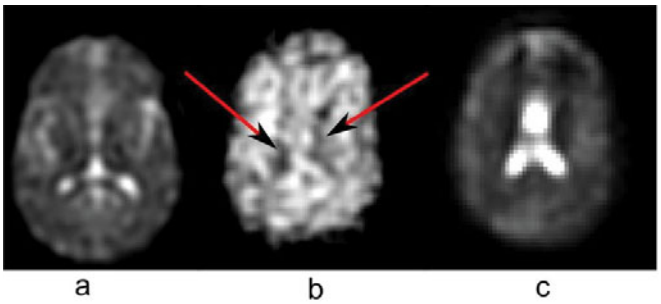

Figure 3: 9.4T in vivo results. TSC weighted SQ (a) and TQF (b) image. (c) shows a T2* weighted image showing the same slice as (b). Signal dropout from CSF in the TQF image is marked with red arrows.

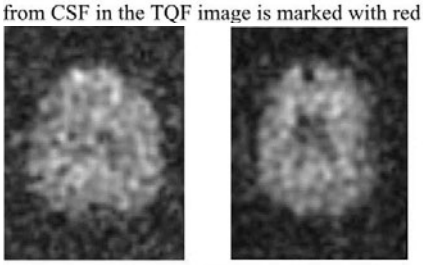

(a) uncorrected (b) motion corrected

Figure 4: Result of motion correction on TQF images. In the uncorrected image (a), the image is smeared. The ventricles are visible in the corrected image (b).

Discussion/Conclusion: *In vivo* results nicely show brain structures, demonstrating the benefits of the high field strength.Triple-quantum filtering removes the CSF signal from the image, but due to partial volume effects, the size of the ventricle appears different in TQ and T2* weighted images. The effectiveness of the motion correction is well appreciable.

It was shown that good quality triple-quantum filtered and single-quantum sodium images can be obtained from a single combined acquisition at ultra-high field strengths.

References:

1. Boada et al. 2005 C Top Dev Biol, 77-101
2. Winter et al. 2001 JMR, 70-78
3. Fiege et al. 2012 MRM, in press
4. Tanase et al. 2005 JMR, 236-53
5. Matthies et al. 2010 JMR, 239-44

689

A novel respiratory triggering scheme for DCE-MRI of mouse liver at 9.4T.

K. Jasinski, T. Skorka, W.P. Weglarz
Magnetic Resonance Imaging, The Henryk Niewodniczanski Institute of Nuclear Physics Polish Adademy of Sciences, Krakow/POLAND

Purpose/Introduction: Dynamic real-time contrast-enhanced MRI of the mouse liver requires acquisition of multiple gradient echo, T_1 weighted images after contrast injection. To reduce motion artefacts respiratory gating is a necessity ensuring data collection during at-rest periods. However, signal variations may persist due to long sequence suspension time when an animal breathe. When the sequence stops waiting for trigger signal, steady state condition is lost due to additional delay considerably longer than the sequence repetition

time (TR) during which longitudinal relaxation takes place. Therefore k-space lines acquired just after the breathe pause gain higher signal what may lead to artefacts and changes in the resulting image amplitude, relatively to the k-space line number. If this occurs when the centre of the k-space is traversed, whole image appears much brighter than the previous one [Fig.1]. This artefact alone makes quantitative image series analysis ambiguous. The idea of the sequence modification was to preserve steady state by continuous excitation of the sample with conditional acquisitions associated with respiratory trigger.

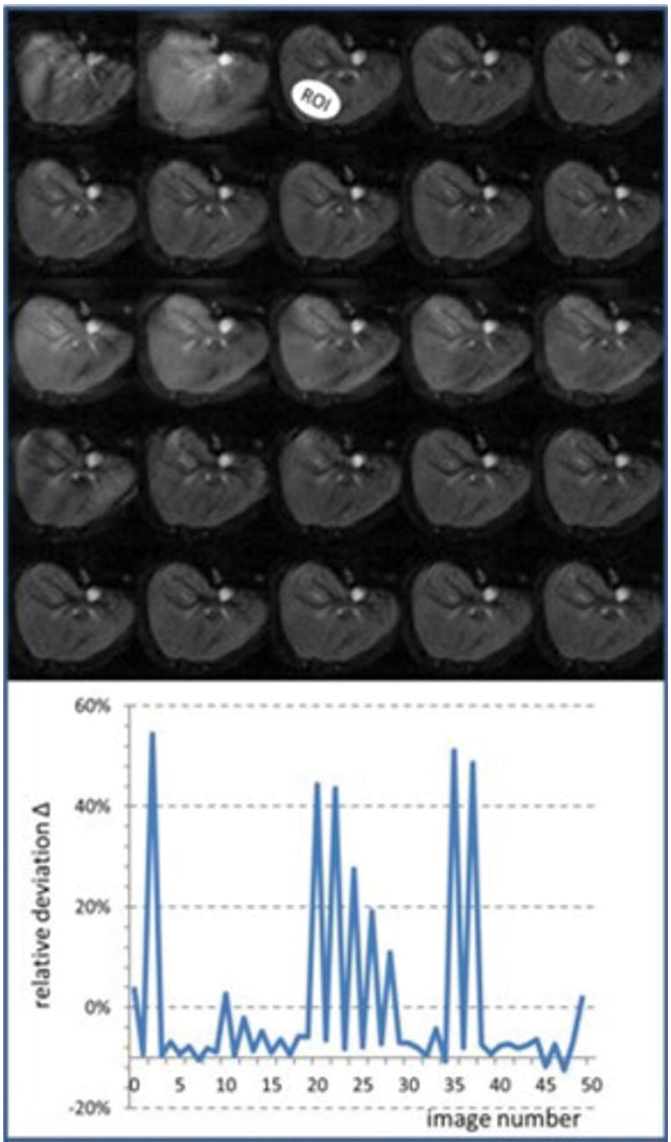

Fig.1. A series of 50 liver images acquired one by one (on average 1.5s per image) with respiratory gating using standard trigger. GEFC sequence parameters are: TR=2ms, TE=10ms, NEX=1, FOV=3x3cm, MTX=128. For clarity only central part of every second image (70x70pix) is shown.

Subjects and Methods: Modified respiratory gated steady-state sequence (GEFCtrig) was derived from standard flow compensated gradient echo GEFC sequence (BrukerAvance III, Paravsion 5.1, (Ettlingen, Germany)). Modification was achieved by application of pulse-program branching controlled by trigger condition dynamically evaluated during run time. Trigger condition is tested after the RF pulse and data acquisition is performed depending on its state [Fig.1]. Phase gradient level and k-space line number are incremented only in the case of data collection what ensures proper k-space traversing. For the in vivo measurements BALB/c mice were anesthetized with 2% isoflurane and placed in the prone position. Respiratory trigger was supplied using pneumatic pillow sensor (SA Instruments Inc., Stony Brook, NY, USA). Images were taken 30 minutes after intravenous injection of Gd-EOB-DTPA (Primovist, Bayer-Shering, Germany, 0.1 mmol/kg) contrast agent. Relative deviation of image intensity was calculated as $\Delta=(x_i-\bar{x})/\bar{x}$, (where x_i is the mean i-th image intensity averaged over desired ROI) for DCE series of GEFC and GEFCtrig images.

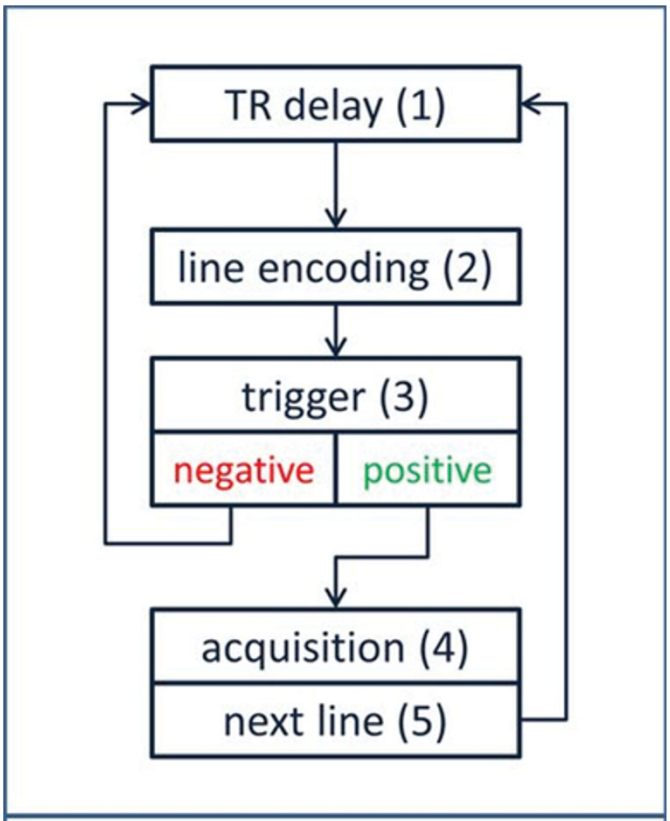

Fig.2. Modified sequence diagram. After repetition time delay TR (1), k-space line is encoded (2) but only for „positive" trigger (3) value the line is acquired (4) and pulse program advances (5) to the next k-space line.

Results: Series of 50 DCE-MR images of the mouse liver with identical parameters were acquired and evaluated (Fig.1 and 3). In the images obtained with the GEFC sequence Δ varied in the range 50%, whereas in case of GEFCtrig this variation is reduced to 10% [Fig.4].

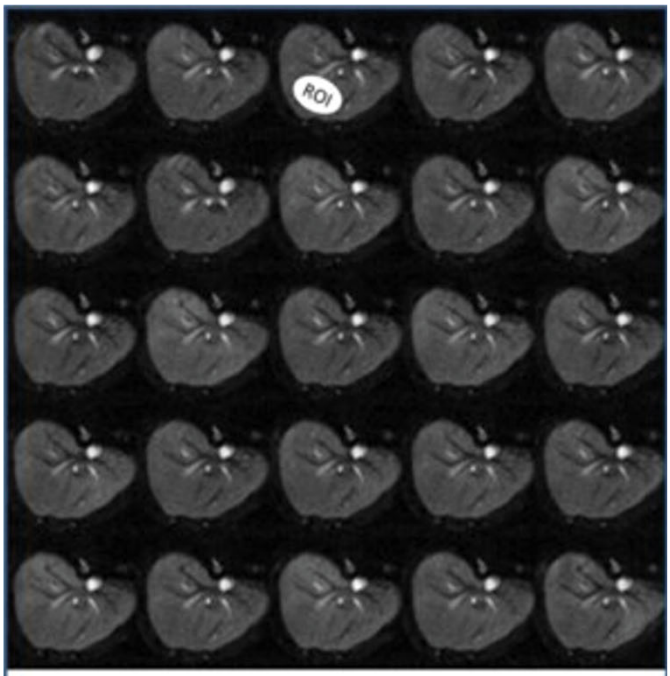

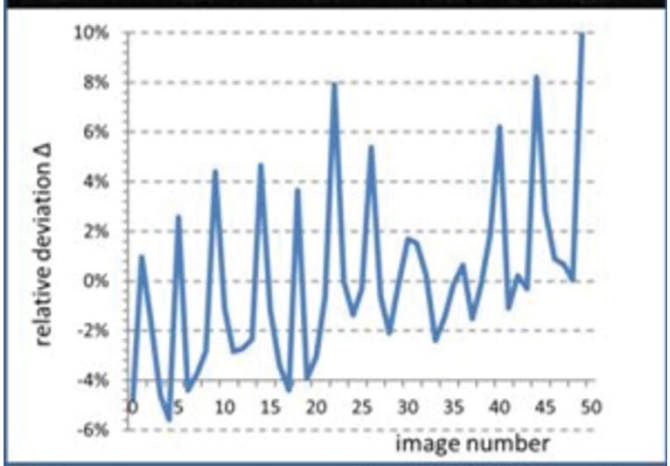

Fig.3. Image series obtained using modified GEFCtrig sequence with identical MR parameters like in Fig. 1. Relative deviation of image to image intensity variation is reduced over 5 times, to less than 10%.

Discussion/Conclusion: It was shown that DCE-MRI T_1 weighted image series benefit from modification of trigger handling. The image to image intensity variation was greatly decreased if compared with standard trigger sequence [Fig.4] thus yielding improved data analysis results.

This research was supported through grant coordinated by JCET-UJ, NoWND-POIG.01.01.02-00-069/09-00.

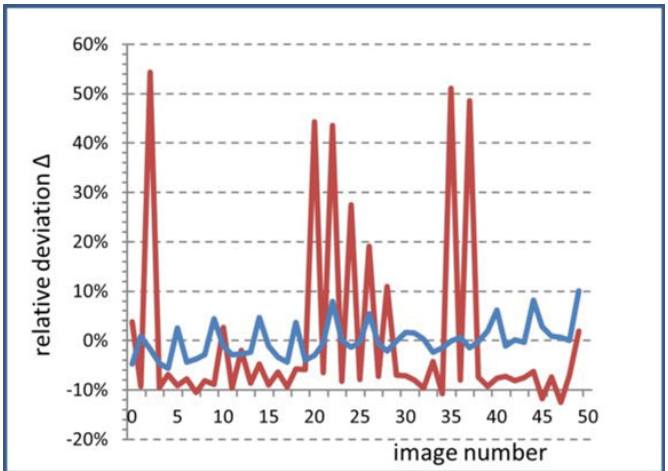

Fig.4. Comparison of results obtained with GEFC (red) and GEFCtrig (blue) sequences. Relative deviation of image intensity calculated over selected ROI is reduced approximately 5 times.

690

Banding Artifact Removal in bSSFP Imaging using Model-Based Iterative Reconstruction

T. Benkert[1], M. Ott[1], M. Blaimer[1], P. Jakob[2], F. Breuer[1]
[1]Magnetic Resonance Bavaria (MRB), Research Center, Würzburg/GERMANY, [2]Experimentelle Physik 5, Lehrstuhl für Physik, Würzburg/GERMANY

Purpose/Introduction: The balanced steady-state free precession (bSSFP) sequence comprises short repetition times and a high intrinsic signal. However, a well-known problem is its sensitivity to off-resonances, yielding severe dark bands in the resulting image. A common procedure to avoid these artifacts is the acquisition of multiple images with different phase-cycles. Afterwards these images can be combined in a specific manner to reduce the artifacts [1]. Another approach is the non-linear pixelwise fit of different phase cycles to the Freeman-Hill formula in order to obtain the corrected signal amplitude and an additional off-resonance map [2]. Although it removes the artifacts reliably, this procedure suffers from a long scan time due to its necessity of several (typically four) fully sampled different images.

In this work, we adapt this method using a model-based iterative reconstruction. This allows the generation of artifact free images with highly undersampled data, resulting in significant scan-time reduction.

Subjects and Methods: Experiments were performed on a healthy volunteer at 1.5T with a 12-channel head-array. Different phase-cycles $\Delta\theta$ with one flip angle (α=45°) were acquired using a 3D-bSSFP-sequence (TR=8ms, voxel size = 1.3x1.3x1.3mm^3). Raw data was retrospectively undersampled using a blocked scheme [3] with undersampling factor 3 respectively 7. Coil-sensitivity profiles C were obtained by adaptive reconstruction [4].

The ellipse-equation of the bSSFP signal [5] was used as a function model. Assuming fixed values for T_1 and T_2 and inserting α and TR, the only unknown parameters are the magnetization M and the off-resonance θ. Performing a model-based iterative reconstruction [3] including the estimated coil profiles, the desired parameters were obtained. Eq.1 shows the corresponding cost function Φ with y being the measured data of channel c and phase-cycle $\Delta\theta$.

$$\Phi(\vec{M},\vec{\theta}) = \frac{1}{2}\sum_{\Delta\theta}\sum_{c}\left\|\vec{F}(\vec{M},\vec{\theta},\Delta\theta,c) - \vec{y}_{\Delta\theta,c}\right\|_2^2$$
$$F = FFT2\left[C_c \cdot M\frac{1-a(T_2,TR)\,e^{i(\theta+\Delta\theta)}}{1-b(\alpha,T_1,T_2,TR)\cos(\theta+\Delta\theta)}\right] \quad (1)$$

Results: Fig.1 shows the fitted magnetization and the off-resonance map of the fully sampled data. Banding-artifacts are completely removed.

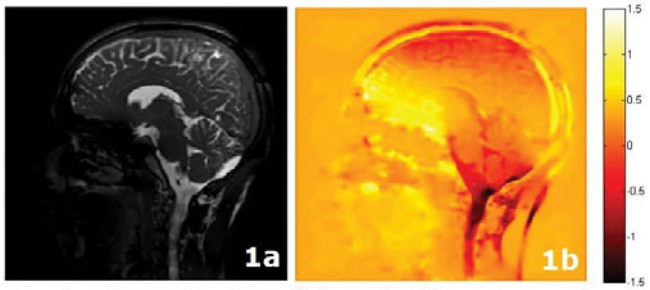

Fig.1: Magnetization (a) and off-resonance map (b), 4 phase-cycles, fully sampled data

Fig. 2 and 3 show the sampling pattern and the results of the undersampled data. The magnetization looks very similar to the one in figure 1a. Only the off-resonance map shows residual artifacts due to undersampling.

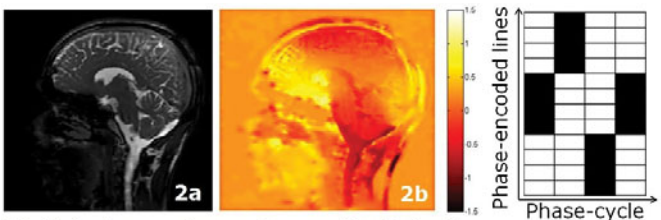

Fig.2: 4 phase-cycles, undersampling factor 3

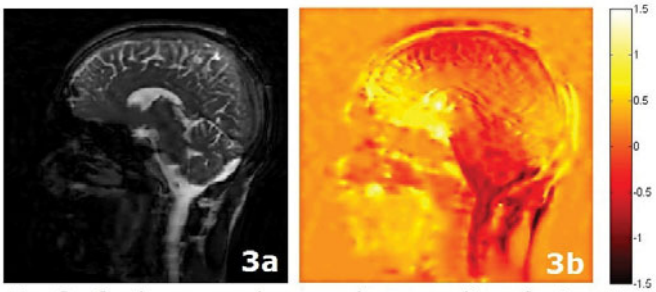

Fig.3: 8 phase-cycles, undersampling factor 7

Discussion/Conclusion: In this work, a novel approach allowing the cancellation of banding-artifacts in bSSFP imaging is presented. Thus, a significant scan-time reduction in comparison to previous published methods [2,5] is achieved. Moreover, an off-resonance map is obtained.

References:

[1] Bangerter et al., MRM,2004,51:1038-1047
[2] Santini et al., Proc. ISMRM,2010,#5027
[3] Sumpf et al., JMRI,2011,34:420-428
[4] Griswold et al., Proc. ISMRM,2002,#2410
[5] Xiang et al., Proc. ISMRM,2010,#6797

691

Image reconstruction in undersampled radial MRI by constrained total variation minimization

S. Wundrak[1], J. Schluttig[2], J. Ulrici[2], E. Hell[2], V. Rasche[1]
[1]Internal Medicine II, University of Ulm, Ulm/GERMANY, [2]GBE, Sirona Dental System, Bensheim/GERMANY

Purpose/Introduction: In case of undersampled MRI direct reconstruction methods like gridding result in images with severe aliasing artifacts. Iterative reconstruction methods using parallel imaging and methods from compressed sensing considerably reduce these artifacts. In contrast to previous work [3,4] the proposed method minimizes the total variation and ensures the data fidelity in an alternating manner, similar to ASD-POCS [1]. This approach leads to a simple implementation and gives great flexibility in the selection of regularization terms. We combine a fast gradient-based algorithm for total variation (TV) minimization (FISTA) [5] and a conjugate gradient (CG) method to ensure the fidelity constraint.

Subjects and Methods: The reconstruction problem is formulated as (1) $min|x|_{TV}$ *s.t.* $|Ax\text{-}b|_2$ (with x: image, *A*:system matrix, *b*:k-space, *ε*:error). Most previous work [3,4] solves an unconstrained formulation. In contrast, we solve the constrained formulation (1) in an alternating manner: a single CG step first enforces the data fidelity constraint and a second step reduces the total variation (Figure 1) using a fast gradient-based algorithm (FISTA)[5] that is applied in image space only. To reach convergence the output of both steps is weighted as described in [2]. The weighting factor λ is calculated (by solving a simple quadratic equation) to keep the increase of the residual error by the TV step less than the decrease by the CG step. The CG residual is adapted accordingly. The algorithm was tested with radial brain images (3T Philips Achieva, radial FFE, TE=4.1 ms, TR=7.0 ms, 1x1x5mm^3, 6 channel head coil, 32 averages).

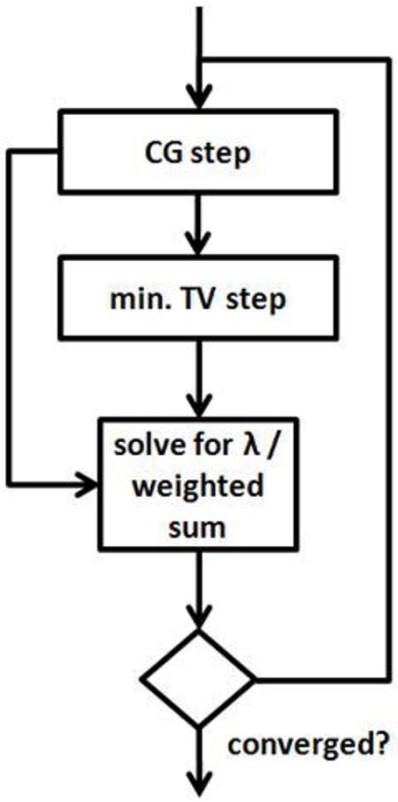

Figure 1: Block diagram of proposed algorithm.

Results: The reconstructed image from 42 k-space profiles (R=9) is, as expected, superior to the gridding reconstruction. Compared to a CG SENSE [6] reconstruction the remaining aliasing artifacts are removed (Figure 1). The reconstruction with 20 iterations took 17 seconds (10 seconds for CG-SENSE) in a MATLAB implementation.

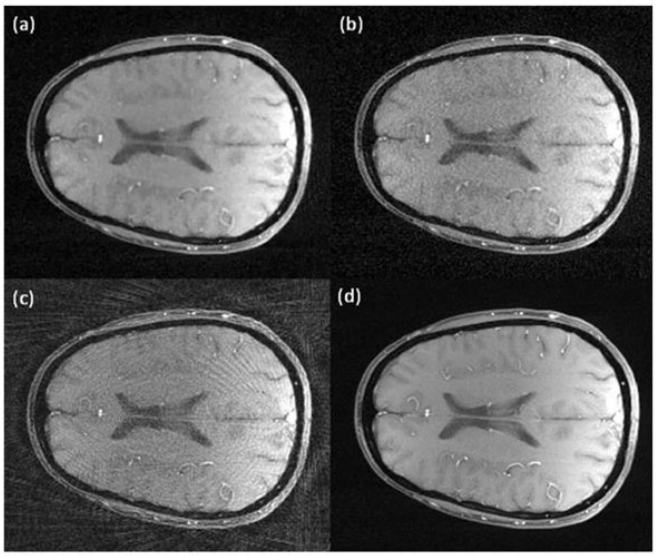

Figure 2: Comparison of (a) constrained TV minimization, (b) CG-SENSE, (c) gridding, and (d) fully sampled data.

Discussion/Conclusion: Constrained TV minimization seems to be a fast, stable and flexible method to reconstruct undersampled radial MRI scans. The reasoning on convergence in [1] should also apply for the proposed method. Using FISTA for TV minimization leads to faster convergence.

References:

[1] Sidky EY, Pan X, 2008, Phys Med Biol, 53:4777-4807.[2] Ritschl L, et al., 2011, Phys Med Biol, 56:1545-1561. [3] Knoll F, et al., 2012, Magn Reson Med, 67:34-41.[4] Lustig M, Donoho D, Pauly JM, 2007, Magn Reson Med, 58(6):1182-95.[5] Beck A, Teboulle M, 2009, IEEE Trans. Image. Proc., 2419-34. [6] Pruessmann KP, et al., 2001, Magn Reson Med, 46:638–551.

692

Ultra-low-field MRI: Imaging at frequencies below 1 kHz

R. Körber[1], I. Hilschenz[2], H. Scheer[1], T. Fedele[3], H. Albrecht[1], A. Cassarà[4], S. Hartwig[1], L. Trahms[1], M. Burghoff[1]
[1]Biosignals, Physikalisch-Technische Bundesanstalt, Berlin, Berlin/GERMANY, [2]Department MQF, University of Leipzig, Leipzig/GERMANY, [3]Neurology, Charité Campus Benjamin Franklin, Berlin/GERMANY, [4]n/a, Centro Fermi, Roma/ITALY

Purpose/Introduction: The objective to investigate the functionality of the human brain led to the development of various methodologies. Those methods lack either spatial resolution (as in EEG or MEG) or temporal resolution (as in fMRI). Another approach which seeks to achieve high temporal and spatial resolution is direct current imaging in which magnetic field changes due to neuronal activity are mapped onto an image. In high field MRI this relies on additional dephasing of the precessing magnetisation around a neuronal activity. However, this has yielded controversial results for in vivo measurements [1]. An alternative would be to exploit the neuronal activity as a "tipping pulse" in the MRI experiment. This requires a static magnetic field with a proton Larmor frequency that corresponds to the frequency of neuronal activity. Electrostimulated somatosensory evoked potentials showed spectral power mainly at around 100 Hz and 700 Hz when analysed 20 ms after stimulation [2]. Thus, to utilize this ac-field as a tipping pulse in MRI, imaging has to be done in a field of 2.5 µT or 17.5 µT.

Subjects and Methods: We designed an ultra-low-field MRI system which is based on a SQUID as the magnetic field sensor. It is operated inside a custom designed magnetically shielded room which suppresses environmental field noise and the earth magnetic field. With this device we performed 2D Fourier gradient echo imaging at frequencies below 1 kHz on phantom samples with T_2 relaxation times as short as 190 ms (about a factor of two longer than observed for brain tissue).

Results: The phantom images taken at 100 Hz and 730 Hz showed that at such low frequencies imaging is possible with a spatial resolution better than 3.5 mm. The extraction of the T_2 times of the phantoms was achieved by evaluating the signal size for different echo times.

Discussion/Conclusion: This study forms a first step towards functional imaging of the human brain based on the resonant mechanism. However, an improvement of the signal to noise ratio is necessary to resolve anatomical structure for in vivo imaging below 1 kHz. Based on phantom studies [3] we can estimate that the minimal detectable current dipole strength observable in this imaging technology is at least one to two orders of magnitude higher than typically physiologically observed values.

References:

[1] Hagberg GE, 2006, Magn Reson Imaging, 24, 483-493
[2] Scheer HJ, 2011 Physiol Meas, 32, N37-79
[3] Höfner N, 2011, Magn Reson Imaging, 29, 1365-1373

693

Multi-Tissue Quantitative T2*-Mapping of the Knee Joint using a Multi-Echo VTE-Sequence at 3 Tesla: Preliminary Results.

G. Riegler[1], S. Apprich[2], O. Bieri[3], S. Zbyn[2], S. Trattnig[1], P. Szomolanyi[1]
[1]Center of Excellence High Field MRI, Department of Radiology, University Hospital of Vienna, Medical School, Vienna/AUSTRIA, [2]MR Centre-Highfield MR, Department of Radiology, Medical University of Vienna/Vienna General Hospital, Vienna/AUSTRIA, [3]Division of Radiological Physics, University of Basel Hospital, Basel/SWITZERLAND

Purpose/Introduction: A new multi-echo, variable echo time (meVTE) sequence enables quantitative MR imaging of tissues with very short T2 relaxation times. The purpose of this study was to evaluate the feasibility of this novel multi-echo VTE sequence at 3T for T2*-mapping of the meniscus (ME), patella tendon (PT), and cruciate ligaments (CL) in the knee joint.

Subjects and Methods: Eighteen consecutive knee patients (8 female; 10 male, mean age 35.7 ±11.6 years) were examined at a 3T whole-body system, using an 8-channel knee coil. Beside standard morphological MRI, a 0.7mm isotropic meVTE-sequence (10 TEs from 0.7 to 22.4 ms; TA 12.16 min) was obtained.T2*-maps were calculated using a mono-exponential fit least square analysis. T2*-values were manually assessed by 2 independent observers using a ROI analysis on 5 consecutive, sagittal slices in the weight bearing region for the anterior and posterior horn of the medial and lateral ME, as well as for the PT. Views for the ACL and PCL were reconstructed using a multiplanar reconstruction tool and evaluated on 3 slices in the same way. Statistical measures of mean T2*-values included an analysis of variance with Duncan post hoc test and Intraclass-Correlation (ICC).

Results: Morphological meniscus grading had a highly significant impact (P <0.001) on T2*-values of the menisci (normal (N=50) 6.0 ±0,9 ms, 95% CI 5.7-6.3 ms; degeneration (N=13) 8.0 ±1,6 ms, 95% CI 7.1-8.9 ms; meniscal tear (N=9) 12.9 ±3.2 ms, 95% CI 10.4-15.4 ms) with significant differences between all groups (P<0.05). The PT was normal in 15 cases (mean T2*value 2.7 ±0,6 ms, 95% CI 2.4-3.1 ms), in 3 cases a tendinitis was found (mean T2*-value 3.9 ±0,.9 ms, 95% CI 1.5-6.3 ms). Mean T2*-relaxation times for the ACL and PCL were 8.4 ±1.6 ms and 8.9 ±1.3 ms. Intra-class correlation between readers for ME, ACL, PCL and PT yielded R^2= 0.962, R^2= 0.594, R^2= 0.648 (P<0.01 for all) and R^2= 0.407 (P=0.042), respectively.

Discussion/Conclusion: T2*-Mapping using a meVTE sequence is able to quantify pathological changes within the ME and PT.

Clinical Relevance

This new multi-echo variable echo-time sequence might have the potential to serve as a one-stop-shopping imaging tool for quantitative T2*-evaluation of several knee joint structures.

694

Temporal Optimisation of Background Suppressesion Pulses in Arterial Spin Labelling (ASL).

R. Wesolowski[1], A. Luxen[2]
[1]Imaging Sciences and Biomedical Engineering, King's College of London, London/UNITED KINGDOM, [2]Cyclotron Research Centre, University of Liege, Liege/BELGIUM

Purpose/Introduction: Background Suppression techniques (BS)[1] have been shown to bring advantages in ASL acquisition, especially at higher fields[2]. Unless complex conjugate subtraction is performed, the ASL signal can be significantly reduced if the modelling for the temporal placement of the BS pulses does not include the contrast difference between the inflowing blood of the selective and non-selective conditions (IN-DIFF). This work has been done to highlight the effects of the BS temporal placement on the ASL signal.
Subjects and Methods: An ASL-FAIR sequence (using FOCI with WET saturation and spatially limited non-selective slab) was implemented on a 3T Siemens Allegra scanner, single channel receive RF coil. Acquisition:GE-EPI; res.:3x3x5mm^3;TR=2560ms;TE=19.99ms;TA=35ms;TI=1500ms; Slices=9;N=60pairs. Assumed T_1 values for White Matter (WM)=800,Grey Matter (GM)=1300,Blood (BL)=1600 and CSF=3700ms. Fitting was done depending on the weighting coefficients emphasising nulling of WM, GM, BL, CSF and maximizing IN-DIFF. BS1 and BS2 timings were optimised for the minimum of sum-of-squares (SumSq), according to the equation: $SumSq=A*1/(IN\text{-}DIFF(TI))^2+B*S_{WM}(TI)^2+C*S_{GM}(TI)^2+S_{BL}(TI)^2+S_{CSF}(TI)^2$; S-signal intensity;A,B,C-weighting coefficients.
Results: Table 1. Numerical estimation of longitudinal magnetisation for brain tissue and inflowing blood for different weighting coefficients (A, B and C) (columns:IN-DIFF, WM, GM, BL, CSF) and corresponding simulated signal reduction (columns:WM and GM %Reduction) and in acquired images both in relation to FAIR-no-BS; last column: Signal of Perfusion-Weighted images relative to the FAIR-no-BS acquisition.

	Simulated.Signals							Acquired.Signals		
	IN-DIFF	WM	GM	BL	CSF	WM (%Reduction)	GM (%Reduction)	WM (%Reduction)	GM (%Reduction)	PW-GM (Signal gain/loss 60Pairs)
a)FAIR-no-BS	0.78	0.83	0.67	0.59	0.32	-	-	-	-	-
b)BS1=544ms, BS2=659ms, A=0,B=2,C=4	0.10	0.06	0.04	0.03	0.02	92%	94%	85%	86%	-17%
c)BS1=985ms, BS2=394ms, A=.1,B=5,C=10	0.41	0.17	0.19	0.19	0.13	80%	71%	75%	70%	+7%
d)BS1=1179ms, BS2=200ms, A=1,B=2,C=4	0.78	0.46	0.41	0.38	0.22	45%	39%	51%	45%	+40%

Fig.1. shows simulated magnetisation signals for different weighting of the SumSq equation and adequate PW images averaged over 60 pairs (top row) and 20 pairs (bottom row).

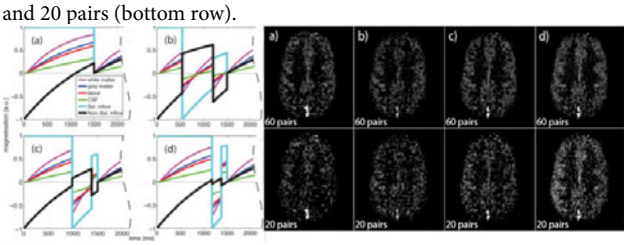

Discussion/Conclusion: In the absence of reconstructed real and imaginary images, needed for the complex conjugate subtraction, temporal placement of the BS pulses can be optimised to consider the highest possible contrast difference between inflowing blood of the selective and non-selective conditions at a cost of partly suppressed static tissue (Fig.1.d,Table.1.d). This approach provides increased SNR (largely emphasised in averaged PW over 20 pairs), much needed in any ASL sequence. PW images confirm the simulated data.
References:
[1]Garcia et al.,MRM,54,336-372,2005.
[2]Gardener et al.,MRM,61,874-882,2009.

695

On-resonance inversion prior to off-resonance irradiation in MT, CEST and rotating frame relaxation experiments

S. Mangia[1], T. Liimatainen[2], M. Garwood[1], S. Michaeli[1]
[1]CMRR - Dept. of Radiology, University of Minnesota, Minneapolis/MN/ UNITED STATES OF AMERICA, [2]Department of Biotechnology and Molecular Medicine A.I. Virtanen Institute for Molecular Sciences, University of Eastern Finland, Kuopio/FINLAND

Purpose/Introduction: Off-resonance irradiation is utilized in a variety of NMR experiments, such as magnetization transfer (MT), chemical exchange saturation transfer (CEST) and rotating frame relaxation experiments. The latter include off-resonance continuous-wave (CW) T1rho and rotating frame relaxations during frequency swept pulses, i.e. adiabatic T1rho and T2rho [1] and relaxation along a fictitious field (RAFF) [2]. Whereas in MT and CEST the off-resonance irradiation is used to saturate one pool of protons that are in exchange with water, in rotating frame relaxation experiments the off-resonance irradiation is used to affect magnetization directly. In general, these off-resonance experiments can produce a steady-state magnetization (Mss). Accurate estimate of Mss is crucial to obtain relaxation parameters, but this is often unachievable in vivo due to RF power limits (SAR). Recently we showed in RAFF and MT experiments that an on-resonance inversion pulse prior to off-resonance irradiation is advantageous for obtaining relaxation parameters and can alleviate the SAR problem [2,3]. Here we extend this approach to other off-resonance experiments.
Subjects and Methods: MT and rotating frame relaxation experiments (adiabatic T1rho, adiabatic T2rho, CW-T1rho and RAFF) were performed on a 4T scanner with parameters described previously [1-3] on 5 human healthy subjects and on a phantom characterized by substantial magnetization transfer effects (i.e., fresh cheese).
Results: Magnetization evolved to steady-state in MT, off-resonance CW-T1rho and RAFF experiments, but not in adiabatic T1rho and T2rho experiments. The steady-state formation did not depend on the initial orientation of magnetization. The robustness of the fitting procedure used to extract relaxation parameters in presence of Mss drastically improved when the on-resonance inversion was applied, ultimately leading to parametric maps with increased tissue specificity as compared to those obtained with the standard acquisitions in which magnetization was initially along the +z axis.
Discussion/Conclusion: The results confirmed the theoretical predictions that Mss is formed whenever the water magnetization evolves in one hemisphere during the off-resonance irradiation. This occurs in MT (and CEST), off-resonance CW-T1rho and RAFF, but not in adiabatic T1rho and T2rho where the magnetization trajectory spans both the positive and negative hemisphere during the adiabatic full passages. The on-resonance inversion preparation prior to off-resonance irradiation is advantageous whenever Mss is formed, either to improve robustness and specificity of the relaxation maps and/or to reduce the acquisition time.
References:
1) Mangia et al. MRI 2009;27:1074-87; 2) Liimatainen et al. MRM 2010;64:983-94; 3) Mangia et al. MRI 2011; 29:1346-50.

696

Long-term Quality Assurance of fMRI and MRS on a 3.0T clinical scanner

E. Alfayate[1], P. García-Polo[2], F. García[1], J.A. Hernández-Tamames[3], R. García-Álvarez[4], J. Álvarez-Linera[5]
[1]Neuroimage, Fundación CIEN, Madrid/SPAIN, [2]Biomedical Technology Centre, Technology University of Madrid, Madrid/SPAIN, [3]Electronical Technology, Universidad Rey Juan Carlos, Móstoles/SPAIN, [4]Clinical Science Development Group, GE Healthcare, Madrid/SPAIN, [5]Radiology, Hospital Ruber Internacional, Madrid/SPAIN

Purpose/Introduction: Functional MRI (fMRI) and Magnetic Resonance Spectroscopy (MRS) are being increasingly used in clinical protocols [1]. Subsequenly, it is crucial to develop a routine quality assurance protocol (QA) of both techniques [2]. This work describes a long-term variability study, as a part of the QA of fMRI and MRS on our institution clinical 3.0 T MR scanner.
Subjects and Methods: QA scans were performed over a period of 12 months (Feb 2011-Feb 2012) on a GE HDxt 3.0T MR scanner using an 8-channel array brain coil. An MRS phantom, mimicking healthy brain metabolite concentrations, was placed at the scanner isocentre 15 minutes prior to each QA adquisition. Phantom temperature together with humidity and temperature of the scanner and the hardware rooms were recorded.
The acquisition protocol consisted of a fMRI using an GRE-EPI pulse sequence with a TR=2506ms, TE=40ms, flip angle=60, slice thickness=3mm, matrix-size=64x64 and 35 slices. The MRS data was acquired using a PRESS pulse sequence with a nominal voxel-size=20x20x20 mm, TE=35ms and a total of 128 scan averages.
fMRI and MRS data were analysed with a Matlab developed Image Temporal-Stability Tool [Fig.1] and the LCModel software [Fig.2][3] respectively. Signal-to-Noise Ratio (SNR) and Signal Fluctuation to Noise Ratio (SFNR) were measured for fMRI data. While for MRS, the Creatine (Cre), Phospho-Coline (PCh), Lactate (Lac), Mio-Inositol (mI) and N-Acetyl-Aspartate (NAA) concentrations were computed.
Signal-stability was analised following previous published methods [1,2]. A warning rule (Shewhart chart [1]) for SNR and SFNR was set to values exceeding the mean±two standard deviations.

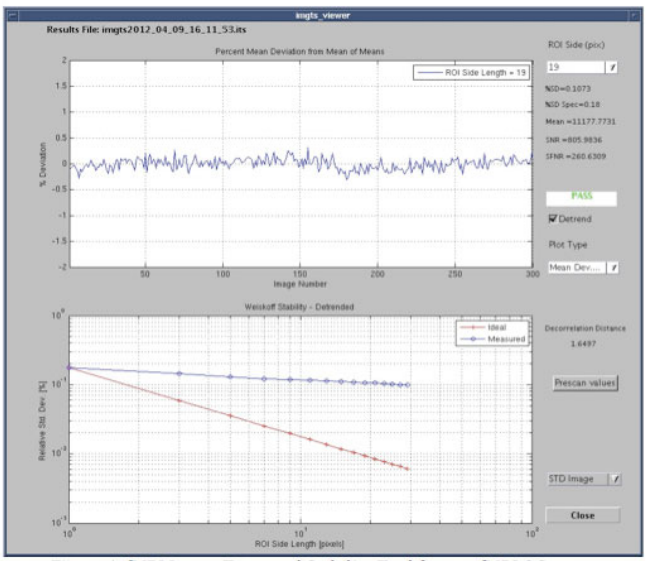

Figure 1. fMRI Image Temporal Stability Tool for one fMRI QC scans

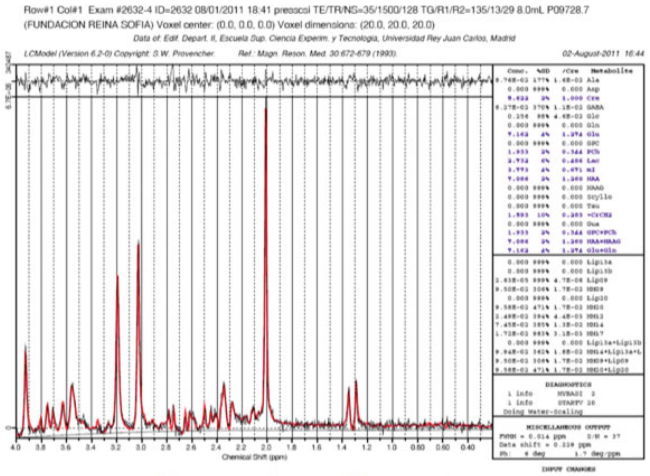
Figure 2. LCModel outcome for one of the MRS phantom acquisitions

Results: SNR and SFNR reached warning values (>mean ± 2 standard deviations) in about 3% and 7% of the repeated measures, respectively. No statistical significant correlation with the registered parameters (scanner-room temperature, technical-room temperature, humidity, percentage of helium volume or helium pressure) [Fig.3] during the fMRI QA study. The Weiskoff stability chart for a fMRI scan [Fig.1-low] also shows that the quality levels are acceptable as the relative fluctuation levels (plotted as %Relative Standard Deviation) follow a decreasing logarithmic line as the ROI increases.
Similarly, Fig.4 demonstrates no statistical significant correlation between metabolite concentrations and these recorded parameters.

PEARSON CORRELATION						
	Temp_Room	Temp_Tec_Room	Humidity	Helium	Helium_Pressure	Temp_Phantom
SNR	-0,1244	-0,0241	-0,0058	0,1010	0,0503	0,0343
SFNR	-0,0725	0,0097	0,0044	-0,0911	-0,1056	0,0506

Figure 3. Pearson Correlation of SNR and SFNR

PEARSON CORRELATION											
	Cre	PCh	PCh/Cre	Lac	Lac/Cre	mI	mI/Cre	NAA	NAA/Cre	GPC+PCh	GPC+PCh/Cre
Temp_Room	0,140	0,139	0,062	0,139	-0,039	0,140	0,015	0,140	0,140	0,139	0,091
Temp_Tec_Room	-0,010	-0,011	-0,002	-0,010	-0,103	-0,010	0,040	-0,009	-0,009	-0,011	-0,035
Humidity	-0,060	-0,060	-0,018	-0,060	-0,004	-0,060	-0,001	-0,061	-0,061	-0,060	-0,054
Helium	-0,018	-0,018	0,048	-0,018	-0,018	-0,018	0,016	-0,018	-0,018	-0,018	0,060
Helium_Pressure	-0,062	-0,062	-0,022	-0,062	0,004	-0,062	0,039	-0,062	-0,062	-0,062	-0,022
Temp_Phantom	-0,009	-0,009	0,025	-0,010	-0,034	-0,008	-0,041	-0,008	-0,009	-0,009	0,060
Hz	0,031	0,031	0,060	0,031	-0,122	0,031	0,114	0,031	0,031	0,031	0,012

Figure 4. Pearson Correlation of Metabolites and Variables

Discussion/Conclusion: Although some data points reached the stablished SNR and SFNR warning values, the results presented here are well within the normal published criteria [1] and no further instrument evaluation was required.
References:
[1] Simmons A. et al.; 1999; MRM 41:1274-1278.
[2] Garcia-Alvarez R. et al.; IPEM; London; July 2003.
[3] Provencher S.W.; MRM 30:672-679; 1993.

697

Signal enhancement of Glycogen by ^{13}C NMR spectroscopy using broadband ^{1}H decoupling and NOE at 7T

E. Serés Roig[1], L. Xin[2], A.W. Magill[1], M. Meyerspeer[3], R. Gruetter[1]
[1]Laboratory for Functional and Metabolic Imaging, Ecole Polytechnique Fédérale de Lausanne, Lausanne/SWITZERLAND, [2]University of Lausanne, Lausanne/SWITZERLAND, [3]Center for Biomedical Engineering and Physics, MR Centre of Excellence, Vienna/AUSTRIA

Purpose/Introduction: ^{13}C MRS is a powerful tool for investigating metabolism in-vivo, allowing non-invasive measurements of tissue Glycogen in human muscle [1]. The challenge of ^{13}C MRS on human scanners at high field is the implementation of ^{1}H-decoupling and NOE [3] while respecting the

IEC guidelines for SAR. In particular, the Waltz16 [2] ^{1}H-decoupling scheme provides broader bandwidth relative to continuous wave (CW). Therefore, the aim of this study was to explore the feasibility of using Waltz16 decoupling in-vivo at 7T and to evaluate the signal enhancement of Glycogen and Glucose using Waltz16 decoupling and NOE in-vitro.

Subjects and Methods: All experiments were performed on a 7T human MR-scanner (Siemens Erlangen/Germany). A ^{13}C-^{1}H RF surface coil was built, consisting of a quadrature ^{1}H coil and a linear ^{13}C coil [4]. In-vitro experiments were performed using a two-compartment phantom: 800mM solution of glycogen (inner compartment) and 8mM solution of 1-^{13}C glucose (outer compartment). A pulse-acquire sequence with adiabatic half-passage excitation (2050µs) was implemented together with Waltz16 and CW ^{1}H-decoupling, and NOE. The decoupling duration and voltage required to achieve broadband decoupling were calibrated in-vitro for Waltz16 and CW schemes. NOE was calibrated and applied in-vitro. All in-vitro experiments were obtained with the following parameter settings: vector size=2048, BW=10 kHz, TR=8060ms, and 64 averages. In-vivo glycogen experiments were performed on human calf using Waltz16 (21ms decoupling duration), vector size=2048, BW=20 kHz, TR=2650ms and 256 averages (Figure1).

Results: The bandwidth of Waltz16 was measured in-vitro, to be 600Hz (10 times of that for CW) (Figure2). The duration of the Waltz16 scheme was adjusted for efficient glycogen and glucose decoupling. The glycogen peak was decoupled by applying 21ms decoupling (Figure3.a), whereas 87ms was required for glucose-α and glucose-β peaks (Figure3.b). The signal enhancement obtained using NOE in-vitro was 1.6 for glycogen, 2.5 for glucose-α, and 2.1 for glucose-β (Figure4).

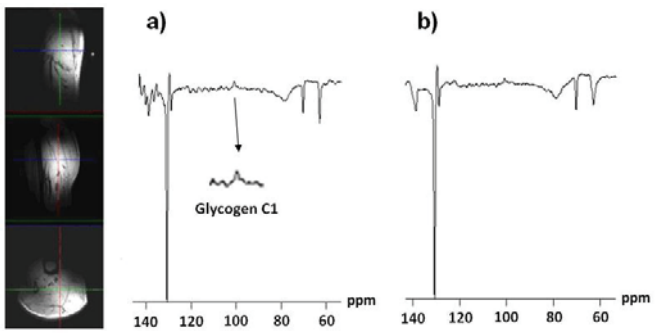

Figure 1: ^{13}C natural abundance signal of glycogen in human calf obtained by pulse-acquire with a) Waltz16 and b) CW decoupling (TR 2650ms, acquisition time 102ms, decoupling time 20ms, 256 averages and vector size 2048).

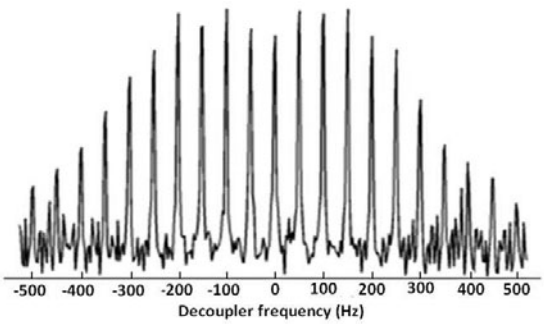

Figure 2: Decoupling bandwidth for Waltz16 measured in vitro by applying the sequence at a range of offset frequencies. Decoupling time = 87ms, TR=3s, BW=20 kHz, acquisition time=102ms, vector size=2048. The bandwidth was evaluated by measuring the frequency range within 80% of the peak height on-resonance, resulting of 600Hz.

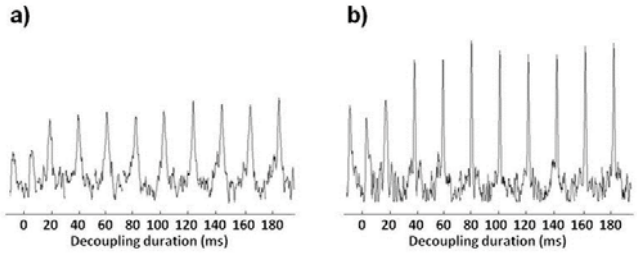

Figure 3: Calibration of the decoupling duration for Glycogen (a) and Glucose beta (b) using Waltz16 at a range of 10% steps of the total acquisition time (i.e.204ms). Glycogen was decoupled at 21ms, whereas Glucose alpha and beta required 87ms decoupling duration.

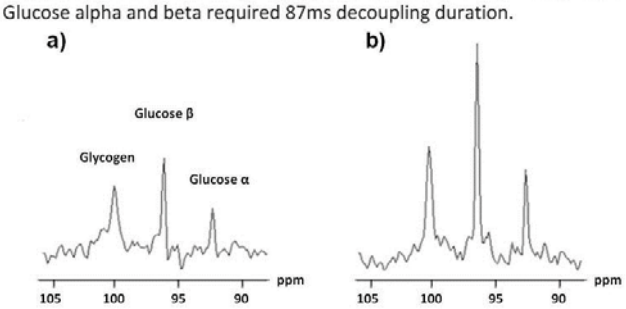

Figure 4: In vitro ^{13}C MRS of Glycogen and Glucose obtained by pulse acquire with Waltz16 (decoupling time = 87ms), TR=8060ms, BW=20 kHz, acquisition time=102ms, vector size=2048, (a) with no NOE, (b) with NOE (44 pulses of 1ms duration and 100ms pause). The enhancement obtained using NOE was 1.6 for Glycogen, 2.5 for Glucose alpha, and 2.1 for Glucose beta.

Discussion/Conclusion: We conclude that it is feasible to apply Waltz16 at 7T to achieve broadband ^{1}H-decoupling in-vivo in human muscle within the IEC guidelines, and this together with NOE enhancement will allow further extention of this technique for ^{13}C MRS measurements such as in human brain.

References:

[1] M.J.Avison PNAS 1988. [2] A.J.Shaka et al, Magn Reson 1983. [3]W.Chen et al, Biochemistry 1993. [4] G. Adriany et al, Magn Reson 1997.

Acknowledgements

Supported by Centre d'Imagerie BioMédicale (CIBM) of the UNIL,UNIGE,HUG,CHUV,EPFL and the Leenaards and Jeantet Foundations.

698

Cardiac MRS: High reproducibility for assesment of myocardial TG

M.C. Sohlin[1], S. Holmquist[2], Å. Carlsson[1], E. Forssell-Aronsson[1], M. Ljungberg[1]

[1]Sahlgrenska University Hospital, Department of Medical physics and Biomedical Engeneering, Göteborg/SWEDEN, [2]Department of Radiation Physics, University of Gothenburg, Göteborg/SWEDEN

Purpose/Introduction: Resent research has found support for the so-called lipotoxicity hypothesis stating that an excess storage of triglycerides within non-adipose tissue may lead to cell dysfunction (1). Localized cardiac MR-spectroscopy (CMRS) is the only method that could facilitate non-invasive localization and quantification of triglycerides within cardiomyocytes (2) and would therefore be an important tool in the search for the unfamiliar link between obesity, cardiovascular disease and diabetic cardiovascular disease. Performing CMRS measurements is not straightforward and complications arise due to cardiac and respiratory motion, and susceptibility effects from the lungs and the blood. In this work, the uncertainties in the CMRS method were estimated by evaluating both intra- and inter-examination reproducibility.

Subjects and Methods: ^{1}H-MRS of human myocardium was performed in one healthy volunteer on two occasions using a 1.5T whole body MRI-system equipped with an MRS research package (Philips Medical Systems, The Neth-

erlands), and 5-channel cardiac-coil for signal reception. On the first occasion the acquisition was repeated six times within one examination. On the second occasion, the examination was again repeated six times, now as separate examinations with repositioning in between. PRESS (TE/TR=35/3000ms) and CHESS was used for volume selection and water suppression. 128 water suppressed dynamics and eight non-water suppressed dynamics (TR=6000ms) were acquired. The spectroscopy scans were cardiac triggered to end systole and respiratory triggered at end expiration using a pencil-beam navigator (3). The VOI (4.5cm^3) was planned within the ventricular septum. The methylene (CH_2) and water peak were quantified using the AMARES algorithm of the jMRUI-package (4). The result was expressed as the quotient between CH_2 and water.
Results: High reproducibility was achieved for the $CH_{2,w}$ signal amplitude in both the intra- and inter-examination measurements. The CV of the $CH_{2,w}$ signal for intra- and inter-examination measurements were 3.8% and 4.7%, respectively.

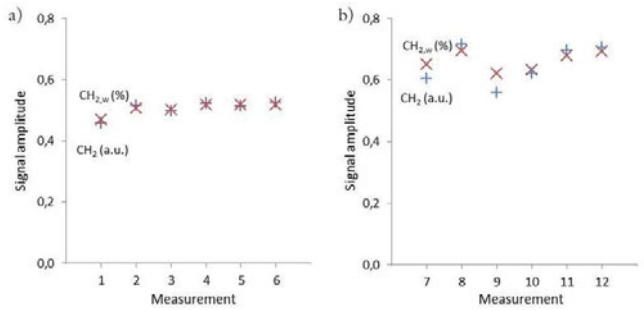

Figure 1 Individual signal amplitudes for CH_2 before(+) and after(x) normalisation with the water signal amplitude from the (a) intra- and (b) inter-examination reproducibility measurements.

Discussion/Conclusion: Very good reproducibility was achievable for the lipid signals of interest indicating that, despite problems with motion and susceptibility effects, CMRS is an extremely promising tool for estimation of myocardial triglyceride content.
References:
1. Wende A. R. et al. (2010) BBA-Mol Cell Biol L 1801(3):311-9.
2. Singhal A. et al. (2009) Prog Nucl Magn Reson Spectrosc 54(3-4):255
3. Kozerke S. et al. (2002) Magn Reson Med 48(2): 380-384.
4. Naressi A. et al. (2001) MAGMA 12, 141-152.

699

Detection of functional lung defects using DC signal gated ^{1}H imaging

A. Fischer[1], M. Gutberlet[2], J. Vogel-Claussen[2], C.O. Ritter[1], D. Hahn[1], H. Köstler[1]
[1]*Institute of Radiology, University of Würzburg, Würzburg/GERMANY,*
[2]*Institute of Diagnostic and Interventional Radiology, Hannover Medical School, Hannover/GERMANY*

Purpose/Introduction: Recently, DC gated imaging has been shown to allow obtaining functional and morphological information of the human lung using standard ^{1}H imaging equipment [1,2] without administering contrast agents. This technique allows obtaining perfusion and ventilation maps similar to standard Fourier Decomposition (FD) [3]. Imaging is performed in free breathing without ECG triggering and, in contrast to FD, no restriction regarding spatial resolution exists. The presented work extends earlier studies [1,2] by initial examiniations of patients. The functional maps obtained by DC gated lung imaging were capable of accurately detecting lung defects which could be confirmed by comparison with established techniques.
Subjects and Methods: DC gated lung imaging was employed as described in [1,2]. By exploiting DC signal variations related to cardiac and respiratory motion, it was possible to retrospectively reconstruct complete cardiac and respiratory cycles. This allowed obtaining perfusion and ventilation maps from four patients (age 22-83). Imaging parameters: Siemens Avanto 1.5T, FLASH, T_R=2.50ms, T_E=0.70ms, matrix 128x128, slice 15mm, α=8°, 64000 quasi-randomly acquired PE steps[1,2], total measurement time 2:40 min. The obtained functional maps were compared to Dynamic Contrast-Enhanced (DCE) MRI (perfusion) and standard FD (ventilation).
Results: In Figure 1, data of a patient (f/22y) suffering from chronic thromboembolic pulmonary hypertension (CTEPH) are shown. A significant perfusion defect in the right lung as well as a small triangular defect in the left lung is recognizable. DC gated lung imaging exhibits these perfusion defects at the same positions with comparable dimensions as in DCE-MRI. The ventilation map shows no perceiveable abnormalities in this patient.

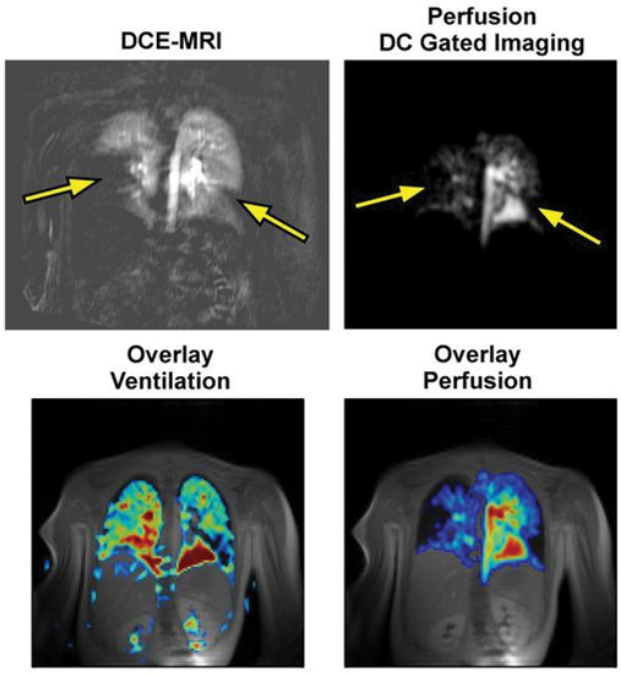

Figure 1

In Figure 2, data of a patient (f/45y) with Bronchiolitis Obliterans Syndrome (BOS) shows that ventilation defects can be equally well detected by DC gated functional lung imaging as in standard FD. As before, the defects appear at the same positions with similar dimensions.

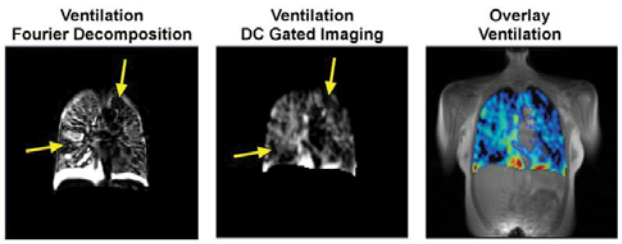

Figure 2

Discussion/Conclusion: The initial results of this work are encouraging with respect to accurately detecting functional pulmonary defects using DC gated imaging. The accuracy of the proposed method was verified using DCE-MRI and standard FD. Examining more patients is currently undergoing. Since spatial resolution is in principle not limited as in standard FD, future work will focus on obtaining higher resolved functional maps using DC gated lung imaging.
References:
[1] Fischer A. et al.; Proceedings 28th ESMRMB Abstract 66 (2011)
[2] Fischer A. et al.; Proceedings ISMRM V. 20 Abstract 1339 (2012)
[3] Bauman G. et. al.; Magn Reson Med V. 62, pp.656-664 (2009)

700

Multiple-quantum reconstruction of triple-quantum filtered data

D.P. Fiege[1], S. Romanzetti[1], F. Boada[2], S.R. Yutzy[2], Y. Qian[2], J. Felder[1], A. Celik[1], N.J. Shah[3]
[1]INM-4, Medical Imaging Physics, Forschungszentrum Jülich GmbH, Juelich/GERMANY, [2]Radiology and Bioengineering, University of Pittsburgh, Pittsburgh/PA/UNITED STATES OF AMERICA, [3]Department of Neurology, RWTH Aachen University, JARA, Aachen/GERMANY

Purpose/Introduction: Triple-quantum filtered (TQF) sodium MRI has been suggested to differentiate the signal from different physiological compartments [1]. The standard three-pulse sequence for triple-quantum coherence preparation creates zero-quantum (ZQ), single-quantum (DQ) and double-quantum (DQ) coherences as well. Usually, these are filtered out by a six-step phase cycling. However, they may also contain valuable information. By applying an additional phase factor to the data before summation of the six phase cycling steps, it is possible to reconstruct these signals from the raw data. We demonstrate this method in vivo on a healthy volunteer.
Subjects and Methods: The TQ preparation, consisting of three RF pulses with variable phases, creates coherences of order zero to three. Usually, only the triple-quantum coherence is of interest, therefore a phase cycling is employed such that all other coherences filter out. The phase difference between the first and third RF pulse, Φ, determines the phase of the coherences: An n-quantum coherence has phase n*Φ [2]. By changing the phase of the ADC in post-processing, the filter can be changed such that one of the coherences remains (and the other three cancel out).
The imaging experiment was performed on a healthy human volunteer on a Siemens 9.4T human whole-body MR scanner (Siemens Medical, Erlangen, Germany) using a home-built sodium birdcage coil (Affinity Imaging, Jülich, Germany). Images were acquired with the SISTINA [3] sequence. Parameters: τ=10.5ms,δ=40us, TE=0.8/10ms. From the same dataset, four images with different filters were reconstructed. The filter can be chosen by multiplying each step with the phase factor corresponding to the step and the desired filter. For illustration, see Figure 1.

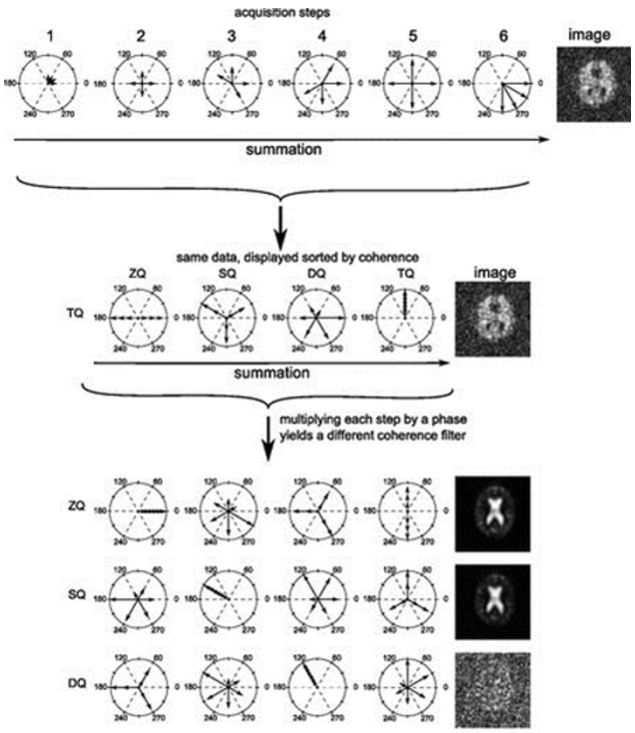

Figure 1: Reconstruction steps for obtaining all coherences. The sum of the six acquisition yields a TQF image (top). This is obvious when the acquisitions are sorted by coherence order. By multiplication of a phase factor, all other coherences are obtained.

Results: Several slices of the contrasts are shown in Figure (2). The ZQF and SQF images show bright CSF. The DQF image displays very low SNR. The TQF shows CSF dark and only matter white.

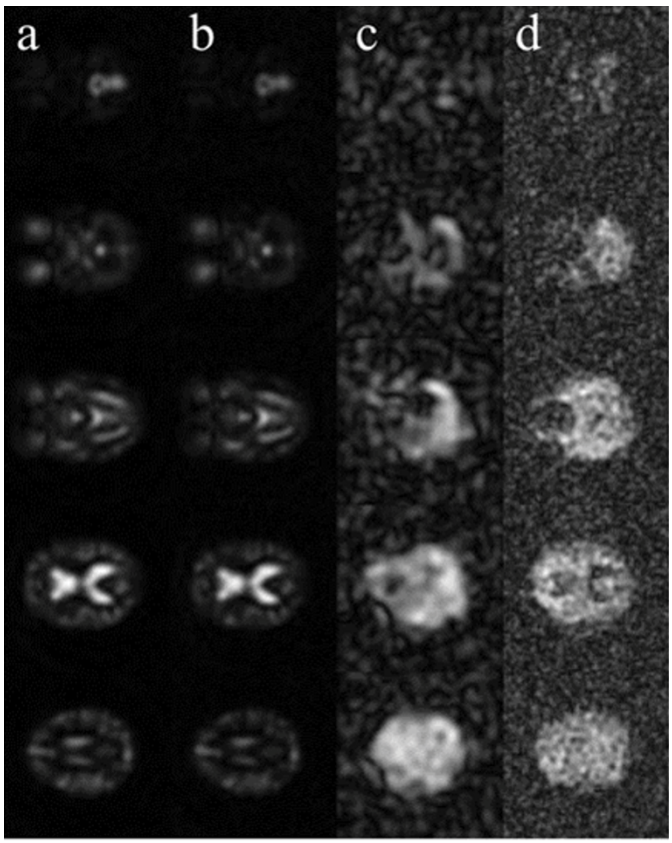

Figure 2: Corresponding slices through the brain of the four coherences. (a) ZQ, (b) SQ, (c) DQ, (d) TQ.

Discussion/Conclusion: The contrast of the SQF and ZQF images reflects their T2 weighting. The CSF with its monoexponential long T2 decay shows bright, while matter is barely visible. The DQF image should exhibit the same contrast as the TQF image, this is not visible because of the low SNR. Future application to diseases may yield valuable information about type and severity.
References:
1. Hancu I, Boada FE, Shen GX. 1999 Magn Reson Med, 1146–1154
2. Levitt MH. Spin dynamics. 2007 Wiley
3. Fiege DP, Romanzetti S, Mirkes CC, Brenner D, Shah NJ. 2012 Magn Reson Med, in press

EPOS™ Poster

Thorax and lung

701

Non-Contrast-Enhanced Perfusion MRI for Preoperative Assessment of Lung Function in Patients with Non-Small-Cell Lung Cancer (NSCLC): Preliminary Results

G. Sommer[1], G. Bauman[2], C. Dränkow[3], C. Heussel[4], H. Kauczor[5], H. Schlemmer[6], M. Puderbach[4]
[1]Radiology and Nuclear Medicine, University of Basel Hospital, Basel/SWITZERLAND, [2]Medical Physics in Radiology, German Cancer Research Center (DKFZ), Translational Lung Research Center Heidelberg (TLRC-H), Member of the German Center for Lung Research, Heidelberg/GERMANY, [3]Thoracic Surgery, Thoraxklinik Heidelberg, Translational Lung Research Center Heidelberg (TLRC-H), Member of the German Center for Lung Research, Heidelberg/GERMANY, [4]Diagnostic and Interventional Radiology, Thoraxklinik Heidelberg, Translational Lung Research Center Heidelberg (TLRC-H), Member of the German Center for Lung Research, Heidelberg/GERMANY, [5]Diagnostic and Interventional Radiology, Heidelberg University Hospital, Translational Lung Research Center Heidelberg (TLRC-H), Member of the German Center for Lung Research, Heidelberg/GERMANY, [6]Radiology, German Cancer Research Center (DKFZ), Translational Lung Research Center Heidelberg (TLRC-H), Member of the German Center for Lung Research, Heidelberg/GERMANY

Purpose/Introduction: Surgery is the only option for curative treatment of NSCLC. As lung function disorders are common comorbidities in patients with NSCLC, knowledge about preexisting lung function defects is important for predicting functional outcome and optimizing surgical procedures. Fourier decomposition MRI (FD-MRI) has been recently introduced as a method for assessment of regional lung function without contrast agents [1,2]. FD-MRI utilizes very short echo-time imaging of the native proton signal with subsequent image registration and spectral analysis to generate perfusion- and ventilation-weighted images. The aim of this ongoing study is to gain initial experience about FD-MRI as a tool for preoperative assessment of regional lung perfusion in NSCLC patients and validate the technique against dynamic contrast enhanced MRI (DCE-MRI) as standard of reference.
Subjects and Methods: Six patients (median age 64y, range 56–74y) with NSCLC of resectable stage were examined at 1.5T (Magnetom Avanto, Siemens, Germany). Time-resolved image data of the lungs were acquired in coronal and sagittal plane using a 2D-bSSFP sequence (TR/TE/TA=1.9/0.8/112ms, 4 images/s, FA=75°, ST=12mm, matrix=128x128). Respiratory motion was corrected with a nonrigid image registration algorithm [3]. Fourier decomposition was used to detect and separate periodic changes of lung proton density caused by respiratory and cardiac cycles. Perfusion-weighted images were created by pixel-wise integration of the cardiac spectral line. For DCE-MRI, a coronal 4D-TWIST sequence (TR/TE=2/0.8ms, FA=25°, ST=5mm, matrix=256x179) was used and subtraction images were calculated. FD- and DCE-perfusion data were analysed visually for perfusion defects.
Results: FD-MRI provided diagnostic image quality in five cases, but failed in one patient. Visual analysis revealed perfusion defects in 6 out of 95 evaluated segments with FD-MRI and 5 segments with DCE-MRI. Concordance rate was 92/95=97%. Two discordances were concerning the middle lobe, and one the right apex (primary tumor location). Fig. 1 shows a sample case of a patient with bulky nodal disease at the right hilum (arrow in d) causing decreased perfusion in the middle lobe (arrowheads). Additional perfusion defects are seen in the right upper lobe including the site of the primary tumor (arrows in a-c).

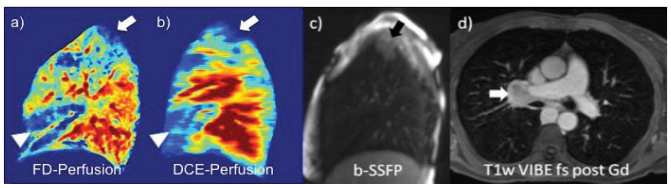

Discussion/Conclusion: Preoperative assessment of regional lung perfusion in NSCLC patients with FD-MRI is feasible and initial results in comparison with DCE-MRI are promising. However, further investigation is required to validate the technique in larger patient cohorts.
References:
[1] Deimling M et al. Proc. ISMRM 2008, Toronto, Canada, p.2202
[2] Bauman G et al. Magn Reson Med 2009, 62(3):656-64
[3] Chefd'hotel C et al. Proc. IEEE (VLSM'2001), Vancouver, Canada

EPOS™ Poster

Vasculature, angiography (excluding brain and coronaries)

702

Detection of intraplaque hemorrhage in carotid atherosclerosis patients: Comparison between 3D T1-weighted fat-suppressed CUBE imaging and 3D T1-weighted fat-suppressed SPGR at 3.0T

P.A. Wielopolski[1], A.C. Van Dijk[1], H.J.M. Verhagen[2], P.J. Koudstaal[3], A. Van Der Lugt[1]
[1]Radiology, Erasmus Medical Center, Rotterdam/NETHERLANDS, [2]Surgery, Erasmus Medical Center, Rotterdam/NETHERLANDS, [3]Neurology, Erasmus Medical Center, Rotterdam/NETHERLANDS

Purpose/Introduction: To compare isotropic three-dimensional (3D) T1-weighted (T1w) fat-suppressed (FS) fast spin echo (FSE) (3D T1w FS CUBE) to T1w FS 3D RF spoiled gradient echo (SPGR) scans in their ability to delineate intraplaque hemorrhage (IPH) in carotid atherosclerosis patients.
Subjects and Methods: After review board approval and informed consents, 40 patients (34 male, 6 female; age range 45–88 years, mean 68) were examined. 15 healthy volunteers were imaged to tune the imaging protocol in relation to signal-to-noise ratio (SNR), voxel size (VS) and acquisition time < 3 min per scan. The study was performed on a 3.0T Discovery MR 750 system (GE Healthcare, Milwaukee, MI, USA) using a radio-frequency (RF) transmit body coil and a 4-channel receive coil (2 channels per carotid artery, Machnet B.V., Roden, The Netherlands). A 2D time-of-flight (TOF) angiogram was used for positioning. For comparisons, 3D scans were reformatted perpendicular to the carotids main axis.
Results: Scanning was performed parallel to the main carotid artery encasing both carotids. The following imaging parameters were set: 5 cm volume, 64 sections 3D T1w FS CUBE with TR/TE=260/10 ms, echo train =8, number of excitations (NEX)=0.5, readout bandwidth (BW)=31.3KHz and VS=0.67 mm^3; 10 cm volume, 128 sections 3D T1w FS SPGR: TR/TE/flip angle=9/1.3 ms/30°, NEX=1.3, BW=62.5 KHz, VS=1.00 mm^3. Seven patients with IPH were selected for analysis. SNR was higher for 3D T1w FS SPGR but similar when a normal FS pulse was used in 3D T1w FS CUBE (default was ASPIR, adiabatic spectral inversion, creating banding artifacts and 30% worse SNR). IPH detection averaged 15% better with 3D T1w FS SPGR and more sensitive to visualize small arterial wall signal irregularities (2 patients, Figure, white arrows). Maximum IPH signal to wall contrast recorded was 4.2 for 3D T1w FS SPGR while 2.4 for 3D T1w FS CUBE (Figure, large yellow arrows). Blood attenuation in 3D T1w FS SPGR was robust and independent from inflow effects, with a maximum signal difference of 3.50 between wall and vessel lumen (average 1.71). Blood suppression was substantially better in 3D T1w FS CUBE (280%) but not uniform. Likewise, calcified plaques were difficult to appreciate from a dark vessel lumen, rendering the 3D T1w FS SPGR scan more useful for overall evaluation of plaque components.

Figure:

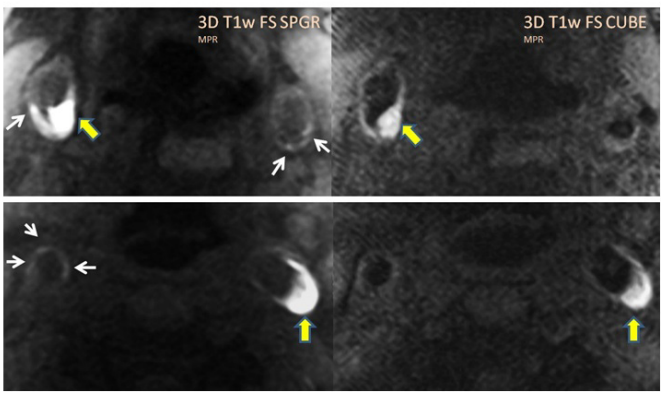

Discussion/Conclusion: 3D T1w FS SPGR provides better visualization of IPH in atherosclerotic plaques and delineates wall irregularities associated with atherosclerotic processes better than 3D T1w FS CUBE.

703

Improved delineation of vulnerable plaques in carotid atherosclerosis patients using contrast enhanced 3D T1-weighted fat-suppressed CUBE imaging at 3.0T

P.A. Wielopolski[1], A.C. Van Dijk[1], H.J.M. Verhagen[2], P.J. Koudstaal[3], A. Van Der Lugt[1]
[1]Radiology, Erasmus Medical Center, Rotterdam/NETHERLANDS, [2]Surgery, Erasmus Medical Center, Rotterdam/NETHERLANDS, [3]Neurology, Erasmus Medical Center, Rotterdam/NETHERLANDS

Purpose/Introduction: To compare isotropic three-dimensional (3D) T1-weighted (T1w) fat-suppressed (FS) fast spin echo (FSE) (3D T1w FS CUBE) to conventional ECG-triggered two-dimensional black blood FSE (2D T1w FS BB FSE) in their ability to delineate vulnerable plaque/lipid core in carotid atherosclerosis patients after contrast administration.
Subjects and Methods: After review board approval and informed consents, 40 patients (34 male, 6 female; age range 45–88 years, mean 68) were examined around the carotid bifurcations. 15 healthy volunteers were also imaged to tune the imaging protocol in relation to signal-to-noise ratio (SNR), voxel size (VS) and imaging time for both 2D T1w FS BB FSE and 3D T1w FS CUBE. The study was performed on a 3.0T Discovery MR 750 system (GE Healthcare, Milwaukee, MI, USA) using a radio-frequency (RF) transmit body coil and a 4-channel receive coil (2 channels per carotid artery, Machnet B.V., Roden, The Netherlands). In patients, 7.5 ml of Gadovist (Bayer HealthCare Pharmaceuticals, Germany) was administered independent of body weight. A 2D time-of-flight (TOF) angiogram was used for positioning. For comparisons, 3D scans were reformatted with the same slice thickness and orientation as the 2D scans.
Results: We settled for the following imaging parameters: fifteen ECG-triggered 2 mm 2D BB FS FSE scans positioned perpendicular to the main carotid artery around the carotid bulb (3 cm volume) with: TE=5.2 ms, echo train (ET)=12, number of excitations (NEX)=1, readout bandwidth (BW)=62.5 KHz and VS=0.68 mm^3; and a para-coronal 3D T1w FS CUBE volume (5 cm) along the main carotid artery with: TR/TE=260/10 ms, ET=8, NEX=0.5, BW=31.25 KHz, VS=0.51 mm^3. Pre-contrast SNR was similar for both sequences, somewhat higher for 2D FS BB FSE with lower heart rates (~50 bpm). Post-contrast enhancement averaged higher for the 3D sequence (range 1.3-2.4, mean 1.9 times in the carotid wall); lower heart rates provided worst T1 weighting as compared to 3D scans (Figure 1). Similar enhancement was found for heart rates around 90 bpm (Figure 2). Lumen definition was better in 2D scans but 3D acquisitions were comparable. Average imaging time for 2D was 5 min 40 s while for 3D constant at 2 min 30 s.

Figure 1:

Lower heart rate (48 bpm).
Carotid plaque (dashed circle)

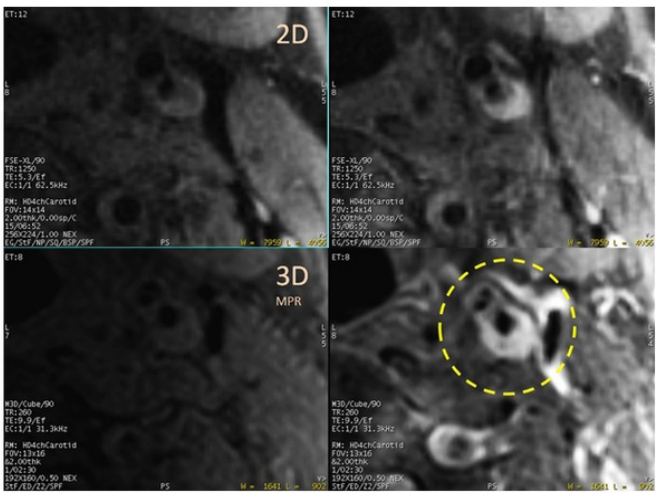

Figure 2:

Higher heart rate (85 bpm),
Carotid plaque (dashed circle); lipid core (arrows)

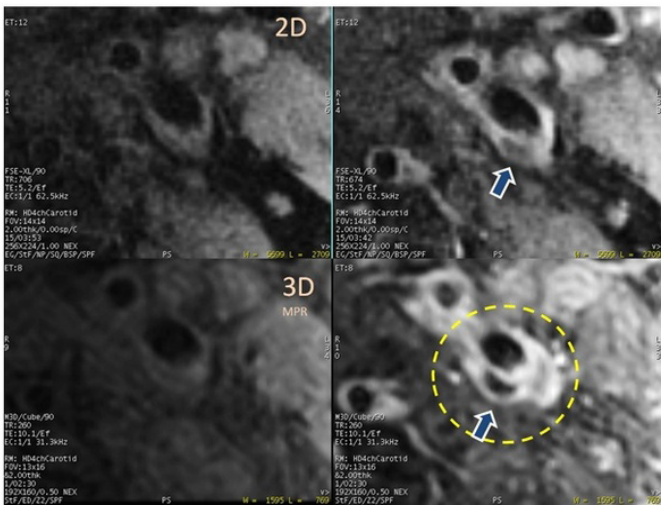

Discussion/Conclusion: 3D T1w FS CUBE provides a time-independent volume acquisition with better enhancement possibilities than ECG-triggered 2D T1w FS BB FSE at half the scan time with similar voxel sizes, SNR and image quality yet making it possible for multi-planar reformatting and full coverage of the carotid arteries.

Paper Poster

Animal models

704

Metabolic profile of inflammation in the hippocampus

X. Combaz[1], M. Cayre[2], Y. Le Fur[3], E. Pecchi[4], S. Courtes[2], S. Confort-Gouny[1], H. Ratiney[5], P.J. Cozzone[6], A. Viola[3]
[1]Université D'aix-marseille, CRMBM UMR CNRS 7339, Marseille/FRANCE, [2]Université D'aix-marseille, IBDML, UMR CNRS 6216, Marseille/FRANCE, [3]Université De La Méditerranée, CRMBM UMR CNRS 7339-Université d'Aix-Marseille, Marseille/FRANCE, [4]Faculte De Medecine La Timone, CRMBM UMR CNRS 7339, MARSEILLE/FRANCE, [5]Creatis, CNRS UMR 5220 – INSERM U1044 – Université Lyon 1 – INSA Lyon, Villeurbanne/FRANCE, [6]Centre De Résonance Magnétique Biologique Et Médicale ('umr 7339'), CNRS, Faculté de Médecine, Aix-Marseille Université, Marseille/FRANCE

Purpose/Introduction: Intracerebral injections are used in animal models of brain pathologies to evaluate the therapeutic impact of drugs, which cannot cross the blood brain barrier. These procedures not only cause lesions at the site of injection, but also may affect brain metabolism as a consequence of inflammation even in distant locations. In order to identify these perturbations we performed an *in vivo* ^{1}H-MRS study of mice receiving an intracerebroventricular (icv) injection of saline and analyzed the metabolic profile of the dendate gyrus, a neurogenic niche in the adult brain.
Subjects and Methods: C57BL/6J mice were explored before and after an icv injection of 2 ml saline isotonic to plasma (at day 1 and 4) on a 11.75 T vertical Bruker AVANCE 500 WB wide-bore MR system (Bruker). Localized ^{1}H-MRS spectra were acquired under isoflurane anesthesia with the PRESS sequence in the dentate gyrus (TE, 20 ms; TR, 1761 ms; 256 averages, 1024 points; water suppression, VAPOR sequence; VOI, 3x1.2x1.350 mm^3). The animals were sacrificed for histology at the end of the protocol. MRS data were processed with CSIAPO software including QUEST[1]. The metabolic database used in this study was constructed after the analysis of 6 brain extracts from C57BL/6J mice by high-resolution ^{1}H-NMR. In total 16 metabolites and 10 macromolecules were fitted. Results were expressed as ratios of the relative area of each metabolite signal to the sum (S) of all metabolite signal areas except macromolecules. A non-parametric statistical analysis was performed. Significance was set to p<0.05.
Results: At day 1 after the icv injection, there was a significant increase in NAA/S (+20%) compared to control values (CT), whereas at day 4, there was a significant increase in aspartate/S (+125 %) and lactate/S (+12%), and a decrease in *scyllo*-Ins/S (-95%) (Fig.1).

Fig.1: Metabolic changes in response to inflammation

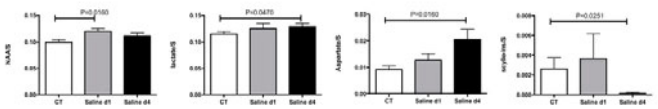

Discussion/Conclusion: The increase in lactate is often observed under inflammatory conditions, whereas the rise in NAA, a marker of neuronal function, is rather unexpected although an anti-inflammatory role has been suggested based on its ability to modulate certain pro-inflammatory cytokines[2]. Aspartate is involved in excitatory pathways and can be more neurotoxic than glutamate in the hippocampus. The report of a decrease of *scyllo*-Ins under inflammation is new and may reflect metabolic and/or osmoregulatory processes.
References:
1. Ratiney, H., et al. NMR Biomed 18, 1-13 (2005).
2. Rael, L.T., et al. Biochem Biophys Res Commun 319, 847-853 (2004).

705

Assessment of neurodegeneration in rat model of vascular dementia using ex vivo magnetic resonance microimaging and histology

A. Gálisová[1], M. Kršňák[2], C. Kronnerwetter[3], A. Kebis[1], K. Ambrušová[4], A. Berg[3], S. Kašparová[1]
[1]Faculty of Chemical and Food Technology, Slovak University of Technology, Bratislava/SLOVAK REPUBLIC, [2]Department of Internal Medicine III, Medical University of Vienna, Vienna/AUSTRIA, [3]Center for Medical Physics and Biomedical Engineering, MR Center of Excellence - Medical University Vienna, Vienna/AUSTRIA, [4]Faculty of Public Health, Slovak Medical University, Bratislava/SLOVAK REPUBLIC

Purpose/Introduction: Cerebrovascular lesions together with advanced age are assumed to be involved in the pathology of sporadic Alzheimer's disease (AD) [1]. A pathophysiological model of vascular dementia (VD) was confirmed as a suitable model mimicking AD-like pathology. Previous studies of VD model were focused on metabolic changes monitored by MR spectroscopy and biochemical tests but no imaging study has been performed yet. Therefore the aim of this study was to assess the hallmarks of AD, like the amyloid plaques and the neuronal loss, by means of *ex vivo* MR microimaging (MRMI) without the use of contrast agent.
Subjects and Methods: Five 11-months-old male Wistar rats were subjected to the three-vessels occlusion in the brain [2]. Six rats of the same age, breed and gender but without surgery served as controls. All rats were sacrificed one month after the surgery and removed brains were fixed in 10%-formaldehyde. MRMI was conducted on the 7T Siemens scanner equipped with the 750mT/m gradient coil insert and 19mm volume resonator. 3D T_2-weighted images were obtained by turbo spin echo sequence (TR=3000ms, TE=83ms, echo train length ETL=19, FA=15°, FOV=17x17mm, matrix 384x384, spatial resolution 44x44x200μm^3, scan time 5h). T_2 maps were reconstructed from the spin echo images (TR=3000ms, FA=180°, 24echoes, TE=8.4-201ms). Signal intensity profiles from hippocampus, contrast-to-noise ratios and T_2 relaxation times were estimated. After MRMI, brain tissues were prepared for histopathology by standard formalin-paraffin method and stained by hematoxylin-eosin.
Results: High quality images provide a detailed view of rat brain anatomy highlighting also different hippocampal layers (Fig.1). No individual amyloid plaques were detected, probably due to rather low age of examined animals. T_2-weighted images revealed differences between control and VD group in MR contrast of cortex (p<0.001), ventricles (p<0.05), CA1 (p<0.01) and CA3 (p<0.05) pyramidal cells and granular cells (p<0.05). Moreover, an elevation of T_2 times was found in these areas (ventricles, cortex, CA1 cells, p<0.001) (Fig.2). The observed changes correspond to histological findings of necrosis in the CA1 subfield seen in Fig.3. Statistical analysis was performed by two sample t-test with significance level 0.05.

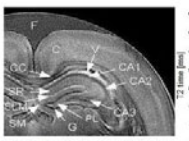

Fig. 1. MRMI image of VD brain highlighting microscopic structural details of the subfields of hippocampus. F – formalin, C – cortex, CC – corpus callosum, V – ventricle, CA1, CA2, CA3 – pyramidal cells, SR – stratum radiatum, SLM – stratum lacunosum moleculare, SM – stratum moleculare, G – granule cell layer, PL – polymorph layer

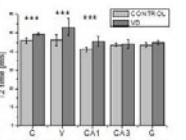

Fig. 2. Bar graph of average T_2 relaxation times calculated from ROI in different areas of hippocampus show significant elevation in cortex, ventricles and CA1 pyramidal cells. Error bars represent standard deviations, ***p<0.001.

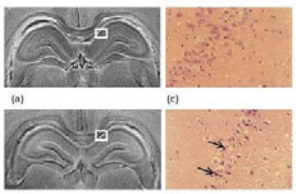

Fig. 3. Comparision of MR images of control (a) and VD (c) group with corresponding histological images (c, d) at magnification 400x. Damaged CA1 pyramidal neurons in the hippocampus are pointed by arrowheads.

Discussion/Conclusion: Our results demonstrated the ability of MRMI to distinguish between healthy and damaged tissue of rat brain on microscopical level. We found prominent signs of damage caused by three-vessels occlusion and necrosis of pyramidal cells in rat hippocampus and confirmed these by histology.
References:
[1] de la Torre,J.C., 2004,Lancet Neurol,3:184, [2] Horecky et al.,2009,J Neurol Sci, 83:178-183

706

MR studies on rat cortex during and after ischemia at 14.1T

H. Lei[1], H. Frenkel[1], R. Gruetter[2]
[1]Department of Radiology, University of Geneva and Lausanne, Lausanne/SWITZERLAND, [2]Department of Radiology, University of Geneva and Lausanne, Geneva Lausanne/SWITZERLAND

Purpose/Introduction: Improved sensitivity and spectral resolution of ^{1}H MRS at high magnetic fields allowed longitudinally studying mouse brain after transient ischemia (1). This opens possibilities in studying specific brain tissue for metabolic alterations during ischemia. The aim of this study was to demonstrate feasibilities of both MRI and MRS studying on rat cortex during ischemia at 14.1T.

Subjects and Methods: Under isoflurane anesthesia mixed with air, four adults Wistar rats (~350g) were prepared to induce a four-vessel-occlusion ischemia on the bench and two were induced in the magnet. Two vertebral arteries were permanently sutured and two occluders along with extension tubes were placed around both carotid arteries for further occlusion in the scanner. Once the preparations were ready, animal heads were stereotaxically fixed with two ear bars and one bite piece, carefully placed in a home-made holder for MR studies. Through the entire MR studies, animals were well maintained under phsyiological conditions.

T_2-weighted images were acquired for precisely identifying cortical tissue and evaluation of vasogenic edema. SPECIAL(2) was applied on cortical tissue during occlusion, which can be done remotely. Once the scans were finished, the occluders were carefully removed and the incision scars were sutured. One day later, T_2-weighted images(1) and diffusion MRI(3) were acquired for identifying edema.

Results: All animals were scanned one day after the occlusions. Under such conditions, 1hr occlusion resulted in some T_2-hyperintensive contrast in brain but not all one day later. Cortical ADC values (Fig-1) were $6.93\pm0.09\times10^{-4}$mm^2/s in rats with cortical lesion and $6.95\pm0.04\times10^{-4}$mm^2/s in rats with metabolic alterations during ischemia even with no T_2-hyper-contrast in cortex one day later. All ADC values of these rats were significantly lower ($p<0.001$, ttest) than $7.38\pm0.11\times10^{-4}$mm^2/s in the healthy controls (3). ^{1}H MR spectra were acquired during ischemia (Fig-2), in which N-acetyl-aspartate), in which N-acetyl-aspartate reduced ~12% towards the end of ischemia.

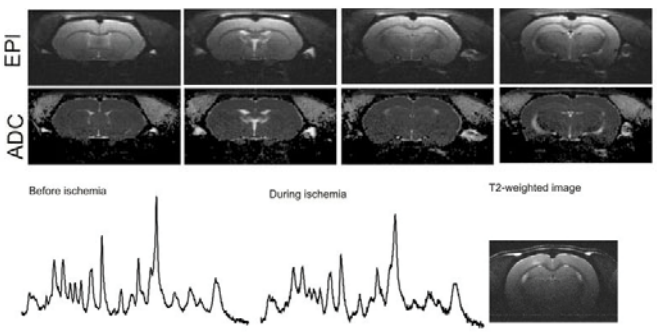

Discussion/Conclusion: We successfully demonstrated that the four-vessel-occlusion stroke model can be remotely preformed when rats were in the 14.1T scanner. This allows us following metabolic evolution before, during and immediately after ischemia. The spectral and other changes could help us understand the consequences of ischemic damages and their restoration of reperfusion remained to be further explored.

References:

1 Lei H et al. JCBFM 2009(29):811;
2) Mlynarik V et al. MRM 2006(56):965;
3) Van de Looij Y et al. MRM 2011(65):732.

707

Multi-parametric MRI investigation of two intracranial glioma models at 7T

P. Porcari, J.K.R. Boult, Y. Jamin, S.P. Robinson
Division of Radiotherapy and Imaging, The Institute of Cancer Research and Royal Marsden NHS Foundation Trust, CR-UK and EPSRC Cancer Imaging Centre, Sutton, Surrey/UNITED KINGDOM

Purpose/Introduction: This study aims to investigate the features and differences between two models of gliomas propagated in mice, rat RG2 [1] and human SF188 [2] using a multi-parametric MRI approach. MRI findings were correlated with specific histopathological features of the tumours.

Subjects and Methods: Twelve female CD1 nude mice were orthotopically implanted with luciferase expressing rat RG2 cells ($5x10^3$ cells, n=6) or human paediatric SF188 cells ($5x10^3$cells, n=6). Tumour establishment and progression were monitored by bioluminescence imaging. MRI measurements were performed using T_2-weighted turbo-spin-echo images, fluid attenuated inversion recovery (FLAIR) imaging, inversion-recovery (IR)-trueFISP scans and diffusion-weighted imaging. The same images were acquired from three healthy (control) mice. Parametric T_1, T_2 and apparent diffusion coefficient (ADC) maps were computed. Mean ADC, T1 and T2 were quantified for regions-of-interest containing tumour, contralateral (CL) area, and the corresponding regions of normal brain in control mice. Immediately after MRI investigation, mice were administered with Hoechst 33342 (15mg/kg, i.v.) and perfusion was subsequently assessed on frozen tissue sections using fluorescence microscopy.

Results: Figure 1 compares images and parametric maps of RG2 (left panel) and SF188 (right panel) glioma models. Coronal T_2-w and FLAIR images, and parametric ADC, T_1 and T_2 maps from a si

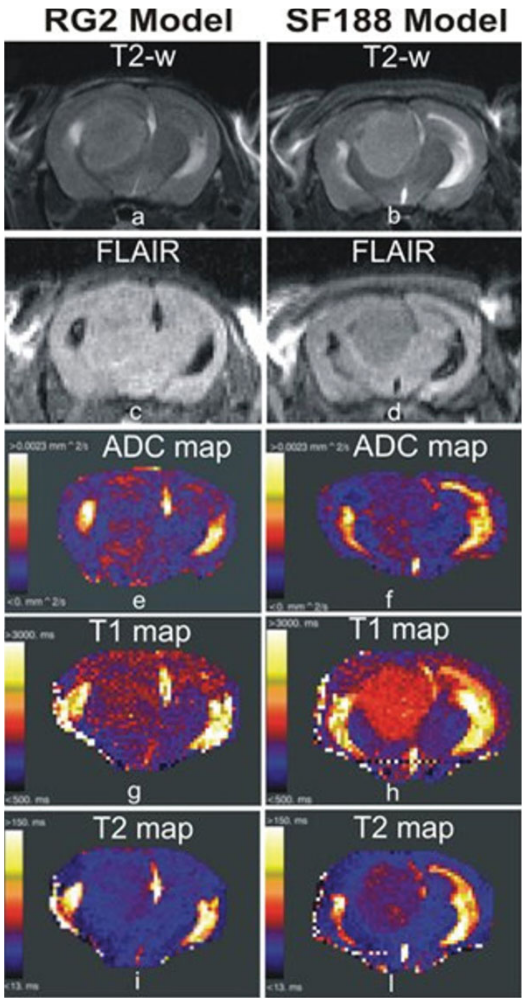

ngle mouse are displayed for each model. T_2-w scans were collected for anatomical reference, and FLAIR images for identifying infiltrative areas of glioma, as it has been clinically adopted [3]. ADC, T_1 and T_2 values derived from tumour and CL area, and from the related brain regions of controls are summarized in the Table. Relaxation times of SF188 tumours are slightly higher than the related values in the RG2 model, whilst ADC values of both tumours showed no differences. This could be explained by a perfusion component, which normally obscures the diffusion behaviour for low b-values (<200s/mm²), preventing discrimination of ADC values derived from each tumour. Indeed, RG2 and SF188 tumours are well vascularised, and more than the surrounding tissue, as confirmed by Hoechst 33342 uptake.

Table Summary of *ADC* values and native relaxation times of tumour (T) and contralateral (CL) area for RG2 and SF188 glioma models, and for the same brain regions of the control group. Data are mean ± 1 s.e.m.

Gliomas	*ADC* values (10^{-4} mm²/s)		T_1 relaxation time (ms)		T_2 relaxation time (ms)	
	T	CL	T	CL	T	CL
RG2	7.16 ± 0.03¶¥	5.04 ± 0.07	1393 ± 5¶¥	1273 ± 13	41.30 ± 0.22¶¥	38.42 ± 0.95
SF188	7.06 ± 0.03¶¥	5.13 ± 0.05	1526 ± 8¶¥	1213 ± 10	50.98 ± 0.41¶¥	36.38 ± 0.43
Control*	5.25 ± 0.13	5.26 ± 0.14	1211 ± 24	1193 ± 15	35.23 ± 0.78	34.19 ± 0.75

* Control data were acquired from complementary brain regions of tumour and CL area.
Statistics: ¶ significantly different from CL area in the same group (unpaired two-tailed t test, $p<0.05$); ¥ significantly different from the related brain regions in the controls (unpaired two-tailed t test, $p<0.05$).

Discussion/Conclusion: This study shows the possibility of characterizing specific features of orthotopic gliomas using a multiparametric MR approach, and can be considered as a starting point for studying analogies and differences between RG2 and SF188 models.

References:

[1] Kemper, EM, 2006, Eur. J Cancer. 3294-303;
[2] Gaspar, M, 2010, Mol. Cancer. Ther. 1219-33;
[3] Kubota, T, 2005, J Mag Reson Imaging 694-700

708

Comparison of different MRI pulse sequences for quantitative T2 measurements in preclinical studies.

W.I. Piędzia, K. Jasinski, W.P. Węglarz
Department of Magnetic Resonance Imaging, Institute of Nuclear Physics PAN, Kraków/POLAND

Purpose/Introduction: MRI is a potential tool for precise measurement of myelin water content for variety of neurodegenerative diseases [1]. Measurements of the short component of multi-exponential T2 decay in neurons may provide valid information about myelin content. However, standard pulse sequences currently available on preclinical MRI scanners are prone to magnetic field inhomogeneities, resulting in alteration of the measured T2 decay. The goal of our study was to compare efficiency for quantitative T2 imaging of multi spin-echo based pulse sequence available on Bruker Biospec 9.4T scanner with custom implemented one utilizing composed refocusing pulse.

Subjects and Methods: Custom implemented Multi-Echo pulse sequence utilizing Levitt – Freeman's composed refocusing 90_0-180_{90}-90_0 pulse and decaying crusher gradients pattern [2] was compared with Multi-Slice Multi-Echo T2 map sequence using Mao refocusing pulse [3]. In addition spectroscopic CPMG sequence [4] with block pulses was used to measure multi-component T2 decay. The same experimental parameters were used for each measurements (TR = 10 s, TE = 10 ms). Number of echoes in imaging experiments was set to 64, while 512 echoes was used in CPMG sequence. Measurements were done using phantom containing three sample tubes filled with two different copper sulfate ($CuSO_4 \cdot 5H_2O$) concentrations and distilled water, as well as using formalin fixed excised rat brain. Image registration and CPMG measurements were carried out using 9.4T/21cm horizontal bore Bruker Biospec MRI scanner. T2 components deconvolution and T2 maps of short and long components were produced using custom developed Matlab (MathWorks, Natick, MA, U.S.A.) scripts.

Results: Table 1 contains results of transverse relaxation times (in ms) obtained in our experiment for each pulse sequence.

	Mao	Levitt-Freeman	CPMG
CuSO4 –short T2	17,6+/-0,9	17,3+/-1,0	17,8+/-0,5
CuSO4 – long T2	76,7+/-1,4	72,4+/-2,0	75,8+/-0,9
H2O	583+/-2	824+/-10	2300+/-50

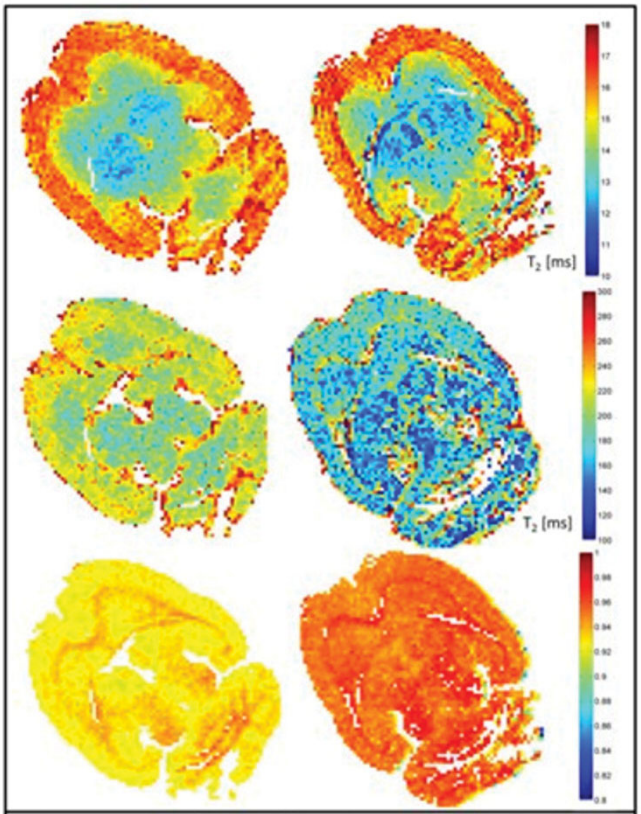

Fig.1. Maps of short and long T_2 components and short component fraction obtained with MSME (left) and composite refocusing pulse sequence (right). Slightly better contrast for short component is observed for image obtained with sequence utilizing composite (Levitt-Freeman) refocusing pulse.

Discussion/Conclusion: Our study demonstrated that sequence utilizing composed refocusing pulse performs better at first few echoes thus allowing for more reliable assessment of short T2 component. Results from phantom measurements suggest that also on the last part of the multiple echo decay this sequence performs better resulting in larger estimated T2 value for long component. The last observation was however not confirmed for fixed brain tissue, where both sequences give comparable results.

References:

[1] D. Grenier *et.al.* Magn.Res.Imag. 20 (2002) 733–741
[2] C.S. Poon, R.M. Henkelman, JMRI 1992; 2:541-553
[3] Bruker: *ParaVision 5.0. Application Manual*
[4] M.D. Hürlimann *et.al.* J.Mag.Reson. 143, 120–135 (2000)

709

In vivo diffusion tensor imaging and tract based spatial statistic in three different mouse models of Alzheimer's Disease

M. Marizzoni[1], E. Micotti[2], M. Lorenzi[1], A. Paladini[2], C. Balducci[2], A. Caroli[3], S. Dix[4], M. O'Neill[4], C. Czech[5], L. Ozmen[5], J. Richardson[6], G. Forloni[2], G. Frisoni[1]
[1]LENITEM Laboratory of Epidemiology, Neuroimaging, & Telemedicine, IRCCS San Giovanni di Dio Fatebenefratelli, Brescia/ITALY, [2]Department of Neuroscience, Mario Negri Institute for Pharmacological Research, Milano/ITALY, [3]Biomedical Engineering Department, Mario Negri Institute for Pharmacological Research, Bergamo/ITALY, [4]Lilly Research Centre, Eli Lilly, Surrey/UNITED KINGDOM, [5]CNS Research, Hoffmann-La Roche AG, Basel/SWITZERLAND, [6]GlaxoSmithKline, GlaxoSmithKline, Stevenage/UNITED KINGDOM

Purpose/Introduction: Diffusion Tensor Imaging (DTI) can be applied for the detection of white matter (WM) alterations in mild cognitive impairment (MCI) [1] and Alzheimer's Disease (AD) [2]. However, WM microstructural alterations have not been well characterized in any mouse model. We report the DTI parameters changes detected in three different mouse models of age-dependent amyloid deposition using the conventional hand drawn regions of interest (ROIs) method and a modified version of a whole brain voxelwise method used in human studies (Tract Based Statistical Analysis protocol (TBSS) [3]).
Subjects and Methods: Wild-type (WT), single APP mutant, PDAPP, double APPxPS-1 mutant TASTPM, and triple TauPS2APP mutant mice were followed from 3 to 20 months. All animals were handled in accordance with European guidelines for animal care. The in vivo diffusion-weighted acquisitions were gained using DTI EPI sequence (19 directions and b-value= 800 s/mm2). Fractional anysotropy (FA) maps were obtained using FSL. Manual analysis. Different regions of interest (ROIs) were manually drawn using the colour coded map. Voxelwise analysis. In order to reliably process the FA images, we developed a processing pipeline based on a modified version of the TBSS. The FA template was computed by iterative affine registration of the individual FA images, and it has been used as a reference space for projecting the individual FA maps. The projected FA values have been used for the subsequent group-wise voxel-by-voxel comparison of the FA distributions.
Results: Manual analysis showed significant FA reduction in different brain structures including corpus callosum, anterior commissure and external capsule of older TASTPM when compared with age-matched WT. Automated approach did not confirmed the anterior commissure FA decrement but showed FA decrease in regions not considered with manual analysis (fimbria, internal capsule). The same areas in single and triple mice were substantially unchanged with aging using both methods.
Discussion/Conclusion: Our results show age-related WM deficits in TASTPM mice promoting them as a potential model to study WM pathology in AD. These findings also indicate that neurodegenerative changes in TASTPM mice can be detected with the automated method, avoiding time-consuming and operator-dependent procedures.
The research leading to these results was conducted as part of the PharmaCog consortium funded by the European Community's Seventh Framework Programme for the Innovative Medicine Initiative under Grant Agreement n°115009 (www.alzheimer-europe.org).
References:
[1] Stahl R, et al. 2007. Radiology; 243(2):483-92.
[2] Liu Y, et al. 2011. Neurobiol Aging. 32(9):1558-71.
[3] Smith SM, et al. 2006. Neuroimage. 31(4):1487-505.

710

Ultra highfield imaging for in vivo phenotyping of genetically modified mouse strains using multidimensional analysis.

M. Meier[1], D. Wedekind[2], H.J. Hedrich[2]
[1]Small Animal Imaging Unit, Hannover Medical School, Hannover/GERMANY, [2]Institute for Laboratory Animal Science, Hannover Medical School, Hannover/GERMANY

Purpose/Introduction: The need for improved tools for characterizing mouse models of human diseases pushes the field of mouse phenotyping using high-field magnetic resonance imaging (hMRI). HMRI can provide important results for comparison of human conditions with mouse disease models. For the evaluation of treatment, monitoring disease progression and as direction for histological investigations it is most powerful. Here we focus on anatomical phenotyping based on the measurement of proton relaxation times, T1 and T2 of organs in mice at 7T. The knowledge of relaxation times is necessary for optimizing imaging contrast. Relaxation times are an important and known way to investigate properties of tissues and to separate normal tissue from diseased tissue.
Subjects and Methods: Relaxation measurements were performed in C57/BL6 mice (N=8) and four other genetically modified strains (N=32) with a Bruker Pharmascan 70/16 in equally sized ROIs in liver, kidney, leg muscle and brain. For data analysis a vector was constructed from the mean T1 and T2 values of the ROI in each organ. From this multidimensional vectors a graphically projection on to a 2D plane was calculated.
Results: Relaxation times in C57/BL6 were comparable to values found in the literature. Interestingly the graphically representation of the vectors of mean T1 and T2 values on the 2D plane makes all 5 groups clearly distinguishable. Due to the low number of animals this still has to be verified.

Location	T1[ms]	T2[ms]
Kidney	1554	59
Leg muscle	1180	43
Liver	980	56
Brain (Cerebellum)	1340	80

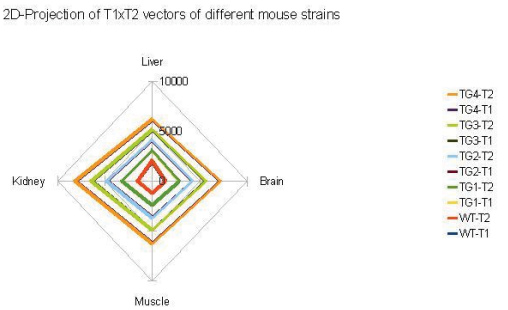

Discussion/Conclusion: One might speculate where differences in relaxation times originate. They were not obvious in organs other than the brain. As the specific weight of the different organs is nearly constant [1], cell density might be ruled out. However, different blood volumes in the various organs could be one source. [2] Blood contains substantial amounts of paramagnetic Fe^{3+}. Thus, relaxation times should be shorter with higher regional blood volume. As the order of T1 relaxation times aligns to the regional blood volume, we assume that Fe^{3+} content contributes to the differences in the relaxation times. However, other factors might still influence the relaxivity as well.
References:
[1] Tang Haiying et al. High-resolution magnetic resonance imaging tracks changes in organ and tissue mass in obese and aging rats. Am J Physiol Regul Integr Comp Physiol, 2001, 282,890–899
[2] Horn Michael et al. 31p-nuclear magnetic resonance spectroscopy of blood: A species comparison. Journal of Cardiovascular Magnetic Resonance, 2000, 2(2),143–149

711

Assessment of dysmyelination in the spinal cord shiverer mice using different imaging modalities at 14.1T

R. Maddage[1], N. Kunz[2], G.A. Lodygensky[3], J.P. Marques[1], R. Gruetter[4]
[1]Functional and Metabolic Imaging, Ecole Polytechnique Fédérale de Lausanne, Lausanne/SWITZERLAND, [2]Division of Child Growth & Development, University of Geneva, Geneva/SWITZERLAND, [3]Department of Pediatrics, Research Center CHU Sainte-Justine, Montreal/CANADA, [4]Department of Radiology, University of Geneva and Lausanne, Geneva Lausanne/SWITZERLAND

Purpose/Introduction: Accurate assessment of myelin in animal models and humans is of prime importance to determine the degree of white matter integrity in injuries and diseases. In the present study, spinal cord dysmyelination of shiverer mice was studied at 14.1T using several quantitative imaging modalities sensitive to myelin such as Quantitative Susceptibility Maps (QSM), Diffusion Tensor Imaging (DTI), T1, T2, T2* maps and Magnetization Transfer Imaging (MT).

Subjects and Methods: Scans were performed on a 14.1T/26 cm scanner (Varian/Magnex Scientific) on excised spinal cords of 5 week-old mice (N=2 shiverer, N=2 control). Tissue samples were fixated with paraformaldehyde by intra-cardiac perfusion[1] and subsequently immersed in PBS for imaging purposes.

QSM: 2D-GE, TR=550ms, TE=14ms/5ms, resolution=78*78*78μm^3. QSM were computed based on a regularized single orientation method[2,3].

DTI: SE with segmented EPI, TR/TE=2000ms/35ms, 21 directions, b=2'200s/mm2, resolution=78*78*2000μm^3.

T_1 mapping Inversion-recovery Look-Locker EPI sequence with 50 inversion times (20ms to 5020ms), TR/TE=30.5s/5.7ms, resolution=78*78*2000μm^3.

T_2 mapping: 2D-SE, 32 echoes (TE:11ms/5ms/166ms), TR=3000ms, resolution=104*104*2000μm^3.

T_2* mapping: 2D-GE, 23 echoes (TE:6ms/2ms/50ms), TR=550ms, resolution=78*78*2000μm^3.

MT: 2D-GE, TR/TE=100ms/4ms, saturation pulse:29ms, 500Hz, FA=950°, resolution=78*78*2000μm^3.

Results: In the MTR, T1 and T2 maps, shiverer WM/GM contrast was significantly diminished/absent (Fig.1) as confirmed by the very close similarity between the WM and GM values (Table 1).

In the other hand, DTI, phase, QSM and T2* map yielded sufficient contrast to distinguish the WM structure in the shiverer (Fig.1). In comparison to the control WM, shiverer WM showed a decrease of the FA (-21%) and increase of radial diffusivity (+43%). Similarly, T2* WM was increased by 30%. QSM indicated a 25% decrease in Δχ (Table 1).

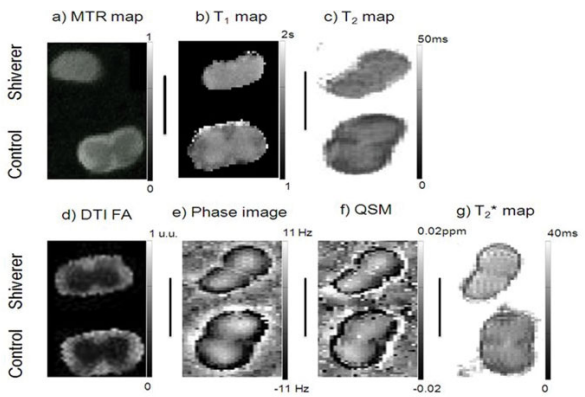

Figure 1. Shiverer and control spinal cords images. In shiverer, a) MTR map, b) T_1 map, c) T_2 map, d) DTI FA map, e) Phase image : images were unwrapped and background field contributions originating from imperfect shimming, air tissue interfaces were filtered using the SHARP algorithm[2] , f) QSM, g) T_2* map. The spinal cord images shown have different orientations as they have been acquired in two separate scans.

		White Matter		Gray Matter	
		Control	Shiverer	Control	Shiverer
MT		0.27 ± 0.02	0.20 ± 0.01	0.19 ± 0.01	0.21 ± 0.01
T_1	*s*	1.42 ± 0.04	1.54 ± 0.02	1.54 ± 0.03	1.59 ± 0.03
T_2	*ms*	15.2 ± 1.3	24.1 ± 0.8	23.4 ± 1.2	26.2 ± 0.9
FA	*u.u.*	0.62 ± 0.12	0.49 ± 0.09	0.16 ± 0.05	0.18 ± 0.05
Trace	10^{-4} *mm²/s*	4.0 ± 0.8	4.8 ± 0.6	4.4 ± 0.4	4.7 ± 0.4
Axial diffusivity	10^{-4} *mm²/s*	7.4 ± 1.4	7.7 ± 0.9	5.1 ± 0.5	5.5 ± 0.5
Radial diffusivity	10^{-4} *mm²/s*	2.3 ± 0.7	3.3 ± 0.6	4.0 ± 0.4	4.3 ± 0.4
Δω	*Hz*	7.9 ± 3.9	5.9 ± 3.3		
Δχ	10^{-2} *ppm*	2.2 ± 0.7	1.6 ± 1.0		
T_2*	*ms*	14.9 ± 2.5	19.3 ± 0.4	23.1 ± 1.5	29.0 ± 2.4

Table 1. Quantitative measurements obtained from the seven imaging modalities (Mean and standard deviation). Δω and Δχ were established as the frequency shift difference between GM and WM.

Discussion/Conclusion: The near absence of WM/GM contrast in the shiverer suggested that T1 and T2 maps could be considered as good clinical markers of dysmyelination, although they are known to also reflect properties such as water mobility and iron concentration. MTR and DTI results obtained are in agreement with literature [4]. FA, phase/QSM and T2* map indicated a less specific sensitivity to myelin content as the shiverer WM structure was still distinguishable even though visible changes were discernible. Further work will be done to extract more quantitative information from the data by using qMT and multi-component T2 techniques as well as histology to evaluate the specificity of each technique.

References:

[1]Lodygensky,Neuroimage2011[2]Schweser,Neuroimage2011[3]de Rochefort,MRM2010[4]Ou,NMRinBiomedecine2009. Supported by CIBM of the UNIL-UNIGE-HUG-CHUV-EPFL, FP7-CONNECT and the Leenaards-Jeantet Foundations.

712

Imaging of the ovine femoral head using IR-prepared 3D Ultrashort TE Pulse Sequences

K. Hemberger[1], P. Jakob[2], D. Haddad[1]
[1]Musculoskeletal MRI, Research Center Magnetic Resonance Bavaria (MRB), Wuerzburg/GERMANY, [2]MRI, Research Center for Magnetic Resonance Bavaria, Wuerzburg/GERMANY

Purpose/Introduction: Avascular femur head necrosis is an increasingly common cause of musculoskeletal disability. Ultrashort TE (UTE) sequences which enable very short TE [1] now offer the potential to estimate the bone water of the femoral head. Combining UTE sequences with long T2 suppression techniques affords high contrast imaging. When imaging the femoral head, voxels contain both long and short T2 species and accurate separation of these components is required. Here we describe the use of IR-prepared 3DUTE [2] for imaging the femoral head of a sheep, the standard animal model for femoral head necrosis. The method was then implemented on a cadaveric haunch of an adult merino sheep.

Subjects and Methods: Measurements were performed on a 1.5T Avanto scanner (Siemens, Erlangen). To verify the effectiveness of the sequence phantom tests were performed on four tubes filled with water, oil and two various concentrations of $MnCl_2$ (resulting in T_2*≈ 0.5ms and 2ms).

The image sequence used in these experiments consisted of a non-selective hard pulse (50μs), followed by a 3D radial ramp sampling UTE k-space acquisition. The IR-prepared sequence consisted of one long hyperbolic secant adiabatic inversion pulse (8ms) with broad spectral bandwidth (1kHz) followed by one UTE acquisition after a time delay TI. The preparation pulse inverts long T2 components while less affecting short T2 protons. When TR is short and the magnetization has reached a steady state fat and water magnetization reach their null point at nearly the same time point resulting in negligible residual longitudinal magnetization at TI.

The acquisition parameters were: TE = 50μs, TR = 40ms, TI = 18.5ms, FoV: 200mm for phantom and 256mm for sheep, 128 readout points. 10K projec-

tions for phantom and 30K for sheep were acquired, leading to total scan time about 6min and 33min.
Results: Fig 1 and Fig 2 show non-prepared and IR-prepared 3DUTE images of phantom and ovine haunch. Despite the deep of the joint (~ 9cm) the femoral head can be shown in an acceptable scan time.

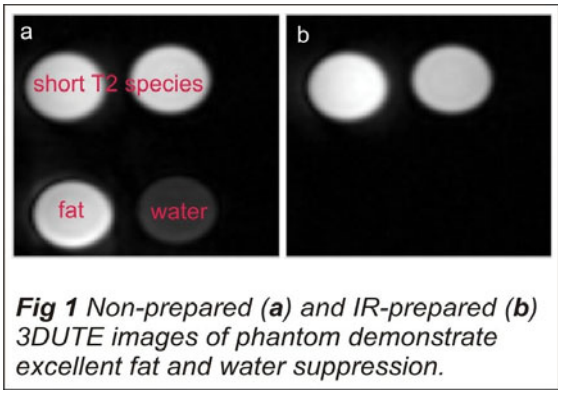

Fig 1 *Non-prepared (**a**) and IR-prepared (**b**) 3DUTE images of phantom demonstrate excellent fat and water suppression.*

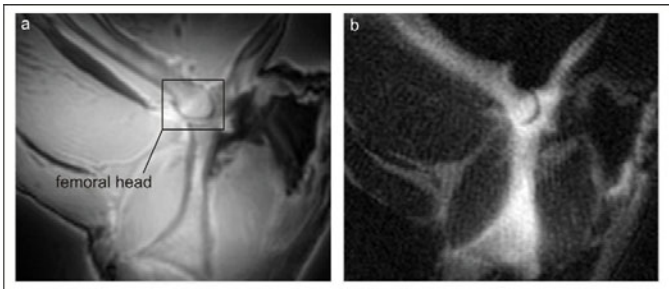

Fig 2 *Non-prepared (**a**) and IR-prepared (**b**) 3DUTE images of an ovine haunch.*

Discussion/Conclusion: IR-prepared 3DUTE is able to provide direct signal of bone water of ovine femoral head with excellent suppression of long T2 components and shows much promises to become a useful method to estimate the bone tissue of femoral head.
References:
1. Rahmer J, MRM 2006; 55:1075-1082; 2. Li C, MRM 2011;
The research leading to these results has received funding by the European Union's Seventh Framework Programme under grant agreement number 242175-VascuBone.

713

MR Imaging for Assessment of Early Treatment Effect in a Mouse Model of Mucosal Melanoma

Y. Sun[1], J. Wang[1], A. Saur[1], A. Lara Albarez[1], F.S. Hodi[2], A.L. Kung[1]
[1]Lurie Family Imaging Center, Dana Faber Cancer Institute, Harvard Medical School, Bostgon/MA/UNITED STATES OF AMERICA, [2]Medical Oncology, Dana Farber Cancer Institute, Harvard Medical School, Boston/MA/UNITED STATES OF AMERICA

Purpose/Introduction: There is a pressing need to develop more efficacious therapies for disseminated mucosal melanoma. Recently, gain of function mutations in c-KIT have been found in subclasses of mucosal melanoma. Nilotinib is a FDA-approved tyrosine kinase inhibitor that targets c-KIT (1). We developed a mucosal melanoma mouse model, and used MRI to assess the early effects of nilotinib treatment.
Subjects and Methods: M6 mucosal melanoma cells were injected subcutaneously in the flank in 13 NOD-SCID-IL2Rnull mice. Mice were imaged weekly to monitor tumor development. When tumors reached about 400 mm^3, 8 mice were treated orally with nilotinib (75 mg/kg) daily for three days, 5 mice were used as controls. MRI experiments were performed on a Bruker 7T BioSpec system. T2 weighted images were acquired to follow tumor growth. T1 and T2 measurements were acquired for evaluation of treatment effects in addition to tumor volume assessment. The tumor volume was quantitated using 3D slicer. Tumors were fixed in 10% buffered formalin, imbedded in paraffin, sectioned, and stained with H&E.
Results: Fig. 1A shows T2 images which revealed tumor heterogeneity as tumors grew. The variation of T2 signal over time may reflect different degrees of necrosis. Fig. 1B shows the tumor growth curve. Fig. 2 shows the comparison of tumor volume, T1 and T2 before and after treatment. Table 1 shows the early effect of treatment (after 3 doses) with nilotinib resulting in significant reduction in tumor volume, T1 and T2, while control animals showed non-significant increases in these values, which was due to the slow growth of the tumor over 3 days. Histologic analysis showed that in the treated tumors, there is increased necrosis and decreased areas of viable tumor in comparison to control tumors.

	Control			Treated		
	Vol	T1	T2	Vol	T1	T2
Pre	430±52	2076±110	79±12	400±74	2078±120	77±20
Post	467±73	2129±143	86±20	263±57	1883±107	65±11
P-value	0.122	0.267	0.115	0.0005	0.0001	0.015

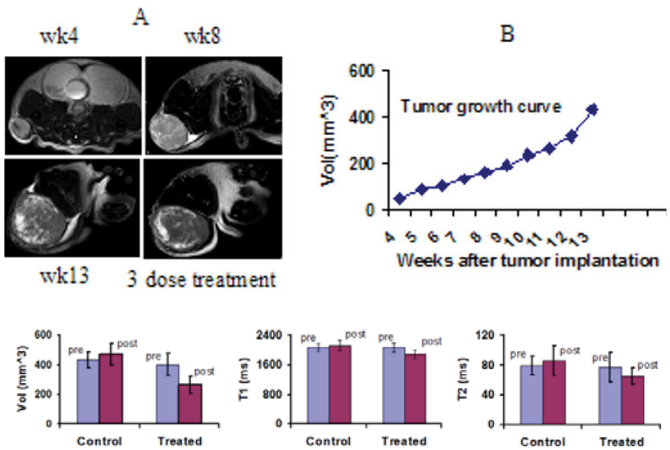

Discussion/Conclusion: Tumor volume, and T1 and T2 values all decreased in response to nilotinib treatment. T1 and T2 have been shown to be shorter in necrotic regions than in regions of viable tissue (2). The decreased T1 and T2 in treated tumors correlated with the increasing fraction of necrotic tissue found on histologic analysis, indicative of sensitivity to nilotinib. Early response to nilotinib treatment was apparent after just 3 treatment doses. Our study demonstrates that T1 and T2, and tumor volume might be used as biomarkers for assessing early response to therapy and selection of effective treatments.
References:
1. X. Jiang et al, Clin Cancer Res, 2008; 14 (23): 7726-7732. 2. I. Jakobsen et al, British J. Cancer, 1995; 71, 456-461.

714

In vivo measurement of sodium T_1 of knee cartilage in a post-operative goat animal model

G. Lykowsky[1], K. Hemberger[1], S. Triphan[1], D. Weber[1], P. Jakob[2], D. Haddad[1]
[1]Research Center Magnetic-Resonance-Bavaria, Wuerzburg/GERMANY, [2]Experimentelle Physik 5, Lehrstuhl für Physik, Würzburg/GERMANY

Purpose/Introduction: Sodium is known to be a sensitive MR imaging biomarker for early diagnosis of knee articular cartilage osteoarthritis (OA) [1]. The goat animal model closely matches the human knee anatomy and can be used to mimic the progressive nature of OA. The measurement of *in vivo* sodium T_1 is essential to allow accurate sodium quantitation [1], fluid suppressed imaging [2] or monitor biochemical changes in tissue [3]. The goal of this abstract is to measure sodium T_1 of different tissues in the post-operative goat knee.
Subjects and Methods: To mimic OA in the goat animal model the medial meniscus of the knee joint was surgically removed. The therefore altered

loading stress on the weight bearing joint leads to degradation of the articular cartilage. Inversion Recovery 2D Ultra Short Echo Time (IR-2D-UTE) sodium imaging was performed post-operative in one subject with the following parameters: B_0=1.5T; 500µs Inversion pulse; TE=0.07ms; resolution=4*4*20mm; TI=1,3,30,70,200ms; TR=250ms+TI; bandwidth=500Hz; projections=1000; total acquisition time=25min; Additionally proton imaging was performed to allow easy anatomical identification of different tissues (Siemens MEDIC, TE=25ms, TR=48ms, resolution=0.4*0.4*0.8mm).
ROIs corresponding to the different tissues were drawn and the mean value of the sodium data fitted to $S=S_0(1-C*\exp(TI/T1))$ [4]. The fitting parameter S is the signal magnitude at inversion time TI, S_0 is the initial magnitude of the signal, C accounts for incomplete inversion due to the short T_2 and imperfect flip angle calibration.
Results: The post-operative proton and sodium images show an aqueous effusion in place of the removed meniscus and in the whole knee (Fig1).

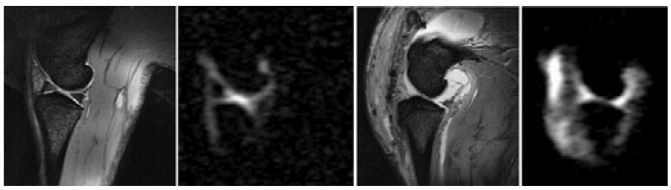

Fig1: From left to right: pre- and post-operative proton and sodium images
The T_1 of cartilage was found to be 23.1±1.1ms. The T_1 of the fluid is significantly higher at 40.8±2.3ms (Fig2). Both, fluid and cartilage T_1 values show high confidence (r_{Square}>0.999) and closely match previously reported values [4].

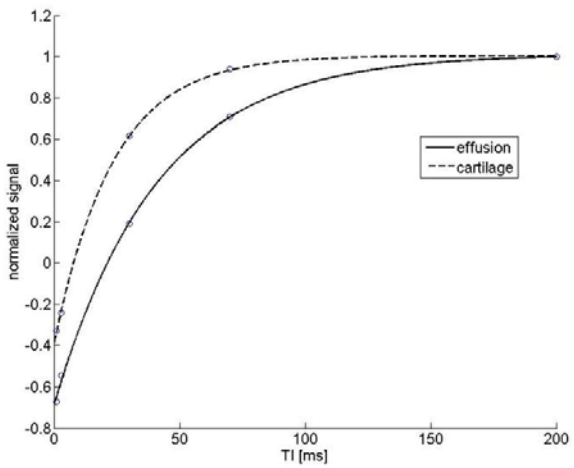

Fig2: Sodium T_1 relaxation curves for cartilage and effusion
Discussion/Conclusion: This preliminary work demonstrates the feasibility of *in vivo* sodium T_1 measurement with a 2D-IR-UTE sequence in acceptable scan time even at low field. The obtained T_1 values may be used to suppress the fluid signal and improve cartilage delineation.
References:
[1] Shapiro, JMR 142:24-31(2000);
[2] Madelin, JMR 207(1):42-52(2010);
[3] Madelin, NMR in Biomedicine 25(4):530-537(2011);
[4] Feldman, Proc. ISMRM Montreal (2011);
Acknowledgements:
Funding by EU FP7 project 241719-ADIPOA.

Paper Poster

Body

715

Texture analyzing of benign and malignant vertebral fractures based on entropy histograms and PARAFAC analysis of MR images

J. Mihailović[1], A. Savić[2], V. Vuković[3], M. Daković[4], **G.G. Bačić**[5]
[1]Magnetic resonance department, National Cancer Research Center, Belgrade/SERBIA, [2]Department of Biophysics, Center for Multidisciplinary Studies, Belgrade/SERBIA, [3]Department of Magnetic Resonance, National cCancer Research Center, Belgrade/SERBIA, [4]Department of Biophysical Chemistry, Faculty of Physical Chemistry, Belgrade/SERBIA, [5]Department of Radiochemistry, Faculty of Physical Chemistry, Belgrade/SERBIA

Purpose/Introduction: Attempts to differentiate benign and malignant vertebral fractures may be difficult, particularly when there is no obvious evidence of malignancy. The role of MRI in the acute phase of vertebral fractures is important although the acute phase of vertebral fractures is the most critical period for defining fracture management. The purpose of this study was to investigate application and implementation of textural analysis based on Haralick texture features and parallel factor analysis (PARAFAC) in clinical practice.
Subjects and Methods: The study included 20 patients, 7 with benign and 13 with malignant vertebral fractures. All patients had undergone conventional MRI scan within 2 months from the time of presenting with the complaint. The 2 month cutoff was chosen because some cases of osteoporotic vertebral fractures remain painful even after conventional treatment. All of the 7 patients were diagnosed with benign vertebral fractures based on pathologic results following needle biopsy. Other 13 patients with malignant vertebral fractures were diagnosed primarily based on pathological results following surgery. MRI examination was performed using a 1.5 T MR system (Avanto; Siemens, Erlangen, Germany). T2 weighted Images were used in this study (3270/87, repetition time (TR) msec/echo time (TE) msec). Analysis of vertebral fractures was based on gray level co-occurrence matrix (GLCM) define for different neighborhood sizes. Analytical step which provides identification and characterization of vertebral fractures was the parallel factor analysis (PARAFAC). Calculations of image entropy and its histogramization were performed in Matlab based script, while the PARAFAC analysis was performed by using The N-way toolbox for Matlab.
Results: The results obtained from PARAFAC analysis had showed the difference in factor shapes and consequently their relative contributions for benign and malignant vertebral fractures based on different neighborhood sizes (Fig. 1). On Fig. 1A and 1B there is only one dominant factor on entropy histograms, but on Fig. 1C there is the second factor with pixel signal intensities much higher from signal intensities derived from benign fractures (arrows), probably due to the cellular infiltrations in malignant fractures. Relative comparison between signal intensities showed that pixel signal intensities from second factor is 84 % higher. Differentiation of acute benign and malignant vertebral fractures with this method was 100% in correlation with clinical findings.

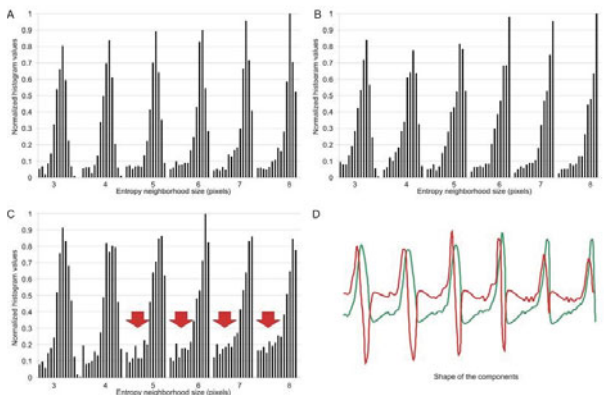

Discussion/Conclusion: Results of this study show that multivariate analysis is a promising analytical method that provides fast, accurate, and easily implementable method for the clinical examination of vertebral fractures.

716

Intra-Ductal Breast Lesions: Diagnostic Accuracy of MR Imaging

M.L.O.D.O. Coelho[1], C. Paulino[2], M. Dias[3], C. Marques[4], M. Gonçalo[4], N. Neves[1], F. Caseiro-Alves[4]
[1]RADIOLOGY, HOSPITAL INFANTE D. PEDRO, AVEIRO/PORTUGAL, [2]RADIOLOGY, HOSPITAIS UNIVERSITARIOS DE COIMBRA, COIMBRA/PORTUGAL, [3]GINECOLOGY, HOSPITAIS UNIVERSITARIOS DE COIMBRA, COIMBRA/PORTUGAL, [4]Radiology, Centro Hospitalar Universitário de Coimbra, Coimbra/PORTUGAL

Purpose/Introduction: The purpose of this study is to evaluate the diagnostic value of magnetic resonance imaging (MRI) in patients with suspicious nipple discharge and/or an intra-ductal breast lesion suspected in other imaging techniques, namely galactography and ultrasound.
Subjects and Methods: We retrospectively analyzed the medical records and images of breast MRI studies performed between February 2010 and April 2012 of women with suspicious nipple discharge or suspected intra-ductal lesion. In the study were included 36 women who had a pathological diagnosis, either histologically proven by surgical specimens (86, 1%) or fine needle aspiration cytology (13,9%).
Results: Of the 36 patients included the mean age was 49 years old, ranging from 28 to 72 years old. The pathological diagnosis distribution revealed 14 papillomas, 6 malignancies and 16 non-surgical lesions, most ectasic ducts with/without usual hyperplasia. 8 of the papillomas and 4 of the malignancies were correctly diagnosed by MRI (the 2 other malignancies were underestimated as typical papillomas), however three of the non-surgical cases were overdiagnosed as papilloma, ductal carcinoma *in situ* (*cdis*) and invasive carcinoma (FP=18,5%). In the 21 patients who had previously done a galactography, we found 52% disagreement between the two techniques – MRI revealing concordance with the pathological findings in 72% of these discordant cases. There were no malignancies missed by MRI and detected as filling defects in galactography, but 3 (14,3% (3/21)) were not visible in either technique. In fact, the global sensitivity and specificity for surgical findings (papilloma, *cdis* and invasive carcinoma) was 75% and 81% and 76,9% and 12,5%, respectively for breast MRI and galactography.
Discussion/Conclusion: Breast MRI is becoming a valuable technique in the diagnosis of suspected intra-ductal neoplasms, and this study supports the recommendation of performing MRI not only as an alternative to galactography when the latter cannot be done or is inconclusive, but also as a complementary contribution to the positive or negative galactography findings.
References:
Lorenzon M, Zuiani C, Linda A, Londero V, Girometti R, Bazzocchi M. Magnetic resonance imaging in patients with nipple discharge: should we recommend it? European Radiology, 2011, May;21(5):899-907
Eiada R, Chong J, Kulkarni S, Goldberg F, Muradali D. Papillary Lesions of the Breast: MRI, Ultrasound, and Mammographic Appearances. AJR 2012; 198:264–271
Ikeda DM, The Requisites: Breast, 2nd Edition, Mosby, Philadelphia, 2010
Kopans, BD, Breast Imaging, 3rd Edtion, Lippincott Williams & Wilkins, Boston, 2007

717

Automated Worklow for 3D CSI Prostate Spectroscopy

R. Neji[1], M. Requardt[1], P. Khurd[2], K. Engelhard[3]
[1]H IM PLM AW ONCO, Siemens AG, Healthcare Sector, Erlangen/GERMANY, [2]Imaging and Visualization, Siemens Corporate Research, Princeton/NJ/UNITED STATES OF AMERICA, [3]Radiology Department, Martha-Maria Hospital, Nuremberg, Nuremberg/GERMANY

Purpose/Introduction: To set automatically the parameters of a 3D CSI prostate spectroscopy measurement: the position, orientation and dimensions of the volume of interest (VOI) and the field of view (FOV), as well as the outer volume saturation bands.
Subjects and Methods: The following measurement workflow is set up:
- A 3D Truefisp scan is run for localization purposes.
- Based on the algorithm in [1], the Truefisp images are segmented and 8 saturation bands are positioned. The frequency of the two highest (resp. lowest) saturation bands in the transverse direction is set to that of water (resp. fat) in order to remove unwanted bladder (resp. lipid) signal. The remaining four saturation bands saturate lipids.
- The VOI is computed as follows: the points belonging to the segmentation mask are projected in the plane perpendicular to the sagittal orientation. A 2D convex hull of the projected points is computed and its minimum area bounding rectangle is obtained [2].
- The edge of the rectangle with the closest orientation to the transverse direction is selected as a slice normal. The second edge is chosen as a phase-encoding direction and the readout direction is lying along the sagittal direction.
- The dimensions of the VOI are given by computing the extents of the segmentation in the above mentioned directions. This defines a 3D box enclosing the prostate. The FOV is adjusted to have the same position and orientation as the VOI. The dimensions of the FOV allow 5 additional oversampled voxels in each direction.
Results: The workflow was tested for 8 patients using a 3D CSI Press sequence on a Siemens 3T Magnetom Skyra with the following parameters: TR = 940ms, TE = 145ms, Averages = 4, BW = 1300Hz, water and lipid saturation, matrix size = 12x12x10. Body Matrix and Spine coils were used for acquisiton. The measurements led to a clinically useful and robust spectral quality, with a computational time of around 30s. The figures below show an example of a measured dataset, the prostate is automatically contoured (manual contour correction not needed) and metabolite maps for choline and citrate are displayed.

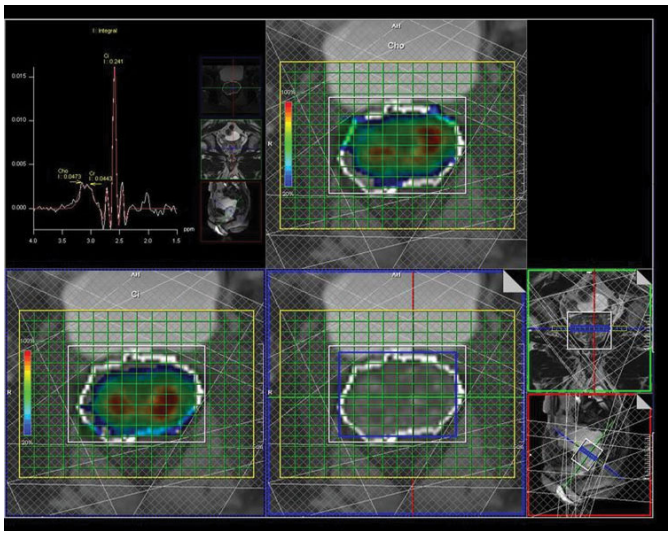

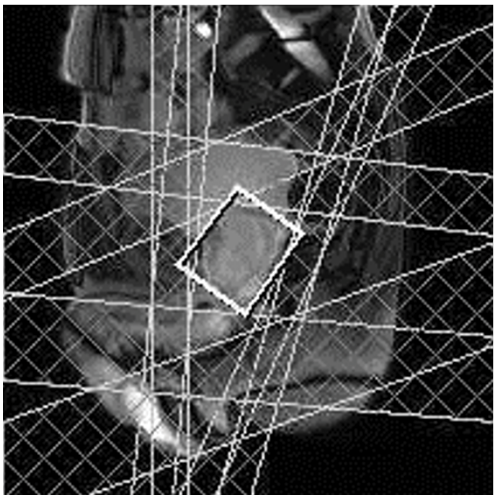

Discussion/Conclusion: The proposed method allows the positioning of a prostate spectroscopy measurement, instead of doing it manually, which is fastidious and time-consuming. A future direction is to use the information provided by the segmentation to build an automated workflow integrating both imaging and spectroscopy.
References:
Khurd P. et al, 2011
Freeman H. and Shapira R., 1975

718

Fat quantification using two different water-fat separation sequences for the diagnosis of diffuse liver disease

C. Kremser, B. Henninger, S. Rauch, W. Jaschke
Dept. of Radiology, Innsbruck Medical University, Innsbruck/AUSTRIA

Purpose/Introduction: Magnetic Resonance Imaging is increasingly being used for the diagnosis of diffuse liver disease. Thereby especially the evaluation of hepatic fat with concurrent hepatic iron overload is of special interest. The purpose of our study was to compare fat quantification of the liver based on two water-fat separation methods as provided by the vendor.
Subjects and Methods: 35 patients with clinical suspicion of diffuse liver disease were investigated on a 1.5T MR scanner (Magnetom Avanto, Siemens, Germany). For the quantification of liver T2*-values a fat saturated multi-gradient-echo sequence with 12 echoes (TR=200ms; TE=0.99ms+n*1.41ms, flip-angle:20°) was used. For fat quantification a conventional spoiled gradient echo in-phase and opposed-phase (IOP) imaging sequence was used (TR=103ms, TE=2.37ms/5.05ms, flip angle: 70°). In addition a 3D chemical shift based water-fat separation sequence (VIBE-DIXON) as provided by the vendor (TR=7.54ms, TE=2.38ms/4.76ms, flip angle: 10°), delivering in-phase, opposed-phase as well as separated fat and water images (f/w), was performed. Fat-signal fraction (FSF) maps were calculated using ImageJ based on the equation $\eta = (IP-OP)/(2*IP)$ and $\eta = F/(W+F)$. IP and OP values were corrected for T2* bias whereas no T2* correction was implemented for the f/w VIBE-DIXON images.
Results: In 9 patients T2* values lower than 10ms were found indicating hepatic iron overload. FSF values for the T2* corrected conventional IOP and VIBE-DIXON IOP images showed good correlation, whereby VIBE-DIXON IOP images lead to higher FSF values consistent with a higher T1 bias. In consequence a higher number of patients (n=26) were diagnosed with a FSF>7% for the VIBE-DIXON IOP method as compared to the conventional IOP method (n=19). For FSF values calculated from VIBE-DIXON fat and water separated images a good correlation between the T2* corrected IP/OP method was found for FSF > 10%, whereas the VIBE-DIXON f/w-FSF values showed lower values than the IOP method. For FSF values < 10% the VIBE-DIXON f/w-FSF showed only small variation with IP/OP-FSF. For patients with hepatic

iron overload (open triangles in figures; T2* < 10ms) large deviations of the VIBE-DIXON f/w-FSF values are seen.

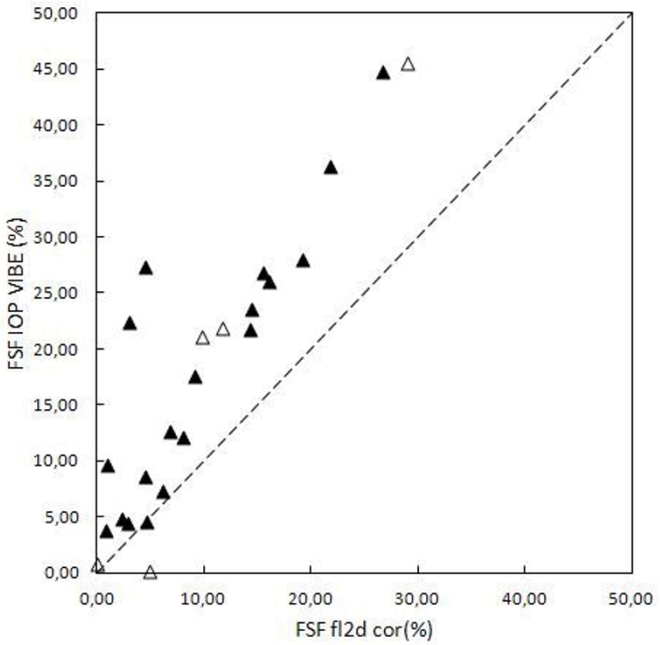

Correlation between T2* corrected FSF values obtained from conventional IOP images and VIBE-DIXON IOP images.

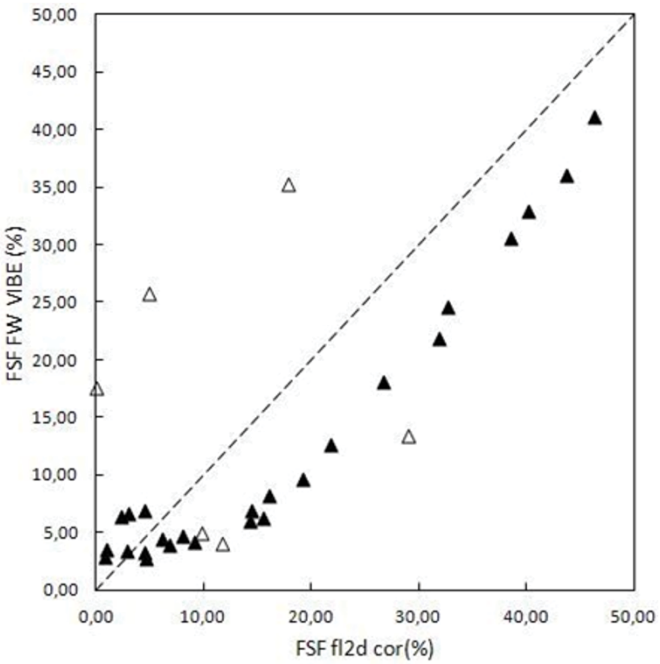

Correlation between T2* corrected FSF values obtained from IOP images (FLASH 2D) and from fat/water separated images (VIBE-DIXON).

Discussion/Conclusion: Fat/water separated VIBE-DIXON images result in good fat suppression; however, FSF values calculated from fat and water images seem to be less reliable as compared to those from IOP images.

719

Quantitative data analysis of the multiphase contrast-enhanced mri in the differential diagnosis of metastatic liver disease of colorectal and pancreatic etiology

Y. Savchenkov, S. Bagnenko, V. Fokin, G. Trufanov
Radiology, Medical military academy, Saint-Petersburg/RUSSIAN FEDERATION

Purpose/Introduction: To develop the method of differential diagnosis metastatic liver lesion of colorectal and pancreatic etiology on the basis of quantitative data analysis of the multiphase magnetic resonance imaging.
Subjects and Methods: We analyzed 57 metastatic liver lesions colorectal (37 lesions) and pancreatic (20 lesions) etiology identified in 20 patients. Contrast agent was entered manually from the calculation of 0.2 ml per 10 kg of body weight with the approximate speed of 1.5-2.5 ml/sec.
All measurements were carried out within a single axial slice (for each pulse sequence separately). The intensity of the MR-signal (SI) was measured in the pathological focus, healthy parenchyma of the liver, the aorta, the inferior vena cava and spleen (as the native, and so on postcontrast imaging) with the construction of the coefficients (the total number of analysed coefficients is 540 for each lesions).
Results: We used single-factor analysis of variance to assess the relationship etiology of metastatic lesion of the liver with the indicators measured in the course of research in quantitative scale.
The most informative coefficients for dynamic multiphase CE MRI were: ($SI_{lesion\ art.phase}/SI_{liver\ art.phase}$)/($SI_{lesion\ ven.phase}/SI_{liver\ ven.phase}$) and ($SI_{lesion\ art.phase}/SI_{aorta\ art.phase}$)/($SI_{lesion\ 3\ min}/SI_{aorta\ 3\ min}$) (F-criterion Fisher 12.04 and 10.61, p<0.001 and="" p="0.002," .="" a="" little="" less="" informative="" demonstrated="" by="" the="" ratio="" of:="" sub=">lesion art.phase/$SI_{aorta\ art.phase}$)/($SI_{lesion\ ven.phase}/SI_{aorta\ ven.phase}$) and ($SI_{lesion\ art.phase}/SI_{liverart.phase}$)/($SI_{lesion\ 3min}/SI_{liver\ 3min}$) (F-criterion Fisher 9.39 and 7.48; p=0.003 and p=0,008, respectively). The metastatic liver lesions of pancreatic etiology characterized by higher values of variables: ($SI_{lesion\ art.phase}/SI_{aorta\ art.phase}$)/($SI_{lesion\ 3\ min}/SI_{aorta\ 3\ min}$) and ($SI_{lesion\ art.phase}/SI_{aorta\ art.phase}$)/($SI_{lesion\ ven.phase}/SI_{aorta\ ven.phase}$) (0.76±0.03, 0.88±0.02 respectively) in comparison with the lesions of colorectal etiology (0.64±0.14 and 0.78±0.02 respectively). At the same time, the significance of relations ($SI_{lesion\ art.phase}/SI_{liver\ art.phase}$)/($SI_{lesion\ ven.phase}/SI_{liverven.phase}$) and ($SI_{lesion\ art.phase}/SI_{liverart.phase}$)/($SI_{lesion\ 3min}/SI_{liver\ 3min}$) above in colorectal metastases (colorectal etiology – 1.08±0.02 and 1.03±0.03, respectively; pancreatic etiology – 0.94±0.03 и 0.88±0.03 respectively).
Discussion/Conclusion: A small number of examined patients don't give us the right to final conclusions at this stage, but the received data are enough to make decision about the effectiveness of the method and good prospects of its application.
References:
Coenegrachts, K., 2009 Magnetic resonance imaging of the liver,p. 72–85
Maniam, S., 2010 MRI: Review of imaging techniques and overview of liver imaging, p. 309–322

720

Vortex formation ratio can be measured using MRI and is decreased in heart failure compared to healthy volunteers

M. Kanski, J. Töger, K. Ehrenborg, M. Carlsson, E. Heiberg, H. Arheden
Department of Clinical Physiology, Skåne University Hospital and Lund University, Lund/SWEDEN

Purpose/Introduction: Heart failure is associated with high mortality and morbidity and new quantitative measures of heart failure are needed. Vortex formation ratio (VFR, also called vortex formation time, VFT) (1) describes optimal vortex blood flow in the left ventricle (LV) during diastole, and has been suggested as a potential new quantitative measure of heart failure (2). Magnetic resonance imaging (MRI) is the gold standard for measurement of LV volumes, and may therefore provide more accurate and observer-independent measurements of VFR. However, VFR has not previously been assessed using MRI.

Therefore, the aims of this study were to investigate if MRI can be used to measure VFR and if VFR measured by MRI differs between healthy volunteers and patients with heart failure.

Subjects and Methods: Healthy volunteers (n=8, 7 male, mean 25 years) and patients with heart failure (dilated cardiomyopathy n=8, 8 male, mean 72 years) underwent cardiac MRI using a 1.5T Philips Achieva scanner (Philips, Best, the Netherlands). LV end-systolic volume (ESV) and the LV volume before atrial contraction (diastatic volume, DV) were measured by manual delineation. The E-wave volume (EWV) was defined as DV - ESV. Mitral valve diameter (D) was defined as the mean between two measurements: a) the 3-chamber long-axis view, and b) the short-axis view of the LV. Based on previous echocardiography studies, VFR was derived as $4/\pi^{*}EWV/D^{3}$. Image analysis was performed using Segment software v1.9 (www.medviso.com/segment). Differences between volunteers and patients were tested using the Mann-Whitney U test.

Results: VFR was significantly lower in patients with heart failure compared to healthy volunteers (3.0±1.0 vs 4.9±0.7, p<0.001). Seven out of eight (87.5%) healthy volunteers had VFR values higher than the highest VFR value in the patient group (heart failure range: 1.0-4.2; healthy range: 3.6-5.8).

Discussion/Conclusion: This is the first study to show that VFR can be measured using MRI. VFR was significantly lower in heart failure compared to healthy volunteers. Since the overlap was small in VFR ranges between healthy volunteers and patients with heart failure, VFR may be used as a quantitative measure of heart failure.

References:

1. Gharib, M. et al. Optimal vortex formation as an index of cardiac health. Proc. Natl. Acad. Sci. U.S.A. 103:6305–6308, 2006.

2. Poh, K. K. et al. Left Ventricular Fluid Dynamics in Heart Failure: Echocardiographic Measurement and Utilities of Vortex Formation Time. Eur Heart J – Cardiovasc Imaging, 13:385-393, 2012.

721

Computer-aided detection in MR perfusion of the heart using Dynamika-software: preliminary results

M. Junghans[1], M. De Booij[1], T. Lenderink[2], M.E.A.P.M. Adriaensen Van Roij[1]

[1]Radiology, Atrium Medisch Centrum Parkstad, Heerlen/NETHERLANDS, [2]Cardiology, Atrium Medisch Centrum Parkstad, Heerlen/NETHERLANDS

Purpose/Introduction: Dynamika (Image Analysis Ltd., Leeds, Great Britain) is a computer-aided detection software developed for analysing and standardising contrast-enhancement in dynamic series automatically. Dynamika has been used in MRI of breast, prostate, and musculoskeletal system. As Dynamika has the ability of motion correction, in theory it could be used in dynamic MR cardiac imaging.

To demonstrate whether Dynamika can analyse dynamic MR cardiac perfusion scans despite cardiac and pulmonary motion.

Subjects and Methods: We retrospectively analysed 46 dynamic MR-cardiac-perfusion-scans performed on 1.5-Tesla-scanner (Avanto, Siemens, Erlangen, Germany) (mean age of patients, 62years; range 34-86 years; 37 (80%) male patients). 39 patients underwent adenosine-stress-scans. Both rest and stress series were included. All dynamic short-axis-scans (n=255) were analysed with Dynamika.

From March 2012 we started using an optimized scan protocol (Table 1). Prospectively 13 consecutive dynamic MR-cardiac-perfusion-scans scanned with the optimized protocol were included (mean age of patients, 66years; range 38-82years; 9 (69%) male patients). Twelve patients underwent adenosine-stress-scans. All dynamic short-axis-scans (n=75) were analysed with Dynamika.

Descriptive statistics and chi-squared-test were performed with Excel for Windows.

Total volume of contrast (Dotarem®, Guerbet, France) was 30 ml per patient.

Results: Dynamika colour maps provide information about the initial rate of enhancement and washout of the heart as well the time of onset of enhancement and washout.

In the first study period, Dynamika was able to analyse and provide interpretable colour maps in 168 out of 180 (93%) dynamic short-axis-scans.

In the second study period, Dynamika was able to analyse and provide interpretable colour maps in 75 out of 75 (100%) dynamic short-axis-scans (P < 0.001).

Figure 1

Colour map of the initial rate of enhancement in a 61-year-old male patient with no abnormal findings at the base of the left ventricle (a). Colour maps of the initial rate of enhancement (b) and washout (c) in a 55- year-old male patient with a hypo-intense region infero-lateral seen at the base of the left ventricle and the image before analysing (d).

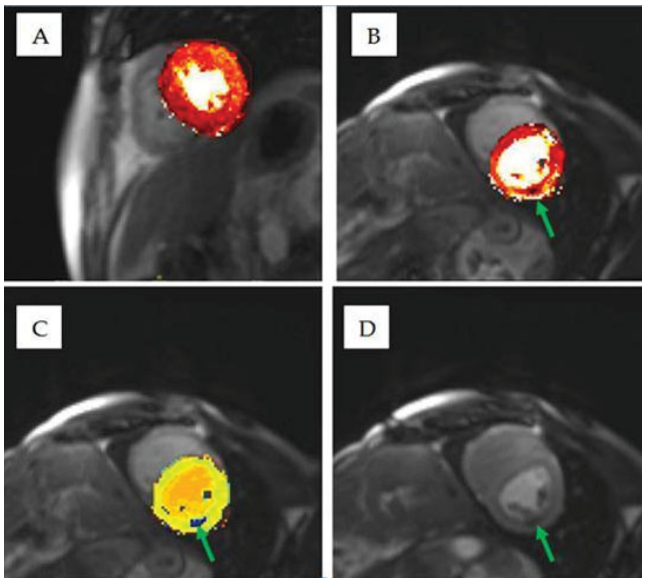

Discussion/Conclusion: Our results show that with an optimized MR-cardiac-perfusion-protocol Dynamika can automatically analyse and provide interpretable colour maps in the vast majority of dynamic perfusion-short-axis-scans of the heart despite potential cardiac and pulmonary motion artefacts. Outcome of Dynamika-software in MR-cardiac-perfusion still needs to be validated.

Table 1

Scan	TrueFISP
Number of slices	3
Slice thickness	8 mm
FoV	250 mm
Resolution	128
Number of measurements	80
Trigger delay	100 ms
TR	189.83 ms
TE	1.04 ms

722

Simplified biexponential model of Diffusion-Weighted Magnetic Resonance Imaging (DW-MRI): a quantitative analysis for prostate tissue characterization

N. Marotti[1], S.F. Carbone[1], G. Belmonte[2], V. Ricci[1], E. Tucci[3], L. Pirtoli[4], L. Volterrani[1]

[1]Radiology Department, University Hospital of Siena, Siena/ITALY, [2]Medical Physics Department, University Hospital of Siena, Siena/ITALY, [3]Urology Department, Ospedale di Grosseto, Grosseto/ITALY, [4]Radiation Oncology Department, University Hospital of Siena, Siena/ITALY

Purpose/Introduction: Diffusion-Weighted Magnetic Resonance Imaging (DW-MRI) signal is accurately described by a biexponential model that allows to assess the real diffusion coefficient (D) and the perfusion fraction (f), using a wide range of b-values and complex calculations.

A simplified biexponential model allows to easier assess ADC (apparent diffusion coefficient), D and f using a less extended range of b-values.
The aim of our study is evaluate whether ADC, D and f, calculated by a simplified biexponential model, may support prostate tissue characterization.
Subjects and Methods: We examined 28 patients with histologically proven prostate cancer by the transrectal ultrasound-guided biopsy. Ten patients were in hormone therapy, 18 patients were not on therapy.
All patients underwent to DW-MRI of prostate with endorectal coil using a 1.5T MR scanner, employing b-values 0 s/mm^2, 600 s/mm^2, 1000 s/mm^2.
We assessed ADC for b=600 s/mm^2 (ADC600), ADC for b=1000 s/mm^2 (ADC1000), diffusion coefficient (D) and perfusion fraction (f) in peripheral prostate (PZ), cancer (TU) and central gland (CG).
We applied to our dataset parametric statistic tests.
Results: ADC600, ADC1000, D and f were strongly lower in TU than in PZ ($p<0.0001$).
ADC600, ADC1000 and f were also significantly lower in TU than in CG ($p<0.0001$). D resulted lower in TU than CG ($p<0.010$).
D is a less strong parameter to differentiate between cancer and CG, probably because of the presence of benign prostatic hyperplasia in CG.
Discussion/Conclusion: A simplified biexponential model of DW-MRI using high b-values (over 600 s/mm^2) provides quantitative parameters (ADC600, ADC1000, D, f) that may support prostate tissue characterization, especially to differentiate cancer and peripheral zone, where the tumor most likely arises.
D is a quantitative parameter, theoretically not affected by the "pseudo-diffusion" due to vascularization.
This quantitative approach to the tissue characterization may overcome some pitfalls of the imaging.
References:

- Le Bihan D et al.Separation of diffusion and perfusion in intravoxel incoherent motion MR imaging.Radiology.1988.
- Mulkern RV et al.Biexponential characterization of prostate tissue water diffusion decay curves over an extended b-factor range.MagnResonImaging.2006.
- Lee SS et al.Quantitative analysis of diffusion-weighted magnetic resonance imaging of the pancreas: usefulness in characterizing solid pancreatic masses.JMagnResonImaging.2008.
- Riches SF et al.Diffusion-weighted imaging of the prostate and rectal wall:comparison of biexponential and monoexponential modelled diffusion and associated perfusion coefficients.NMR Biomed.2009.
- Shinmoto H et al.Biexponential apparent diffusion coefficients in prostate cancer. MagnResonImaging.2009.
- Döpfert J et al.Investigation of prostate cancer using diffusion-weighted intravoxel incoherent motion imaging. MagnResonImaging.2011.

723

Evaluation of a Knowledge-Based 6-Plane Automatic Slice-Alignment Method for Cardiovascular Magnetic Resonance Imaging at 3 T

S. Kuhara[1], K. Yokoyama[2], R. Ishimura[2], T. Nitatori[2], S. Nitta[3], T. Shiodera[3], T. Takeguchi[3]
[1]MRI Systems Development Department, Toshiba Medical Systems Corporation, Otawara-shi/JAPAN, [2]Department of Radiology, Kyorin University Faculty of Medicine, Mitaka-shi/JAPAN, [3]Corporate Research & Development Center, Toshiba Corporation, Kawasaki-shi/JAPAN

Purpose/Introduction: We have developed an automatic slice-alignment method that employs a combination of knowledge-based recognition techniques and image processing techniques to determine six cardiac planes at the same time. In our previous report, we showed that the proposed method can detect the cardiac planes more quickly and accurately than the conventional method [1-3] at 1.5 T [4, 5]. In the present report, we assess the usefulness of this method in actual clinical cases at 3 T.
Subjects and Methods: ECG-gated 2D steady-state free precession (SSFP) axial multislice images were acquired using a 3-T MRI scanner (Vantage™ Titan 3T, Toshiba Medical Systems) during a single breath-hold. The scanning conditions were TR/TE=3.4/1.7, matrix=198x256, and slice thickness=7 mm (no gap), with a scanning time of less than approximately 20 s. Using the proposed method combining knowledge-based recognition techniques and image processing techniques, the positions of the mitral valve, cardiac apex, left ventricular outflow tract, tricuspid valve, and right ventricular corner were detected to determine the long-axis and three short-axis orientations to define the 4-chamber, 2-chamber, and 3-chamber views. The angular error of the normal vector of each view between the automatically determined results and manual annotations was measured. Thirty clinical datasets were scored for diagnostic accuracy by two physicians (1: unacceptable, 2: marginal but diagnostically useful, 3: good, 4: excellent). The interobserver error was also measured for two experienced physicians and one experienced operator to evaluate the angular error.
Results: The proposed method successfully detected the six planes in all cases. The average scores for the short-axis, 4-chamber, 2-chamber, and 3-chamber views were 3.35±0.94, 3.23±0.94, 3.20±0.92, and 3.32±0.87, respectively. The angular error values for the short-axis, 4-chamber, 2-chamber, and 3-chamber views were 5.83±5.57, 7.97±6.24, 11.81±6.11, and 7.97±6.61 degrees, respectively, and were lower than the interobserver error values, which were 5.92±3.18, 10.24±7.36, 22.98±33.54, and 9.12±4.55 degrees, respectively.
Discussion/Conclusion: We have proposed a slice-alignment method based on knowledge-based recognition techniques combined with image processing techniques to simplify cardiac scan planning. The results showed that the proposed method can provide sufficient accuracy for plane determination even at 3 T, although the image quality of SSFP multislice images is usually degraded compared to those acquired at 1.5 T.
References:

[1] BPF Lelieveldt et al. Radiology 2011, 221:p537-542
[2] RD Darrow et al. ISMRM 2009:p1800
[3] X Lu et al. MICCAI 2011, 6893:p479-486
[4] S Nitta et al. ESMRMB 2011, No. 726
[5] S Nitta et al. SCMR 2012, No. 269

724

Assessment of myocardial lipid accumulation: Optimisation of in vivo ^{1}H magnetic resonance spectroscopy (MRS) measurement protocol.

M. Kršňák[1], G. Reiter[2], M. Chmelík[3], M. Gajdošík[3], D. Jankovic[1], Y. Winhofer[1], A. Luger[1], M. Krebs[1]
[1]Department of Internal Medicine III, Medical University of Vienna, Vienna/AUSTRIA, [2]Medical Division, Siemens Healthcare, Wien/AUSTRIA, [3]MR Centre of Excellence, Department of Radiology, Medical University of Vienna, Vienna/AUSTRIA

Purpose/Introduction: Patients with type 2 diabetes mellitus (DM2) are at higher risk for cardiomyopathy which is associated with myocardial lipid (MYCL) accumulation. MYCL can be assessed by proton MRS. Different approaches of elimination of artifacts of breathing- and cardiac movement on the precision of the measurement have been proposed and are evaluated in this study.
Subjects and Methods: In all protocols ECG-triggered localized single voxel ^{1}H MRS (PRESS, TE= 30 ms; TR according to heart beat) was performed on 3T system (Siemens, Germany) on healthy volunteers and DM2 patients. Different protocols included: (i) no additional correction for the breathing movement (FB-NC, n=20); (ii) prospective acquisition correction during free breathing (FB-PACE, n=22); (iii) standard magnetic field and frequency adjustments as well as signal acquisition performed during multiple breath-holds (BH-ST, n=33), and (iv) user configurable magnetic field adjustments based on gradient recalled double echo acquisition field map as well as frequency adjustment and MRS acquisition applied during multiple breath-holds (BH-GRE, n=36). Quality of the spectra was assessed by the linewidth of water signal ($FWHM_{H20}$) from spectra acquired without water suppression. Signal acquired with weak water suppression in subsequent acquisitions was used to quantify the amplitude of methylene- and methyl group signals from MYCL and coefficient of variation (CV) of MYCL from test-retest measurements was compared to evaluate the precision of the measurement in different protocols.
Results: Best spectral quality was achieved using the BH-GRE ($FWHM_{H20}$; BH-GRE: 15±3Hz, BH-ST: 21±7Hz, FB-PACE: 21±8Hz, FB-NC: 25±8Hz). This effect was accompanied by the improvement in CV of MYCL measurement (CV; BH-GRE: 20%, BH-ST: 24%, FB-PACE: 39%, FB-NC: 45%).

	Acquisition Scheme			
	BH - GRE	BH – ST	FB – PACE	FB - NC
FWHM H_2O [Hz]	15 ± 3	21 ± 7	21 ± 8	25 ± 8
FWHM Range [Hz]	9 -22	9 - 36	8 - 39	11 - 40
CV – MYCL [%]	20	24	39	45

Discussion/Conclusion: In conclusion advanced option for the adjustment of magnetic field homogeneity in connection with the signal acquisition during multiple breath-holds improves the quality of MYCL assessment by ^{1}H MRS.

References:

This study was supported by Jubiläumsfond of Austrian National Bank (P#13249).

725

Myocardial T_1 mapping in free breathing with motion correction at 3T: a pilot study

H. Clique[1], A. Menini[1], H.M. Cheng[2], P. Marie[3], J. Felblinger[1], M. Beaumont[4]

[1]U947, INSERM, Nancy/FRANCE, [2]Medical Biophysics, University of Toronto, Toronto/ON/CANADA, [3]Département de médecine nucléaire, CHU de Nancy, Nancy/FRANCE, [4]CIT801, INSERM, Nancy/FRANCE

Purpose/Introduction: T_1 mapping is a useful quantitative MR technique for cardiac tissue characterization and contrast agent concentration measurements. Because of cardiac and respiratory motion, cardiac T_1 mapping remains challenging. A variable flip angle approach using standard clinical sequences[1], that integrates B_1 correction, had been proved on subjects with a 'controlled' free-breathing (double gating) at 3T[2]. In this work, a free-breathing approach with GRICS reconstruction[3] was evaluated in the same conditions.

Subjects and Methods: Two healthy volunteers (1 men, age 24 and 33) underwent a cardiac examination on a 3T MR system.

A rapid 3D T_1-mapping method, based on variable flip angles (FA)[1], was employed (Matrix 128x128x16, TR/TE= 4/1.8 ms, FA=2, 5, 11°, Slice Thickness=8mm, Trigger Delay=300 to 500ms, depending on heart rate). Four sets of 3 sequences were performed; one during controlled breathing and the three others during free breathing. Sequences were triggered on ECG. Excitation field correction (B_1) was performed from two EPI acquisitions (same parameters with FA_1/FA_2=60/120° and 120/240°)[1].

T_1 maps were obtained using home made T_1 computation[1] Matlab softwares integrating GRICS reconstruction for free breathing.

The left ventricle myocardium was divided into 6 segments according to the AHA recommendations[4]. Mean pixel value of each ROI was used to compute 6 myocardial T_1 values. Then, B_1 error was estimated on each ROI and used to correct myocardial T_1 values.

Results: Originally, T_1 values obtained during controlled breathing were not homogeneous over the whole myocardium whereas B_1 correction was applied. Mean of T_1 values was 1289 ± 162 ms, the T_1 of two septal segments being the lowest. With the free breathing reconstruction, T_1 values were balanced over the different segments compared to previous ones. Mean of free breathing myocardial T_1 values was 1376±103 ms.

Discussion/Conclusion: Using motion compensated reconstruction and iterative motion estimation, good quality T_1 maps were obtained from free breathing acquisitions. Due to cardiac gating troubles (heart rate variations), some T_1 values were not properly estimated, especially on the septum wall. This free-breathing T_1 computation method can be applied on other moving organs or applied with perfusion.

References:

[1]Cheng, HLM, 2006, MRM, 566-574; [2]Poinsignon, H, 2011, ISMRM, [3] Ménini, A, 2010, ISMRM; [4]Cerqueira, MD, 2002, Circulation, 539-542.

726

MR based volumetry of musculature in the lower extremity in 156 subjects and relations of findings to age, gender, anthropomorphic characteristics and a diet intervention.

C. Schabel[1], M. Böttcher[1], F. Springer[2], U. Grosse[3], N. Stefan[4], A. Fritsche[4], F. Schick[5], J. Machann[6]

[1]Section on Experimental Radiology, Department of Diagnostic and Interventional Radiology, University Hospital Tübingen, Tübingen/GERMANY, [2]Diagnostic and Interventional Radiology, University Hospital of Tübingen, Tübingen/GERMANY, [3]Department of Radiology, Section on Experimental Radiology, Tuebingen/GERMANY, [4]Department of Internal Medicine, Division of Endocrinology, Diabetology, Angiology, Nephrology and Clinical Chemistry, University Hospital Tübingen, Tübingen/GERMANY, [5]Section on Experimental Radiology, University Hospital Tübingen, Tübingen/GERMANY, [6]Section on Experimental Radiology, Institute for Diabetes Research and Metabolic Diseases (IDM) - Metabolic Imaging - of the Helmholtz Center Munich at the University of Tübingen, Tübingen/GERMANY

Purpose/Introduction: The quantification of muscular volume (MV) in the lower extremities by MRI in slightly obese patients with high risk for diabetes type 2 and its correlation with anthropomorphic and metabolic characteristics before and after a lifestyle intervention with caloric restriction and endurance training.

Subjects and Methods: One hundred fifty-six patients (94w, 62m, mean age 45.5±11.1years, mean BMI w=29.7±3.5 and m=29.7±3,5kg/m^2) underwent whole body MRI to quantify MV, subcutaneous and visceral adipose tissue. The volumetry was based on axial T1-weighted fast spin-echo images with TE/TR of 12ms/490ms, slice thickness 10mm, 10mm gap, five sections per acquisition and 10cm table incrementation. Patients were imaged from fingers to toes in prone position with arms extended using a body coil. Post processing was performed by a custom written MATLAB program with a semi-automated segmentation of muscular and adipose tissue using a threshold technique. MV was exemplary determined on the lower extremity, ranging from the heel bone to the head of femur. Metabolic characteristics were examined by glucose clamp and aerobic capacity by ergospirometry. Examinations were repeated after 6-9 month of lifestyle intervention.

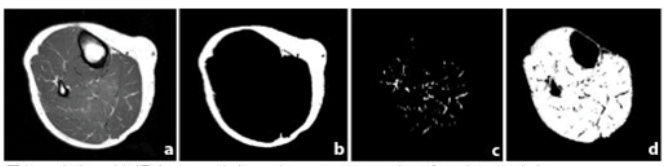

T1-weighted MR image (a) and postprocessing for determining subcutaneous fat (b), intramuscular lipids (c) and muscular tissue (d).

Results: As expected, males showed significantly more MV than females (m=22.5±2.3 vs. w=15.9±2.2 liter, p<0.01), whereby MV correlated well with weight (r_w=0.78 and r_m=0.63), BMI (r_w=0.59 and r_m=0.39) and volume of fat (r_w=0.36 and r_m=0.22). By contrast MV correlated inversely with the patient's age in men more than in women (r_m=-0.36, r_w=-0.16). Dependence of MV on insulin sensitivity was not significant (r_w=-0.-23 and r_m=0.03). For both genders, MV was hardly correlated with aerobic fitness (r_w=-0.02 and r_m=0.13). The lifestyle intervention caused a mean loss of weight, BMI, body fat and muscle volume by 2.5kg, 0.8 kg/m^2, 0.5% and 0,27litres respectively, whereby correlation remained widely unaffected except the inverse correlation between MV and age decreased (r_w=-0.05 and r_m=-0.28). Relative muscle volume increased significantly (p<0.001).

	Muscular volume	
	Women	Men
Age	-0.13	-0.36
Weight	0.78	0.63
BMI	0.59	0.39
Fat volume	0.36	0.22
Aerobic fitness	-0.02	0.13

Correlation coefficients of muscular volume in the lower extremities.

Discussion/Conclusion: Muscular volume was correlated with weight, BMI and volume of fat for both genders, whereby men tended to lose more muscle volume while aging corresponding to [1]. Insulin sensitivity seemed to be independent from muscle volume. A lifestyle intervention caused a loss of weight and MV whereas relative MV increased [2].

References:

[1] C.Wang,GeriatrGerontolInt.,2012;10.1111/j.1447-0594.2012.00851
[2] J.Machann,Radiology,2010;257(2):353-63

727

Ultra short echo time (UTE) MR imaging with off-resonance saturation for characterization of pathologically altered Achilles tendons at 3 Tesla.

U. Grosse, P. Martirosian, R. Syha, G. Groezinger, F. Schick, F. Springer
Department of Radiology, Section on Experimental Radiology, Tuebingen/GERMANY

Purpose/Introduction: Off-resonance radiofrequency (rf) saturation pulses applied prior to regular excitation in MR sequences can be used to modify signal contrast based on magnetization transfer (MT) and direct saturation (DS) effects. Assessment of MT provides quantitative insight into the interactions of free water protons and protons bound to macromolecules [1,2].
Clinical applicability and value of UTE sequences combined with off-resonance saturation pulses was tested in healthy, paratendinopathic and tendinopathic Achilles tendons in-vivo at 3 Tesla. For this purpose, applied off-resonance frequencies of saturation pulses were varied systematically between 1000 and 5000 Hz.
Subjects and Methods: Sixteen healthy volunteers as well as fourteen patients with clinical and morphological signs of an Achilles mid-portion tendinopathy and paratendinopathy (as indicated by conventional MRI and ultrasound) were examined. A 3D ultrashort echo time (UTE) sequence in combination with a Gaussian off-resonance saturation pulse (frequency offset: 1000, 1500, 2000, 3000, 4000 and 5000 Hz) was used to modify the detectable MR signal intensity from the Achilles tendon. Off-resonance saturation ratio (OSR) was calculated pixel-wise or in selected regions of interest as the relative reduction in signal intensity under selective off-resonance saturation in relation to a reference measurement without any saturation pulse.
Results: OSR in tendons of healthy volunteers ranged from 0.52 ± 0.06 (1000 Hz) to 0.24 ± 0.02 (5000 Hz), whereas symptomatic tendinopathic tendons (0.35 ± 0.04 to 0.17 ± 0.02) and asymptomatic tendinopathic tendons (0.41 ± 0.06 to 0.21 ± 0.02) showed significantly lower mean OSR values. Symptomatic paratendinopathic tendons (0.43 ± 0.06 to 0.23 ± 0.01) presented lowered OSR values as well (difference to healthy subjects is not significant). In all groups, mean differences between pathologically altered and healthy tendons were especially pronounced for off-resonance frequencies of less than 3000 Hz.
Discussion/Conclusion: Off-resonance Saturation Ratio (OSR) values provide a sensitive and quantitative marker for assessment of pathological microstructure alterations in mid-portion tendinopathy of the Achilles tendon. Off-resonance frequencies of 3000 Hz or more lead to negligible DS effects, and MT effects almost exclusively contribute to the MRI signal decrease, reflecting interactions between macromolecules and free water protons. Higher mean differences of the OSRs between healthy and impaired cases were found for saturation pulses with less than 3000 Hz off-resonance frequency, indicating that also DS effects contribute to useful tissue contrast in pathologically affected tendons.

References:

[1] Hodgson RJ et al. 2011, Magn Reson Med, 65(5):1372-1376.
[2] Syha R et al. 2011, Rofo, 183(11):1043-1050.

728

What is the relationship between contrast enhanced and diffusion weighted MR parameters in peripheral zone prostate tumours?

L.J. Bains, D.G. Chong, M. Ith, H.C. Thoeny
Dept. of Diagnostic, Interventional and Pediatric Radiology (DIPR), University & Inselspital Bern, Bern/SWITZERLAND

Purpose/Introduction: Both DW and DCE MRI both provide information about tumour diffusion and perfusion characteristics which may be useful in the detection and monitoring of prostate tumours. However, the relationship between parameters calculated using the two techniques is unclear, with previous studies finding no or limited correlations between theoretically similar parameters[1,2]. The purpose of this study was to investigate the relationship between DCE and DW MRI parameters in peripheral zone (PZ) prostate cancers.
Subjects and Methods: Twenty patients with confirmed PZ tumours underwent 3T MR imaging prior to prostatectomy. Diffusion weighted imaging (DW MRI) was performed with 8 b-values. Diffusion coefficients were estimated using all b-values (ADC_{total}), and of b-values from 0-130 (ADC_{low}, expected to contain information on perfusion) and 270-900 s/mm² (ADC_{high}, expected to primarily represent diffusion).
DCE MRI volumes were acquired for approximately 5 minutes using a T1-weighted sequence with temporal resolution of 4 s. A two compartment model of tracer kinetics was used to calculate perfusion F, fractional plasma volume v_p, fractional extravascular-extracellular volume v_e, and permeability surface area product PS.
Pairwise Pearson correlations between DCE and ADC parameters with p-values below 0.05 were considered significant.
Results: Significant correlations of v_e with ADC_{high} (figure 1) and v_e with ADC_{total} suggest that related information on tissue interstitial space is provided by DCE and DW MRI; tissues with increased interstitial space demonstrate more interstitial diffusion. The negative correlation observed between PS and ADC_{low} in PZ tumours (figure 2) is ambiguous; one explanation is that tumours with higher pseudodiffusion show greater perfusion due to capillaries which are less prone to "leakage", leading to lower PS. No significant correlations were observed for other parameters.

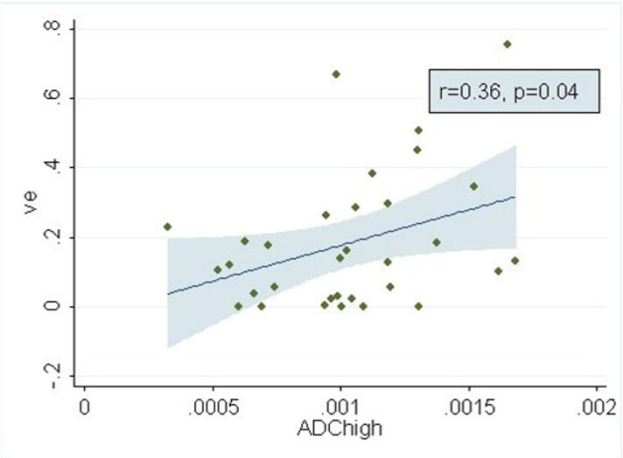

Figure 1Correlation between ADC_{high} and v_e in PZ tumours and normal contralateral tissue

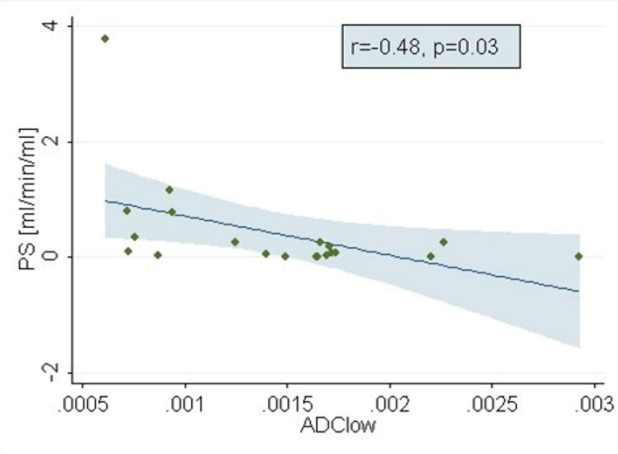

Figure 2 Correlation between ADC_{low} and PS in PZ tumours

Discussion/Conclusion: These preliminary results suggest that both DCE and DW MRI provide related information on diffusion in the prostate interstitial space. As previously seen in the breast and liver[1,2], DW and DCE tissue vascularisation and perfusion parameters do not show a simple relationship in PZ prostate tumours. Further investigation in other tissues is needed to determine the relationship between these parameters and the underlying tissue physiology.

References:

[1] Arlinghaus LR et al. 2011. Magn Reson Imaging. 29(9):630-8
[2] Patel J et al. 2010. J Magn Reson Imaging. 31(3):589-600

Paper Poster

Contrast media: Molecular and cellular imaging

729

A new model for visualization of contrast agent release from thermosensitive lipososmes induced by laser based hyperthermia

L. Willerding[1], S. Limmer[1], M. Hossann[1], A. Zengerle[1], M. Reiser[2], R.D. Issels[1], L. Lindner[3], M. Peller[2]
[1]Department Of Internal Medicine Iii, Ludwig-Maximilians-University Hospital Munich, Munich/GERMANY, [2]Institute For Clinical Radiology, Ludwig-Maximilians-University Hospital Munich, Munich/GERMANY, [3]Ccg Hyperthermia, Helmholtz Zentrum Muenchen, German Research Centre for Environmental Health, Munich/GERMANY

Purpose/Introduction: Thermosensitive liposomes (TSL) are potential drug carriers for improved chemotherapy, by which targeting and triggering is achievable if temperature can be controlled locally [1]. A TSL-formulation with prolonged circulation time and fast content release was developed for hyperthermia (HT) temperature levels >41°C [2]. Content release above a critical temperature (T_m) can be visualized by co-encapsulation of an MRI contrast agent (CA-TSL). Visualization may allow temperature and dose monitoring during HT [3]. Feasibility was shown in mice before using a water bath for HT [4]. To allow a dedicated non-invasive HT of the tumour a new laser based HT setup should be developed and tested in vivo.
Subjects and Methods: Experiments were performed in 2 rats with tumours located on both hind legs. In each animal, one tumour (Tu1; 0.5cm³/0.8cm³) was superficially heated to 41°-42°C by a 940nm laser. Temperature was monitored with an intratumoral temperature probe. After heat-up CA-TSL (Gd-DTPA-BMA-0.6mmol/kg; DPPC/DSPC/DPPG250/20/30(mol/mol)) [2] were injected i.v.. 1min prior to 60min after injection MR-images were continuously acquired using a fl3D-sequence (TE=2.1ms; TR=6.3ms; α=40°; FoV=78*63mm²; spat.res.=0.4*0.4*2.5mm³; dt=7.49s) at 3T. Before and after HT, T1-parameter maps were determined using a variable-flip-angle method (α=[2.5°;5°;10°;19°], TR=9.7ms, FoV=78*63mm²; spat.res=0.5*0.5*2.5mm³). Contrast agent concentration changes were calculated as c(t)=(1/T1post–1/T1pre)/r1; (r1=4.3[L/(mmol*s)]) [5].
Results:

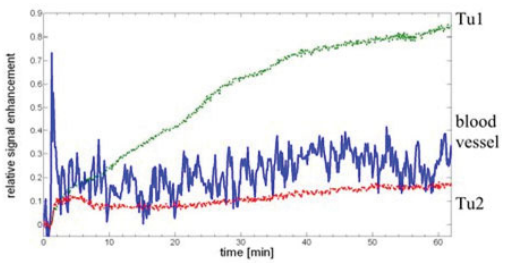

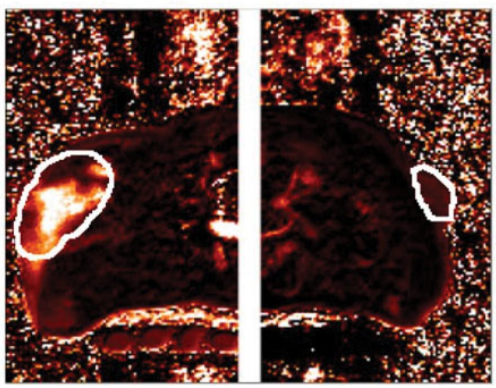

Dynamic signal enhancement up to 84/87% during HT was detected in the heated tumours Tu1. In the non-heated tumours Tu2 signal increased within one minute after injection by 13/16% and was constant (±5%) thereafter. Signal from a blood vessel showed peak enhancement during first pass and an increased signal level of ~18-20% thereafter. The CA-concentration post 60min HT calculated from T1-relaxation change was in the range of 0.20/0.30mmol/L in Tu1 and 0.02/0.04mmol/L in Tu2.
Discussion/Conclusion: The strong signal increase in the heated tumour compared to the minor increase in the non-heated tumour demonstrated HT-induced release of CA and the effectiveness of the new heating device. This is supported by the small signal changes in the blood vessel. Visualization compared to HT in mice induced by water bath [4] was significantly improved. Furthermore in vitro experiments in rat plasma show a similar release kinetic of TSL compared to human plasma [6]. This seems important for further experiments to characterize drugs release from TSL.
References:
[1] Koning et.al. PharmRes (2010) [2] Lindner, et.al. ClinCancRes (2004) [3] Viglianti et.al. MRM (2006) [4] Peller, et.al. InvestRadiol (2008) [5] Rohrer et.al. InvestRadiol (2005) [6] Schmidt et.al. ESHO (2009)

730

A novel superparamegnetic particle shows no splenic accummulation, improved pharmacokinetics and optimal properties for perfusion imaging.

D. Calle[1], G. Bannenberg[2], S. Cerdán[1], F. Moreno[2]
[1]Laboratory Of Imaging And Spectroscopy By Magnetic Resonance Imaging, Instituto de Investigaciones Biomedicas, Madrid/SPAIN, [2]I+d, Solutex S.A., Nanotex S.A., Alcobendas (Madrid)/SPAIN

Purpose/Introduction: Superparamagnetic contrast agents are normally used to reduce the T_2 and T_{2*} relaxation times enhancing the sensitivity of MRI diagnosis and providing new probes for T_{2*} based imaging methods including perfusion. However, commercial superparamagnetic nanoparticles are coated with dextran and present significant non specific binding to vascular structures, long retention times in liver and spleen and are not devoid of potential toxicity due to accumulation during repeated administration to patients. We report here on a new superparamagnetic nanoparticle coated with polyacrylic acid that shows excellent properties for perfusion imaging, large T_{2*} relaxivity, no appreciable non-specific binding to vascular structures, undetectable spleen retention and remarkably fast hepatic elimination rate, decreasing the risk of cummulative effects after repeated dosing.
Subjects and Methods: The superparamagnetic nanoparticles used in this study were developed by Nanotex Co. These nanoparticles are composed of a ferromagnetic core (Fe_3O_4) coated with polyacrylic acid. To investigate the in vivo the pharmacokinetic properties by MRI, we obtained T_{2*} weighted images in a 7T Bruker Pharmascan and the corresponding T_{2*} maps of coronal sections across the thorax and abdomen of Swiss CD1 mice (n=12) before intravenous administration of the nanoparticles (15 and 30 micromol Fe/kg) and at increasing times after administration (1, 3, 6, 24, 48, 168h). For the perfusion imaging experiments we used rats carrying implanted C6 glioma tumors. Briefly, we injected a bolus (0.1 mL) of the nanoparticle suspension (15 micromol Fe/kg) in the tail vein of rats and followed by MRI the dynamics of T_{2*} contrast with time.
Results:
The pharmacokinetics of the novel nanoparticle show, after administration (15 micromol Fe/kg), a fast decline in hepatic T_{2*} followed by very rapid clearance from hepatic tissue and complete recovery of the precontrast T_{2*} within approximately 24 hours (Fig.1).

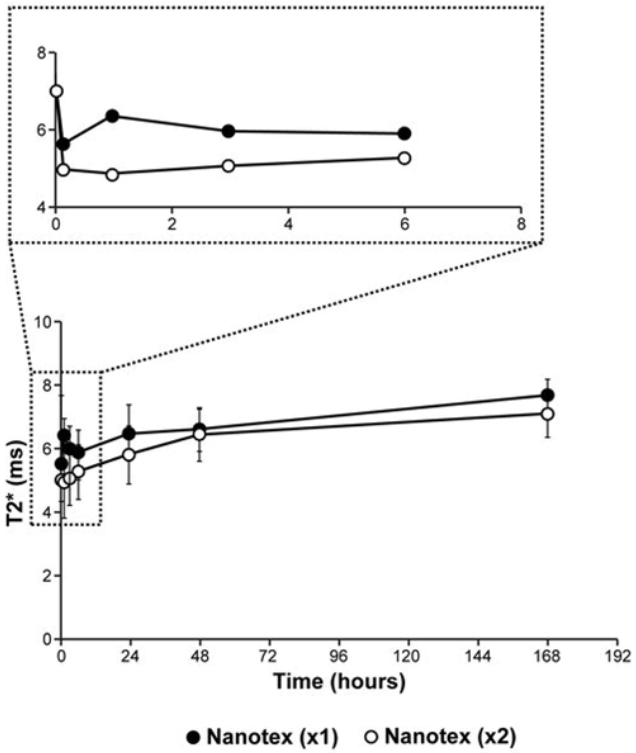

When the dose was doubled (30 micromol Fe/kg), a significantly increased relaxation effect in the liver was observed while the fast elimination rate was maintained. The agent was not accumulated in the spleen. The perfusion study (Fig.2) shows a very favourable first passage kinetics and recovery through the cerebral microvasculature with values of CBF (22.86±4.62 mL/100g)/min), CBV (1.41± 0.06 mL/100g) and MTT (3.55± 1 s-1).

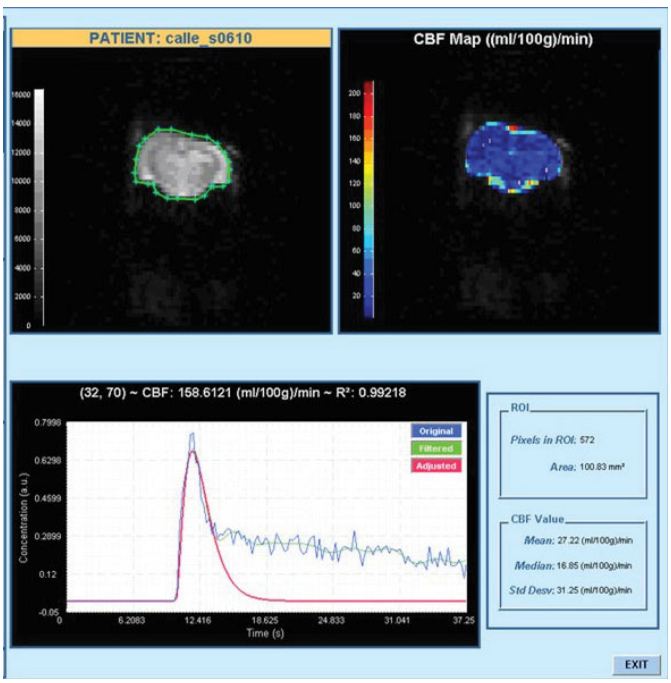

Discussion/Conclusion: We report on a novel superparamagnetic nanoparticle with no detectable splenic retention, favorable pharmacokinetic properties, no appreciable toxicity and optimal performance with perfusion imaging by the bolus tracking method.

731

Cystine-functionalized superparamagnetic nanoparticles effects on human immune cells ex vivo

L. Delogu[1], **S. Dolci**[2], V. Domenici[2], R. Madeddu[3], R. Manetti[4], G. Pampaloni[2], F. Sgarrella[1], C.A. Veracini[5]
[1]Dipartimento Di Scienze Del Farmaco, Università di Sassari, Sassari/ITALY, [2]Dipartimento Di Chimica E Chimica Industriale, University of Pisa, Pisa/ITALY, [3]Dipartimento Di Scienze Del Farmaco, Università di Pisa, Sassari/ITALY, [4]Dipartimento Di Medicina Clinica, Sperimentale E Oncologica, Università di Sassari, Sassari/ITALY, [5]Dipartimento Di Chimica, Università di Pisa, PISA/ITALY

Purpose/Introduction: Nanomedicine is an emerging field of research, which deals with the development and use of different classes of nanomaterials and nanoparticles for therapeutic and diagnostic purposes, such as Superparamagnetic iron oxide nanoparticles (SPION). Toxicity of SPIONs is an important issue when thinking to the potential use of them as MRI contrast agents. In this work, we study new cystine-functionalized SPIONs [1].
Subjects and Methods: Our attention focuses on a wide variety of human immune cells *ex vivo (*T and B lymphocytes, NK cells and monocytes) looking at the relatively cell percentage and at their functionality in presence of different doses of cystine-functionalized SPIONs [1].
Human cells were obtained from informed healthy male donors (25 to 50 years old). Cell separation and experiments were performed immediately after blood drawing. Details of the method and preparation will be reported in the presentation.
Results: We analyzed the effects of SPION on cells directly isolated from human peripheral blood (PBMCs). First we wanted to assess whether the presence of SPION at 50, 100 and 200 ug/ml could have an impact on the relatively cell percent after 24 hours incubation.
Cell percentage was not affected in all cell population with the only exception of monocytes. Anti-CD14 is a common marker for the identification of monocytes, the strong decrease of monocytes in presence of SPION was dose dependent. SPION did not cause any change for T, B, and NK cells, however, we wanted to understand if the cell functionality, for those cell types, was preserved. The activation is a critical key to investigate on functionality changes in the immune system. We focused on the major activation markers (CD25, CD69,CD30) in presence of different doses of SPION. In all activation assay performed, SPION didn't impact cell activation.
Discussion/Conclusion: Our results, on human cells *ex vivo*, showed that SPION in different doses didn't affect the cell percentage for T, B, and Natural Killer cells. The decrease we found for monocytes population is probably not surprising as these phagocytic cells need to respond to foreign materials. More assay on isolated monocytes to assess the real possible toxicity of SPION are in progress.
References:
[1] "Precursors of Magnetic Resonance Imaging Contrast Agents Based on Cystine-coated Iron-oxide Nanoparticles", Sara Dolci, Vincenzo Ierardi, Anton Gradišek,Zvonko Jagličić, Maja Remskar, Tomaž Apih, Mario Cifelli, Guido Pampaloni,Carlo Alberto Veracini and Valentina Domenici, CURRENT PHYSICAL CHEMISTRY, accepted.

732

Lanthanide-based Lipoparticles as Bimodal Magnetic Resonance/ Optical Imaging Probes with Potential BBB Permiability

S. Lacerda[1], C. Bonnet[1], A. Pallier[1], S. Villette[1], S. Petoud[1], C. Pichon[1], E.J. Toth[2]
[1]Cbm, Centre de Biophysique Moleculaire, Orleans/FRANCE, [2]Cnrs, Centre de Biophysique Moléculaire, Orleans/FRANCE

Purpose/Introduction: Current nuclear-imaging methods, as optical imaging offer high sensitivity while others, as MRI, give high-resolution. Consequently *multimodality imaging* provides complementary information in pharmaceutical and medical applications. Nanotechnology has greatly facilitated diagnosis and treatment of central nervous system diseases, and the delivery of anticancer drugs to specific sites, overcoming the multi drug resistance problems.

Nanoparticles incorporating contrast-generating materials make the focus of contrast agent research, especially for MRI, offering improved contrast, high payloads, long circulation times and the ease of including multiple imaging properties in one single entity, plus a targeting moiety.[1]
The majority of new drugs for the brain do not cross the BBB. Therefore, the search for novel drug delivery technologies is driven by the need to increase efficacy, improve safety and patient compliance in the cure of highly social impact diseases, in particular cancer.
Subjects and Methods: Herein we present novel bimodal MR/O Imaging nanolipoplatform probes, capable of BBB permeability. They are liposomes or lipoprotein-like particles that include (i) amphiphilic Ln^{3+} complexes (Gd^{3+}/Nd^{3+}/Yb^{3+}-pyOC12)[2] as imaging probes for MR and Optical imaging, (ii) chromophore (anthracene) and (iii) Apolipoprotein ApoE4 (target towards LDL receptors, located in the BBB or tumour cancer cells).
The particles where synthesised by the dry film method[3] and characterized by DLS, AFM, Gel Electrophoresis and Fluorescence of Tryptophan residues. Their NMRD and luminescence properties were studied. *In cellulo* studies were performed using a co-culture of b.End3/C6 cells *in vitro* BBB model.[4]
Results: The particles show high relaxivities; the sensitization of the Nd^{3+}/Yb^{3+} is possible by the inclusion of anthracene, and more importantly, the ApoE4 enables BBB permeability in an *in vitro* BBB model.
Discussion/Conclusion: These results open promising perspectives in bimodal MR/O imaging probes targeted to the BBB or cancer cells overexpressing LDL receptors.
References:
(1) Cormode, D.P.; Jarzyna, P.A.; Mulder, W.J.M.; Fayad, Z.A., **2010**, *Adv. Drug Deliv. Rev.*, *62*, 329.
(2) Bonnet, C.S.; Pellegatti, L.; Buron, F.; Shade, C.M.; Villette, S.; Kubíček, V.; Guillaumet, G.; Suzenet, F.; Petoud, S. and Tóth, É., **2010**, *Chem. Commun.* *46*, 124.
(3) Cormode, D.P.; Chandrasekar, R.; Delshad, A.; K.C. Briley-Saebo, K.C.; Calcagno, C.; Barazza, A., Mulder, W.J.M.; Fisher, E.A. and Fayad, Z.A., **2009**, *Bioconj. Chem.*, *20*, 937.
(4) Li, G.; Simon, M.J.; Cancel, L.M.; Shi, Z-D.; Ji, X.; Tarbell, J.M.; Morrison III, B. and Fu, B.M., **2010**, *Ann. Biomed. Eng.*.

733

Exploring the fate of cell-internalized MRI Gd-based contrast agents

E. Di Gregorio[1], E. Gianolio[1], R. Stefanìa[1], S. Aime[2]
[1]*Chemistry-university Of Turin, Molecular Imaging center, Torino/ITALY,* [2]*Chemistry-university Of Turin, Molecular Imaging Center, Torino/ITALY*

Purpose/Introduction: In vivo MRI tracking of labelled cells is still a topic of huge interest. Most often the cells are labelled with Iron Oxide nanoparticles. However, Gd-chelates have also been proposed. The threshold for the MRI visualization of a cell is in the order of 10^7-10^9 Gd-chelates per cell. Such a high payload of stable Gd(III)-chelates seems to be well tolerated by the cellular machinery as low cytotoxicity has been reported for several cell types. Cell viability tests are usually carried out at short times after incubation and no study of the "fate" of cell internalized Gd-complexes at longer time has been reported. The knowledge of the *in cellulo* behavior of Gd-complexes may also provide some new insight into the understanding of the etiology of pathologies related to the release of Gd^{3+} ions such as NSF (Nephrogenic Systemic Fibrosis).
Subjects and Methods: J774.A1(murine macrophages) and NIH-3T3(murine fibroblasts) cells were incubated with two commercial contrast agents (Gd-DTPA, Gd-HPDO3A), washed extensively and reincubated for 1-4 days. The total amount of internalized Gd(III) was determined through a relaxometric method and the amount of intact Gd-complex was determined by mass spectrometry. Cells lysates were characterized by registration of NMRD profile on a fast field-cycling stelar relaxometer.
Results: Up to 4 days no sign of transformation for both complexes internalizated in fibroblasts was detected. Vice versa, a net difference in the behavior of Gd-DTPA and Gd-HPDO3A has been observed when the Gd-complexes are internalized into macrophages. Whereas Gd-HPDO3A maintains its integrity also after four days into macrophages, only ca. half of intact Gd-DTPA was determinated. The herein reported data clearly reflects the ability of macrophages to transform Gd-DTPA in respect to fibroblasts which appears to reflect the specific ability of macrophage enzymatic armoury to attack xenobiotics. These exogenous molecules are able to iper-activate NF-kB pathway that promotes the expression of a high levels of pro-inflammatory cytokines and various metallo-enzymes such as Mn-SOD as demonstrated by Western blot analysis.

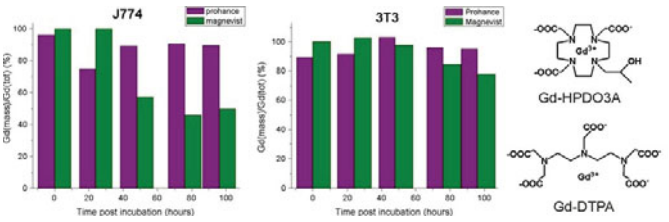

Discussion/Conclusion: The observed behaviour can be accounted in terms of the different stability and rigidity of the two investigated systems being the Gd-HPDO3A more robust and stable. The degradation of Gd-DTPA in macrophages calls for more attention in the cell labeling and cell-targeting procedures with Gd(III) complexes.
References:
Aime S *et al* J. Magn.Reson.Imag. 2002, 16, 394-406.
De Galdo F *et al* Ann Rheum Dis 2010, 69:2024-2033.

734

In vitro determination of calibration curves for a pure and an emulsified semifluorinated alkane as prerequisite for ^{19}F-oximetry

S. Kegel[1], G. Glatting[1], B. Theisinger[2], C. Tsagogiorgas[3], L.R. Schad[4], S. Kirsch[4]
[1]*Medizinische Strahlenphysik/strahlenschutz, Klinik Für Strahlentherapie Und Radioonkologie, Universitätsmedizin Mannheim, Mannheim/GERMANY,* [2]*Research And Development, Novaliq GmbH, Heidelberg/GERMANY,* [3]*Klinik Für Anästhesiologie Und Operative Intensivmedizin, Universitätsmedizin Mannheim, Mannheim/GERMANY,* [4]*Computer Assisted Clinical Medicine, Medical Faculty Mannheim, Heidelberg University, Mannheim/GERMANY*

Purpose/Introduction: Incorporation of spatial distribution of oxygen partial pressure (pO_2) in the radiotherapy treatment plan could improve cancer treatment. There is a linear correlation between pO_2 and relaxation rate R1 of the longitudinal magnetization for fluorine compounds[1]. Previous research was focused on perfluorocarbons like PFCE[2] (Figure1a) or HFB[3] (Figure1b). Contrary to these, semifluorinated alkanes (SFA) are amphiphilic. They can solve oxygen and carry lipoproteins or lipid based drugs. Emulsions of SFA show outstanding long term stability and low Ostwald ripening [4].
To our knowledge, there are no publications related to measurement of pO_2 using SFA and MRI. Therefore, this in vitro study investigated the relation between R1 and pO_2 of pure and emulsified SFA.
Subjects and Methods:

Figure1: a)PFCE b)HFB c)F6H8

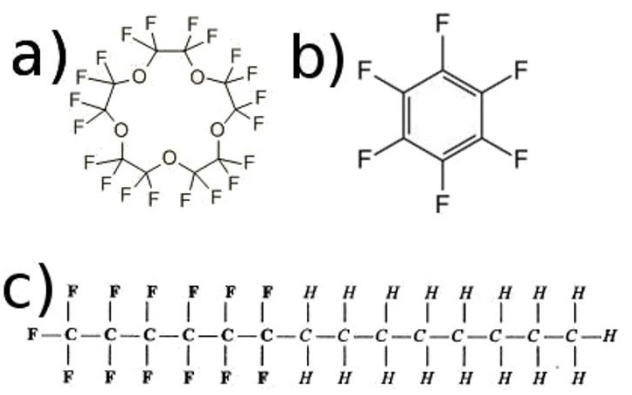

Measurements were performed using a Bruker 9.4 T animal scanner (Bruker, Ettlingen, Germany) and a $^{1}H/^{19}F$-surface resonator. Perfluorohexyloctane (F6H8) from Novaliq (Heidelberg, Germany) was measured in a glass vial containing 5 ml of the liquid sample. The molecule ($C_{14}F_{13}H_{17}$) is shown in Figure1c.
After 20 min of bubbling, relaxation rate R1 was measured with a saturation recovery sequence (TR=20 s, Recovery time T_rec=0 – 10000 ms, 16 increments). Mixtures of nitrogen and oxygen (0%, 10%, 21%, 30%...100% Oxygen in steps of 10%, θ=20°C, p_{air}=765 mmHg) were examined. All measurements were repeated with ST084 (Novaliq), a heat sterilized oil-in-water emulsion (40w% F6H8 as dispersed phase).
Results:

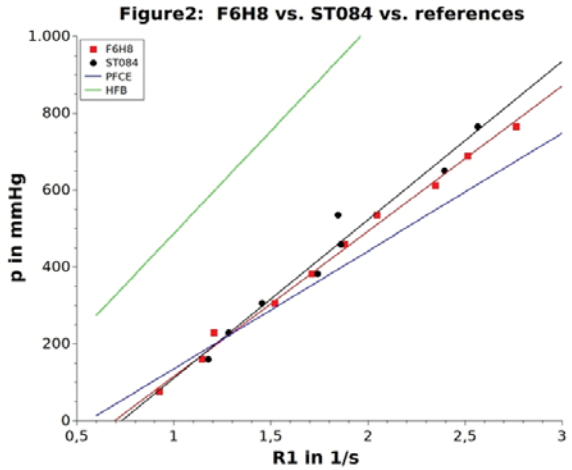

Relaxation rates R1 for pure F6H8 and ST084 with different levels of oxygen were measured and calibration lines calculated. A linear relationship pO_2[mmHg]= a*R1[s^{-1}]+b between pO_2 and the relaxation rate R1 was found with a = 378±9 s*mmHg and b=-262±16 mmHg (R^2>0,9952) for F6H8 compared to a=413±29 s*mmHg and b=-302±54 mmHg (R^2>0,9708) for ST084 (Figure 2).

Discussion/Conclusion: There is no significant difference in R1 for ST084 and F6H8. References [2,3] show similar responding behaviour compared to PFCE (a~306 s*mmHg) and HFB (a~533 s*mmHg).
We demonstrated that both F6H8 and ST084 can be used to measure pO_2 in vitro. The obtained calibration line is necessary for further examinations of pO_2 in tissue.
References:
[1] Magat and Jordan, et al. Med.Phys. 2010; 37(10):5434-41
[2] Dardzinski, B. et al. Magn Reson Med. 1994; 32(1):88-97
[3] Jordan, B. et al. Magn Reson Med. 2009; 61(3):634-8
[4] Meinert, H. et al. Biomaterials, Artificial Cells & Immob Biotech 1993, 21, 583-595

735

Optimization of pulse sequences for molecular MRI of glioma

B. Blasiak[1], S. Barnes[2], W.P. Weglarz[3], T. Foniok[1], A. Obenaus[2], D. Ponjevic[1], J. Matyas[1], B. Tomanek[1]
[1]*Clinical Neurosciences, University of Calgary, Calgary/AB/CANADA,* [2]*Radiation Medicne, Loma Linda University, Loma Linda/CA/UNITED STATES OF AMERICA,* [3]*Magnetic Resonance Imaging, The Henryk Niewodniczanski Institute of Nuclear Physics Polish Adademy of Sciences, Krakow/POLAND*

Purpose/Introduction: MRI is of particular importance in imaging of high-grade gliomas due to their rapid growth [1] and a median survival rate of only 9 months. Standard contrast enhanced MRI does not provide sufficiently high specificity for tumor diagnosis and therefore targeted contrast agents are used [2]. These contrast agents comprise superparamagnetic nanoparticles shortening T_2 and T_2^*. While concentration and dose of the targeted contrast agents have been investigated here we analyze different pulse sequences used for molecular imaging of an animal model of glioma (n=3). We studied standard pulse sequences, gradient echo (GE) and spin echo (SE), as well as a pulse sequence with flow compensating gradients (GEFC)]. The goal of the study was to optimize and compare CNR using SE, GE and GEFC for contrast-enhanced molecular MRI at 9.4T. An *in vivo* animal model was used to evaluate each pulse sequence.
Subjects and Methods: As a tumor mouse model was used [1]. Iron oxide nanoparticles (NPs) functionalized with IGFBP7-sdAb [2] specific to glioma vasculature.
A 9.4T/21cm magnet was used. 200µl of the contrast agent (2mgFe/ml) was administered via tail vein. Three pulse sequences were tested: SE, GE and GEFC before and 20min after injection. For all sequences FOV=2×2cm. For GE and GEFC: TR=500ms,50kHz bandwidth,30 degree flip angle. TE 3,7,11,15, 19ms for GE; for MESE: TR=5000ms;6 echoes,10ms apart.. For the flow compensation (GEFC) short TEs and the first order flow compensation gradients in three directions were used. CNR was calculated within ROIs covering tumor and corresponding area in the contralateral brain.
Results: Pre-injection GE and GEFC MR images showed very low contrast while pre-injection SE MRI showed good contrast between tumor and healthy brain tissues. Following contrast agent administration, the absolut values of CNR increased significantly for both GE and GEFC pulse sequences, while CNR for SE decreased (Fig. 1). The absolute values of CNR for GE and SE were not significantly different at 20 min after injection, however the contrast was reversed: tumor was darker than normal tissue in GE and brighter in SE MRI. CNR was higher with GEFC 20min after injection when compared to GE and SE (Table 1).

	Pre injection	Post injection
GEFC	-0.2	-7.4
GE	-0.1	-5.3
SE	7.0	5.2

Table 1. Comparison of CNR between the tumor and brain regions using SE, GE and GEFC pulse sequences pre and 20 min post *iv* tail injection of the contrast agent. The negative CNR value indicates that tumor is darker than normal brain.

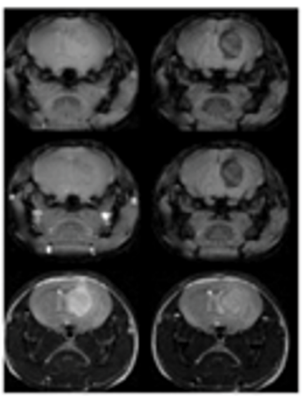

Fig. 1. MR images of the tumor bearing mouse using GE, GEFC and SE (top to bottom) pre (left) and post (right) *iv* tail injection.

Discussion/Conclusion: The results of the studies suggest that the best CNR is provided by GEFC compared to SE and GE pulse sequences. These results also demonstrate that CNR in molecular MR imaging using targeted contrast agents can be improved if the optimal pulse sequence is used.
References:
1.Blasiak,MagnResImag2010;28:784-789;2.Tomanek,Neuro-Oncology,2012,14(1):53-63.

Paper Poster

Diffusion

736

Parameter dependence of diffusion coefficient estimations using IVIM imaging

S.I. Goncalves[1], J. Simoes[1], F. Caseiro-Alves[1], M. Castelo-Branco[2]
[1]Radiology, University Hospital Coimbra, Coimbra/PORTUGAL, [2]Coimbra, ANIFC, Coimbra/PORTUGAL

Purpose/Introduction: Intra-voxel incoherent motion (IVIM) imaging [1] differentiates between true diffusion (*D*), diffusion due to perfusion (*D**), and quantifies perfusion fraction (*f*). Although its applicability has been demonstrated, little has been said over the effect of chosen b-value range (*br*) and T2 relaxation (*T2r*) on diffusion parameter estimation. The goal is to provide quantitative evidence of the effect of *br* and *T2r* on the estimation of the diffusion parameters using IVIM.
Subjects and Methods: Liver signal was simulated, noise added and *T2r* included.Sampling in the low *br* was varied and the error associated with the estimations of *D*, *D** and *f* computed. Liver data from 9 volunteers were acquired in a 3T imaging system (Magnetom Trio Tim, Siemens Medical Solutions, Erlangen, Germany) with a 4-channel body-coil. FOV=400×400 mm, 3.12×3.12 mm in-plane resolution, 1 slice 10 mm thick, TR/TE = 4954/71 ms, parallel imaging factor 2, 5 averages, 16 b-values. Diffusion coefficients were computed with different b-value combinations from regions-of-interest in the liver.
Results: D* is the most sensitive parameter to the magnitude of noise and to the density of low *br* sampling (fig. 1). The error is minimized for *deltab=5* but also for *deltab=20*. Extending TE (fig. 2) increases the error associated with D* especially for *deltab=10* than for *deltab=15, 20*. Figure 3 shows a scatter plot of the in-vivo estimations of D* and f for several choices of b-values and it indicates that D* depends heavily on the choice of b-values (Table 1).

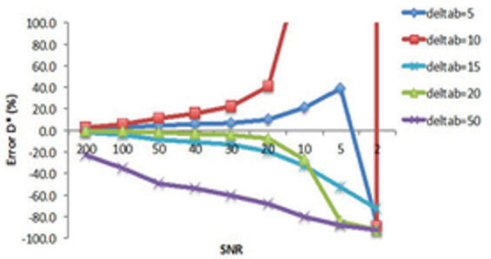

Figure 1. *deltab=5* (0, 5, 10, 15, 20, 25, 30, 40, 50, 60, 70, 80, 100, 200, 300, 400, 500, 600, 800), *deltab=10* (0, 10, 20, 30...), *deltab=20* (0, 20, 40, 60, 80...) and *deltab=50* (0, 50, 100...)

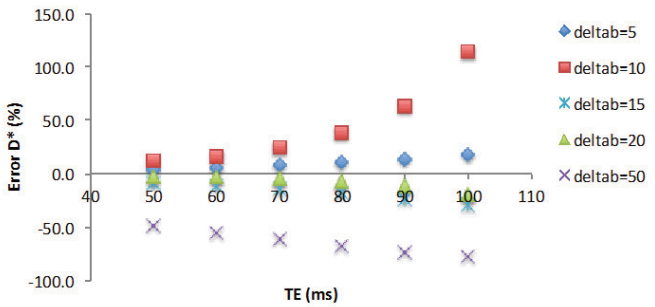

Figure 2. See text

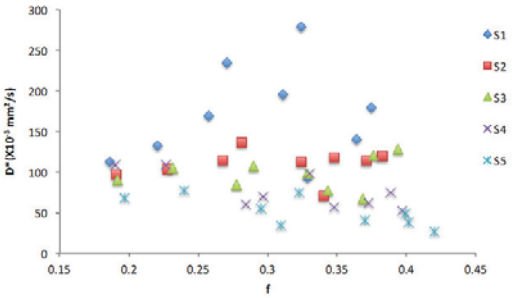

Figure 3. Volunteer data. Estimations with different ranges of b-values: S1 (0, 5, 10, 15, 20, 25, 30, 35, 40, 50, 70, 90, 100, 200, 400, 800), S2 (0, 10, 20, 30, 40, 50, 70, 80, 90, 100, 200, 400, 800), S3 (0, 15, 30, 50, 70, 90, 100, 200, 400, 800), S4 (0, 20, 40, 70, 90, 100, 200, 400, 800), S5 (0, 50, 100, 200, 400, 800)

Table 1 - Average estimations for volunteer data

	D (×10⁻³ mm²/s)	D* (×10⁻³ mm²/s)	f
S1	1.109±0.202	170±60	0.29±0.06
S2	1.109±0.202	109±18	0.30±0.07
S3	1.109±0.202	97±20	0.31±0.07
S4	1.109±0.202	76±21	0.32±0.07
S5	1.109±0.202	51±18	0.32±0.08

Discussion/Conclusion: Parameters depend on the sampling density of b-values in the lower range and increasing the overall number of b values does not necessarily imply more accuracy in the estimations. An a-priori choice of b-values considering the SNR and perfusion properties of the tissue should be done [1]. However, we suggest that in addition, focusing on the sampling density of the low *br* and on the appropriate choice of TE, considering the relaxation properties of the tissue, should be considered.
References:
[1] Lemke, A., Stieltjes, B., Schad, L. R., Laun, F. B., (2011) Toward an optimal distribution of b-values for intravoxel incoherent motion imaging, Magnetic Reson Imaging, 29: 766-776.

737

Analysis of Chronotype Alternations by TBSS

J. Rosenberg[1], I.I. Maximov[2], M. Reske[2], F. Grinberg[2], N.J. Shah[1]
[1]Neurology, Universitätsklinikum Aachen, Aachen/GERMANY, [2]Inm-4, Forschungszentrum Jülich, Jülich/GERMANY

Purpose/Introduction: Individual daily rhythms such as vitally important physiological mechanisms entrain differently to environmental cycles, earlier or later during the day. Human subjects can be classified according to their rhythm as early, late or intermediate chronotypes: an endogenous, self-sustained genetic disposition in sleep and wakefulness [1] reflecting preferences in circadian rhythms. Early chronotypes tend to wake up at early hours and find it difficult to remain awake beyond their usual bedtime. Late chronotypes go to bed late at night. Recent behavioural studies verified that chronotype affects performance on cognitive tasks [2], e.g. participants perform more efficiently when tested in their chronotype-specific optimal time of day. Cerebral correlates underlying these fluctuations in cognitive performance have not been investigated in sufficient depth. The present study aims to investigate chronotype specific alternations using the Diffusion Tensor Imaging (DTI) technique.
Subjects and Methods: 56 healthy male, early (EM, n = 15), intermediate (IM, n= 18) and late (LM, n = 23) chronotypes underwent MRI and DTI measurements 10 to 12 hours after their individual wake up time. *In vivo* diffusion-weighted images in humans were acquired with a whole-body 3T Siemens scanner with 30 encoding diffusion gradients. Diffusion weighting was 1000 s mm². Statistical analysis was performed with TBSS/FDT tools [3,4] from FSL [5]. Pair comparisons of fractional anisotropy (FA) and mean diffusivity (MD) maps between EM/IM, EM/LM and IM/LM groups were performed. 50000 permutations applied in the "randomize" FSL function were used.

Results: Statistical analysis demonstrated that there is no significant difference in the MD/FA maps between EM/IM and between EM/LM, respectively. However, comparison of IM/LM identified brain regions where intermediate subjects show significantly higher FA than late chronotypes. LM reached significant higher MD values than the IM group (Figure 1).

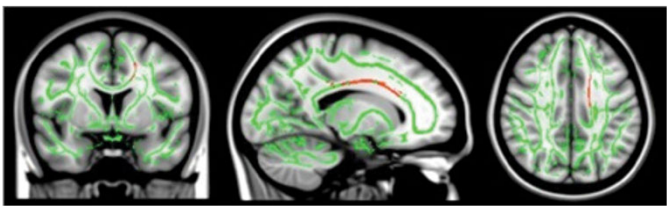

Figure 1. Coronal, saggital and axial projections of the statistically significant regions of FA values in IM/LM.

Discussion/Conclusion: Preliminary results support the hypothesis that chronotype-specific alternations can be characterized by microstructural differences. Additional TBSS analysis based on axial/radial diffusivity maps and other rotational invariants with increasing subject population will be provided. Importantly, results will have implications for working hours, shift work and in the future may also help to explain processes in relevant neuropsychiatric disorders such as depression.

References:

[1] Vink et al., 2001; ChronoInt., 809-822.
[2] Schmidt et al., 2009; Science, 516-519.
[3] Smith et al., 2006; NeuImage, 1487-1505.
[4] Behrens et al., 2003; MRM 50, 1077-1088.
[5] Woolrich et al., 2009; NeuImage 45, 173-186.

738

Disentangling tract-specific scalar measures by tractographic backprojection

J. Andreotti[1], A. Griffa[2], T. Dierks[1], P. Hagmann[2], A. Federspiel[1], V.J. Wedeen[3]
[1]Department Of Psychiatric Neurophysiology, University Hospital of Psychiatry, Bern/SWITZERLAND, [2]Department Of Radiology , CHUV-UNIL, Lausanne/SWITZERLAND, [3]Building 149, Room 2301, MD, Medicine, Albert Einstein College of Medicine, Charlestown/UNITED STATES OF AMERICA

Purpose/Introduction: The objective of the project is to extract white matter (WM) tract-specific scalar measures from voxel-wise scalar MR measures disentangling contributions from fiber crossings. The model makes two important assumptions: first that the scalar measure in a given voxel is the weighted sum of contributions from different tracts passing through that voxel and second that there exists a unique tract-specific scalar measure for each fiber tract, i.e. the measure is constant along the tract.

Subjects and Methods: Data for a single subject were acquired on a Trio Siemens with 32-channel head coil with a q4half Diffusion Spectrum Imaging sequence [4]. Tractography was computed with a deterministic streamline algorithm adapted to account for multiple directions in a voxel [1].

Fiber tracts considered for the analysis are defined using the tractography algorithm results.

The model assumes that the scalar measure in a specific voxel is given by the weighted sum of the tract-specific measures. The weight of a tract is estimated using the proportion of streamlines of each tract, corrected by its length. Measures of all WM voxels are considered in a unique linear system in order to extract the fiber tract-specific scalar measures.

Results: First tests of the method were done using simulated data in order to assess robustness to noise. Results show a good stability to noise, as all voxels are used to estimate fiber tract specific measures. In addition, the model has been tested on the ADC map of a real dataset. Results show very small differences (see Figure 1 and 2). The structure of differences is non random showing larger differences near WM borders. This is probably do to partial volume effects.

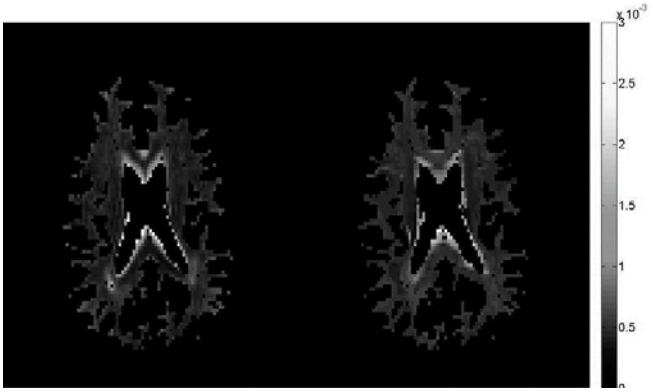

Fig.1: original and estimated WM ADC map

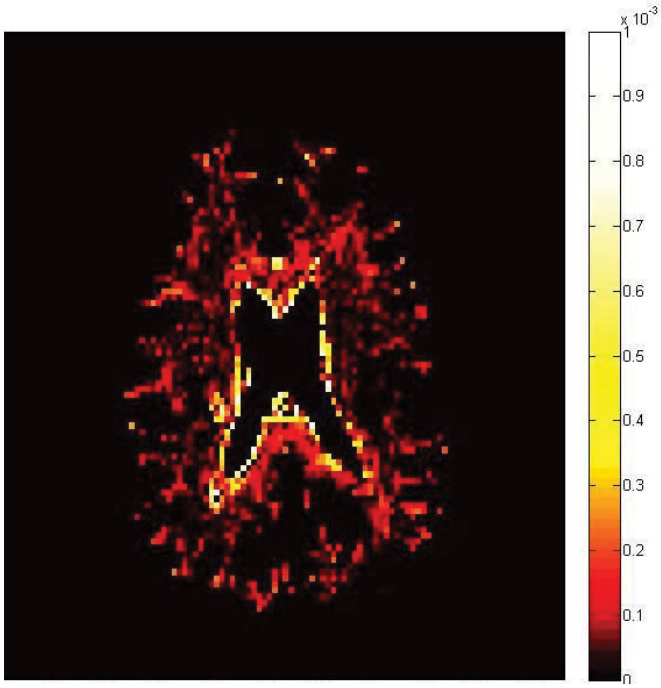

Fig.2: absolute difference

Discussion/Conclusion: Tract-specific scalar measures are critically relevant in order to optimally characterize fiber tract physiologic properties and related function([2],[3]). Voxel measures suffer from tract cross-correlations due to fiber crossings and related partial volumes. Based on two assumptions it is possible to decorrelate fiber-tract scalar properties by formulating the problem as a well defined invertible linear system. Such approach enables to obtain tract-specific scalar measures that are not influenced by crossing tracts and enable to improve connectome maps.

References:

[1] Hagmann P. et al., 2008, Plos Biol, 6:1479-1493
[2] Jbabdi S. et al., 2011, Brain Connect., 1(3): 169-183
[3] Rademacher J., et al., 1999, NeuroImage, 9(4):393-406
[4] Wedeen V.J. et al., 2005, Magn Reson Med, 54:1377–1386

739

White matter differences in juvenile myoclonic epilepsy and patients with generalized tonic-clonic seizures-only revealed by diffusion tensor imaging

M. Uppman[1], I. Savic[2], P. Lindström[3], T. Li[4]
[1]Department Of Medical Physics, Karolinska University Hospital, Stockholm/SWEDEN, [2]Department Of Women's And Children's Health, Karolinska Institute, Stockholm/SWEDEN, [3]Department Of Clinical Neuroscience, Karolinska Institute, Stockholm/SWEDEN, [4]Department Of Clinical Science, Intervention And Technology, Karolinska Institute, Stockholm/SWEDEN

Purpose/Introduction: The current classification of epilepsies states absence of anatomical abnormalities in syndromes of idiopathic generalized epilepsy (IGE). Contrary, and relaying on data from studies with different imaging techniques, our group has forwarded the hypothesis that IGE is associated with specific cerebral changes which differ between patients with juvenile myoclonic epilepsy (JME), and epilepsy with generalized tonic-clonic seizures-only (GTCS-only), e.g. [1]. In the present study we used DTI to further test the hypothesis.
Subjects and Methods: We studied 18 patients with JME (age=30.11±7.73 years, male/female=3/15), 15 with GTCS-only (age=35.27±12.96 years, male/female=10/5), and 34 healthy controls (age=31.67±9.02 years, male/female=17/17) on a 3T Siemens. Unpaired t-test showed no significant age difference between groups. DTI scan was repeated twice using SE-EPI with; 30 DWI directions, voxel size=2x2x3 mm^3, TE/TR=91/5200 ms, and b=1000 s/mm^2. Data was processed using AFNI and FSL's TBSS [2]. Statistical significance was assessed in two ways; i) all controls as an age-matched control group with gender as exploratory variable; ii) Separate the controls into age- and gender-matched groups for each patient group.
Results: First analysis showed decreased FA ($p<0.05$) in JME patients compared to controls in the genu/splenium of corpus callosum (gCC/sCC), the left anterior corona radiate (ACR_L), the right anterior limb of the internal capsule (ANIC_R) and the right superior portion of CC connecting to the left premotor cortex (PC). There was very significant FA difference in the body of CC (bCC) ($p<0.005$) (Figure 1). The mean FA values were extracted for these ROIs showing significant difference, Table 1.
The two statistical approaches yielded comparable results. Hence, gender-missmatch cannot account for the observed white matter difference.

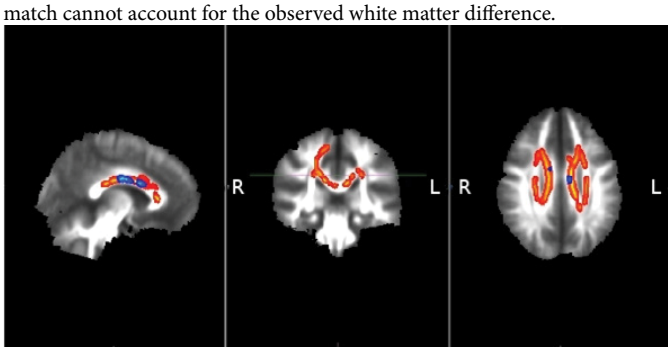

Figure 1: Statistical analysis of the DTI shows significant lower FA in patients with JME compared to controls (red: $p<0.05$, blue: $p<0.005$)

Table 1: FA values (mean±std) of the detected ROIs in the subject groups.

Region	Control	GTCS-only	JME
sCC	0.518±0.038	0.510±0.042	0.505±0.039
gCC	0.515±0.056	0.514±0.028	0.495±0.057
bCC	0.486±0.035	0.465±0.043	0.457±0.048
ACR_L	0.386±0.027	0.382±0.035	0.374±0.024
ALIC_R	0.484±0.054	0.469±0.051	0.450±0.045
PC	0.427±0.036	0.417±0.036	0.405±0.036

Discussion/Conclusion: DTI results show significant white matter differences between patients with JME and GTCS-only. The detected regions correspond to the connections to the premotor/motor areas, frontal cortex and the thalamocortical pathways. These results are consistent with a recent publication using tractography [3]. IGE syndromes should, therefore, be considered heterogeneous, as indicated by our results.
References:
1. Savic, I., 2004, Neuroimage, 163-72
2. Smith, S.M., 2006, Neuroimage, 1487-505
3. Liu, M., 2012, Epilepsia, 2267-75

740

On the optimal b-value range in diffusion kurtosis imaging

E. Farrher, F. Grinberg, N.J. Shah
Institute Of Neuroscience And Medicine - 4, Forschungszentrum Juelich GmbH, Juelich/GERMANY

Purpose/Introduction: Diffusion kurtosis imaging (DKI) is an important method for the quantification of non-Gaussian diffusion [1]. It is applicable in the moderate range of b-values below $bm=3/(D\times K)$, where D and K are the apparent diffusivity and kurtosis, respectively [1]. Here, we study the impact of the chosen b-value range on DKI metrics and assess the optimal range which allows a sufficient non-exponentiality but does not exceed bm.
Subjects and Methods: Measurements were performed in a whole-body 3T Siemens Trio scanner. The twice-refocused spin-echo diffusion-weighted EPI sequence was applied for 6 gradient directions. DKI metrics were evaluated [2] using the kurtosis equation,

$$S(b) = \exp\left(-bD + (bD)^2 K/6\right)$$

for 21 ranges of b-values between 0 and b_n, where b_n was varied from 1000s/mm^2 to 5000s/mm^2.The maps of bm were evaluated from the fitted values of D and K by iteratively increasing b_n with the step of 200s/mm^2 until the condition $b_n<bm$ was violated. This procedure was performed for each gradient direction individually. The maps of mean diffusivity (MD) and mean kurtosis (MK) are defined as the average over gradient directions.

Results: Figure 1a illustrates how the chosen b-value range affects the evaluation of MK. The dependence of the DKI metrics on b_n is demonstrated by the histograms in Figures 1b and 1c.

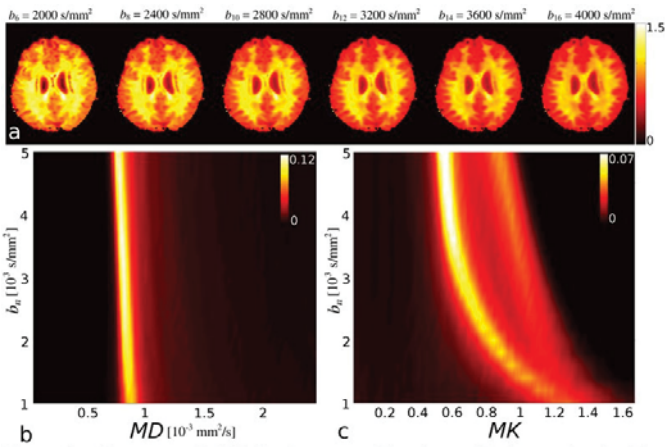

Figure 1. The maps of MK for 6 ranges of b-values with increasing b_n (a). The histograms of MD (b) and MK (c), from the whole range of b_n.

Whereas the peak of MD in Figure 1b is only slightly dependent of b_n, both peaks in the histograms of MK (Figure 1c) tend to shift towards lower values with increasing b_n. Figures 2a and 2b show the evaluated maps of bm for two selected gradient directions; Figure 2c shows the map of bm averaged over all gradient directions.

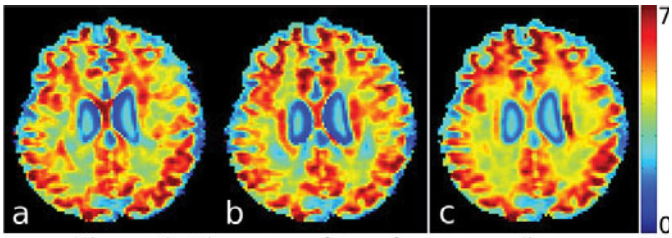

Figure 2. The maps of *bm* for two gradient directions (a,b) and the map of ‹*bm*› (c).

One can see that *bm* depends on the gradient direction and is inhomogeneous across the brain. Figures 3a and 3b show the maps of *MK* for the conventional (0-2000s/mm^2) (a) and optimised, voxel-dependent, *b*-value range (b).

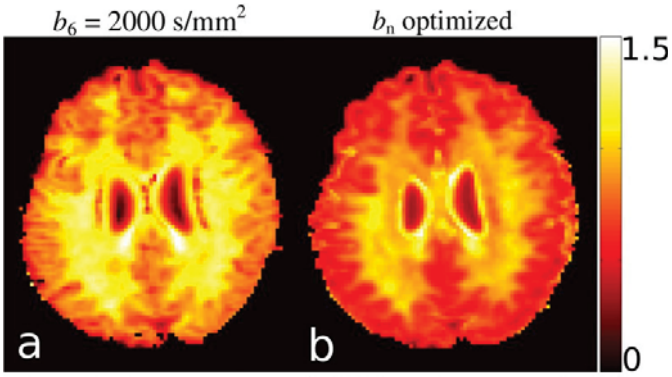

Figure 3. A comparison of *MK* from the conventional value for b_n (a) and the optimized b_n (b).

Discussion/Conclusion: We demonstrated that the optimal range of *b*-values for kurtosis evaluation depends on the gradient direction and tissue type. Implementation of a voxel-based estimation of *bm* helps to improve the accuracy of evaluation of DKI metrics and reduces its dependence on the selection of specific gradient orientations and *b*-value sets.

References:

[1]Jensen,J.H.,Helpern,J.A.,Ramani,A.,Lu,H.,Kaczynski,K.,2005.*Magn.Reson. Med.***53,**1432-1440.[2]Grinberg,F.,Farrher,E.,Kaffanke,J.,Oros-Peusquens,A.-M.,Shah,N.J.2011.*Neuroimage***57**,1087-1102.

aper Poster

unctional imaging

41
scrimination of tactile trajectories on the fingertip: an fMRI study

Q. Alhussain, A. Benattayallah, J. Fulford, I. Summers
llege Of Engineering, Mathematics And Physical Sciences, Exeter university, eter/UNITED KINGDOM

rpose/Introduction: Previous studies [1,2] have identified brain regions ociated with tactile movement (coherent or random). The present study in-stigates whether cortical activation depends on the nature of the movement, ing stimuli moving in two dimensions over the fingertip (as opposed to the e-dimensional movement over the tongue investigated by Matteau *et al.* [3]).
bjects and Methods: Ten volunteers participated (all male, 24-40 years). ages (EPI, TR = 3s, TE = 45ms, 39 slices of 3mm thickness, in-plane resolu-n 3x3mm were continuously acquired during which repeated blocks were esented comprising 9s tactile stimulus followed by 9s rest period, 5s response riod and a further rest varying between 21 and 33s. The vibrotactile display s contactors at 2mm spacing in a 5×5 array on the fingertip, driven by pi-oelectric mechanisms which can operate at 40Hz in a high-magnetic-field. muli were of three types (Figure 1): a "circle" consisting of 9 rotations around e fingertip, "random" followed a path of no obvious shape, and "stationary" volved alternating diagonals of a 2×2 square (giving sufficient modulation to nimise adaptation). Following stimuli presentation, subjects were required identify the stimulus type via button pressing feedback.
g. 1. Stimuli as a sequence of timeframes over the array (dots indicate ap-rent stimulus): (a) circle, (b) random (part of), (c) stationary.

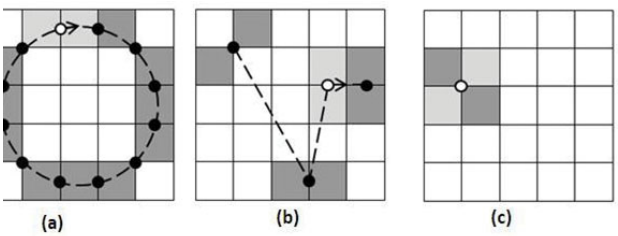

sults: When the stimuli identification feedback was assessed one subject is unable to correctly identify at a rate higher than random chance and is removed from subsequent analysis. The remaining subjects correctly ntified the stimuli 82% overall. Functional MRI data were analysed using M8 software. A preliminary analysis suggests little difference in activation ensity for circle and random stimuli (Figure 2). However, the data allows e activity for incorrect and correct responses to be differentiated – the next ge of analysis will take advantage of this.
g. 2. Activations in a single subject, fixed effects, $p<0.001$, uncorrected (left: cle stimulus *vs* rest; right: random stimulus *vs* rest).

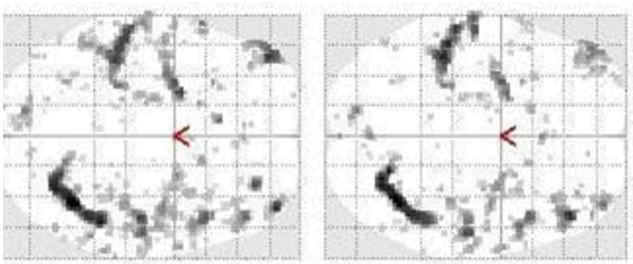

knowledgment: We are grateful to Philips Healthcare for scientific support

Discussion/Conclusion: The results show the array can be successfully used to represent different types of tactile movement and thus, can be used for fMRI studies. Preliminary findings suggest that despite shape discrimination similar cortical regions of the brain are activated.
References:
[1] Vanello N *et al.* (2004) Proc. HBM 2004, TU323
[2] Summers IR *et al.* (2009) J. Acoust. Soc. Amer. 125, 1033-39
[3] Matteau I *et al.* (2010) Brain Res. Bull. 82, 264-70.

742
Haplotype trend regression analysis improves detection efficacy of SCL6A4 effects on amygdala activation

R.N. Boubela[1], K. Kalcher[1], W. Huf[2], U. Rabl[2], T. Hofmaier[2], V. Szilagyi[2], H. Esterbauer[3], C. Windischberger[1], L. Pezawas[2], **E. Moser**[1]
[1]Center For Medical Physics And Biomedical Engineering, Medical University of Vienna, Wien/AUSTRIA, [2]Division Of Biological Psychiatry, Department Of Psychiatry And Psychotherapy, Medical University of Vienna, Wien/AUSTRIA, [3]Department Of Laboratory Medicine, Medical University of Vienna, Vienna/AUSTRIA

Purpose/Introduction: Genetic variability within the serotonin transporter gene (SCL6A4) such as a frequently studied tandem repeat polymorphism in its promoter region (5-HTTLPR) plays a crucial role in the neurobiological understanding of developmental effects of serotonin (5-HT) signaling and its neural consequences [1]. Amygdala hyperreactivity is the most prominent finding in S-allele carriers of 5-HTTLPR so far[6]. However, single genetic variants such as 5-HTTLPR exhibit only subtle statistical effects in even large neuroimaging samples. Hence, we studied SCL6A4 haplotypes with the goal to increase detection efficacy of genetically driven SCL6A4 on a neural level, an approach that has recently been taken for iCOMT[2].
Subjects and Methods: 128 healthy subjects performed a 10 minute emotional fMRI paradigm (3T Siemens Magnetom TIM Trio, 12-channel head coil, GRE single shot EPI sequence, TE/TR=42/2000ms, 96x96 matrix, 210mm square FOV, 20 axial slices, 4mm thickness, 1mm gap, 280 volumes) in which pictures of fearful faces and geometric shapes were presented to the subjects. Images were corrected for slice-timing and motion[3], normalized on the MNI152 template, smoothed with a 8mm FWHM Gaussian kernel and masked using an amygdala atlas[4]. Task effect of fearful faces versus geometrical forms was estimated using a general linear model (GLM). All preprocessing was computed in AFNI. 5-HTTLPR, STin2 as well as the SNP rs25531 were genotyped with standard procedures and subjects with Sg variant were excluded from the analysis due to their rare occurrence (n=4). Haplotype trend regression (HTR), calculated in R 2.14.1 (see Table), was applied to estimate the influence of haplotypes on amygdala BOLD response. F-tests were employed to assess whether the HTR explained significantly more variance than the simpler triallelic 5-HTTLPR genotypization[5].
Results: Activation maps calculated via GLM are shown in Fig. 1a. Significantly higher explained variance in the model using HTR compared to the model with the triallelic 5-HTTLPR genotypization was found in a cluster of 42 voxels (peak p=0.007) in the right amygdala (Fig.1b). Haplotype effects on amygdala activation are given in Fig.2.

Estimated Haplotype Frequencies

5-HTTLPR	rs25531	STin2.x	haplotype frequency
L	a	10	29.87%
L	a	12	23.68%
L	g	12	6.22%
L	g	9	1.50%
S	a	10	5.30%
S	a	12	32.13%
S	g	10	1.30%

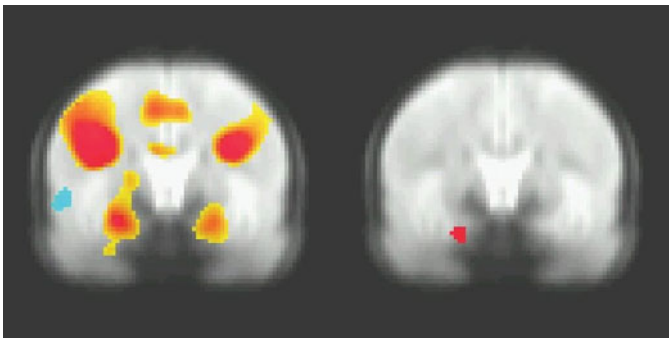

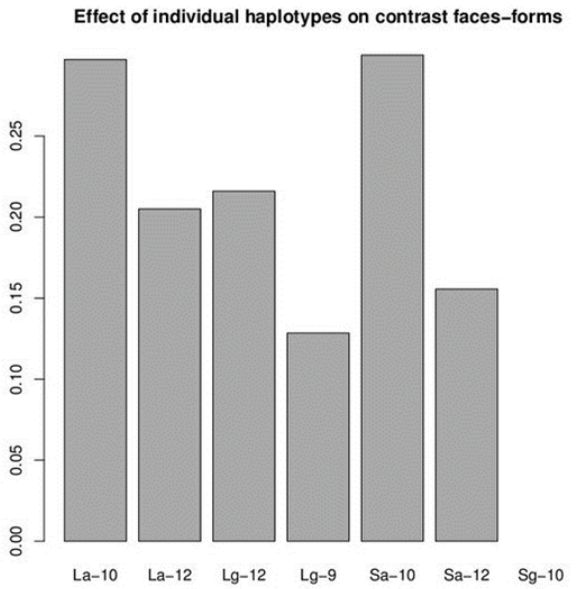

Discussion/Conclusion: HTR can be used to better predict the effect of depression-related genes on amygdala function in healthy subjects. The haplotypes La-10 and Sa-10 are associated with an increase, and haplotypes Lg-9 and Sa-12 with a decrease in amygdala response when viewing fearful faces. Further research may investigate potential effects of haplotype on connectivity in brain networks, particularly involving the anterior cingulate cortex[1].

References:

[1]Pezawas,L.et_al.Nat_Neurosci_8,828-834(2005).
[2]Meyer-Lindenberg,A.et_al.Mol_Psychiatry_11,867-877,797(2006).
[3]Sladky,R.et_al.Neuroimage_58,588-94(2011).
[4]Amunts,K.et_al.Anat_Embryol_210,343-352(2005).
[5]Zalsman,G.et_al.Am_J_Psychiatry_163,1588-1593(2006).
[6]Hariri,AR.et_al.Science_297,400-403(2002).

743

Assessment of Arterial Spin Labeling for functional localization of active and passive motor tasks.

I. Boscolo Galazzo[1], F.B. Pizzini[2], S.F. Storti[1], E. Formaggio[3], A. Bertoldo[4], P. Manganotti[1]
[1]Department Of Neurological, Neuropsychological, Morphological And Movement Sciences, University of Verona, Verona/ITALY, [2]Department Of Neuroradiology, General Hospital, Verona/ITALY, [3]Neurophysiology, IRCCS San Camillo Hospital, Venice/ITALY, [4]Department Of Information Engineering, University of Padova, Padova/ITALY

Purpose/Introduction: Functional magnetic resonance imaging (fMRI) using Arterial Spin Labeling (ASL) is emerging as a useful technique for spatial mapping of brain activity. It allows to localize and also estimate cerebral blood flow (CBF) changes induced by different tasks[1]. The purpose of this study was to assess the applicability of ASL to detect brain activations during active and passive movements compared to the gold standard, i.e. fMRI based on the blood-oxygenation-level-dependent (BOLD) contrast[2].

Subjects and Methods: Eight healthy volunteers were studied on a Siemens Allegra 3T. A pulsed Q2TIPS-PICORE sequence was used for the ASL acquisition in a block design with eight cycles of rest/task of 30s each (TR/TE/TI_2=3000/16/1400ms).The BOLD fMRI protocol consisted of six 30s cycles of task alternated to rest (TR/TE=3000/30ms). During active movement, they flexed and released their right hand, while passive movement was applied by one investigator by repeating the same task.

The fMRI data were analyzed with a General Linear Model approach, using a design matrix with 2 covariates for BOLD, while 4 covariates were assumed to model ASL data[3]. Since the low signal-to-noise-ratio (SNR) of the ASL technique[1], two different thresholds for ASL and BOLD data were chosen for the statistical significance.

Results: In the group analysis, for active-movement task, ASL showed activations in the contralateral sensorimotor cortex (SMI), supplementary motor area (SMA), ipsilateral cerebellum, inferior parietal lobe and thalamus ($p < 0.01$ uncorrected). BOLD also showed the same network of areas, but with more consistent activations ($p < 0.005$ Bonferroni)(Fig.1).

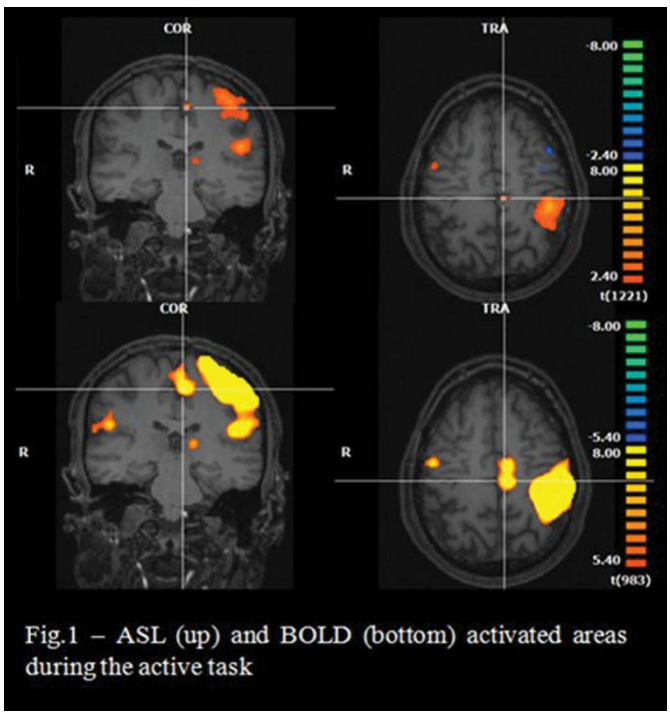

Fig.1 – ASL (up) and BOLD (bottom) activated areas during the active task

For passive-movement task, ASL activities were limited to SMI and SMA, whereas with BOLD no differences between the areas involved during active and passive tasks were detected(Fig.2).

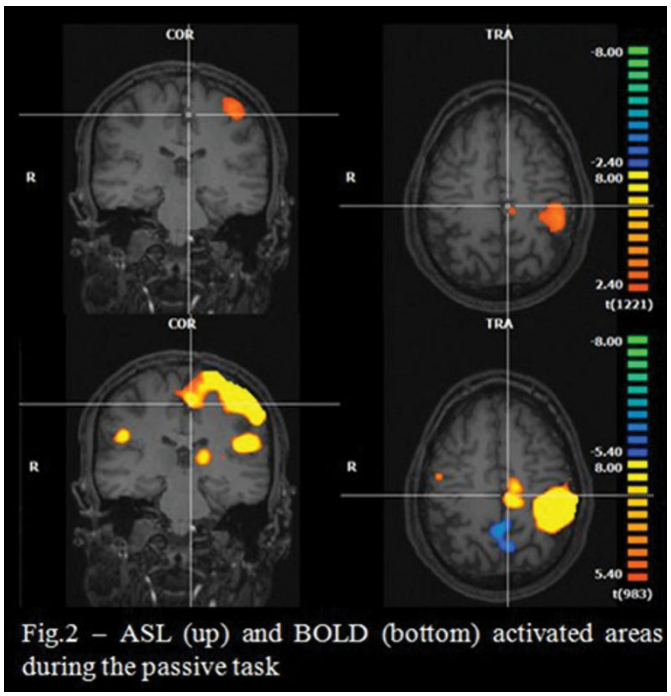

Fig.2 – ASL (up) and BOLD (bottom) activated areas during the passive task

In the quantitative measurement of CBF, during active movement the mean values averaged across all subjects for SMI and SMA were 80±13(mean±std) and 52±11ml/100gr/min for task and rest respectively, whereas during passive task the mean values were 65±20 for movement and 50±14ml/100gr/min for rest.

Discussion/Conclusion: Our results suggest ASL fMRI can be usefully applied to detect brain activations during different tasks, despite its low SNR, and can provide a quantitative measurement of CBF. ASL gives more focal activations in comparison to BOLD, even with different statistical thresholds. Differently from BOLD, ASL identifies less activated areas for passive than active condition, probably due to lower CBF variations, as confirmed by CBF estimation.

References:

[1]Detre JA et al., 2002, Clin.Neurophysiol,113:621-634
[2]Bandettini P et al., 1992, MRM, 25:390-397
[3]Mumford JA et al., 2006, NeuroImage,33:103-114

Paper Poster

Hardware

744

Quad channel PIN diode driver.

Y. Pilloud, R. Gruetter
Lifmet, CIBM-EPFL-LIFMET-SB, Lausanne/SWITZERLAND

Purpose/Introduction: In some experiments, like Arterial Spin Labelling (ASL), with multiple surface and/or volume coils, one coil is loading the other. PIN diodes can be used as switches to detune the unused coils. This circuit is designed to be integrated in a Varian magnet leg and digitally controlled by the console by a TTL signal (0 to +5V). The PIN diodes are polarized through the RF coaxial cables to avoid extra connections.
Subjects and Methods: The circuit is splitted in two parts linked by an opto-coupler to avoid ground loops between the RF and digital signals.
The control signal is applied through two triggers/inverters U1A/U1B and the switch S1.They allow to invert the polarity if needed. The optoisolator U2 creates a galvanic separation between the logic and the RF grounds. The signal is amplified by the darlington transistors Q1 and Q2 to the desired level. The current through the PIN diode (MA4P1250, M/A-COM) D11 is controlled by R5. The two chokes L1 and L12 create the DC path and block the RF signal. Only three extra components (D11, C15, L12) are needed on the coil circuit to be detuned.
The whole circuit takes place on a PCB and is powered by the magnet leg.

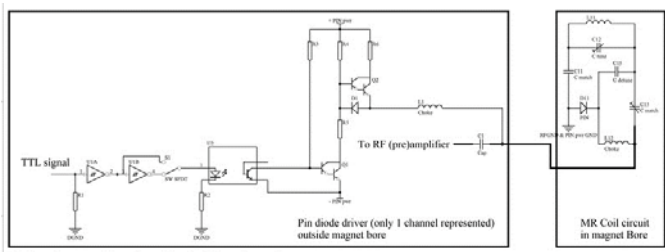

Fig 1. : schematic of one channel with a MR coil example.

Results: The switch is driving -10mA (ON) and +12V (OFF). Plots from the network analyzer (Agilent E5071C) are shown in the four figures below. The bandwidth is flat at 0.3 dB from 40 MHz to 650 MHz. VSWR is lower than 1.2 in the range 100-600 MHz. The separation between two adjacent channels is better than 70 dB. The switching ON time is 1 µs and 1.5 µs for OFF time.

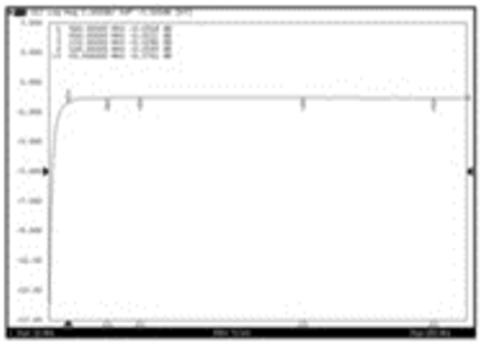

Fig. 2: S12, switch bandwith and insertion loss.

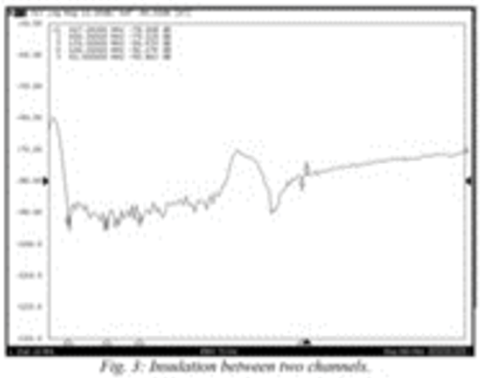

Fig. 3: Insulation between two channels.

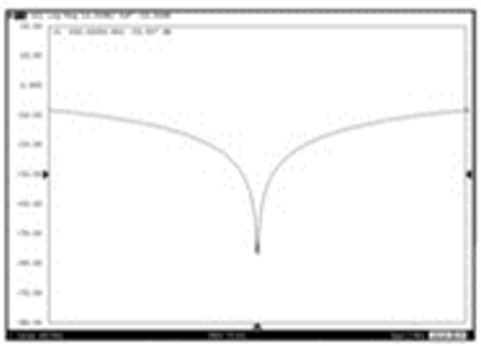

Fig. 4: Coil tuned and matched at 400 MHz.

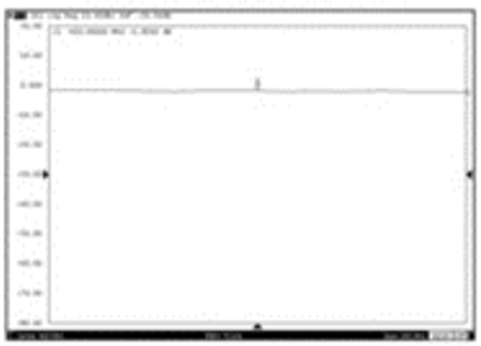

Fig. 5: Coil detuned at 400 MHz.

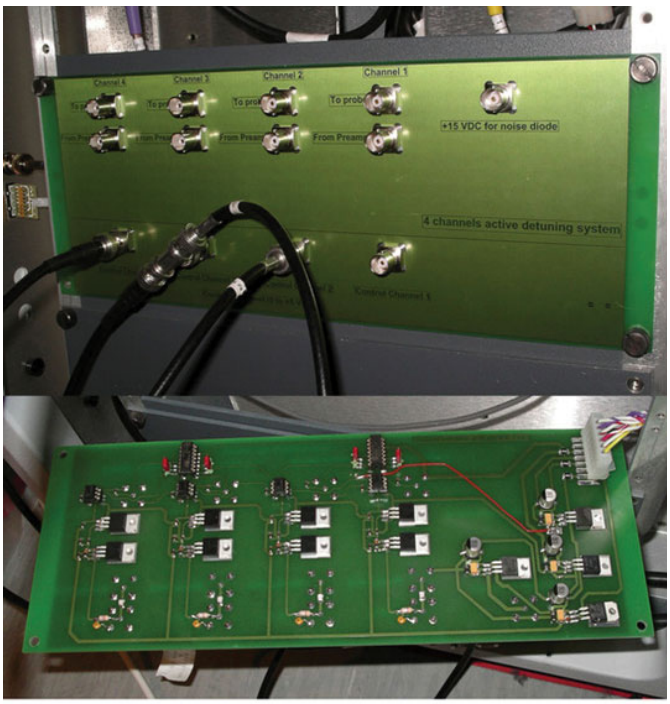

Fig. 6: View of both sides of the 4 channels PIN diode driver included voltage regulators.

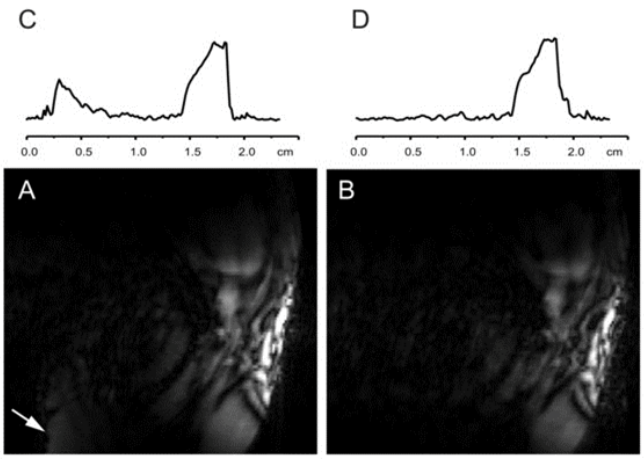

Fig. 7. Comparison of sagittal GRE images without/with active detuning. A and B are GRE images acquired using the neck coil as transceiver without and with active detuning image coil on top of the tagging coil. The arrow (in A) indicated the apparent signal intensity difference when comparing with B.

Discussion/Conclusion: The original ASL experimental setup required two separate RF power amplifiers to drive tagging and imaging coils. The PIN diode driver presented here simplifies the setup; the polarity of each channel can be inverted with a switch. The circuit can be easily extended and scaled to a higher number of channels, a larger bandwith or a higher power rating. During tuning and matching, the PIN diodes can be polarized or blocked simply by changing the switch position

References:

Lei H et al. Conf Proc IEEE Eng Med Biol Soc. 2011;2011:6993-6.
W.E. Doherty and R.D.Joos, 'The PIN diode designers handbook', Microsemi Corp., 1998
NMR Probeheads, Imperial College Press, 2006.

Acknowledgements: This study was supported by CIBM of the UNIL, UNIGE, HUG, CHUV, EPFL and Leenaards and Jeantet Foundations.

745

Respiration-Induced B_0 Fluctuations in the Rat Brain at 9.4 Tesla

I. Dragonu, N. Baxan, A. Merkle, J. Hennig, D. Von Elverfeldt, M. Zaitsev
Dept. Of Radiology, Medical Physics, University Medical Center Freiburg, Freiburg/GERMANY

Purpose/Introduction: At high B_0 field the susceptibility difference between tissues and air produces greater field inhomogeneities leading to potential shimming problems. Furthermore, B_0 may vary during the experiment for several reasons: physiological motion such as breathing [1], subject motion and hardware imperfections. This work investigates respiration-induced B_0 fluctuations in the rat brain at 9.4T including dependence on slice orientation.
Subjects and Methods: All experiments were performed on a 9.4T Bruker BioSpin animal scanner using an EPI sequence incorporating FID navigators. TR was readjusted to be 1.2 times smaller than the period of the respiration cycle, and the flip angle to the Ernst angle assuming a T_1 value of 2200ms [2]. The B_0 fluctuations were evaluated in three different volumes of interest (VOI): two stacks of transverse slices with different positioning along the z-axis and one stack with sagittal orientation. B_0 fluctuations during the respiratory cycle were estimated using the phase information of the complex FID. After phase unwrapping, a linear fit was performed on the phase values of the FID with the B_0 variation being proportional to the slope of the resulting fit. This operation was applied for each individual channel and subsequently combined using a magnitude weighted mean.
Results: Fig.1(a) displays one example of the B_0 fluctuation in a slice located in the cerebellum, illustrating an average variation of 17.95Hz peak-to-peak. The spatial variation of the peak-to-peak amplitude in the z-direction for the VOI containing the cerebellum is shown in Fig.1(b) for three individual dynamic scans and the resulting second order polynomial fit. The variation along the z-axis depicts a polynomial behaviour suggesting variable Z^2 shim values. The second order coefficient of the resulting polynomial fit is equal to 0.9Hz/mm^2. The peak-to-peak amplitudes of the frontal brain (see Fig.1c) can be approximated with a linear behaviour along the z-axis with a slope of -0.57Hz/mm. A relatively flat behaviour was observed in the sagittal orientation with peak-to-peak amplitudes with a mean value of 10.73Hz.

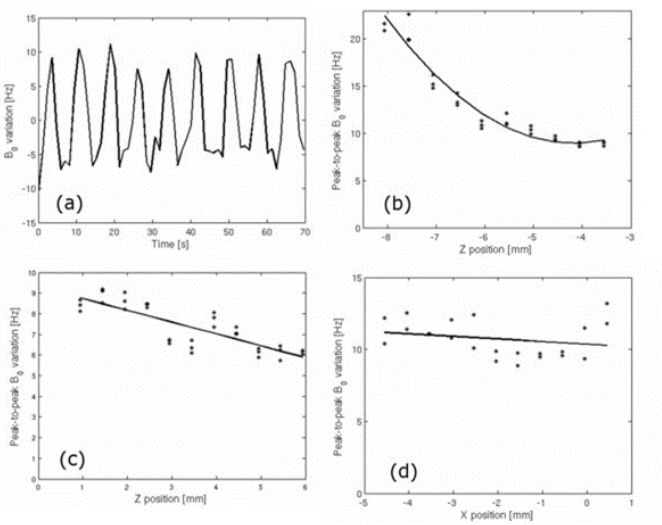

Fig 1: a) Global B0 fluctuation in a slice located in the cerebellum (average peak-to-peak = 17.95 Hz), b) Spatial variation of peak-to-peak amplitude along z-axis in a region of interest containing the cerebellum. c) Spatial variation of peak-to-peak amplitude along z in the frontal brain. d) The spatial dependence along the x-axis was analysed using the sagittal slices.

Discussion/Conclusion: The respiration-induced B_0 fluctuations were investigated at 9.4T in different regions of the rat brain. This work demonstrates that the observed magnetic field fluctuations are significant and that the peak-to-peak B_0 fluctuations are dependent on the slice orientation and position.

References:

[1] Van de Moortele PF *et al.* MRM 2002; 47:888-895.
[2] Kuo Y-T *et al.* JMRI 2005 21:334-339.

746

8 Channel Interventional Head Receive Array for Transcranial MR Guided Focused Ultrasound

F. Resmer[1], B. Werner[2], T. Lanz[1]
[1]-null-, RAPID Biomedical GmbH, Rimpar/GERMANY, [2]Center For Mr Research, University Children's Hospital Zurich, Zuerich/SWITZERLAND

Purpose/Introduction: Transcranial MR guided Focused Ultrasound (TcMRgFUS) is a new treatment modality for image-guided, non-invasive neurosurgery. However, intra-interventional high-quality MR imaging is challenging due to mechanical constraints and electronic complexity imposed by the ultrasound transducer setup. Here, a dedicated 8 channel interventional MR head receive array has been developed to support the TcMRgFUS intervention.

Subjects and Methods: The front-end of the InSightec ExAblate 4000 Brain system (InSightec Ltd., Tirat Carmel, Israel) consists of a large phased array transducer supported by a mechanical 4-axis positioner. A stereotactic frame immobilizes the patient's cranium inside the transducer (Fig. 1).

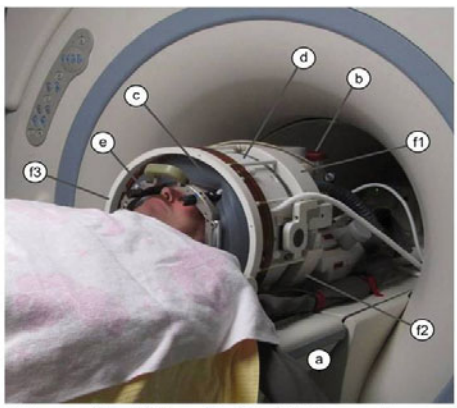

Fig. 1: MR array (Rapid Biomedical GmbH, Rimpar, Germany) in clinical use. Transducer setup: (a) MR table, (b) 4-axis positioner, (c) membrane, (d) transducer enclosure, (e) stereotactic frame, (f1) anterior MR array, (f2) posterior MR array, (f3) MR array front ring.

The MR array (inner diameter 345mm, outer diameter 375mm, length 240mm) wraps tightly around the transducer (Fig. 1). It comprises an anterior section and a posterior section of 4 receive channels each. Every channel contains an active and a passive decoupling circuit and is connected to a low impedance preamplifier [1] via a 50 Ω matching network followed by a phase shifter for preamplifier decoupling [1]. Next neighbour elements are decoupled with shared inductors [2].

Results: Both, handling and reproducibility are improved compared to formerly used phased-array, wrap around coils. Image SNR is slightly improved due to the improved filling factor but quantification is difficult due to poor stability and reproducibility of volunteer immobilization. Figure 2 shows identically acquired 3D-T1IR images as used for stereotactic navigation. The Rapid coil provides more anatomical resolution and consequently allows to reduce acquisition time for navigation imaging from 19' to 9' while preserving navigation precision.

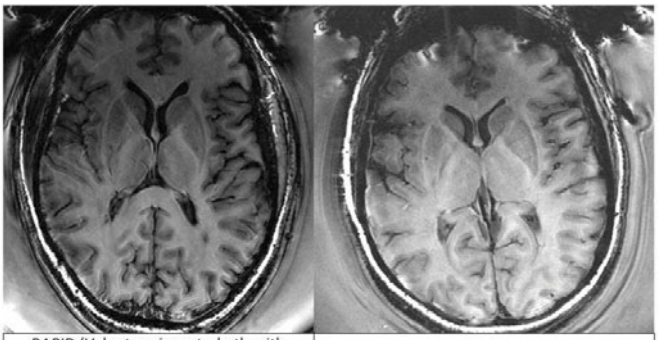

Figure 2: Comparison of a 3D-T1IR Navigation scan with Rapid coil and 8CH-TORSO phased-array.

The MR array was certified as a medical device and has been successfully tested in ongoing clinical phase I studies for functional TcMRgFUS neurosurgery [3] and TcMRgFUS tumor surgery (Fig. 1). It offers full head coverage and parallel imaging capability.

Discussion/Conclusion: The TcMRgFUS environment is very challenging for MR imaging owing to the system electronics of the phased array ultrasound transducer, its copper shielded transducer surface with water bath and the stereotactic fixation of the patient head. Here we demonstrate the advantages of integrating an MR array into the TcMRgFUS frontend: handling, reproducibility and scanning time could be improved. We believe that the SNR could be further increased by an individual in-situ fine tuning as each element is affected differently by the transducer setup.

References:

[1] P. Roemer et al., MRM 16: pp.192 (1990)
[2] J. Wang, Proc. ISMRM 4 p.1434 (1996)
[3] D. Jeanmonod, et al., Neurosurg Focus 32 (1):E1, 2012

Paper Poster

Neuro

747

Post-mortem structural MR imaging of diethylene glycol - embalmed brain specimens

M.M. Ribeiro[1], M. Carreiras[2], H. Martins[3], H.A. Ferreira[4], D. Pais[5], J.G. O´neill[5], J.C. Maurício[6]
[1]Sciences And Technology Of Radiation, Polytechnic Institute of Lisbon, Lisbon/PORTUGAL, [2]Sciences And Technology Of Radiation And Human Anatomy, Polytechnic Institute of Lisbon and Medical Sciences Faculty, Lisbon/PORTUGAL, [3]Radiology, Polytechnic Institute of Lisbon - Scholl of Heath Technology, Lisbon/PORTUGAL, [4]Ibeb, Sciences Faculty of Lisbon University, Lisbon/PORTUGAL, [5]Human Anatomy, Medical Sciences Faculty of Lisbon University, Lisbon/PORTUGAL, [6]Imaging, Euromedic - Tomar, Tomar/PORTUGAL

Purpose/Introduction: Post-mortem MR imaging is a good method to establish correlations between neuroimaging and neuroanatomy and to provide pathological information.The common solutions used to break the autolysis process in post-mortem (pm) tissues are formaldehyde based. To prevent hazards and promote health protection of users against formaldehyde toxicity, we have been replacing these solutions with diethylene-glicol (DEth-Glic). DEth-Glic has shown efficacy as a brain-fixation solution concerning the plasticity, consistency and color of the tissues but nothing is known concerning its suitability for MR imaging. In this study, we investigated Deth-Glic fixated pm brains properties regarding structural MR imaging.

Subjects and Methods:

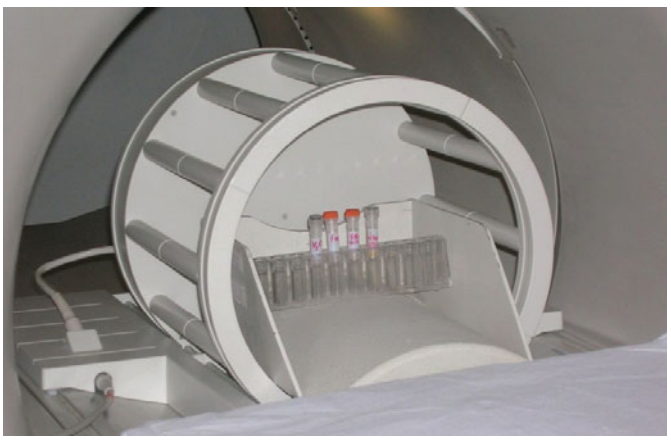

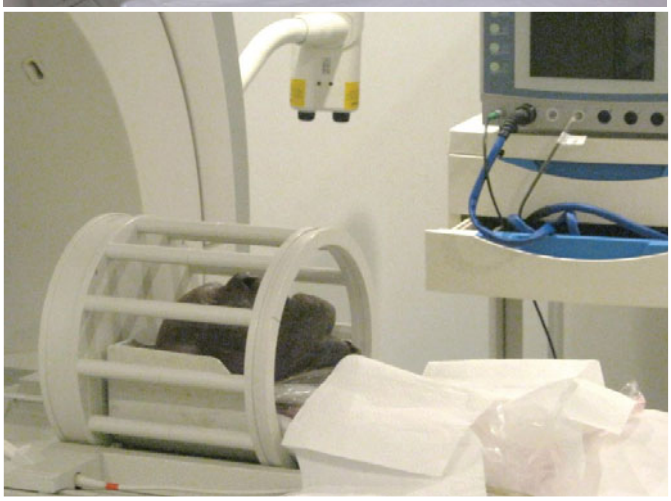

T1 and T2 relaxation values of DEth-Glic pure in flagon were determined using multiple inversion and echo times sequences, in a Philips Gyroscan Intera scanner (Fig1). With the consent of the Cadavers Donation Office of the Medical Sciences Faculty, 8 brains from deceased subjects (2008-2009) were studied. The cadavers presented different causes of death. They were embalmed immediately after dead via the femoral artery (5-10 liters DEth-Glic perfunded) and were conserved in high freezing at -30ºC. Cadavers' brains were scanned at room temperature using a 1.5T MR system and a receiving bird cage coil (Fig2). T1w sagittal, T2w-FLAIR and T1w-IR transversal plan sequences were obtained. ROI(s) were placed at the basal ganglia(BG) and corpus callossum(CC). MR signal intensities(SI) were measured and Contrast-to-Noise Ratio(CNR) values were calculated from BG and CC. Finally, CNR values were compared to values obtained with same sequences from 4 healthy living subjects.

Results:

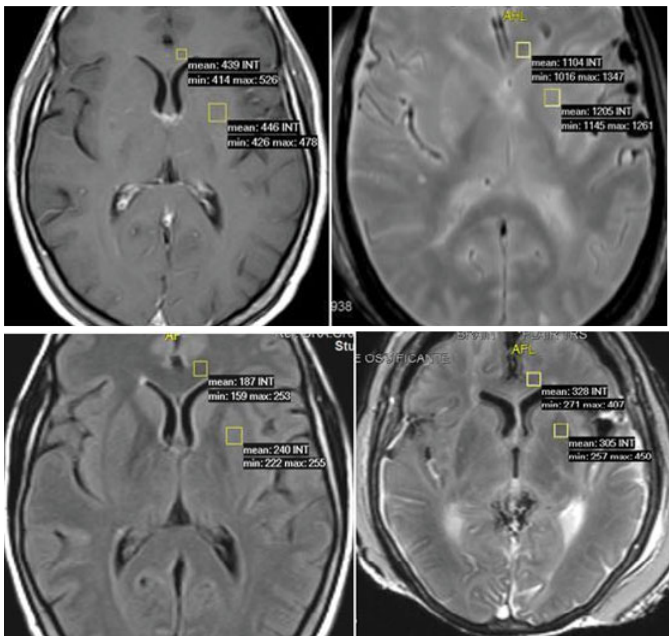

The T1 and T2 values of the DEth-Glic samples were 221ms and 112ms, respectively. We observed that DEth-Glic perfused brains have adequate SI for structural anatomy visualization in all the studied MR weightings (Fig 3; 4). Additionally, pm brain images showed different gray/white matter visualization in comparison with living brain images. For pm images, CNR values were 106,03 and 918,73 in the T1w and T2w-FLAIR sequences. For living brain images CNR values were 608,4 and 572,53. Finally, we found significant differences (p=0,0061, Mann-Withney test) in CNR of pm and living brain for both T1w and T2w-sequences.

Discussion/Conclusion: We conclude that DEth-Glic as a fixating solution, in pm brains perfused and immersed for 3,5 years, provides enough signal intensity and increased contrast between brain anatomic structures in comparison with images taken from living brains.

References:

1.Helmes G.et al.*Proc.Intl.Soc.Mag.Reson.Med.*19(2011).
2.De Groot J.et al.B*rain*(2001),124:1635-1645.
3.Kato H.et al.*Med.Phys.*(2005),32(10):3199-3208.
4.Dawe R.et al.*Mag.Reson.Med.*(2009),61:810-818.
5.Pfefferbaum A.et al.*Neuroimage.*(2004),21:1585-1595.

748

Radiotherapy of glioblastoma : absence of acute dose-dependent changes in DTI-derived metrics

T. Hope, R. Salo, J. Vardal, C. Larsson, I. Rasmussen, A. Bjørnerud
Intervention Centre, Rikshospitalet, Oslo University Hospital, Oslo/NORWAY

Purpose/Introduction: Irradiation of the head is a standard component in the treatment of primary brain tumors. Depending on the total irradiation dose, patients invariably experience cognitive changes after cerebral radiotherapy (CRT). Previous studies have suggested that diffusion tensor imaging (DTI) can detect radiation induced changes already in the acute phase in normal appearing white matter (NAWM) in patients undergoing CRT (1,2). In this study we hypothesized that radiation dose-dependent NAWM changes can be detected with DTI in the acute phase of CRT.

Subjects and Methods: 17 glioblastoma-patients were imaged at 3 Tesla with serial DTI measurements before CRT, every two weeks during the six-week course of CRT and thereafter every three months until death. Patients received a total of 55-60 Gy in 30 fractions. Relevant DTI-derived metrics (Fractional Anisotropy, Mean Diffusivity, Longitudinal Diffusivity, Radial Diffusivity) were computed for all time points.

Individual radiation dose maps were used to separate NAWM into 5 regions depending on total dose received: <12 Gy, 12-41Gy, 41-48Gy, 48-54Gy and >54 Gy.

The time evolution of DTI-derived metrics were comprehensively assessed through histogram analysis (mean, standard deviation, skewness, kurtosis), analysis of variance and correlations to radiation dose absorbed.

Results:

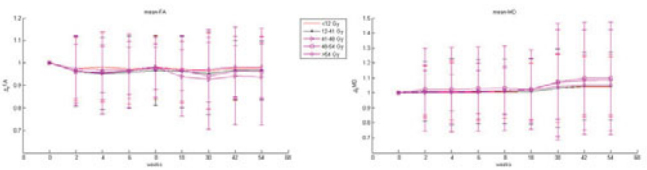

Although significant changes in mean values of all DTI metric could be detected already after 2 weeks of CRT, these changes did not correlate to radiation dose (fig 1). Other measured histogram parameters also failed to reveal any significant dose-related change in any of the investigated DTI-metrics.

Discussion/Conclusion: Applying detailed analysis of the time evolution of DTI-derived metrics, no significant dose-related changes in NAWM were observed in glioblastoma-patients undergoing CRT during therapy. Previous studies report dose-dependent changes in different DTI-metrics, however, our study cannot confirm these findings. Several ongoing studies investigate changes in DTI-derived metrics in tumor tissue and compare with regions of 'stable' NAWM (3) and although no dose-dependent effect could be detected in our study, an overall effect on estimated DTI-metrics in NAWM was observed - violating this assumption.

References:

(1) Nagesh V et al. Radiation-Induced Changes in Normal-Appearing White Matter in Patients With Cerebral Tumors: A Diffusion Tensor Imaging Study, IJROBP 2008; 70:1002 - 1010

(2) Haris M et al. Serial diffusion tensor imaging to characterize radiation-induced changes in normal-appearing white matter following radiotherapy in patients with adult low-grade gliomas. Radiat Med 2008;26:140-150.

(3) Moffat BA et al. Functional Diffusion Map: An Imaging Biomarker for the Early Prediction of Cancer Treatment Outcome Neoplasia. 2006; 8(4): 259–267

749

Automatic procedure for measuring brain tumor volumetric change

R. Salo[1], A. Server Alonso[2], C. Saxhaug[3], B. Breivik[3], I. Rasmussen[4], A. Bjørnerud[1]
[1]Intervention Centre, Oslo University Hospital, Oslo/NORWAY, [2]Department Of Radiology, Oslo Univerisity Hospital, Oslo/NORWAY, [3]Department Of Radiology, Oslo University Hospital, Oslo/NORWAY, [4]Intervention Centre, Rikshospitalet, Oslo University Hospital, Oslo/NORWAY

Purpose/Introduction: Tumor growth rates may be early biomarkers of expected survival time in patients with high grade gliomas. Identification of early surrogate markers for treatment response may improve survival of brain tumor patients by providing more time for secondary therapeutic interventions. Manual identification of volumetric growth is extremely time consuming, and thus unavailable in radiological practice; automatic procedures need to be developed.

Subjects and Methods: An automatic approach of measuring volumetric brain tumor changes using serial 3D-FLAIR and contrast-enhanced 3D T1-weighted (T1CE) image series was used to segment relevant tumor components: tumor-induced hyper-intensity on FLAIR and contrast enhancement. The procedure was 1) brain extraction [1], 2) magnetic field inhomogeneity removal [2], 3) intensity thresholding of volumes of interest by 2nd order relative entropy-based thresholders [3], 4) combining the clusters to produce relevant tumor VOIs. Serial imaging was performed in a radiochemotherapeutic monitoring study. A total of 44 data-sets from 11 post-surgical glioblastoma patients were included in the analysis. Tumor VOIs obtained from the automated procedure (tumor defined to include contrast-enhancement and necrosis) were compared to VOIs hand-traced by three experienced neuro-radiologists. Core VOIs, defined as the VOIs common to all experts were defined and the difference in number of tumor VOI voxels between each expert and the automated method was measured.

Results: The automatic method was able to produce tumor volumes within expert variation in 55% of cases. Excluding patients where the automatic method included voxels from outside the brain (due to inferior quality of brain-extraction) resulted in 25 examinations with 80% of the cases being within expert variation. Figure 1 shows a sample case with the three expert tumor VOIs shown in addition to the automatically defined VOI.

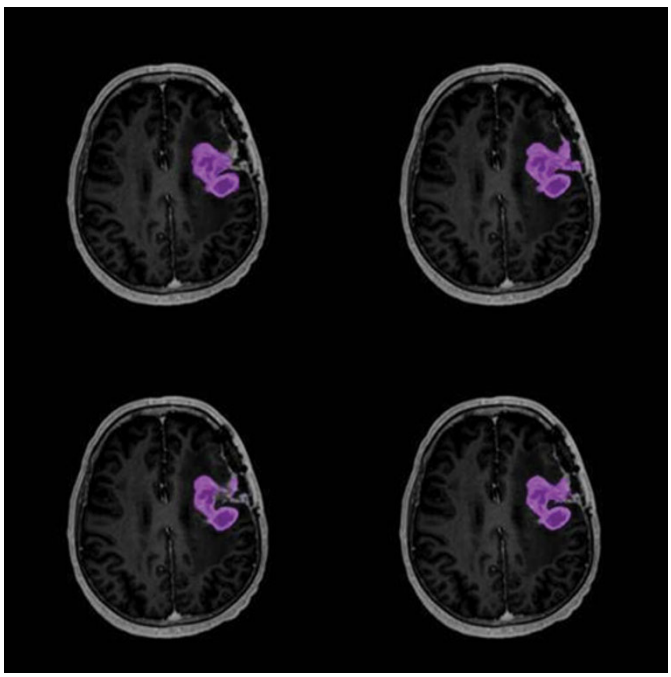

Fig 1. Three expert tumor VOIs and automatically defined VOI (lower right).

Discussion/Conclusion: We propose an automatic method for tumor delineation and volumetric quantification providing tumor VOIs in good agreement with experts' definitions in glioblastoma patients. The presence of contrast enhancement in extra-axial regions combined with imperfect brain extraction remains a challenge for fully automated tumor extraction methods in the brain.
References:
[1] Smith SM, 2002, Fast robust automated brain extraction., Human Brain Mapping, 17:143-155
[2] Likar B, Viergever MA, Pernuš F, 2001, Retrospective Correction of MR Intensity Inhomogeneity by Information Minimization., IEEE Trans Med Imaging, 20:1398-1410.
[3] Chang CI, Du Y, Wang J, Guo SM, Thouin PD, Survey and comparative analysis of entropy and relative entropy thresholding techniques., IEE Proc. Vis. Image Signal Process., 153:837-850.

750

Metabolic profiling of RG2 glioma using in-vivo ^{1}H MRS and ex-vivo HRMAS ^{1}H MRS

V. Stupar[1], N. Coquery[2], R. Farion[1], E. Barbier[2], C. Rémy[3], **F. Fauvelle**[4]
[1]Inserm, U836, Grenoble/FRANCE, [2]Gin, Université Joseph Fourier, Grenoble/FRANCE, [3]Gin, Preclinical MRI Facility, Grenoble/FRANCE, [4]Nmr Laboratory, IRBA-CRSSA, La Tronche/FRANCE

Purpose/Introduction: *In vivo* ^{1}H MRS provides metabolic information regarding tumour growth and response to treatment. A wider range of metabolites can be obtained *ex vivo* in biopsies using ^{1}H HRMAS MRS. The aim of the study was to assess the ability of both approaches to discriminate tumour from normal tissue using multivariate pattern recognition methods in a rat glioma model.
Subjects and Methods: Fischer rats (n=7) were orthotopically implanted with RG2 glioma cells at day 0. *In vivo* ^{1}H MRS was performed on well-established tumour at day 14. At day 15, the tumour bulk and the contralateral striatum were rapidly isolated and frozen.
In-vivo ^{1}H MRS was performed at 7 Tesla. Tumour and contralateral spectra were acquired in a 3x3x3mm^3 voxel with a PRESS sequence (TE/TR=20/2500 ms, tAcq 17min). HRMAS ^{1}H MRS was performed at 9.4 Tesla, 4°C within 16min using a CPMG pulse sequence [1].
The signals were processed using the "substract-QUEST" algorithm [2] of the jMRUI-sofware. Simulated spectra of 20 metabolites were included in the basis set for HRMAS MRS and 10 metabolites for MRS. The total spectrum intensity was used for normalization.
Quantified data were loaded in the SIMCA-P software (Umetrics, Sweden) as variables and scaled to unit variance before Projection to Latent Structure-Discriminant Analysis (PLS-DA) [3]. Cross-validation led to a quality factor R2Y and a predictive factor Q2. A good Q2 (>0.5) allows the model to be used for prediction. The results were visualized by plotting the first two principal components of the analysis against each other.
Results: *In vivo* and *ex vivo* spectra gave similar results in tumour with an increase of total Choline compounds (tCho) and a decrease of NAA, total Creatine compounds (tCr) (**Fig.1**). HRMAS MRS provided additional information in tumour metabolism: an increase of Alanine and Glycine, a decrease of GABA, the identification of choline components (Cho, PC, GPC) and the emergence of Hypotaurine. Both analyses yielded robust statistical models with a clear separation between tumour and contralateral striatum (**Fig.2**).

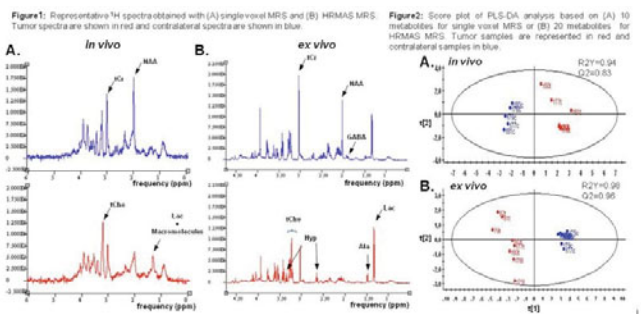

Figure1: Representative ^{1}H spectra obtained with (A) single voxel MRS and (B) HRMAS MRS. Tumor spectra are shown in red and contralateral spectra are shown in blue.

Figure2: Score plot of PLS-DA analysis based on (A) 10 metabolites for single voxel MRS or (B) 20 metabolites for HRMAS MRS. Tumor samples are represented in red and contralateral samples in blue.

Discussion/Conclusion: Quantification with jMRUI is reliable since metabolic profiles from contralateral striatum are well grouped. The PLS-DA models are robust despite inter-individual variability and highly predictive (high Q2 values). Further studies are needed to validate this approach for evaluation of treatment efficiency of glioma in preclinical research.
References:
[1] Wieruszeski et al., *JMR*, 2001, [2] Ratiney et al., *NMR biomed.*, 2005, [3] Holmes et al., *NeuroRx*, 2006.

751

Does multi-modal magnetic resonance imaging at 1.5 Tesla help to detect specific alterations within the brainstem of patients with Parkinson's disease

M.F. Schocke[1], R. Esterhammer[1], M. Nocker[2], C. Scherfler[2], W. Poewe[2], K. Seppi[2]
[1]Department Of Radiology, Medical University Innsbruck, Innsbruck/AUSTRIA, [2]Department Of Neurology, Medical University Innsbruck, Innsbruck/AUSTRIA

Purpose/Introduction: To evaluate multi-parametric magnetic resonance imaging (MRI) for the detection of specific alterations sensitive to complementary tissue characteristics (i.e. tissue iron deposition and microstructural disorganization) within subcortical structures in Parkinson's disease (PD).
Subjects and Methods: The authors prospectively studied MRI of 33 patients with PD and 26 age- and gender-matched healthy controls. Mean diffusivity (MD), fractional anisotropy (FA) as well as the relaxation rates R2 and R2* were evaluated in the caudate nucleus (NC), the putamen (PU), the globus pallidus (GP), the thalamus (TH), the corpus callosum (CC), the middle cerebellar peduncle (MCP) as well as the substantia nigra (SN) and segments of the SN.
Results: The MD was significantly increased in the SN and its subregions, while the FA was decreased in the caudal SN (ist das level 3). Both R2 and R2* were significantly increased in the SN. There were further significant R2 increases in the GP, Thalamus, MCP and dentate nucleus. In a further step, parameters were combined for the differentiation of PD and controls. A receiver operator characteristic analysis in the caudal SN revealed that diagnostic accuracy (sensitivity 0.85 and a specificity 0.77) was highest, when combining MD and R2* (ADC x R2*).
Discussion/Conclusion: This study suggest that microstructural alterations in the SN related to tissue iron deposition and microstructural disorganization as assessed with multi-parametric MRI might be useful for the evaluation of PD.
References:
Scherfler C, Schocke MF, Seppi K, Esterhammer R, Brenneis C, Jaschke W, Wenning GK, Poewe W: Voxel-wise analysis of diffusion weighted imaging reveals disruption of the olfactory tract in Parkinson's disease. Brain 2006, 129:538-542.
Vaillancourt DE, Spraker MB, Prodoehl J, Abraham I, Corcos DM, Zhou XJ, Comella CL, Little DM: High-resolution diffusion tensor imaging in the substantia nigra of de novo Parkinson disease. Neurology 2009, 72:1378-1384.
Peran P, Cherubini A, Assogna F, Piras F, Quattrocchi C, Peppe A, Celsis P, Rascol O, Demonet J, Stefani A, Pierantozzi M, Pontieri FE, Caltagirone C, Spalletta G, Sabatini U: Magnetic resonance imaging markers of Parkinson's disease nigrostriatal signature. Brain 2010, 133:3423-3433.
Du G, Lewis MM, Styner M, Shaffer ML, Sen S, Yang QX, Huang X: Combined R2* and diffusion tensor imaging changes in the substantia nigra in Parkinson's disease. Mov Disord 2011, 26:1627-1632.

752

Effects of Nutrition and Physical Activity on Brain Structure and Brain Metabolite Concentrations in Alcohol Dependence

S. Gazdzinski[1], A. Mon[2], T.C. Durazzo[2], M. Vertinski[2], D.J. Meyerhoff[2]
[1]Mri Core Facility, Nencki Institute for Experimental Biology, Warsaw/ POLAND, [2]Radiology And Bioimaging, University of California San Francisco, San Francisco/UNITED STATES OF AMERICA

Purpose/Introduction: Alcohol dependence is associated with poor nutrition and sedentary lifestyle. In neuroimaging studies of healthy light-drinkers and alcohol dependent individuals, we and others have shown lower N-acetylaspartate (**NAA**, marker of neuronal viability), lower glucose utilization, and certain brain structural changes, particularly in frontal lobe – a region that is preferably injured in alcohol dependence.[1] Here, we evaluated whether less physical activity and more caloric intake is associated with brain abnormalities in alcohol dependence.
Subjects and Methods: We studied 18 male alcohol dependent individuals in treatment (ALC) at 1.5T with MPRAGE (TR/TI/TE=10/300/4 ms) and multislice^{1}H MRSI (TR/TI/TE=1800/300/25 ms) in 3 parallel planes through the centrum semiovale, nuclei of the basal ganglia, and cerebellum. Brains were parcelated into anatomically defined regions with automated probabilistic segmentation combined with automated atlas-based region labeling of major lobes, cerebellum, and subcortical structures. Regional atrophy-corrected metabolite concentrations of NAA, choline-containing compunds, myo-inositol, and creatine containing metabolites were calculated by combining MRSI and segmented MRI data. Nutrition and physical activity over a year preceding the study were evaluated with standardized questionnaires (NutritionQuest, Berkeley, CA). Correlations were evaluated with Spearman's ρ.
Results: More daily fat intake was associated with smaller frontal gray matter volume (ρ=-0.42, p=0.04). Larger daily caloric intake was associated with lower NAA in parietal gray matter (ρ = - 0.42, p=0.05). Higher caloric expenditure (a measure of physical activity) was associated with higher temporal white matter NAA (ρ=+0.57, p=0.008). Unexpectedly, higher daily caffeine intake was associated with greater whole-brain gray matter volume (ρ=+0.50, p=0.017) and higher temporal gray matter NAA (ρ = +0.42, p=0.05). Thiamine intake mediated some of these relationships.
Discussion/Conclusion: These preliminary analyses suggest that neurobiological injury in ALC, which has been shown to be related to cognitive dysfunction[2], is partially mediated by nutrition and sedentary lifestyle. Other factors such as subclinical depressive disorders, liver disease, or cigarette smoking may have contributed to the relationships and will be evaluated in larger samples.
Sponsored by NIH AA10788 (DJM).
References:
1. Gazdzinski, S., et al, 2010, ACER, p. 2089-96. 2. Sullivan EV., 2003, ACER, p. 1409-19.

753

Metabolic changes in the central auditory system accompanying presbycusis

M. Dezortova[1], D. Wagnerova[1], O. Profant[2], J. Syka[2], M. Hajek[1]
[1]Mr-unit, Department Of Diagnostic And Interventional Radiology, Institute for Clinical and Experimental Medicine, Prague 4/CZECH REPUBLIC, [2]Institute Of Experimental Medicine, Academy of Sciences of the Czech Republic, Prague/CZECH REPUBLIC

Purpose/Introduction: The age-related hearing loss, presbycusis, is caused by lesions at different levels of the auditory pathway, the loss of active hair cells, and by deteriorated temporal processing of sound. Previous studies on animals showed a decrease in inhibitory neurotransmitters in the auditory cortex [1]. The goal of our study was to investigate changes in metabolite concentrations in the central auditory cortex in humans using MR spectroscopy (MRS).
Subjects and Methods: Fifty-three subjects underwent audiologic and MRS examination. Audiologic testing consisted of high frequency pure tone audiometry, spontaneous, transiently evoked and distortion products of otoacoustic emmissions and speech audiometry. MRS was performed at 3T system (Siemens) using a single voxel technique (TR/TE/NA=5000ms/30ms/64; volumes 8 and 18 ml) centered around the Heschl gyrus in both temporal lobes. MRS data were analyzed by LCModel, water signal was used as an internal reference for the calculation of metabolic concentrations. Corrections for the cerebrospinal fluid were applied. The statistical evaluation was performed using One-Way ANOVA with Turkey's Multiple comparison test.
All the subjects provided an informed consent according to the ISO 9001:2008 norm.
Results: Subjects were divided into three groups according to their audiologic results: young controls (YC; physiologic hearing, age: 24.3±2.3 yrs), elderly controls (EC; normal presbycusis, age: 67.3±1.9 yrs), elderly patients (EP; expressed presbycusis, age: 71.2±5.2 yrs). No asymmetry between hemispheres was found. YC significantly ($p<0.01$) differed from EC and EP in concentrations of glutamate, sum of glutamate and glutamine (Glu+Gln) and total N-acetylaspartate (NAA). No differences were found between EC and EP (Table 1). Significant changes ($p<0.05$) between all individual groups were found in lactate concentration measured from large volume.
Discussion/Conclusion: The decrease in glutamate and Glu+Gln concentrations between young and elderly subjects may suggest a loss of the function of excitatory transmission in the central auditory cortex with age. Although it could be a consequence of age-related brain atrophy in general (indicated by NAA decrease), we speculate that the trend of decreasing glutamate and Glu+Gln concentrations in elderly subjects is a result of decreased signaling caused by the hypofunctional inner ear confirmed by moderately (EC group) or strongly (EP group) decreased otoacoustic emissions. Although MRS is not sensitive enough to distinguish different levels of the presbycusis, it confirmed metabolic changes in the auditory cortex related to hearing impairment.
References:
[1]Burianova J et al. Exp Gerontol 2009;44(3):161-169
Acknowledgements
Supported by GACR P304/10/1872 and MZCR Institutional grant 00023001IKEM.

Table 1: Metabolite concentrations [mM] in auditory cortex

Group	GABA	Gln	Glu	Ins	Lac	Cho	NAA	Cr	Glu+Gln
VOI 8 ml									
young controls	1.77	4.05	14.27	7.74	0.74	2.20	12.30	10.19	18.33
elderly controls	1.56	3.57	13.08	8.57	1.04	2.33	11.14	10.20	16.64
elderly patients	1.79	4.23	11.80	8.00	1.26	2.16	10.79	9.83	16.03
VOI 18 ml									
young controls	1.22	1.76	12.10	7.59	0.53	2.00	11.32	9.54	13.86
elderly controls	1.61	2.01	10.14	7.68	0.84	2.15	9.97	9.40	12.17
elderly patients	1.64	1.70	9.43	7.41	1.10	1.95	9.49	8.77	11.13

VOI - volume of interest, GABA - γ-aminobutyrate, Gln - glutamine, Glu - glutamate, Ins - myo-Inositol, Lac - lactate, Cho - choline compounds, NAA - N-acetylaspartate and N-acetylaspartylglutamate, Cr - creatine and phosphocreatine, * - $p<0.05$, ** - $p<0.01$, *** - $p<0.001$

754

ROC analysis of mI/NAA in healthy elderly, MCI and AD at 3 T and 1.5 T

R. Tarducci[1], P. Mecocci[2], P. Chiarini[3], L. Pelini[2], P. Floridi[3], G. Gobbi[1]
[1]Medical Physics Department, Az. Ospedaliera di Perugia, Perugia/ITALY, [2]Institute Of Gerontology And Geriatrics, University of Perugia, Perugia/ ITALY, [3]Dept. Of Neuroradiology, Az. Ospedaliera di Perugia, perugia/ITALY

Purpose/Introduction: Proton Magnetic Resonance Spectroscopy (1HMRS) has been proposed as a diagnostic tool in the early phase of dementia. In this study we measured the 1HMRS metabolites in the posterior cingulate gyrus and in the medial occipital lobe at 1.5T and 3.0 T in a cognitively healthy elderly (Clinical Dementia Rating (CDR) scale score = 0), subjects with amnesic mild cognitive impairment (MCI) (CDR = 0.5) and patients with mild (CDR = 1) Alzheimer's disease (AD). The purpose is to compare 1.5T to 3.0T MRS in discriminating healthy elderly subjects from subjects with MCI and mild AD.
Subjects and Methods: Following the protocol proposed by Kantarci (1) double voxel 1H MRS at 1.5 T and 3.0T were performed. 1H MR spectroscopy voxels were placed over the posterior cingulate gyrus and the medial occipital lobe. An echo time of 35 ms and repetition time of 2000 ms were used in acquisitions from the VOIs. Statistics were performed by means of ANOVA with Bonferroni post hoc test for comparison between groups, correlation analysis between metabolites MMSE score and ROC curve analysis for sensitivity and specificity.

Results: No differences were observed in occipital medial lobe. In the posterior cingulate region at 3 T mI/NAA in AD significantly differed from HC ($p<0.01$) and MCI ($p<0.01$). Receiver operating characteristics (ROC) analysis was used to compare the diagnostic accuracy of mI/NAA ratios in distinguishing patients with AD from elderly control subjects and MCI at 1.5 and 3 T. Area under curve (AUC) were 0.61 at 1.5 T and 0.98 at 3T when comparing AD and MCI; 0.61 for 1.5 T and 0.93 for 3 T in comparing AD and controls.
Discussion/Conclusion: 1H MRS at 3T showed that:
a) mI/NAA measured in posterior cingulate area is the best marker to distinguish HC, MCI and mild AD
b) mI/NAA significantly differ from AD and HC and MCI
c) ROC curves: at 3 T showed that a value of 0.24 of mI/NAA had the best sensitivity and specificity to distinguish mild AD from HC and MCI. These aspects were not observed at 1.5 T. So, we can conclude that measurement of mI/NAA at 3T 1H MRS is a useful tool to evaluate mild AD.
References:
[1] K Kantarci, "1H Magnetic resonance spectroscopy in dementia"; The British Journal of Radiology, 80 (2007), S146-S152

755

Brain Temperature Changes with Abstinence from Alcohol – a Proton Magnetic Resonance Spectroscopy Study

S. Gazdzinski[1], A. Mon[2], T.C. Durazzo[2], D.J. Meyerhoff[2]
[1]Mri Core Facility, Nencki Institute for Experimental Biology, Warsaw/POLAND, [2]Radiology And Bioimaging, University of California San Francisco, San Francisco/CA/UNITED STATES OF AMERICA

Purpose/Introduction: Previous neuroimaging studies of abstinent and actively drinking alcohol-dependent individuals, including ours, have demonstrated widespread brain abnormalities, as well as lower brain perfusion and lower glucose metabolism that partially normalize with abstinence from alcohol.[1,2,3] Temperature changes can be probed from the difference in chemical shifts between water and N-acetyl-aspartate (**NAA**) peaks.[2] We hypothesize that increasing metabolic rates during early abstinence from alcohol increase brain temperature.
Subjects and Methods: Eight alcohol dependent individuals (ALC) were scanned at one week of abstinence (after acute withdrawal), at one month, and at six months of abstinence with STEAM (TE/TM/TR = 12/12/2000ms, 128 scans) on a Bruker/Siemens 4T. Spectra were obtained from 8 mL voxels in the anterior cingulate cortex (**ACC**) and the parieto-occipital cortex (**POC**). The water peaks were acquired immediately afterwards from identical voxels, with absence of movement between scans carefully evaluated on scout images. Brain temperature T and its changes were calculated with the formula by Corbett[4]: $T = -82.33(\delta_{water} - \delta_{NAA}) + 255.94$ [^{O}C], where δ_{water} and δ_{NAA} denote chemical shifts of water and NAA peaks, respectively.
Results: Between the first week and first month of abstinence from alcohol, measured brain temperature decreased by $(0.70\pm0.57)^{0}$C in ACC ($p=0.005$) and by $(0.38\pm0.38)^{0}$C in POC ($p=0.03$). No significant changes in brain temperature were observed between one month and six months of abstinence in this sample ($p>0.17$).
Discussion/Conclusion: These preliminary results do not support our hypothesis of increasing brain temperature with abstinence from alcohol. The observed temperature decreases could be accounted for by improving perfusion (i.e., more efficient heat dissipation) during early abstinence from alcohol.[3]
References:
1. Gazdzinski S. et al., 2006,ACER, p. 947-58. 2. Volkow, N., et al, 1994, Am J Psychiatry, p. 178-183. 3. Mon A., et al, 2009, ACER, p. 1314-21. 4. Corbett R. et al., 1999, Am J Neuroradiology, p. 1852-7.

756

Brain structure and neurochemistry in Autism Spectrum Disorders

A.C. Pereira[1], I.R. Violante[2], S. Mouga[1], G. Oliveira[3], M. Castelo-Branco[1]
[1]Ibili - Faculty Of Medicine, University of Coimbra, Coimbra/PORTUGAL, [2]Ibili, Faculty Of Medicine, University of Coimbra, Coimbra/PORTUGAL, [3]Neurodevelopment And Autism Unit From Child Center, Pediatric Hospital of Coimbra, Coimbra/PORTUGAL

Purpose/Introduction: MRI and H1-MRS allow the in vivo non-invasive study of brain morphology and neurochemistry.
Impairments observed in people diagnosed with Autism Spectrum Disorders (ASD) have been linked to brain regions such as the frontal lobe and the basal ganglia because of their role in executive functions and social cognition[1][2], which are known to be impaired in ASD[3][4].
Using MRI and H1-MRS we characterized brain morphometry and neurochemistry in males diagnosed with ASD. Our interest in the frontal lobe and basal ganglia is grounded on the aim to identify brain alterations in the ASD group that could be related to the spectrum symptomatology and direct future investigation on disease-related clinical clusters.
Subjects and Methods: We included twelve male participants with ASD (12-33 years., mean±SD 16.9±6.3), with no history of seizures or epilepsy and no intellectual disability.
The control group included twelve age-matched male participants (12-32 years, mean±SD 19.6±7.1), with no history of psychiatric or neurological conditions.
Participants were scanned on a 3T Siemens TimTrio scanner using a 12-channel birdcage head coil.
Two anatomical T1-weighted MPRAGE sequences were acquired for morphometric analysis. Freesurfer was used to obtain cortical thickness and subcortical volumes.
A 3cm3 single-voxel located in the bilateral anterior cingulate cortex was acquired using PRESS to obtain main brain metabolites concentrations: NAA, Cho, Ins, Cre+PCr (tCr) and Glx, quantified using LCModel.
Results: Subjects with ASD presented increased volumes of the left and right caudate nucleus ($p=0.03$ and $p=0.02$). Additionally, we observed increased cortical thickness in the ASD group in the medial orbitofrontal cortex ($p=0.02$) and left frontal pole ($p=0.05$).
Evidence of increased cortical thickness was observed in the ASD group being restricted to the left medial orbitofrontal cortex ($p=0.02$) and left frontal pole ($p=0.05$).
Spectroscopic analysis revealed decreased NAA+NAAG/tCr levels in subjects with ASD ($p=0.036$), (ASD group: n=7, 12-33 years; mean±SD = 19.5 ± 7.2; control group: n=8, 12-32 years; mean ± SD = 23.2 ± 6.0).
Discussion/Conclusion: Our approach enabled the detection of frontal and striatal differences in the brain morphometry and neurochemistry in the ASD group. These are present, as expected, in regions implicated in functions that are believed to be impaired in autism. Future studies combining anatomy, neurochemistry and behavior might help identify clinical subgroups with well defined biological and behavioral phenotypes.
References:
[1] Alvarez,J. A. & Emory,E., 2006, Neuropsychol. Rev,16-1:17-24
[2] Overwalle,F. V., 2009, Hum. Brain Mapp.,30:829–858
[3]-Hill,E. L., 2004, Trends Cogn. Sci.,8-1:26-32
[4] Sabbagh,M. A., 2004 Brain Cognition,55:209–219

757

Quantitative cerebral water mapping in chronic kidney disease during the haemodialysis cycle using 3T MRI

Z. Abbas[1], K. Reetz[2], A. Costa[2], V. Gras[1], T. Gross[3], S. Mirzazade[2], F. Eitner[3], J. Flöge[3], J.B. Schulz[2], N.J. Shah[1]
[1]Forschungszentrum Jülich, Institute of Neuroscience and Medicine - 4, Jülich/GERMANY, [2]Department Of Neurology, Faculty of Medicine, JARA, RWTH Aachen University, Aachen/GERMANY, [3]Division Of Nephrology, RWTH Aachen University, Aachen/GERMANY

Purpose/Introduction: Patients with chronic kidney disease (CKD) undergoing haemodialysis are at risk of cognitive impairment given the high prevalence of stroke, cardiovascular risk factors, uremia inflammation and multiple metabolic disturbances. Cerebral water shifts such as oedema may play an important role in CKD patients [1]. In this study, we aim to quantify brain water content in CKD patients before and after haemodialysis.
Subjects and Methods: Quantitative assessment of cerebral water content of five, CKD patients and age-gender matched healthy control group, was performed. Measurements were based on [2, 3] the estimation of the proton density (PD) using MRI at 3T. The MRI measurement in both groups was performed at two time points, i) before and ii) 12 hours after haemodialysis in CKD patients. The measured water content maps were calibrated to the CSF signal, which is assumed to have the same intensity as of pure water. Whole brain coverage was achieved with an in-plane resolution of 1 mm and a slice thickness of 2 mm within 15 minutes of acquisition.

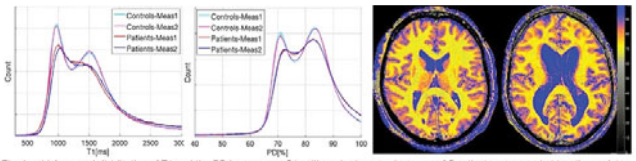

Fig. 1: a-b) Averaged distribution of T1 and the PD in a group a 5 healthy volunteers and a group of 5 patients, measured at two time points. c-d) Axial PD maps of the brain in an healthy volunteer and a patient.

Results: The water content measurements performed at 3T showed higher SNR and a good agreement with the results reported previously at 1.5T [2, 4]. Fig. 1: a-b, displays histograms of T1 (ms) and Proton density (PD) (%). The water content and longitudinal relaxation time (T1) measurements in the healthy group did not vary between two time points (separated by 24 hours). This demonstrates the stability of the MRI protocol and the possibility of testing the hypothesis of a normalisation of the water content immediately after dialysis.
Discussion/Conclusion: The water content distribution in the CKD brains showed global increase in the white matter (Fig. 1b, shift of the white-matter associated peak to the right of approximately 3%) whereas the grey matter seemed to be unaffected in CKD patients compared to controls. Comparing the water content distribution before and after haemodialysis in CKD patients, we were unable to demonstrate significant changes. However, this might be due to the small sample size. Although no focal abnormalities (e.g. stroke) in any subject were found, some patients demonstrated global atrophy compared to controls (Fig. 1d). These preliminary data are the first in CKD patients and are promising to enhance our understanding of cognitive impairment and haemodialysis in this disease.
References:
[1] Sarnak(2005). Cognitive Functions in Dialysis Patients.
[2] Shah (2008). *NeuroImage* 41, 706-717.
[3] Gras (ISMRM 2011). *Proc.Intl.Soc.Mag.Reson.Med.*19. p.4449.
[4] Abbas (ISMRM 2012). *Proc.Intl.Soc.Mag.Reson.Med.* p.1073.

758

Influence of Retinal Dystrophy on Brain Cortex Structure in Retinitis Pigmentosa

S. Ferreira[1], A.C. Pereira[1], C. Mateus[1], A. Reis[2], B. Quendera[1], M.D.R. Almeida[3], E. Silva[2], M. Castelo-Branco[1]
[1]Visual Neuroscience Laboratory, IBILI - Faculty of Medicine - University of Coimbra, Coimbra/PORTUGAL, [2]Centre For Hereditary Eye Diseases, Department Of Ophthalmology, University Hospital Coimbra, Coimbra/PORTUGAL, [3]Vision Genetics And Neurogenetics Laboratory, Center for Neuroscience and Cell Biology, Coimbra/PORTUGAL

Purpose/Introduction: To study the influence of rod-cone dystrophy on visual cortical organization, by characterizing retinal structure and function, and cortical structure of two subjects with Retinitis Pigmentosa due to rhodopsin gene mutations.
Subjects and Methods: Two male subjects (Subject I: 57y.o., mutation p.Tyr60His in exon1; Subject II: 60y.o., mutation p.Arg69Cys in exon1) were examined with: Color Fundus Photography; Cirrus Optical Coherence Tomography (OCT); Cambridge Colour Test; Static Perimetry (Humphrey 10-2); Microperimetry (MP1); Pattern (using checkerboards), Full Field (using flashes), and Multifocal Electroretinography (ISCEV standards, Espion2).
Brain structural images were obtained with a 3T Siemens TimTrio scanner (T1-weighted MPRAGE sequences; voxel size of 1x1x1mm^3). Cortical thickness and surface area of Brodmann Areas were obtained with FreeSurfer 5.0.0. The four subjects' hemispheres were compared with eight controls' hemispheres (age- and gender-matched): IBM SPSS Statistics 19, Mann-Whitney test at α=0.05, uncorrected and with Bonferroni correction for multiple comparisons.
Results: Subject I had profound visual impairment, as documented by low visual acuity, and inability to perform the psychophysical measurements. Subject II showed alterations in all cone pathways and a restricted visual field of 5º. Both subjects demonstrated: isoelectric Pattern and Full Field ERG responses; a significant decrease in P1-wave amplitude for all rings and a significant delay in implicit time, in multifocal ERG; a significant reduction in RNFL thickness (and in retinal thickness for subject I), in OCT.
Local thickness was preserved in subjects' visual cortex, but, interestingly, it was significantly increased in motor cortex regions: BA4a and BA6 (p=0.017 and p=0.042, uncorrected). V2 and MT surface areas were significantly reduced (p=0.011 and p=0.027, uncorrected). With Bonferroni correction, only V2 surface area was significantly reduced [1].
Discussion/Conclusion: Visual cortex thickness appears to be unchanged in Retinitis Pigmentosa, but the cortical surface area is reduced. Due to the early onset of this disease, neurodevelopmental changes occur in the visual cortex, that are in line with the idea of peripheral vision loss and consequent reduction of cortical substrates. Future studies should address the impact of peripheral visual loss on dorsal stream and motor cortex organization and function.
References:
[1] Van De Graaff, K. M., 2002, McGraw-Hill, Chapter 11, 363-367.

Paper Poster

Processing and quantification

759

Quantitative assessment of very low lipid concentrations in a calf-phantom and in human musculature by fat-selective imaging with spatial-spectral excitation

X. Mao, P. Martirosian, H. Graf, F. Schick
Sektion Für Experimentelle Radiologie, Abteilung Für Diagnostische Und Interventionelle Radiologie, Eberhard-Karls-Universität Tübingen, Tübingen/GERMANY

Purpose/Introduction: Assessment of low amounts of lipids in tissues as musculature and liver is crucial for metabolic research. For example insulin resistance is known to be correlated with a significantly increased concentration of intramyocellular lipids [1]. However, musculature stores lipids in adipocytes (EMCL) and as small droplets in myocytes (IMCL) [2]. MRS revealed the muscular lipids (IMCL + EMCL) of the human calf in a range of 0.5% (m. tibialis anterior) up to 10% (m. soleus) [2].
Goals of this work were to (1) optimize measurement parameters for quantification of fat fractions as low as 1‰ in a calf phantom and to (2) test the feasibility for in-vivo measurements using fat-selective spatial-spectral rf pulses in combination with spin-echo acquisition.
Subjects and Methods: All experiments were performed on 3 T MR-scanner with 8-channel-knee-coil using a sequence consisting of equidistant unipolar modified binomial sub-pulses [Fig.1] followed by spin-echo acquisition. A phantom [Fig.2a] was designed with a geometry similar to human calf [Fig.2b]. Thistle oil was chosen to simulate subcutaneous lipid and bone-marrow, 0.1–1.0% milk-fat fractions were applied to model muscular lipids in a calf-phantom.
Firstly, variations of significant sequence parameters (BW, TE, AV, TR and FFT) were implemented systematically pursuing the highest SNR_{fat} in calf-phantom and human-calf. Secondly, fat contents in both were measured with the optimized parameter-setting [Tab.1] and evaluated quantitatively. Milk- and muscular-fat contents were quantified using signal intensity of adjacent thistle-oil and bone-marrow respectively. Finally, results were compared to spectroscopic analysis using a STEAM sequence.

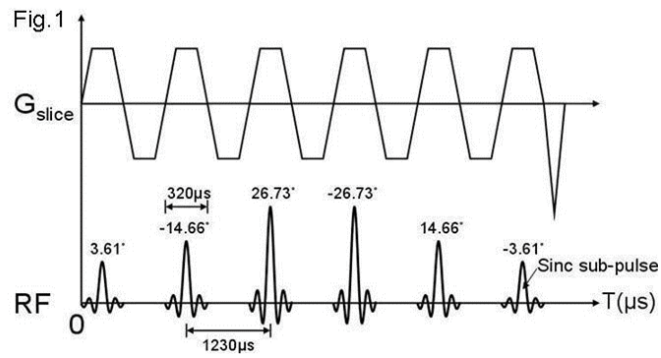

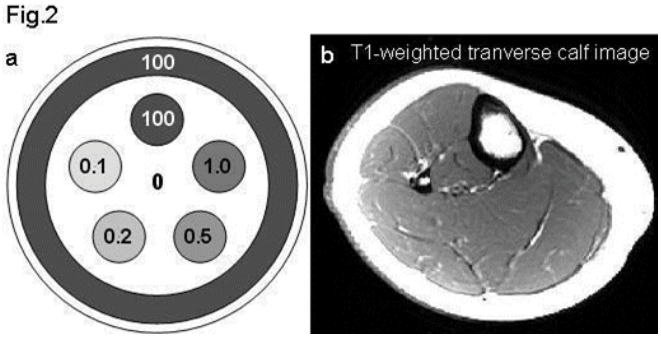

Tab.1:

Parameters	Phantom	Musculature
Pixel-size	1.0×1.0x10mm³	1.17×1.17x10mm³
Bandwidth	91Hz/pixel	40Hz/pixel
TE	14ms	28ms
TR	500ms	450ms
Measuring time	8:32min	9:36min

Results: Solution with 1‰ fat content could be clearly distinguished from pure water. An SNR of 4280 for pure fat was obtained in examinations with 8.5minutes of measuring time in phantom-studies, whereas water was suppressed down to the noise-level [Fig. 3a]. Fat signal intensity was linear increasing with fat content. Muscular fat was also well displayed in images of human lower leg (examination time 9.5 minutes) [Fig.3b]. Results from MRI and MRS correlated well [Tab.2].

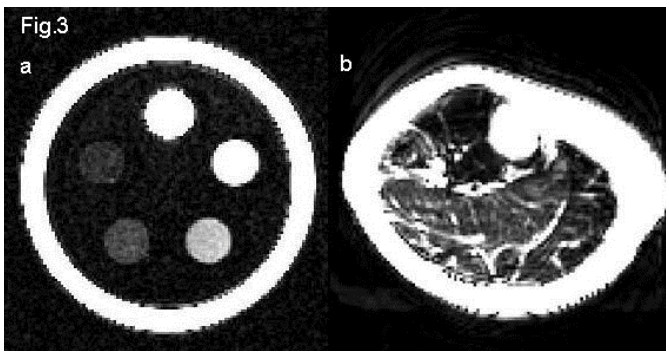

Table.2:

		MRI		^{1}H-MRS	
		mean SI±SD	Fat-content(%)	Integral	Fat-content(%)
calf-phantom	thistle-oil	2996.4 ± 26.7	----------	32440	----------
	1% milk-fat	31.3 ± 1.4	1.021	337.4	1.040
	0.5% milk-fat	15.7 ± 1.0	0.501	166.8	0.514
	0.2% milk-fat	6.7 ± 1.1	0.200	66.9	0.206
	0.1% milk-fat	3.8 ± 0.8	0.103	38.6	0.119
	noise	0.9 ± 0.7	----------	--------	----------
human-calf	bone-marrow	1851.9±144.9	----------	18590	
	m.-soleus	52.4 ± 15.7	2.839	538.1	2.895
	m.-tibialis	13.7 ± 5.1	0.739	129.2	0.695
	noise	0.8 ± 0.7	----------	--------	----------

Discussion/Conclusion: Optimized fat-selective MRI with spectral-spatial excitation provides a robust noninvasive tool for assessment of muscular fat at 3T.
References:
1. Schick F. MRI of muscular fat. (2002) Magn Reson Med. 47: 720–727
2. Schick F. Comparison of localized proton NMR signals of skeletal muscle and fat tissue in vivo: two lipid compartments in musle tissue. (1993) Magn Reson Med. 29: 158–167

760

VBM with viscous fluid registration of grey matter segments in SPM

J.M.S. Pereira[1], J. Acosta-Cabronero[2], G. Pengas[2], L. Xiong[3], P. Nestor[2], G. Williams[2]
[1]Ibili - Faculty Of Medicine, University of Coimbra, Coimbra/PORTUGAL, [2]Department Of Clinical Neurosciences, University of Cambridge, Cambridge/UNITED KINGDOM, [3]Neurology Department, Zhongnan Hospital of Wuhan University, Wuhan/CHINA

Purpose/Introduction: DARTEL (Diffeomorphic Anatomical Registration Through Exponentiated Lie Algebra) has been presented as an improvement for the registration of grey matter (GM) probability maps used in voxel based morphometry (VBM) (1). Results with this method, however, show little anatomical detail and the likely presence of false negatives (2). This work suggests

a viscous fluid registration method as an alternative to DARTEL to enhance the detail of VBM results.

Subjects and Methods: Controls (n=21), AD subjects (n=16), SD subjects (n=10), and n=17 patients with mild cognitive impairment (MCI) had volumetric T1-weighted MRI scans acquired on a Siemens Trio 3T system using a 3D-MPRAGE sequence with 1.25mm^3 voxel size. Scans were preprocessed (3), and were then registered, segmented and modulated using the unified segmentation in SPM8 (http://www.fil.ion.ucl.ac.uk/spm/software/spm8/) (4). The resulting modulated GM maps were then registered again to a randomly selected control subject GM segment. This second, higher degrees-of-freedom registration was performed using a published implementation of a viscous fluid algorithm (5). VBM analyses were performed with the basic SPM GM maps, with DARTEL, and using the viscous fluid registration (Fluid). The GM segments were smoothed with an 8mm Gaussian kernel and the total intracranial volume (TIV) was used as a nuisance covariate.

Results:

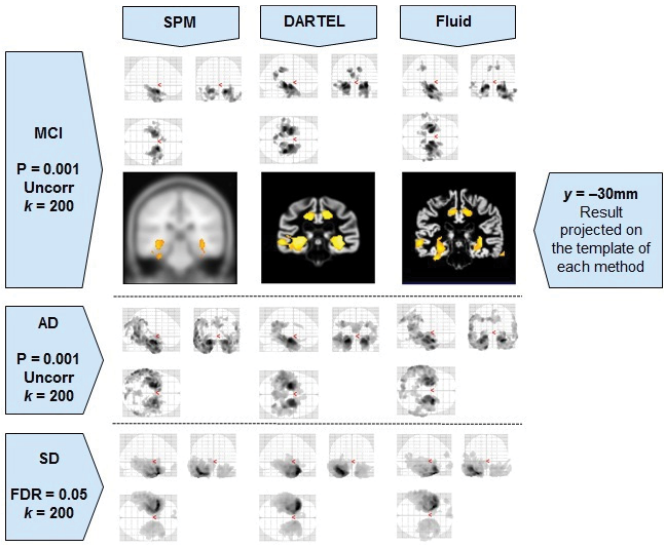

The Figure shows the VBM results with the statistical threshold and extent threshold (*k*) used. The Fluid registration algorithm enhanced the findings of both SPM and DARTEL, while removing some areas of significance that were, given what is known for these pathologies, most likely false positives, notably in the AD and MCI cohorts. Compared to DARTEL, the results obtained with the Fluid algorithm retained greater anatomical detail. DARTEL destroys the results' anatomical detail, especially in severely atrophic regions that appear as amorphous areas.

Discussion/Conclusion: Fluid registration enhanced the sensitivity of VBM while retaining anatomical detail, showing evidence for improvement over both SPM and DARTEL. The Fluid registration method was able to provide detailed results for both a very focal atrophy (SD) and in milder, more diffuse atrophy (AD, MCI). When compared to DARTEL and SPM, the VBM outputs with Fluid were more contiguous and anatomically localised. These results suggest that a high-degree of freedom registration algorithm, with very little regularisation, may be useful to re-register the probability maps in order to improve VBM results.

References:

(1) Ashburner,Neuroimage 2007;38:95-113;
(2) Pereira et al.,Neuroimage 2010;49:2205–2215;
(3) Acosta-Cabronero et al,Neuroimage 2008;39:1654-1665;
(4) Ashburner et al,Neuroimage 2005;15:839-851;
(5) Christensen et al,IEEE Transactions on Image Processing 1996;5:1435-1447.

761

Feasibility Study of an Automatic Planning Assist System for Cardiac Magnetic Resonance Examinations

S. Nitta[1], T. Takeguchi[1], S. Kuhara[2], R. Ishimura[3], K. Yokoyama[3], T. Nitatori[3]
[1]Corporate Research & Development Center, Toshiba Corporation, Kanagawa/JAPAN, [2]Mri Systems Division, Toshiba Medical Systems Corporation, Tochigi/JAPAN, [3]Department Of Radiology, Kyorin University Faculty of Medicine, Tokyo/JAPAN

Purpose/Introduction: Planning assist systems for cardiac MR examinations are important for realizing easier operation and shorter examination times. Previous studies have focused on slice alignment using 2 or 3 plane localizer images [1,2], a single volume [3], or axial multislice images [4,5]. However, more basic settings for patient positioning and local shimming were not automatic in previous studies. In this paper, we propose a new automatic planning assist system for such settings employing an atlas-based segmentation technique with a well-designed registration method.

Subjects and Methods: An ECG-non-gated 3D fast field echo (FFE) single volume covering the entire chest area was acquired using a 1.5-T MRI scanner (Excelart Vantage™ powered by Atlas, Toshiba Medical Systems) during a single breath-hold with TR/TE=3.7/1.3, FOV=500x350x350 mm^3 (coronal slab), readout encode steps=256, phase encode steps=64, and slice encode steps=35. The scanning time was around 9 seconds. Our proposed method is based on a registration technique of several steps to achieve good accuracy with acceptable processing cost. First, the input volume is normalized in contrast by a histogram expansion technique and in size based on patient body size before registration. Then, the input volume is transformed to match a prepared model volume in which the area of the heart has been annotated. Finally, the transformation is used to estimate the entire heart region of the input. To evaluate accuracy, the Euclidean distances of the six sides of a circumscribed cuboid of the cardiac area between the results and manual annotations were measured.

Results: The proposed method successfully segmented the entire heart region for 24 datasets from 13 healthy volunteers. Processing was completed in approximately 2 seconds (2.4-GHz CPU, single-thread processing). The average distance error values for the left, right, anterior, posterior, head, and foot sides were 5.50±4.00, 2.69±1.94, 3.52±2.47, 4.32±3.12, 9.95±14.11, and 7.10±11.43 mm, respectively.

Discussion/Conclusion: We propose a new automatic planning assist system employing atlas-based segmentation techniques for couch movement and local shimming settings. The experimental results showed that the proposed method can detect the entire heart region quickly and accurately. In addition, a fully automatic planning assist system can be achieved by combining the results of this study with our previous work on slice alignment methods [4,5].

References:

[1] BPF Lelieveldt et al. Radiology 2011, 221:p537-542
[2] RD Darrow et al. ISMRM 2009:p1800
[3] X Lu et al. MICCAI 2011, 6893:p479-486
[4] S Nitta et al. ESMRMB 2011, No. 726
[5] S Nitta et al. SCMR 2012, No. 269

762

3D Reconstruction and Quantitative Analysis of Carotid Artery Geometry using 2D-TOF, 3D-TOF MR Angiography and Multi-Detector CT Angiography

C. Zhu, A.J. Patterson, O.M. Thomas, U. Sadat, M.J. Graves, J.H. Gillard
University Department Of Radiology, University of Cambridge, Cambridge/ UNITED KINGDOM

Purpose/Introduction: Stroke is the leading cause of death and disability worldwide, representing 4.4 million deaths every year and causing 5,000 disabilities per million people [1]. Carotid geometry parameters have been shown to be closely related to adverse hemodynamic conditions and may contribute to plaque formation, progression, destabilization, and rupture [23]. This study aims to quantify geometric risk factors by applying 3D automatic segmenta-

tion methods to 2D-TOF, 3D-TOF MR angiography and multi-detector CT angiography (MDCTA).
Subjects and Methods: Subjects and Methods: 16 patients with >30% carotid stenosis identified by ultrasound underwent contrast enhanced MDCTA in a Siemens16- (n=7) or 64-section (n=9) multi-detector CT scanner. 2D-TOF and 3D-TOF MR angiography was performed in a GE 1.5 tesla MRI system with a 4 channel phased-array neck coil. Scan parameters are in Table.1. The 3D geometry was directly reconstructed from MDCTA and MRA datasets using an open-source segmentation toolkit (Vascular Modelling Toolkit, VMTK [4]) (Figure.1). Geometric factors as defined by Thomas et al [3], were automatically calculated and compared between methods.

Table.1

	In-Plane-Resolution	Trough-Plane-Resolution	TR/TE
MDCTA	0.3mm*0.3mm	0.6-0.8mm	N/A
2DTOF	0.43mm*0.43mm	2mm	16.6/4.1(ms)
3DTOF	0.63mm*0.63mm	1mm	23/4.5(ms)

Figure.1

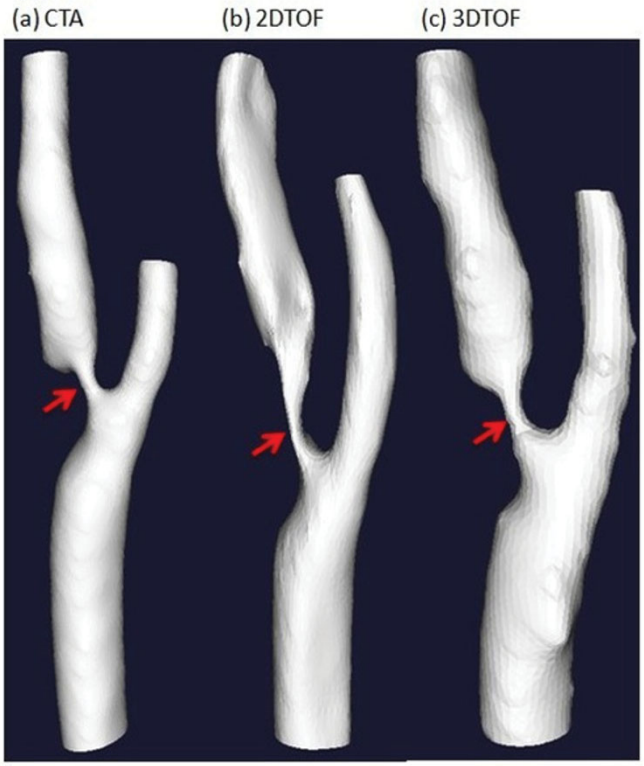

Results: Measurements of ICA inplanarity using 2DTOF and 3DTOF were in poor agreement with MDCTA with an inter-class correlation coefficient (ICC) = 0.19 (2DTOF) and 0.10 (3DTOF). Measurements of proximal/distal area ratios using 2DTOF and 3DTOF had satisfactory or good agreement with MDCTA (proximal area ratio: ICC = 0.52 for 2DTOF, ICC = 0.84 for 3DTOF; distal area ratio: ICC = 0.49 for 2DTOF, ICC = 0.69 for 3DTOF).
Discussion/Conclusion: Using high-resolution MDCTA as a gold standard, both 2D and 3D TOF MRA are not able to reliably measure ICA planarity but they can achieve satisfactory agreement in measuring proximal/distal area ratios. 3D TOF tends to have better agreement with MDCTA than 2D TOF in area ratios quantification. TOF MRA is still limited in quantitative measurement of geometric risk factors. This is mostly due to the signal void artifact around the bifurcation, where complex blood flow often occurs. 3D high-resolution MRI with motion-sensitive driven-equilibrium (MSDE) blood suppression [5] can suppress the signal from complex flow and therefore potentially delineate the lumen boundary better. We are currently investigating such techniques for geometrical analysis of the carotid bifurcation.
References:
[1] Hankey GJ. Arch Neurol 1999;56(6):748-54.
[2] Malek AM, Alper SL, JAMA 1999;282(21):2035-42.
[3] Lee SW, et al Stroke 2008;39(8):2341-7.
[4] www.vmtk.org.
[5] Balu N, et al Magn Reson Med 2011;65(3):627-37.

763

The effect of the kernel size in 3D-GRAPPA algorithms

J. Chung[1], D. Kim[2], D. Kang[2], Y. Kim[2], S. Ogawa[2], Z. Cho[2]
[1]Biomedical Engineering, Eulji University, Seongnam Gyeonggi-do/KOREA, [2]Neuroscience Research Institute, Gachon University, Incheon/KOREA

Purpose/Introduction: In volumetric parallel imaging (PI), a 3D k-space data is undersampled along the two phase encoding directions. The undersampled data can be reconstructed by a number of GRAPPA-based techniques [1-2]. The extended 3D-GRAPPA (EX-3D-GRAPPA), which is an extended version of the conventional GRAPPA, with cross shaped auto-calibration signal (cross-ACS) has shown good performance by reducing aliasing and noise artifacts [3]. However, this method requires a large amount of computation and memory capacity. In this study, we propose a single-kernel 3D-GRAPPA (SK-3D-GRAPPA) to reduce the computation time.
Subjects and Methods: EX-3D-GRAPPA method uses (R-1) weighting matrices and is carried out for (R-1) times in the matrix inversion because it uses (R-1) different kernels to estimate the weighting matrices. Fig. 1(a) represents the EX-3D-GRAPPA sampling scheme using three kernels for three weighting matrices in R = 4 (2x2). On the other hand, SK-3D-GRAPPA uses only one kernel to reconstruct the points differently located in a block (Fig. 1 (b)). Moreover, it provides a simplified process in which an operation of the matrix inversion is performed only once.

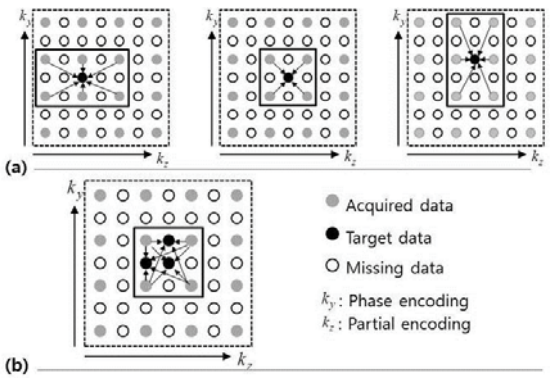

Figure 1. Reconstruction scheme (a) EX-3D-GRAPPA (b) SK-3D-GRAPPA

Brain phantom was acquired on a 3T scanner (Verio, Siemens) with a 12-channel head coil using 3D gradient-echo: TR = 20 ms, TE = 14 ms, flip angle = 25°, FOV = 210x210 mm², slice thickness = 0.8 mm, and matrix size = 256x256x208. The experiments were performed on ACS with the various readout lines (Fig. 2). The number of ACS lines for the two phase encodings was 48 lines each and reduction factor R = 4 (2x2) was used. The kernel size was determined: (a) EX-3D GRAPPA (3x4x3, 3x4x4, 3x3x4), (b) SK-3D-GRAPPA (3x4x4). To evaluate the algorithm itself, the reconstructed images did not contain ACS data.

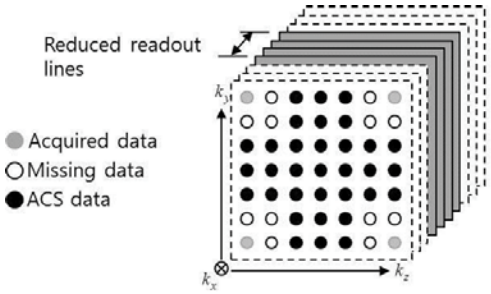

Figure 2. Reference scheme (Cross-ACS)

Results: Fig. 3 shows the result from: (a) Full-EX-3D-GRAPPA, (b) Full-SK-3D-GRAPPA, (c) 48-EX-3D-GRAPPA, and (d) 48-SK-3D-GRAPPA. The images using the SK-3D-GRAPPA are similar to those using the EX-3D-GRAPPA. The images using reduced-ACS are enhanced comparable to the images using full-ACS. The root-mean-square (RMS) error of the reconstructed image and computation time are presented in Table 1. The aliasing artifact is saturated at a certain number of readout lines [4].

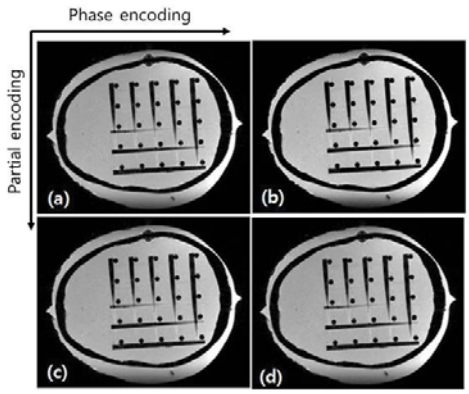

Figure 3. Results (slab = 139) from (a) EX-3D-GRAPPA, ACS with full readout lines (b) SK-3D-GRAPPA, ACS with full readout lines (c) EX-3D-GRAPPA, ACS with 48 readout lines (d) SK-3D-GRAPPA, ACS with 48 readout lines

Table 1. RMS error of the reconstructed images* (Total computation time**)

	256 lines	128 lines	88 lines	48 lines	28 lines
EX-3D-GRAPPA	0.0015 (5923.3 s)	0.0015 (842.0 s)	0.0015 (719.2 s)	0.0015 (624.9 s)	0.0016 (589.3 s)
SK-3D-GRAPPA	0.0015 (1182.2 s)	0.0015 (370.7 s)	0.0015 (322.5 s)	0.0015 (285.4 s)	0.0016 (268.6 s)

* Reference image fully sampled in k-space: mean = 0.9248, variance = 1.6448
** Computation environment: 3.3 GHz, 15.39GB of RAM, MATLAB programming

Discussion/Conclusion: This study demonstrates that the SK-3D-GRAPPA using ACS with reduced readout lines is efficient for simplifying the computing process and reducing time, while providing good quality images.

References:

[1] Griswold etal MRM 2002;47:1202-10
[2] Breuer etal MRM 2006;56:1359-64
[3] Chung etal ESMRMB 2012 submitted
[4] Wang etal MRM 2012;67:1042-53

764

Semi-automated renal segmentation in-vivo based on non contrast-enhanced T1 and T2 weighted images to separate renal cortex, medulla, and pelvis

S. Will, P. Martirosian, C. Würslin, F. Schick
Section On Experimental Radiology, University clinic Tuebingen, Tuebingen/ GERMANY

Purpose/Introduction: Volumetric analysis of the entire kidneys and their cortical and medullar components might lead to generation of biomarkers for identification and monitoring of pathologies. Former approaches to renal segmentation[1-3] have been based on MR-images recorded after administration of contrast agent.
The work presented in the following aims on segmentation of kidneys from the surrounding structures in a first step and on further differentiation of cortex, medulla, and pelvis in a second step from two set of T1- and T2-weighted MR-images without contrast media.
Subjects and Methods: For adaptation of sequence types and parameters five healthy volunteers were examined on a 1.5T MR-scanner (Magnetom Sonata, Siemens Healthcare, Germany). A clinical setting with an anterior and posterior array coil was applied for signal detection.
T2-weighted HASTE sequences with spectral fat suppression were applied aiming at high contrast between kidneys and surrounding tissues as liver, spleen, and perirenal fat. Coronal slice orientation was chosen for recording a set of images covering both kidneys completely within a breath-hold. Contrast behavior and quality of segmentation were tested for sequence parameter settings with variable TE (80-120ms).
T1-weighted images spoiled 2D GRE images were acquired with variable flip angles (30-90°; TR=132ms, TE=2.44ms) in order to maximize the contrast between renal cortex and medulla.
A reference mask of the entire kidneys was created on the basis of gray scale segmentation of T2-weighted images. Renal Cortex, medulla, and pelvis were subsequently separated by the contrast of T1 images.
Because of possible displacements of the kidneys, T1- and T2-weighted images were registered via SPM prior to further processing.
Results: Suitable imaging parameters for T2-weighted imaging were TE=95ms, FA=150, FoV=256×256mm², slice thickness(ST)=5mm, BW=781Hz/Px and for T1-weighted GRE imaging FA=70°, FoV=256×256mm², ST=5mm, BW=260Hz/Px.

Fig .1 shows the T1- and T2-weighted images obtained using above mentioned suitable sequence parameters as well as segmentation results. Good separation of both kidneys and successful segmentation of internal renal anatomical structures such as cortex, medulla and pelvis were possible using simple signal thresholds. Visual segmentation of T1-weighted images was found in good agreement with semi-automatic segmentation.

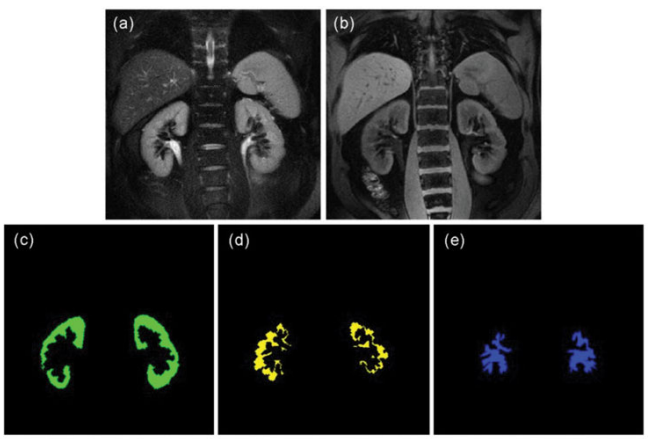

Fig. 1: T2-weighted image (a) to separate the entire kidneys from the surrounding tissues. T1-weighted image (b) with adapted sequence parameters for a good contrast between renal cortex (c), medulla (d) and pelvis (e).

Discussion/Conclusion: The presented technique provides reliable segmentation of renal cortex, medulla and pelvis using sets of (breath-hold) T1- and T2-weighted images without need of contrast media. Breathing related geometric differences of both data sets require a dependable registration.
The method will further be investigated regarding correctness and reproducibility in a current running study on 12 subjects.
References:
[1]A.Mikheev,ISMRM,2012.
[2] Y.Tang,IJIIP,2010
[3]B.Chevaillier,EUSIPCO,2008.

765

A comparison study of GRAPPA algorithms for volumetric parallel imaging

J. Chung[1], D. Kim[2], D. Kang[2], Y. Kim[2], S. Ogawa[2], Z. Cho[2]
[1]Biomedical Engineering, Eulji University, Seongnam Gyeonggi-do/KOREA, [2]Neuroscience Research Institute, Gachon University, Incheon/KOREA

Purpose/Introduction: In volumetric parallel imaging (PI) [1-3], a 3D dataset is undersampled along two phase encoding directions with a reduction factor of R (R = Ry x Rz, where Ry and Rz are reduction factors in y and z directions, respectively). To reconstruct the undersampled data, a 2D-GRAPPA-operator (2D-GRAPPA-OP) can be used [2]. Another way of reconstruction can be performed using the 3D-GRAPPA [2-3]. In this study, an optimal method for volumetric PI will be investigated by comparing these two methods, and the extension of the 3D GRAPPA (EX-3D-GRAPPA) will be explained in detail.
Subjects and Methods: Fig. 1 shows the schematic description of 2D-GRAPPA-OP, 3D-GRAPPA, and EX-3D-GRAPPA in R = 4 (2x2). In comparison to 2D-GRAPP-OP, which only uses a 2D kernel without extending the kernel in the other phase encoding direction (Fig. 1(a)), and 3D-GRAPPA, which uses both 2D and 3D kernels (Fig. 1(b)), EX-3D-GRAPPA uses 3D kernels, which are spread in all of directions (Fig. 1(c)).

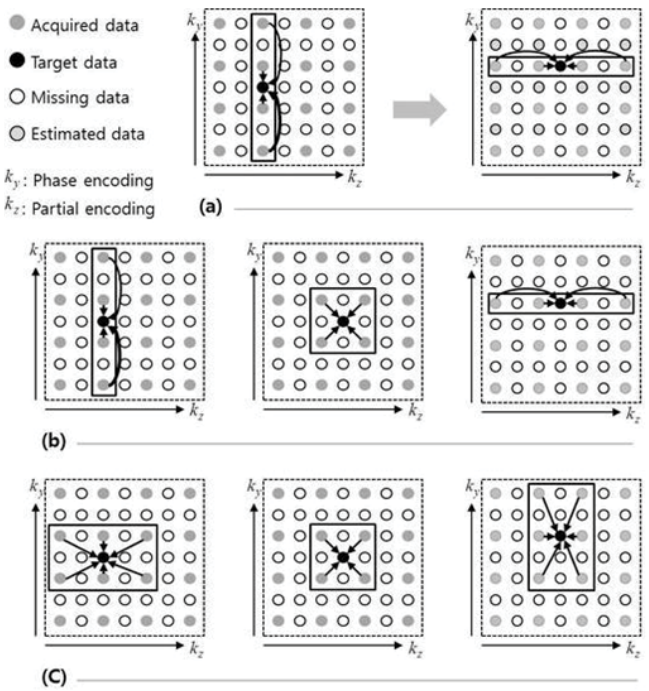

Figure 1. Reconstruction scheme (a) 2D-GRAPPA-OP (b) 3D-GRAPPA (c) EX-3D-GRAPPA

The experiments were carried out on a 3T scanner (Verio, Siemens) with a 12-channel head coil. Brain phantom data were acquired using 3D gradient-echo: TR = 20 ms, TE = 14 ms, flip angle = 25°, FOV = 210x210 mm², slice thickness = 0.8 mm and matrix size = 256x256x208. The data were undersampled and two types of auto-calibration signal (ACS) data, each consisting of 48 lines, were used to estimate weighting matrices because the performance is dependent on the ACS shapes (square-ACS, cross-ACS). Cross-ACS improves the image quality compared to square-ACS [4]. To evaluate the algorithm itself, the reconstructed images did not contain the ACS data. The kernel sizes were determined: (a) 2D-GRAPPA-OP (3x4x1, 3x1x4), (b) 3D GRAPPA (3x4x1, 3x4x4, 3x1x4), and (c) EX-3D-GRAPPA (3x4x3, 3x4x4, 3x3x4).

Results: Fig. 2 represents the images reconstructed with the cross-ACS: (a) 2D-GRAPPA-OP, (b) 3D-GRAPPA and (c) EX-3D-GRAPPA. As shown in Fig. 2, EX-3D-GRAPPA can reduce aliasing and noise artifacts (Fig. 2(c)).

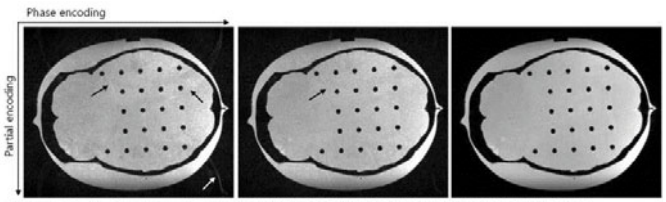

Figure 2. Results from Cross-ACS (a) 2D-GRAPPA-OP (b) 3D-GRAPPA (c) EX-3D-GRAPPA (slab=103)

Discussion/Conclusion: 2D-GRAPPA-OP may possibly propagate an estimation error occurring in the phase encoding direction. On the contrary, 3D-GRAPPA can reduce the aliasing artifact because it performs the reconstruction of two phase encoding directions at once. However, for noise reduction, 2D-GRAPPA-OP is better than 3D-GRAPPA [2]. Due to the 3D kernel spreading in all directions, the EX-3D-GRAPPA is robust to both noise and aliasing artifacts.
References:
[1] Wang etal MRM 2005;54:738-42
[2] Breuer etal MRM 2006;56:1359-64
[3] Lustig etal MRM 2010;64:457-71
[4] Wang etal MRM 2012;67:1042-53

766

Application of Anisotropic Diffusion Phantom for DTI experiments

A. Krzyżak
Department Of Magnetic Resonance Tomography, Institute of Nuclear Physics PAN, Kraków/POLAND

Purpose/Introduction: In order to accurately determine the diffusion tensor, we must precisely calculate the b-matrix, which depends on the parameters characterizing the imaging sequence [1].
In this study we propose a novel method for which we adopted the name of **BSD-DTI** (B-matrix Spatial Distribution in DTI) [2].The method calculates the spatial distribution of the b-matrix components using a set of **ADPs** -Anisotropic Diffusion Phantoms [2] that are characterized by the known spatial distribution of the diffusion tensor. The BSD-DTI technique demonstrates the accuracy improvement of water diffusion tensor determination in comparison to the standard methods used in commercial MRI systems.
Subjects and Methods: MRI measurements of the phantoms carried out on 9.4T Bruker BioSpin scanner using volumetric RF coil (ID 72 mm) and DTI standard Spin-Echo sequence.
Investigations were performed at temperature 22 °C using a homogenous water phantom F1 (a bottle with a diameter of 5 cm filled with distilled water) and anisotropic diffusion phantom F2. F2 was built in the form of a brick (with side length 5cm) composed of an array of thin glass plates (100 um) separated by H^2O layers (20 um).
The main DTI experiment consisted of calculating the diffusion tensors for F1, in five slices and 16 ROIs (2x2mm) for each slice. Then, for the same source data and ROIs, the diffusion tensors were calculated using the BSD-DTI method. The remaining DTI parameters are shown in Table 1.

Tab 1. DTI parameters for investigation of phantom F1.

Parameter	Value
TE - Echo Time	40 ms
RT- Repetition Time	2.5 s
NA - Number of Averages	4
Slice thickness	2 mm
Separation time between slices	5 mm
Slice orientation	coronal
Number of diffusion gradients directions	6
Number of b_0 scans	1
δ, Δ – Diffusion and separation time	2 ms, 20 ms
b effective	650 s/mm^2

The spatial distribution of diffusion tensors for F2 was determined with the same MR parameters except for the number of diffusion gradients directions, which were 32.
The mean eigenvalues for the Water Diffusion Tensors for each slice were obtained by averaging data from16 ROIs.

Results: The comparison of water diffusion tensor of F1 phantom achieved by standard Bruker DTI procedures and with correction performed by BSD-DTI technique is shown in the Table 2.

Tab. 2 The comparison of eigenvalues of water diffusion tensor calculated using standard procedures for Bruker BioSpin System and BSD-DTI method. The data are presented as Mean value averaging from 16 ROIs and SD.

slice	D [mm2/s]	SD1	SD1 %	D [mm2/s]	SD2	SD2 %	IMP %
	Bruker			BSD-DTI			
1	0,002262135	0,000134	5,94	0,002258168	0,0001	4,45	25,06
2	0,002244421	0,000133	5,91	0,00224135	7,43E-05	3,32	43,95
3	0,002244703	0,000134	5,96	0,002246216	7,05E-05	3,14	47,33
4	0,002247061	0,00014	6,22	0,002253005	7,36E-05	3,27	47,46
5	0,002259484	0,000145	6,41	0,002264983	5,91E-05	2,61	59,27

The relative improvement indicator IMP calculated as (SD1-SD2)/SD1 shows the increase in accuracy for determining the diffusion tensor eigenvalues.

Discussion/Conclusion: The presented results confirm the usefulness of our method for accuracy improvement of diffusion tensor calculation and possible reduction of the DTI measurement time. It also seems to be valuable for the verification of calculated b-matrix.

References:

1. Basser PJ et al JMR(1994)103:247-254
2. Krzyzak AT EP09755104.8

Acknowledgments

Ministry of Science and Higher Education of Poland for grant N518413238
Prof. L.R. Jaroszewicz from Military University of Technology, Warsaw, for constructing the set of anisotropic diffusion phantoms-ADP.

767

Quantification of Tumor Responses to Radiosurgery Using Tensor Invariants

A. Hamamci[1], N. Kucuk[2], K. Karaman[3], K. Engin[2], G. Unal[1]
[1]Electronics Engineering, Sabancı University, Istanbul/TURKEY, [2]Radiation Oncology, Anadolu Medical Center, Kocaeli/TURKEY, [3]Radiology, Anadolu Medical Center, Kocaeli/TURKEY

Purpose/Introduction: The response of the brain tumors to the radiosurgery is quantified by using measures derived from the invariants of the Lagrange strain tensor.

Subjects and Methods: CE-T1-spgr volumes of 4 Glioblastoma-Multiforme and 12 Acoustic-Neuroma patients, acquired before and after radiosurgery,were included.

In the pre-processing stage,MRI volume acquired after the radiosurgery therapy is aligned to the one obtained before therapy,rigidly using the "Block Matching" method[1].In both volumes,brain tumors are segmented using the "Tumor-cut" method[2].Deformation field from the former to the latter binary tumor volumes is calculated using the "Diffeomorphic Deamons" method[3]. In continuum mechanics,Lagrange strain tensor is used to represent finite deformations of the body.Let u(x) be the displacement field from the former binary tumor volume to the latter one.The invariants I_1,I_2,I_3 of the Lagrange strain tensor associated with this deformation is calculated for each voxel as shown in Figure 1.

$$I_1(\boldsymbol{T}) = \boldsymbol{T}\cdot\boldsymbol{I} = tr(\boldsymbol{T}) = \boldsymbol{T}_{mm}$$
$$I_2(\boldsymbol{T}) = \frac{1}{2}[(\boldsymbol{T}\cdot\boldsymbol{I})^2 - (\boldsymbol{T}\cdot\boldsymbol{T}^T)] = \frac{1}{2}[(\boldsymbol{T}_{mm})^2 - \boldsymbol{T}_{mn}\boldsymbol{T}_{nm}]$$
$$I_3(\boldsymbol{T}) = det(\boldsymbol{T})$$

where T is the Lagrange Strain Tensor: $\boldsymbol{T} = \frac{1}{2}[\boldsymbol{C} - \boldsymbol{I}]$

C is the Right Green Deformation Tensor: $\boldsymbol{C} = \boldsymbol{F}^T\boldsymbol{F}$

and F is the Deformation Gradient Tensor: $\boldsymbol{F} = \boldsymbol{I} + \nabla_x \boldsymbol{u}$

Figure 1:Calculation of the tensor invariants.

To derive global measures of the total change,we calculated integral and co-efficient of variation (CV=Std.Dev./Mean) of each scalar invariant maps in Figure 2.

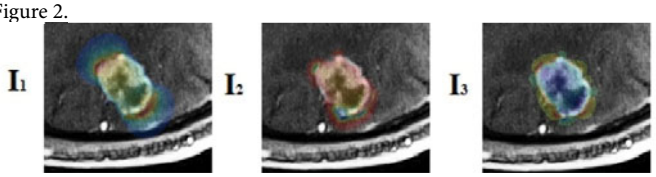

Figure 2:Tensor invariants overlayed on a sample slice.
We scored each case as in Table 1.

Table 1:Scoring Convention

CLINICAL OUTCOME	RADIOLOGICAL ASSESSMENT
-1:Reduced Symptoms	-1:Reduced Size
0:Stability	0:Unchanged
+1:Increased Symptoms	+1:Increased Size

Results:

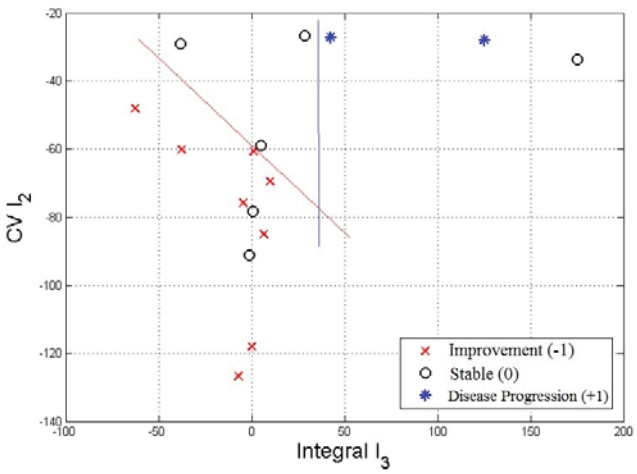

Figure 3:Coef.of Variation-I2 v.s.Integral-I3 plot of the cases with different clinical outcomes.
Kruskal-Wallis test indicates; the volume change (p=0.33) and the first invariant (p=0.44),which corresponds to dilation,show less importance in explaining the clinical outcome,whereas the variation of the second invariant (p=0.05) which is a measure of the strain magnitude and the integral of the third invariant (p=0.10) which doesn't have a clear physical interpretation plays a more important role(see Figure 3).

RADIOLOGY ASSESSMENT / PROPOSED METHOD

CLINICAL OUTCOME	+1	0	-1
+1	2 / 2	0 / 0	0 / 0
0	1 / 1	3 / 3	2 / 2
-1	1 / 0	5 / 0	2 / 8

Figure 4:Comparison of the radiology assessment with the proposed method For clinically unchanged and worsened cases,both radiological assesment and the proposed method resulted in the same prediction performance,whereas considering the best linear classifier applicable,the method outperformed the basic global measurements used in the radiological assessment for those cases with clinical improvement,as in Figure 4.

Discussion/Conclusion: The results presented show that the analysis of the deformation fields of tumor changes using methods of solid mechanics might provide results that are more correlated to the clinical outcomes of the therapy than considering only the volume or largest diameter measurements.
The results need further validation on larger datasets and the effect of the regularization while obtaining the deformation field should be considered.
References:
[1]S.Ourselin,et.al.,*MICCAI2000,LNCS V1935,(2000).*
[2]A.Hamamci,et.al.,*IEEE-Trans.Med.Imaging,31(3),(2012).*
[3]T.Vercauteren,et.al.,*Neuroimage,45(1Suppl),(2009).*

768

An application of texture analysis for the evaluation of the long-axis myocardial motion velocity maps derived from MR Tagged mouse heart images

A. Osiak[1], M. Suchanek[1], B. Tomanek[2], T. Skorka[1]
[1]*Department Of Magnetic Resonance Imaging, The H. Niewodniczański Institute of Nuclear Physics Polish Academy of Sciences, Kraków/POLAND,*
[2]*Institute For Biodiagnostics, National Research Council, Calgary/CANADA*

Purpose/Introduction: One of major applications of tagged cardiac images analysis is visualization of the motion grids, muscle strain maps or velocity vector fields of a moving organ. However that representation does not reveal more detailed information about the displayed quantity characteristics within myocardial segments. Our goal was to find an optimal method of longitudinal left ventricle (LV) motion quantification considering the velocities map as the starting-point. We based the segmental kinetics parameterization on the texture analysis concepts.
Subjects and Methods: Two FVB mice and two TgGαq*44 with different stage of cardiomyopathy were examined (9.4T Bruker BioSpec, GEFC sequence, SPAMM tagging module). The four-chamber imaging projection was chosen with tag stripes orientated perpendicularly to the long axis of LV. 10 phases/cardiac cycle were acquired.
The HARP-based Optical Flow image analysis [1] was performed for direct computation of the longitudinal velocity fields within myocardium. The local distribution of the velocities projection on LV long axis was assessed within seven segments (17-Segment Model) using histogram parameters (moments and quantiles). The Principal Component Analysis (PCA) was employed for finding groups of the parameters differentiating myocardial segments against each other and their changes over cardiac cycle. All image processing algorithms were written in MATLAB (MathWorks, USA), for the PCA Origin (OriginLab, USA) was used.
Results: The computed velocity vector fields and its long-axis projection maps in different cardiac cycle phases for mouse heart at the early stage of cardiomyopathy and the control mouse are presented in Fig.1.

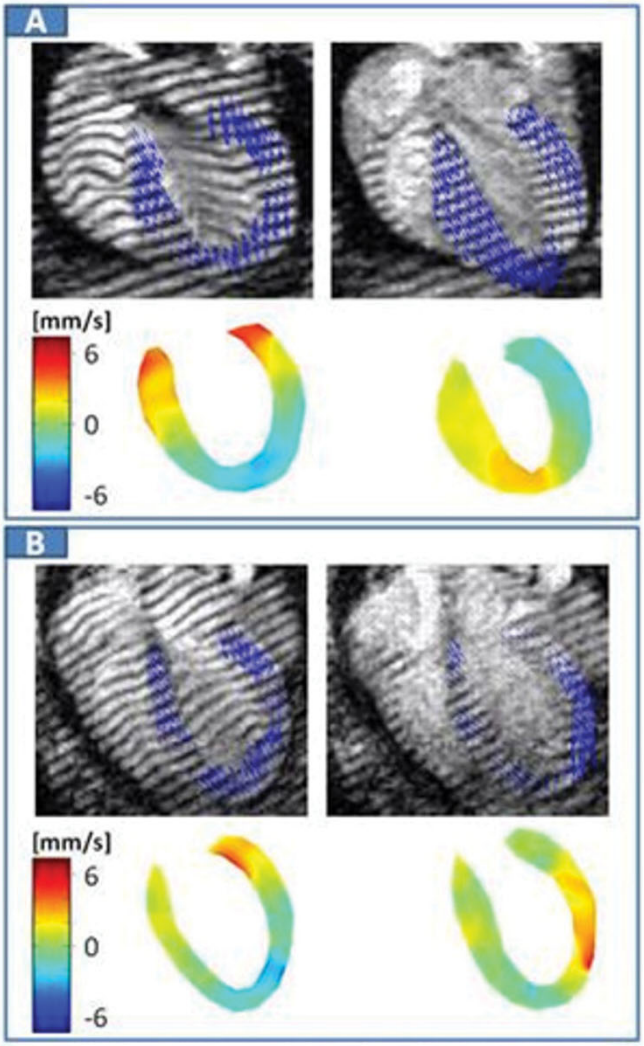

Fig. 1. A) The velocity vector field (top) and the color map of its long-axis projection (bottom) in different cycle phases of healthy heart (left: isovolumetric contraction, right: isovolumetric relaxation). **B)** The respective images for heart disease. The red color (positive values) indicates velocities at long-axis direction while the blue color (negative values) represents the opposite direction.

The PCA pointed four parameters grouped in three factors differentiating LV segments and enclosing major information about time-dependent local velocity changes: skewness, kurtosis, interquartile range and mean. The analysis identified combination of kurtosis and skewness as the main component reflecting variability. These factors also reveal differences between healthy and malfunctioning myocardium (Fig. 2).

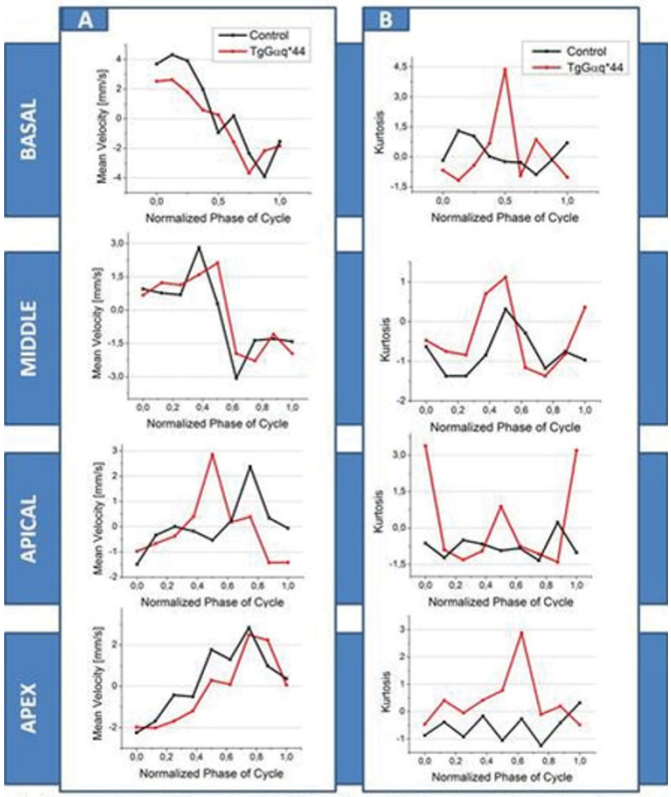

Fig. 2. Comparison of Mean Velocity **(A)** and Kurtosis **(B)** evolution through cardiac cycle for selected Control and TgGαq*44 subjects (the same as in **Fig.1**) at the free-wall side. From top to bottom segments: basal, middle, apical and apex. The kurtosis for each segment differentiates control and heart disease better than the mean value does.

Discussion/Conclusion: The proposed analysis showed the feasibility of the alternative representation of the velocity maps with the use of simplified texture analysis (limited to the histogram parameters). Each LV segment could be described by set of quantities giving more information about myocardial contractility. Time-dependent characteristics of these parameters seem to be compliant for the same segments within the same group and differ between subjects. Thus the method could be good extension of the typically used MR tagging-based functional visualization.

Work supported by European Union (grant coordinated by JCET-UJ, No WND-POIG.01.01.02-00-069/09-00).

References:

[1] Osman NF, Prince JL. Phys Med Biol 2000;45:1665–1682

769

Quantification of Perfusion in Murine Myocardium: A Retrospectively Triggered Arterial Spin Labeling Sequence using Parallel Imaging

F.T. Gutjahr[1], T. Kampf[1], X. Helluy[2], P. Winter[1], C. Ziener[3], P. Jakob[2], W. Bauer[4]

[1]*Experimentelle Physik 5, Universität Würzburg, Würzburg/GERMANY,*
[2]*Experimentelle Physik 5, Lehrstuhl für Physik, Würzburg/GERMANY,*
[3]*Radiology, German Cancer Research Center, Heidelberg/GERMANY,*
[4]*Medizinische Klinik Und Poliklinik I, Universitätsklinikum Würzburg, Würzburg/GERMANY*

Purpose/Introduction: In this work a method for quantification of perfusion in murine myocardium is proposed. The method is based on T_1 mapping after slice selective and global inversion using an Inversion Recovery Snapshot FLASH (IRSF)[1]. Retrospective triggering enables continuous acquisition of data. The Look-Locker condition is strictly maintained without the need for dummy pulses greatly reducing the hardware's realtime capacity limit.

Random sampling in phase direction is used to deal with the irregular heart and respiratory rate of the animals. This leads to undersampling in k-t-space. The undersampled data is reconstructed using parallel imaging techniques[2].

Subjects and Methods: Experimental work was performed on a 7T BioSpec using a 72mm transmit coil and a 29mm 4-channel receive array. The animals (NMRI mice, Charles River Laboratories) were anesthetized by isoflourane.

An IRSF sequence using Cartesian random phase encoding was implemented. The sequence parameters were: Matrix size: 68x58, Field of View: 30x20mm², imaging slice thickness: 2mm, selective inversion slice thickness: 6mm, TR: 3.3ms, readouts: 3000, waiting period: 15s, 25% echo position.

The study protocol consists of 32 global and 32 slice selective inversions. Cardiac and respiratory information and a TTL signal from the MRI system for each readout pulse is recorded, which allows for retrospective triggering. Each readout is assigned a relative position in the heart period. Data sampled during the end diastole is selected for reconstruction. For every accepted k-space center a frame is reconstructed by collapsing the data within a time window around the k-space center. Remaining missing lines are reconstructed using GRAPPA[2] with a 2x5 kernel.

Results:

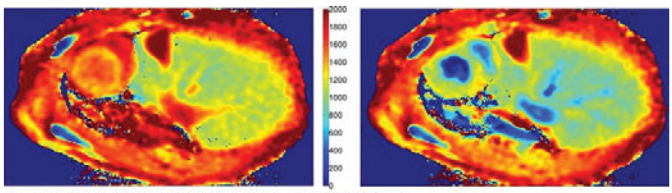

Fig 1: Global (left) and slice selective T_1 map (right) [ms]

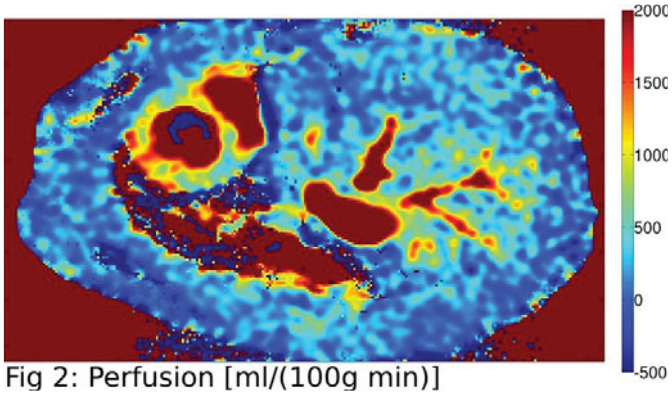

Fig 2: Perfusion [ml/(100g min)]

Exemplary T_1 and perfusion maps are shown in figure 1 and 2. K-space lines were selected from an enddiastolic window covering 20% of the heart period and collapsed over a 32TR time window.

Quantitative T_1 and perfusion maps of murine myocardium were acquired. The perfusion values were in good agreement with literature values [1]. Using parallel reconstruction the window size of accepted data can be reduced leading to a more accurate reconstruction.

Discussion/Conclusion: Retrospective IRSF is a robust alternative to its prospectively triggered counterpart for quantification of myocardial perfusion. Its reduced real-time capacity limit should allow it to be implemented on a broad range of scanners. The application of parallel imaging with GRAPPA reconstruction improves the reconstructed image quality and therefore allows for more accurate reconstruction of quantitative perfusion values.

References:

1 Streif JUG, Magn Reson Med (2005);53:584-592;
2 Grisworld MA, Magn Reson Med(2002);6:1202-1210

770

Assessment of Self-Gated Cardiac Reconstruction Quality in Mouse at 9.4T using Piecewise Linear Regression Method

M. Jablonska[1], U. Tyrankiewicz[1], A. Osiak[1], H. Figiel[2], T. Skorka[1]
[1]Department Of Magnetic Resonance Imaging, H. Niewodniczanski Institute of Nuclear Physics - PAN, Krakow/POLAND, [2]Department Of Medical Physics And Biophysics, AGH University of Science and Technology, Krakow/POLAND

Purpose/Introduction: Self-gated cardiac MR imaging technique allows for retrospective reconstruction considering cardiac and respiratory movements [1, 2]. Increasing the number of images reconstructed from the collected data results in more accurate Time-Area Curves (TAC). However such images are reconstructed from lower amount of the data what results with decreased SNR and may decrease endocardium segmentation accuracy. The aim of this work was to assess piecewise linear regression (PLR) as the method for the TAC modeling depending on temporal resolution and acquisition speed.
Subjects and Methods: Six data sets of the mouse short-axis midventricular slice were collected (3 at rest and 3 after low β-adrenergic stimulation with dobutamine) using self-gated FLASH sequence at 9.4 T (IntraGate Angio, BioSpec 94/20 USR, Bruker, Germany). Data sets differed with the number of repetitions per phase line (30, 60 and 120). Images were reconstructed using IntraGate software (Bruker BioSpin) for 15, 30 and 60 time-frames (Figure 1). TACs were generated using LV segmentation (Segment, Medviso AB, Sweden). PLR was used for the TACs modeling giving number of TAC segments according to Akaike Information Criterion used for optimal model selection [4]. Both methods were implemented in Matlab (MathWorks, USA).

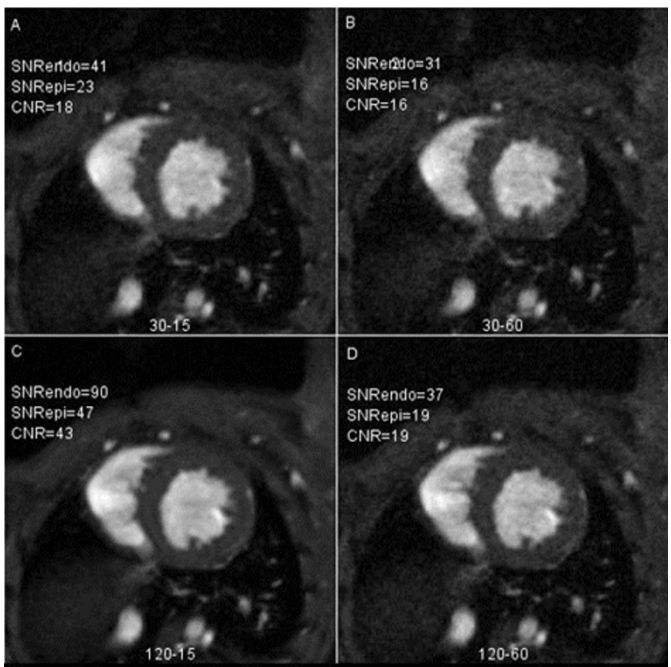

Figure 1. An example of midventricular cross-section of murine heart taken in end-diastole from cine series (IntraGate FLASH with FA = 19, TE/TR = 1.32/8.0ms, FOV = 3x3cm, matrix = 192x192, slice = 0.8mm). A) 15 frames reconstructed with 30 repetitions; B) 60 frames with 30 repetitions; C) 15 frames with 120 repetitions; D) 60 frames with 120 repetitions.

Results: Curves reconstructed at 15 frames were not influenced by number of acquisitions and were mostly composed of 4 segments similar in shapes. Increase in the number of reconstructed frames shortened duration of the systole and distinguished several diastolic segments corresponding to the cardiac physiological phases (Figure 2). Irrespective of the reconstruction scheme, obtained global cardiac parameter values as calculated at rest and during stress were similar. TACs from high time resolving series of reconstructed images were fitted with more cardiac phases than those reconstructed with fewer time-frames (measured with the same acquisition time) (Table 1).

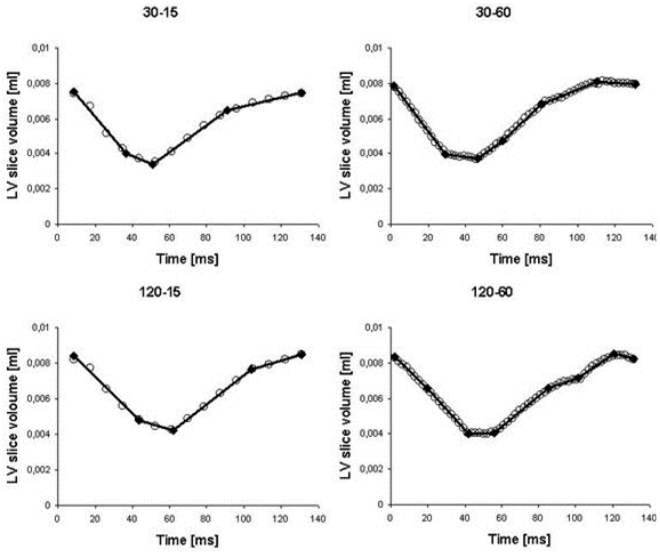

Figure 2. An example of TACs modeled with the use of piecewise linear regression. A) 15 points fitted with 4 segments; B) 60 points fitted with 6 segments; C) 15 points fitted with 4 segments; D) 60 points fitted with 7 segments.

Table 1. Cardiac parameters values at rest (B) and after dobutamine (D) in different reconstruction schemes.

Reconstruction scheme	No of Segm.	FAC [%]	ESA [ul]	EDA [ul]	ER [ul/ms]	FR [ul/ms]	ERt [ms]	IVRT [ms]	DT [ms]
B30-15	4	52%	3.5	7.4	0.12	0.08	51	—	—
B30-30	5	53%	3.8	8.0	0.10	0.08	42	9.0	—
B30-60	6	55%	3.7	8.1	0.13	0.09	33	13.8	—
B120-15	4	50%	4.3	8.5	0.10	0.08	62	—	—
B120-30	6	58%	3.6	8.6	0.13	0.12	46	15.7	—
B120-60	7	54%	3.7	8.1	0.12	0.07	36	8.2	—
D30-15	4	49%	3.9	7.7	0.09	0.06	44	19.7	—
D30-30	7	63%	2.5	6.7	0.14	0.10	33	9.4	—
D30-60	8	56%	2.9	6.6	0.09	0.07	43	—	32.0
D120-15	3	48%	4.1	7.9	0.08	0.05	54	23.0	—
D120-30	5	53%	3.6	7.7	0.08	0.08	55	5.1	17.3
D120-60	8	58%	3.3	7.8	0.09	0.08	34	11.8	9.4

FAC, Fractional Area Change; ESA, End-Systolic Area; EDA, End-Diastolic Area; ER, Ejection Ratio; FR, Filling Ratio; ERt, ER time; IVRT, Isovolumic Relaxation Time; DT, Decelaration Time.

Discussion/Conclusion: The PLR as the fast and objective method gives an opportunity for the more profound TAC analysis. It allowed for the such transient phenomena as the IVRT and DT detection and quantification as well as the other time segments. The application of the PLR extends the analysis protocol and allows for semi-automatic assessment of the TAC individual systolic and diastolic cardiac phases and also for the LV global function giving a complete set of parameters.
Grant coordinated by JCET-UJ, NoWND-POIG.01.01.02-00-069/09-00.
References:
[1] Bovens S.M., 2011, NMR Biomed 24:307-315
[2] Heijman E., 2007, NMR Biomed 20:438-447
[3] Krishnamurthy R., 2010, JMRI 31:872-880
[4] Jablonska M., 2011, Advanced Bioimaging Technologies Conference.

771

How different MR protocol parameters affect the estimation of a simplified CHARMED model: a study on simulated data

J. Andreotti[1], C. Kiefer[2], T. Dierks[1], A. Federspiel[1]
[1]Department Of Psychiatric Neurophysiology, University Hospital of Psychiatry, Bern/SWITZERLAND, [2]Institute Of Diagnostic And Interventional Neuroradiology, University Hospital of Bern, Bern/SWITZERLAND

Purpose/Introduction: The aim of the project is to analyze the effect of varying the MR protocol parameters on the estimation of a simplified CHARMED model. Simulated data for ten sequences with 90-144 measurements are compared.
Subjects and Methods: The white matter model assume two separate compartments providing distinguished signals as in [1,2,3]. The first compartment represent the intra-axonal population of water molecules and axons are modeled as cylinders of radius R. The signal for the extra-axonal compartment is modeled by a DT model.
First estimates for the direction of maximal diffusion, the diffusion coefficients and the proportion of the compartments are given by fitting an exponential model with baseline [4]. Then, a MCMC algorithm assuming a Rician noise is used to estimate the whole model [1,2].
Simulated data are generated for 200 random combinations of radii, compartments' proportions, diffusion coefficients and fiber orientation. In addition 200 combinations with 2 or 3 radii are generated. Ten sequences with different combinations of gradient strength, number of gradients' directions and gradient and diffusion times are tested with different SNR levels.
Results: The estimates of the first step of the estimation correlate well with the simulated parameters. However, except for the fiber's orientation estimation, the absolute error is reduced up to 10 times with the MCMC algorithm (depending on sequence and SNR level).
In general, sequences with 8-10 points estimated in every direction are more efficient. The estimation is improved when sequences with different gradients' strengths and diffusion times are used.

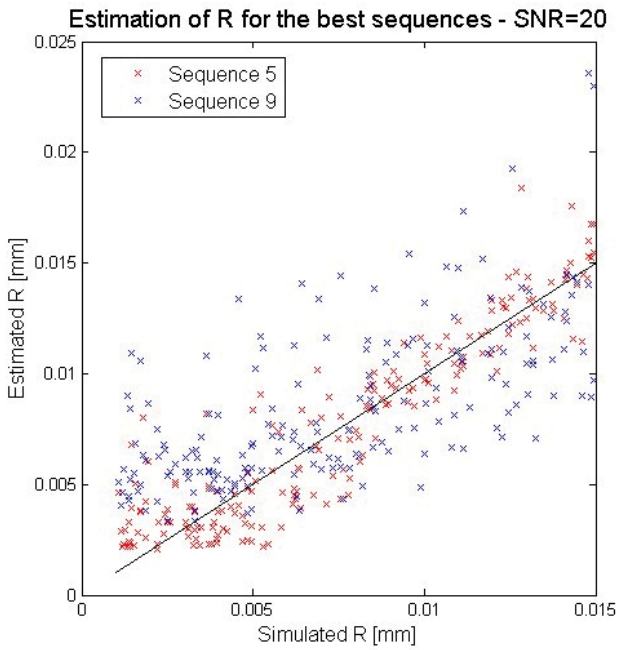

Fig.1: Simulated vs estimated R for the best sequences with 12 and 30 gradients directions.
When the signal is simulated with more than one radius, the sequences with 8-10 q-values in every direction seem more stable and the parameter R correlate well with the mean of the radii.

Discussion/Conclusion: This work allows to evaluate the possibility of assessing properties of the fiber structure using a combination of the methods of [2] and [4] on simulated data.
Results give information on the correlations between parameters, the quality of the estimation with different sequences and the possibility of using the simpler model in a complex situation with more axons' radii.
References:
[1] Alexander D.. et al., 2008, Magn Reson Med, 60:439-448
[2] Alexander D.. et al., 2010, NeuroImage., 52: 1374–1389
[3] Assaf Y., et al., 2004, Magn Reson Med, 52:965-978
[4] Peled S. et al., 2007, IEEE Trans Med Imaging, 26: 1448-1455
[5] van Gelderen et al., 1994, J. Magn Reson, 103:255–260

772

Reduction of fat signal contamination in kooshball uTE lung imaging using retrospective self navigation

K.M. Lagerstrand[1], L.E. Olsson[2]
[1]Diagnostic Radiation Physics, Sahlgrenska University Hospital, Goeteborg/SWEDEN, [2]Department Of Radiation Physics, Lund University, Malmö/SWEDEN

Purpose/Introduction: 3D MRI with radial *k*-space acquisition and ultra short echo time (uTE) has been proposed for human lung imaging[1]. 3D uTE imaging is usually performed without fat suppression, since most available techniques will reduce the already low SNR, increase the echo or scan time, and/or produce image artifacts[2].
We aimed to evaluate the influence and contamination of the fat signal on 3D uTE lung imaging with and without retrospective self navigation (RSN) of the respiratory cycle.
Subjects and Methods: Twelve healthy volunteers, recruited with informed consent, were scanned during free breathing using a 1.5T Philips Achieva MR system with a 3D kooshball uTE sequence [COR, FoV=500 mm², voxel=5 mm², radial density=170%, TE=0.7-2.3 ms, TR=4 ms, α=10°, NSA=8]. For one volunteer, an extended measurement was performed with TE=0.16-10 ms and NSA=1. After completed measurements, reconstruction of images synchronized to the expiration phase of the respiratory cycle (acceptance window=7 mm) was performed with RSN[3].
The signal level for different TE:s, with and without RSN was determined in lung and muscle (Fig 1). For the lungs, the T2* value ($T2^*_{lung}$) was estimated assuming mono exponential signal decay with TE. The noise level of the images was estimated as the SD of the signal intensity measured in air (Fig 1). The smoothing of the images was estimated in a central image of the thorax by the gradient of a signal profile orthogonal through the lung–liver boundary.
Results: Without motion compensation, signal from fat was smeared out over the whole image (Fig 2). RSN effectively improved the image quality of the lungs by reducing the influence of fat on $T2^*_{lung}$ (Fig 3), decreasing the noise level ~1.5 times and reducing the smoothing effect in the image (Fig 4) without degrading the contrast.

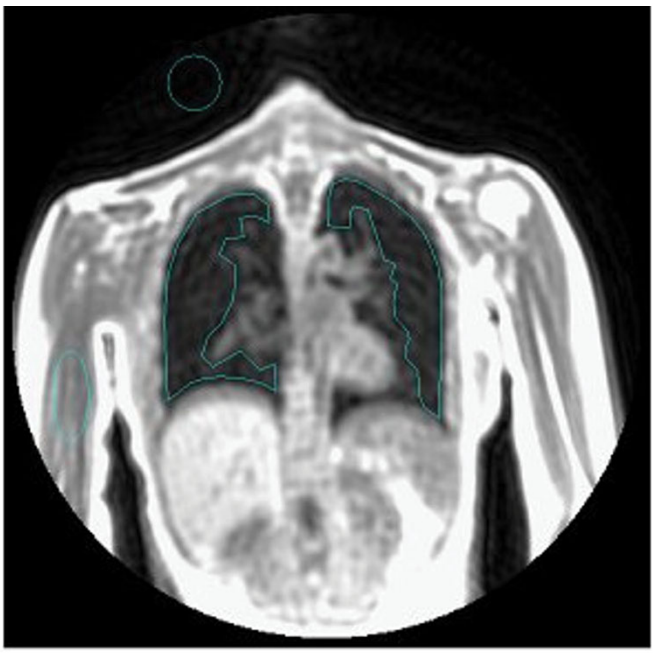

Figure 1. Positions of the ROI:s used in the analysis; in lungs, muscle and air outside the body.

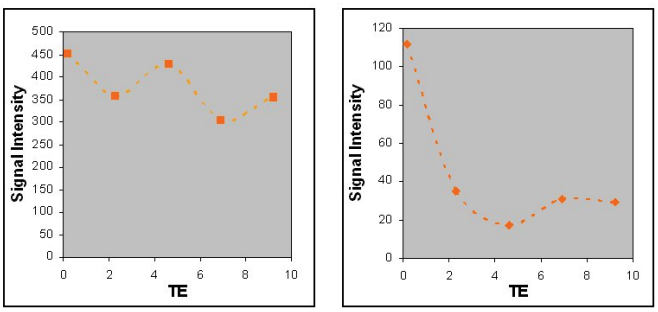

Fig 2. The signal intensity levels in a) muscle and b) lung for the extended measurement plotted as a function of TE. Large differences in signal intensity level and decay rate between the tissues were shown. In both tissues, a low frequency modulation in the signal from the in and out of phase behaviour of the contaminating fat signal was shown.

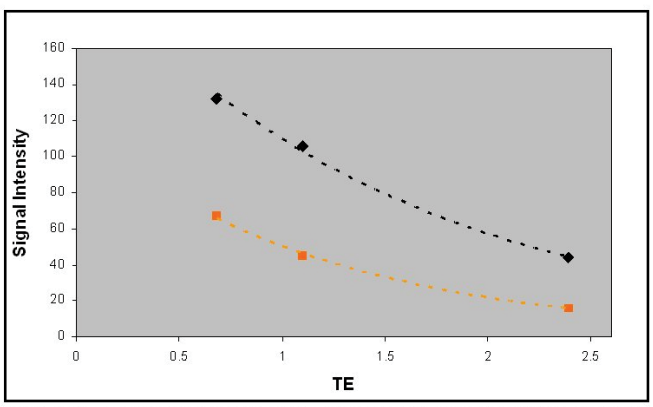

Figure 3. Signal decay curves in lung averaged over all volunteers with (■) and without (◆) RSN. During the time period used for the $T2_{lung}$* estimation, the in and out of phase behaviour of fat significantly modified the lung signal and resulted in an overestimation of the true $T2^*_{lung}$ value. The influence of fat was reduced in the RSN images and resulted in a faster decay and a reduction in the estimated $T2^*_{lung}$ value from 1.5 to 1.2 ms. The lower signal intensity with RSN is an effect of lower NSA.

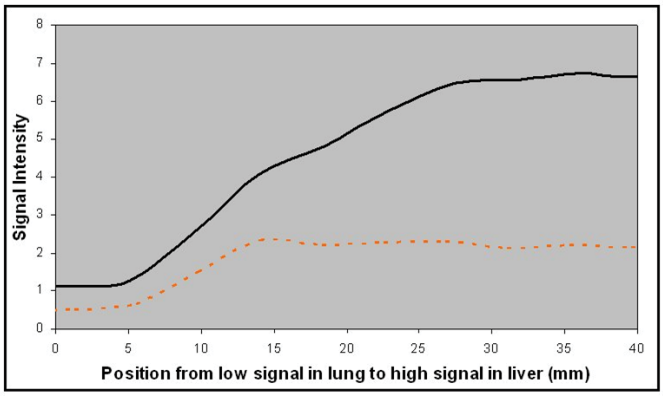

Figure 4. Signal intensity profiles orthogonal to the lung-liver boundary. The profiles were averaged over al volunteers with (dotted line) and without (solid line) RSN. The profile for the RSN image displayed lower signa intensity due to lower NSA, but a sharper boundary between lung and liver with a faster increase from low signa in lung to high signal in liver.

Discussion/Conclusion: Breathing artifacts severely hamper kooshball uTE lung imaging both qualitatively and quantitatively when fat is present in the imaged region. The fat contamination degrades the lung image and decreases the accuracy of $T2_{lung}$* as the signal decay reflects not only the T2* relaxation of lung tissue, but also the in and out-of-phase behavior of the fat signal in the lung voxels. Motion compensation reduces this influence, but at the expense of increased scan time. Development of effective fat reduction techniques should therefore be a priority.

References:

1. MRM 2010;64(5):1491-8
2. Clin Radiol 2003;58:1–19
3. MRM 2010;64:401–7

773

Registration Based Estimates of Lung Ventilation

Å. Kjørstad[1], D.M.R. Corteville[1], F. Horn[2], F.G. Zöllner[3], E. Hodneland[4], C. Fink[5], L.R. Schad[1]

[1]Computer Assisted Clinical Medicine, Heidelberg University, Mannheim/ GERMANY, [2]Academic Radiology, University of Sheffield, Sheffield/UNITED KINGDOM, [3]Computer Assisted Clinical Medicine, Medical Faculty Mannheim, Heidelberg University, Mannheim/GERMANY, [4]Department Of Mathematics, University of Bergen, Bergen/NORWAY, [5]Institut Für Klinische Radiologie Und Nuklearmedizin, Heidelberg University, Mannheim/ GERMANY

Purpose/Introduction: Ventilation measures the volume of air per unit time that enters and leaves the lung. It is one of the main physiological parameters of lung function. As injury or disease can alter lung function both globally and locally, local measures of ventilation can be clinically important. Current gold standard methods for extracting local ventilation-related information in MRI require the use of contrast agents such as hyperpolarized gases. However, the preparation and administration of these gases require advanced and expansive equipment which is not widespread.

It has been suggested that the deformation field obtained from image registration of lung images can be used to calculate local ventilation [1,2], and a close correlation has been shown between ventilation measurement done by xenon CT and registration-based estimates of ventilation [3]. We show that image registration of a standard lung sequence at 1.5T can provide both local and quantifiable information about lung ventilation.

Subjects and Methods: To measure the exact volume of ventilation five bags of different sizes (0.6L, 1.0L, 1.6L, 2.0L, and 2.5L) were used. One subject was instructed to hold his breath, breathe into the bag until it was full, and then hold his breath again. This was repeated 5 times for each bag. 3D images were acquired during both breath holds using a 3D VIBE sequence on a 1.5T scanner (Magnetom Avanto, Siemens Healthcare, Erlangen, Germany) with FA=8°, FOV=450x450mm², TR=2.6ms, TE=0.9ms, slice thickness= 5mm and matrix=128x128x44.

The initial lung volume was segmented using a region growing technique. The volume change was then calculated using a fluid registration model with the residual complexity similarity measure [4].

Results: The image registration was able to accurately measure the global ventilation (Fig 1). The local distribution of ventilation inside the lungs seems realistic, with a clear gravitational effect present and a gradient value in accordance with literature [5] (Fig 2 and 3).

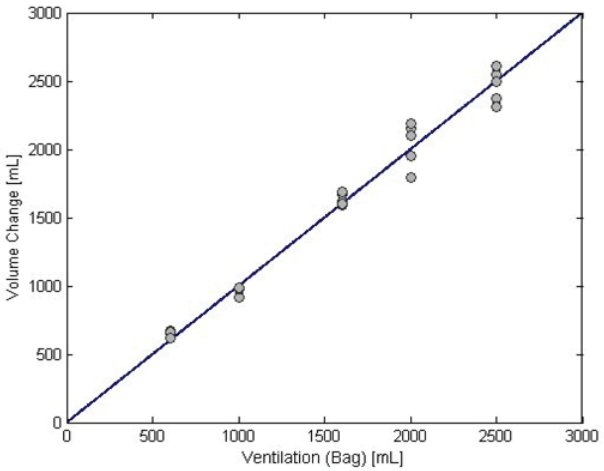

Figure 1: Scatter plot of registration-based estimates of ventilation vs. known bag ventilation. Correlation > 0.99

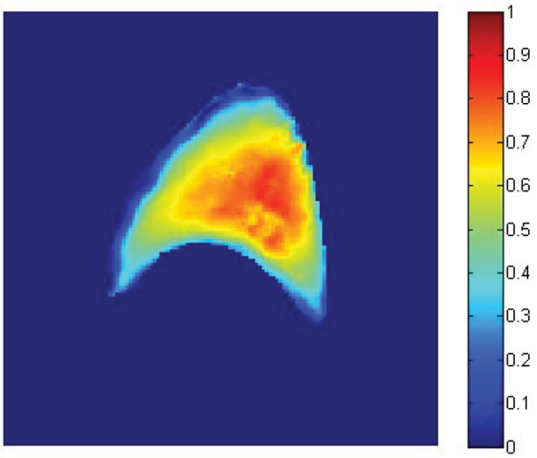

Figure 2: Specific expansion in a sagittal slice. Note the gravitational gradient from anterior to posterior.

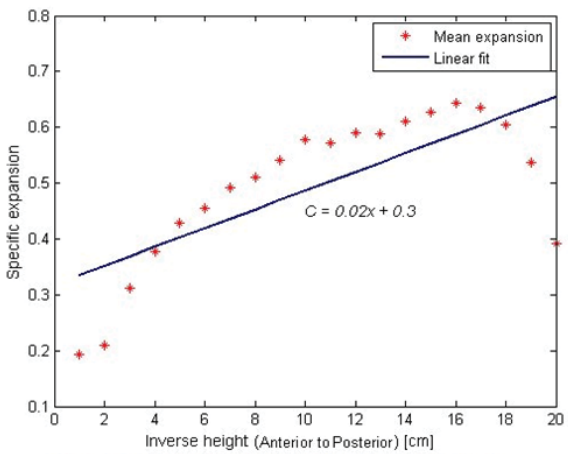

Figure 3: Mean specific expansion vs. inverse height

Discussion/Conclusion: Using non-rigid image registration we can estimate global ventilation and acquire valuable local information inside the lung without using hyperpolarized or inert gases.

References:

[1]: Guerrero T, 2006, Phys in Med and Bio, 51:777-791;
[2]: Sundaram TA, 2005, Med Image Anal, 9:524–537;
[3]: Reinhardt J.M, 2008, Med Image Anal, 12:752-763;
[4]: Myronenko A, 2010, IEEE Trans Med Im, 29:1882–91;
[5]: Sà RC, 2010, J Appl Physiol, 109:1950-1959;

Acknowledgments: This work was supported by EU FP7 PI-net.

Paper Poster

Sequences and techniques

774

Quantitative pH analysis with sodium ^{13}C-Bicarbonate at small pH variations

D.J. Scholz[1], O. Khegai[2], A. Otto[1], R.F. Schulte[2], M. Schwaiger[3], S. Ziegler[3], A. Haase[1], M.I. Menzel[2]
[1]*Institute Of Medical Enigeering (imetum), TU München, Garching/ GERMANY,* [2]*Dbt, GE Global Research- Europe, Garching/GERMANY,* [3]*Nukleamedizin, Klinikum rechts der Isar, München/GERMANY*

Purpose/Introduction: In vivo determination of the spatial distribution of pH is a challenging task.[1, 2] Metabolic magnetic resonance imaging using hyperpolarized bicarbonate ($H^{13}CO_3^-$) may help to close this clinically important gap.[3] The pH includes information about type and severity of a disease like tumors and inflammation. Bicarbonate helps to regulate the pH-value in mammalian tissues tightly. Under acidic conditions it acts as proton acceptor and forms carbonic acid (H_2CO_3), which dissociates to water (H_2O) and carbon dioxide (CO_2). The ratio of the two levels of bicarbonate and dioxide can be used to determine the spatial distribution of the environmental pH-value of the investigated sample with the help of the Henderson-Hasselbalch equation.[3]

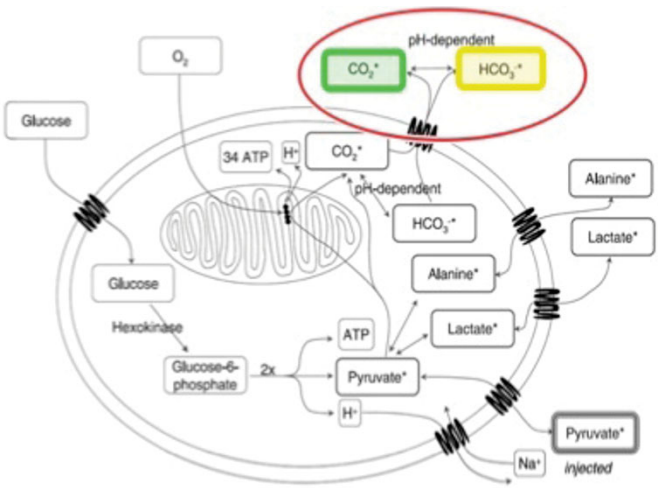

Subjects and Methods: Hyperpolarization[4] allows the detection the ^{13}C-Bicarbonate. A solvent technique, combining heating and ultrasonic treatment, was developed for Sodium ^{13}C-BiC. For the subsequent dissolution H2O/ D_2O + EDTA was used. Quantitative Experiments were performed with pH buffers varying in a small pH-range to estimate the sensitivity of the method.
Results: A stable solid-state polarization buildup could be observed after 90 minutes. The liquid state polarization reached polarization levels of 16 +/- 5 %, and a relaxation time of 60 +/- 10 s in H_2O and 115 +/- 10 s in D_2O seconds (25 mMol final concentration). On average a signal to noise ratio at thermal equilibrium of 25 was achieved. The dependence of the conversion of ^{13}C-BiC to ^{13}C-Dioxide on pH is depicted in Fig. 2, the spectra do no depict any unwanted side products. Different concentrations of OXO-radical and Gadolinium were investigated to show their influence on solid-state polarization time, polarization level and liquid state polarization.

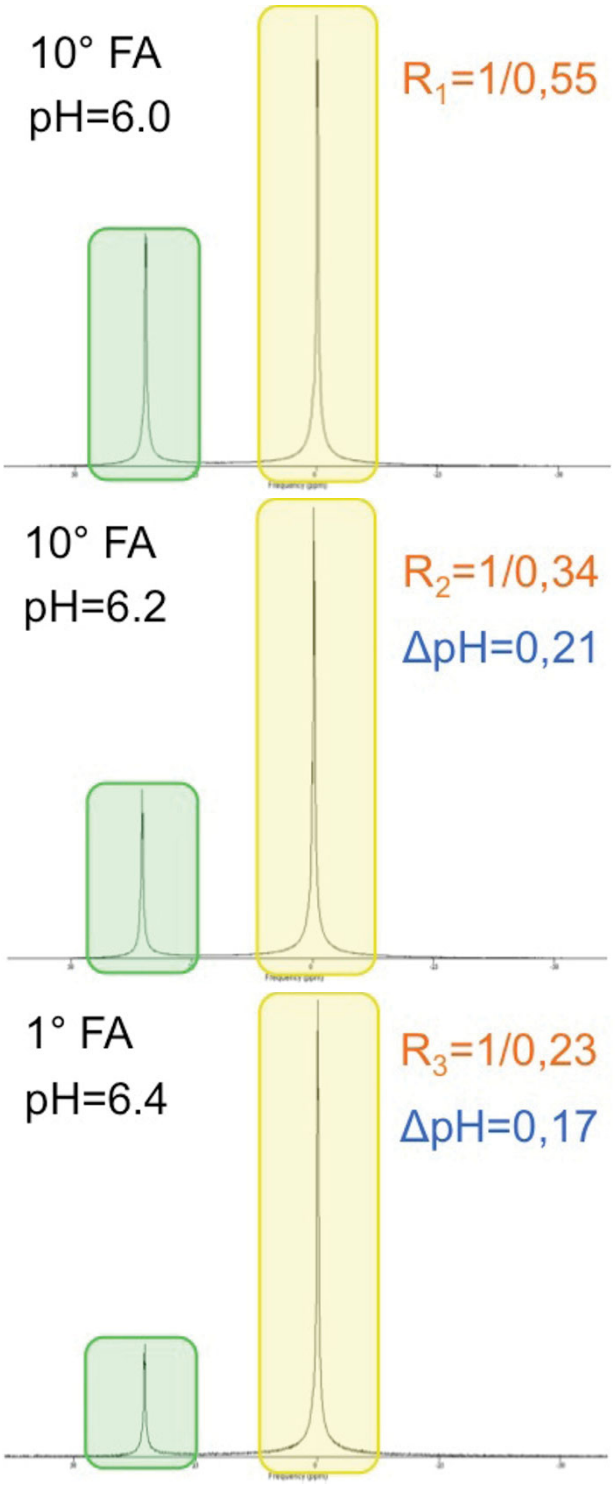

Discussion/Conclusion: A stable procedure and chemical formulation for hyperpolarization of Sodium ^{13}C-BiC was developed, which constitutes the first steps to in-vivo application for pH mapping. Due to the level of polarization, the sufficient long T1 and the good signal to noise ratio ^{13}C-BiC and the converted $^{13}CO_2$ show promising MR signal intensities in the physiological range of pH for subsequent in vitro and in vivo measurements.
References:
[1] Stubbs, M. et al., 1992, *NMR Biomed* 351-359. [2] Ward, K. M et al., 2000, *Magnet Reson Med,* 799-802. [3]. Gallagher, F.A et al., 2008, *Nature* 940-943. [4] Ardenkjær-Larsen, J.H. et al., 2003, *Proc Natl Acad Sci* 10158 -10163.

775

MR Thermometry for Head and Neck Hyperthermia: Experimental Verification of Simulations for Guiding Setup Design.

W.C.M. Numan[1], L.W. Hofstetter[2], G. Kotek[3], J.F. Bakker[4], E.W. Fiveland[2], G.C. Houston[5], G. Kudielka[6], G.C. Van Rhoon[1], D.T.B. Yeo[2], **M.M. Paulides**[1]

[1]Radiation Oncology; Hyperthermia Unit, Erasmus MC, ROTTERDAM/NETHERLANDS, [2]Mr Lab, Diagnostics & Biomedical Technologies, GE Global Research, Niskayuna/UNITED STATES OF AMERICA, [3]Radiology, Erasmus MC, Rotterdam/NETHERLANDS, [4]Radiation Oncology; Hyperthermia Unit, Erasmus MC - Daniel den Hoed Cancer Center, Rotterdam/NETHERLANDS, [5]Applied Science Laboratory, GE Healthcare Technologies, 's-Hertogenbosch/NETHERLANDS, [6]Europe, GE Global Research, Munchen/GERMANY

Purpose/Introduction: In Rotterdam, head and neck hyperthermia (HT) is a standard addition to re-irradiation. HT is controlled using interstitial fiber-optic temperature probes and hyperthermia treatment planning, based on electromagnetic (EM) simulations. Often, invasive placement of temperature sensors is cumbersome, painful and not without risk on complications, so we are developing non-invasive magnetic resonance thermometry (MRT) as alternative. In this work, we experimentally verified our EM and thermal simulation tools through probe and MRT measurements, for guiding the development of new hybrid MR-HT applicator prototypes.

Subjects and Methods: The experimental setup consisted of the lower half of a cylindrical HT antenna array[1]. Muscle equivalent material[2] was placed on top of the setup as an additional absorber (figure 1). A four-sensor fiber-optic probe was inserted into the absorber to continuously document the temperature. MR imaging was performed using a 1.5T MR450w wide-bore scanner (GEHC, WI). The proton resonance frequency shift (PRFS) MRT method was applied and sunflower oil surrounding the top muscle phantom was used for B0 drift correction[3]. Heating was applied using 60s periods of RF power (75W, 434MHz at two antennas), interspaced by 45s periods for MRT measurements. This cycle of heating and cooling was repeated 11 times over a 19min period, followed by monitoring of thermal decay. A high-resolution 3D scan, taken during the experiment, facilitated in adaptation of the applicators CAD-model to accurately recreate the experimental setup and identify the exact position of the temperature probes. EM and thermal simulations were accurately modeled on 1.3mm Yee-grid using an FDTD algorithm (SEMCADX, Speag, CH). Dielectric and thermal parameters were taken from literature[1]. Since the water-bolus was included in the simulations, no thermal bounds were required. Applied RF power and losses (S11-values) were recorded during the whole experiment to allow accurate reproduction of the input power.

Results: Predicted temperature time profiles closely follow the measured ones (Figure 3). The average difference remains below 0.55°C (Table 1). The correlation coefficient between simulated and measured temperatures is high (R2>0.98). Figure 2 shows that the general focus (5°C-contour) of simulations and MRT match well, but indicate a discrepancy in unheated sections (0°C-2°C) outside the ROI.

Discussion/Conclusion: A high correlation has been shown between simulated and measured temperature distributions, both in absolute value as in focus shape. This study validates our approach using simulation-guided hybrid MR-HT prototype development and advocates the use of a sufficient temperature gradient to improve MRT measurement accuracy.

References:

1. Paulides;2007;IntJRadiatOncolBiolPhys; 68(2):612-20.
2. Ito;2001;ElectronCommJpn;84(4):67-77.
3. De Poorter;1995;MRM;33:74-81.

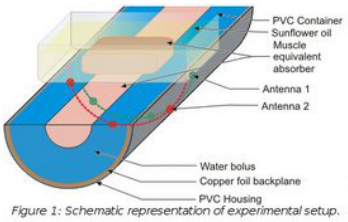

Figure 1: Schematic representation of experimental setup.

	Measurement-Simulation	
	RMSE [°C]	R^2
	0.16	0.99
	0.14	0.99
	0.12	0.99
	0.05	0.98

Table 1: Root mean square error and correlation coefficient of simulate data.

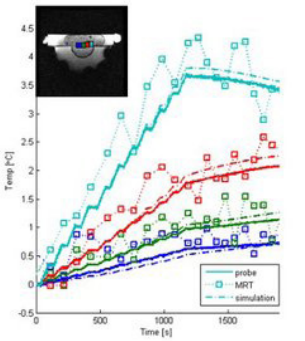

Figure 2: Time-temperature curve of probe, MRT and simulation data for 4 probe locations.

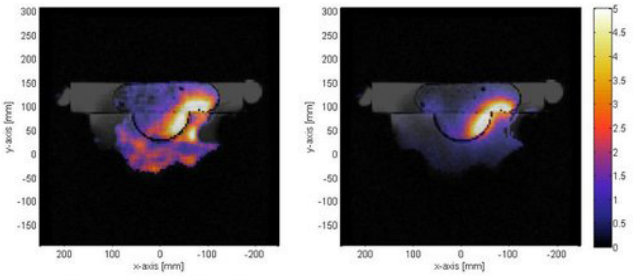

Figure 3: Thermal distribution captured by MRT(left) and simulation(right) at t = 840s

776

Pulse Optimization and a Method to Correct Off-Resonance Induced Errors for Bloch-Siegert B_1^+ Mapping

M. Koehler, T. Speckner

H Im Mr Plm-sd Sws Sit, Siemens Healthcare, Erlangen/GERMANY

Purpose/Introduction: A promising technique for fast and robust B1+ mapping is the Bloch-Siegert method [1], where an off-resonant pulse follows an excitation pulse and generates a $(B1+)^2$ dependent phase shift. In this work, an off-resonant pulse is tailored in order to maximize the phase shift while limiting other, unwanted effects. Furthermore, a method to reduce off-resonance induced errors is proposed.

Subjects and Methods: As suggested in [1], a Fermi pulse is employed to generate the Bloch-Siegert phase shift. Using Bloch simulations, the parameters of the Fermi pulse (duration, edge width, edge position and modulation frequency) are optimized to meet the following conditions: limited on-resonance excitation (< 1% below 800 Hz), a maximum Bloch-Siegert phase shift for a given B1+ amplitude, a limited pulse duration and a limited dependence of the phase shift on the flip angle of the preceding excitation pulse. For an off-resonance frequency of 800 Hz, a relative error below 6% is desired. To further reduce this error, a modified calculation of the phases is proposed (compared to $\Delta\Phi=(|\Phi_+-\Phi_-|)/2$ as in [1]), see Fig. 1.

$$\Delta\phi = \frac{2}{\frac{1}{|\phi_{ref} - \phi_+|} + \frac{1}{|\phi_{ref} - \phi_-|}}$$

ϕ_{ref} : Phase of reference scan without Fermi pulse

ϕ_+, ϕ_-: Phases of scan with Fermi pulse above/below water resonance

FIGURE 1: Proposed method to calculate the phase difference used for the calculation of the B1+ magnitude.

Then, ΔΦ is used to calculate the B1+ magnitude as described in [1].
A STEAM-based Bloch-Siegert sequence [2] was implemented on a 3 T MR scanner (MAGNETOM Skyra, Siemens, Erlangen). Both phantom and in-vivo studies were performed.

Results: Even small variations of the Fermi pulse parameters influence the performance significantly. In Fig. 2, the optimized Fermi pulse is shown together with a pulse which has somewhat steeper edges. The optimized parameters are displayed in Fig. 2; the optimized modulation frequency is 2400 Hz relative to the water resonance. Exemplarily, Fig. 3 shows the dependence of the Bloch-Siegert phase shift on the flip angle of the preceding excitation pulse for the two pulses shown in Fig. 2. The off-resonance induced error of the optimized pulse is shown in Fig. 4. This error can be reduced to below 1%.

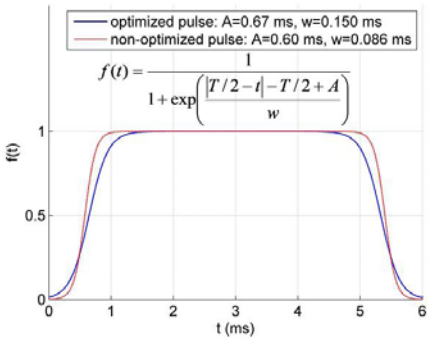

Figure 2: Optimized and non-optimized Fermi pulse (normalized). The pulse duration is T=6 ms, the parameters A and w are shown in the legend.

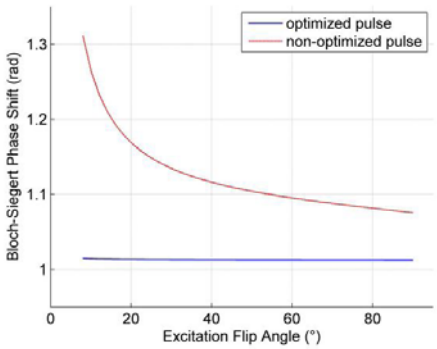

Figure 3: Simulated Bloch-Siegert phase shift as a function of the flip angle of the excitation pulse for the optimized pulse and the non-optimized pulse shown in Fig. 1. The simulation was performed for a B1+ amplitude of 10 µT.

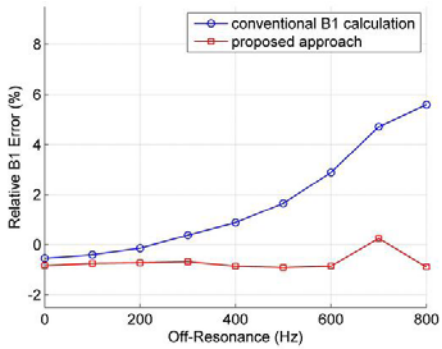

Figure 4: Relative error of the measured B1+ amplitude for off-resonance frequencies up to 800 Hz, measured with an oil phantom at 3 T. The Phases were calculated according to the approach described in [1] and the approach proposed in this work.

Discussion/Conclusion: The importance of optimizing the Fermi pulse parameters is apparent from Fig. 3. For a straightforward B1+ calculation, it is desired to disentangle the effects of excitation flip angle variations and the phase shift generated by the Fermi pulse. The relative error of 6% for an off-resonance of 800 Hz might be acceptable; however it can be almost eliminated applying the proposed method.

References:

[1] Sacolick, LI. et al., 2010, MRM, 63:1315-1322.
[2] Nehrke, K. and Börnert, P., 2011, Proc. ISMRM 19:4411.

777

Clinical workflow optimized Calibration-Method for Stereo-Optical Tracking in MRI

M. Hoßbach[1], **J. Gregori**[2], S. Wesarg[1], M. Günther[3]
[1]Cognitive Computing & Medical Imaging, Fraunhofer IGD, Darmstadt/GERMANY, [2]Mevis, Fraunhofer, Bremen/GERMANY, [3]Mevis, Fraunhofer MEVIS, Bremen/GERMANY

Purpose/Introduction: Though motion tracking for head motion compensation in MRI has been a research topic for some time [1-4], literature is not giving much attention to the calibration of such systems. We present a method to calibrate the coordinate systems of a stereo-optical camera setup mounted to the MRI head coil and show that, though using a simple setup and visible light [1], it is possible to achieve a sub-millimeter tracking precision.
Subjects and Methods: MRI compatible video cameras acquiring images of 768x576 pixels at 25fps are mounted to a camera holder which is attached to the MRI head coil and calibrated using text-book methods. Blue water-filled spheres positioned throughout the whole imaging volume are detected in images of the tracking cameras as well as MRI scans in order to register the coordinate systems of both camera system and MRI scanner. A heuristic-enhanced brute-force approach is used to match detected spheres in the different images. Then, a rigid transformation is calculated and applied to the cameras' external parameters to align the coordinate systems.
The precision was evaluated using leave-one-out cross-validation both for the camera calibration and the scanner coordinate system registration, considering the number of spheres. Also, a prediction of the achievable tracking accuracy was made: Considering that only features on the patient's face are used for tracking, the influence of jitter in feature detection on the position of a point on the forehead and at the back of the head was measured.
Results: Leave-one-out cross validation showed that the cameras' locations and orientations are correct within 0.1 mm and 0.01 degrees, using at least 18 spheres. Evaluation of the MRI coordinate system registration showed an average reprojection error of 0.37 mm. The resulting calibration transformation is correct within 0.05 mm and 0.05 degrees.
Influence of a feature point jitter of 0.5 pixels is 0.03 mm for a point close to the cameras, 0.3 mm for a point close to the back of the patient's head. Tracked poses are correct within 0.17 mm and 0.001 degrees.
Discussion/Conclusion:
We showed that using a simple setup of two MR compatible cameras mounted to the MRI head coil, it is possible to achieve a sub-millimeter tracking precision for patient head motion compensation in MRI.
References:

1. Hoßbach, *VISAPP,* 2010, 453-456
2. Maclaren et al, *MagnResonMed,* 2010, 63, 162-170
3. Zaitsev et al, *NeuroImage,* 2006, 31, 1038-1050
4. Forman et al, *MedImAnal,* 2011, 15, 708-719

778

Pulsed 3D ASL at 7 Tesla: Initial Results

K. Schewzow, A.I. Schmid, E. Moser
Center For Medical Physics And Biomedical Engineering, Medical University of Vienna, Wien/AUSTRIA

Purpose/Introduction: Arterial spin labeling (ASL) represents a non-invasive assessment of tissue perfusion. The potential benefits of this technique at 7 Tesla are the increased perfusion weighted (PW) signal due to higher SNR and the longer T_1-relaxation times, allowing for longer inflow and imaging times. There are, however, also challenges in ASL at ultra high field, arising from B_0/B_1 inhomogeneities, shorter T_2/T_2^* times and SAR constrains. The goal of this work is to implement and optimize pulsed ASL with 3D-GRASE readout[1] for 7T with respect to image quality and SAR.
Subjects and Methods: For the acquisition of the PW images the pulsed ASL technique with FAIR labeling scheme and segmented 3D-GRASE readout was used. BASSI inversion pulses[2] were implemented for global and slice selective inversion (μ=7.2, β=1214, b_0=20) (Fig.1). Saturation pulses were applied after the inversion to reduce the static tissue signal. Measurements in vivo were carried out on a 7T Siemens Magnetom scanner with transmit/receive 32-channel head coil (Nova Medical, USA). Imaging parameters: FOV=256×256×54mm³ , 128×55×18 matrix, 4/8 slice partial Fourier, 100% slice oversampling, EPI-factor=19, turbo-factor=19, 3 segments, TR/TE/TI=7500/20/2000ms, 200ms Q2TIPS duration, inversion slab-thickness=64 mm; 16 repetitions, 12 min scan time. Quantitative perfusion maps were calculated in three healthy subjects (two male, one female, mean age 27±2 years) using $f=\lambda/2TI\times\Delta M(TI)/M_0\times\exp(TI/T_1)$ (λ=0.98, T_1=2100ms). Perfusion maps were registered to a standard brain using FSL, a gray matter mask was applied to calculate the mean gray matter perfusion.

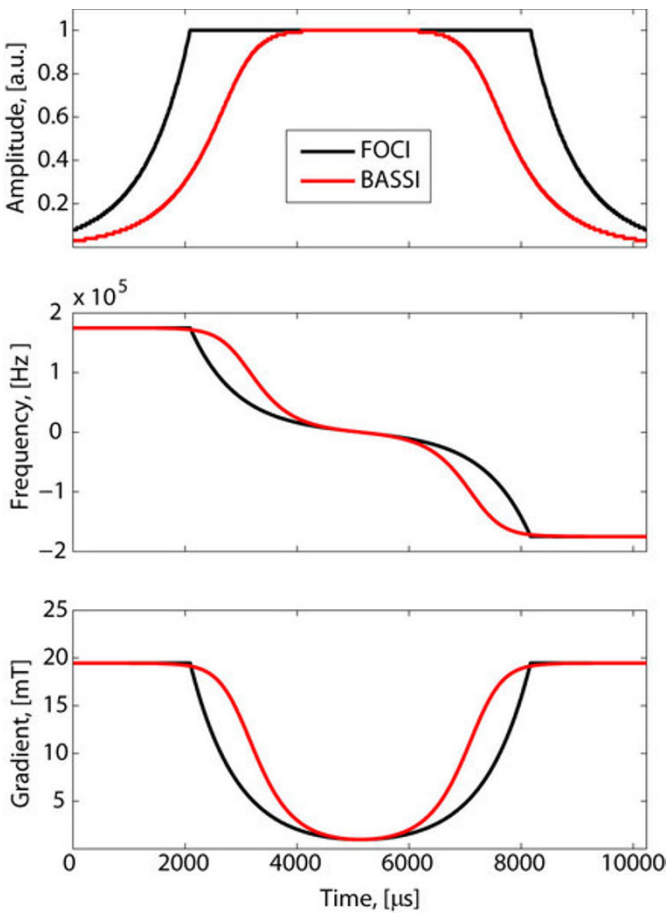

Fig1: Amplitude (top), Frequency (middle) and Gradient (bottom) of FOCI (black) and BASSI (red) pulses.

Results: The GM perfusion values in three volunteers were 83±38, 55±21 and 104±35 ml/100g/min with mean SNR of ~30 in GM. Fig.2 shows the perfusion maps of 18 slices of one volunteer.

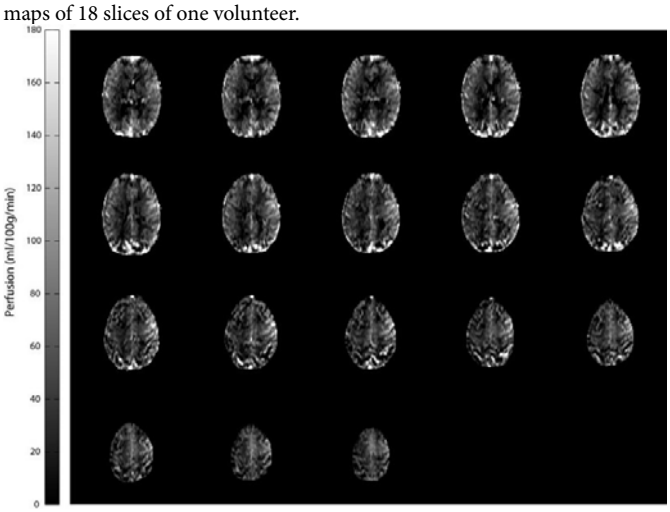

Fig2: Perfusion maps obtained in a healthy volunteer at 7 Tesla.

Discussion/Conclusion: 3D perfusion maps of high resolution and good SNR could be obtained at 7 Tesla. TR was chosen as a compromise between T_1-relaxation, SAR and scan time. SAR could be significantly reduced through BASSI-pulses, requiring 31% less energy compared to FOCI-pulses[2], therefore the total deposited energy including Q2TIPS saturation and many refocusing pulses could be kept within legal limits. The calculated CBF values are in good agreement with previous results[1,3].
References:
[1] Gunther et al, MRM, 2005
[2] Warnking et al, MRM, 2004
[3] Gardener et al, MRM 2009

779

Slice Profile Adapted Radio Frequency Pulses for Simultaneous Gradient and Spin Echo EPI Using the Shinnar-Le-Roux Algorithm

B. Fernandez[1], M. Czisch[2], P. Le Roux[3]
[1]*Global Applied Science Laboratory, GE Healthcare, Munich/GERMANY,*
[2]*Rg Neuroimaging, Max Planck Institute of Psychiatry, Munich/GERMANY,*
[3]*Applied Science Lab, GE Healthcare, Palaiseau/FRANCE*

Purpose/Introduction: The interest for simultaneous or combined gradient and spin echo echo planar imaging (EPI) sequence (called here hybrid EPI) has grown for different applications [1-3] like fMRI [3]. A difficulty with this sequence is to have the same slice profile for both the gradient-echo (GRE) and the spin-echo (SE). This problem has been investigated for spectral-spatial excitation pulses [4]. Here, we focus on the design of selective excitation and refocusing pulse for the hybrid EPI with a fat saturation pre-pulse.
Subjects and Methods: In order to keep the minimum achievable TE of the SE, the RF pulses duration has not been lengthened compared to the RF pulse used in the original SE-EPI sequence (referred as original RF pulse; excitation: least-square design, 5ms duration, 886Hz bandwidth; refocusing: linear phase Shinnar-Le-Roux (SLR) [5], 3.2ms duration, 905Hz bandwidth). Both excitation and refocusing pulse has been designed using SLR [5] with minimum phase because it allows a more selective slice profile compared to its linear phase counterpart [5]. Others design parameters for the excitation pulse was: 90° flip angle, 5ms duration, 600Hz bandwidth, and for the refocusing pulse: 170° flip angle, 3.2ms duration, 900Hz bandwidth. Common parameters were 0.1% in-band and 1% out-band ripples. The slice profiles of the original and the proposed pulses were computed in simulation. Additionally, the slice volume (the integral of the main lobe of the transverse magnetization along z) relative to the ideal slice volume were compared. Finally, the pulses were implemented in the hybrid sequence (figure 1) on a 3T GE scanner.

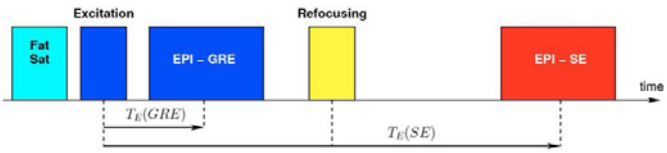

Results: Simulation results are summarized in figure 2.

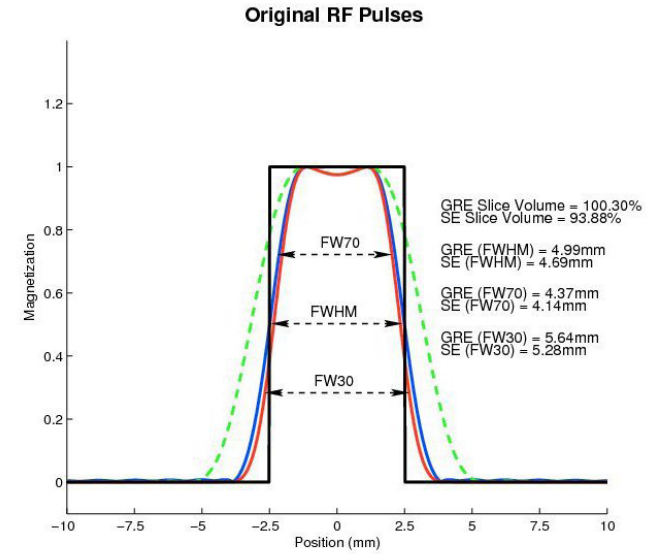

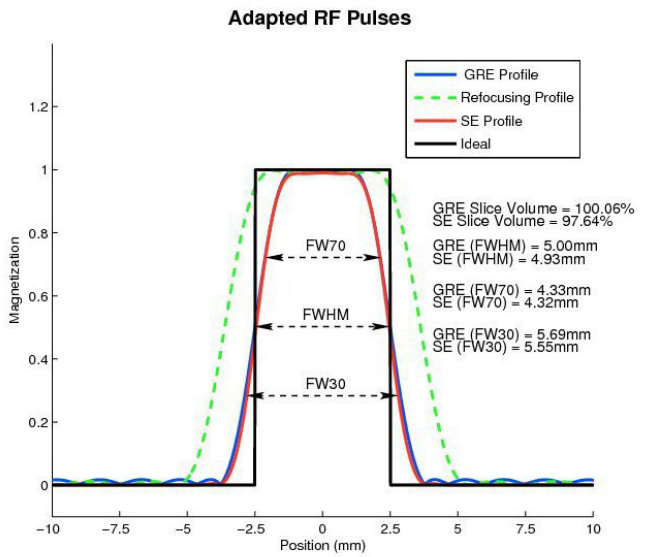

For the original pulses, the difference between the GRE and SE profile in term of full width at 30%, 50% and 70% of the maximum was 0.36, 0.3 and 0.23 mm, respectively and for the adapted pulses, it was 0.14, 0.07 and 0.01 mm, respectively. Examples images acquired on a phantom are displayed in figure 3.

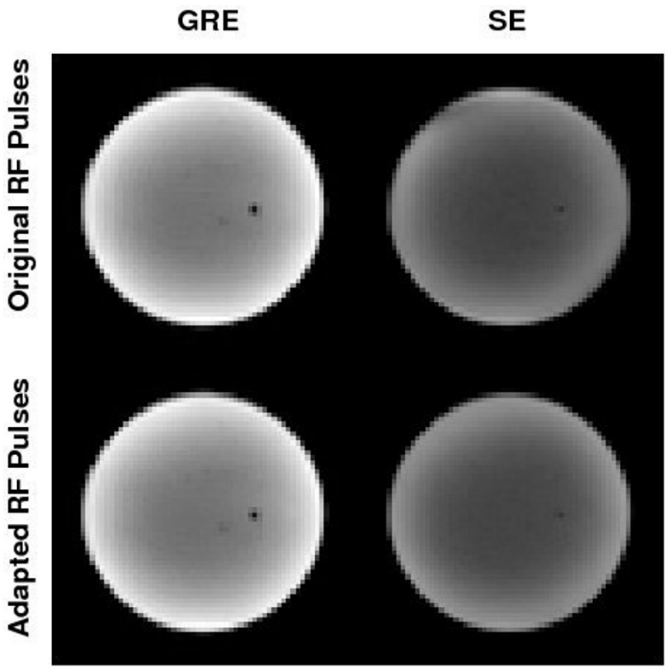

Discussion/Conclusion: The presented results show that we can get similar slice profile for the GRE and the SE without lengthening the pulse duration by using minimum phase SLR pulses. The effect of profile mismatch has been investigated in the case of R2/R2* imaging [4], suggesting that this mismatch also affects fMRI. SLR pulses should be used for a valid comparison of GRE and SE for fMRI and investigate the effect.

References:

[1] Kiselev V,2005,MRM,53:553-563.
[2] Schmiedeskamp H, 2011,In press.
[3] Schwarzbauer C,2010,NeuroImage,49:316-326.
[4] Schmiedeskamp H,2012,67:378-388.
[5] Pauly J,1991,IEEE-TMI,10:53-65.

780

Ex vivo high-resolution MR (7T) microscopy of the human hippocampus

I. Zucca[1], R. Coras[2], R. Garbelli[3], G. Milesi[3], C. Frassoni[3], A. Mastropietro[1], A. Muhlebner[2], A. Hess[4], E. Aronica[5], I. Blümcke[2], R. Spreafico[3]
[1]Scientific Direction, Neurological Institute Carlo Besta, Milano/ITALY, [2]Department Of Neuropathology, University Hospital Erlangen, Erlangen/GERMANY, [3]Clinical Epileptology And Experimental Neurophysiology, Neurological Institute Carlo Besta, Milano/ITALY, [4]Experimental And Clinical Pharmacology And Toxicology, University of Erlangen Nuremberg, Erlangen/GERMANY, [5](neuro)pathology, Academic Medical Centre, Amsterdam/NETHERLANDS

Purpose/Introduction: The human hippocampus (HI) is morphologically affected in many neurological disorders such mesial temporal lobe epilepsy (MTLE). Its internal structure remains difficult to recognize by conventional MRI studies. In present study, we aimed to anatomically delineate all subregions and layers of the HI combining high-resolution 7T-MRI and microscopy from same tissue specimen.

Subjects and Methods: Eight formalin-fixed post-mortem HI specimens were examined using a 7T-MRI scanner (BioSpec 70/30 USR, Bruker, Ettlingen, Germany) equipped with a BGA12S gradient system capable of 400mT/m. T2-weighted imaging both three-dimensional (3D-T2WI) and high-resolution two dimensional (2D-T2WI) on coronal planes with different angulations were acquired to anticipate the arched shape of the hippocampal head. For high-resolution 2D-T2WI : in plane resolution 40X40µm², slice thickness 0.5mm, repetition time (TR) echo time (TE)=6000/60 ms and an acquisition time

(TA) 15h. For 3D-T2WI: resolution 150X150X150 μm³, TR/TE=6000/60ms and TA 60h. For Diffusion Tensor Imaging (DTI): EPI sequence, in plane resolution 120X120μm², slice thickness 0.7mm, number of diffusion directions 126, b-value=2500, TR/TE=15000.0ms/60.0ms and TA 26h12min. Fractional anisotropy maps and color fiber orientation maps were computed. Histological analysis of the same specimens was performed to validate 7T-MRI. Serial sections of 50 μm were prepared using a vibratome (VT1000S, Leica, Heidelberg, Germany) and Violet, Thionin, Luxol Fast Blue and Black Gold were performed (Garbelli et al. 2011). Each stained section was digitized with a Nikon slide scanner and co-registered by Amira 5.3.3 software with the corresponding MR images of the same slab/specimen.

Results: High-resolution 2D-T2WI identified all subcompartments and layers along the entire anterior-posterior axis of the HI. MRI-intensity differences between anatomical boundaries were confirmed by histological matching and could be assigned to ten recognizable layers. These findings were best visible at the hippocampal mid-body-level. We were able to distinguish these hippocampal subregions also in the hippocampal head with 3D-T2WI and angulated coronal planes. From DTI data we were able to visualize intrahippocampal projections and fiber tracts connecting the hippocampus and mesial temporal lobe.

Discussion/Conclusion: Our findings rely on the basic concept of precise co-registration of MRI and histology and allowed a reliable visualization of anatomical HI-microarchitectures. These findings will provide a valuable tool for clinical and preclinical investigations of patho/physiological conditions in patients suffering from diseases affecting the hippocampus and adjacent brain regions such as MTLE.

References:

Garbelli R et al. 2011-Neurology-76(13):1177-85.

781

Shim improvement in 3T breast imaging by slice-dependent shim update

S. Lee[1], E.T. Tan[1], A. Govenkar[2], I. Hancu[1]
[1]Mri Laboratory, GE Global Research, Niskayuna/UNITED STATES OF AMERICA, [2]Software Development, Extenprise Inc, Pune/INDIA

Purpose/Introduction: Susceptibility-induced B_0 inhomoeneity is a leading cause of image artifact in high-field diffusion-weighted imaging (DWI) in breast. We have previously shown that B_0 homogeneity in bilateral breast can be significantly improved by strategic placement of the shim region-of-interest (ROI) in linear shimming [1] whereas volumetric second- and third- order shimming is relatively inefficient [2]. Based on off-line shim simulation applied to in-vivo B_0 maps from twelve volunteers, we demonstrate here that slice-by-slice linear shim update can significantly improve the B_0 homogeneity in axial multi-slice breast imaging.

Subjects and Methods: Multi-slice axial breast B0 maps were obtained from twelve healthy volunteers with 3-point-Dixon-based fat-water separation and iterative reconstruction (IDEAL). The B0 maps were previously verified to be in good agreement with body-susceptibility-induced B0 calculation in breast [2]. Shim simulation was performed on each subject's B0 maps in which both slice-by-slice and bulk linear shimming with rectangular ROI were applied. Slices with >50 cm² breast area in the image were chosen for processing. The shim ROI included both breasts but excluded the heart and axilla.

Results:

Figure 1

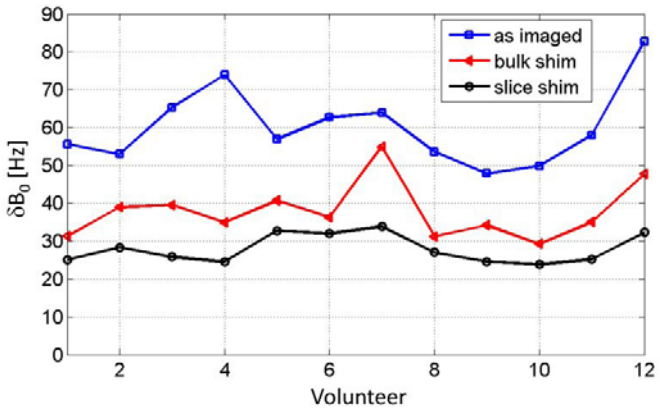

Table 1. Comparison of shim results: as imaged (volume shim with whole body ROI), bulk-shim (volume shim with rectangular ROI over breasts), slice-shim (slice-dependent shim with rectangular ROI over breasts).

12-volunteer-averaged B_0 inhomogeneity	as imaged	60.3 Hz
	bulk-shim	37.9 Hz
	slice-shim	28.0 Hz
Improvement with respect to as-imaged maps	bulk-shim	36.6%
	slice-shim	52.8%

Figure 1 shows the B_0 inhomogeneity (defined as the standard deviation in each slice averaged over all slices considered) in 12 volunteers for: (1) bulk shim with a whole-body ROI (blue), (2) bulk shim with a rectangular ROI (red), (3) slice-dependent shim (black). The volunteer-averaged data are shown in Table 1.

Discussion/Conclusion: B0 homogeneity in axial breast imaging can be substantially improved by employing slice-dependent shim updating with only linear gradients. The method effectively compensates B0 variation of XZ^n and YZ^n type, which is present due to the breast shape effect and asymmetric disposition of heart and lungs. Work is under way to implement slice-dependent linear shim and center frequency updating in a standard 3T breast DWI protocol.

References:

[1] Hancu et al, MRM 2012, doi: 10.1002/mrm.24307
[2] Lee et al, JMRI 2012, in press

Grant support: NIH/NCI 1R01CA154433-01A1

782

Effects of sequence parameters on reliability of multi-exponential T2 measurements

H. Adriaensen[1], **M. Musse**[1], S. Quellec[1], A. Vignaud[2], F. Mariette[1]
[1]Tere, Irstea, Rennes cedex/FRANCE, [2]Siemens Healthcare, Siemens Healthcare, Saint-Denis/FRANCE

Purpose/Introduction: Most biological tissues exhibit multi-exponential relaxation behaviour which characterisation is useful for assessment of human diseases [1] and for non-clinical fields as plant sciences [2]. Besides relaxation curve sampling problems, the reliability of T2 quantification depends on multiple factors. Crusher gradients, used for spurious echoes suppression produce signal loss *f* and the apparent T2 decreases. Diffusion of water molecules throughout the gradients generated by susceptibility inhomogeneities T2' and diffusion acting imaging gradients T2" [2] also affects T2 quantification: 1/T2-apparent=1/T2-intrinsic+1/T2'+1/T2" (Eq-1), with $1/T2' \sim \langle gz^2 \rangle TE^2D$ (Eq-2) ($\langle gz^2 \rangle$-mean square distribution of the local field gradients, TE-Echo Time, D-self-diffusion constant) and $1/T2'' \sim G^2\delta^2D(\Delta-\delta/3)/TE$ (Eq-3) (G-gradient strength, δ-gradient duration, Δ-distance from the gradient lobe centres). The impact of the technical parameters on the signal depends on T2

values and can thus lead to erroneous interpretation for multi-exponential relaxation. Therefore, TE and crusher momentum effects on bi-exponential T2 measurements were investigated.

Subjects and Methods: Experiments were performed on a 1.5T scanner (Avanto, Siemens) with a 512-echo CPMG-MRI sequence. Four solutions of T2=26, 125, 502 and 1248ms (reference MRI values for: TE=7.1ms; crusher-momentum=5x10^{-6}T.s/m) in 50%-50% volume ratio was combined generating six different elements with bi-exponential relaxation.

The effects of (1) crusher-momentum and (2) TE were investigated from images acquired with: (1) crusher-momentum=5, 25 and 50x10^{-6}T.s/m; TE=12ms and (2) TE=7.1, 9.1 and 12ms; crusher momentum=5x10^{-6}T.s/m.

In the second case, a tri-exponential transverse relaxation in porous system (apple) was also explored.

Results: Diffusion effects led to T2 decrease when the crusher momentum increased (Fig-1), especially for long-T2 components. The experimental results matched well with the predicted trend (Eq-3). The relative intensity (I_R) ratio close to 50%-50% was not affected.

T2 changes due to the diffusion throughout readout gradients (Eq-3) and to the signal loss *f* were not significant in the range of TE investigated. Consequently, T2 in the phantom was not affected by TE changes (Fig-2). However, in the porous apple tissues, susceptibility effects (Eq-2), induce the decrease of T2 (and changes in I_R) with TE increase, the phenomenon being marked for long-T2 components (Fig-3).

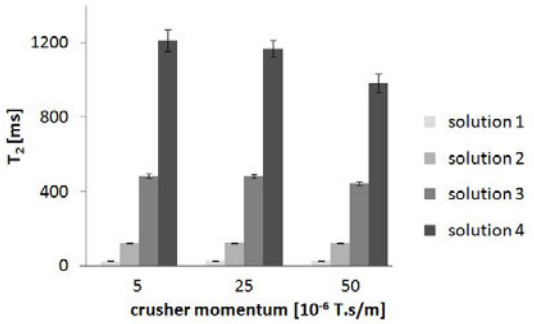

Figure 1: Effect of crusher momentum in the phantom. T_2 values as a function of crusher momentum for a bi-exponential decay measured in the phantom. Vertical bars correspond to standard deviations. TE was set to 12 ms for all experiments.

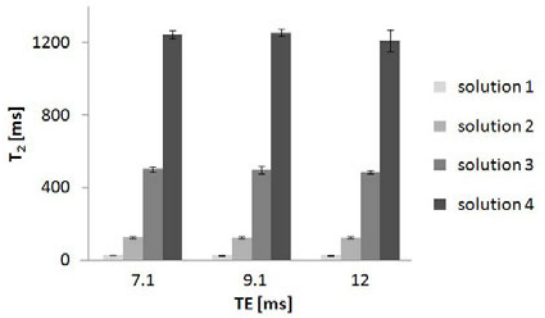

Figure 2: Effect of TE in the phantom. Mean T_2 values as a function of TE in the bi-exponential configuration. Vertical bars correspond to standard deviations. A constant crusher of 5 x 10^{-6} T.s/m was used.

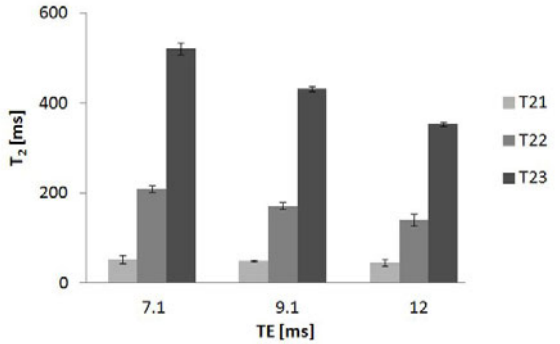

Figure 3: Effect of TE in the apple. T_2 relaxation signal was fitted by using a three-exponential function. Mean T_2 values of three different samples as a function of TE in the apple. Vertical bars correspond to standard deviations. A constant crusher of 5 x 10^{-6} T.s/m was used.

Discussion/Conclusion: T2 and associated signal intensity quantification depend on technical factors in the imaging sequence. The sequence parameters have to be optimised for reliable measurements with regards to the various effects and tissues under investigation, especially when susceptibility effects are expected.

References:

1. Storas T.H. et al., 2008, J.Magn.Reson.Imaging, 1166-72
2. Edzes H.T. et al., 1998, Magn.Reson.Imaging, 185-196

783

T2 & T2ρ maps: Sequence Development and Clinical Impact on Joint Study

L. Balbi[1], D. Greco[1], S. Innocenti[1], C. Sirignano[2], G. Palma[2], E. Soscia[2], B. Alfano[2], M. Salvatore[2]
[1]Mri R&d, Esaote S.p.A., Genoa/ITALY, [2]Ibb, CNR, Naples/ITALY

Purpose/Introduction: To assess the value of T2- and T2ρ-maps obtained by a dedicated MRI system as a diagnostic tool for the evaluation of the knee joint cartilage.

Subjects and Methods: We have studied 24 patients scheduled for arthroscopy on a dedicated MRI system (Esaote G-Scan – 0.25 T) with two optimized Steady-State Free-Precession (SSFP) sequences. The related signal equations were inverted voxel-by-voxel to obtain quantitative PD-, T1- and T2-maps of the whole joint. The T2ρ-map of the joint was derived as harmonic mean of T1 and T2.

3D Sharc, T2- and T2ρ-maps were evaluated in consensus by two radiologists at fixed range scales to find cartilage defects.

The number of focal or diffuse cartilage alterations detected by MRI images by means of each kind of map was then compared to the number cartilage defects found by surgeons during arthroscopy.

Results: As for the evaluation of diffuse cartilage alterations, SSFP, T2-maps and T2ρ-maps were positive in 4, 35 and 24 cases, respectively. Moreover SSFP revealed 3 focal cartilage alterations, T2-maps revealed 48 and T2ρ-maps revealed 70.

The arthroscopic correlation was poor for the SSFP (20% of agreement), and good with T2 and T2ρ maps (95% of agreement).

Discussion/Conclusion: Our initial results show that both T2- and T2ρ-maps provide extra information on the health status of knee cartilage, even in absence of morphological evidence of alteration on native 3D images; in particular, T2ρ-maps appeared more sensitive than T2-ones.

784

Quick water-selective imaging of tendons, ligaments and cortical bone: Feasibility of detailed tissue characterization by T2* and magnetization transfer

F. Springer, U. Grosse, R. Syha, C. Schabel, G. Steidle, P. Martirosian, F. Schick
Department Of Diagnostic And Interventional Radiology, Section On Experimental Radiology, University Hospital, Tübingen/GERMANY

Purpose/Introduction: Solid-like tissues (e.g. tendons, ligaments or cortical bone) have short effective transverse relaxation times (T2*) and comprise a rather low spin density. By means of ultrashort echo time (UTE) sequences MR signal even from these tissues can be acquired and provides the possibility to characterize these tissues by their MR-specific properties. To increase contrast to surrounding long-T2 tissues (muscle, fat) various long-T2 saturation strategies have been developed but most of these methods require long pre-saturation pulses or inversion times which are clearly too long for clinical applications [1]. Thus, we developed a quick water-selective (WE) 3D UTE sequence with variabel echo time and additionally implemented an off-resonance saturation pulse for magnetization transfer (MT) imaging [2].
Subjects and Methods: A 1-1 double WE excitation pulse was incorporated into a 3D UTE sequence with centric radial k-space sampling. Two short non-slice-selective rectangular RF pulses (Trf=0.1ms) were implemented with a time interval of 1150µs inbetween to allow a spin dephasing of 180° for methylene spins at 400Hz off-resonance frequency (at 3T). Spoiling was implemented before each WE excitation block to achieve a steady-state only for the longitudinal magnetization. T2* of the investigated tissue was evaluated by TE variation and 2-parameter fitting of the observed mono-exponential signal decay. For MT preparation a Gaussian-shaped off-resonance saturation pulse (Trf=5.12ms, FA=300deg) was implemented before each WE block. The contrast to long-T2 tissues i.e. muscle/fat was optimised analytically for a broad range of relaxation times [2]. Exemplarily, in-vivo measurements of healthy volunteers were performed on a 3T whole-body MR scanner (Siemens Healthcare, Erlangen, Germany) and T2* and MT ratios (MTR) were calculated for a variety of solid-like tissues.
Results: Using the newly developed 3D WE-UTE sequence solid-like tissues could be successfully visualized with improved contrast to surrounding long-T2 tissues. Variation of echo times and implementation of off-resonance saturation pulses allowed for a detailed characterization of MR specific tissue properties (T2*, MTR). Tissues with extremely fast signal decay (T2*<1ms) experience a marked signal decay already during/ inbetween RF pulses resulting in a less efficient WE excitation.

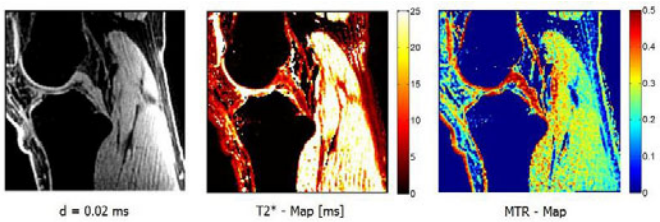

Figure 1: Evaluation (T2*, MTR) of the knee with a 8-channel transmit/receive knee coil: TR=10.3ms, d=0.02-6.02ms, FA=8°, FoV=128mm³, BW=1000Hz, TA=2:09min, 0.8mm isotropic resolution. MT pulse: Gaussian-shaped, 5.120ms duration, FA=300°, 10kHz off-resonance

Discussion/Conclusion: Using the newly developed quick water-selective 3D UTE sequence in combination with additional MT-preparation pulses solid-like tissues with fast signal decay can now be characterized by their MR-specific properties (T2*, MTR) with improved contrast to surrounding long-T2 tissues (muscle, fat) which may help to identify early degenerative changes in clinical examinations.
References:
[1] Du J, 2011, Magn Reson Imaging, 470-82.
[2] Springer F, ISMRM 2012 Melbourne, ePoster 3316.

785

Triple-quantum filtered ^{23}Na imaging using a phased-array receive coil at 9.4T

D.P. Fiege[1], S. Romanzetti[1], F. Boada[2], S.R. Yutzy[2], Y. Qian[2], J. Felder[1], A. Celik[1], N.J. Shah[1]
[1]Inm-4, Medical Imaging Physics, Forschungszentrum Jülich GmbH, Juelich/ GERMANY, [2]Radiology And Bioengineering, University of Pittsburgh, Pittsburgh/PA/UNITED STATES OF AMERICA

Purpose/Introduction: Sodium MRI suffers from a low in vivo SNR. Especially triple-quantum filtering (TQF) methods that differentiate signals from different compartments are low in signal [1]. The use of multi-channel receive coils to improve coil sensitivity is therefore highly desirable. However, this enlarges the raw data significantly and complicates the reconstruction, especially if a B0 correction is performed. In this work we present the workflow and demonstrate imaging results on a phantom at 9.4T.
Subjects and Methods: A phantom comprising two agarose and three sodium concentrations in six compartments was used on a Siemens 9.4T human whole-body scanner (Siemens Medical, Erlangen, Germany). A birdcage transmit, 8 channel receive coil (Affinity Imaging, Jülich, Germany) was employed. The SISTINA sequence [2] was used for imaging (voxel size 5.7mm isotropic, TR=150ms, tau=10ms, delta=40us, TE=0.8/10ms, TA=16 min). A two-times six step phase cycling was employed to correct for B0 inhomogeneities [3,4]. All data were reconstructed off-line in Matlab (The Mathworks, Natick, NA). Figure 1 shows the flowchart of the reconstruction. First, the averages (acquisitions with all parameters equal) are combined. Then, each of the two six-step phase cycles is combined separately. Sum-of-squares addition is used for combining the two cycles and the eight coil channels. The final image then contains all 36 averages.

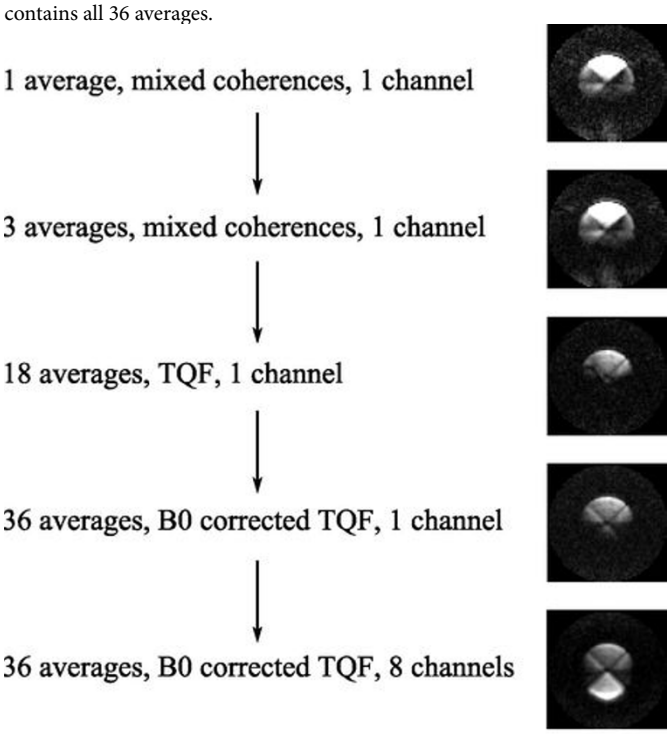

Figure 1: Flow chart of the reconstruction steps. Phase-cycling steps and averages are combined as complex images before sum-of-squares combination of B0 correction and channel combineation.

Results: Figure 2 shows several slices through the phantom. The first slices are dominated by partial volume effects and distortions due to the inhomogeneous field. The centre of the phantom displays very good SNR, however, the intensity drops off towards the edges. The last slices are again dominated by artefacts due to phantom geometry.

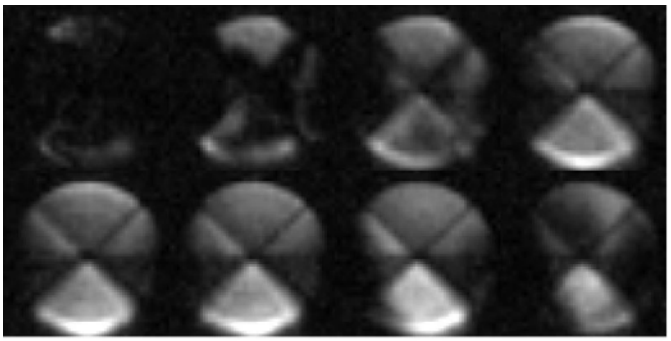

Figure 2: Several slices through the phantom from top (top left) to bottom (bottom right).

Discussion/Conclusion: Triple-quantum filtered sodium imaging at 9.4T using a phased-array coil is feasible. Data combination yields proper TQF images if the steps are carried out in the correct order, i.e. all phase cycling is performed in a complex fashion. The resulting images show promising SNR. Inhomogeneous signal intensity across the phantom could be corrected by correcting for B1+ and B1- profiles.

References:

1. Hancu I, Boada FE, Shen GX. 1999 Magn Reson Med, 1146–1154
2. Fiege DP, Romanzetti S, Mirkes, CC, Brenner D and Shah NJ. Magn Reson Med, in press
3. Fleysher L, Oesingmann N, Inglese M. 2010 NMR Biomed, 1191-1198
4. Matthies C, Nagel AM, Schad LR, Bachert P. 2008, J Magn Reson 239-244

786

MRI phantoms – are there alternatives to agar?

A. Hellerbach, V. Schuster, A. Jansen, J. Sommer
Department Of Psychiatry And Psychotherapy, University Marburg, Marburg/GERMANY

Purpose/Introduction: MR-phantoms are useful for evaluation of system performance, examination of intra-site and inter-site variability and testing of new imaging techniques. There have been several attempts to develop tissue-equivalent MR-phantoms using agarose[1,2],agar[3],carrageenan[4],polyvinyl alcohol(PVA)[5] and polysaccharide(TX-150 and TX-151)[6,7]. Although various types of phantom materials have been suggested, most common are water and agar phantoms. Agar phantoms have the advantage of being less susceptible to vibration. With regard to the construction of diffusion(DTI) phantoms, embedding fibre objects in a gel would be advantageous to reduce artefacts on boundaries and avoid aqueous movements. Agar could be suitable for this, but it needs thermal treatment (80°C-100°C) during preparation and it is not immune to fungi without toxic additives. Therefore the aim of this study was to analyse different gelling agents to provide a new phantom material for embedding fibre phantoms.

Subjects and Methods: We analysed the gelling properties of sodium alginate, xanthan, superabsorbent polymer(SAP) and PNC400 (sodium carbomer). Hydrated gels were simply prepared by mixing the agents with distilled water at room temperature. Concentrations range from 0.1% to 5%. Test phantoms were prepared in autoclaved 500ml propylene containers. Measurements of T1 and T2 relaxation times were made using a 3T MR scanner (Magnetom Trio,Siemens Medical Solutions). A DTI phantom was created by winding polyester fibres on a cylindrical polyamide spindle[8]. The fibre phantom was measured in aqueous and gel environment.

Results: Test gels based on sodium alginate and xanthan did not show any advantages over agar gels. They show a strong bubble formation and gel breakdown. Moreover xanthan is highly susceptible to fungi. Both SAP and PNC400 are immune to fungi, have a short gel setting time and do not need thermal treatment during preparation. Gels based on SAP are very elastic and inhomogeneous whereas PNC400 provides a homogeneous and temporally stable gel. T1 and T2 relaxation times are longer than those of human tissue, but can be adjusted with contrast agents. Advantage of gel for DTI phantoms is visible in figure1B. FA map(B) shows less distortions compared to measurement in aqueous solution(A).

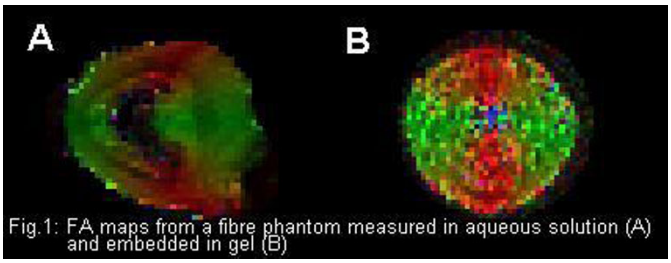

Fig.1: FA maps from a fibre phantom measured in aqueous solution (A) and embedded in gel (B)

Discussion/Conclusion: PNC400 promises to be a good candidate for a new tissue-equivalent MR-phantom material. The gelling agent is easy to handle, inexpensive and it provides a homogeneous and temporally stable gel. The relaxation times can be varied in a wide range, so it is capable of mimicking human tissue.

References:

[1]Mitchell,M.D. et al.,1986,MRI,263-266
[2]Howe,F.A.,1988,MRI,263-270
[3]Mathur-De Vre,R.et al.,1985,MRM,176-179
[4]Yoshimura,K.et al.,2003,MRM,1011–1017
[5]Mano,I. et al.,1986,MRM,921-926
[6]Groch,M.W.et al.,1991,MRI,417-421
[7]Mazzara,G.P. et al.,1996,MRI,639-648
[8]Laun,F.,2009,MRI,541-548

787

Narrow-band artefact correction in multiple-channel acquisitions: application to EEG recorded during fMRI

M.F.P. Leite[1], T.I.G. Murta[1], S. Vullermoz[1], D. Carmichael[1], P.M.P. Figueiredo[2], L. Lemieux[1]
[1]Dcee, ION-UCL, London/UNITED KINGDOM, [2]Dbe, IST, Lisboa/PORTUGAL

Purpose/Introduction: The recording of electroencephalographic data with functional MRI (EEG-fMRI) offers the possibility to study the spatiotemporal dynamics of brain activity. Although well-known artefacts induced on the EEG data by the fMRI acquisition can be largely removed by previously developed techniques[1], additional artefacts are commonly present due to factors of specific scanning environments. We aimed to address this issue by proposing a correction method for multiple-channel data subject to frequency-band limited electromagnetic noise from sources that have coherent amplitudes and phase-differences over time.

Subjects and Methods: The proposed method consists of:

- band-pass filtering the signal in the narrowest band(s) comprising all the artefact frequency components;
- singular-value-decomposition in the channel dimension of the filtered signal;
- averaging of the 1st and 2nd eigenvariates weighted by their singular values, yielding the estimate of the artefact time course;
- calculation of the harmonic conjugate of the estimated artefact using the Hilbert transform; the artefact template consists of the estimated artefact time course and its harmonic conjugate;
- subtraction of the artefact template from the original data.

We applied this method to EEG data acquired simultaneously with fMRI. The EEG was previously corrected for scanner gradient artefacts using the standard methodology [1].

Results: The spectra and time-frequency amplitude profiles for two representative EEG channels affected by an artefact that satisfies the above assumptions are illustrated in Fig.1. One can observe on Fig.2 that the 1st and 2nd eigenvariates display a similar time-frequency amplitude profile, while the 3rd is apparently artefact free. The phase difference between the 1st and 2nd eigenvariates in the artefact-related frequencies is pi/2 (Fig.3).
After artefact template removal, the data appear artefact free with no apparent depression in the spectra between 92.7 and 93.7 Hz (Fig.4), consistent with minimal loss of information.

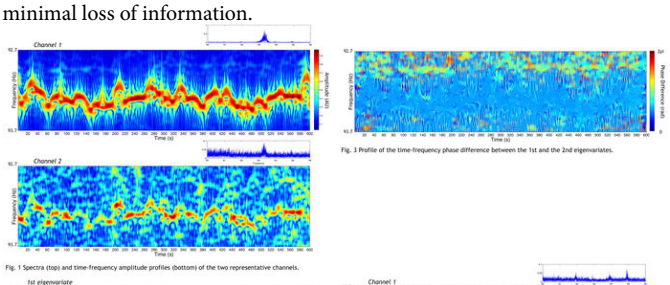

Fig. 1 Spectra (top) and time-frequency amplitude profiles (bottom) of the two representative channels.

Fig. 3 Profile of the time-frequency phase difference between the 1st and the 2nd eigenvariates.

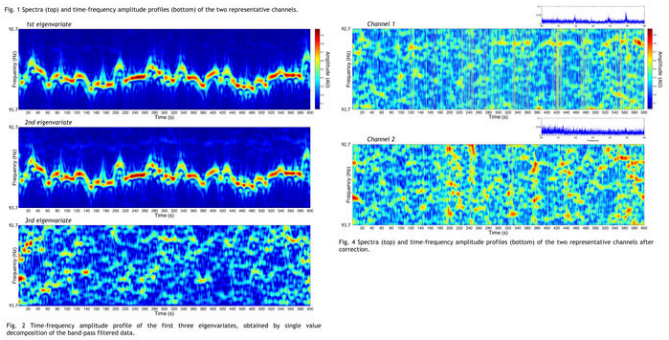

Fig. 2 Time-frequency amplitude profile of the first three eigenvariates, obtained by single value decomposition of the band-pass filtered data.

Fig. 4 Spectra (top) and time-frequency amplitude profiles (bottom) of the two representative channels after correction.

Discussion/Conclusion: The proposed method was able to successfully remove band-limited artefacts with varying frequency content over time, which are coherent but have with different phases across channels, from EEG data acquired simultaneously with fMRI. The correction procedure eliminates one degree of freedom in the channel dimension (average of the 1st and 2nd eigenvariates) and one degree of freedom in the temporal domain (phase estimation) and in this sense is optimal in terms of data loss. Furthermore, this data loss is limited to the frequency band affected by the artefact, which is ensured by the first filtering step in calculating the artefact template.
References:
[1] Allen et al. 2000 NeuroImage 12 pp-230-239

788

The reliability of GABA measurements in phantom and human brain by MRS at 3T

O. Voevodskaia[1], M. Uppman[2], M. Karlsson[3], T. Li[4]
[1]Department Of Applied Physics, Royal Institute of Technology, Stockholm/SWEDEN, [2]Department Of Medical Physics, Karolinska University Hospital, Stockholm/SWEDEN, [3]Siemens Healthcare, Siemens, Upplands väsby/SWEDEN, [4]Department Of Clinical Science, Intervention And Technology, Karolinska Institute, Stockholm/SWEDEN

Purpose/Introduction: ^{1}H MRS is a non-invasive technique that allows metabolic quantification inside the human body. GABA (γ-aminobutyric acid) is the primary inhibitory neurotransmitter in the central nerve system. Altered levels of GABA are associated various neurological and psychiatric disorders, e.g. schizophrenia [1] and epilepsy. The resonance frequencies of GABA overlap with other metabolites, resulting in uncertainty of GABA measurements using standard MRS techniques. The aim of our study was to implement the MEGA-PRESS sequence, optimize the acquisition protocol, and develop a post-processing routine for the quantification of GABA.
Subjects and Methods: To improve GABA detection, the MEGA-PRESS sequence [2] based on J-difference editing was implemented on a Siemens 3 T clinical MRI scanner. Brain phantoms with 3.9 and 7.8 mM GABA were measured. TE, TR, voxel size, number of measurements and selective frequency/bandwidth of the MEGA-pulses were varied for optimization. The *in-vivo* study involved 8 healthy volunteers (male/female=6/2, age=27.9±6.1). An in-house program based on MATLAB was used for post-processing of the time-domain raw data.
Results: As expected, the phantom study showed a twofold increase in GABA signal between the 3.9 and 7.8 mM phantoms. Voxel size and the number of measurements had only minor effects on the accuracy of the phantom measurements (Tables 1 and 2). However, the technique can only yield about 50% of the available signal at 3T, as reported previously [3]. Optimal acquisition parameters were established as follows: TE/TR=72ms/2500ms and selective pulse at 1.8 ppm relative water with FWHM of 0.9 ppm, which was used for the *in-vivo* study. The NAA/GABA ratio measured *in-vivo* was 0.24±0.05 (mean±std).

Table1: Quantification of GABA relative to NAA in the 3.9 mM phantom.

	NAA/GABA
Actual ratio	0.31
128 measurements	0.15
256 measurements	0.15
512 measurements	0.13

Table2: Quantification of GABA relative to NAA in the 7.8 mM phantom.

	NAA/GABA
Actual ratio	0.62
15x15x15mm^3	0.35
20x20x20mm^3	0.29
30x30x30mm^3	0.30

Discussion/Conclusion: Careful shimming to minimize the magnetic field inhomogeneities is crucial for GABA quantification using the MEGA-PRESS sequence. The phantom studies demonstrated robust results independent of voxel size and number of measurements. *In-vivo* studies are less reliable due to various effects, such as, inter-subjects variability, GABA concentration distribution, and motion artifacts, in addition to the imperfect shimming effect. It is preferable to achieve FWHM <15 Hz. We are currently conducting studies involve epilepsy patients.
References:
[1] Ongür D., 2010, Biol Psychiatry, (7):667-70
[2] Mescher M., 1998, NMR Biomed, (11):266-272
[3] Kaiser L.G, 2008, NMR Biomed, (21):22-32

Paper Poster

Vascular and perfusion

789

Automatic Segmentation and Analysis of Carotid and Middle Cerebral Artery using Black-Blood 3D Variable Flip Angle FSE (CUBE) MRI

C. Zhu, A.J. Patterson, M.J. Graves, J.H. Gillard
University Department Of Radiology, University of Cambridge, Cambridge/ UNITED KINGDOM

Purpose/Introduction: Atherosclerotic plaques presenting within extra- and intra-cranial arteries are known to be risk factors for subsequent stroke. High resolution carotid vessel wall MRI can visualize high-risk morphologic factors of plaques in vivo and help patient risk stratification [1]. 3D imaging approaches are promising for its large coverage and high SNR efficiency [2]. 3D FSE acquisitions use variable-flip-angle refocusing pulses to maintain signal over a longer ETL, and have been shown to demonstrate a high signal-to-noise ratio (SNR) efficiency as well as intrinsic black-blood effects compared with conventional 3D FSE sequences [3]. Motion-sensitized driven-equilibrium (MSDE) provides better blood suppression than traditional inflow saturation(IS) and double inversion-recovery (DIR) methods [4]. Automatic segmentation methods applied to 3D FSE allow morphologic quantification of atherosclerotic plaques. This study aims to investigate the automatic segmentation and analysis of carotid and middle cerebral artery (MCA) using such 3D FSE sequence combined with MSDE blood suppression.

Subjects and Methods: Two healthy volunteers and one patient with >30% carotid stenosis indentified by ultrasound underwent black-blood 3D FSE (CUBE, GE, modified to incorporate MSDE blood suppression) of the carotids in a 1.5T GE MRI system using a 4-channel phased-array neck coil . One healthy volunteer underwent 3D black-blood CUBE of the MCA using a standard 8-channel head coil. T1w and T2w CUBE for carotid: TR/TE(T1):440ms/10.8ms; TR/TE(T2):1800ms/58.9ms; 0.625mm*0.625mm in-plane-resolution, 1.2mm slice thickness. T2w CUBE for MCA: TR/TE=2500ms/79.6ms; 0.75mm*0.75mm in-plane-resolution, 1.2mm slice thickness. The lumen boundary of the carotid and MCA were automatically segmented by in-house MATLAB software and reconstructed using the vascular toolkit (VMTK[5]). 3D geometry and central lines of the arteries were generated automatically. Diameter and area stenosis was automatically calculated using in-house software. Automatic reformatted 2D images which were perpendicular to the vessel central lines were generated using VTK.

Results: Strong black-blood effect and good image quality were achieved in both the MCA (Figure.1) and carotid (Figure.2) by 3D MSDE CUBE MRI. Arterial geometry was successfully segmented and measures of stenosis were derived. Reformatted 2D images which were perpendicular to the central lines were successfully generated, which clearly showed the actual plaque burden.

Figure.1

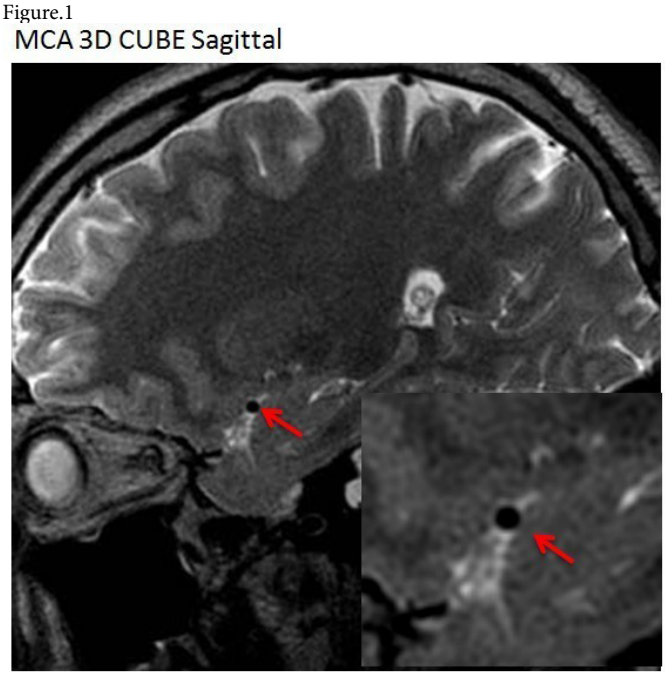

Figure.2

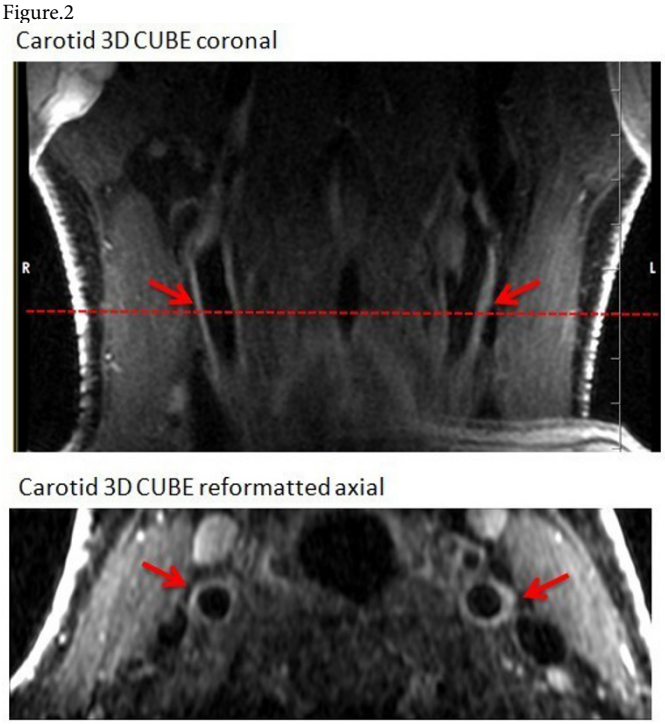

Discussion/Conclusion: Automatic segmentation and analysis using 3D MSDE CUBE MRI can favour the morphologic quantification of carotid and middle cerebral artery.

References:

1. Underhill et,al. *Nat Rev Cardiol* 2010;7(3):165-73.
2. Balu et,al. *J Magn Reson Imaging* 2008;27(4):918-24.
3. Busse et,al. *Magn Reson Med* 2008;60(3):640-9.
4. Wang et,al. *J Magn Reson Imaging* 2010;31(5):1256-63.
5. www.vmtk.org.

790

Correlation of Intravoxel Incoherent Motion MR Imaging with dynamic contrast-enhanced MRI in brain tumors

M. Schneider, M. Ingrisch, B. Ertl-Wagner, M. Reiser, O. Dietrich
Institute For Clinical Radiology, Ludwig-Maximilians-University Hospital Munich, Munich/GERMANY

Purpose/Introduction: Intravoxel incoherent motion (IVIM) MRI can be used to obtain information about tissue microcapillary perfusion properties based on diffusion-weighted acquisitions[1]. The validity of this information remains controversial due to technical and methodological difficulties. Therefore, we compare perfusion-related parameters obtained by IVIM measurements with cerebral blood volume and flow (CBV,CBF) retrieved from dynamic-contrast-enhanced (DCE) MRI[2,3] in tumorous and normal-appearing brain tissue.
Subjects and Methods:

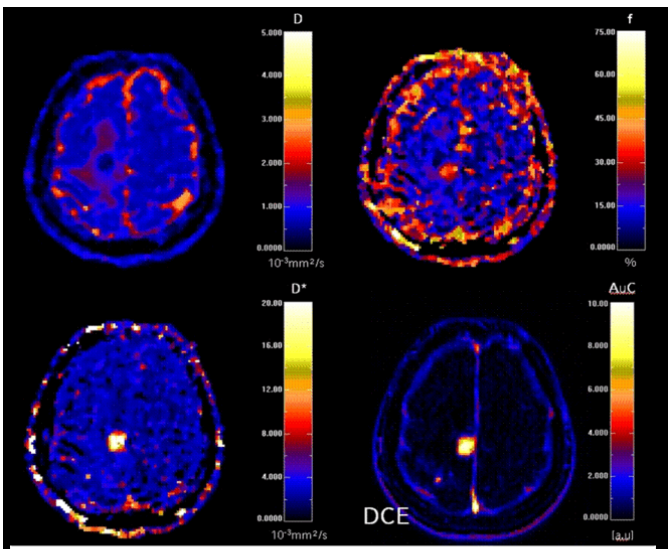

Fig.1: Comparison of voxel-wise calculated parameter maps from IVIM measurements with DCE area-under-the-curve map

6 patients with brain tumors were examined on a 3-Tesla whole-body MRI system. IVIM measurements were performed with a single-shot EPI sequence (spatial resolution 1.7×1.7×3mm³ (20slices), TR/TE=5000/60ms, 3 averages, 10 b-values (0-1000s/mm²)). Subsequently, the patients underwent DCE-MRI using an view-sharing 3D gradient-echo sequence (TE/TR=0.86/2.29ms) acquiring 200 volumes after double-bolus injection of 0.1mmol/kg Gadobutrol (temporal resolution 2.1s, spatial resolution 2×2×3mm³). Regions of interest (ROIs) were placed in tumorous tissue (excluding necrosis) and normal-appearing brain tissue. The IVIM parameters *D* (tissue diffusivity), *f* (perfusion fraction) and *D**(pseudo diffusivity) were determined by fitting the data to a biexponential model[1]. DCE data was analyzed with a 2-compartment exchange (2CX), uptake (2CU), and Tofts (2CT) model[2,4]; for each ROI, the most appropriate model was selected with the Akaike Information Criterion[3].
Results: Median values and standard deviations of IVIM and DCE parameters are presented in Table1; Table2 shows Pearson's correlation coefficients and their p-values. IVIM parameter maps display similar features as DCE-MRI area-under-the-curve maps (Fig.1).

Table1: Median values(±standard deviation) of IVIM and DCE parameters

	f [%]	*D*[mm²/10³s]	*D**[mm²/10³s]	CBV [ml/100ml]	CBF [ml/100ml/min]
Tumorous tissue	18.82±4.61	0.97±0.19	3.63±0.63	3.14±1.96	32.59±22.63
Normal appearing tissue	10.68±2.12	0.67±0.08	3.09±0.36	0.56±0.19	8.58±16.97

Table2: Pearson's correlation coefficients (and p-values) between IVIM and DCE parameters

	D	f	*D**	f×D*
CBV	**r=0.558;p=0.0106**	**r=0.606;p=0.0046**	**r=0.495;p=0.0266**	**r=0.759;p=0.0001**
CBF	**r=0.513;p=0.0206**	**r=0.661;p=0.0015**	r=0.214;p=0.3643	**r=0.669;p=0.0013**

Discussion/Conclusion:

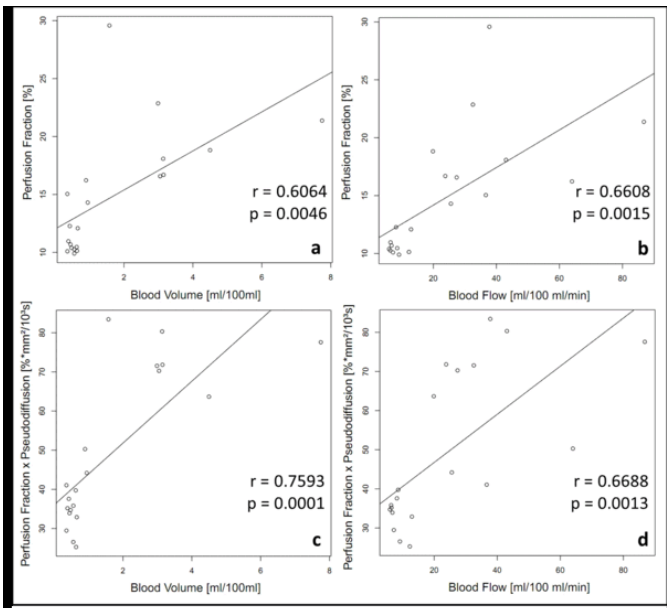

Fig.2: Correlation between *f* and CBV (a); *f* and CBF (b); the product *f*×*D** and CBV (c); *f*×*D** and CBF (d)

The IVIM perfusion fraction *f* correlates well with CBV and CBF (Fig.2), indicating that IVIM yields perfusion-related information. The fact that there is no significant correlation between *D** and CBF suggests that the CBF increase in the examined tumors is rather due to a higher capillary count than increased blood velocity. The product *D**×*f*, which reflects a "makeshift flow"[5], correlates best with both CBV and CBF (Fig.2) and is therefore likely to be the best indicator for tissue-perfusion changes.
References:
[1]Le Bihan D et al. Radiology 1988;168:497-505,[2]Sourbron et al. MRM 2009;62:205-217,[3]Glatting G et al. Med Phys 2007;34:4285-4292,[4]Ingrisch M et al. Invest Radiol 2012;47:252-258,[5]Le Bihan&Turner MRM 1992;27:171-178.

791

Sampling requirements in DSC-MRI

K.M. Bakke, A. Bjørnerud
The Intervention Centre, Oslo University Hospital, Oslo/NORWAY

Purpose/Introduction: Dynamic Susceptibility Contrast(DSC) is based on the tracing of an intravascular bolus of contrast agent(CA) with a sampling time(Ts) fast enough to capture the CA bolus passage; the order of a few seconds in most tissues. Measuring hemodynamic parameters from DSC images requires deconvolution that includes a regularization. Regardless of method, regularization acts as a low-pass filter with loss of high frequency components in the estimated tissue residue function. Regularization thus leads to a reduction in the effective sampling requirement of the input data.
Purpose: To systematically estimate sampling requirements in DSC-MRI based on simulations and clinical data.
Subjects and Methods: Simulations: A gamma-variate shaped arterial input function(AIF) was convolved with an exponential residue function. Fixed values of Cerebral Blood Flow(CBF)=50ml/100g/min and Mean Transit Time(MTT)=4s was used. After adding Gaussian noise, the curves were downsampled and deconvolved using truncated SVD[1] (0.2 threshold), and CBF was estimated.
Patient data: DSC data with a nominal Ts=1.5s from 101 patients were downsampled by consecutive averaging to yield datasets with Ts=3.0s, 4.5s and 6.0s. CBF-maps were generated using truncated SVD, and average CBF in unaffected white matter(WM) was compared in the downsampled, to the reference(Ts=1.5s) images.
Results: Figure 1 shows mean, normalized CBF from 500 simulations as a function of Ts. Increasing Ts has little effect on CBF for Ts<3s. Figure 2 and 3 shows mean CBF(WM) in 101 patients at Ts=3.0s and 4.5s, compared to Ts=1.5s, confirming the minimal effect on CBF at Ts-values <=3s. Figure 4 shows CBF-maps generated at all Ts-values in a sample patient.

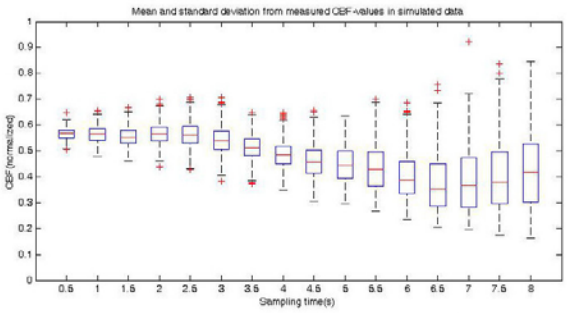

Figure 1: Mean, normalized CBF-values from 500 simulations as a function of sampling time.

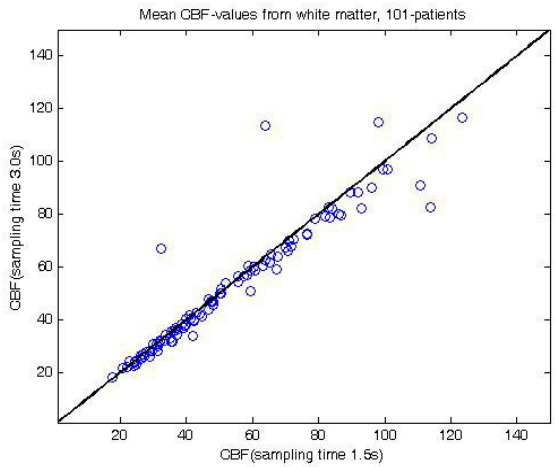

Figure 2: Mean white matter CBF-values for 101 patients, comparing 3.0s to 1.5s sampling time.

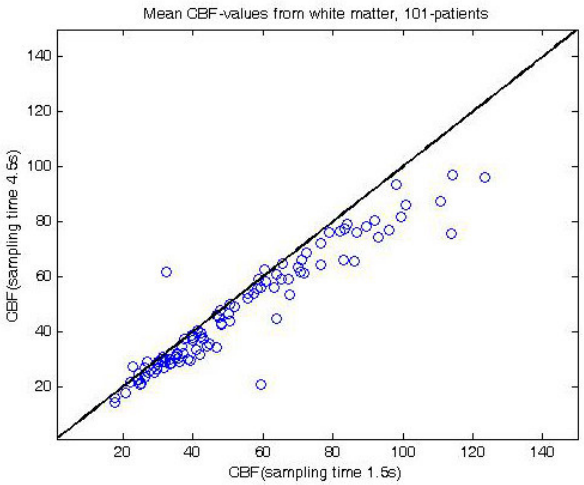

Figure 3: Mean white matter CBF-values for 101 patients, comparing 4.5s to 1.5s sampling time.

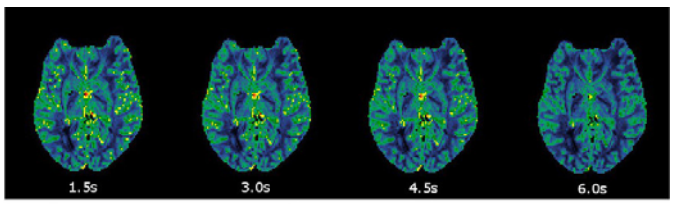

Figure 4: CBF-maps from a sample patient at all TS-values.

Discussion/Conclusion: The temporal sampling requirement in cerebral DSC-MRI may be lower than expected from tissue MTT alone, due to the low-pass effect induced by regularization. We found CBF-estimates to be almost independent of sampling time for Ts-values between 0.5-3.0s, whereas higher Ts-values caused increasing CBF-underestimation; a result confirmed in clinical DSC data. Sampling requirements will to some extent depend on regularization method and threshold, as well as actual tissue MTT, but since tumor and vascular pathology typically leads to an increase in MTT relative to WM[2], our results should be indicative of the lower limit of Ts required in clinical DSC-MRI in the brain.
Conclusion: A sampling time of 3s was found to be adequate for DSC-MRI in the brain. Longer sampling times lead to increasing CBF-underestimation.
References:
[1] Østergaard, L. et al., 1996, Magn. Reson. Med., 715–725.
[2] Bjørnerud, A. et al., 2011, J. Cereb. Blood Flow Metab., 2041- 2053.

792

Effects of percutaneous transluminal angioplasty on muscle perfusion in patients with peripheral arterial occlusive disease: preliminary results.

G. Grözinger
Department Of Diagnostic And Interventional Radiology, University Hospital Tübingen, Tuebingen/GERMANY

Purpose/Introduction: The aim was to evaluate the effect of percutaneous transluminal angioplasty (PTA) of the superficial femoral artery (SFA) or the iliac artery (IA) on the perfusion of the calf musculature of patients with intermittent claudication.
Subjects and Methods: Eight patients (mean age, 65.2+/-9.6 years) with symptomatic peripheral arterial occlusive disease (PAOD) caused by SFA or IA stenosis were investigated before and after PTA. Patients underwent MRI perfusion measurement 1 to 5 days before and 4 to 6 weeks after PTA. A T2*-weighted pseudo-continuous Arterial Spin Labeling (pcASL) echo-planar MR-imaging technique was applied. Sequence parameters were as followed: Labeling time (TL)1200ms, Postlabeling delay (LD) 1400 ms, Echo time (TE) 19 ms, TR 2750 ms, Matrix: 64x64, slice thickness 8mm. As tag and control

scans were acquired responsively the effective temporal resolution was 5.5 seconds. Absolute values of perfusion were calculated using a modified Bloch-Equation. The perfusion measurements were acquired at mid-calf level during reactive hyperemia at 3 T. This transient hyperperfusion of the muscle tissue was provoked by 5 minute suprasystolic cuff compression. Soleus muscle was evaluated. Data from the eight patients was pooled for data analysis. Key parameters describing the perfusion signal curve included maximum perfusion (P_{max}), time-to-peak to reach maximum perfusion (TTP) and Duration of hyperemia (T_{hyp}). Paired t-tests were applied for statistic comparison.
Results: Between baseline and post-PTA, P_{max} increased from 85 +/-40 ml/(100g x min) to 245 +/- 101 ml/(100g x min), ($p<0.05$). In cumulative data TTP decreased from 49.5s to 16.5s. Duration of hyperemia decreased from 82.5s to 55s.

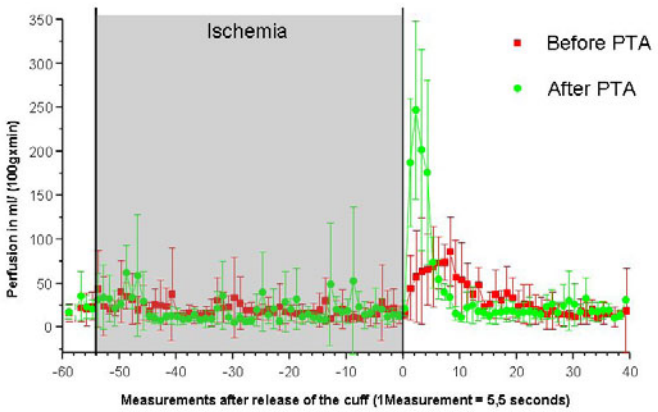

Discussion/Conclusion: In conclusion, pcASL-MRI reveals changes of the key parameters P_{max}, TTP, and T_{hyp} after successful PTA of the calf muscles during reactive hyperemia and seems to be a promising tool for monitoring of an interventional treatment.

793

Assessment of mono-exponential model with Pseudo Continuous ASL data

M. Castellaro[1], I. Boscolo Galazzo[2], D. Peruzzo[1], F. Arrigoni[3], F. Triulzi[4], A. Bertoldo[1]
[1]Department Of Information Engineering, University of Padova, Padova/ITALY, [2]Department Of Neurological, Neuropsychological, Morphological And Movement Sciences, Section Of Clinical Neurology, University of Verona, Verona/ITALY, [3]Neuroimaging Unit, Scientific Institute IRCCS Eugenio Medea, Bosisio Parini (LC)/ITALY, [4]Neuroimaging Unit, Fondazione IRCCS Ca' Granda, Ospedale Maggiore Policlinico, Milano/ITALY

Purpose/Introduction: The quantification of Cerebral Blood Flow (CBF) with Pseudo Continuous Arterial Spin Labeling (pCASL) [1] usually assumes a mono-exponential model [2], whose amplitude includes contributes that can be estimated or fixed to literature values. The decay of the exponential comprehends the T_1 decay of the magnetized blood (T_{1b}), provided the assumption that the post delay time (PDT) is long enough [2]. The aim of our study was to assess the range of reliability of the assumptions frequently used in the mono-exponential model.
Subjects and Methods: We performed a multi-PDT pCASL acquisition on a 3T Philips Achieva with a 32-channels coil in 6 healthy controls (TR/TE=5000/16ms, 6 slices, label duration 1.65s, PDT from 1210ms up to 2810ms with step of 200ms). To evaluate the reliability of a mono-exponential model in describing the data in the range of validity of the PDT assumption, we fitted both a generic mono-exponential and a bi-exponential model to the pCASL data acquired using a nonlinear least squares estimator. We selected the best model on the basis of the Akaike Information Criteria (AIC). Afterwards, we investigated the validity of assuming a literature constant value for the exponential decay in both gray (GM) and white matter (WM).
Results: The mono-exponential model results the best in the large majority of voxels (95%). The estimates for the decay term show a non-uniform distribution in the whole brain 0.89±0.51 (median±sd), in GM 0.84±0.46 and in WM 1.14±0.58 (Fig. 1). This indicates that the common assumption of fixing the exponential term to the T_{1b} decay value [2,3] is prone to introduce a significant bias in CBF estimates. Indeed, by fixing the exponential term to T_{1b}, the estimates obtained for the amplitude term, which is proportional to the CBF, are significantly different ($p<.05$) from the previous ones for each subject. Moreover, the distribution of the ratio between the two estimated amplitudes, which reflects the bias on CBF estimation, is 1.87±5.34 (Fig. 2).

Fig. 1 - Distributions of the decay of the mono-exponential model

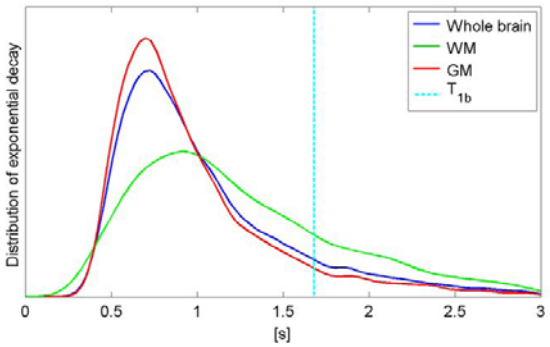

Fig. 2 - Box plot of the distribution of the ratio of the amplitudes

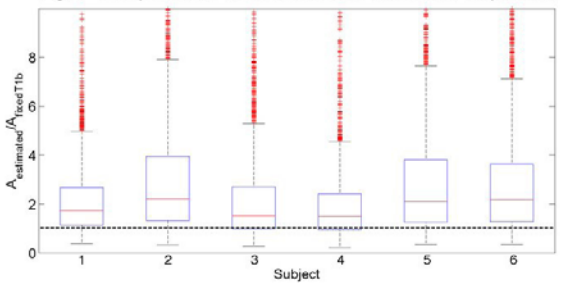

Discussion/Conclusion: Our study confirms that the best model to describe pCASL multi-PDT data when PDT>1200ms (i.e. the bolus arrival time) is a mono-exponential model. The decay term is non-uniform in the whole brain. Furthermore, our findings show that using a fixed T_{1b} decay for pCASL data causes amplitude estimation error and, consequently, biased CBF estimation.
References:
[1] Dai W.Y. et al., 2008, MRM, 60:1488–1497
[2] Alsop D.C. et al., 1996, JCBFM, 16:1236-49
[3] Wang J. et al., 2005, Radiology, 235:218-28

794

Single post-labeling versus multi post-labeling pCASL: evaluation of differences in cerebral blood flow estimation

I. Boscolo Galazzo[1], M. Castellaro[2], D. Peruzzo[2], F. Arrigoni[3], F. Triulzi[4], A. Bertoldo[2]
[1]Department Of Neurological, Neuropsychological, Morphological And Movement Sciences, University of Verona, Verona/ITALY, [2]Department Of Information Engineering, University of Padova, Padova/ITALY, [3]Neuroimaging Unit, Scientific Institute IRCCS Eugenio Medea, Bosisio Parini (LC)/ITALY, [4]Neuroimaging Unit, Fondazione IRCCS Ca' Granda, Ospedale Maggiore Policlinico, Milano/ITALY

Purpose/Introduction: Arterial spin labeling (ASL) has become a valuable technique for cerebral blood flow (CBF) quantification. Its newly proposed method, pseudo-continuous ASL (pCASL), provides higher SNR and labeling efficiency compared to conventional sequences [1].
pCASL images are typically acquired at a single post-labeling delay (PLD), which becomes the crucial parameter [2].

In this study, we aimed to select the best PLD for pCASL and to evaluate the differences incurred in perfusion quantification even when using the optimum single PLD, by comparing CBF values from a multi PLD pCASL acquisition.

Subjects and Methods: Six healthy volunteers (26÷32 years, M/F=3/3) were scanned on a Philips 3T Achieva with a 32-channel head coil. pCASL parameters were: TR/TE=5000/16ms, 6 slices, 1650ms labeling and 9 delay times covering the interval 1210-2810ms with steps of 200ms.

The mono-compartment model published in [3] was assumed for the voxelwise CBF estimation by using the multiple PLD data set (CBF_{multi}) as well as single PLD point separately (CBF_{single}).

The root mean square error (RMSE) between the multi pCASL data and the model prediction with single PLD point estimates was calculated for gray and white matter (GM,WM) and compared to find the PLD which minimized RMSE. The ratio CBF_{single}/CBF_{multi} was also assessed to evaluate under/overestimation with the single PLD approach.

Results: Fig.1 shows the RMSE curves with PLD≥1200ms, i.e. the range of validity of the mono-exponential model. In 5/6 subjects the minimum is reached for PLD=1410ms (1/6 PLD =1610ms), while PLDs≥2000ms lead to a worse CBF_{single} estimation.

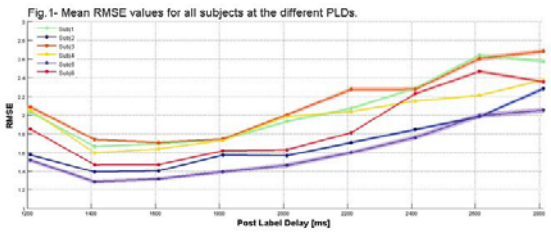

Boxplot (fig.2) shows the CBF ratios, using the optimal PLD to estimate the CBF_{single}: the average values among all subjects are 0,64±0,2 and 0,5±0,3(mean±std) for GM and WM respectively. This corresponds to a marked understimation of CBF_{single} values (~30%GM and ~50%WM), due to the fact single point data are assumed in the identification process without measurement error.

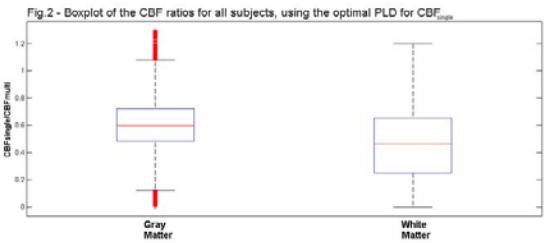

Discussion/Conclusion: Using the information from multi PLD data and analyzing separately each single point, we derived a procedure to identify the optimal PLD for a given sequence setup. We suggest for a 3T scanner a PLD range of 1400-1600ms. Ratio values<1 indicate that, even at the optimal PLD, the single point approach leads to a marked underestimation of CBF that has to be considered especially in clinical practice.

References:

[1] Dai W et al., 2008, MRM, 60:1488-1497
[2] Wang J et al., 2002, MRM, 48:242-254
[3] Alsop DC et al., 1996, JCBFM,16:1236-1249

795

Perfusion changes in response to hypercapnia in free breathing or ventilated C57Bl/6 mice.

T. Dresselaers[1], S. Caers[1], T. Struys[2], A. Van Santvoort[1], U. Himmelreich[1]
[1]Biomedical Mri Unit / Mosaic, Imaging And Pathology, KULeuven, Leuven/ BELGIUM, [2]Biomedical Research Institute, Department Of Functional Morphology, Lab Of Histology, University Hasselt, Hasselt/BELGIUM

Purpose/Introduction: Regional cerebral perfusion is relevant for the evaluation of mouse models of human diseases and their relation to vascular disorders. Arterial spin labeling (ASL) provides a means for quantifying cerebral blood flow (CBF) in a noninvasive and longitudinal manner. Recent ASL applications in mice include models of stroke [1] and Alzheimer's disease [2]. Besides basal flow, the increase in CBF to a hypercapnic challenge might be a more sensitive marker of vascular defects. In this study, we determined the reproducibility of a pulsed ASL protocol and the impact of different anesthetics on the cerebral vascular response (CVR) in mice.

Subjects and Methods: C57J/BL6 mice (9 weeks) were scanned in a 9.4T/200 Biospec (Bruker) using a 7cm linearly resonator and an actively-decoupled surface coil. Perfusion maps were recorded using a FAIR protocol (10 TI: 300-3000ms) with RARE readout. A dynamic ASL protocol was also used during the challenge (TI 1500ms). Animals were scanned under free breathing conditions (two sessions within 1 week) or ventilated [3] with either isofluorane anesthesia or a ketamine/xylazine mixture (muscle relaxant rocuronium/pancuronium), respectively. Hypercapnia was induced by either exposure to 5%CO2/95%O2 or a hypoventilation procedure.

Results: CBF values were similar for both free breathing sessions: mean difference = 16 ± 27, 9 ± 22, 10 ± 37 ml/100g/min (n=6), for cortex, hippocampus and thalamus, respectively. The inter-observer variability was similar: 0.1 ± 6.0, -4.5 ± 9.6 and -0.2 ± 3.6 ml/100g/min (order as above). A 5%CO2 challenge under free breathing isofluorane anesthesia did not elicit a reproducible increase in CBF. A similar observation was made in the ventilated group under isofluorane anesthesia. Under ketamine-xylazine anesthesia an increase in CBF was observed during both the carbogen as during the hypoventilation challenge (fig1).

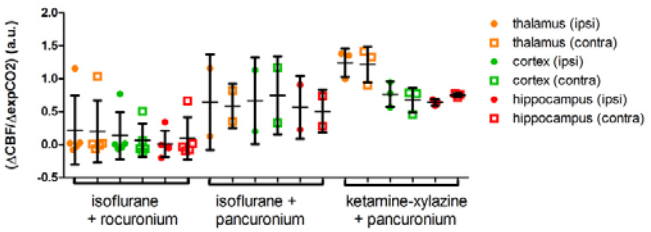

Fig1.Effect of anesthesia on the cerebral vascular response (CVR)

Discussion/Conclusion: The reproducibility in CBF levels of two sessions was good with only 10-13% variability. This variability could partly be explained by the limited resolution and the difficulty of accurately delineating the different regions as evident from the inter-observer variability. A reproducible vascular response was mostly absent under isoflurane, likely due to the vasodilating effect of this anesthetic. For the ketamine/xylazine anesthesia, reproducible CBF and CVR levels were found in good agreement with a previous study using urethane and alpha-chloralose as anesthetics [3].

References:

1. Thomas D.L., JMRI 2005. **22**(6): 741-744.
2. Mueggler T., et al. J. Neurosc. 2002. **22**(16): 7218-7224.
3. Oosterlinck, W.W., et al., MRM 2011. **66**(3): 802-811.

796

Investigation of an Experimental Determination of Labeling Efficiencies for Perfusion Measurements with Pseudocontinuous Arterial Spin Labeling

S. Rüfer[1], M. Helle[2], A. Woehner[1], O. Jansen[1]
[1]Institute Of Neuroradiology, University Hospital Schleswig-Holstein, Kiel/GERMANY, [2]Innovative Technologies Research Laboratories, Philips Technologie GmbH, Hamburg/GERMANY

Purpose/Introduction: Perfusion measurements based on ASL enable the calculation of cerebral blood flow (CBF). A crucial parameter is the labeling efficiency α as it is directly related to perfusion signal [1]. Efficiency could be influenced e.g. by field inhomogeneities, flow velocity or susceptibility effects [2]. For perfusion quantification, α is often derived from simulations not taking into account such influences. Recently, a method for experimental determination of the efficiency of pCASL was introduced [3]. We applied this method to superselective pCASL [4], comparing the results to numerical simulations.

Subjects and Methods: In 12 healthy volunteers, labeling efficiencies in 17 ICAs were determined according to [3] using labeling excitation of superselective pCASL on a Philips 3T Achieva. In addition, efficiency was measured for all vessels simultaneously with non-selective pCASL. A single image slice was positioned 2.5cm above the labeling plane and acquisition started immediately after excitation. Sequence parameters: voxel size 0.8x0.8x8mm3, segmented EPI readout, TR=850ms, TE=6.4ms, Matrix 320x320, labeling duration 1.65s, scan time 2:15min/vessel. Efficiencies were calculated pixel wise by complex subtraction from magnetization signal. To obtain mean values, manually drawn ROIs were placed on the target artery using reasonable thresholds avoiding partial volume effects.

Numerical simulations of the inversion efficiency, based on Bloch equations, were performed for comparison purposes.

The measured efficiencies were investigated in a second experiment by moving the labeling spot from the targeted ICA by offsets of 1-6mm in 7 volunteers, and compared to simulation results.

Results: The mean efficiency for 17 ICAs is $\alpha_{ICAs,s}$=0.65±0.07 for selective and $\alpha_{ICAs,ns}$=0.70±0.05 for non-selective excitation, and the values range from 0.51-0.78. The simulated values are $\alpha_{sim,s}$=0.61 and $\alpha_{sim,ns}$=0.82 (Fig.1).

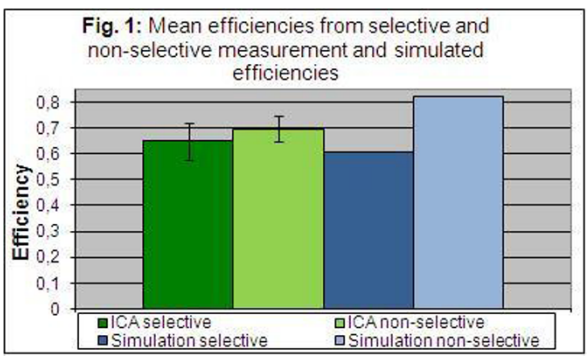

Fig. 1: Mean efficiencies from selective and non-selective measurement and simulated efficiencies

A paired t-test verifies, that efficiencies measured selectively or non-selectively differ significantly for ICAs ($p<0.001$).

The mean efficiencies for the experiment and the simulated efficiencies decrease for increasing offsets from the target artery (Fig.2).

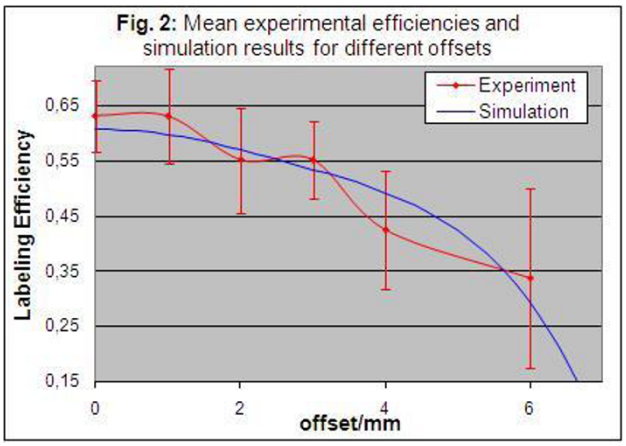

Fig. 2: Mean experimental efficiencies and simulation results for different offsets

Discussion/Conclusion: The range of measured efficiencies shows variations between persons and arteries due to differing labeling locations, artery diameters, physiologic conditions or even subject motion. Especially for selective measurements the mean efficiency is reduced compared to non-selective simulations so that simulated values usually used for quantification [5] may result in an underestimation of CBF. Our simulations, especially those in Fig. 2 show good agreement with experiments, but may be compared to other methods like [2] for further evaluation of the results.

References:

1. van Osch,2009,MRM,62,165-173
2. Aslan,2010,MRM,63,765-771
3. Jahanian,2011,NMRbiomed,24,1202-1209
4. Helle,2010, MRM,64,777-786
5. Wu,2007,MRM,58,1020-1027

Clinical Review Poster

Animal studies

797

BSA-USPIO enhanced atherosclerotic plaque MRI: A surrogate complex to mimic Gadofluorine enhanced fibrous plaque detection?

P. Opriessnig[1], G. Almer[2], D. Frascione[2], R. Prassl[2], H. Mangge[3], R. Stollberger[1]
[1]Institute Of Medical Engineering, Graz University of Technology, Graz/AUSTRIA, [2]Institute Of Biophysics And Nanosystems Research, Austrian Academy of Sciences, Graz/AUSTRIA, [3]Clinical Institute For Medical And Chemical Laboratory Diagnosis, Medical University of Graz, Graz/AUSTRIA

Introduction: Atherosclerosis is a chronic inflammatory disease of the arterial walls, ending in clinical manifestations. Gadolinium chelates and iron oxide probes represent the two major families of MR contrast agents, both successfully applied in atherosclerotic plaque MRI. Whereas the latter one is recognized as safe, a possible association between nephrogenic systemic fibrosis and gadolinium based agents is supposed [1]. Gadofluorine, a gadolinium based blood pool agent, exploits the altered vascular permeability of injured regions and albumin as vehicle to penetrate the lesion and bind to several extracellular matrix constituents within the extracellular space of the fibrous plaque [2]. Ultrasmall superparamagnetic iron oxides (USPIOs) employed as surrogate marker for plaque inflammation [3] were successfully functionalized for Vascular Cell Adhesion Molecule (VCAM)-1 [4]. The purpose of this preliminary study was to investigate whether fibrous plaque detection by Gadofluorine can be translated to iron oxide nanoparticles coated with bovine serum albumin (BSA).
Cases: Rabbits fed a western diet or normal chow underwent a baseline and 24h post contrast measurement of the descending thoracic aorta including a dark blood multi-contrast protocol on a human 3Tesla platform. Equivalent doses of 50umol/kg b.w. Gadofluorine P (n=5) and 40-50umol Fe/kg b.w. (n=2) were administered intravenously.
The *Gadofluorine P experiments* revealed for the WT/NZW/WHHL a change in rSI of 2/4/30% in the normal chow group and an rSI change for the NZW/WHHL of 30, 78% in WD group (Figure 1). The *BSA-USPIO experiments* revealed for the NZW on normal chow no alteration (4%) whereas the NZW on WD showed a 16% reduction (Figure 2).

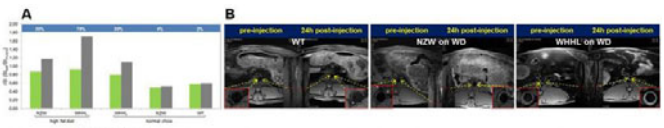

Figure 1. Gadofluorine P enhanced T1w plaque MRI of the descending thoracic aorta. **panel A:** bar plot displays semi-quantitative rSI of rabbit walls at baseline and post infusion time points either fed a normal chow or WD. rSI = SI_{wall} / SI_{muscle}; *blue bar*: rSI_{change} = rSI_{post} - rSI_{pre}; WT, NZW, WHHL on normal chow: 2, 4, 30% change; NZW, WHHL on WD: 30, 78% change. **panel B:** T1w pre and post infusion images. WD, western diet (cholesterol rich diet); WT, wild type; rSI, relative signal intensity.

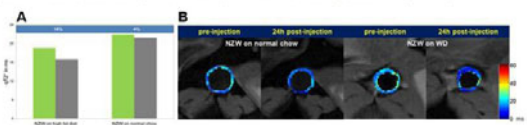

Figure 2. BSA-USPIO enhanced meGRE plaque MRI of the descending thoracic aorta. **panel A:** bar plot displays quantitative T2* relaxation times of rabbit walls at baseline and post infusion time point *either* fed a normal chow or WD. *blue bar*: $qT2^*_{change}$ = $qT2^*_{post}$ / $qT2^*_{pre}$. NZW on WD: 16% change and NZW on normal chow 4% change. **panel B:** $T2^*w$ pre and post infusion images superimposed with wall $T2^*$ maps.

Discussion: *Gadofluorine-P enhanced MRI* clearly reveals an accumulation in all cases of pathological transformed vessel walls. Furthermore, the accumulation of the contrast agent in injured walls is animal model and diet dependent. WHHL without dietary triggering exhibit similar enhancement behaviour as do NZW on WD. The *BSA-USPIO experiments* show a disease induced uptake of the complex in the wall mediated by the particles albumin surface. An increased selective migration into the vessel wall similar to Gadolfuorine-P is supported by the fact that in a preliminary investigation [5] a four-fold higher dosage of glycin saturated control particles was required to achieve a comparable drop in vessel wall signal.

References:
[1] Kei, PL, 2008, Singapore Med J, 181-185
[2] Meding, J, 2007, Contrast Media Mol Imaging, 120-129
[3] Ruehm, SG, 2001, Circulation, 415-422
[4] Kelly, KA, 2005, Circ Res., 327-336
[5] Opriessnig, P, 2011, ESMRMB Proceedings

798

WITHDRAWN

Clinical Review Poster

Body

799

MRI and other imaging findings of Intrathoracic Desmoid Tumor

B. Nazir
Deptt Of Oncologic Imaging, NATIONAL CANCER CENTER, SINGAPORE/ SINGAPORE

Cases: A 45 year old male with complaints of right chest pain.
MRI Scan revealed a large intrathoracic-extrapulmonary softtissue mass with lobulated margins The upper part of the mass was moderately hyperintense on T 1 -weighted images and markedly hyperintense on T 2 -weighted and STIR images and marked enhancement on contrast-enhanced images.The lower part of the mass was isointense or minimally hyperintense on T 1 -weighted images and markedly hypointense on T 2 -weighted and STIR images relative to the muscle signal . Mild contrast enhancement was seen on IV contrast in this part of the mass. Corresponding DWI and ADC map showed abscence of diffusion restriction.

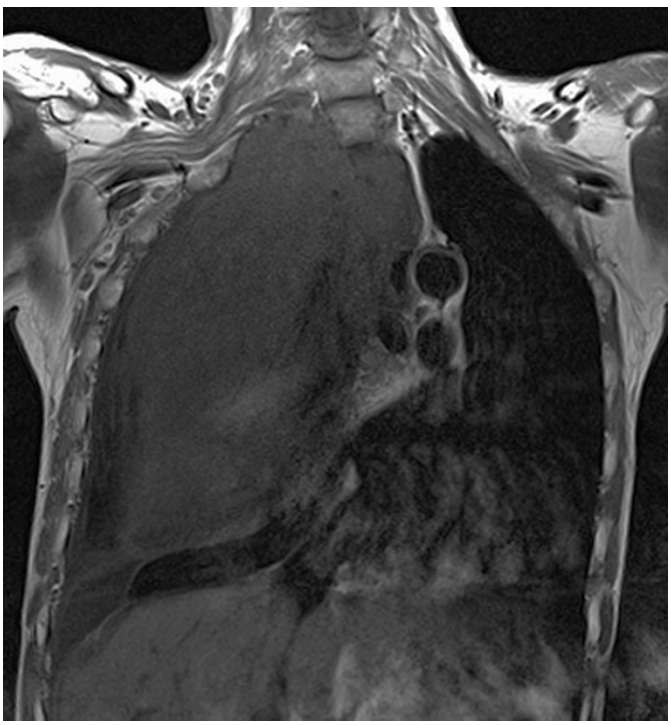

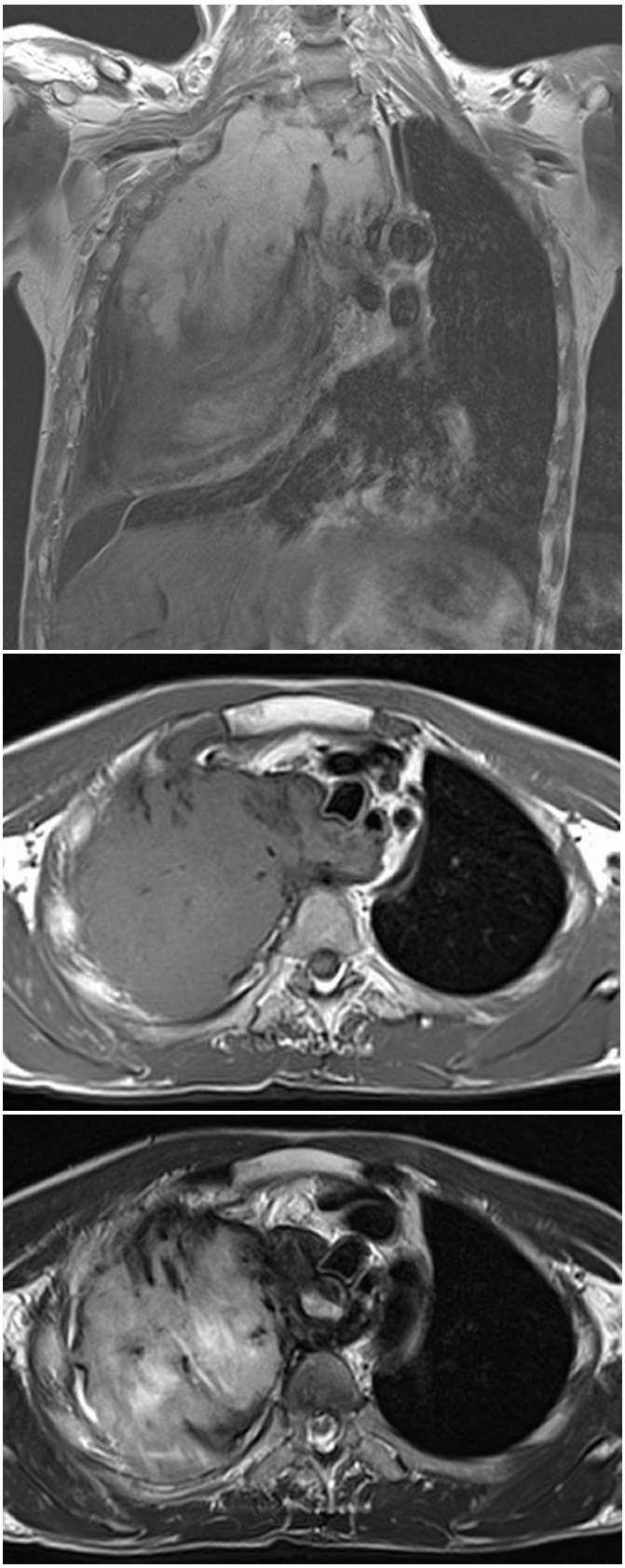

Discussion: Vandevenne et al described three stages of evolution in desmoid tumors . The first stage: increased cellularity, large extracellular fluid spaces and paucity of collagen deposition. Second stage: The collagen deposition . Third

stage:marked hypocellularity, desiccation, shrunked extracellular spaces and exuberant collagenization. This knowledge may be important in understanding its variable appearance on imaging.
MRI signals reflect amaount of collagen, water, cellularity and vascularity of the tumor. Because of predominant fibrous nature of tumor, the MR signals are expected to be hypointense on both T 1 and T 2 images, but counterintutively, this pattern is only seen in 30% of tumor . Usually, they show inhomogenous isointensity or mild hyperintensity on T 1 images, and mild to moderate heterogenous hyperintensity on T 2 images which is not very different from any other softtissue tumor . Low intensity areas and bands if seen correspond to collagen deposition or hypocellularity and is said to be characteristic although not specific. In early stage, tumor is more cellular and less fibrotic with larger extracellular fluid spaces, and therefore it appears hypointense on T 1 and hyperintense on T 2 images. In the third stage, the tumor is mainly composed of collagen, and therefore appears hypointense in both T 1 and T 2 images.
References:
1. Meyerson SL, D'Amico TA. Intrathoracic desmoid tumor: brief report and review of literature. J
Thorac Oncol 2008;3:656-9.
2. Kaplan J, Davidson T. Intrathoracic desmoids: report of two cases. Thorax 1986; 41:894-895.

800

A semi quantitative MRI method for assessing skeletal involvement in type I Gaucher disease.

V. Komninaka[1], **D. Kolomodi**[2], T. Marinakis[3], K. Repa[4], D. Christoulas[5], E. Terpos[5]
[1]Haematology, LAIKO GENERAL HOSPITAL, ATHENS/GREECE, [2]Radiology, LAIKO GENERAL HOSPITAL, Athens/GREECE, [3]Department Of Hematology, Georgios Gennimatas General Hospital, Athens/GREECE, [4]Department Of Hematology, Polykliniki General Hospital, Athens/GREECE, [5]Department Of Clinical Therapeutics, Univercity of Athens School of Medicine, Athens/GREECE

Introduction: Gaucher disease (GD) is a lysosomal storage disease . Bone complications are common in the non-neuronopathic form of GD (formerly type I) . MRI imaging is the most sensitive procedure for assessing skeletal involvement in patients with Gaucher disease and semi quantitive MRI is a very useful procedure for evaluating the bone marrow burden. The aim of this study was to prove and develop a semi quantitative scoring system to determine by MRI the bone marrow involvement . We implemented T1-weighted spin echo sequence , PDfs (to compare the detected changes on T1w sequence) and short time inversion recovery sequences (STIR) (for evaluation of the activity of the disease). We performed ROI evaluation of bone infiltration on T1W images in affected areas compared with those of healthy regions and in conjunction with measurements taken from subcutaneous fat of both thighs of these patients. We therefore introduced the following classification:
STAGE I:ROI estimated to be above the 50% of that of healthy regions
STAGE II:ROI estimated to fluctuatebetween 30% and 50%of the values detected in healthy regions
STAGE III :ROI estimated to fluctuate between 25% and 30% of the values measured in unaffected regions
STAGE IV: Detection of distal epiphyseal infiltration on T1 and STIRsequences
We derived a strong correlation of high values with low grade disease and low values with high grade disease respectively.
In conclusion, our study suggests that the above semi quantitave method is easy to perform and is a sensitive MR technique which could be useful for evaluation and monitoring of bone marrow disease .
Cases: We studied 27 adult patients (15M/12F, median age 44.5 years, range: 18-71 years) with type IGaucher
Discussion: We performed a thorough comparison of T1W and PDfs images targeting in the detection of the remodeling process of the affected bone. In all patients we performed ROI evaluation of bone infiltration on T1W images in affected areas compared with those of healthy regions and in conjunction with measurements taken from subcutaneous fat of both thighs of the same patients. The normal values were derived from healthy individuals .
References:
Hollak C,Maas M,Akkerman FM,HermanG,PastoresGM,AertsH,denHeeten A,Roca M, MotaJ Terk MR,Daniel WW.Goldblatt,FletcherIM,MagnaldiS. Dixon quantativechemical shift imaging as a sensitive tool of evaluating bone marrow response to enzyme suupplementation therapy in type 1 Gaucher disease.
Replacement therapy for inherited enzyme deficiency.
MR imaging of bone marrow changes in Gaucher disease

801

Strain at the Proximal Iliac Insertion of the Fascia Lata - MR Imaging Findings

P. João[1], R. Breni[2], M. Abreu[2]
[1]Imagiologia, HFF, LISBOA/PORTUGAL, [2]Radiologia, HMD, Porto Alegre RS/BRAZIL

Introduction: The *Fascia Lata* is a fibrous structure that envelops the external surface of the thigh and gluteal muscles. Its exact anatomy is subject to debate, but one can recognize a proximal multipoint insertion at the pelvic bones and inguinal ligament. Beyond the iliac tubercle, the fascia becomes thicker and inserts distally at the lateral tibial tubercle (Gerdy´s tubercle), being designated as iliotibial band.
The symptomatology described in relation to the iliotibial band is pain in the anterolateral region of the thigh and knee due to repetitive sliding over the lateral femoral condyle. It is commonly found in the context of sports activity, particularly in long-distance runners, soccer players or cyclists.
Much less frequent is the reference to symptoms arising in its proximal insertion, occurring in similar ocupational context, which include progressive pain localized at the hip, worsened by effort.
Magnetic Ressonance (MR) imaging is the most accurate method to evaluate these structures, showing increased signal intensity on T2-weighted images in the areas of inflamation.
Cases:

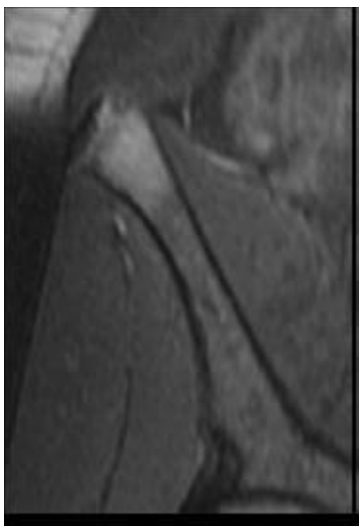

1- 14-year-old male, athlete (runner), with pain referred pain to the right iliac crest: MR shows homolateral apophysitis in the area of isertion of the fascia lata

2- 39-year-old, marathonist, with pain referred to the left iliac crest. MR with signs of fasceitis in the iliac insertion of the fascia lata

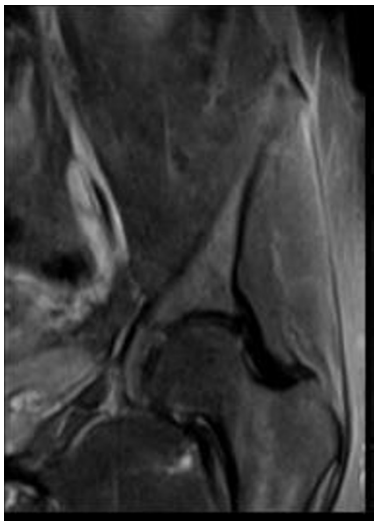

3- 42-year-old female, occasional runner, with pain referred to the left iliac crest. MR with thickening and inflamation of the fascia lata near its iliac insertion.

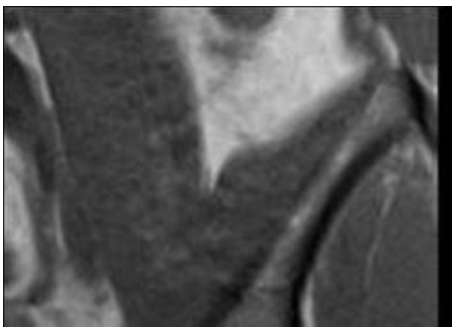

Discussion: Pathology related to the proximal insertion of the Fascia Lata/ Iliotibial is seldom referred in the literature or in common clinical pratice. However one can suspect that lesions at this location may be somewhat underdiagnosed and treated in a non-specific way (for example as pathology of the coxofemoral joint).
Its presence should be suspected if local symptoms (i.e. pain) arise, specially in a context of repeated physical activity that may put stress on this structure. If MR imaging is subsequently performed the Radiologist should have this possible diagnosis in mind and therefore ensure that the anatomical regions of interest are included and evaluated in the study.
References:
Sher I, 2011, "Proximal Iliotibial Band Syndrome - what is it and whre is it?", Skeletal Radiol 40:1553-1556
Stoller D, 2004 "Diagnostic Imaging-Orthopedics", Amirsys 5-70 to 5-73
Herbert K, 2008 AJR Am J Roentgenol 190:1487-91
Murphy B, 1992 "Iliotibial friction syndrome: MR imaging findings" Radiology 185:569-571

802

Shoulder entrapment neuropathies in the shoulder – know what do they look like on MRI and avoid being yourself entrapped

P.D. Afonso[1], L. Gargate[1], J. Strecht[1], C. Spritzer[2]
[1]Radiology, Hospital Beatriz Angelo, Loures/PORTUGAL, [2]Radiology, Duke University Medical Center, NC/NC/UNITED STATES OF AMERICA

Introduction: MRI has an important role in identifying direct and indirect signs of shoulder entrapment neuropathies and can confirm the presence of nerve compression, depict space-occupying lesions, and exclude other intrinsic pathology of the shoulder that can present in similar fashion to entrapment neuropathy. In this pictorial tour, the relevant anatomy, causes, clinical findings, and MRI appearances of nerve injury and muscle denervation of the shoulder girdle are presented.
Cases: We have retrospectively reviewed the senior authors' MRI database. All cases were imaged with T1WSE, T2WFSE or STIR, using a 1.5T or a 3T magnet. We illustrate this pictorial review with selected, MRI images of suprascapular nerve entrapment, quadrilateral space syndrome and Parsonage Turner syndrome.
Discussion: Nerve injuries of the shoulder are uncommon but not rare causes of shoulder pain. Diagnosis is traditionally based on clinical and electromyographic findings, which do not determine the exact cause or anatomic site of entrapment nor denervation.
Improvements in MRI technique have helped in detecting changes in the signal intensity of nerves and in detecting perineural pathology, becoming the primary imaging technique in the evaluation of shoulder entrapment syndromes and playing an important role in the precise location of nerve compression, aid in the identification of the morphologic cause and duration of muscle denervation and refining the differential diagnosis.
Knowledge of the relevant anatomy, cause, and imaging findings is important in making a potentially treatable diagnosis, avoiding confusion with rotator cuff inflammatory, traumatic or neoplastic processes, and obviating biopsy or surgical intervention.
References:
-Yanny S, Toms A. MR Patterns of Denervation around the Shoulder AJR 2010, 195: W157-163
-Gaskin A, Helms C. MR and Clinical Findings of Parsonage-Turner Syndrome. Radiology. Vol 240: Number 2 – August 2006
-Bencardino J; Rosenberg Z. Entrapment Neuropathies of the Shoulder and Elbow in the Athlete. Clin Sports mED 25 (2006) 465-487
-Scalf et al. AJR 2007; 187:W39-44

803

Coxalgia, evaluation with conventional MR and MR arthrography

V.V. Mascarenhas, H. Marques, A. Guerra, P. Rego, A. Gaspar
Centro De Imagiologia, Hospital da Luz, Lisbon/PORTUGAL

Introduction: Hip pain is a common clinical issue. MR imaging is of paramout importance in evaluating femoro-acetabular pathology.
The differential diagnosis of hip pain
is broad and includes intra-articular and extra-articular pathology, and mimickers including the joints of the pelvic ring.
The main goals are to review
intra-articular and extra-articular causes of hip pain as well to discuss imaging features and main differential diagnosis issues.
Cases: We selected particular cases from 650 MR examinations performed in our institution, between October 2007 and November of 2011.
In this review, we discuss the causes of intra-articular hip pain that can be diagnosed with specific imaging modalities namely MRI/Arthro MRI: labral tears, loose bodies, femoroacetabular impingement, ligamentum teres' tears and chondral damage.
Extra-articular diagnoses are also discussed, including: iliopsoas tendonitis, snapping hip, iliotibial band and greater trochanteric bursitis, . Other diagnoses reviewed include femoral neck stress fracture, adductor strain, piriformis syndrome, sacroiliac joint pain and osteitis pubis.
Discussion: Current imaging modalities allow a more precise evaluation of hip pain.
In recent years, our understanding of the functional anatomy around the hip has improved. In addition, because of advancements in MRI, the diagnosis of soft tissue causes of hip pain has also improved thus broadening the differential diagnosis.
Hip pain is a common clinical problem and often difficult to correctly assess only by clinical parameters. Knowledge of different clinical entities and their imaging appearances is therefore essential for every radiologist (in general and specialized practice).
References:
1) Troum OM, The young adult with hip pain: diagnosis and medical treatment. Clin Orthop Relat Res. 2004 Jan

2) David Stoller. Magnetic resonance Imaging in orthopaedics and sports Medicine.
3) Resnick et al. Bone and Joint Imaging, 3rd edition

804

Rheumatoid artrhitis and Seronegative Spondyloarthropaties: Evaluation with basic and advanced MRI

V.V. Mascarenhas, H. Marques, A. Guerra, D. Afonso, A. Gaspar
Centro De Imagiologia, Hospital da Luz, Lisbon/PORTUGAL

Introduction: Rheumatoid artrhitis and Seronegative Spondyloarthropaties are a common cause of pain in young and adult individuals, with imaging providing critical information in the diagnostic work-up. After viewing this exhibit, viewers will be able to:
1. Become familiar with the different athritides and their most common presenting clinical signs and symptoms.
2. Be able to identify the imaging signs and features of these disorders within different modalities and particularly with basic and dynamic MRI.
3. Understand the role of imaging in the diagnostic work-up and management of Rheumatoid artrhitis and Seronegative Spondyloarthropaties.
Cases: We reviewed selected cases among 210 patients with clinical suspicion of rheumatological disease.
The purpose of this exhibit is:
1. To provide a pictorial review of rheumatoid arthritis and related diseases, including ankylosing spondylitis, psoriatic arthritis and reactive arthritis among others.
2. To highlight the different imaging features associated with these diseases, and how they appear with MR imaging (unenhanced, enhanced, and dynamic imaging).
3. To review the common clinical presentations and
treatments options of these disorders.
Discussion: After reviewing this cases the final work-up was structured as follows:
1. Pathophysiology of Rheumatoid artrhitis and Seronegative Spondyloarthropaties
2. Review of clinical presentations and diagnostic workup
3. Review of imaging findings with examples using different
modalities but with emphasis on MR imaging:
- Plain Film
- CT
- 3Tesla MRI (unenhaced, enhanced and dynamic imaging)

4. Discuss clinical significance and treatment options
References:
1. Diagnostic Imaging - Orthopaedics; Stoller et al
2. Bone and Joint Imaging, , Resnick et al, 3rd edition
3. Imaging rheumatic diseases. Reynolds A. Radiol Technol. 2012 May;83(5):467-89.
4. Evaluating joint destruction in rheumatoid arthritis**:** is it necessary to radiograph both hands and feet?. Knevel R, Kwok K, de Rooy D, Posthumus M, Huizinga T, Brouwer E, van der Helm-van Mil A. Ann Rheum Dis. 2012 May 12. [Epub ahead of print]

805

MR imaging findings of musculoskeletal (MSK) infections in the foot – a pictorial tour

P.D. Afonso[1], A. Gaspar[1], V.V. Mascarenhas[1], C. Spritzer[2]
[1]Radiology, Hospital da luz, Lisbon/PORTUGAL, [2]Radiology, Duke University Medical Center, NC/NC/UNITED STATES OF AMERICA

Introduction: Infections of the musculoskeletal (MSK) system comprise a spectrum of disorders determined by specific tissue involvement i.e.soft tissues, bones and joints. This is particularly challenging in the foot where multiple structures are tightly packed together.
Its well known that MRI is the imaging modality of choice for MSK infections and allows to verify the presence of pedal infection and its extent. Contrast-enhanced MRI is often employed but has been a focus of debate among musculoskeletal radiologists, and many avoid contrast administration due to increased expense, longer magnet time and safety issues.
In this pictorial tour, we intend to review the primary and secondary signs of pedal osteomyelitis and soft tissue infections with T1 weighted and fluid-sensitive sequences, as well as show examples where gadolinium administration may effect image interpretation.
Cases: Selected examples from 80 MRI examinations retrospectively reviewed with the clinical indication of infection of the foot/ankle and/or toes will be presented. All were imaged with T1WI SE, T2WFSE or STIR and post-contrast T1 WSE, performed at either 1.5T or 3.0 T. Patients electronic clinical records were reviewed and imaging findings were correlated with clinical history and final diagnosis.
Discussion: Pedal musculoskeletal infections continues to be a common malady in clinical practice and appears to be increasing, particularly in patients with diabetes and who are immunocompromized.
MRI is cost effective and currently the best imaging modality to evaluate MSK infections. MRI confirms the presumed clinical diagnosis, delineates the extent of disease and its complications and also localizes target areas for intervention. Primary signs of osteomyelits include abnormal marrow signal on all pulse sequences. Secondary signs, including bony destruction and adjacente soft tissue abnormalities increase specificity. Contrast administration appears most useful for chronic osteomyelitis and characterization of soft tissue abnormalities including abscess, phlegmon, sinus and fistulous tracts. The presence of Charcot arthropathy remains a confounder in this population group.
References:
Kappoor A et al. Magnetic Resonance Imaging for Diagnosing Foot Osteomyelitis A meta-analysis. Arch Intern Med. 2007; 167:125-132
Miller T et al. Fat-suppressed MRI of musculoskeletal infection- fast T2-weighted techniques versus gadolinium-enhanced T1-weighted images. Skeletal Radio 1997; 26:654-658
JH Kan at al. Clinical impact of gadolinium in the MRI diagnosis of musculoskeletal infection in children. Pediatr Radiol (2010) 40:1197-1205
W. Morrison et al. Diagnosis of Osteomyelitis: Utility of Fat-Suppressed Contrast-enhanced MR Imaging; Radiology 1993; 189: 25-257

806

Recognizing false positives and negatives of diffusion MRI

A. Iglesias Castañon[1], M. Arias González[1], B. Nieto Baltar[1], J. Mañas Uxo[1], P. Sucasas Hermida[2], Á. Nieto Parga[3]
[1]Unidad De Diagnóstico Por Imagen (galaria), COMPLEJO HOSPITALARIO UNIVERSITARIO DE VIGO, Vigo/SPAIN, [2]Unidad De Diagnóstico Por Imagen, Institution Complejo Hospitalario Universitario de Vigo Galaria, Vigo/SPAIN, [3]Department Unidad De Diagnóstico Por Imagen, Institution Complejo Hospitalario Universitario de Vigo Galaria, Vigo/SPAIN

Introduction: DWI provides better detection and delineation of lesions increasing the contrast between normal and tumor tissues and quantitative information reflecting tissue cellularity and organization.
DWI and ADC mapping are becoming important image biomarkers in tissue characterization, cancer detection and response to treatment assessment, as the have quickly widespread because do not require contrast administration and can be obtained quite easily and quickly.
However it can present several false positive and false negative situations: the T2 shine-through effect, slow-flowing blood, some magnetic susceptibility artifacts, densely cellular tissue or tumors with low cellular density and we must be aware of that.
Cases: T2 shine-through effect
Slow-flowing blood
Magnetic susceptilbility artifacts
Densely cellular tissue:
- Normal tissue: Neurological tissue (brain, spinal cord, peripheral nerves), hematopoietic bone marrow, most glands, spleen, kidneys, lymph nodes…
- Non cellular structures: abscesses, inflammatory collections, proteinaceous and hemorrhagic cysts...
- Inflammation
- Fibrosis

Tumors with low cellular density: cystic, mucinous or necrotic tumors

Discussion:

- Hyperintensity on DW-MRI does not always mean malignancy
- Some pathological or technical related features can explain restricted diffusion in otherwise benign lesions
- To avoid misinterpretation of findings on DW-MRI a correlation with ADC maps, morphological images and clinical data is mandatory

References:

- Qayyum, A. Diffusion-weighted Imaging in the Abdomen and Pelvis: Concepts and Applications. RadioGraphics 2009; 29:1797-1810
- Evaluation with Intravoxel Incoherent Motion Echo-planar MR Imaging. Radiology 1999; 210: 617-623.
- Koh DM, Collins DJ. *Diffusion-weighted MRI in the body: applications and challenges in oncology. AJR Am J Roentgenol 2007;188(6):1622–1635.*
- Neil JJ. *Measurement of water motion (apparent diffusion) in biological systems. Concepts Magn Reson 1997;9:385–401*
- Thoeny HC, De Keyzer F. *Extracranial applications of diffusion-weighted magnetic resonance imaging. Eur Radiol 2007;17(6):1385–1393*
- Bammer R. *Basic principles of diffusion-weighted imaging. Eur J Radiol 2003;45(3):169–184*
- Whittaker CS, Coady A, Culver L, Rustin G, Padwick M, Padhani AR. *Diffusion-weighted MR imaging of female pelvic tumors: a pictorial review. RadioGraphics 2009;29(3):759–774; discussion 774–778*
- Parikh T, Drew SJ, Lee VS, et al. *Focal liver lesion detection and characterization with diffusion-weighted MR imaging: comparison with standard breath-hold T2-weighted imaging. Radiology 2008; 246(3):812–822*

807

Abdominal and Pelvic Carcinoid tumors: Magnetic Resonance Imaging Pictorial Review

J.M. Palas[1], A. Matos[1], F.V. Gomes[2], M. Ramalho[1], C. Bagulho[1]
[1]Radiology, Hospital Garcia de Orta, Almada/PORTUGAL, [2]Imagiologia, Hospital de Faro, Faro/PORTUGAL

Introduction: Our purpose is to illustrate the appearance of abdominal and pelvic carcinoid tumors on magnetic resonance imaging (MRI).
MR is an excellent imaging method for detection of larger primary and secondary abdominal and pelvic carcinoid tumors. These tumors usually appear of low signal intensity on T1-weighted sequences and moderate high signal on T2-weighted sequences. Following intravenous gadolinium, there is characteristic marked homogeneous enhancement, reflecting its highly vascular nature.
Cases: Carcinoid tumors are a fascinating group of neuroendocrine neoplasms. Carcinoids can arise in a very wide variety of sites, most frequently occurring in the gastrointestinal tract (70%), followed by the tracheobronchial system. A computerized search in our radiological database reports for carcinoid tumors in patients who had abdominal or pelvis MRI examinations was performed and allowed us to find carcinoid tumors arising from duodenum, jejunum, ileum, appendix, rectum, pancreas, liver (metastases) and mesentery.
Discussion: MRI plays a central role in the localization and staging of carcinoid tumors and in monitoring the treatment response. Imaging is often challenging, and a combination of anatomic and functional techniques is usually required, depending on the tumor type and location. Therefore, radiologists must be aware of the contribution of each imaging modality in the assessment of different neuroendocrine tumors.
References:

Angela D. Levy, Leslie H. Sobin, Gastrointestinal Carcinoids: Imaging Features with Clinicopathologic Comparison, RadioGraphics 2007; 27:237–257
Andrew F. Scarsbrook, Arul Ganeshan, Jane Statham, Rajesh V. Thakker, Andrew Weaver, Denis Talbot, Philip Boardman, Kevin M. Bradley, Fergus V. Gleeson, Rachel R. Phillips, Anatomic and Functional Imaging of Metastatic Carcinoid Tumors, RadioGraphics 2007; 27:455– 476
Karen M. Horton, Ihab Kamel, Lawrence Hofmann, Elliot K. Fishman, Carcinoid Tumors of the Small Bowel: A Multitechnique Imaging Approach, AJR March 2004 vol. 182no. 3 559-567
Angela D. Levy, Leland D. Taylor, Robert M. Abbott, Leslie H. Sobin, Duodenal Carcinoids: Imaging Features with Clinical-Pathologic Comparison, Radiology 2005; 237:967–972

808

Liver Fat-Containing Lesions: Magnetic Resonance Imaging Pictorial Review

J.M. Palas[1], A. Matos[1], F.V. Gomes[2], M. Ramalho[1], C. Bagulho[1]
[1]Radiology, Hospital Garcia de Orta, Almada/PORTUGAL, [2]Imagiologia, Hospital de Faro, Faro/PORTUGAL

Introduction: Our purpose is to to illustrate and describe the appearance of liver fat-containing lesions on magnetic resonance imaging (MRI).
Detection and characterization of these lesions is commonly achieved with MRI. Several MRI sequences aid in the detection of fat, including fat suppression or dual gradient echo two-point Dixon techniques with fat-only or water-only datasets and chemical shift imaging with in- and out-of-phase gradient-echo technique, helping in differentiation of the lipid composition of the lesion (macroscopic fat vs. intracellular fat).
Cases: Fat-containing lesions of the liver represent a broad spectrum of congenital, metabolic, inflammatory, traumatic and neoplastic processes. These include fatty liver (diffuse, geographic, focal, subcapsular, multifocal, perivascular and ultra-high liver fat deposition), hepatocellular carcinoma, adenomas, lipomas and angiomyolipomas, lipopeliosis and others.
Discussion: The presence of fat components within a lesion combined with other imaging features allow definite diagnosis or greatly narrow the differential diagnosis. MRI is currently the most specific imaging technique for demonstration and characterization of microscopic and macroscopic fat.
References:

Srinivasa R. Prasad, Hanlin Wang, Humberto Rosas, Christine O. Menias, Vamsi R. Narra, William D. Middleton, Jay P. Heiken, Fat-containing Lesions of the Liver: Radiologic Pathologic Correlation, RadioGraphics 2005; 25:321–331
Okka W. Hamer, Diego A. Aguirre, Giovanna Casola, Joel E. Lavine, Matthias Woenckhaus,Claude B. Sirlin, Fatty Liver: Imaging Patterns and Pitfalls, RadioGraphics 2006; 26:1637–1653
Ceyla Basaran, Musturay Karcaaltincaba, Deniz Akata, Nevzat Karabulut, Devrim Akinci, Mustafa Ozmen, Okan Akhan, Fat-Containing Lesions of the Liver: Cross-Sectional Imaging Findings with Emphasis on MRI, AJR:184, April 2005
Elmar M. Merkle, Rendon C. Nelson, Dual Gradient-Echo In-Phase and Opposed Phase Hepatic MR Imaging: A Useful Tool for Evaluating More Than Fatty Infiltration or Fatty Sparing, RadioGraphics 2006; 26:1409 –1418
Kyoung Won Kim, Min Ju Kim, Seung Soo Lee, Hyoung Jung Kim, Yong Moon Shin, Pyo-Nyun Kim, Moon-Gyu Lee, Sparing of Fatty Infiltration Around Focal Hepatic Lesions in Patients with Hepatic Steatosis: Sonographic Appearance with CT and MRI Correlation, AJR 2008; 190:1018–1027

809

Correlation between MRI and Laparoscopy findings on severe endometriosis

A. Guerra, A. Setúbal, **V.V. Mascarenhas**, L.R. Orvalho, H. Marques, A. Gaspar
Imagiology, Hospital da Luz, Lisbon/PORTUGAL

Introduction: The endometriosis is an important gynaecologic disorder that primarily affects women of reproductive age, often causing chronic pelvic pain and infertility.
The aim of this study was to review the MRI findings of women with severe endometriosis.
Cases: We did the correlation between MRI and laparoscopy findings of the women, who had signs and symptoms of severe endometriosis. All women (100) did a pelvic MRI with protocol for endometriosis before surgery and all the MRI exams and surgery were perform by the same Radiologist and Surgeon .
With this sample, the authors review and documented almost forms of severe endometriosis in these diagnostic technics.
Discussion: The standard of reference for the diagnosis and staging of endometriosis is laparoscopy. The majority of the disease was seen at MRI. Knowledge

of the variety of MRI appearances of endometriosis is important for guiding laparoscopic examination.

References:

Pelvic endometriosis: MR imaging spectrum with laparoscopic correlation and diagnostic pitfalls. KG Bis, TG Vrachliotis, R Agrawal, A N Shetty, A Maximovich and H Hricak. Radiographics May 1997 17:3 639-655.
Endometriosis: Radiologic-Pathologic Correlation. Paula J. Woodward, Roya Sohaey and Thomas P. Mezzetti, Jr. Radiographics January 2001 21:1 193-216.

810

MR findings of various causes of acute abdominal pain in pregnant women

J.Y. Son, C.I. Shin, J.K. Han, B.I. Choi
Radiology, Seoul National University Hospital, Seoul/KOREA

Introduction: Acute abdominal in pregnant patients presents unique diagnostic and therapeutic challenges. Although ultrasound (US) is the primary imaging investigation in the diagnostic evaluation of the pregnant patient, the use of magnetic resonance imaging (MRI) in the evaluation of acute abdominal pain in pregnant women is increasing.
Cases: Acute appendicitis, hemoperitoneum, heterotopic pregnancy, engorged gonadal vessel, ovary torsion.
Discussion: MRI can provide a systematic cross-sectional evaluation of the entire abdomen without exposing the fetus to ionizing radiation. MRI is often used in the obstetric setting for imaging maternal and fetal diseases and has recently been suggested as a promising tool for evaluation of acute appendicitis in pregnant patients. MRI is very useful in the evaluation of the acute abdomen during pregnancy.
References:

Radiographics 2007; 27:721
Radiographics 2012; 32:317

811

The value of MRI evaluation in Endometriosis – A Pictorial Review

E. Batista[1], T.M. Cunha[2]
[1]Radiology, Hospital Curry Cabral - CHLC, 166/PORTUGAL, [2]Radiology, Instituto Português de Oncologia Francisco Gentil, EPE, Lisbon/PORTUGAL

Introduction: Endometriosis is defined as the presence of functional endometrial glands and stroma outside the uterine cavity. This ectopic tissue is hormonally responsive and may undergo bleeding, leading to inflammation, fibrosis and adhesion formation, which can result in pelvic pain and infertility. The most common locations of endometriosis are the ovaries and uterine ligaments, pelvic peritoneum, fallopian tubes, recto-sigmoid colon and bladder. Deep pelvic endometriosis, defined as endometrial tissue implants penetrating more than 5mm under the peritoneal surface, is not as common as superficial peritoneal endometriosis, but is more frequently related with clinical symptoms and infertility.
Cases: The authors will present cases from their institution, illustrating the typical and less common locations of endometriosis and it's characteristic appearance on MRI.
Emphasis will be given to MRI findings in deep pelvic endometriosis, by showing different locations and outlining the advantages and limitations of this technique in their evaluation.
Discussion: Laparoscopic surgery still remains the gold standard for the location of peritoneal implants in the pelvis, but often, direct inspection of some lesions is not possible, due to adhesions. MRI is the best imaging technique to preoperatively detect and stage endometriosis, providing a useful roadmap to proper program surgical intervention. For this evaluation a dedicated MR protocol is needed and patient preparation is also recommended.
Frequently, MRI findings are subtle and a careful imaging analysis paired with knowledge of the clinical context is fundamental not to overlook lesions that can be related with patient symptoms.
References:

1.Bis KG, Vrachliotis TG, Agrawal R et al. Pelvic endometriosis: MR imaging spectrum with laparoscopic correlation and diagnostic pitfalls. 1997 Radiographics; 17:639-55
1.Jarlot C, Anglade E, Paillocher N et al. Caracteristiques IRM de l'endométriose profunde: correlation aux résultats coelioscopiques. 2008 J Radiol; 89:1745-54
2. Chamié LP, Blasbalg R, Gonçalves MO et al. Accuracy of magnetic resonance imaging for diagnosis and preoperative assessment of deeply infiltrating endometriosis. 2009 Int J Gynecol Obstet; 106:198-201
3.Marcal L, Nothaft MA, Coelho F, Choi H. Deep pelvic endometriosis: MR imaging. 2010 Abdominal Imaging; 35:708-15
4. Saba L, Guerriero S, Sulis R et al. Learning curve in the detection of ovarian and deep endometriosis by using Magnetic Resonance: comparison with surgical results. 2011 Eur J Radiol; 79:237-44.

812

Manifestations and Complications of Endometriosis— the possibility of magnetic resonance imaging

E. Yukhno, I. Trofimenko, G. Trufanov, S. Serebryakova, T. Gribanova, V.V. Ryazanov
The Department Of Radiology And Nuclear Medicine, Military Medical Academy, St. Petersburg/RUSSIAN FEDERATION

Introduction: Endometriosis plays an important role in infertility, chronic pelvic pain. The variety of disease clinics depends on the localization of endometriotic infiltrates and associated complications, which accounts for the difficulty of diagnosis and high incidence of recurrence of the disease and significantly impairs quality of life.
Cases: 103 patients with different kinds of endometriosis and pelvic pain syndrome have been investigated by MRI unit (1.5 T). Scanning protocol included T1 and T2 spin-echo sequences and fat suppression. We used the technique of non-contrast MR urography. The diagnosis was confirmed intraoperatively with histology and morphology, and materials research.
Discussion: MRI showed high sensitivity and specificity (over 90%) in detecting peritoneal lesions. The main limitation of the method - detection of small size heterotopias (<3 mm). The most often localization of endometrioid heterotopias were the ovaries, at least – fallopian pipe and retrocervicel space, colon and appendix, the wall of the bladder, ureters, urethra. MRI endometrioid heterotopias were represented by cysts with evidence of chronic hemorrhage, surrounded by a zone of fibrosis. They were characterized by high intensity of MR signal on T1-WI and low - on T2-WI - the effect of "T2 shading". Loss of signal on T2-weighted images in these cysts is caused by high concentrations of protein and iron, as a result of cyclical bleeding and reflects the chronic nature of the process. The heterogeneous signal intensity in patients with endometriosis was due to the different stages of degradation of blood products (blood clots, clots) ($p < 0.005$). Scar adhesions and changes in paraovarial tissue were observed in every third patient with endometrial cysts ($p < 0.005$). In the retroutherical space endometrial infiltration was found as a structure of low MR signal, spread laterally to one or both utero-sacral ligaments. Obliteration of retrocervikal space along with infiltrate spread to the wall of the rectum in this group we met in 58% of the surveyed complained of a painful bowel movements. With such a localization in 24% of cases infiltration of the ureter took place with prestenothic extension. In 9% of the patients complaining of disuria diagnosed endometriosis utero-vesical ligaments and the bladder wall was diagnosed as a local thickening with haemorrhagic inclusions.
In endometriosis in the broad ligament of the uterus endometric infiltration in 23% of the Fallopian tube was included with the development of obstructive hydrosalpinx. All examined patients had been treated for infertility for a long time.

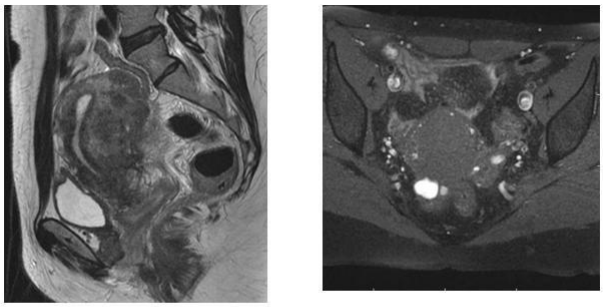

T2- WI sag T1- WI FS tra

Fig.3. Endometriosis retrotservikal space in 35-year-old woman.

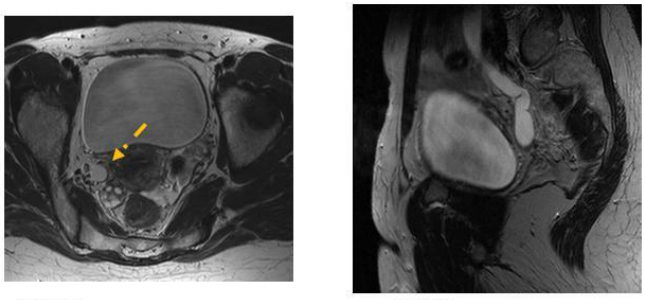

T2- WI tra T2- WI sag

Fig.4. Endometriosis retrotservikal space, hydrouretheronephrosis in 29-year-old woman.

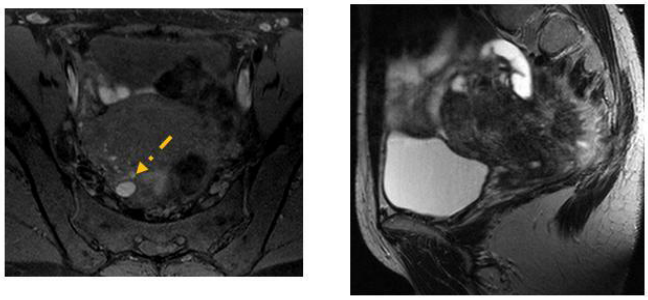

T1- WI FS tra T2- WI sag

Fig.5. Endometriosis in the broad ligament, hydrosalpinx in 33-year-old woman.

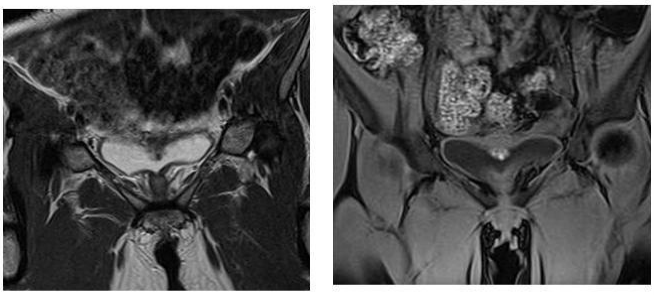

T2- WI cor T1- WI FS cor

Fig.6. Endometriosis of the bladder in 24-year-old woman.

813

WITHDRAWN

814

MR-Elastography of the Liver: Comparison and Performance evaluation of the Piezoelectric and Pneumatic Actuators

J.R. Loureiro[1], M. Mada[2], T.A. Carpenter[3]
[1]Wolfson Brain Imaging Centre, Addenbrooke's Hospital, Cambridge/ UNITED KINGDOM, [2]Wolfson Brain Imaging Centre, Wolfson Brain Imaging Centre, Cambridge/UNITED KINGDOM, [3]Wolfson Brain Imaging Centre, University of Cambridge, Cambridge/UNITED KINGDOM

Purpose/Introduction**:** Magnetic Resonance Elastography is a non-invasive technique that can spatially map and quantitatively describe displacement patterns corresponding to strain waves, in tissue-like materials. [1] One main issue with MRE is the design of an actuation system to enable adequate mechanical excitation within the magnetic field of the magnetic resonance imager. Pneumatic, electromagnetic, and piezoelectric actuation systems have been employed for MRE examinations of the skeletal muscle, the brain, and abdominal organs such as the liver. The purpose of this study is to evaluate and compare two actuator systems, piezoelectric- and pneumatic-based, for liver MRE.

Subjects and Methods: The piezoelectric actuator consists of a piezoceramic stack connected to a lever to amplify the displacement to a few millimetres. A wooden rod is fixed to the lever and its end is placed on the volunteers' abdomen (Fig. 1).The actuator is driven by a high voltage amplifier and a function generator, situated outside the RF cage.

The custom-built pneumatic actuator is based on Ehman's [2] design and consists of a commercial active subwoofer driven by a function generator, both placed outside the magnet room. The sound waves are transmitted through a PVA hose attached to a plastic bottle to act as a passive actuator.

Both actuators were tested on the same volunteer on a 3T MRI and data was analysed using the complex inversion of the shear wave algorithm [3].

Motion deflection tests, using both actuators, were carried out, in-vitro, on a phantom (Fig.2) at various frequencies and amplitudes, using an accelerometer. Acceleration data was post-processed and converted into displacement measurements.

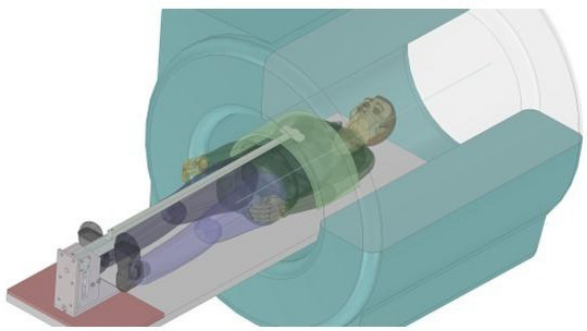

Fig. 1 Schematic representation of the piezoelectric system: liver setup.

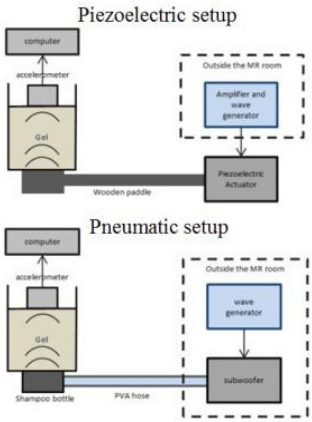

Fig. 2 Schematic figure of the motion measurements setup for both system actuators.

Results: Fig. 3 shows displacement values obtained with both designs. Liver experiments were also performed at 3 different frequencies (Fig.4). Spatial mean values were obtained at each frequency and are shown in the table below.

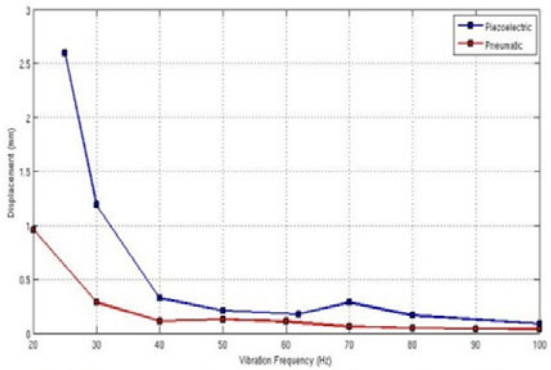

Fig. 3 Displacement values obtained for the piezoelectric (blue) and pneumatic (red) designs at 9 different vibration frequencies.

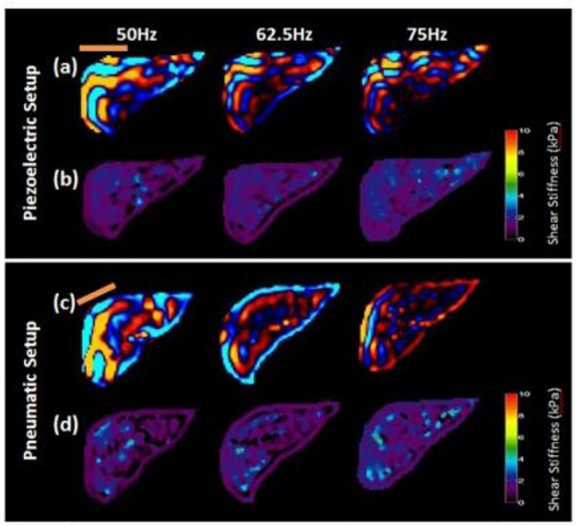

	50Hz	62.5Hz	75Hz
$\bar{G}_{Piezoelectric}$(kPa)	2.509	2.758	2.907
$\bar{G}_{Pneumatic}$(kPa)	2.256	2.383	2.887

Fig. 4 Liver elasticity results obtained for the piezoelectric (a) and (b) and pneumatic (c) and (d) systems. The orange lines in (a) and (c) represent the position of the actuators respectively. Global mean shear modulus values are depicted in the table below.

Discussion/Conclusion: The piezoelectric proved to be able to induce a higher displacement on tissue. Wave images (Fig. 4 (a), (c)) and reconstructed shear stiffness maps (Fig. 4 (b), (d)) appear more uniform using the piezoceramic device. Despite having noisier maps, the pneumatic system still presents similar values compared with the ones found with the piezoelectric setup. The piezoelectric actuator can achieve higher frequencies and provide more reliable quantitative measurements. Nevertheless, other factors such as cost and complexity are a disadvantage with the piezoelectric system.

References:

[1] Muthupillai, R. (1996). MRM, 36: 266-274.
[2] Ehman. (2006). Patent: N.º US 7,034,534 B2. United States.
[3] Papazoglou, S. (2008). Phys. Med. Biol., 53: 3147-3158.

815

Diffüsion Weighted imaging in early sacroiliitis

Y. Durum[1], C.-. Çevikol[2], A.U. Şenol[3]
[1]Radiology, Adnan Menderes Üniversty of Medicine, Aydın/TURKEY, [2]Radiology, Akdeniz Üniversity of medicine, Antalya/TURKEY, [3]Radiology, Akdeniz Üniversty of Medicine, Antalya/TURKEY

Introduction: Early diagnosis of acute sacroiliitis and related disorders are quite important for preventing the irreversible results of these diseases (such as ankylosis) and increasing the efficiency of treatment. Magnetic Resonance Imaging (MRI) is the most important modality in early diagnosis. Routine MR examinations should include STIR and contrast enhanced fat saturated T1-weighted sequences. In our study, we evaluated the role of DWI MRI sequence in the diagnosis of acute sacroiliitis. Interobserver and intraobserver reliability is also evaluated.

Cases: Seventy patients suffering from back pain and underwent sacroiliac joint MRI between october 2008 and december 2009 were retrospectively evaluated. Patien sunder 18 year old and had MRI examinations without contrast were excluded. Total 84 sacroiliac joints of 42 patient'sroutine MRI examinations and DWI sequences (b100, b600, b1000) were evaluated retrospectively. Evaluations were made independently without any information about patient's name and clinical findings. First, DWI MRI examinations were evaluated by two radiologist seperately (one of the radiologist made another evaluation after one week). After one month, sacroiliac joint MRI's of the patients were evaluated for osteitis and bone marrow enhancement (positive MRI) by two radiologists and decisions were made by consensus.

For the diagnosis of acute sacroiliitis, sensitivity and specificity values of DWI MRI were calculated as 75% and 87,5% respectively in 84 sacroiliac joints. By using Cohen'sKappa Test, moderate interobserver correlation (kappa=0,512) and weak intraobserver correlation (kappa=0,369) was found.

Discussion: Inconclusion, DWI MRI examinations are non-invazive (contrast material administration is not needed), sensitive, fast diagnostic method in the diagnosis of acute sacroiliitis. Besides, DWI MRI may have a potential as a screening method in suspected cases, if supported with large studies.

References:

1) Bozgeyik Z,Özgöçmen S, Karakoç E.Role of Diffüsion-Weighted MRI in the detection of Early Active Sacroiliitis.AJR 2008;191:980-986.
2) Algın O,Gokalp G, Baran B, Ocakoğlu G, Yazıcı Z. Evulation of Sacroiliitis: contrast enhanced MRI with substraction tecnique.Skeletal Radiology 2009;38(10)983-8.
3) Allthoof CH, Feist E, Burova E at all. Magnetic Resonance imaging of active sacroiliitis: do you really need godalinium?Eur J Radiol 2009;71(2)232-6.

816

Magnetic Resonance Tractography as a tool to evaluate pubovisceral muscle morphological changes.

S. Brandão[1], T. Da Roza[2], M. Parente[2], T. Mascarenhas[3], I. Ramos[1], R.N. Jorge[2]
[1]Radiology, Centro Hospitalar de São João, Oporto/PORTUGAL, [2]Idmec, FEUP, Oporto/PORTUGAL, [3]Depart. Of Gynecology|obstetrics, Centro Hospitalar de São João, Oporto/PORTUGAL

Introduction: Pelvic floor dysfunction may be caused by *levator ani* disruption. Functional consequences depend on which portion is involved. Pubovisceral muscle includes pubococcygeal and puborectal muscles, which form a sling around the rectum and vagina to promote urogenital hiatus closure.
Magnetic Resonance Imaging (MRI) enables detailed analysis of muscle disruption and thickness abnormalities that are associated with stress urinary incontinence (SUI), even in asymptomatic women with minor muscle asymmetry[1].
Diffusion tensor imaging (DTI) measures the directionality of water protons motion, providing information regarding tissue architectural organization. Tractography is the visualization of tracts or fibers as resulting from DTI post-processing. As muscles are highly anisotropic structures and water molecules move preferably along them, it is expected that pelvic floor muscles could be depicted by DTI.
Cases: Anatomical T2-w and diffusion-weighted images were acquired at rest, parallel to the puborectal line, from a healthy 29-year-old nulliparous woman, at 3Tesla (Fig.1).

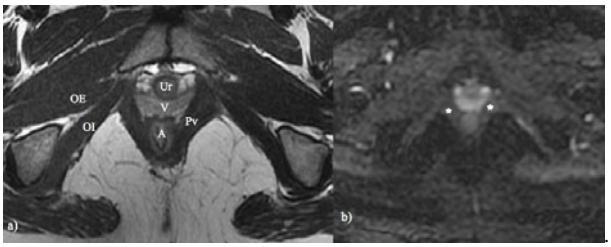

External contour of the pubovisceral muscle was manually performed on the T2-w images to create a 3D model (Fig.2).

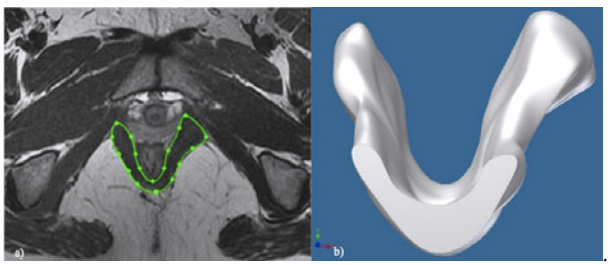

Afterwards, ABAQUS™ was used to build a 3D model based on finite element method (FEM). Simulation of intra-abdominal pressure was applied perpendicular to the muscle to depict fiber direction (Fig.3b-d).

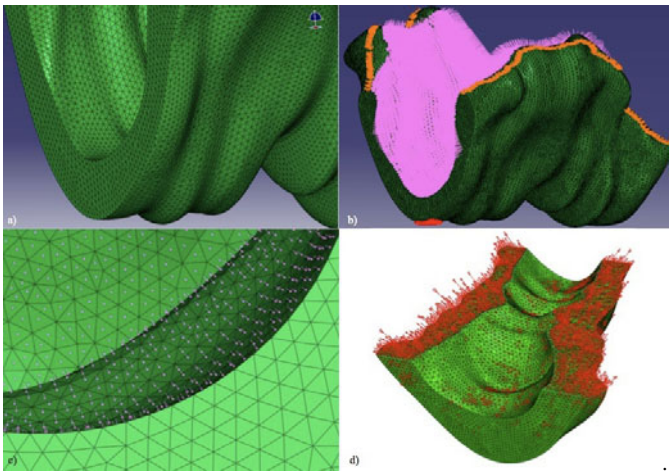

DTI images obtained in 60 directions were post-processed for fiber tractography using Diffusion Toolkit (Fig.4a).

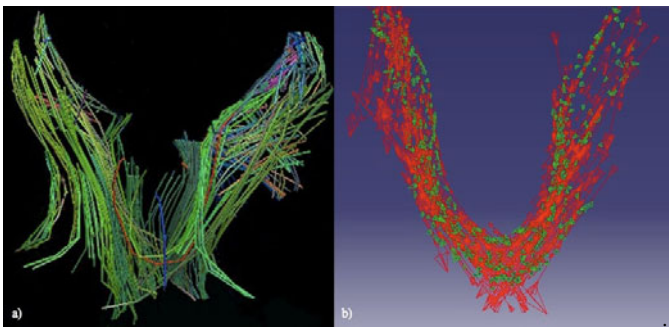

Discussion: Asymmetry of pubovisceral muscle as specific SUI finding is controversial. Some authors have emphasized that a homogeneous low signal and symmetric shape are imaging features of negative diagnosis for SUI[2], while others found left-to-right side differences on asymptomatic women[3], or subtle thickness differences between SUI and continent women[4].
In this pilot study, the left side of the pubovisceral muscle was thicker than the right side (1.315 against 0.89cm).
Fiber tractography enabled to determine pubovisceral muscle anterior-to-posterior direction and left side irregularity that were concurrent to that achieved on the FEM model slice (Fig.4b).
These simulation tools based on FEM consider muscle as being a homogeneous material. Further research based on DTI parameters and fiber tractography may bring new information about muscle fibers shape, density, pennation and eventually internal (dis)arrangement, which could help to characterize abnormal patterns of biomechanical response on apparently normal muscles.
References:
[1] Morgan, DM, 2010, Int Urogynecol J Pelvic Floor Dysfunct., 47–52
[2] Tunn, R et al., 2006, Eur J Obstet Gynecol Reprod Biol., 239–245.
[3] Singh, K et al., Obstet Gynecol., 2002, 433–438
[4] Kim, JK et al., 2003, AJR, 1037–1044

817

Approach to the Noncooperative Patient in Abdominal MRI - T1W sequences

F.V. Gomes[1], J. Palas[2], A. Matos[2], M. Ramalho[2]
[1]Imagiologia, Hospital de Faro, Faro/PORTUGAL, [2]Radiologia, Hospital Garcia de Orta, Almada/PORTUGAL

Introduction: Magnetic resonance imaging (MRI) has become an essential technique in the evaluation of the abdomen.
A subset of patients pose a great technical challenge, given that many MR sequences for the abdomen require the patient to sustain their breath for about

15 seconds. These include children, agitated or sedated patients, in whom different sequences are required in order to obtain images of sufficient quality.
Respiratory triggering or navigation techniques are routinely incorporated in T2-weighted imaging in noncooperative patients. The challenge remains when it comes to avoiding breathing artifacts in T1-weighted (T1W) images. T1W images are of particular importance due to the acquisition of in-phase (IP) and out-of-phase (OP) images, and their use in dynamic contrast studies. The present review discusses and illustrates alternativeT1W approaches in noncooperative patients, recently described in the literature.
Cases: Illustrative cases of uncooperative patients will be shown.
Discussion: T1W gradient-echo (GRE) in-phase and out-of-phase imaging is an essential component of comprehensive abdominal MR exams. It is useful for the study of fat-containing lesions and to identify various disease states related to the presence of fat in the liver. 2D GRE is still considered the best approach for this purpose. It has been shown that Magnetization-Prepared Gradient Recalled Echo (MP-GRE) sequences acquired in free-breathing manner produce quality images in patients unable to hold their breath. In a different study, this technique was compared with 2D GRE IP and OP images in the evaluation of hepatic steatosis and produced clinically useful images in evaluating liver fat in noncooperative patients. The utility of this sequence in the characterization of adrenal lesions in noncooperative patients, has also been described.
3D-GRE with fat supression is currently the method of choice for post contrast MRI, which is also vulnerable to breathing artifacts. Free breathing 3D GRE with radial data sampling has been established in thoracic and cardiac imaging. Recently, a preliminary evaluation of free-breathing 3D GRE with radial data sampling acquisition in abdominal MRI was performed and compared with a standard 3D GRE volumetric interpolated breath-hold examination. Despite the small number of patients, it is suggested that 3D GRE with radial data sampling is a feasible quality alternative.
In conclusion, recent advances in motion resistant T1W sequences for abdominal imaging have shown diagnostic capability for evaluating patients unable to cooperate with suspending respiration.
References:
1.Ramalho et al 2012 Acta Radiologica
Azevedo et al 2011 AJR
3.Ramalho et al 2011 AJR
4.Herédia et al 2011 JMRI

818

Regional quantification of Cystic fibrosis using hyperpolarized Xe-129 and Chemical Shift Imaging

C. Fernandes[1], S. Reis[2], K. Ruppert[1], J. Mugler Iii[1], I. Ruset[3], W. Miller[1], W. Hersman[3], J. Mata[1]
[1]Radiology & Medical Imaging, University of Virginia, Charlottesville/ UNITED STATES OF AMERICA, [2]Imaging, Institute of Biophysics and Biomedical Engineering, Lisbon/PORTUGAL, [3]Imaging, Xemed, Durham/ UNITED STATES OF AMERICA

Introduction: Cystic fibrosis (CF) is a genetic disorder in which the defective gene causes the production of unusually thick and viscous mucus that builds-up in the airways, leading to inflammation and infection of lung structures [1]. Our technique makes use of hyperpolarized Xe-129 (hp Xe-129) gas and chemical shift imaging (CSI), for non-invasively obtaining, in a single breath-hold (<15 seconds), three dimensional regional characterization of gas ventilation, and gas uptake-exchange in lung tissue and in red blood cells (RBC) separately. Here we demonstrate the feasibility of this method for assessing gas distribution in multiple lung compartments in subjects with CF and in healthy subjects.
Cases: Eight independent clinical studies were performed in six volunteers: 3 healthy and 3 previously diagnosed with CF; one healthy and one CF were imaged twice for a repeatability study. All scans were done in a 1.5T clinical system (Avanto, Siemens Medical Solutions) using a linear transmit/receive RF coil built in-house and tuned to the Xe-129 frequency. For each acquisition, 700±100mL of hp Xe-129 gas (polarization ~35-50%; Xemed, NH) mixed with oxygen and room air was inhaled by the subject, followed by a breath-hold during the entire pulse-sequence acquisition. Xe-129 CSI post-processing was performed using the 3DiCSI (Columbia University, NY) software package. The free-induction decay corresponding to each voxel of the 18x18 matrix was Fourier transformed and the integral of each peak was calculated for each slice. Multiple regional defects (no detectable signal) were observed in all lung compartments in the CF population, demonstrating that current CSI map resolution is sufficient to detect focal disease (Figure 1). Furthermore, Xe-129 CSI results were capable of clearly distinguishing CF from healthy population, with mean ratios of the gas dissolved in tissue to RBC of 3.12±1.55 and 0.61±0.03, respectively (Figure 2). CF subjects presented a higher tissue/RBC ratio probably due to heterogeneous inflammation and thickening of the lung tissue walls [2]. For the two performed reproducibility studies, the mean difference of the tissue/RBC ratios between the two consecutive acquisitions of the same subject were 7%±4% for the CF, and 10%±6% for the healthy subject (Figure 2).

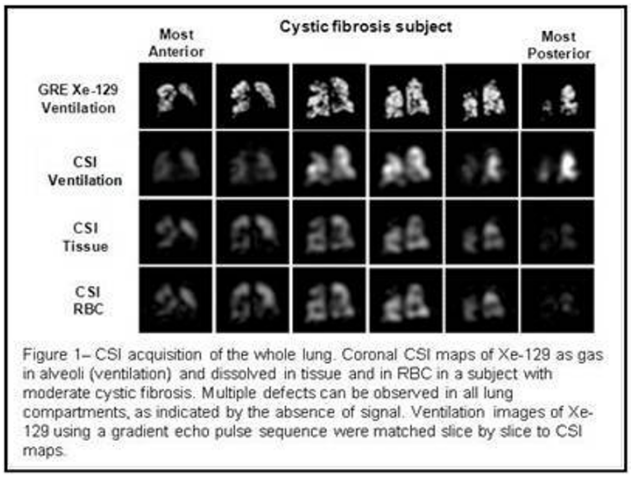

Figure 1– CSI acquisition of the whole lung. Coronal CSI maps of Xe-129 as gas in alveoli (ventilation) and dissolved in tissue and in RBC in a subject with moderate cystic fibrosis. Multiple defects can be observed in all lung compartments, as indicated by the absence of signal. Ventilation images of Xe-129 using a gradient echo pulse sequence were matched slice by slice to CSI maps.

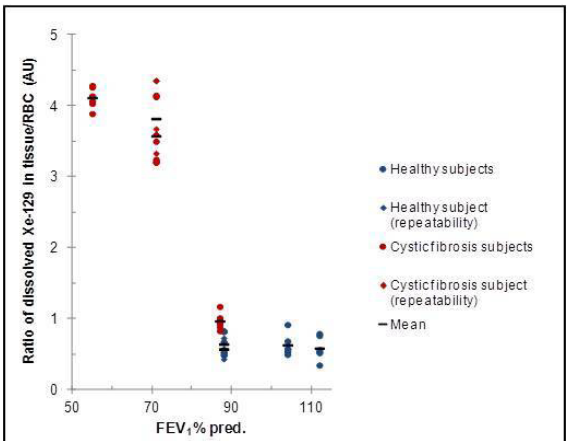

Figure 2 - Correlation between lung measurements. Quantification of the ratio of Xe-129 dissolved in tissue to RBC through the CSI technique demonstrates a clear distinction between healthy and cystic fibrosis subjects. Also, CSI maps appear to be more sensitive to disease severity than current spirometry measurements (note that the very mild CF shows a higher ratio of tissue/RBC, whereas the corresponding FEV_1 is almost in the healthy range).

Discussion: The preliminary data presented here let us hypothesize that our technique is able to provide, in a single short breath-hold, detailed physiological information, without requiring the use of ionizing radiation.
References:
[1] Cystic Fibrosis Foundation, 2012; ().
[2] Tiddens, H., et al., 2000, Eur Respir J, 15: 735-42.

819

Accuracy of DWI-STIR and DWI-SPAIR fat-suppression techniques in ADC quantification and visibility of breast lesion identification at 3Tesla

M.L. Nogueira[1], S. Brandão[2], E. Matos[3], J. Loureiro[2], I. Ramos[4]
[1]Radiology, Hospital de São João/Faculty of Medicine of Oporto and School of Health Technology of Oporto/Polytechnic Institute of Oporto, Oporto/PORTUGAL, [2]Radiology, Hospital de São João/Faculty of Medicine of Oporto University, Oporto/PORTUGAL, [3]Health Community, Institute Biomedical Sciences Abel Salazar of Oporto University, Oporto/PORTUGAL, [4]Head Department Of Radiology, Hospital de São João/Faculty of Medicine of Oporto University, Oporto/PORTUGAL

Introduction: Controversy exists on what is the best fat-suppression technique for breast diffusion-weighted magnetic resonance imaging (DW-MRI) at 3Tesla because of the increased sensitivity to gradient and magnetic field in-homogeneities that may result on poor quality images [1,2].
Our purposes is to assess the effect of fat-suppression technique on Apparent Diffusion Coefficient (ADC) of breast malignant lesions, in what relates lesion visibility on DWI-Short Tau Inversion Recovery (STIR) and DWI-Spectrally Adiabatic Inversion Recovery (SPAIR) images, and also evaluate the effect of b1000 and b2000s/mm² on ADC calculation and lesion visual depiction to distinguish cellular grade.
Cases: Fifty women with suspected malignant breast lesions performed breast MRI examinations. The protocol includes morphological T1w and T2w pulse sequences and dynamic contrast enhancement acquisition. DWI-STIR and DWI-SPAIR were added before gadolinium injection.
For quantitative analysis, comparison between lesion mean signal intensity (SI) and ADC values on the two DWI pulse sequences was performed. ADC values were calculated based on b50-b1000 and b50-b2000s/mm² diffusion-weighting. For qualitative assessment, lesions were reviewed *a posteriori* in a random order, in consensus by two observers. Lesion visibility was rated using a 3-point scale (1-poor; 2-good; 3-excellent). Differences between STIR and SPAIR scores were analysed with the t-test for paired samples and the concordance in lesion visibility with Kappa coefficient.
There was significant difference between mean SI values for the 61 lesions found by the two fat suppression techniques (b50s/mm² p<0,001; b1000s/mm² p<0,001; b2000s/mm² p<0,001). Despite that, mean ADC values were not different between DWI-STIR and DWI-SPAIR for the same b-value (ADC_b1000 p=0,95; ADC_b2000 p=0,29) (Figure 1).

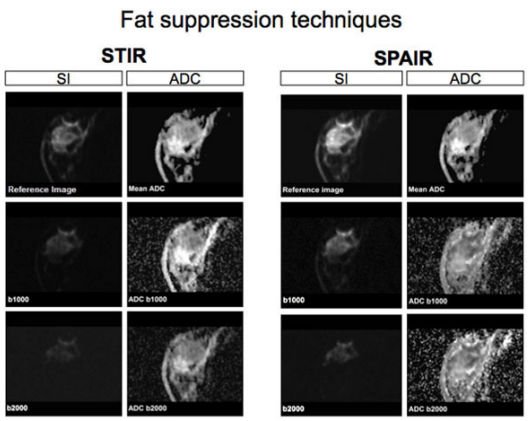

When we consider lesion histology type, we only found a significant difference in ADC at b2000 s/mm² for invasive lobular carcinoma (p=0,035). Lesion visual analysis showed good and moderate visibility between DWI-STIR and DWI-SPAIR on b1000s/mm² (Kappa=0,62) and b2000s/mm² (Kappa=0,56) respectively.
Discussion: For breast DWI, fat suppression techniques is critical because the variable content of fatty tissue. Considering the physics characteristics of both fat suppression techniques [3], possible explanation for our results is that SPAIR is more prone to susceptibility effects from air–fat interface, inframammary folds and chemical shift artefacts resulting in more magnetic in-homogenity that disturbs uniform fat suppression then STIR. However, visual assessment DWI-SPAIR is not affected.
References:
[1] Khouli, R et al., 2010, Radiology, 64-73
[2] Woodhams, R et al., 2011, RadioGraphics, 1059-1084
[3] Baron, P et al., 2010, NMR Biomed, 399-405

820

Bilobed Gallbladder (Vesica Fellea Divisa).

I.T. Rakici[1], A. Ozturk[2]
[1]Radiology, Aksaray Devlet Hastanesi, Aksaray/TURKEY, [2]Radiology, Bakırköy Ruh Sinir Hastalıkları Hastanesi, Istanbul/TURKEY

Introduction: Gallbladder duplication is a rare congenital malformation, occurring in about one per about 4000 births. Pre-operative diagnosis is extremely important as if diagnosed during surgery; the per-operative location of the second gallbladder may be difficult or even be missed. We are reporting a case of double gallbladder with its Magnetic Resonance imaging features as it is very rare.
Cases: A 65 year old man patient with renal cancer incidentally found bilobed gallbladder during MR imaging.

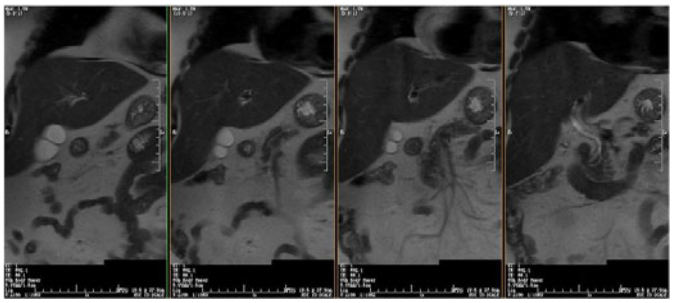

Figure 1: Coronal T2- weighted MRI image shows common bile duct, two different fundus and corpus.

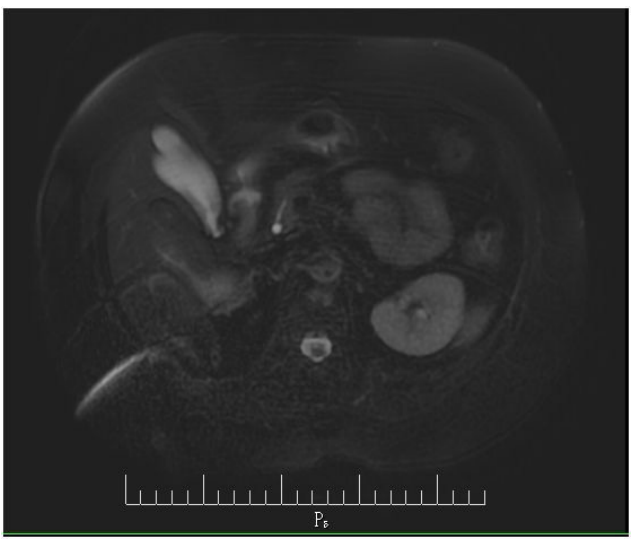

Figure 2: Axial fat saturated T2- weighted MRI image shows the connection between two fundus before common bile duct.

Discussion: Duplication of the gallbladder is a rare congenital anomaly, occurring in about one per 4000 births Double gallbladders are classified according to the Boyden's classification. The two main types of duplications are vesica fellea divisa or bilobed gallbladder and vesica fellea duplex or true duplication, with two different cystic duct (1). The various modalities like ultrasound, Oral cholecystogram (OCG), scintigraphy, ERCP, PTC, CT scan and MRI can be used pre-operatively to diagnose double gallbladder (2). In symptomatic

patient, cholecystectomy is recommended with the excision of both the gallbladder even if the disease is present only in one lobe (3)

References:
1- Boyden EA. The accessory gallbladder: an embryological and comparative study of aberrant biliary vesicles occuring in man and the domestic mammals. Am J Anatomy 1926;38: 177-231.
2- Mazziotti S, Minutoli F, Blandino A, Vinci S, Salamone I, Gaeta M. gallbladder duplication: MR Cholangiography demonstration. Abdom Imaging 2001; 26(3): 287-89.
3- Gigot J, Van Beers B, Goncette L, et al. Laparoscopic treatment of gallbladder duplication-A plea for removal of both gallbladder. Surg Endosc 1997; 11(5):479-82.

821

Pubovisceral muscle measurements in urinary incontinence.

S. Brandão[1], T. Da Roza[2], S. Duarte[3], T. Mascarenhas[4], R.N. Jorge[2]
[1]Radiology, Centro Hospitalar de São João, Oporto/PORTUGAL, [2]Idmec, FEUP, Oporto/PORTUGAL, [3]Depart. Of Gynecology|obstetrics, Centro Hospitalar de São João, oporto/PORTUGAL, [4]Depart. Of Gynecology|obstetrics, Centro Hospitalar de São João, Oporto/PORTUGAL

Introduction: The levator ani muscle divisions have an important role on continence, and changes in morphology are associated with pathological conditions, namely urinary incontinence. Muscle morphology can be evaluated through magnetic resonance imaging (MRI) and ultrasound [1,2]. Some authors suggest that thickness abnormalities are associated with pelvic floor dysfunction, which represents an important public health concern [3]. Therefore, it is expected that in women with urinary incontinence the abnormal thickness are larger when compared with continent women.
Cases: Translabial 3D/4D ultrasound and anatomical T2-w images of the pelvic floor were obtained from 11 young nulliparous women (7 clinically diagnosed as incontinent). Ultrasound images were acquired using a 7MHz transducer at rest, at an angle of 70º, to be parallel to the plane of minimal dimensions. T2-w MR images were acquired by means of a 3T scanner, at rest, parallel to the puborectal line to be coincident to the ultrasound.
We compared continent and incontinent women pubovisceral muscle thickness (cm), on right and left sides, at the level of midvagina on the axial MR and ultrasound images(fig.1).

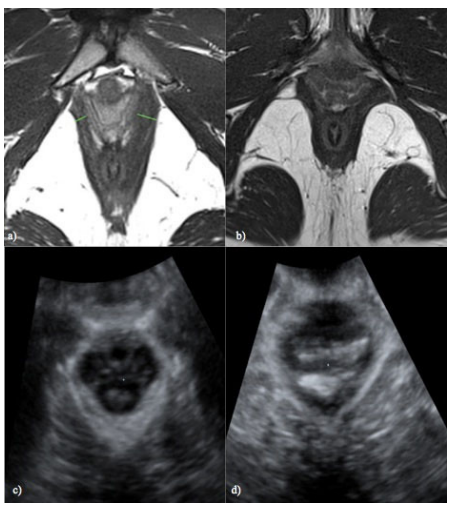

Our results showed a thicker left side of the muscle (0.7±0.25) when compared to the right side (0.91±0.26) for the continent women (p=0.038) (fig.1a,c), while for the incontinent, thickness was very similar (0.58± 0.17 for the right side and 0.59±0.11 for the left side)(fig.1b,d). Ultrasound and MRI thickness values were compared and ultrasound showed the same relation between right and left sides, although the measures were all lower, and the difference was greater (0.15±0.59) when compared to MRI (0.09±0.69). There was a weak correlation between US and MRI measurements.

Discussion: Translabial ultrasound is the usual imaging method to evaluate pelvic floor muscles morphology at rest, contraction and Valsalva Maneuver, when clinical findings are suggestive of UI. Despite that, MRI is more accurate to evaluate subtle muscle changes. Differences between left and right portions of pubovisceral muscle have already been described on both continent and incontinent women[4,5]. This is an important parameter to account to, especially on physiologycal conditions as contraction and Valsalva. Therefore, further research should investigate if these imaging planes and measurements should be included on the MR protocol.

References:
[1]Dietz, HP *et al.*, 2005, Ultrasound Obstet Gynecol, 580–585
[2]Law, YM *et al.*, 2008, AJR, S45–S53
[3]Fielding, JR, *et al.*, 1996, J Magn Reson Imaging, 961–963
[4]Singh, K *et al.*, Obstet Gynecol., 2002, 433–438
[5]Kim, JK *et al.*, 2003, AJR, 1037–1044

822

WITHDRAWN

823

Mimics of ovarian cancer in MR imaging

E. Batista[1], T.M. Cunha[2]
[1]Radiology, Hospital Curry Cabral - CHLC, 166/PORTUGAL, [2]Radiology, Instituto Português de Oncologia Francisco Gentil, EPE, Lisbon/PORTUGAL

Introduction: Ovarian cancer findings in imaging are well known. They include lesion size (>4cm), thickness of the walls and septa (>3mm) and solid or mixed solid and cystic components architecture, including papillary projections, nodularity, various degrees of necrosis and hemorrhage and tumor vessels determining contrast enhancement. Since it is common to find advanced disease at initial presentation (FIGO III-IV), ancillary findings such as infiltration of pelvic organs or sidewall, peritoneal implants, ascites and adenopathy, increase the diagnostic confidence for ovarian cancer.
However, despite well-established imaging criteria, findings in malignant and benign lesions overlap and mimics of ovarian cancer contribute to the complexity of imaging interpretation.
Cases: The authors will present a pictorial review of ovarian cancer mimics and provide a systematic approach for imaging interpretation and their differentiation, using MRI as a problem solver, according to the ESUR Guidelines 2010. For practical purposes, ovarian cancer mimics presented will be divided in solid pelvic/adnexal lesions (uterine leiomyioma, atypical fibrothecoma, dysgerminoma, Brenner tumor, mature solid teratoma, ovarian lymphoma and massive ovarian edema and ovarian metastasis) and complex adnexal lesions (endometrioma, dermoid tumor without fat, cystadenofibroma, struma ovarii tumor, ovarian metastasis, tubo-ovarian abscess, ovarian torsion and ovarian hyperstimulation syndrome).
Discussion: The pretreatment determinations of the location, size and likelihood of malignancy of a lesion are becoming increasingly important, as treatment options for adnexal masses become more sophisticated and patient specific. A systematic stepwise approach to imaging analysis associated with the knowledge of MR specific findings in ovarian cancer is fundamental for identifying the multiple ovarian cancer mimics. Subdividing ovarian cancer mimics into groups according to their morphologic features helps narrowing down the differential diagnosis.

References:
1.Hricak H, Chen M, Coakley FV et al. Complex adnexal masses: detection and characterization with MR imaging – multivariate analysis. 2000 Radiology; 214(1): 39-46
2. Bazot M, Nassar-Slaba J, Thomassin-Naggara I et al. MR imaging compared with intraoperative frozen-section examination for the diagnosis of adnexal tumors: correlation with final histology. 2000 Eur Radiol; 16:2687-1699
3.Kim KA, Park CM et al. Benign ovarian tumors with solid and cystic components that mimic malignancy. 2004 AJR; 182:1259-1265
4.Imaoka I, Wada A et al. Developing an MR imaging strategy for diagnosis of ovarian masses. 2006 Radiographics; 26:1431-1448

6. Forstner R, Sala E, Kinkel K, Spencer JA. ESUR guidelines: ovarian cancer staging and follow-up. 2010 Eur Radiol; 20(1): 25-35
7.Forstner R et al. MRI in ovarian cancer. 2012 Imaging in Medicine; 4(1): 59-75.

824

Choroidal Melanoma: the role of magnetic resonance imaging from diagnosis to management

C. Mandel[1], N. Bergen[1], C. Phillips[2]
[1]Radiology, Peter MacCallum Cancer Centre, East Melbourne/AUSTRALIA, [2]Radiation Oncology, Peter MacCallum Cancer Centre, East Melbourne/ AUSTRALIA

Introduction: Choroidal melanoma is the commonest primary tumour of the globe. It usually progresses more slowly than skin melanoma. Eye-conserving treatment is becoming more common. Magnetic resonance imaging has an important role in determining treatment options, planning radiotherapy and follow up of patients after treatment.
Cases: We present images form our cohort of patients to illustrate:
1 the imaging appearances of choroidal melanoma
2 the appearances of commoner complications such as retinal detachment and
3 how anatomy is important in determining appropriate treatment options
4 the role of MRI in planning treatment
5 the use of MRI in follow-up.
We also present images from radiotherapy planning to illustrate how MRI is used and the importance of careful attention to technique.
Discussion: The anatomy of the globe determines the pattern of spread of choroidal melanoma: this is important in determing the most appropriate treatment options. Local lymph node metastases only occur when the sclera is breached. The commonest site of metastasis is the liver.
Overall 5 year survival is 77% but 50% of patients have metastases by 15 years. Thinner tumours have a better prognosis.
There are now a variety of treatment options for choroidal melanoma. These include observation, brachytherapy, a variety of external beam radiotherapy options, enucleation and exenteration. Long-term survival is not compromised by non-surgical treatments.
The choice of treatment depends on the location of the tumour within the globe, proximity to the optic nerve, spread beyond the globe and patient preferences.
Magnetic resonance imaging is very important in management and careful attention to technique is critical because of the very small size of the tumours and the need to precisely target the radiation beam.
We use a combination of thin-section, high-resoltion images of the globe and whole head sequences in order to fuse the images with the planning CT in the radiotherapy planning software.
References:
The Collaborative Ocular Melanoma Study: an Overview. Margo C. Cancer Control 2004; 11:304-309
Choroidal Melanoma: Natural History and Management Options. Bell DJ, Wilson MW. Cancer Control; 11:296-303
Mortality in Patients With Small Choroidal Melanoma The Collaborative Ocular Melanoma Study Group Arch Ophthalmol. 1997;115(7):886-893
Screening for Metastasis From Choroidal Melanoma: The Collaborative Ocular Melanoma Study Group J Clinical Oncology 2004; 22:2438-2444
Accuracy of Diagnosis of Choroidal Melanomas in the Collaborative Ocular Melanoma Study. The Collaborative Ocular Melanoma Study Group *Arch Ophthalmol.* 1990;108(9):1268-1273
Mortality in Patients With Small Choroidal Melanoma The Collaborative Ocular Melanoma Study Group Arch Ophthalmol. 1997;115(7):886-893

Clinical Review Poster

Head and neck

825

Crucial Magnetic Resonance Imaging (MRI) anatomy of the head and neck in cancer staging.

G. Guzman Perez-Carrillo[1], J.P. Hogg[2]
[1]Radiology, Centro de Diagnostico, SA, Granada/SPAIN, [2]Radiology, West Virginia University- Robert C. Byrd Health Sciences Center, Morgantown/WV/UNITED STATES OF AMERICA

Introduction: Our purpose is to provide an educational exhibit illustrating the crucial head and neck anatomy in magnetic resonance imaging (MRI) utilized in the correct local staging of head and neck cancers. The approach is based on anatomic localization with an emphasis on the anatomy of the oral cavity, nasal sinuses, nasopharynx, oropharynx, hypopharynx, larynx, nodal levels, deep cervical spaces, fascial planes and use of diffusion wighted images (DWI) to identify possible regions of locoregional tumor that need more meticulous characterization and evaluation.
Cases: Retrospective case review of a broad range of pathologically and clinically proven cases of head and neck neoplasms accumulated from 2000-2012 at a tertiary referral university medical center and from 2010-2012 at a large private practice clinic which provides MRI service to the local university medical center. These are organized by location of the primary neoplasm and pertinent anatomy for the local staging. High quality anatomical and DWI images are used to illustrate the findings. Some of the cases will be accompanied by histopathological correlation.
Discussion: Staging of head and neck can present a diagnostic challenge. Critical anatomy that needs to be recognized and evaluated for the correct staging of these tumors is fundamental to optimize patient care and outcome. The viewer of this exhibit will gain or refresh information about critical MRI anatomy for the staging of head and neck cancers useful in clinical practice and for preparation for certifying examinations. The images provided aid in recognition of critical anatomical structures that must be thoroughly evaluated and categorized in order to arrive at the correct diagnosis.
References:
Drake RL. Gray's Anatomy for Students. Philadelphia: Elsevier/Churchill Livingstone, 2005.
Cochard LA. Netter's Atlas of Human Embryology. Teterboro, NJ: Icon Learning Systems, 2002.
Larsen WJ. Human Embryology. New York: Churchill Livingstone, 2001.
Hermans R. Diffusion-weighted MRI in head and neck cancer. Curr Opin Otolaryngol Head Neck Surg. 2010 Apr;18(2):72-8.
Vandecaveye V, De Keyzer F, Dirix P, Lambrecht M, Nuyts S, Hermans R. Applications of diffusion-weighted magnetic resonance imaging in head and neck squamous cell carcinoma. Neuroradiology. 2010 Sep;52(9):773-84.
Fong D, Bhatia KS, Yeung D, King AD. Diagnostic accuracy of diffusion-weighted MR imaging for nasopharyngeal carcinoma, head and neck lymphoma and squamous cell carcinoma at the primary site. Oral Oncol. 2010 Aug;46(8):603-6.
Mack MG, Rieger J, Baghi M, Bisdas S, Vogl TJ. Cervical lymph nodes. Eur J Radiol. 2008 Jun;66(3):493-500.

826

Imaging the lacrimal glands with magnetic resonance

R.G. Saru[1], T.A. Ferreira[2]
[1]Radiology, University Emergency Hospital, Bucharest/ROMANIA, [2]Radiology, Leiden University Medical center, 2300 RC Leiden/NETHERLANDS

Introduction: The lacrimal glands are located in the anterior, superior and lateral aspect of the orbital cavity, in the extraconal space.
Cases: The aim of this presentation is to provide an overview of the role of MR in characterization of masses of the lacrimal gland and also its normal anatomy. The differential diagnosis of unilateral lacrimal gland masses, in particular of nonaggressive an aggressive lesions will be shown. The differential diagnosis of bilateral lacrimal gland lesions will be shown.
Several pathologies including capillary hemangioma, cysts, inflammatory lesions such as pseudotumor and sarcoidosis, several benign and malignant tumors such as pleomorphic adenoma, adenoid cystic carcinoma, lymphoma will be discussed. Perineural extension following the lacrimal nerve will also be emphasized.
Discussion: In conclusion, magnetic resonance is a useful tool in imaging the lacrimal gland.

827

The feasibility of Phosphorus-31 SWIFT dental MRI

Y. Sun[1], D. Idiyatullin[2], M. Garwood[2], A. Heerschap[1]
[1]Radiology, Radboud University Medical Center, Nijmegen/NETHERLANDS, [2]Center For Magnetic Resonance Research, University of Minnesota, Minneapolis/MN/UNITED STATES OF AMERICA

Purpose/Introduction**:** Several pilot studies have demonstrated the potential of applying MRI in dental imaging (1,2). But it's still challenging even with ultrashort echo time (UTE) sequences, the most mature technique in visualizing very short T_2 tissues (3). The recently developed Sweep Imaging With Fourier Transformation (SWIFT) technique offers high-resolution 3D images of hard and soft tissue within clinically relevant scanning times (4). However, the main content of human tooth is hydroxylapatite, a crystalline calcium phosphate. Thus ^{31}P SWIFT would directly provide images of calcium phosphate constituents. In this study, the feasibility of ^{31}P SWIFT dental imaging was examined.
Subjects and Methods: The extracted human molar was imaged in a 9.4T MR system (Agilent- Varian) with a home-built double channel surface coil. Proton SWIFT imaging was acquired with an excitation bandwidth of 125kHz, flip angle (FA) 15°, TR of 2.5ms, FOV of 3*3*3cm, and a matrix of 256*256*256, the total acquisition(TA) time is 100 seconds. Phosphorus SWIFT imaging was acquired with an excitation bandwidth of 45kHz, FA of 3.6°, oversampling factor of 8, TR of 200ms, FOV of 3*3*3cm, and a matrix of 64*64*64,TA around 4mins. The relaxation times of ^{31}P spins were also measured.
Results: On ^{1}H SWIFT images, a clear delineation of enamel, dentin and pulp is visible, early stage caries lesions could also be identified. For ^{31}P, the measured T_2* was 100 microsecond and T_1 was 130 seconds, which necessitates a small flip angle and rapid data acquisition. The ^{31}P images clearly reflect the shape and size of the tooth, further delineation of molar structures is also possible: the enamel shows higher signal intensity due to high content of mineral hydroxylapatite. In contrast pulpal tissue did not appear on the ^{31}P images because of the extremely low phosphate concentration.
Discussion/Conclusion:
In this study, the feasibility of ^{31}P SWIFT dental imaging was demonstrated for the first time. SWIFT imaging of ^{31}P requires extremely fast transmit/receive switching, which could be further optimized to enhance imaging quality and spatial resolution.
^{31}P SWIFT has potential value in tooth imaging because of its direct measurement of the phosphorous signal. Apart from dental imaging, it might be attractive in diagnostics of osteoporosis and other bone disease because of mineral breakdown. The versatility of the SWIFT provides many possibilities for improvements.
References:
1.Baumann et al. 1993 2. Wu et al.1996 3.Bracher et al. 2011 4.Idiyatullin et al.2011

Clinical Review Poster

Neuro

828

WITHDRAWN

829

Carnosine Brain's concentration measurement through magnetic resonance spectroscopy

E.F. Cardoso[1], B.F. Pastorello[1], V.D.S. Painelli[2], G. Artioli[2], B. Gualano[2], A.H. Lancha Junior[2], B. Foerster[1], C.D.C. Leite[1], M.C.G. Otaduy[1]
[1]Instituto De Radiologia - Ressonância Magnética, Hospital das Clínicas da Faculdade de Medicina da Universidade de São Paulo, São Paulo - SP/BRAZIL, [2]Biodinâmica Do Movimento Humano, Escola de Educação Física e Esporte - USP, São Paulo - SP/BRAZIL

Introduction: Carnosine (β-alanyl-L-histidine) is a dipeptide present in human brain. Although its physiological role is still under investigation many beneficial actions have been attributed to it, such as being an antioxidant, antiglycating and a free-radical scavenger. This fact raises the hypothesis that it might be useful in the prevention and treatment of neurodegenerative disorders as Parkinson's and Alzheimer's disease also in epilepsy.
As the molecule of carnosine is very similar to homocarnosine (which is also a dipeptide composed by gamma-aminobutyric acid (GABA) and histidine) the pool brain's concentration of these dipetides can be estimated through MR spectroscopy[1].
In this abstract, we describe a modified technique that enables to quantify the concentration of homocarnosine / carnosine in the brain. Recently our group showed that MR spectroscopy is able to demonstrate increase in muscle carnosine after dietary supplementation[2]. This technique might have a major impact in the research of neurodegenerative disorders, in order to clarify the role of these dipeptides in its pathophysiology and pathogenesis.
Cases: Experiments were performed at Phillips Intera 3 T using a 8-channel head coil. Single voxel spectroscopy was performed with STEAM technique using the following parameters: TR: 1840 ms; TE: 9.9 ms; TM: 37 ms. Research mode enabled us to modify the frequency of resonance in order to increase sensitivity to the spectral frequency region of carnosine (8 ppm).
Voxel was positioned at anterior cingulated gyrus (voxel size: 3x3x3 cm) in 4 healthy volunteers. In order to evaluate reproducibility spectroscopy was repeated in all volunteers at the same day, one volunteer repeated the exam every week during one month.
In order to quantify the metabolites we used jMRUI software (www.mrui.uab.es) considering only the second peak of carnosine (8 ppm).
This method was robust enabling quantification and reproducibility similar to major spectroscopy peaks such as NAA. In the single subject we evaluated for 4 weeks no large differences was observed.
Discussion: This technique enables to estimate the concentration carnosine / homocarnosine in the brain. In the near future we want to evaluate if the technique is able to detect differences in carnosine due to disease or treatment effects.
References:
1. Rothman DL et al. Homocarnosine and the measurement of neuronal pH in patients with epilepsy. *Magn Reson Med* 1997;38:924-929
2. Del Favero S et al. Beta-alanine (Carnosyn) supplementation in elderly subjects (60-80 years): effects on muscle carnosine content and physical capacity. *Amino Acids* 2011

830

Characterization of Focal Openings of the Blood-Brain Barrier at Different Time Points Using MR guided Focused Ultrasound Surgery

M. Costa, C. Fernandes, M. Wintermark, A. Klibanov, J. Mugler Iii, J. Mata
Radiology And Medical Imaging, University of Virginia, Charlottesville/ UNITED STATES OF AMERICA

Introduction: The use of therapeutic agents in the brain is limited by the blood-brain barrier (BBB). Focal or regional opening of the BBB in a non-invasive and controlled way may provide the administration of specifically targeted therapeutic agents to a localized area. One approach is to use Magnetic Resonance guided Focused Ultrasound (MRgFUS), that allows applying low amounts of energy to produce acoustic pressure at a desired frequency, using MR images to guide the treatment [1]. This permits to break microbubbles and open the BBB in a very focal area.
The purpose of this work was to characterize the opening of the BBB temporally, during the 60min. immediately post-sonication with microbubbles, to determine the optimal time window to administer intra-venous brain therapeutic agents.
Cases: Three Sprague-Dawley rats (~250g) underwent MRgFUS using a focused ultrasound system (FUS, Canada) composed of a single transducer, operating at 1.06MHz. Each animal received one or two sonications immediately after the injection of 2cc of microbubbles. Each sonication had a duration of 120sec.; acoustic pressure=1MPa; burst time=10ms; period=5sec. All scans were done in a 3T clinical system (Trio, Siemens Medical Solutions) using a TX/RX surface radiofrequency loop coil. MR imaging was performed after multiple injections of 0.2cc of Gadodiamide (Omniscan, GE Healthcare, Canada), using a contrast-enhanced protocol (CE-T1w), at baseline, 15min., 30min. , 45min. and 60min. post-sonication; FOV=60x60mm^2; in-plane resolution=0.3x0.3mm^2; slice thickness=2.0mm; TR/TE=110/3.2ms.
Focal opening of the BBB was observed in all cases at 30min. post-sonication (Fig. 1B&2). At 30-45min. post-sonication the SNR of the focal point was highest with a 2.1 increase (Fig. 1&2). The area of contrast extravasation kept increasing until the last time point at 60min. post-sonication (Fig. 2), to a mean value around 2.3 times the initial value immediately after sonication. After 30min. the borders of the area of extravasation were less defined and appeared more diffuse (Fig. 1C).

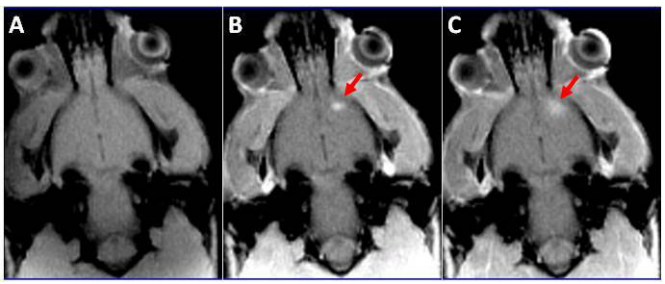

Figure 1A: Baseline CE-MRI of in-vivo rat brain model. **B:** 30 minutes post-sonication with microbubbles. Note the very well defined borders of the focal BBB opening (red arrow), very suitable for precise delivery of therapeutic agents to the brain. **C:** 60 minutes post-sonication. Note the diffuse and wider area of BBB opening (red arrow), more suitable for larger extended deliveries of therapeutic agents, for example to the areas around a brain tumor. All images are from the same animal.

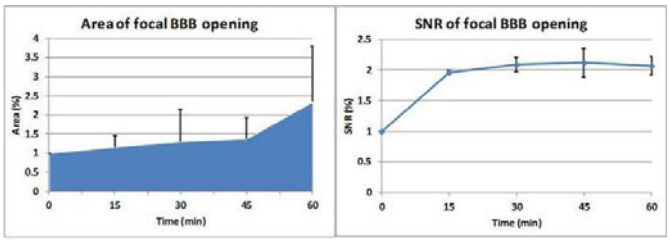

Figure 2: Temporal quantification and characterization of focal openings of the BBB, induced by MRgFUS with microbubbles. **Left:** Percentage area opened over time, post-sonication. Note the steady increase all the way to 60 minutes. **Right:** Increase of SNR over time up to 30 minutes post-sonication, followed by a slight decrease until 60 minutes. Error bars represent STD.

Discussion: From this preliminary animal study, we found that for highly localized delivery of intravenous therapeutic agents to the brain, the optimal delivery time is around 30min. after sonication using the parameters above and microbubbles. For therapeutic delivery in larger areas of the brain we may have to wait at least 60min. before injecting an agent via I.V. Since the area of open BBB was still increasing for all animals 60min. post-sonication, future studies should probe this at longer time periods.

References:

[1] McDannold, N., et al., 2005, Ultrasound Med. Biol., 31:1527-1537.

831

4D flow analysis in brain aneurysms using 3D radial phase contrast MR imaging

P. Roca[1], M. Edjlali-Goujon[1], C. Rabrait[2], K. Johnson[3], O. Wieben[4], D. Trystram[1], O. Naggara[1], J. Meder[1], C. Oppenheim[1]
[1]Department Of Neuroradiology, Sainte-Anne Hospital, Paris/FRANCE, [2]Clinical Science Development Group, GE Healthare, Buc/FRANCE, [3]Department Of Medical Physics, University of Wisconsin, Madison, madison/UNITED STATES OF AMERICA, [4]Department Of Medical Physics, University of Wisconsin, Madison/WI/UNITED STATES OF AMERICA

Introduction: The impact of flow on the aneurysm wall may be an important factor for pathogenesis and for the assessment of rupture risk. The 3D PC-VIPR MR pulse sequence [1] is a non-invasive approach that provides dynamic 3D velocity measurements, enabling the in-vivo study of blood flow pattern in aneurysms with high spatial and temporal resolution. Here we present the first application of this sequence for the 4D flow analysis of one human aneurysm with a high risk of rupture.

Cases: 3D PC-VIPR data with retrospective cardiac gating were acquired on a 3T MR scanner (GE Healthcare) after injection of 15 mL of contrast agent (Gd-DTPA). Two velocity encodings were used to obtain information on fast (80cm/s) and slow flows (30cm/s). Each 3D volume covering the whole brain was imaged in about 5 minutes with an isotropic spatial resolution of 0.86mm. All radial projections were pooled to compute time-averaged 3D velocity maps. In addition, 3D PC-VIPR data at individual time frames within the cardiac cycle (8 phases) were reconstructed using an adaptive width temporal filter [2] leading to 4D velocity maps, used to calculate pressure difference maps. Among our patients population with brain vascular disorders, we show here a case presenting an anterior ethmoidal type IV arterio-veinous fistula, and a 10-mm aneurysm of a cortical vein of drainage.

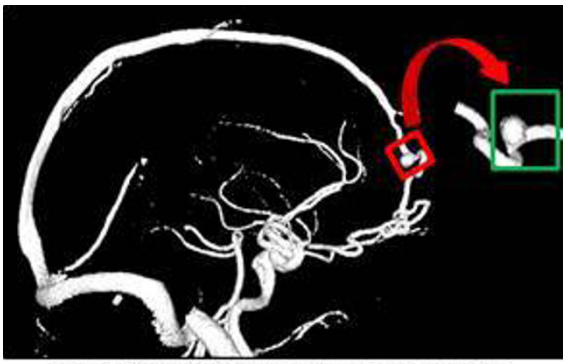

Figure1. PC VIPR vessels segmentation. Aneurysm is in red square, and view used in Fig. 2 in green.

Using streamlines originating from different planes, we identified a spiral flow pattern with low velocities at the apex of the vortex and a zone of flow disturbance. We selected the systolic phase based on time-resolved velocity data. The pressure maps showed a low pressure differential within the aneurysm, as found in a canine model of recirculation flow pattern [2], with smaller values at the vortex core, in line with computational fluid dynamic studies [3].

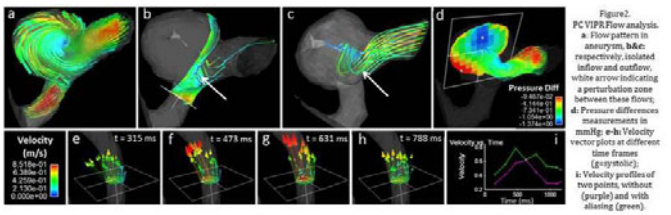

Figure2. PC VIPR Flow analysis. a: Flow pattern in aneurysm, b&c: respectively, isolated inflow and outflow, white arrow indicating a perturbation zone between these flows; d: Pressure differences measurements in mmHg; e-h: Velocity vector plots at different time frames (g=systolic); i: Velocity profiles of two points, without (purple) and with aliasing (green).

Discussion: This methodology sheds some new light in the quantitative description of complex blood-flow patterns with a significant improvement in spatial resolution compared to similar 4D Flow MR sequences [4], [5]. In addition, time-resolved 3D PC-VIPR data allows to identify the systolic time frame and pressure patterns. A better understanding of hemodynamics in ruptured and unruptured aneurysms may help in improving our treatment paradigms and patients follow-up.

References:

[1] Gu T et al., AJNR, 26:743-749, 2005.; [2] Moftakhar R et al., AJNR, 28:1710-1714, 2007; [3] Jeong, J et al., J Fluid Mechanics, 285:69-94, 1995. [4] Isoda, H et al., Neuroradiology, 52: 921-8, 2010; [5] Meckel S et al., Neuroradiology, 50:473-484, 2008.

832

Comparison of gradient and spin echo arterial spin labeling (GRASE-ASL), pseudo continuous arterial spin labeling (pCASL) and dynamic susceptibility-weighted contrast-enhanced (DSC) perfusion in carotid stenosis.

F. Kellner-Weldon[1], M. El-Koussy[1], M. Mono[2], K. Jann[3], R. Verma[1], A. Federspiel[3], J. Slotboom[1], M. Zbinden[1], R. Wiest[1], **C. Kiefer**[1], G. Schroth[1]
[1]Neuroradiology, University Hospital Bern, Bern/SWITZERLAND, [2]Neurology, University Hospital Bern, Bern/SWITZERLAND, [3]Department Of Psychiatric Neurophysiology, University Hospital of Psychiatry, Bern, Bern/SWITZERLAND

Introduction: The aim of this study was to compare two arterial-spin-labeling (ASL) techniques, namely gradient-and-spin-echo-arterial-spin-labeling (GRASE-ASL), pseudo-continuous ASL (pCASL) and dynamic-susceptibility-weighted contrast-enhanced (DSC) perfusion in patients with carotid artery disease (CAD).

Cases: MRI was performed in 20 patients (mean stenosis measured by MR-Angiography, NASCET, 80.2 %, std 15.6). Measurements included pCASL-

CBF[1] (pCBF) (label-delay 1.5 s, label-time 1.72s), GRASE-ASL[2] (14 time points over 2.8 s, bolus-peak-time (bpt), model/non-model-based CBF (m/aCBF), and DSC-perfusion (relative cerebral blood flow (cbf) and ttp (time to peak)[3,4]). Data sets (figure1) were coregistered and normalized[5]. Amide software[6] was used to place four territorial regions on each hemisphere[7]. Pearson correlation was calculated for ratios of each region(left/right).

Good overall correlation between bpt and ttp. In areas where pCBF measured <0ml/min/100g (mean size/mm^3 507.5, std 302.8), mCBF was 33.51ml/min/100g. Mean mCBF in areas with bpt <1000 and >2000ms was 46.71(std 10.83) and 20.82(std 8.2)ml/min/100g, respectively. Ratios of >30% bpt in MCA territory correlate with low pCBF. Table1 shows overall correlation.

ratios of territories	Significant correlation	No significant correlation
ttp and bpt	All 0.64	
pCBF and cbf	MCA 0.51	
mCBF and pCBF		All 0.02
mCBF and cbf		All 0.13
bpt and pCBF		All -0.2
Bpt and pCBF in ratio of>10% (MCA)		0.26
Bpt and pCBF in ratio of>20% (MCA)		-0.19
Bpt and pCBF in ratio of>30% (MCA)	-0.51 (MCA), -0.83 (PCA), -0.54 (all)	
bpt and aCBF in >80% unilateral stenosis	MCA -0.52	

Table 1. over all correlation ACA= territory of anterior cerebral artery, MCA= territory of middle cerebral artery, PCA= territory of posterior cerebral artery, BSG= basal ganglia territory; bpt(ms), mCBF (ml/min/100g), pCBF (ml/min/100g), ttp (sec), aCBF and cbf (relative)

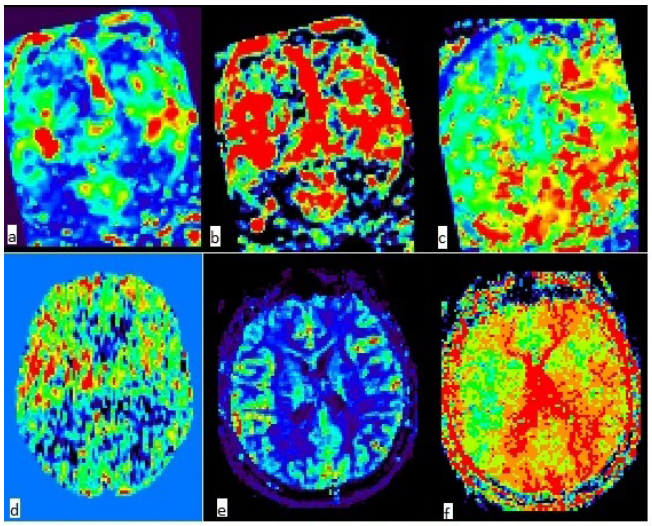

Figure 1.Pat. with unilateral occlusion of the left ICA; a) aCBF, b)mCBF, c)bpt, d)pCBF, e) cbf; f) ttp

Discussion: The timeparameters ttp and bpt show consistent results. The good correlation between prolonged bpt and low aCBF/pCBF in the MCA-territory makes GRASE-ASL a possible indicator of hypoperfusion and/or poor collateralization. PCASL with 120 measurements suffers intrinsic low SNR and yields non-physiologic pCBF while GRASE-ASL delivers physiologic values. ASL methodology in the clinical setting of CAD is technically challenging and requires further optimization.

References:

1 E. C. Wong, R. B. Buxton and L. R. Frank, "A Theoretical and Experimental Comparison of Continuous and Pulsed Arterial Spin Labeling Techniques for Quantitative Perfusion Imaging," Magnetic Resonance in Medicine, Vol. 40, No. 3, 1998, pp. 348-355

2 M. Guenther, K. Oshio and D. A. Feinberg, "Single-Shot 3D Imaging Techniques Improve Arterial Spin Labeling Perfusion Measurements," Magnetic Resonance in Medi- cine, Vol. 54, No. 2, 2005, pp. 491-498.

3 Meier P, Zierler KL. On the theory of the indicator-dilution method for measurement of blood flow and volume. J Appl Physiol 1954;6:731–44

4 Ostergaard L, Sorensen AG, Kwong KK, et al. High resolution measurement of cerebral blood flow using intravascular tracer bolus passages. Part II: Experimental comparison and preliminary results. Magn Reson Med 1996;36:726–36.

5 SPM8, Welcome Department of Cognitive Neurology, London, UK

6 Loening AM, Gambhir SS, " AMIDE: A Free Software Tool for Multimodality Medical Image Analysis", Molecular Imaging, 2(3):131-137, 2003.

7Damasio H: A computed tomographic guide to the identification of cerebral vascular territories. Arch Neurol 1983;40:138–142

833

Mapping of Primary Auditory Cortex using high-resolution fMRI.

T. Wolak, M. Rusiniak, A. Pluta, M. Lewandowska, L. Sliwa, H. Skarzynski, P.H. Skarzynski

Bioimaging Research Center, World Hearing Center, Nadarzyn-Kajetany/ POLAND

Introduction: The technical progress that has occurred in recent years has allowed MR imaging of submillimetre resolution. It is possible to obtain structural images with an isotropic resolution of approximately 0.3 mm. However, the acquisition of images needed to cover the whole brain takes a few minutes. While it is acceptable for structural imaging of the brain, in the case of imaging of brain function is not acceptable. fMRI acquisition of whole head is very fast but the resolution of images is rather poor. Even for 3T scanners it typically amounts 3x3x3mm (57 slices with a thickness of 3 mm, image matrix 64x64 pixels, Field of View 192x192, voxel volume is 27 mm3) with acquisition speed of 19 slices per second. The aim of this study was to develop protocols for acquisition of functional images of auditory cortex with high spatial resolution and comparing results acquired with different resolutions.

Cases: The study was conducted at 3T Magnetom Trio scanner located in the Bioimaging Research Center. The largest size of an image matrix that can be achieved is 128x160 pixels. The highest resolution of whole brain which can be achieved is 1.2x1.5x1.8 mm. Comparing high- resolution images with low-resolution images it can be seen that activation is localized only in the cortex of the brain (Fig.1).

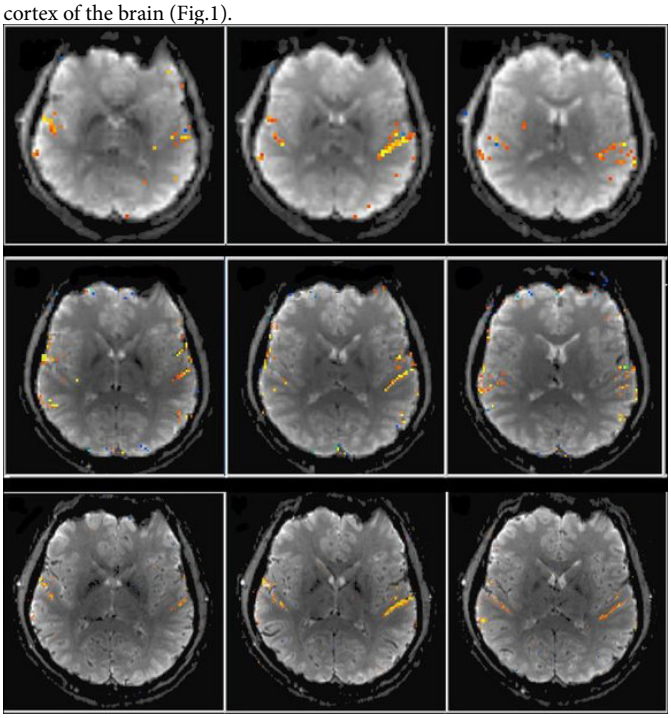

Even after interpolation of EPI images to overlay in the structural images (Fig.2) the localization of the activations in the gray matter is still very precise.

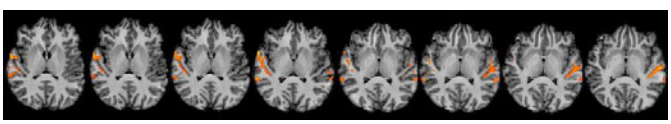

Discussion: First, higher resolution is associated with prolongation of the acquisition time (see Tab.1).

Voxel size [mm]	Matrix size [pixels]	Voxel volume [mm3]	Acquisition speed [images/s]	TR [ms] for acquisition of whole head	Nr of slices to cover whole head
3x3x3	64x64	27	17	2650	47
2x2x2	96x96	8	13	5400	70
1.2x1.5x1.8	128x160	3.24	12	7000	78

It reduces the temporal resolution of the functional study. Secondly, higher resolution means reducing the voxel size, thus reducing the signal to noise ratio. To keep unchanged the signal to noise ratio, it is necessary to use 32-channel coil. Third, smaller voxel means greater influence of movement artifacts in the image. Displacement or rotation of the patient's head should not exceed one millimeter. It is not recommended to apply a filter to the smoothing of functional images because it destroys the effect of high resolution (Fig.3).

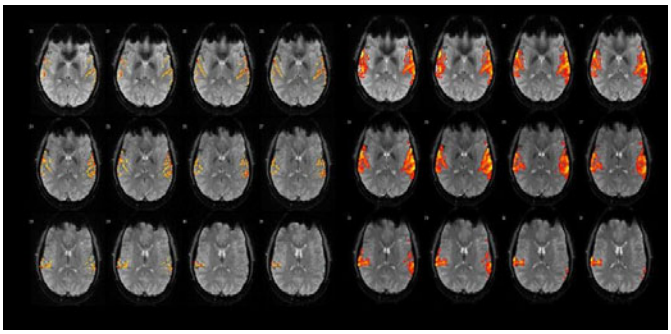

High resolution fMRI is essential for precise mapping of auditory cortex.

834

Time duration estimation of daily activities investigated by fMRI

G. Hossu[1], T. Rivasseau-Jonveaux[2], A. Simler[1], A. Trognon[3], M. Batt[3], J. Felblinger[4], M. Braun[5]

[1]Cic-it, CHU de Nancy, Vandoeuvre les Nancy/FRANCE, [2]Service De Gériatrie Hôpital De Brabois, Centre Mémoire de Ressources et de Recherche de Lorraine, Vandoeuvre les Nancy/FRANCE, [3]Département De Psychologie, Groupe de Recherche sur les Communications, Laboratoire INTERPSY, EA 4432, Nancy/FRANCE, [4]U947, INSERM, Nancy/FRANCE, [5]Iadi, Université de Lorraine, Nancy/FRANCE

Introduction: During Alzheimer disease(AD), alterations of temporality (time experienced by consciousness) are not well understood, both in terms of frequency/evolution and in terms of the underlying neuropsychological processes. However this aspect of the disease needs to be more investigated. Based on neuropsychological tests[1], we have put forward innovative functional MRI paradigms to estimate areas involved in the time duration estimation of daily activities in AD patients; these preliminary results are presented.

Cases: Eleven healthy subjects over fifty years old were examined (study approved by our institutional review board). Brain MRI examinations including anatomical and functional MRI imaging, were performed on a 3T scanner with an eight channel coil. A video projector and a display screen MRI compatible were used in order to show the tasks to the volunteers. If necessary, amagnetic glasses were adapted to correct subjects' visual acuity.

For each task (thirty seconds duration including ten working periods), three photographs(fig.1) were selected which represent the beginning, the progression and the end of an activity.

Figure1: example of daily activity shown to the volunteer

During the first exercise, the subject was asked to mentally describe projected pictures of daily life activities, mute and mental only. A second exercise, dealt with the presentation of images joined to the specific question:"how long does it take to complete this action?" A control task consisted in calculations was acquired for both exercises, alternated with working periods. Differences in BOLD signal in ON and OFF conditions were evaluated by SPM8 software.

Discussion: Group activations during the first exercise involved 19-37 Brodmann areas. Activations during the second exercise involved 16, 19 Brodmann areas and thalamus bilaterally (R>L), bilateral hippocampi and parahippocampal gyrus (BA 27-35), BA 6,8,45 (R>L) to the lateral orbitofrontal cortex. Comparing the two exercises(fig.2), the activations answered the question: "How long it takes to make the action?", when the volunteer observes the image of the action. We can conclude that in our volunteer group, activations occurred on BA 39-40 at left; the visual network is at bilateral BA 17-18, and bilateral cerebellar; left precentral is at BA 4-6 representing the cortical reactivation of the hand-eye couple.

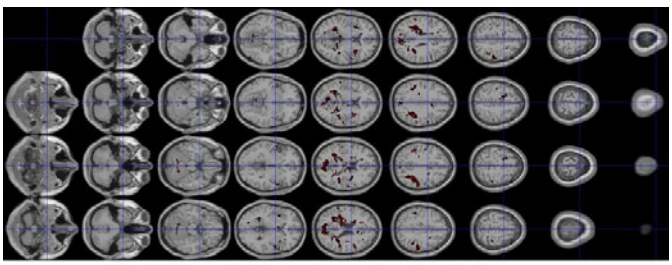

Figure2: Group activation match, second exercise vs the first one

This original neuropsychological methodology based on EDAVIE scale[1], was successfully adapted to fMRI experiment. In order to improve our understanding of cognitive processes and areas of the brain involved in time estimation during daily activities; further investigations will be performed in a larger study including healthy volunteers and AD patients.

References:

[1] Rivasseau-Jonveaux, Annales Médico Psychologiques,2012
[2] Rubia, Acta Neurobiologiae Experimentalis,2004

835

Progressive ataxia with an unknown signal in 1H MR brain spectra

M. Dezortova[1], K. Brozova[2], M. Hajek[1]
[1]Mr-unit, Dept. Diagnostic And Interventional Radiology, Institute for Clinical and Experimental Medicine, Prague 4/CZECH REPUBLIC, [2]Department Of Child Neurology, Thomayer Hospital, Prague 4/CZECH REPUBLIC

Introduction: In this study we report a case that represents, to our knowledge, an unknown disease characterized by a new, as yet undescribed signal in 1H MR spectra of the brain.
Cases: We repeatedly examined a female patient with progressive ataxia and spasticity since infancy, dependent on a wheelchair since 13 y/o. Her mild mental retardation is not progressing. She is without any other pathologic systemic involvement and abnormalities in biochemical tests.
Her parents and older sister are without neurological problems. In her family tree we only found two cases of males with multiple sclerosis.
The first MRI at the age of 2 years indicated leukodystrophy. Another MR examination including MRS was performed when she was 14, 16 and 18 y/o. 1H MR spectroscopy consisted of PRESS sequence with TR/TE=5000/30, 80, 135 and 270 ms. Her mother and sister underwent the same MR examination protocol. The volume of interest of 5.2 ml and positions in the frontoparietal white matter were kept the same in all examinations in all subjects.
Spectra were evaluated by LCModel technique. The results were compared with a control group routinely used for clinical purposes.
Mother and sister of the patient did not show any pathological findings on MR images. Also, the metabolite profiles were similar to the control levels.
In the patient, MRI revealed supratentorial dystrophic changes predominantly affecting the white matter, with progressive atrophy.

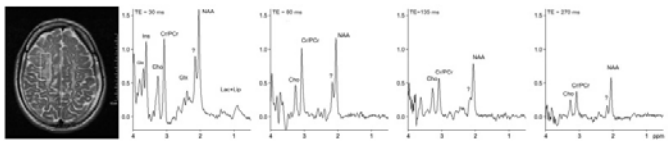

MR spectroscopy revealed low NAA and choline and high myo-inositol (Table). In addition, a new signal visible at 2.13±0.01 ppm was repeatedly detected. This signal was visible even in spectra with a long TE (Figure). Its intensity as well as the calculation using LCModel with modified databasis resulted in cca 2.4 mM concentration.

Table. Metabolite concentrations [mM] calculated by the LCModel technique with segmentation to CSF content. (NAA – N-acetylaspartate, Cr/PCr – creatine/phosphocreatine, Cho – choline compounds, Ins – myo-inositol, Glx – glutamate/glutamine, Met – methionine)

	NAA	Cr/PCr	Cho	Ins	Glx	Met
Patient (16 yrs)	6.3 ± 0.3	6.9 ± 0.3	1.2 ± 0.1	15.4 ± 0.6	8.2 ± 1.1	2.4 ± 0.2
Patient (18 yrs)	5.3 ± 0.2	6.5 ± 0.2	1.2 ± 0.1	12.2 ± 0.8	7.4 ± 0.8	2.2 ± 0.2
Sister (22 yrs)	12.0 ± 0.2	7.1 ± 0.2	2.4 ± 0.1	5.6 ± 0.4	8.7 ± 0.9	-
Mother	12.9 ± 0.1	8.2 ± 0.2	2.4 ± 0.1	5.6 ± 0.3	6.8 ± 0.5	-
Control range	11.7 - 13.0	7.4 - 8.5	2.3 - 2.6	6.0 - 7.3	8.2 - 10.4	-

Discussion: Only findings that could help in the diagnosis were found in the MR spectra. The new signal was assigned to a methyl or even an acetyl group of a small and relatively mobile molecule or as a simple radical of a larger rigid molecule.
From the potential candidates, we highlighted methionine (namely its methyl group) as the key compound although its disturbance is usually associated with liver pathology. Nevertheless, the laboratory tests including methionine have been in the normal range. Thus, only the central nervous system seems to be affected.
Maybe there are some unpublished MR spectra or other clinical data that could support our results.
References:
The study was supported by the MZCR institutional project 00023001IKEM.

836

Study of valves permeability in hydrocephalus patients with ventricular shunt by quantitative phase-contrast magnetic resonance

R. Sanz-Requena, J. Forner-Giner, L. Marti-Bonmati, A. Alberich-Bayarri, G. Garcia-Marti
Radiology, Hospital Quiron Valencia, Valencia/SPAIN

Introduction: Malfunctioning of ventricular shunt valves in normal pressure hydrocephalus (NPH) patients is usually shown as several clinical symptoms, including convulsions and increased intracranial pressure. In imaging studies, this abnormal performance of the valve is observed as an increased ventricular size. However, in some patients there is a malfunctioning of the valve without increased ventricles, due to scars in the ventricle wars and the surrounding tissues.
We propose the combination of conventional MR and quantitative phase-contrast MR (PC-MR) to follow up NPH patients after ventricular shunt. The conventional MR study can be used to assess ventricular changes, while the quantitative assessment of cerebrospinal fluid (CSF) flow by PC-MR can be used to assess valve permeability.
Cases: Ten NPH patients (six with non-obstructive NPH and four with obstructive NPH) with clinical suspicion of valve obstruction were studied with PC-MR (Philips 3T, TR/TE/FA=16ms/8ms/10º, 25 images/cycle, voxel size=0.33x0.33x5mm, encoding velocity=15cm/s, acquisition plane perpendicular to the shunt catheter). None of them showed significant changes in ventricular size in comparison to previous studies.Valve permeability was assessed by manually placing a ROI on it and calculating CSF flow through a cardiac cycle.

- Non-obstructive group:
- Three patients showed flow absence in the valve.
- Two patients showed normal functioning of the valve.
- One patient showed slight flow through the valve, possibly related to an incomplete obstruction.
- Obstructive group:
- Two patients with stenosis at the aqueduct of Sylvius showed flow.
- Two patients with tumors: one showed permeability and the other did not.

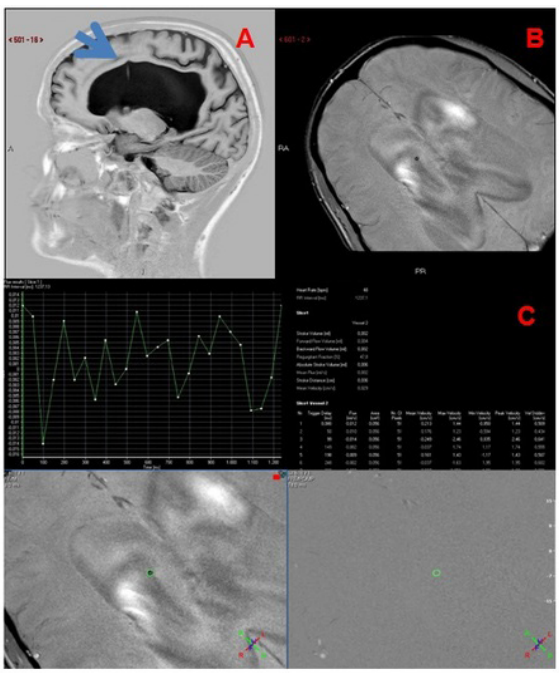

Example of a non-permeable catheter. A) Sagittal plane with the shunt catheter (arrow). 2) Perpendicular plane to the catheter . C) Results of the CSF flow quantitative analysis. The oscillations in the curve are only due to image noise.

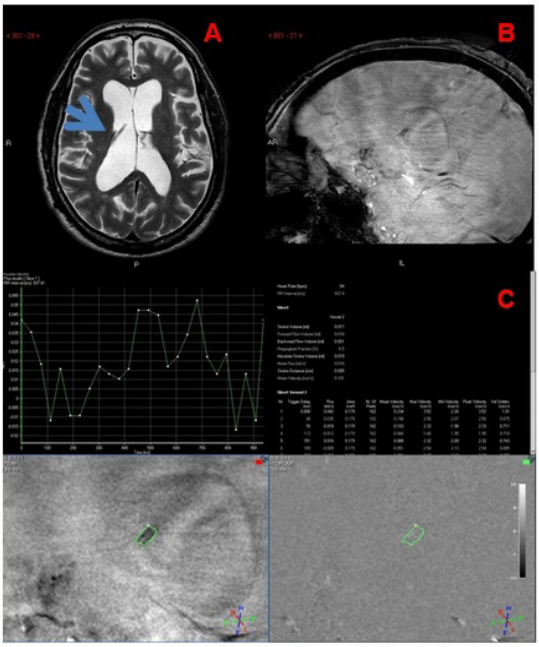

Example of a permeable catheter. A) Axial plane with the shunt catheter (arrow). 2) Perpendicular plane to the catheter . C) Results of the CSF flow quantitative analysis. Although the flow curve shows oscillations caused by image noise, it can be seen that there is net flow following the cardiac cycle.

Discussion: When a shunting catheter malfunction is suspected, it is recommended to perform a brain MR and an abdominal CT to study the distal end of the catheter. In this context, PC-MRI can be used to assess permeability, independently of changes in ventricular size. When permeability is negative it is recommended to perform a further study including an exogenous tracer. If positive, it can be concluded that the valve works correctly.
Some studies report CSF flow inversion in NPH patients with ventricular shunting, from caudocranial (permeable catheter) to craniocaudal (non-permeable) in systole. In this series of patients we have not observed this situation.
In conclusion, PC-MR with quantitative assessment of CSF flow can be used to evaluate the permeability of catheters after ventricular shunt in NPH patients.
References:
Kesava Reddy G et al. Neurosurgery 2011;69:774-80.
Barkovich AJ. Pediatric neuroimaging. 1995; p. 439–475.

837

Ectopic Neurohypophysis

I.T. Rakici[1], A. Ozturk[2]
[1]Radiology, Aksaray Devlet Hastanesi, Aksaray/TURKEY, [2]Radiology, Bakırköy Ruh Sinir Hastalıkları Hastanesi, Istanbul/TURKEY

Introduction: Ectopic Neurohypophysis is an anomaly of the Pituitary gland with short stature due to Growth hormone deficiency. MRI is the modality of choice in diagnosing this condition.
Cases: A 17 year old boy patient with abnormal 24 hr Growth hormone secretory pattern and peak Growth hormone levels less than 10ng/ml during provocative stimulation tests.

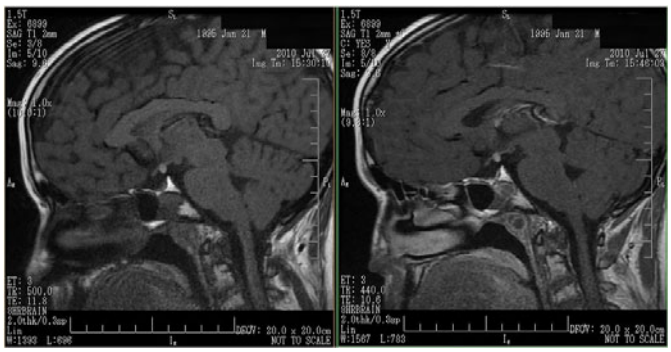

Figure 1: Pre and post contrast enhanced T1- Weighted Sagital images showing anterior pituitary gland, absent Pituitary stalk and Ectopic Posterior Pituitary signal located in the infindibulum.

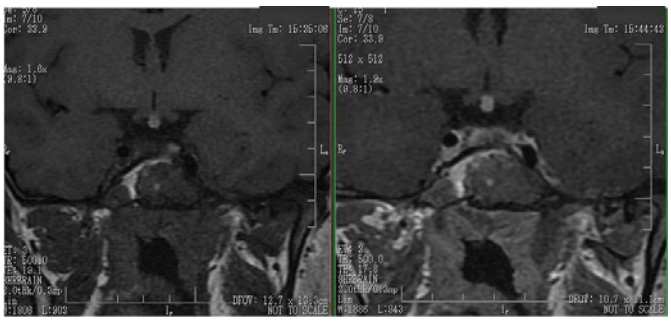

Figure 2: Pre and post contrast enhanced T1- Weighted Coronal images showing anterior pituitary gland, absent Pituitary stalk and Ectopic Posterior Pituitary signal located in the infindibulum.

Discussion: Posterior Pituitary Ectopia is an anomaly of the Pituitary gland associated with short stature and Growth Hormone deficiency. It is presumed to result from birth trauma causing a dysfunction between the Adenohypophysis and Neurohypophysis and is associated with deficiency of Anterior Pituitary hormones but preservation of Neurosecretory hormones (1).
The differential diagnosis of a Suprasellar bright spot include Rathkes Cleft Cyst, Subacute haemorrhage (in thrombosed Aneurysm), Haemorrhagic neoplasm, Post operative status, Lipoma, Dermoid, Traumatic transection of Stalk, Hypophysectomy, Sarcoidosis and Histiocytosis (1).
On MR the Sella appears smaller than normal on T1W images, the homogeneous signal of normal Pituitary is absent or small, with the absence of proximal pituitary stalk. A focal bright signal spot is seen in the proximal portion of the Infundibulum or the Tuber Cinereum which
represents the ectopic position of the Neurohypophysis. (1,2).
References:
1- Kiranmayı A, Nunna SVV, Chamarti SK, Mukarrab AM. Ectopic Neurohypophysis - A Case Report. Ind J Radiol Imag. 2006, 16:2:179-180.
2- Kılınç İ, Gökalp D, Özmen CA. Ectopic Neurohypophysis in Patient with Pituitary Dwarfism: A Case Report. Dicle Tıp Dergisi. 2008, Cilt: 35, Sayı: 3, (192-195).

838

Superficial Siderosis of the Central Nervous System - a small series review

B.C. Gomes[1], A.C. Ribeiro[2], J. Nunes[1], P. Gouveia[1], R.P. Pais[1]
[1]Serviço De Neurorradiologia, Hospital Geral, Centro Hospitalar e Universitário de Coimbra, Coimbra/PORTUGAL, [2]Serviço De Neurologia, Hospital Geral, Centro Hospitalar e Universitário de Coimbra, Coimbra/PORTUGAL

Introduction: Superficial Siderosis (SS) of the Central Nervous System (CNS) is a rare entity in which chronic recurrent subarachnoid hemorrhage (SAH) leads to the accumulation of cytotoxic hemosiderin in the subpial layer of the

CNS. It is a cause of insidious neurological deterioration, most frequently presenting with a classic triad of symptoms of bilateral sensorineural hearing loss, cerebellar ataxia and myelopathy. Magnetic Resonance Imaging (MRI) is the diagnostic modality of choice showing pathognomonic features of hemosiderin accumulation on the CNS surfaces.

Cases: The authors present four cases of SS of the CNS with different causes and emphasize the role of MRI. Three men and one woman, presented with an average age of 40 years with bilateral sensorineural hearing loss (two cases), cerebellar ataxia (two patients) and myelopathy (one case). Complete imaging study of the CNS was obtained in all patients, showing the characteristic rims of hypointensity around the surface of the cerebral hemispheres, cerebellum, brainstem, cranial nerves and spinal cord on T2 and especially in Gradient-Echo T2 weighted images. The causes of the SAH were a filum terminale ependymoma in one patient, post-traumatic cervical pseudomeningoceles in another patient and a previously resected CNS tumor of the posterior cranial fossa in the third patient. In the fourth case, despite of the extensive etiological investigation, no identifiable cause of recurrent SAH was identified. The filum terminale ependymoma was surgically resected, the second patient refused any neurosurgical intervention. One patient with sensorineural hearing loss was treated with bilateral auditory prosthesis and iron-chelating therapy and the other with a cochlear implant.

Discussion: The most common reported causes of SS are CNS tumors, head or back trauma and vascular lesions (arteriovenous malformations or aneurysms). However the source of SAH remains unidentified in up to 35% of cases. Once the diagnosis is established by MRI, the source of recurrent SAH must be must be recognized and corrected when possible, as to prevent the natural course of progressive and irreversible neurological deficit. In the early stage of the disease the MRI features can be very subtle, and so an accurate clinical assessment and high suspicion are essential.

References:

Kumar, N., 2010, Neuroimaging in Superficial Siderosis: an in-depth look, Am J Neuroradiol, 31:5-14

Kumar, N., et al., 2006, Superficial Siderosis, Neurology, 66:1144-1152

Levy, M., et al., 2007, Superficial siderosis: a case report and review of the literature, Nature Clinical Practice Neurology, 3(1):54-58

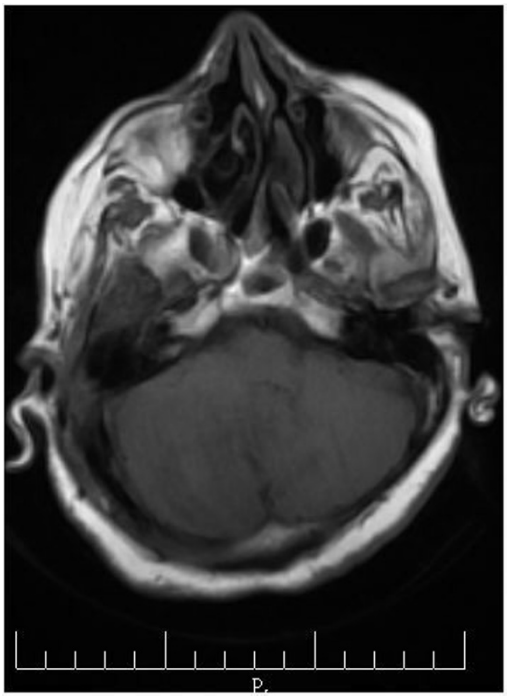

Figure 1: T1-weighted image. the mass was predominantly hypointense and had typical prominent hypo- and isointense striations.

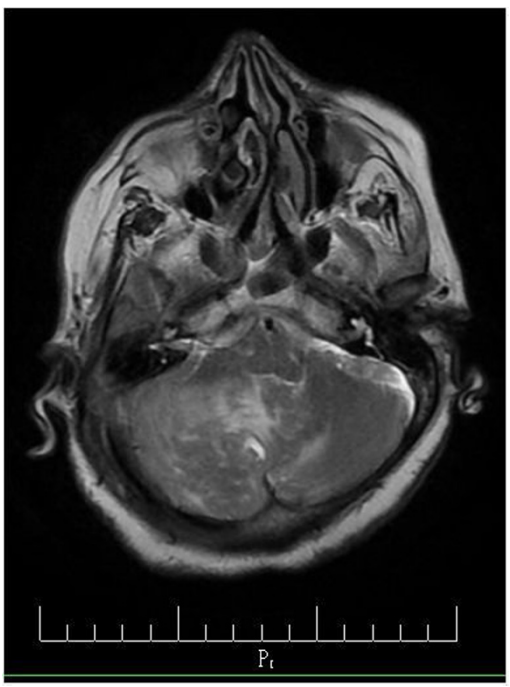

Figure 2: T2-weighted image. the mass was predominantly hyperintense and had hyper- and isointense striations with respect to gray matter.

839

Dysplastic Cerebellar Gangliocytoma (Lhermitte-Duclos Disease)

I.T. Rakici[1], A. Ozturk[2]

[1]Radiology, Aksaray Devlet Hastanesi, Aksaray/TURKEY, [2]Radiology, Bakırköy Ruh Sinir Hastalıkları Hastanesi, Istanbul/TURKEY

Introduction: Lhermitte-Duclos disease is a rare disorder of cerebellum that characterized by a slowly enlarging mass lesion. It most frequently seen between the 2nd and the 4th decades. In elderly ages is extremely rare. In this report, we described a 64- year old woman, who had Lhermitte-Duclos disease which was diagnosed by MRI findings and cofirmed by histopathology.

Cases: A 64-year-old woman presented with long-standing occipital headache, progressive ataxia. She had no other important history. Papilledema was noted at fundoscopy. She was operated and pathology result was " dysplastic cerebellar gangliocytoma".

On multiplanar MR images (Figs 1–4), the cerebellum appeared enlarged.

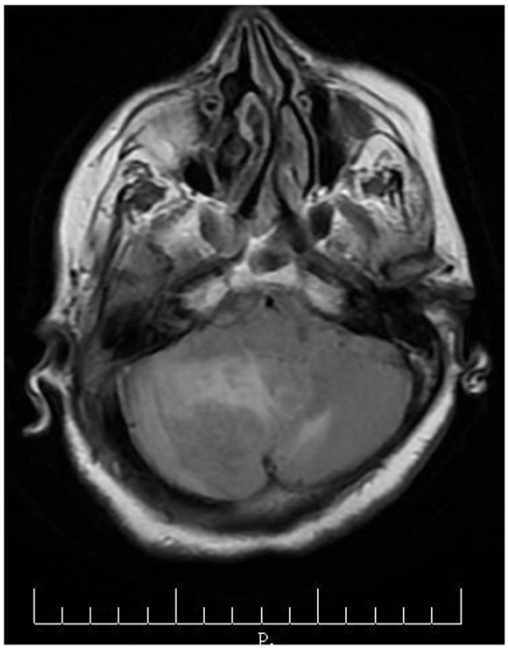

Figure 3: Fluid-attenuated inversion-recovery (FLAIR) image. The mass remained heterojen hyperintense.

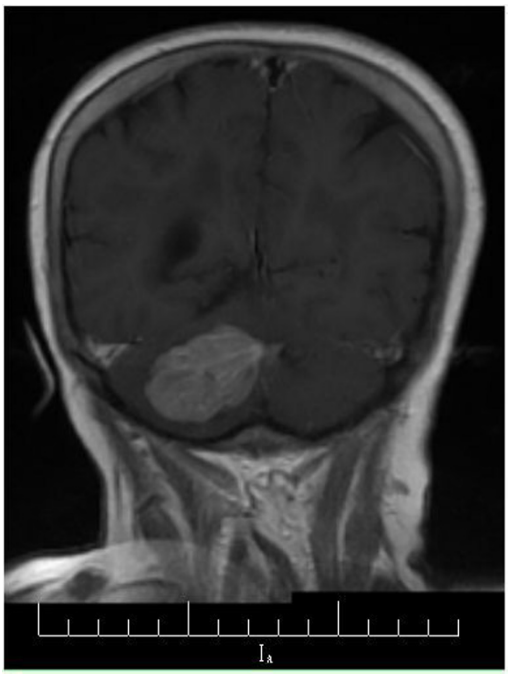

Figure 4: Coronal T1-weighted contrast-enhanced image. Diffuse enhancement was noted.

Discussion: Dysplastic cerebellar gangliocytoma is a rare hamartomatous disorder. Lhermitte and Duclos reported the first case of cerebellar ganglion cell tumor in 1920 (1). MR imaging reveals a cerebellar mass with a typical striated, corduroy, or tiger-striped folial pattern that consists of alternating bands on both T1- and T2-weighted images (2). Dysplastic cerebellar gangliocytoma is seen most frequently in young adults (average age, 34 years). There is no sex predilection. In elderly ages is extremely rare (3). It may have a hamartomatous, neoplastic, or congenital malformative origin (4). The only other lesion that may produce similar findings is cerebellar infarction, but the clinical presentation is usually very different. Despite the benign nature, surgical excision is the treatment of choice (5).

References:
1- Lhermitte J, Duclos P. Sur un ganglioneurome diffus du cortex du cervelet. Bull Assoc Fr Etude Cancer 1920; 9: 99–107.
2- Meltzer CC, Smirniotopoulos JG, Jones RV. The striated cerebellum: an MR imaging sign in Lhermitte-Duclos disease (dysplastic gangliocytoma). Radiology 1995;194:699–703.
3- Roessmann U, Wongmongkolrit T. Dysplastic gangliocytoma of cerebellum in a newborn: case report. J Neurosurg1984;60:845–847.
4- Robinson S, Cohen AR. Cowden disease and Lhermitte-Duclos disease: characterization of a new phakomatosis. Neurosurgery2000;46:371–383.
5- Bayat MRH, Sarawan J. Case Report: CT and MRI findings in Lhermitte-Duclos Disease. SAJR. 2005; February:30-31.

840

MRI Findings of Primitive Neuroectodermal Tumours of The Brain

E. Aktas[1], **N. Ciledag**[2], B. Gulpinar[1], B. Savran[1], H. Kaygusuz[1], K. Arda[1]
[1]Radiology, Ankara Oncology Research and Education Hospital, Ankara/TURKEY, [2]Radiology, Ankara onkoloji eğitim ve araştırma hastanesi, ANKARA/TURKEY

Introduction: Primitive neuroectodermal tumors (PNETs) are rare group of central nervous system malignencies. They may be located supratentorially or infratentorially in cranium. Primary cerebral neuroblastomas and pinealoblastomas are supratentorial PNETs. These are rare in adult population and are frequently seen in childhood(1). Their MR findings have only been reported in a few cases in English literature. This article presents MR findings of three proven cases of PNET.
Cases: Case 1. A 26-year old male admitted to our hospital with headache. MRI showed multicystic masses with periferic enhancement and surrounding minimal periferic edema. Pathology was confirm the diagnosis as PNET.
Case 2. A 31-year old man has suffered from nausea and vomitting for one month. We saw a hemorrhagic mass with periferal edema at left parietal lobe and right frontal lobe on MRI.
Case 3. A 22-year old man admitted to hospital with confusion and somnolence. A large sized hemorrhagic mass, which was showed heterogene enhancement was seen at frontotemporal lobe on MRI.
Discussion: PNETs are occasionally associated with cysts, necrosis, calsification and intratumoral hemorrhage (2). We could not see calsification on CT but three cases had hemorrhagic mass. The lesions appear as iso- or hyperdense on CT, hypointense and hyperintense on T1- and T2- weighted MR imaging, and heterogeneously enhanced after contrast administration. Surrounding brain edema varies from slight to marked. Multicystic apperance of PNETs are similar to astroblastoma. Astroblastoma, glioblastoma multiforme and ependymoma were thougt in differential diagnosis. The optimal treatment for PNET has not yet been established. If possible, a total resection of the tumors and adjuvant radiotherapy and chemotherapy are standart (2).
References:
1. Ohba S, Yoshida K, Hirose Y, Ikeda E, Kawase T. A supratentorial primitive neuroectodermal tumor in an adult: a case report and review of the literature. J Neurooncol. 2008;86:217-224.
2. Shingu T, Kagawa T, Kimura Y, Takada D, Moritake K, Hoshii Y. Supratentorial primitive neuroectodermal tumor in an aged patient case report. Neurol Med Chir. 2005;45:530-535.

Software Exhibits

Data analysis - MRI and MRS

841

BrainCON: software tool for graph theory based multimodal brain connectivity analysis and visualization

T. Spisák[1], G. Opposits[1], S.A. Kis[1], B. Clemens[2], M. Emri[1]
[1]Department Of Nuclear Medicine, University of Debrecen, Debrecen/ HUNGARY, [2]Department Of Neurology, Kenézy Hospital Ltd., Debrecen/ HUNGARY

Purpose of the software: Graph theory based structural and functional brain connectivity analysis is a novel method providing new insights into the dynamics and complexity of the brain by modeling it's regional interactions[1]. Due to the heterogeneity and dynamic development of the applied mathematical models and analysis techniques the software support of this field is still poorly accomplished[2].
Our purpose was to develop a user friendly software system dedicated for the analysis and visualization of multimodal brain connectivity data based on EEG, fMRI and DTI data.
Methods/Implementation: The software system has modular architecture which provides the opportunity to rapidly follow the latest improvements of connectivity analysis and visualization methods by incremental development. Reconstruction of brain networks is modality dependent and can be performed with various state-of-the-art software tools, eg. BrainLOC[3], Matlab and R for fMRI, FSL or Matlab softwares for DTI and NeuroGuide for EEG-LORETA data. These software tools can be easily fitted into the processing pipeline of the system. The resulting connectivity matrices can be displayed and thresholded interactively. Various interchangeable components are present for global (eg. small-worldness), modular (eg. community detection, modularity scores) and nodal (eg. various hub-scores) analysis of binary and weighted graphs in both individual and population level[4]. Cost-integration[5] technique was implemented to solve the problem of thresholding networks. Interpreting the results is aided by real-time 2D and 3D "galss brain" visualization techniques and various plots.
The program is built upon the MultiModal Medical Imaging software library system(www.minipetct.com/m3i) and runs on Windows 7 and Windows Xp operation systems and various Linux distributions (www.minipetct.com/braincon). The hardware requirements of the application match the current average PC configurations used in medical image analysis.
The software system was implemented mainly in C++ and partly in R.
Features illustrated at the exhibit: At the exhibit connectivity data analysis is demonstrated using variuos modalities.
Different methods are evaluated on the same data, connectivity patterns and hub-scores corresponding to brain regions are visualized in 3D.

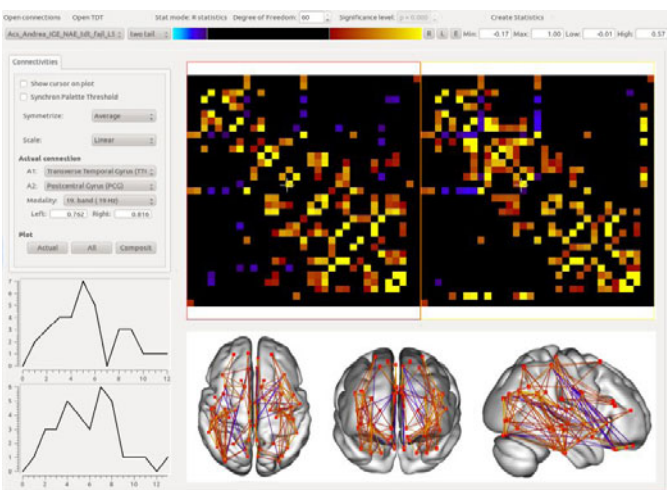

References:
[1] Sporns, O., The human connectome: a complex network, Annals of the New York Academy of Sciences, 1224(1):109-125, 2011. [2] Leergaard et. al., Mapping the Connectome: Multi-Level Analysis of Brain Connectivity, Frontiers in Neuroinformatics, 6, 2012. [3] Spisák, T. et. al., Region management toolkit for atlas-space image processing, MAGMA 24 (S1):543, 2011. [4] Rubinov, et. al., Complex network measures of brain connectivity: uses and interpretations, Neuroimage, 52(3):1059-1069, 2010. [5] Ginestet et. al., Brain network analysis: separating cost from topology using cost-integration, PloS1, 6(7):e21570, 2011.

842

Connectomist-2.0: a novel diffusion analysis toolbox for BrainVISA

D. Duclap, A. Lebois, B. Schmitt, O. Riff, P. Guevara, L. Marrakchi-Kacem, V. Brion, F. Poupon, J. Mangin, C. Poupon
I2bm, CEA NeuroSpin, Gif-sur-Yvette/FRANCE

Purpose of the software: Connectomist-2.0 is a novel software dedicated to the analysis of diffusion-weighted (DW) MRI data usable as a BrainVISA toolbox. Connectomist-2.0 aims at providing all the required pipelines to study the structural human brain connectivity from DW-MRI data, including quality check of the data, local modeling of the diffusion process, fiber tracking, clustering, automatic bundle labeling, computation of connectivity matrices of regions of interest (ROI), tract-based statistics.
Methods/Implementation: The user interface and pipelines of Connectomist-2.0 were developed using python. The image processing routines were written in C++ for computational efficiency. The viewer was developed using pyanatomist [2] and matplotlib python modules.
Connectomist-2.0 can run on a standard Linux workstation, and can be connected to a Linux cluster to reduce the computation time when it is available, using the soma-workflow python module [3]. When dealing with multiple subjects, computation can be distributed on the processors of a single machine using a simple multithreading strategy or on the nodes of a cluster when soma-workflow is available to process the database of subject more efficiently.
Features illustrated at the exhibit: The software was organized into 10 pipelines:
- Quality check, detection and correction of artifacts and definition of the Q-space sampling (see figure(1))
- Local modeling of the diffusion process using popular HARDI models of the literature (DTI, Q-Ball Imaging, DOT, CSD, SDT, DSI) to obtain fields of orientation distribution functions (ODF) (see figure(2))
- Computation of tractography masks from T1-weighted MRI data replacing standard FA-based masks (see figure(3))
- Tractography on the entire brain using streamline deterministic or probabilistic tractography techniques (see figure(4))
- Filtering of fibers based on morphometric criterions (length, curvature, tortuosity, density of fibers) or selection of fibers using ROIs
- Computation of connectivity matrices between sets of volume- or surface-based ROIs (see figure(5))
- Intra-subject fiber clustering to automatically construct white matter (WM) bundles at the individual level (see figure(6))
- Inter-subject fiber clustering to automatically identify WM bundles common to the subjects of a population
- Automatic labeling of bundles constructed from the previous pipelines (see figure(7)

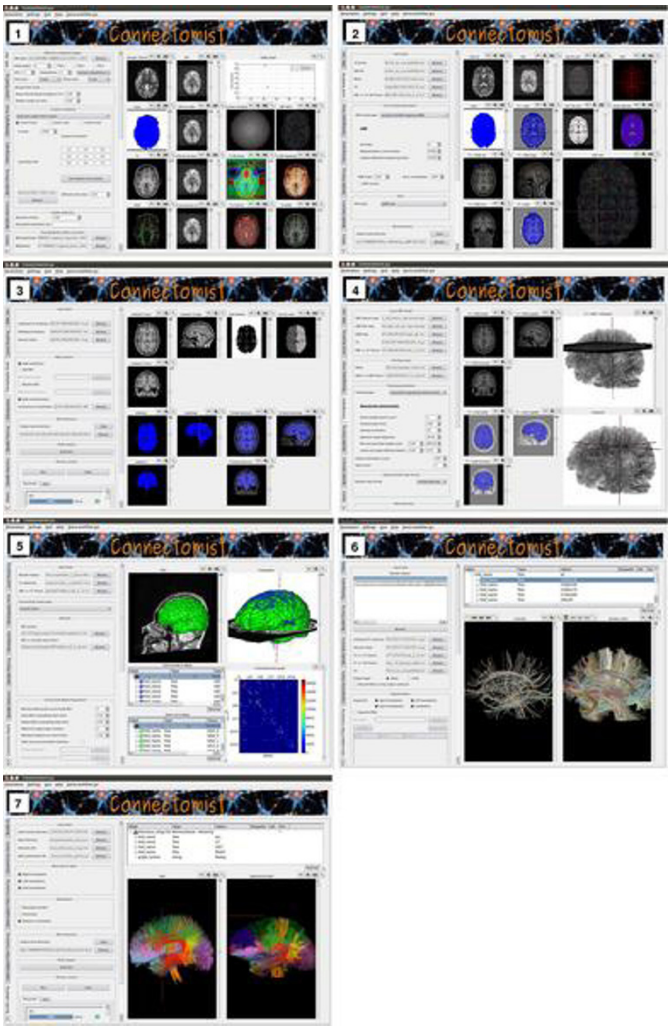

References:
[1] Geffroy D et al, 2011, BrainVISA: a complete software platform for neuroimaging, in Python in neurociences workshop, Paris
[2] Rivière D et al, 2011, Anatomist: a python framework for interactive visualization of neuroimaging data, in Python in neurociences workshop, Paris
[3] Laguitton S et al, 2011, Soma-Workflow: open source software platform for neuroimaging, in Python in neurociences workshop, Paris

843

UMMPerfusion: A Tool for Quantitative Perfusion Analysis in a Clinical Workflow

F.G. Zöllner[1], G. Weisser[2], S.P. Sourbron[3], S. Kaiser[1], M. Reich[1], S.O. Schoenberg[2], L.R. Schad[1]
[1]Computer Assisted Clinical Medicine, Medical Faculty Mannheim, Heidelberg University, Mannheim/GERMANY, [2]Department Of Clinical Radiology And Nuclear Medicine, University Medical Center Mannheim, Heidelberg University, Mannheim/GERMANY, [3]Division Of Medical Physics, University of Leeds, Leeds/UNITED KINGDOM

Purpose of the software: To develop a generic Open Source MRI perfusion analysis tool for quantitative parameter mapping to be used in a clinical workflow and methods for quality management of perfusion data.
Methods/Implementation: The software implements several well established MRI perfusion models previously presented in PMI [1] as a plugin for the Open Source DICOM workstation OsiriX [2]. Our plugin features a deconvolution analysis based on truncated singular value decomposition [3], a 1-compartment model [4], 2-compartment models for uptake and exchange [5], and the modified Toft's model [4].
In OsiriX, image data can be easily retrieved from a PACS without transferring the data to an offline system. The data is therefore directly available to the plugin. Quantification of the perfusion data can be performed on basis of a region-of-interest (ROI) or pixel-wise analysis. In the latter case, parameter maps are calculated as shown in Fig 1.

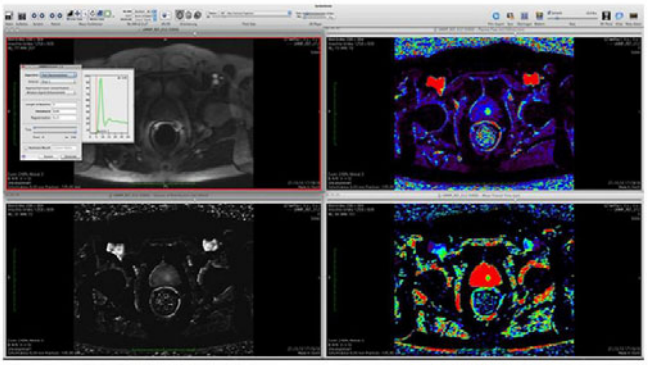

Fig. 1: Visualization of perfusion analysis results by our plug-in using. Top left: the original data set (3D + time), top right: plasma flow, lower left: volume of distribution, lower right: mean transit time. Data originates from a prostate MR exam. Data was evaluated using a voxel-wise deconvolution approach.

For quality management of the perfusion data, we implemented a graphical user interface that has a plot of the selected arterial input function (AIF) which is updated when the ROI of the AIF is changed and a graphical visualization of the number of baseline volumes selected (see Fig. 2). Thereby, selecting a false AIF might be reduced.

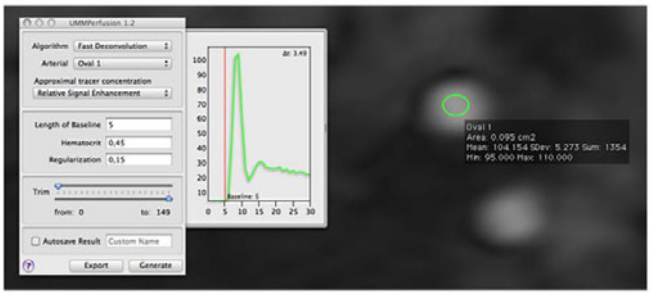

Fig. 2: Graphical user interface of the perfusion plug-in. The arterial input function (green curve) selected by the user is shown in an online updated chart. Also the current setting of the baseline (red line) is depicted.

Furthermore, we implemented a report (see Fig. 3) that logs all settings made during the analysis of the perfusion data, including a plot of the AIF. Thereby data analyses could be reviewed at later stage and possible errors could be detected.

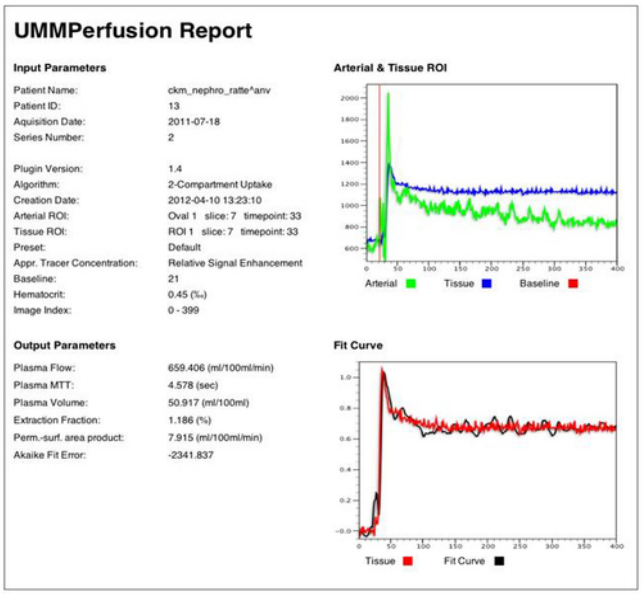

Fig. 3: Report generated from fitting a 2 compartment model to an example data set. Upper left: fit parameters used, lower left: calculated physiological parameters, top right: arterial input function and tissue signal curve (averaged over ROI), lower right: model fit.

The report and all calculated parameter maps are stored with the patient record in the OsiriX DICOM database and thus, could be transferred into a PACS system for further processing. Our software is Open Source and available at http://www.opossumm.de/ including source code documentation and a user manual. It was tested with OsiriX 3.9.4 and Mac OSX 10.6/10.7.

Features illustrated at the exhibit: The exhibit will adress both users and developers. For the user, we will demonstrate our plugin on different data sets and show how to use the plugin. For developers, we will briefly outline the implementation and point out how to extend our software (e.g. add new perfusion models).

References:

[1] Sourbron et al., ESMRMB 2009, p.756
[2] Rosset A, et al., J Digit Imaging 17:205-216, 2004
[3] Sourbron S, et al., Phys Med Biol 52:429-447, 2007
[4] Tofts PS, et al., J Magn Reson Imaging 10:223-232, 1999
[5] Sourbron SP, Buckley DL, Phys Med Biol 57:R1-R33, 2012

844

Extendable Multimodality GPU enabled Computing Framework with specific illustration of DTI & DCE-MRI

D.K.S. Rathore[1], R.K.S. Rathore[2], R.K. Gupta[3], P. Sahoo[2]
[1]Imaging R&d, Advanced Digital Imaging Solutions Laboratory, India, Kanpur/INDIA, [2]2department Of Mathematics And Statistics, Indian Institute of Technology, Kanpur/INDIA, [3]Department Of Radiodiagnosis, Sanjay Gandhi Post Graduate Institute of Medical Sciences, Lucknow/INDIA

Purpose of the software: A worldwide interest in handling multiple modalities of MRI and associated protocols has generated a requirement for tools and frameworks[1,2] for fast processing of data. We propose a plugin based architecture, Image Apprentice[17] (Figure 1), that allows extending support for GPU[3] (or, CPU) based post-processing algorithms.

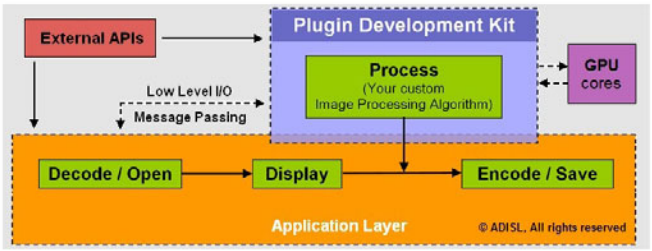

Methods/Implementation: Methodology and results of present analysis tool (Figure 2) have been validated in referenced publications[4-13]. The tool is supported on a PC with Microsoft® Windows® and (optionally) NVIDIA CUDA™ enabled GPU. Plugins can be developed using Microsoft® Visual Studio®.

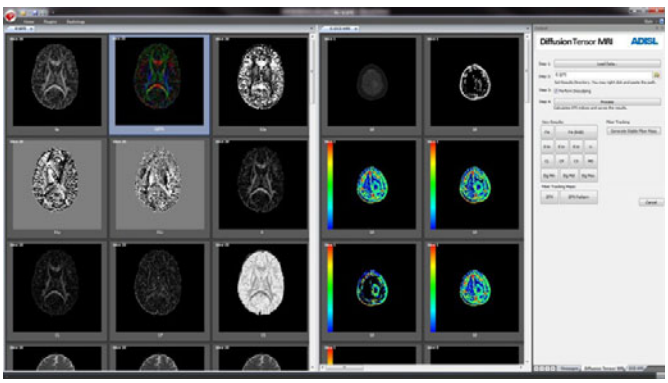

Features illustrated at the exhibit: We will illustrate post-processing of DTI and DCE-MRI data over a GPU.

DTI -

- Descalping[5] - removes non-brain anatomies from b0 images.
- Processing[6,14] – Voxel wise tensor field is diagonalized using the analytical diagonalization method to obtain the eigen values, eigen vectors and then DTI metrics.
- Fiber Tracking - White Matter structures separated using Principal Eigen Vector Field Segmentation (PEVFS)[7]approach. Single click on obtained segments provides seed point for Streamline Fiber Tracking Algorithm[15].
- Visualization - 3D Visualization using VTK[16].

DCE-MRI -

- Descalping[5].
- Pre-contrast tissue parameter estimation and quantitation of absolute tracer concentration from measured signal intensity[8].
- A piecewise linear model for automatic estimation of BAT and other segmentation parameters like slope of line segments[9].
- Automatic measurement of AIF along with PVE correction for individual patients[10].
- Both, tracer kinetic/generalized tracer kinetic and first pass analysis models with correction of leakage effect on CBV estimation[8,10,18].
- ROI analysis.

References:

[1] Rathore D et al, 2011, ESMRMB 28, 761
[2] Rathore DK et al, 2011, ISMRM 19, 4891
[3] http://en.wikipedia.org/wiki/CUDA
[4] Rishi Awasthi et al, 2010, JCAT. Jan, 34(1):82-8.
[5] Purwar A et al, 2006, ISMRM 14.
[6] Ankur et al, 2006, ESMRMB 23.
[7] Shruti et al, 2009, ISMRM 17.
[8] Singh A et al, 2007, JMRI, 26:871-880.
[9] Singh A et al, 2007, ISMRM-ESMRMB (2240).
[10] Rathore RKS et al, 2008, ISMRM, 1884.
[11] Haris M, et al., 2008, JCAT, 32:955-65
[12] Haris M, et al., 2008, Clinical Radiol, 63:562-574
[13] Haris M, et al., 2008, Neuroradiology, 50(6):531-40

[14] Hasan, KM, et al, 2001 JMRI, 13: 769-780.
[15] Basser PJ, et al, 2000, MRM, 44:625– 632
[16] www.vtk.org
[17] www.adislindia.com
[18] Tofts PS, et al., 1999, JMRI, 10:223-32

845

BrainMOD: 4-dimensional multimodal medical image analysis software

T. Spisák, S.A. Kis, G. Opposits, I. Lajtos, L. Balkay, M. Emri
Department Of Nuclear Medicine, University of Debrecen, Debrecen/ HUNGARY

Purpose of the software: Within the Central Nervous System Imaging project (http://www.eniac-csi.org/) of the ENIAC consortium, the need has emerged for a general multimodal visualization platform which facilitates the evaluation of data produced by new enhanced devices developed in the project. Taking advantage of multi-source post-processed data, this software aims to help interpreting complex intra-modal relationships. The modalities involved are PET, MRI, EEG, EIT.
According to the project proposal, our purpose was to develop a software for interactive user-friendly 2D and 3D visualization of post-processed multimodal medical imaging data. Important requirements were to manage dynamic image data and explicitly support the use of various enhanced brain imaging techniques.
Methods/Implementation: The input of the software are MR structural data, fMRI and PET dynamic data and activation maps (GLM, ICA), EEG/EIT based static functional maps and dynamic data, other EEG and fMRI related time series (eg. hemodynamic response functions, independent component analysis time courses), volumes-of-interests of segmentation data and EEG/EIT marker positions. Besides conventional 2D image fusion features, the software provides numerous ways to reveal intra-modal dynamic relationships. Volumes-of-interests can be delineated manually or automatically aided by various segmentation algorithms or brain atlases[1]. Time series curves can be generated from the image data and on these various operations can be performed (eg. resampling, filters, correlation, convolution).
Three dimensional surfaces can be reconstructed, visualized and colored by multiple parameters (eg. dynamic functional information).
The program is built upon the MultiModal Medical Imaging software library system (www.minipetct.com/m3i) and runs on Windows 7 and Windows Xp operation systems and various Linux distributions. The hardware requirements of the application match the current average PC configurations used in medical image analysis.
The software system was implemented in C++.
Features illustrated at the exhibit: At the exhibit the features of the software are illustrated by performing a comparsion analysis of EEG-fMRI activation maps vs. resected area and evaluating the overlap between fMRI parametric maps computed by Independent Component Analysis and standard resting-state network templates[2].

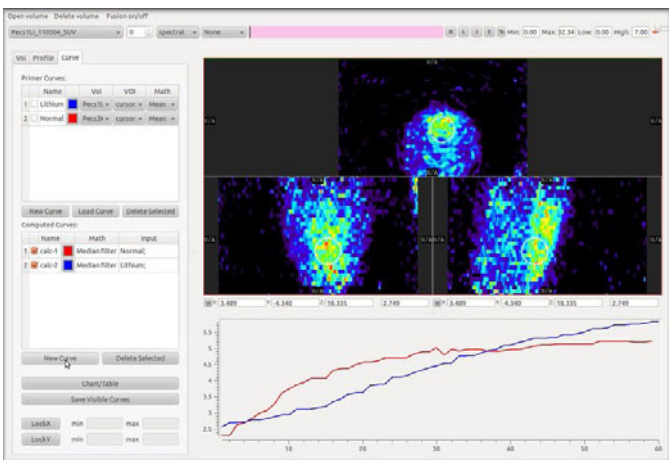

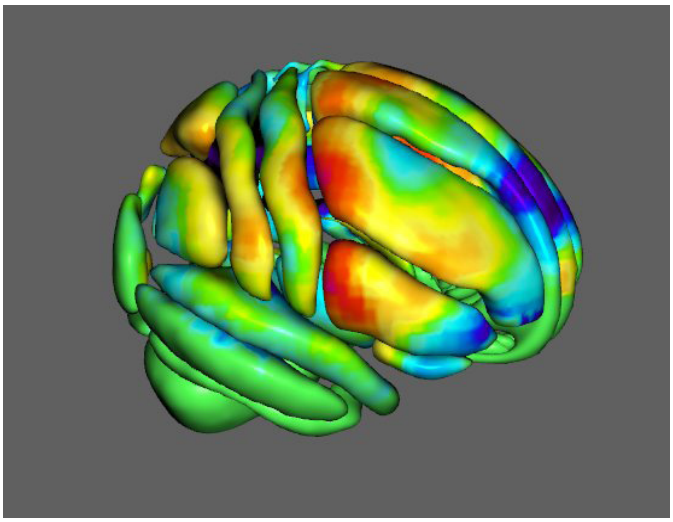

References:
[1] T. Spisák, M. Koselák, G. Opposits, S. A. Kis, L. Trón, A. Jakab, E. Berényi, M. Emri, Region management toolkit for atlas-space image processing, MAGMA 24 (S1):543, 2011.
[2] Shirer, WR and Ryali, S. and Rykhlevskaia, E. and Menon, V. and Greicius, MD, Decoding subject-driven cognitive states with whole-brain connectivity patterns, Cerebral Cortex, 22(1):158-162, 2012.

846

QMapIt, an ImageJ-plugin, for quantitative multi-parametric analysis of DICOM images

M.G. Kaul, G. Adam
Department Of Diagnostic And Interventional Radiology, University Medical Center Hamburg-Eppendorf, Hamburg/GERMANY

Purpose of the software: QMapIt offers an operation system independent platform for multi-parametric analysis of MRI data in a framework embedded in the image processing software ImageJ [1]. This has the main advantage that tasks can be modulized and the stored results can be piped to further tools to analyse more complex processes.
Methods/Implementation: All quantitative tools can by assessed by an interactive graphical user interface. The selective import of DICOM data is managed by DicomSort'n'Select (DSnS) [2]. The configurable DSnS provides technical information about the scans to further ImageJ plugin tools. Several sessions can be imported and labelled. A session can consist on several image stacks which are grouped images that belong together like time-series. Since each session is labelled the plugins can recognize the data that is needed to perform the analysis. For instance, T1-maps have to be calculated from a series a different T1weighted images. The resulting T1-maps are stored as DICOM files. These can be imported and be combined with the DCE measurements to calculate concentration maps to perform in the next step pharmacokinetic modelling (see figure). Another example is vessel-size-imaging (VSI) that is related to T2- and T2*-maps that are acquired before and after contrast agent administration. For the storage of DICOM files the DCM4che libraries [3] are used. A pixelwise timeline fitting and visualisation framework was developed using a Levenberg-Marquardt fit algorithm [4], extended to support multi-core processors for speeding up the fitting procedure and covariance analysis to estimate errors. All incorporated plugins (T2RelaxIt, T1RelaxIt, ADCIt, IVIMIt, VSIIt, DCEIt) are developed in Java using Eclipse [5] and are also running as standalone plugins in ImageJ.
Example of a workflow for pharmacokinetic modelling (see figure):
First stage: Import of T1weighted data, calculation of T1-maps and stored as DICOM files.
Second stage: Import of T1-maps and dynamic-contrast-enhanced (DCE) data, calculation of concentration (C-) maps

Third stage: Import of C-maps; ROI-based arterial-input-function (AIF) estimation than pharmacokinetic modelling

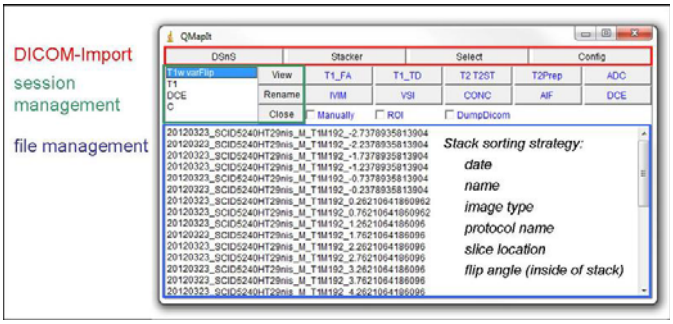

Features illustrated at the exhibit: * Selective import of DICOM files with DicomSort'n'Select (DSnS)
* Calculation of T1-maps (variable angle T1_FA and saturation/inversion recovery T1_TD)
* Merging 3D-T1-maps with 4D-DCE measurements to generate 4D-concentration maps
* Pharmacokinetic modelling (Tofts model)
* Plugins available for mapping of T2 (also with T2Prep), T2*, ADC, IVIM, VSI, and DCE

References:

[1] rsbweb.nih.gov/ij
[2] Kaul MG, Ernst T, Adam G. DicomSort´n´Select, an ImageJ-plugin, for sorting, selecting of DICOM images and providing a technical data interface. ESMRMB (2011)
[3] dcm4che.org
[4] scribblethink.org
[5] eclipse.org

847

An integrated framework to produce classifiers for MRS data and to visualise them into a decision-support system

M. Julià-Sapé[1], S. Ortega-Martorell[2], A. García-Chacón[1], C. Arús[2]
[1]Departament De Bioquímica I Biologia Molecular, Universitat Autònoma de Barcelona, Cerdanyola del Vallès/SPAIN, [2]Centro De Investigación Biomédica En Red En Bioingeniería, Biomateriales Y Nanomedicina, CIBER-BBN, Cerdanyola del Vallès/SPAIN

Purpose of the software: To develop semi-automated classifiers based on MRS data and to visualise their predictive outcome.
Methods/Implementation: SpectraClassifier 3.0.09 (1) is a java solution that uses statistical machine learning techniques, for helping spectroscopists to analyse and classify *in-vivo* and *ex-vivo* ^{1}H-MRS data. SpectraClassifier minimises the user's learning process curve, and allows straightforward display and evaluation of results obtained. SpectraClassifier is composed by five modules: classifier design (for specifying inputs to the classifier and obtaining relevant features), data exploration (for analysing the spectra type population structure and visually comparing spectra), visualisation (for visualising PCA and LDA results up to 3D), evaluation (for validating results) and reports (to review/export results), Classifier history, Multi-voxel reports (for visualizing PCA and LDA results of Multi-voxel based classifiers) and Batch Analysis (for obtaining classifiers in batch mode). For obtaining relevant features, SpectraClassifier offers three methods: Sequential-Forward, Sequential-Backward and PCA; and LDA is the technique implemented to separate up to four classes. As well, a confusion matrix, a Receiver Operator Characteristics (ROC) curve, balanced error rate and methods like cross-validation, leave-one-out and bootstrapping are available to evaluate classifiers. The INTERPRET DSS 3.02 (2) is another Java solution to visualise classifiers previously generated with SpectraClassifier using SV ^{1}H-MRS data obtained at 1.5T *in-vivo* from patients affected by abnormal brain masses. The INTERPRET DSS is aimed to help radiologists with the characterisation of unseen data.

Features illustrated at the exhibit:
- To identify the inputs needed to develop a classifier with the different data types, SV, MV, and HRMAS.
- To import training datasets, group tumours into classes, select a method for obtaining relevant features, and create the classifier.
- To visualise spectra and relevant features (by means of the exploration module) and the latent space of PCA or LDA results up to 3D (by means of the visualisation module).
- To evaluate the quality of the developed classifier, by at least, the bootstrapping method, the balanced error rate, the confusion matrix and the ROC curve.
- To learn how to use the batch mode.
- To review the results obtained and export them into one of the allowed formats.
- To learn how to enter new cases into the INTERPRET DSS and how to build one's own database.

References:

1. Ortega-Martorell, S., et al.(2010), BMC Bioinformatics, 11:106 [http://gabrmn.uab.es/sc].
2. Perez-Ruiz, A., et al. (2010) BMC Bioinformatics, 11:581.

848

Automated analysis of ACR phantom images

T. Mäkelä[1], T. Ihalainen[2], O. Sipilä[2]
[1]Department Of Physics, University of Helsinki, Helsinki/FINLAND, [2]Helsinki Medical Imaging Center, Hospital District of Helsinki and Uusimaa, Helsinki/FINLAND

Purpose of the software: Phantom-based image quality estimation is an essential part of any modern MRI scanner quality control (QC) programme. The accreditation phantoms designed by the American College of Radiology (ACR) [1] are widely used in MR equipment acceptance and quality assurance testing [2] and the suggested analysis [3] can be carried out manually on any radiology workstation. The primary purpose of this project was to automate this somewhat tedious procedure and furthermore decrease the subjectivity of the results.
Methods/Implementation: A MATLAB (v.7.11, MathWorks., Natick, MA) program running on a standard PC was written for sorting and analysing images acquired of the ACR head and knee multi-purpose phantoms. Similar work has been done earlier only for the ACR head phantom [4]. Graphical user interface allows the operator to either view and confirm the results or modify parameters and reanalyse the images. The reliability of the software was verified by using simulated test images imitating degraded MR acquisitions. Finally, a comparison was made between manual and automated analyses of 30+ sets of images. Data were available from fourteen scanners of three major manufacturers with field strengths of 1, 1.5 and 3 teslas.
Features illustrated at the exhibit: Implemented subroutines estimate signal-to-noise ratio, geometric accuracy (see figure), slice location and thickness, resolution, image intensity uniformity and ghosting artefact using basic image processing methods. The program produces also a summary table which can be read into any major spreadsheet software. The advantages of computer aided analysis were evident. Tailor-made tools for each step improved objectivity and reduced time consumption (from 40 minutes to less than two minutes per set). Increased sensitivity of certain methods (e.g. ghosting) resulted in findings that were previously missed in visual investigations.

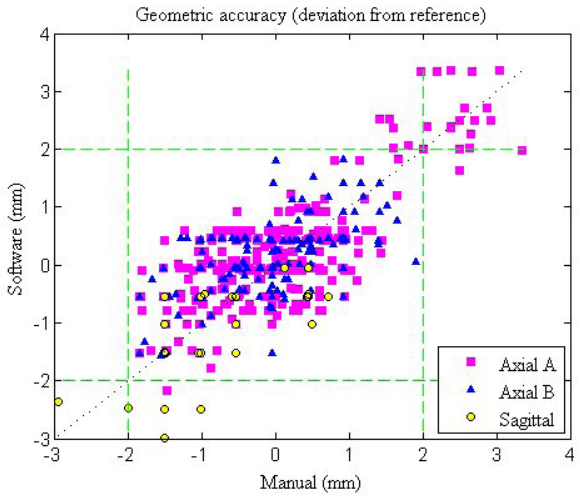

Figure: Comparison between manual and automated measurements of geometric accuracy. The dashed green lines indicate the action criteria recommended by the ACR.

References:
[1] Weinreb J. et al., 2005, J Am Coll Radiol, 2:494-503
[2] Ihalainen T. et al., 2011, Acta Oncol, 50(6):966-972
[3] Phantom Test Guidance for the ACR MRI Accreditation Program, American College of Radiology, Reston, VA, 2005
[4] Panych L.P. et al., 2010, Proc. ISMRM, Stockholm, Sweden, 5071

849

WITHDRAWN

850

CartiQ - Software for calculation and evaluation of quantitative MRI maps (e.g. T1, T2 maps)

C. Siversson
Department Of Medical Radiation Physics, Lund University, Malmo/ SWEDEN

Purpose of the software: The CartiQ software is a complete multi-platform software suite for doing quantitative MRI analyses (e.g. T1, T2). The software can be used for a variety of clinical applications where quantitative MRI is desired. A prominent such application for which the software is very well suited is quantitative cartilage evaluations (including delayed Gadolinium Enhanced MRI of Cartilage, dGEMRIC [1]). The software comes with an intuitive user interface, complete with all functionality required for drawing and evaluating regions of interests within the images.
Further functionality, such as additional types of quantitative calculations and templates for cartilage delineation, are provided through separate plugins.
Methods/Implementation: - Written in C/C++
- Available for Windows, Linux and Mac OS X.
- T1 maps are calculated from Inversion Recovery [2], Variable Flip Angle (DESPOT1) [2] and Look-Locker [3] type images.
- T2 maps are calculated from multiple spin echo images
- Both 2D and 3D data is supported
- Complete DICOM support
Features illustrated at the exhibit: Calculation and evaluation of T1 maps for dGEMRIC cartilage assessment
References:
1. Bashir A et al (1999), Magn Reson Med 41(5): 857-865.
2. Gupta R et al (1980), Journal of Magnetic Resonance 38: 447-452.
3. Brookes J A et al (1999), J Magn Reson Imaging 9(2): 163-171.
4. Henderson E et al (1999), Magn Reson Imaging 17(8): 1163-1171.

Software Exhibits

Decision-support systems

851

Curiam BT kids, a Clinical DSS for pediatric brain tumour diagnosis

J. Vicente, C. Sáez, S. Tortajada, E. Fuster-Garcia, M. Esparza, M. Robles, J.M. Garcia-Gomez
Ibime, Universitat Politècnica de València, Valencia/SPAIN

Purpose of the software: Curiam BT kids is a Clinical Decision Support System (DSS) for brain tumour (BT) diagnosis in children. It is presented as a sister version of Curiam BT [1], and includes a set of diagnostic classifiers aimed to discriminate the most common pediatric BT types.
The high performance of these classifiers makes Curiam BT kids a suitable tool to obtain accurate diagnostic information on the tumour type prior to initial surgery. Thus, it can help in the surgical decision-making, allow timely adjuvant therapy planning and aid discussion with the family.

Methods/Implementation: SV 1H-MRS (1.5T PRESS, PROBE or STEAM, TE 20-32 ms, and PRESS, 135-136 ms) from 90 patients histopathologically diagnosed with medulloblastoma (MED), ependymoma (EPEN) and pilocitic astrocytoma (PILOA) acquired in a multi-centre study were used to train and evaluate Linear Discriminant Analysis classifiers.
The classifiers addressed three clinically relevant diagnostic classifications. A stringent evaluation of the diagnostic accuracy was performed based on resampling and high diagnosis performance was achieved (see Table 1).

Table 1 Balanced Accuracy Rate (BAR) of the classifiers in Curiam BT kids

Question Acquisition	Short-TE	Long-TE	Short-TE+ Long-TE
(PILOA, EPEN) vs MED	0.88	0.85	0.94
PiLOA vs MED	0.92	0.94	0.95
PILOA vs EPEN vs MED	0.76	0.70	0.92

70% of the BT in children are MED, PILOA or EPEN. Nevertheless, the predictive ability of the classifiers when classifying other tumour types was also evaluated. The classifiers were able to effectively separate other low-grade tumour types from embryonal tumour types with a Balanced Accuracy Rate (BAR) of 1.0 when using the information from both Short-TE and Long-TE to answer this diagnostic classification. With this result, the applicability of Curiam BT kids is extended up to the 83% of the BT childhood cases.
Features illustrated at the exhibit: Curiam BT kids is an effective non-invasive pre-operative tool to aid in the definition of the tumour resection strategy. It offers a high diagnostic accuracy based on MRS data for the non-invasive characterization of common childhood BT. It automatically pre-process 1H-MRS data from major manufacturers and allows a diagnosis classification by combining the metabolite information of Short-TE and Long-TE MRS data. Classification is also possible with either TE alone, offering in any case, a visual representation of the classifier projection for case analysis and comparison. Free evaluation licenses are available under request.

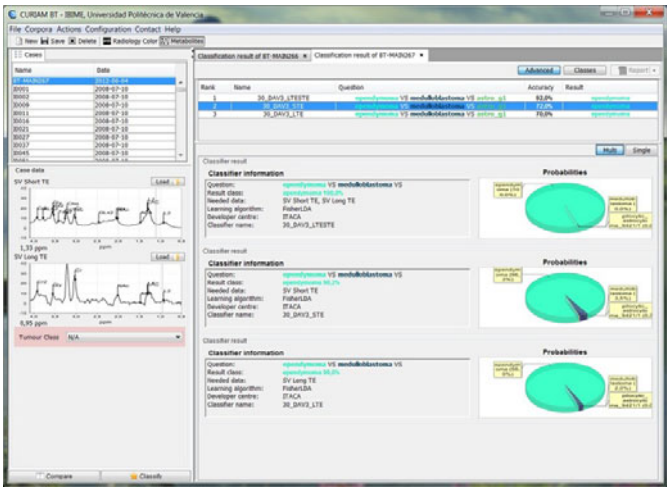

References:
[1] ESMRMB 2009 Congress Book of Abstracts, Info-RESO, DOI:10.1007/s10334-009-0178-y, Page 538.
[2] ISPNO 2012 Congress Book of Abstracts, in press.

852

ProstateAnalyzer: GUI in Medical Domain with Management of DICOM Images of Prostate Cancer

C. Mata[1], P. Walker[2], A. Lalande[2], F. Brunotte[2], A. Oliver[1], J. Marti[1]
[1]*Computer Vision And Robotics Group, Universitat de Girona, Girona/SPAIN,*
[2]*Department Of Mr Spectroscopy, University Hospital, Dijon/FRANCE*

Purpose of the software: Medical support analysis systems are becoming increasingly important in assisting experts to supply more accurate and well informed diagnoses. Although there is increased interest in the management, storage and retrieval of digital images for diagnoses, most hospitals need specific and tailored software solutions to solve the management of data and its access in the network. In this paper, we propose a framework that comprises visualization and analysis for MR imaging of the prostate and a new storage system of clinical diagnoses in a single package. ProstateAnalyzer is such a network-based database system allowing the management of both MRI and spectroscopy data sets, and the possibility of performing basic mathematical operation images.
Methods/Implementation: ProstateAnalyzer has been designed as a web-based application within a Zend Apache server, also used as a MySQL database server for data storage. The application links a database of DICOM images with a XML server which stores a set of clinical cases (annotation files). Figure 1 shows the proposed architecture and the hardware needed to run the ProstateAnalyzer. This tool is implemented as a Java-based applet application to facilitate the inclusion of medical findings on existing prostate studies. These studies are created by means of XML files to annotate tumors and other pathologies provided by experts.

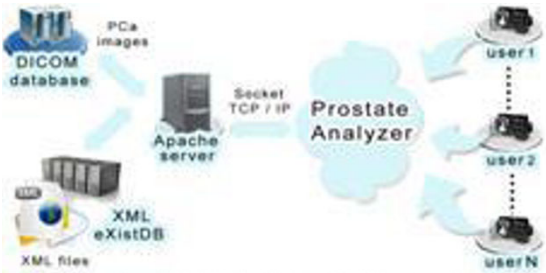

Figure 1: Network-based database system designed to implement the framework

Features illustrated at the exhibit: The main features of the software are based on four techniques of visualization: 3D T2-weighted imaging, Diffusion-Weighted Imaging with ADC maps, Perfusion-Weighted Imaging and 3D-MR Spectroscopy. These visualization capabilities are combined with basic post-processing tasks such as user-specific ROI, surface and volumetric measurements, ADC values, perfusion signal-time curves and individual spectrum visualization. A medical tool has been developed in order to globalize all these features in the same software and facilitate data management.
Figure 2: Multiple and user-specific ROI on 3D T2-weighted images.
Figure 3: Example of basic operations on ADC images.

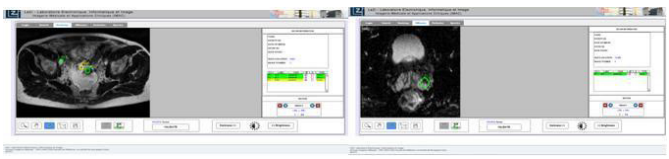

Figure 4: ROI analyses on perfusion images with corresponding signal-time curves.

Figure 5: 3D-spectroscopic imaging study

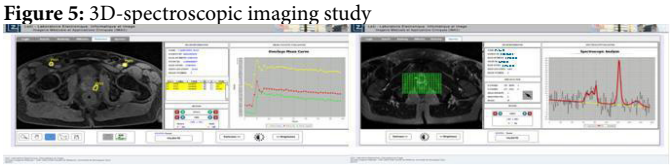

One of the most evident advantages provided by the tool is an improved create/recover/update prostate diagnosis provided by different experts. It is an efficient way to share and save information concerning the state of diagnoses. The tool offers the possibility to work remotely via the web and represents an improvement in data management. Taking into account how rapidly clinical databases are growing, ProstateAnalyzer will be an important contribution to the management of our database of more than 1000 patient data sets.

853

My appetite: A novel software tool to identify appetite disorders.

A. Benítez[1], G. Peláez-Brioso[1], **B. Lizarbe**[2], P. Lopez-Larrubia[3], S. Cerdán[1], L. Lago-Fernández[4], M. Sánchez-Montañés[4]
[1]Modelos Experimentales De Enfermedades Humanas, Instituto de Investigaciones Biomédicas "Alberto Sols", Madrid/SPAIN, [2]-null-, Instituto Investigaciones Biomedicas "Alberto Sols", Madrid/SPAIN, [3]-null-, Instituto Investigaciones Biomedicas "Alberto Sols" CSIC-UAM, Madrid/SPAIN, [4]Escuela Politécnica Superior, Departamento De Ingeniería Informática, Universidad Autónoma de Madrid, Madrid/SPAIN

Purpose of the software: Obesity is a pandemic syndrome, one of the most prevalent and morbid diseases in developed countries. It is caused by a disorder of the feeding behavior, which is controlled by intrahypothalamic orexigenic and anorexigenic neurons. The diagnosis of obesity is often made by body measurements including weight, but it would be more precise to assess its development directly at the hypothalamic level.
We provide here a software package to evaluate in vivo and automatically the "fed" or "fasted" state of the hypothalamus in the mouse and human brains, using Diffusion Weighted Imaging data sets with multiple b values. The program may be useful to assess hypothalamic function in obesity and other eating disorders.
Methods/Implementation: A total of eight mice were investigated either "fed ad libitum" or "fasted for 48h". For each mouse, axial images showing the hypothalamus were obtained in both conditions. For each case, DWI were acquired with the diffusion gradient oriented in three orthogonal directions (left-right L-R, anterior-posterior A-P and head-foot H-F). DWI were acquired using a spin-echo Stejskal-Tanner sequence, with an in plane resolution of 128 x 128 pixels, every pixel being described by a 33 component vector representing intensity values along each of the three orthogonal directions. A similar approach was used to obtain DWI dataset from six human volunteers, receiving normal diet (fed) or after 24h of fasting (fasted). Fisher's discriminant analysis was then applied to the DWI data sets in order to find the linear projection that best discriminates the pixels belonging to a fed or fasted animal or human. The discriminant function obtained may be used later to classify additional data into one of the two classes.
Our package is able to accept DWI data sets from mouse or human brains, providing automatically a classification of the new image in a scale of "appetite index" 0 (fed)-100 (fasted).
Features illustrated at the exhibit: We illustrate the operation of the program (Fig. 1) with a set of sample DWI images from the mouse or human brains using the data base described in Methods. The user may enter external data base into the application, use preeexisting data base already configured in the software package or a combination of both. Features include: Input of Data, Display, Processing and classification (Fig. 2), Results expressed as "Appetite Index" (Fig. 3).

Fig. 1. Initial GUI of software package *My Appetite*

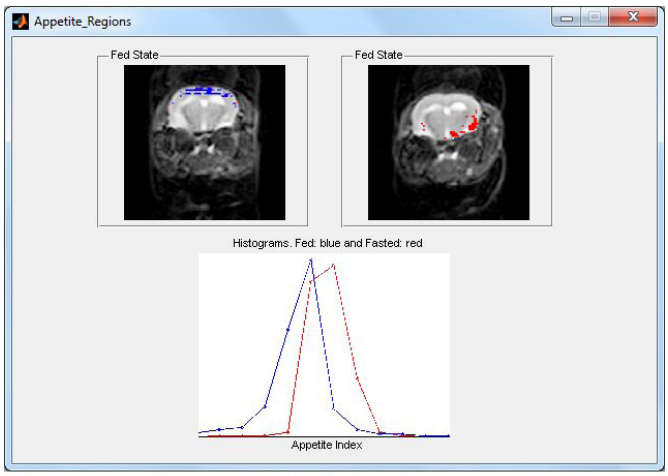

Fig. 2. Top panel: Example of classification where representative "appetite index" images from the brain of fed (blue pixels) or fasted (red pixels) mice are shown. **Bottom panel**: Representation of Fisher's projection (fed-blue dots/fasted-red dots).

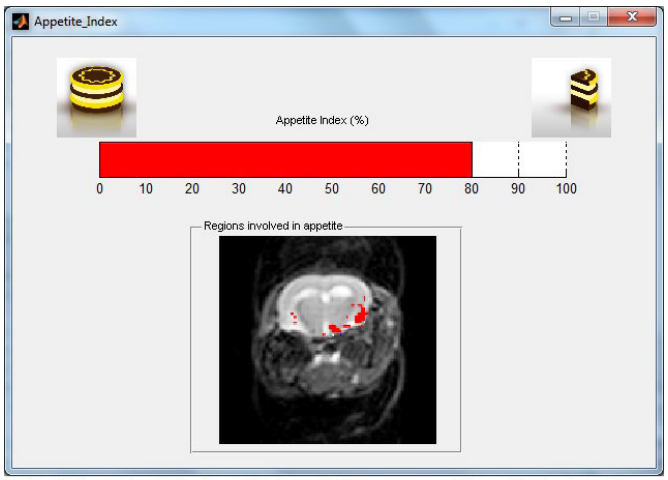

Fig. 3. Example of the "appetite index" of a mouse and the active brain regions (red pixels) in fasted state.

Software Exhibits

Other

854

ArchiMed : A research PACS

E. Micard[1], D. Husson[1], F. Odille[2], J. Felblinger[1], C. Pasquier[1]
[1]Cit 801, INSERM, Vandoeuvre-lès-Nancy/FRANCE, [2]Iadi, Université de Lorraine, Vandoeuvre-lès-Nancy/FRANCE

Purpose of the software: Clinical research, especially in MRI, produces a large amount of data. Centralized data storage system is essential to transfer research works to clinical applications effectively, in accordance to legal requirements and research obligations.
ArchiMed is a complete storage and visualization solution developed for clinical research. Fully integrated into clinical environment (MRI, others devices, ...), it ensures all data storage, quality control and connections with processing research tools *(fig.1)*.
Unlike clinical Picture-Archiving-and-Communication-System (PACS)[1], our solution is able to store all kind of files (DICOM, MR-RAWDATA, ...) with associated metadata and allows "batch processing" for large-scale studies. Finally, to respect French Public Health Code, ArchiMed architecture and associated data workflow ensure preservation and confidentiality of clinical research data.

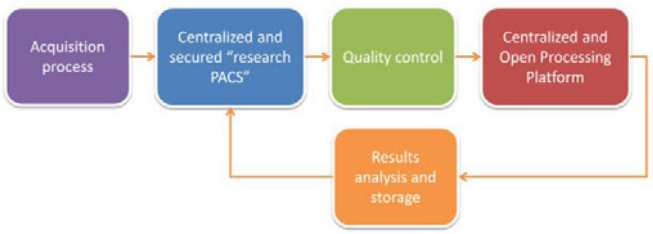

Fig. 1 : Data workflow

Methods/Implementation: To address the requirements stated previously, three main prerequisites must be met: easy integration, interoperability and quality insurance.
Integration :

Table1. Technical choices

	Technology	Justification
Architecture	Client/Server Service-Oriented-Architecture	Scalable, Multi-clients, secured
Platform	JAVA-EE[2], Glassfish[3]	Open, multi-OS
Database	Object-Relational-mapping[4]	Compatible with standard Database-Management-Systems
Security	LDAP[5] authentication	OS login integration

ArchiMed is a distributed Java-EE application with Service Oriented Architecture *(fig.2)*. Server part of application can be installed on every Operating-System with Java™ and linked to any Database-Management-System (MySQL, Oracle,...)
Authentication is based on LDAP[5] (like Active-Directory). Thus, it uses operating system login credentials.

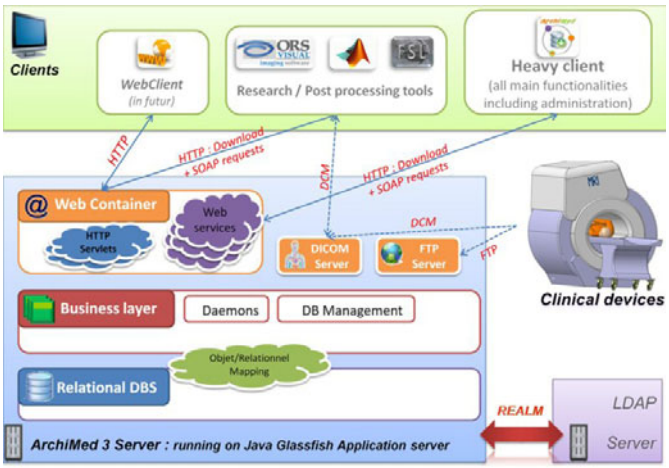

Fig. 2 : ArchiMed services-oriented architecture

Interoperability *(Fig.3)* :
Web Services[6] and Servlets[7] make ArchiMed interoperable on HTTP[8]. C++, Java or Web application, can query database and upload/download files. To connect ArchiMed to research environment and post-processing tools, users can use/develop interface-plugin (FSL and Matlab® plugins are already implemented)
To connect ArchiMed to clinical environment, a DICOM[9] implementation is used. ArchiMed, behaving like a DICOM node, can receive/send images from/to clinical devices, PACS or workstation. Otherwise, specific files like MR raw-data, are sent via FTP.

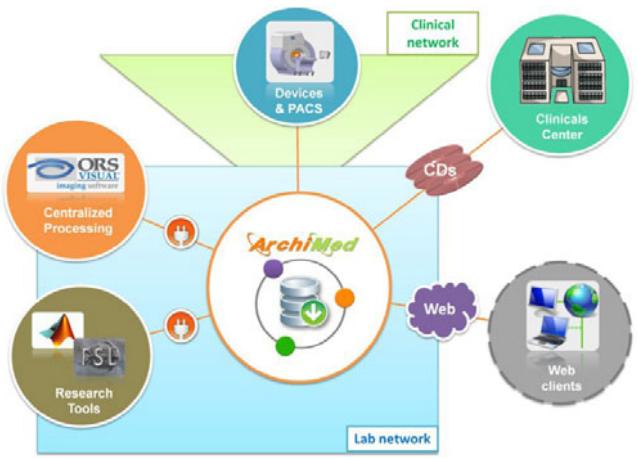

Fig. 3 : ArchiMed interactions

Quality insurance
To insure confidentiality, there are group/user restrictions on authorized studies. Furthermore, a manual validation is mandatory before final insertion. Study expert checks data validity and anonymize patient identifying data.
To ensure data integrity and preservation, ArchiMed storage facilities builds in standard backup and archiving system.
Features illustrated at the exhibit: Data/images integration, visualization and interactions with Matlab, FSL and a 3D plateform will be demonstrated using virtualized local server.

Fig. 4 : ArchiMed client GUI

References:
[1]Choplin, R.H., Boehme, J.M.,Maynard, C.D.: Picture archiving and communication systems:an overview.Radiographics. 12,127-129(1992).
[2]Java.EE.at.a.Glance, http://www.oracle.com/technetwork/java/javaee
[3]GlassFish-Open.Source.Application.Server, http://glassfish.java.net
[4]Mapping.Objects.to.Relational.Databases, http://www.agiledata.org/essays/mappingObjects.html.
[5]Koutsonikola, V., Vakali, A.: LDAP: Framework, Practices, and Trends (2004)
[6]Web.Services.Architecture, http://www.w3.org/TR/ws-arch/
[7]Java.Servlet.Technology.Overview, http://www.oracle.com/technetwork/java/javaee/servlet
[8]HTTP-Hypertext.Transfer.Protocol, http://www.w3.org/Protocols/
[9]DICOM:Digital.Imaging.and.Communication.in.Medicine, http://medical.nema.org

855

SendMeClever - Web based tool for transfering MR data

F. Jiru, M. Hajek
Mr-unit, Department Of Diagnostic And Interventional Radiology, Institute for Clinical and Experimental Medicine, Prague/CZECH REPUBLIC

Purpose of the software: Research cooperation between different MR sites often requires sharing of MR data and MR related computing resources. For transferring MR data with sensitive personal information use of secured data transfer protocols (such as SSL/https or sFTP) or data anonymization are mandatory. Difficult access to tools providing these services may lead to using alternative data exchange services (such as FTP or email) that compromise data security.
In this contribution SendMeClever application for MR data exchange conforming to above mentioned security requirements is introduced.
Methods/Implementation: SendMeClever is a web application running in conventional web browser (Fig.1) that enables:
1) Sending email like messages with large attachments over secured https connection. This simplifies data description in the message because cryptic names for personal data in MR data headers are not required. The whole directory structure containing e.g. selected MR study can be selected as an attachment.
2) Processing MR data in the attachment prior to the delivery to the recipient using extendable processing utilities. SendMeClever currently implements DICOM anonymization which obviates separate data anonymization before sending. Additional processing functionality can be installed in the form of SendMeClever plug-in that can be created following SendMeClever plug-in specifications.
3) Sending attachment data to Java Message Service (JMS) provider for asynchronous data processing. Each recipient may register connection to the JMS provider (so called processing queue) where the delivered data will be forwarded to. Data can then be automatically read by recipient's program and processed. This functionality provides effective sharing of MR processing tools among different sites.
Several independent user groups each having own group administrator and one common super-administrator can share SendMeClever functionality.

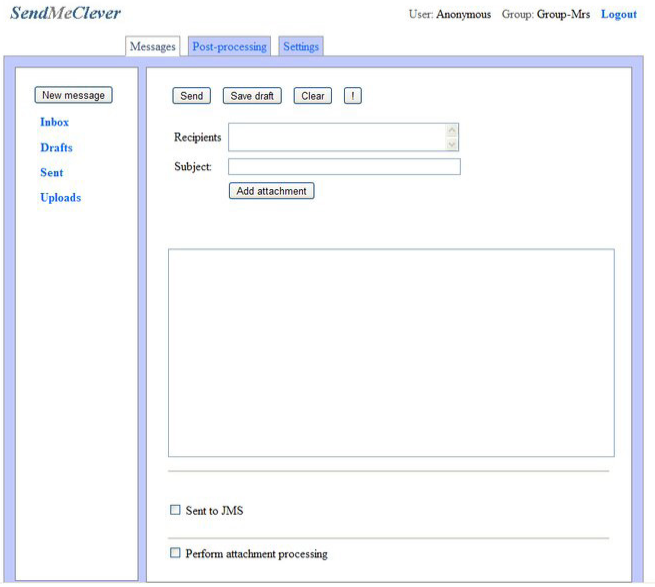

Fig.1

The application has been implemented in Java programming language on top of the Spring-3 platform. The schematic description of data flow in the SendMeClever application is shown in Fig.2. The selected attachment data are compressed and transferred to SendMeClever server using Java applet. Attachment data are then optionally processed and stored along with the corresponding message in the PostgreSQL database. In addition, the data are together with specified processing instructions optionally sent to recipient's data processing queue registered at the Apache MQ (JMS provider). For security reasons the CleverSent server is intended to be hosted in the network of one of cooperation partners. TheCleverSent application will be released as an open source after documenting and testing.

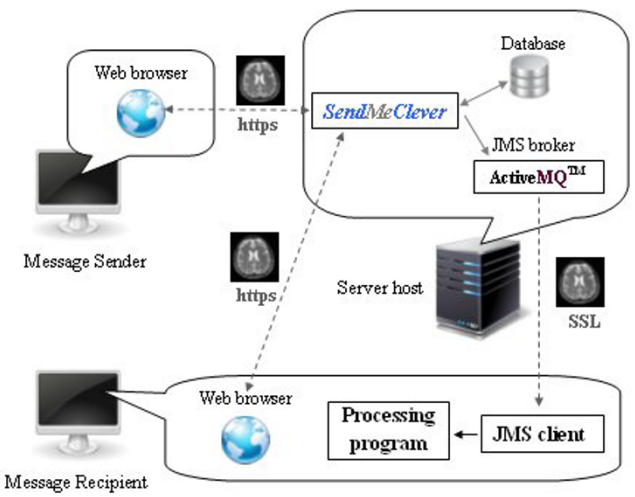

Fig.2.
Supported by MZCR Institutional grant 00023001IKEM

Features illustrated at the exhibit: Overall functionality of SendMeClever program will be shown.
Acknowledgements:
grant sponsor: IGA MZ CR (NT12288-5)

856

Images Preview with a Dynamic Acquisition Real-time System (DARTS)

C. Meyer[1], **P. Vuissoz**[2], J. Felblinger[3]
[1]Iadi, Université de Lorraine, Nancy/FRANCE, [2]Iadi U947, INSERM, Nancy/FRANCE, [3]Pôle Imagerie, CHU Nancy, Nancy/FRANCE

Purpose of the software: Magnetic Resonance Imaging is an intrinsically slow acquisition process. Sequences can take minutes to run and images are displayed only after the whole sequence is complete. The proposed software displays partial images as soon as they are acquired using a real-time communication framework with the scanner. Thus, adjustments to the scan parameters can be decided and the sequence aborted and restarted, if judged necessary, without having to wait for a useless sequence to complete. This new technique allows for a constant feedback of the acquisition process and reduces the machine to human feedback loop delay.
Methods/Implementation: A 3T MRI scanner (Signa HDxt, General Electric, Milwaukee, WI) with an 8-channel cardiac coil and a 2D cartesian fast gradient recalled echo sequence was used to acquire CINE data from a volunteer (scan time : 4 minutes).
MR coils data are received as soon as they are acquired using the Raw Data Server software version 15M4 offered by the vendor (subject to research agreement). Since only k-space raw data is transferred by this mean, the sequence was modified to send the trajectory (i.e. phase encoding step) at each TR. Those two separate signals were acquired with distinct threads and stored in two queues in memory. Only raw data that were associated with a phase encode step (and vice versa) were used to fill zero-initialized partial k-spaces. The latter were transformed into images using the FFTW3 library [1] and displayed (along with general user interface) using Qt4 [2]. The "views per transfer" parameter of the Raw Data Server was controlling the refresh rate of the images previewing.
Our software runs on a standard PC with a Linux operating system (kernel version 2.6.33.5) patched for reduced latency (rt-patch 22). An Ethernet connection with the MR cabinet permits bi-directional communication between the running sequence (EPIC environment) and our software.
Features illustrated at the exhibit: At the exhibit, the software will illustrate (fig. 1) its two main features while an actual acquisition previously recorded will be simulated: (i) preview images will be displayed and (ii) the trajectory of acquisition in k-space will be shown, both in real-time.

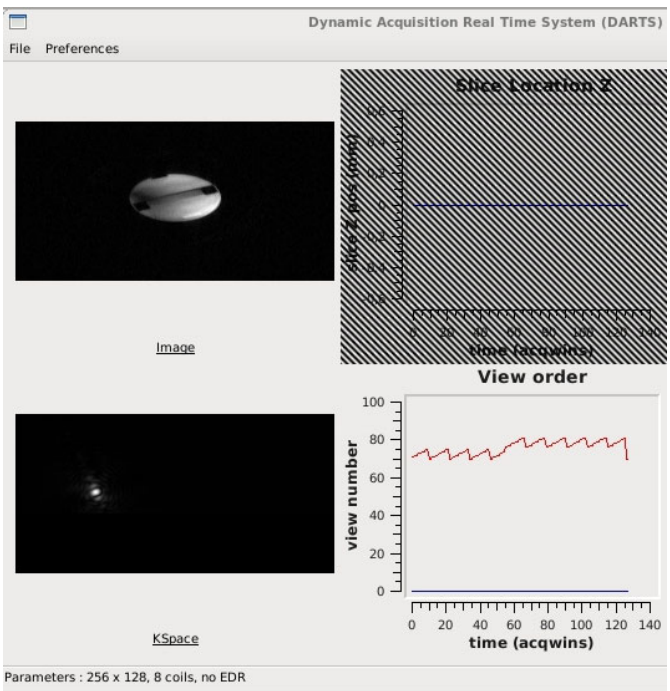

Figure 1: User interface showing preview of partial acquisition (left) and trajectory (right). About 3/4 of data were acquired at the time of screenshot. Segmented CINE acquisition is represented as a "serrated" trajectory ("View order" plot).

References:

[1] Frigo M., 2005, Proc. IEEE, 216-231
[2] Blanchette J., 2007, Prentice Hall, ISBN 0132354160

857

openEMS – A Free and Open Source FDTD Software Package, Supporting Cartesian and Cylindrical Coordinates Ideally Suited for MRI Applications

T. Liebig, A. Rennigs, D. Erni
General And Theoretical Electrical Engineering (ate), University of Duisburg-Essen, Duisburg/GERMANY

Purpose of the software: OpenEMS [1] is a fully-vectorial three-dimensional finite-difference time-domain (FDTD) simulation platform supporting Cartesian as well as cylindrical coordinates. In bioelectromagnetics the FDTD method has already been established as one of the most powerful numerical tools for designing e.g. complex radio frequency (RF) systems for advanced MRI scanners. Although the relevant RF structures used in MRI systems are confined to a cylindrical shape, the pertinent commercial FDTD software packages (e.g. SEMCAD X, XFdtd, EMPIRE XCcel, etc.) do not explicitly foster cylindrical meshing, whereas the cylindrical version of openEMS is ideally suited for handling e.g. thin conformal structures such as the resonant birdcage coil shown in Fig.1. The coil is discretized using a rather coarse mesh without displaying any stair-casing effects, rendering the numerical analysis highly efficient. In the context of a multi-channel traveling-wave MRI system we have recently demonstrated [2] that openEMS can handle multiple conformal ring antennas where any Cartesian FDTD implementation is supposed to completely fail.

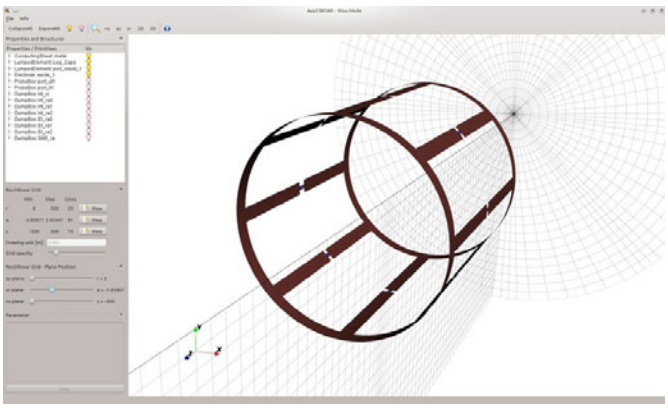

Fig. 1: Low-pass birdcage coil being well resolved by the cylindrical version of openEMS.

Methods/Implementation: The cylindrical (equivalent circuit-based [1]) FDTD scheme is mostly identical to the Cartesian counterpart and therefore apt for a generic highly optimized iteration engine as implemented in openEMS using C++ with multi-threading support. OpenEMS is memory and speed efficient and can be deployed on any personal computer running Linux or Windows – and with the support of MPI, openEMS is even ready to run on a Linux cluster (or a supercomputer).
Features illustrated at the exhibit: OpenEMS relies on a user friendly Matlab/Octave interface for scripting purposes and a graphical user interface as a structural 2D/3D viewer (cf. Fig. 1). The interface and a couple of ready-made MRI examples (e.g. birdcage-coils) will be elucidated at the exhibit. Furthermore we will promote an integrated user interface between the well-known "Birdcage Builder" from the Penn State Center for NMR Research [3] and openEMS advancing a fast comprehensive full-wave coil design.

References:
[1] Liebig, T., openEMS website: http://openEMS.de
[2] Liebig, T., et al., ESMRMB 2011, Oct. 6-8, Leipzig, Germany, paper 49, (2011).
[3] Chin, C.-L., et al., Concepts Magn. Reson., 15(2), 156-163, (2002).